2025 7th International Conference on Smart Power & Internet Energy Systems

(SPIES 2025)

October 17-20, 2025

Shanghai, China



2025 7th International Conference on Smart Power & Internet Energy Systems (SPIES 2025)

Copyright ©2025 by the Institute of Electrical and Electronics Engineers, Inc. All rights reserved.

Copyright and Reprint Permission:

Abstracting is permitted with credit to the source. Libraries are permitted to photocopy beyond the limit of U.S. copyright law for private use of patrons those articles in this volume that carry a code at the bottom of the first page, provided the per-copy fee indicated in the code is paid through Copyright Clearance Center, 222 Rosewood Drive, Danvers, MA 01923.

Other Copying, reprint, or reproduction requests should be addressed to IEEE Copyrights Manager, IEEE Service Center, 445 Hoes Lane, P. O. Box 1331, Piscataway, NJ 08855-1331.

Conference XPLORE COMPLIANT Version

IEEE Catalog Number: CFP25V85-ART
ISBN: 979-8-3315-5473-6

Conference USB Version

IEEE Catalog Number: CFP25V85-USB
ISBN: 979-8-3315-5472-9

2025 7th International Conference on Smart Power & Internet Energy Systems

(SPIES 2025)

Table of Contents

Preface.....x

Conference Committees.....xi

➢ **High Voltage Transmission and Insulation Technology**

Research on Breakdown Performance of DC Model Cable Based on Chinese Cross-linked Polyethylene Insulating Material.....1

Wang Chuan-Bo, Jiao Yong-hui, Xu Peng-cheng, Han Ben, Pang Gong-he, Jiao kun, Xu Shi-ming, Ye Jian-cheng

Insulator Defect Target Detection Based on Improved YOLOv5s.....6

Yugang Li, Zheng Chen, Zheng Zhang, Jiabao Zhu

Influence of Structural Geometry and Contamination Characterics on the Surface Electric Field distribution of HVDC Insulators.....12

Minghao Du, Donglai Wang, Chengze Li, Shuo Gao

Anfis-Based Insulation Condition Diagnosis for Power Capacitors Using Secondary Side Information.....18

Yanlong ZHAO, Xuanyang LIU, Zihao LI, Fei LI, Weichen YAN

➢ **High Voltage Power Transmission System and Key Equipment Status Monitoring**

Global Optimization of Micro-Meteorological Station Siting for Ultra-High-Voltage Transmission Lines.....23

Qingtian Ge, Kai Yang, Wenke Pan, Ye Feng, Huayue Huang, *Jiangjiao* Xu

Research on Aerial Image Localization and Classification of Transmission Equipment Based on the C2f-CAA Mechanism.....30

Weisong Liang, Yonghua Wen, Haimei Cen, Huiying You, Shaojun Qi, Xueying Huang, Yongqiu Liu, Huarong Wang

Design of Self-Powered Energy-Harvesting Power Supply for Three-Phase Cable Temperature Monitoring Device..34

Hong Lei, Zhaohong Wang, Lu Zeng, Jiale Chen, Sheng Li

Improving General-Purpose LLM Models for Power Cable Tasks Using Structured Context Engineering.....41

Tong Wu

➢ **Control Models, Parameter Optimization, and Performance Evaluation in Power Systems**

Electric Arc Simulation Validations and Switchgear Applications.....46

Wenkai Shang, Shihu Ma, Meng Li, Oleg Chernukhin, Runan Mo, Somasekhar Machani, Chuan Lu, Yumin Xiao, Isaac Liu

Redefining Grid-Connected Control: A Polar-Coordinate Based Synchronized Virtual Oscillator Framework.....53

Hoach The Nguyen, Ameena Saad Al-Sumaiti, Khalifa Al Hosani, Ahmed Al-Durra, Mohamed Shawky El-Moursi

Electromagnetic Simulation Model of Switching Power Supply 59
Wu Jianchao, Li Xinxin, Lv Hui, Liu Mi, Ji Zhipo, Wan Chengan

Unintentional Islanding Detection Method based on Voltage and Reactive Power Adjustment in Grid-Forming Inverter Systems 65
Yejin Choi, Inchan Hong, Jaehoon Jung, Seungmin Jung, Yeuntae Yoo

Suppression of Inrush Current in Rectifier Transformer of Mobile DC De-icing Device 70
Junjie Zhao, Wentong Chen, Yuqun Fang, Xiaoyu Zhou, Bo Zhang, Wu Wen

A Multi-stage Features and Attention Mechanism-Embedded Time Convolutional Network-Based Power System Transient Stability Assessment Method 75
Yutong Wang, Xiaobo Wang, Xinyao Zhu, Haiqiang Zhou, Shengjun Wu, Shuhuan Li

Research and Simulation on Multi-Mode Operation Control Strategy of Combined Diesel and Energy Storage Power Supply System 81
Cunping Wang, Yanxia Chen, Ruoxi Liu, Jing Zeng, Yifan Wu, Shuchang Wan

Development of Piezoelectric Vibration Energy Harvester (VEH) for Machine Condition Monitoring Purpose 87
Riady Siswoyo Jo, Rachel Lee Xin

- **Distribution System and Distribution Network**

AC and DC Power Flow Calculation Method in Distribution Networks Based on Power Electronic Transformers 93
Zhen Zheng, Yinan Huang, Wenwen Chen, Xiao Yang, Haijun Xing

Deployment of IoT Technologies for Phase Balancing in Low-Voltage Power Distribution 99
Aship Chaudhary, Samundra Gurung, Rabindra Maharjan, Priyanshu Rouniyar, Sashank Shrestha, Yubraj Chimoriya

A Unified Energy Management System Framework for Active Distribution Networks with Hybrid Energy Storage and Decentralized Voltage Control 105
Ahmed Bedawy, Yutaka Sasaki, Chiraz Krifa, Yoshifumi Zoka, Naoto Yorino

A Robust Optimization Method for Distribution System Considering Mobile Emergency Resource under Extreme Weather 112
Di Yang, Jun Lu, Jisheng Jia, Mingyi Qiu, Lei Sun, Fei Zeng, Jiahao Sun, Haijun Xing

A Transformer-based Approach for Operating Situation Prediction in Distribution Networks 118
Li Zeke, Chen Bin, Guo Jiuyu, Fan Haiwei, Ding Linglong, Liu Bijing

Hierarchical Multi-objective Collaborative Optimization of electric Vehicle, Station and Distribution Network Considering Reactive Power Compensation Capacity of V2G Charging Piles 123
Tao He, Suwo Wu, Chongcheng Zhou, Xingzhuang Li, Aiqing Yu

Multi-Time-Scale Adaptive Defense Response Strategy for Cyber-Physical Distribution Systems 129
Yang Liu, Mi Wen, Yunsheng Xue, Jiaju Yu, Yi Gao, Qiuling Yu

A Random Forest based Construction Method of New Distribution Network Planning Evaluation Indicators 135
Ning Luo, Wei Xiong, Yuan Zhang, Jinsen Liu, Ludong Chen, Hongyan He, Pengcheng Zhang, Guo Chen

Distribution Network Power Quality and Potential Impact on Electric Vehicle Charging 142
Mohd Zamri Che Wanik, Muneera Al-Qahtani, Abdullah Abdul Jabbar, Mohamed Khalid Gad

Grid Partitioning Method for Distribution Networks Considering the Clustering of Flexibility Resources 148
Yuanbing Xiao, Mingzhu Ren, Taotao Ma, Zhen Zheng, Duhong Wang, Yehui Ma, Shijie Zhuang, Haijun Xing

Hysteresis Control with Variable Coefficients Based on a Physics-Mechanism-Data Hybrid Modeling Approach 155
Weijie Tang, Fan Yang, Bingcheng Zhou, Tao He, Xiaoyan Sun, Zhilei Qiu, Gaiping Sun

➢ **New Motor Function Control and Parameter Optimization**

Performance Evaluation of Asymmetric Six-Phase Induction Motors Using an Improved DTC-SVPWM Technique 160
Kaniz Suburna, Shirazul Islam, Atif Iqbal, S. M. Muyeen

A Frequency-Tracking Quasi-Proportional Resonant Approach for Harmonic Suppression in PMSM 166
Siqi Peng, Chuchen Yang, Zhiwen Zhang, Kun Zhu

Research on Model-Free Predictive Current Control Strategy for Axial Flux-Switching Shaftless Rim Driven Motor 172
Chenxuan Zhang, Ziyi Tai, Haoyu Wang, Yifei Ren, Wei Zhang

Improved Sensorless Full-Speed Range Composite Control Strategy for IPMSM 177
Siqi Peng, Zhiwen Zhang, Kun Zhu, Chuchen Yang

Analytical Calculation Method for Parasitic Capacitance of Annular Excitation Winding in Non-uniformly Distributed Motors 184
Jiaqiang Zou, Shengbo Mo, Qianqian Liu, Ruxin Chen, Shushu Zhu

Parameter Identification of Permanent Magnet Synchronous Motor Based on IRBMO Algorithm 190
Siqi Peng, Kun Zhu, Chuchen Yang, Zhiwen Zhang

An Equivalence Method for PMSG-based Wind Farm with Virtual Synchronous Generator Control Considering the Whole Dynamic Process 196
Peicong Zhu, Qiang Ma, Shaoguang Chen, Haiqiang Zhou, Tai He, Yujie Wang

Experimental Study on Thermal Management Control of Liquid Immersion Cooling Package Module for Vehicle EPS Motor Driving 203
Hojong Kwak, Jaehyuk An, Sewoong Ahn, Byeongyu Kim, Simon Cho, Hyoseo Choi, Jian Lee, and Young-Jae Min

Research on the Temperature Field of Shaftless Rim-Driven Motor Based on a Three-Dimensional Integrated Water-Cooling Structure 207
Li Chen, Jishuang Zhang, Tao Zhu, Leyan Xu, Wei Zhang

➢ **Operation Status Monitoring and Fault Diagnosis in New Power Systems**

High-Resolution FBG Interrogation Using Microwave Photonics for Real-Time Temperature Monitoring of Power Equipment 211
Minhao HU, Xuecheng KONG, Fei LI, Weichen YAN

Development of a B-type Leakage Current Sensor for Wide Range Accurate Detection 215
Yi Wei, Jian Zhibo, Liang Guobang, Huang Mingxin, Zhang Wenzhen, Huang Menghua

Research on the Analytical-Model-Based Setting Method for Leakage Magnetic-Field Differential Protection for Transformer Early Fault 220
Ping Zeng, Wei Bao, Qian Feng, Jiayu Lian, Xiangli Deng, Hang Tu

Neural Network-Based Detection of Open and Closed-Circuit Faults in Single-Phase Voltage Source Inverters 229
George Owusu, Joshua Afosa-Baffoe

A Novel Traveling Wave Fault Location Method for MMC-HVDC Transmission Lines Based on Complementary Ensemble Empirical Mode Decomposition and Hilbert Transform 234
Xiangyang Liu, Zhong Tang, Haoyang Cui, Hong Qian

Transient Fault Analysis of Renewable Energy DC Collection and Transmission System with High-Voltage DC-DC Converters 240
Dazhen Xu, Zhibo Zhang, Zhiguang Lin, Jianjun Ma, Miao Zhu

An Enhanced Multi-Source Domain Adaptation Framework for Grounding Fault Diagnosis in Urban Rail Transit Systems under Varying Operating Conditions 246
Bo Chen, Qiaoyue Li, Guifu Du, Yanrong Ren

A Transformer Fault Diagnosis Approach Based on WCGAN-GP and Multimodal Deep Feature Fusion 252
Ping Zeng, Wei Bao, Desheng Zhou, Zhaoxin Du, Yuqing Shen, Xiangli Deng

➢ **Stable Operation and Reliability Evaluation of Smart Grid**

An Improved Cloud Drift Optimization Based Two-Layer MPC for Economic Dispatch of Microgrids with Hybrid Energy Storage 259
Peixin He, Chenyuhao Ma, Daming Zhou, S. M. Muyeen

A Layered Optimization Scheduling Method of Energy Storage Stations for Supporting Grid-Province Coordination 265
Wei Ma, Bin Xu, Ze Li, Bingjian Fan, Zhe Li, Guigang Han

KG-SA-GNN: Knowledge-Guided Self-Attention Graph Networks for Imbalanced Fault Detection in Smart Grids 271
Yi Guo, Yi Kuang, Bin Duan, Sheng Li

Stochastic Programming for Capacity Expansion Planning Method Considering Extreme Scenarios 278
Shu Xia, Yuan Zhang, Yue Yu, Enyu Jiang, Chen Wang

Research on the Evaluation of Autonomous Controllability of Power Grid Dispatching Technical Support Systems 285
Li Zhao, Bijing Liu, Xiaosong Zhu, Jiancheng Guo, Yong Yang

Power System and Reliability Analysis of Geothermal and Hydrogen Storage-Orientated Grid-Connected Smart Grid for Mining and Agricultural Application: A Global Perspective 292
Md. Nimul Hasan, Sk. A. Shezan, Md. Fatin Ishraque, SM Muyeen, Innocent Kamwa

➢ **Electric Load Model and Forecasting Calculation**

Day-Ahead Net Load Forecasting Based on Similar-Period Selection and CNN-BiLSTM-Attention 298
Wei Wang, Shunfu Lin, Bo Zhou, Liang Qian

Multi-dimensional Feature-Fusion-Based Cooling and Heating Load Identification Model for Distribution Substations 303
Bingbing Lu, Fan Yang, Jun Liu, Jiashuai Li, Gaiping Sun, Ziqi Ye

Distributed Energy Dispatch for Energy Community Using Decision-oriented Net-load Prediction 308
Yibo Ding, Jian Zhao, Jiaqi Ruan, Zhao Xu

Proportional-Integral-and-Data-Driven Load Frequency Controller for Microgrid Systems 313
Weichao Wang, Ronghu Chi, Yang Liu

An Adaptive Model Predictive Load Frequency Control Strategy for Low-Inertia Power Systems 318
Hayato Nagaosa, Yutaka Sasaki, Helin Yang, Yoshifumi Zoka, Naoto Yorino, Ahmed Bedawy, Weichao Wang

A Multi-Scale Spatio-Temporal Model for Eletric Load Forecasting 324
Muyang Tian, Ruirui Ji, Xin Xin, Chenxi Bai, Tong Jia, Anjie Song

Short-term Hybrid Forecasting Method for Multi-type Customer Loads in Extreme Weather Based on BiLSTM-Seq2seq Model 330
Gaiping Sun, Jiashuai Li, Ronghui Liu, Deyong Yu, Shunfu Lin, Ziqi Ye

- **Modern Integrated Energy Systems and New Energy Storage Technologies**

Multiscale Modeling and Electrochemical Validation of PEM Electrolyzer-Coupled Hybrid Energy Storage Systems 336
Haotian MA, Shangfeng DU, Georgios Nikiforidis

Research on Integrated Energy System Planning Considering Multiple Uncertainties and Operational Risks 341
Zhuoxiang Wu, Shunfu Lin, Jin Tan, Liang Qian

Medium-Long Term Balance Analysis Considering Extreme Scenarios at Multi-time Scales 347
Weijie Wu, Sui Peng, Zhengmin Zuo, Yixin Li, Shucan Zhou, Shijie Lin

Distributed Photovoltaic Cluster Power Forecasting Based on an Improved Graph Attention Network Model 351
Yanping Zhu, Pan Chen, Yueguang Zhang, Yi Feng, Jingzhe Shan, Liang Wang, Tianrun Wen, Delin Zhao, Yuntian Liu

Research on the Development Paths of New Energy Industry in Rural Areas for Dual Carbon Goals 356
Yanfei Pan, Qiong Li

- **Advanced Control Technology and Energy Optimization Scheduling in High Proportion New Energy Power Systems**

An Optimal Scheduling Strategy for Virtual Power Plant Participating in Peak Regulation Considering Industrial Load Production Processes 360
Jin Mao, Liang Yin, Fang Wang, Xiaoli Wang

Online Energy Management of FCHEVs based on Multi-Time Scale Dynamic Game Theory 367
Zhuang Tian, Junqi Wang, Yigeng Huangfu, S. M. Muyeen, Daming Zhou

Optimal Placement of Constrained Micro PMUs Using Phasor Measurement based State Estimation 373
Seungyeop Baek, Jinhyeok Kim, Byeongchang Lim, Yeuntae Yoo

Influence of New Energy Power Fluctuation on the Power System Frequency Safety Under High New Energy Penetration 379
Wenbo Yang, Zhen Huang, Lei Chen, Kaiyuan Hou, Deming Xia, Xingwei Xu

Research and Development Status of Domestic and Foreign Solid Power Controllers and Industrialization Insights 387
Xu Wang, Huiyao Li, Mi Liu, Xing Liu, Bei Zhang

Virtual Inertial Response and Frequency Regulation Control Method for Combined Systems of Renewable Energy and Hybrid Energy Storage 393

Wenxin Guo, Ruifeng Zhao, Yumin Li, Jiangang Lu, Huijuan Tan, Shiming Li

Joint Estimation of State of Charge and State of Health for Lithium-Ion Batteries Based on Singular Value Decomposition and Multi-Innovation Adaptive Unscented Kalman Filter Algorithm 400

Tao Ren, Jin Jiang, Sheng Li

- **Wind Farm Simulation and Wind Power Generation System**

Short-term wind PV output and electrical load forecasting for microgrids based on peak-valley weighted CNN-BiLSTM 407

Yu Huiqun, Meng Yanyu, Yang Yifan, Qiu Yaming

Inertia Evaluation Method for Power Systems with Integration of Wind Farms Under Colored Measurement Noise 412

Yongkang Luo, Mingjiang Liu, Yu Zhang, Ziwen Liu, Xingwei Che, Xiangyu Meng

Wind Speed Prediction for Smart Grid Using a Hybrid GNN-Transformer Model 418

Huayue Huang, Shaoyu Mao, Ye Feng, Wenke Pan, Qingtian Ge, Jiangjiao Xu

A Fuzzy Adaptive Parameter Control Method for Wind Farm Active Frequency Support Considering Wind Speed Difference 424

Jiangwei Bi, Zhongyuan Yao, Tianyi Huang, Haiqiang Zhou, Yi Zheng, Youwei Zhang

- **Electricity Market and Demand Analysis**

The Bidding Strategy of Energy Storage in the Power Spot Market Based on the Adaptive McCormick Method..... 430

Hao Tong, Jiang Li, Zishuo Zhang

Decision Optimization for Virtual Power Plants Participating in the Coupled Electricity-Carbon Market..... 436

Na Wang, Tiantian Chen, Chen Wang, Pengwei Wang, Linxuan Zhao, Jing Liu

Credit Evaluation Method for New Market Entities Based on Credibility Entropy Evidence Theory..... 442

Kong Shuqin, Sheng Jiansheng, Tian Lin, Zheng Wei, Wu Jinghui, Xue Shumin

An Electricity Price Forecasting Method Based on Multimodal Temporal Decomposition Framework Under the Mid-to-long-term Market Environment..... 449

Xiejun Du, Junjie Li, Kun Wang, Yan Shen

A trading settlement analysis model for the southern regional electricity market based on big data intelligent computing 457

Zhang Ge, Ding Junce, He Shiyang, Wen Qingyang

Peer-to-Peer Energy Trading and the Development of Grid-Blockchain Simulation Platform..... 462

Mohd Zamri Che Wanik, Usman Zafar, Asrani Lit, Nazreen Junaidi, S. M. Muyeen

Study on Dual-Time-Scale Mid-to-Long-Term Spot Electricity Procurement Optimization Model Considering Inter-Provincial Channel Constraints 468

Ying Fan, Pengfei Zhang, Na Wang, Yuxin Chen, Huan Zhou, Gaiping Sun

Risk-Averse Optimization of Medium and Long-Term Power Procurement Under Multi-Dimensional Uncertainty 473

Ronghui Liu, Weicheng Wang, Gaiping Sun, Shunfu Lin

➢ **Electric Vehicles and Power Supply Systems**

EV Charging Scheduling in Residential Areas: A Multi-Objective Approach Based on MOIPSO 479

YueJun Li, Bin Duan, Yi Kuang

Economic Analysis of Replacing a Combustion Vehicle with an Electric Vehicle Supported by Residential Photovoltaic Systems in Brazil 485

Daywes Pinheiro Neto, Isabela Lopes Magalhães, Thiago Augusto Mendes, Letícia Chaves Ucker, Anto´nio Paulo Coimbra, Pedro Moura, Aníbal Traça de Almeida

Multi-objective Optimization Strategy of Electric Vehicle Charging and Discharging Based on User Demand Response and Stackelberg Game 491

Sheng Li, Yonghong Lan, Zhouzhou Xu, Hong Lei

➢ **Author Index**

Preface

2025 7th International Conference on Smart Power & Internet Energy Systems (SPIES 2025) has been successfully held in Shanghai, China during October 17-20, 2025. The major goal of the conference was to bring academic scientists engineers and industry researchers together to exchange and share their experiences and research results, and discuss the practical challenges encountered and the solutions adopted.

SPIES 2025 is sponsored by Shanghai University of Electric Power, China and technically co-sponsored by IEEE PES and IEEE IAS. And it is also technically supported by University of Vaasa, Macquarie University, Chiang Mai University, Université de Bretagne Occidentale, University of Nottingham and Auckland University of Technology, Journal of Shanghai University of Electric Power and Virtual Teaching and Research Section for Electrical Engineering and Automation Specialization of the Ministry of Education. It is my honor to serve as the General Chair of this premier conference. I am happy to share that we have been able to put together a good technical program covering research papers, keynote speeches and invited speeches by renowned researchers for both academic and industry audiences.

I would like to express my sincere appreciation to the Honorary Chair, General Co-Chairs, Advisory Chairs, Program Chairs, Technical Program Committee, as well as all the members of various Committees, who shared different responsibilities and contributed to this conference. My thanks and gratitude to all the authors who submitted papers and all the attendees.

During the conference, the Honorary Chair, Prof. Chunhua Gu, the President of Shanghai University of Electric Power, China made the opening remark for the conference. Prof. M. Fotuhi-Firuzabad from Sharif University of Technology, Iran, Prof. Hua Geng from Tsinghua University, China, Prof. Syed M Islam from Federation University, Australia, Prof. S. M. Muyeen from Qatar University, Qatar, Prof. Weilin Li from Northwestern Polytechnical University, China and Prof. Pinjia Zhang from Tsinghua University, China have shared Keynote Speeches with us. Prof. Yu Wu from Northwestern Polytechnical University, China, Prof. Yu Wang from Chongqing University, China, Prof. Yiqi Liu from Northeast Forestry University, China, Prof. Zhenzhi Lin from Zhejiang University, China and Prof. Hui Hou from Wuhan University of Technology, China delivered Invited Speeches at the conference. It was a golden opportunity for students, researchers and engineers to interact with experts on technical matters, research methodology, career advice, future vision, and other aspects.

After more than one year's preparation, we received more than 140 submissions from China, Japan, Malaysia, Republic of Korea, United States, Ghana, United Arab Emirates, United Kingdom and other countries. The submitted topics include High Voltage Transmission and Insulation Technology, High Voltage Power Transmission System and Key Equipment Status Monitoring, Control Models, Parameter Optimization, and Performance Evaluation in Power Systems, Distribution System and Distribution Network, New Motor Function Control and Parameter Optimization and other topics. More than 100 Technical Program Committee Members participated in the review process. Thanks for their great efforts and excellent work. Finally, 84 papers are accepted and all the participants have presented their papers during the conference in different sessions.

I hope SPIES 2025 has provided an international platform for the global power and energy experts from academia, industry, utilities, and service providers to exchange ideas and experiences on emerging and enabling technologies, and also offered great opportunities for all participants to establish academic relationships and to find global partners for the future cooperation. Finally, I would extend my sincere gratitude to all delegates, and wish to meet all of you again in the future.



General Chair
Prof. Dongdong Li
Shanghai University of Electric Power, China

Committees

Honorary Chair
Prof. Chunhua Gu, Shanghai University of Electric Power, China

General Chairs
Prof. Dongdong Li, Shanghai University of Electric Power, China
Prof. Jing Ma, Shanghai University of Electric Power, China

General Co-Chairs
Assoc. Prof. Xiaolu Li, Shanghai University of Electric Power, China
Prof. Shunfu Lin, Shanghai University of Electric Power, China

Advisory Chairs
Prof. Adrian Ioinovici, Shanghai University of Electric Power, China
Prof. S M Muyeen, Qatar University, Qatar
Prof. Mohamed Benbouzid, University of Brest, France
Prof. Ahmed Al-Durra, Khalifa University, UAE

Program Chairs
Prof. Ali Arefi, Murdoch University, Australia
Assoc. Prof. MD Rakibuzzaman Shah, Federation Unviersity, Australia

International Steering Committee
Prof. Syed Islam, Federation University, Australia
Prof. Innocent Kamwa, Laval University, Canada
Prof. Marcelo G. Simoes, University of Vaasa, Finland
Prof. Farhad Rachidi-Haeri, Swiss Federal Institute of Technology (EPFL), Switzerland
Prof. Mohamed Benbouzid, Brest University, France
Prof. Aman Maung Than Oo, Macquarie University, Australia

Publicity Chairs
Prof. Fan Yang, Shanghai University of Electric Power, China
Assoc. Prof. Yin Yao, Shanghai University of Electric Power, China
Asst. Prof. Arman Oshnoei, Aalborg University, Denmark
Asst. Prof. Jiangjiao Xu, Shanghai University of Electric Power, China

Chapter Chairs
Prof. Yufei Wang, Shanghai University of Electric Power, China
Assoc. Prof. Gaiping Sun, Shanghai University of Electric Power, China

Technical Committee Chairs
Prof. Yang Mi, Shanghai University of Electric Power, China
Assoc. Prof. C Dhanamjayulu, Vellore Institute of Technology, India

Publication Chairs
Prof. Ronghui Liu, Shanghai University of Electric Power, China
Asst. Prof. Haris Khalid, University of Dubai, UAE
Dr. Hafiz bin Ismail, Universiti Teknologi Petronas, Malaysia

Special Session/Tutorial/Workshop Chair
Prof. Aiqing Ma, Shanghai University of Electric Power, China

Technical Program Committee Members
Kumar T. Nandha, University of Nottingham Malaysia, Malaysia
Yuefeng Liao, Zhengzhou University, China
Ying-Yi Hong, Chung Yuan University
AHMAD SHUKRI BIN ABU HASIM, National Defence University of Malaysia, Malaysia
TAN CHING SIN, Universiti Tenaga Nasional, Malaysia
Huamin Jie, Nanyang technological university, Singapore
Siti Rohani Sheikh Raihan, University of Malaya, Malaysia
N. K. Srivastava, National Institute of Technology, India
Gheorghe Grigoras, Gheorghe Asachi Technical University of Iasi, Romania
Irdayanti binti Mat Nashir, Universiti Pendidikan Sultan Idris, Malaysia
Ameena Al Sumaiti, Khalifa University, UAE
Chia-Chi Chu, NTHU
Ayubi Bilal Iqbal, ShanDong University, China
Songtao Huang, Huazhong University of Science and Technology, China
Mingxu Xiang, Chongqing University, China
Maciej Dzikuć, University of Zielona Góra, Poland
Gheorghe-Daniel Andreescu, Politehnica University Timisoara, Romania
Foo Yi Shyh Eddy, Nanyang Technological University, Singapore
Guoming Ma, North China Electric Power University, China
Tao Lin, Wuhan University, China
Hamed Aly, Dalhousie University, Canada
Jiebei Zhu, Tianjin University, China
Muhammad Rizwan, Sultan Qaboos University, Oman
Chuah Joon Huang, University of Malaya, Malaysia
Motiur Reza Mohammed, Khalifa University, UAE
Mrityunjay Kumar Mishra, Khalifa University, UAE
Mohd Zamri Che Wanik, Hamad Bin Khalifa University, Qatar
Erchin Serpedin, Texas A&M University at Qatar, Qatar
Hamzeh Aljarajreh, Australian University, Kuwait
Jinsong Li, Dalian University of Technology, China
Elmootazbellah Elnozahy, King Abdullah University of Science and Technology, Saudi Arabia
Kei Eguchi, Fukuoka Institute of Technology, Japan
Song Han, Guizhou University, China
Chunhua Liu, City University of Hong Kong, China
Mohsin Jamil, Memorial University of Newfoundland, Canada
Abdelsalam Elhaffar, Sultan Qaboos University, Oman
Tariq Jamil Saifullah Khanzada, King Abdulaziz University, Saudi Arabia
Tareg Ghaoud, Dubai Electricity and Water Authority, United Arab Emirates
Constantinos S. Psomopoulos, University of West Attica, Greece
Ayedh H. Alqahtani, Public Authority for Applied Education and Training, Kuwait
Madhuri Katira, Atmiya University-Rajkot, India
Qian Xiao, Tianjin University, China
Saleh Edhah, Khalifa University, UAE
Maamar Taleb, University of Bahrain, Bahrain
M Aizaz Farid, RMIT University, Australia
Yun Yang, Nanyang Technological University, Singapore
Mao Yuan, Zhejiang University of Technology, China
Hilal Said Al Hadi, Muscat Electricity Distribution Company, Muscat, Sultanate of Oman

Hossam Gaber, Ontario Tech University, Canada
Mohamad Nassereddine, University of Wollongong in Dubai, United Arab Emirates
Furkan Dincer, Kahramanmaras Sutcu Imam University, Turkiye
Yanawati Binti Yahya, Universiti kuala lumpur, Malaysia
Krishna Kumar, Lund University, Sweden
Daywes Pinheiro Neto, Federal Institute of Goiás, Brazil
Omar Hanafy Abdalla, Helwan University Cairo, Egypt
Sajan K. Sadanandan, Dubai Electricity and Water Authority, United Arab Emirates
Kenza Maher, Qatar Environment and Energy Research Institute (QEERI) Hamad Bin Khalifa University (HBKU), Qatar Foundation (QF)Doha, Qatar
Miguel Ramirez-Gonzalez, ZHAW, Switzerland
Prakash Dwivedi, National Institute of Technology (NIT), India
Mohd Azrik Bin Roslan, Universiti Malaysia Perlis, Malaysia
Rini-Nur Hasanah, Brawijaya University, Indonesia
Raúl Sarrias-Mena, University of Cádiz, ETSI Algeciras, Spain
Hau Lee Cheun, Universiti Tunku Abdul Rahman, Malaysia
Mohammadali Abbasian, University of Warwick, UK
Somporn Sirisumrannukul, King Mongkut's University of Technology North Bangkok (KMUTNB), Thailand
Supachai Prainetr, Nakhon Phanom University, Thailand
Der-Cherng Liaw, NCTU
Edward Ofoegbu, Leeds Beckett University, United Kingdom
Mehdi Baharizadeh, University of Southern Denmark, Denmark
Luis M. Fernández-Ramírez, University of Cádiz, ETSI Algeciras, Spain
Sansanee Auephanwiriyakul, Chiang mai University, Thailand
Mohd Izhar Bin Abu Bakar, Universiti Kuala Lumpur British Malaysian Institute, Malaysia
Hao Tu, University of Kansas, USA
Shujia Li, MORNSUN, China
Soham Ghosh, Arizona State University, USA
Yugang Li, Qufu Normal University,China
Jia Yao, Nanjing University of Science and Technology, China
Junliang Liu, Chongqing University, China
Na Zhi, Xi’an University of Technology, China
Senthil Nathan Thangaraj, AMD-Xilinx, USA
Prerna Jain, Malaviya National Institute of Technology Jaipur, India
Cao Sunliang, The Hong Kong Polytechnic University, Hong Kong SAR, China
Khoa Dang Hoang, University of Huddersfield, UK
Lalit Goel, Nanyang Technological University, Singapore
George Owusu, University of Mines and Technology, Ghana
Lei Chen, Tsinghua University, China
Qiaoyue Li, Suzhou City University, China
Ahmed Bedawy, Hiroshima University, Japan
Weichao Wang, Qingdao University of Science and Technology, China
Wei Zhang, Nantong University, China
Yonghua Wen, Guangdong University of Science and Technology, China
Yutaka Sasaki, Hiroshima University, Japan
Weichen Yan, Zibo Polytechnic University, China
Haiqiang Zhou, Hohai University, China
Bo Zhang, Wuhan University, China
Abu Zaharin Ahmad, Universiti Malaysia Pahang, Malaysia
Zhiyi Li, Zhejiang University, China
Xiaokang Liu, Sichuan University, China
Wei Xiong, Guizhou University, China, China

Haoran Zhao, Shandong University, China, China
Hongshun Liu, Shandong university, China, China
Enyu Jiang, Shanghai University of Electric Power, China
Fangyuan Li, Zhengzhou University, China
Sundari Ramabhotla, Florida Polytechnic University, USA

Research on Breakdown Performance of DC Model Cable Based on Chinese Cross-linked Polyethylene Insulating Material

Wang Chuan-Bo
State Key Laboratory of Technology and Equipment for Defense against Power System Operational Risks
Nari Technology Co., Ltd
Nanjing, Jiangsu, 211106, China
603187843@qq.com

Jiao Yong-hui
State Key Laboratory of Technology and Equipment for Defense against Power System Operational Risks
Nari Technology Co., Ltd
Nanjing, Jiangsu, 211106, China
584328330@qq.com

Xu Peng-cheng
State Key Laboratory of Technology and Equipment for Defense against Power System Operational Risks
Nari Technology Co., Ltd
Nanjing, Jiangsu, 211106, China
xupc09@163.com

Han Ben
State Key Laboratory of Technology and Equipment for Defense against Power System Operational Risks
Nari Technology Co., Ltd
Nanjing, Jiangsu, 211106, China
hanben@sgepri.sgcc.com.cn

Pang Gong-he
State Key Laboratory of Technology and Equipment for Defense against Power System Operational Risks
Nari Technology Co., Ltd
Nanjing, Jiangsu, 211106, China
px116139@163.com

Jiao kun
State Key Laboratory of Technology and Equipment for Defense against Power System Operational Risks
Nari Technology Co., Ltd
Nanjing, Jiangsu, 211106, China
jiaokun@sgepri.sgcc.com.cn

Xu Shi-ming
State Key Laboratory of Technology and Equipment for Defense against Power System Operational Risks
Nari Technology Co., Ltd
Nanjing, Jiangsu, 211106, China
xushiming@sgepri.sgcc.com.cn

Ye Jian-cheng
State Key Laboratory of Technology and Equipment for Defense against Power System Operational Risks
Nari Technology Co., Ltd
Nanjing, Jiangsu, 211106, China
yejiancheng@sgepri.sgcc.com.cn

***Abstract*—In order to simulate the structure and production process of high-voltage direct current (DC) cables more efficiently, the preferred Chinese low-density polyethylene-based resin, nanoparticles and additives are added, and the high-voltage DC cable insulation material is mixed by a twin-screw extruder, which can solve the problem of difficult dispersion of nanoparticles. In addition, the HVDC cable insulation material production process was used to produce model cables with insulation thicknesses of 3.4mm, 5.5mm and 7.6mm, and DC breakdown experiments with different temperatures and different terminal accessories were carried out to evaluate the feasibility of Chinese insulation materials as HVDC cable insulation materials. The test results show that the cable material has excellent DC breakdown performance at different insulation thicknesses and temperatures. Moreover, it is found that different termination forms can increase the breakdown voltage of the cable, and the overall breakdown level of the cable can be improved by improving the terminal accessories in the future.**

Keywords—Cross-linked polyethylene, Nanocomposite, model cable, DC Breakdown Strength

I. INTRODUCTION

Cross-linked polyethylene (XLPE) is the most widely used insulating material for power cables due to its low price and excellent mechanical and electrical properties. However, the reason that limits the development of direct current cables comes from the accumulation of space charge under continuous long-term electric fields and the charge exchange under electrothermal coupling fields, resulting in extreme changes in electric field insulation failures [1]. The goal of DC cable insulation modification is to suppress space charge accumulation and increase volume resistivity, especially at high temperatures when the cable is loaded [2-4]. Therefore, in cable design and cable testing, the role of electrical stress and thermal stress needs to be considered at the same time. In order to suppress the problem of charge accumulation in space, introducing traps in the wide bandgap of XLPE is a straightforward and effective solution to these problems. Nanoparticles have been used as trap inducers for many years [5-8]. The nano-filler material system can improve the comprehensive performance of the cable [9].

Although the space charge factor has a great influence on the electrical performance of DC cables, the specific influence mechanism is still inconclusive, and the influence cannot be quantified, so the cable design relies more on the test of DC breakdown field strength. The breakdown field strength varies with the size of the insulation, as the larger the volume of the insulation, the greater the number and size of defects that typically lead to degradation and breakdown [10]. The design of

979-8-3315-5472-9/25/$31.00 ©2025 IEEE

an HVDC cable would require very high short-term breakdown strength [11].

In this paper, the nano-doped polyethylene technology was used to produce high-voltage DC cable materials, and the surface-modified nanoparticles were selected to facilitate the fusion with polyethylene materials. And the twin-screw extruder was used to produce the cable insulation masterbatch with better dispersion. Then the insulation masterbatch and polyethylene were mixed according to a certain proportion and additives were add to produce the high-voltage DC cable material by using the single-screw extruder. Considering the economy and efficiency of the test, the performance of the cable material was verified by the way of the production model cable test. Considering the breakdown field strength and the insulation thickness were related, three model cables with different thicknesses were produced for the test. Two forms of no cable accessories and cable accessories, and the conductor temperature of normal temperature and 90℃ were used in the test. The short-term breakdown voltage of the model cable is tested.

II. Methods and Materials

A. Material Preparation

The base resin was LDPE produced by Yangzi-BASF, a petrochemical manufacturer in Nanjing. The primary particle size of the inorganic nanoparticles was about 20 nm and the specific surface area was 100-150m^2/g. The imported antioxidant 300 was used as the auxiliary agent with a density of 1.1g/cm^3 and the ash content less than or equal to 0.05%. Dicumyl peroxide (DCP) was used as the cross-linking agent.

B. Masterbatch Production Process

The difficulty of nanocomposite polyethylene materials is the dispersion of nanoparticles, and the necessary condition for inorganic nanoparticles to achieve nanoscale dispersion in the polymer melt is that the dispersion force transmitted by the polymer melt to the nanopowder must be greater than the local or overall aggregation force of the nanopowder. In order to increase the interfacial adhesion between nanoparticles and polymers and improve the dispersion properties of nanoparticles,inorganic nanopowders with surface modification treatment were adopted. A twin-screw extruder is used to mix polyethylene and nanoparticles to improve the mechanical stress dispersion and make the inorganic nanopowder and polyethylene fused evenly.

LDPE, nano filler, additives are added to the twin-screw extruder through the feeder, respectively. The feeder has a function of precise dynamic metering to ensure the quality accuracy in the feeding process during continuous production. After each component is fully mixed by strong shearing of the twin screw, some agglomerated nanoparticles and gel-like polyethylene are filtered out through a filter. Then the mixture entered the underwater pelletizer, and the particles were pelletized in the deionized ultrapure water environment. The particles entered the dryer for drying and screening to obtain masterbatch. Figure 1 is the flow chart of high-voltage DC masterbatch preparation. The whole manufacturing process was carried out in the ultra-clean room, and the overall cleanliness level of the ultra-clean room reached 10,000 levels.

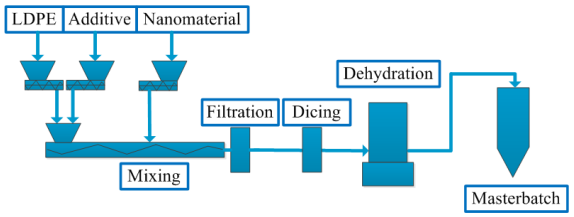


Fig. 1. Schematic diagram of Chinese HVDC masterbatch

In order to obtain Chinese high-voltage DC cable material, the masterbatch and polyethylene are mixed according to the mass ratio of 1:10, then mixed and extruded by a reciprocating single-screw extruder. After filtering through a filter screen, a certain proportion of cross-linking agent was added after underwater pelletizing. The DC cable material preparation flow chart is shown in Figure 2.

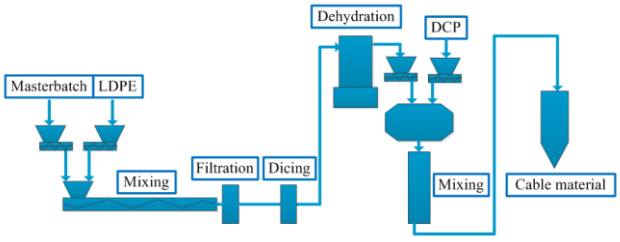


Fig. 2. Schematic diagram of chinese HVDC cable material

C. SEM Observations

The uniform dispersion is the premise for the DC cable material to obtain good electrical properties，To observe the dispersion of space charge inhibitor in the base material, the microscopic morphology of the section of polyethylene insulating material was observed by SEM. As in Figure 3, the nanoparticles were almost free of agglomeration in LDPE and were very uniformly dispersed in the resin matrix.

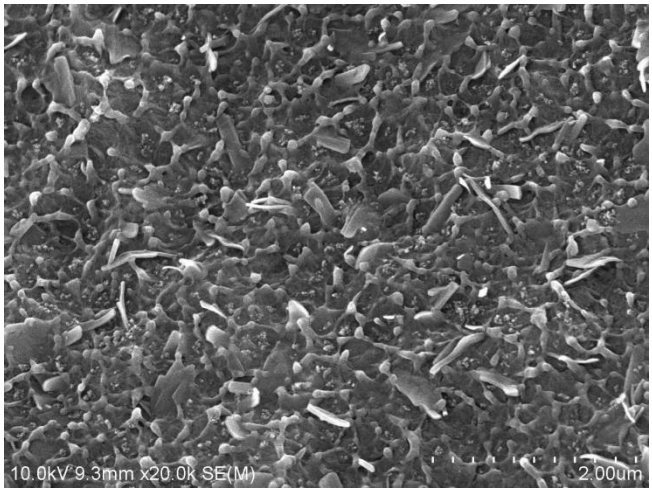


Fig. 3. SEM diagram of Chinese cable material.

D. Model Cable Structure

The self-developed DC cable material A was selected. The manufacturing capacity and test requirements of the cable

factory were comprehensively considered, and three insulation thicknesses of DC model cables were designed and prepared, with insulation thicknesses of 3.4mm, 5.5mm, and 7.6mm, and numbered A1, A2, and A3, respectively. The cable shielding material was made of LE0550DC grade shielding material produced by Borealis. Considering the convenience of installing the cable termination, the conductor diameter was adjusted to ensure that the outer diameter of the cable was consistent on the basis of the design insulation thickness. The rest of the structure was uniformly designed, with a conductor shield thickness of 1.0 mm and an insulating shield of 0.8 mm. Figure 4 is a diagram of the cable structure.

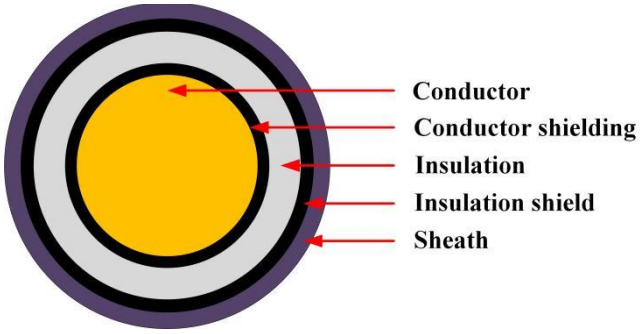


Fig. 4. Schematic diagram of the cable structure

E. Process parameters

To maintain consistency with the HVDC cable production process, the model cable employed a three-layer co-extrusion process to ensure that the inner and outer shielding layers were closely bonded to the insulation layer. The main extrusion process parameters are shown in Table 1.

TABLE I. EXTRUSION PROCESS PARAMETERS

Parameter	Conductor shielding	Insulation	Insulating shielding
Melting temperature/℃	118	118	120
Rotate speed/(r/min)	7.4	15.9	10.3
Extrusion speed/(m/min)	3.12	3.12	3.12

III. RESULTS AND DISCUSSION

A. DC Breakdown Test Method

The breakdown test included normal temperature breakdown and high temperature breakdown. The normal temperature breakdown conductor temperature was the room temperature, and the high was 90°C. During the test, 20m were taken for each model cable, and the two ends of the cable were processed according to Figure 5. There were two kinds of terminal configuration schemes for the DC breakdown test of the model cable. One case is that there is no cable termination, and the other was an integrated prefabricated cold-shrinkable silicone rubber terminal.

The DC model cable breakdown experiment was carried out in the high-voltage DC experimental hall. If the cable needed to be heated, the two ends of the cable were connected with copper bars, and heated to the test temperature with a through-core transformer. Figure 6 is a schematic diagram of the test wiring. During the test, the conductor was connected to DC high voltage and the cable was grounded by the outer shield. The voltage was increased in two stages. In the first stage, the voltage was increased at a rate of 5 kV/s to 50 kV. In the second stage, the voltage was increased at a rate of 1 kV/s until the cable breaks down. Three tests were performed for each cable.

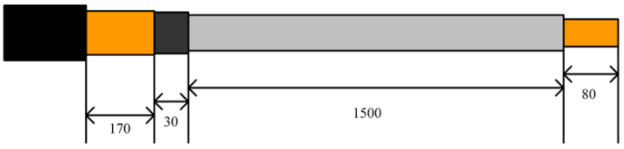


Fig. 5. Handle the dimensions at both ends of the cable

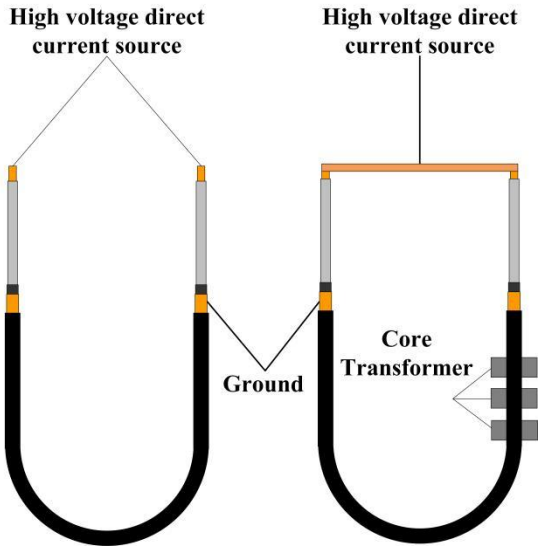


Fig.6. Schematic diagram of test wiring.

B. No cable Terminations at Room Temperature Test Results

When there are no terminals at both ends of the cable, it is equivalent to using air as the external insulation. The DC breakdown voltage of this type of cable was tested. The test was divided into two cases, one with the conductor temperature at room temperature and the other with the conductor temperature not less than 90°C. Table 2 is the test results of model A1 cable, Table 3 is the test results of model A2 cable, and Table 4 is the test results of model A3 cable.

TABLE II. A1 MODEL CABLE BREAKDOWN

No.	Conductor temperature /℃	Breakdown field strength /(kV/mm)	Average breakdown field strength /(kV/mm)
1	16	27.6	27.4
2	16	28.0	
3	16	26.5	
4	90.1	20.6	18.9
5	90.2	17.6	
6	90.2	18.5	

As can be seen from Table 2, the insulation thickness of a certain model cable was 3.4mm. When the conductor temperature is 90℃, its breakdown field strength is 69% of that at room temperature.

TABLE III. A2 MODEL CABLE BREAKDOWN

No.	Conductor temperature /℃	Breakdown field strength /（kV/mm）	Average breakdown field strength /（kV/mm）
1	15	27.3	
2	15	27.6	27.1
3	15	26.4	
4	90.2	18.2	
5	90.5	16.4	18.2
6	90.0	20	

As can be seen from Table 3, the insulation thickness of a certain type of cable is 5.5mm. When the conductor temperature is 90℃, its breakdown field strength is 67% of that at room temperature.

TABLE IV. A3 MODEL CABLE BREAKDOWN

No.	Conductor temperature /℃	Breakdown field strength /（kV/mm）	Average breakdown field strength /（kV/mm）
1	16	26.3	
2	16	27.0	26.8
3	16	27.2	
4	90.3	17.1	
5	90.0	18.0	18.1
6	90.1	19.2	

As can be seen from Table 4, the breakdown field strength of the model cable with an insulation thickness of 7.6 mm when the conductor temperature is 90°C is 67% of that at room temperature.

As can be seen from Table 2-4, the insulation breakdown field strength decreases only slightly with the increase of insulation thickness at both room temperature and high temperature, and the results show that the performance of the cable material is relatively stable.

C. Equipped with Terminal Test Results

The DC breakdown voltage test of this type of cable was carried out with integrated pre-cooled heat shrinkable silicone rubber terminals installed at both ends of the cable. The test was divided into two cases: the conductor temperature was room temperature and the conductor temperature was not less than 90°C. Table 5 shows the test results of Class A1 cables, Table 6 shows the test results of Class A2 cables, and Table 7 shows the test results of Class A3 cables.

TABLE V. A1 MODEL CABLE BREAKDOWN

No.	Conductor temperature /℃	Breakdown field strength /（kV/mm）	Average breakdown field strength /（kV/mm）
1	12	41.5	
2	12	40.9	41.2
3	12	41.2	
4	90.5	31.5	
5	90.0	32.4	31.3
6	90.3	30	

As can be seen from Table 5, the breakdown field strength of the model cable with an insulation thickness of 3.4 mm at a conductor temperature of 90°C was 76% of that at room temperature. Compared with Table 2, the breakdown voltage of the model cable equipped with integrated prefabricated cold shrinkable silicone rubber termination was higher than that of the model cable without terminal at room temperature, regardless of the normal temperature or high temperature state. And it was 1.73 times at high temperature. It showed that under this terminal, the high-temperature breakdown performance was improved even more.

TABLE VI. A2 MODEL CABLE BREAKDOWN

No.	Conductor temperature /℃	Breakdown field strength /（kV/mm）	Average breakdown field strength /（kV/mm）
1	14	40	
2	14	38.2	39.1
3	14	39.1	
4	90.0	32.7	
5	90.5	30.9	30.9
6	90.7	29.1	

As Table 6 showed, the breakdown field strength of the model cable with an insulation thickness of 5.5 mm at a conductor temperature of 90°C was 79% of that at room temperature. Compared with Table 2, it suggested that the breakdown voltage of the model cable equipped with integrated prefabricated cold shrinkable silicone rubber termination was higher than that of the model cable without terminal at room temperature, regardless of the normal temperature or high temperature state. It was 1.7 times at high temperature. The results indicated that under this terminal, the high-temperature breakdown performance was improved even more.

TABLE VII. A3 MODEL CABLE BREAKDOWN

No.	Conductor temperature /℃	Breakdown field strength /（kV/mm）	Average breakdown field strength /（kV/mm）
1	13	39.5	
2	13	38.3	38.5
3	13	37.8	
4	90.1	31.6	
5	90.8	30.3	30.5
6	90.3	29.6	

As can be seen from Table 7, the breakdown field strength of the model cable with an insulation thickness of 7.6 mm at a conductor temperature of 90°C was 79% of that at room temperature. Compared with Table 2, it indicated that the breakdown voltage of the model cable equipped with integrated prefabricated cold shrinkable silicone rubber termination was higher than that of the model cable without termination at room temperature or high temperature, with a breakdown voltage of

1.4 times at room temperature and 1.68 times that of high temperature. It suggested that under this terminal, the high-temperature breakdown performance was improved even more.

D. Comparative Analysis

Fig. 7 shows the variation of the breakdown field strength of the model cable with the thickness of the insulation under the room temperature and 90℃. From room temperature to 90℃, regardless of the form of the terminal, the DC breakdown field strength of the model cable decreased significantly. The insulation thickness ranged from 3.4mm to 7.6mm, and the DC breakdown field strength of the model cable only decreased slightly with little change, regardless of the form of termination. The test results showed that the production of 100kV HVDC cable using this cable material met the insulation performance requirements. It was concluded that different terminal forms of insulation thickness had a great impact on the breakdown performance of model cables, which was the key factor to determine the dielectric strength. And matching suitable cable terminations can improve the upper limit of insulation capacity. In the future, when studying the Chinese insulated cable materials, the Chinese accessory terminal materials and structures should be developed and the insulation performance of cable materials should be fully explored to explore the possibility of producing high-voltage DC cables with higher voltage levels.

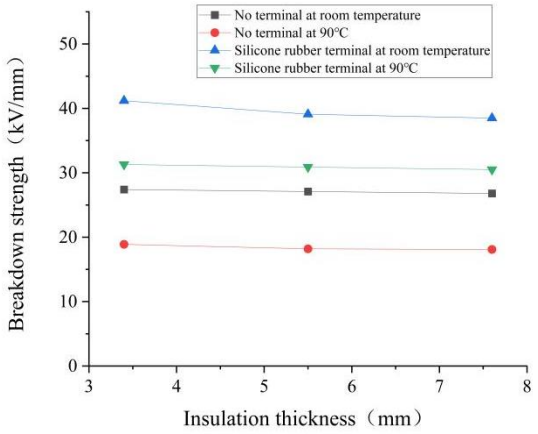


Fig. 7. Breakdown field strength of model cables with different thicknesses

IV. Conclusion

1) Temperature had a great influence on the breakdown performance of DC cables, and the breakdown field strength at 90℃ only accounted for 70%-80% of the breakdown field strength at room temperature under the same insulation thickness.

2) Different terminal forms of insulation thickness had a great impact on the breakdown performance of model cables, which was the key factor to determine the dielectric strength, and matching suitable cable terminals could improve the upper limit of insulation capacity.

3) The insulating material could be used to manufacture 100kV DC cables, and in the future, when studying the Chinese insulated cable materials, the Chinese accessory terminal materials and structures should be developed and the insulation performance of cable materials should be fully explored to explore the possibility of producing high-voltage DC cables with higher voltage levels.

References

[1] Yang, Xu, et al. Modulated electrical performance of cross-linked polyethylene by grafted charge-attracting molecules for high voltage direct current cable insulation. Materials & Design 240 (2024): 112884.

[2] Du, Boxue. Polymer insulation applied for HVDC transmission. Springer Nature, 2020.

[3] Chen, George, et al. Review of high voltage direct current cables. CSEE Journal of Power and Energy Systems 1.2 (2015): 9-21.

[4] Katakai, Shoshi. Behind the scenes of the development of DC XLPE power cables. SEI Tech. Rev. 91 (2020): 5-14.

[5] Li, Zhonglei and Du, Boxue. Polymeric insulation for high-voltage dc extruded cables: challenges and development directions. IEEE Electrical Insulation Magazine 34.6 (2018): 30-43.

[6] Ma, Haoyu, et al. Improved dielectric and electromagnetic interference shielding performance of materials by hybrid filler network design in three-dimensional nanocomposite films. Materials & Design 226 (2023): 111666.

[7] Ru, Jiasheng, et al. Enhanced energy storage properties of thermostable sandwich-structured BaTiO3/polyimide nanocomposites with better controlled interfaces. Materials & Design 197 (2021): 109270.

[8] Zhang, Tiandong, et al. Non-linear electrical conductivity of ethylene-propylene-diene monomer-based composite dielectrics by tuning inorganic fillers. High Voltage 8.4 (2023): 781-790.

[9] Lewis, T. J. Nanometric dielectrics. IEEE Transactions on Dielectrics and Electrical Insulation 1.5 (2002): 812-825.

[10] Mazzanti, Giovanni. Updated review of the life and reliability models for HVDC cables. IEEE Transactions on Dielectrics and Electrical Insulation 30.4 (2023): 1371-1390.

[11] Montanari, Gian Carlo, et al. Criteria influencing the selection and design of HV and UHV DC cables in new network applications. High Voltage 3.2 (2018): 90-95.

Insulator Defect Target Detection Based on Improved YOLOv5s

Yugang Li
Qufu Normal University
Rizhao,China
liyugang@qfnu.edu.cn

Zheng Chen
Qufu Normal University
Rizhao,China
chenzheng@qfnu.edu.cn

Zheng Zhang
Qufu Normal University
Rizhao,China
1376351138@qq.com

Jiabao Zhu
Qufu Normal University
Rizhao,China
15564272581@163.com

***Abstract*—Traditional deep learning-based insulator defect detection algorithms often face the dilemma between network model lightweighting and detection accuracy. This paper proposes a method that integrates the ShuffleNetV2 neural network model into the Backbone structure of the YOLOv5s network model and adds an ECA attention mechanism layer to the last layer of the Backbone. In the Neck structure of YOLOv5s, the traditional PANet structure is replaced with a BiFPN structure. Compared to the original YOLOv5s, the size of the improved network model is reduced from 13.7 MB to 7.7 MB, a decrease of 6 MB. The model's detection accuracy, measured by the mean Average Precision (mAP) value, increases from 92.2% to 94.5%, an improvement of 2.3%. While enhancing the network's accuracy, the proposed method also achieves a more lightweight network model.**

Keywords—Target Detection; YOLOv5; BiFPN; ECA Attention Mechanism

I. INTRODUCTION

Insulators, which function as insulating control devices that provide insulation and protection for transmission lines on power towers, are crucial for the safe operation of power systems [1-3]. Periodic safety inspections of transmission lines and regular checks for insulator defects are essential for maintaining the normal operation of these lines [4]. To ensure this, significant resources are allocated annually for the inspection and maintenance of transmission lines. The advent of drone technology has revolutionized power line inspection, enabling automation in power operations and making inspections simpler and more flexible while effectively reducing labor costs [5]. Drones can replace human workers in high-altitude and high-risk operations, thereby reducing inspection risks and enhancing safety and convenience. Early drone inspection methods involved aerial photography followed by manual analysis of the captured images by staff. However, due to the large volume of inspection work and the vast amount of image data, this approach often resulted in missed detections or misjudgments of insulator defects caused by human fatigue or inattention. In recent years, advancements in artificial intelligence have significantly improved the accuracy and speed of insulator defect detection, bringing new developments to insulator fault detection technology.

Rizhao Natural Science Foundation NO.RZ2022ZR18.

Over 20 years ago, P. Viola and M. Jones first achieved real-time face detection. In honor of their outstanding contributions, the detection algorithm they used in their experiments is referred to as the "Viola-Jones detector" [6-7]. In 2005, the Histogram of Oriented Gradient (HOG) proposed by N. Dalal and B. Triggs [8] significantly improved upon the scale-invariant feature transform and contextual environment of that time [9]. It remains the foundation for some of the highly used classic object detectors today.

In recent years, deep learning-based object detection algorithms have become mainstream in industrial applications. These algorithms are primarily divided into single-stage and two-stage object detection methods. There are many types of two-stage object detection algorithms, including RCNN [10], Fast-RCNN [11], and Faster-RCNN [12]. These methods are characterized by high detection accuracy, but they have complex models, large data volumes, and consequently high memory usage, making rapid detection unattainable.

Single-stage object detection algorithms have developed rapidly in recent years, with several types of algorithms emerging, such as the YOLO [13] series and SSD [14]. These algorithms reduce model complexity and enable faster object detection, making them the most popular methods in industrial applications currently. This paper focuses on the detection of insulator faults in aerial images captured by drones. Based on the mainstream YOLOv5 detection algorithm, we have improved the network model by replacing the backbone network with the ShuffleNetV2 architecture [15] and adding an ECA attention mechanism. In the Neck part, the traditional PANet [16] is replaced with the BiFPN structure [17]. Compared to the traditional YOLOv5 algorithm, the improved network reduces the model size while increasing detection accuracy. It can be better applied to the identification of insulator targets and fault detection in drone aerial inspections.

II. RELATED WORK

A. Overview of YOLOv5

YOLOv5s consists primarily of four components: Input, Backbone, Neck, and Output. Among these, the Backbone and Neck are the principal network structures.

The Backbone is the primary network structure of the model. It incorporates the CSP (Cross-Stage Partial Network)

architecture, which is inspired by CSPNet. This architecture copies and transfers basic features extracted from the lower layers of the data to the next module via a dense block. This process allows the data features to be fully detached from the lower layers, thereby reducing unnecessary model parameters and computational load. It addresses the issue of repeated gradients that often occur in large networks, enhances the backbone's ability to extract information, and reduces network inference time. YOLOv5s employs two types of CSP modules. The CSP-1 structure is used in the Backbone, while the CSP-2 structure is used in the Neck. The primary difference is that CSP-2 replaces the residual module in CSP-1 with a convolutional layer.Compared to previous YOLO series, YOLOv5s introduces a new Focus module in its Backbone. The core operation of the Focus module is to slice the original image. As illustrated in the figure, it first performs pixel sampling between adjacent areas and then recombines them by category. After recombination, the number of channels increases from 3 to 12, representing a fourfold expansion.

The Neck part of YOLOv5s employs an FPN [18] + PAN [19] structure. Its primary purpose is to extract deeper features from the information provided by the Backbone and perform feature fusion. The FPN layer conducts top-down feature propagation and fusion to obtain detailed feature maps. Subsequently, two PAN layers perform bottom-up fusion of low-level and high-level features, enabling high-level feature maps to incorporate low-level features. This combination of top-down FPN and bottom-up PAN structures facilitates the fusion of parameter information obtained from multiple detections, which is beneficial for detecting small targets and enhances the network's feature extraction capability.

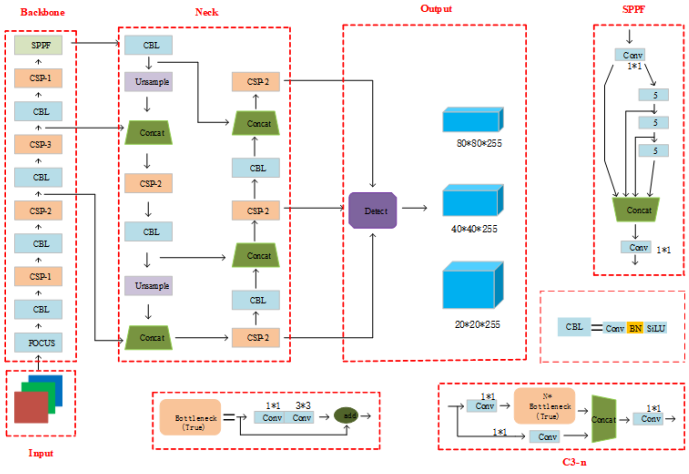


Fig. 1. YOLOv5s network structure

III. METHODS

A. Improvement of the Neck Structure

BiFPN (Weighted Bidirectional Feature Pyramid Network) extends PANet's direct top-down and bottom-up feature concatenation by introducing cross-scale feature fusion. For feature fusion within the same layer, it not only extracts features from adjacent feature fusions but also incorporates feature fusion from the same-layer feature map. When performing feature fusion across different regions, it assigns different weights to them based on their importance, thereby increasing their proportion in the feature fusion process. This approach is illustrated in Equations (1) and (2).

$$Out = \sum_i I_i \tag{1}$$

$$Out = \sum_i \frac{\omega_i * I_i}{\sum_i \omega_i + \epsilon} \tag{2}$$

Where ω_i represents the weights learned for different feature modules. I_i represents the input feature vectors from different layers. ϵ is a value taken to prevent the denominator from being zero, usually 0.0001.

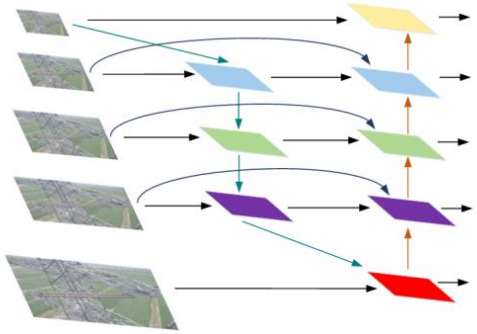


Fig. 2. Schematic diagram of BiFPN structure

B. Improvement of the Backbone Structure

This paper employs the ShuffleNetV2 structure to replace the backbone layers of YOLOv5s and reconstruct the feature extraction network. Traditional convolution methods are characterized by channel density, employing costly dense 1×1 convolutions. Each convolution is performed within its own channel before feature fusion, and if there are N convolutions, N channels are required. ShuffleNetV1 addresses this issue by using group convolution, as shown in Figure 3(a), to apply sparse channel connections on the 1×1 layer, thereby reducing computational load. However, group convolution has limitations: the output from a group is only related to the input of that group and cannot receive information from other groups, failing to achieve information transfer between channels. To address this, ShuffleNetV1 introduces a novel channel shuffle operation based on group convolution. As shown in Figure 3(b), after the first convolution calculation, features from different channels are scattered separately. During the next group convolution, these scattered features are recombined, ultimately achieving channel shuffling and allowing information flow between different channels.

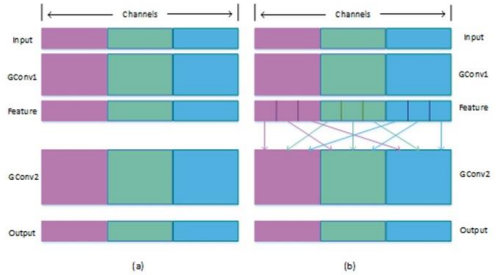


Fig. 3. Group convolution and channel mixing

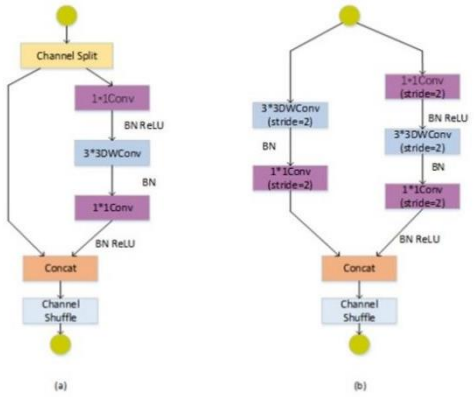


Fig. 4. ShuffleNetV2 network structure

ShuffleNetV2 is an improvement over ShuffleNetV1. ShuffleNetV1 relies heavily on pointwise group convolutions, which necessitate a larger number of channels and consequently increase memory access costs. Moreover, the use of non-equal-width channels in ShuffleNetV1 further exacerbates computational demands.

To address these issues, the ShuffleNetV2 network structure introduces a channel split operation. The input is split along the channel dimension into two branches. One branch is directly routed to the output, while the other undergoes a sequence of operations: a 1×1 Conv convolution, a 3×3 DWConv depthwise convolution, and another 1×1 Conv convolution. These three convolutions maintain a stride of 1 and preserve the number of input and output channels. After convolution, the two branches are concatenated, and channel shuffling is performed to enable information exchange between them. Compared to this approach, an alternative configuration (b) omits channel splitting and doubles the number of output channels. However, due to the use of building blocks with a stride of 2, the height and width of the feature map are halved, thereby preventing an increase in the network's FLOPs. Therefore, integrating ShuffleNetV2 as the Backbone module in YOLOv5s can significantly reduce the model size while improving model accuracy.

C. ECA

In response to the issue of interference from the surrounding environment in insulator target detection and defect recognition tasks. An ECA attention mechanism is added to the network algorithm. The attention mechanism, while scanning the entire image, allocates attention to the input information through weight training. During the network training process, the network is made to focus on the insulator parts in the image and suppress irrelevant information from the surrounding environment.

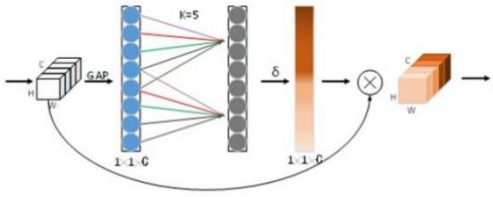


Fig. 5. ECA-Net

The ECA attention mechanism is a channel attention mechanism. It can be directly added to the network model. It performs global average pooling on the input features. Without affecting the network channel size or feature extraction capability. The following figure illustrates the working principle of ECA-Net. After pooling, a 1D convolution of size K is used for local cross-channel interaction. When solving object detection tasks on different datasets, the size of K is uncertain. However, the size of the convolution kernel K has a certain mapping relationship with the channel dimension C. As shown in Equation (3) and (4).

$$C = \varphi(K) = 2^{(\gamma K - b)} \tag{3}$$

$$K = \varphi(C)\sigma = \left|\frac{\log_2 C}{\gamma} + \frac{b}{\gamma}\right|_{odd} \tag{4}$$

Therefore, a nonlinear formula can be introduced to determine the size of K. where γ and b are the adjustment parameters, and $|x|_{odd}$ is the smallest odd number rounded up by x.

D. Improve the Overall Network Structure

The improved network structure is depicted in Figure 6. Compared to the original network model, this structure replaces the original backbone network with the ShuffleNetV2 architecture, thereby reducing the number of layers and the number of parameters in the backbone part of the network. Additionally, an ECA channel attention mechanism is incorporated into the final layer of the backbone network, enhancing the network's ability to capture important information across channels. In the Neck structure, a weighted feature pyramid structure is employed. This enables the Concat modules in layers 17 and 20 of the network to extract information from the previous layer while also obtaining information from layers 4 and 2 in a weighted manner, thereby enhancing the network's feature fusion capability.

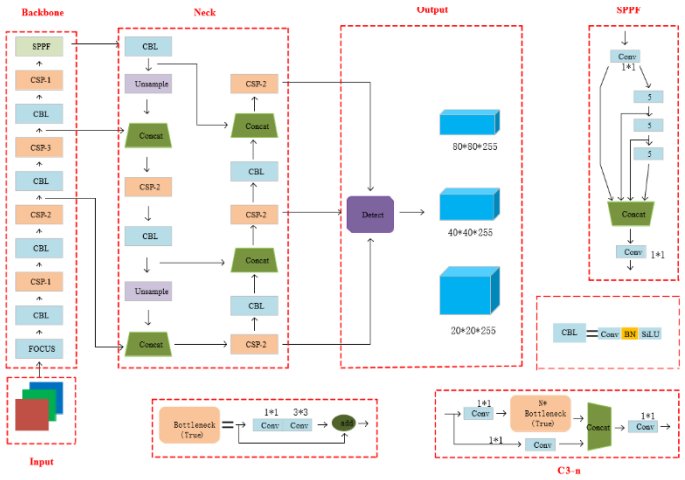


Fig. 6. Improved YOLOv5s network structure

IV. EXPERIMENTS

A. Datasets

The dataset utilized in this experiment is an open-source insulator image dataset available online. It comprises 1,500 real

captured images, which are augmented with an additional 4,500 images using methods such as flipping, scaling, and adjusting brightness, resulting in a total of 6,000 insulator images. The images are annotated using the LabelImg software, with annotation results saved by default in the PASCAL VOC format as XML files. The annotated objects are labeled as "insulator" and "defect." The dataset is divided into training and testing sets in an 8:2 ratio using Python.



Fig. 7. Insulator images

B. Experimental Parameter Setting

In order to verify the performance of the improved network, this paper builds a relevant experimental platform. The specific experimental environment is shown in Table 1.

TABLE I. EXPERIMENTAL ENVIRONMENT

name	Relevant configuration parameters
operating system	Windows10
CPU	12th Gen Intel(R) Core(TM)i5-12400F
GPU	NVIDIA GeForce RTX 3060
Deep learning framework	Pytorch1.7.1
YOLOv5	Pycharm 2022.1.4
Accelerate the environment	CUDA10.2

Each set of experiments uses the same initial learning rate of 0.0001, batch setting of 8, initial momentum setting of 0.9, number of 200 epoch training rounds, and weight decay coefficient of 0.0005.

V. RESULTS

A. Evaluation Indicators

Object detection metrics are generally categorized into detection accuracy metrics and detection speed metrics. To quantitatively analyze the detection experimental results, this paper primarily employs Precision to evaluate detection accuracy, Recall to assess the completeness of the search, and mean Average Precision (mAP) to measure the overall detection performance of the model.

The test results of the classifier are categorized into four types: TP (True Positives, correct identification of positive samples), TN (True Negatives, correct identification of negative samples), FP (False Positives, incorrect identification of positive samples), and FN (False Negatives, incorrect identification of negative samples). Precision refers to the proportion of correctly identified positive samples out of all samples identified as positive by the classifier. The calculation formula is shown in Equation (5):

$$P = \frac{TP}{TP+FP} \times 100\% \tag{5}$$

Recall refers to the proportion of positive samples correctly determined by the classifier to all correct decisions. The calculation formula is shown in Equation (6):

$$R = \frac{TP}{TP+FN} \times 100\% \tag{6}$$

Average precision AP refers to the area enclosed by the curve with P as the horizontal axis and R as the vertical axis. The calculation formula is shown in Equation (7):

$$AP = \int_0^1 PdR \tag{7}$$

After finding the AP, the mAP value can be obtained by averaging the AP value obtained many times, and the calculation formula is as shown in Equation (8):

$$mAP = \frac{\sum_{i=1}^{n} AP_i}{n} \tag{8}$$

The indicators of detection speed used in this paper are mainly single detection speed and frame rate (FPS), the larger the FPS value, the faster the network model can process the image.

B. Ablation Experiment Comparison

To analyze the performance improvement of each modification to the network model, ablation experiments were conducted, as shown in Table 2. The experiments were based on the YOLOv5s network model. The Neck part was first improved by replacing it with BiFPN. Subsequently, the ECA channel attention mechanism was incorporated. Finally, the Backbone part was modified to use ShuffleNetV2. Comparisons were made among the different network models through these experiments.

TABLE II. ABLATION EXPERIMENTAL RESULTS

Network model	P(%)	R(%)	mAP(%)	Single inspection time (s)	FPS	Model size (MB)
YOLOv5	91.3	90.9	92.2	0.017	52	13.7
YOLOv5+Bifpn	93.9	90.6	93.1	0.019	48	15.8
YOLOv5+Bifpn+ECA	93.9	91.9	94.3	0.020	45	13.7
YOLOv5+Bifpn+ECA +ShuffleNetV2	93.4	93.4	94.5	0.016	55	7.7

As shown in Table 2, the original YOLOv5s network has a Precision (P) of 91.3% and a mean Average Precision (mAP) of 92.2%. After incorporating BiFPN, these values increased to 93.9% and 93.1%, respectively. The Recall (R) value did not change significantly. The model size increased from 13.7 MB to 15.8 MB, while the Frames Per Second (FPS) decreased from 52 to 48. This indicates that detection accuracy improved at the expense of detection speed. After adding the ECA channel

attention mechanism, the R value and mAP value increased from 90.6% and 93.1% to 91.9% and 94.3%, respectively. The Precision (P) value remained relatively unchanged. The model size decreased from 15.8 MB to 13.7 MB, while the FPS decreased from 48 to 45. This suggests that detection accuracy improved, but detection speed decreased. After replacing the Backbone with ShuffleNetV2, the Precision (P) value and mAP value remained relatively unchanged, while the Recall (R) value increased from 91.9% to 93.4%. The model size decreased from 13.7 MB to 7.68 MB, and the detection time per image decreased from 0.020 s to 0.016 s. Consequently, the FPS increased from 45 to 55. This indicates that both detection accuracy and detection speed improved.

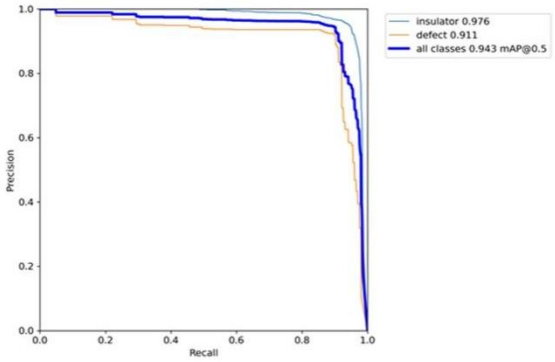


Fig. 8. Comparison of mAP results of four different network models

C. Comparative Experiments

To further validate the performance of the improved network model. This paper compares the improved YOLOv5s algorithm with the original YOLOv5s, SSD, and YOLOv3 algorithms. The models are compared using two metrics: mAP value and model size. The results are shown in Table 3.

TABLE III. COMPARE EXPERIMENTAL RESULTS

Network model	mAP(%)	FPS
YOLOv5s	92.2	52
SSD	77.0	38
Faster R-CNN	87.8	12
YOLOv5s+Bifpn+ECA+ShuffleNetV2	94.5	55

As shown in the table, compared with the SSD and YOLOv3 algorithms, YOLOv5 achieves a higher mAP value with a smaller network model. Compared to the original YOLOv5s, the mAP value increased from 92.2% to 94.5%, an improvement of 2.3 percentage points. The model size decreased from 13.7 MB to 7.7 MB, a reduction of 6 MB.

Figures 9, 10, 11, and 12 present the detailed partial detection results for the four models. From these detailed results, it is evident that the SSD algorithm has the lowest detection accuracy, with missed detections of insulator bodies and both misdetected and missed detections of insulator defects. The Faster R-CNN algorithm can accurately recognize the insulator body but exhibits misdetected insulator detail defects. Both the original YOLOv5s and the improved YOLOv5s algorithms can correctly identify the insulator body and its defects, with the improved YOLOv5s algorithm demonstrating a higher recognition rate and the best overall detection performance.

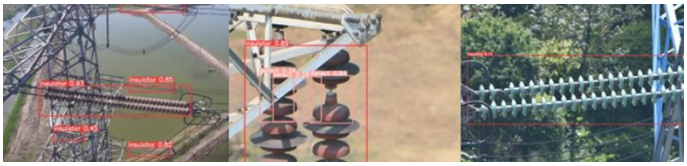


Fig. 9. SSD Partial Inspection Results



Fig. 10. Faster R-CNN partial detection results

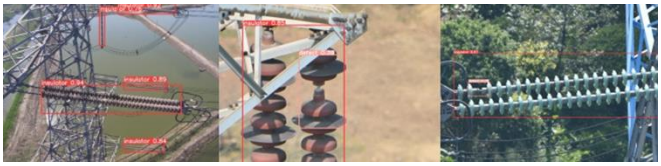


Fig. 11. YOLOv5s partial detection results

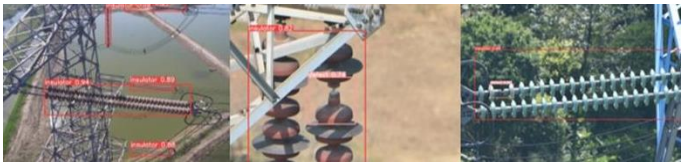


Fig. 12. Improved YOLOv5s Partial Detection Results

VI. CONCLUSION

To address the issues of low accuracy and slow detection speed in insulator target recognition and fault detection for transmission lines, this paper proposes a novel improved YOLOv5s algorithm. The Backbone structure of the original YOLOv5s is replaced with ShuffleNetV2, which reduces the size of the network model. An ECA channel attention mechanism is added to the last layer of the Backbone, enhancing the network's representation ability and reducing interference from irrelevant information. The FPN+PAN structure in the Neck part is changed to a BiFPN structure, improving the network's feature fusion capability. Experimental results show that, compared to the original YOLOv5s network, the size of the improved network model is reduced from 13.7 MB to 7.7 MB, a reduction of 6 MB. The mAP value increased from 92.2% to 94.5%, an improvement of 2.3%. These enhancements effectively improve the accuracy of insulator defect detection in transmission lines and reduce the risk of power grid damage caused by missed or incorrect detection of insulators during inspection.

ACKNOWLEDGMENT

This work was supported in part by the Rizhao City Natural Science Foundation (Grant Number. RZ2022ZR18).

REFERENCES

[1] Gao F, Wang J, Kong Z, et al. Recognition of insulator explosion based on deep learning[C]//2017 14th international computer conference on wavelet active media technology and information processing (ICCWAMTIP). IEEE, 2017: 79-82.

[2] Huang X, Shang E, Xue J, et al. A multi-feature fusion-based deep learning for insulator image identification and fault detection[C]//2020 IEEE 4th Information Technology, Networking, Electronic and Automation Control Conference (ITNEC). IEEE, 2020, 1: 1957-1960.

[3] Antwi-Bekoe E, Zhan Q, Xie X, et al. Insulator recognition and fault detection using deep learning approach[C]//Journal of Physics: Conference Series. IOP Publishing, 2020, 1454(1): 012011.

[4] Liu J, Liu C, Wu Y, et al. An improved method based on deep learning for insulator fault detection in diverse aerial images[J]. Energies, 2021, 14(14): 4365.

[5] Yan D. Research and application status of industrial robot control system[C]//2018 3rd International Conference on Mechanical, Control and Computer Engineering (ICMCCE). IEEE, 2018: 16-20.

[6] Viola P, Jones M. Rapid object detection using a boosted cascade of simple features[C]//Proceedings of the 2001 IEEE computer society conference on computer vision and pattern recognition. CVPR 2001. Ieee, 2001, 1: I-I.

[7] Lammertsma P. Viola-Jones' face detection claims 180k features[J]. Stack Overflow, 2009, 10(11).

[8] Dalal N, Triggs B. Histograms of oriented gradients for human detection[C]//2005 IEEE computer society conference on computer vision and pattern recognition (CVPR'05). Ieee, 2005, 1: 886-893.

[9] Jafari F, Basu A. Saliency-Driven Hand Gesture Recognition Incorporating Histogram of Oriented Gradients (HOG) and Deep Learning[J]. Sensors, 2023, 23(18): 7790.

[10] Pang J, Chen K, Shi J, et al. Libra r-cnn: Towards balanced learning for object detection[C]//Proceedings of the IEEE/CVF conference on computer vision and pattern recognition. 2019: 821-830.

[11] Zhao Z Q, Bian H, Hu D, et al. Pedestrian detection based on fast R-CNN and batch normalization[C]//Intelligent Computing Theories and Application: 13th International Conference, ICIC 2017, Liverpool, UK, August 7-10, 2017, Proceedings, Part I 13. Springer International Publishing, 2017: 735-746.

[12] Yang S, Fang B, Tang W, et al. Faster R-CNN based microscopic cell detection[C]//2017 international conference on security, pattern analysis, and cybernetics (SPAC). IEEE, 2017: 345-350.

[13] Redmon J, Divvala S, Girshick R, et al. You only look once: Unified, real-time object detection[C]//Proceedings of the IEEE conference on computer vision and pattern recognition. 2016: 779-788.

[14] Liu W, Anguelov D, Erhan D, et al. Ssd: Single shot multibox detector[C]//Computer Vision–ECCV 2016: 14th European Conference, Amsterdam, The Netherlands, October 11–14, 2016, Proceedings, Part I 14. Springer International Publishing, 2016: 21-37.

[15] Ma N, Zhang X, Zheng H T, et al. Shufflenet v2: Practical guidelines for efficient cnn architecture design[C]//Proceedings of the European conference on computer vision (ECCV). 2018: 116-131.

[16] Wang K, Liew J H, Zou Y, et al. Panet: Few-shot image semantic segmentation with prototype alignment[C]//proceedings of the IEEE/CVF international conference on computer vision. 2019: 9197-9206.

[17] Tan M, Pang R, Le Q V. Efficientdet: Scalable and efficient object detection[C]//Proceedings of the IEEE/CVF conference on computer vision and pattern recognition. 2020: 10781-10790.

[18] Ghiasi G, Lin T Y, Le Q V. Nas-fpn: Learning scalable feature pyramid architecture for object detection[C]//Proceedings of the IEEE/CVF conference on computer vision and pattern recognition. 2019: 7036-7045.

[19] Li G, Fan Y, Lai Y, et al. Coronavirus infections and immune responses[J]. Journal of medical virology, 2020, 92(4): 424-432.

[20] Hu X, Kong D, Liu X, et al. FM-STDNet: High-Speed Detector for Fast-Moving Small Targets Based on Deep First-Order Network Architecture[J]. Electronics, 2023, 12(8): 1829.

[21] Sha J, Wang J, Hu H, et al. Development of an Accurate and Automated Quality Inspection System for Solder Joints on Aviation Plugs Using Fine-Tuned YOLOv5 Models[J]. Applied Sciences, 2023, 13(9): 5290.

[22] Zhang H, Zhou F, Ma C, et al. MCMNET: Multi-Scale Context Modeling Network for Temporal Action Detection[J]. Sensors, 2023, 23(17): 7563.

[23] Fang S, Zhang B, Hu J. Improved mask R-CNN multi-target detection and segmentation for autonomous driving in complex scenes[J]. Sensors, 2023, 23(8): 3853.

[24] Nursikuwagus A, Munir R, Khodra M L. Hybrid of deep learning and word embedding in generating captions: Image-captioning solution for geological rock images[J]. Journal of Imaging, 2022, 8(11): 294.

Influence of Structural Geometry and Contamination Characterics on the Surface Electric Field distribution of HVDC Insulators

Minghao Du
School of Electrical Engineering Shenyang Institute of Engineering
Shenyang, China
12024201309@stu.sie.edu.cn

Donglai Wang*
Key Laboratory of Regional Multi-Energy System Integration and Control of Liaoning Province Shenyang Institute of Engineering
Shenyang, China
wangdl@sie.edu.cn

Chengze Li
State Grid Shenyang Electric Power Supply Company State Grid Liaoning Electric Power Co., Ltd.
Shenyang, China
lcz1724192328@163.com

Shuo Gao
School of Electrical Engineering Shenyang Institute of Engineering
Shenyang, China
12024201118@stu.sie.edu.cn

***Abstract*—Electric field strength distribution on the insulator surface is an important factor to determine its insulation performance. To explore the influence of various factors on the surface electric field of insulators, 3D models of insulators under different working conditions are constructed based on finite element technology, and the effects of voltage level, structural parameters, and surface state on the surface electric field intensity are systematically studied. The results show that with the increase of voltage level, the electric field intensity on the insulator surface will show an obvious increasing trend, which puts forward higher requirements for its insulation performance. Structural parameters such as the diameter of the umbrella skirt and the distance between umbrellas have a significant control effect on the electric field distribution. Increasing the radius of the umbrella skirt can increase the creepage distance, thus effectively reducing the maximum field strength at the edge of the umbrella skirt and improving the uniformity of the electric field distribution. Appropriately decreasing the distance and increasing the umbrella skirt are beneficial to improving the surface electric field and achieving the optimal field strength distribution. Contamination layer and water droplet adhesion on the insulator surface will induce a local concentration of electric field strength by changing surface conductivity, thus significantly increasing the risk of insulation failure. The research results can provide theoretical support and data reference for insulator structure optimization design, operation, and maintenance strategy formulation, and fault prevention.**

Keywords—Electric field, High voltage, Insulator structure, Surface texture component

I. INTRODUCTION

High-voltage direct current (HVDC) system operation reliability has been paid more attention of long distance power transmission. As an indispensable key insulation component in DC transmission lines, insulators shoulder the dual missions of electrical insulation and mechanical bearing, and the distribution characteristics of their surface electric fields are directly related to the insulation performance and service life of equipment [1-4]. Once the surface electric field intensity exceeds the critical value, it is easy to induce partial discharge, surface flashover, and other faults, which pose a serious threat to the safe and stable operation of the power grid [5-6]. Therefore, it is of great theoretical significance and engineering value to deeply analyze the influence mechanism of the surface electric field of insulators for optimizing their structural design and improving the insulation reliability of the system.

Scholars have carried out extensive research on the electric field characteristics of insulators. Ref. [7] explores the effects of pollution layer, water droplets and other factors on the surface electric field of insulators with different profile types, and proves that optimizing the umbrella skirt structure is helpful to improve the performance of insulators. Ref. [8] combined with numerical simulation and experimental test, the surface charge distribution law of polymer insulator under AC and DC voltage is analyzed, and it is found that charge accumulation will significantly lead to electric field distortion; Ref. [9] focuses on the influence of ring non-uniform pollution on DC flashover characteristics of suspension insulators, and reveals the relationship among flashover voltage, surface pollution layer resistance and leakage current. Ref. [10] discusses the influence of the coupling effect of surface charge and air humidity on the DC flashover voltage of polymer insulators, and points out that the synergistic effect of environmental factors can not be ignored. Although the existing research has preliminarily clarified the influence of a single factor on the electric field distribution, there are still three shortcomings: it focuses only on single environmental or structural factors, lacking analysis of voltage level-structural parameter-surface state coupling. It offers mostly qualitative optimization of structural parameters without quantitative rules or synergistic mechanisms. And it fails to clarify how pollution layers and water droplets differ in distorting electric fields, hindering engineering guidance.

This paper constructs three-dimensional models of insulators under different working conditions based on finite element method, and quantifies the influence of the coupling of voltage grade, structural parameters, and surface state on the surface

This work was supported by the National Natural Science Foundation of China (Grant No. 52407011).

electric field distribution. A collaborative optimization of "umbrella skirt diameter-umbrella spacing" is proposed, which provides a quantitative basis for insulator structure optimization by comparing the changes of electric field and creepage distance under different parameter combinations. The differential influence mechanism of the pollution layer and water droplets on the electric field is revealed, which provides theoretical support for the formulation of a differential operation and maintenance strategy.

II. 3D Finite Element Calculation Model of Insulator

A. Establishment of Finite Element Simulation Model

According to the physical structure of a typical DC insulator [11], a 3D simulation model including mandrel, umbrella skirt, fittings, equalizing ring, and air field is built by using finite element technology, as shown in Fig. 1. In the model, the high voltage terminal is connected to the conductor and DC voltage is applied. The low-voltage terminal is connected to the beam and set to zero potential. To give consideration to both calculation accuracy and efficiency, the model is reasonably simplified: considering the electric field on the surface of the focused insulator, the electric field distribution of the transmission line is mainly concentrated on the conductor itself, so the influence of the transmission line is ignored, and the umbrella skirt is simulated with silicone rubber material. A coaxial cylindrical air field is set on the periphery of the insulator, and the boundary is set to the far-field condition, which simulates the infinite electric field environment and avoids the interference of boundary reflection on the calculations [7].

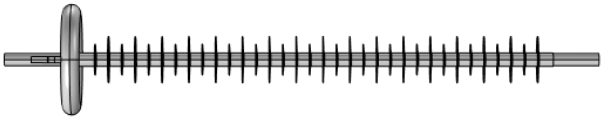


Fig. 1. 3D simulation model of insulator

B. Material Parameters and Boundary Conditions

The dielectric constant and conductivity of each material in the model are set according to the actual engineering parameters, as shown in TABLE. 1. Among them, for the setting of surface state, the polluted layer is simulated by the model with equivalent dielectric constant of 2.8 and conductivity of 1×10^{-11} S/m, and the water droplets are simulated by the parameters with dielectric constant of 81 and conductivity of 0.03 s/m to reflect the characteristics of wet environment [8]. The boundary conditions are set as follows: DC voltages of 110 kV, 220 kV, and 500 kV are applied to the high-voltage terminal, and the low-voltage terminal is grounded, which is set to 0; The outer boundary of the airfield is set to zero charge condition, and the surface of the insulator is set to continuous boundary.

TABLE I. Properties of Structural Materials of Insulators

Material	Dielectric coefficient	Electrical conductivity(S/m)
Air	1.0	1×10^{-30}
Umbrella skirt	3	1×10^{-12}
Core rod	6	1×10^{-12}
Armour clamp	10^{11}	5.998×10^{7}
Equalizing ring	10^{12}	1×10^{8}
Dirt	2.8	1×10^{-11}
Water droplet	81	0.03

C. Calculation of Electric Field and Potential

The distribution of the electrostatic field is solved based on the following equation [12]:

$$\oint_S D \cdot dS = Q_{enc} \tag{1}$$

where D is the electric displacement vector, $D=\varepsilon E$, ε is the dielectric constant, E is the electric field strength, and Q_{enc} is the free charge surrounded by the closed surface S.

When DC voltage U is applied to the high voltage terminal of the insulator, in the simplified model, the relationship between electric field intensity E and voltage U can be expressed as:

$$E = \frac{U}{d} \tag{2}$$

where d is the equivalent insulation distance, indicating that the voltage level directly determines the magnitude of the electric field strength. The electric field strength can also be calculated by the negative gradient of potential:

$$E = -\nabla V \tag{3}$$

The magnitude of the potential gradient reflects the strength of the electric field, and the direction points to the direction where the potential decreases fastest.

III. Results and Discussion

In order to study the influence of different factors on the insulator surface, the analysis path shown in Fig. 2 is selected. This path extends from the high voltage end to the low voltage end along the insulator surface, which is used to extract and analyze the surface electric field intensity data efficiently.

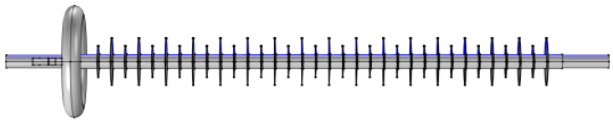


Fig. 2. Path Selection

In this study, three groups of simulation schemes are designed by using the control variable method to explore the influence of voltage level, structural parameters, and surface state, respectively.

A. Simulation Results of Different Voltage Levels

The structural parameters and surface cleanliness of insulators were determined, and DC voltages of 110 kV, 220 kV, and 500 kV were applied, respectively. By comparing and analyzing the distribution of field strength at different voltage levels, the correlation between voltage amplitude and field strength characteristics is quantified.

The potential distribution and electric field intensity distribution of the whole 3D model are simulated and calculated. The results show that the surface electric field intensity increases linearly with the increase of voltage level under the same insulator structure parameters. Fig. 3 and Fig. 4 show the typical electric field intensity and potential distribution nephograms at 110 kV, respectively. It can be seen that the insulator potential

decreases approximately linearly and uniformly along the electric field direction; The overall electric field distribution is relatively uniform, but the maximum electric field intensity is concentrated in the joint between the mandrel and the hardware, which is easy to cause electric field concentration due to the sudden change of geometric structure. The potential gradient and electric field intensity near the two ends of the insulator are relatively large, which accords with the basic principle of electrostatic field and verifies the rationality of the simulation results.

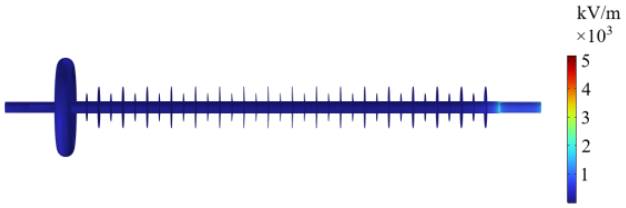


Fig. 3. 3D electric field simulation model of insulator

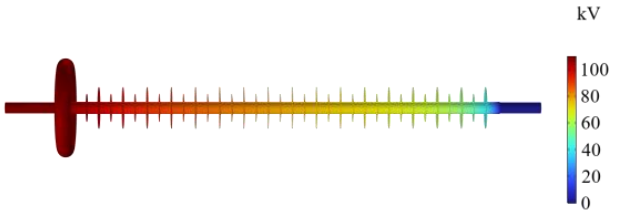


Fig. 4. 3D potential simulation model of insulator

Comparing the electric field distribution curves along the analysis path in Fig. 5 and Fig. 6, it can be seen that the corresponding electric field distribution patterns are highly similar under different voltage levels, and only the amplitude increases linearly with the increase of voltage. Specifically, the electric field intensity e and the applied voltage meet a strict linear proportional relationship. This law fully verifies the linear characteristics of the DC insulator system under the studied conditions. Based on this, the unit voltage method can be used to simplify the calculation of electric field analysis of insulators with different voltage levels: after accurately solving the electric field distribution under a certain reference voltage, the field intensity distribution of other voltage levels can be obtained by scaling.

The surface field strength of insulators is negatively correlated with insulation life. The higher the voltage level, the greater the rated surface field strength. High field strength will aggravate the migration of contaminated ions on the insulator surface, accelerate the leakage current and material corrosion, and thus shorten the insulation life. The data show that the maximum surface field strength of insulators at 500 kV is 12000 kV/m, which is 1.76 times higher than that at 4340 kV/m at 110 kV, and the aging risk is significantly increased. Therefore, for high voltage insulators such as 500 kV, it is necessary to shorten the aging detection period and find defects in time. At the same time, silicone rubber materials with better aging resistance should be selected to offset the life decay caused by high field strength through material performance optimization.

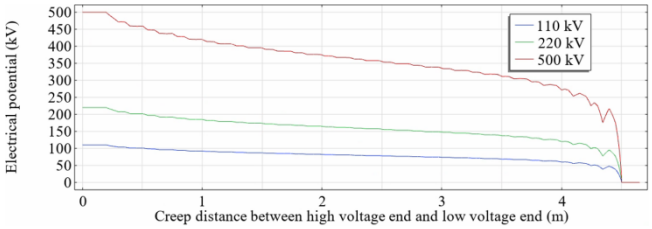


Fig. 5. Influence of different voltage levels on overall potential

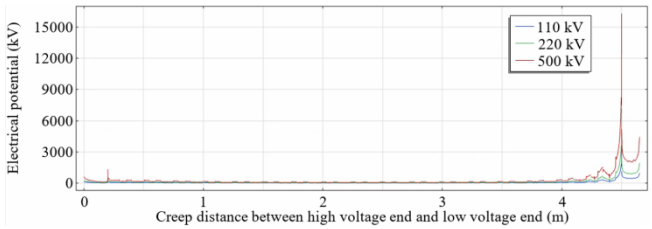
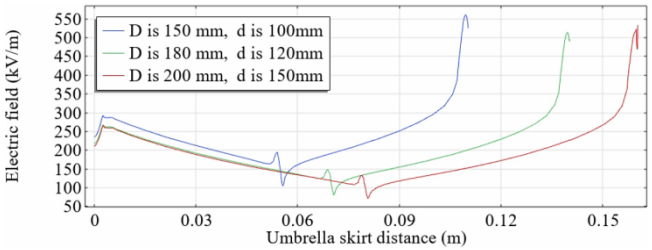


Fig. 6. Influence of different voltage levels on the overall electric field

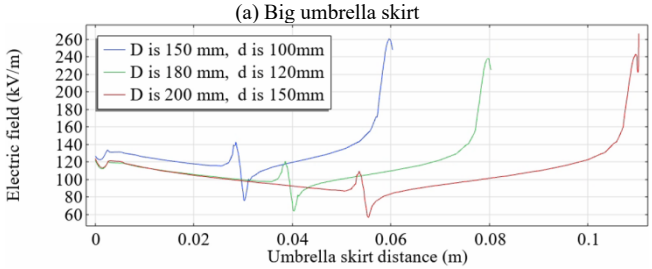
B. *Simulation Results of Different Insulator Structural Parameters*

Under a fixed voltage level of 110 kV and a clean surface, the influence of umbrella skirt diameter and umbrella spacing was studied.

The influence of umbrella skirt diameter: three diameter schemes are designed by adopting the alternating structure of a big umbrella skirt and a small umbrella skirt.



(a) Big umbrella skirt



(b) Small umbrella skirt

Fig. 7. Surface electric field of insulator at low voltage side under different umbrella skirt diameters

The simulation focuses on the influence of the structural parameters of the insulator. In the experiment, the fixed voltage level is 110 kV and the surface state is clean, and the variables are set to carry out the research: the first programme is that the big umbrella skirt is 150 mm and the small umbrella skirt is 100 mm; The second programme is that the big umbrella skirt is 180 mm and the small umbrella skirt is 120 mm; programme 3 is 200 mm for big umbrella skirt and 150 mm for small umbrella skirt. The distance between the big and small skirts is fixed at 44 mm.

The simulation results are shown in Fig. 7, taking the large and small umbrellas on the low-voltage side as examples. When the diameter of the big umbrella skirt is increased from 150 mm to 200 mm, the maximum field strength at the edge of the big umbrella skirt is reduced from 140.2 kV/mm to 110.1 kV/mm, which is 21.68%. This is because increasing the diameter of the umbrella skirt will increase the creepage distance and make the electric field distributed in a longer path, thus reducing the electric field intensity per unit length and reducing the local field intensity concentration. Although the materials are the same, the potential and electric field intensity at different nodes along the surface of insulators are significantly different, which shows that the surface geometry is the key factor to determine the distribution of electric field along the surface.

As shown in Fig. 8, as the diameter of the umbrella skirt increases from 150 mm to 200 mm, the creepage distance of the insulator also increases accordingly. This structural change realizes the remarkable optimization of the electric field distribution through multiple mechanisms: firstly, the larger umbrella skirt diameter expands the effective conductive area of the insulator surface, so that the electric field energy that might have been concentrated locally can be evenly dispersed along a longer surface path, which fundamentally avoids the excessive concentration of energy in local areas and lays the foundation for the reduction of the overall field strength. For the traditional electric field concentration area (which is easy to cause dense electric field lines due to the sudden change of geometric structure), the "aggregation effect" of electric field lines is obviously weakened after the creepage distance increases, and its electric field intensity is reduced from 3560 kV/m to 2680 kV/m, with a decrease of 24.7%. At the same time, the increase of the creepage distance is equivalent to prolonging the "discharge path" of the electric field, which directly reduces the average electric field intensity per unit length, and makes the average electric field intensity of the insulator decrease from 59.464 kV/m to 44.087 kV/m, with a decrease of 25.9%. This result fully shows that increasing the diameter of the umbrella skirt can effectively improve the electric field characteristics of key areas and the whole insulator and reduce the risk of insulation failure by optimizing the electric field energy distribution and path length.

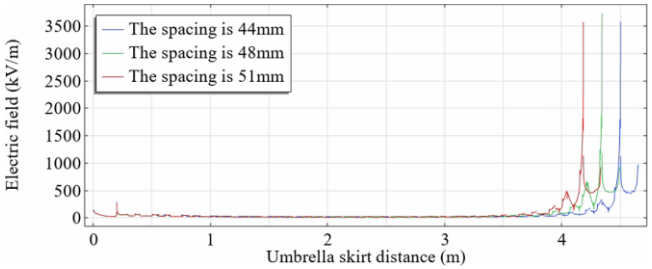
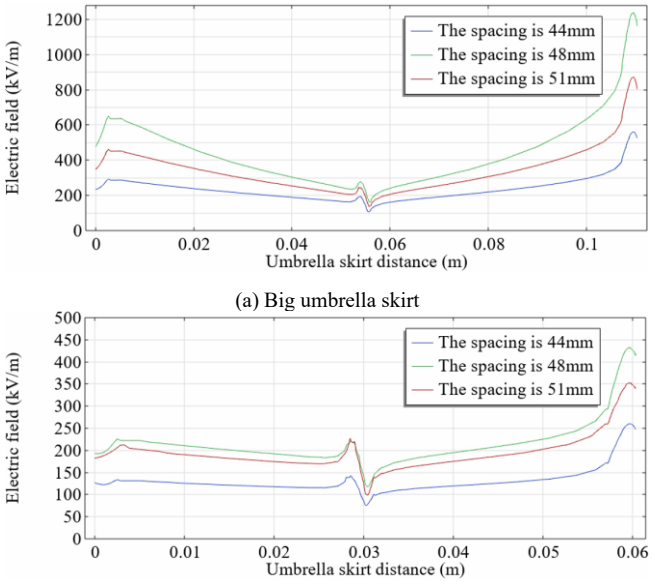


Fig. 8. Electric field distribution on creepage distance from high voltage side to low voltage side under different diameters of umbrella skirt

Considering the effect of the change of umbrella skirt spacing on the surface electric field of insulators, two additional research schemes are designed in this study. In the scheme, the basic parameter configuration is defined first: the diameter of the big umbrella skirt is 150 mm, and the diameter of the small umbrella skirt is 100 mm. On this premise, two limiting indices are set. The fourth programme has a spacing of 48 mm, and the fifth programme has a spacing of 51 mm. The simulation results are shown in Fig. 9. Taking the big and small umbrella skirts on the low-voltage side as an example, the umbrella spacing has a significant influence on the electric field distribution, especially the field strength between the umbrella skirts and the edge of the umbrella skirt. Under the condition of the same insulator length, increasing the distance between umbrella skirts will reduce the creepage distance and the number of umbrella skirts, which will make the electric field distributed in a shorter path, and then lead to the enhancement of the surface electric field. Therefore, properly reducing the spacing and increasing the number of umbrella skirts can increase the path of electric field distribution, disperse the intensity of the electric field, and improve the surface electric field.



(a) Big umbrella skirt

(b) Small umbrella skirt

Fig. 9. Electric field on the surface of low voltage side umbrella skirt under different spacing of insulator size umbrella skirt

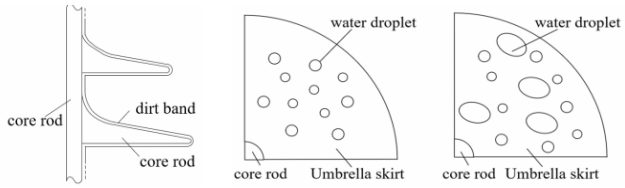
At the same time, reducing the intensity of the local electric field can improve the flashover voltage of insulators in operation, thus significantly reducing the risk of line tripping. At the same time, increasing the creepage distance reduces the surface leakage current, which helps to delay the thermal aging of insulators. In addition, when the distance between umbrellas is reduced from 51 mm to 44 mm, the increased number of umbrellas prolongs the distribution path of the electric field, which can increase the pollution lightning voltage by more than 15%. This design is especially suitable for selecting insulators in heavily polluted industrial areas.

C. Simulation Results of Different Surface States

With a fixed voltage level of 110kV and the structural parameters of insulators unchanged, as shown in Fig. 10, four typical surface states are simulated: (a) clean state; (b) Uniform pollution coverage, with a pollution layer thickness of 1 mm; (c) a small amount of water droplets adhere; (d) a large number of water droplets are attached. The fixed pollution thickness of 1 mm is adopted according to the typical pollution level in the actual environment. Although it may not capture all the changes

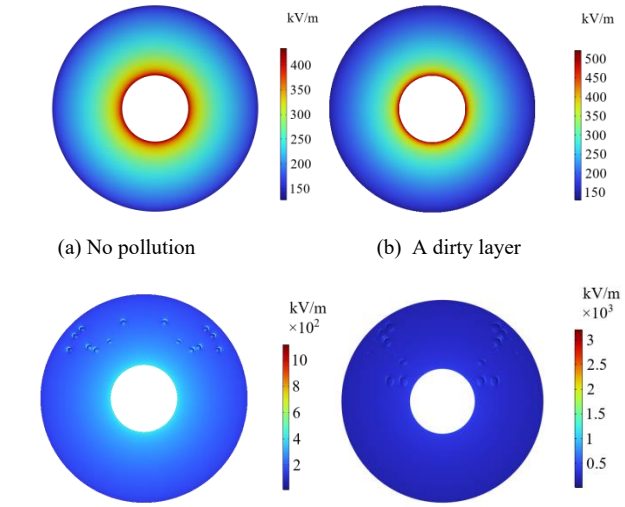
in the real world, it provides a representative baseline for comparing the relative impact of pollution. By comparing and analyzing the characteristics of field strength distortion, the influence mechanism of the surface state is clear.

The fixed voltage level is 110 kV, and the structural parameters of insulators are unchanged. The distortion effect of field strength is explored by simulating four typical surface states: clean state, polluted cover state, small amount of water droplets attached state, and large amount of water droplets attached state. The typical surface states involved in the experiment are as shown in Fig. 10: (a) covered with dirt, (b) covered with a small amount of water droplets, and (c) covered with a large amount of water droplets. By comparing and analyzing the characteristics of field intensity distortion in different states, the influence mechanism of surface states on the electric field characteristics of insulators is clarified.



(a) Contaminated layer (b) Small water droplets (c) Large water droplets

Fig. 10. Different surface States of umbrella skirts



(a) No pollution (b) A dirty layer

(c) Small number of water droplets (d) Large number of water droplets

Fig. 11. Surface electric field distribution of large umbrella skirt at low pressure side under different surface conditions

As shown in Fig. 11, the electric field distribution under different surface conditions is simulated by taking the large umbrella skirt on the low-voltage side as an example. The electric field distribution in the clean state is relatively uniform, and the maximum field strength appears at the junction of the umbrella skirt and the mandrel, about 434 kV/m; The increase of contaminated layer leads to the increase of surface conductivity, which is because the conductivity of the contaminated layer is higher than that of the insulator itself, making it easier for current to flow on the surface, which in turn leads to the increase of overall surface field strength. The maximum field strength is still at the junction of umbrella skirt and mandrel, but the value rises to about 525 kV/m; In the state of a small amount of water droplets, the dielectric constant of water droplets is much larger than that of insulators and air, which will lead to the concentration of electric field lines to water droplets, causing obvious local electric field distortion, and the maximum field strength will transfer to the contact edge between water droplets and the umbrella skirt; When there are a large number of water droplets, with the increase of the number of water droplets, more electric field lines gather at the edge of water droplets, and the local field strength distortion is more obvious, and the peak value of field strength further increases. Surface contamination mainly leads to an increase in the overall field strength level. However, the adhesion of water droplets mainly causes strong local electric field concentration distortion, and the degree of distortion increases with the increase of water droplets, which significantly increases the risk of partial discharge and flashover.

IV. Conclusion

Based on the finite element simulation technology, this paper systematically studies the influence of voltage level, structural parameters, and surface state on the surface electric field intensity distribution of high voltage DC insulators, and draws the following main conclusions. And draw the following main conclusions.

(1) The surface electric field intensity is in strict linear proportion to the applied voltage. The increase in voltage level not only linearly increases the amplitude of surface field strength, but also objectively aggravates the potential insulation risk due to the increase in absolute value. Therefore, in insulator design, it is necessary to calculate the surface field strength threshold in linear proportion according to the target voltage level to avoid insulation failure caused by excessive field strength; In the testing process, the field strength distribution test and insulation withstand voltage test under different voltages should be carried out to ensure that the insulators are suitable for the operation requirements of voltage levels.

(2) The diameter of the umbrella skirt and the distance between umbrellas are the key structural parameters to control the electric field distribution. Increasing the radius of the umbrella skirt will increase the creepage distance, effectively reduce the maximum field strength at the edge of the umbrella skirt, and improve the uniformity of the electric field distribution. Appropriately reducing the umbrella spacing and increasing the number of umbrella skirts will help to improve the surface electric field and achieve the best field strength distribution. This points out the direction for the optimal design of insulator structure: in the design, the electric field distribution can be optimized by increasing the radius of umbrella skirts, reasonably reducing the distance between umbrellas and increasing the number of umbrella skirts; When testing, we should focus on the surface field strength distribution data under different umbrella skirt parameter combinations, establish the corresponding relationship between structural parameters and field strength performance, and provide testing basis for the selection of optimal structural scheme..

(3) The surface pollution layer usually improves the overall electric field intensity level of the insulator surface. The adhesion of water droplets leads to serious distortion and

concentration of the local electric field, and the point of maximum field strength moves to the edge of the water droplets, and the peak field strength increases significantly with the increase in water droplets. This discovery requires that the future insulator design should strengthen the antifouling and hydrophobic properties, such as adopting a new antifouling coating or optimizing the shape of the umbrella skirt to reduce the adhesion of pollutants and water droplets. In the test system, it is necessary to add the polluted environment simulation test and the electric field distribution test under the state of water droplet attachment to verify the electric field stability and insulation reliability of insulators under complex working conditions.

ACKNOWLEDGMENT

This work was supported by the National Natural Science Foundation of China (Grant No. 52407011).

REFERENCES

[1] H. Liu., “Innovative practice of ±1100kV UHVDC transmission project,” Journal of China Electrical Engineering,” vol. 40, no. 23, pp. 7782-7792, 2020.

[2] L. Cui., M. Ramesh, “Prediction of flashover voltage using electric field measurement on clean and polluted insulators,” International Journal of Electrical Power & Energy Systems, vol. 116, pp. 105574, March 2020.

[3] C. Liu, Y. Wu, J. Liu, et al, “Insulator faults detection in aerial images from high-voltage transmission lines based on deep learning model,” Applied Sciences, vol. 11, no. 10, pp. 4647, May 2021.

[4] S. Ji., Y. Jia, Y. Xu, et al, “A method for measuring electric field distribution along insulator surfaces based on electroluminescence effect and its image processing algorithm,” IEEE Transactions on Dielectrics and Electrical Insulation, vol. 29, no. 3, pp. 939-947, April 2022,

[5] A. Salem, R. Abd-Rahman, W. Rahiman, et al, “Pollution flashover under different contamination profiles on high voltage insulator: Numerical and experiment investigation,” IEEE Access, vol. 9, pp.37800-37812, March 2021.

[6] S.Mohammadnabi, K.Rahmani. "Influence of humidity and contamination on the leakage current of 230-kV composite insulator," Electric Power Systems Research, vol. 194, pp. 107083, May 2021.

[7] S. M. El-Refaie, Abd Elrahman, M. K. Mohamed, “Electric field distribution of optimized composite insulator profiles under different pollution conditions,” Ain Shams Engineering Journal, vol. 9, no. 4, pp. 1349-1356, December 2018.

[8] J. Mahmoodi, M. Mirzaie, A.A. Shayegani-Akmal, “Surface charge distribution analysis of polymeric insulator under AC and DC voltage based on numerical and experimental tests,” International Journal of Electrical Power & Energy Systems, vol. 105, pp. 283-296, 2019.

[9] Z. Zhang, J. zhao, D. zhang, et al, “Study on the dc flashover performance of standard suspension insulator with ring-shaped non-uniform pollution,” High Voltage, vol. 3, no. 2, pp. 133-139, June 2018.

[10] A. Mohammed, L.Jeff , M.William, “New experimental study on the DC flashover voltage of polymer insulators: combined effect of surface charges and air humidity,” High Voltage, vol. 4, no. 4, pp. 316-323, October 2019.

[11] H. Benguesmia, N. M’ziou, A. Boubakeur, “Simulation of the potential and electric field distribution on high voltage insulator using the finite element method,” Diagnostyka, vol.19, no. 2, pp. 41-52, 2018.

[12] W. Du, X. Yu, Y. Wang, et al, “Study on spatial electric field distribution characteristics of composite insulators under different surface conditions,” Automation and Instrumentation, vol. 10, pp. 110-114, 2024.

Anfis-Based Insulation Condition Diagnosis for Power Capacitors Using Secondary Side Information

Yanlong ZHAO
State Grid Zibo Power Supply Company
Ylzhao_sjtu@163.com

Xuanyang LIU
State Grid Zibo Power Supply Company
654361102@qq.com

Zihao LI
State Grid Zibo Power Supply Company
877719314@qq.com

Fei LI
State Grid Zibo Power Supply Company
stategrid888@163.com

Weichen YAN
College of Intelligent Manufacturing
Zibo Polytechnic University
ywc859955132@126.com

***Abstract*—To facilitate the realization of the 30·60 Dual Carbon Objectives, China is expediting the establishment of a new-type power system, with AI-enhanced intelligent monitoring of grid equipment being one of the key priorities. Aiming to overcome the limitations of conventional power capacitor fault diagnosis methods that either require power outages or rely heavily on empirical judgments, this study presents a diagnostic method for power capacitor insulation defects by analyzing secondary-side parameters including resistive current, capacitance, and dielectric loss using ANFIS to evaluate both moisture ingress and aging degradation levels. The training dataset, consisting of actual defect characteristics obtained from online monitoring and outage tests, demonstrates good agreement between ANFIS outputs and real insulation conditions, confirming the method's diagnostic accuracy. The proposed approach has been successfully implemented in practical operations at State Grid Zibo Power Supply Company, providing valuable reference for online monitoring and fault diagnosis of power equipment.**

Keywords—Second-side information; power capacitor; ANFIS; insulation defects

I. INTRODUCTION

Power capacitors are widely used for reactive power compensation and filtering in power systems. During operation, they gradually age under the long-term effect of operating voltage and current, and sometimes discharge due to overvoltage [1]. Common abnormal phenomena of capacitors include external fuse blowing, internal fuse blowing caused by internal component breakdown, and bulging caused by internal overheating (which may be caused by dielectric aging or capacitor component breakdown without internal fuse blowing). All these will be reflected in changes in capacitor capacitance or dielectric loss angle. The dielectric loss angle reflects the active power loss caused by insulation aging or discharge of power capacitors. The method of periodic preventive offline testing for capacitors has a long cycle, low applied voltage, and inconsistent test conditions with operating status, making it difficult to reflect the real operating conditions under high voltage conditions [2]. Online monitoring of capacitor capacitance and dielectric loss angle can timely detect capacitor abnormalities or latent faults, thereby effectively preventing capacitor explosion. Current research on online monitoring of capacitors mainly focuses on the monitoring of leakage current on the grounding side of capacitors and the measurement and calculation of dielectric loss angle.

China's installed capacity of reactive power compensation devices has reached nearly 1 billion kvar, with shunt capacitor banks constituting the majority. While these capacitor installations play crucial roles in maintaining power system stability [3], improving power quality, reducing grid losses, and enhancing transmission capacity [4], insufficient attention to refined operation and maintenance has led to high failure rates of power capacitors during operation [5]. The non-repairable nature of these failures and the overall low utilization rate of capacitor equipment have become persistent challenges in the power industry. Current diagnostic methods for power capacitor insulation defects primarily rely on online monitoring and outage testing. While online monitoring enables real-time data acquisition during operation, its diagnostic accuracy largely depends on empirical judgments, often leading to misidentification and missed detection of insulation faults. Conversely, conventional outage testing, though widely adopted as a standard detection approach, inevitably reduces equipment utilization rates and incurs significant labor and financial costs due to necessary power interruptions.

To address these limitations, this study proposes an enhanced online monitoring method utilizing secondary-side measurements combined with an Adaptive Neuro-Fuzzy Inference System (ANFIS) to improve the diagnostic accuracy of power capacitor insulation defects. The proposed approach is trained using actual defect data obtained from both online monitoring and outage tests, with its effectiveness validated through comparative analysis between ANFIS outputs and real insulation conditions.

Funding Project:
Group Innovation Fund of Zibo Power Supply Company, State Grid Shandong Electric Power Company (2022Q2)

979-8-3315-5472-9/25/$31.00 ©2025 IEEE

II. METHODOLOGIES

A. Principle of ANFIS

In order to diagnose the insulation state of power capacitors, this paper applies the Adaptive Network-based Fuzzy Inference System (ANFIS) to the insulation state diagnosis of power capacitors. It gives full play to the advantages of fuzzy logic and neural networks, and improves the reliability and adaptability of the insulation state diagnosis of power capacitors. The ANFIS primarily employs the Takagi-Sugeno (T-S) fuzzy model [6], and its classic two-input single-output structure is illustrated in Fig. 1.

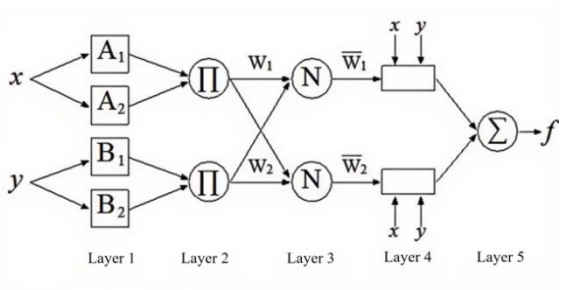


Fig. 1. ANFIS model structure

(1): Layer 1: Fuzzification Layer (Input Variable Layer)

The first layer is the fuzzification layer, where A_i and B_i correspond to the fuzzy sets of the input variables. The nodes in this layer are adaptive, and their outputs represent the membership degrees of the input variables. The output can be expressed as Eq. (1):

$$\begin{cases} O_{1i} = \mu_{A_i}(x) \\ O_{2i} = \mu_{B_i}(y) \end{cases} \tag{1}$$

Where i=1,2 and O_{1i} and O_{2i} denote the membership degrees of the fuzzy sets; and μ is the membership function (MF). The selection of the MF determines the premise parameters. In this study, the Gaussian function is adopted as the MF, defined in Eq. (2):

$$\mu_{\text{Gauss}i} = \exp\left(-\left(\frac{x-c_i}{a_i}\right)^2\right) \tag{2}$$

Where, a_i and c_i are the premise parameters, which determine the shape of the MF.

(2): Layer 2: Rule Inference Layer (Firing Strength Layer)

The second layer computes the firing strength of each fuzzy rule, denoted by the **Π** operator in the structure. The output of each node represents the firing strength of a rule in Eq. (3):

$$w_i = \mu_{A_i}(x)\,\mu_{B_i}(y) \tag{3}$$

Where i = 1, 2, and w_i is the firing strength.

(3): Layer 3: Normalization Layer

The third layer normalizes the firing strengths of all rules, represented by N in the structure. The normalized firing strength is computed as Eq. (4):

$$\bar{w}_i = w_i \Big/ \sum_i w_i \tag{4}$$

Where i=1,2, and $\bar{w}_i$ is the normalized firing strength.

(4): Layer 4: Defuzzification Layer (Consequent Layer)

The fourth layer computes the output of each rule based on the normalized firing strengths denoted by Eq.(5).

$$O_{4i} = \bar{w}_i f_i = \bar{w}_i\left(p_i x + q_i y + r_i\right) \tag{5}$$

Where i=1,2; p_i, q_i and r_i are the consequent parameters; and O_{4i} is the output signal.

(5): Layer 5: Output Layer (Aggregation Layer)

The fifth layer aggregates all defuzzified outputs into the final system output, represented by a fixed node in the structure:

$$f = \sum \bar{w}_i f_i = \frac{\sum w_i f_i}{\sum w_i} \tag{6}$$

Where i=1,2; f is the total system output; and f_i is the output of the i-th rule.

B. Insulation Defect Feature

Main insulation defect features are: ①Resistive component of current I_R,②Dielectric loss tan δ and ③Capacitance C.

The procedure for deriving insulation defect features from secondary-side measurements is outlined below.

(1)The secondary voltage signal U is obtained from the voltage transformer (TV) connected to the power capacitor.

(2)The operating voltage U_c of the power capacitor is calculated using Eq. (7).

$$U_C = \frac{U}{1-\beta} \tag{7}$$

Where, U is secondary voltage signal; U_c is operating voltage; β is reactor ratio.

(3) The current signal I is acquired from the current transformer (TA) connected to the power capacitor.

(4) The current signal I from the TA is subjected to Fourier transform (FT) to derive the resistive current I_r and the capacitive current I_c.

(5)The dielectric loss tanδ is calculated in Eq. (8), using the capacitive current I_c and resistive current I_r obtained through Fourier transform.

$$\tan\delta = \frac{I_R}{I_C} = \frac{1}{2\pi f\left(\varepsilon\frac{S}{d}\right)\bullet\left(\rho\frac{d}{S}\right)} = \frac{1}{2\pi f\varepsilon\rho} \tag{8}$$

(6)The active power P of the power capacitor circuit is computed using Eq. (9).

$$P = I_r \times U \tag{9}$$

(7)The capacitance C of the power capacitor is determined by applying Eq. (10).

$$C = \frac{P}{\omega \times U_C^2 \times \tan\delta} \tag{10}$$

Where, ω is angular frequency.

III. Results and Analysis

A. Training of ANFIS

This study selects a 10 kV capacitor bank (Model: BFM11/√3-334-1W) in operation at a substation of State Grid Zibo Power Supply Company as the research subject. The original dataset is constructed based on the actual insulation condition of power capacitors, derived from both real-time measurement data acquired by online monitoring devices and field outage test data. From the original dataset, 48 representative samples were extracted for training purposes. The moisture level and aging level of the 48 samples is shown in Tab. 1.

TABLE I. The Moisture Level and Aging Level of the Training Samples

Moisture level	No. of samples	Aging level	No. of samples
0	12	0	10
1	12	1	13
2	12	2	14
3	12	3	11

According to the above calculation steps, training error curve of ANFIS is shown in Fig.2.

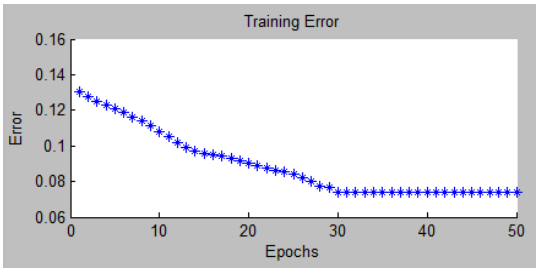


Fig. 2. Training error curve of ANFIS

As shown in Fig. 2, the ANFIS achieves an error reduction to 0.075 after approximately 30 training epochs, demonstrating significant performance advantages for real-time insulation condition diagnosis.The comparison between the ANFIS output and the actual moisture level are presented in Fig. 3.

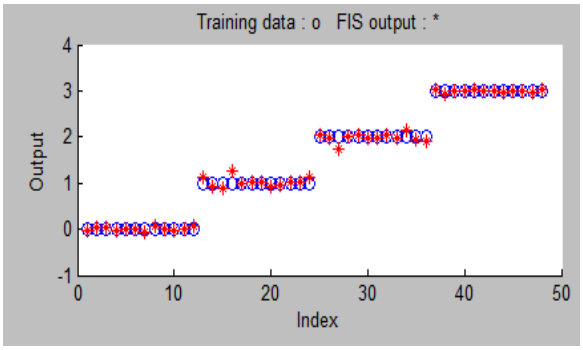


Fig. 3. ANFIS output and the actual moisture level

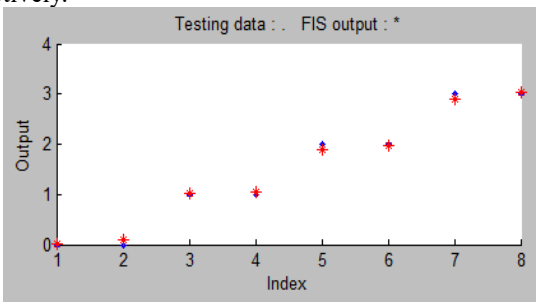
B. Test of ANFIS

8 representative datasets were selected as test samples, with detailed specifications provided in Tab. 2.

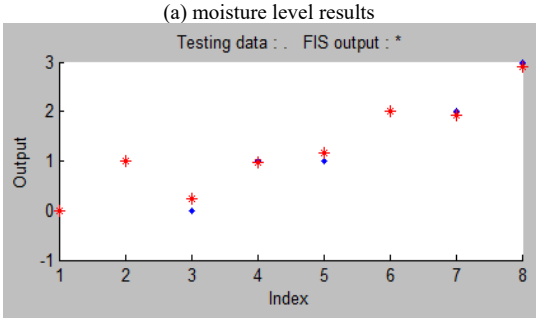
TABLE II. Samples Used in the Test

No.	C/μF	tanδ/%	I_R/mA	moisture level	aging level
1	26.36	0.030	15.77	0	0
2	26.44	0.036	18.99	0	1
3	26.65	0.032	17.01	1	0
4	26.71	0.035	18.65	1	1
5	26.85	0.037	19.82	2	1
6	26.84	0.042	22.47	2	2
7	27.09	0.039	21.08	3	2
8	27.16	0.045	24.38	3	3

The samples from Tab.2 were used to evaluate both moisture levels and aging levels of power capacitor insulation in the ANFIS, with the corresponding test results illustrated in Fig. 4, respectively.



(a) moisture level results



(b) aging level results

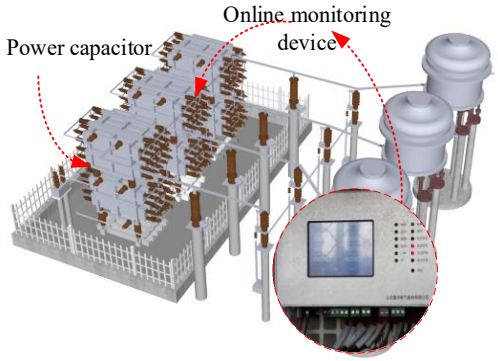
Fig. 4. Test results of moisture level and aging level in samples

The ANFIS-derived moisture ingress levels and aging degradation levels of the power capacitors demonstrate strong agreement with the actual insulation defects, confirming the system's diagnostic accuracy for both moisture and aging insulation defect in the test samples.

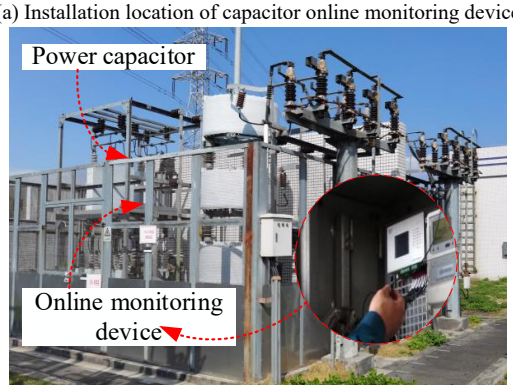
C. Comparison of Methods

Currently, some online monitoring systems for shunt capacitors in substations monitor the ground current of capacitors, which cannot monitor the working conditions of individual capacitors. Although some systems can monitor the current and voltage parameters of individual capacitors, they

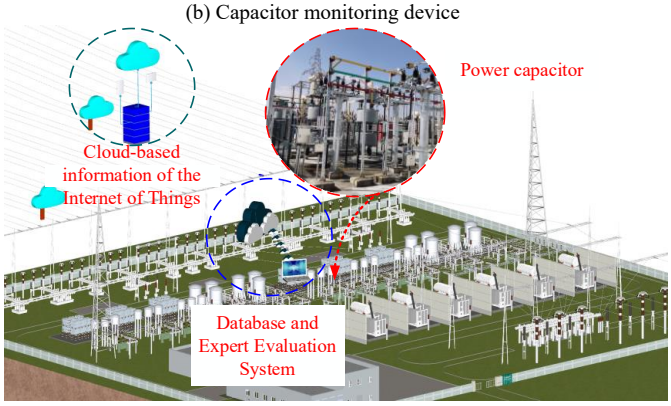
require both current and voltage signals of the capacitors to be transmitted to the monitoring unit through signal lines, resulting in numerous leads and complex wiring. In some systems, the capacitor monitoring device is at high potential, and the capacitor current signal needs to be measured through an optical current transformer or transmitted via optical fiber, resulting in poor technical and economic efficiency. This paper realizes the online monitoring and fault analysis of substation power capacitors based on IoT technology, and the practical application project is shown in Fig. 5.



(a) Installation location of capacitor online monitoring device



(b) Capacitor monitoring device



(c) Internet of things of monitoring device

Fig. 5. On-line monitoring site of power capacitors

IoT technology can realize remote monitoring and control of equipment through remote monitoring technology, timely detect equipment failures, and perform remote maintenance and management, improving equipment operational efficiency. Through remote monitoring technology, power capacitors can achieve remote monitoring and control, thereby realizing intelligent management of the equipment. At the same time, remote monitoring technology can improve the operational efficiency and reliability of equipment and reduce the possibility of equipment failures. As shown in Figure 6, the power capacitor online monitoring system transmits data through IoT and cloud databases, and uses wireless communication between capacitor monitoring points, avoiding insulation problems between high and low voltage systems, and featuring flexible networking, simple installation and easy expansion.

To objectively evaluate the accuracy of the proposed method, it is compared with the approaches presented in references [8] and [9], as summarized in Tab. 3.

TABLE III. ACCURACY COMPARISON WITH LITERATURE

Data source	Method	Accuracy/%
Shiue-Der Lu , et al [8]	PNN	95%
	ENN	82%
	Extension theory	80%
	LVQ	78%
	BPN	72%
Xiangbing Zhao, et al[9]	SVM	91.43%
	DBN	94.83%
Proposed method		90-95%

As can be seen from Tab. 3, the proposed method achieves satisfactory accuracy and can be considered an effective approach.

IV. CONCLUSION

This study proposes a novel insulation defect diagnosis method for power capacitors based on secondary-side information. The approach utilizes resistive current I_R, capacitance C, and dielectric loss tanδ as insulation defect feature, employing ANFIS to simultaneously assess both moisture ingress levels and aging degradation.

The training dataset, consisting of actual defects obtained from online monitoring and outage tests, demonstrates good agreement between ANFIS outputs and real insulation conditions, confirming the method's diagnostic accuracy.

The proposed approach has been successfully implemented in practical operations at State Grid Zibo Power Supply Company, providing valuable reference for online monitoring and fault diagnosis of power equipment.

REFERENCES

[1] Kumar N, Prakash C, Grebennikov A, et al. High-efficiency broadband parallel-circuit class E RF power amplifier with reactance-compensation technique[J]. IEEE Transactions on Microwave Theory and Techniques, 2008, 56(3): 604-612.

[2] Xu H, Zhang X, Liu F, et al. A reactive power sharing strategy of VSG based on virtual capacitor algorithm[J]. IEEE Transactions on Industrial Electronics, 2017, 64(9): 7520-7531.

[3] Xue Y, Zhang X P. Reactive power and AC voltage control of LCC HVDC system with controllable capacitors[J]. IEEE transactions on power systems, 2016, 32(1): 753-764.

[4] Bisanovic S, Hajro M, Samardzic M. One approach for reactive power control of capacitor banks in distribution and industrial networks[J]. International Journal of Electrical Power & Energy Systems, 2014, 60: 67-73.

[5] Miao Y, Cheng H. An optimal reactive power control strategy for UHVAC/DC hybrid system in east China grid[J]. IEEE Transactions on smart grid, 2014, 7(1): 392-399.

[6] Qin W, Wang P, Han X, et al. Reactive power aspects in reliability assessment of power systems[J]. IEEE Transactions on Power Systems, 2010, 26(1): 85-92.

[7] Zhao J, Wang L, He X, et al. Substation Reactive Power Optimization Considering Capacitor Operation Regulation Cost[C]//2024 4th International Conference on Intelligent Power and Systems (ICIPS). IEEE, 2024: 59-62.

[8] Lu S-D, Sian H-W, WangM-H, Kuo C-C. Fault diagnosis of power capacitorsusing a convolutional neural network combined with thechaotic synchronisation method and the empirical modedecomposition method[J]. IET Sci Meas Technol. 2021;15:551–561.

[9] Zhao X, Zhang X, Ren P. Fault diagnosis and identification of power capacitor based on edge cloud computing and deep learning[J]. Mathematical Problems in Engineering, 2020, 2020(1): 3120805

Global Optimization of Micro-Meteorological Station Siting for Ultra-High-Voltage Transmission Lines

Qingtian Ge
The Ultra High Voltage Branch
Shanghai Electric Power Company
Shanghai, China
jingtian2812@163.com

Kai Yang
School of Electrical Engineering
Shanghai University of Electric Power
Shanghai, China
Yangk0524@163.com

Wenke Pan
The Ultra High Voltage Branch
Shanghai Electric Power Company
Shanghai, China
15621638899@163.com

Ye Feng
The Ultra High Voltage Branch
Shanghai Electric Power Company
Shanghai, China
m18521762101@163.com

Huayue Huang*
The Ultra High Voltage Branch
Shanghai University of Electric Power
Shanghai, China
huanghua.yue@163.com
*Corresponding author

Jiangjiao Xu
School of Electrical Engineering
Shanghai University of Electric Power
Shanghai, China
jiangjiao.xu@shiep.edu.cn

***Abstract*—Micro-meteorological monitoring along ultra-high-voltage (UHV) transmission corridors is crucial for risk-aware operation, but limited station counts and uneven layouts create a persistent accuracy–cost trade-off. Empirical spacing rules secure coverage yet do not guarantee reconstruction accuracy in complex terrain, whereas optimization-based siting often lacks an interpretable sampling scale and a unified evaluation. We present a physics- and data-driven framework that couples an empirically estimated correlation scale with constrained global optimization, semivariograms from historical records define a maximum inter-station spacing used as a hard coverage constraint, then a genetic algorithm minimizes weighted-interpolation error subject to right-of-way, accessibility, and minimum-separation constraints and is benchmarked under a unified protocol against uniform and terrain-weighted layouts. In a real UHV corridor, the framework achieves full coverage with a maximum spacing of about 8 km and reduces wind-speed reconstruction error relative to uniform placement—RMSE from 2.41 to 2.10 m/s , MAE from 2.14 to 1.88 m/s , and MAPE from 26.93% to 23.82% —while improving network compactness. By linking an interpretable correlation scale with global optimization, the approach provides a practical basis for planning, staged densification, and rapid emergency deployment of corridor monitoring networks.**

***Index Terms*—Ultra-high-voltage (UHV) transmission; micro-meteorological monitoring; optimal station placement; maximum station spacing; genetic algorithm (GA).**

I. Introduction

In the context of the national dual-carbon goals and the ongoing energy transition, the high penetration of renewable generation and large cross-regional power transfers, together with the rising frequency of extreme weather, these have markedly increased the power system's sensitivity to meteorological uncertainty [1]. Transmission corridors have therefore become focal assets for risk exposure assessment and resilience enhancement. With the rapid deployment of new-type power systems and ultra-high-voltage (UHV) long-distance transmission, ensuring the safety and resilience of corridors under extreme events and local micro-meteorological disturbances has emerged as a central operational concern. Deploying micro-meteorological monitoring systems along corridors enables timely detection of hazards such as strong winds and icing, thereby improving grid reliability and operational safety [2]. However, wind speed exhibits pronounced spatiotemporal variability, a limited number of stations cannot adequately characterize the regional wind field, and suboptimal station layouts lead to substantial interpolation errors. When official meteorological stations are sparse, both the number and spatial arrangement of stations strongly affect wind-speed interpolation accuracy. Uneven layouts can create local monitoring blind spots and amplify estimation errors [3].

Environmental monitoring network optimization broadly follows two methodological lines. First, empirical and geostatistical heuristics, stations are often placed uniformly or by proximity, prioritizing coverage over information gain [4]. Semivariograms are used to infer wind-field correlation scales and set upper bounds on inter-station spacing, yet such threshold-driven rules do not guarantee optimal interpolation accuracy and can degrade in complex terrain or strongly heterogeneous surface conditions [5]. Second, optimization-based formulations cast siting as a constrained combinatorial problem that minimizes a prescribed performance functional (e.g., interpolation error, coverage, cost) under engineering constraints. The problem is akin to optimal PMU placement, known to be NP-complete, and thus typically addressed with approximate algorithms. Recent work combines exact (mixed-

979-8-3315-5472-9/25/$31.00 ©2025 IEEE

integer) optimization with metaheuristics (genetic algorithms, particle swarm, simulated annealing) and related intelligent search for environmental sensing networks [6], but most ignore corridor-specific right-of-way or accessibility constraints, resulting in impractical layouts. In summary, empirical schemes are easy to deploy but under-exploit data value, whereas optimization-based approaches can deliver superior performance at the expense of computational burden and reliance on model priors. Consequently, objective definitions and constraint representations must be tailored to the application scenario to achieve balanced trade-offs [7].

To overcome the limitations of traditional approaches, recent research has advanced along two primary directions. First, multiobjective and intelligent optimization integrates error, cost, and coverage within a unified formulation and solves the siting problem using heuristic or intelligent algorithms (e.g., stepwise genetic algorithms for national air-quality network redesign that simultaneously reduce redundancy and improve coverage [8], and genetic programming in greenhouse microclimate settings that selects sensor locations and weights to approach dense-network accuracy with few sensors [9]), yet its high computational complexity and sensitivity to sparse corridor wind data make it hard to scale for large UHV corridors. Such methods coordinate competing objectives but often entail high computational complexity, sensitivity to data and hyperparameters, and limited interpretability. Second, physics-model fusion and surrogate modeling couple mechanistic simulations with search procedures or employ statistical emulators to accelerate optimization (e.g., chemical-transport–model-based network design that improves pollutant-field reconstruction accuracy [10], and kriging emulators enabling minute-scale, nationwide rain-gauge siting [11]), but mechanistic simulations are too slow for UHV corridor emergency station deployment, and surrogates poorly generalize across diverse corridor terrains. While these approaches offer stronger physical interpretability and numerical fidelity, they still face challenges in computational cost, surrogate generalization, and the explicit representation of engineering constraints.

With advances in sensing and artificial intelligence, increasingly sophisticated station–siting approaches are emerging. On one hand, deep integration of high-fidelity numerical simulation and intelligent optimization is gaining traction. Lang *et al.* [12] combine computational fluid dynamics (CFD), mixed-integer linear programming (MILP), and artificial neural networks (ANNs) for large-scale hazardous-gas monitoring, markedly improving source-localization accuracy and configuration efficiency. Araki *et al.* [13] couple a chemical transport model with a search algorithm to optimize air-monitoring networks, enhancing pollutant-field reconstruction accuracy and robustness. On the other hand, reinforcement learning and deep learning are explored for policy search in sensor-network configuration. Zhou *et al.* [14] employ a deep-RL framework based on graph convolutional networks (GCNs) and DDPG to solve optimal PMU placement, improving system observability and state estimation under complex operating conditions. Annoni *et al.* [15] propose sparse-sensor placement for wind-farm control, maintaining control performance while substantially reducing sensor count and deployment cost. They optimize for observability or windfarm control, not UHV micro-meteorological interpolation. At a more macroscopic level, multi-hazard integrated monitoring and systematized network design are advancing. Khan *et al.* [16] review IoT and emerging sensors for multi-risk early warning, summarizing progress in layout optimization and intelligent algorithms. Verghese and Nema [17] synthesize objective functions and constraint representations for air-quality monitoring networks, providing a structured basis for indicator systems and method selection across domains. While advancing physical-model coupling and intelligent decision-making, existing approaches remain hindered by implementation complexity, reliance on data and priors, and limited handling of engineering constraints—highlighting the need for a practical, interpretable, and transferable siting framework for UHV corridors.

To tackle the precision–cost trade-off, corridor constraints, and emergency needs, we propose an integrated UHV siting framework combining correlation thresholds, constrained global optimization, and unified evaluation. A semivariogram yields spacing limits for density planning, a genetic algorithm with penalties encodes ROW, accessibility, and safety constraints, and a deployment protocol balances coverage and uniformity, providing candidate sites and densification guidelines for routine and emergency rollouts.

The main contributions of this study are as follows:

- We propose a quantitative inter-station spacing method grounded in the wind field's statistical correlation structure, estimating the correlation range via a semivariogram and deriving a $d_{\max}$ threshold that provides a principled basis for network-density planning and blind-spot diagnosis, with block cross-validation and terrain-sensitivity analyses confirming robustness and interpretability.
- We develop a genetic-algorithm siting model that explicitly encodes corridor right-of-way limits, site accessibility, and minimum safety clearances, incorporates penalty and solution-repair mechanisms with adaptive crossover–mutation under a joint objective of error, coverage, and spatial uniformity, and conducts global search for feasible solutions while yielding deployable candidate sites and staged deployment guidance.
- In a real transmission-corridor case, the proposed approach reduces wind-field reconstruction error and improves coverage and spatial balance relative to uniform and terrain-weighted baselines, ablation studies identify the "correlation-threshold + constrained global optimization" coupling as the principal source of gains, and the framework transfers smoothly to temperature/humidity variables and corridors of differing geometry.

The rest of this paper is organized as follows. Section II introduces model. The experimental result is given in Section III. Finally, Section IV concludes this paper and threads a light on some potential future directions.

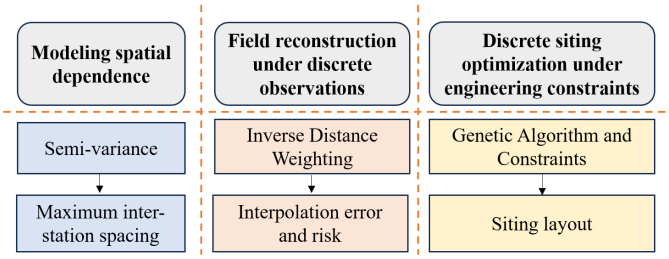


Fig. 1. Three-part overview—spatial dependence, reconstruction, and constrained siting.

II. Methods

The design of spatial observation networks and the reconstruction of field variables can be organized around three fundamental questions: (i) *modeling spatial dependence*, which characterizes the co-variation of the field with spatial lag and thereby yields a principled scale for sampling density [18]. (ii) *field reconstruction under discrete observations*, namely interpolation at unobserved locations using weighted-averaging schemes. and (iii) *discrete siting optimization under engineering constraints*, so as to obtain a network layout whose overall error is controllable under limited resources. To maintain notational consistency and transparency of reasoning, this section formalizes the canonical theoretical tools for each of the above problems [19]. A concise schematic of these relationships is shown in Fig. 1, where semivariance and the correlation length inform a maximum inter-station spacing, IDW-based reconstruction yields interpolation error/risk, and a GA under engineering constraints determines the siting layout. Details of every part will be introduced below.

A. Spatial Correlation and Semivariogram

Under the common assumptions of second-order stationarity and isotropy, the covariance of a scalar random field $Z(\mathbf{s})$ (e.g., wind speed) depends on the spatial lag vector $\mathbf{h}$ only through its Euclidean norm $h = \|\mathbf{h}\|_2$. The *theoretical semivariogram* is defined as

$$\gamma(h) \;=\; \tfrac{1}{2}\,\mathrm{Var}\big[\,Z(\mathbf{s}+\mathbf{h}) - Z(\mathbf{s})\,\big] \tag{1}$$

where $\gamma(h)$ denotes the semivariance at lag distance h and $\mathrm{Var}[\cdot]$ is the variance operator.

The corresponding *empirical semivariogram* (Matheron estimator) is:

$$\widehat{\gamma}(h) \;=\; \frac{1}{2\,|\Omega(h)|}\sum_{(i,j)\in\Omega(h)} \big(Z(\mathbf{s}_i) - Z(\mathbf{s}_j)\big)^2 \tag{2}$$

where $\Omega(h) = \{(i,j) : \|\mathbf{s}_i - \mathbf{s}_j\| \in [\,h-\Delta h,\; h+\Delta h\,]\}$ is the set of point pairs whose separation falls in the bin centered at h. $|\Omega(h)|$ is its cardinality, and Δh is the bin width.

To obtain a smooth and interpretable dependence structure, $\widehat{\gamma}(h)$ is typically fitted by a parametric model. A common choice is the *exponential* model:

$$\gamma_{\boldsymbol{\theta}}(h) \;=\; c_0 \;+\; c_1\Big(1 - e^{-h/a}\Big) \tag{3}$$

with parameter vector $\boldsymbol{\theta} = (c_0, c_1, a)$. Here c_0 is the *nugget* (microscale variability and measurement noise), c_1 is the *structured variance*, and $c_0 + c_1$ approximates the *sill*. The parameter $a > 0$ controls the correlation length. The associated correlation function is $\rho(h) = \exp(-h/a)$. Distances on the order of a provide a practical upper bound for sampling spacing, balancing information redundancy among neighboring samples and the reduction of interpolation variance. Analogous interpretations apply to the spherical and Gaussian models.

B. Inverse Distance Weighting (IDW)

Given discrete observations $\{(\mathbf{s}_i,\, Z(\mathbf{s}_i))\}_{i=1}^{n}$, the Shepard–type inverse distance weighting (IDW) estimator reconstructs the field at a query location $\mathbf{p}$ by a locally weighted average:

$$\widehat{Z}(\mathbf{p}) = \frac{\displaystyle\sum_{i\in\mathcal{N}(\mathbf{p})} w_i(\mathbf{p})\, Z(\mathbf{s}_i)}{\displaystyle\sum_{i\in\mathcal{N}(\mathbf{p})} w_i(\mathbf{p})}, \qquad w_i(\mathbf{p}) = \big(d(\mathbf{p},\mathbf{s}_i) + \varepsilon\big)^{-p} \tag{4}$$

Here, $\mathcal{N}(\mathbf{p})$ denotes the spatial neighborhood of $\mathbf{p}$ (e.g., k-nearest neighbors or a fixed-radius ball). $Z(\mathbf{s}_i)$ is the observation at site $\mathbf{s}_i$. $d(\mathbf{p},\mathbf{s}_i)$ is the Euclidean distance. $p > 0$ is the power parameter controlling the decay of weights with distance, and $\varepsilon \geq 0$ is a small regularization to avoid singularity when $\mathbf{p} = \mathbf{s}_i$. With normalized weights $\lambda_i(\mathbf{p}) = w_i(\mathbf{p}) / \sum_{j\in\mathcal{N}(\mathbf{p})} w_j(\mathbf{p})$, the estimator satisfies $\sum_i \lambda_i(\mathbf{p}) = 1$ and hence is a convex combination of local observations (boundedness). Exactness holds at data sites when $\varepsilon = 0$, i.e., $\widehat{Z}(\mathbf{s}_j) = Z(\mathbf{s}_j)$. Increasing p (or shrinking the neighborhood) yields a more local, higher-variance but lower-bias estimate, whereas decreasing p (or enlarging the neighborhood) produces a smoother, lower-variance but potentially higher-bias estimate, reflecting the classical bias–variance trade-off.

To encode directional dependence or corridor-like accessibility, the Euclidean distance in (4) can be replaced by an anisotropic metric:

$$d_M(\mathbf{p},\mathbf{s}_i) \;=\; \big\|\,M\big(\mathbf{p}-\mathbf{s}_i\big)\big\|_2 \qquad M \in \mathbb{R}^{2\times 2} \tag{5}$$

where d_M measures distance under the linear transformation M, enabling IDW to emphasize preferred directions or penalize cross-corridor movement. Geodesic distances on graphs may be used analogously when obstacles or terrain induce non-Euclidean accessibility.

C. Combinatorial Siting under Engineering Constraints with Genetic Algorithms (GA)

Given a set of candidates $\mathcal{S} = \{\mathbf{c}_1, \ldots, \mathbf{c}_M\}$ and an existing network $\mathcal{S}_0$, the siting task is cast as a constrained binary optimization. Let the decision vector $\mathbf{x} = (x_1, \ldots, x_M)^\top \in \{0,1\}^M$ indicate whether candidate $\mathbf{c}_i$ is selected ($x_i = 1$) or not ($x_i = 0$). Using a fixed interpolator to reconstruct the field

from the union of existing and newly selected sites, the risk functional is:

$$\min_{\mathbf{x}\in\{0,1\}^M} \mathcal{J}(\mathbf{x}) = \int_{\mathcal{D}} \left(\widehat{Z}_{\mathbf{x}}(\mathbf{u}) - Z(\mathbf{u})\right)^2 \mathrm{d}\mathbf{u} \quad (6)$$

where $\mathcal{D} \subset \mathbb{R}^2$ is the spatial domain of $Z(\mathbf{u})$ is the true (unknown) scalar field. $\widehat{Z}_{\mathbf{x}}(\mathbf{u})$ denotes the interpolated field obtained from $\mathcal{S}_0 \cup \{\mathbf{c}_i : x_i = 1\}$. and $\mathcal{X}$ is the feasible set encoding engineering constraints (e.g., a budget on the number of new sites, minimum separation from incumbents/infrastructure, and corridor accessibility). In computation, $\mathcal{J}(\mathbf{x})$ is evaluated via a discrete sum over a representative set of locations (and times, if applicable).

A genetic algorithm (GA) provides a practical metaheuristic for (6). Its core components include: *encoding* (binary string for $\mathbf{x}$), *fitness* (a monotone transform of $-\mathcal{J}$), *selection/crossover/mutation* operators, and *constraint handling* (feasibility repair or penalty). A common penalty formulation augments the objective by:

$$\widetilde{\mathcal{J}}(\mathbf{x}) = \mathcal{J}(\mathbf{x}) + \lambda\,\Psi(\mathbf{x}) \quad (7)$$

where $\lambda > 0$ is a penalty coefficient and $\Psi(\mathbf{x}) \geq 0$ measures the degree of constraint violation (e.g., cumulative shortfall of pairwise distances from a prescribed minimum, number of selections outside the accessible corridor, or excess over the site budget). This framework does not rely on convexity or differentiability and is therefore suitable for NP-hard combinatorial siting with appropriate operators and tuning, GA consistently yields high-quality solutions in engineering practice. The algorithm iteratively performs population initialization, penalized fitness evaluation, selection, crossover, mutation, and population update until the termination criterion is satisfied. A schematic of the GA iteration procedure is shown in Fig. 2.

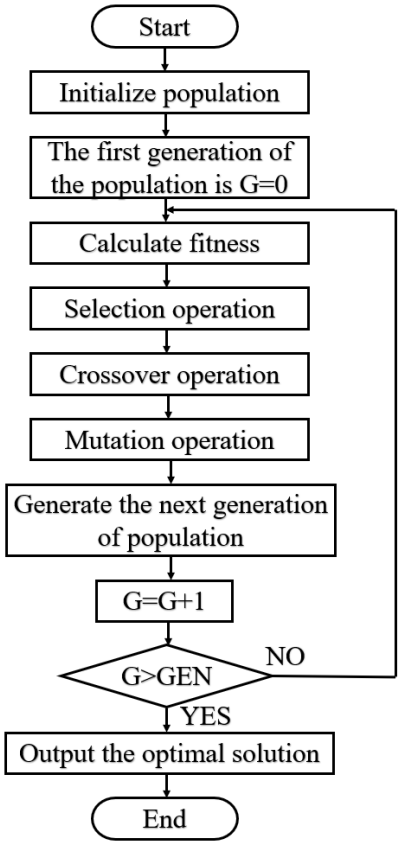


Fig. 2. Genetic algorithm (GA) iteration flowchart.

III. Experiments

This section provides an empirical evaluation of the proposed sensor-siting optimization for wind-speed sensing within transmission corridors. The experimental setting and data sources, configurations of existing and candidate stations, and the principal hyperparameters for the interpolation model and the optimizer are specified. Performance is quantified by MAE, RMSE, MAPE, Coverage@$d_{\max}$, and the average nearest-station distance. Results are benchmarked against representative siting strategies and are accompanied by diagnostic visualizations (composite metric curves, error as a function of nearest-station distance, and the resulting station layout).

A. Scenario & Dataset

An in-situ wind-speed dataset was collected along a transmission corridor of size 20×4 km^2 over a full diurnal cycle discretized into $T = 12$ time slices. Twelve incumbent stations, primarily aligned with the corridor centerline with small cross-track offsets, recorded wind-speed time series. After acquisition, quality control and harmonization were applied, including time synchronization, removal of spikes/outliers, missing-value flagging, and unification of coordinates and reference height. For evaluation and visualization under a common corridor coordinate system (x, y), a raster product with 200 m spatial resolution was generated while preserving the original station-level series.

Candidate sites were proposed based on field survey and accessibility constraints, forming a quasi-regular mesh with along-corridor spacing $\approx$ 2 km and cross-track spacing $\approx$ 1 km. Locations within 300 m of any incumbent station were excluded to enforce minimum separation. The empirical semivariogram computed from the incumbent network provided a practical correlation range of $\approx$ 8 km. This value is adopted as $d_{\max}$ and reused in subsequent metrics such as Coverage@$d_{\max}$. Table I lists representative coordinates of incumbent and candidate sites in corridor coordinates (meters).

B. Baselines and Optimizer Configuration

a) Baselines: To quantify the effect of adding stations on interpolation quality, four station-placement schemes are compared under a unified evaluation protocol and identical sampling. Let $K_{\text{new}} = 8$ denote the number of added stations unless stated otherwise.

TABLE I: Representative coordinates of incumbent and candidate sites (corridor coordinates, unit: m).

Name	x_{m}	y_{m}
Incumbent 1	1000.0	103.04
Incumbent 2	2636.36	571.29
Incumbent 3	4272.73	38.77
Candidate 1	1000.0	-1600.0
Candidate 2	3000.0	-1600.0
Candidate 3	5000.0	-1600.0

TABLE II: Genetic algorithm hyperparameters and constraints.

Parameter	Setting	Notes
Population size	30	
Generations	30–40	early stop allowed
Selection	Tournament (size 3)	
Mutation rate	0.2 (swap)	
Added sites K_{new}	8	per run
Min. distance to incumbents	300 m	hard constraint
IDW power p	2	shared across schemes
Test points P	1000 @ 6 times	shared across schemes

- **ExistingOnly**: keep the 12 incumbent stations only (lower-bound baseline).
- **UniformCenterline+Existing**: add K_{new} stations evenly spaced along the corridor centerline and merge with incumbents.
- **TerrainWeighted+Existing**: score candidate sites by local terrain relief, select the top K_{new} sites and merge with incumbents.
- **GAOptimized+Existing**: from the full candidate set, select K_{new} sites by a genetic algorithm (GA) that minimizes the sum of squared interpolation errors aggregated over multiple times and locations, merge with incumbents.

b) Evaluation protocol: Interpolation uses inverse-distance weighting (IDW) with power $p = 2$. The test set comprises $P = 1000$ points sampled from the corridor raster and evaluated at six time slices. The same spatial–temporal sample is used for all schemes to ensure fairness. Error metrics include MAE, RMSE, and MAPE (computed after excluding samples with wind speed $v < 0.5\,\mathrm{m/s}$). The average nearest-station distance is also reported. Coverage is computed with $d_{\max} \approx 8\,\mathrm{km}$ as established in Sec. III-A. All settings and preprocessing are held fixed across schemes.

c) GA configuration and constraints: A global search is performed with a GA under engineering constraints: any selected site must be at least $300\,\mathrm{m}$ from incumbent stations. Random seeds are fixed for reproducibility. Key hyperparameters are summarized in Table II.

C. Evaluation Metrics

All schemes are evaluated under a unified protocol. Let P denote the number of spatial evaluation locations (sampled from the $200\,\mathrm{m}$ raster) and let T_{eval} be the number of time slices used for testing. The total number of spatio–temporal samples is $N = P \times T_{\mathrm{eval}}$. For location $p \in \{1, \ldots, P\}$ and time $t \in \{1, \ldots, T_{\mathrm{eval}}\}$, let $v_{p,t}$ be the observed wind speed and $\hat{v}_{p,t}$ its estimate.

a) MAE: The mean absolute error aggregates absolute deviations over all samples:

$$\mathrm{MAE} \;=\; \frac{1}{N} \sum_{t=1}^{T_{\mathrm{eval}}} \sum_{p=1}^{P} \left| \, \hat{v}_{p,t} - v_{p,t} \, \right| \tag{8}$$

b) RMSE: The root mean squared error emphasizes larger deviations:

$$\mathrm{RMSE} \;=\; \sqrt{\frac{1}{N} \sum_{t=1}^{T_{\mathrm{eval}}} \sum_{p=1}^{P} \left(\hat{v}_{p,t} - v_{p,t} \right)^2} \tag{9}$$

c) MAPE: To avoid distortion at near–zero wind speeds, MAPE is computed only on samples with $v_{p,t} \geq \tau$, where $\tau = 0.5\ \mathrm{m/s}$ unless stated otherwise. Let $\mathcal{I}_\tau = \{(p,t) : v_{p,t} \geq \tau\}$ and $N_\tau = |\mathcal{I}_\tau|$:

$$\mathrm{MAPE} \;=\; \frac{100\%}{N_\tau} \sum_{(p,t) \in \mathcal{I}_\tau} \left| \frac{\hat{v}_{p,t} - v_{p,t}}{v_{p,t}} \right| \tag{10}$$

d) Coverage@ $d_{\max}$: Spatial coverage characterizes the fraction of evaluation locations that lie within $d_{\max}$ of at least one station. Let $\mathcal{S} = \{\mathbf{s}_j\}$ denote the set of (incumbent + added) stations for a given scheme, and define $d_{\min}(\mathbf{p}_p) = \min_{\mathbf{s}_j \in \mathcal{S}} \|\mathbf{p}_p - \mathbf{s}_j\|_2$. With $d_{\max} \approx 8\ \mathrm{km}$ (Sec. III-A):

$$\mathrm{Coverage@}d_{\max} \;=\; \frac{1}{P} \sum_{p=1}^{P} I\{\, d_{\min}(\mathbf{p}_p) \leq d_{\max} \,\} \tag{11}$$

where $I(\cdot)$ denotes the indicator function.

e) Average nearest-station distance: As a network compactness proxy (negatively correlated with coverage):

$$\bar{d} \;=\; \frac{1}{P} \sum_{p=1}^{P} d_{\min}(\mathbf{p}_p) \tag{12}$$

Unless otherwise specified, the same spatio–temporal evaluation set $\{(\mathbf{p}_p, t)\}$ is shared across all schemes to ensure fair comparison.

D. Main Results and Analysis

Table III summarizes the results under the unified sampling and evaluation protocol (Sec. III-C). GAOptimized+Existing attains the lowest errors among the four schemes: relative to UniformCenterline+Existing, RMSE decreases from 2.41 to $2.10\ \mathrm{m/s}$ (-12.9%), MAE from 2.14 to $1.88\ \mathrm{m/s}$ (-12.1%), and MAPE from 26.93% to 23.82% (-11.6%). With $d_{\max} \approx 8\ \mathrm{km}$, all schemes reach $\mathrm{Coverage@}d_{\max} = 1.0$. Hence performance differences are mainly reflected by error metrics and the compactness measure $\bar{d}$, which decreases from $1183\ \mathrm{m}$ (ExistingOnly) to $926\ \mathrm{m}$ (GAOptimized+Existing).

Fig. 3 plots mean absolute error against the nearest-station distance. For both the incumbent and optimized networks, errors increase with distance, indicating sensitivity to network

TABLE III: Overall comparison across station-placement schemes (wind in m/s, MAPE in %).

Scheme	MAE	RMSE	MAPE(%)	Coverage@ $d_{\max}$	$\bar{d}$ (m)
ExistingOnly	2.97	3.26	37.51	1.00	1183
UniformCenterline+Existing	2.14	2.41	26.93	1.00	1026
TerrainWeighted+Existing	1.94	2.18	24.60	1.00	955
GAOptimized+Existing	1.88	2.10	23.82	1.00	926

Note: MAPE excludes samples with $v < 0.5\,\mathrm{m/s}$, Coverage@ $d_{\max}$ uses $d_{\max} \approx 8\,\mathrm{km}$.

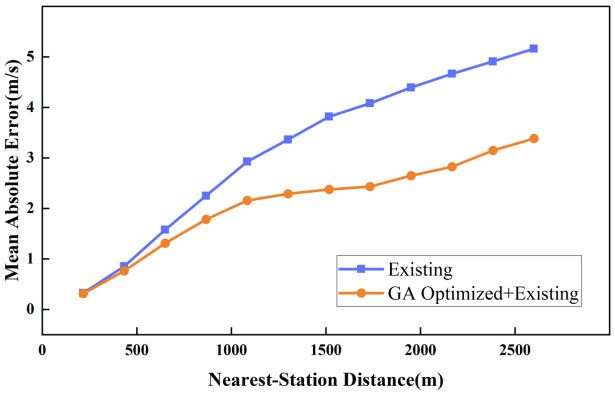


Fig. 3. Mean absolute error versus nearest-station distance.

density, while the optimized curve remains lower across all distance bins, with the largest gap at greater distances.

Fig. 4 shows that the GA reallocates sensors to terrain-aware positions—densifying corridor ends to curb edge variance, shifting laterally toward ridge–valley transitions, and selectively infilling large nearest-station gaps. This shortens local distances in complex terrain and yields a more uniform sensing field, consistent with the lower error curve and larger gains in high-distance bins. In essence, it converts the same coverage budget from redundant overlap into targeted variance reduction, improving accuracy without sacrificing corridor-wide reach. This placement reduces large-$d_{\min}$ voids and enriches high-gradient regions, which stabilizes interpolation locally and yields the aggregate improvements reported in Table III.

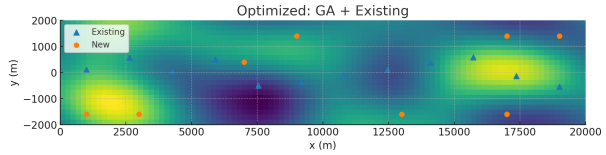


Fig. 4. Final GA-optimized layout of additional stations (lighter=ridges, darker=valleys).

IV. CONCLUSION

Targeting the practical challenges of sparse stations, uneven layouts, and complex engineering constraints in micro-meteorological networks along UHV transmission corridors, this study proposes an integrated framework that couples statistical correlation thresholds, constrained global optimization, and unified evaluation. This paper estimates the wind-field correlation scale via an empirical semivariogram and derive a maximum inter-station spacing $d_{\max}$. This paper then formulates a genetic-algorithm siting model constrained by corridor right-of-way, site accessibility, and minimum safety distances, and benchmark it under a unified protocol against uniform and terrain-weighted baselines. Empirical results show that, with coverage requirements satisfied, the proposed approach markedly reduces wind-field reconstruction error and enhances spatial uniformity and network compactness, thereby providing actionable guidance for planning, expansion, and rapid emergency densification of corridor monitoring networks.

While the proposed approach demonstrates effectiveness in error control and layout uniformity, anisotropy and non-stationarity of corridor wind fields remain critical issues for further study. Our next step is to model directional correlation structures by constructing directional variograms and deriving a directional spacing threshold $d_{\max}(\theta)$. To replace weighted interpolation with regression kriging and co-kriging that explicitly incorporate covariates such as topographic relief, surface roughness, and wind-rose distributions. and to embed the directional threshold jointly with engineering constraints into genetic-algorithm or mixed-integer optimization frameworks. This will yield rapidly deployable densification strategies and further improve reconstruction accuracy and engineering suitability under complex terrain and prevailing-wind conditions.

REFERENCES

[1] J. Xu, T. Zheng, Y. Dang, F. Yang, and D. Li, "Distributed deep reinforcement learning for data-driven water heater model in smart grid," *IEEE Transactions on Smart Grid*, vol. 16, no. 4, pp. 2900–2912, 2025.

[2] G. Zhang, J. Wang, W. Jiang, M. Li, J. Liu, and S. Ren, "Study on optimization of placement method for transmission line monitoring devices based on probability of meteorological disasters," in *Journal of Physics: Conference Series*, vol. 2785, p. 012071, IOP Publishing, 2024.

[3] M. Radić, L. Šerić, and M. Bugarić, "Evaluation of spatial interpolation methods for wind speed and direction: A case study in split-dalmatia county," *The International Archives of the Photogrammetry, Remote Sensing and Spatial Information Sciences*, vol. 48, pp. 193–200, 2025.

[4] J. S. Apte and C. Manchanda, "High-resolution urban air pollution mapping," *Science*, vol. 385, no. 6707, pp. 380–385, 2024.

[5] E. M. Delmelle and P. Goovaerts, "Second-phase sampling designs for non-stationary spatial variables," *Geoderma*, vol. 153, no. 1-2, pp. 205–216, 2009.

[6] M. M. Ahmed, M. Amjad, M. A. Qureshi, M. O. Khan, and Z. M. Haider, "Optimal pmu placement to enhance observability in transmission networks using ilp and degree of centrality," *Energies*, vol. 17, no. 9, p. 2140, 2024.

[7] B. Suslu, F. Ali, and I. K. Jennions, "Understanding the role of sensor optimisation in complex systems," *Sensors*, vol. 23, no. 18, p. 7819, 2023.

[8] H. Gao, J. Liu, P. Lin, G. Hu, L. Patruno, Y. Xiao, K. Tse, and K. Kwok, "An optimal sensor placement scheme for wind flow and pressure field monitoring," *Building and Environment*, vol. 244, p. 110803, 2023.

[9] O. S. Ajani, E. Aboyeji, R. Mallipeddi, D. Dooyum Uyeh, Y. Ha, and T. Park, "A genetic programming-based optimal sensor placement for greenhouse monitoring and control," *Frontiers in Plant Science*, vol. 14, p. 1152036, 2023.

[10] A. Henriquez, A. Osses, L. Gallardo, and M. D. Resquin, "Analysis and optimal design of air quality monitoring networks using a variational approach," *Tellus B: Chemical and Physical Meteorology*, vol. 67, no. 1, p. 25385, 2015.

[11] R. L. T. Henriksen, J. B. Hubrechts, J. K. Møller, P. Knudsen, and J. W. Pedersen, "Large-scale rain gauge network optimization using a kriging emulator," *Journal of Hydrology*, vol. 637, p. 131360, 2024.

[12] Y. Lang, M. X. Y. Ng, K. X. Yu, B. Chen, P. C. Tan, K. W. Tan, W. H. Lam, P. Siwayanan, K. S. Kim, T. S. Y. Choong, *et al.*, "A novel cfd-milp-ann approach for optimizing sensor placement, number, and source localization in large-scale gas dispersion from unknown locations," *Digital Chemical Engineering*, vol. 14, p. 100216, 2025.

[13] S. Araki, K. Iwahashi, H. Shimadera, K. Yamamoto, and A. Kondo, "Optimization of air monitoring networks using chemical transport model and search algorithm," *Atmospheric Environment*, vol. 122, pp. 22–30, 2015.

[14] X. Zhou, Y. Wang, Y. Shi, Q. Jiang, C. Zhou, and Z. Zheng, "Deep reinforcement learning-based optimal pmu placement considering the degree of power system observability," *IEEE Transactions on Industrial Informatics*, vol. 20, no. 6, pp. 8949–8960, 2024.

[15] J. Annoni, T. Taylor, C. Bay, K. Johnson, L. Pao, P. Fleming, and K. Dykes, "Sparse-sensor placement for wind farm control," in *Journal of Physics: Conference Series*, vol. 1037, p. 032019, IOP Publishing, 2018.

[16] A. Khan, S. Gupta, and S. K. Gupta, "Multi-hazard disaster studies: Monitoring, detection, recovery, and management, based on emerging technologies and optimal techniques," *International journal of disaster risk reduction*, vol. 47, p. 101642, 2020.

[17] S. Verghese and A. K. Nema, "Optimal design of air quality monitoring networks: a systematic review," *Stochastic Environmental Research and Risk Assessment*, vol. 36, no. 10, pp. 2963–2978, 2022.

[18] J. Xu, K. Li, and D. Li, "Multioutput framework for time-series forecasting in smart grid meets data scarcity," *IEEE Transactions on Industrial Informatics*, vol. 20, no. 9, pp. 11202–11212, 2024.

[19] M. Bartos and B. Kerkez, "Observability-based sensor placement improves contaminant source identification in river networks," in *AGU Fall Meeting Abstracts*, vol. 2021, pp. H25X–1303, 2021.

Research on Aerial Image Localization and Classification of Transmission Equipment Based on the C2f-CAA Mechanism

Weisong Liang
Guangdong University of Science and Technology
School of Mechanical and Electrical Engineering
Dongguan, China
2862161215@qq.com

Yonghua Wen*
Guangdong University of Science and Technology
School of Mechanical and Electrical Engineering
Dongguan, China
wen_yonghua@163.com
*Corresponding author

Haimei Cen
Guangdong University of Science and Technology
School of Mechanical and Electrical Engineering
Dongguan, China
1298258280@qq.com

Huiying You
Guangdong University of Science and Technology
School of Mechanical and Electrical Engineering
Dongguan, China
1985972705@qq.com

Shaojun Qi
Guangdong University of Science and Technology
School of Mechanical and Electrical Engineering
Dongguan, China
yzazhg@sina.com

Xueying Huang
Guangdong University of Science and Technology
School of Mechanical and Electrical Engineering
Dongguan, China
huangxueying4@gdust.edu.cn

Yongqiu Liu
Guangdong University of Science and Technology
School of Mechanical and Electrical Engineering
Dongguan, China
332448843@qq.com

Huarong Wang
Guangdong University of Science and Technology
School of Mechanical and Electrical Engineering
Dongguan, China
464984479@qq.com

***Abstract*—Aiming at the problem of aerial image localisation classification of power transmission equipment, this study proposes a method for aerial image localisation classification of power transmission equipment based on the C2f-CAA mechanism. The method improves the residual convolutional neural network method by using the contextual anchor attention mechanism and the cross-stage partial double convolution module, so that the model is theoretically reduced in computational complexity. At the same time, the X-Small detection head and cross-connection strategy are used to complete the feature extraction fusion process, and finally the bounding box regression module is completed based on the CIoU algorithm. The experimental results show that the accuracy and FPS of this model in insulator target localisation reaches 93% and 243 respectively, which indicates that this model has a positive effect in reducing computational complexity and small target detection.**

Keywords—power transmission equipment, positioning classification, attention mechanism, residual convolutional neural network

I. INTRODUCTION

Transmission equipment primarily refers to outdoor power system components such as insulators, towers, and transmission lines. As a critical component of the power transmission system [1-2], its stability is a key factor in assessing power system safety. Therefore, transmission equipment inspection has become one of the routine maintenance tasks for power companies.

With the advancement of drone inspection technology, power companies are transitioning from traditional manual inspection methods to intelligent monitoring methods for line maintenance. Among these, Reference [3] proposes a multi-drone collaborative inspection operation based on the combination of drones and operational vehicles, demonstrating the feasibility of drones in transmission line inspections. Reference [4] introduces high-speed state detection of insulators using aerial images, pushing intelligent inspections to new heights.

Unfortunately, existing transmission equipment target detection primarily relies on simple transfer learning using convolutional neural networks, lacking algorithmic specificity for target localization and featuring overly complex computational models.

Meanwhile, the context anchor attention mechanism, with its advantages of low complexity and effective feature extraction, has become an effective method for aerial image target detection. Literature [5] models remote geographic features and local information using the context anchor attention mechanism, achieving high-precision geographic information modeling. Literature [6] proposes an adaptive attention network, utilizing a context information adaptive fusion module to efficiently process high-resolution remote sensing image semantic segmentation. Reference [7] proposes a context-anchor attention mechanism detection method based on small object detection, successfully constructing an application framework for edge device target detection. This indicates that the context-anchor attention mechanism has a strong application background in the

1. Supported by Natural Science Project of Guangdong University of Science and Technology (GKY-2024KYQNK-7)
2. Supported by College Student Innovation Training Program of Guangdong University of Science and Technology（GK2025015）

field of aerial image target localization, but remains in its infancy in the context of power equipment inspection.

Therefore, we propose a transmission equipment aerial image localization and classification model based on the context anchor attention mechanism. This model performs feature extraction using the context anchor attention mechanism, completes feature fusion using the XSmall detection head and cross-connection strategy, and finally constructs a bounding box regression module based on CIoU.

II. Model Section

For the problem of aerial image localization and classification of power transmission equipment, we propose a lightweight localization and classification model based on a context anchor attention mechanism, whose complete architecture is shown in Fig.1. Specifically, this model is constructed based on the residual architecture framework[8] for the backbone and neck parts, while combining the Cross-stage partial 2-fusion (C2f) module[7] with the context anchor attention mechanism (Context Anchor Attention, CAA) [9] to improve the C2f-CAA module. It utilizes the three-level max pooling operation of the fast spatial pyramid pooling module (Spatial Pyramid Pooling-Fast, SPPF)[10] to extract multi-scale features, and finally employs the X-Small detection head for efficient detection of small targets such as insulators.

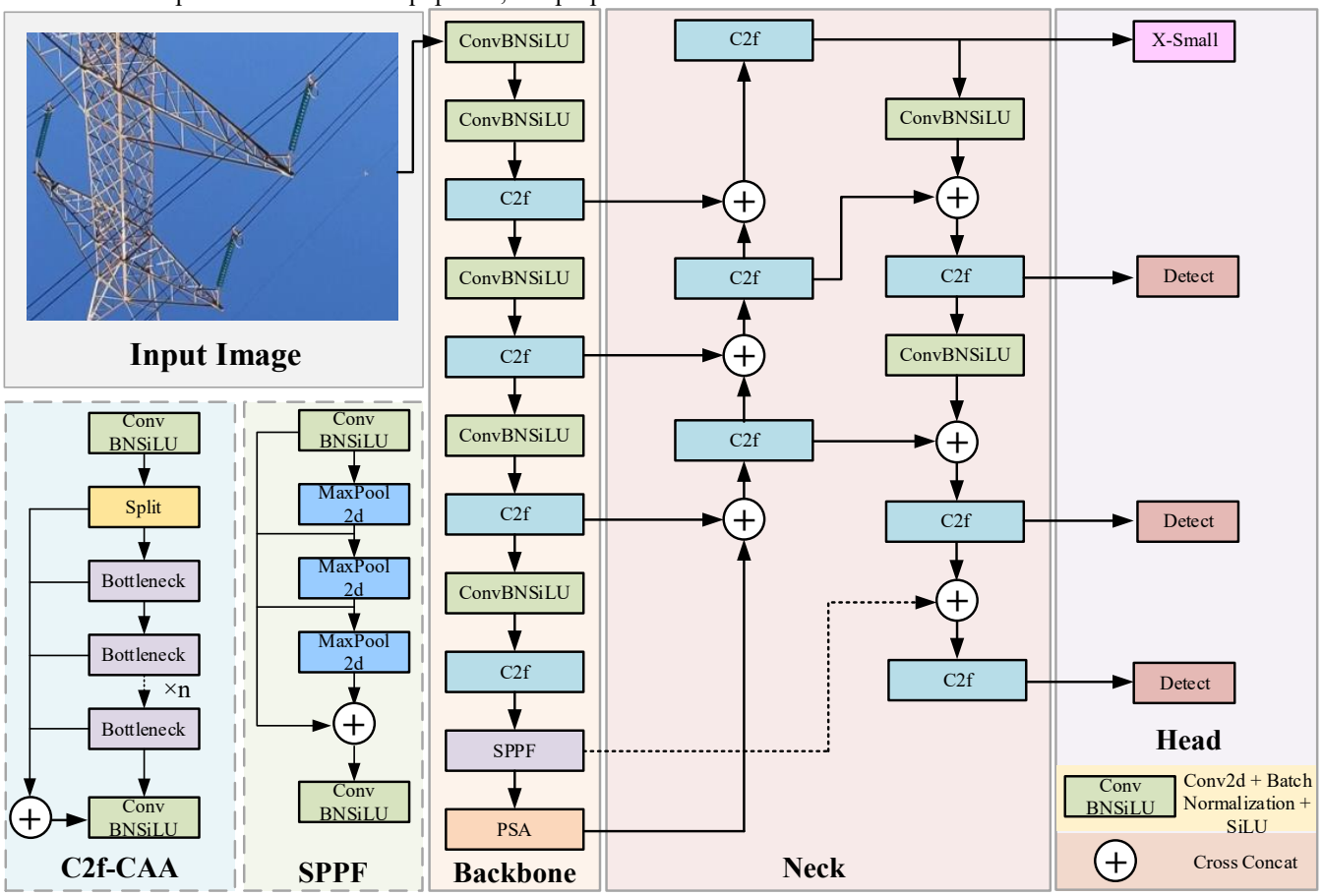


Fig. 1. Overall framework of the aerial image localization and classification model for transmission equipment based on the C2f-CAA mechanism

A. *Lightweight Residual Convolutional Neural Network Framework*

A lightweight residual neural network is trained for the feature extraction problem of transmission equipment. The network skeleton consists of C2f-CAA module, Partial Self Attention (PSA) module, Feature Pyramid Network (FPN)[11] (left structure of Neck part) and Path Aggregation Network (PAN) [12] (right structure of Neck part), which can effectively extract the features of transmission equipment. Its general framework is shown in Fig. 1.

B. *C2f-CAA Module*

In order to improve the processing speed and efficiency of convolutional networks, we introduce C2f-CAA to improve the feature extraction process. This module was firstly used for small target localisation classification of aerial images and is applicable to the field of UAV target detection. Specifically, the module provides smoother gradient transition for the convolutional process through SiLU function activation, and completes the channel importance weighting through average pooling operation $\mathcal{P}_{avg}$ and point-by-point convolution operation $\mathrm{Conv}_{1\times1}$.

$$\mathbf{F}_{l-1}^{pool} = \mathrm{Conv}_{1\times1}(\mathcal{P}_{avg}(\mathbf{X}_{l-1})) \tag{1}$$

$$\mathbf{A}_{l-1} = \mathrm{Sigmoid}(\mathrm{Conv}_{1\times1}(\mathbf{F}_{l-1}^{pool})) \tag{2}$$

where F_{l-1}^{pool} is the feature obtained from the 1*1 convolution operation, the weighting matrix $A_{l-1} \in IR^{C_l \times H_l \times W_l}$.

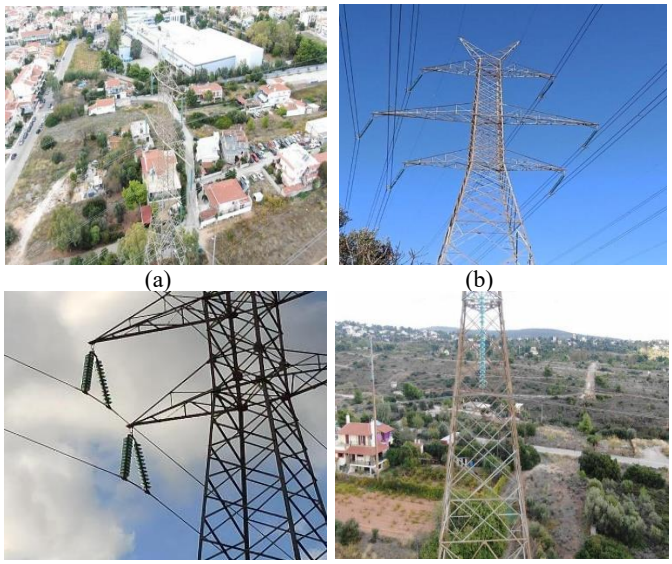
C. X-Small Detection Head

Facing the challenge of detecting small targets such as insulators in aerial images, we use the X-Small detection head for tiny object recognition. Taking the input images (512*640) in the dataset as an example, when they reach the detection head, the generated feature maps have resolutions of 64*80, 32*40 and 16*20 pixels. This leads to the problem of missed and wrong detection of devices like insulators on aerial images. To improve the detection of small targets, we introduce the X-Small detection branch[7], which reduces the PAN network to two levels, thus preserving more image features at a fine-grained level.

III. Experimental Section

A. Data Sets

We use the TIC dataset[13], which includes 2,056 images (512x640) of the transmission line network in northeastern Attica, Greece, and three object category labels (i.e., towers, insulators, and conductors), and divide the training set and validation set in an 8:2 ratio. This is a mature and challenging drone aerial photography dataset of transmission equipment.



(a) (b) (c) (d)

Fig. 2. Example images of the dataset, (a) taken at a top angle, (b) and (c) taken at an elevation angle, and (d) taken at a side angle.

B. Experimental Equipment

This experimental environment uses NVIDIA GeForce RTX 3080 Laptop GPU as the GPU processor while the CPU processor is AMD Ryzen 9 5900HX with Radeon Graphics.

C. Experimental Indicators

In order to better quantify the localisation classification effect, we introduce the mainstream performance metrics in the target detection domain: precision, recall and mean average precision (mAP).

$$\mathrm{Precision} = \frac{\mathrm{TP}}{\mathrm{TP}+\mathrm{FP}} \tag{3}$$

$$\mathrm{Recall} = \frac{\mathrm{TP}}{\mathrm{TP}+\mathrm{FN}} \tag{4}$$

where TP is true positive, FP is false positive and FN is false negative.

$$AP = \int_0^1 p(r)dr \tag{5}$$

$$\mathrm{mAP} = \frac{1}{k}\sum_{i=1}^{k} AP_i \tag{6}$$

where $p(r)$ is the precision of the recall function. mAP is the value obtained for the averaging operation of the AP values for the three categories (towers, transmission lines, and insulators), while mAP_{50} is the detection result in the case where the IoU is not less than 0.5.

D. Comparison Experiment

In order to quantify the detection effect of this model, we construct a comparison experiment using the TIC validation set as input. From Table 1 we can see that our proposed model is more than 1% higher than the other two mainstream models for target detection in terms of precision and recall, with a mAP50 of more than about 2%, while the FPS metric is lower by more than 30. It indicates that the model possesses a positive impact in terms of detection precision and computational complexity.

TABLE I. COMPARATIVE EXPERIMENTS OF TARGET RECOGNITION MODELS

Model	Precision	Recall	mAP_{50}	FPS
Yolov6s	0.639	0.695	0.717	315
Yolov7s	0.666	0.711	0.723	278
C2f-CAA	0.70	0.721	0.741	243

Meanwhile, in order to explore the reasons for the low average precision, we take the precision and recall of different categories of transmission equipment as inputs to construct the Precision-Recall graph, as shown in Fig. 3. It can be seen that for the target detection effect of insulators and towers category, the AP50 value of this model reaches 85.7% and 93.1% respectively, which has good detection effect. However, in the detection effect of linear targets in the transmission line category, the AP50 of this model is only 43.5%, which indicates that this model needs to be further improved in the detection of linear targets.

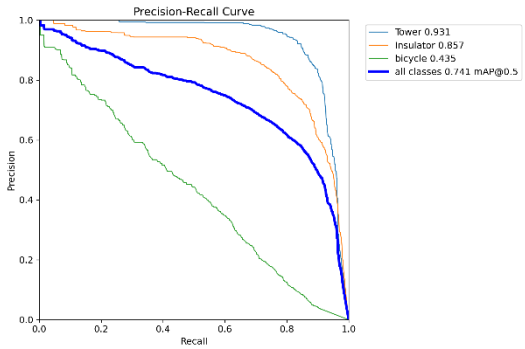


Fig. 3. Precision-Recall curve diagram

E. Operational Effect

The field pictures containing transmission equipment are visualized and verified, and the actual results of its operation are shown in Fig.4. From the figure, it can be found that the present model possesses a positive impact in the detection of small targets such as insulators, but there are still some limitations in the transmission line part.

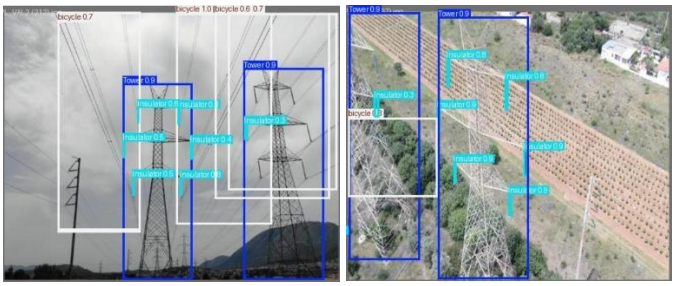


Fig. 4. Actual running effect of the model

IV. SUMMARIZE

In this paper, we propose an aerial image localization and classification model for power transmission equipment based on C2f-CAA mechanism, which realizes efficient localization and classification of power transmission equipment (towers, transmission lines and insulators). At the same time, it improves the recognition accuracy of small targets of insulators in aerial images, reduces the computational complexity of the model, and provides new ideas for the intelligent recognition of power transmission equipment UAVs. However, the present model still has some deficiencies in transmission line-based linear target detection, and we will next improve it around the linear target detection problem.

REFERENCES

[1] G. Liu, Y. Wen, Y. Gu, F. Guo, J. Zhou, &X. Zhang, et al. “Monitoring of composite insulators in transmission lines: a hydrophobicity diagnostic method using aerial images and residual neural networks.” IEEE T. Power Delivery, vol. 38, no. 4, pp. 2500-2509, Aug. 2023

[2] G. Liu, Y. Wen, Y. Gu,et al. Decision Tree Clusters: Non-destructive detection of overheating defects in porcelain insulators using quantitative thermal imaging techniques[J].Measurement, 2025, 241(000).

[3] H. Zheng, W. Hongxing, Z. Tianpei and Y. Bin, "The Collaborative Power Inspection Task Allocation Method of “Unmanned Aerial Vehicle and Operating Vehicle”," IEEE Access, vol. 9, pp. 62926-62934, 2021.

[4] Y. Li, B. Hu, S. Wei, D. Gao and F. Shuang, "Simplify-YOLOv5m: A Simplified High-Speed Insulator Detection Algorithm for UAV Images," IEEE T. Instrum. and Meas., vol. 74, pp. 1-14, 2025.

[5] Z. Chen, X. Han and X. Ma, "Combining Contextual Information by Integrated Attention Mechanism in Convolutional Neural Networks for Digital Elevation Model Super-Resolution," IEEE T Geosci. Remote, vol. 62, pp. 1-16, 2024.

[6] Y. Chen, Q. Zhang, X. Wang, Q. Dong, M. Kang, &W. Jiang, et al., "AANet: Adaptive Attention Networks for Semantic Segmentation of High-Resolution Remote Sensing Imagery," IEEE J-Stars, vol. 17, pp. 14640-14655, 2024.

[7] Z. Song, Y. Zhang and A. A. R. M. A. Ebayyeh, "EDNet: Edge-Optimized Small Target Detection in UAV Imagery - Faster Context Attention, Better Feature Fusion, and Hardware Acceleration," 2024 IEEE Smart World Congress (SWC), Nadi, Fiji, pp. 829-838, 2024.

[8] K. He, X. Zhang, S. Ren and J. Sun, "Deep Residual Learning for Image Recognition," 2016 IEEE Conference on Computer Vision and Pattern Recognition (CVPR), Las Vegas, NV, USA, pp. 770-778, 2016.

[9] X. Cai, Q. Lai, Y. Wang, W. Wang, Z. Sun, and Y. Yao, ”Poly Kernel Inception Network for Remote Sensing Detection,” in 2024 IEEE/CVF Conference on Computer Vision and Pattern Recognition (CVPR), Seattle, WA, USA, pp. 27706-27716, 2024.

[10] K. He, X. Zhang, S. Ren, and J. Sun, ”Spatial pyramid pooling in deep convolutional networks for visual recognition,” IEEE T. Pattern Anal., vol. 37, pp. 1904–1916, 2015.

[11] T. -Y. Lin, P. Dollár, R. Girshick, K. He, B. Hariharan and S. Belongie, "Feature Pyramid Networks for Object Detection," 2017 IEEE Conference on Computer Vision and Pattern Recognition (CVPR), Honolulu, HI, USA, 2017, pp. 936-944.

[12] S. Liu, L. Qi, H. Qin, J. Shi and J. Jia, "Path Aggregation Network for Instance Segmentation," 2018 IEEE/CVF Conference on Computer Vision and Pattern Recognition, Salt Lake City, UT, USA, 2018, pp. 8759-8768.

[13] Elisavet Bellou. (2024). Tower Insulator Conductors (TIC) Powerline Dataset with Object Detection Models [Dataset]. Retrieved from https://github.com /Elizbellou/TIC-Powerline-Dataset-and-Detection-Models

Design of Self-Powered Energy-Harvesting Power Supply for Three-Phase Cable Temperature Monitoring Device

Hong Lei
School of Automation and Electronic Information
Xiangtan University
Xiangtan,China
13187387993@163.com

Zhaohong Wang
School of Automation and Electronic Information
Xiangtan University
Xiangtan,China
trancemania@xtu.edu.cn

Lu Zeng
School of Automation and Electronic Information
Xiangtan University
Xiangtan,China
18873267200@163.com

Jiale Chen
School of Automation and Electronic Information
Xiangtan University
Xiangtan,China
17369240992@163.com

Sheng Li
School of Automation and Electronic Information)
Xiangtan University
Xiangtan,China
3067265199@qq.com

***Abstract*—To address the power supply issue for temperature measurement devices on transmission line three-phase cables, this study investigates the magnetic field characteristics around three-phase cables and proposes a novel energy harvesting solution. This paper designs an energy harvesting current transformer (EHCT) suitable for extracting energy from the magnetic field around three-phase cables, along with subsequent rectification/filtering circuits and voltage stabilization circuits. An excessive power supply voltage ripple coefficient can severely affect the measurement accuracy of temperature monitoring devices. Therefore, this paper designs a high-gain, ultra-low-output-voltage-ripple DC-DC converter, which effectively solves the problems of low output voltage and excessive voltage ripple after the energy from the EHCT passes through the rectification/filtering circuits. To verify the accuracy of the proposed energy harvesting solution, a 3D simulation model of the EHCT was built using Ansys Electronics to validate its output performance, while a complete circuit simulation model of the energy harvesting system was constructed in Simulink. Simulation results show that the EHCT can achieve an output power of approximately 330 mW, and the final output voltage of the proposed energy harvesting circuit reaches about 5 V with a voltage ripple coefficient below 0.01%. This energy harvesting solution can provide a sufficiently high and stable output voltage, enabling reliable power supply for low-power cable temperature monitoring devices.**

Keywords—Three-phase cable, energy-harvesting current transformer (EHCT), DC-DC converter

I. INTRODUCTION

With the acceleration of urbanization and continuous growth of power loads, high-voltage cable tunnel laying has become the mainstream choice for urban power grid expansion [1]. Cross-linked polyethylene (XLPE) power cables are widely used in urban power systems at various voltage levels for transmission and distribution networks due to their excellent characteristics. Studies show that when the surface temperature of XLPE insulated cables exceeds the rated value by 8%, their service life decreases by 50%, and when exceeding by 15%, the life sharply drops to 25% [2]. However, thermal effects caused by dense laying of multi-circuit cables are becoming increasingly prominent[3]. The operating temperature of cables is strongly correlated with their insulation aging state, and high-precision temperature measurement of cables (within ±0.1°C) is crucial for ensuring grid safety, optimizing operational efficiency, and extending equipment lifespan [4][5].

Due to the special environment around three-phase cables, providing reliable power for temperature monitoring devices is challenging. Dedicated power lines would significantly increase costs, while battery power depends on battery lifespan and requires regular replacement, failing to meet long-term operational requirements. Therefore, the currently widely used method is to generate electricity using the magnetic field around power cables through energy-harvesting current transformers (EHCTs). Research and application of EHCTs suitable for single-phase cables are already quite mature, but studies on EHCTs for three-phase cables are rarely published by scholars. Since the magnetic field characteristics of three-phase cables are fundamentally different from those of single-phase cables, EHCTs designed for single-phase cables are not suitable for three-phase cables. In reference [6], Lu Yongling et al. designed a C-type magnetic core EHCT by analyzing the distribution characteristics of the normal magnetic flux density around cables. This design increases winding space but sacrifices the advantage of high magnetic flux density near the cables. In reference [7], Di Yunpeng et al. designed a three-split winding EHCT by neglecting the magnetic field cancellation phenomenon near one phase conductor.

To address these challenges, this paper proposes a novel energy harvesting scheme featuring a hexa-split winding EHCT,

979-8-3315-5472-9/25/$31.00 ©2025 IEEE

accompanied by optimized rectification-filtering and voltage stabilization circuits. The voltage ripple coefficient of the power supply critically impacts the measurement accuracy of high-precision cable temperature monitoring systems. Elevated ripple levels introduce interference in analog signal conditioning circuits and analog-to-digital converters (ADCs), thereby amplifying measurement errors. To resolve this, we developed a high-gain low-output-voltage-ripple DC-DC converter, ensuring both the output voltage magnitude and ripple level satisfy the operational requirements of cable temperature monitoring devices. The schematic diagram of the proposed design is illustrated in Fig. 1.

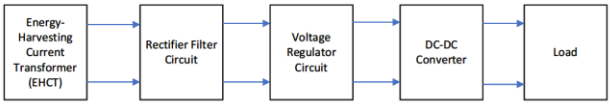


Fig. 1. Schematic Diagram of the Energy Harvesting Scheme Framework.

II. Design of Six-Split Winding Energy-Harvesting Current Transformer

A. Analysis of Design Principles for Energy-Harvesting Current Transformers

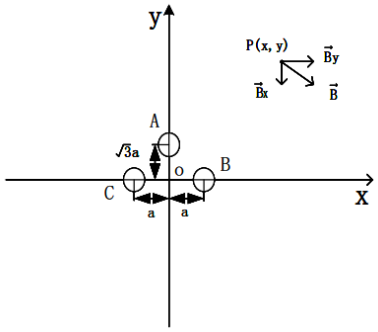


Fig. 2. Computational Model of Three-Phase Cable Magnetic Field.

As shown in Fig. 2, point P(x, y) represents an arbitrary position outside the three-phase cables. The three-phase current expressions are respectively:

$$\begin{cases} i_A = I_M \,\mathrm{Sin}(100\pi t)(A) \\ i_B = I_M \,\mathrm{Sin}(100\pi t - 2\pi/3)(A) \\ i_C = I_M \,\mathrm{Sin}(100\pi t + 2\pi/3)(A) \end{cases} \tag{1}$$

where I_M denotes the amplitude of the three-phase alternating current. According to the Biot-Savart Law, the magnetic flux density generated by phase-A current at point P is given by:

$$B_A = \frac{u_0 i_A}{2\pi} \times \frac{1}{\sqrt{x^2 + (y - \sqrt{3}\mathrm{a})^2}} \tag{2}$$

The rectangular coordinate components of this magnetic flux density are respectively:

$$\begin{cases} B_{Ax} = \dfrac{u_0 i_A}{2\pi} \times \dfrac{y - \sqrt{3}\mathrm{a}}{x^2 + (y - \sqrt{3}\mathrm{a})^2} \\ B_{Ay} = \dfrac{u_0 i_A}{2\pi} \times \dfrac{x}{x^2 + (y - \sqrt{3}\mathrm{a})^2} \end{cases} \tag{3}$$

According to the superposition principle, the total magnetic flux density at point P is given by:

$$\begin{cases} B_x = B_{Ax} + B_{Bx} + B_{Cx} \\ B_y = B_{Ay} + B_{By} + B_{Cy} \\ B = \sqrt{B_x^2 + B_y^2} \end{cases} \tag{4}$$

Based on Faraday's Law of Electromagnetic Induction:

$$e(t) = -\frac{d\phi(t)}{dt} = -\frac{dB(t)}{dt} S \tag{5}$$

The magnitude of the induced voltage e(t) on the energy-harvesting CT winding is related to the instantaneous variation of the magnetic flux density B and the core cross-sectional area S . As shown in Equations (1) to (9), the mutual cancellation effect of the magnetic fields generated by each of the three-phase currents becomes more pronounced with increasing vertical distance from the cable. This implies that the magnetic flux density at locations far from the three-phase cables is nearly zero. When the cable length is assumed to be infinite, the magnetic flux density magnitudes are equal at points equidistant vertically from the cable. Increasing the core cross-sectional area under a fixed number of winding turns increases the winding length, thereby raising the internal resistance of the coil windings. This elevates energy losses. Therefore, when designing the parameterized structure of the energy-harvesting CT, the inner and outer diameters of the circular magnetic core should be set to reasonable values based on the cable conductor diameter to ensure that enlarging the core cross-sectional area enhances the induced voltage. The core cross-sectional area is effectively increased by expanding the core thickness along the cable's axial direction (i.e., the core's radial dimension).

Additionally, according to the right-hand screw rule, the magnetic field surrounding a single-phase cable forms concentric circular magnetic flux lines around the conductor, with the field direction flipping once per cycle following the sinusoidal current's polarity reversal. In contrast, the magnetic field distribution around three-phase cables exhibits fundamentally different characteristics. As derived from the three-phase current expressions, at any instant, two phases share identical current directions opposing the third phase. Applying the right-hand screw rule reveals that the resultant magnetic field around three-phase cables constitutes an alternating rotating magnetic field, analogous to the rotating field generated in three-phase generator rotors.

To validate this analysis, electromagnetic simulation analysis of the magnetic field surrounding three-phase cables was conducted using Ansys Electronics software. The simulation results are shown in Fig. 4.

Based on the above analysis, a six-split winding EHCT can be designed, with its structural configuration shown in Fig. 3. For the three-split winding design, each winding occupies an electrical angle range of 120°, where partial magnetic field vectors cancel each other (phase difference ⩾ 90°). In contrast, the six-split winding design restricts each winding to a 60° electrical angle range, enabling more concentrated magnetic field vector superposition (smaller phase differences) and consequently generating a higher resultant electromotive force (EMF) vector.

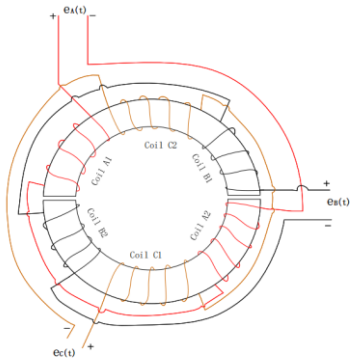
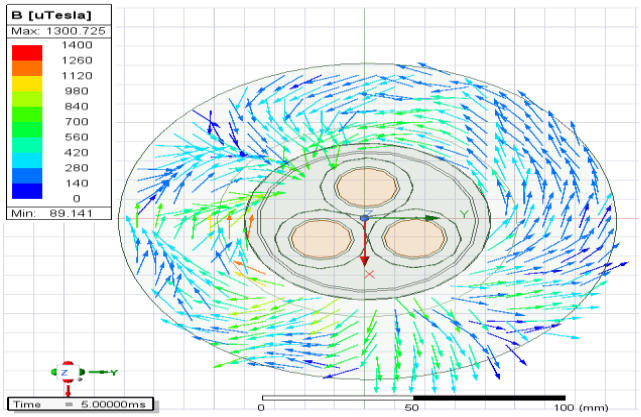
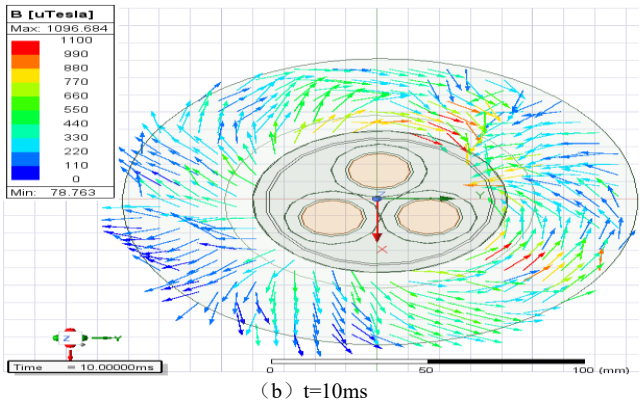


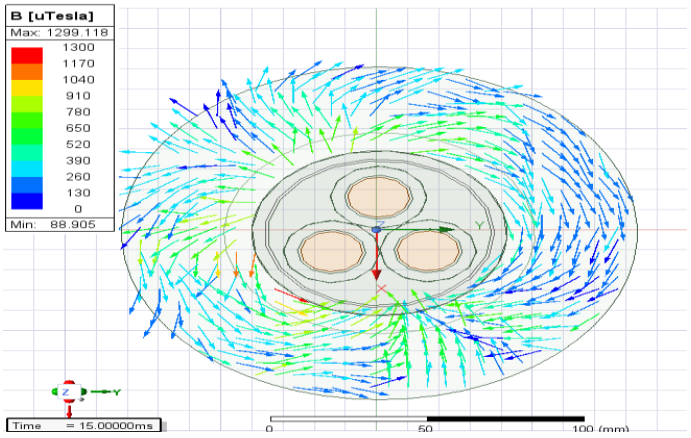
Fig. 3. Structural diagram of six-split winding energy-harvesting current transformer.



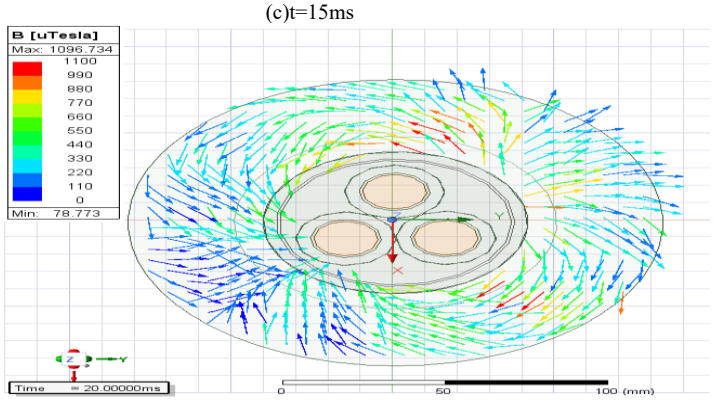
(a) t=5ms



（b）t=10ms



(c)t=15ms

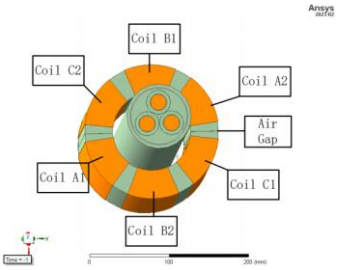


(d)t=20ms

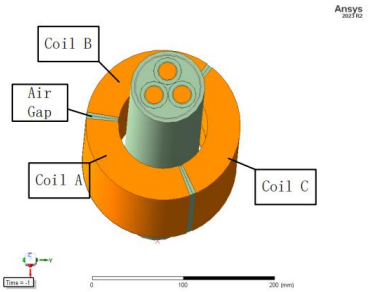
Fig. 4. Vector Distribution Diagrams of Magnetic Flux Density at Different Time Instants.

B. *Simulation Analysis of the Energy-Harvesting Current Transformer*

Simulation analysis was performed on the six-split winding EHCT proposed in this paper and the three-split winding EHCT proposed in [7]. A three-dimensional simulation model of a three-core cable (model YJV22-8.7/15kV 3×300) and simulation models of both EHCTs were established using Maxwell 3D in Ansys Electronics, as shown in Fig. 5. A field-circuit coupling model was built in Simplorer, with each phase winding of the EHCT connected to a 9Ω load. The current amplitude per phase conductor on the cable was set to 260A. Both CT MEHs had 420 turns per phase. The structural parameters of the split-type circular magnetic core were: inner radius r_1=50mm, outer radius r_2=85mm, thickness d=160mm. The magnetic core material was silicon steel sheet DW310-35. The structural parameters of the three-phase cable are listed in TABLE I.



(a) Six-split winding energy-harvesting current transformer



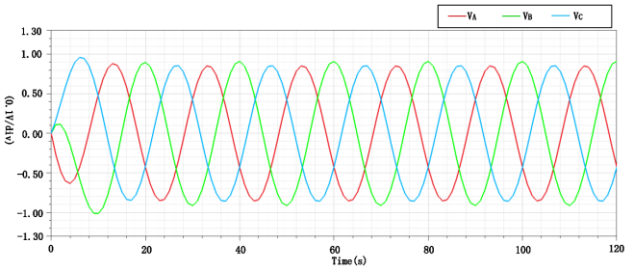
(b) Three-split winding energy-harvesting current transformer

Fig. 5. Three-dimensional simulation model diagram of three-core cable and energy-harvesting current transformer.

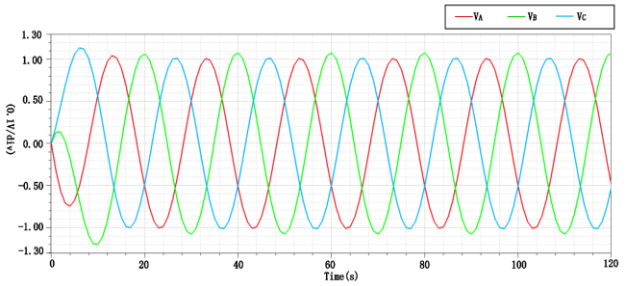
TABLE I. GEOMETRIC PARAMETERS OF THE THREE-PHASE CABLE

Cable structure	Parameters/mm	Cable structure	Parameters/mm
conductor radius	10	outer sheath thickness	4
conductor shield thickness	1	cable outer radius	41
insulation layer thickness	4.5	——	——
filler layer radius	36	——	——
armor layer thickness	1	——	——

The simulation results of the output induced voltage for both EHCTs are shown in Fig. 6. Compared with the three-split winding EHCT, the six-split winding EHCT shows an approximate increase of 160mV in the amplitude of each phase's induced voltage and about 70mW in output power, with a total output power of approximately 330mW, which can meet the power requirements of some low-power temperature measurement devices. From the simulation results, it can be observed that the performance of the six-split winding EHCT is superior to that of the three- split winding EHCT.



(a) Output voltage waveform of the three-split winding energy-harvesting CT



(b) six-split winding energy-harvesting CT

Fig. 6. Output voltage waveforms of both energy-harvesting CTs.

III. LOW-RIPPLE HIGH-GAIN DC-DC CONVERTER

To address the issue that the output power of the energy-harvesting current transformer after rectification and filtering exhibits insufficient output voltage and excessive voltage ripple, which cannot meet the strict power supply requirements of temperature monitoring equipment, a high-gain DC-DC converter with ultralow output voltage ripple is designed. Its topology is shown in Fig. 7.

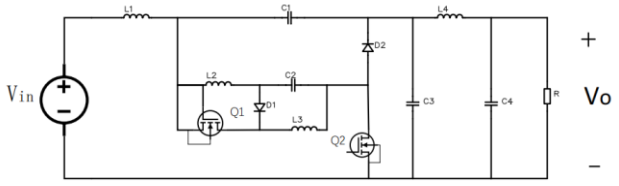


Fig. 7. Topology of the Converter.

A. Analysis of Operating Principle

The converter employs two MOSFETs that turn on and off simultaneously, characterized by simple structure and easy implementation. To analyze the performance of the proposed converter, all devices are assumed to be ideal. The converter operates in Continuous Conduction Mode (CCM) with two operational states: ON and OFF.The duration of the ON state is DTs, where D is the duty cycle and Ts is the switching period. As shown in Fig. 8, during the ON state : MOSFETs Q_1 and Q_2 are turned on , Diodes D_1 and D_2 are reverse-biased (cut off),The inductor current increases linearly.

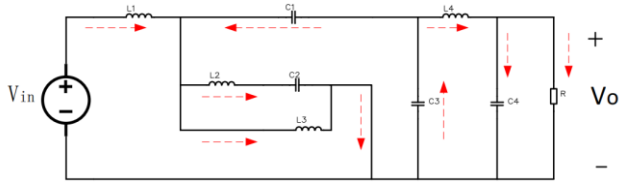


Fig. 8. Equivalent Circuit Diagram When Switching Tubes Are Conducting.

The turn-off mode is shown in Fig. 9, where MOSFETs Q_1, Q_2, and Q_3 are turned off, while diodes D_1 and D_2 conduct. The inductor and input voltage jointly release energy to the capacitor, which is then loaded through the diodes.

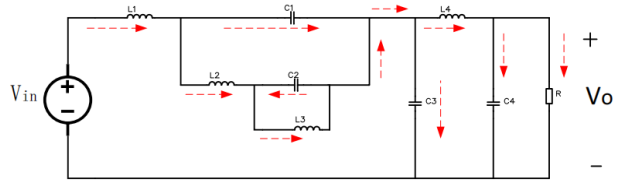


Fig. 9. Equivalent Circuit During Switch Turn-Off.

Based on the volt-second balance of inductors and the ampere-second balance of capacitors, the converter's gain G, capacitor voltages, and inductor currents can be derived as follows:

$$G = \frac{V_O}{V_{in}} = \frac{1}{(1-D)^2} \tag{6}$$

$$\begin{cases} V_{C1} = \dfrac{2D - D^2}{(1-D)^2} V_{in} \\ V_{C2} = \dfrac{D}{1-D} V_{in} \\ V_{C3} = V_O = \dfrac{1}{(1-D)^2} V_{in} \end{cases} \tag{7}$$

$$\begin{cases} I_{L1} = I_{L3} = \dfrac{1}{(1-D)^2} I_O \\ I_{L2} = \dfrac{1}{1-D} I_O \\ I_{L4} = I_O \end{cases} \tag{8}$$

From the above analysis, it can be concluded that the following relationships hold within each switching cycle:

$$\begin{cases} L_1 \dfrac{di_{L1}(t)}{dt} \approx V_{C3} - V_{C1} - V_{in} = 0 \\ L_4 \dfrac{di_{L4}(t)}{dt} \approx V_{C3} - V_O = 0 \end{cases} \tag{9}$$

Therefore, theoretical analysis demonstrates that inductors L_1 and L_4 exhibit near-zero current ripple per switching cycle, indicating the converter achieves zero input-output current ripple characteristics.

B. Design of Inductor and Capacitor Parameters

Since the aforementioned theoretical analysis is based on the small-ripple approximation, in practical circuit operation, the capacitor voltages inevitably exhibit minor fluctuations within each switching cycle. Therefore, Equation (10) is adopted for designing inductor L_1, where $\Delta VC1$ and $\Delta VC3$represent the voltage ripples of capacitors C_1 and C_3, respectively, and $\lambda L1$ denotes the current ripple coefficient.

$$L_1 \geq \frac{V_{C3} + \Delta V_{C3} - V_{C1} - \Delta V_{C1} - V_{in}}{\lambda_{L1} \times I_{L1}} DT_S \tag{10}$$

Inductor L_4 is designed using Equation (11), where f_s represents the switching frequency of the DC-DC converter.

$$L_4 \geq \frac{100}{(2\pi f_s)^2 C_4} \tag{11}$$

To ensure the converter operates in Continuous Conduction Mode (CCM), the parameters of inductors L_2, L_3 and capacitors C_1, C_2, C_3, C_4 are designed as follows:

$$\begin{cases} L_2 \geq \dfrac{(V_{in} + V_{C2})DT_S}{I_{L2}} \\ L_3 \geq \dfrac{V_{in} DT_S}{I_{L3}} \end{cases} \tag{12}$$

$$\begin{cases} C1 \geq \dfrac{I_{L2} + I_{L3} - I_{L1}}{\lambda_{C1} V_{C1}} DT_S \\ C_2 \geq \dfrac{I_{L2}}{\lambda_{C2} V_{C2}} DT_S \\ C_3 \geq \dfrac{I_{L2} + I_{L4}}{\lambda_{C3} V_{C3}} DT_S \\ C_4 = C_3 / 5 \end{cases} \tag{13}$$

λ_{C1}, λ_{C2}, and λ_{C3} represent the voltage ripple coefficients of capacitors C_1, C_2, and C_3, respectively.

C. Simulation Analysis of the Converter

Simulation analysis of the proposed converter is performed based on the actual selected component parameters, with the component parameters listed in TABLE II. and the simulation model shown in Fig. 10.

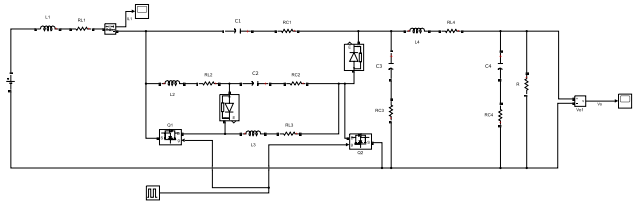


Fig. 10. Figure of the simulation model for the proposed converter in this paper.

TABLE II. SIMULATION PARAMETERS OF THE CONVERTER

Components	Parameters
Inductor L1	L1=600uH，R_{L1}=100m Ω
Inductor L2	L2=680uH，R_{L2}=180m Ω
Inductor L3	L3=100uH，R_{L3}=15m Ω
Inductor L4	L4=200uH，R_{L4}=30m Ω
Capacitor C1	C1=8uF，R_{C1}=80m Ω
Capacitor C2	C2=80uF，R_{C2}=20m Ω
Capacitor C3	C3=100uF，R_{C3}=15m Ω
Capacitor C4	C4=20uF，R_{C4}=50m Ω
Diodes	V_D=0.3V，R_D=8m Ω
MOSFETs	R_Q=3m Ω
Load R_{Load}	R=250 Ω

R_{L1} and R_{L2} represent the equivalent series resistances of inductors L1 and L2, respectively. R_{C1} and R_{C2} denote the equivalent series resistances of capacitors C1 and C2, respectively. R_{Q1} and R_{Q2} indicate the drain-source on-resistances of MOSFETs Q1 and Q2, respectively. R_{D1} and R_{D2} are the internal resistances of diodes D1 and D2, respectively; V_{D1} and V_{D2} are the forward conduction voltage drops of diodes D1 and D2.

The output voltage of the converter considering parasitic parameters is:

$$V_O = \frac{V_{in} - B(D)}{(1-D)^2 + \frac{A(D)}{R}} \tag{14}$$

where

$$A(D) = \frac{R_{L1}}{(1-D)^2} + R_{L4} + \frac{2R_{C3}D(2-D)}{1-D} + (1-D)\left\{\frac{D[2R_{C1} + (2-D)R_{C3} + R_{L2} + R_{C2}]}{1-D} + \frac{D(2-D)R_{Q2}}{(1-D)^2} + R_{D2} + R_{L2}\right\} + \frac{D[R_{C1} + (2-D)R_{C3} + R_{C2}]}{1-D} + \frac{D(2-D)R_{Q2} + D(R_{L3} + R_{Q1})}{(1-D)^2} + \frac{R_{D1} + R_{L3}}{1-D} \tag{15}$$

$$B(D) = (1-D)^2 V_{D2} + (1-D)V_{D1} \tag{16}$$

Through calculation, when Vin=0.4V, to achieve Vo=5V, D ≈0.777. The simulation results of the converter output voltage Vo and input current I_{L1} are shown in Figs. 11 and 12.When the duty cycle D=0.775, the output voltage Vo=5V, which is nearly consistent with the theoretical analysis. The simulation results show that the input current ripple coefficient is about 0.2%, and the output current ripple coefficient is less than 0.01%, indicating that zero input-output current ripple has been achieved. Simulation results demonstrate that the proposed converter exhibits high voltage gain and ultra-low input and output current ripple characteristics.

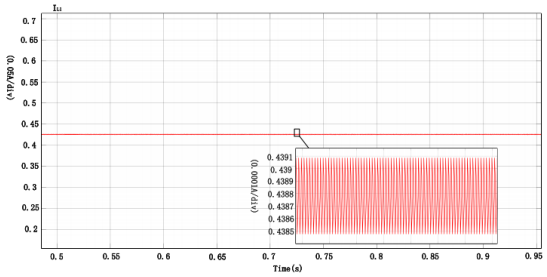


Fig. 11. Input current waveform of the converter.

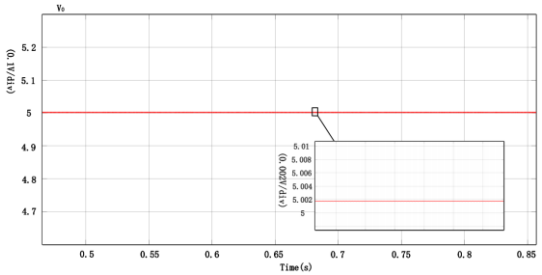


Fig. 12. Output voltage waveform of the converter.

D. Comparative Analysis

In this section, the converter proposed in this paper is compared with those proposed in other literature for the energy harvesting field. TABLE III. shows the comparisons of step-up ratio, component count, input/output current ripple, and voltage gain.

The voltage gain curves of the converter topologies proposed in[10], [11], [12] and the converter topology proposed in this paper are plotted, as specifically shown in Fig. 13.

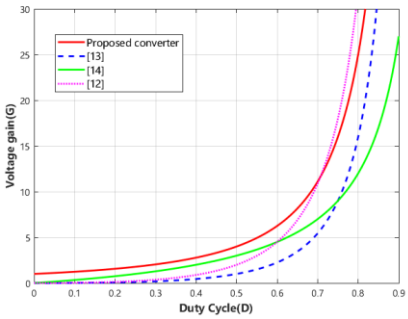


Fig. 13. Comparison Diagram of Converter Voltage Gain.

TABLE III. COMPARISON OF DIFFERENT CONVERTERS

Reference	[10]	[11]	[12]	This paper
Number of switching tubes	1	1	1	2
number of diodes	7	5	3	2
number of inductors	3	3	4	4
number of capacitors	2	3	6	4
input/output current ripple	Non-zero	Non-zero	Non-zero	0
voltage gain (G)	$\frac{2D^2}{(1-D)^2}$	$\frac{D^2}{(1-D)^2}$	$\frac{3D}{1-D}$	$\frac{1}{(1-D)^2}$

From the above comparison, it can be seen that the topology proposed in this paper achieves higher gain than other converters with a similar number of components, uses fewer diodes to reduce losses, and realizes zero input-output ripple.

IV. SYSTEM SIMULATION MODEL CONSTRUCTION AND SIMULATION RESULTS

To verify the overall performance of the energy harvesting system, a simulation model of the entire circuit was built using Simulink, as shown in Fig. 15. According to the simulation analysis of the EHCT in Section 1.2 of this paper, the output of the EHCT is three-phase electricity. However, during actual operation, the current amplitude on the cable fluctuates by ±(10-30)%. Therefore, a three-phase voltage source with equal amplitude and time-varying amplitude was used to simulate the EHCT. As analyzed earlier, when the simulated current fluctuates around ±30%, the output voltage of the EHCT fluctuates between 0.7V and 1.3V. Thus, the waveform of the three-phase voltage source was set as shown in Fig. 14.

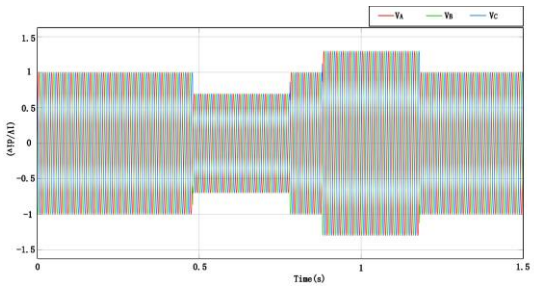


Fig. 14. Waveform of three-phase voltage source.

The output voltage of the energy-harvesting current transformer fluctuates around 0.4V after rectification, filtering, and voltage stabilization, but with significant voltage variations. After passing through the DC-DC converter, the output voltage reaches VO=5V. After passing through the DC-DC converter, the output voltage reaches VO=5V. The final output voltage waveform of the circuit is shown in Fig. 16. It can be observed that once the circuit reaches steady state, even when the current amplitude on the cable fluctuates within ±30%, the output voltage of the circuit remains stable at approximately 5V, with a maximum voltage ripple coefficient of about 1%. The proposed energy-harvesting scheme in this paper provides an output voltage that is sufficiently high and stable to meet the power supply requirements of temperature monitoring equipment.

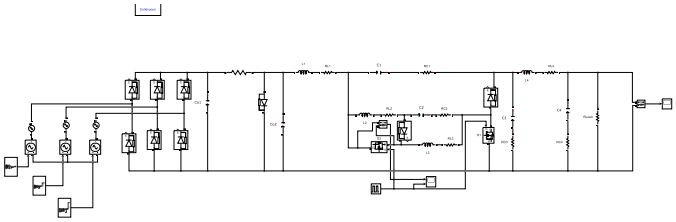


Fig. 15. Circuit model in Simulink.

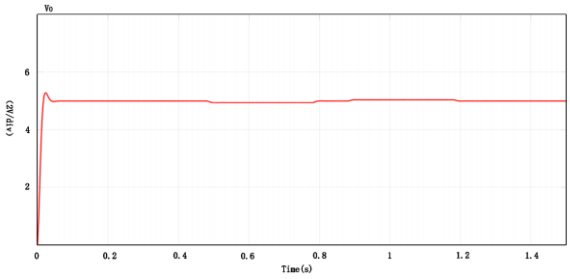


Fig. 16. Final output voltage waveform of the circuit.

V. Conclusion

This paper theoretically analyzes and simulates the amplitude and vector distribution characteristics of the magnetic flux density around three-phase cables, demonstrates why single-cable energy harvesting current transformers (EHCTs) are unsuitable for three-phase cables, and accordingly designs a six-segment winding EHCT. Compared with EHCT structures designed by other researchers, the three-cable EHCT proposed in this paper exhibits improvements in both output voltage and output power, with a per-phase output voltage increase of 120 mV and an output power increase of 70 mW. Furthermore, the self-designed DC-DC converter is theoretically analyzed in this study. Simulations verify that it possesses high-gain and low-output-voltage-ripple characteristics: with an input voltage of only 0.4 V, it achieves an output voltage of 5 V, an input current ripple of less than 0.2%, and an output current ripple of less than 0.01%. This effectively addresses the issues of low voltage and excessive ripple after the output of the EHCT undergoes rectification, filtering, and stabilization. A comprehensive simulation analysis of the proposed energy harvesting system shows that the final output voltage of the proposed solution remains stable at around 5 V. Even when the current amplitude of the three-phase cable fluctuates within ±30%, the maximum voltage ripple is only about 1%, ensuring that the final output voltage of the energy harvesting circuit meets the operational requirements of most low-power temperature monitoring devices. This provides a new solution for powering cable temperature measurement systems. Additionally, the proposed converter demonstrates excellent performance and can be extended to other energy harvesting fields such as photovoltaics.

References

[1] Y. Yan, T. Zhu, N. Zhang, et al. "Electromagnetic environment influencing factors for AC/DC cables in common trenches," Transactions of China Electrotechnical Society, vol. 37, no. 6, pp. 1329-1337, 2022. DOI: 10.19595/j.cnki.1000-6753.tces.l90547.

[2] Z. Lin, H. Zhou, L. Niu, et al. "Thermal-flow field coupling analysis of EHV power cables under tunnel laying conditions," Electric Power Engineering Technology, vol. 41, no. 3, pp. 216-223, 2022..

[3] Yasui T, Takeda N, Yokoo Y, et al. Temperature and Pressure Distribution Simulations of 3-km-Long High-Temperature Superconducting Power Cable System With Fault Current for 66-kV-Class Transmission Lines [J]. IEEE Transactions on Applied Superconductivity, 2017, 27(4): 1-5.

[4] Downie J D. Maximum Capacities in Submarine Cables With Fixed Power Constraints for C-Band, C+L-Band, and Multicore Fiber Systems [J]. Journal of Lightwave Technology, 2018, 36(18): 4025-4032.

[5] Song Y, Chen W, Wan F, et al. Online Multi-parameter sensing and condition assessment technology for power cables: A Review [J]. Electric Power Systems Research, 2022, 210: 108140.

[6] YONGLING LU, ZHEN WANG, ZIQUAN LIU, et al. Study on the Magnetic Field Characteristics of Three-phase Cables and Efficient Energy Extraction Methods[C]//2023 International Conference on Advances in Electrical Engineering and Computer Applications: AEECA 2023, Dalian, China, 18-19 August 2023, [v.1]. 2023:360-369.

[7] Di Y, Gao Y, Wang Y, et al. Design of Draw-out Power Supply for On-line Monitoring System of Three-core Power Cables [C]. 2021 3rd Asia Energy and Electrical Engineering Symposium (AEEES), 2021: 616-620.

[8] Monagle D, Ponce E A, Leeb S B. Rule the Joule: An Energy Management Design Guide for Self-Powered Sensors [J]. IEEE Sensors Journal, 2024, 24(1): 6-15.

[9] YIDONG ZHAO, HAN PENG, HONGFEI XIAO, et al. A Lightweight Self-Powered Module Based on Magnetic Energy Harvesting for Transmission Line Remotely Sensing[C]//2024 IEEE 10th International Power Electronics and Motion Control Conference: IPEMC2024-ECCE Asia, Chengdu, China, 17-20 May 2024, [v.1]. 2024:4565-4571.

[10] S. Liu, B. Wang, G. Zhu, et al. "A quadratic Buck-Boost converter based on switched-inductor," Transactions of China Electrotechnical Society, vol. 37, no. S1, pp. 190-197, 2022. DOI: 10.19595/j.cnki.10006753.tces.L90479.

[11] N. Zhang, G. Zhang, K. W. See and B. Zhang, "A Single-Switch QuadraticBuck-Boost Converter With Continuous Input Port Current and Continuous Output Port Current," IEEE Trans. Power Electron., vol. 33, no. 5, pp. 4157-4166, May 2018.

[12] M R Banaei, S G Sani. Analysis and implementation of a new SEPIC-Based single-Switch Buck-Boost DC-DC converter with continuous input current [J]. IEEE Transactions on Power Electronics,2018,33 (12):10317-10325.

Improving General-Purpose LLM Models for Power Cable Tasks Using Structured Context Engineering

Tong Wu
State Grid Xiamen Power Supply Company
Xiamen, China
t_wu96@163.com

***Abstract*—With the rapid development of large language models (LLMs), their performance on general tasks has approached human-level capabilities. However, challenges remain in applying these models to specific professional domains, such as insufficient domain knowledge and limited problem comprehension. This paper proposes a knowledge enhancement method based on context engineering. Using DeepSeek-R1-Distill-Qwen-32B as the experimental subject, the method embeds fault cases, textbook knowledge, and real-world problem descriptions from the field of power cables into the context in a structured manner. This significantly improves the model's performance in the domain. Experimental results show that, compared with AI systems that do not employ context engineering, the proposed method achieves a notable increase in accuracy across multiple professional question sets. The study demonstrates that combining context engineering with high-quality data can rapidly and effectively enhance a general-purpose language model's domain knowledge and problem-solving capabilities without fine-tuning of the model.**

Keywords—LLM, context engineering, power cable

I. INTRODUCTION

In recent years, large language models (LLMs) have made groundbreaking advances in the field of natural language processing (NLP), demonstrating impressive capabilities in tasks such as text generation, question answering, and code generation. However, these models are primarily trained on large-scale general-purpose corpora and often lack sufficient knowledge in specific professional domains. As a result, their performance in real-world engineering applications—such as understanding complex problems or providing expert-level advice—remains suboptimal.

Given the high degree of specialization in power system tasks, general-purpose utility functions are often difficult to directly adapt[1–2]. Therefore, it is necessary to train more efficient, domain-specific large-scale models in a targeted manner. Some researchers look for full-scale training of large language models (LLMs) to achieve specific task objectives. Common approaches include data parallelism[3], pipeline/model parallelism[4], and hybrid parallelism[5].

Funding Project: Research Project of State Grid Fujian Electric Power Co., Ltd. *"An Intelligent System for Power Cable Monitoring and Fault Diagnosis Based on Optical Fiber Sensing"* (Project ID: 52134024000Z).

Taking power system planning as an example, the stochastic nature of renewable energy output and the susceptibility of equipment safety margins to environmental factors make safe and efficient system planning challenging. Beyond employing hybrid training strategies for LLMs to integrate multi-source data and multi-device models, it is also essential to incorporate safety and low-carbon constraints into the loss function, thereby balancing risk and cost.

Another line of research focuses on parameter fine-tuning. Since pretraining LLMs on general text corpora cannot sufficiently encode power domain knowledge, parameter fine-tuning addresses this limitation by training only a subset of parameters, effectively transferring downstream task data into the model. For instance, some studies extend pretrained models by introducing additional parameters or layers, such as adapters[6], while others selectively fine-tune higher-level network structures, such as adjusting only model biases[7] or specific layers[8]. In addition, low-rank representations have been employed to minimize the number of trainable parameters[9], and combining multiple fine-tuning methods has been shown to further improve performance[10].

In the context of power system control, LLMs can be trained on large volumes of offline data to accumulate knowledge and experience for handling complex operational scenarios. In online scheduling, however, feasible dispatch regions and environmental feedback often exhibit sudden changes. By introducing adapters, soft prompts, and other fine-tuning methods, online models can perform rolling inference under multiple constraints—such as power flow convergence, transient stability, and steady-state security—while autonomously exploring the solution space and mastering optimal grid control patterns.

A further approach is embedding domain knowledge into the model. For professional-grade power domain LLMs, domain knowledge must be in-depth, real-time, and accurate. Power grid knowledge graphs (KGs) can capture and represent complex spatiotemporal relationships among grid operating conditions, multi-level equipment entities, and related events via graph-based modeling[11–14].

Traditional solutions typically rely on fine-tuning or instruction tuning methods, which involve retraining the model with large amounts of domain-specific data to enhance its

979-8-3315-5472-9/25/$31.00 ©2025 IEEE

specialized capabilities. However, these approaches are often associated with high computational costs, expensive data annotation requirements, and complex deployment processes, making them difficult to scale in resource-constrained or fast-iteration application scenarios.

To address these challenges, this paper proposes a method for enhancing the domain-specific capabilities of language models without fine-tuning, referred to as Context Engineering. By carefully designing structured information within the model's input context, the approach integrates typical fault cases, textbook knowledge, and real-world problems from the field of power transmission cables. This allows the model to incrementally "acquire" domain knowledge during the dialogue process, thereby improving its understanding and problem-solving abilities.

Using DeepSeek-R1-Distill-Qwen-32B as the experimental model, the study conducts a series of experiments centered on the power transmission cable domain. By comparing the performance with that of models using unoptimized context inputs, the effectiveness of the context engineering approach in enhancing the model's domain-specific capabilities is systematically evaluated. This work not only offers a lightweight and efficient solution for applying general-purpose language models in specialized fields but also provides valuable insights into how AI can assist engineering professionals in solving practical problems.

II. Methodology of Context Engineering

A. Design Philosophy of Context Engineering

Context Engineering is a lightweight approach that enhances a language model's domain expertise by optimizing input structure and dynamically injecting high-quality domain knowledge[15]. Unlike traditional fine-tuning methods, context engineering does not involve modifying model parameters. Instead, it embeds domain knowledge into the conversational context in a structured manner through well-designed input content and information layout, enabling the model to "temporarily acquire" a specialized knowledge system during inference.

The design philosophy of context engineering in this study is based on three core principles:

Problem-Oriented: Contexts are constructed around questions commonly raised by technical personnel in real-world scenarios, ensuring that the model's understanding aligns with authentic work contexts.

Case-Driven: Representative fault cases related to power transmission cables are carefully selected to serve as material for the model to "learn from" and "reason through," thereby improving its contextual understanding and application capabilities.

Knowledge Completion: To address general language models' limitations in understanding technical terminology and principles, key knowledge points are extracted from textbooks and embedded into the context in a concise and structured format, providing essential support for the model's reasoning.

B. Implementation Framework of Context Engineering

The implementation framework of the proposed context engineering method consists of the following steps:

(1) Problem Analysis and Scenario Setup

First, common question types encountered by technical personnel during cable operation and fault handling are collected and categorized into four main groups: fault diagnosis, cause tracing, emergency response, and technical solution optimization. Additionally, problem descriptions are simulated based on real-world expressions to ensure that the inputs reflect authentic language and operational context.

(2) Case and Knowledge Base Construction

A dataset comprising 200 representative fault cases of power transmission cables is constructed. Each case includes a fault description, environmental context, handling process, and final conclusion. Meanwhile, 50 key knowledge points are extracted from power cable maintenance textbooks—covering topics such as cable structure principles, common fault types, diagnostic methods, and technical standards—to form a reusable knowledge base.

(3) Context Structure Design

For each question category, a standardized context template is designed. The basic structure includes:

Problem Statement: The specific question is posed using language typical of field engineers or technicians.

Relevant Cases: One or two historical fault cases closely related to the question are included.

Knowledge Prompt: Two to three textbook-derived knowledge points relevant to the question are inserted.

Instruction: The model is explicitly prompted to respond as a domain expert, conducting analysis and offering solutions.

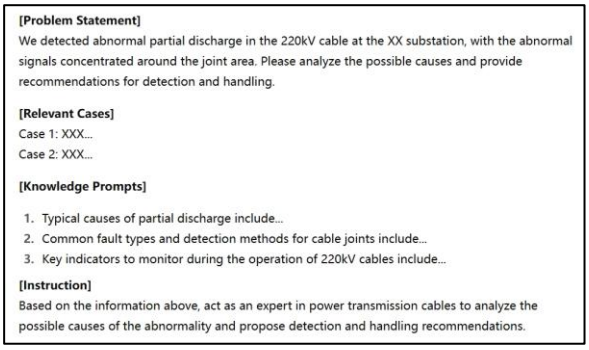


Fig. 1. An example structure of the context

An example structure of the context is shown in Fig.1.

(4) Dynamic Context Generation and Injection

Based on the user's question, the system performs keyword matching and semantic analysis to dynamically select the most relevant content from the case base and knowledge base. It then automatically generates a complete context and feeds it as input to DeepSeek-R1-Distill-Qwen-32B for reasoning and response.

C. Baseline Comparison

To evaluate the effectiveness of context engineering, two baseline systems were designed for comparison:

Baseline A: The question is input directly without any contextual information.

Baseline B: The question is provided along with a brief background description, but without embedded cases or knowledge prompts.

By comparing the performance of these baseline systems, the study assesses the role of context engineering in improving the model's answer accuracy and domain-specific expertise.

III. Experiments and Results

The goal of this experiment is to evaluate the effectiveness of the context engineering approach in improving the accuracy and professionalism of DeepSeek-R1-Distill-Qwen-32B when answering questions in the domain of power transmission cables. The focus is on examining whether domain knowledge acquisition and problem-solving capabilities can be significantly enhanced through optimized contextual input, without any model fine-tuning.

A. Question Bank and Dataset Construction

To comprehensively assess the effectiveness of context engineering, three types of test question banks were constructed, comprising a total of 300 questions. These cover various knowledge dimensions and application scenarios within the power cable domain:

TABLE I. Construction of Question Banks

Question Bank Type	Number of Questions	Description
Fault Diagnosis	120	Presents abnormal phenomena; requires analysis of causes and fault location
Treatment Suggestions	100	Provides specific fault scenarios; requires proposed detection and handling methods
Knowledge Application	80	Open-ended questions combining textbook knowledge with applied understanding

All questions were annotated by five engineers with over five years of experience in power cable operation and maintenance, ensuring that the problem descriptions reflect real-world scenarios and that reference answers carry authoritative industry insights.

B. Experimental Groups and Comparison Plan

Three experimental groups were designed for comparison:

Baseline A (No Context): Only the question is input, with no background or knowledge prompts provided.

Baseline B (Brief Background Description): The input includes the question and a brief scenario description, but no embedded cases or knowledge prompts.

Proposed Method (Context Engineering): Applies the full context engineering approach described in this paper, embedding relevant cases and textbook knowledge.

All experiments were conducted using the DeepSeek-R1-Distill-Qwen-32B model under consistent model parameters and inference environments to ensure fairness.

C. Evaluation Metrics

To evaluate the model's performance under different context inputs, the following metrics were used:

Top-1 Accuracy: Whether the model's first response matches the reference answer.

Professionalism Score: Rated by five power cable experts based on the technical accuracy and professionalism of the response, with a maximum score of 10.

Practical Effects: Assesses whether the model's response is executable and provides meaningful guidance in actual engineering contexts, with a maximum score of 5.

D. Experimental Results

(1) Top-1 Accuracy

TABLE II. Top-1 Accuracy Comparison

Question Bank Type	Baseline A	Baseline B	Proposed Method
Fault Diagnosis	48.3%	61.7%	82.5%
Treatment Suggestions	42.0%	57.0%	79.0%
Knowledge Application	55.0%	68.8%	86.3%
Average Accuracy	48.4%	62.5%	82.6%

(2) Professionalism Score

TABLE III. Professionalism Score Comparison

Question Bank Type	Baseline A	Baseline B	Proposed Method
Fault Diagnosis	5.2	6.8	8.9
Treatment Suggestions	4.8	6.5	8.7
Knowledge Application	6.0	7.3	9.1
Average Score	5.3	6.9	8.9

(3) Practical Effects

TABLE IV. Practical Effects Comparison

Question Bank Type	Baseline A	Baseline B	Proposed Method
Fault Diagnosis	2.3	3.5	4.7
Treatment Suggestions	2.0	3.2	4.5
Knowledge Application	2.7	3.8	4.8
Average Score	2.3	3.5	4.7

E. Result Analysis

Experimental results show that the Proposed Method using context engineering significantly outperforms both Baseline A and Baseline B across all three evaluation metrics. In particular, for fault diagnosis and treatment suggestion questions, the

accuracy improved by more than 30%, while scores for professionalism and practical usefulness also increased substantially. These results demonstrate that well-designed contextual inputs—embedding high-quality cases and textbook knowledge—can effectively compensate for the limitations of general-purpose language models in mastering specialized knowledge within professional domains.

IV. Discussion

A. Advantages of Context Engineering

The context engineering approach proposed in this study demonstrates significant potential for rapidly enhancing the domain capabilities of general-purpose large language models (LLMs) in resource-constrained environments. Compared with traditional methods that rely on model fine-tuning and retraining, context engineering offers several notable advantages:

(1) Lightweight and Cost-Effective

Context engineering is entirely input-optimization-based, requiring no additional model training or parameter adjustment. This avoids the substantial computational and data annotation costs associated with fine-tuning, enabling ordinary enterprises and small to medium-sized teams to enhance LLMs with domain expertise at a low cost.

(2) Flexibility and Real-Time Adaptability

Unlike fine-tuned models that require redeployment, context engineering allows dynamic adjustment of context content and structure according to specific application scenarios and question types. This enables rapid iteration and scenario switching—making it particularly suitable for complex professional domains like power transmission cables, where problem types are diverse and situational complexity is high.

(3) Improved Problem Understanding and Reasoning Capabilities

By embedding structured cases and knowledge points into the context, the model can develop "situational awareness" during problem-solving. This reduces reliance on memorized general corpora from training and enhances the model's performance in understanding problems, analyzing causes, and proposing solutions with greater relevance and logical coherence.

B. Limitations and Challenges

Despite the promising results achieved, the context engineering approach still faces several inherent limitations and challenges:

(1) Limitations of Context Window Length

Current LLMs are still constrained by the physical limit of their context window size. When problem scenarios are complex and require numerous cases and knowledge points, it remains a challenge to efficiently organize information within a limited window while ensuring completeness and model comprehension. This is an area that requires further exploration.

(2) Quality of Case and Knowledge Base Construction

The effectiveness of context engineering is highly dependent on the quality and coverage of the case base and knowledge base. If the selected cases are not representative or the extracted knowledge points are not precise enough, it can negatively impact the model's ability to understand the problem and provide professional responses. Therefore, constructing high-quality domain knowledge bases is critical for the broader application of context engineering.

(3) Sensitivity to Question Phrasing

Although context engineering improves the model's mastery of domain knowledge, it remains sensitive to the way users phrase their questions. If a question is poorly described, vague, or illogical, the model may still produce incorrect responses. Hence, future research should focus on integrating natural language understanding techniques to guide and optimize how users formulate questions, thereby improving the system's practical usability.

C. Prospects for Broader Application

Despite the above challenges, the context engineering approach proposed in this study holds significant potential for application in other professional domains beyond power transmission cables. Examples include:

Fault Diagnosis and Operation Support in Power Systems: Extending the approach to other scenarios such as substations, distribution networks, and energy storage systems.

Intelligent Customer Support Systems for Equipment Manufacturers: Assisting technical support personnel with fast, accurate solutions to product-related issues.

Intelligent Teaching Assistants for Engineering Education: Providing students with personalized, case-driven learning and Q&A experiences based on textbook content.

Furthermore, as the context window capacity of future LLMs expands and methods for injecting multimodal data (such as images, tables, and real-time data) become more sophisticated, the proposed method could evolve to integrate diverse information formats—further enhancing the model's scene understanding and problem-solving capabilities.

V. Conclusion

This paper addresses the challenge of inadequate domain knowledge mastery in large language models (LLMs) and proposes a context engineering-based knowledge enhancement method. By embedding typical fault cases and textbook knowledge points into a well-structured input context, the general-purpose LLM DeepSeek-R1-Distill-Qwen-32B demonstrated improved professionalism and practicality in the field of power transmission cables.

Experimental results show that the proposed context engineering method significantly enhances the model's accuracy, expertise, and practical usability across various question types—such as fault diagnosis, treatment recommendations, and knowledge application—without requiring any fine-tuning. Compared to traditional baseline methods, the AI system utilizing context engineering achieved over 30% improvement in answer accuracy across all test sets, and the quality of its responses received consistent recognition

from domain experts. These findings validate the effectiveness and practicality of the method in enhancing domain-specific knowledge.

The main contributions of this work are:

- Proposing a lightweight, flexible, and training-free context engineering method for enhancing domain knowledge in LLMs;
- Constructing a high-quality case base and knowledge base tailored to the power transmission cable domain, and systematically validating the effectiveness of context engineering in boosting model expertise;
- Providing a viable path for deploying general-purpose LLMs in other specialized domains, particularly in resource-constrained or rapid deployment scenarios.

However, this study also recognizes several ongoing challenges faced by the context engineering approach, including limitations in context window length, high demands on data quality, and sensitivity to question phrasing. Future research will focus on the following directions:

- Leveraging larger context windows and multimodal data to optimize information organization and expression in complex scenarios;
- Building more structured and comprehensive domain knowledge graphs to further enhance the model's understanding and application of logical relationships between knowledge points;
- Investigating best practices for user query formulation and intelligent guidance strategies to improve the model's comprehension accuracy and robustness in real-world interactions.

In summary, the context engineering method proposed in this paper offers a novel and practical approach to rapidly enhancing the domain capabilities of general-purpose LLMs without fine-tuning, and holds strong potential for engineering applications and broader Application.

REFERENCES

[1] X. Han, J. GUO, T. PU, et al. Theoretical foundation and directions of electric power artificial intelligence (I): hypothesis analysis and application paradigm. Proceedings of the CSEE, 2023, 43(8):2877-2890.

[2] Q. Sun, L. Yang, H. Zhang. Smart energy−applications and prospects of artificial intelligence technology in power system. Control and Decision, 2018, 33(5):938-949.

[3] S. Rajbhandari, O. Ruwase, J. Rasley, et al. Zeroinfinity: breaking the GPU memory wall for extreme scale deep learning. International Conference for High Performance Computing, Networking, Storage and Analysis, November 14-19,2021, St. Louis, USA.

[4] D. Narayanan, M. Shoeybi, J. Caspe, et al. Efficient large-scale language model training on GPU clusters using megatron-LM. International Conference for High Performance Computing, Networking, Storage and Analysis, November 14-19, 2021, St. Louis, USA.

[5] L. Zheng, Z. Li, H. Zhang, et al. Alpa: automating interand intra-operator parallelism for distributed deep learning. 6th USENIX Symposium on Operating Systems Design and Implementation, July 11-13, 2022, Carlsba, USA.

[6] N. Houlsby, A. Giurgiu, S. Jastrzebski, et al. Parameter-efficient transfer learning for NLP. International Conference on Machine Learning, June 9-15, 2019, Long Beach, USA.

[7] E. Ben Zaken, Y. Goldberg, S. Ravfogel. BitFit: simple parameter-efficient fine-tuning for transformer-based masked language-models. 60th Annual Meeting of the Association for Computational Linguistics, May 22-27, 2022, Dublin, Ireland.

[8] D. Vucetic, M. Tayaranian, M. Ziaeefard, et al. Efficient fine-tuning of BERT models on the edge, IEEE International Symposium on Circuits and Systems (ISCAS), May 27-June 1, 2022, Austin, USA.

[9] A. Aghajanyan, S.Gupta, L. Zettlemoyer. Intrinsic dimensionality explains the effectiveness of language model fine-tuning. 59th Annual Meeting of the Association for Computational Linguistics and the 11th International Joint Conference on Natural Language Processing, August 1-6, 2021.

[10] M R. Karimi, J. Henderson, S. Ruder. Compacter: efficient low-rank hypercomplex adapter layers. Advances in Neural Information Processing Systems, 2021, 34: 1022- 1035.

[11] X. Zhang, D. Liu, B. Li, et al. Research on the framework and construction model of information driven knowledge graph of large power grid operation situation. Proceedings of the CSEE, 2024, 44(11):4167-4181.

[12] S. Pan, L. Luo, Y. Wang, et al. Unifying large language models and knowledge graphs: a roadmap. IEEE Transactions on Knowledge and Data Engineering, 2024, 36(7):3580-3599.

[13] L. Yang, H. Chen, Z. Li, et al. Give us the facts: enhancing large language models with knowledge graphs for factaware language modeling. IEEE Transactions on Knowledge and Data Engineering, 2024, 36(7):3091-3110.

[14] H. Zhu, D. Xu, Y. Huang, et al. Graph structure enhanced pre-training language model for knowledge graph completion. IEEE Transactions on Emerging Topics in Computational Intelligence, 2024, 8(4):2697-2708.

[15] M. Mosbach, T. Pimentel, S. Ravfogel, et al. Few-shot fine-tuning vs. in-context learning: A fair comparison and evaluation. Annual Meeting of the Association for Computational Linguistics, 2023.

Electric Arc Simulation Validations and Switchgear Applications

Wenkai Shang
ANSYS Germany GmbH
Otterfing, Germany
wenkai.shang@ansys.com

Shihu Ma
ANSYS, Inc
Boulder, CO, USA
shihu.ma@ansys.com

Meng Li
ANSYS, Inc
Canonsburg, PA, USA
meng.li@ansys.com

Oleg Chernukhin
ANSYS, Inc
Waterloo, Canada
oleg.chernukhin@ansys.com

Runan Mo
ANSYS, Inc
Canonsburg, CA, USA
runan.mo@ansys.com

Somasekhar Machani
ANSYS, Inc
Bengaluru, Indian
somasekhar.machani@ansys.com

Chuan Lu
ANSYS, Inc
Canonsburg, PA, USA
chuan.lu@ansys.com

Yumin Xiao
ANSYS, Inc
Canonsburg, PA, USA
yumin.xiao@ansys.com

Isaac Liu
ANSYS, Inc
Canonsburg,PA,USA
isaac.liu@ansys.com

***Abstract*-In this paper, we focus on the validation of numerical simulation of electric arcs in gas. The core of the electric arc reaches a local thermal equilibrium (LTE) state, which primarily determines its behaviour. In contrast, the regions near the anode and cathode and outside the arc core are in a non-LTE condition. This work mainly discusses the modelling of the near-anode and near-cathode regions and the arc core. We use a magnetostatic approach to calculate the Joule heating loss and the Lorentz force within the arc. To model the regions near the anode and cathode, we introduce nonlinear conductivity dependent on current density to simulate voltage drops near the electrodes. The anode and cathode surface losses are then determined based on these voltage drops. Computational fluid dynamics (CFD) simulations are used to calculate the electrical conductivity and temperature of the arc at each iteration. Multi-species models that incorporate local species concentrations are used to account for metal and insulation vapor. Various thermal radiation models can be applied to improve the accuracy of electric arc simulations. High-performance computing (HPC) is used to meet computational demands and reduce simulation time. To validate the proposed simulation workflow, we focus on two benchmark cases and compare the simulated results with the experimental results from literature. Switchgear electric arc simulation is a challenging topic, due to complex physics, examples are shown as application of the simulation workflow to understand the complex electric arc process.**

Keywords-LTE electric arc, near anode and cathode voltage drop, nonlinear resistance sheet, arc simulation validation, weakly coupled simulations, and switchgear electric arc simulations.

I. INTRODUCTION

Studies of electric arcs related to switchgear operation date back to the 1900s [1]. These studies encompass a wide range of physical phenomena, including thermal dynamics, electron emission, high-temperature gas equilibrium, solid-phase transitions at electrode surfaces, behaviour of high-temperature and high-pressure partially ionized plasma, turbulence modelling, and thermal radiation characteristics. In recent years, significant advancements have been made through investigations and simulations, particularly those based on computational fluid dynamics (CFD) software [2–9].

In this work, we present a weakly coupled electric arc simulation workflow that focuses on validating numerical accuracy. One advantage of using a weakly coupled approach with ANSYS System Coupling is that each solver can independently achieve well-converged results. Additionally, different meshes can be used for different solvers, enabling each to more effectively model its intended physics.

The electromagnetic solver ANSYS Maxwell is used to solve Maxwell's equations and calculate the volume Joule loss, the Lorentz force, and the surface Joule loss density related to the arc. In the near-anode and near-cathode regions, the electrode surfaces are modeled as nonlinear resistive sheets to capture the non-local thermal equilibrium (NLTE) behavior of the electric arc. Nonlinear magnetic material properties can also be included, which is important for low-voltage switchgear applications.

The CFD solver ANSYS Fluent is used to solve the Navier–Stokes equations, which yield temperature and pressure fields. The energy equation includes both volume and surface Joule losses, and the momentum equation incorporates the Lorentz force. The workflow accounts for temperature- and pressure-dependent gas properties and integrates a species transport model to simulate the evaporation of metal and insulating materials due to localized high temperatures.

To ensure a coherent physical representation, predefined electrode motion is consistently applied in both the electromagnetic and CFD simulations. Additionally, an external circuit based on a Functional Mock-up Unit (FMU) can be coupled with the electromagnetic solver to study the interaction between arc voltage and circuit current. This coupling is essential to understanding the current-limiting behaviour of low-voltage circuit breakers.

979-8-3315-5472-9/25/$31.00 ©2025 IEEE

ANSYS System Coupling manages the exchange of the following between the solvers: Lorentz force, Joule loss, and bulk electrical conductivity. It also handles data mapping across different meshes and coordinates the sequential execution of electromagnetic and computational fluid dynamics (CFD) solvers. Figure 1 shows the general simulation workflow.

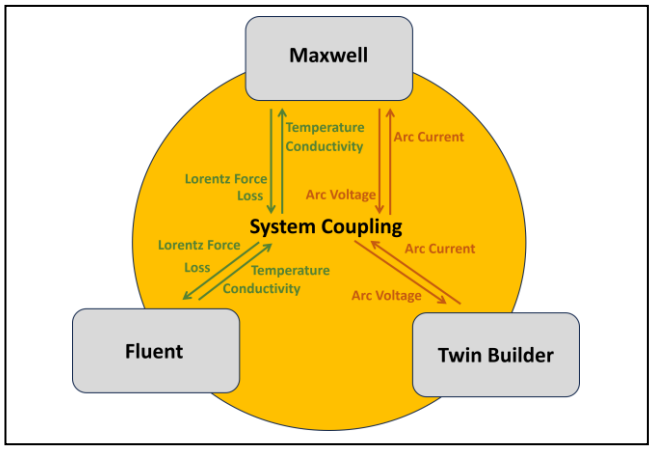


Figure 1. Simulation workflow and data exchange between different solvers.

II. NUMERIC SOLUTIONS IN DIFFERENT SOLVERS

A. *Workflow managing and data mapping through System Coupling*

The data transfer process consists of two main components, each of which executes its own set of algorithms [10].

Mapping uses data from a source mesh to compute corresponding data on a target mesh. It includes various algorithms that perform the following tasks:

- Associate source and target locations
- Generate data for target locations

Supplemental processing is applied to the data before and/or after mapping. Several algorithms are employed to:

- Reconstruct data at mesh locations
- Apply ramping and under-relaxation factors
- Perform unit conversions as needed
- Implement Quasi-Newton stabilization

The mapping algorithms ensure accurate data transfer, and supplemental processing enhances convergence between different solvers. Additionally, multiple cores can be utilized to speed up the data mapping process.

B. *Electromagnetic Solutions with Magnetostatics:*

A finite element magnetostatic solution is used to solve magnetic field, incorporating updated conductivity and temperature data from the fluid dynamic solver [10].

The current density in any conductive object can be solved for using the following equations:

$$\nabla \cdot (\sigma \nabla \varphi) = 0 \tag{1}$$

$$\boldsymbol{J} = \sigma \boldsymbol{E} = -\sigma \nabla \varphi \tag{2}$$

Here, $\sigma(x, y, z)$ represents the conductivity (S/m) of the material, and $\varphi(x, y, z)$ represents the electric potential (V), $\boldsymbol{J}$ is current density (A/m^2), $\boldsymbol{E}$ is electric field (V/m).

The magnetic field strength $\boldsymbol{H}$ (A/m) is then solved using Ampere`s law:

$$\nabla \times \boldsymbol{H} = \boldsymbol{J} \tag{3}$$

and the continuity of flux for magnetic flux density $\boldsymbol{B}$ (T):

$$\nabla \cdot \boldsymbol{B} = 0 \tag{4}$$

Then, the Lorentz force density $\boldsymbol{J} \times \boldsymbol{B}$ (N/m^3) and the Joule loss density σE^2 (W/m^3) are simulated and mapped to the CFD solver.

For non-local thermal equilibrium plasmas near the anode and cathode regions, we introduce a nonlinear resistive thin film of thickness L (m) and with conductivity σ dependent on the current density J to model the behaviour of the near anode and cathode region [2, 3]:

$$\sigma(J) = L\frac{c + J^d}{a + bJ^{d-1}}, \tag{5}$$

a , b, c and d are empirical constants [2, 3]. The values for the anode are: 3.0 x 10^8, 5, 1.1 x 10^{14}, and 2, respectively. The values for the cathode are: 3.0 x 10^8, 10, 1.1 x 10^{14}, and 2, respectively, these values are validated from our simulation results to get correct total arc voltage. This nonlinear relationship applies to both the anode and cathode surfaces. The ohmic loss at the root of the arc P (W) can be calculated as $L \rightarrow 0$, from a volume resistance integration to a surface resistance integration:

$$P = \lim_{L \to 0} \int_S \frac{J^2}{f(J)} dS, \tag{6}$$

$$f(J) = \frac{c + J^d}{a + bJ^{d-1}}. \tag{7}$$

This approach enables accurate extraction of anode and cathode drop values without the need to model non-LTE plasma in these regions, thereby simplifying the simulation workflow, and avoiding to model a very thin 3D layer, which makes the simulation much more efficient and accurate.

Surface heat flux is simulated by using the following equations for cathode and anode [1]:

$$Cathode: Q_c = k_i P + k_i J(V_i - \emptyset_c) \tag{8}$$

$$Anode: Q_a = k_e P + k_e J \emptyset_a \tag{9}$$

where P (W) is the nonlinear resistive sheet loss from equation (6) and the five coefficients for air and copper electrode are:
-k_i (=0.15) is the cathode ion current to total current ratio.
-k_e (=0.85) is the anode electron current to total current ratio.
-V_i (=15.58 V) is the air ionization potential.
-$\emptyset_c$, $\emptyset_a$ (=4.65 eV) are the work functions of the copper material at the cathode and anode respectively.

On the anode side, the current is primarily carried by electrons, while on the cathode side, it is predominantly carried

by ions. The ion current ratio, denoted as k_i, typically ranges from 0.1 to 0.2 [1]. For other gases or electrode materials, these values should be adjusted accordingly.

The surface heat flux is mapped from magnetostatic solver to CFD solver and assigned as a boundary condition to the corresponding surface to account for the influent in the electrode surface temperature calculation.

In Magnetostatic solver, motion can be defined as contact motion from experimental test results in the form of a tabular data set or as an analytical expression. Surface or object motion can also be defined. Linear or rotational motion can also be defined as needed.

The arc current can be defined as time-dependent, or derived from the circuit simulation.

C. The Fluid Dynamics Solution

The fluid dynamics solver uses the finite volume method to solve the Navier-Stokes equations with the following equations and considering: the Lorentz force density to the momentum equation; volumetric Joule heating and volumetric radiation losses q_{rad} (W/m^3) to energy equation [10]:

Continuity equation:

$$\frac{\partial \rho}{\partial t} + \nabla \cdot (\rho \boldsymbol{V}) = S_m \tag{10}$$

ρ (kg/m^3) is the gas density, t is time (s) and $\boldsymbol{V}$ (m/s) is velocity vector, S_m (kg/m^3) is the mass source term.

Momentum equation:

$$\frac{\partial (\rho \boldsymbol{V})}{\partial t} + \rho(\boldsymbol{V} \cdot \nabla)\boldsymbol{V} = -\nabla p + \mu \nabla^2 \boldsymbol{V} + \boldsymbol{J} \times \boldsymbol{B} \tag{11}$$

Here, p is pressure (Pa), μ is dynamic viscosity, $\boldsymbol{J} \times \boldsymbol{B}$ is the Lorentz force density (N/m^3).

Energy equation:

$$\frac{\partial (\rho h)}{\partial t} + \nabla \cdot (\rho h \boldsymbol{V}) = \nabla \cdot (\lambda \nabla T) + \sigma E^2 - q_{rad} \tag{12}$$

Here, h is the enthalpy, λ is thermal conductivity (W/mK), T is temperature (K), σE^2 is the Joule loss density (W/m^3), q_{rad} (W/m^3) is the energy source due to the thermal radiation.

When the evaporation of metal or insulation is considered the following continuity equation instead of equation (10) is solved for gas, metal and insulation vapour:

$$\frac{\partial (\rho Y_i)}{\partial t} + \nabla \cdot (\rho \boldsymbol{V}\, Y_i) = -\nabla \cdot \boldsymbol{F_i} + S_i \tag{13}$$

Y_i is mass fraction, $\boldsymbol{F_i}$ is diffusion flux (kg/m^{2}s), S_i is mass source, i represents gas, metal and insulation vapour.

To account for thermal radiation, the net emission formulation proposed by Lowke for an isothermal sphere with a radius of R_p is used [11]. [11-14] describe the net emission coefficient (NEC) approach, in which thermal radiation loss under thermodynamic equilibrium conditions are considered. In this context, the emission and absorption coefficient follows Kirchhoff s law. The radiation energy source term in the energy equation can ultimately be expressed as follows:

$$q_{rad} = 4\pi\varepsilon_n \tag{14}$$

Here, ε_n is the net emission coefficient, which is related to temperature, spectral intensity, emission and absorption coefficients. It is used as the thermal radiation loss term for validation. Alternative thermal radiation models may also be applied, provided that suitable material data is available.

The electrical conductivity is calculated using the simulated temperature and pressure from the CFD solver, and then mapped back to the electromagnetic solver for further analysis.

Motion can be defined using the dynamic mesh in CFD solver. Either a velocity profile or a displacement table can be used to define the motion of the electrodes. Different dynamic-mesh methods can be employed here, such as layered mesh or re-mesh for moving objects. Linear and rotational motion can also be modeled in CFD solver.

We use a user-defined function (UDF) to handle temperature- and pressure-dependent thermal dynamics and transport properties. We treat the material properties under the LTE assumption for electric arc core region. Therefore, thermal transport and dynamic properties are considered as a collective property of all species at different temperatures and pressures. Murphy [15] studied the properties of air ranging from 300 K to 30,000 K and modelled it as a mixture of nitrogen, oxygen, argon, and carbon dioxide. The species molar ratio was calculated by minimizing the Gibbs free energy. The transport coefficients are determined by the Chapman-Enskog method and tabulated prior to simulation. In this work, we use the transport coefficients from Murphy's study.

There are different turbulence models can be incorporated for the effect of turbulence through CFD viscous model [10]. Here, the SST $k-\omega$ model from F. R. Mentor is adopted for the effect of turbulence considering the simulation accuracy and simulation time [10], [16-17].

Due to the highly dynamic nature of electric arcs, small time steps are typically required in CFD solver. Two solutions can be used to speed up the simulation: The most common way is parallel computing, which directly expedites matrix solving. Another way is the sub-time step solution. Within each system coupling time step, Fluent divides it into N smaller sub-time steps. This technique allows for the use of larger time steps for coupling but smaller time step for CFD simulation.

D. Circuit simulation in ANSYS Twin Builder

The transient external circuit simulation accounts for the impact of electric arc voltage on the arc current, which is particularly critical for low voltage switchgear exhibiting current limiting behavior. The electric arc voltage, obtained from the magnetostatic simulation, is applied as a voltage source in the circuit simulation. The resulting current from the circuit simulation is then used as the excitation input for the magnetostatic analysis. Therefore, accurate simulation of the arc voltage is essential for determining the correct arc current.

III. Steady-state and Transient Simulation Validation and Comparison with Literature.

To validate the accuracy of our simulation workflow, we used two publications on LTE electric arc simulation and tests. Both cases show good agreement with the literature's results.

A. Steady-state, wall-stabilized LTE argon arc

As described in references [13, 14], this simulation workflow models a wall-stabilized cylindrical argon arc with 5 mm diameter and current of 100 A. We compared our workflow with the results reported in [13]. This simple yet effective model incorporates corresponding experimental measurements, and the simulated results align well with the test data, as illustrated in Figure 2 [14].

The NEC approach is used for validation purposes. There are also other thermal radiation models that can be used. For the NEC model [13-14], the radius of the isothermal sphere (Rp) is important for an accurate simulation result. In [14] different Rp values of 0 mm, 0.5 mm, 1.5 mm and 2.5 mm are used for the simulation. Thermal radiation is considered in the simulation as a loss term in the energy equation via a user-defined function (UDF).

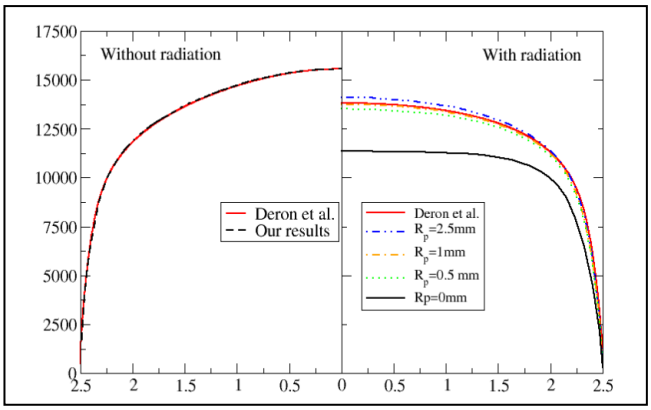


Figure 2. Simulated temperature with and without thermal radiation, x axis is radius (mm), y axis is temperature (K) [13].

Figure 3 shows the simulated temperature distribution without thermal radiation. Figure 4 shows the temperature distribution when thermal radiation is considered, using the net emission coefficient method [13, 14].

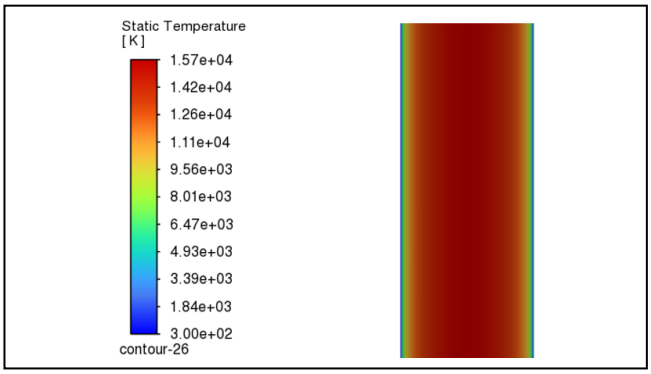


Figure 3. Simulated Wall-Stabilized Argon arc at 100 A without thermal radiation shows a temperature of 15725 K at the axis.

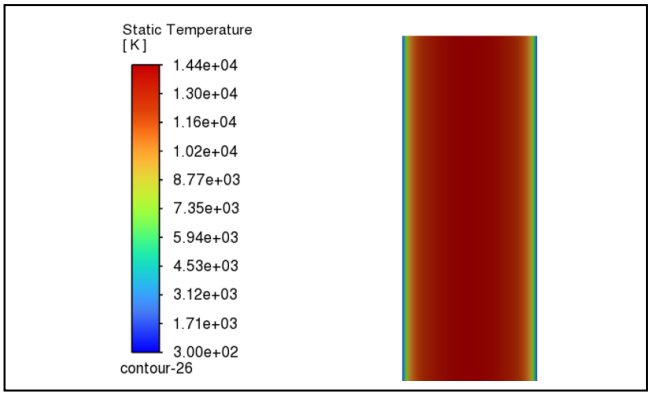


Figure 4. Simulated Wall-Stabilized Argon arc at 100 A with thermal radiation, the temperature at the axis is 14409 K.

B. Transient Arc Simulation of a Parallel Rail

An experimental investigation of a parallel rail system with various configurations at atmosphere air condition was conducted in [18]. For our study, we modeled two 15 mm wide, 120 mm long rails with an 18 mm gap and 1 mm thick electrodes to valid our simulation workflow. Both ends have an open venting, and both sides have electrical insulation walls. The current is transient and reaching a peak of 900 A at 2.2 x 10^{-3} s taken from the literature. We considered arc displacement and arc voltage to be the key parameters for evaluating the model.

A nonlinear resistive sheet was incorporated into the magnetostatic model based on Equation (1). Surface heat flux is accounted for using Equations (4) and (5) to simulate electrode surface temperatures. To capture the effect of thermal radiation on the surrounding walls, the discrete ordinates (DO) radiation model is applied [10].

As illustrated in Figure 5, the simulated arc displacement shows good agreement with the measured results.

These differences may be due to variations in motion measurement techniques and arc initiation methods. In the literature, it uses an optical method to obtain an average displacement value with multiple tests with measurement scatter. In our simulation, we track arc displacement by monitoring peak current density locations on the cathode and anode. The experiment uses a 0.1 mm diameter exploding electric conductive wire to initiate the arc, In the simulation, the arc is initiated by applying a constant heat source to a 1mm diameter cylinder. After stabilization, the arc voltage in both the experiment and simulation should converge to the same level.

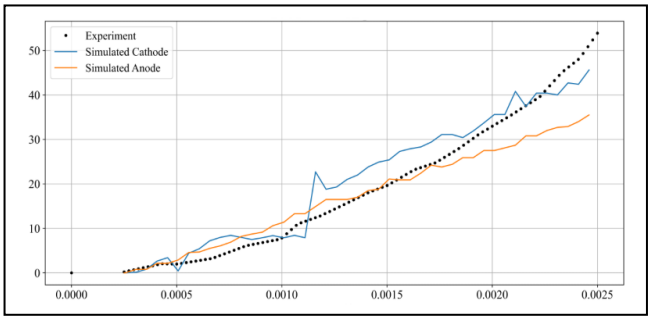


Figure 5. The arc motion is compared with experimental results from the literature [18]. The x axis represents time (s), and the y axis represents displacement (mm).

Figure 6 shows the typical arc temperature distribution on the middle cross section. Figure 7 shows the 3D Iso temperature contour surface with 15000 K.

After arc initiation using a fuse wire, the measured arc voltage decreases from an initial higher voltage phase to a steady range of 60 – 70 V. As shown in Figure 8, the simulated arc voltage in the range of 50 - 70 V.

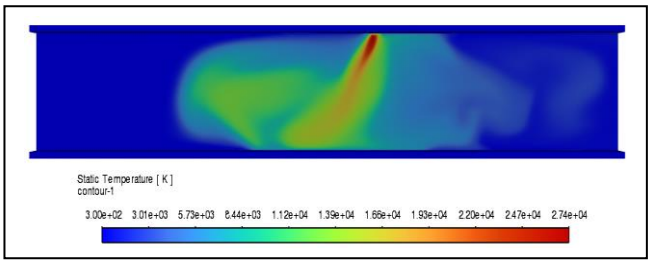


Figure 6. Temperature distribution in the middle plane, upper electrode is cathode, and lower electrode is anode.

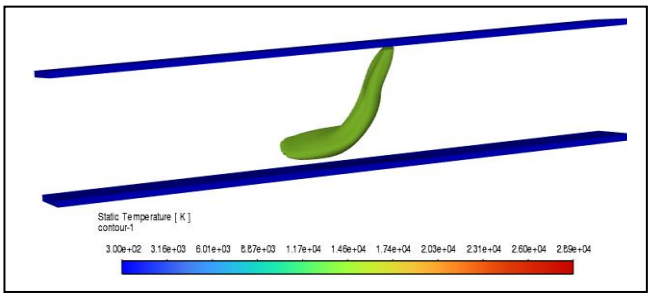


Figure 7. 3D Iso temperature contour surface with 15000 K, upper electrode is cathode, and lower electrode is anode.

From the simulation, the electric arc moves faster on the cathode side than on the anode side. This is mainly because the arc is more concentrated on the cathode side, resulting in a higher Lorentz force density and faster movement.

The total arc voltage consists of three main parts: the voltage drops near the anode and cathode, and the voltage drop in the arc column. Simulated total arc voltage indicates that nonlinear resistive sheets properly represent the behavior of electric arc voltage drop near the anode and cathode. The results can be fine-tuned by adjusting the four coefficients in equation (5). The coefficients from the literature already produce correct total simulated arc voltage. Another possible cause of the difference is the different initiation of the arc, which results in a different total arc voltage. In the test, an electric wire with a diameter of 0.1 mm is used, which introduces a more dynamic initial phase with a smaller initial arc diameter and a higher initial arc column voltage drop. In the simulation, we heat up the initial region with a constant heat source and 1 mm diameter initial arc, which results in a lower initial arc column voltage drops. These differences will also cause differences in total arc voltage.

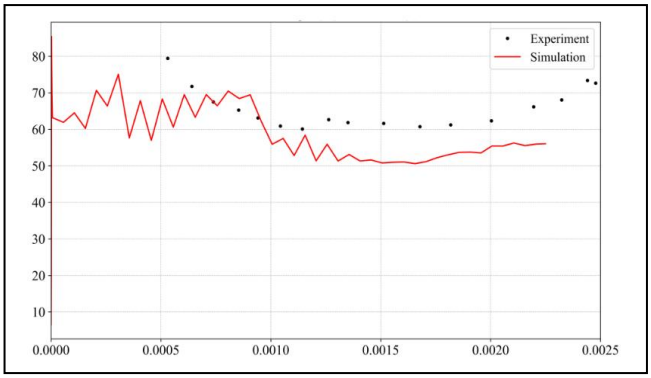


Figure 8. Simulated total arc voltage compared with test results from literature [18]. The x axis is time (s) and the y axis is voltage (V).

In testing and simulations, we observe a slightly V shaped total arc voltage by excluding the explosion of the electric wire at the beginning of the test. This can be explained as follows: Initially, the arc is relatively concentrated in cold surroundings, resulting in a higher total arc voltage. At a certain point, the total arc voltage decreases due to the increased overall temperature. After some time, the arc length increases more than the gap distance due to the different velocities of the cathode and anode. The increased arc length then increases the arc column voltage and increases also the total arc voltage.

IV. Application of Electric Arc Simulations

A. Transient electric arc simulation of low-voltage circuit breakers with constant current and electrode motion

The nonlinear material properties of the magnetic extinguishing plate and electrode motion are considered in the magnetostatic solver for low voltage switchgear, as they have strong impacts of the electric arcing process.

With 100 A DC, the arcing process can be simulated during contact opening. The arc is initiated at the small gap shown in Figure 9 and is driven by the Lorentz force from the initial arc point through the arc runner to the arc chute area shown in Figure 10. As expected, the arc moves properly to the arc quenching plates.

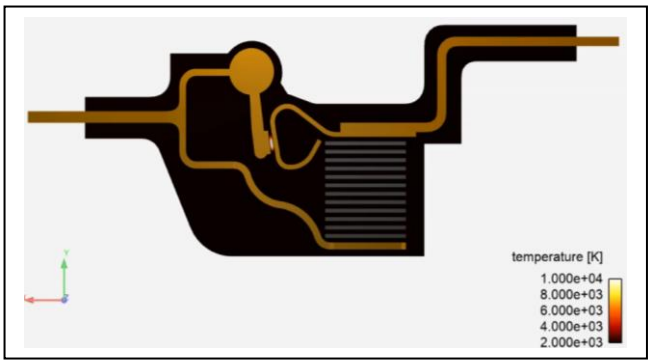


Figure 9. The arc is initiated between the electrodes.

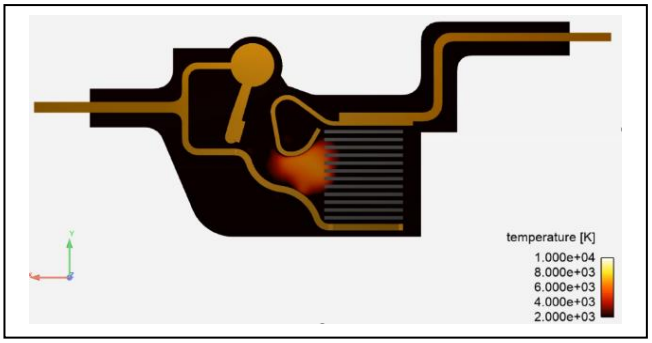


Figure 10. The arc moves toward the arc quenching plate.

B. *Simulation of internal electric arc failure*

Internal arc failure is a severe test for switchgear. According to the industry standard, switchgear must pass this test under defined criteria.

Figure 11 shows a substation control room model based on [19]. Previously, there was no satisfactory solution for simulating internal arcs that considered arcing physics. In this study, we simulate a real arc inside the switchgear room using a three-phase short-circuit current with a high DC component.

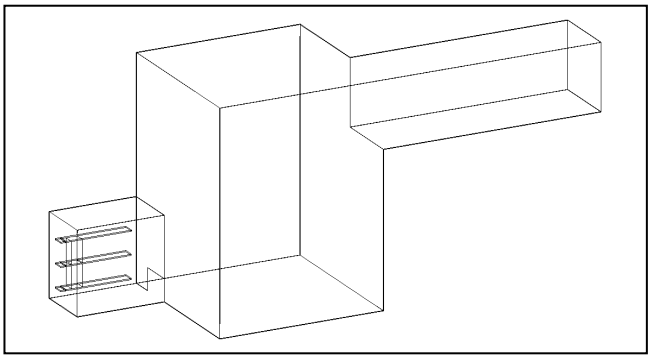


Figure 11. The internal arc simulation model.

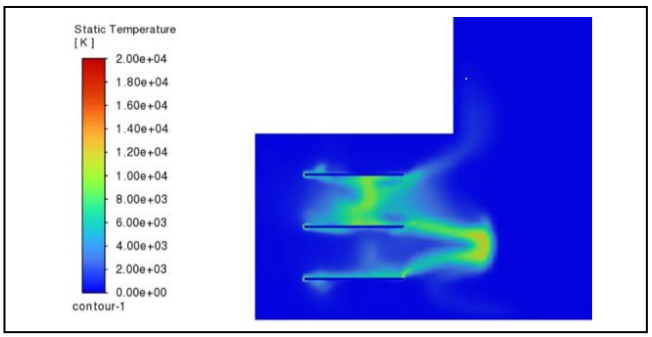


Figure 12. The electric arc is driven from left to the right by Lorentz force.

By observing the movement of the electric arc inside the switchgear, one can determine where the arc could remain and identify areas where the switchgear could potentially burn through. This information can then be used to improve switchgear design and performance.

Due to the high current and the Lorentz force, the electric arc is driven to the right side by the Lorentz force, as shown in Figure 12.

C. *The impact of metal and insulation material vapor on electric arc*

During high-current electric arcs, vapor containing metal and insulating material can be released from the electrode. Equations (4) and (5) can be used to model surface heat flux and simulate surface temperatures on electrode surfaces. Then, based on equation (13), the evaporation of metal from metal electrodes can be modeled correctly. Figure 13 shows the metal species injected from the electrode surface into the electric arc.

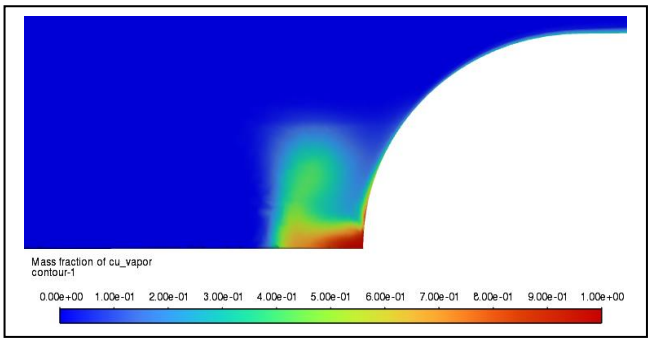


Figure 13. Copper vapor is released from the electrode surface.

Due to thermal heating from nearby electric arcs, ablation of insulation material can be modeled for insulated surfaces, especially for high current arcs. Insulation vapor can alter pressure and temperature distributions, as well as electric arc behavior at current zero. This can affect electric arc extinction, especially in high-voltage puffer-type circuit breakers.

V. Summary and Conclusions

In this work, we present a weakly coupled simulation workflow for modeling electric arcs using various solvers within the ANSYS eco system. We then validate the results by comparing them with those reported in the literature. It is an easy-to-use workflow. It is demonstrated through two case studies in which simulation results are compared with experimental data and the results show good agreement, the differences can be explained as the different initiation of the electric arc in test and simulation.

Solver-specific strategies can be applied to reduce the overall computational cost of long simulations without compromising accuracy. This simulation approach can be applied to many electric arc related applications, such as low, medium, and high voltage circuit breakers; pyro fuses; electrical contactors; load breakers; plasma wind tunnels; thermal plasma sources; ignition spark plugs; arc welding systems; and arc melting furnaces.

Acknowledgments

The authors would like to thank our management team for their support in developing this simulation workflow. Special thanks go to Anna Kvarnström, Jeremy McCaslin, Marius Ruso, Devin Crawford, Melanie Michon, Jay Cosentino, Atul Verma,

Bo He, Mark Solverson, Eric Bracken, and Vincent Lue. Thanks also to Fatitha Ouchar and Cyril Van de Steen from Safran for their collaborations.

REFERENCES

[1] T.H. Lee, Physics and Engineering of High Power Switching Devices. The MIT Press, 1975.

[2] M. Lindmayer, E. Marzahn, A. Mutzke, T. Rüther and M. Springstubbe, "The process of arc-splitting between metal plates in low voltage arc chutes," in IEEE Holm Conference on Electrical Contacts, Seattle, WA, USA, 2004.

[3] C. Rümpler,"Lichtbogensimulation für Niederspannungsschaltgeräte," Dissertation, Technische Universitat Ilmenau, Ilmenau, Germany, 2009.

[4] M. Rong, F. Yang, Y. Wu, A. B. Murphy, W. Wang and J. Guo, "Simulation of Arc Characteristics in Miniature Circuit Breaker," IEEE Transactions on Plasma Science, vol. 38, no. 9, pp. 2306-2311, 2010.

[5] K. Korytchenko, E. Poklonskiy, D. Vinnikov and D. Kudin, "Numerical Simulation of Gas-Dynamic Stage of Spark Discharge in oxygen," BAHT, vol. 4, no. 86, pp. 155-160, 2013.

[6] R. Bianchetti, A. Adami, L. Fagiano, R. Gati, L. Hofstetter, K. Elissa, "Arc Simulation in Low Voltage Switching Devices, a Case Study," Plasma Physics and Technology, vol.2, no.1, pp.5-8, 2015.

[7] B. Galletti, M. Schwinnea, M. Buffonia, P. U. Cristini, "Two-dimensional axisymmetric modeling of the magnetic field for high-voltage gas circuit breakers," Plasma Physics and Technology, vol.10, no.3, pp.141-145, 2023.

[8] R. B. Chechare, C. Rümpler, S. A. Sabri, S. J. Barot and A. Kittur "Multiphysics arc simulation of a miniature circuit breaker for prediction of short circuit interruption performance," in IEEE Holm Conference on Electric Contacts, 2024, pp. 166.

[9] J. Engelbrecht, S. Gorchakov, R. Methling, P. Pietrzak, and C. Franck "Study of transient arc properties near current zero in an experimental CO2 high-voltage circuit," Journal of Physics D: Applied Physics, vol.58, no.55, March 2025.

[10] ANSYS Maxwell, Fluent, Twin Builder, System Coupling help documents, 2025R1.

[11] J. J. Lowke, "Predictions of Arc Temperature Profiles Using Approximate Emission Coefficients for Radiation Losses," J. Quant. Spectrosc. Radiat. Transfer, vol. 14, no. 2, pp. 111-122, 1974.

[12] Y. Naghizadeh-Kashani, Y. Cressault and A. Gleizes, "Net emission coefficient of air thermal plasmas," Journal of Physics D: Applied Physics, vol. 35, no. 22, pp. 2925-2934, 2002.

[13] C. Deron, Ph. Riviere, M-Y. Perrin, and A. Soufiani. "Coupled radiation, ` conduction, and joule heating in argon thermal plasmas, " Journal of Thermophysics and Heat Transfer, vol.20, no.2, pp 211-219, 2006.

[14] F. Ouchar, C. Van de Steen , Ph. Riviere, T. Lebey , A. Soufiani. " Influence of Radiation Modelling on the Simulation of Wall Stabilized Electrical Arc," in IEEE Holm Conference on Electric Contacts, 2024.

[15] A. B. Murphy, "Transport Coefficients of Air, Argon-Air, Nitrogen-Air, and Oxygen-Air Plasmas," Plasma Chemistry and Plasma Processing, vol. 15, no. 2, pp. 279-307, 1995.

[16] F. R. Menter, "Zonal Two Equation k-ω Turbulence Models for Aerodynamic Flows", AIAA Paper 93-2906, 1993.

[17] F. R. Menter, "Two-Equation Eddy-Viscosity Turbulence Models for Engineering Applications", AIAA Journal, vol. 32, no 8. pp. 1598-1605, 1995.

[18] Jingjing Lu, "Caractérisation du comportement du plasma dans un disjoncteur basse tension par le développement d'un outil numérique et d'expériences associées," dissertation, Université Toulouse 3 Paul Sabatier, Toulouse, France, 2020.

[19] Xiang Zhang, "Modellierung der Auswirkungen von Störlichtbögen in elektrischen Anlagen," dissertation, Rheinisch-Westfälische Technische Hochschule Aachen, Aachen, Germany, 2002.

Redefining Grid-Connected Control: A Polar-Coordinate Based Synchronized Virtual Oscillator Framework

Hoach The Nguyen
Smart OR Lab, Advanced Power and Energy Center, Electrical Engineering Department, Khalifa University
ORCID: 0000-0002-9781-0856
Email: nguyen.hoach@ku.ac.ae

Ameena Saad Al-Sumaiti
Smart OR Lab, Advanced Power and Energy Center, Electrical Engineering Department, Khalifa University
Abu Dhabi, UAE
ORCID: 0000-0002-7742-8596
Email: ameena.alsumaiti@ku.ac.ae

Khalifa Al Hosani
Advanced Power and Energy Center, Electrical Engineering Department Khalifa University
ORCID: 0000-0002-2043-483X
Abu Dhabi, UAE
Email: khalifa.halhosani@ku.ac.ae

Ahmed Al-Durra
Advanced Power and Energy Center, Electrical Engineering Department Khalifa University
ORCID: 0000-0002-6629-5134
Abu Dhabi, UAE
Email: ahmed.aldurra@ku.ac.ae

Mohamed Shawky El-Moursi
Advanced Power and Energy Center, Electrical Engineering Department Khalifa University
ORCID: 0000-0001-6695-5342
Abu Dhabi, UAE
Email: mohamed.elmoursi@ku.ac.ae

Abstract— **This paper introduces a control framework for inverter-based resources using externally synchronized oscillators. Polar-coordinate control laws regulate phase, frequency, and magnitude without PLLs, dq-transforms, or trigonometric functions. Large-signal stability and convergence are proven via Lyapunov analysis. The framework supports direct power control, grid-forming features, and simple digital implementation. Simulations and experiments show fast synchronization, accurate regulation, and resilience in weak grids, unifying grid-following, grid-support, and grid-forming modes under one approach.**

Index Terms— Grid synchronization, polar coordinate control, power electronics, renewable energy integration, inverter-based resources, weak grids.

I. Introduction

The increasing penetration of inverter-based resources (IBRs) such as solar PV, wind turbines, and storage is transforming modern power systems [1], [2]. With renewables projected to supply over 85% of global electricity by 2050 [3], [4], challenges of synchronization and stability are intensifying under weak-grid and high-renewable conditions [5], [6], [7], requiring robust grid-connected control strategies [8].

Conventional inverter control relies on phase-locked loops (PLLs) with dq-frame transformations [9], [10] but PLLs introduce instability in weak grids [8], [11], [12] and interact unfavorably with power control, causing oscillations [13], [14]. Alternatives such as frequency-locked loops (FLLs) [15], virtual synchronous machines (VSMs) [16], [17], droop control [18], and virtual oscillator control (VOC) [19] have been investigated, yet suffer from slow dynamics, residual PLL dependence [20], limited synchronization accuracy, or lack of stability proofs [21], [22].

Kuramoto-inspired oscillator models [23] suggest self-synchronization and grid-forming capability without PLLs, but practical adoption is hindered by simplifying assumptions, difficult parameter tuning, and lack of large-signal analysis. Similarly, dq-frame approaches [9] add complexity and sensitivity to unbalances [24], while direct power control lacks precision [25]. Ensuring large-signal stability of inverter-dominated systems remains an open problem, with Lyapunov-based methods promising but challenging for conventional controllers [26].

In summary, state-of-the-art approaches face three main limitations: (1) reliance on PLLs with stability risks, (2) structural complexity due to transformations and filtering, and (3) absence of rigorous large-signal stability guarantees.

This paper introduces synchronized generalized virtual oscillators (Syn-GVOs) with polar-coordinate control to address these gaps. The framework: (1) synchronizes to grids without PLLs or dq transformations, (2) decouples phase/frequency and magnitude dynamics to eliminate coupled instability risks, (3) establishes large-signal stability via Lyapunov methods, and (4) validates performance through simulations and experiments under weak-grid conditions.

The paper is organized as follows: Section II introduces the Syn-GVO framework and polar-coordinate formulation; Section III provides stability analysis; Section IV describes implementation in grid-connected control; Section V presents experiments; and Section VI concludes.

II. New Concepts of Synchronized Virtual Oscillators and Polar-Coordinate Control

This section introduces a new concept of synchronized virtual oscillators (Syn-VOs) with decoupled polar-coordinate control laws, independently regulating magnitude and frequency/phase while ensuring large-signal stability.

A. Comparative High-Level Designs

Fig. 1(a) depicts conventional PLL-based dq-frame control with PI loops. Fig. 1(b) shows the proposed Syn-VO architecture using nonlinear limit-cycle oscillators in polar

979-8-3315-5472-9/25/$31.00 ©2025 IEEE

coordinates. The key difference is synchronization: conventional loops rely on a single PLL referencing the grid, whereas Syn-VO loops self-synchronize to upstream and external reference signals. This decentralized approach removes the reliance on a common PLL, enhancing flexibility and robustness. Loops adapt autonomously under disturbances, improving system resilience.

B. Concepts of Syn-VOs and Polar-Coordinate Control

Linear PI control in grid-connected systems struggles to track original sinusoidal signals, which explains the conventional reliance on PLL-based dq-frame transformations (Fig. 1(a)). This paper introduces Syn-VOs with polar-coordinate control to track sinusoidal signals directly, avoiding redundant transformations.

Balanced three-phase signals are represented as rotating vectors in αβ-frame:

$$\vec{x} = xe^{j\theta} = x_\alpha + jx_\beta \text{ for simplicity} \quad (1)$$

where the arrow superscript ($\vec{x}$) represents complex numbers or vector, x is the magnitude, θ is the phase-angle. The vector component in $\alpha\beta$–frame is x_α and x_β, and j is an imaginary unit.

The external reference signal is assumed to be a sinusoidal signal represented by a vector with slowly changed magnitude and frequency as follows:

$$\vec{x}^* = x^* e^{j\theta^*} = x_\alpha^* + jx_\beta^*, \dot{x}^* \approx 0, \dot{\omega}^* = \ddot{\theta}^* \approx 0 \quad (2)$$

The superscript (*) denotes the reference signal, and single/double dots (.) & (..) indicate first- and second-order time derivatives.

This paper assumes slow variations in reference magnitude and frequency within a single sampling period, which is typical for power electronic systems. High-order control could handle fast changes, but the slow-variation assumption is sufficient for the applications considered here.

The dynamics of the signal can be written in both polar- and Cartesian coordinates such as:

$$\dot{\vec{x}} = \dot{x}_\alpha + j \times \dot{x}_\beta = (\dot{x}/x + j \times \dot{\theta})\vec{x} \quad (3)$$

where $\dot{x}/x$ represents the relative changes of magnitude and $d\theta/dt$ represent the angular speed or frequency of the signal.

The Syn-GVOs are proposed with the following decoupled closed-loop feedback in polar-coordinates:

$$\dot{\vec{x}} = (f_m + j \times f_\theta)\vec{x} \quad (4a)$$

$$f_m = \mu_m(x^* - x)/x \quad (4b)$$

$$f_\theta = \omega_{nom} + \mu_\omega \sin(\theta^* - \theta) + \mu_\theta \int \sin(\theta^* - \theta)dt \quad (4c)$$

ω_{nom} is the nominal angular frequency of the external signal. In (4), the control gains for each decoupled dynamics of magnitude, frequency, and phase angle are μ_m, μ_ω, and μ_θ, respectively.

As shown in the next subsection, the closed-loop laws (4b)–(4c) guarantee large-signal stability and asymptotic convergence of x to x^* in both magnitude and frequency/phase.

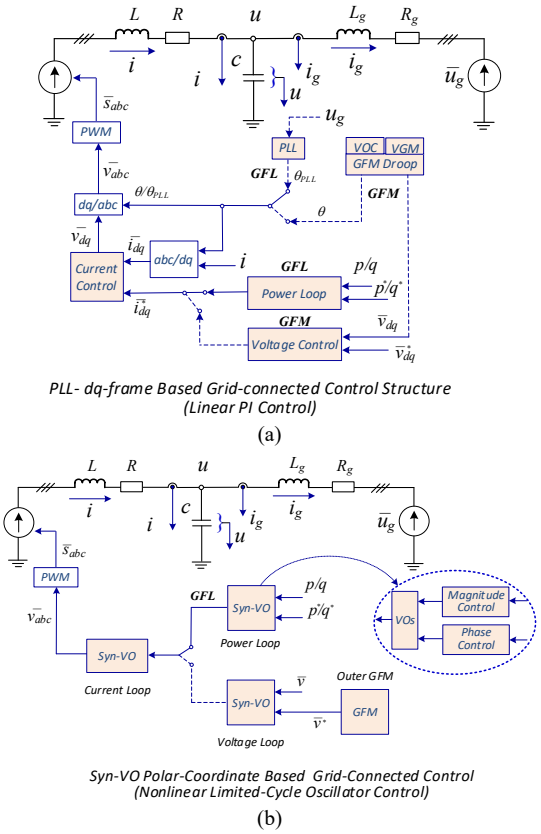


Fig. 1 Comparative control structures for grid-connected control.

While other nonlinear control laws could achieve similar convergence, (4b)–(4c) is used here for simplicity. Alternative laws may be applied for different dynamic signals in specific electronic applications, which are beyond this paper's scope.

III. Decoupled Closed-Loop Dynamic Designs and Lyapunov-Based Stability Proof

This subsection provides proof of large-signal stability of the Syn-VO proposed in (4) and details on the implementation.

A. Asymptotic Stability of Decoupled Control Laws

Substituting (4) into (3), the decoupled closed-loop dynamics are obtained as:

$$\dot{x} = \mu_m(x^* - x) \quad (5a)$$

$$f_\theta = \dot{\theta} = \omega_{nom} + \mu_\omega \sin(\theta^* - \theta) + \mu_\theta \int \sin(\theta^* - \theta)dt \quad (5b)$$

The dynamic (5a) shows exponential convergence of the magnitude to the reference one by a direct solution of the differential equations (5a):

$$x = x^* + \Delta x_0 e^{-\mu_m t} \to x^*|_{t\to\infty, \mu_m>0} \quad (6)$$

The solution (6) shows that stability of magnitude dynamic is ensured with positive gain, $\mu_m > 0$ under exponential trajectory with a rate determined by the gain.

The asymptotic convergence of phase angle in (5b) is proved by the following derivation and Lyapunov method:

$$\begin{cases} f_\theta = \omega = \dot{\theta} = \omega_{nom} + \mu_\omega \sin\delta_\theta + \mu_\theta \int \sin\delta_\theta dt \\ \dot{\delta}_\omega = -\mu_\omega \delta_\omega \cos(\delta_\theta) - \mu_\theta \sin\delta_\theta \end{cases} \quad (7)$$

where $\delta_\theta = \theta^* - \theta$, $\delta_\omega = \omega^* - \omega$ (8)

The asymptotic stability of dynamics (7) for both frequency and phase angle can be proved by the following Lyapunov function:

$$L_\theta = \frac{\delta_\omega^2}{2} + \mu_\theta\left(1 - \cos\left(\delta_\theta\right)\right) > 0 \;\forall(\delta_\omega \neq 0 \;\&\; \delta_\theta \neq 0) \quad (9a)$$

$$\dot{L}_\theta = -\mu_\omega \delta_\omega^2 \cos(\delta_\theta) \leq 0 \quad \left| -\pi/2 < \delta_\theta < \pi/2 \right. \quad (9b)$$

It is worth noting that for the application of virtual oscillators, the condition of $\{-\pi/2 < \delta_\theta < \pi/2\}$ can be ensured by changing the initial condition of the oscillator's phase angle ($\theta_0 = \theta|_{t=0}$). The initial condition guarantees stability in the large-signal sense instead of the small-signal approximation as conventional PLL-methods.

B. Implementation of Grid-Connected Control

Fig. 2 shows the Syn-VO implementation. Its digital realization uses simple integration blocks, eliminating the need for trigonometric functions common in PLL-based control. This reduces computational overhead, memory usage, and numerical errors, improving robustness and determinism. The simplified structure enables faster control loops, better scalability for multi-inverter systems, and suitability for resource-constrained embedded platforms like DSPs, FPGAs, or microcontrollers.

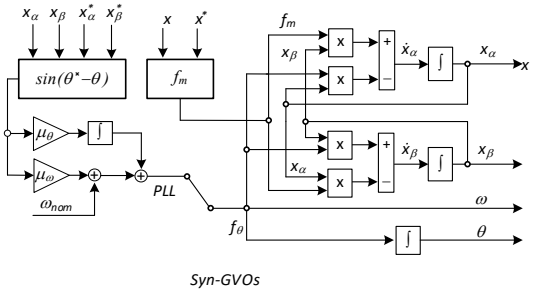


Fig. 2 Implementation diagram of Syn-GVOs with decoupled dynamics for magnitude and phase/frequency.

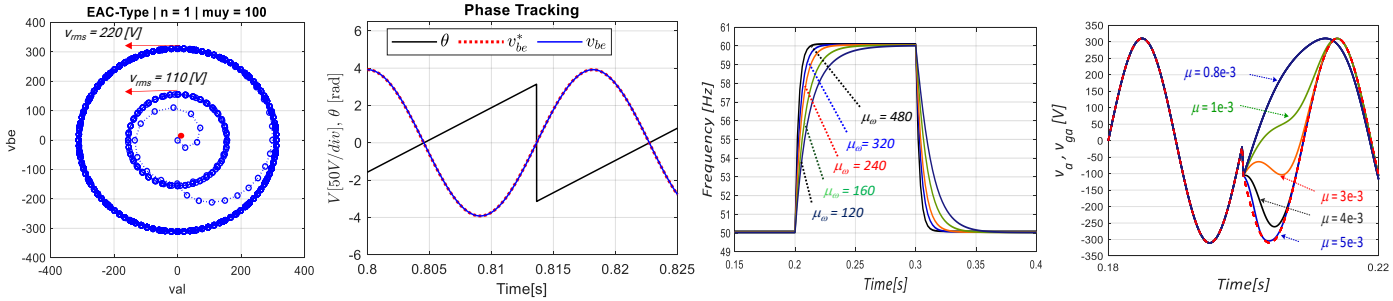


Fig. 3 Tracking features of the proposed Syn-GVO, (a) Magnitude tracking and limited cycle convergence of Syn-VOs, (b) Phase tracking of stable frequency signal, (c) Frequency step-change tracking performance under difference gains, (d) Tracking performance of phase in transient states.

Removing trigonometric dependencies decouples Syn-VO control from grid-frequency assumptions, allowing robust synchronization under varying or distorted grids. The phase-angle error is computed directly from the $\alpha\beta$-frame (10).

$$\sin(\theta^* - \theta) = (x_\alpha x_\beta^* - x_\alpha^* x_\beta)/(xx^*) \quad (10)$$

Fig. 3 shows Syn-VO dynamics: (a) stable limit-cycle under a 110 V→220 V magnitude step, (b) accurate phase tracking with zero steady-state error, and (c–d) frequency step and transient phase responses under different gains. These results confirm Syn-VO's robustness and suitability for grid-interfacing applications.

IV. New Grid-Connected Control with Syn-VOs

This subsection presents the Syn-GVO implementation in grid-connected control using cascaded design for a system of grid-connected IBR with LCL filter as seen in Fig. 4

A. Inner Loop Current Control

The Syn-GVO is applied to the inner current loop in grid-connected control (Fig. 1(b)), with the control law derived from the RL filter dynamics and designed closed-loop dynamics as follows:

$$d\vec{i}/dt = \left(\vec{v} - \vec{u} - R\vec{i}\right)/L \quad (11)$$

$$d\vec{i}/dt = \left(f_m + j \times f_\theta\right)\vec{i} \quad (12)$$

Substituting (11) int (10), the current control law is determined as:

$$\vec{v} = \vec{u} + (R + Lf_m + j \times Lf_\theta)\vec{i} \quad (13)$$

$$\begin{cases} f_m = \mu_m\left(i^* - i\right)/i, \sin(\theta_i^* - \theta_i) = \left(i_\alpha i_\beta^* - i_\alpha^* i_\beta\right)/\left(i^* i\right) \\ f_\theta = \omega_{nom} + \mu_\omega \sin(\theta_i^* - \theta_i) + \mu_\theta \int \sin(\theta_i^* - \theta_i) dt \end{cases} \quad (14)$$

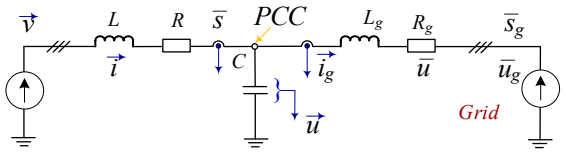


Fig. 4. IBR connected to a grid and its grid-connected control.

B. Redefinition of Grid-Following and Grid-Forming Control

In grid-following mode, the powers can be regulated by Syn-VO as follows:

$$d\vec{s}/dt = \left(\dot{u}/u + \dot{i}/i + j\times\dot{\theta}_u - j\times\dot{\theta}_i\right)\times\vec{s} = (f_{ms} + j\times f_{\theta s})\times\vec{s} \quad (15)$$

where f_{ms}, $f_{\theta s}$ are relevant polar-coordinate closed-loop control function of powers following the general rules in (4). Specifically, the powers are dc-signal in this control which can be considered a specific sinusoidal signal with zero frequency.

1) *Power Tracking with GFL*: The purely grid-following control mode assumes of a stable voltage at the PCC as:

$$\dot{u}/u \approx 0, \dot{\theta}_u = \omega_{nom} \quad (16a)$$

Hence, the GFL control law with power tracking set at the PCC for the RL-branch is expressed from (15) as:

$$d\vec{i}^*/dt = \left(f_{ms} + j\times\left(\omega_{nom} - f_{\theta s}\right)\right)\vec{i}^* \quad (16b)$$

2) *Voltage control with GFM*: When the inner current control loop is employed to regulate the point of common coupling (PCC) voltage under grid-forming (GFM) control, the outer voltage control loop can be designed using a Syn-VO with limit-cycle behavior.

This GFM structure enables the generation of a stable voltage reference using the self-synchronizing properties of Syn-VO, ensuring robust voltage regulation even under weak grid conditions or grid disturbances.

$$d\vec{u}/dt = (\vec{i}^* - \vec{i}_g)/C = (f_{mu} + j\times f_{\theta u})\times\vec{u} \quad (17a)$$

$$\vec{i}^* = \vec{i}_g + C(f_{mu} + j\times f_{\theta u})\times\vec{u} \quad (17b)$$

where f_{mu}, $f_{\theta u}$ are relevant polar-coordinate closed-loop control function of capacitor voltage tracking a reference. The reference u^* in (17b) can be defined according to grid-forming (GFM) control principles. In particular, the following control formulation represents a GFM strategy in which the Syn-VO is synchronized with the injected grid current:

$$d\vec{u}^* = f_{mu}. - \mu_q \sin(\theta_i - \theta_u^*) + j\times(\omega_{nom} + \mu_p \cos(\theta_i - \theta_u^*)) \quad (18a)$$

The grid-forming control law expressed in equation (18a) corresponds to droop characteristics in the steady state, where the active and reactive power outputs can be proportionally allocated according to the rated capacity of each inverter-based resource (IBR).

$$u^* = u_{nom} - d_p Q, \quad \omega^* = \omega_{nom} + d_p P \quad (18b)$$

where P, Q are the active and reactive powers, respectively.

Equation (18a) is a simplified form of (4), where the Syn-VO reference voltage synchronizes to the grid current using only the frequency term ($\mu\theta = 0$), omitting phase coupling. This highlights a key distinction: in grid-forming (GFM) control, Syn-VOs track the grid current, while in grid-following (GFL) control, they track the grid voltage. This unified framework explains the suitability of GFM for weak grids and GFL for stiff grids, linking both strategies under a single Syn-VO formulation.

V. Experimental Validation

This section presents comparative studies and experimental validations demonstrating the effectiveness of the proposed control strategy.

A. Experimental Setup

Fig. 5 shows an inverter-based system with three IBRs supplying three corresponding loads, interconnected via Line-12 and Line-23. Each node includes loads with active/reactive power (P, Q) and RLC components. Load-3.2 at Node 3 is toggled to examine dynamic responses. Key system parameters are listed in Table 1.

Three scenarios are considered to evaluate the proposed control framework:

- Scenario 1: Droop-Based Grid-Forming Control. All IBRs operate under droop-based GFM control, sharing active power proportionally (5:4:1 for IBR1–3) without centralized coordination.
- Scenario 2: Decentralized OPF-Based Dispatch. IBR1 acts as a swing node regulating frequency and voltage, while IBR2 and IBR3 are precisely dispatched to P_2*=3 kW and P_3*=2 kW, maintaining synchronization via grid-forming behavior.

TABLE I. Inverter-Based System under Competitive Studies

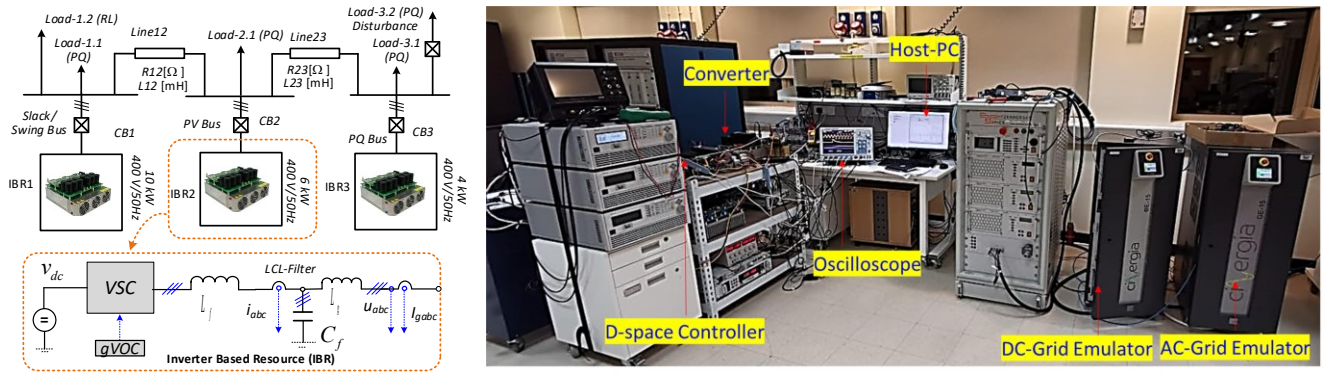
***IBR and Load Parameters* (50Hz/400V)**	**IBR1:** 10 [kW], 2L-VSC LCL-1 = 5.0 [mH] + 0.1 [Ohm], 260 [uF], 1.5 [mH] + 0.1 [Ohm]	**Load-1.1**: 2.0 [kW], 1.0 [kVAr] Load-1.2: 10.0 [kW], 5.0 [kVAr]
	IBR2: 8 [kW], 2L-VSC LCL-2 = 5.0 [mH] + 0.1 [Ohm], 260 [uF], 1.5 [mH] + 0.1 [Ohm]	**Load-2.1**: 3.0 [kW], 1.5 [kVAr]
	IBR3: 2 [kW], 2L-VSC LCL-3 = 5.0 [mH] + 0.1 [Ohm], 260 [uF], 1.5 [mH] + 0.1 [Ohm]	**Load-3.1:** 5.0 [kW], 3.0 [kVAr]
***Lines Parameters* (50Hz/400V)**	**Line12:** R12 = 0.15[Ω], L12= 3.0 [mH]	**Line23:** R23 = 0.15[Ω], L23 = 3.0 [mH]

The whole platform is configured under the power-HIL concept for verification purposes. The power-HIL structure enables the verification of comparative control methods with the real-time response of the physical devices.

B. Comparative Grid-Forming Behaviors (Scenario-1)

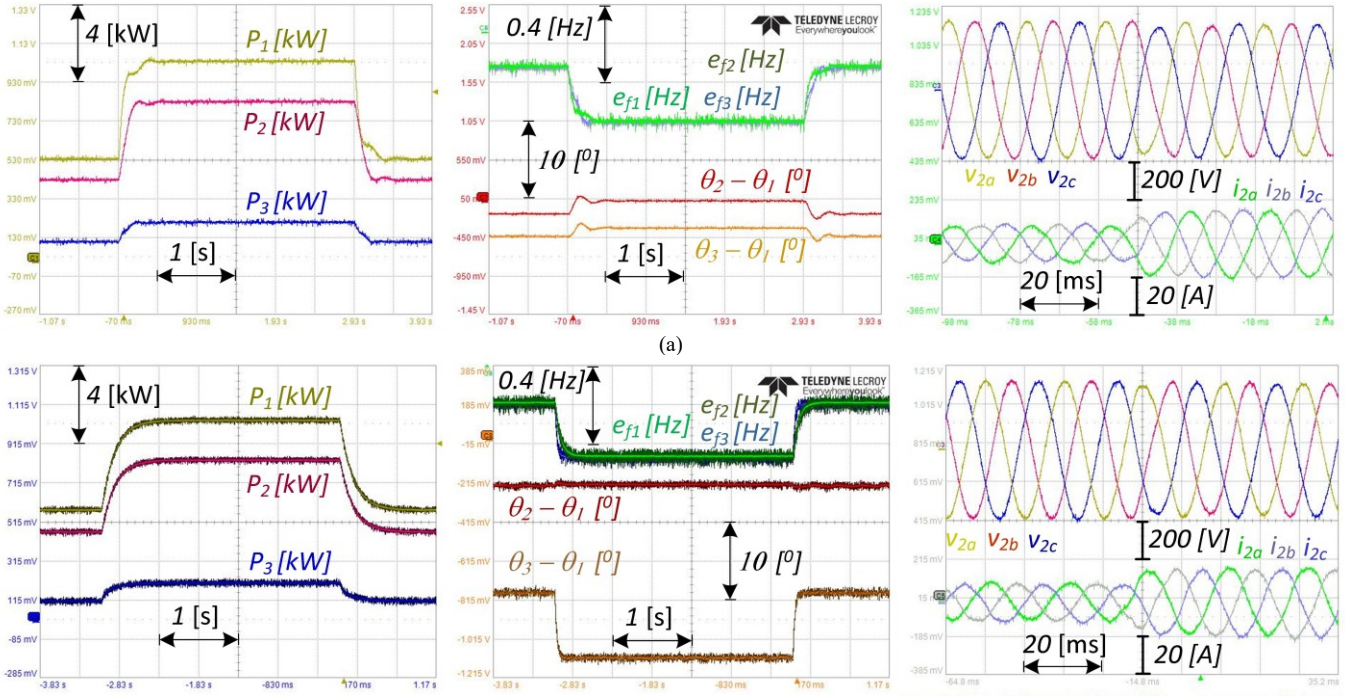
Fig. 6 compares droop control and the proposed Syn-VO under Scenario 1, with a power ratio of 5:4:1 for IBR1–3. Both schemes use identical droop laws, but Syn-VO relies on time-domain virtual oscillators with autonomous synchronization, whereas conventional droop uses PI controllers in the dq-frame. In Fig. 6, the experimental results validate advancement of the proposed method. That is, significant differences are observed in the phase synchronization of Syn-VO via the coupled oscillator principle compared to conventional PI-loop droop controllers. The smooth transition between synchronized modes due to the disturbance contributes to the overall system's stability and reduces the transient time against load disturbance. In *Scenario-1*, with the results shown in Fig. 6, the parameter settings for the whole power system are only the ratio drop gains (d_p and d_q) of each IBR. The parameter settings for each Syn-VO are as simple as the droop control by directly setting the droop gain ratio depending on the rated-power ratio of each IBR, and this ratio of shared powers remains despite the

load changes.



(a) (b)

Fig. 5. Photograph of the experiment platform with power- hardware in loop.



(a)

(b)

Fig. 6. (*Scenario*-1) Experimental validation of grid-forming performance, (a) Conventional droop with PI dq-based current control, (b) Proposed Syn-VO without precise dispatch control options.

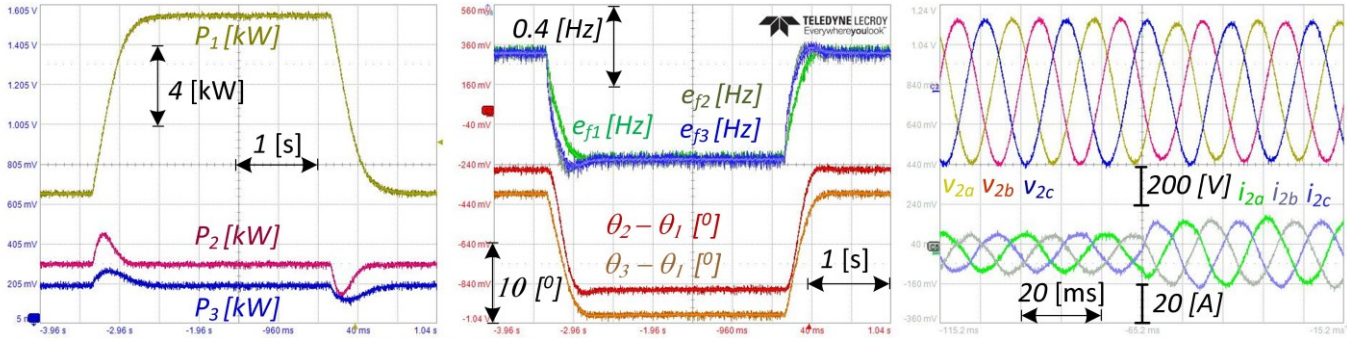


Fig. 7. (*Scenario*-2) Experiment results with precise-dispatch control of active powers at IBR2 & IBR3, results from the proposed Syn-VO framework.

C. Comparative Grid-Following Behavior (Scenario-2)

Conventional dVOC can achieve dispatchable control if P^* and Q^* are feasible for the system [27], [28]. However, real-time dispatch is challenging because precalculated setpoints can drift due to dynamic load and source changes. Thus, conventional dVOC relies heavily on system-wide parameter settings to maintain accurate power flow under varying conditions.

Recent dVOC implementations with local power dispatch still face challenges as GFL control, since operating states can drift without system-wide coordination. To address this, dispatch types are classified as slack/swing, PV, and PQ nodes, enabling near-optimal power allocation. The proposed Syn-VO framework achieves precise local dispatch using only local settings, avoiding the uncontrolled drift of conventional dVOC.

In *Scenario-2* shown in Fig. 7, conventional dVOC required resetting all IBR controllers when Load-2.1 changed to maintain P_2 and P_3, whereas Syn-VO maintains correct dispatch without adjustments. Active powers P_2 and P_3 remain at 3 kW and 2 kW, with load variations handled by IBR1. Fig. 7 also shows smooth transient response, fast synchronization, and high-quality currents/voltages from IBR2, with measured THDs of 2.5% and 3.65% for voltage and current.

VI. Conclusion

This paper presents a unified Syn-VO control framework for both grid-forming (GFM) and grid-following (GFL) inverter modes. Using a polar-coordinate structure, Syn-VO captures droop-like GFM behavior and precise GFL power regulation, enabling flexible dispatch of inverter-based resources. Simulations and experiments show superior synchronization, current regulation, and accurate active/reactive power control. The results highlight Syn-VO's potential as a robust solution for inverter-dominated systems, while providing a theoretical foundation that unifies GFM and GFL concepts.

Acknowledgment

This work was supported by the Advanced Power and Energy Center (APEC) of Khalifa University, Abu Dhabi, UAE.

References

[1] B. Kroposki *et al.*, "Achieving a 100% Renewable Grid: Operating Electric Power Systems with Extremely High Levels of Variable Renewable Energy," *IEEE Power and Energy Magazine*, 2017, doi: 10.1109/MPE.2016.2637122.

[2] H. T. Nguyen *et al.*, "Fast Harmonic Rejecting Control Design to Enable Active Support of Charging Stations to Micro-Grids under Distortion," *IEEE Transactions on Transportation Electrification*, 2023, doi: 10.1109/TTE.2023.3241392.

[3] International Renewable Energy Agency, *IRENA (2019), Global Energy Transformation: A Roadmap to 2050*. 2019.

[4] N. T. Hoach, *et al.*, "Independent Time-Delay Signal Cancellation for Fast Harmonic-Sequence Filters Targeting Arbitrary Sequences and Frequencies," *IEEE Trans Industr Inform*, vol. PP, pp. 1–13, 2024, doi: 10.1109/TII.2024.3383510.

[5] J. Matevosyan *et al.*, "Grid-forming inverters: Are they the key for high renewable penetration?," *IEEE Power and Energy Magazine*, vol. 17, no. 6, pp. 89–98, 2019, doi: 10.1109/MPE.2019.2933072.

[6] E. Ebinyu, O. Abdel-Rahim, D. E. A. Mansour, M. Shoyama, and S. M. Abdelkader, "Grid-Forming Control: Advancements towards 100% Inverter-Based Grids—A Review," 2023. doi: 10.3390/en16227579.

[7] N. Hoach *et al.*, "Enhanced Performance of Charging Stations via Converter Control under Unbalanced and Harmonic Distorted Grids," *IEEE Transactions on Power Delivery*, pp. 1–10, 2021, doi: 10.1109/TPWRD.2021.3052319.

[8] Q. Salem, B. B. Fawaz, R. Aljarrah, and M. Karimi, "Grid Forming Converters for Low Inertia Systems-Capabilities and Limitations: A Critical Review," *IEEE Open Journal of the Industrial Electronics Society*, vol. 6, pp. 775–801, 2025, doi: 10.1109/OJIES.2025.3566213.

[9] Q. Hu, L. Fu, F. Ma, and F. Ji, "Large Signal Synchronizing Instability of PLL-Based VSC Connected to Weak AC Grid," *IEEE Transactions on Power Systems*, 2019, doi: 10.1109/TPWRS.2019.2892224.

[10] X. Gao, D. Zhou, A. Anvari-Moghaddam, and F. Blaabjerg, "Seamless Switching Method between Grid-Following and Grid-Forming Control for Renewable Energy Conversion Systems," *IEEE Trans Ind Appl*, vol. 61, no. 1, pp. 597–606, 2025, doi: 10.1109/TIA.2024.3471728.

[11] N. Jaalam, N. A. Rahim, A. H. A. Bakar, C. K. Tan, and A. M. A. Haidar, "A comprehensive review of synchronization methods for grid-connected converters of renewable energy source," 2016. doi: 10.1016/j.rser.2016.01.066.

[12] Y. Zhang, H. Pen, and X. Zhang, "Stability Control of Grid-Connected Converter Considering Phase-Locked Loop Frequency Coupling Effect," 2024, doi: 10.3390/en17143438.

[13] W. Zhou, Y. Wang, R. E. Torres-Olguin, and Z. Chen, "DQ Impedance Reshaping of Three-Phase Power-Controlled Grid-Connected Inverter for Low-Frequency Stability Improvement under Weak Grid Condition," *ECCE 2020 - IEEE Energy Conversion Congress and Exposition*, pp. 1678–1685, Oct. 2020, doi: 10.1109/ECCE44975.2020.9236052.

[14] S. Silwal, "Enhanced controllers for voltage-sourced converters interfaced with weak ac power grids," *Theses and Dissertations*, Dec. 2019.

[15] G. Wang, P. Sun, X. Du, and L. Zhou, "Dynamical performance of frequency-locked loop synchronization method under asymmetric grid voltage condition," *Diangong Jishu Xuebao/Transactions of China Electrotechnical Society*, 2015.

[16] F. Wald, Q. Tao, and G. De Carne, "Virtual Synchronous Machine Control for Asynchronous Grid Connections," *IEEE Transactions on Power Delivery*, 2024, doi: 10.1109/TPWRD.2023.3235149.

[17] S. D'Arco and J. A. Suul, "Equivalence of virtual synchronous machines and frequency-droops for converter-based Microgrids," *IEEE Trans Smart Grid*, 2014, doi: 10.1109/TSG.2013.2288000.

[18] M. Kosari and S. H. Hosseinian, "Decentralized Reactive Power Sharing and Frequency Restoration in Islanded Microgrid," *IEEE Transactions on Power Systems*, 2017, doi: 10.1109/TPWRS.2016.2621033.

[19] B. B. Johnson, S. V. Dhople, A. O. Hamadeh, and P. T. Krein, "Synchronization of parallel single-phase inverters with virtual oscillator control," *IEEE Trans Power Electron*, vol. 29, no. 11, pp. 6124–6138, 2014, doi: 10.1109/TPEL.2013.2296292.

[20] Y. Zhou, X. Xiong, X. Li, and P. Cheng, "Effects of PLL in the Damping Unit of a Gird-Connected VSG," in *PEAC 2022 - 2022 IEEE International Power Electronics and Application Conference and Exposition, Proceedings*, 2022. doi: 10.1109/PEAC56338.2022.9959193.

[21] M. Wang, S. Niu, *et al.*, "A Power Decoupling Control Strategy for Virtual Oscillator Controlled Grid-Forming Inverters Based on Impedance and Voltage Compensation," in *PEAS 2023 - 2023 IEEE 2nd International Power Electronics and Application Symposium, Conference Proceedings*, 2023. doi: 10.1109/PEAS58692.2023.10395108.

[22] S. Azizi Aghdam and M. Agamy, "Virtual oscillator-based methods for grid-forming inverter control: A review," *IET Renewable Power Generation*, vol. 16, no. 5, pp. 835–855, 2022, doi: 10.1049/rpg2.12398.

[23] J. Zhao and T. Iwasaki, "Orbital Stability Analysis for Perturbed Nonlinear Systems and Natural Entrainment via Adaptive Andronov-Hopf Oscillator," *IEEE Trans Automat Contr*, 2020, doi: 10.1109/TAC.2019.2906429.

[24] J. Zhang, X. Niu, M. Du, Z. Qi, and Q. Li, "Research on control strategy of cascade STATCOM under unbalanced system voltage," in *China International Conference on Electricity Distribution, CICED*, 2012. doi: 10.1109/CICED.2012.6508710.

[25] M. A. H. Mujammal, *et al.*, "Novel Direct Power Control Based on Grid Voltage Modulated Strategy Using Artificial Intelligence," *Smart Grids and Sustainable Energy*, vol. 9, no. 2, pp. 1–15, Dec. 2024, doi: 10.1007/S40866-024-00225-1/FIGURES/14.

[26] X. Zhang, J. He, H. Ma, Z. Ma, and X. Ge, "Stability Enhancement Methods of Inverters Based on Lyapunov Function, Predictive Control, and Reinforcement Learning," *Stability Enhancement Methods of Inverters Based on Lyapunov Function, Predictive Control, and Reinforcement Learning*, pp. 1–164, Jan. 2022, doi: 10.1007/978-981-19-7191-4.

[27] X. He, V. Haberle, I. Subotic, and F. Dorfler, "Nonlinear Stability of Complex Droop Control in Converter-Based Power Systems," *IEEE Control Syst Lett*, vol. 7, pp. 1327–1332, 2023, doi: 10.1109/LCSYS.2023.3236276.

[28] F. Dörfler and D. Groß, "Control of Low-Inertia Power Systems," 2023. doi: 10.1146/annurev-control-052622-032657.

Electromagnetic Simulation Model of Switching Power Supply

Wu Jianchao
Dept. of Electronic Products
Beijing Spacecraft
Beijing, China
wujianchao20062007@163.com

Li Xinxin
Dept. of Electronic Products
Beijing Spacecraft
Beijing, China
13301309127@163.com

Lv Hui
Dept. of Electronic Products
Beijing Spacecraft
Beijing, China
735804726@qq.com

Liu Mi
Dept. of Electronic Products
Beijing Spacecraft;
Harbin Institute of Technology
Beijing, China
liumi0065@163.com

Ji Zhipo
Dept. of Electronic Products
Beijing Spacecraft
Beijing, China
13810475501@163.com

Wan Chengan
Dept. of Electronic Products
Beijing Spacecraft
Beijing, China
wan001@vip.sina.com

***Abstract*— Electromagnetic compatibility (EMC) of aerospace power modules is crucial for ensuring stable and reliable operation of the entire spacecraft. To meet the high power and high efficiency demands of aerospace power supplies, GaN power devices with high switching frequency characteristics are gradually being incorporated into aerospace power supply designs. The high dv/dt and di/dt characteristics of GaN power devices have significant impacts on the parasitic parameters of sensitive circuits, such as driver circuits, posing a significant challenge to EMC design. In particular, in complex electromagnetic environments (such as external interference, power-on pulses, and capacitive loads), effective methods for quantitatively assessing interference in sensitive links are lacking. This paper develops an accurate high-frequency simulation model for a space-use buck power module. By extracting the parasitic parameters of key sensitive links (drive circuit and power circuit on the printed circuit board (PCB)) , core components and structural shells, a system-level simulation environment that can accurately reflect its high-frequency characteristics is constructed. This model enables quantitative analysis of the induced noise voltage/current caused by electromagnetic interference at any location along the sensitive link, transcending the limitations of traditional qualitative testing. Simulation and experimental results demonstrate that the model is highly accurate with a relative error of 10.3% . This research provides theoretical tools and engineering foundations for precise EMC design and fault prediction in aerospace power supplies, significantly improving the first-pass rate for EMC design of power supply products.**

Keywords—switching power supply, electromagnetic compatibility, high-frequency conduction simulation

I. INTRODUCTION

With the accelerated construction of major national space infrastructure such as manned space flight, Beidou navigation, and low-orbit satellite internet, spacecraft platforms have put forward stringent requirements on the power density, conversion efficiency, and reliability of their core unit power systems[1-2].The operating environment of spacecraft is complex and harsh, including space electromagnetic environment interference and man-made electromagnetic attacks, with interference frequency bands ranging from tens of MHz to more than ten GHz[3-4]. Its operating conditions are complex and changeable, and high-power bus power outages and switching moments will also generate GHz transient pulse interference[5]. Gallium nitride power switches, with their extremely high electron mobility and excellent switching characteristics, have become an important technical approach to achieve miniaturization, lightweighting, and high efficiency of aerospace power supplies. The picosecond switching speed of gallium nitride devices produces extremely high voltage and current change rates, resulting in the electromagnetic interference energy distribution tending to high frequency[6]. At high frequencies, the previously negligible printed circuit board, device package parasitic parameters, and distributed parameter effects of the structural become extremely prominent. They constitute a complex coupling path, which has caused strong interference to the key sensitive links of the power supply. These interferences can cause power supply performance degradation at best, or even hardware damage at worst. Therefore, the EMC design of power supply is crucial to ensuring their long-term, stable, and reliable operation in orbit.

In recent years, domestic and foreign scholars have conducted extensive research on the analysis and prediction of EMI in power supplies. Early research by NASA, JPL, the European Space Agency and other foreign institutions focused on interference source modeling, such as the precise behavioral model of power switching devices[7] and the frequency-dependent loss model of magnetic components[8]. In terms of the influence of parasitic parameters, scholars generally use two-dimensional/three-dimensional electromagnetic field simulation tools (such as ANSYS Q3D, CST) to extract and model key loops[9]. In terms of sensitivity analysis, studies usually treat the entire feedback loop as a black box and test its overall anti-interference performance through injection methods[10]. However, most of these methods remain at the qualitative or semi-quantitative analysis level at the system level or port level, making it difficult to accurately locate the weak links within the link and provide quantitative noise amplitude information. In addition, although some studies have mentioned the electromagnetic coupling effect between structural parts such as

979-8-3315-5472-9/25/$31.00 ©2025 IEEE

metal casings and circuits[11], there is still a lack of research that systematically integrates it into the overall power supply simulation model as a distributed parameter and conducts quantitative analysis.

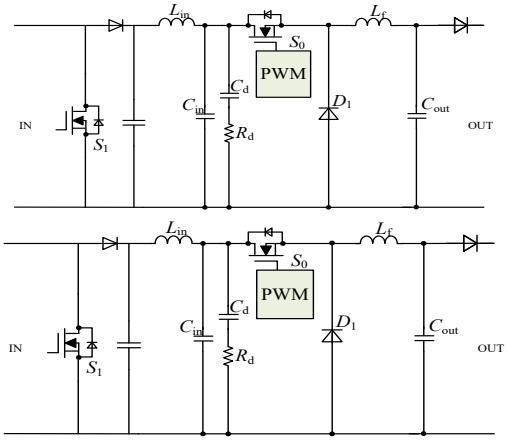
Domestic universities and research institutes have proposed many excellent methods in switching power supply modeling[12]and conducted EMI filter design[13]. Some studies have begun to focus on the extraction of PCB parasitic parameters to improve simulation accuracy[13-14]. But in general, domestic research is still largely following foreign technology routes. Most work focuses on the suppression of conducted emissions and the optimization design of filters. For the sensitivity issues within the system, especially the precise analysis from "qualitative" to "quantitative", it is still in its infancy. Research that incorporates the influence of structure into the power supply simulation model and uses it to predict the response of internal nodes is even rarer.

In summary, current research on power supply EMI, both domestically and internationally, has evolved from simple interference source modeling to a comprehensive consideration of propagation paths and sensitive devices. However, existing technologies still suffer from two significant shortcomings: First, the analysis granularity is insufficient, lacking the ability to quantitatively and traceably analyze nodes within sensitive links; second, the model is incomplete, with most models ignoring the effects of distributed parameters introduced by the mechanical structure, leading to discrepancies between high-frequency simulation predictions and measured results. Therefore, this paper conducts precise modeling of the high-frequency distributed parameters of the PCB and mechanical structure for an aerospace switching power supply module. This enables quantitative analysis of the impact of electromagnetic interference at any point in the sensitive link, thereby filling the technological gap between traditional qualitative design and precise quantitative prediction.

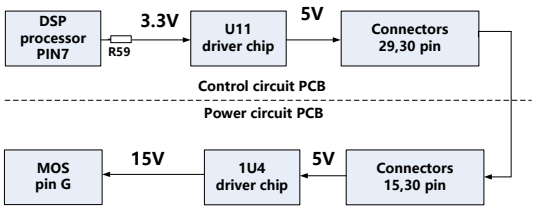
II. High-frequency Simulation Modeling and Parameter Extraction

A. Target Power Module Introduction

A typical aerospace power module with a 100V input voltage and a 28V output bus voltage adopts a buck topology, as shown in Figure 1. a) below:



a) Schematic diagram of power supply topology



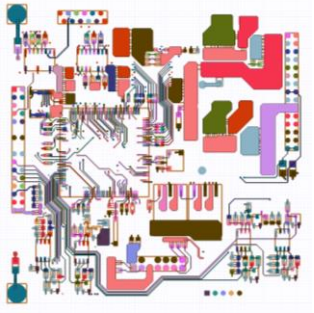
b) Connection relationship between control circuit and power

Fig. 1. Critical path selection.

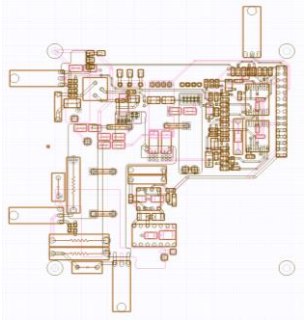
Its core circuitry includes the power circuitry for power conversion and the control circuitry for stable drive, located on the power and control circuit boards, respectively. The control and power circuit boards are located on the upper and lower layers of the metal housing, respectively. Signals between the two printed circuit boards are transferred via connectors.

B. 3D LAYOUT Creation

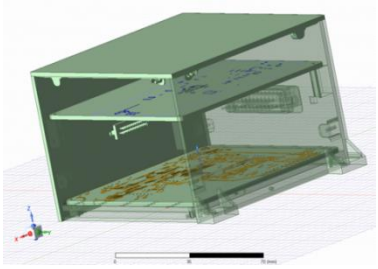
HFSS simulation software was used to establish a high-frequency conduction simulation model for a switching power supply.First,the power circuit printed circuit board and the control circuit printed circuit board were imported into HFSS. The stackup relationship and material information for each printed circuit board were designed to ensure that the thickness and material were consistent with the actual product.The structure file was then imported into HFSS, and the structure and the two printed circuit boards were assembled in the software, as shown in the figure below .



a) Power circuit board



b) Control circuit board



c) Casing

Fig. 2. 3D LAOUT creation.

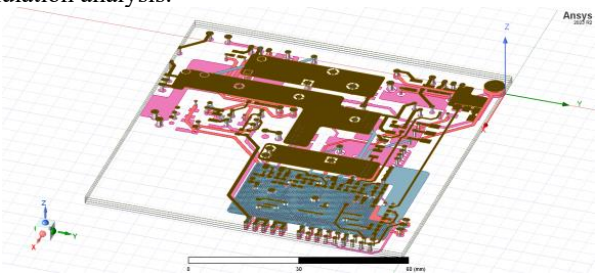
C. S-parameter Extraction of Key Links and Structures

Because the physical path of a switching power supply is extremely complex, extracting high-frequency parasitic parameters along the entire path would be computationally intensive, making it difficult to achieve convergence. By analyzing the power and control loops of the power module's critical links, the 3D layouts of the complete power and control

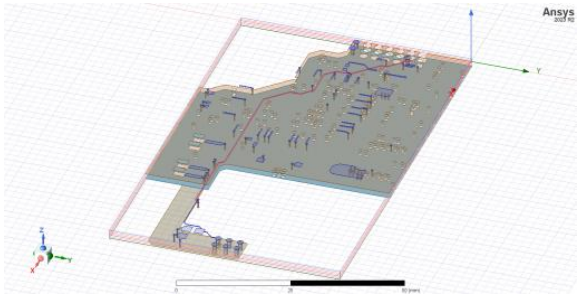
circuit boards were tailored. Based on Figure 1b), the core components and NETs in the power and signal circuits were screened to form the target analysis path. Figure 3a) shows the critical path of the power circuit board, and Figure 3 b) shows the critical path of the control circuit board.

In HFSS, the power and control circuit boards have been assembled and installed on the structural structure . Select the grounded components in the key links of the power and control circuits. In this example, these are filter capacitors C3, C10, C11, C23, and C24. The mounting hole R in the structure is selected as the EARTH point.

Based on the circuit connections and current flow , define the source (current inflow) and sink (current outflow) for each independent net in HFSS . Once this is complete, perform a frequency sweep to simulate and analyze LRC parasitic parameters . The calculation results for the power circuit, control circuit, and structure are packaged to generate device models (including high-frequency parasitic parameters) for circuit simulation analysis.



a) Power circuit



b) Control circuit

Fig. 3. Critical path S-parameter extraction

D. Establish SPICE Models for Core Components

Utilizing PEmag's extensive manufacturer material library, you can quickly build transformer and inductor design models and link them to Maxwell 2D for electromagnetic analysis. Simulation results can be generated as .cir files, which are SPICE models.

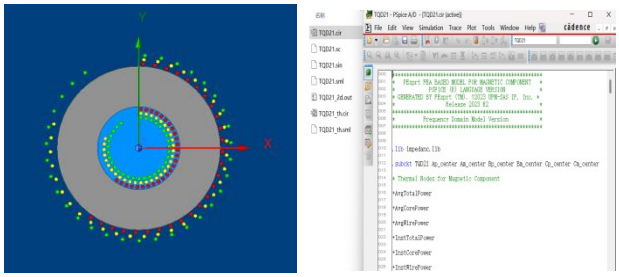


Fig. 4. Transformer magnetic simulation model and SPICE model

E. Establishing Simulation Loop

Create a power supply analysis loop as shown in Figure 5 below, with an input voltage of 100V and an output voltage of 28V. Interference injection in the 100V Input. In ANSYS circuit analysis software, based on circuit principles, connect the core component SPICE models (either self-built or downloaded from the official website), the power circuit model, the control circuit model, and the structural model to form a simulation analysis loop, as shown in Figure 6 (the circuit connections are complex and cannot be displayed aesthetically).This loop comprehensively considers the parasitic parameters of the core components, the packaging structure, and the parasitic parameters of the printed circuit board link.the interference waveform can be analyzed at any location in the link.

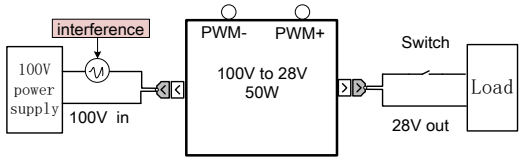


Fig. 5. Schematic diagram of power supply analysis circuit

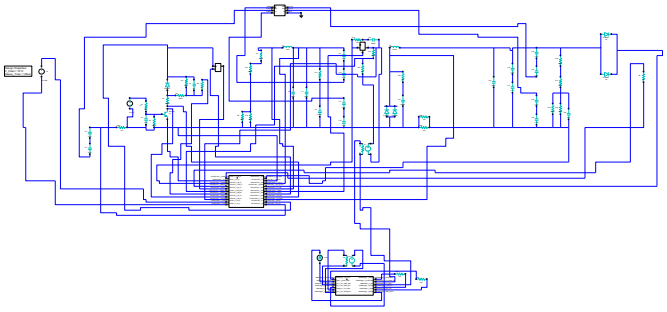


Fig. 6. Simulation circuit

III. Simulation Analysis

A. Interference Source Settings

Because switching power supplies use parallel lines for power transmission and lack normalized impedance, injection testing is difficult. To ensure consistency between test and simulation, this paper uses the measured waveform obtained with an oscilloscope on the input bus during the irradiation experiment as the simulated injection waveform.

The interference radiation source in this paper is a first-order Gaussian pulse with a pulse peak-to-peak time width of 0.7ns. Its time domain expression is generally approximated as shown in the following formula [15].

$$g(t) = k\frac{t-t_0}{\tau}\cdot e^{-\frac{4\pi(t-t_0)^2}{\tau^2}} \quad (1)$$

Where, k is the peak correction coefficient; t_0 is the pulse delay, τ and is the pulse width constant.

The experiment used far-field plane wave irradiation with a radiation source field strength of 20 kV/m . The waveform coupled into the switching power supply input was roughly

similar to that of the irradiation source : both were Gaussian pulses, with a peak-to-peak voltage pulse duration of 1.25 ns and a waveform oscillation decay duration of 15 to 20 ns . The maximum coupled voltage amplitude was 306.8 V, as shown in the figure 7.

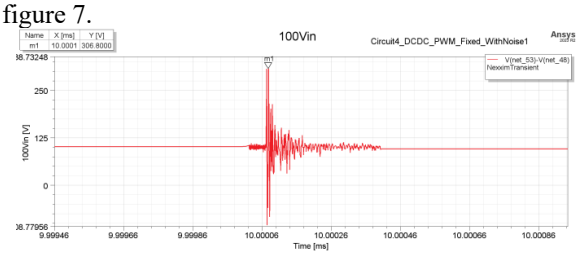


Fig. 7. Inductive overvoltage waveform injected into the input terminal

B. *Interference Injection Simulation*

As described above, an active circuit was established and an interference source was injected. The interference waveform was obtained from the irradiation test, with a maximum amplitude of 306.8V. The simulation results show that interference was superimposed on the 28V output voltage. As shown in the figure below, the output interference waveform is roughly similar to the input interference waveform: the peak-to-peak duration of the voltage pulse at the switching power supply input is 1.25ns, the waveform oscillation decays for 15ns to 20ns , and the maximum voltage amplitude is 306.8V. The peak-to-peak duration of the voltage pulse at the switching power supply output is 2.5ns , the waveform oscillation decays for 50ns to 60ns , and the maximum voltage amplitude is 169.73V.

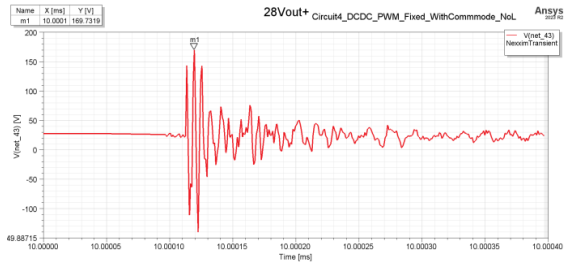
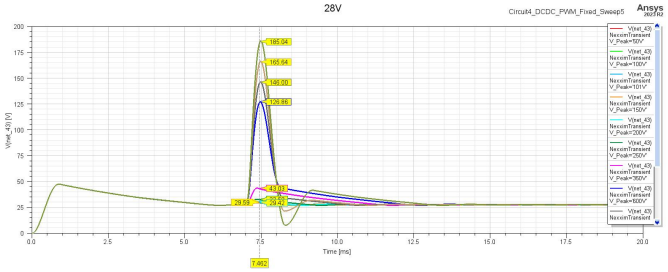


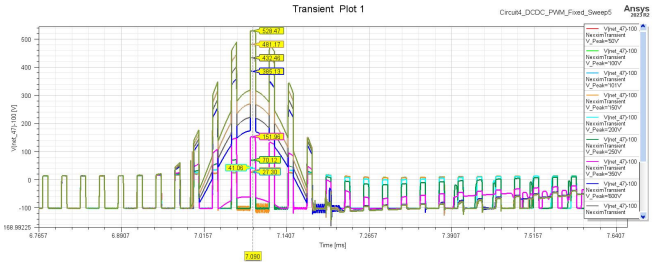
Fig. 8. Simulated value of output interference waveform

C. *Transmission Law Analysis*

By setting different values for the injection source's peak-to-peak voltage pulse and pulse width, we simulated and studied the transmission characteristics of the interference pulse 's peak value and pulse width in the power supply circuit. The results are shown in the figure below.

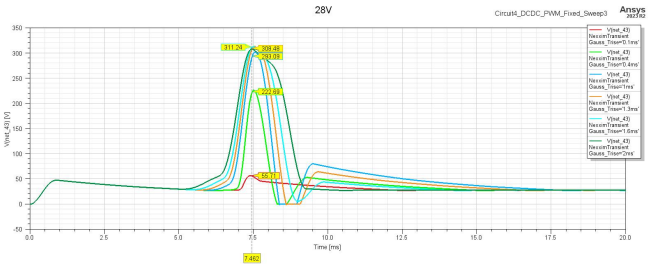


a) 28V output terminal

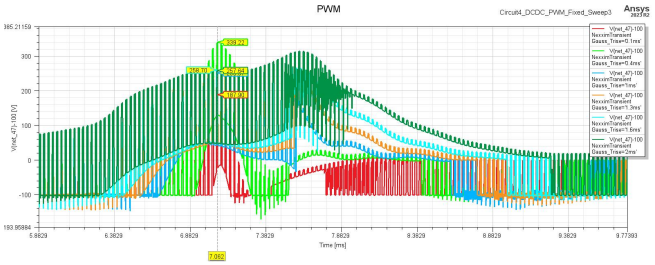


b) PWM signal terminal

Fig. 9. Different peak values of induced overvoltage



a) 28V output terminal



b) PWM signal terminal

Fig. 10. induced over-voltage with different pulse widths

IV. Experimental Verification

A. *Experimental Process*

As shown in the figure below, a test verification platform was constructed.

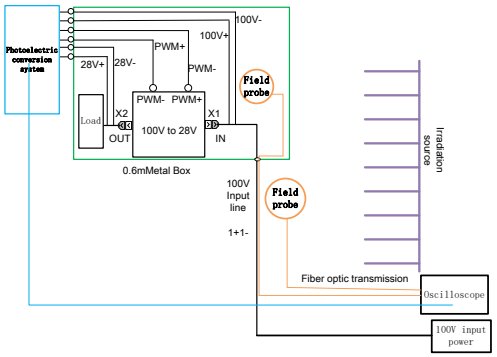


Fig. 11. Schematic diagram of test layout.

The power supply circuit for the power module was configured consistent with the simulation. Far-field irradiation was used , using a Gaussian pulse source with a peak-to-peak duration of 0.7 ns and a field strength of 20 kV/m . The power module was placed in a 0.6-cubic-meter metal box to simulate cabin conditions. The box was fully shielded to prevent direct interference from the radiation source on the power supply output and signal interruption. Six SMA flange RF connectors were installed on the side of the box facing away from the antenna, connecting to the power supply's 100V positive input, 100V negative input, 28V positive output, 28V negative output, PWM positive, and PWM negative terminals. The RF connectors were connected to an oscilloscope via an optoelectronic system to prevent interference with the monitoring circuit. A field strength probe was connected to the oscilloscope via optical fiber to monitor both internal and external field strengths

B. Test Results

The following figure shows the interference voltage waves monitored at the input and output terminals when the radiation source field strength is 20 kV/m . An attenuator was used to protect the oscilloscope during the experiment . The maximum input voltage is 146 mV, and the attenuator factor is 2100, resulting in a maximum input voltage of 306.6 V. This waveform is used as the interference source injection waveform in the simulation.the maximum interference voltage at the output terminal of the switching power supply is 128.2 mV, and the attenuation factor is 1200. Therefore, the output interference voltage should be 1200 times the value displayed on the oscilloscope , for a maximum value of 153.84 V.

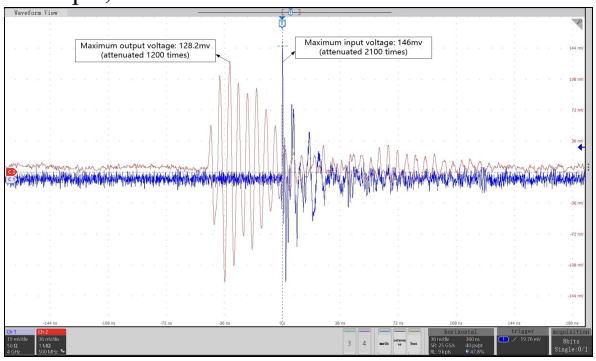


Fig. 12. Input and output interference waveform test values

C. Results Comparison

The simulation results of the maximum output coupling voltage are compared with the experimental results, where V_s is the simulation result and V_t is the experimental result, as shown in the following table. The relative error is 10.3%.

TABLE I. COMPARISON BETWEEN SIMULATION AND TEST

Coupling voltage	**V_s / (kV/m)**	**V_t / (V)**	**e_{max} /%**
Input	306.8V	306.8V	The simulation uses experimental values
Output	169.73V	153.84V	10.3
$e_{max} = \lvert V_s - V_t \rvert / V_t$			

V. CONCLUSION

This paper establishes a high-frequency conduction simulation model for switching power supplies and conducts quantitative research on the transmission characteristics of interference voltage from the input to the output of the switching power supply. This model comprehensively considers the high-frequency characteristics of core magnetic components, the parasitic parameters of printed circuit board traces, and the structure. In high-frequency simulation analysis, the experimental error is only 10.3%. It can be widely used to study the transmission characteristics and transmission patterns of voltage and current pulse interference in switching power supply links, laying the foundation for EMC design, electromagnetic protection design, and discharge damage research. Subsequent research will focus on two aspects: first, conducting digital model simulation of chip devices to establish a more accurate interference analysis model; second, conducting research on the impact of power supply system impedance characteristics on interference transmission, covering power supply models of various topologies.

ACKNOWLEDGMENT

This work was supported by the National Science and Technology Major Project under Grant 2024ZD06049XX.

REFERENCES

[1] Tong Qiang, Qu Lu, Liu He, et al. Design of distributed power system for satellite based on universal power module[J].Journal of Power Supply, 2022, 20(5): 15-21.

[2] He Xiong, Chen Yonggang, Wang Li, et al. Research on power supply controller for distributed aerospace power supply system[J].Journal of Power Supply, 2022, 20(5): 5-13.

[3] William A.Radasky.Use of IEC E1 HEMP Standards to Determine the Coupled Levels and Impacts of Induced Currents to Power Substation Control House Yard Cables[J].2022 IEEE:537-540.

[4] Edward B.Savage and Willliam A.Radasky.Experimental Studies of E1 HEMP Coupling and Propagation Effects for Power Substation Yard Cables[J].2022 IEEE:496-500.

[5] Li Jianping, Wu Ming, Lu Wei, et al. Engineering developmentof GEO high-power power supply and its in-orbit application[J].Chinese Journal of Power Sources, 2019, 43 （5）:864-868 .

[6] Chen Yonggang, Peng Cheng, Zhi Shubo, et al. Development and application of gallium nitride power devices in aerospace power supply. Electronic Design Engineering, 2024, 32(20): 50-56, 61.

[7] Wong K L, Huang W T, Chen P Y, et al. Modeling of Common-Mode Noise for a Buck Converter With Heat Sink and Free Air[J]. IEEE Transactions on Electromagnetic Compatibility, 2017, 59(4): 1196-1205.

[8] Wang S, Lee F C, Chen D Y, et al. Effects of Parasitic Parameters on EMI Filter Performance[J]. IEEE Transactions on Power Electronics, 2004, 19(3): 869-877.

[9] Müeller J, Schmuelling B, De Doncker R W. Calculation of the Transfer Function of an EMI Filter Considering the Coupling Between Common-Mode and Differential-Mode[J]. IEEE Transactions on Power Electronics, 2015, 30(10): 5652-5661.

[10] Zhang X, Ruan X, Tse C K. Prediction of Conducted EMI in Switching Power Supplies Based on Numerical Calculation and Neural Networks[J]. IEEE Transactions on Power Electronics, 2020, 35(5): 5134-5144.

[11] Christopoulos C, Thomas D W P, ADD A.The Application of Transmission-Line Modeling (TLM) to Electromagnetic Compatibility Problems[J]. IEEE Transactions on Electromagnetic Compatibility, 1995, 37(2): 185-191.

[12] Qian Zhaoming, Zhang Junming, Lü Zhengyu, et al. Electromagnetic interference analysis model of switching power supply power converter [J]. Transactions of the Chinese Society of Electrotechnical Engineering, 2010, 25(5): 1-10.

[13] Chen Henglin, Zhou Luowei, Luo Quanming. Electromagnetic compatibility prediction of switching power supply system based on three-dimensional field-circuit coupling[J]. Proceedings of the CSEE, 2014, 34(3): 431-438.

[14] Li Hong, Zhao Yang, Li Shijin, et al. Analysis of conducted electromagnetic interference characteristics of Buck converter based on parasitic parameters[J]. Transactions of the Chinese Society of Electrotechnical Engineering, 2018, 33(16): 3891-3900..

[15] Zhou Bihua, Chen Bin, Shi Lihua. Electromagnetic pulse and its engineering protection[M]. Beijing, National Defense Industry Press. 2003.1

Unintentional Islanding Detection Method based on Voltage and Reactive Power Adjustment in Grid-Forming Inverter Systems

Yejin Choi
Department of Electrical Engineering
Myongji University
Yongin, Republic of Korea
ehdrh0301@mju.ac.kr

Inchan Hong
Department of Electrical Engineering
Myongji University
Yongin, Republic of Korea
hic05141@mju.ac.kr

Jaehoon Jung
Department of Electrical Engineering
Myongji University
Yongin, Republic of Korea
pho1103@mju.ac.kr

Seungmin Jung
Department of Electrical and Computer Engineering
University of Seoul
Seoul, Republic of Korea
seungminj@uos.ac.kr

Yeuntae Yoo
Department of Electrical Engineering
Myongji University
Yongin, Republic of Korea
ytyoo@mju.ac.kr

***Abstract*—As the proportion of inverter-based resources (IBRs) in the power systems increases, the problem of the grid inertia is becoming increasingly significant. To address this challenge, there is ongoing research into grid-forming (GFM). The prevalent inverter control method, known as the grid-following (GFL), is susceptible to faults and does not have the ability to maintain voltage and frequency. However, grid-forming inverters (GFMIs) overcome these shortcomings. Nevertheless, due to its ability to autonomously generate voltage and frequency, there is difficult to detect unintentional islanding, and there is a potential risk of encountering a Non-Detection Zone (NDZ) may occur. This paper analyzes the response characteristics of GFMIs when the reference values of voltage and reactive power injected into the GFMI are changed using PSCAD/EMTDC. Furthermore, it proposes a innovative unintentional islanding detection method (IDM) applicable to GFMIs, which is based on the rate of change voltage and reactive power before and after the reference adjustment.**

Keywords—Grid-Forming Inverter, Grid-Following Inverter, Unintentional Islanding Detection, Non-Detection Zone

I. INTRODUCTION

In recent years, there has been an growing corporation of inverter-based resources (IBRs) into power systems has heightened the significance of addressing the issue of system inertia. Traditional power system operations have primarily relied on synchronous generators, which are electromagnetically linked to the grid and provide the necessary inertia to sustain system stability during disturbances. However, as reliance on IBRs increases, the available inertia diminishes, rendering the system more susceptible to failures. This shift has contributed to prolonged blackouts attributed to inertia deficiencies, particularly in Europe, where there is a substantial dependence on renewable energy sources.

To address the shortcomings associated with the IBRs in terms of inertia provision, the grid-forming inverter (GFMI) control has become a prominent focus of research. The prevailing inverter control methodology, known as grid-following (GFL), does not exert direct control over voltage and frequency. This approach relies on Phase Locked Loop (PLL) technology to achieve synchronization with the grid by continuously tracking the grid's phase angle, which renders the accuracy of voltage measurement critical and susceptible to potential failures. In contrast, GFMIs function as voltage sources capable of independently adjusting both voltage magnitude and phase, thereby enabling self-synchronization with the grid [1-2]. Furthermore, GFM systems incorporate a voltage control loop and generate a phase angle based on variations in active power, thereby emulating the operational characteristics of synchronous generators [3-4].

However, the increasing integration of GFMIs into the power system can lead to the autonomous generation of frequency and voltage, resulting in the emergence of a Non-Detection Zone (NDZ) and raising concerns regarding unintentional islanding [5-6]. Unintentional islanding, unlike microgrids which are intentionally operated in isolation from the grid, refers to a state of disconnection from the grid due to a fault. In such instances, the stability of voltage and frequency may be compromised, and if reconnection to the power system occurs while there is a phase mismatch, there exists a significant risk of equipment damage due to overvoltage and overcurrent conditions [6].

Traditionally, the Non-Islanding Inverter Test as specified by the IEEE Std 929-2000 (now incorporated into IEEE 1547-2018) is conducted by connecting an RLC parallel load at the Point of Common Coupling (PCC) and comparing the power delivered by the inverter in relation to the power utilized by the load [7-8]. When the system is connected, the inverter is responsible for supplying the power that is not provided by the grid. However, if the inverter is operating in an isolated state and supplying all the power required by the load while maintaining voltage and frequency, it does not satisfy the test criteria.

Furthermore, various islanding detection methods (IDMs), including the active [9], passive [10], hybrid [11-12], and deep learning-based approaches [13-14], have been actively studied. The capability of GFMIs to maintain voltage and frequency presents a significant challenge in terms of islanding detection.

979-8-3315-5472-9/25/$31.00 ©2025 IEEE

Consequently, there is a pressing need for the development of new IDMs that are suitable for GFMIs [6].

This study conducts a comparative analysis of the control logic employed in GFM and GFL control logic, and we introduce novel IDMs specifically for GFMIs. Distinct from GFLIs, GFMIs incorporates an additional control loop that autonomously generates voltage and frequency. Consequently, during an islanding event, GFMIs assume the role of the primary voltage generator and adjusts its output in accordance with any changes in the voltage reference. However, in response to alterations in the reactive power reference, GFMIs do not adjust its output to match the reference, as it prioritizes the stability of the voltage and only provides the reactive power necessary to sustain the actual voltage level. This islanding detection approach leverages the unique response characteristics of GFMIs.

II. Inverter Control Method

A. Grid-Following Control

The GFMIs initially monitor the phase angle continuously by analyzing the voltage at the PCC. Utilizing this phase angle, the voltage and current within the DQ frame are subsequently generated [15]. The calculations for active power and reactive power within the DQ frame are calculated using (1) and (2).

$$P_{dq} = \frac{3}{2}(v_d \cdot i_d + v_q \cdot i_q) \quad (1)$$

$$Q_{dq} = \frac{3}{2}(v_q \cdot i_d - v_d \cdot i_q) \quad (2)$$

Provided that synchronization with the grid is effectively accomplished, the value of v_d approaches nearly zero, allowing for the active and reactive power to be estimated as shown in (3) and (4).

$$P_{dq} \approx \frac{3}{2}(v_d \cdot i_d) \quad (3)$$

$$Q_{dq} \approx \frac{3}{2}(-v_q \cdot i_d) \quad (4)$$

In this context, the direct current component i_d significantly impacts the regulation of active power, while the quadrature current component i_q plays a essential role in the regulation of reactive power.

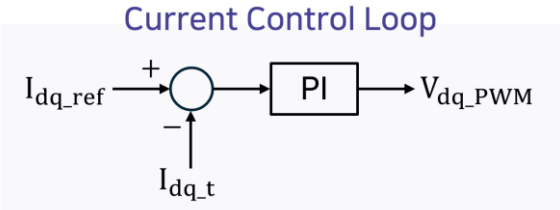


Fig. 1. GFL – Current Control Loop

Consequently, within the power control loop of GFLI systems, the reference values for active and reactive power, along with the output measurements of the inverter's active and reactive power, are utilized to calculate the reference currents I_{d_ref} and I_{q_ref} through the application of proportional-integral (PI) controllers.

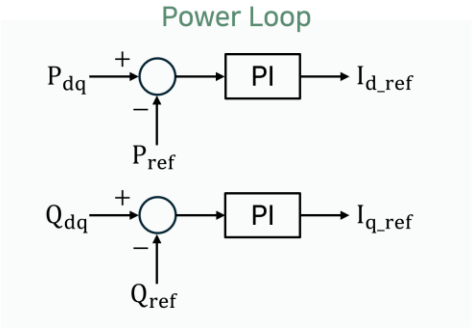


Fig. 2. GFL – Power Control

This is then input to the PWM as V_{d_ref} and V_{q_ref} by performing PI control with i_d and i_q in the current control loop. This structure operates as a closed loop, and eventually the GFLIs generate the desired PQ output. The comprehensive structure of the GFL is illustrated in Fig 3.

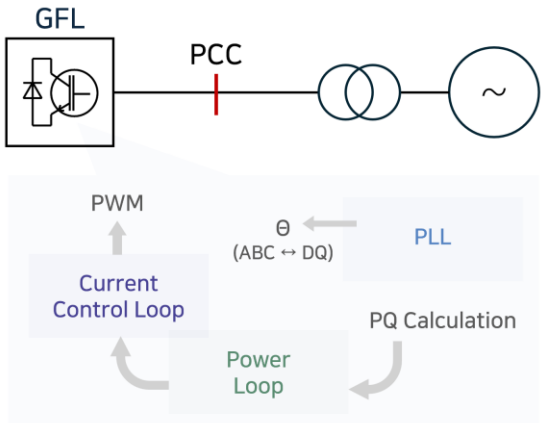


Fig. 3. The overall structure of GFL Control

B. Grid-Forming Control

GFM control significantly differs from GFL control in that it does not employ a PLL and incorporates a voltage control loop. In the outer control loop, rather than utilizing a PLL, the P_{ref} and P_{dq} are regulated using PI control to determine the frequency in accordance with the P-ω droop characteristic. Similarly, reactive power control is implemented using a Q-V droop strategy. In (5) and (6), m and n is the droop coefficients for the P-ω and Q-V droop controllers, respectively [16].

$$w_{ref} = w_{rated} - m(P_{dq} - P_{ref}) \quad (5)$$

$$V_{d_ref} = V_{rated} - n(Q_{dq} - Q_{ref}) \quad (6)$$

The phase angle is subsequently generated by integrating the sum of this frequency and a predefined frequency reference. The frequency reference is established from the outset to facilitate the generation of the phase angle, with only the droop component of the active power discrepancy being included in the calculations, thereby ensuring frequency stability even in the event of system disturbances. Additionally, in the outer loop, the

reactive power mismatch, when multiplied by the droop coefficient, is combined with the voltage reference value to compute the voltage reference V_{d_ref}.

In the inner loop, both voltage and current control mechanisms are implemented. Initially, in the voltage control phase, the V_{d_ref} determined in the outer loop and the V_d are subjected to PI control to derive the reference current I_{d_ref}. In this study, given that the Q-axis is assumed to be zero, the reference voltage for the Q-axis V_{q_ref} is consequently set to zero. Therefore, the actual V_q and PI control are employed to compute the reference current for the Q-axis I_{q_ref}. The current control approach utilized here mirrors the current control methodology typically employed in GFL systems.

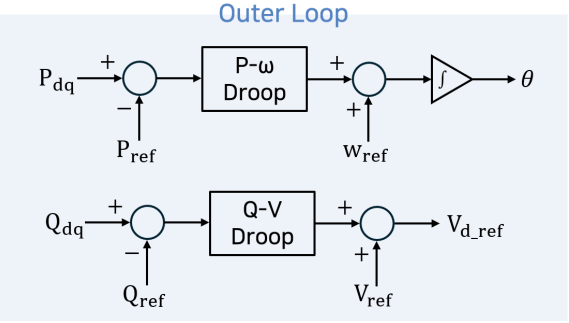


Fig. 4. GFM – Voltage Control Loop

The comprehensive structure of the GFM is illustrated in Fig 5.

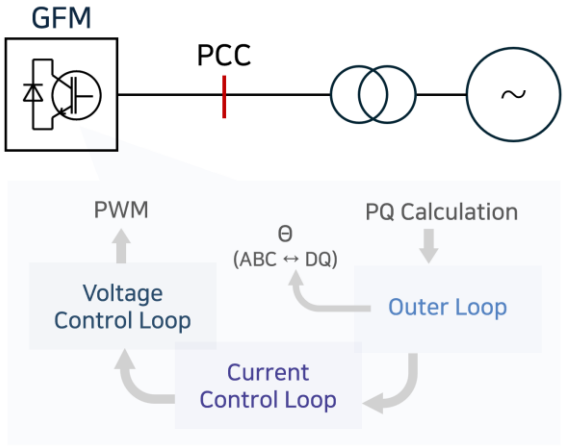


Fig. 5. The overall structure of GFM Control

III. Unintentional Islanding Detection Method

During islanding events, GFLIs, despite supplying power equivalent to the load's requirements, lack the capability to sustain voltage levels. Consequently, although they may maintain frequency temporarily, voltage levels decline rapidly, leading to the immediate activation of the circuit breaker.

In contrast, GFMIs possess the ability to modulate reactive power to maintain voltage stability during islanding. As a result, the voltage may decrease slightly but it is expected to fluctuate only within a safe operational range.

A. Voltage Reference Adjustment

When the reference voltage value is modified while the system is connected to the AC grid, the GFMIs adjust in accordance with the grid voltage. Conversely, during islanding conditions, the GFM units assume the primary role in voltage generation, thereby adhering to the newly established voltage reference. Consequently, the index for detecting islanding based on voltage can be articulated through the following (7).

$$V_{ratio} = \left|\frac{V_{ss_new} - V_{ss_prev}}{V_{ref_new} - V_{ref_prev}}\right| = \left|\frac{\Delta V_{ss}}{\Delta V_{ref}}\right| \quad (7)$$

V_{ref_prev} and V_{ref_new} are the voltage reference values before and after in the GFMI. V_{ss_prev} and V_{ss_new} are the corresponding steady-state voltage values at each point. V_{ratio} indicates the relative change in steady-state voltage in response to the voltage reference adjustment. If $V_{ratio} \approx 1$, IDM can be determined as an islanding state.

B. Reactive Power Reference Adjustment

In the non-islanding condition, adjustments to the reactive power reference can be transmitted to the AC grid, resulting in convergence towards the newly established reactive power reference. Conversely, during islanding state, there is no sink for the surplus reactive power. Given that both excessive and insufficient reactive power can influence voltage levels, the reactive power remains relatively unchanged before and after the onset of islanding, particularly when voltage is stabilized due to the operational characteristics of GFM systems. Therefore, the index for islanding detection based on reactive power can be expressed as (8).

$$Q_{ratio} = \left|\frac{Q_{ss_new} - Q_{ss_prev}}{Q_{ref_new} - Q_{ref_prev}}\right| = \left|\frac{\Delta Q_{ss}}{\Delta Q_{ref}}\right| \quad (8)$$

Q_{ratio} represents the proportional variation in steady-state reactive power resulting from changes to the reactive power reference. If $Q_{ratio} \approx 0$, it can be classified as an islanding condition.

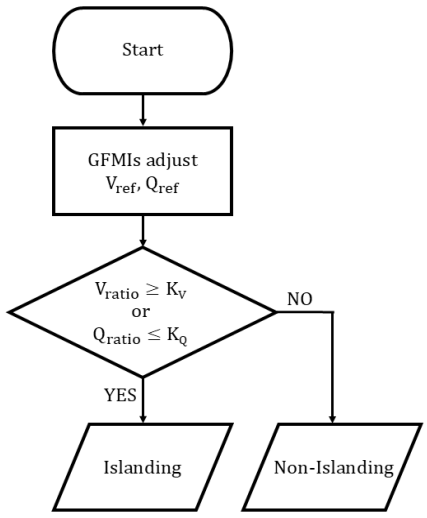


Fig. 6. Flowchart of GFM unintentional islanding detection method

If the criteria for islanding detection related to both voltage and reactive power are met, the system is classified as being in an islanding condition, as illustrated in Fig 6.

IV. Simulation

This study utilized PSCAD/EMTDC as the simulation tool. The model consisted of two GFLIs, one GFMI, and a load. Simulations were conducted to analyze both non-islanding and islanding scenarios by controlling the connection and disconnection of the AC side grid after a single-line-to ground fault on phase A.

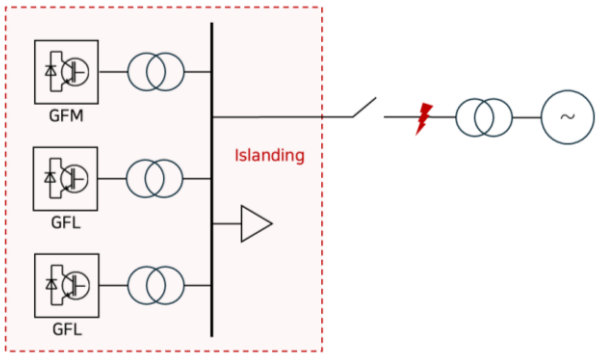


Fig. 7. The islanding simulation system

It is important to note that the GFMI is required to be connected when the grid frequency is close to 60 (Hz) to operate stably. Therefore, it was safely started-up by operating as a GFL mode at first and then switching to a GFM mode at 2 (s).

TABLE I. Paramers Is Used In This Study

Parameter	*Value*	*Unit*
MVA Rating of each Inverters	50	MVA
Initial Voltage Reference	13.8	kV
Active Power Reference	35	MW
Initial Reactive Power Reference	0.066	PU
Frequency Reference	60	Hz
Active Power of Load	105	MW
Reactive Power of Load	0	MVAR
Transformer Voltage	154/13.8	kV
Voltage Ratio, K_v	0.8	-
Reactive Power Ratio, K_Q	0.4	-

Fig 8 illustrates the dynamic response of each inverter under islanding condition when a phase A ground fault occurs at 10 (s) and lasts for 0.05 (s). The AC side grid is isolated at 10.02 (s) only in the case of islanding, meaning that fault recovery is managed exclusively by the inverters. Fig 8 indicates that GFMI supplies more fault current than GFLIs, thereby contributing to fault recovery. Furthermore, GFMI temporarily delivers a significant amount of active and reactive power, supporting system stabilization. As a result, the grid voltage and frequency are rapidly restored due to the fault recovery capability of the GFMI.

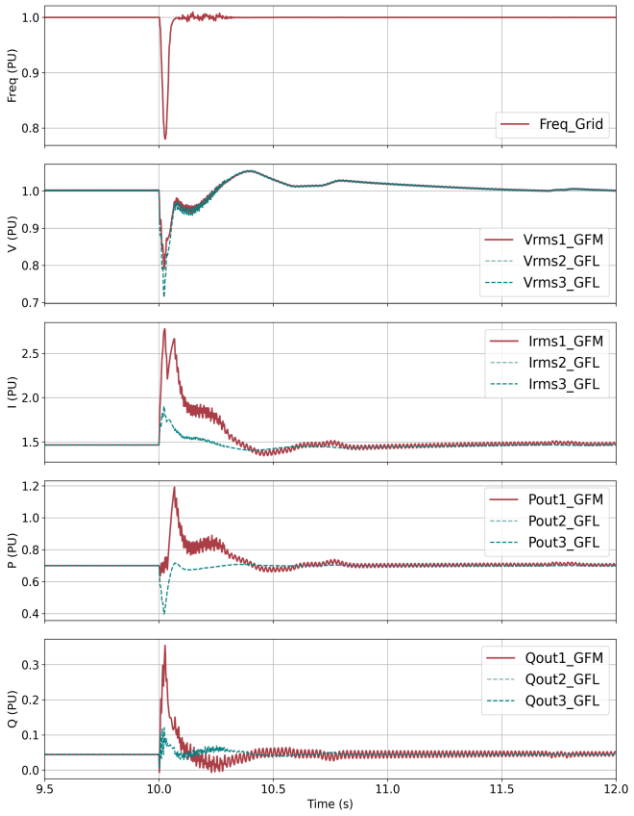


Fig. 8. The dynamic responses of the system after a single-line-to ground fault on phase A: Grid frequency, Voltage (RMS), Current (RMS), Active power, and Reactive power of each inverter.

The IDM module based on C code was implemented in PSCAD/EMTDC. This module determines islanding conditions by calculating the V_{ratio} and Q_{ratio} between the steady-state values before and after change in the V_{ref} or Q_{ref}. To obtain the steady-state values, voltage and reactive power which are the inverter's output are averaged over one cycle. After a reference changes, the computation of the new steady-state is delayed by 2 (s) to allow system transients to settle, and islanding detection is performed at the end of this delay.

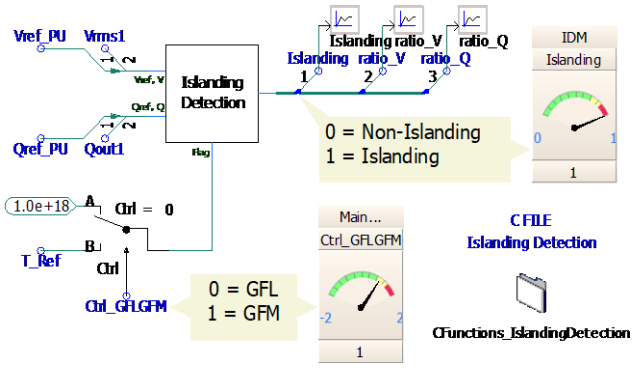


Fig. 9. The IDM module based on C code

A. *Grid forming Response to V Reference Adjustment*

The GFLI was not analyzed independently due to the absence of a loop for voltage regulation. Since the voltage generation during islanding is maintained by a GFMI, the V_{ratio} closes to 1 under islanding conditions, and nearly 0 under non-islanding conditions. This behavior is illustrated in Fig 10, where the V_{ref} is adjusted from 1 to 1.05, 1.1 and 1.15 (PU).

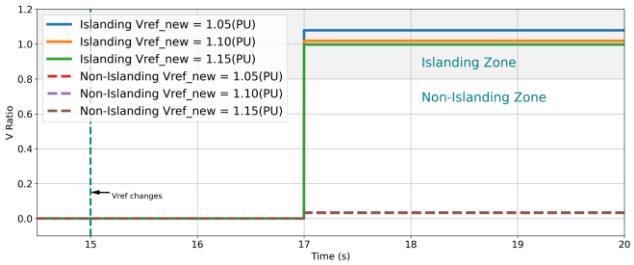


Fig. 10. The comparison of V_{ratio} under islanding and non-islanding conditions

B. *Grid forming Response to Q Reference Adjustment*

The Q_{ref} was changed from 0.066 to 0.3, 0.6 and 0.9 (PU). In contrast to the case of the voltage case, the Q_{ratio} approaches 1 under islanding condition and is nearly 0 under non-islanding conditions. This behavior of Q_{ratio} is illustrated in Fig 11.

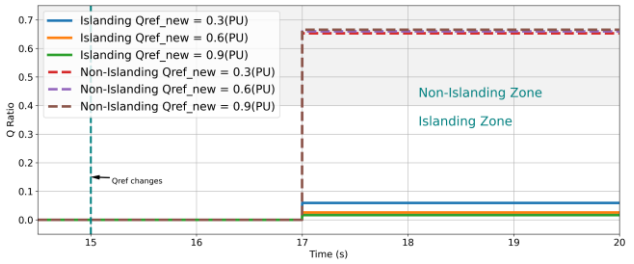


Fig. 11. The comparison of Q_{ratio} under islanding and non-islanding conditions

V. Result

This study presents a novel method for unintentional islanding detection specifically designed for GFMIs. The proposed approach utilizes the unique response characteristics of GFMI, particularly its behavior to follow voltage reference adjustments during islanding without reacting to changes in reactive power references. The proposed algorithm was implemented as a module based on C code, and its performance was observed through simulation. Future research will aim to establish suitable threshold values for the detection indices introduced in this method. Furthermore, the potential applicability of this detection strategy to other inverter control paradigms, including grid-supporting and grid-feeding modes, will be explored.

Acknowledgment

This work was supported by Korea Institute of Energy Technology Evaluation and Planning (KETEP) grant funded by the Korea government (MOTIE) (RS-2023-00234563, Development of power system modeling & analysis and interoperability evaluation technology applied with grid forming based on distributed energy), (No. RS-2023-002317052, Development of an Open Integrated Platform for Distributed Renewable Energy Systems).

References

[1] J. Rocabert, A. Luna, F. Blaabjerg, and P. Rodríguez, "Control of power converters in AC microgrids," IEEE Trans. Power Electron., vol. 27, no. 11, pp. 4734–4749, Nov. 2012, doi: 10.1109/TPEL.2012.2199334.

[2] R. Rosso, X. Wang, M. Liserre, X. Lu, and S. Engelken, "Grid-forming converters: Control approaches, grid-synchronization, and future trends—A review," IEEE Open J. Ind. Appl., vol. 2, pp. 93–109, 2021, doi: 10.1109/OJIA.2021.3074028.

[3] N. Mohammed, H. H. Alhelou, and B. Bahrani, Eds., *Grid-forming power inverters: Control and applications*, 1st ed. Boca Raton, FL, USA: CRC Press, 2023, doi: 10.1201/9781003302520.

[4] D. B. Rathnayake, C. Zhan, T. Xie, Y. Liu, and M. S. El Moursi, "Grid forming inverter modeling, control, and applications," IEEE Access, vol. 9, pp. 114781–114807, 2021, doi: 10.1109/ACCESS.2021.3104617.

[5] B. Bahrani, H. Ye, F. Blaabjerg, J. Driesen, and M. Liserre, "Grid-forming inverter-based resource research landscape: Understanding the key assets for renewable-rich power systems," IEEE Power Energy Mag., vol. 22, no. 2, pp. 18–29, Mar.–Apr. 2024, doi: 10.1109/MPE.2023.3343338.

[6] T. Liu, X. Wang, F. Liu, K. Xin, and Y. Liu, "Islanding detection of grid-forming inverters: Mechanism, methods, and challenges," IEEE Electrific. Mag., vol. 10, no. 1, pp. 30–38, Mar. 2022, doi: 10.1109/MELE.2021.3139206.

[7] IEEE Standard Coordinating Committee 21, "IEEE recommended practice for utility interface of photovoltaic (PV) systems," IEEE Std 929-2000, 2000, doi: 10.1109/IEEESTD.2000.91304.

[8] IEEE Standard Association, "IEEE standard for interconnection and interoperability of distributed energy resources with associated electric power systems interfaces," IEEE Std 1547-2018 (Revision of IEEE Std 1547-2003), pp. 1–138, Apr. 2018, doi: 10.1109/IEEESTD.2018.8332112.

[9] Q. Sun, J. M. Guerrero, T. Jing, J. C. Vasquez, and R. Yang, "An islanding detection method by using frequency positive feedback based on FLL for single-phase microgrid," IEEE Trans. Smart Grid, vol. 8, no. 4, pp. 1821–1830, Jul. 2017, doi: 10.1109/TSG.2015.2508813.

[10] S. Hasan and S. S. Saleh, "A new passive islanding detection technique for a microgrid based on transient energy," IET Gener. Transm. Distrib., vol. 16, pp. 2476–2500, 2022, doi: 10.1049/gtd2.12468.

[11] H. Amini, A. Mehrizi-Sani, and R. Noroozian, "Hybrid islanding detection of an inverter-based high-noise microgrid," IEEE Access, vol. 13, pp. 73161–73172, 2025, doi: 10.1109/ACCESS.2025.3563679.

[12] A. Arif, K. Imran, Q. Cui, and Y. Weng, "Islanding detection for inverter-based distributed generation using unsupervised anomaly detection," IEEE Access, vol. 9, pp. 90947–90963, 2021, doi: 10.1109/ACCESS.2021.3091293.

[13] A. Khamis, H. Shareef, E. Bizkevelci, and T. Khatib, "A review of islanding detection techniques for renewable distributed generation systems," Renew. Sustain. Energy Rev., vol. 28, pp. 483–493, 2013, doi: 10.1016/j.rser.2013.08.025.

[14] R. Chandrakar, R. K. Dubey, and B. K. Panigrahi, "Deep learning-based islanding detection method for droop-controlled grid-forming inverters," IEEE J. Emerg. Sel. Topics Ind. Electron., vol. 6, no. 2, pp. 687–698, Apr. 2025, doi: 10.1109/JESTIE.2024.3512937.

[15] A. Yazdani and R. Iravani, *Voltage-sourced converters in power systems: Modeling, control, and applications*. Hoboken, NJ, USA: IEEE Press/Wiley, 2010.

[16] J. Liu, Y. Miura, and T. Ise, "Comparison of dynamic characteristics between virtual synchronous generator and droop control in inverter-based distributed generators," IEEE Trans. Power Electron., vol. 31, no. 5, pp. 3600–3611, May 2016, doi: 10.1109/TPEL.2015.2465852.

Suppression of Inrush Current in Rectifier Transformer of Mobile DC De-icing Device

1st Junjie Zhao
Jinhua Power Supply Company
State Grid Zhejiang Electric Power Co., Ltd.
Jinhua, China
200824976@qq.com

2nd Wentong Chen
Jinhua Power Supply Company
State Grid Zhejiang Electric Power Co., Ltd.
Jinhua, China
chen_wentong_jh@126.com

3rd Yuqun Fang
Jinhua Power Supply Company
State Grid Zhejiang Electric Power Co., Ltd.
Jinhua, China
326947638@qq.com

4th Xiaoyu Zhou
State Grid Zhejiang Electric Power Co., Ltd.
Hangzhou, China
515834041@qq.com

5th Bo Zhang
School of Electrical Engineering and Automation
Wuhan University
Wuhan, China
zhangbo7973@126.com

6th Wu Wen
School of Electrical Engineering and Automation
Wuhan University
Wuhan, China
632187905@qq.com

***Abstract*—During the de-icing operation of high voltage overhead transmission lines using a mobile DC de-icing device, the energization of the rectifier transformer will produce inrush current, which causes the relay protection to operate and makes the DC de-icing device unable to work. This paper conducts simulations on the inrush current of the rectifier transformer in a mobile DC de-icing device using a 10kV emergency generation vehicle as the AC power source. The influence of the winding connection type of the rectifier transformer on the inrush current is analyzed. This paper proposes an operation method of stepping up from zero voltage for the unloaded rectifier transformer by using the generator excitation control system of the generator in the emergency generation vehicle. The simulation results show that when the Δ/Y connected rectifier transformer is energized, the inrush current amplitude can reach 516.5A. With the application of the stepping up from zero voltage operation of the rectifier transformer, the inrush current can be limited to less than 1.0A. This ensures the mobile DC de-icing operation of transmission lines can be carried out safely and smoothly.**

Keywords—rectifier transformer, inrush current, mobile DC de-icing device, emergency generation vehicle, stepping up from zero voltage

I. INTRODUCTION

Transmission line icing is one of the main natural disasters threatening the safe and stable operation of power grids. Transmission line icing will cause conductor galloping and line sag increase, leading to transmission line tower collapse. These problems are more serious in high altitude, low temperature, rainy and snowy areas. DC de-icing technology is an effective method to solve the problem of transmission line icing [1-3]. It utilizes a three-phase bridge rectifier circuit to convert AC power into DC power, treating the icing line as a load. The DC current in the conductor heats the line to melt the ice. Compared with AC short-circuit de-icing technology, DC current de-icing requires significantly less reactive power and achieves the same ice-melting effect with much smaller power supply capacity, and it is the most widely used de-icing technology at present.

The DC de-icing devices for transmission lines can be categorized into fixed devices and mobile devices. For the de-icing work in EHV and UHV transmission lines, fixed DC de-icing devices are predominantly implemented. They are typically installed in substations or converter stations, and have large power capacities and occupy a large area, the maximum de-icing current exceeds 2kA [4]. The mobile DC de-icing devices, with the rectifier module integrated into transportable units, can be flexibly deployed in different substations based on de-icing operation requirements. Due to transportation constraints, the capacity and weight of the mobile DC de-icing device are limited. Currently, mobile DC de-icing devices utilizing emergency generation vehicle are primarily applied for de-icing work of short transmission lines in the power distribution system. The length of these lines usually does not exceed 4km, and the de-icing current does not exceed 600A.

Since ground wires have higher resistance compared to conductors of transmission lines, the de-icing current of the ground wires is lower, and the power supply capacity required for the segmented ground wire de-icing operation is smaller. The 10 kV emergency generation vehicles can be adopted as the AC power sources for the mobile de-icing operation of segmented ground wires, and they can be deployed near the sections of iced transmission lines. This can improve de-icing efficiency while reducing the power supply capacity, and the flexibility of de-icing operations is further enhanced.

When using the 10 kV emergency power generation vehicle for the DC de-icing operations, due to the limited capacity of the generator, which is mostly in the range of 1000kW-3000kW and the rated power factor is 0.8, the output current of the generator

This work is funded by State Grid Zhejiang Electric Power Co., Ltd. and the research project number is 5211JH24000B.

979-8-3315-5472-9/25/$31.00 ©2025 IEEE

is between 69A-206A. Therefore, a rectifier transformer must be used to reduce the output voltage and increase the output current in order to meet the requirements of the de-icing current for transmission line conductors or ground wires de-icing operations.

During the startup of the DC de-icing device, when an unloaded rectifier transformer is energized, the inrush current is induced due to the nonlinear magnetic property and hysteresis effect of the transformer core. This inrush current may trigger relay protections of the transformer or the generator, causing the generator to shut down and resulting in the failure of the de-icing operation.

The magnitude of inrush currents depends on the magnetic hysteresis characteristics, the transformer core structure and the voltage phase angle at the time of energization. To suppress inrush current, the iron core demagnetization techniques and the phase-angle controlled closing technology have been proposed [5-7]. However, the iron core demagnetization requires complex wiring and time-consuming procedures, has a poor operational efficiency. The phase-angle controlled closing technology needs complex switch control system and requires historical data of iron core magnetization, which is suitable for substations with fixed transformer and power supply parameters. For the mobile DC de-icing device, the parameters of the power supply and rectifier transformer are not fixed, it is impossible to accurately obtain historical data of the iron core magnetization. Neither of the above two technologies is suitable for suppressing the inrush current of rectifier transformers in mobile DC de-icing operations. For the mobile DC ice-melting device powered by the emergency generation vehicle, the output voltage of the generator can be controlled via the excitation regulator, and the inrush current can be effectively suppressed by minimizing the generator output voltage through the excitation regulator when the rectifier transformer is energized.

In this paper, the inrush current characteristics of the rectifier transformer in the mobile DC de-icing device, which is supplied by the 10kV/1000kW emergency power generation vehicle, are simulated with the application of ATP-EMTP software. To ensure the implementation of mobile DC de-icing operations in transmission lines, the suppression measure for inrush current of the rectifier transformer based on generator output voltage control is investigated.

II. Structure and Parameters of Mobile DC De-icing Device

A. Mobile DC De-icing Device

The mobile DC de-icing device consists of the emergency generation vehicle, the rectifier transformer, the rectifier, the power filter, the circuit breakers, etc., as shown in Fig. 1.

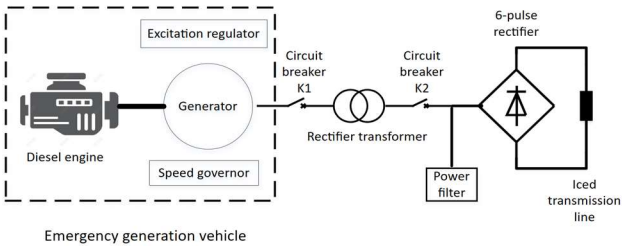


Fig. 1. Structure of a mobile DC de-icing device.

B. Generator Parameters

The generator parameters of the emergency generation vehicle are shown in Table I and Table II, the rated voltage of the generator is 10.5kV, the rated capacity is 1.25MVA, the rated power factor is 0.8 and the number of generator poles is 4.

TABLE I. Electrical Parameters of Generator

Parameter	Value(p.u.)
R_a, Armature resistance	0.010
X_d, Synchronous reactance d axis	1.839
X_q, Synchronous reactance q axis	0.955
X_l, Leakage reactance	0.116
X_d', Transient reactance d axis	0.191
X_q', Transient reactance q axis	0.600
X_d'', Subtransient reactance d axis	0.152
X_q'', Subtransient reactance q axis	0.183
X_0, Zero sequence reactance	0.220

TABLE II. Time Constants of Generator

Time constant	Value(s)
T_d,Open circuit time constant in d axis	0.711
T_q, Open circuit time constant in q axis	1.000
T_d', transient time constant in d axis	0.125
T_q', transient time constant in q axis	0.850
T_d'', subtransient time constant in d axis	0.035
T_q'', subtransient time constant in q axis	0.004

C. Rectifier Transformer Parameters

The parameters of the rectifier transformer in the mobile DC de-icing device are shown in Table III, and Fig. 2 shows the nonlinear characteristics of the transformer core.

TABLE III. Parameters of the Rectifier Transformer

Rated voltage (kV)	Rated capacity (MV • A)	Short circuit impedance (%)	Winding connection type
10/3	1	5	Δ/Y

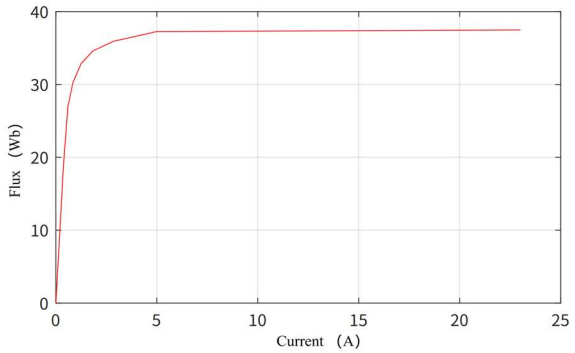


Fig. 2. Nonlinear characteristics of rectifier transformer core.

III. Analysis of Inrush Current in Rectifier Transformer

A. Influence Factor

When an unloaded transformer is energized, the inrush current of the transformer is influenced by various factors, such as the residual flux of the transformer core, the switching angle of the circuit breaker, the system voltage, the system capacity

and the transformer parameters. Among all the influencing factors, the residual flux of the iron core and the switching angle of the circuit breaker are the main factors affecting the inrush current of the transformer [7-9].

The steady-state output voltage of the generator in the emergency generation vehicle is shown in (1).

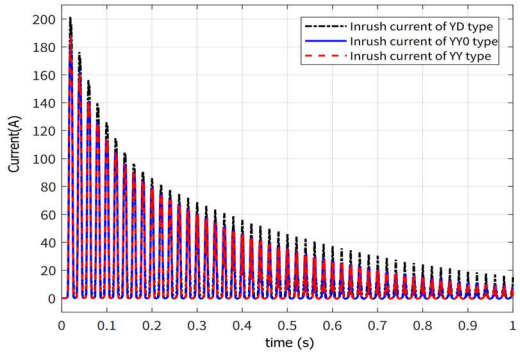
$$\begin{cases} u_A(t) = U_m \sin(\omega t + \alpha) \\ u_B(t) = U_m \sin(\omega t + \alpha - 120°) \\ u_C(t) = U_m \sin(\omega t + \alpha + 120°) \end{cases} \quad (1)$$

In (1), U_m=8.16 kV, ω=314rad/s, α is the switching angle when t is 0. For the inrush current of transformer phase A, when there is no residual flux, the amplitude of the excitation inrush current is maximum when α is 0° or α is 180°. When there is residual flux, if the residual flux is positive, the inrush current is maximum when α is 0°. If the residual flux is negative, when α is 180°, and the inrush current is maximum [9].

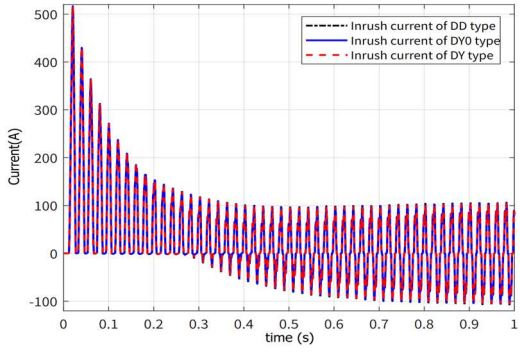
In addition, the connection type of the three-phase winding of the transformer also has a certain impact on the inrush current. In this paper, the influence of the transformer windings connection type on the inrush current will be mainly analyzed.

B. Inrush Current with Various Windings Connection Type

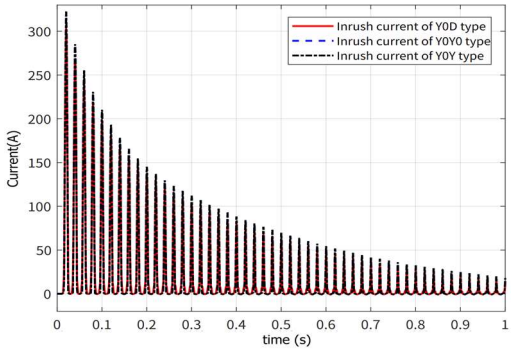
Based on the nonlinear characteristics of the rectifier transformer core, assuming the residual flux is 28% of the saturation magnetic flux and α is 0°, the inrush currents with various windings connection types of the rectifier transformer in the mobile DC de-icing device are simulated with the application of ATP-EMTP. The simulation results are shown in Fig.3 and Table IV.



(a)



(b)



(c)

Fig. 3. Inrush current waveform of rectifier transformer with various windings connection type. (a) Y-type connection on the primary side of the transformer. (b) Δ-type connection on the primary side of the transformer. (c) Y0-type connection on the primary side of the transformer.

TABLE IV. AMPLITUDES OF INRUSH CURRENTS

Winding connection type	Inrush current (A)
Y/Δ	201.6
Y/Y	188.2
Y/Y0	188.2
Δ/Δ	516.2
Δ/Y	516.5
Δ//Y0	516.5
Y0/Δ	303.2
Y0/Y	322.6
Y0/Y0	322.6

When the Δ-Y connected rectifier transformer is energized, the inrush current amplitude can reach 516.5A, which is 5.3 times of the generator rated current. The inrush current may trigger relay protections of the transformer or the generator, resulting in the failure of the de-icing operation.

According to the simulation results, when the primary side of the transformer winding adopts a Δ-type connection, the third harmonic current can pass through the winding coil, and the winding voltage is the generator line voltage. When the winding of the primary side is Y0 connected, the third harmonic current can also flow in the winding coil, and the winding voltage is the phase voltage. When using Y-type connection wiring, the third harmonic current cannot flow in the winding. Therefore, the inrush current of the transformer using the Y-type connection at the primary side is smaller than the current of the Δ-type and Y0-type connections.

IV. SUPPRESSION OF INRUSH CURRENT

A. Operation of Stepping up from Zero Voltage

To suppress the inrush current when the no-load rectifier transformer is energized, this paper adopts the operation of stepping up from zero voltage of the transformer, which is often used for checking large capacity power transformers before the impact closing test. The application of this operation can avoid damage to the transformer caused by the impact voltage in the test. Usually, an emergency diesel generator is used as its test power source. Since the mobile DC de-icing device is powered by the generator of the emergency power vehicle, the operation of stepping up from zero voltage can be applied for the suppression of inrush current during the rectifier transformer energization.

The operation of stepping up from zero voltage of the transform are as follows.

- Connect the unloaded rectifier transformer before starting the generator of the emergency generator vehicle.
- Start the diesel engine and increase the generator speed from 0 to the rated speed.
- Control the excitation regulator to synchronously increase excitation current and increase the voltage of the generator from 0 to the rated voltage.

The excitation current control diagram of the generator during the generator starting process is shown in the Fig.4.

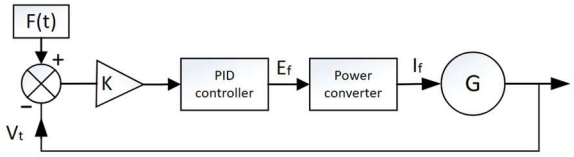


Fig. 4. Excitation current control diagram of the generator.

In Fig.4, V_t is the voltage at the output terminal of the generator and it is expressed in per unit value, K is a proportional amplifier, E_f is the excitation voltage control signal, I_f is the excitation current of the generator, F (t) is the excitation current control function for the generator starting process, as shown in (2).

$$F(t)=\begin{cases}0.1t & 0<t<t_0\\ 1 & t_0\le t<t_s\end{cases} \tag{2}$$

In (2), t_0 is the time for the generator to reach its rated speed, t_s is the total starting time of the generator. For the generator in the emergency generation vehicle, t_0 is 3s and t_s is 40s.

B. Simulation Analysis

For the simulation of the generator starting process, K is 100, the parameters of the PID control unit are set to K_p=0.2, K_i=20 and K_d=0. The residual flux of the rectifier transformer is 28% of the saturation magnetic flux, α is 0° and the transformer windings adopt △/Y connection. The generator frequency, the generator voltage, the transformer excitation current and the magnetic flux of the transformer core during the starting process of the generator are simulated.

The frequency curve during the starting process of the generator is shown in Fig. 5.

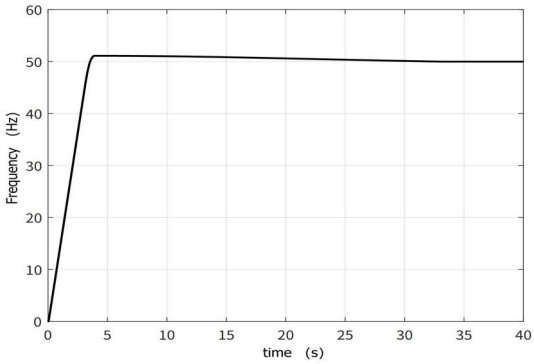


Fig. 5. Frequency curve during the starting process.

The generator voltage curve and waveforms during the starting process of the generator is shown in Fig.6.

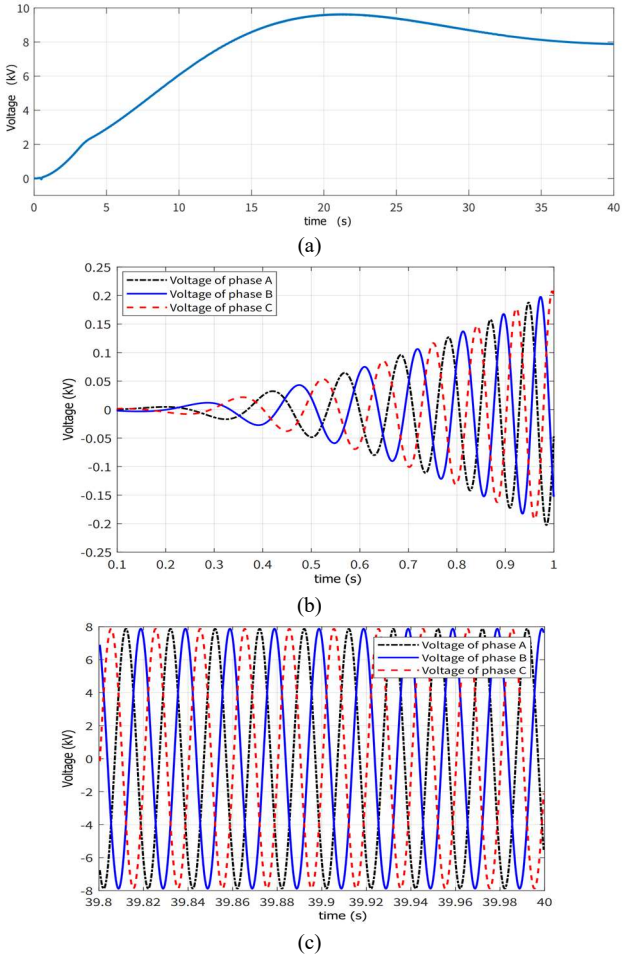
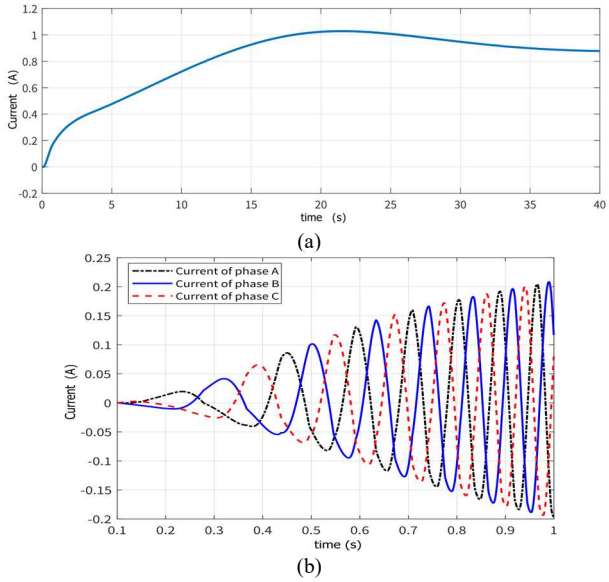
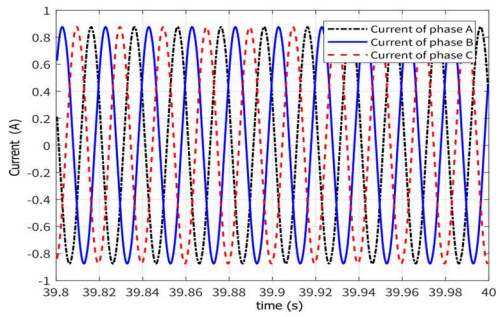


Fig. 6. Voltage curve and waveforms of the generator during the starting process. (a) Curve of voltage amplitude. (b) Voltage waveform within the first second of startup. (c) Voltage waveform after startup completion.

Fig.7 shows the curve and waveforms of the transformer excitation current during the starting process of the generator.

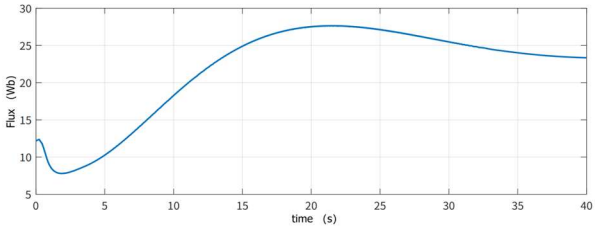




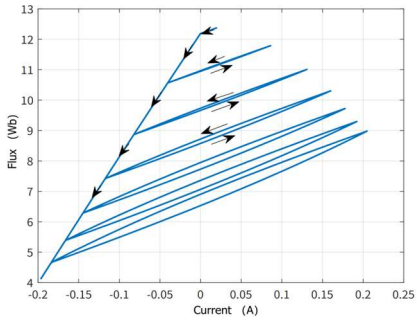
(c)

Fig. 7. Transformer excitation current curve and waveforms during starting process. (a) Curve of excitation current amplitude. (b) Current waveform within the first second of startup. (c) Current waveform after startup completion.

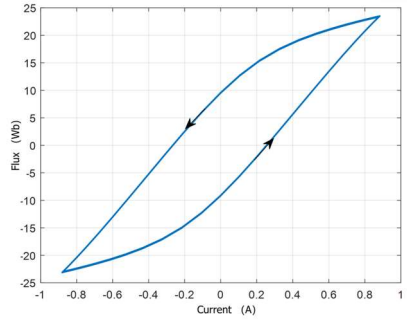
Fig.8 shows the magnetic flux curve and hysteresis loop of transformer core during the starting process of the generator.



(a)



(b)



(c)

Fig. 8. Magnetic flux curve and hysteresis loop of transformer core during the starting process. (a) Curve of iron core magnetic flux. (b) Hysteresis loop within the initial startup time. (c) Hysteresis loop after startup completion.

As the speed of the generator increases, the terminal voltage of the generator oscillates from 0 to the rated voltage. At the beginning of the starting process, the hysteresis loop of the transformer core oscillates around a small range of residual magnetism, and the center of the hysteresis loop gradually shifts towards the zero residual magnetism point. The oscillation range of the hysteresis loop gradually increases, but it is basically in the linear region of the hysteresis loop. During the starting process of the generator, the magnetizing current of the transformer is less than 1A. With the application of stepping up from zero voltage operation, the inrush current can be effectively eliminated when the unloaded rectifier transformer is energized.

V. Conclusion

This paper analyzes the inrush current during the rectifier transformer energization in a mobile DC de-icing device, which is supplied by the 10kV/1000kW emergency generation vehicle. The suppression measure of the inrush current is proposed.

The inrush current of the rectifier transformer is not only affected by the residual flux of the iron core and the switching angle of the circuit breaker, but also by the connection type of the transformer winding. For the Δ /Y connected rectifier transformer, the inrush current amplitude can reach 516.5A. When the primary side of the transformer adopts Δ type connection, the excitation inrush current is the highest. When using Y type connection, the excitation inrush current can be reduced. The stepping up from zero voltage operation of the transformer can effectively reduce the inrush current when the unloaded rectifier transformer is energized. With the application of the stepping up from zero voltage operation, the inrush current can be limited to less than 1.0A. To reduce the inrush current of the rectifier transformer in the mobile DC de-icing device, it is recommended to use a Y connection on the primary side of the transformer winding and adopt the stepping up from zero voltage operation during the transformer energization.

References

[1] X. Zhou, Y. Zhu, Y. Zhang and H. Li, “A Review of Anti-icing and De-icing Technology of Overhead Ground Wire,” 2022 International Symposium on Electrical, Electronics and Information Engineering (ISEEIE), Chiang Mai, Thailand, 2022, pp. 282-286.

[2] J. Feng et al., “Study on De-Icing Technology of High Altitude Wind Power Transmission Line,” 2023 International Conference on Power System Technology (Power Con), Jinan, China, 2023, pp. 1-6.

[3] Q. Yang, “Mechanism of Transmission Line Icing in High Altitude Area and Optimization of De-Icing Technology Algorithm,” 2025 International Conference on Electrical Drives, Power Electronics & Engineering (EDPEE), Athens, Greece, 2025, pp. 1112-1118.

[4] J. Lu, J. Hu, Z. Fang, “Experimental investigation on ice-coating and ice-melting of large-section current carrying conductors for UHVDC transmission project,” Power System Technology, vol. 37, no. 5, pp. 1258-1264, May 2013.

[5] J. H. Brunke and K. J. Frohlich, “Elimination of transformer inrush currents by controlled switching. I. Theoretical considerations,” in IEEE Transactions on Power Delivery, vol. 16, no. 2, pp. 276-280, April 2001.

[6] F. de León, A. Farazmand, S. Jazebi, D. Deswal and R. Levi, “Elimination of Residual Flux in Transformers by the Application of an Alternating Polarity DC Voltage Source,” in IEEE Transactions on Power Delivery, vol. 30, no. 4, pp. 1727-1734, August 2015.

[7] R. Zhang, Z. Gan, et al., “Controlled switching strategies to eliminate the inrush current of converter transformer,” Power System Protection and Control, vol. 47, no.15, pp.69-77, August 2019.

[8] J. Lv, M. Hou, J. Deng, Z. Pan, Z. Zhang and J. Gao, “Analysis of factors affecting the inrush current in converter transformers,” China HVDC and Power Electronics Annual Meeting of CSEE (DCPE 2024), Tianjin, China, 2024, pp. 153-160.

[9] C. Liu, F. Chen, “Research on Simulation of Inrush Current in Transformer Based on PSCAD/EMTDC,” Transformer, vol. 57, no. 5, pp. 44-47, May 2020.

A Multi-stage Features and Attention Mechanism-Embedded Time Convolutional Network-Based Power System Transient Stability Assessment Method

Yutong Wang
Electrical and Power Engineering School
Hohai University
Nanjing, China
yutongwang_66@163.com

Xiaobo Wang
Systems and New Energy Technology Center, Jiangsu EPRI
State Grid Jiangsu Electric Power Company Co., Ltd
Nanjing, China
wangxb0324@foxmail.com

Xinyao Zhu
Systems and New Energy Technology Center, Jiangsu EPRI
State Grid Jiangsu Electric Power Company Co., Ltd
Nanjing, China
xy_zhu@foxmail.com

Haiqiang Zhou
Electrical and Power Engineering School
Hohai University
Nanjing, China
js.hq@163.com

Shengjun Wu
Systems and New Energy Technology Center, Jiangsu EPRI
State Grid Jiangsu Electric Power Company Co., Ltd
Nanjing, China
wsj333@163.com

Shuhuan Li
Electrical and Power Engineering School
Hohai University
Nanjing, China
18953891779@163.com

***Abstract*—A multi-stage features and attention mechanism-embedded time convolutional network-based transient stability assessment (TSA) method is proposed. Firstly, the multi-stage features are constructed with pre-fault, during-fault and post-fault time sequence, and the time convolutional network (TCN) is used to efficiently capture the causal correlation ship between time series in parallel. Secondly, balance of the samples is improved by adjusting the sample composition and the weight of the loss function during training. The model's ability to fit the classification boundary is enhanced through sample augmentation. Then, the attention mechanism is embedded in the TCN to capture the high-value features and improve the interpretability of the model. It helps the TCN to evaluate the power system transient stability more accurately. Finally, the proposed TSA algorithm is validated with the modified IEEE 39-bus system including 3 wind generators. Simulation results show that the TCN-based TSA method has good accuracy and efficiency.**

Keywords—transient stability assessment, time convolutional network, attention mechanism, sample balance, wind generator

I. INTRODUCTION

The large-scale integration of renewable energy into the new power system has reduced its voltage and frequency support capability, which has resulted in frequent tripping events of renewable energy units. Transient stability is a challengeable issue for the new power system. The power system with high-penetration new energy has multiple uncertainties. The Monte Carlo method [1] is computationally too time-consuming to be used in practice. Although probabilistic analysis methods such as Gaussian mixture model [2] and point estimation [3] can calculate the probability of the power system transient stability analytically, but the accuracy and the applicability in various scenarios still need to be improved.

In recent years, with the rapid development of artificial intelligence technology [4], machine learning methods have been widely used in power system TSA. Reference [5] proposes a support vector machine (SVM)-based TSA model. The state variables of the generators are chosen as input. The SVM-based method is demonstrated to have better accuracy than other shallow network-based models while exhibiting limitations in high-dimensional feature extraction. In deep learning, reference [6] utilizes a convolutional neural network (CNN) to extract temporal features from transient processes. However, as the network depth increases, training complexity significantly rises. Reference [7] proposed an improved long short-term memory (LSTM) network enhancing the TSA accuracy effectively., However, features cannot be extracted by model in parallel due to its intricate gating mechanisms and recurrent structure. Reference [8] introduces a time convolutional network (TCN) to capture temporal features in transient processes, improving assessment accuracy with low computational cost. However, TCN has poor interpretability. Reference [9] uses a Transformer encoder-based TSA method, which has strong assessment performance and interpretability but cannot fully exploit the causal relationships in temporal features.

To improve sample balance, Reference [10] uses an adaptive cross-entropy loss function to increase the weight of unstable samples and improve model evaluation bias, but ignores the importance of boundary samples for model training. References

This work is supported by the Science and Technology Program of SGCC (No. J2024158).

979-8-3315-5472-9/25/$31.00 ©2025 IEEE

[11-12] obtain and enhance boundary sample sets based on the TSA results of pre-trained CNN model without consideration of how close the samples are to the physical stability boundary.

Overall, there are still several limitations which remains to be disclosed: 1) The impact of temporal features on TSA has been few studied, and the model's interpretability was few considered; 2) Improving sample balance and how to improve the model evaluation performance has not been studied sufficiently.

A multi-stage features and AMETCN-based TSA method is proposed. Firstly, the multi-stage features are constructed with pre-fault, during-fault and post-fault time sequence, and TCN is used to efficiently capture the causal correlation between time series in parallel. Secondly, to improve sample balance, enhance the model's ability to fit the classification boundary by adjusting the sample composition and the weight of the loss function during training. Then, to capture the high-value features and improve the model interpretability, attention mechanism is embedded to enable TCN to evaluate the transient stability accurately. Finally, the accuracy and efficiency of the proposed TSA model are applied in the modified IEEE 39 system with wind turbines to verify its effectiveness.

II. Muti-stage Features-Based Time Convolutional Network Transient Stability Assessment Model

Transient stability is the ability of the synchronous generators(SGs) to maintain coherency and transit to a new steady state operation mode or return to the original steady state after a large disturbance in the power system. The most fundamental issues are how to choose features and suitable deep neural network when the machine learning (ML) technology is applied in TSA.

A. Multi-stage Features of Transient Stability

Data-driven TSA models usually use the pre-fault system state as input features, collecting samples under various scenarios. The model is trained by samples to establish a mapping relationship between steady-state features and system transient stability. Single moment features-based TSA models are relatively simple and provide faster evaluation speeds. However, new power system exhibits strong nonlinear and time-varying characteristics. During faults, discrete control actions such as fault ride-through, current limitation, recovery of renewable generators and the interactive effects of voltage and frequency result in complex post-fault dynamic responses. Relying solely on the information provided by the steady-state operation point makes it difficult to predict system transient stability accurately. The post-fault trajectories of the system contains the dynamical causal relationships. Therefore, it is more suitable to assess the transient stability according to the trajectories in a short period after the fault.

The evolution of system faults can be divided into three stages: pre-fault, during-fault, and post-fault stage, as shown in Fig. 1. 1 point is taken in a steady state before the fault. When the fault occurs at t_f, 6 points are taken at relatively short intervals due to the intense dynamic changes during the fault. When the fault is cleared at t_c, assume that integration continues for 0.1s after the fault is cleared. According to EEAC theory, the post-fault motion trajectory of the equivalent system on the $P-\delta$ plane has an important impact on the transient stability of

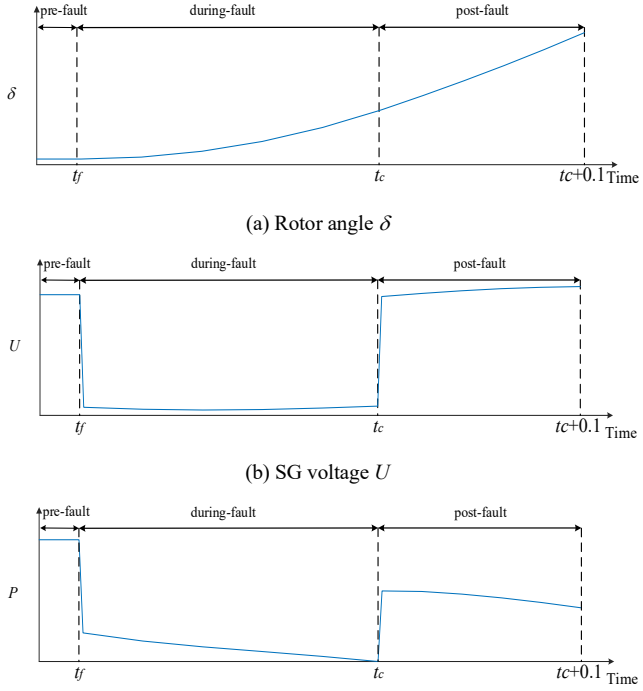


Fig. 1. Schematic diagram of multi-stage features sampling

the system. Therefore, 5 points are taken at equal intervals within the period of [t_c , t_c +0.1]. The dynamical features collected at t_k (k=1,2,…,12) are used in TSA.

Considering that the dynamic characteristics of generators and new energy generators have a significant impact on transient stability, the features at t_k are depicted as:

$$\boldsymbol{X}^{(k)} = \left[\boldsymbol{X}_{\mathrm{G}}^{(k)},\ \boldsymbol{X}_{\mathrm{W}}^{(k)} \right] \tag{1}$$

$\boldsymbol{X}_{\mathrm{G}}^{(k)}$ can be expressed as:

$$\boldsymbol{X}_{\mathrm{G}}^{(k)} = \left[\boldsymbol{X}_{\mathrm{G1}}^{(k)}, \boldsymbol{X}_{\mathrm{G2}}^{(k)}, \ldots, \boldsymbol{X}_{\mathrm{G}n}^{(k)} \right] \tag{2}$$

$\boldsymbol{X}_{\mathrm{G}i}^{(k)} = [\delta_{gi}^{(k)}, \omega_{gi}^{(k)}, P_{gi}^{(k)}, U_{gi}^{(k)}]$, $\delta_{gi}^{(k)}$, $\omega_{gi}^{(k)}$, $P_{gi}^{(k)}$, $U_{gi}^{(k)}$ are the rotor angle, rotor speed, active power, and voltage amplitude of the ith SG, n is the number of SGs. $\boldsymbol{X}_{\mathrm{W}}^{(k)}$ can be expressed as:

$$\boldsymbol{X}_{\mathrm{W}}^{(k)} = \left[\boldsymbol{X}_{\mathrm{W1}}^{(k)}, \boldsymbol{X}_{\mathrm{W2}}^{(k)}, \ldots, \boldsymbol{X}_{\mathrm{W}m}^{(k)} \right] \tag{3}$$

$\boldsymbol{X}_{\mathrm{W}i}^{(k)} = \left[P_{\mathrm{w}i}^{(k)}, Q_{\mathrm{w}i}^{(k)}, U_{\mathrm{w}i}^{(k)} \right]$, $P_{\mathrm{w}i}^{(k)}$, $Q_{\mathrm{w}i}^{(k)}$, $U_{\mathrm{w}i}^{(k)}$ are the active power, reactive power, and voltage amplitude of the ith wind turbine, m is the number of wind turbine units.

Compared with single-point features as model inputs, the multi-stage features in this paper provide evaluation model with continuous correlation between the features, making the model capture the mapping relationship between the temporal

evolution patterns of multi-stage features and TSA results, thereby improving model evaluation performance.

B. *Time Convolutinal Network-Based Transient Stability Assessment Model*

LSTM, CNN and TCN are commonly used to process time series. LSTM has a complex gating mechanism and low computational efficiency. And CNN extracts local information by stacking convolutional kernels to ultimately obtain the global information, and has high computational complexity. Whereas the TCN can process temporal features in parallel, resulting in high training efficiency. It can also expand the receptive field flexibly to capture causal relationship between features over longer time spans at a low computational cost, thereby improving evaluation accuracy. Therefore, TCN is used as the TSA model in this paper.

TCN consists of stacked residual blocks. The structure of the residual module is shown in Fig. 2. Each residual block has two identical convolution units, each of them including causal dilation convolution, weight normalization layer, ReLU layer and dropout layer. The residual connection can solve gradient vanishing in deep neural networks.

The core of TCN lies in the use of causal dilation convolution to extract temporal features, which extracts the output of *t* only obtained by the previous convolution layer and the historical data through the convolution calculation, which ensures the continuity and causality of the extracted temporal features.

Multi-stage features have a long time span and a large amount of data. Causal convolution needs to increases the network parameters and reduces the model training efficiency to capture the temporal features of longer time. Therefore, the introduction of dilation factor can expand the receptive field of causal convolution for historical data [13].The causal dilation convolution is calculated as follows:

$$G(t)=\sum_{r=0}^{s-1}F_n(r)x_{t-dr} \tag{4}$$

$G(t)$ is the output of the convolution layer at t; $F_n(r)$ is the rth convolution kernel; x_{t-dr} is input of the convolution layer at t-dr; d is the dilation factor; s is the size of the convolution kernel.

III. Sample Balance Improvement Method

In TSA, the small number of unstable and boundary samples makes the loss of stable samples dominate the gradient descent direction [14], which severely restricts the model from learning the features of unstable and boundary samples, making it difficult to improve model evaluation performance. Therefore, it is necessary to improve sample balance.

Define boundary samples from model classification boundaries and transient stability physical boundaries. The model classification boundary is defined according to the cross-entropy loss:

$$l_{CE_i}=-\frac{1}{C}\sum_{j=1}^{C}y_{i,j}\ln p_{i,j} \tag{5}$$

C is the number of sample categories, $y_{i,j}$ and $p_{i,j}$ represent the sample labels and the probability of classifying the sample as j.

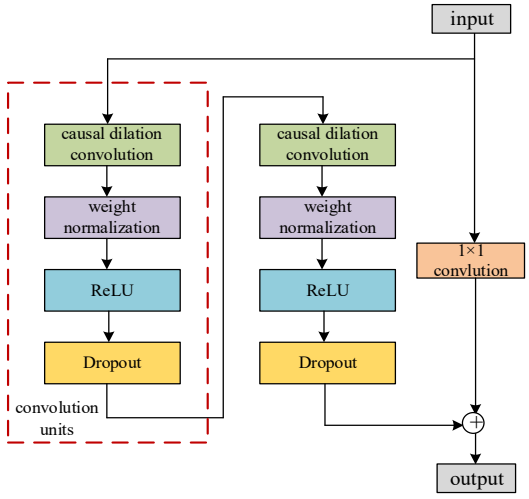


Fig. 2. Structure of residual block

The samples are divided into severely misclassified samples, model classification boundary samples, and correctly classified samples by (5). Usually, it is regarded as a boundary sample when l_{CE_i} satisfies $0.1054<l_{CE_i}<2.3026$.

η_{TSI} is the transient stability margin. The closer its value is to 0, the closer the sample is to the transient stability physical boundary. η_{TSI} is defined as follows:

$$\eta_{\mathrm{TSI}}=\frac{360^{\circ}-\left|\Delta\delta_{\max}\right|}{360^{\circ}+\left|\Delta\delta_{\max}\right|} \tag{6}$$

$\Delta\delta_{\max}$ is the maximum rotor angle difference between any two SGs in the system during the simulation time. When η_{TSI} satisfy $-0.6\leqslant\eta_{\mathrm{TSI}}\leqslant 0.2$, the sample is close to the transient stability boundary. At the data level, the generative adversarial network (GAN) is used to enhance the two types of boundary samples[12].

Adjusting the weights of the loss function during training and regulating the direction of gradient updates can help avoid bias in model classification. The improved Focus Loss (FL) function is expressed as:

$$\begin{aligned}L_{ce}&=-w_s y(1-p)^{\gamma}\log p-w_{us}(1-y)p^{\gamma}\log(1-p)\\&=\begin{cases}-w_s(1-p)^{\gamma}\log p & \text{y=1}\\-w_{us}p^{\gamma}\log(1-p) & \text{y=0}\end{cases}\end{aligned} \tag{7}$$

y represents the label, where 1 indicates a stable sample and 0 indicates an unstable sample; p represents the probability of predicting the sample as stable, and 1-p represents the probability of predicting the sample as unstable; and w_s, w_{us} represent the category balance factors for stable and unstable samples, which are inversely proportional to the proportion of samples of that category in the dataset; γ is the boundary sample modulation factor, which dynamically adjusts the loss by setting

an appropriate value to enhance the model's learning ability of boundary samples and weaken the influence of non-boundary samples.

IV. Attention Mechanism-Embedded Transient Stability Assessment Model

A. Attention Mechanism-Based Feature Interpretation

The multi-stage features of TSA include abundant fault information. However, using causal dilation convolution alone makes it difficult to extract the correlations between different features, preventing the model from capturing the important features that play a key role in TSA. Therefore, an attention mechanism is introduced to extract global feature information, providing high-value input data for TCN to extract local temporal features. The model adjusts the focus on features dynamically according to the attention weight matrix obtained through linear transformation of the attention mechanism, thereby enhancing the model's perception of multi-stage features and its interpretability. The feature expressions output by the multi-head attention mechanism are described in detail in Reference [9]. The average of the attention weights obtained from all self-attention heads is used to measure the importance of features[15]:

$$\tilde{\mathrm{A}}(Q,K)=\frac{1}{h}\sum_{i=1}^{h}\mathrm{Softmax}\left(\frac{\boldsymbol{Q}_i\boldsymbol{K}_i^{\mathrm{T}}}{\sqrt{d_k}}\right) \tag{8}$$

$\mathrm{Softmax}(\boldsymbol{Q}_i\boldsymbol{K}_i^{T}/\sqrt{d_k})$ is single-head attention weight, the weight values are in the range of 0-1; d_k is the scaling factor; h is the number of heads in multi-head attention; $\boldsymbol{Q}_i$ and $\boldsymbol{K}_i$ are the matrixes obtained by the query matrix and key matrix after linear transformation.

The attention weight matrix reflects the model's dynamic weight allocation for features, which is not constrained by the distance between features. Therefore, the multi-head attention mechanism has a global receptive field, which can focus on the key features that have a significant impact on the TSA results. After feature adaptive weight, the model can mine deeper temporal features and guide the selection of features, thereby enhancing the model's interpretability.

B. AMETCN-Based Transient Stability Assessment Method

The procedures of the AMETCN-based power system TSA is as follows.

1) Sample generation. A large number of samples are obtained through time-domain simulation. The sample labels are determined by (6). When $\eta_{\mathrm{TSI}}<0$, the sample is unstable; when $\eta_{\mathrm{TSI}}>0$, the sample is stable.

2) Sample balance improvement. Boundary samples are screened and enhanced according to Equations (5) and (6). The enhanced samples are added to the original sample set to form the enhanced sample set.

3) Offline training stage. The training set is used for AMETCN model training, using an improved FL function to minimize the loss function until the loss converge, which indicates model training completion.

4) Online application stage. The test set is simulated as real-time measurement data from the PMU and input into the model to quickly obtain evaluation results.

V. Case Study

A. Case System

The effectiveness of AMETCN-based TSA method is verified in the modified IEEE39 system with wind turbines which is shown in Fig. 3. In this system, the SGs are replaced by wind turbines at bus 32, 33 and 37 which installed capacities are 800 MVA, 800 MVA and 880 MVA. All loads are modeled in constant impedance and all sample data are simulated from PSASP7.4.

The simulation samples are set up as follows. The load fluctuates between 80 %~120 % and varies in 5 % each step, and the output of wind turbines fluctuates between 20 %~100 % and changes in 20% each step. Adjust the output of the SGs accordingly to ensure the power balance and maintain the voltage in the range of 0.95 p.u. ~1.05 p.u. The fault is set as a three phases short circuit fault, the fault duration is set to be 0.15 s, 0.2 s and 0.25 s respectively, the simulation time is set to 5 s, and the fault location is 20 %, 50 %, and 80 % of the total length of the lines. The 33 transmission lines except bus 16-19 are selected as fault lines. Totally, 13 365 samples are generated, including 7 403 stable samples and 5 962 unstable samples.

B. Effect of Sample Balance on the Transient Stability Assessment

To evaluate the performance of model, indices such as the overall evaluation accuracy A_c, the false judgment rate of stable samples P_{fs}, and the missed judgment rate of unstable samples P_{fu} are calculated by:

$$A_c=\frac{T_S+T_U}{T_S+T_U+F_S+F_U} \tag{9}$$

$$P_{fs}=\frac{F_S}{T_S+T_U+F_S+F_U} \tag{10}$$

$$P_{fu}=\frac{F_U}{T_S+T_U+F_S+F_U} \tag{11}$$

where F_{S} and T_{U} are the numbers of incorrect and correct evaluation in the unstable samples. F_{U} and T_{S} are the numbers of incorrect and correct evaluation in the stable samples as shown in Table I.

The boundary samples are screened effectively according to the method proposed in section Ⅲ of this paper. Then, the proportion of boundary samples is increased to 6 %, 12 % and 24 % of the original dataset. The performance on the original dataset and the enhanced dataset is compared in Table Ⅱ.Table II shows that with the increasing proportion of boundary samples in the sample set, P_{fs} and P_{fu} decrease significantly, and A_c increases, which proves that the boundary sample enhancement method can effectively improve the model evaluation performance.

The improved loss function can make the TSA model more sensitive to minor class samples and avoid model bias. The evaluation performance is shown in Table III.

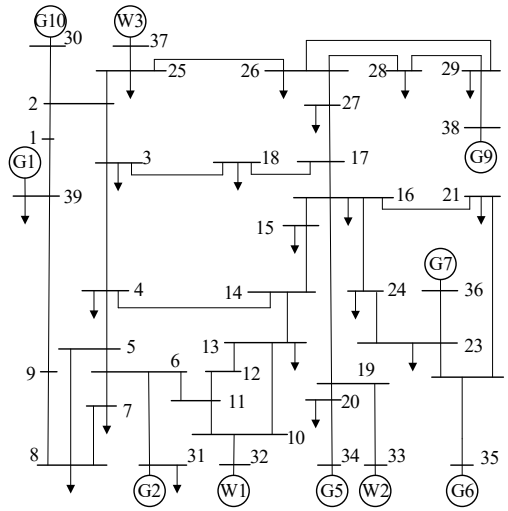


Fig. 3. The structure of modified IEEE 10-generator 39-bus system

Compared with the binary cross-entropy and weighted cross-entropy loss function, the model accuracy with the improved FL function is increased by 0.74% and 0.68%, P_{fs} is reduced by 22.35% and 9.59%, and P_{fu} is reduced by 50.46% and 53.04% respectively. As the sample category balance factor is introduced into the improved FL function, the influence of large number of stable samples participating in the adjustment of model training parameters is reduced. At the same time, the introduction of boundary sample modulation factor makes the model pay more attention to boundary samples during the training process and enhance the model's classification ability of boundary sample.

C. *Model Interpretability Analysis*

The attention mechanism is used for model interpretability analysis due to its feature weight visualization. The attention weight magnitude reflects the feature's importance. Features with larger attention weights have a greater impact on the model's classification results.

The temporal attention distribution is illustrated in Fig. 4. Notably, the attention weights exhibit significantly higher values during steady-state operations and the post-fault period. These two time regions are located at the beginning and later stages of the multi-stage features, with a relatively long time span. They reflect critical transient stability characteristics and have higher value for TSA. Therefore, the model allocates higher attention distribution to features in time regions with longer spans, enhancing the feature representation with higher attention weight, thereby increasing the influence of corresponding temporal features on the TSA results.

To verify the effectiveness of the model attention weight distribution, the steady state moment and the post-fault period are extracted as high-attention features for training and evaluation. The during-fault features are used as the low-attention features. The model is trained by high and low-attention features, and the evaluation results are compared with the model trained by the multi-stage features. The experimental results show that the good performance can be reached by using only the high-attention features for TSA, which indicates that the temporal features with high-attention to the evaluation results can be identified through the attention mechanism, which is consistent with the attention distribution in Fig. 4. Compared with the low-attention features, the transient stability information contained in high-attention features is relatively rich, which has a greater impact on the TSA results of the model. The attention mechanism can provide more effective information for the model and improve the model performance by realizing the global interaction between features at different moments.

TABLE I. CONFUSION MATRIX

Prediction Label	**Actual Label**	
	Stable	Unstable
Stable	T_S	F_U
Unstable	F_S	T_U

TABLE II. EFFECT OF BOUNDARY SAMPLE ENHANCEMENT ON TRANSIENT STABILITY ASSESSMENT

Sample Set	**Evaluation Indices**		
	A_c / %	P_{fs} / %	P_{fu} / %
Original sample set	98.05	0.97	0.97
Boundary samples enhanced to 6% of the sample set	98.44	0.64	0.92
Boundary samples enhanced to 12% of the sample set	98.53	0.74	0.74
Boundary samples enhanced to 24% of the sample set	98.79	0.66	0.54

TABLE III. EVALUATION RESULTS OF DIFFERENT LOSS FUNCTIONS

Loss Function	**Evaluation Indices**		
	A_c / %	P_{fs} / %	P_{fu} / %
Binary cross-entropy function	98.06	0.97	0.97
Weighted cross-entropy function	98.12	0.64	0.92
Improved FL function	98.79	0.74	0.74

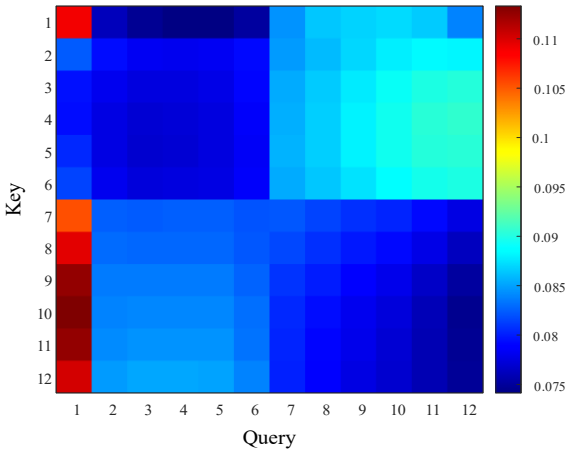


Fig. 4. Attention distribution for different temporal data

TABLE IV. EVALUATION RESULTS OF DIFFERENT ASSESSMENT MODELS

TSA Models	Evaluation Indices			Evaluation Time/s
	A_c / %	P_{fs} / %	P_{fu} / %	
SVM	97.28	1.15	1.57	0.071
LSTM	97.94	0.79	1.27	0.089
CNN	97.16	1.69	1.15	0.068
AMETCN	98.79	0.66	0.54	0.055

D. Comparison with other TSA methods

SVM, LSTM and CNN are selected to construct the comparison model in this paper. SVM uses linear kernels with regularization parameters of 1.0. The number of neurons in the hidden layer of LSTM is {64,128,32}, and one fully connected layer is set. CNN consists of 2 layers of convolution, pooling, and activation layers, as well as 2 fully connected layers and the softmax layer, with a convolutional kernel size of 3 and a maximum pooling layer step size of 2. The above deep models all use the Adam learning algorithm and the weighted FL cross-entropy loss function, γ is 2, and TSA model is constructed by the multi-stage features and the enhanced sample set. The performance comparison of models is shown in Table IV.

Experimental results show that compared with the deep model, SVM, a traditional machine learning method, has poor performance, and the ability of extracting high-dimensional features is limited, so it is not suitable for TSA. Deep learning models such as LSTM and CNN can better capture complex relationships in data, but the evaluation performance of the proposed methods in this paper is better than that of the other two deep models.

In the proposed model, TCN can use convolutional kernels across time steps to capture the causal relationship between temporal features in parallel, reducing the computational burden. The attention mechanism is embedded on the basis of TCN. The model realizes the rapid interaction between global features through attention mechanism and makes full use of the high-value temporal information of the power system, so the TSA performance is improved.

VI. CONCLUSION

A multi-stage features and AMETCN-based TSA method is proposed. Simulation tests are carried out on the IEEE39 system with wind turbines, and the following conclusions are obtained.

1) TCN can capture the causal relationship between multi-stage features through parallel computation of stacked convolutional units, thereby accelerating training speed. On this basis, the embedded attention mechanism make the model capture features with high attention weights. As a result, the proposed model performs well in TSA and has good model interpretability.

2) Boundary sample enhancement improves sample balance by adjusting the sample composition. While improving the FL function makes the model more focused on unstable samples and boundary samples by changing the weight of the loss function.

ACKNOWLEDGMENT

This work is supported by the Science and Technology Program of SGCC (No. J2024158).

REFERENCES

[1] T. Odun-Ayo and M. L. Crow, "Structure-preserved power system transient stability using stochastic energy functions," IEEE Transactions on Power Systems, vol. 27, no. 3, pp. 1450-1458, 2012.

[2] Z. YU, C. SHEN, F. LIU, and L. TANG, "Transient stability-constrained economic dispatch considering windpower uncertainty," Proceedings of the CSEE, vol. 40, no. 22, pp. 7270-7282, 2020.

[3] S. Xia, X. Luo, K. W. Chan, Z. Ming, and G. Li, "Probabilistic transient stability constrained optimal power flow for power systems with multiple correlated uncertain wind generations," IEEE Transactions on Sustainable Energy,vol. 7, no. 3, pp. 1133-1144, 2016.

[4] H. Lv and H. Tang, "Machine learning methods and their application research," 2011 2nd International Symposium on Intelligence Information Processing and Trusted Computing, pp. 108-110, 2011.

[5] L. LIU, Y. LI, Y. J. CAO, J. H. TANG, J. F. ZHU, D. YANG, et al, "Transient rotor angle stability prediction method based on SVM and LSTM network," Electric Power Automation Equipment, vol. 40, no. 2, pp. 129-139, 2020.

[6] F. TIAN, X. X. ZHOU, D. Y. SHI, Y. CHEN, Y. H. HUANG, and Z. H. YU, "Power system transient stability assessment based on comprehensive convolutional neural network model and steady-state features," Proceedings of the CSEE, vol. 39,no.14, pp. 4025-4032, 2019.

[7] Z. J. XIE, D. X. ZHANG, X. Q. HAN, and W. HU, "Research on transient stability assessment method of power system based on improved long short term memory network," Power System Technology, vol. 48, no. 3, pp. 998-1010, 2024.

[8] L. ZHANG, J. AN, and Y. B. ZHOU, "Transient stability assessment of power system based on temporal convolution and graph attention network," Automation of Electric Power Systems, vol. 47, no. 7, pp. 114-122, 2023.

[9] J. S. FANG, C. R. LIU, C.B. SU, H. X. LIN, and L. ZHENG, "Multi-stage transient stability assessment of power system based on self-attention transformer encoder," Proceedings of the CSEE,vol. 43, no. 15, pp. 5745-5759, 2023.

[10] J. X. HU, J. LIU, Y. S. LI, S. S. CHEN, G. Y. XU, and X. L. CHEN, "Adaptive transient stability assessment method based on Gan key sample enhancement and transfer learning," Journal of North China Electric Power University, pp.1-14, http: //kns.cnki.net/kcms/detail/13.1212.TM.20231212.1209.004. Accessed 18 Aug. 2025.

[11] S. C. ZHOU, Y. LUO, X. C. YI, Y. N. WU, D. LI, and C. LEI, "Two-stage transient stability assessment of power system based on boundary enhanced hybrid sampling," Electric Power Automation Equipment, vol. 44, no. 4, pp. 143-150, 2024.

[12] C. SHI, J. LIU, Z. H. LIANG, Y. S. LI, and X. L. CHEN, "Transient stability assessment of power system based on GAN and multi-channel CNN power system technology," Power System Technology, vol. 46, no. 8, pp. 3191-3202, 2022.

[13] L. XIAO, J. ZHANG, Y. HE, Y. LIU, and Y. C. YE, "Power system transient stability assessment based on temporal convolution and adaptivegraph convolution network". Power System Technology, pp. 1-13, https://doi.org/10.13335/j.1000-3673.pst.2024.1724, Accessed 18 Aug. 2025.

[14] S. X. FAN, Z. N. ZHAO, J. B. GUO, S. C. MA, T. Z. WANG, and D. Q. LI, "Review on data-driven power system transient stability assessment technology". Proceedings of the CSEE, vol. 44, no. 9, pp. 3408-3428, 2024.

[15] Y. X. YANG, W. YAO, X. Z. DENG, Y. T. LAN, W. HUANG, and S. T. DONG, et al, "Frequency stability index prediction based on Koopman time series extension and CNN-Transformer model". Power System Technology, pp. 1-15, https://doi.org/10.13335/j.1000-3673.pst.2024.0686, Accessed 18 Aug. 2025.

Research and Simulation on Multi-Mode Operation Control Strategy of Combined Diesel and Energy Storage Power Supply System

Cunping Wang
State Grid Beijing Electric Power Research Institute
State Grid
Beijing, China
100075
wangcunping163@163.com

Yanxia Chen
State Grid Beijing Electric Power Research Institute
State Grid
Beijing, China
100075
chenbepc@163.com

Ruoxi Liu
State Grid Beijing Electric Power Research Institute
State Grid
Beijing, China
100075
liuruoxi0121123@163.com

Jing zeng
School of Automation
Wuxi University
Wuxi, China
214105
24402133@stu.cwxu.edu.cn

Yifan Wu
School of Automation
Wuxi University
Wuxi, China
214105
2245939328@qq.com

Shuchang Wan
School of Internet of Things Engineering
Wuxi University
Wuxi, China
214105
18399672363@163.com

***Abstract*—This paper addresses the coordinated control problem of multi-mode operation in a photovoltaic-diesel generator-energy storage microgrid system under the context of renewable energy integration. A joint operation strategy based on the collaborative control of photovoltaic systems, diesel generators, and energy storage systems is proposed. By constructing five operational modes, the strategy achieves dynamic source-load matching and ensures stable system operation. The backup power mode guarantees rapid response during main grid failures, the load balancing mode optimizes energy distribution under low-load conditions, the peak shaving mode collaboratively handles load peaks, the fuel-saving mode reduces fuel consumption through the economic load rate of diesel generators, and the fast power balancing mode suppresses sudden power fluctuations. Simulation results based on MATLAB/Simulink demonstrate that the proposed strategy effectively enhances system stability and economic performance, supports smooth grid-connected/islanded transitions, and meets power demand under various operating conditions. The research findings provide a theoretical foundation and technical reference for microgrid systems with high penetration of renewable energy, contributing significantly to the advancement of clean energy applications and the sustainable development of power systems.**

Keywords—PV-diesel-energy storage microgrid, multi-mode operation, coordinated control, renewable energy integration

I. Introduction

Under the backdrop of renewable energy integration, multi-energy microgrids have become a research hotspot. To address the challenges posed by the volatility of renewable energy, this project focuses on the coordinated control of PV-diesel-energy storage (PV-DG-ESS) systems, investigating key technologies such as diesel-storage capacity allocation, frequency regulation, and grid-connected/islanded transition [1]. Compared to traditional single/dual-mode operation, the study emphasizes breakthroughs in the joint regulation of PV, diesel generators (DGs), and energy storage [2], developing an integrated operational strategy for new power systems to enhance stability and economic efficiency [3].

For PV-DG-ESS systems, a coordinated control strategy with five operational modes is proposed. Backup power mode ensures rapid response and uninterrupted power supply during main grid failures[4]. Load balancing mode optimizes energy distribution under low-load conditions[5]. Peak shaving mode coordinates diesel generators and energy storage to handle load peaks[6][7]. Fuel-saving mode reduces fuel consumption by operating DGs at their economic load rate. Fast power balancing mode mitigates PV output fluctuations and load variations[8].

The project validates control performance through MATLAB/Simulink simulations, providing theoretical and technical support for uninterrupted maintenance operations in distribution grids with high renewable energy penetration [9]. This will significantly enhance the reliability of non-interruption maintenance operations, reduce operational costs, promote the widespread adoption of clean energy, and facilitate sustainable energy system development, thereby supporting the establishment of a modern, efficient and eco-friendly power grid system [10].

II. Structure and Modeling of PV-Diesel-Energy Storage Microgrid System

A. Overall System Model

The PV-diesel-energy storage (PV-DG-ESS) microgrid system consists of photovoltaic (PV) generation, diesel

generators (DGs), energy storage devices, and inverters, capable of supporting both grid-connected and islanded operation modes while enabling multi-source coordinated control. In terms of simulation modeling, the study focuses on analyzing the control characteristics of diesel generators and energy storage systems. Separate and joint operational simulation models were developed, along with corresponding mathematical models and control strategies. The overall design is shown in Figure 1. Research on reconfigurable distribution network technology emphasizes the exploration of coordinated PV-DG-ESS operation modes [11], as well as energy management strategies under special operating conditions, aiming to optimize the cooperative frequency regulation and power allocation mechanisms between diesel generators and energy storage[12]. An integrated scheduling strategy was proposed, featuring a PV-DG-ESS energy management scheme based on load forecasting and mode switching [13]. This ensures safe and stable uninterrupted maintenance operation under high PV penetration conditions.

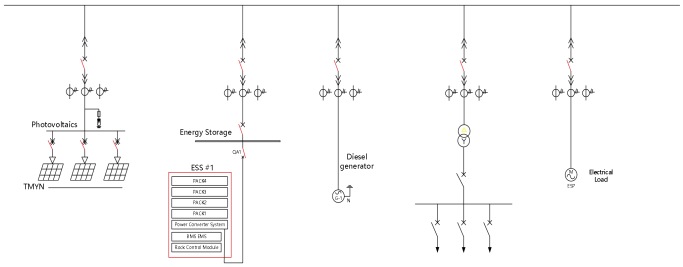


Fig. 1. Topology diagram of the diesel-Energy storage hybrid power generation system

B. Mathematical Model of Diesel Generator System

In MATLAB simulations of diesel generators, the governor gain serves as the core parameter for regulating rotational speed dynamics. By controlling fuel injection to compensate for speed deviations, this parameter directly affects both system response speed and stability. The higher the gain value, the greater the correction intensity of speed deviation, the response speed is improved but easy to cause oscillation; the lower the gain value, the slower the response, but the system stability is enhanced. The governor's primary function is to maintain constant engine speed [14]. When load variations cause actual speed to deviate from the setpoint, the governor rapidly adjusts fuel supply through closed-loop feedback, ensuring real-time matching between mechanical power and electrical load. This dynamic equilibrium guarantees stable generator operation while optimizing fuel efficiency. For simulation modeling, precise gain tuning is essential. The working principle is shown in Figure 2. It usually uses PID algorithm to realize the proportional amplification of speed deviation, integral elimination of steady-state error and differential suppression of oscillation [15], and balance between fast response and overshoot suppression, and finally achieve the grid connection requirement of speed fluctuation rate ≤0.25% [16].

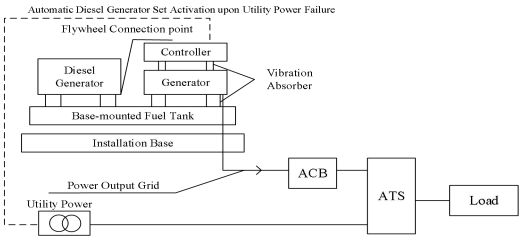


Fig. 2. Working principle of diesel generator

C. Mathematical Model of Energy Storage System

The mathematical model of energy storage systems characterizes their dynamic behavior and operational constraints through multi-dimensional parameters [17]. The general model of energy storage battery is shown in Figure 3. The bidirectional asymmetric charge-discharge efficiency endows the system with non-symmetric energy transfer characteristics [18]. The system monitors the SOC change rate and energy throughput in real time to establish overcharge/overdischarge protection mechanisms and optimize the power distribution strategy of the energy storage system. This model achieves a unified representation of electrochemical characteristics and electrical responses through the synergy between SOC and circuit parameters, providing a theoretical basis for grid-connected control and capacity configuration of energy storage systems [19].

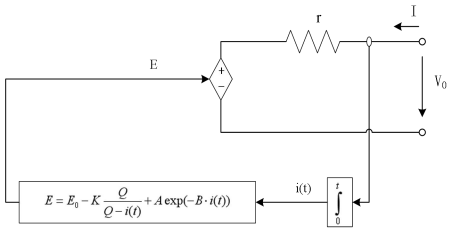


Fig. 3. A general model of energy storage batteries

D. Photovoltaic System Model

The principle of photovoltaic power generation is that when sunlight shines on a semiconductor, the semiconductor absorbs light energy and produces the photovoltaic effect, converting photon energy into electrical energy for power generation. The equivalent circuit of a photovoltaic cell is shown in Figure 4. Photovoltaic cells have a structure similar to that of a PN junction, with the characteristics of the PN junction represented by a diode. The equivalent circuit includes a photogenerated current source I_{ph}, a parallel resistor R_{sh}, and a series resistor Rs [20].

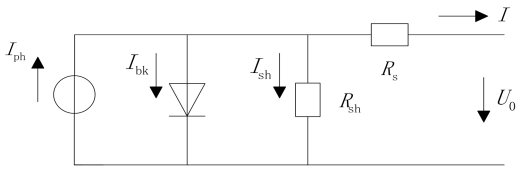


Fig. 4. Equivalent circuit diagram of photovoltaic cell

III. Coordinated Operation Strategy for PV-Diesel-Storage System

A. Five Operational Modes

Based on the coupling relationship between load power demand and PV output characteristics, the system establishes five operational modes with corresponding switching conditions, as well as operating states for both diesel generators and energy storage[21]. The specific mode classifications are as follows, shown in Figure 5.

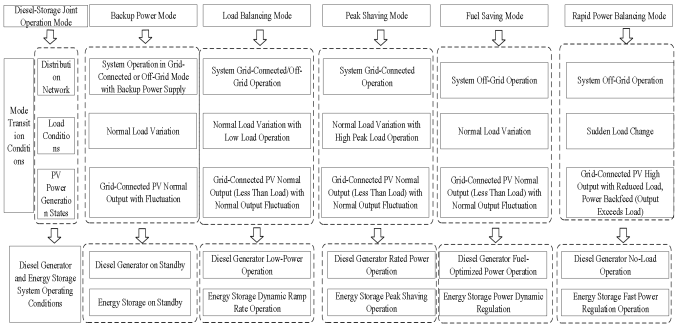


Fig. 5. Mode switching flow chart

1) Backup power mode

When the main power grid fails, the system switches to standby power mode, with diesel generators and energy storage systems working together to supply power [22]. The energy storage rapidly establishes voltage support within milliseconds (<10ms), while the diesel generator starts relatively slowly, gradually reaching its rated power. The operational strategy is shown in Figure 6. Upon detecting that the grid voltage is 0, the energy storage instantly purchases high-power Vf from the grid, and the diesel generator gradually increases its startup power, while the energy storage power decreases[23]. The diesel and storage systems then operate in parallel off-grid until balance is achieved.

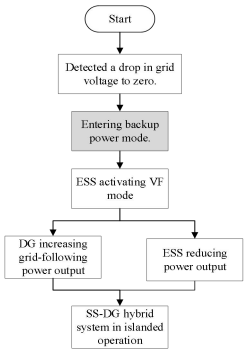


Fig. 6. Power backup mode operation flow chart

2) Load balancing mode

During low load and photovoltaic output limitation periods (such as at night or on overcast days), the system adopts an energy storage-led load balancing mode, as shown in Figure 7. At this time, diesel generator power gradually decreases to standby reserve, while the energy storage adjusts its power output dynamically to respond to load demand[24]. This strategy ensures that energy storage takes priority in power supply, with diesel generators serving only as a supplement [25], achieving a balance between economic operation and reliable power supply.

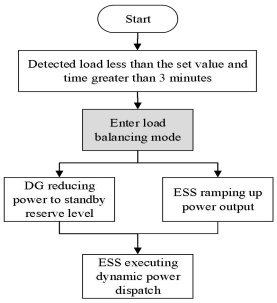


Fig. 7. Load balancing mode operation flow chart

3) Peak shaving mode

When the load is at a high value or overloaded, the system initiates peak shaving mode to protect the diesel generator set from damage[26]. As shown in Figure 8, the diesel power increases to over 90%, and it always operates at high power. The energy storage power decreases and adjusts the remaining power in real-time according to load changes[27], effectively controlling the peak power fluctuations. PV Power Generation States.

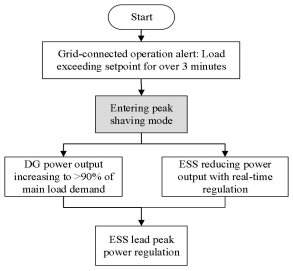


Fig. 8. Peak shaving mode operation flow chart

4) Fuel saving mode

When the load is running normally, in the region where the fuel supply of the diesel generator is limited, the economic operation of the diesel generator unit is given priority and enters the fuel saving mode as shown in Figure 9. At this time, the diesel generator power always runs at 80% of the rated power point to achieve the best fuel efficiency[28]. The energy storage adjusts the real-time power to maximize the efficiency and reduce carbon emissions.

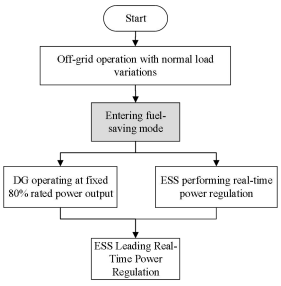


Fig. 9. Fuel saving mode operation flow chart

5) Rapid power balance mode

In the face of sudden power changes, such as a sudden increase in load or a decrease in photovoltaic output, the system enters a rapid power balancing mode to prevent frequency collapse[29]. As shown in Figure 10, when the system is operating off-grid and the load changes by more than 30% of the system's rated value within 30 seconds, the diesel generator reduces its operation to no-load mode, while the energy storage system quickly adjusts its real-time power and regulates the leading power change [30].

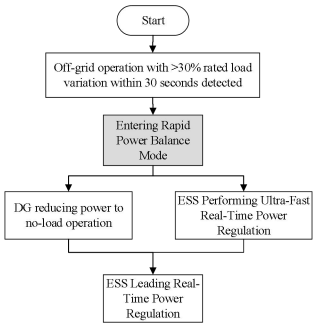


Fig. 10. Quick power balance mode flow chart

IV. SIMULATION VERIFICATION

Based on the above five combined operation strategies of photovoltaic, biomass and energy storage systems, a MATLAB simulation model of combined operation of photovoltaic, biomass and energy storage systems is built, in which the power generation of biomass is 50kW, the energy storage power is 20kW, the load power is adjustable from 0 to 100kW, and the photovoltaic power is 30kW. The five modes are simulated and verified. The overall simulation model is shown in Figure 11.

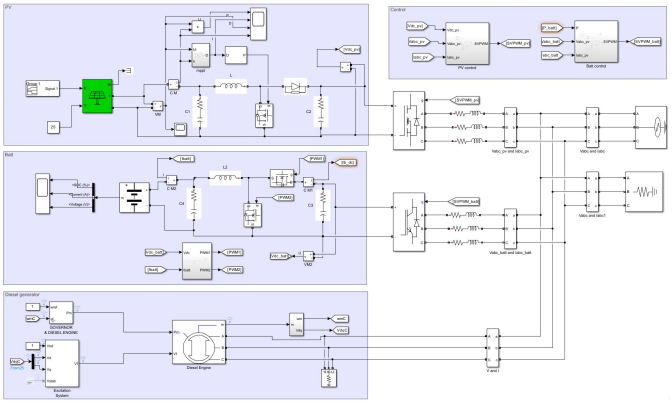
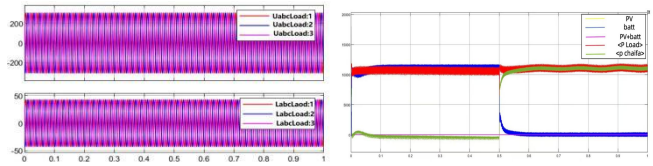


Fig. 11. Overall simulation model diagram

Operation mode 1: Standby power mode

In the integrated diesel and battery system, the municipal power is supplied by the battery when normal. After the municipal power fails, the diesel generator starts, initially supporting the load with the battery, then gradually taking over the power supply. The simulation results are shown in Figure 12, the load is 10kW for 1s. After the rated 50kW(380V), 0.5s of the diesel generator fails, the battery power gradually decreases, and the diesel generator becomes the primary power source, verifying the reliability of the backup mode.

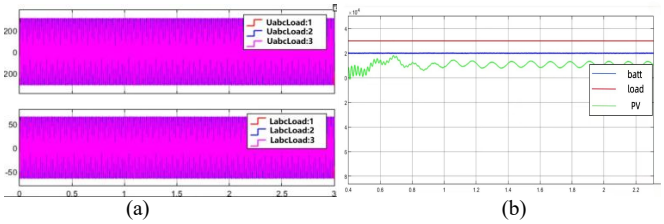


(a) (b)

Fig. 12. (a) Overall power simulation diagram of standby power supply (b) Load voltage and current in standby power mode

Operation mode 2: Load balancing mode

When operating at low load, prioritize energy storage power supply (20kW), reducing diesel generator operation (10kW supplement), to enhance efficiency and economy. Energy storage offers advantages such as frequency regulation, noise-free operation, and zero emissions, making it particularly suitable for enclosed environments like underground parking lots, where it can replace diesel engines to reduce wear and maintenance costs. Photovoltaic systems and diesel engines should be shut down during low load to optimize the system. In the simulation, the load is 30kW, the energy storage voltage is 400V, and the three-phase voltage is 380V. The results show that the mode of main energy storage supply and diesel engine supplementation is effective, with no output from photovoltaic systems or the main grid, verifying the feasibility of the strategy. The simulation results are shown in Figure 13.

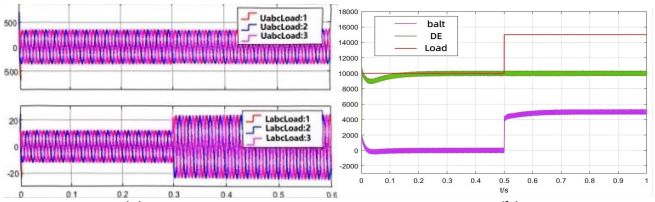


(a) (b)

Fig. 13. (a) Load balance mode loads voltage and current (b) Overall power diagram of load balancing mode

Operation mode 3: Peak shaving mode

Diesel and energy storage work together to handle peak loads, with the storage system taking on short-term spikes, reducing diesel operation intensity, and decreasing fuel consumption and emissions. This approach is suitable for scenarios with significant differences between peak and off-peak hours (such as shopping malls and factories), reducing reliance on the main grid and electricity costs. In the simulation (0.7s, before load 13-25kW), 0.2s: diesel (20kW) and energy storage (2kW) supply power together; 0.2-0.25s during peak load, energy storage assists in load reduction; 0.25-0.5s during low load, diesel supplies power and charges the energy storage; after 0.5s, joint power supply resumes to verify the effectiveness of the mode. The simulation results are shown in Figure 14.

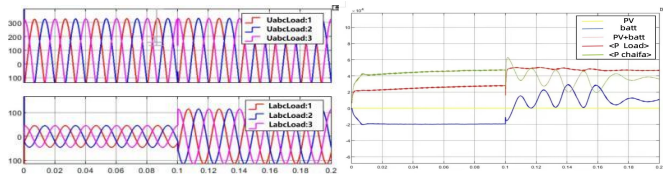


(a) (b)

Fig. 14. (a) Peak shaving mode load voltage and current (b) Overall power diagram of peak shaving mode

Operation mode 4: Fuel saving mode

Energy storage regulates the diesel generator load rate to 80% (optimal fuel efficiency) through charging and discharging, suitable for fuel-constrained scenarios (such as islands and deserts). In the simulation (at 0.2s, before the load 20-50kW), 0.1s, the diesel generator (40kW) supplies power to a 20kW load and charges the energy storage; after 0.1s, the load increases to 50kW, with the energy storage compensating for the difference, achieving both energy savings and economic benefits. The results are shown in Figure 15.

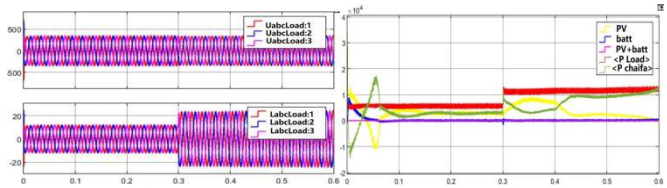


(a) (b)

Fig. 15. (a) Fuel saving mode load voltage current (b) Overall power simulation diagram of fuel saving mode

Operation mode 5: Fast power balance mode

In response to load sudden changes, the energy storage system responds in milliseconds, while diesel generators maintain stable voltage and pv systems keep maximum output. The simulation simulates a load increase from 5kW to 10kW within 0.3 seconds and load fluctuations. The results are shown in Figure 16. During islanded operation, the system maintains dynamic balance, verifying the energy storage's ability to withstand shocks. The results show that when the load or PV changes, the diesel generator power is flexibly adjusted to ensure grid stability, meeting design expectations.



(a) (b)

Fig. 16. (a) Rapid power balances the load voltage and current (b) Power simulation diagram of fast power balance mode

To sum up, when the load is newly connected and the irradiance is increased at the same time, it can be clearly seen that the output power of diesel generator decreases correspondingly, while the photovoltaic power increases; after the photovoltaic power decreases, the power of diesel generator can increase to maintain the stable operation of the main network, which is consistent with the design theory, so the correctness of the simulation mode is verified.

V. Conclusion

This paper constructs an integrated photovoltaic, thermal storage, and energy storage system, proposing a coordinated active/reactive power control strategy to achieve dynamic source-load matching through five operating modes. The system integrates photovoltaic MPPT, energy storage SOC management, and for coordinated thermal storage control, supporting both grid-connected and off-grid dual-mode operation: constant power control is used during grid connection, while voltage stabilization control switches in off-grid mode, with PI regulation ensuring a smooth transition. Simulation based on MATLAB/Simulink has verified the system's rapid response capability under load disturbances; however, static parameter settings result in significant overshoot and longer adjustment times, necessitating the introduction of dynamic tuning algorithms for optimization. The research findings provide technical references for microgrids and distributed energy systems, and can be extended to areas such as intelligent scheduling and fault prediction, promoting the engineering application of hybrid new energy systems.

References

[1] Y. Zhang, W. Zhang, B. Li, H. Wang, "Segmented grid restoration strategy based on PV-storage hybrid system," Journal of Electric Power Engineering and Technology, vol. 43, no. 4, pp. 26–35, 2024.

[2] D. Li, "Research on hierarchical control-based energy management strategy for islanded microgrid with wind-PV-diesel-storage," M.S. thesis, Univ. of Electron. Sci. & Technol. China, Chengdu, China, 2013.

[3] C. Wu, H. Li, D. Liu, Y. Chen, "An improved PSO algorithm for economic load dispatch in power systems," Power System Protection and Control, vol. 44, no. 10, pp. 44–48, 2016.

[4] C. Jin, B. Zhou, X. Ai, M. Chen, "Optimal energy storage capacity configuration considering PV-storage participation in frequency response," Global Energy Interconnection, vol. 1, no. 3, pp. 1–10, 2018.

[5] X. Sun, X. Geng, Y. Zhou, "A novel multifunctional converter for hybrid renewable power systems," Acta Energiae Solaris Sinica, vol. 40, no. 12, pp. 3501–3512, 2019.

[6] Q. Peng, S. Ouyang, J. Zhang, L. Wang, "Cluster partition method for distribution networks with high-penetration distributed PV considering multi-section source-load matching," Southern Power System Technology, pp. 1–13, 2024. [Online]. Available: [URL]

[7] L. Kong, X. Tang, Z. Qi, W. Zhang, "Dynamic energy dispatch strategy for PV-diesel-storage microgrid," Power System Protection and Control, vol. 40, no. 20, pp. 6–12, 2012.

[8] Y. Zou, J. Qian, L. Li, S. Wang, "Review on research and application of diesel generators in microgrids," China Water Transport, vol. 21, no. 11, pp. 50–52, 2021.

[9] X. Zang, "Optimization of governor control system for standby diesel generators," Instrumentation Customer, vol. 28, no. 10, pp. 80–84, 2021.

[10] K. Zhu, Y. He, W. Jiang, "Comparative study on grid-forming control strategies for PV-storage hybrid systems," Power Capacitors & Reactive Power Compensation, vol. 44, no. 5, pp. 1–9, 2023.

[11] Y. Wang, J. Yang, Y. Zhao, "Wind-PV-storage joint frequency regulation strategy based on SOC and power margin adjustment," Power System and Clean Energy, vol. 40, no. 4, pp. 150–158, 2024.

[12] S. Zhao, "Supercapacitor control strategy based on bidirectional DC/DC converter," Electrical Engineering Materials, no. 4, pp. 81–83, 2024, doi: 10.16786/j.cnki.1671-8887.eem.2024.04.018.

[13] G. Lin, Y. Huang, "A non-isolated high-gain three-port DC-DC converter," Electric Machines and Control, vol. 27, no. 2, pp. 98–111, 2023.

[14] Y. Ma, K. Qian, Q. Yan, "Hierarchical control for islanded DC microgrid with PV-storage-load coordination," Power Capacitors & Reactive Power Compensation, vol. 44, no. 1, pp. 129–135, 2023.

[15] Y. He, X. Xing, S. Yu, "Two-level emergency power supply strategy with energy storage and diesel generator," Marine Electric & Electronic Technology, vol. 41, no. 9, pp. 30–34, 2021.

[16] Z. Rao, Z. Yang, Y. Wang, "Optimal configuration method for regional large-scale hybrid power station based on source-load matching," Acta Energiae Solaris Sinica, vol. 45, no. 8, pp. 1–8, 2024.

[17] J. Han, Z. Du, H. Jiang, "Nonlinear robust control for wind-storage systems in isolated grids," Journal of Xi'an Jiaotong University, vol. 57, no. 9, pp. 152–161, 2023.

[18] J. Li, K. Luo, H. Guo, "Integrated PV-storage microgrid and its control strategy," Power Electronics, vol. 56, no. 11, pp. 101–105, 2022.

[19] Y. Zhang, K. Kang, C. Tang, "A networking method and control strategy for AC/DC hybrid microgrids," Electrotechnics Electric, no. 7, pp. 27–31, 2024.

[20] S. Tian, H. Wang, Y. Wang, "Operation control strategy for multi-converter microgrid in grid-connected/islanded modes," Journal of Baotou Vocational & Technical College, vol. 24, no. 4, pp. 39–43, 2023.

[21] LIU Huiwen, WANG Shengtie, LIU Guangchen, Operation strategy of optimal capacity configuration for microgrid with WT-PV-DE-BES [J]. Acta Energiae Solaris Sinica,2022,43(9):453-460.

[22] ZHONG Cheng, CHU Wenhao, LI Xiaoming, Optimal dispatch of photovoltaic storage diesel microgrid considering energy storage life[J]. Electrotechnical Application, 2023, 42(11): 9-15.

[23] GUO Y, MING B, HUANG Q, Variation-based complementarity assessment between wind and solar resource in China[J]. Energy Conversion and Management, 2023, 278: 116726.

[24] ZHANG Kun, WANG Shenghao, LI Zhi, Research on optimal ratio of wind and PV and energy storage optimization configuration in regional power grid[J]. Northeast Electric Power Technology, 2024, 45(4): 23-28.

[25] WANG Jialin, ZHANG Chunyan, AI Sheng, Modeling and analysis of multi-energy isolated microgrid with wind-PV-diesel-storage in islands and reefs[J]. Journal of Naval University of Engineering, 2024, 36(2): 79-86.

[26] LI Ming, YIN Xiaoyu, DONG Xiaoling, Research on multi-objective capacity allocation optimization of photovoltaic microgrid in power internet of Things[J]. Electronic Design Engineering, 2024, 32(5): 165-168.

[27] Fan Ailong, Yan Xinping, Li Zhongkui, The Demand, Path and Prospect of Green and Low-Carbon Development in China's Shipping Industry [J] Ship and Ocean Engineering, 2024,53 (4): 1-5+12

[28] XIAO Jiajie, LI Peiqiang, MAO Zhiyu. Battery energy storage participating in secondary frequency regulation based on fuzzy allocation factor[J]. Power System Technology, 2023, 47(9): 3568-3575.

[29] Wang Liaowei, Sun Heng, Ding Yanming, The Current Development Status of the Global biodiesel Industry and Its Impact on the Safety of vegetable Oil in China [J] China Oils and Fats, 2024,49 (5): 8-13.

[30] Wang Tianhe, Ma Junrui, Wang Ruojin, Analysis of the Current Situation and Future Development of the Fuel Oil Market [J] Petroleum and Petrochemical Green and Low-Carbon, 24, 9 (1): 8-12.7.

Development of Piezoelectric Vibration Energy Harvester (VEH) for Machine Condition Monitoring Purpose

Riady Siswoyo Jo
School of Engineering,
Faculty of Engineering and Technology,
Sunway University,
No. 5, Jalan University,
Bandar Sunway, 47500 Selangor Darul Ehsan, Malaysia
riadyj@sunway.edu.my

Rachel Lee Xin
School of Engineering and Physical Sciences
Heriot-Watt University Malaysia
1, Jalan Venna P5/2,
Precinct 5, 62200 Putrajaya, Malaysia
xl75@hw.ac.uk

***Abstract*—This paper presents the development of a vibration energy harvester (VEH) that is applicable for machine condition monitoring purpose. Piezoelectric transducer-based VEH module is designed to harvest energy from vibrating machine. Combination of several VEH modules, either in series or parallel connections allow consolidated harvesting of the vibration energy. The harvested energy can be used to power remote sensors that are able to monitor the conditions of the vibrating machine, e.g. temperature, vibration amplitudes, etc. This paper also explores the design of vibration energy harvesting circuit and investigates the configuration that can bring about the best output power performance through experiments with different loading conditions. In the experiments, the source of vibration utilized is a direct forced vibration from a vibrating machine, resembling practical industrial scenarios where the VEH module and remote sensors are placed near rotating or reciprocating machines. Results show that the harvested energy at certain loading conditions are sufficient to supply for low-power remote sensors.**

***Keywords*—Vibration Energy Harvester, Wireless Sensors, Machine Condition Monitoring, Circuit Design, Piezeoelectric Transducer**

I. Introduction

The rising use of sensors that collect large amount of physical information has resulted from the expansion of automated systems across several industries. These sensors can be utilized in a variety of applications, including weather monitoring and agricultural applications, as well as detecting physiological parameters for biomedical applications and the equipment conditions in industrial settings.

Sensors are normally powered by sources derived from the power grids or portable sources, such as batteries. Alternative power sources, such as solar power or wind power, were employed in rural areas when connection to the power grid is limited [1].

In industrial and biomedical applications, the presence of long wires to supply electricity limits movement and reduces reliability [2]. Furthermore, due to advancement in microelectronics, power requirements of many sensors have been reduced to the range of mW (milliwatts), which adds to the impracticality of using wired power sources. Although the usage of batteries was the first alternative option to wired power source, replacing and servicing these batteries may not be cost effective in the long run.

As a result, self-sufficient sensors that can harvest energy from their surroundings are required. Sensors can be powered by a variety of energy sources, including microbial fuel cells, solar, wind and thermal energy [3], [4].

However, as vibration energy can be abundantly found in moving machinery and busy bridges [5], harvesting vibration energy becomes a viable alternative to supply power to sensors due to its potential as a high-power density source [6].

There are three common methods used in vibration energy harvesters (VEH), which are electromagnetic, electrostatic, and piezoelectric. Electromagnetic energy harvester is based on Faraday's law of electromagnetic induction, electrostatic energy harvester is based on Coulomb's Law, and piezoelectric energy harvester utilizes piezoelectric effect, which is the ability to produce charges under mechanical stress [5].

However, it was found that piezoelectric harvesting has a higher energy density, high voltage, and a simpler system compared to other vibration energy harvesting methods. Research on piezoelectric method of energy harvesting shows promising result for the application to power remote sensors, although only a few has reached the stage of being released in the market [7].

Some studies presented the use of Synchronized Switch Harvesting on Inductor (SSHI) circuits in connection with a piezoelectric sensor when forming an energy harvester. In a traditional AC-DC circuit, the generated voltage and output current are out of phase, causing a loss in power. The SSHI circuit flips the voltage to reduce the capacitive term on the capacitor, which is a tendency for the capacitor to resist changes in voltage that causes a phase shift between the

979-8-3315-5472-9/25/$31.00 ©2025 IEEE

current and voltage. This is done by having a resonant circuit between the capacitor of the piezoelectric transducer and an external inductor [8]. However, when the AC voltage from the piezoelectric sensor is put through a full-bridge rectifier, the issue of phase shifts between the current and voltage can be eliminated because a DC voltage has been produced. This is similar to a simplified piezoelectric battery charging circuit as suggested by [9].

In industrial applications, machine condition monitoring has been an important topic as practitioners are finding ways to efficiently plan for predictive maintenance of machinery [10].

Recent innovations in machine condition monitoring include portable machine condition sensors, one well-known example being the SKF QuickCollect sensor that monitor machine velocity, acceleration and temperature, that can be easily attached and removed from the machines in factory settings. The data from this sensor can be requested real-time through a mobile device as the sensor is wirelessly connected through Bluetooth. Despite its ease-of-use, the sensor itself is powered by batteries that need to be charged daily for full-day use [11].

To this end, this paper explores the development of a piezoelectric Vibration Energy Harvester (VEH) that is aimed to be used for wireless machine condition monitoring sensors by harvesting the energy from vibrating machines.

II. Design of VEH Modules

A. VEH Module Circuit Design

Modular design approach is applied in designing the VEH to facilitate scalability. Multiple VEH modules can be connected in different circuit configurations based on use cases and power requirements. The schematic diagram of a single VEH module is shown in Fig. 1.

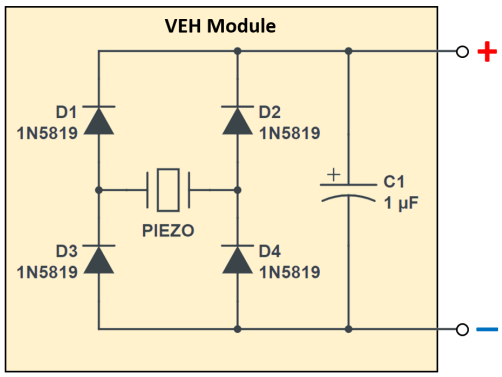


Fig. 1. Schematic diagram of a single VEH module

For each module, a piezoelectric transducer is placed to harvest vibration energy and it produces potential difference when it is exposed to vibration. In this study, the piezoelectric transducer used is a 35-mm diameter disc-type piezoelectric transducer with resonant frequency of 2.6±0.5kHz.

As the potential difference across the piezoelectric transducer terminals is alternating, a full-wave rectifier circuit is used to convert the wave to positive polarity with respect to the negative terminal of the circuit (marked in blue). The diodes used for the full-wave rectifier circuit is 1N5819 Schottky diodes.

A smoothing 1μF capacitor is connected at the output of the rectifier, which is also the output of the VEH module, marked by the positive (red) and negative (blue) terminals.

B. Series and Parallel VEH Configurations

There are two basic configurations that a VEH power supply can be developed using the VEH module discussed above. First is by connecting several VEH modules in series as shown in Fig. 2 and second is by connecting several VEH modules in parallel as shown in Fig. 3.

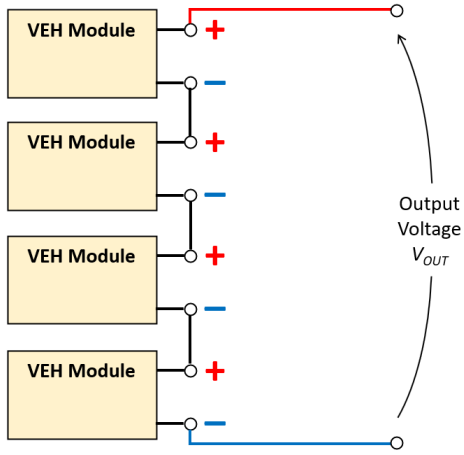


Fig. 2. Circuit connection for Series VEH configuration

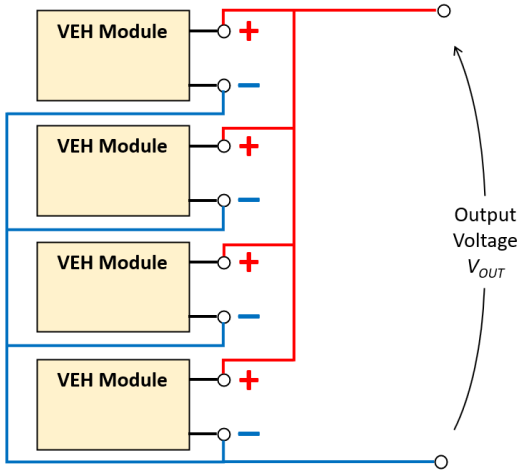


Fig. 3. Circuit connection for Parallel VEH configuration

Assuming that all VEH modules are harvesting identical vibration energy instantaneously, a series VEH configuration may boost the output voltage V_{out}, while a parallel VEH configuration may increase output current. This is similar to how battery cells can be connected in series or parallel or

a combination of both to achieve the power (which involves voltage and current) requirements of different applications.

III. Experimental Setup

An experimental setup is developed to investigate how different VEH configurations harvest vibration energy and produce electrical power. In this study, the focus of the experiment is to evaluate the output electrical power from the VEH when a vibrating machine is running.

A. Vibrating Machine Platform

A DC brushed motor with an eccentric mass is used as the source of vibration in this experiment. The DC motor is powered by an external constant power supply at the rated voltage of 5V and it has the rated speed of 3980RPM.

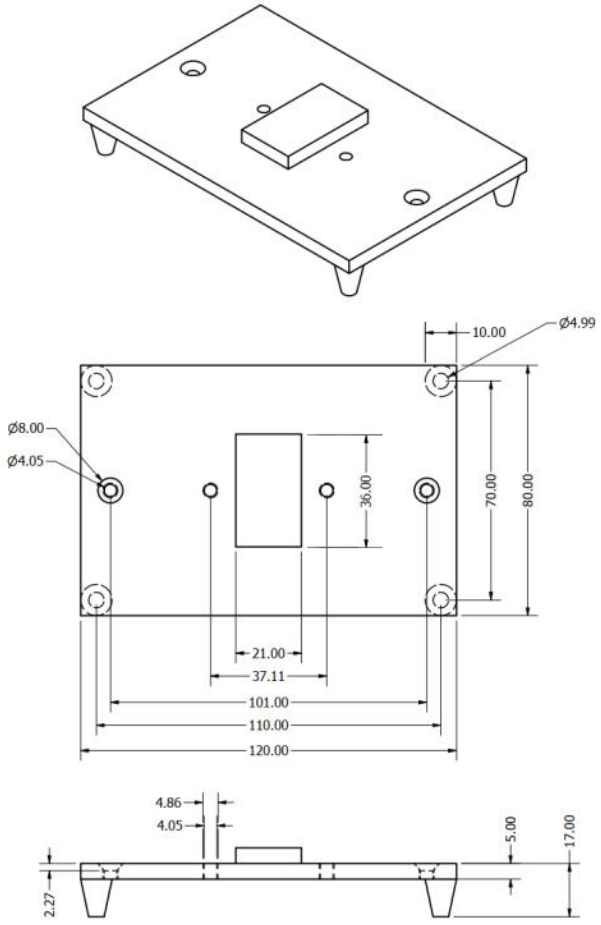


Fig. 4. Dimensions of the 3D printed platform in mm

A platform and a motor bracket are fabricated to keep the DC motor in place. Fig. 4 shows the dimensions of the platform in mm and Fig. 5 shows the assembly of the platform, bracket and vibrating machine. The rotation of the DC motor shaft shall cause vibration due to the mounted eccentric mass and this vibration is used to emulate vibrations in rotating or reciprocating machines in factory settings.

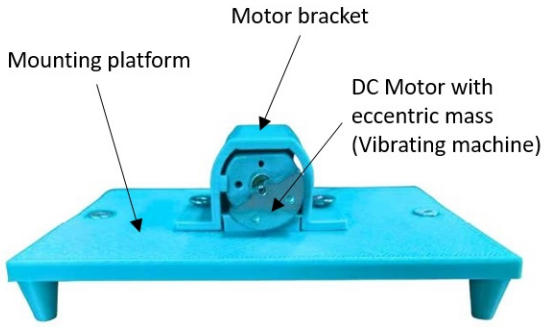


Fig. 5. Assembly of 3D printed platform, bracket and vibrating machine

B. Full Mechanical Setup

The vibrating machine platform discussed above is mounted on a wooden floor (Fig. 6) through two mounting bolts. The vibrating machine platform is also sitting on four piezoelectric transducers that are placed on the wooden floor.

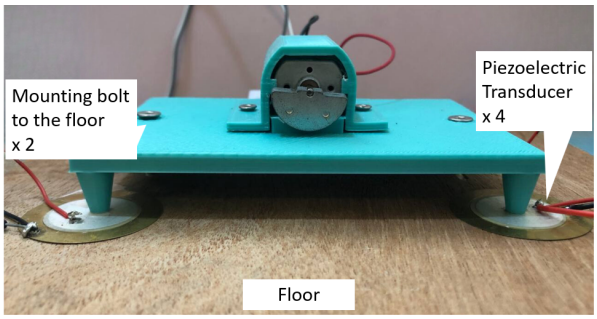


Fig. 6. Full mechanical setup of the vibration energy harvesting experiment

IV. Results and Discussion

The output performance of the VEH is investigated through load experiments. The four piezoelectric transducers attached on the vibrating machine platforms are connected either in series or parallel configurations.

A. Load Experiment for Series VEH Configuration

In the load experiment for series VEH configuration, the four VEH modules are connected in series and the output voltage V_{out} (Fig. 2) is observed through an oscilloscope. Before connecting any load to the output terminals of the VEH, a no-load (open-circuit, $R_L = \infty$) waveform is collected and is shown in Fig. 7, with an average voltage of V_{out} = 35.2V. Voltage ripples with peak-to-peak amplitude of about 2V can be observed in the waveform.

Several external resistive loads ranging from R_L = 5.1Ω up to 100MΩ are connected to the VEH output terminals in order to study the effect of the external load on the output of the VEH.

A sample output voltage waveform when an external resistive load of R_L = 22kΩ is shown on Fig. 8. Here, the

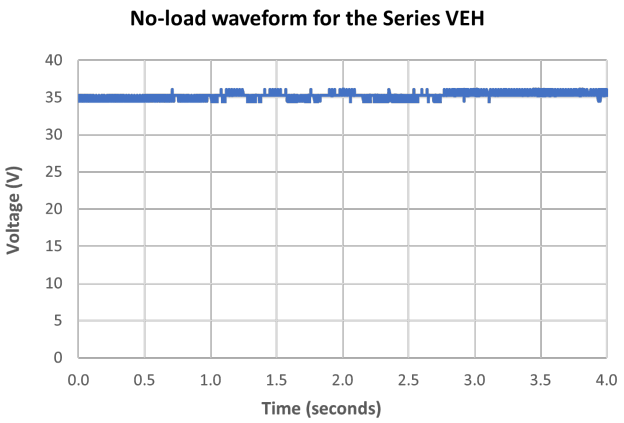


Fig. 7. Output voltage waveform of Series VEH configuration at no-load condition

average output voltage has dropped to V_{out} = 2.92V with peak-to-peak voltage ripple of about 2V.

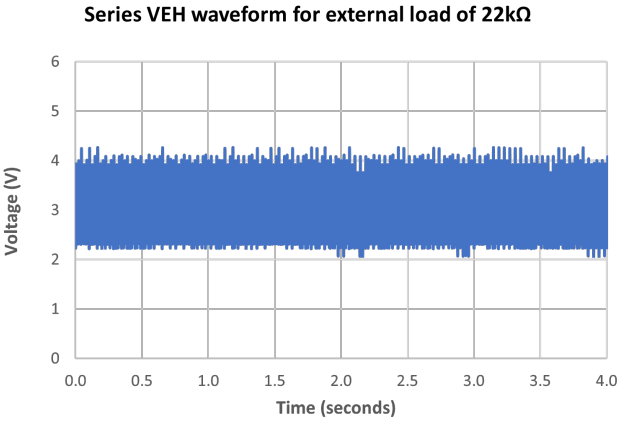


Fig. 8. Output voltage waveform of Series VEH configuration when an external resistive load of 22kΩ is connected

Results for the output performance for series VEH under different loading conditions is shown in Fig. 9, where the output power P_{out} is the power dissipated across the load resistance R_L:

$$P_{out} = \frac{{V_{out}}^2}{R_L} \quad (1)$$

It can be seen that the maximum power for this experiment occurs at R_L = 500kΩ, with V_{out} = 20.9V and P_{out} = 0.874mW. This can give an indication to what the internal impedance of the VEH circuit is. Based on maximum power transfer theorem, the maximum power transfer is delivered to a load if it is identical to the internal impedance of the supply, which means, at this operating condition of forced vibration, the VEH circuit has an internal impedance that is at the vicinity of 500kΩ.

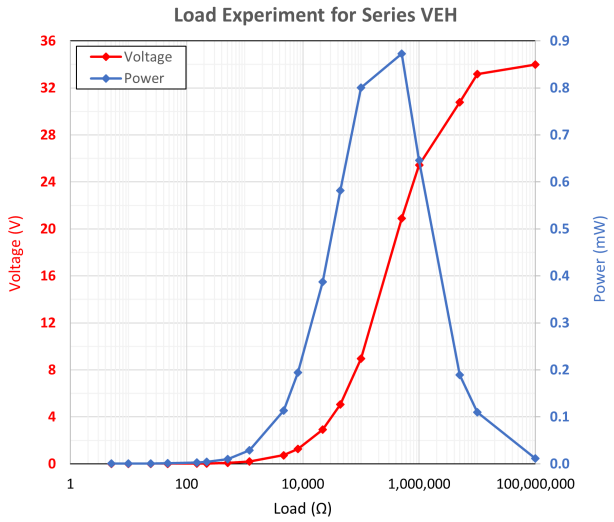


Fig. 9. Output voltage and power of the Series VEH configuration under different loading conditions

B. Load Experiment for Parallel VEH Configuration

Similar to the previous experiment, the load experiment for parallel VEH configuration is conducted when the four VEH modules are connected in parallel (Fig. 3). The output waveform of the parallel VEH at no-load (open-circuit, $R_L = \infty$) is shown in Fig. 10, with an average voltage of V_{out} = 13.1V. No significant voltage ripple is observed in this case.

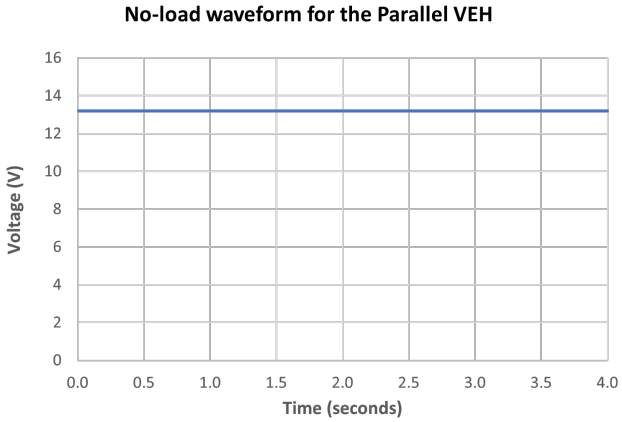


Fig. 10. Output voltage waveform of Parallel VEH configuration at no-load condition

A sample output voltage waveform when an external resistive load of R_L = 22kΩ is shown on Fig. 11. The average output voltage has dropped to V_{out} = 3.57V with peak-to-peak voltage ripple of about 0.7V.

Results for the output performance for parallel VEH under different loading conditions is shown in Fig. 12.

In the parallel VEH experiment, the maximum power for this experiment occurs at R_L = 44kΩ, with V_{out} = 5.18V and P_{out} = 0.609mW. Considering the maximum power transfer

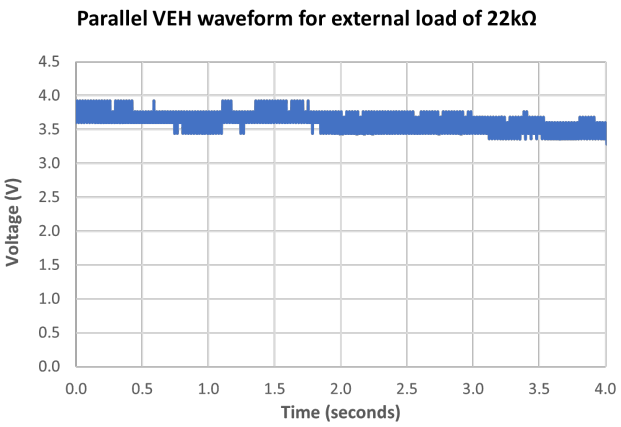


Fig. 11. Output voltage waveform of Parallel VEH configuration when an external resistive load of 22kΩ is connected

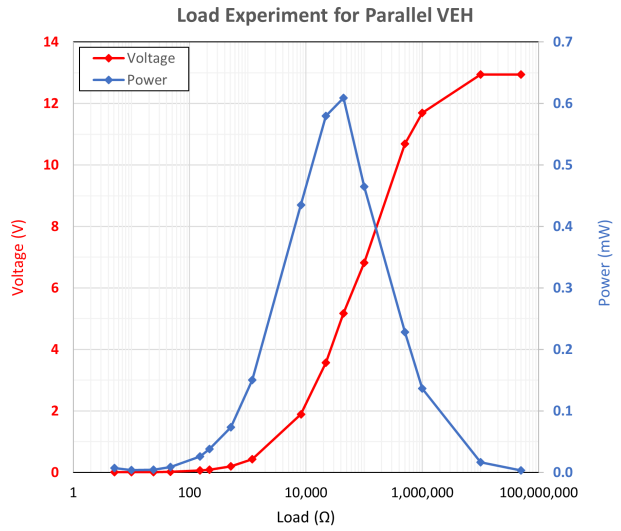


Fig. 12. Output voltage and power of the Parallel VEH configuration under different loading conditions

theorem, it can be implied that at this operating condition of forced vibration, the VEH circuit has an internal impedance that is at the vicinity of 44kΩ.

C. Comparisons between Series and Parallel VEH Configurations

Looking at the load experiment results for series and parallel VEH configurations, it is evident that the series configuration is able to generate higher output voltage as the total voltage is the sum of the outputs of all the transducers. However, parallel VEH configuration allows the smoothing out of the output voltage as the parallel configuration effectively averages the outputs of all the transducers and therefore has better voltage ripple performance.

The internal impedance of the piezoelectric transducers is also dependent on the frequency of the vibration and minimum impedance of piezoelectric transducers occurs at the resonant frequency. The piezoelectric transducers used in the experiment has a resonant frequency of 2.6±0.5kHz, and although the minimum impedance is not available in the specifications, the minimum impedance may be as low 1kΩ. In this paper, the vibrating machine rated frequency is 3980RPM = 66.3Hz, which is around 40 times lower than the resonant frequency. At this frequency, the internal impedance of the VEH is much higher than the minimum impedance.

If the internal impedance of a single piezoelectric transducer is Z_0, assuming that all four piezoelectric transducers are undergoing identical mechanical vibration, the equivalent series impedance of four piezoelectric transducers is Z_{series} = 4 Z_0 and the equivalent parallel impedance of four piezoelectric transducers is $Z_{parallel}$ = Z_0 / 4. The ratio of the equivalent series impedance to the equivalent parallel impedance can be given as:

$$\frac{Z_{series}}{Z_{parallel}} = \frac{4Z_0}{Z_0/4} = 16 \tag{2}$$

In practical situations, expecting all piezoelectric transducers to simultaneously produce identical outputs is not possible as all four modules are not undergoing the exact same vibration. Having said that, the load resistance for the maximum power in the series VEH experiment is found to be around 500kΩ and the load resistance for the maximum power in the parallel VEH experiment is found to be around 44kΩ, which gives a ratio of 500kΩ/44kΩ = 11.4, a difference of 29% from the ideal ratio of 16 given by Eq. (2).

D. Suitability for Machine Condition Monitoring Applications

To evaluate the suitability of using the developed VEH for machine condition monitoring, a set of sensors and data acquisition device is considered. Variables that are common to be monitored for machine condition include temperature and acceleration.

Several low-power temperature and acceleration sensors are available in the market. For example, Analog Devices TMP35 Temperature Sensor is able to measure a temperature range of 10 to 125°C and takes a supply voltage of as low as 2.7V and an operating supply current of 50μA, which corresponds to power supply of 0.135mW [12]. Bosch BMA400 accelerometer is able to measure acceleration in multiple ranges up to ±16 times the gravitational acceleration, with a minimum supply voltage of 1.72V and an operating supply current of 14.5μA, corresponding to 0.0249mW [13]. A total power consumption for the sensor is therefore about 0.16mW.

A typical wireless sensor node shall require a data acquisition device that is able to transmit wireless data. An example of possible device that can be used in this application is Arduino MKR WAN 1310, a microcontroller with LoRaWAN capability to transmit and receive wireless signals [14]. The supply voltage to Arduino MKR WAN 1310 is 5V with a current consumption of minimum 104μA, this

gives a power consumption of 0.520mW. As Arduino MKR WAN 1310 provides a regulated 3.3V supply to peripherals, this supply is suitable to power up the external sensors mentioned above.

To summarize, the wireless sensor network may consume a total power of less than 0.7mW. Of course, it is also necessary that a DC-DC converter to be used to provide for 5V supply required by the Arduino MKR WAN 1310.

Based on the current VEH setup, it is possible to find a range of outputs to which the output voltage is above 5V and the output power is above 0.7mW from the series VEH configuration (Fig. 9) while the parallel configuration (Fig. 12) is not able to supply for power requirement beyond 0.609mW.

For this particular suggested application, a series VEH may be able to be used for the machine condition monitoring application. In the industrial scenarios, which typically have much larger vibration amplitudes and perhaps running on higher frequencies, piezoelectric VEH provides sustainable alternative power source for wireless machine condition monitoring devices.

V. Conclusion and Future Works

This paper presents the development of a VEH based on piezoelectric transducers for the purpose of machine condition monitoring. The miniature vibrating machine system is developed to observe the output performance of VEH modules under different circuit configurations. Results show that the developed VEH can be used to supply wireless machine condition monitoring devices.

Nonetheless, several limitations and challenges are observed in the current work, these being opportunities for future works. First, experiments involving different types and sizes of piezoelectric transducers can be carried out. Secondly, to efficiently harvest vibration energy, the operating frequency should also be taken into account. Thirdly, to minimize power loss while supplying to the load circuit, impedance or load matching can be carried out based on the operating frequency of the machine. Finally, combinations of multiple VEH modules connected in different configurations, such as series-parallel connections used commonly in battery modules may increase the harvested vibration energy. Practical implementation of the VEH for machine condition monitoring shall also take into account the possible load requirements as well as output regulation circuitry.

Using VEH for low-power sensors allow for many future applications, especially on the Internet-of-Things (IoT) technologies, where IoT wireless sensor networks are implemented in various areas, such as agriculture and healthcare [15], [16]. Sustainable and and small form-factor source of energy such as VEH provides a promising alternative to other sources of renewable energies such as wind or solar energy.

References

[1] A. F. De Leon and F. R. G. Cruz, "Water level monitoring and flood warning system using light detection and ranging (lidar) sensor with hybrid renewable solar-wind power," in *2021 IEEE 13th International Conference on Humanoid, Nanotechnology, Information Technology, Communication and Control, Environment, and Management (HNICEM)*, 2021, pp. 1–5.

[2] E. Sardini and M. Serpelloni, "Passive and self-powered autonomous sensors for remote measurements," *Sensors*, vol. 9, no. 02, pp. 943–960, 2009.

[3] T. Li, C. Li, C. Han, Y. Jiang, L. Chen, Y. Xu, Y. Li, and H. Deng, "Distinct voltage signals of sediment microbial fuel cell sensors in sensing various contaminants," *Electroanalysis*, vol. 36, no. 6, p. e202300394, 2024.

[4] J. Prasad and R. K. Tripathi, "Series and hybrid connection of sediment microbial fuel cell for powering led," in *2017 14th IEEE India Council International Conference (INDICON)*, 2017, pp. 1–5.

[5] A. Mohanty, S. Parida, R. K. Behera, and T. Roy, "Vibration energy harvesting: A review," *Journal of Advanced Dielectrics*, vol. 9, no. 04, p. 1930001, 2019.

[6] L. Dong, A. B. Closson, C. Jin, I. Trase, Z. Chen, and J. X. Zhang, "Vibration-energy-harvesting system: Transduction mechanisms, frequency tuning techniques, and biomechanical applications," *Advanced materials technologies*, vol. 4, no. 10, p. 1900177, 2019.

[7] N. Sezer and M. Koç, "A comprehensive review on the state-of-the-art of piezoelectric energy harvesting," *Nano Energy*, vol. 80, p. 105567, 2021.

[8] X. Wang, Y. Xia, G. Shi, H. Xia, Z. Chen, Y. Ye, and Z. Zhu, "A self-powered rectifier-less synchronized switch harvesting on inductor interface circuit for piezoelectric energy harvesting," *IEEE Transactions on Power Electronics*, vol. 36, no. 8, pp. 9149–9159, 2021.

[9] H. A. Sodano, D. J. Inman, and G. Park, "Generation and storage of electricity from power harvesting devices," *Journal of intelligent material systems and structures*, vol. 16, no. 1, pp. 67–75, 2005.

[10] P. Samant, M. Bhushan, A. Kumar, R. Arya, S. Tiwari, and S. Bansal, "Condition monitoring of machinery: A case study," in *2021 6th International Conference on Signal Processing, Computing and Control (ISPCC)*. IEEE, 2021, pp. 501–505.

[11] SKF, *SKF QuickCollect Sensor User Manual Rev. B*, 2020. [Online]. Available: https://www.skf.com/binaries/pub12/Images/0901d1968094e9ec-CMDT-391-CMDT-391-Ex-QuickCollect-Sensor-UM-EN-Rev-B-15V-090-00090-100_tcm_12-592191.pdf

[12] AnalogDevices, *TMP35/TMP36/TMP37 (Rev. H) Datasheet*. [Online]. Available: https://www.analog.com/media/en/technical-documentation/data-sheets/TMP35_36_37.pdf

[13] Bosch, *BST Data Sheet Datasheet*. [Online]. Available: https://www.bosch-sensortec.com/media/boschsensortec/downloads/datasheets/bst-bma400-ds000.pdf

[14] Arduino, *Arduino MKR WAN 1310 — Arduino Official Store*. [Online]. Available: https://store.arduino.cc/products/arduino-mkr-wan-1310

[15] K. T. Chew, R. S. Jo, M. Lu, V. Raman, and P. H. H. Then, "Organic black soldier flies (bsf) farming in rural area using libelium waspmote smart agriculture and internet-of-things technologies," in *2021 IEEE 11th IEEE Symposium on Computer Applications & Industrial Electronics (ISCAIE)*. IEEE, 2021, pp. 228–232.

[16] M. S. Farooq, O. O. Sohail, A. Abid, and S. Rasheed, "A survey on the role of iot in agriculture for the implementation of smart livestock environment," *IEEE Access*, vol. 10, pp. 9483–9505, 2022.

AC and DC Power Flow Calculation Method in Distribution Networks Based on Power Electronic Transformers

Zhen Zheng
State Grid Shanghai Electric Power Company Qingpu Power Supply Company
Shanghai, 201700 China
upczz@126.com

Yinan Huang
State Grid Shanghai Electric Power Company Qingpu Power Supply Company
Shanghai, 201700 China
3253572494@qq.com

Wenwen Chen
State Grid Shanghai Electric Power Company Qingpu Power Supply Company
Shanghai, 201700 China
354765399@qq.com

Xiao Yang *
School of Electrical Engineering, Shanghai University of Electric Power,
Shanghai, 200090 China
19511569055@163.com
*Corresponding author

Haijun Xing
School of Electrical Engineering, Shanghai University of Electric Power,
Shanghai, 200090 China
xinghj@shiep.edu.cn

***Abstract*—To characterise the multi-port power coupling characteristics of power electronic transformers, this research proposes a method for calculating power flow in AC and DC distribution networks incorporating PETs. Firstly, by constructing a multi-port power flow decoupling model for PETs based on controlled source pairs, the power coupling characteristics of the power conversion elements under voltage control and power control modes are characterised. Secondly, an alternating iteration algorithm is employed to achieve efficient collaborative solution for AC and DC systems. Finally, power flow calculations for an enhanced 26-node AC and DC hybrid distribution network in a specific region demonstrate that the proposed method satisfies the requirements for power flow calculations in distribution networks incorporating PETs. The proposed PET power flow decoupling model accommodates multi-voltage level AC and DC buses. It accurately calculates both PET port power flows and internal power flow distributions under both voltage control and power control modes, whilst exhibiting a low number of iterations and rapid convergence.**

Keywords—power electronic transformer, AC/DC distribution network, alternating iteration method

I. INTRODUCTION

With the advancement of the dual carbon goals, the penetration rate of distributed generation (DG) sources such as wind and photovoltaic power has significantly increased within distribution networks, altering grid structures and operational characteristics. While high-penetration renewable energy integration enhances clean energy levels, its randomness, volatility, and intermittency pose challenges to the safe and stable operation of distribution grids [1,2]. To enhance DG integration capacity and operational flexibility, hybrid AC-DC distribution grids have emerged as a key development direction. Power electronic transformers (PETs), serving as core equipment for multi-voltage-level AC/DC power conversion and regulation [3,4], play a pivotal role in the smooth control of renewable energy. However, the multi-port strong coupling and complex internal conversion stages of PETs render their power flow characteristics difficult to analyse. This limits the application of traditional power flow calculation methods, constraining the planning and economic operation of systems incorporating PETs [5].

In power flow calculations for hybrid AC/DC distribution networks, existing research predominantly focuses on systems incorporating voltage-source converters (VSCs), with insufficient attention given to refined modelling of multi-port PETs. Reference [6] established steady-state equivalent circuits for modular multilevel converters (MMC) and double active bridge (DAB) converters within PETs, equating the DAB to a series connection of a square-wave power source and a transformer Π-circuit. Reference [7] independently modelled VSCs and DABs, describing AC-DC side relationships via DC voltage utilisation rates. While these models account for internal topologies, they do not fully resolve port coupling issues. Some studies simplify PET modelling, such as Reference [8] which equates it to PQ or PV nodes, yet overlooks internal power coupling and losses, resulting in limited accuracy. Algorithmically, simultaneous solution methods enable integrated system analysis. However, PET's strong nonlinearity complicates Jacobian matrix construction, leading to poor convergence and low efficiency [9]. Alternating iteration methods reduce complexity by decoupling AC and DC subsystems [10]. Reference [11] proposes an alternating iteration method, constructing an equivalent controlled-source pair to decouple PET port coupling, thereby enhancing efficiency and accuracy.

To account for the multi-port power coupling characteristics

This work is supported by Science and Technology Project of State Grid Shanghai Electric Power Co.,Ltd (No. 520934250004)

979-8-3315-5472-9/25/$31.00 ©2025 IEEE

of PET, this paper proposes a method for calculating power flows in AC/DC distribution networks incorporating PET. A controlled-source decoupling model is constructed, combined with an alternating iteration algorithm to circumvent the challenges of the Jacobian matrix. Validation through a 26-node enhanced case study demonstrates that the proposed algorithm achieves accurate power flow calculations under master-slave control, with fewer iterations and faster convergence.

II. PET AC/DC Hybrid Distribution Network Power Flow Model

A. PET Decoupled Model for Tidal Current Calculation

PET contains different structures of converters such as VSC1, DAB, VSC2, etc., which need to be modelled separately to calculate the tidal currents of each part.

$$P_{\text{loss-ACi}} = \sum_{i=\text{h,l}} a_{i0} + a_{i1}|I_{ai}| + a_{i2}|I_{ai}|^2 \tag{1}$$

where: $P_{\text{loss-AC}}$ is the loss of PET AC port [12], due to the zero-voltage switching control of DAB, its power loss is small, and the power loss of PET is mainly concentrated in VSC. Where a_{i0}, a_{i1}, a_{i2} are the i^{th} fixed loss, linear loss and squared loss coefficient, respectively; the subscripts h and l are the medium-voltage side and low-voltage side, respectively.

$$\begin{cases} \dot{U}_{\text{fm}} = \dot{U}_{\text{m}} + Z_{\text{tr}}(P_{\text{m}} - \text{j}Q_{\text{m}})/U_{\text{m}}^{*} \\ \dot{U}_{\text{am}} = \dot{U}_{\text{fm}} + [(P_{\text{m}} - \text{j}Q_{\text{m}})/U_{\text{m}}^{*} + \dot{U}_{\text{fm}}/Z_{\text{ch}}]Z_{\text{lh}} \\ S_{\text{am}} = \dot{U}_{\text{am}}[(P_{\text{m}} - \text{j}Q_{\text{m}})/U_{\text{m}}^{*} + \dot{U}_{\text{fm}}/Z_{\text{ch}}]^{*} \end{cases} \tag{2}$$

$$\begin{cases} \dot{I}_{\text{st}} = \dot{I}_{\text{lh}} - \dfrac{\dot{U}_{\text{fm}}}{Z_{\text{ch}}} \\ \dot{U}_{\text{m}} = \dot{U}_{\text{fm}} + \dot{I}_{\text{st}} Z_{\text{tr}} \\ \dot{U}_{\text{am}} = \dot{U}_{\text{fm}} - \dot{I}_{\text{am}} Z_{\text{lh}} \\ S_{\text{am}} = \dot{U}_{\text{am}} \cdot I_{\text{lh}}^{*} \\ \dot{I}_{\text{am}} = \dot{I}_{\text{lh}} \end{cases} \tag{3}$$

where: $U_{\text{fm}}\angle\delta_{\text{fm}}$ is the medium-voltage filter capacitor voltage; $U_{\text{am}}\angle\delta_{\text{am}}$ is the VSC1 AC output voltage; S_{am} is the medium-voltage filter reactor branch power flow; Z_{tr} is the equivalent impedance of the VSC1 converter transformer; Z_{lh} and Z_{ch} are the filter reactor reactance and capacitive reactance of VSC1 respectively; $\dot{I}_{\text{st}}$ is the converter transformer branch current; $\dot{I}_{\text{lh}}$ is the filter reactor branch current; S_{am} represents the branch power flow of the medium-voltage filter reactor; $U_{\text{m}}\angle\delta_{\text{m}}$ denotes the medium-voltage AC terminal voltage; S_{m} signifies the converter transformer branch power flow; the superscript '*' denotes conjugate. When VSC1 employs power-station control, its power flow equation is given by Equation (2). The values $U_{\text{am}}\angle\delta_{\text{am}}$, $U_{\text{fm}}\angle\delta_{\text{fm}}$, and S_{am} can be calculated using the reference values $P_{\text{m}}^{\text{ref}}$, $Q_{\text{m}}^{\text{ref}}$, or $U_{\text{m}}^{\text{ref}}$ at the medium-voltage AC side point of common coupling (PCC); When VSC1 employs voltage-source control, its power flow equation is given by Equation (3). This requires calculating $U_{\text{fm}}\angle\delta_{\text{fm}}$ and $U_{\text{am}}\angle\delta_{\text{am}}$ via $\dot{I}_{\text{st}}$ and $\dot{I}_{\text{lh}}$, followed by iterative solution of the above equations using Newton's method to determine P_{m} and Q_{m} at the medium-voltage PCC point.

$$\begin{cases} P_{\text{al}} + P_{\text{loss-ACl}} + P_{\text{dl}} = 0 \\ U_{\text{dl}} = U_{\text{dvl}} + (P_{\text{dvl}}/U_{\text{dvl}})Z_{\text{dl}} \\ P_{\text{D}} = U_{\text{dl}}(P_{\text{dvl}}/U_{\text{dvl}} - P_{\text{dl}}/U_{\text{dl}}) \end{cases} \tag{4}$$

where: Z_{dl} is the equivalent impedance of the DAB2 line; U_{dvl} is the low-voltage DC port voltage; U_{dl} is the DAB low-voltage DC output voltage; P_{dl} is the DC-side injection power of VSC2; P_{dvl} is the power injected into the low-voltage DC distribution network; $P_{\text{loss-ACl}}$ is the active power loss in the power conversion stage of VSC2. The DAB can similarly be categorised into power stations and voltage stations according to the PET control scheme. When DAB-2 operates as a low-voltage power station or voltage station, only the initial iteration values differ. Combining the injected power into the low-voltage DC distribution network P_{dvl} and the injected power from VSC2 P_{al}, calculate U_{dl} and P_{D}.

$$\begin{cases} U_{\text{dm}} = U_{\text{dvh}} + (P_{\text{dvh}}/U_{\text{dvh}})Z_{\text{dm}} \\ P_{\text{dm}} = P_{\text{D}} + U_{\text{dm}}(P_{\text{dvh}}/U_{\text{dvh}}) \end{cases} \tag{5}$$

$$\begin{cases} P_{\text{am}} + P_{\text{loss-ACh}} + P_{\text{dm}} = 0 \\ P_{\text{dm}} - P_{\text{D}} = U_{\text{dm}} I_{\text{dvh}} \\ U_{\text{dm}} = U_{\text{dvh}} + I_{\text{dvh}} Z_{\text{dm}} \end{cases} \tag{6}$$

where: Z_{dm} is the equivalent impedance of the DAB1 line; U_{dvh} is the medium-voltage DC port voltage; U_{dm} is the medium-voltage DC output voltage of the DAB; P_{dm} is the DC-side injection power of VSC1; P_{dvh} is the power injected into the medium-voltage DC distribution network; $P_{\text{loss-ACh}}$ is the active power loss in the power conversion stage of VSC1. When VSC1 operates as a medium-voltage voltage source, the power flow equation for DAB-1 is given by Equation (5). Combining this with the transmission power of DAB-1 P_{D}, calculate U_{dm} and P_{dm}. When VSC1 operates as a medium-voltage power source, the power flow equation for DAB-1 is given by Equation (6). Combining this with the active power injected by VSC1 P_{am} to the DC side and the transmission power of DAB-2 P_{D}, calculate U_{dm} and I_{dvh}.

$$\begin{cases} \dot{U}_{\text{fl}} = \dot{U}_{\text{l}} + Z_{\text{C}}(P_{\text{l}} - \text{j}Q_{\text{l}})/U_{\text{l}}^{*} \\ \dot{U}_{\text{al}} = \dot{U}_{\text{fl}} + [(P_{\text{l}} - \text{j}Q_{\text{l}})/U_{\text{l}}^{*} + \dot{U}_{\text{fl}}/Z_{\text{L2}}]Z_{\text{L1}} \\ S_{\text{al}} = \dot{U}_{\text{al}}[(P_{\text{l}} - \text{j}Q_{\text{l}})/U_{\text{l}}^{*} + \dot{U}_{\text{fl}}/Z_{\text{L2}}]^{*} \end{cases} \tag{7}$$

where: Z_{L1}, Z_C, Z_{L2} and represent the equivalent inductive reactance, capacitive reactance, and inductive reactance of the LCL-type filter respectively; $U_1\angle\delta_1$ denotes the low-voltage AC terminal voltage; denotes the low-voltage filter capacitor voltage; $U_1\angle\delta_1$ denotes the AC output voltage of the VSC2; S_{al} denotes the power flow in the inductive reactance branch of the LCL-type linear filter. Compared to VSC1, the tidal current calculation equation of VSC2 differs only in its input and output variables, due to the connection to the low-voltage distributed power supply, and its voltage source/power source control mode difference in the initial value of the tidal current iteration. The rest of the voltage and current can be calculated based on known quantities.

In summary, the PET decoupling model needs to be clarified: VSC1, DAB and VSC2 are modelled separately, with variables such as VSC loss coefficients (h MV side, l LV side), DAB line equivalent impedance, etc.; VSC1 and DAB are divided into power/voltage control modes, with the former using the PQ/PV node characteristics, and the latter differing in the initial value of the iteration only, while the initial value of iteration of VSC2 varies with the control mode due to the connection to the low-voltage DG.

B. AC/DC Distribution Network Trend Calculation Model with PET Ports

In the equivalent circuit of a low-voltage direct current distribution network, its topology exhibits the characteristic features of a typical radial single-feeder configuration. The initial node 0 represents the PET low-voltage direct current port, with a voltage corresponding to the PET low-voltage direct current port voltage. The terminal node n connects to the DG, while intermediate nodes i ($1\leqslant i\leqslant n$-1) are each connected to active loads. The power flow calculation model for DG connection to PET via direct current is as follows:

$$\begin{cases} P_G = U_{Pn} I_G \\ P_{Pi} = U_{Pi} I_{Pi} i = 1,...,n-1 \\ U_{Pi} - U_{P(i+1)} = Z_{Pi(i+1)} (I_{P(i-1)i} - \dfrac{P_{Pi}}{U_{Pi}}) i = 1,...,n-1 \\ U_{Pi} - U_{P(i-1)} = -Z_{P(i-1)i} (I_{Pi(i+1)} + \dfrac{P_{Pi}}{U_{Pv}}) i = 2,...,n \end{cases} \quad (8)$$

where: I_G and P_G denote the DG injection current and power respectively; Z_{Pij} and I_{Pij} represent the equivalent impedance and branch current between nodes i and j respectively; U_{Pi} denotes the voltage at node i; P_{Pi} denotes the active power of the load at node i. Power flow direction: The PET controls the terminal voltage via port voltage U_{dvl}, i.e., given $U_{P0} = U_{dvl}$, injecting power into the network P_{dvl}; the load at each intermediate node i (i=1,…,n−1) consumes active power, while the DG at terminal node n injects power P_G as a current source; branch current I_{Pij} at node i satisfies Kirchhoff's current law. Combining DG injection power P_G with Kirchhoff's current law, the Newton method is employed to compute node voltages U_{Pi} and load currents I_{Pi}.

The low-voltage AC distribution network adopts a radial structure, with the PET low-voltage port serving as the primary node 0. Line nodes are sequentially connected to loads, with the terminal connected to DG. Its power flow calculation model is as follows:

$$\begin{cases} S_G = \dot{U}_{Cn} \dot{I}_G^* \\ S_{Ci} = \dot{U}_{Ci} \dot{I}_{Ci}^* i = 1,\ldots,n-1 \\ \dot{U}_{Ci} - \dot{U}_{C(i+1)} = Z_{Ci(i+1)} (I_{C(i-1)i} - \dfrac{S_{Ci}^*}{\dot{U}_{Ci}^*}) i = 1,\ldots,n-1 \\ \dot{U}_{C(i+1)} - \dot{U}_{Ci} = -Z_{C(i-1)i} (I_{Ci(i+1)} + \dfrac{S_{Ci}^*}{\dot{U}_{Ci}^*}) i = 2,\ldots,n \end{cases} \quad (9)$$

where: $\dot{I}_G$ represents the current injected by DG, Z_{Cij} and I_{Cij} denote the equivalent impedance and branch current between nodes i and j respectively, $U_{Ci}\angle\delta_{Ci}$ denotes the voltage at node i, and S_{Ci} denotes the apparent power of the load at node i. Power flow direction: The PET controls the upstream terminal voltage via port voltage $U_1\angle\delta_1$, i.e., given $U_1\angle\delta_1 = U_{C0}\angle\delta_{C0}$, the DG injects power S_G into terminal node n as a power source. This power is transmitted stepwise through line impedance Z_{Cij} to the upstream load node. Current $\dot{I}_G$ flows out from node n along branch $I_{C(n-1)n}$ towards node n-1. During transit through each node, part of the current branches to local load S_{Ci}, while the remaining current continues towards the PET port. Ultimately, net power is injected into the PET converter system via its low-voltage AC port.

Through the medium-voltage DC port interconnection in the PET, this paper employs master-slave control to construct a ring network. Nodes are categorised into three types for power flow solution: balancing nodes (voltage reference), voltage station nodes (known voltage), and power station nodes (requiring power equations).

$$\Delta P_{dvmi} = P_{dvmi} - U_{dvmi} \sum_{j\in N_{dc}} Y_{dvij} U_{dvmj} = 0 \quad (10)$$

$$[\Delta P_{dvm}] = -[J_m][\Delta U_{dvm}] \quad (11)$$

$$\begin{cases} J_{mii} = \dfrac{\partial \Delta P_{dvmi}}{\partial U_{dvmi}} = -2Y_{dvii} U_{dvmi} - \sum_{j\in N_{dc} j\neq i} Y_{dvij} U_{dvmj} \\ J_{mij} = \dfrac{\partial \Delta P_{dvmi}}{\partial U_{dvmj}} = -Y_{dvij} U_{dvmi} \end{cases} \quad (12)$$

$$U_{dvm}^{(k+1)} = U_{dvm}^{(k)} + (-J_m^{-1})^{(k)} \Delta P_{dvm}^{(k)} \quad (13)$$

where: ΔP_{dvmi} denotes the error in the active power balance equation for node i; P_{dvmi} and U_{dvmi} represent the injected power and voltage at node i, respectively; Y_{dvij} is the admittance between nodes i and j; N_{dc} denotes the set of node indices in the medium-voltage DC distribution network, where $i \in N_{dc}$; ΔP_{dvm} is the vector of errors in the active power

balance equations for the n-1-r power station nodes; ΔU_{dvm} is the voltage correction vector for the n-1-r nodes; J_{m} is the Jacobian matrix. The superscript (k) denotes the parameter value at the kth iteration; The subscript -1 denotes the inverse operation.

For the medium-voltage AC distribution network containing PET trend calculation, the controllable mode equates the PET medium-voltage AC ports to PV or PQ nodes in order to use the traditional algorithm, according to which the nodes are divided into nodes: n-1-r PQ nodes, r PV nodes, which are required to build n-1 active, n -1-r reactive power balance equations.

$$\begin{cases} \Delta P_i = P_i - U_i \sum\limits_{j \in N_{\mathrm{ac}}} U_j (G_{ij} \cos\delta_{ij} + B_{ij} \sin\delta_{ij}) = 0 \\ \Delta Q_i = Q_i + U_i \sum\limits_{j \in N_{\mathrm{ac}}} U_j (B_{ij} \cos\delta_{ij} - G_{ij} \sin\delta_{ij}) = 0 \end{cases} \tag{14}$$

$$\begin{bmatrix} \Delta \boldsymbol{P} \\ \Delta \boldsymbol{Q} \end{bmatrix} = -\begin{bmatrix} \boldsymbol{H} & \boldsymbol{N} \\ \boldsymbol{M} & \boldsymbol{L} \end{bmatrix} \begin{bmatrix} \Delta \boldsymbol{\delta} \\ \Delta \boldsymbol{U} / \boldsymbol{U} \end{bmatrix} \tag{15}$$

$$\begin{cases} H_{ii} = \dfrac{\partial \Delta P_i}{\partial \delta_i} = Q_i + U_i^2 B_{ii} \\ H_{ij} = \dfrac{\partial \Delta P_i}{\partial \delta_j} = -U_i U_j (G_{ij} \sin\delta_{ij} - B_{ij} \cos\delta_{ij}) \end{cases} \tag{16}$$

$$\begin{cases} N_{ii} = \dfrac{\partial \Delta P_i}{\partial U_i} U_i = -P_i - U_i^2 G_{ii} \\ N_{ij} = \dfrac{\partial \Delta P_i}{\partial U_j} = -U_i U_j (G_{ij} \cos\delta_{ij} + B_{ij} \sin\delta_{ij}) \end{cases} \tag{17}$$

$$\begin{cases} M_{ii} = \dfrac{\partial \Delta Q_i}{\partial \delta_i} = -P_i + U_i^2 G_{ii} \\ M_{ij} = \dfrac{\partial \Delta Q_i}{\partial \delta_j} \\ = U_i U_j (G_{ij} \cos\delta_{ij} + B_{ij} \sin\delta_{ij}) B_{ij} \cos\delta_{ij}) \end{cases} \tag{18}$$

$$\begin{cases} L_{ii} = \dfrac{\partial \Delta Q_i}{\partial U_i} U_i = -Q_i + U_i^2 B_{ii} \\ L_{ij} = \dfrac{\partial \Delta Q_i}{\partial U_j} U_j = -U_i U_j (G_{ij} \sin\delta_{ij} - B_{ij} \cos\delta_{ij}) \end{cases} \tag{19}$$

where: P_i and Q_i denote the active and reactive power injected at node i respectively; U_i is the voltage at node i; δ_{ij}, G_{ij} and B_{ij} represent the phase angle difference, conductance, and admittance between nodes i and j respectively; N_{ac} is the set of node indices in the medium-voltage AC distribution network, where $i \in N_{\mathrm{ac}}$. $\Delta \boldsymbol{P}$ and $\Delta \boldsymbol{\delta}$ denote the error vector of the n-1 active power balance equations and the node voltage phase angle correction vector respectively; $\Delta \boldsymbol{Q}$ and $\Delta \boldsymbol{U}$ denote the error vector of the n-1-r reactive power balance equations and the node voltage magnitude correction vector, respectively; $\boldsymbol{H}$, $\boldsymbol{N}$, $\boldsymbol{M}$, $\boldsymbol{L}$ are Jacobian subblock matrices.

III. Tidal Current Calculation Method Based on Alternating Iteration Method

The methods for calculating power flow in hybrid AC-DC systems primarily encompass simultaneous solution approaches and alternating iteration techniques [13]. The alternating iteration method decouples the framework to independently solve equations for AC and DC subsystems, utilising interface variables to exchange results. This approach offers advantages such as straightforward integration into existing architectures and flexible handling of operational constraints. This paper adopts this approach for multi-PET hybrid AC/DC distribution networks, employing a subnetwork iteration strategy: first independently calculating power flows for each subnetwork, then alternately updating PET port coupling variables to achieve system-level convergence. The specific workflow involves decoupling the PET module, solving the power flow equations, and alternately updating variables. The algorithmic flow for the alternating iteration method in hybrid AC/DC systems is illustrated in Fig. 1.

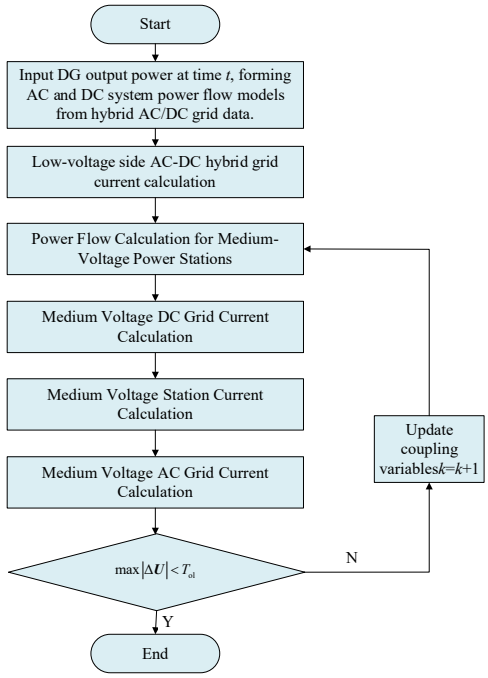


Fig. 1. Flowchart of alternating current iteration algorithm for AC-DC hybrid system

IV. Case Study Analysis

A. Case Study Introduction

To validate the power flow model and the proposed power flow algorithm, a 26-node AC distribution network in a certain region was expanded into a hybrid AC/DC distribution network incorporating multiple PETs and multiple voltage levels. Its topology is illustrated in Fig. 2. Within this network, PETs were connected at the terminals of different branches of the 26-node medium-voltage AC distribution network in the region, totalling three units. The medium-voltage DC ports form a three-terminal DC ring network, while the low-voltage AC/DC ports connect to the low-voltage AC/DC distribution networks respectively. Distributed wind/photovoltaic power generation is connected at the branch terminals. The specific simulation parameters for

PET are detailed in [16]. The loss coefficients for VSC1 are: a_{h0} =0.0001, a_{h1} =0.005, a_{h2} =0.2; those for VSC2 are: a_{l0} =0.0001, a_{l1} =0.1316, a_{l2} =1.38. Active loads of 0.38 MW are connected at nodes 28, 32, and 36 respectively. Active loads of 0.2 MW, 0.4 MW, and 0.18 MW are connected at nodes 30, 34, and 36 respectively. 38 nodes respectively connected active loads of 0.18 MW, while nodes 40, 42, and 44 were connected to active loads of 0.2 MW, 0.4 MW, and 0.18 MW respectively. Nodes 51 and 45 were connected to reactive loads of 0.02 Mvar and 0.5 Mvar respectively, with the total distribution network load being 4.866 + j1.671 MVA.

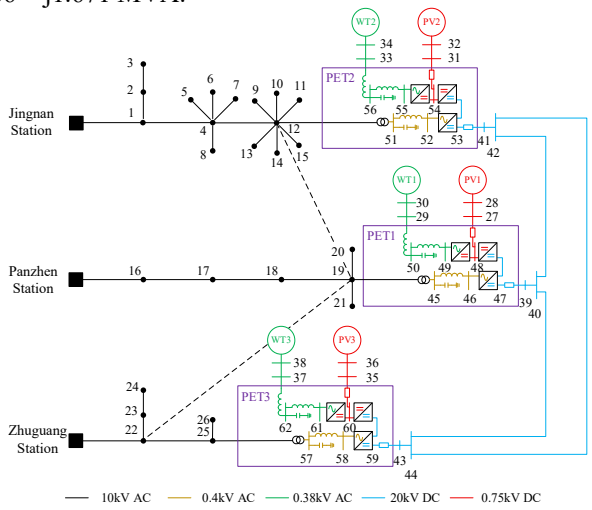


Fig. 2. Improvement of 26-node AC-DC hybrid distribution network topology in a region

B. *Verification of Current Computational Methods*

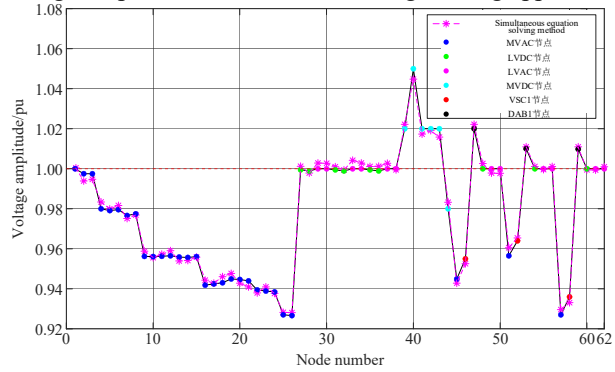
In master-slave control mode, the PET regulates the low-voltage AC/DC port voltages. Node 39 serves as the master station for the medium-voltage DC ring network voltage, while all other PET ports employ power station control. The control quantities and reference values for each PET port are detailed in Table 1.

TABLE I. PET CONTROL VOLUME AND REFERENCE VALUE DURING MASTER-SLAVE CONTROL

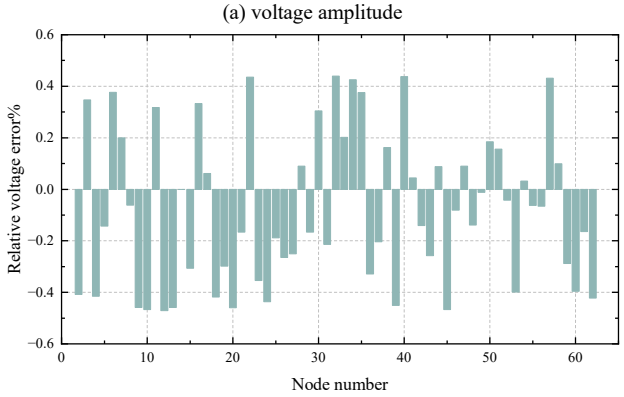
Parameters	Reference Value		
	PET1	***PET2***	***PET3***
P_s	-0.01	—	0.01
Q_s	0	0.01	0
U_{dch}	—	1.05	—
U_{dcl}	1	1	1
U_l	1	1	1
δ_l	0	0	0

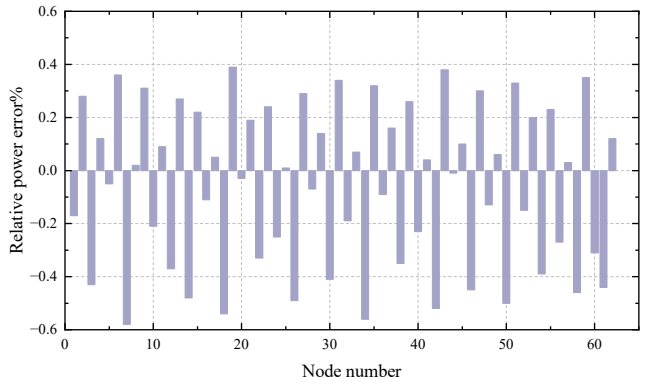
In master-slave control mode, the voltage distribution of the hybrid AC-DC distribution network is illustrated in Fig. 3(A). The coupled solution method, by directly characterising the global interdependencies between variables, yields more accurate computational results in strongly coupled scenarios and exhibits lower power flow calculation errors for the proposed model. The model's accuracy is evaluated using the coupled solution method's results as a benchmark. Within the medium-voltage AC distribution network segment, node voltages across branches generally exhibit a trend of either gradually decreasing towards the network's periphery or increasing at the periphery. In the medium-voltage DC ring network segment, node voltages are approximately uniform, tending towards the reference value of the master station voltage. Conversely, within the low-voltage AC/DC distribution network segment, the integration of wind/solar power generation results in a phenomenon of peripheral voltage elevation. These voltage distribution characteristics align with the patterns observed in hybrid AC/DC distribution networks. Furthermore, the error margin between the proposed algorithm and traditional simultaneous solution method calculations falls within the range [-0.47%, 0.44%], as illustrated in Fig. 3(B), thereby validating the proposed algorithm's efficacy. Furthermore, for branch power and node injection power, the error between the alternating iteration method and the simultaneous solution method lies within the range [-0.61%, 0.39%], satisfying the validity of the computational results.

The iterative convergence curve for the AC-DC hybrid distribution network is shown in Fig. 3(C). The proposed algorithm requires only three alternating iterations to reduce the error to 10^{-6}, with a computation time of 1.8800 seconds. In contrast, the simultaneous solution method still exhibits an error exceeding 10^{-6} at the fourth iteration, taking 3.0400 seconds to compute, demonstrating significantly slower convergence than the alternating iteration method. This demonstrates that the alternating iteration method, by decoupling the AC and DC systems for sequential solution, effectively circumvents the complex Jacobian matrix computation issues arising from unified modelling in the simultaneous solution approach. Consequently, it substantially reduces computational load per iteration, providing an efficient and accurate solution for weakly coupled AC/DC systems. This offers significant value in reducing computational time costs for engineering applications.

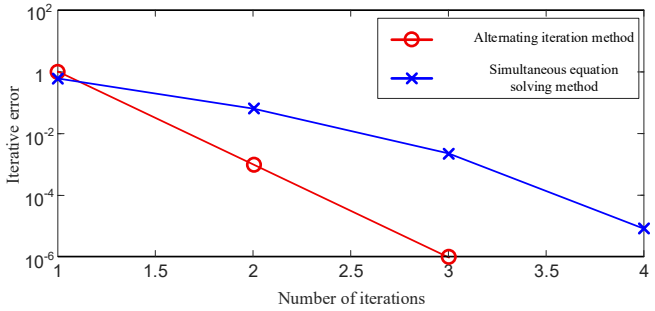


(a) voltage amplitude





(b) Relative error of voltage and power



(c) Algorithm Iteration Convergence Curve

Fig. 3. Master-slave power flow results

V. Conclusion

Based on decoupling the coupling relationships between power electronic transformer ports via controlled sources, this paper constructs a decoupled model for power flow calculation in power electronic transformers. This model characterises the power conversion properties of multi-voltage level AC/DC buses through equivalent controlled sources, enabling precise analysis of port power flows and internal power distribution under both voltage control and power control modes. Furthermore, an alternating iteration method was employed to design a flow calculation framework for hybrid AC/DC distribution networks incorporating multiple power electronic transformers. A stepwise solution strategy for decoupled subsystems significantly reduced the dimension of the Jacobian matrix. Simulation validation demonstrates that the proposed algorithm achieves high-precision power flow calculations under master-slave control, with convergence error reduced to 10^(−6). Moreover, the average number of iterations is lower than that of the simultaneous solution method, highlighting its computational efficiency advantage in weakly coupled systems.

Acknowledgment

This work is supported by Science and Technology Project of State Grid Shanghai Electric Power Co., Ltd (No. 520934250004)

References

[1] BERJAWI A E H, WALKER S L, PATSIOS C, et al. An evaluation framework for future integrated energy systems: A whole energy systems approach[J]. Renewable and Sustainable Energy Reviews, 2021, 145: 111163.

[2] ZHENG Waisheng, RAO Hong. Flexible Grid-forming Technology and Its Application in New Power System [J]. Automation of Electric Power Systems, 2024: 1-10.

[3] CAO Y, NGO K, DONG D. A Scalable Electronic-Embedded Transformer, a New Concept Toward Ultra-High-Frequency High-Power Transformer in DC–DC Converters[J]. IEEE Transactions on Power Electronics, 2023, 38(8): 9278-9293.

[4] PEI Zhongchen, LIU Chuang, WANG Shiyou, ZHU Di1, et al. Equivalent Modeling and Small Signal Stability Analysis of Three-stage Power Electronics Transformer [J]. Power System Technology, 2023, 47(8): 3426-3439.

[5] MENZI D, YANG A, CHHAWCHHARIA S, et al. Novel Three-Phase Electronic Transformer[J]. IEEE Transactions on Power Electronics, 2024, 39(5): 5027-5033.

[6] BARANWAL R, CASTELINO G F, IYER K, et al. A Dual-Active-Bridge-Based Single-Phase AC to DC Power Electronic Transformer With Advanced Features[J]. IEEE Transactions on Power Electronics, 2018, 33(1): 313-331.

[7] XU J, GAO C, DING J, et al. High-Speed Electromagnetic Transient (EMT) Equivalent Modelling of Power Electronic Transformers[J]. IEEE Transactions on Power Delivery, 2021, 36(2): 975-986.

[8] GUERRA G, MARTINEZ-VELASCO J A. A Solid State Transformer model for power flow calculations[J]. International Journal of Electrical Power & Energy Systems, 2017, 89: 40-51.

[9] WANG Xuekui, PENG Chunhua, SUN Huijuan. Power Flow Calculation of AC/DC Hybrid Power Grid Considering VSC Control Strategy [J]. Proceedings of the CSEE, 2023, 43(10): 3731-3742.

[10] SONG Zhiqiang,HUANG Yaohui,ZHAO Huashi, et al. Applicability analysis of power flow calculation methods for AC/DC hybrid connected power grid with multi-type DC [J]. Electric Power Automation Equipment, 2024, 44(4): 190-196.

[11] CHAI Yunze, Zhang Baohui, Bo Zhiqian. Alternating Iterative Power Flow Algorithm for Hybrid AC/DC Networks Containing DC Grid Basedon Voltage Source Converter [J]. Automation of Electric Power Systems, 2015, 39(7): 7-13.

[12] GENG Qi, HU Yan, HE Jianzong, et al. Optimal Power Flow for Hybrid AC/DC Grid With Power Electronic Transformer [J]. Power System Technology, 2019, 43(9): 3288-3298.

[13] LI Zhicheng.Optimal Power Flow and Self-healing Reconfiguration for AC/DC Power Systems with VSC-Based MTDC [D]. Beijing Jiaotong University, 2017.

[14] GAO Fanqiang, Li Zixin, Li Yaohua, et al. 10kV-3MV·A Four-Port Power Electronic Transformer for AC-DC Hybrid Power Distribution Applications [J]. Transactions of China Electrotechnical Society, 2021, 36(16): 3331-3341.

[15] SHI Xujiang. Research on Operation Optimization of Power Electronic Transformer Embedded AC/DC Distribution Network [D]. Southeast University, 2021.

Deployment of IoT Technologies for Phase Balancing in Low-Voltage Power Distribution

Aship Chaudhary
Equagen Engineers PLLC
Kathmandu, Nepal
aship.chaudhary@equagen.com

Samundra Gurung
Kathmandu University
Dhulikhel, Nepal
samundra.gurung@ku.edu.np

Rabindra Maharjan
Equagen Engineers PLLC
Kathmandu, Nepal
rabindra.maharjan@equagen.com

Priyanshu Rouniyar
Equagen Engineers PLLC
Kathmandu, Nepal
priyanshu.rouniyar@equagen.com

Sashank Shrestha
Equagen Engineers PLLC
Kathmandu, Nepal
sashank.shrestha@equagen.com

Yubraj Chimoriya
Kathmandu University
Dhulikhel, Nepal
yubrajchimoriya@gmail.com

***Abstract*—Voltage Unbalance (VU) is a significant power quality issue in low-voltage (LV) distribution feeders, particularly when voltage drops approach allowable limits and residential loads are unequally distributed across the three phases. The increasing penetration of single-phase rooftop solar photovoltaic (PV) systems further worsens this problem by introducing asymmetrical power injection, leading to greater per-phase loading variation and increased VU. High levels of VU can increase network losses and cause malfunctions or premature failure of three-phase equipment, such as induction motors. To mitigate this, a distributed intelligent load transfer scheme is proposed to dynamically reduce VU by redistributing residential loads among phases. A central controller installed at the distribution transformer monitors power consumption in each house using Internet of Things (IoT) technology and determines optimal load transfers. These transfers are executed via static transfer switches with a three-phase input and a single-phase output, installed at each residence to allow flexible phase reassignment. A short pi-model distribution line with unbalanced loading conditions is developed in MATLAB/Simulink to simulate the proposed scheme. The simulation results demonstrate the effectiveness of the approach in reducing voltage unbalance and improving the overall performance of the feeder.**

***Index Terms*—Phase balancing, Distribution substation, IoT, Control strategies, Microcontroller, MySQL database, Python script, WIFI communication.**

I. Introduction

In many parts of southern Asia, low-voltage (LV) residential feeders are typically three-phase, four-wire systems supplied by Dyn three-phase transformers. While most houses have a single-phase power supply, larger houses may have three-phase connections. With the increasing popularity of distributed energy resources like solar PV, the variability in per-phase loads and voltage unbalance are expected to rise, potentially causing damage to equipment like three-phase motors and increasing network losses. Utilities often manually balance loads among phases to minimize unbalance, but this research proposes dynamically transferring single-phase residential loads between phases to reduce voltage unbalance and power mismatch.

A new LV network consumer allocation method reduced phase imbalance from 1.287 to 1.003 and daily energy losses by 65.23%, tested on a rural network [1]. A model using static transfer switches redistributes customers and PVs in LV feeders via NSGA-II, minimizing losses and maintaining voltages in MATLAB–OpenDSS simulations [2]. A PRD control method for LVDNs with rooftop solar uses measurable PRD data, effectively mitigating unbalance in non-AMI networks; simulations confirm performance [3]. A load balancing method uses Deterministic Crowding for customer phase redistribution, minimizing switches, achieving imbalance targets, and improving service quality with fewer smart meters, validated on real data [4]. A novel compensation method using voltage sensitivity analysis and symmetrical components mitigates single-phase DER-induced unbalance, outperforming existing approaches in VUF threshold compliance and stability [5]. Automated phase balancing with remote-controlled switches reduces interruptions and losses in unbalanced feeders; IDECO's hybrid FFBPNN–RBFNN approach proves most effective in MATLAB simulations [6]. A genetic algorithm optimizes distribution transformer phase arrangements for balancing and loss reduction, validated on a feeder with 28 load points in simulations [7]. A customized power park employing shunt and series compensators protects sensitive loads from unbalance and distortion; PSCAD/EMTDC simulations validate these strategies [8]. Five voltage unbalance definitions (CIGRE, NEMA, IEEE, IEC) are compared to evaluate effectiveness in quantifying unbalance and mitigating its adverse impacts [9]. A distributed control using Dynamic Switching Devices (DSDs) mitigates voltage unbalance in LV systems with single-phase PVs by autonomously swapping phases based on local voltage sensitivity, minimizing Voltage Unbalance Factor (VUF) without communication or central control [10]. A study on 11/0.4 kV LV networks using MATLAB/Simulink found acceptable voltage only up to 0.5 km. For 0.8–5 km, voltage drop and unbalance exceeded limits, requiring voltage boosting devices [11]. An intelligent residential load transfer scheme mitigates voltage unbalance by shifting household

979-8-3315-5472-9/25/$31.00 ©2025 IEEE

loads between phases via a central controller and static transfer switches. MATLAB and PSCAD/EMTDC analyses confirm improved balance with dynamic phase selection using real-time loads [12]. A residential load transfer device mitigates LV unbalance by remotely swapping phases using MQTT with LoRa + 4G. An improved multi-population genetic algorithm (IMPGA) optimizes strategies, with experiments verifying reduced three-phase unbalance [13]. A static load transfer switch (SLTS) with an optimization algorithm for bipolar LVDC networks mitigates unbalance and neutral losses. EMTP simulations on a 1500 V system show real-time reconfiguration reducing loss and maintaining balanced voltages [14]. A novel voltage deviation indicator and control strategy mitigate unbalance in LV feeders with single-phase renewables and uneven loads. A three-phase inverter with optimization-based control enables asymmetric injection, with simulations confirming improved quality and reduced losses [15]. An improved d-q-o and PI controller-based Dynamic Voltage Restorer (DVR) for 11/0.4 kV networks mitigates unbalance. MATLAB/Simulink simulations showed $\pm 5\%$ correction over 0.5–5 km by injecting series compensating voltages [16]. A radial LV feeder modeled in MATLAB/Simulink analyzed voltage unbalance from uneven single-phase PV integration. Three scenarios showed VU levels of 9.87%, 7.68%, and 5.93%, exceeding the 3% IEEE 45-2002 limit, requiring PV regulation [17]. A Soft Open Point (SOP)-based control strategy mitigates unbalance in feeders by regulating power flow and injecting negative- and zero-sequence currents. MATLAB/Simulink and hardware-in-the-loop tests validate balanced voltages under unbalanced and fault conditions [18]. An optimal genetic algorithm-based SVC placement mitigates load unbalance from uneven single-phase distribution. Simulations on real feeders show optimally placed SVCs reduce voltage imbalance and losses, achieving cost-effective balancing under varying conditions [19].The paper studies three-phase unbalance in distribution networks, focusing on its impact on power losses and transformer loading. It suggests improved definitions incorporating zero-sequence unbalance, supported by empirical data from TNWDS substations. [20]. Voltage Unbalance True Definition (VUTD) is defined, based on IEEE Std. 1996 [20] and IEC Std. 61000-4-27, as:

$$\text{VUTD}_{\text{IEEE 1996}} = \left|\frac{V_-}{V_+}\right| = \left|\frac{V_{ab} + \alpha^2 V_{bc} + \alpha V_{ca}}{V_{ab} + \alpha V_{bc} + \alpha^2 V_{ca}}\right| \quad (1)$$

where V- and V+ are respectively negative and positive sequence voltages. ANSI standard for "Electric Power Systems and equipment voltage ratings" should be designed to limit the maximum VU to 3% when measured at the electric utility endpoints at no-load conditions.

II. Voltage Unbalance Definition

Voltage unbalance (VU) in a three-phase electrical system arises when the magnitudes of the phase voltages are unequal and/or the phase angles deviate from the ideal 120° separation. Accurate quantification of voltage unbalance is essential for maintaining power quality, particularly in systems with sensitive or unbalanced loads. Commonly accepted definitions are outlined below:

- Phase Voltage Unbalance Rate (PVUR) – IEEE Std. 936-1987 [20]: Defines unbalance as the ratio of the difference between the maximum and minimum phase voltages to their average:

$$PVUR_{\text{IEEE936}} = \frac{\max(V_a, V_b, V_c) - \min(V_a, V_b, V_c)}{\frac{V_a+V_b+V_c}{3}} \quad (2)$$

- Phase Voltage Unbalance Rate – IEEE Std. 112-1991 [20]: Uses the maximum deviation of each phase voltage from the average, normalized by the average of line voltages:

$$PVUR_{\text{IEEE112}} = \frac{\max(|V_a - V_{\text{avg}}|, |V_b - V_{\text{avg}}|, |V_c - V_{\text{avg}}|)}{\frac{V_{ab}+V_{bc}+V_{ca}}{3}} \quad (3)$$

where $V_{\text{avg}} = \frac{V_a+V_b+V_c}{3}$.

- Line Voltage Unbalance Rate (LVUR) – NEMA Std. MG1-1993 [20]: Defined similarly to PVUR but based on line voltages:

$$LVUR_{\text{NEMA}} = \frac{\max(|V_{ab} - V_{\text{line}}|, |V_{bc} - V_{\text{line}}|, |V_{ca} - V_{\text{line}}|)}{\frac{V_{ab}+V_{bc}+V_{ca}}{3}} \quad (4)$$

where $V_{\text{line}} = \frac{V_{ab}+V_{bc}+V_{ca}}{3}$.

- CIGRE Definition – 1986 Report [20]: Provides a non-linear voltage unbalance expression based on line voltage magnitudes:

$$VU_{\text{CIGRE}} = \sqrt{\frac{1 - \sqrt{3 - 6\beta}}{1 + \sqrt{3 - 6\beta}}} \quad (5)$$

where,

$$\beta = \frac{|V_{ab}|^4 + |V_{bc}|^4 + |V_{ca}|^4}{(|V_{ab}|^2 + |V_{bc}|^2 + |V_{ca}|^2)^2} \quad (6)$$

III. System Overview

Overall system consists of two controllers; the Center controller in the control room and the phase sequencing controller, P1, P2, P3,...., Pn at each node in the feeder and is depicted in Figure 1.

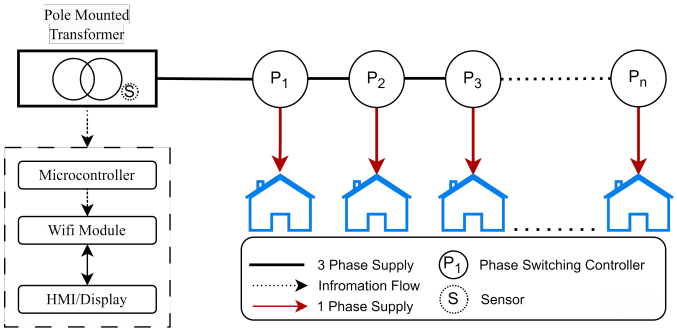


Fig. 1: Block Diagram of the Overall System

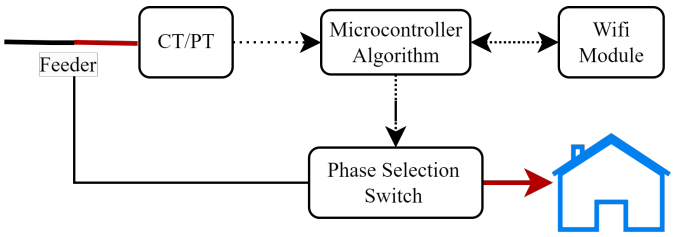


Fig. 2: Block Diagram of Phase Switching Controller (P1)

CT and PT in substation transformer sends analog signals of step-down current and voltage. This analog voltage is converted into digital by the ADC. The converted data is calculated by Arduino to find the respective voltage and current flowing at the substation. These voltages and currents are stored in my SQL database server. These data are transferred through the WIFI module to the WIFI server as shown in Figure 2. From the WIFI server, this data is stored in the database. The database is accessed by a python script.

Each phase switching controller has an Arduino that takes signals from the CT/PT to calculate current and voltage. This data is also stored in a common database, i.e., both the center controller and each phase switching controller store data in the same database. Storing of data takes place in a similar process to data from the central controller as illustrated by Figure 3.

These data are analyzed by the python script, and it calculates the voltage unbalance factor (VUF) at the distribution substation. If VUF is less than 5% or a predefined value, it locates the unbalanced phase. After locating an unbalanced phase, it sends one of the phase switching controllers (based on priority) to change the phase through the WIFI module to Arduino at the respective phase switching controller.

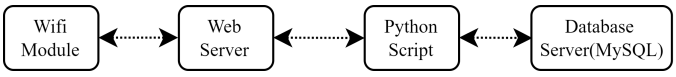


Fig. 3: Block Diagram for Communication with Web Server

Also, the operator in the control room can monitor the data on the web page. Communication between Arduino and the Database server takes 4 steps which can be best described by block diagram.

1. Arduino makes HTTP requests to the webserver.
2. The web server runs a python script.
3. Python script gets data from the HTTP request, processes the data, and then interacts with the MySQL database.
4. Python script processes the result and returns the result to Arduino via HTTP response.

IV. System Design

A. Planning and Algorithm Development

The research commenced with setting clear goals and defining methods. An algorithm was then developed to precisely outline the system's intended operation.

B. Circuit Design and Code

A detailed circuit diagram was crafted to provide a visual representation of the system, aiding in the setup of hardware components. Subsequently, Arduino code was written based on the established algorithm. The code underwent iterative adjustments throughout the project's progression.

C. Simulation and Modeling

Utilizing Proteus software, the circuit model was simulated to validate its authenticity and functionality. Additionally, Simulink was employed to construct a model of a transmission line, facilitating the examination of electrical parameters.

D. Hardware Testing and Placement

Components underwent rigorous testing on a breadboard before being integrated into a permanent configuration. The hardware setup closely mirrored the simulated design, ensuring consistency and reliability.

E. Circuit Diagram

The diagram illustrates the power flow and control mechanisms of the system, including the power source, transmission line model, load configurations, and control devices.

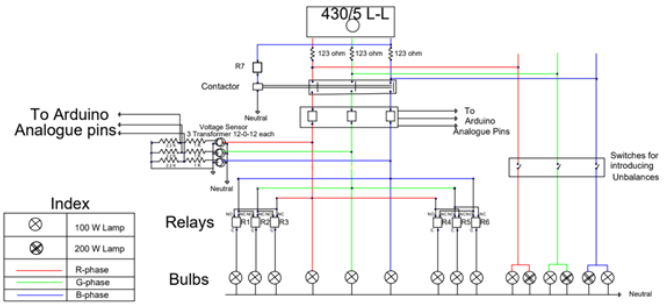


Fig. 4: Power Circuit Diagram

1) Power Circuit Diagram: Figure 4 gives an overview of the overall power circuit of the system with all the relay and load connections.

2) Control Circuit Diagram: The control circuit employs Arduino and NodeMCU to measure RMS voltage and current. Arduino controls the relay based on web server commands, while NodeMCU logs data and communicates over the internet, as shown in Figure 5.

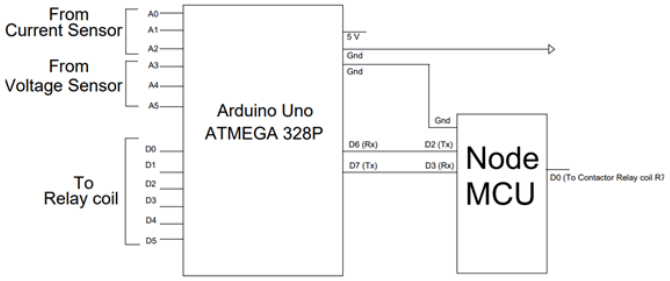


Fig. 5: Control Circuit of the System

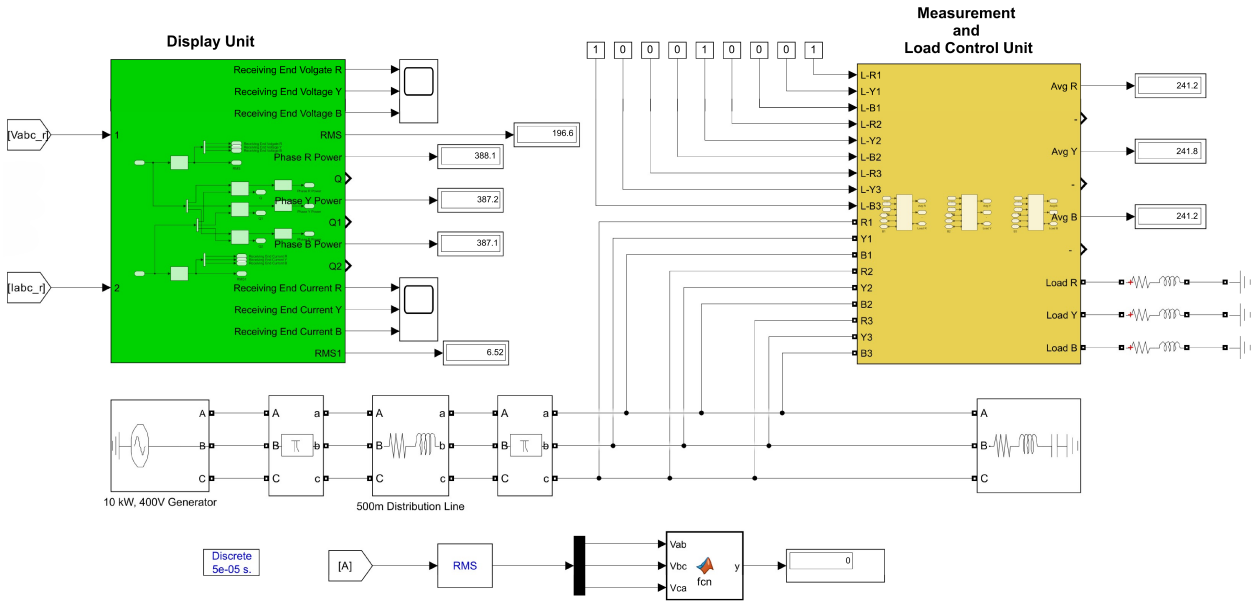


Fig. 6: Simualtion model in MATLAB

V. System Analysis and Result

A. Simulation in MATLAB

1) Unbalanced Load (VUF=6.819): The system is modeled in Simulink, where a 10 KW, 400 V generator is taken for simulation. The power is transported through a 500 m distribution line. There are a total of 4 loads. One of the loads is 3 phase Load while the other loads are a single-phase load as represented by the system modeled in simulink shown in Figure 6. The instantaneous graph of receiving end voltage with unequal phase magnitudes and deviation from the ideal 120° phase separation is shown in Figure 7. This results in a Voltage Unbalance Factor (VUF) of 6.819. The asymmetry in waveforms indicates the presence of negative and zero sequence components, which can cause increased losses, torque pulsations in motors, and reduced equipment lifespan.

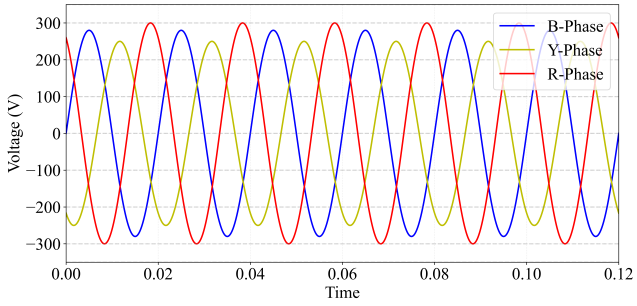


Fig. 7: Instantaneous graph of receiving end voltage at VUF=6.819

2) Balanced Load (VUF=0): Under balanced loading conditions using identical generator and transmission parameters, all four loads were configured as symmetrical three-phase elements, achieving Voltage Unbalance Factor (VUF) of 0. Figure 8 demonstrates optimal three-phase performance with uniform voltage magnitudes of approximately 283V peak across all phases and perfect sinusoidal characteristics free from harmonic distortion. The phase relationships maintain precise 120° electrical separation, confirming absence of negative and zero sequence components. This balanced operation eliminates circulating currents, minimizes transformer losses, and ensures optimal motor performance without thermal stress validating the importance of proper load distribution in maintaining power quality.

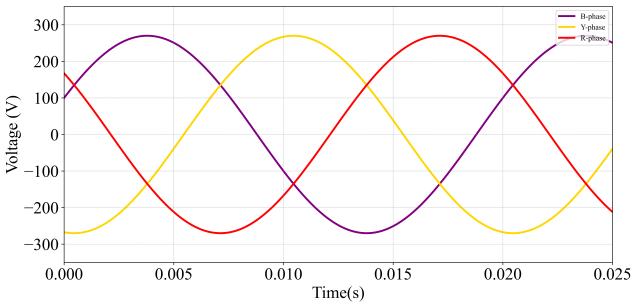


Fig. 8: Instantaneous graph of receiving end voltage at VUF=0

VI. Hardware Implementation

This follows a systematic voltage unbalance detection algorithm that continuously monitors three-phase voltage levels. The system begins by measuring voltage and current across all phases (R, Y, B) and determines the maximum and minimum voltage values.

The algorithm employs a two-tier decision structure, as shown in Figure 9:

- Primary Check: If the voltage difference between the maximum and minimum phases exceeds 15% of the rated voltage, the system proceeds to identify the specific type of unbalance.
- Secondary Classification: The system distinguishes between:
  - Double Phase Unbalance: When multiple phase combinations simultaneously exceed the 15% threshold relative to the maximum voltage.
  - Single Phase Unbalance: When only one phase shows a significant deviation.

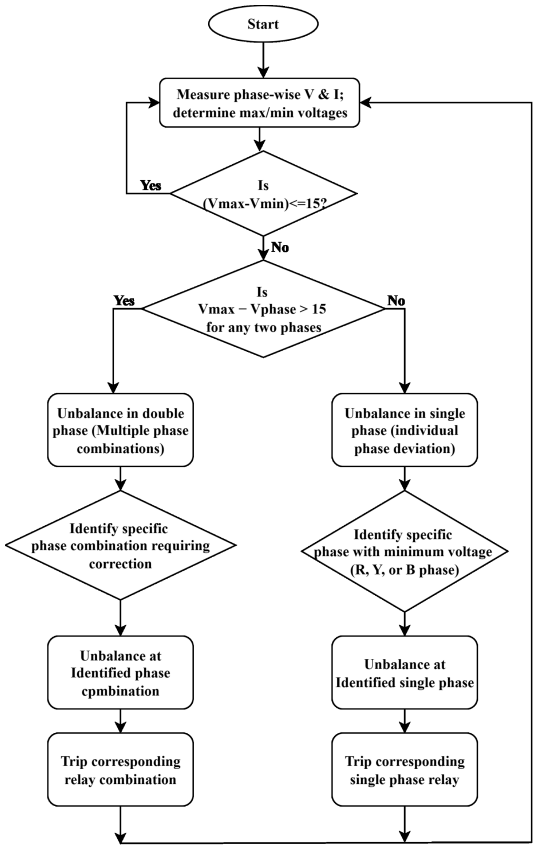


Fig. 9: Methodology of hardware implementation

Protection Action: Based on the classification, the system triggers appropriate relay combinations:

- For double phase unbalance: Activates specific relay combinations corresponding to the affected phase pairs.
- For single phase unbalance: Trips the individual phase relay associated with the minimum voltage phase.

Continuous Monitoring: If no unbalance is detected, or after corrective action, the system returns to continuous monitoring mode, ensuring real-time protection against voltage unbalance conditions.

The central controller, located at the distribution transformer, uses IoT to remotely monitor each house's power consumption and decides which houses should be switched from one phase to another. This transfer is performed using a static transfer switch that has a three-phase input and a single-phase output, providing power to each house. A short pi-model transmission line with varying loads on different phases is simulated in Simulink to analyze voltage, current, and power magnitudes, as well as waveforms, before and after phase unbalance.

The system uses an Arduino-controlled contactor to manage the power supply to a set of lamps, activated by relay R7 for remote control. Voltage and current measurements are taken for twelve 100-W and three 200-W lamps. Under balanced conditions, nine 100 W lamps are used. Unbalanced conditions are created using switches to control three 100 W and three 200 W lamps. All loads connect to the common pin of the relays. In their normally closed (NC) position, lamps connected to Relays R1 and R4 receive power from the R-phase supply, Relays R2 and R5 from the Y-phase, and Relays R3 and R6 from the B-phase. The Arduino program detects unbalances and activates the corresponding relays to redistribute the loads. For example, if the R-phase is loaded, the Arduino detects the unbalance and trips Relays R1 and R4, switching the R1 lamp to Y-phase and the R4 lamp to B-phase, thus restoring balance.

TABLE I: RYB voltage at different load conditions

Condition		R-Phase (V)	Y-Phase (V)	B-Phase (V)
Balanced		140	133	141
Unbalance	Loading at R-Phase	81.7	136.1	140.7
	Loading at Y-Phase	139.8	82.7	141.1
	Loading at RY-Phase	80	83	147
	Loading at YB-Phase	143	85	87

From Table I, it can be concluded that introducing an unbalance in any phase results in a voltage reduction for that specific phase. For instance, under balanced conditions, all phases are at close to 140 Volts. However, when an unbalance occurs in one phase, such as the R-phase, the voltage in the R-phase drops significantly. Similarly, if lamps are loaded on both the R and Y phases, the voltages in these phases decrease, while the voltage in the B-phase increases. The circuit is initially designed and simulated in Proteus, and finally, the hardware model of the system is developed and operated in the lab as shown in Figure 10.

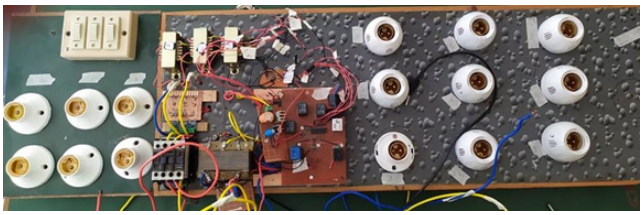


Fig. 10: Developed hardware setup

A web-based interface was developed to monitor system parameters and record measurements in real time. The home page, shown in Figure 11, provides access to RMS voltage, RMS current, and active power values, along with system status control and a data log viewer.

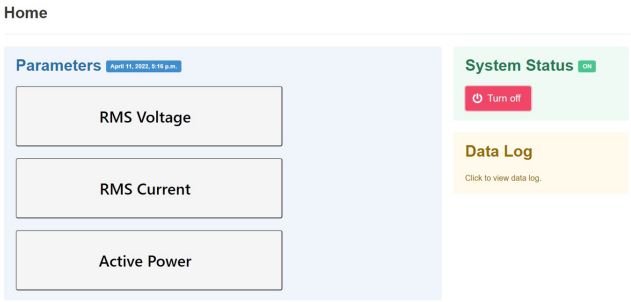


Fig. 11: HMI of web page

The data logging page Figure 12 records timestamped measurements of phase voltages, currents, and power for all phases, enabling continuous performance tracking and historical analysis of the system. This functionality assists in evaluating load behavior, diagnosing abnormalities, and validating overall system performance over time, making it an essential tool for operational decision-making.

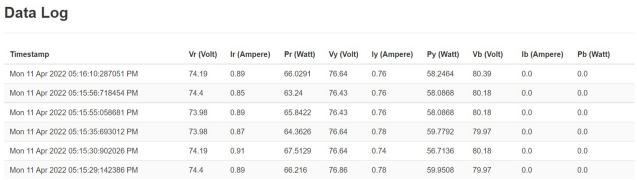


Fig. 12: Data logging

VII. Conclusion

This paper presents a distributed intelligent load transfer scheme that mitigates voltage unbalance in low-voltage distribution networks by dynamically redistributing residential loads across phases. The system utilizes an IoT-enabled central controller at the distribution transformer to monitor individual household power consumption and determine optimal load transfer strategies. Static transfer switches with three-phase input and single-phase output are deployed at each residence to enable flexible load redistribution.

MATLAB/Simulink simulations validate that the system effectively reduces voltage unbalance and improves distribution feeder performance under unbalanced loading conditions. The system delivers enhanced voltage quality, reduced network losses, and equipment protection from voltage imbalance damage.

Future work should focus on implementing this system in real-world distribution networks to evaluate its long-term reliability and performance. Further improvements could include deploying solid-state switches like Thyristors or IGTOS for faster load transfers. Additionally, addressing cybersecurity challenges for IoT communication and exploring machine learning algorithms to adapt to varying load conditions could enhance the system's effectiveness in dynamic environments.

References

[1] G. Grigoras, M. Gavrilas, B.-C. Neagu, O. Ivanov, I. Triștiu, and C. Bulac, "An efficient method to optimal phase load balancing in low voltage distribution network," in *2019 International Conference on ENERGY and ENVIRONMENT (CIEM)*, pp. 323–327, IEEE, 2019.

[2] A. Heidari-Akhijahani, A. Safdarian, and M. Lehtonen, "Unbalance mitigation by optimal placement of static transfer switches in low voltage distribution feeders," *IET Generation, Transmission & Distribution*, vol. 14, no. 20, pp. 4612–4621, 2020.

[3] B. Liu, K. Meng, Z. Y. Dong, P. K. Wong, and X. Li, "Load balancing in low-voltage distribution network via phase reconfiguration: An efficient sensitivity-based approach," *IEEE Transactions on Power Delivery*, vol. 36, no. 4, pp. 2174–2185, 2020.

[4] V. A. Jimenez, A. L. Will, and D. F. Lizondo, "Phase reassignment for load balance in low-voltage distribution networks," *International Journal of Electrical Power & Energy Systems*, vol. 137, p. 107691, 2022.

[5] N. Kongtrakul, W. Wangdee, and S. Chantaraskul, "Comprehensive review and a novel technique on voltage unbalance compensation," *IET Smart Grid*, vol. 6, no. 4, pp. 331–358, 2023.

[6] L. Alhmoud, Q. Nawafleh, and W. Merrji, "Three-phase feeder load balancing based optimized neural network using smart meters," *Symmetry*, vol. 13, no. 11, p. 2195, 2021.

[7] T.-H. Chen and J.-T. Cherng, "Optimal phase arrangement of distribution transformers connected to a primary feeder for system unbalance improvement and loss reduction using a genetic algorithm," in *Proceedings of the 21st International Conference on Power Industry Computer Applications. Connecting Utilities. PICA 99. To the Millennium and Beyond (Cat. No. 99CH36351)*, pp. 145–151, IEEE, 1999.

[8] A. Ghosh, "Performance study of two different compensating devices in a custom power park," *IEE Proceedings-Generation, Transmission and Distribution*, vol. 152, no. 4, pp. 521–528, 2005.

[9] A. K. Singh, G. K. Singh, and R. Mitra, "Some observations on definitions of voltage unbalance," in *2007 39th North American Power Symposium*, pp. 473–479, IEEE, 2007.

[10] A. Kharrazi and V. Sreeram, "Mitigation of voltage unbalance in distribution feeders using phase switching devices: A decentralized control approach based on local measurements," *IEEE Transactions on Power Delivery*, vol. 37, no. 4, pp. 2875–2885, 2021.

[11] P. T. Ogunboyo, R. Tiako, and I. Davidson, "Investigation of voltage unbalance profile in low voltage electrical distribution network with normal mode operation using matlab," *International Journal of Engineering Research in Africa*, vol. 35, pp. 60–76, 2018.

[12] F. Shahnia, A. Ghosh, G. Ledwich, and F. Zare, "Voltage unbalance improvement in low voltage residential feeders with rooftop pvs using custom power devices," *International Journal of Electrical Power & Energy Systems*, vol. 55, pp. 362–377, 2014.

[13] G. Bao and S. Ke, "Load transfer device for solving a three-phase unbalance problem under a low-voltage distribution network," *Energies*, vol. 12, no. 15, p. 2842, 2019.

[14] G.-H. Gwon, C.-H. Kim, Y.-S. Oh, C.-H. Noh, T.-H. Jung, and J. Han, "Mitigation of voltage unbalance by using static load transfer switch in bipolar low voltage dc distribution system," *International Journal of Electrical Power & Energy Systems*, vol. 90, pp. 158–167, 2017.

[15] L. Neukirchner, P. Görbe, and A. Magyar, "Voltage unbalance reduction in the domestic distribution area using asymmetric inverters," *Journal of cleaner production*, vol. 142, pp. 1710–1720, 2017.

[16] O. P. Taiwo, R. Tiako, and I. E. Davidson, "An improvement of voltage unbalance in a low voltage 11/0.4 kv electric power distribution network under 3-phase unbalance load condition using dynamic voltage restorer," in *2017 IEEE PES PowerAfrica*, pp. 126–131, 2017.

[17] P. K. AINAH and L. TONDIE, "Voltage unbalance issues with uneven distribution of single-phase pv system on lv distribution network," 2024.

[18] R. You and X. Lu, "Voltage unbalance compensation in distribution feeders using soft open points," *Journal of Modern Power Systems and Clean Energy*, vol. 10, no. 4, pp. 1000–1008, 2022.

[19] M. Talebi, A. Kazemi, A. Gholami, and M. Rajabi, "Optimal placement of static var compensators in distribution feeders for load balancing by genetic algorithm," in *18th International Conference and Exhibition on Electricity Distribution (CIRED 2005)*, pp. v5–70, IET, 2005.

[20] M. T. Bina and A. Kashefi, "Three-phase unbalance of distribution systems: Complementary analysis and experimental case study," *International Journal of Electrical Power & Energy Systems*, vol. 33, no. 4, pp. 817–826, 2011.

A Unified Energy Management System Framework for Active Distribution Networks with Hybrid Energy Storage and Decentralized Voltage Control

Ahmed Bedawy[1], Yutaka Sasaki[1], Chiraz Krifa[1], Yoshifumi Zoka[1], Naoto Yorino[1,2]
[1] Graduate School of Advanced Science and Engineering, Hiroshima University, Higashi-Hiroshima, Japan
[2] National Institute of Technology (KOSEN), Kure College, Kure, Japan
a.bedawy@ieee.org

Abstract— **High penetration of renewable energy sources (RES) and inverter-based resources (IBRs) in active distribution networks presents two major operational challenges: maintaining voltage quality and managing the variability of distributed generation. This paper proposes a unified Energy Management System (EMS) framework that brings together several established methods into one conceptual platform. The first component is a neural network-based forecasting module for photovoltaic (PV) generation and load demand, which supports a two-stage storage management strategy, day-ahead mixed-integer linear programming (MILP) scheduling, and intraday model predictive control (MPC) corrections, for the coordinated operation of battery energy storage systems (BESS) and hydrogen energy storage systems (HESS). The second component is a sensitivity-based voltage control layer, implemented using a multi-agent system (MAS) to coordinate voltage regulators and inverter reactive power in real time. While the forecasting-based storage management and the decentralized voltage control operate as separate modules in the current study, the proposed framework outlines how they could be combined in future work. Each algorithm is validated individually through simulations on benchmark distribution test feeders, demonstrating reduced voltage deviations, minimized tap changes, improved energy scheduling, and enhanced state-of-charge (SOC) and level-of-hydrogen (LOH) tracking.**

Keywords—Energy management system, voltage control, battery energy storage, hydrogen energy storage, neural network forecasting, active distribution network

I. INTRODUCTION

The rapid integration of renewable energy sources (RESs) and inverter-based resources (IBRs) into active distribution has accelerated the transition toward sustainable and decarbonized power systems. While this transformation offers environmental and economic benefits, it also introduces new operational challenges. Among these, maintaining voltage quality under fluctuating and bidirectional power flows, and managing the variability of distributed generation to ensure reliable supply-demand balancing. High photovoltaic (PV) penetration can cause significant voltage deviations and reverse power flows, while the stochastic nature of RES generation complicates supply-demand balancing and storage scheduling [1]–[3].

Energy Management Systems (EMS) have emerged as essential platforms for optimizing the operation of modern distribution networks. A robust EMS must coordinate diverse functions, including forecasting, scheduling of distributed energy resources (DERs), energy storage management, and real-time voltage regulation [4]–[7]. Recent research has demonstrated significant advances in each of these functions individually; however, their integration into a single, implementable EMS architecture remains underdeveloped, particularly in systems with high RES penetration and mixed storage technologies.

In previous works, the authors have developed and validated four complementary methods relevant to this goal:

- **A hierarchical EMS architecture** for coordinating DERs and control devices in active distribution networks[8]–[10].
- **A hybrid storage management strategy** using day-ahead mixed-integer linear programming (MILP) and intraday for coordinated operation of energy storage systems[11]–[14].
- **A neural network-based forecasting module** for PV generation and load demand, currently applied to improve storage scheduling decisions [15], [16].
- **A sensitivity-based voltage control** implemented using a multi-agent system (MAS), to coordinate voltage regulators and inverter power in a decentralized manner [17], [18].

This paper presents a conceptual unified EMS framework that brings these methods together within a single operational design for active distribution networks. While the current work validates each algorithm independently, the proposed architecture defines clear operational interfaces, such as preserving reactive power headroom for voltage control in storage scheduling and allowing real-time voltage trends to influence future dispatch plans that enable coordinated deployment in future implementations. This separation allows each layer to function independently while enabling coordinated operation through the EMS's centralized management and communication infrastructure.

The novelty of this work lies in combining:

- Decentralized MAS-based voltage regulation using both inverters and voltage regulators,
- Forecast-based hybrid BESS–HESS scheduling for long-term energy balancing, and
- A unified EMS control and communication structure that allows these functions to coexist without sacrificing real-time responsiveness.

979-8-3315-5472-9/25/$31.00 ©2025 IEEE

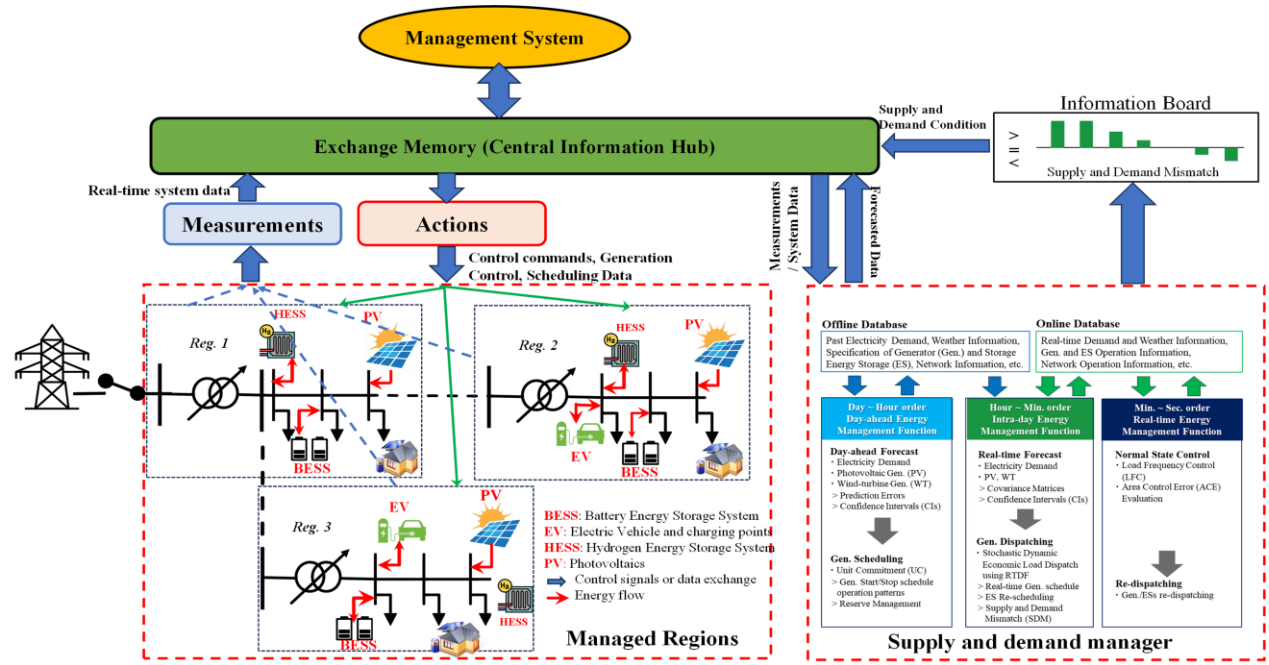


Fig. 1. Unified EMS framework with hybrid storage and decentralized voltage control for active distribution networks.

The remainder of this paper is organized as follows: Section II presents the proposed unified EMS architecture. Section III describes the methodology of the unified EMS. Section IV details mathematical formulation of the EMS functions. Section V presents individual simulation results for each function. Section VI concludes the paper and outlines the future work.

II. Proposed Unified EMS Framework

The proposed unified EMS framework integrates energy scheduling, neural network (NN)-based forecasting, energy storage management, and decentralized voltage control into a single operational platform for active distribution networks. Figure 1 illustrates the architecture, which is composed of three main functional domains: Managed Regions, the Supply and Demand Manager, and the Exchange Memory that acts as the central information hub. The framework aims to handle both long-term energy balancing and fast-response voltage regulation utilizing the NN-based forecasting techniques.

A. Exchange Memory as Central Information Hub

The Exchange Memory serves as the bidirectional information layer between the managed regions, voltage control, and the supply-demand management functions. It stores both real-time measurements from field devices and processed forecasting results, allowing each module to operate with consistent, up-to-date information. This centralized exchange eliminates the need for multiple point-to-point communication links, improving scalability and coordination.

B. Managed Regions and Distributed Assets

The network is divided into Managed Regions, each containing a mix of DERs and IBRs, including PV generation, BESS, HESS, and electric vehicle (EV) charging facilities. Energy flows (red arrows in Fig. 1) indicate active power transfer, while data/control flows (blue and green arrows) represent information exchange via the Exchange Memory. Each region also contains voltage regulation devices, such as on-load tap changers (OLTCs), step voltage regulators (SVR), and inverter-based reactive power control, operating in a decentralized manner using local measurements.

C. Supply and Demand Manager

The Supply and Demand Manager is responsible for balancing generation and consumption through a three-tier process:

1. **DA: Day-Ahead Management (Offline Database)**: Utilizes historical demand, weather, and generation data to perform NN-based forecasting of PV and load profiles. The forecasts feed MILP optimization for unit commitment, storage scheduling, and reserve allocation.
2. **ID: Intraday Management (Online Database)**: Incorporates updated real-time measurements, short-term forecasts, and system state data to run model predictive control (MPC)-based adjustments for storage dispatch and generation re-optimization.
3. **Real-Time Management**: Executes fast re-dispatch commands to generation and storage assets, including frequency and voltage-sensitive actions, ensuring supply-demand matching under rapidly changing conditions.

D. Coordination Between Energy Scheduling and Voltage Control

A key integration feature is that forecast-based supply-demand conditions from the supply and demand manager are shared through the exchange memory with local voltage control agents. This enables proactive voltage regulation, where local controllers can anticipate high PV output or low-load scenarios and adjust reactive power dispatch before voltage limits are violated. While voltage control remains decentralized for speed and resilience, this forecast integration adds a predictive element that enhances stability.

E. Communication and Implementation Considerations

The exchange memory is conceived as a logically centralized, physically distributed database to ensure both low-latency access and redundancy. Communication between the managed regions and the supply and demand manager can be implemented over standardized protocols, ensuring interoperability with existing utility infrastructure.

F. Advantages of the Framework

- **Scalability:** Supports additional DERs, storage devices, or control functions without redesigning the entire system.
- **Resilience:** Maintains voltage quality even during sudden generation or load changes.
- **Flexibility:** Allows independent operation of modules while providing a pathway for coordinated control in future implementations.

G. Scope of Current Work

In this study, each module, forecasting, storage scheduling, and voltage control, is evaluated individually to demonstrate its performance. Integration into a unified, continuously operating EMS cycle will be addressed in future work.

III. Methodology

The unified EMS framework integrates the energy management, NN-based forecasting, voltage control, and hybrid energy storage within a coordinated architecture. This section outlines the computational models, control strategies, and operational workflows for each component.

A. Neural Network (NN) Forecasting Module

The forecasting module predicts short-term PV generation and load demand using a feedforward NN with backpropagation training. Historical weather data (irradiance, temperature) and past load profiles are used as inputs. The model is trained offline and updated periodically to account for seasonal variations. Forecast horizons include:

- **DA** predictions for MILP scheduling.
- **ID** rolling forecasts for MPC corrections.

Forecast results are stored in exchange memory, where they are accessible to both the supply and demand manager and local voltage control agents for proactive decision-making.

B. Energy Management and Scheduling

The EMS scheduling function operates on two levels:

1. **DA MILP Optimization**: Minimizes total operational cost while respecting technical constraints (SOC limits, hydrogen tank capacity, generation limits). The optimization allocates charging/discharging of BESS and HESS, and dispatches PV generation.
2. **ID MPC Control**: Adjusts dispatch plans in real time using updated forecasts and measurements, minimizing deviations from scheduled targets.

The EMS ensures balanced operation between storage systems and improves renewable energy.

C. Voltage Control Strategy

Voltage regulation is performed through a decentralized, sensitivity-based control algorithm implemented in MAS. Two types of devices are coordinated:

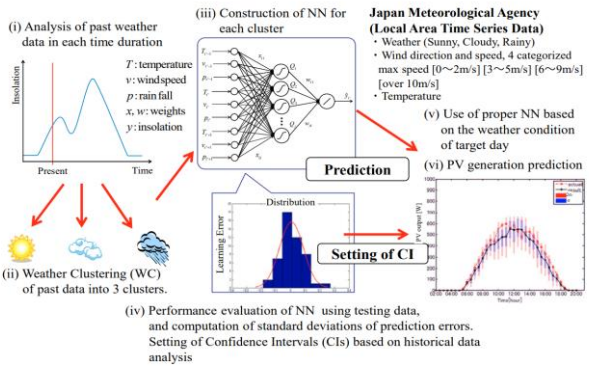


Fig. 2. The PV neural network-based forecasting.

- **Voltage Regulators (OLTCs, SVRs)**: Tap-changing transformers adjusting setpoints based on voltage sensitivity.
- **Inverter-Based Resources (IBRs)**: Provide dynamic reactive power support according to sensitivity analysis.

Local controllers receive real-time measurements from their respective managed regions and can optionally use forecast-based supply-demand conditions from the exchange memory to anticipate voltage stress events.

D. Hybrid Energy Storage Management

The system employs both BESS and HESS to achieve complementary operational objectives:

- **BESS**: Provides fast-response power balancing and supports short-term energy needs.
- **HESS**: Offers seasonal and medium-term storage, allowing surplus renewable energy to be stored as hydrogen via electrolyzer and later reconverted through fuel cells.

The hybrid configuration helps to handle both fast transient and long-duration imbalances, improving overall resilience.

E. Integration through Exchange Memory

All modules communicate via exchange memory, ensuring consistent and synchronized data exchange. This allows:

- Forecasting outputs to guide storage dispatch.
- Real-time measurements to trigger corrective actions.
- Optional data sharing between energy scheduling and voltage control for predictive voltage management.

IV. Mathematical Formulation

The unified EMS framework employs mathematical models for supply and demand management with NN-based forecasting, hybrid energy storage scheduling (BESS and HESS), and the voltage control function. Together, these ensure predictive scheduling, real-time balancing, and network stability. The following summarizes the key formulations for these functions.

A. Supply and Demand Manager with Forecasting Function

The supply and demand manager serves as the predictive core of the proposed unified EMS, ensuring accurate scheduling and balancing of resources by integrating an NN-based PV and demand forecasting. The process, developed in [16], follows a multi-step methodology that guarantees reliable DA and real-time predictions. Unlike traditional demand-supply balancing schemes that rely on real-time measurements, the supply and

demand manager integrates a forecasting function to anticipate future operating conditions and make proactive decisions.

The supply and demand manager employs the NN-based forecasting module to generate DA and ID predictions of PV output and load demand, as shown in Fig. 2. To ensure high-fidelity forecasts, raw meteorological and historical PV datasets are pre-processed before model input. The Japan Meteorological Agency (JMA) provides 3-hourly forecasts of temperature (*T*), wind speed (*v*), precipitation probability (*p*), and weather classification (sunny, cloudy, rainy, and snowy). Each class of the NN is trained by using the corresponding class of data. Specifically, if the Agency's forecasted data for the target time is sunny, the predictions are made by the NNs that are trained using the sunny cluster data. Each weather-specific network is a three-layer feedforward NN, trained with backpropagation. Inputs include triplets of (*T*, *v*, *p*) from *t'–1*, *t'*, and *t'+1* (representing temporal context), while outputs are predicted solar radiation. This structure embeds short-term weather dynamics, e.g., cloud movement, directly into the model. Prediction errors are statistically analyzed to determine ±σ and ±2σ confidence intervals representing uncertainty bounds. After that, forecasted solar radiation is converted to PV output. For ID corrections, the supply and demand manager employs Spatial Radiation Correlation Analysis between multiple PV sites. By leveraging cross-site correlations and time lags induced by cloud movement, real-time forecasts are refined from 3-hour to 5-minute resolution by interpolation and correlation adjustment.

Forecasting data is stored in exchange memory and shared with both the scheduling optimizer and the real-time voltage control agents.

B. Hybrid Storage Scheduling (BESS and HESS)

The EMS incorporates a two-stage optimization to coordinate BESS and HESS. The main objective is to minimize grid transaction cost (1), ensuring economic operation while maintaining supply-demand balance and storage reliability. The EMS optimizes the charge/discharge schedules of BESS and HESS through a two-stage framework: DA-MILP and ID-MPC. In the first stage, a MILP model is used to determine optimal charging and discharging schedules of BESS and HESS over a 48-hour horizon. Forecasted data of PV generation, load demand, and electricity prices are used as inputs.

Objective Function:

$$min \sum_{t=1}^{T} \{u_t (C_t^{buy} + C^{buy}) P_t^{buy} - (1-u_t)(C_t^{buy} + C^{buy}) P_t^{sell}\} \quad (1)$$

Where, P_t^{buy}, P_t^{sell} are the power quantities traded with the energy market. C_t^{buy}, C_t^{sell} are the electricity prices of the power transactions. C^{buy}, C^{sell} are the energy powers cost. The binary variable u_t activates energy purchase or sale operations.

The objective function (1) is subject to power balance, electrolyzer limits, fuel cell limits, level of hydrogen (LOH), BESS state of charge (SOC), and energy buy/sell limits.

Since PV and demand forecasts are uncertain, deviations from the DA plan are corrected through an MPC strategy. The MPC is executed every 15 minutes over a rolling 4-hour horizon. The MPC enhances robustness by dynamically adapting the operation of BESS and HESS based on updated forecasts and measurements. This rolling optimization ensures that short-term imbalances are corrected, reducing reliance on costly grid imports and maintaining operational flexibility.

This formulation allows the EMS to minimize costs by scheduling storage operations (charging during low-price hours and discharging during peak-price hours). By combining fast-acting BESS with high-capacity HESS, the EMS achieves both temporal flexibility (minutes to hours) and seasonal balancing capability (hours to days). This coordinated strategy minimizes costs while maintaining grid support.

C. Voltage Control Functions

To maintain voltage quality in distribution networks with high renewable-based DER and IBR penetration, the EMS incorporates sensitivity-based voltage regulation through OLTC/SVR adjustments and inverter reactive power control.

1) Voltage Regulator Control

The **objective** is to minimize voltage deviation V_{Dev}:

$$Min\, V_{Dev} = \sum_{i=1}^{n} (V_i - V_r)^2 \quad (2)$$

V_i: Voltage at node *i*.
V_r: Reference voltage.
n: Total number of monitored nodes.
subject to voltage and tap constraints:

$$V_{min} \le V_i \le V_{max}, \quad \forall i \quad (3)$$

$$T_{min} \le T_j \le T_{max}, \quad \forall j \quad (4)$$

where T_j is the tap position of voltage regulator *j*, approximated using sensitivity analysis (4).

$$\Delta \boldsymbol{V} = \frac{\partial \boldsymbol{V}}{\partial \boldsymbol{T}} \cdot \Delta \boldsymbol{T} \quad (5)$$

The sensitivity index *S* guiding optimal tap adjustments is:

$$S_j(t) = R_j \sum_{i=1}^{n} (V_i - V_r) . \frac{\partial V_i}{\partial T_j} \quad (6)$$

The sensitivity index, shown in (6), indicates the effectiveness of a unit tap change in reducing voltage deviation. A practical approach to minimizing (2) involves utilizing the sensitivity index. In *optimal control*, the regulator with the maximum sensitivity index is selected. In *suboptimal control*, each regulator acts independently if its index exceeds a threshold set by the system operator.

2) Reactive Power Control of Inverters

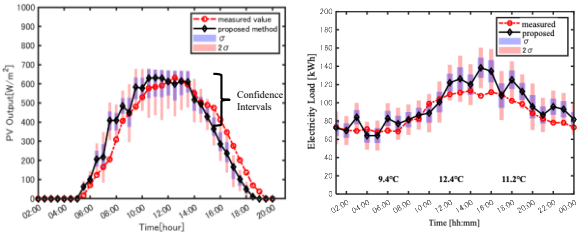
The inverter provides localized voltage support via reactive power adjustments:

$$Q_{inv} = -k(V_{inv} - V_r), \;\; k = \frac{\Delta Q}{\Delta V} \quad (7)$$

where V_{inv} is the inverter node voltage, V_r is a reference voltage, and *k* is the sensitivity factor. These control rules are subject to the inverter capacity (S_{inv}) in (8) and voltage limits (3).

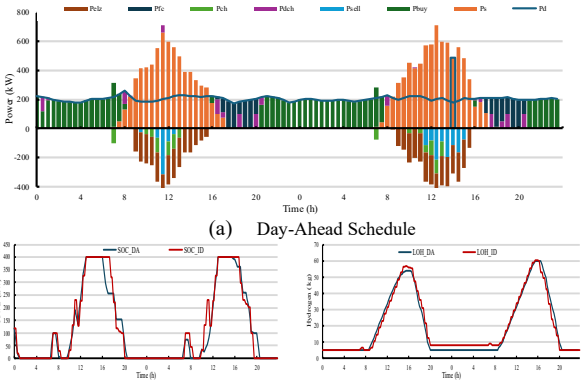
$$P_{inv}^2 + Q_{inv}^2 \le S_{inv}^2, \quad \forall inv \quad (8)$$

Reactive power adjustments follow sensitivity-based control:



(a) PV forecast (b) Load forecast

Fig. 3. PV and load NN-based forecasting results.



(a) Day-Ahead Schedule

(b) SOC adjustment (c) LOH adjustment

Fig. 4. HESS and BESS Management for Sunny Day.

$$\Delta Q_{inv,i} = k \cdot (V_{max} - V_i) \cdots if\ V_i > V_{max} \quad (9)$$

$$\Delta Q_{inv,i} = k \cdot (V_{min} - V_i) \cdots if\ V_i < V_{min} \quad (10)$$

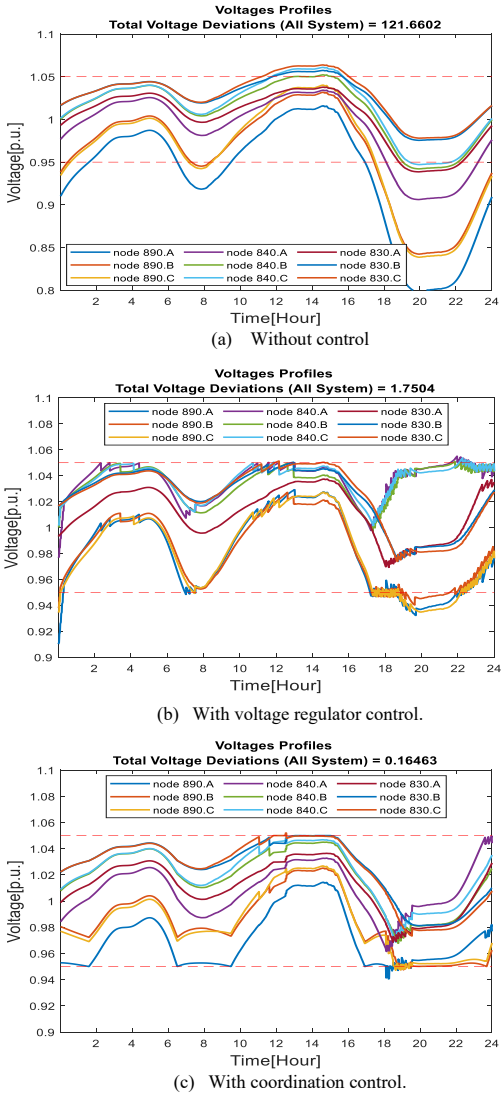
When full system Jacobian data are unavailable, local sensitivities can be estimated using historical EMS data and local voltage-reactive power measurements.

The voltage is controlled through two stages, the inverter and the OLTC/SVR. In each area, voltage regulators and inverters coordinate to achieve a common goal. The inverters manage rapid, short-term voltage fluctuations, while voltage regulators handle longer-term challenges. By setting appropriate thresholds and time delays for the regulators, the inverters are given priority to respond to persistent voltage deviations. Voltage regulators only intervene if the inverters cannot correct the voltage within the specified delay period. This proposed framework provides an effective voltage control strategy while aiming to minimize the number of tap changes.

The exchange memory ensures seamless communication between data sources, control devices, and regional subsystems. The hierarchical structure enables localized control strategies while maintaining global system optimization, ensuring efficient coordination across regions. This structured approach ensures the effective execution of voltage control functions, leveraging the EMS's hierarchical design to control voltage and optimize system performance.

V. Results and Discussion

This section presents the performance evaluation of the proposed EMS framework, which integrates (i) the supply-demand manager with forecasting, (ii) BESS-HESS coordinated management through two-stage optimization, and (iii) sensitivity-based voltage control. Results are analyzed in terms of forecasting accuracy, energy scheduling efficiency, economic benefits, and voltage regulation effectiveness.

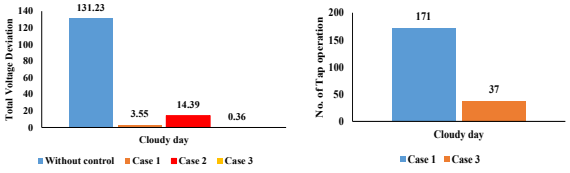


(a) Without control

(b) With voltage regulator control.

(c) With coordination control.

Fig. 5. Voltage profiles of IBR nodes for sunny day.



(a) Total voltage deviations (b) No. of Tap operations

Fig. 6. Comparison of the voltage control case studies for cloudy day.

A. Supply and Demand Forecasting Performance

Fig. 3 shows PV generation (a) and power demand (b) of a typical consumer connected to distribution system. Due to space limitations, only the DA forecast results are shown. Compared to measurement data, our proposed method achieved relatively good forecasts with a prediction error of less than 10%.

B. Energy Storage Management and Economic Evaluation

The performance of the proposed two-stage energy management strategy is evaluated using a six-bus distribution system comprising residential and industrial load profiles, PV units, HESS, and BESS. The forecasted PV generation and load demand profiles are obtained using the NN-based prediction model trained on historical data. DA scheduling is carried out using a MILP formulation to minimize grid transaction costs. ID deviations are handled using an MPC framework to adjust storage dispatch dynamically.

Fig. 4(a) presents the DA schedule for a representative sunny day. High solar availability enables the EMS to schedule extensive HESS charging alongside BESS charging during surplus generation periods. The EMS also schedules occasional grid export, thereby maximizing self-consumption and minimizing reliance on external supply. During low-solar hours, HESS and BESS discharge operations are coordinated to satisfy demand with minimal energy purchases from the grid. The integrated approach reduced transaction costs compared to DA scheduling alone.

In Fig. 4(b) and (c), the ID trajectories closely follow the DA reference while dynamically adapting to forecast errors and sudden load variations. Frequent adjustments in the SOC profile demonstrate the controller's ability to maintain BESS operation near its planned trajectory while avoiding constraint violations. Similarly, the LOH profile confirms that hydrogen production and consumption schedules are dynamically modified to correct deviations, ensuring sufficient energy availability during peak demand hours. These results highlight the role of coordinated BESS-HESS scheduling in enhancing system economics while maintaining reliability.

C. Voltage Regulation Performance

The final set of results evaluates the voltage control functions integrated within the EMS using the IEEE 34-bus distribution test feeder with several PV units acting as IBRs. Fig. 5 compares node voltage profiles for sunny PV voltage profiles under different control modes. Without control, significant deviations outside the permissible ±5% range are observed. Voltage regulator control alone mitigates large excursions but remains insufficient during periods of high PV injection. Inverter-based reactive power control improves local voltage, yet some overvoltage risks persist. The combined strategy, which integrates both regulator and inverter control, effectively maintains all voltages within operational limits, confirming the complementarity of the two actions.

The quantitative benefits are reported in Fig. 6 for a cloudy day PV profile. The combined strategy reduces maximum voltage deviations, eliminates overvoltage events, and minimizes the number of tap operations compared to regulator-only control. These results confirm that integrating inverter flexibility with traditional regulator control provides a robust solution for voltage regulation in active distribution systems.

VI. Conclusion

This paper presented a comprehensive EMS framework that integrates three key functions: (i) supply-demand management with NN-based forecasting, (ii) coordinated operation of BESS and HESS through a two-stage scheduling strategy, and (iii) real-time voltage regulation using sensitivity-based control of regulators and inverters. Unlike previous works that address these modules independently, the proposed framework consolidates them into a unified platform for active distribution networks with high renewable energy penetration.

Simulation studies demonstrated the effectiveness of each module individually. The forecasting module provided accurate DA predictions of PV generation and load demand, enabling cost-effective scheduling. The two-stage storage management strategy effectively reduced grid transaction costs while maintaining the operational constraints of both BESS and HESS. Furthermore, the integrated voltage control function ensured that node voltages were kept within permissible limits, minimizing overvoltage and under-voltage events and reducing regulator tap operations. Collectively, these results confirmed the capability of the proposed EMS framework to enhance both the economic and technical performance of active distribution networks. However, the current evaluation is limited to individual module validation rather than a fully integrated system test.

Future research will focus on evaluating the unified EMS under fully integrated scenarios, where all modules operate simultaneously on large-scale distribution networks. Additional directions include incorporating market-based demand response, exploring reinforcement learning and AI for predictive optimization, uncertainty handling, multi-agent coordination for scalability, and real-world deployment in utility-scale distribution networks.

References

[1] L. Zhang, Y. Chu, Y. Xu, and W. Guo, "Quantitative assessment and optimization strategy of flexibility supply and demand based on renewable energy high-penetration power system," *Energy Informatics*, vol. 7, no. 1, pp. 1–18, Dec. 2024, doi: 10.1186/S42162-024-00431-2/FIGURES/12.

[2] D. Sampath Kumar, O. Gandhi, C. D. Rodríguez-Gallegos, and D. Srinivasan, "Review of power system impacts at high PV penetration Part II: Potential solutions and the way forward," *Solar Energy*, vol. 210, pp. 202–221, Nov. 2020, doi: 10.1016/j.solener.2020.08.047.

[3] N. Yorino, S. Sekizaki, K. Adachi, Y. Sasaki, Y. Zoka, A. Bedawy, T. Shimizu, and K. Amimoto, "A novel design of single-phase microgrid based on non-interference core synchronous inverters for power system stabilization," *IET Generation, Transmission and Distribution*, 2022, doi: 10.1049/gtd2.12455.

[4] P. Sharma, K. K. Saini, H. D. Mathur, and P. Mishra, "Improved Energy Management Strategy for Prosumer Buildings with Renewable Energy Sources and Battery Energy Storage Systems," *Journal of Modern Power Systems and Clean Energy*, vol. 12, no. 2, pp. 381–392, Mar. 2024, doi: 10.35833/MPCE.2023.000761.

[5] P. Du, B. Huang, Z. Liu, C. Yang, and Q. Sun, "Real-Time Energy Management for Net-Zero Power Systems Based on Shared Energy Storage," *Journal of Modern Power Systems and Clean Energy*, vol. 12, no. 2, pp. 371–380, Mar. 2024, doi: 10.35833/MPCE.2023.000535.

[6] L. Angel Iturralde Carrera, J. Cesar Ramirez-Ceballos, E. Molina-Santana, F. Antonio Castillo Velasquez, C. F. Mayra, J. M. Alvarez-Alvarado, and J. Rodriguez-Resendiz, "Integration of Energy Management and Efficiency System for Buildings With Zero Carbon Emissions: A Case of Study," *IEEE Access*, vol. 12, pp. 64237–64251, 2024, doi: 10.1109/ACCESS.2024.3396816.

[7] X. Liu, T. Zhao, H. Deng, P. Wang, J. Liu, and F. Blaabjerg, "Microgrid Energy Management with Energy Storage Systems: A Review," *CSEE Journal of Power and Energy Systems*, vol. 9, no. 2, pp. 483–504, Mar. 2023, doi: 10.17775/CSEEJPES.2022.04290.

[8] Y. Sasaki, N. Takahashi, Y. Zoka, N. Yorino, A. Bedawy, C. Krifa, and S. Sekizkai, "Day-ahead Generation Scheduling with Information Gap

Decision Models," *IFAC-PapersOnLine*, vol. 58, no. 13, pp. 152–157, Jan. 2024, doi: 10.1016/J.IFACOL.2024.07.475.

[9] S. K. Mumbere, S. Matsumoto, A. Fukuhara, A. Bedawy, Y. Sasaki, Y. Zoka, N. Yorino, and Y. Tanioka, "An energy management system for disaster resilience in islanded microgrid networks," *2021 IEEE PES/IAS PowerAfrica, PowerAfrica 2021*, Aug. 2021, doi: 10.1109/POWERAFRICA52236.2021.9543282.

[10] Y. Sasaki, N. Yorino, Y. Zoka, and F. Wahyudi, "Robust stochastic dynamic load dispatch against uncertainties," *IEEE Trans Smart Grid*, vol. 9, no. 6, pp. 5535–5542, Nov. 2018, doi: 10.1109/TSG.2017.2690360.

[11] K. S. Mumbere, Y. Sasaki, N. Yorino, Y. Zoka, Y. Tanioka, and A. Bedawy, "A Resilient Prosumer Model for Microgrid Communities with High PV Penetration," *Energies (Basel)*, vol. 16, no. 2, 2023, doi: 10.3390/en16020621.

[12] K. S. Mumbere, Y. Sasaki, N. Yorino, Y. Zoka, A. Bedawy, and Y. Tanioka, "An Interconnected Prosumer Energy Management System Model for Improved Outage Resilience," *2022 IEEE PES/IAS PowerAfrica, PowerAfrica 2022*, 2022, doi: 10.1109/POWERAFRICA53997.2022.9905352.

[13] Y. Sasaki, M. Ueoka, Y. Uesugi, N. Yorino, Y. Zoka, A. Bedawy, and M. S. Kihembo, "A Robust Economic Load Dispatch in Community Microgrid Considering Incentive-based Demand Response," in *IFAC-PapersOnLine*, Jan. 2022, vol. 55, no. 9, pp. 389–394. doi: 10.1016/j.ifacol.2022.07.068.

[14] Y. Sasaki, Y. Uesugi, N. Yorino, Y. Zoka, M. K. Samuel, K. Chiraz, S. Sekizaki, and A. Bedawy, "A Robust Energy Management Controller for Microgrid Operations Considering Generator's Feasibility and Energy Trading," 2023. doi: 10.1109/ISGTEUROPE56780.2023.10408343.

[15] Y. Sasaki, M. Ueoka, N. Yorino, and Y. Zoka, "Dynamic Economic Load Dispatch Considering Incentive-based Demand Response," *2021 IEEE PES Innovative Smart Grid Technologies - Asia, ISGT Asia 2021*, 2021, doi: 10.1109/ISGTASIA49270.2021.9715596.

[16] L. Ma, N. Yorino, Y. Sasaki, Y. Zoka, K. Khorasani, and A. B. Rehiara, "A Simple and Reliable Photovoltaic Forecast for Reliable Power System Operation Control," *IFAC-PapersOnLine*, vol. 51, no. 28, pp. 161–166, Jan. 2018, doi: 10.1016/J.IFACOL.2018.11.695.

[17] A. Bedawy, N. Yorino, K. Mahmoud, and M. Lehtonen, "An Effective Coordination Strategy for Voltage Regulation in Distribution System Containing High Intermittent Photovoltaic Penetrations," *IEEE Access*, vol. 9, pp. 117404–117414, Aug. 2021.

[18] A. Bedawy, N. Yorino, K. Mahmoud, Y. Zoka, and Y. Sasaki, "Optimal Voltage Control Strategy for Voltage Regulators in Active Unbalanced Distribution Systems Using Multi-Agents," *IEEE Transactions on Power Systems*, vol. 35, no. 2, pp. 1023–1035, Sep. 2020, doi: 10.1109/TPWRS.2019.2942583.

A Robust Optimization Method for Distribution System Considering Mobile Emergency Resource under Extreme Weather

Di Yang
State Grid Shanghai Electric Power Company Pudong Power Supply Company
Shanghai, 200210 China
yang_ti@163.com

Jun Lu
State Grid Shanghai Electric Power Company Pudong Power Supply Company
Shanghai, 200210 China
354765399@qq.com

Jisheng Jia
State Grid Shanghai Electric Power Company Pudong Power Supply Company
Shanghai, 200210 China
806858536@qq.com

Mingyi Qiu
State Grid Shanghai Electric Power Company Pudong Power Supply Company
Shanghai, 200210 China
3059929248@qq.com

Lei Sun
State Grid Shanghai Electric Power Company Pudong Power Supply Company
Shanghai, 200210 China
sisi101212229@163.com

Fei Zeng
State Grid Shanghai Electric Power Company Pudong Power Supply Company
Shanghai, 200210 China
482151894@qq.com

Jiahao Sun*
School of Electrical Engineering, Shanghai University of Electric Power
Shanghai, 200090 China
sunjh443@163.com
*Corresponding author

Haijun Xing
School of Electrical Engineering, Shanghai University of Electric Power
Shanghai, 200090 China
xinghj@shiep.edu.cn

***Abstract*—To enhance distribution network resilience against extreme weather, this paper proposes a coordinated strategy synergizing Mobile Energy Storage Systems (MESS) and repair crews. A two-stage optimization framework is presented. A robust optimization model determines the optimal pre-positioning of resources, considering photovoltaic (PV) and load uncertainties at the pre-disaster prevention stage. At the post-disaster restoration stage, a multi-period dispatch model dynamically coordinates the spatiotemporal movement of MESS, including relocation and battery swapping, with the progress of repair crews to accelerate critical load restoration. The effectiveness of the algorithm is verified on the IEEE33-node distribution system.**

Keywords—Distribution network resilience, Mobile Energy Storage Systems, repair crews, extreme weather

I. INTRODUCTION

In recent years, a global trend of increasingly frequent and intense extreme weather events has emerged. For example, in September 2024, Typhoon Bebinca caused power outages in substations, transmission lines, and local distribution areas across the power grids of Zhejiang, Shanghai, and other regions. Similarly, in 2020, extreme high temperatures in California led to a surge in air conditioning loads, triggering widespread blackouts. Such events pose unprecedented impacts on power systems, particularly on distribution networks, exposing their vulnerability to sudden extreme weather phenomena.[1] As the critical link between the generation side and the user side, the stable operation of the distribution network is fundamental to the daily life of residents, industrial production, and the proper functioning of other key infrastructure[2].

The increasing frequency and severity of extreme weather events are widely considered to be closely related to global climate change. This trend necessitates a paradigm shift in power grid planning and operational strategies, moving from a traditional post-hoc, reactive response model to a proactive, preventive, and adaptive reinforcement model. Consequently, building a distribution network system with continuous adaptive capacity, structural robustness, and dynamic operational capabilities to effectively cope with frequent and far-reaching climate shocks has become a core objective for current and future development[3].

In response to different types of extreme weather disasters, scholars have conducted extensive targeted research. Regarding typhoon disaster response, reference [4] proposed a resilience enhancement strategy for urban distribution networks based on Vehicle-to-Grid (V2G) technology, which guides electric vehicles to participate in power restoration by formulating a post-disaster reverse power transmission incentive mechanism. Reference [5] considered the spatiotemporal evolution characteristics of typhoons, established a spatiotemporal characteristic matrix for distribution line failure rates, and employed a robust optimization model to determine the optimal configuration and operational strategy for mobile energy storage. From the perspective of coordinating multiple distributed resources, reference [6] proposed a two-stage power supply restoration strategy. Reference [7] introduced a resilience assessment and differentiated planning scheme for new power systems, establishing a relationship model between system load and line failure rates under high temperatures.

Research on enhancing distribution network resilience primarily focuses on three stages: pre-disturbance prevention, intra-disturbance resistance, and post-disturbance recovery. Among the various technical measures, MESS have become one of the most effective tools for improving the disaster resistance of distribution networks due to their high flexibility, rapid response speed, and relatively low deployment costs. The optimal configuration and dispatch of mobile energy storage are key issues in enhancing distribution network resilience. Reference [8] proposed a two-stage resilience enhancement strategy: in the pre-disaster prevention stage, a two-stage robust optimization model is used to solve for the configuration of mobile energy storage; in the post-disaster recovery stage, a mixed-integer second-order cone programming model is

This work is supported by Science and Technology Project of State Grid Shanghai Electric Power Co.,Ltd(No. 52092125000A).

established based on multi-source coordination. Reference [9] focused on the integrated distribution-transportation network system, proposing a multi-scenario spatiotemporal coordinated optimal dispatch strategy for mobile energy storage vehicles. For severe convective disasters, reference [10] proposed a power system resilience assessment method that considers the pre-positioning of mobile energy storage.

This paper investigates the optimal configuration and dispatch of emergency resources under extreme weather. First, addressing the needs for peak shaving and fluctuation suppression in distribution networks with high PV penetration, a multi-objective optimization model is constructed that balances economy, vulnerability, and mobile energy storage capacity to determine its size and placement. Subsequently, under fault conditions induced by extreme scenarios such as typhoons and high temperatures, a two-stage resilience enhancement model is proposed, encompassing pre-disaster initial deployment and post-disaster coordinated emergency recovery. This model accelerates the restoration of critical loads in each period through the cross-nodal migration.

II. Modeling of Fault Scenarios

The generation of fault scenarios is not the primary focus of this study; its main purpose is to provide driving data for the optimization model. In constructing the typhoon scenario, this paper utilizes the geospatial information of the lines and sets typhoon path parameters to establish the Batts model for typhoons, which is used to deduce the temporal evolution of line failure probabilities. Subsequently, through Monte Carlo sampling and the k-means clustering algorithm, a representative set of time-series fault scenarios is selected. For the extreme high-temperature scenario, this paper uses historical response samples of high temperature versus load over multiple days, combined with an equipment temperature versus failure rate model, to extract the most representative load scenarios and their corresponding failure rates.

III. Pre-Disaster Model

A. . Objective Function

In the pre-disaster stage, our primary objective is to strategically pre-position emergency resources to minimize potential operational costs. The objective function therefore minimizes the sum of deployment costs and the anticipated load shedding costs under worst-case scenarios. We formulate this as a two-stage robust optimization problem to determine the optimal number and locations of mobile energy storage units. This model explicitly accounts for the high uncertainty of PV generation and load demand inherent in extreme weather events. The detailed formulation and the C&CG solution methodology are further elaborated in Part D.

$$\min_{\alpha_{i,0}^{\mathrm{ME}},\alpha_{i,0}^{RC},\alpha_{ij}} \max_{P_i^{\mathrm{PV}},P_i^{load}} \min_{\substack{P_i^{\mathrm{Lshd}},Q_i^{\mathrm{Lshd}},P_i^{\mathrm{DG}},Q_i^{\mathrm{DG}},\\ P_{ij},Q_{ij},V_i^{\mathrm{sqr}},I_{ij}^{\mathrm{sqr}}}} \sum_{i\in\Omega_{\mathbb{N}}} (C^{\mathrm{ME}}\alpha_{i,0}^{\mathrm{ME}} + C^{RC}\alpha_{i,0}^{RC} + w_i P_i^{\mathrm{Lshd}}) \tag{1}$$

where: $\Omega_{\mathbb{N}}$ is the set of load nodes; $\alpha_{i,0}^{\mathrm{ME}}$ and $\alpha_{i,0}^{RC}$ are binary variables, representing the connection status of MESS and repair crews with node *i*. α_{ij} is the status of branch; P_i^{Lshd} and Q_i^{Lshd} are the active and reactive power of load shedding; P_i^{DG} and Q_i^{DG} are the active and reactive power output of DGs; P_{ij} and Q_{ij} are the active and reactive power flow on branch; V_i^{sqr} and I_{ij}^{sqr} are the squared nodal voltage and squared branch current; C^{ME} and C^{RC} are the costs of pre-positioning a single MESS unit and repair crew; w_i is the unit cost of load shedding at node ; P_i^{PV} is the PV output and $P_{\mathrm{i}}^{\mathrm{load}}$ is the load at node *i*.

B. First-Stage Constraints

1) Mobile Energy Resource Constraints

The number of mobile energy resources available for pre-positioning is limited, and all devices are assumed to have identical parameters. Furthermore, a maximum of one device can be pre-positioned at any given node.

$$\sum_{i\in\Omega_{\mathrm{N}}} \alpha_{i,0}^{ME} \leqslant N_{\max}^{ME}, \sum_{i\in\Omega_{\mathrm{N}}} \alpha_{i,0}^{RC} \leqslant N_{\max}^{RC} \tag{2}$$

where: $N_{\max}^{ME}$ is the upper limit on the number of MESS units in the pre-positioning stage, and $N_{\max}^{RC}$ is the upper limit on the number of repair crews. The binary nature $\alpha_{i,0}^{\mathrm{ME}}$ and $\alpha_{i,0}^{RC}$ of and restricts each node to being pre-assigned at most one MESS unit or repair crew.

2) Distribution Network Radial Topology Constraints

We employ an improved single-commodity flow model to enforce a radial network topology during restoration.

$$\sum_{ij\in\Omega_{\mathrm{B}}} \alpha_{ij} = N_{\mathrm{B}} - \sum_{i\in\Omega_{\mathrm{N}}} S_i^{\mathrm{VS}} \tag{3}$$

$$\sum_{j\in\delta(i)} F_{ij} - \sum_{k\in\gamma(i)} F_{ki} = F_i^{\mathrm{VS}} - 1 \tag{4}$$

$$-M_1 S_i^{\mathrm{VS}} \leqslant F_i^{\mathrm{VS}} \leqslant M_1 S_i^{\mathrm{VS}} \tag{5}$$

$$-M_1 \alpha_{ij} \leqslant F_{ij} \leqslant M_1 \alpha_{ij} \tag{6}$$

where: Ω_B is the set of branches; N_{B} is the total number of nodes; $\delta(i)$ and $\gamma(i)$ are the sets of child and parent nodes of node *i*; F_{ij} is the virtual power flow on branch; F_i^{VS} is the virtual power generated at node *i*; and M_1 is a large positive number.

C. Second-Stage Constraints

1) Load Shedding Constraints

Assuming a fixed power factor for the load, the load shedding power constraints can be expressed as follows:

$$0 \leqslant P_i^{\mathrm{Lshd}} \leqslant P_{i,\max}^{\mathrm{L}} \tag{7}$$

$$Q_i^{\mathrm{Lshd}} = \frac{Q_{i,\max}^{\mathrm{L}}}{P_{i,\max}^{\mathrm{L}}} P_i^{\mathrm{Lshd}} \tag{8}$$

where: $P_{i,\max}^{L}$ and $Q_{i,\max}^{L}$ are the maximum active and reactive power of the load.

2) Distributed Generation Output Constraints

The DG output constraints are as follows :

$$-\sum_{i\in M} \alpha_i^{\mathrm{DG}} P_{i,\max}^{\mathrm{DG}} \leqslant P_i^{\mathrm{DG}} \leqslant \sum_{i\in\{M,D,P\}} \alpha_i^{\mathrm{DG}} P_{i,\max}^{\mathrm{DG}} \tag{9}$$

$$-\sum_{i\in\{M,D,P\}} \alpha_i^{\mathrm{DG}} Q_{i,\max}^{\mathrm{DG}} \leqslant Q_i^{\mathrm{DG}} \leqslant \sum_{i\in\{M,D,P\}} \alpha_i^{\mathrm{DG}} Q_{i,\max}^{\mathrm{DG}} \tag{10}$$

$$\cos\varphi_{i,\min}^{\mathrm{DG}} \leqslant \frac{P_i^{\mathrm{DG}}}{\sqrt{(P_i^{\mathrm{DG}})^2 + (Q_i^{\mathrm{DG}})^2}} \leqslant \cos\varphi_{i,\max}^{\mathrm{DG}} \tag{11}$$

where: *M*, *D* and *P* are the sets of nodes with MESS, DGs, and PV; α_i^{DG} represents the connection status of each type of DG with node *i*; $P_{i,\max}^{\mathrm{DG}}$ and $Q_{i,\max}^{\mathrm{DG}}$ are the upper limits for active and reactive power output of DGs; $\cos\varphi_{i,\max}^{\mathrm{DG}}$ and $\cos\varphi_{i,\min}^{\mathrm{DG}}$ are the upper and lower limits of the DG power factor, which are identical for PV.

3) Distribution Network Operational Constraints

The power flow characteristics of the radial distribution network are modeled using the set of linear DistFlow equations, which define the relationship between nodal voltages and branch power flows.

$$\sum_{j\in\delta(i)} P_{ij} - \sum_{j\in\gamma(i)} (P_{ji} - R_{ji} I_{ji}^{\mathrm{sqr}}) = P_i^{\mathrm{DG}} - P_{i,\max}^{\mathrm{L}} + P_i^{\mathrm{Lshd}} \tag{12}$$

$$\sum_{j\in\delta(i)} Q_{ij} - \sum_{j\in\gamma(i)} (Q_{ji} - X_{ji} I_{ji}^{\mathrm{sqr}}) = Q_i^{\mathrm{DG}} - Q_{i,\max}^{\mathrm{L}} + Q_i^{\mathrm{Lshd}} \tag{13}$$

$$\begin{aligned} M_1(\alpha_{ij} - 1) \leq V_i^{\mathrm{sqr}} - V_j^{\mathrm{sqr}} - 2(R_{ij}P_{ij} + X_{ij}Q_{ij}) + \\ (R_{ij}^2 + X_{ij}^2)\frac{P_{ij}^2 + Q_{ij}^2}{V_i^{\mathrm{sqr}}} \leqslant M_1(1 - \alpha_{ij}) \end{aligned} \tag{14}$$

$$V_{i,\min}^{\mathrm{sqr}} \leqslant V_i^{\mathrm{sqr}} \leqslant V_{i,\max}^{\mathrm{sqr}} \tag{15}$$

$$0 \leqslant I_{ij}^{\mathrm{sqr}} \leqslant \alpha_{ij} I_{ij,\max}^{\mathrm{sqr}} \tag{16}$$

$$\left\| \begin{matrix} 2P_{ij} \\ 2Q_{ij} \\ I_{ij}^{sqr} - V_i^{sqr} \end{matrix} \right\|_2 \leq I_{ij}^{sqr} + V_i^{sqr} \tag{17}$$

where: R_{ij} , X_{ij} represent branch resistance and reactance; $V_{i,\max}^{\mathrm{sqr}}$, $V_{i,\min}^{\mathrm{sqr}}$ represent the upper and lower limits of node voltage squared terms; $I_{ij,\max}^{\mathrm{sqr}}$ represents the upper limit of branch current squared term.

To address the operational uncertainties stemming from PV output and load fluctuations, we incorporate robust optimization principles by defining the uncertain variables within a box uncertainty set, as shown in equation (18).

$$U = \begin{cases} P_{i,t}^{PV} = \hat{P}_{i,t}^{PV} + \Delta P_{i,t}^{PV,max} \cdot \beta_{i,t}^{PV}, \quad \forall i,t \\ P_{i,t}^{L} = \hat{P}_{i,t}^{L} + \Delta P_{i,t}^{L,max} \cdot \beta_{i,t}^{L}, \quad \forall i,t \\ -1 \leq \beta_{i,t}^{PV} \leq 1, \quad \forall i,t \\ -1 \leq \beta_{i,t}^{L} \leq 1, \quad \forall i,t \\ \sum_{i,t} |\beta_{i,t}^{PV}| \leq \Gamma^{PV} \\ \sum_{i,t} |\beta_{i,t}^{L}| \leq \Gamma^{L} \end{cases} \tag{18}$$

where: $\hat{P}_{i,t}^{PV}$ and $\hat{P}_{i,t}^{L}$ represent the predicted values of PV output and load at node *i*; ΔP_i^{pv} and ΔP_i^{L} represent the maximum fluctuation magnitudes of PV output and load; β_i^{pv} and β_i^{ℓ} are variables indicating the level of fluctuation; Γ^{pv} and Γ^{L} are uncertainty budgets.

D. Model Reconstruction

The pre-positioning problem is reformulated as a two-stage robust optimization model[11]. First-stage decisions regarding resource allocation are made before the uncertainty is realized. Subsequently, second-stage recourse actions are determined to optimize system operation and minimize costs for the worst-case scenario.

$$\min_{y\in Y} \left\{ C_{pre}(y) + \max_{u\in U} \min_{x\in X(y,u)} C_{shed}(x) \right\} \tag{19}$$

$$\begin{cases} y &= \{\beta_i, \alpha_{ij}, ...\} \\ u &= \{P_t^{PV}, P_t^{L}, ...\} \\ x &= \{P_{cut}, P_{dg}, ...\} \end{cases} \tag{20}$$

where: *y* is the vector of first-stage decision variables, including binary variables for resource allocation and network topology; *u* is the vector of uncertain variables representing a specific disaster scenario; and *x* is the vector of second-stage recourse variables for system operation. $C_{pre}(y)$ represents the first-stage pre-disaster costs, which include the deployment costs for MESS and repair crews. $C_{shed}(x)$ represents the second-stage post-disaster recourse costs, consisting of the costs from load shedding.

This min-max-min problem is computationally intractable. Therefore, the C&CG algorithm is employed for its solution, which decomposes the original problem into a Master Problem (MP) and a Subproblem (SP).

$$\eta^*(y^*) = \max_{u\in U} \min_x \left\{ C_{shed}(x) \middle| \text{ Second-stage constraints for given } y^*, u \right\} \tag{21}$$

$$\begin{cases} \min_{y,\eta} \quad C_{pre}(y) + \eta \\ \text{s. t.First-stage constraints (e. g., (3), (4))} \\ \eta \geq C_{shed}(x_k), \quad \forall k = 1,...,K \\ \text{s. t.Second-stage constraints for scenario } u_k \\ y \in Y, \eta \in \mathbb{R} \end{cases} \tag{22}$$

The MP acts as the decision-maker that proposes an optimal resource allocation, while the SP acts as an adversary that finds the worst-case scenario to challenge the allocation's robustness.

IV. Post-Disaster Model

A. Objective Function

After a disaster occurs, the distribution network loses its main grid supply. The duration of the fault is predicted based on the disaster's intensity and the number of available repair resources. The objective is to minimize the weighted sum of load shedding power during the fault period.

$$\min \sum_{t\in\Omega_T} \sum_{i\in\Omega_N} w_i P_{i,t}^{\text{Lshd}} \tag{23}$$

where: Ω_T is the set of time periods during the fault; $P_{i,t}^{\text{Lshd}}$ is the active power of load shedding at node *i* at time *t*.

B. Spatiotemporal Dynamic Dispatch Constraints for Mobile Energy Storage

$$\sum_{i\in\Omega_{\text{ME}}} \alpha_{i,j,t_0}^{\text{ME}} = \alpha_{j,0}^{\text{ME}} \tag{24}$$

$$\alpha_{i,j,t}^{\text{ME}} + \alpha_{i,k,t+\Delta t}^{\text{ME}} \leqslant 1 \quad \forall \Delta t < T_{i,j,k}^{\text{ME}}(t) + T_0^{\text{ME}} \tag{25}$$

$$\sum_{j\in\Omega_{\text{N}}} \alpha_{i,j,t}^{\text{ME}} \leqslant 1 \tag{26}$$

$$U_{i,t}^{\text{Mch}} + U_{i,t}^{\text{Mdch}} \leqslant \sum_{j\in\Omega_{\text{N}}} \alpha_{i,j,t}^{\text{ME}} \alpha_{i,j,t+1}^{\text{ME}} \tag{27}$$

$$0 \leqslant P_{i,t}^{\text{Mch}} \leqslant U_{i,t}^{\text{Mch}} P_{i,\max}^{\text{Mch}} \tag{28}$$

$$0 \leqslant P_{i,t}^{\text{Mdch}} \leqslant U_{i,t}^{\text{Mdch}} P_{i,\max}^{\text{Mdch}} \tag{29}$$

$$0 \leqslant Q_{i,t}^{\text{Mch}} \leqslant U_{i,t}^{\text{Mch}} Q_{i,\max}^{\text{Mch}} \tag{30}$$

$$0 \leqslant Q_{i,t}^{\text{Mdch}} \leqslant U_{i,t}^{\text{Mdch}} Q_{i,\max}^{\text{Mdch}} \tag{31}$$

$$E_{i,t+\Delta t}^{\text{ME}} = E_{i,t}^{\text{ME}} + P_{i,t}^{\text{Mch}} \eta_i^{\text{Mch}} \Delta t - \frac{P_{i,t}^{\text{Mdch}}}{\eta_i^{\text{Mdch}}} \Delta t \tag{32}$$

$$E_{i,\min}^{\text{ME}} \leqslant E_{i,t}^{\text{ME}} \leqslant E_{i,\max}^{\text{ME}} \tag{33}$$

where: Ω_{ME} is the set of pre-positioned MESS units; T_0 is the time the fault occurs; $U_{i,t}^{\text{Mch}}$ and $U_{i,t}^{\text{Mdch}}$ are binary flags for charging and discharging, with a value of 1 indicating the respective state; $P_{i,t}^{\text{Mch}}$ and $P_{i,t}^{\text{Mdch}}$ are the active charging and discharging powers; $Q_{i,t}^{\text{Mch}}$ and $Q_{i,t}^{\text{Mdch}}$ are the reactive charging and discharging powers; $P_{i,\max}^{\text{Mch}}$ and $P_{i,\max}^{\text{Mdch}}$ are the upper limits for active charging and discharging powers; $Q_{i,\max}^{\text{Mch}}$ and $Q_{i,\max}^{\text{Mdch}}$ are the upper limits for reactive charging and discharging powers; η_i^{Mch} and η_i^{Mdch} are the charging and discharging efficiencies; $E_{i,\max}^{\text{ME}}$ and $E_{i,\min}^{\text{ME}}$ are the upper and lower limits of the state of charge (SOC).

This paper enhances the spatiotemporal dispatch constraints of MESS by adding constraints for online battery swapping.

$$\sum_{t\in T} \sum_{i\in M} \sum_{j\in\Omega_{BS}} \gamma_{i,j,t} \leq N_{batt}^{max} \tag{34}$$

$$E_{i,t+1} = E_{i,t}(1 - \sum_{j\in\Omega_{BS}} \gamma_{i,j,t}) + E_i^{max} \sum_{j\in\Omega_{BS}} \gamma_{i,j,t} + \eta_{ch} P_{i,t}^{ch} \Delta t - \frac{P_{i,t}^{dch} \Delta t}{\eta_{dch}}, \quad \forall i, \forall t \tag{35}$$

$$u_{i,t}^{ch} + u_{i,t}^{dch} + \sum_{j\in\Omega_{BS}} \gamma_{i,j,t} \leq 1, \quad \forall i, \forall t \tag{36}$$

where: $\gamma_{i,j,t}$ is a binary variable, which equals 1 if MESS unit *i* performs a battery swap at node *j* during time period *t*; N_{batt}^{max} is the total number of available spare batteries.

C. Repair Crew Model

1) Repair Crew Spatial Constraints

$$\sum\nolimits_{m\in F\cup R\setminus\{k\}} x_{k,m,c} - \sum\nolimits_{m\in F\cup S\setminus\{k\}} x_{m,k,c} = 0, \quad \forall c \in C, k \in F \tag{37}$$

$$\begin{cases} \sum_{m\in F\cup R} x_{k,m,c} = 1, \quad \forall c \in C, k \in S \\ \sum_{k\in F\cup S} x_{m,k,c} = 1, \quad \forall c \in C, m \in R \\ \sum_{m\in F\cup S} x_{k,m,c} = 0, \quad \forall c \in C, k \in R \\ \sum_{k\in F\cup R} x_{k,m,c} = 0, \quad \forall c \in C, m \in S \end{cases}, \quad \begin{matrix} x_{k,k,c} = 0 \\ \forall c \in C \\ k \in F \cup S \cup R \end{matrix} \tag{38}$$

$$y_{k,c} = \sum_{m\in F\cup R} x_{k,m,c}, \quad \forall c \in C, k \in F \tag{39}$$

$$\sum_{c\in C} y_{k,c} \leq 1, \quad \forall k \in F \tag{40}$$

where: $x_{k,m,c}$ and $y_{k,c}$ are binary decision variables. Additionally, C is the set of dispatched repair crews, F is the set of faulted lines, and S and R are the start and end point sets for all repair crews.

2) Repair Crew Temporal Constraints

$$t_{k,c}^{arr} + t_{k,c}^{rep} \cdot y_{k,c} + t_{km,c}^{tra} - t_{m,c}^{arr} \le (1 - x_{k,m,c})H, \quad \forall k \in F \bigcup S, m \in F \bigcup R, c \in C \tag{41}$$

$$\begin{cases} \sum_{t=1}^{T_{all}} t \cdot f_{k,t} \ge \sum_{c \in C} (t_{k,c}^{arr} + t_{k,c}^{rep} y_{k,c}), \\ \sum_{t=1}^{T_{all}} t \cdot f_{k,t} < \sum_{c \in C} (t_{k,c}^{arr} + t_{k,c}^{rep} y_{k,c}) + 1, \end{cases} \quad \forall k \in F \tag{42}$$

where: $t_{k,c}^{arr}$ is the arrival time of crew c at faulted line k; $t_{k,c}^{rep}$ is the time required for crew c to repair line k; $t_{k,m,c}^{tra}$ is the travel time for crew c from line k to line m; $f_{k,t}$ is a binary variable.

In the post-disaster recovery phase, the load shedding, DG output, and distribution network operational states in each time period must still satisfy their respective constraints.

V. Case Study

This paper selects a modified IEEE 33-bus distribution system for simulation analysis, with the network structure shown in Fig.1. All computations were performed in the MATLAB R2024b environment on a personal computer with an Intel Core i7-14650HX processor and 32 GB of RAM, utilizing the Gurobi 12.0.2 solver[12]. Important user nodes are 1, 2, 6, 7, 8, 19, 20, 21, 22, 23, 24, 31, the remaining nodes are ordinary users. Parameters of DEGs and PV are listed in TABLE I. and TABLE II.

To validate the reliability of the proposed model, four different fault scenarios were established. Scenarios 1 and 2 are fault scenarios under typhoon conditions, while Scenarios 3 and 4 are fault scenarios under high-temperature conditions.

TABLE I. Parameters of DEGs

	Max Active Power/kW	Max Reactive Power/kvar	Location Nodes
DEG1, DEG2, DEG3	200	180	3, 7, 10
DEG4, DEG5	120	100	20, 28

TABLE II. Parameters of PV

	PV1	PV2	PV3	PV4	PV5
Forecasted Max Power Output/kW	120	300	360	240	180
Location Node	12	19	22	24	33

TABLE III. Faulted Branches Under Different Scenarios

Scenario	Faulted Branches
Scenario 1	13 19 20 24 25 35
Scenario 2	2 6 16 18 23
Scenario 3	1 5 8 20
Scenario 4	2 12 14 18

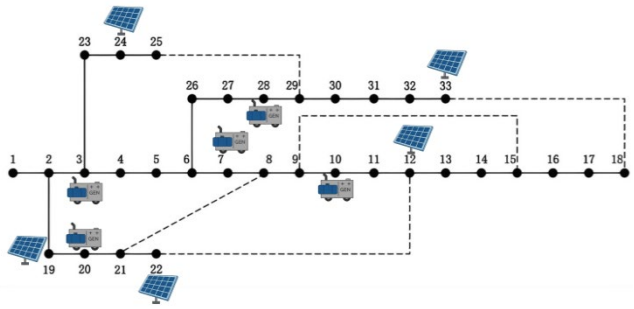


Fig. 1. Structure of the modified IEEE 33-bus distribution network

To evaluate the effectiveness of the proposed coordinated strategy, we define the following four comparative schemes: Scheme A: Coordinated pre-positioning of both resources; Scheme B: Pre-positioning of repair crews only; Scheme C: Pre-positioning of MESS units only; Scheme D: No pre-positioning.

The model is computationally efficient, with average solution times of 79.50s (pre-disaster) and 21.79s (post-disaster). Fig. 2 shows that Scheme A has the lowest total pre-disaster pre-positioning cost in all scenarios, each scenario about 28–30% lower than Scheme D. Though pre-positioning adds deployment costs, it cuts load-shedding costs overall. Using a single resource (Schemes B or C) helps only a little; coordinated deployment works much better. Optimally combining MESS for fast power supply with repair crews for line restoration uses resources most efficiently and minimizes post-disaster load loss.

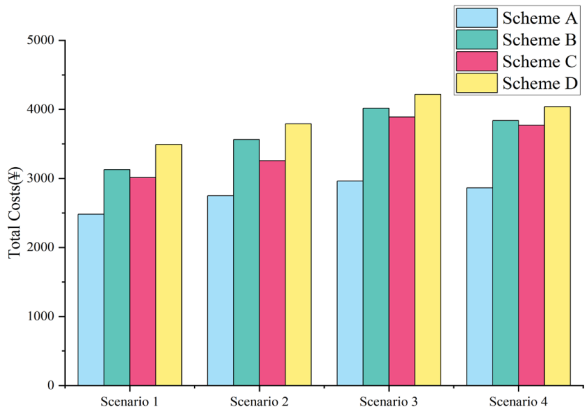


Fig. 2. Pre-deployment costs under different schemes

Fig. 3 shows that immediately after the disaster, widespread line faults cause a high load shedding ratio. As repair crews restore lines and mobile energy storage systems connect at critical nodes to provide temporary power, supply capability recovers and shedding declines. In Scenarios 3 and 4, all important loads are fully restored between hours 8 and 9, approaching zero shedding, which verifies that the proposed multi-period dispatch effectively coordinates MESS and repair crews for rapid recovery.

Fig. 4 illustrates the dynamic dispatch results for the MESS under Scenario 1.In Scenario 1, MESS pre-positioned at nodes

7 and 23 promptly connect and discharge to support critical loads, while repair crews restore lines in sequence. As the topology changes, the model repositions MESS and performs battery swaps at hours 5 and 7. With most lines repaired, main-grid supply resumes; after hour 9, MESS discharge subsides, indicating near-stable operation.

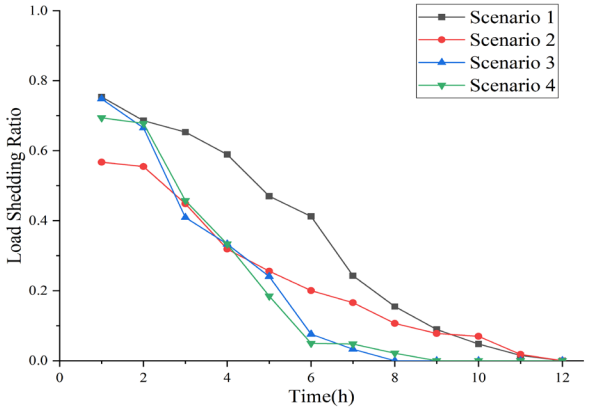


Fig. 3. Load shedding ratio under different scenarios

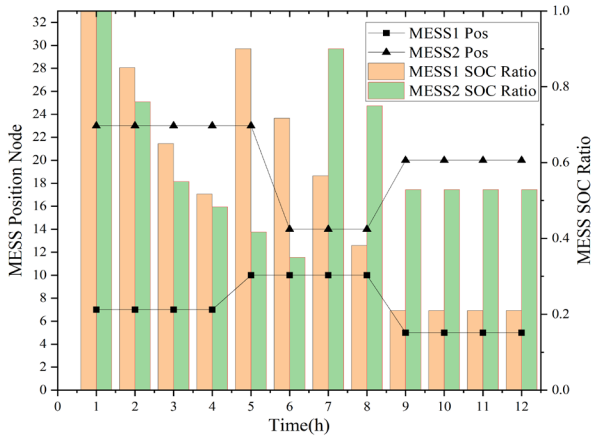


Fig. 4. Dynamic Dispatch Results for Mobile Energy Storage Systems

VI. Conclusion

To enhance distribution network resilience under extreme weather, a coordinated strategy utilizing Mobile Energy Storage Systems (MESS) and repair crews was developed, featuring a two-stage optimization model that covers pre-disaster prevention and post-disaster recovery. The main conclusions are as follows:

1)The two-stage robust optimization model effectively addresses the uncertainties of PV output and load. Compared to strategies with only a single resource or no pre-positioning, the coordinated pre-positioning scheme significantly reduces load-shedding costs under adverse scenarios and mitigates system operational risks. A rational plan also enables emergency resources to respond rapidly after a disaster, improving resource utilization efficiency.

2)The multi-period optimization model dynamically dispatches the location, charging, and swapping of MESS, coupling these actions with the progress of repair crews. This dynamic recovery mode leverages the synergistic advantages of rapid power supply from MESS and physical line repairs, which significantly reduces load-shedding losses and accelerates the restoration process for critical loads.

Future research could focus on two key areas. First, adopting more advanced time-varying vulnerability models would more accurately capture the dynamic and stochastic processes of line failures under disasters. Second, developing a co-optimization model for coupled power-transportation networks would allow for a deeper investigation into the interaction between emergency resource dispatch and grid restoration strategies, especially under conditions like traffic congestion or road damage, leading to more practical recovery plans.

Acknowledgment

This work is supported by Science and Technology Project of State Grid Shanghai Electric Power Co.,Ltd (No. 52092125000A).

References

[1] B. Chen and J. L. Liao, “Technology for improving distribution network disaster-prevention capabilities for intercurrent natural disasters areas under extreme weather: Review and prospect,” Electric Power Construction, vol. 46, no. 1, pp. 107–121, 2025.

[2] Y. Q. Wang, W. X. Li, J. Han, et al., “Review of evaluation and improvement of distribution network resilience under extreme weather,” Electric Power Construction, vol. 46, no. 3, pp. 1–15, 2025.

[3] H. P. Jia, C. W. Wu, D. N. Liu, et al., “Review on the resilience of new power systems with flexible resources under extreme weather conditions,” Electric Power Construction, early access, 2025. [Online].

[4] Q. M. Yang, G. F. Li, C. H. Bie, et al., “Vehicle-to-grid-based resilience promotion strategy for urban distribution network under typhoon disaster,” Automation of Electric Power Systems, vol. 46, no. 12, pp. 130–139, 2022.

[5] Y. S. Wang, H. Deng, X. Wang, et al., “Optimal configuration and operation strategy of mobile energy storage in distribution network considering spatial-temporal evolution of typhoon,” Automation of Electric Power Systems, vol. 46, no. 9, pp. 42–51, 2022.

[6] M. H. Li, Q. M. Yang, G. F. Li, et al., “Two-stage power supply recovery strategy of resilient distribution network based on the coordination of multiple distributed resources in typhoon scenario,” High Voltage Engineering, vol. 50, no. 1, pp. 93–104, 2024.

[7] J. Y. Luo, H. J. Xing, W. B. Quan, et al., “Resilience assessment and differentiated planning of new power systems under extreme high temperatures,” Automation of Electric Power Systems, vol. 49, no. 3, pp. 135–144, 2025.

[8] Y. H. Wang, W. X. Liu, Q. Yao, et al., “Pre-layout and dynamic scheduling strategy of mobile energy storage for resilience enhancement of distribution network,” Automation of Electric Power Systems, vol. 46, no. 15, pp. 37–45, 2022.

[9] X. Luo, Y. H. Huang, and B. Y. Xiong, “Multi-scenario spatial-temporal collaborative optimal scheduling strategy for mobile energy storage vehicles based on distribution network and road network integration,” Smart Power, vol. 51, no. 8, pp. 30–37, 66, 2023.

[10] Z. Li, J. Wang, S. F. Liu, et al., “Resilience assessment of power system considering mobile energy storage pre-arrangement under severe convective disaster,” Advanced Technology of Electrical Engineering and Energy, vol. 44, no. 2, pp. 44–54, 2025.

[11] H. Yuan, Y. Shen, and X. Xie, “A novel robust optimization method for mobile energy storage pre-positioning,” Applied Energy, vol. 379, art. no. 124810, 2025.

[12] Gurobi Optimization. [EB/OL]. [2024-9-10]. https://www.gurobi.com/

A Transformer-based Approach for Operating Situation Prediction in Distribution Networks

Li Zeke
State Grid Fujian Electric Power Co., Ltd.
Fuzhou, Fujian, China
350001
lizeke@139.com

Chen Bin
State Grid Fujian Electric Power Co., Ltd.
Fuzhou, Fujian, China
350001
13506990860@139.com

Guo Jiuyu
State Grid Fujian Electric Power Co., Ltd.
Fuzhou, Fujian, China
350001
guo_jiuyu@fj.sgcc.com.cn

Fan Haiwei
State Grid Fujian Electric Power Co., Ltd.
Fuzhou, Fujian, China
350001
fanhighway@163.com

Ding Linglong
State Grid Fujian Electric Power Co., Ltd.
Fuzhou, Fujian, China
350001
16963599@qq.com

Liu Bijing
NARI Group Corporation
State Grid Electric Power Research Institute Co., Ltd.
Nanjing, Jiangsu, China
211106
liubijing@sgepri.sgcc.com.cn

***Abstract*—Accurate perception and prediction of distribution network operating conditions are critical for enabling rapid response and risk mitigation, especially under extreme scenarios such as large-scale integration of renewable energy, sudden load fluctuations, or equipment failures. In response to the growing measurement capabilities and increasing operational complexity of active distribution networks, this paper proposes a Transformer-based method for predicting distribution network operating conditions. First, a time series forecasting model based on the Transformer architecture is constructed, leveraging the model's ability to extract features and capture both temporal patterns and correlations among key operational elements from large volumes of measurement data, thereby significantly improving prediction accuracy. Next, a heuristic optimization algorithm based on Ant Colony Optimization (ACO) is employed to explore the hyperparameter space and determine the optimal configuration for the proposed model, further enhancing its predictive performance. Finally, the feasibility and effectiveness of the proposed method are validated using the IEEE 33-bus test system.**

Keywords—Distribution Network, Transformer Model, Attention Mechanism, Ant Colony Optimization, Operational Situation Prediction

I. INTRODUCTION

In recent years, as China continues to advance toward its "carbon peak and carbon neutrality" goals, the scale of domestic clean energy generation has expanded rapidly. Among various renewable energy sources, photovoltaic (PV) power generation has become the primary form due to its flexibility in deployment, abundant solar resources, and zero emissions[1].With the increasing complexity of distribution network structures, the operational situation of active distribution networks is becoming more difficult to discern, making it necessary to carry out research on situational prediction for such networks[2][3]. In particular, under extreme operating conditions—such as voltage violations caused by renewable energy fluctuations, sudden load surges, or equipment failures—the operational risks of distribution networks increase significantly. Without effective situational awareness and forecasting mechanisms, such scenarios may lead to degraded power quality or even localized outages. Therefore, enhancing situational awareness under extreme conditions is of critical importance.

Situational awareness in distribution networks emphasizes the real-time and accurate cognition of the current system operating status, while situational prediction focuses on the prospective judgment of future system state changes. Together, they form critical components for power grid operation analysis and decision support. Currently, situational prediction methods for distribution networks can be broadly categorized into data-knowledge-driven approaches and physics-mechanism-driven approaches [4]. With the improvement in measurement capabilities in modern distribution networks, data-driven situational prediction methods have been explored in greater depth. Common deep learning models—such as Convolutional Neural Networks (CNN)[5], Long Short-Term Memory networks (LSTM)[6], and Gated Recurrent Units (GRU)[7]—have achieved significant results in situational prediction tasks. For instance[8] proposed a hierarchical method for distribution networks based on the information entropy principle and applied LSTM networks for state identification using data from Phasor Measurement Units (PMUs). In[9], an improved Deep Convolutional Generative Adversarial Network was used to augment electrical measurement data in distribution networks, while Support Vector Data Description was employed to set early warning boundaries, improving both the accuracy and speed of situational prediction. However, these studies generally fail to account for the varying importance of input features across large-scale datasets. Given the strong spatial and temporal correlations inherent in distribution networks, it is critical to fully leverage the model's ability to learn operational

The Science Project of Fujian Electric Power Company (Project No. 521300240002), titled "Research and Application of Key Technologies for Dispatch Support Systems under Extreme Conditions."

situations from diverse feature parameters and across different time segments.

To address this issue, some researchers have introduced attention mechanisms into time series prediction models to enhance their accuracy. For example,[10] used an LSTM network with an integrated attention mechanism to analyze transient stability in power systems, providing a new approach to situational prediction in distribution networks. In[11], a frequency attention module was incorporated into a temporal convolutional network to improve residual blocks and enhance wind power forecasting accuracy. Similarly,[12]applied temporal attention mechanisms to a bidirectional LSTM model for short-term load forecasting, further improving accuracy through sequence component reorganization. In[13], Particle Swarm Optimization (PSO) was used to address the hyperparameter selection challenge in LSTM models, with applications in power equipment status prediction. Although the aforementioned studies introduce attention mechanisms into the power industry, they generally lack a deeper understanding and analysis of the operational situation in active distribution networks based on these methods.

To bridge this gap, this paper proposes a Transformer-based early warning method for operational situation prediction in distribution networks. To handle high-dimensional time series data, a Transformer model integrating multi-head attention mechanisms—capturing both feature-wise and temporal attention—is developed. Additionally, a heuristic optimization algorithm based on Ant Colony Optimization (ACO) is employed to fine-tune the model's hyperparameters, effectively improving its performance. Using historical measurement data of loads and wind power, the proposed model predicts future power values of key operational elements—such as node loads and wind generation—within the distribution network. By performing power flow calculations across multiple time segments, a real-time, accurate, and intuitive representation of the network's operational situation is obtained. Finally, the effectiveness and accuracy of the proposed method are validated through comparative experiments with other forecasting models and case studies on an improved IEEE 33-bus distribution system.

II. Operational Situation Prediction Method for Distribution Networks

A. Transformer-Driven Prediction of Distribution Network Operating Conditions

Given the outstanding performance of Transformer models [14] in time series processing, this paper employs Transformer as a feature extractor to capture temporal features from sequential measurement data in distribution networks. The standard Transformer architecture is a sequence-to-sequence model composed of an encoder and a decoder. To better capture the dynamic characteristics and temporal dependencies in both source and target domain data, this study adopts only the encoder module, which maps the input into a high-dimensional domain-invariant feature matrix.

The encoder module is composed of a stack of multiple identical encoder layers. Each encoder consists of two sub-layers: a multi-head self-attention mechanism and a fully connected feedforward neural network. Residual connections are applied around each sub-layer, followed by layer normalization after the addition operation, which enhances the model's stability and representational capacity.

Before being fed into the multi-head attention mechanism, the input data X_t must first undergo positional encoding. The positional encoding is computed using sine and cosine functions, as defined by the following equations:

$$F_{PE}(F_{pos}, 2j) = \sin(F_{pos} / 10000^{\frac{2j}{d_{model}}}) \tag{1}$$

$$F_{PE}(F_{pos}, 2j+1) = \cos(F_{pos} / 10000^{\frac{2j}{d_{model}}}) \tag{2}$$

$$X_i = \text{Embedding}(X_t) + \text{F}_{PE}(X_t) \tag{3}$$

In the equations: F_{pos} denotes the position of each feature value in the time series; j represents the dimension of the positional encoding; d_{model} is the model dimension; X_i is the encoded vector.

After positional encoding, the encoded input data X_i is fed into the multi-head attention mechanism. This mechanism enables deep extraction of nonlinear features from time series data by assigning higher weights to important information and lower weights to less relevant information. As shown in Fig. 1, the multi-head attention mechanism consists of a self-attention layer, a concatenation layer, and a linear transformation layer. The self-attention layer includes a dot-product module and a softmax function module. In the multi-head attention mechanism, the positionally encoded time series is input into multiple parallel self-attention networks to compute the attention value matrix for each network.

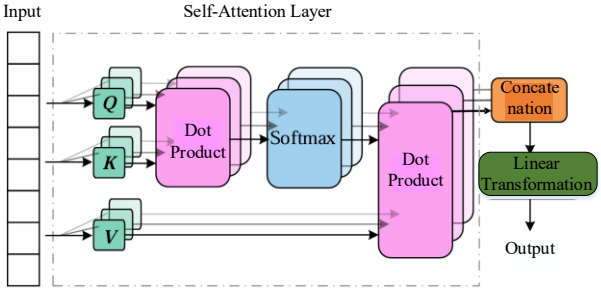


Fig. 1. Structure of multi-head attention mechanisms

B. Hyperparameter Optimization Based on Ant Colony Optimization

To enhance the adaptability of the proposed Transformer model under source-load fluctuation scenarios in active distribution networks, frequent hyperparameter adjustments are required during both training and prediction processes. To improve the efficiency and effectiveness of this tuning process, Ant Colony Optimization (ACO) is introduced for hyperparameter optimization.

In the ACO-based hyperparameter optimization process, the first step is to define the search ranges for the hyperparameters of the Transformer time series prediction model. These ranges are then integrated with the ACO algorithm to design the solution path space.

In this study, p hyperparameters of the Transformer model are optimized. The optimization process is modeled as a path consisting of p+1 nodes, from the starting point to the endpoint. Due to the varying precision levels of each hyperparameter, the number of paths between adjacent nodes differs accordingly. Thus, a total of p+1 nodes are defined, and the overall number of possible paths is determined based on the optimization precision of each hyperparameter, as shown in the following equation:

$$N_{\text{Road}} = \prod_{i=1}^{p} A_i \tag{4}$$

In the equation: N_{Road} denotes the total number of paths; A_i represents the resolution of the *i*-th hyperparameter; p is the total number of hyperparameters.

A transition probability function is constructed to model the movement of ants during the iterative search process. The transition probability represents the likelihood of an ant moving from the current hyperparameter combination to another. This probability is influenced by the pheromone concentration on the corresponding path — the higher the pheromone concentration, the greater the transition probability. The pheromone levels are dynamically updated throughout the iteration process.

$$p_{ij}^{k} = \begin{cases} \dfrac{[\tau_{ij}(t)]^{\alpha} \cdot [n_{ij}(t)]^{\beta}}{\sum_{s \in allow_k} [\tau_{is}(t)]^{\alpha} \cdot [n_{is}(t)]^{\beta}}, s \in allow_k \\ 0, s \in allow_k \end{cases} \tag{5}$$

In the equation: t denotes the iteration number; k is the index of the ant; p_{ij}^{k} represents the probability of ant k moving from path i to path j at iteration t; $\tau_{ij}(t)$ is the pheromone concentration; $n_{ij}(t)$ is the heuristic function, representing the heuristic value of path j when the ant is currently on path i; α and β are the influence factors of the pheromone concentration and the heuristic function, respectively; $allow_k$ denotes the predefined set of hyperparameter paths, with the search direction set to be unidirectional.

During the iterative process of the Ant Colony Optimization algorithm, ants traveling from the starting point to the endpoint release pheromones along their paths. Shorter paths—representing better solutions—lead to a higher pheromone concentration, reinforcing the desirability of those paths. Therefore, it is necessary to define a performance evaluation metric to represent path length.

In this study, the Root Mean Square Error (RMSE) is used as the path length metric. RMSE is particularly effective at highlighting paths with large errors, making it suitable for eliminating suboptimal hyperparameter combinations and accelerating the convergence of the optimization process.

$$n_i(t) = \frac{1}{RMSE} \tag{6}$$

The pheromone update models in Ant Colony Optimization (ACO) include the Ant-Cycle model, Ant-Quantity model, and Ant-Density model. In the Ant-Cycle model, the pheromone increment is related to the entire path represented by a specific hyperparameter combination, and the pheromone is updated only after an ant completes the full path search. In contrast, the Ant-Quantity model updates the pheromone after each step, with the increment related to the partial path explored by the ant.

In this study, the Ant-Cycle model is adopted for pheromone update control. The total amount of pheromone is set to a fixed value, and the pheromone increment depends solely on the overall path selected by the ant. After a complete path search is performed, the pheromone is updated based on the global path. Additionally, a pheromone evaporation rate is introduced to prevent premature convergence and enhance the model's ability to find the global optimal solution.

$$\tau_j(t+1) = (1-\rho)\tau_j(t) + \Delta\tau_j^{k}, 0 < \rho < 1 \tag{7}$$

$$\Delta\tau_j^{k} = \frac{Q}{RMSE} \tag{8}$$

In the equation: ρ denotes the pheromone evaporation rate; $\Delta\tau_j^{k}$ represents the pheromone increment deposited by ant k after traversing path j. This increment is determined by the ratio between a fixed global pheromone quantity Q and the path length, which is measured by the Root Mean Square Error (RMSE).

Compared with the Ant-Quantity and Ant-Density models, the Ant-Cycle model is better suited for the complex environment of hyperparameter optimization in artificial neural networks, as it helps avoid premature convergence to a locally optimal hyperparameter configuration.

C. Workflow of ACO-Based Optimization for the Transformer Model

In the Transformer model, Ant Colony Optimization (ACO) is used to optimize various hyperparameters, including the learning rate, dropout rate, and the number of units in the attention mechanism. The Root Mean Square Error (RMSE) is selected as the fitness function to guide the path search, aiming to find the optimal set of hyperparameters. The specific optimization process is illustrated in Fig. 2.

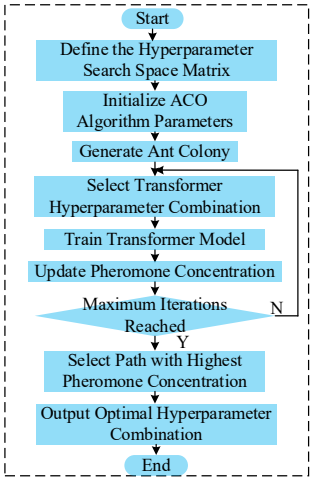


Fig. 2. Flowchart of Transformer hyper-parameter optimization search for ACO

III. Case Study Analysis

The case study is conducted using an improved IEEE 33-bus distribution system, as shown in Fig. 3. Wind turbines are connected at buses 16, 20, and 31, with rated capacities of 1000 kW, 500 kW, and 500 kW, respectively. Historical load power data and environmental data from a certain region over the past two months are selected, along with actual wind power output data from a wind farm located in a western region during the same period. All data are sampled at 15-minute intervals and have undergone outlier processing. The historical load and wind power data are normalized to per-unit values based on their respective rated capacities, and then scaled according to the rated load and wind power values of the IEEE 33-bus system. These scaled values are used as the historical input data for loads and wind power in the simulation. The proposed model is applied to predict the 24-hour ahead trend of load demand and wind power output at each node in the system. Subsequently, active distribution network power flow calculations are performed to obtain the real-time operational situation of the distribution system.

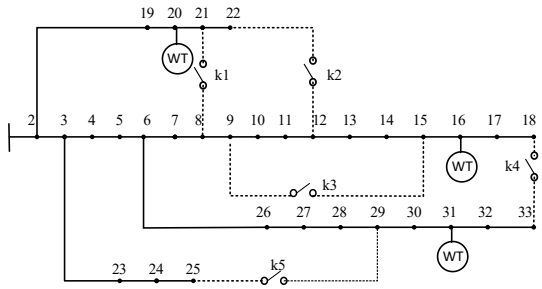


Fig. 3. Improved IEEE 33 node system

A. Analysis of Ant Colony Optimization Results

First, the optimization performance of the selected Ant Colony Optimization (ACO) algorithm on the proposed Transformer model is verified. During the hyperparameter tuning process, several key hyperparameters of the Transformer are optimized, including the number of hidden neurons in each module, learning rate, dropout rate, and batch size. To evaluate the performance, the ACO algorithm is compared with Particle Swarm Optimization (PSO) and Genetic Algorithm (GA). The optimization fitness values of the Transformer hyperparameters obtained through iterative training using the three algorithms are shown in Fig. 4.

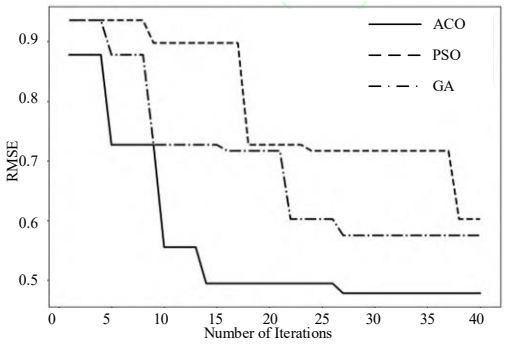


Fig. 4. Comparison of Optimal Root Mean Square Error of Optimization Algorithms

The parameters for each algorithm are configured as follows: for ACO, the number of ants k is set to 50; the pheromone importance factor α and the heuristic importance factor β are set to 2 and 4, respectively; the pheromone evaporation rate is set to 5%, the total pheromone quantity is set to 100, and the maximum number of iterations is 40. The Root Mean Square Error (RMSE) is used as the fitness function for all three algorithms (ACO, PSO, and GA).

As illustrated in Fig. 4, the ACO algorithm demonstrates superior convergence and fitness performance compared to the PSO and GA algorithms. The Genetic Algorithm (GA) tends to converge to local optima, resulting in suboptimal hyperparameter solutions with poor fitness. Although the Particle Swarm Optimization (PSO) algorithm converges quickly, it exhibits limited capability in further exploring the solution space, often leading to suboptimal solutions as well.In contrast, the Ant Colony Optimization algorithm is more effective in exploring the solution space thoroughly, making it better suited for hyperparameter optimization of the proposed Transformer model. Therefore, ACO is adopted in subsequent experiments for hyperparameter tuning.

B. Analysis of Wind Power Forecasting Results

To further validate the forecasting performance of the proposed model, a comparative analysis is conducted among the proposed method, the original Transformer model (without hyperparameter optimization), and the LSTM model. The wind power forecasting results of each model are shown in Fig. 5.

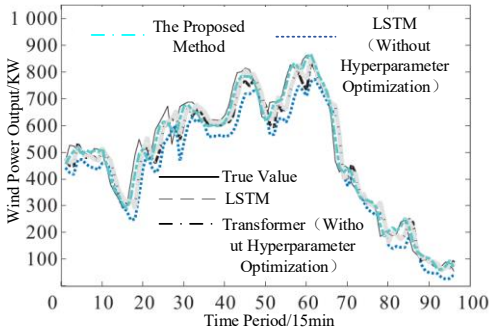


Fig. 5. WT output prediction results of different models

A numerical analysis of the results shown in Fig. 6 reveals that the proposed Transformer model significantly outperforms the baseline LSTM model, with a reduction of 66.06% in RMSE, a 71.74% reduction in MAE, and a 13.48% improvement in R^2. This indicates that the proposed Transformer architecture provides substantial improvements over the standard LSTM model. Compared with the Transformer model without hyperparameter optimization, the RMSE is reduced by 54.29%, MAE by 55.24%, and R^2 is improved by 5.54%, demonstrating the effectiveness of incorporating the ACO algorithm. Furthermore, compared with the TA-LSTM model, the proposed method achieves a 57.82% reduction in RMSE, a 58.86% reduction in MAE, and a 6.85% improvement in R^2. These results suggest that the integration of modal decomposition and intelligent optimization contributes to better adaptability and significantly enhances prediction accuracy.

C. *Analysis of Load Forecasting Results*

A similar comparative analysis is conducted for the load power at Node 9. The load forecasting results are shown in Fig. 6, and the forecasting performance metrics of each model are summarized in Table 1. The analysis of the load forecasting results leads to similar conclusions, indicating that the proposed Transformer model outperforms the other three comparative models and demonstrates superior prediction performance.

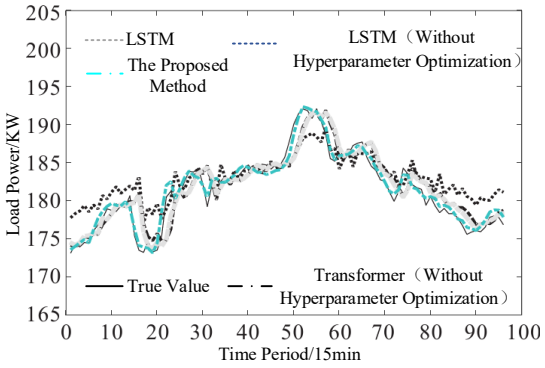


Fig. 6. Load Forecasting Results of Different Models

TABLE I. COMPARISON OF EVALUATION INDEXES OF POWER LOAD PREDICTION RESULTS

Prediction Model	e_{RMSE}/kw	e_{MAE}/kw	R^2
The Proposed Method	0.8027	0.6452	0.9712
Transformer（Without Hyperparameter Optimization）	2.0098	1.4359	0.8191
LSTM	2.1215	1.5896	0.8045
LSTM (Without Hyperparameter Optimization)	3.0115	2.4546	0.6057

IV. CONCLUSION

In this paper, an improved IEEE 33-bus distribution system is selected as a typical case study. A Transformer model optimized by the Ant Colony Optimization (ACO) algorithm is applied to forecast wind power and load in the distribution network. The main conclusions are as follows:1)The Transformer network incorporating both feature attention and temporal attention modules can effectively capture multi-scale correlations within complex measurement data. This significantly improves the accuracy of wind power and load forecasting.2)The heuristic ACO-based hyperparameter optimization algorithm shows strong adaptability to Transformer models with attention mechanisms. By constructing a path-based hyperparameter search space, the proposed method effectively tunes complex model parameters and enhances the performance of the Transformer-based situational awareness module.

REFERENCES

[1] KANG Chongqing, YAO Liangzhong .Key Scientific Issues and Theoretical Research Framework for Power Systems with High Proportion of Renewable Energy[J].Automation of Electric Power Systems,2017,41(9):2-11.

[2] GE Leijiao, LI Yuanliang, CHEN Yanbo,et al.Key Technologies of Situation Awareness and Implementation Effectiveness Evaluation in Smart Distribution Network[J].High Voltage Engineering,2021,47(7):2269-2280.

[3] HUANG Manyun, WEI Zhinong, SUN Guoqiang,et al. Review of Distribution System Situation Awareness Based on Data Mining: Modeling, Algorithms and Challenges[J]. Proceedings of the CSEE,2022,42(18):6588-6599.

[4] Fan Xixi, Wang Guoqiang, Luo He, et al. Short-term electricity load forecasting based on N-BEATS with auxiliary encoders[J]. Power System Technology, 2024, 48(04): 1612-1621.

[5] Sekhar C, Dahiya R. Robust framework based on hybrid deep learning approach for short term load forecasting of building electricity demand[J]. Energy, 2023, 268: 126660.

[6] Lv L, Wu Z, Zhang J, et al. A VMD and LSTM based hybrid model of load forecasting for power grid security[J]. IEEE Transactions on Industrial Informatics, 2021, 18(9): 6474-6482.

[7] LIN Weiqing, MIAO Xiren, XIAO Sa, et al. Forecasting method for thermal state parameters in ultra-high voltage transformers based on spatial-temporal features mining [J]. Proceedings of the CSEE, 2024, 44(3): 1649-1662.

[8] TIAN Shuxin, LI Kunpeng, WEI Shurong,et al.Security Situation Awareness Approach for Distribution Network Based on Synchronous Phasor Measurement Unit[J].Proceedings of the CSEE,2021,41(2):617-632.

[9] LI Xiaolu, CHEN Siyu, LIU Jinsong,et al.A Method for Distribution Network Operation Situation Warning Based on Data Augmentation[J/OL].Power System Technology,1-13[2024-07-18].

[10] XIE Zhijun, ZHANG Dongxia, HAN Xiaoqing,et al.Research on Transient Stability Assessment Method of Power System Based on Improved Long Short Term Memory Network[J].Power System Technology,2024,48(3):998-1010.

[11] LIU Tianhong, QIAO Xianzhu, JIAN Libin,et al.TCN Short Term Wind Power Prediction by Introducing Attention Mechanism and Parameter Optimization[J/OL].Proceedings of the CSU-EPSA,1-7[2024-07-18].

[12] YI Yanwen, LOU Suhua.Short-term Power Load Forecasting Based on Sequence Component Recombination and Temporal TCN-BiLSTM[J/OL].Proceedings Self-attention Mechanism of Improved the CSU-EPSA,1-11[2024-07-18].

[13] ZHANG Qixiao, DONG Peng, WANG Kewen,et al.Residual Service Life Prediction for Aircraft Engines Based on Bayesian Optimal Long Short-term Memory Network[J].Fire Control & Command Control,2022,47(4):85-89.

[14] Wang C, Wang Y, Ding Z, et al. A transformer-based method of multienergy load forecasting in integrated energy system[J]. IEEE Transactions on Smart Grid, 2022, 13(4): 2703-2714.

Hierarchical Multi-objective Collaborative Optimization of electric Vehicle, Station and Distribution Network Considering Reactive Power Compensation Capacity of V2G Charging Piles

Tao He
Department of Distribution Network
State Grid Shanghai Electric Power Company, Jiading Power Supply Company
Shanghai, China
hetao2005@163.com

Suwo Wu
Department of Distribution Network
State Grid Shanghai Electric Power Company, Jiading Power Supply Company
Shanghai, China
565821929@qq.com

Chongcheng Zhou
Department of Operation and Maintenance
State Grid Shanghai Electric Power Company, Jiading Power Supply Company
Shanghai, China
874391303@qq.com

Xingzhuang Li
Department of Electrical Engineering
Shanghai University of Electric Power
Shanghai, China
1169063614@qq.com

Aiqing Yu
Department of Electrical Engineering
Shanghai University of Electric Power
Shanghai, China
yuaiqing@shiep.edu.cn

***Abstract*—In response to the voltage fluctuation challenges induced by the high integration of electric vehicles (EVs) into power grids, this research presents a two-tier collaborative control strategy for charging stations. The strategy leverages the surplus capacity of vehicle-to-grid (V2G)-capable charging piles to achieve reactive power demand response. By constructing a residual capacity model of charging piles considering spatiotemporal coupling characteristics, a two-stage optimization framework is developed to achieve coordinated optimization between active regulation of charging loads and reactive power demand response. This approach aims to enhance the capacity utilization rate of charging facilities while ensuring grid voltage quality. Simulation results demonstrate that the proposed model not only achieves optimal charging costs for EVs within charging stations but also significantly improves the capacity utilization efficiency of charging infrastructure, ultimately achieving overall optimal voltage quality at the grid nodes where charging stations are connected.**

Keywords—V2G, charging piles, EV Charging Station, Reactive Power Compensation, voltage quality

I. INTRODUCTION

Against the backdrop of the "dual carbon" goals, the popularization of EVs has driven the low-carbon transformation in the transportation sector. Projections indicate that by 2030, the global electric vehicle (EV) fleet will attain 140 million units, accompanied by a charging demand of 550 TWh [1]. To address this charging requirement, China is advancing the deployment of charging infrastructure at an accelerated pace, with the number of charging piles anticipated to reach 3.263 million by 2026 [2]. However, current charging facilities generally face the challenge of low comprehensive utilization efficiency, and there is an urgent need to tap into their available potential[3]. Among them, V2G charging piles can not only optimize the operation of the distribution network at the end of feeders but also improve the capacity utilization rate of charging piles, thus showing considerable application prospects.

The reactive power compensation capacity of charging piles has been extensively validated by numerous studies. In [4], a comprehensive review is conducted on diverse power electronic conversion topologies of single-phase charging piles, accompanied by an in-depth analysis of the reactive power compensation performance of chargers under these respective topologies. Meanwhile, [5] delves into the power electronic topologies of two representative three-phase EV chargers, both featuring bidirectional charging and discharging capabilities. From a practical application perspective, [6] conducts an intensive study on the reactive power exchange between end-users and power electronic transformers within the power grid, exploring its implications for the voltage profile of the distribution network. Drawing inspiration from the Swiss power grid, [7] formulates a centralized and computationally feasible control strategy grounded in optimal power flow theory. This strategy not only enables the optimization of real-time operation

The paper is supported by Research on Multi-Objective Optimal Operation and Control Technology of V2G Charging Piles with Power Quality Governance Function (52093124000A).

979-8-3315-5472-9/25/$31.00 ©2025 IEEE

in active distribution networks but also integrates voltage support as an ancillary service for the transmission network.

In recent years, domestic and international academic communities have conducted systematic investigations into the optimal dispatching of reactive power compensation for charging pile clusters. [8] considers the charging demand of vehicles, calculates the output power of charging piles through a model predictive control algorithm, and then each charging station shares power and voltage prediction data to realize coordinated control, ultimately optimizing the voltage quality of the charging station nodes in the distribution network. [9]puts forward a V2G reactive power compensation application mode under the hierarchical scheduling of grid and operator, which cooperates with orderly charging to utilize the remaining capacity of charging piles for reactive power-voltage compensation of the power grid. [10]puts forward a V2G reactive power scheduling strategy that combines the non-dominated sorting genetic algorithm and the local optimization algorithm with global objectives, aiming at optimizing load fluctuation, charging cost, and voltage quality. However, in the above studies, the active power interaction between charging piles and the power grid is unidirectional, and the charging power is a fixed value, which fails to give full play to the bidirectional power transmission function of V2G charging piles and the adjustability of charging power.

Based on the above analysis, a hierarchical multi-objective optimization model for vehicle-station-grid considering the reactive power compensation capacity of V2G charging piles is constructed. The upper layer realizes the goal of cost minimization through "flexible scheduling of bidirectional power under time-varying electricity prices", and the lower layer achieves the goal of minimizing voltage deviation through "cluster reactive power coordinated compensation with dynamic coupling of active and reactive power". The hierarchical multi-objective optimization model forms a new mechanism of "charging service + power grid support" coordinated optimization, which improves the operational economy of charging stations and the stability of the distribution network.

II. Charging Load Characteristics and Principle of Reactive Power Compensation for Charging Piles

A. EVs Charging Demand Generation

The spatial and temporal distribution of EV charging loads is influenced by vehicle owners' behavioral characteristics, with distinct travel patterns and charging habits observed among different types of EV owners. Simulations utilize the initial SOC measurements documented in BMW China's MINI E field trial cohort[11]. The initial charging SOC data follows a normal distribution, as shown in Equation (1):

$$f(x)=\frac{1}{\sigma\sqrt{2\pi}}\exp(-\frac{(x-\mu)^2}{2\sigma^2}) \tag{1}$$

Where the values of μ and σ are 0.35 and 0.052 respectively. In addition, the range of initial charging SOC in this paper is set to 0.2~0.5.

When charging, EV users will select a desired SOC that can both meet their travel needs and be beneficial to battery health. Combined with the above-mentioned initial charging SOC, the charging demand of EVs can be calculated, as shown in Equation (2):

$$\Delta Q_{\max}=(SOC_e-SOC_0)Q \tag{2}$$

Where SOC_e is the desired SOC, set to 0.95; SOC_0 is the initial charging SOC; Q is the capacity of the battery pack in the EV.

B. Principle of Reactive Power Compensation for Charging Piles

At present, the active-reactive power operating limit domain of intelligent charging piles capable of bidirectional four-quadrant charging is shown in Fig. 1.

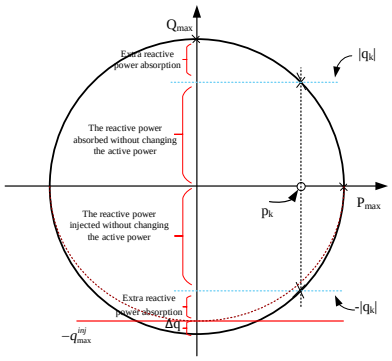


Fig. 1. Active-reactive power operating limit domain of the charging pile

As can be seen from the figure, V2G charging piles can operate in four quadrants. When an EV is connected to an intelligent charging pile for charging, A bidirectional flow of active and reactive power exists between the charging pile and the power grid, while only active power flows between the EV's power battery and the charging pile. Therefore, the reactive power regulation of the charging pile will not directly affect the service life of the EV's power battery[12]. Based on the above analysis, the V2G charging piles in this paper mainly work in the third and fourth quadrants.

The power transmission capacity of the charging pile is limited by its inherent capacity. This is based on the conventional bidirectional four-quadrant charging topology utilized in intelligent charging piles, [13] has further derived the active-reactive power constraints for the operation of intelligent charging piles:

$$\begin{cases} p^2+q^2\le S^2, & q\ge 0 \\ \left(p^2+q^2\right)\cdot\left(1-\dfrac{\omega L_c}{V_s^2}\cdot q\right)^2\le S_{\max}^2, & q<0 \end{cases} \tag{3}$$

To meet the capacitor requirements, the above capacity constraints indicate that the reactive power operation of the charging pile is asymmetric. Considering special cases, when the charging pile does not perform active charging (i.e., p=0), the reactive power injected into the power grid reaches the maximum:

$$q_{\max}^{\text{inj}} = \frac{\sqrt{1+4\cdot\frac{\omega L_c}{V_s^2}\cdot S_{\max}} - 1}{2\cdot\frac{\omega L_c}{V_s^2}} \tag{4}$$

Therefore, when the V2G charging pile is in an interactive state with the power grid, its reactive power constraints are as follows:

$$-q_{\max}^{\text{inj}} \le q \le S_{\max} \tag{5}$$

III. A Hierarchical Multi-Objective Model of Vehicle, Station and Grid Based on V2G Technology

The hierarchical dispatching architecture of vehicle-station-grid based on reactive power compensation of V2G charging piles is shown in Fig. 2. EV users send charging information to the charging station, which integrates the information and optimizes the charging power under the premise of meeting the charging demand. Then, the remaining reactive power capacity is calculated based on the active power and sent to the power grid department. The power grid department analyzes the voltage situation through power flow calculation, and issues regulation instructions to the charging station in combination with reactive power optimization strategies. After receiving the instructions, the charging station allocates reactive power demands and regulates V2G charging piles to perform reactive power compensation for the power grid. This method can achieve dual optimization of charging costs and power grid voltage quality.

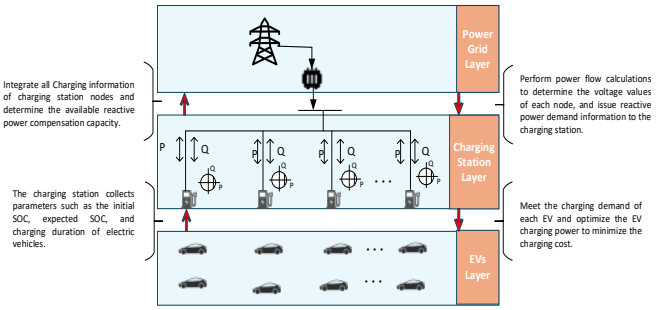


Fig. 2. Hierarchical Dispatching Architecture of Vehicle, Station and Grid Based on Reactive Power Compensation of V2G Charging Piles

Due to the small capacity of a single charging pile, it is necessary to aggregate the reactive power of multiple charging piles to form a resource cluster with large capacity and long duration. By controlling the charging piles in the charging station to achieve aggregated response and converge the reactive power response capacity of each charging pile, the voltage quality of the distribution network can be effectively optimized.

A. Upper-Level Optimization Model

Before solving the upper-level model, EVs are first categorized using a grouping model in[14]. This allows the upper-level optimization model to utilize smaller-scale grouped samples for modeling, effectively reducing the dimensionality of decision variables and the computational effort required for model solving. The upper-level optimization model aims to minimize the charging cost of EVs in the charging stations within the distribution network area, and its objective function is as follows:

$$\min f = \sum_{i=1}^{N}\sum_{t=1}^{n} e_t^{dt} p_{ti} \Delta t \tag{6}$$

Where N is the sample size of each group of EVs; n is the number of uniform time intervals divided from period T; Δt is the time interval; e_t^{dt} is the electricity purchase price in time period t; p_{ti} is the charging power of the i-th EV in time period t.

The constraints that the upper-level optimization model needs to satisfy are as follows:

a) EV charging power constraint:

$$-S_{\max} < p_{ti} \le S_{\max} \tag{7}$$

Where $S_{\max}$ is the maximum capacity of the charging pile.

b) EV charging energy constraint:

$$\sum_{i=1}^{N}\sum_{t=1}^{n} p_{ti}\Delta t - \Delta Q_i = 0 \tag{8}$$

Where ΔQ_i is the charging demand of the i-th EV.

c) Power output constraints.:

$$\begin{cases} \sum_{t=1}^{n}\sum_{i=1}^{N} P_{ti} - p_{\text{ST}}^{\text{A}}(t) \le 0 \\ P_{\text{ST}}^{\text{A}}(t) = \dfrac{\sum_{i=1}^{N}\Delta Q_i}{\Delta Q}(P_{\text{ST}}^{\max}(t) - P_L(t)) \end{cases} \tag{9}$$

Where $P_{\text{ST}}^{\text{A}}(t)$ is the maximum power output allocated to the EV group in time period t; ΔQ is the total charging demand of the EV cluster in the charging station; $P_{\text{ST}}^{\max}$ is the maximum active power output of the transformer; $P_L(t)$ is the conventional load in time period t.

B. Lower-Level Optimization Model

1) Lower-Level Optimization Objective Function

The main purpose of the lower-level optimization model is to minimize the overall voltage deviation at the connection node of the charging station within the distribution network area. For any charging station, the control objective is to minimize the overall voltage deviation at the distribution network node connected to the charging station in each time period, and its objective function is as follows:

$$\min f_2 = \sum_{j=1}^{m}(V_j^{EVC} - 1)^2 \tag{10}$$

Where m is the total number of charging stations built in the distribution network, and V_j^{EVC} is the voltage of charging station j in time period t.

2) State equation of the charging station node voltage

EVs charging stations are built at distribution network nodes. When the active power and reactive power of an EV charging station change, they will affect the voltage of the distribution network node, and the voltage will change accordingly. Therefore, it is necessary to establish a state equation for the distributed joint control of active and reactive power in EVs charging stations to predict the changes in the voltage of charging station nodes when active power and reactive power change. For any charging station j, its state equation is as follows:

$$\Delta V(t) = S_P \bullet \Delta P(t) + S_Q \bullet \Delta Q(t) \tag{11}$$

$$\Delta V(t) = \begin{bmatrix} V_1^{EVC}(t) - V_1(t) \\ \vdots \\ V_m^{EVC}(t) - V_m(t) \end{bmatrix} \tag{12}$$

$$\Delta P(t) = \begin{bmatrix} P_1^{EVC}(t) \\ \vdots \\ P_m^{EVC}(t) \end{bmatrix} \tag{13}$$

$$\Delta Q(t) = \begin{bmatrix} Q_1^{EVC}(t) \\ \vdots \\ Q_m^{EVC}(t) \end{bmatrix} \tag{14}$$

$$P_j^{EVC}(t) = \sum_{i=1}^{n} P_j^i(t) \tag{15}$$

$$Q_j^{EVC}(t) = \sum_{i=1}^{n} Q_j^i(t) \tag{16}$$

Where $\Delta V(t)$ is the increment of the voltage at the node where each charging station is located in the t-th time period; S_P and S_Q are the sensitivity matrices of node voltage with respect to active and reactive power increments, respectively; $\Delta P(t)$ and $\Delta Q(t)$ are the changes in active power and reactive power of charging station j at time t; $V_j^{EVC}(t)$ and $V_j(t)$ are the voltage at the node where charging station j is located in the t-th time period and the voltage at that node when no charging station is built, respectively; $P_j^{EVC}(t)$ and $Q_j^{EVC}(t)$ are the sum of the active power of each charging pile in charging station j and the sum of the reactive power compensated by each charging pile to the power grid in the t-th time period, respectively.

3) Constraints of the Lower-Level Optimization Model

The goal of the lower-level optimization model is to optimize the voltage quality of the node where the charging station performs reactive power compensation to the distribution network. It is subject to the constraints of the charging station's voltage and reactive power capacity as follows:

$$V_{j,\min}^{EVC} \le V_j^{EVC} \le V_{j,\max}^{EVC} \tag{17}$$

$$0 \le Q_j^{EVC}(t) \leqslant Q_{j,\max}^{EVC}(t) \tag{18}$$

$$Q_{j,\max}^{EVC}(t) = \sum_{i=1}^{N_j} \left(\sqrt{\left(S_j^{\max,i}\right)^2 - \left[P_j^i(t)\right]^2} - \Delta q_s \right) \tag{19}$$

Where $V_{j,\min}^{EVC}$ and $V_{j,\max}^{EVC}$ are the minimum and maximum voltages of the node where charging station j is located, respectively; $Q_{j,\max}^{EVC}(t)$ is the remaining capacity of charging station j, which is also the maximum reactive power capacity that charging station j can compensate to the distribution network; N_j is the number of charging piles in charging station j; $S_j^{\max,i}$ is the rated capacity of charging pile i in charging station j; $P_j^i(t)$ is the active power of charging pile k in charging station j during time period t; Δq_s is the reactive power loss of the charging pile during reactive power compensation.

IV. Simulation and Analysis

A. Simulation Parameter Settings

This paper uses the IEEE 33-bus system as a case study to simulate the proposed hierarchical multi-objective optimization method for charging stations considering the reactive power demand response of V2G charging piles. The grid topology is shown in Fig. 3. In the figure, the nodes marked with boxes are the access nodes of the charging stations. The base power of the IEEE 33-bus grid is set to 100 MVA, the base voltage is 12.66 kV, and node 1 is set as the slack node; the capacity of each charging station's distribution transformer is 600 kV·A, with a power factor of 0.9.

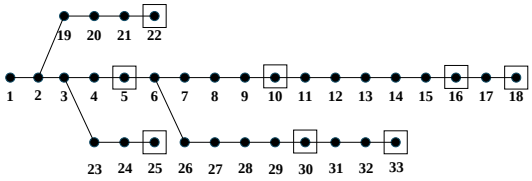


Fig. 3. IEEE 33-bus power grid topology

The parameter settings of the charging station are as follows: Each charging station is equipped with 96 charging piles, and each pile has a rated capacity of 10 kVA; the optimization period is from 9:00 to 18:00; the battery capacity of EVs is 30 kW·h. Each charging station has a transformer with a capacity of 600 kV·A and a power factor of 0.9; it is assumed that the charging station is a campus charging station, with fixed charging time.

B. The Optimization Effect of Charging Cost

By solving the upper-level optimization model, the charging curve of EVs under the optimized charging mode adopted in this paper can be obtained, as shown in Fig. 4.

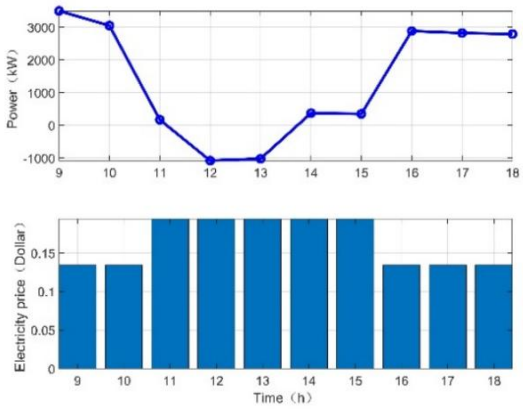


Fig. 4. Charging curve under the optimized charging mode

The figure also includes the distribution of time-of-use electricity prices. Since the optimization period is from 9:00 to 18:00, this period only covers the peak-time electricity price of 0.1939$/kWh (11:00-15:00) and the off-peak (regular) time electricity price of 0.1341$/kWh (9:00-10:00 and 16:00-18:00), with no valley-time electricity price included. It can be seen from the EV charging curve in the figure that EV charging is mostly concentrated in the off-peak (regular) price periods, with very little charging in the peak price period, while EVs only discharge during the off-peak (regular) price periods. To highlight the superiority of the optimized charging mode adopted for EVs in this paper in reducing charging costs, a comparison is made with the traditional EV charging mode.

The charging costs of all EVs in various charging modes are shown in the table below.

TABLE I. THE CHARGING COSTS IN VARIOUS CHARGING MODES

Charging mode	***TCM***	***OCM***
Charging cost ($)	2049.43	1609.57
Reduction (%)	—	27.33

C. Reactive Power Compensation Effect

By solving the lower-level optimization model, the node voltage after the charging station utilizes the remaining capacity of the on-site V2G charging piles to perform reactive power compensation for the connected node (after EVs are integrated into the grid) can be obtained. To quantitatively compare the improvement effect of voltage quality before and after reactive power compensation, the voltage quality index is defined as follows:

$$E = \frac{\sum_{j=1}^{m} \left| V_j - 1 \right|}{m} \tag{20}$$

where E is the voltage quality index; V_j is the voltage of charging station j; m is the number of charging stations.

The voltage quality index E represents the voltage deviation rate, where a smaller E indicates more stable voltage. After EVs are integrated into the grid, the voltage quality of the nodes where the charging stations are located before and after reactive power compensation is shown in the table below.

TABLE II. VOLTAGE QUALITY BEFORE AND AFTER REACTIVE POWER COMPENSATION

Time (h)	***Before compensation（Per Unit Value）***	***After compensation（Per Unit Value）***	***Increase Rate（%）***
9	0.0993	0.0523	47.38
10	0.0938	0.0465	50.42
11	0.0609	0.0144	76.39
12	0.0484	0.0087	81.94
13	0.0489	0.0089	81.79
14	0.0627	0.0156	75.07
15	0.0631	0.0159	74.78
16	0.0918	0.0447	51.28
17	0.0911	0.0443	52.48
18	0.0907	0.0425	53.17

As shown in the table, the effects of reactive power compensation are particularly significant during peak electricity pricing periods. This is because the active power delivered to the grid by EVs is relatively low during peak times, resulting in a substantial amount of available capacity for reactive power compensation at the V2G charging stations.

After utilizing the remaining capacity of the V2G charging stations for reactive power compensation at the corresponding nodes, the power flow distribution in the distribution network will change, thereby affecting the node voltages throughout the entire distribution network. Fig.5 shows the distribution of node voltages in the IEEE 33-bus system after reactive power compensation by the electric vehicle charging station during the optimization period.

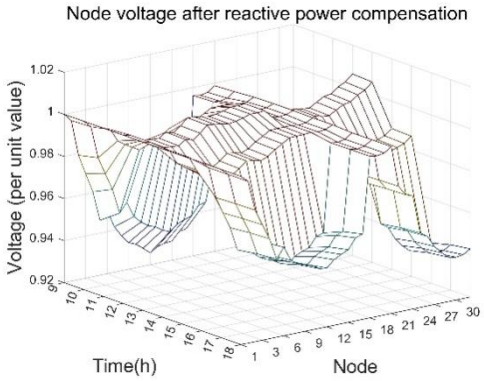


Fig. 5. The distribution of node voltages in the IEEE 33-bus system

As shown in the figure, the distribution of node voltages in the IEEE 33-bus system during peak and off-peak periods is significantly different. The overall voltage level of the distribution network during peak times is better than that during off-peak times. This phenomenon occurs because EVs deliver active power to the grid during peak periods, which effectively adds a power source to the original load at the nodes, reducing the active load and consequently decreasing voltage losses.

Furthermore, the reactive capacity utilized by the V2G charging stations for reactive power compensation during peak times is greater than that during off-peak periods. In peak times, the V2G charging stations function both as active power sources, supplying active power to the grid, and as reactive power sources, providing reactive power compensation to the grid, creating a synergistic effect of "active support + reactive compensation."

V. CONCLUSION

This paper addresses the voltage fluctuation issues in distribution networks caused by the high penetration of EVs and proposes a hierarchical multi-objective collaborative optimization model for V2G charging stations that integrates reactive demand response. The following conclusions were obtained through example analysis:

1) The upper-layer optimization model significantly reduces users' charging costs through the bidirectional adjustment of V2G charging and discharging power. Under a time-of-use pricing mechanism, this strategy guides EVs to avoid peak charging periods, resulting in a 27.33% reduction in charging costs compared to the TCM.

2) The lower-layer model utilizes the remaining capacity of the charging stations to achieve dynamic compensation of reactive power, significantly improving the voltage quality of the grid. Especially during peak pricing periods, V2G charging stations can create a synergistic effect of "active support + reactive compensation," leading to a more pronounced improvement in voltage quality. Additionally, the V2G charging station reactive power optimization strategy effectively reduces network losses across various branches.

3) The dual-layer architecture effectively reduces the complexity of the model through active-reactive decoupling control. Furthermore, this dual-layer architecture balances user economics and grid stability, demonstrating the feasibility of charging stations providing both "charging services + grid support."

ACKNOWLEDGMENT

This research is funded by the technology project of Jiading Power Supply Company, State Grid Shanghai Electric Power Company “Research on Multi-Objective Optimal Operation and Control Technology of V2G Charging Piles with Power Quality Governance Function ”(52093124000A).

REFERENCES

[1] Hu Yucai, Lu Zhanghao, Wei Jiajing. Interpretation of 2021-2035 New Energy Vehicle Industry Planning [J]. Internal Combustion Engine and Parts,2022(06):167-169.

[2] Qiao Dong. Research on the Site Selection Planning of Multi-Type Charging Facilities for Urban Electric Vehicles [D]. China University of Geosciences, 2024..

[3] I. S. Jacobs and C. P. Bean, “Fine particles, thin films and exchange anisotropy,” in Magnetism, vol. III, G. T. Rado and H. Suhl, Eds. New York: Academic, 1963, pp. 271–350.

[4] Liu Xiaofei, Zhang Qianfan, Cui Shumei. Transactions of China electrotechnical society,2012,27(2):121-127.

[5] Zhang Kai, Yin Zhongdong, Yang Xiaotian, Yan Zhuowu, Huang Yongzhang. Power grid reactive power compensation based on V2G reactive power scheduling[J]. Electric power construction,2018,39(01):40-47..

[6] Yang Shuqiang, GUO Li, LIU Jiaoyang, et al. Photovoltaic access planning based on compression and voltage regulation strategy [J]. Automation of electric power systems,2018,42(15):31-38..

[7] N. I. Mohammad Afandi, “Management of Voltages in LV Networks,”APQRC,2020.

[8] Liu Si, Shen Guang, Hu Jindi, et al. A Control Strategy for Reactive Power Compensation of Electric Vehicle Charging Stations Utilizing Residual Capacity. Journal of Zhejiang Electric Power, 2021, 40(05): 14-19.

[9] Zhang Kai, Yin Zhongdong, Yang Xiaotian, et al. Reactive Power Compensation of the Power Grid Based on V2G Reactive Power Scheduling. Electric Power Construction, 2018, 39(01): 40-47.

[10] He Kuiyuan, Yu Jiangtao, Zhu Qi, et al. Hierarchical Reactive Power Dispatch Strategy for Electric Vehicle Charging Stations under V2G Mode. Electrical Drive, 2024, 54(10): 39-49.

[11] China Automotive Technology & Research Center. Report on the Development of Chin-a’s New Energy Auto Industry; Social Sciences Academic Press: Beijing, China, 2013.

[12] Zhang Bingxu. Research on Energy Management Optimization Strategy of Active Distribution Network in the Grid-Connected Scenario of Electric Vehicles [D]. North China Electric Power University (Beijing), 2021.

[13] Chang Xiao. Research on Reactive Power Optimization Method Based on V2G [D]. Taiyuan University of Science and Technology, 2020.

[14] Lixing Chen, Xueliang Huang, Hong Zhang and Yinshen Luo, A study on coordinated optimization of electric vehicle charging and charging pile selection[J], Energies, 2018, 11(6):1350-1365.

Multi-Time-Scale Adaptive Defense Response Strategy for Cyber-Physical Distribution Systems

Yang Liu
College of Electric Power Engineering
Shanghai University of Electric Power
Shanghai, China
liuyang1124004567@163.com

Mi Wen
College of Computer Science and Technology
Shanghai University of Electric Power
Shanghai, China
miwen@shiep.edu.cn

Yunsheng Xue
School of Computer and Information Technology
Beijing Jiaotong University
Beijing, China
24110105@bjtu.edu.cn

Jiaju Yu
College of Computer Science and Technology
Shanghai University of Electric Power
Shanghai, China
jiajuyu@mail.shiep.edu.cn

Yi Gao
College of Computer Science and Technology
Shanghai University of Electric Power
Shanghai, China
gaoyi23221@gmail.com

Qiuling Yu
College of Computer Science and Technology
Shanghai University of Electric Power
Shanghai, China
qiulingyu@mail.shiep.edu.cn

***Abstract*—With the increasing digitalization and intelligence of power distribution systems, the deep integration of physical and cyber layers has exposed cyber-physical distribution systems (CPDS) to complex and dynamic threats. Existing defense resource strategies are often static and lack the flexibility to adapt to the spatio-temporal evolution of risks, leading to inefficient resource usage and delayed responses. To address this, we propose a multi-time-scale adaptive defense response strategy for power CPDS. The proposed approach integrates real-time risk assessment and dynamic defense resource allocation into a Markov Decision Process (MDP) model, which accounts for risk stage transitions and asynchronous defense actions. A deep reinforcement learning framework is developed to optimize decision-making under multi-scale temporal constraints, enabling intelligent scheduling of defense resources. Experimental results demonstrate that the strategy effectively mitigates risk propagation and enhances defense efficiency, offering both theoretical insight and practical value for resilient power CPS security.**

Keywords—cyber-physical distribution systems, multi-time-scale, defense resource optimization, deep reinforcement learning, adaptive response strategy

I. INTRODUCTION

With the rapid development of digitalization and intelligence in power systems, distribution networks have evolved into Cyber-Physical Distribution Systems (CPDS), which tightly integrate sensing, communication, and control functions. However, this high degree of coupling also exposes CPDS to significant security threats from the cyber domain, such as false data injection, denial-of-service attacks, and command manipulation [1], [2]. In distribution systems, such attacks are becoming increasingly intelligent, diverse, and persistent. Traditional defense strategies—characterized by static resource allocation and single-scale response mechanisms—are no longer adequate for coping with complex, evolving threats [3-5] .Therefore, there is an urgent need to develop an adaptive defense resource response strategy that leverages the spatio-temporal characteristics of CPDS to enhance security and risk control [6-8].

Current research on defense mechanisms for CPDS primarily falls into three categories: anomaly detection and intrusion identification based on intrusion detection systems (IDS) [9], Attack inference and risk evaluation methods grounded in physical modeling [10], Defense resource allocation strategies based on optimization or game theory [11]. In [12] , a deep learning-based intrusion detection and mitigation system is proposed for smart grids, capable of detecting, classifying, locating intrusions, and predicting current waveforms, thereby enhancing system observability and response capability under cyberattacks. In [13], a clustering-based PMU intrusion detection system is proposed to identifies the number and location of attacks and recovers accurate state estimation under multiple intrusions. In[14], a cascading failure risk assessment and mitigation method is proposed based on security-constrained AC optimal power flow and critical line flow limiting, effectively identifying high-risk lines and reducing cascading risk. In[15], a nonzero-sum game with incomplete information is proposed for optimizing defense resource allocation against DDoS attacks in CPPSs, incorporating task delays and multidimensional node value analysis to ensure effective protection under limited resources. However, these approaches exhibit several limitations. On the spatial level, they lack flexibility in dynamically reallocating defense resources to address the uncertainty of threat propagation. On the temporal level, they often fail to model the staged evolution of attacks and optimize responses accordingly. As a result, achieving precise and effective defense in multi-time-scale dynamic environments remains an open challenge.

This work was supported in part by the National Key Research and Development Program of China No. 2023YFB2704705; in part by the National Natural Science Foundation of China under Grant No. U23B2021.

979-8-3315-5472-9/25/$31.00 ©2025 IEEE

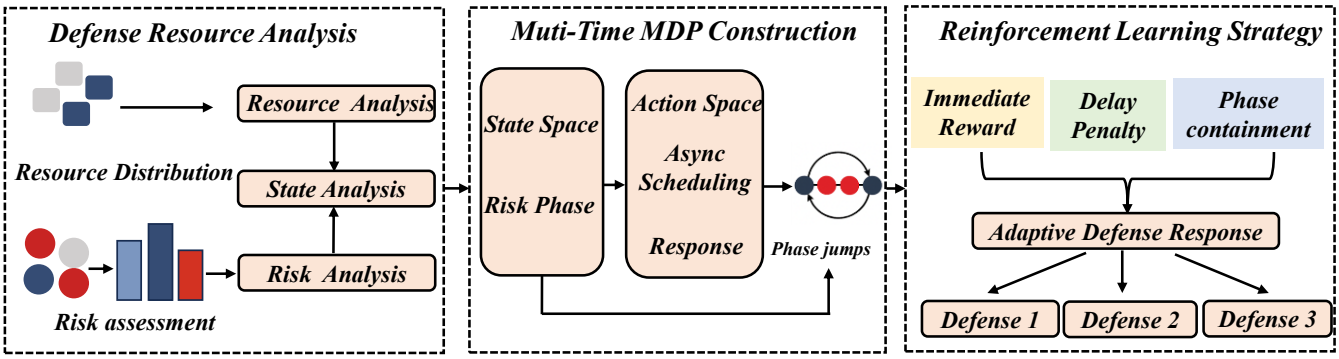


Fig. 1. The overall framework of the proposed.

To address these challenges, this study proposes a deep reinforcement learning-based multi-time-scale adaptive defense resource response strategy for power CPDS. The proposed approach integrates risk assessment results, system state dynamics, and defense resource information into a Markov Decision Process (MDP) model that incorporates risk stage transitions and asynchronous action mechanisms. A deep reinforcement learning framework is employed to train the response policy end-to-end, enabling adaptive decision-making across different time scales and resource constraints. This approach enhances defense effectiveness against complex, evolving cyber threats. The overall framework of the proposed is shown as Fig. 1.

The main contributions of this work are as follows:

- Introducing multi-time-scale modeling into the defense resource response problem for CPDS, enabling a stage-based dynamic defense perspective.
- Constructing an asynchronous MDP model that incorporates risk stage transitions and integrates spatio-temporal risk evolution.
- Designing a deep reinforcement learning framework tailored for asynchronous actions and delayed rewards to improve policy optimization.
- Validating the effectiveness and generalizability of the proposed method in representative CPDS attack scenarios.

The remainder of this paper is organized as follows. Section II details the construction of the multi-time-scale MDP model and the design of the reinforcement learning strategy. Section III presents experimental settings and performance evaluations. Section IV concludes the paper and discusses future research directions.

II. The Multi-Time-Scale MDP Model and Reinforcement Learning-Based Strateg

A. State and Action Space Construction in Multi-Time-Scale MDP

To enable dynamic and adaptive scheduling of defense resources in CPDS, a well-structured state space is required to represent not only the system's operational status but also the distribution of risk and the evolution phase of potential attacks. Conventional MDP formulations often consider simplified system states, such as node load or binary attack labels, which fail to capture the multi-layer interactions among cyber, physical, and defense domains. Therefore, this work designs a state representation that incorporates risk awareness, resource deployment status, and phase indicators. The state vector s_t at time t can be expressed as

$$s_t = [\mathbf{r}_t, \mathbf{d}_t, \mathbf{l}_t] \tag{1}$$

where $\mathbf{r}_t$ is the risk status vector, which can be predicted dynamically by a prior risk assessment model, reflecting the spatial distribution of potential threats. $\mathbf{d}_t$ is the resource deployment status, which indicates the type and location of defense resources currently deployed, providing constraints for feasible action selection. $\mathbf{l}_t$ is the risk phase label, representing the current stage of the attack lifecycle, which enables anticipatory and context-aware decision-making.

At the same times, to overcome the limitations of traditional defense scheduling models that assume synchronous actions, we propose an asynchronous and multi-scale defense action space tailored for CPDS. In real-world settings, different types of defense resources (e.g., isolation switches, authentication modules, or topology reconfiguration policies) vary in both their deployment delay and activation duration. Therefore, the action space must explicitly model such asynchronous behaviors to enable effective policy learning across different time scales. At each time step t, the agent can choose an action a_t^i for each node i from the following options:

(1) No action: Maintain the node's current status.

(2) Fast response: Deploy resources that take immediate effect.

(3) Slow response: Apply actions that require several time steps to activate.

(4) Resource withdrawal: Reclaim deployed resources for reallocation. Each action is encoded as a discrete decision value. The system-level action vector is defined as

$$a_t = [a_t^1, a_t^2, \ldots, a_t^N] \tag{2}$$

where N is the number of nodes, and $a_t^i \in A$ denotes the action type applied to node i. To explicitly model temporal asynchrony, an execution delay function $\delta(a_t^i)$ is introduced, representing the number of steps required for action a_t^i to take effect. This enables the policy to account for diverse response latencies and improves its adaptability to real-world dynamics.

In multi-time-scale defense strategy modeling, accurately capturing the dynamic evolution of CPDS states over time is foundational to constructing an effective reinforcement learning framework. System state transitions are not only driven by defense resource scheduling actions but are also heavily influenced by the progression of adversarial behaviors and their nonlinear interactions with the physical layer. Particularly, in scenarios where attacks exhibit phase-transition-like behaviors, the system may evolve in a discontinuous and nonlinear fashion. Hence, it is essential to develop a transition model that accounts for both delayed action effects and risk phase jumps, suitable for multi-scale temporal decision-making. Accordingly, we define the system transition at time t as

$$s_{t+1} = \mathcal{F}(s_t, a_t, \delta(a_t), \omega_t) \tag{3}$$

where s_t is the system state, a_t is the defense action. $\delta(a_t)$ represents the action delay function, indicating whether the action takes effect immediately or in subsequent steps. $\omega_t \sim \mathcal{P}$ denotes exogenous disturbances such as attack behavior or load variability. $\mathcal{F}$ is the transition function, possibly implemented by a simulator, a data-driven model, or a physics-informed differentiable system.

This transition mechanism comprises two coupled components: Delayed Effect of Defense Actions and Risk Phase Jump Modeling. In Delayed Effect of Defense Actions, given that real-world deployment of defense resources often involves actuation delays, we introduce an action delay function $\delta(a_t^i) \in \mathbb{N}$ for node i. If the delay condition is not met, the action is queued and does not affect s_{t+1} directly until it matures. In Risk Phase Jump Modeling, attacks typically unfold across distinct phases (e.g., reconnaissance, infiltration, control, disruption). We define a finite phase set $\mathcal{L} = \{l_1, l_2, ..., l_K\}$ and model its transition using as

$$\mathbb{P}(l_{t+1} |\ l_t, s_t, a_t) \tag{4}$$

This allows for non-sequential and abrupt transitions, such as escalation from infiltration to disruption under poor protection and high load. Defense actions modify this probability distribution. For instance, successful isolation increases $\mathbb{P}(l_{t+1} = l_t)$, effectively delaying escalation.

Moreover, the performance of reinforcement learning hinges on the quality of the reward design. To guide the policy toward minimizing risk and optimizing resource usage across multiple time scales, we construct a composite reward function as

$$r_t = \lambda_1 \cdot R_t^{\text{risk}} + \lambda_2 \cdot R_t^{\text{res}} + \lambda_3 \cdot R_t^{\text{delay}} \tag{5}$$

where R_t^{risk} is rewards reductions in overall system risk (e.g., decrease in average node risk), encouraging proactive containment of attacks. R_t^{res} is penalizes inefficient use of defense resources (e.g., excessive or unnecessary deployments). R_t^{delay} rewards successful planning and utilization of delayed actions, emphasizing their long-term benefits. The weights λ_i balance these components according to task priorities. Additionally, a phase jump penalty is applied when the system escalates from a less critical to a more critical risk stage (e.g., from intrusion to disruption), promoting early intervention in risk progression.

At the same times, to further enhance temporal abstraction and policy interpretability, we adopt a nested multi-time-scale MDP structure based on the Options Framework. This framework enables the policy to operate at two levels: a high-level controller selects a macro-action, which invokes a sequence of low-level primitive actions over multiple time steps. Each option $o \in \mathcal{O}$ is defined as

$$o = (\mathcal{I}_o, \pi_o, \beta_o) \tag{6}$$

where $\mathcal{I}_o$ is the seting of states in which the option is available; π_o is the internal policy of the option (e.g., fast isolation strategy, slow recovery protocol); β_o is the termination condition for when to exit the option. The advantage of the nested MDP structure is temporal abstraction, which can separation of high-level planning and low-level execution.

B. Reinforcement Learning Strategy Design and Training Mechanism

To effectively learn and optimize the scheduling policy of multi-time-scale defense resources, this study adopts a RL)framework to model the previously defined MDP as a sequential decision-making problem. Given the challenges posed by high-dimensional states, asynchronous actions, and delayed feedback in CPDS, we design a deep RL strategy capable of handling asynchronous decision structures and achieving scalable policy optimization. The RL agent aims to learn a policy $\pi(a_t |\ s_t)$ that maximizes the expected cumulative discounted reward, which can be expressed as

$$\pi^* = \arg\max_\pi \mathbb{E}\left[\sum_{t=0}^{T} \gamma^t r_t\right] \tag{7}$$

where $\gamma \in (0,1)$ is the discount factor, r_t is the immediate reward defined by the task-specific function, T denotes the time horizon. The objective is to obtain a near-optimal sequence of resource scheduling actions $\{a_t\}$ that minimizes system-

wide risk, maximizes resource efficiency, and enables cooperative responses across different temporal scales.

Meanwhile, To enhance policy expressiveness and learning stability, we adopt an Actor-Critic architecture with two core components: Actor Network and Critic Network. The Actor Network meaning that takes the current state s_t and outputs a probability distribution $\pi(a_t | s_t; \theta)$ over possible actions. Critic Network meaning that estimates the value $Q(s_t, a_t; \omega)$ of each state-action pair, serving as a baseline for policy gradient updates.

Due to the asynchronous nature of defense actions—where different actions exhibit varying activation delays—traditional synchronous policy update mechanisms often fail to attribute rewards accurately to their originating decisions, thus compromising learning effectiveness. To address this issue holistically, we integrate a temporally-aware learning mechanism that jointly considers action delay tracking, reward alignment, and temporal consistency in experience sampling. Specifically, an action delay buffer is maintained to store pending actions and ensure they are aligned with the state transitions in which their effects manifest. Meanwhile, temporal credit assignment is achieved using methods such as eligibility traces or TD(λ), allowing the agent to correlate delayed rewards with earlier decisions that triggered them. To further ensure time-consistent training dynamics, we implement a temporal replay buffer that retains windowed sequences of experience tuples, preserving the temporal dependencies necessary for multi-scale learning. These components are seamlessly embedded within a policy gradient framework, where algorithms such as Proximal Policy Optimization (PPO) or Soft Actor-Critic (SAC) are adopted to achieve a balance between policy stability and effective exploration.

The training process follows a structured pipeline designed to support asynchronous action dynamics and ensure stable policy optimization. Initially, the actor and critic networks are parameterized and deployed within a CPDS simulation environment, where they interact with evolving system states to generate state-action-reward trajectories. Asynchronous effects introduced by delayed action execution are explicitly handled through the integration of delay buffers and temporal alignment mechanisms, ensuring that learning signals are correctly attributed. Policy and value functions are then jointly updated using an Actor-Critic framework, guided by experience replay and temporal consistency constraints. Throughout the training cycle, periodic evaluations are conducted to monitor policy performance and convergence behavior. To prevent overfitting and enhance training robustness, techniques such as early stopping and reward smoothing are employed, which help regulate gradient updates and promote stable convergence across varying temporal scales.

III. Case Study

To validate the effectiveness of the proposed multi-time-scale defense resource scheduling strategy, we using a CPDS simulation consisting of a cyber-physical dual-layer structure. The physical layer is modeled using the IEEE 33-bus distribution network, while the cyber layer includes node-level communication topology, intrusion detection interfaces, and control agents. The attack scenarios involve typical false data injection (FDI), topological perturbation, and staged composite attacks simulating a lifecycle from stealth to disruption.

A. Simulation Setup

The training environment is implemented in Python with PyTorch. The reinforcement learning strategy is trained using the Proximal Policy Optimization (PPO) algorithm over 10,000 episodes, with a maximum of 100 steps per episode.

To comprehensively evaluate the performance of the proposed approach, we compare it with the following baseline strategies:

- Rule-based response (Rule): A static policy that assigns protection based on node-level risk rankings.
- Single-scale RL (Single-RL): A synchronous reinforcement learning model that disregards action delays and phase transitions.
- Greedy strategy (Greedy): Always selects the highest-risk node for defense deployment at each step.

To evaluate strategy performance from multiple dimensions, the following metrics are employed:

- Cumulative Risk (CR): The weighted sum of all node-level risks over the entire simulation horizon;
- Resource Efficiency (RE): The average amount of risk reduced per unit of deployed defense resource;
- Response Latency (ResL): The average delay between issuing a defense action and its actual effect;
- Phase Containment Ratio (PCR): The proportion of successful prevention of risk phase transitions;
- Convergence Speed: The number of training episodes required for the policy to stabilize.

B. Results and Analysis

As shown in Fig. 2, we comprehensively evaluate the proposed multi-time-scale reinforcement learning strategy against several baseline approaches across four key performance dimensions. In terms of CR, the proposed strategy achieves the lowest risk level, with a 37.5% reduction compared to the rule-based method, which highlights the benefits of incorporating phase-aware modeling and asynchronous scheduling. RE, the proposed method demonstrates the highest utilization rate, suggesting its strong adaptability under constrained defense resources. Although the ResL is slightly higher than that of the Greedy strategy due to asynchronous decision execution, it remains within a controllable range, reflecting a favorable trade-off between timeliness and defense quality. In the aspect of PCR, our strategy successfully suppresses 89.4% of stage transitions, nearly doubling the performance of the rule-based approach.

These results collectively demonstrate that the integration of multi-time-scale decision-making and phase transition awareness significantly improves the robustness, responsiveness, and efficiency of defense strategies in complex and dynamic cyber-physical distribution systems.

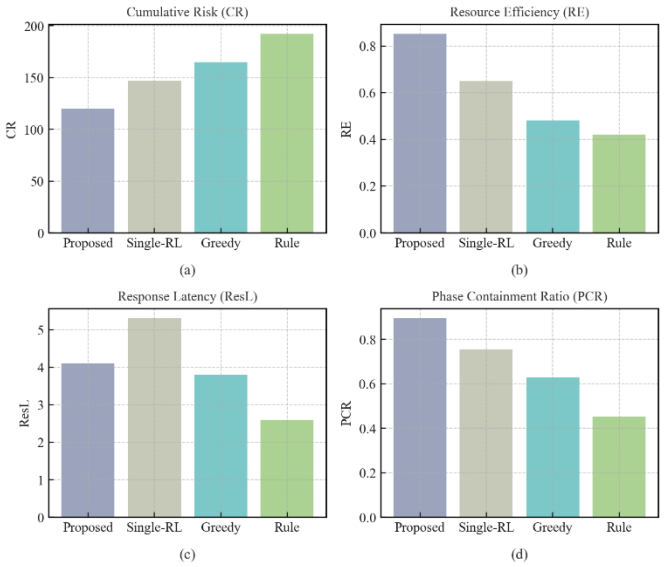


Fig. 2. Performance comparison of different defense strategies across four metrics: (a) CR, (b) RE, (c) ResL, and (d) PCR.

Fig. 3. illustrates the convergence trajectories of CR for the proposed strategy and the baseline Single-RL strategy during training. The proposed method exhibits faster convergence, achieving stable performance within approximately 1,000 episodes, whereas Single-RL converges more slowly and exhibits larger fluctuations. Throughout the entire training process, the CR values under the proposed policy remain consistently lower, indicating superior learning efficiency and stability. These results verify the advantage of incorporating asynchronous action modeling and phase-aware learning in enhancing policy robustness and generalization.

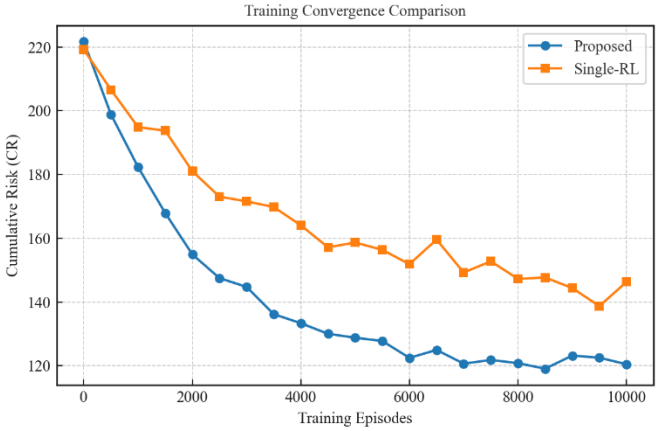


Fig. 3. Training convergence of CR for the proposed multi-time-scale RL strategy versus the Single-RL baseline.

TABLE I. PERFORMANCE COMPARISON

Time scale	*CR*	*ResL*	*RE*	*PCR*
Short-only	152	3.2	0.61	0.71
Short +Medium	134	3.7	0.72	0.8
Ours	120	4.1	0.85	0.894

As shown in Table I, the performance of different defense strategies under varying time-scale configurations is compared. The proposed multi-time-scale strategy achieves the best performance, with a CR of 120 and a PCR of 0.894, outperforming single-scale counterparts. This demonstrates the necessity of temporal coordination in complex cyber-physical threat environments.

IV. CONCLUSION

This paper presents a multi-time-scale adaptive defense resource response strategy for CPDS, addressing the mismatch between static deployment and dynamic threats. By incorporating phase-aware modeling, asynchronous action scheduling, and a deep RL framework, the proposed method enables intelligent and temporally coordinated resource allocation. An MDP formulation is designed to capture system dynamics and risk evolution, while an actor-critic-based algorithm supports policy learning under delayed and asynchronous conditions.

Simulation results demonstrate that the proposed strategy achieves lower cumulative risk, higher resource efficiency, and stronger phase containment capability compared to rule-based, greedy, and single-scale RL baselines. It also exhibits faster convergence and improved robustness under varying time-scale settings. Future work will investigate uncertainty modeling, hierarchical coordination, and online adaptation to enhance scalability and real-time applicability in complex CPDS environments.

REFERENCES

[1] S.J. Davis et al., “Net-zero emissions energy systems,” Science, vol. 360, no. 6396, Jun. 2018, Art. no. eaas9793.

[2] T. V. Vu, B. L. H. Nguyen, Z. Cheng, M.-Y. Chow, and B. Zhang, “Cyber-physical microgrids: Toward future resilient communities,” IEEE Ind. Electron. Mag., vol. 14, no. 3, pp. 4–17, Sep. 2020.

[3] Y. Liu, H. Xin, Z. Qu, and D. Gan, “An attack-resilient cooperative control strategy of multiple distributed generators in distribution networks,” IEEE Trans. Smart Grid, vol. 7, no. 6, pp. 2923–2932, Nov. 2016.

[4] A. C. Santos, A. C. B. Delbem, J. B. A. London, and N. G. Bretas, “Node-depth encoding and multiobjective evolutionary algorithm applied to large-scale distribution system reconfiguration,” IEEE Trans. Power Syst., vol. 25, no. 3, pp. 1254–1265, Aug. 2010.

[5] Y. Liu, M. Wen, H. Wen, R. Deng, S. Peng, and N. Guo, “False data injection attacks in power distribution systems considering the characteristics of distributed photovoltaic,” IEEE Trans. Ind. Informat., vol. 21, no. 3, pp. 2023–2032, Mar. 2025..

[6] R. Deng, P. Zhuang, and H. Liang, "False data injection attacks against state estimation in power distribution systems," IEEE Trans. Smart Grid, vol. 10, no. 3, pp. 2871–2881, May 2019.

[7] S. Wei, Z. Wu, J. Xu, and Q. Hu, "Multiarea probabilistic forecasting aided interval state estimation for FDIA identification in power distribution networks," IEEE Trans. Ind. Informat., vol. 20, no. 3, pp. 4271–4282, Mar. 2024.

[8] S. Peng, Z. Zhang, R. Deng, and P. Cheng, "Localizing false data injection attacks in smart grid: A spectrum-based neural network approach," IEEE Trans. Smart Grid, vol. 14, no. 6, pp. 4827–4838, Nov. 2023.

[9] J. Wu, Z. Zhao, C. Sun, R. Yan, and X. Chen, "Fault-attention generative probabilistic adversarial autoencoder for machine anomaly detection," IEEE Trans. Ind. Informat., vol. 16, no. 12, pp. 7479–7488, Dec. 2020.

[10] Q. Dai, L. Shi, and Y. Ni, "Risk assessment for cyberattack in active distribution systems considering the role of feeder automation," *IEEE Trans. Power Syst.*, vol. 34, no. 4, pp. 3230–3240, Jul. 2019.

[11] A. Farraj, E. Hammad, A. Al Daoud, and D. Kundur, "A game theoretic analysis of cyber switching attacks and mitigation in smart grid systems," *IEEE Trans. Smart Grid*, vol. 7, no. 4, pp. 1846–1855, Jul. 2016.

[12] A. Aljohani, M. AlMuhaini, H. V. Poor, and H. M. Binqadhi, "A deep learning-based cyber intrusion detection and mitigation system for smart grids," *IEEE Trans. Artif. Intell.*, vol. 5, no. 8, pp. 3902–3914, Aug. 2024.

[13] Z. S. Khalafi, M. Dehghani, A. Khalili, A. Sami, N. Vafamand, and T. Dragičević, "Intrusion detection, measurement correction, and attack localization of PMU networks," *IEEE Trans. Ind. Electron.*, vol. 69, no. 5, pp. 4697–4706, May 2022.

[14] Y. Dai, M. Noebels, R. Preece, M. Panteli, and I. Dobson, "Risk assessment and mitigation of cascading failures using critical line sensitivities," *IEEE Trans. Power Syst.*, vol. 39, no. 2, pp. 3937–3948, Mar. 2024.

[15] B. Yan, P. Yao, T. Yang, B. Zhou, and Q. Yang, "Game-theoretical model for dynamic defense resource allocation in cyber-physical power systems under distributed denial of service attacks," *J. Mod. Power Syst. Clean Energy*, vol. 12, no. 1, pp. 41–51, Jan. 2024.

A Random Forest based Construction Method of New Distribution Network Planning Evaluation Indicators

Ning Luo
Power Grid Planning & Research Center
Guizhou Power Grid Co., Ltd.
Guiyang, China
LUO18785069512@163.com

Wei Xiong
College of Electrical Engineering
Guizhou University
Guiyang, China
wxiong@gzu.edu.cn

Yuan Zhang
College of Electrical Engineering
Guizhou University
Guiyang, China
2324816737@qq.com

Jinsen Liu
Power Grid Planning & Research Center
Guizhou Power Grid Co., Ltd.
Guiyang, China
guizhoujsliu@163.com

Ludong Chen
Power Grid Planning & Research Center
Guizhou Power Grid Co., Ltd.
Guiyang, China
ljj_143@163.com

Hongyan He
Power Grid Planning & Research Center
Guizhou Power Grid Co., Ltd.
Guiyang, China
1097997121@qq.com

Pengcheng Zhang
Power Grid Planning & Research Center
Guizhou Power Grid Co., Ltd.
Guiyang, China
zhangpcgz@163.com

Guo Chen
Center College of Electrical Engineering
Guizhou University
Guiyang, China
2824539574@qq.com

***Abstract*— To address the challenge of static rigidity in the indicator system for evaluating new distribution grid planning, a random forest (RF) based constructing method of planning evaluation indicators for new distribution networks is proposed. First, typical planning scenarios are built and matched through quantitative analysis of county-level distribution grids in terms of regional energy positioning and digital intelligence dimensions. Based on the proposed scenario-driven approach, candidate indicators are initially screened based on expert experience, followed by an objective quantitative assessment of indicator importance using the RF model. This ultimately results in an evaluation indicator system highly adaptable to different scenarios. Validation using a typical county-level case study demonstrates that the proposed method can accurately match the core evaluation dimensions and key indicators under different scenarios, effectively distinguish the advantages and disadvantages of planning schemes, and significantly enhance the scientific rigor and specificity of planning evaluations.**

Keywords—New distribution system; Distribution network planning and evaluation; Evaluation index system; Scenario construction; Random Forest

I. INTRODUCTION

The development of new power systems is driving a profound transformation of distribution grids from traditional passive networks to complex energy ecosystems that integrate high proportions of renewable energy consumption with flexible interaction between power generation, transmission, load, and storage[1]-[3]. This transformation has rendered traditional planning and evaluation methods and indicator systems based on static physical constraints inadequate for measuring emerging core values such as system flexibility and intelligence, as well as for adapting to regional heterogeneity. The effectiveness of these methods and systems is now facing severe challenges. Therefore, researching and constructing a differentiated scenario indicator system that can precisely respond to diverse development paths has become an urgent need in the field of distribution network planning.

Many researchers have conducted numerous valuable explorations in the construction of evaluation indicator systems for power grid planning. Existing research has primarily focused on establishing comprehensive evaluation frameworks that reflect the characteristics of power systems, such as multi-dimensional indicator systems that balance safety and flexibility [4], or the application of methods like fuzzy comprehensive evaluation [5]. Although these efforts have significantly enriched the dimensions and methods of evaluation, the indicator systems they have constructed generally exhibit static and universal characteristics, typically designed for a specific objective or general scenario, and lack a systematic methodology capable of flexible and dynamic adjustments based on specific regional characteristics and development orientations.

In terms of scene construction methods, existing research has made significant progress. For example, a method for generating joint wind power generation scenes applicable to multiple wind farms has been proposed [6], temporal correlation has been introduced to construct source-load joint operation scenes[7], or probabilistic models have been used to generate uncertainty scenes[8]. However, the refined scene analysis results from these methods rarely provide feedback to the evaluation metric system itself. Meanwhile, data-driven technologies have garnered significant attention due to their powerful ability to extract deep features from massive datasets. Random Forest (RF), with its exceptional ability to handle high-dimensional, nonlinear data and its inherent feature importance assessment mechanism, has been successfully applied in multiple areas of power systems to objectively quantify and identify decisive influencing factors from complex variables[9][10]. However,

Supported by the National Natural Science Foundation of China (52367005); the Innovation Program of China Southern Power Grid Co., Ltd. (GZKJXM20222468).

despite RF's outstanding performance in feature importance assessment, its systematic application in distribution network planning evaluation, particularly when combined with scenario construction and expert experience, remains an urgent research gap to be addressed.

In response to the aforementioned challenges, this paper proposes a novel method for constructing evaluation indicators for distribution network planning based on random forests. First, the distribution network is analyzed in terms of regional energy positioning and digital intelligence dimensions, and typical planning scenarios are constructed and matched. Candidate indicators are then preliminarily screened based on expert experience. Subsequently, the RF model is employed to objectively quantify the importance of the candidate indicators, identifying and selecting an indicator set that aligns with the specific scenario objectives. Finally, through empirical analysis of typical counties, this method was validated as capable of constructing an evaluation indicator system that dynamically adapts to different scenario characteristics, significantly enhancing the specificity and flexibility of planning evaluation.

II. Establishing a Comprehensive Indicator System for New Distribution Systems

This study is based on a comprehensive set of candidate indicators that fully reflect the development needs of new distribution grids. The indicator system is constructed around five core dimensions: clean and low-carbon, safe and abundant, economical and efficient, flexible and intelligent, and supply-demand coordination. It includes 5 first-level, 13 second-level, and 56 third-level indicators[11](see Fig.1 for the detailed structure of the system). This comprehensive indicator system fully covers the key performance areas of new distribution grids, providing a solid foundation for subsequent data-driven indicator refinement tailored to different scenarios.

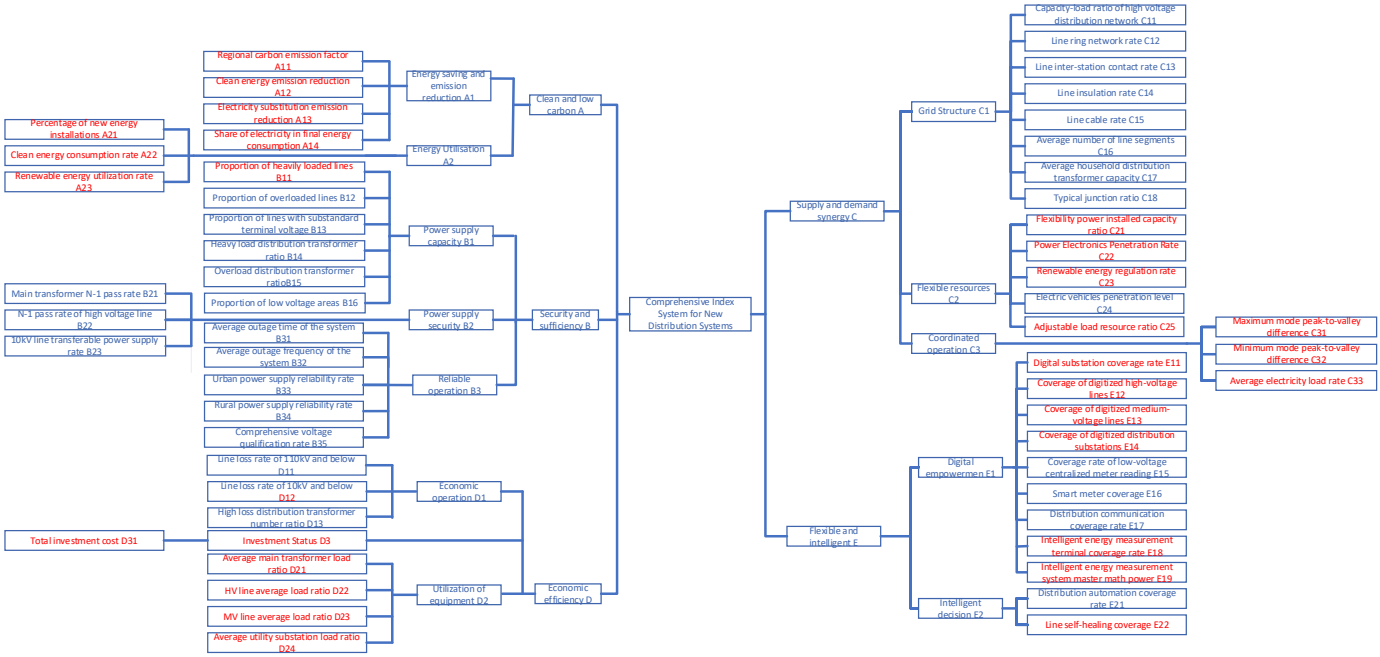


Fig. 1. Comprehensive Index System for New Distribution Systems

III. Differentiated Planning Scenario Classification Method

To reflect the integration of patio-temporal resources in different scenarios, we drew on the power supply area division methods related to construction standards in the technical guidelines for distribution network planning and design. We differentiated the planning scenarios based on two core dimensions: regional energy positioning and digital intelligence level.

A. Regional Energy Positioning

Regional energy positioning is the primary dimension for constructing differentiated scenarios, aiming to precisely define the role of the county distribution grid in the energy system and its core development tasks. Based on the relative relationship between energy density and load size, two types are ultimately identified, with the specific formula and judgment criteria shown in Table 1 below:

1) Energy-importing type: Local energy resources are scarce or limited in development, and the region mainly relies on external energy imports to meet its load demand.

2) Energy-exporting type: The region has abundant exploitable clean energy resources, and its local energy production capacity far exceeds its demand, giving it significant potential for energy exports.

$$D = \frac{Total\ installed\ capacity(MW)}{Power\ supply\ area(km^2)} \quad (1)$$

$$\partial = \frac{Maximum\ power\ consumption(MV)}{Power\ supply\ area(km^2)} \quad (2)$$

Where D represents Energy Density and ∂ represents Load Density.

TABLE I. REGIONAL ENERGY POSITIONING ASSESSMENT TABLE

	Load Density ∂	Regional Energy Positioning
Energy Density D	$\geqslant$	Energy-exporting type
	$<$	Energy-importing type

B. Degree of Digitalization

The degree of digital intelligence is the core dimension for measuring the level of digital coverage in the perception, communication, and key equipment segments of a new-type distribution grid. To objectively quantify this characteristic, a "Digital Empowerment Composite Index (*DSI*)" has been established. This index comprehensively evaluates the overall coverage level of digital substations, high-voltage lines, medium-voltage lines, and distribution transformers within a region. Based on the evaluation values of this comprehensive index, the level of digital intelligence is categorized into two grades: high and low. The specific criteria for this classification are outlined in Table 2:

TABLE II. DIGITAL INTELLIGENCE LEVEL ASSESSMENT TABLE

INDICATOR NAME	NUMERICAL VALUE	GRADING SYSTEM
DSI	⩾75%	High-level digital intelligence configuration
	<75%	Low-level digital intelligence configuration

C. Typical Scenario Classification

Based on the aforementioned analysis of regional energy positioning and digital intelligence levels, four representative planning scenarios were ultimately identified, as shown in Table 3 below.

TABLE III. TYPICAL SCENARIO CLASSIFICATION TABLE

TYPICAL SCENARIOS	REGIONAL ENERGY POSITIONING TYPES	DEGREE OF DIGITALIZATION
Scene 1	Energy-importing type	Low-level digital intelligence configuration
Scene 2	Energy-importing type	High-level digital intelligence configuration
Scene 3	Energy-exporting type	Low-level digital intelligence configuration
Scene 4	Energy-exporting type	High-level digital intelligence configuration

IV. DIFFERENTIATED INDICATOR CONSTRUCTION METHOD BASED ON EXPERT EXPERIENCE

The construction of an indicator system for new distribution grid planning must respond to the differences in macro-development environments across various regions, particularly factors such as policy orientations (e.g., support for new energy, power market reforms, etc.) and economic development trends. These factors directly determine the importance and applicability of specific indicators in different planning scenarios. To accurately capture these macro-level influences, the Expert Scoring Method is employed to achieve an initial scenario-based differentiation of the indicator system.

Invite 5–10 senior experts from the fields of power grid planning, new energy, and related research areas to independently and anonymously score the importance of each indicator in the comprehensive indicator system based on the development needs of specific scenarios (scoring range: 0–1). Subsequently, by calculating the mean S_i and standard deviation σ_i of each indicator's expert scores, and setting dual screening thresholds for importance $S_i > 0.6$ and consistency $\sigma_i < 0.3$, the core indicators that are universally recognized as important and consistent by the expert group are identified and retained.

V. FLEXIBLE INDICATOR CONSTRUCTION METHOD BASED ON RANDOM FORESTS

Although the expert scoring method can initially screen out indicators that are consistent with subjective experience and macro-level guidance, to further enhance the objectivity and accuracy of indicator selection, a random forest model is introduced to assess the importance of the expert-selected indicator set, thereby establishing a final distribution network planning evaluation indicator system that can adapt to the needs of different scenarios.

Random Forest (RF)[12]takes the preliminary screened indicator set $S = \left(x_1, x_2, ..., x_j\right)$ as input and identifies the core indicator subset that has the most significant impact on achieving the scene objective by calculating the contribution of each indicator to improving the model's prediction accuracy. The importance of each indicator I_j^m is calculated by accumulating the reduction in impurity it brings at all split nodes. The final feature in the overall random forest importance score formula is as follows:

$$I_j^m = \sum(\omega_t \times \Delta_j(t)) \tag{3}$$

$$I_j^{RF} = \frac{1}{T}\sum_{m=1}^{T} I_j^m \tag{4}$$

$$\Delta_j(t) = MSE(t) - (\frac{N_L}{N_t} \times MSE(t_L) + \frac{N_R}{N_t} \times MSE(t_R)) \tag{5}$$

In the formula: I_j^{RF} represents the importance of indicator x_j in the entire random forest, ω_t is the sample weight of node t, T is the total number of decision trees, $MSE(t_L)$ and $MSE(t_R)$ are the mean square errors of the left and right child nodes, respectively, and N_L and N_R are the sample sizes of the left and right child nodes, respectively.

VI. CASE STUDY ANALYSIS

To validate the practicality and effectiveness of the novel distribution network planning evaluation indicator construction method based on random forests proposed in this paper, a county was selected for case study analysis. The relevant data was supplemented based on the "14th Five-Year Plan for Distribution Network Planning" and appropriately anonymized. The basic situation is shown in Table 4.

A. Analysis of Basic County Conditions and Scenario Classification

TABLE IV. REGIONAL CHARACTERISTICS ANALYSIS TABLE

FEATURE DIMENSION	INDICATORS	CURRENT YEAR	PLANNING YEAR
Regional Energy Positioning	Total installed capacity (MW)	0.038	1.738
	Maximum power supply load (MW)	130.23	132.5
	D	0.00025	0.0117
	∂	0.8799	0.8952
	Energy Type Determination	Energy-importing type	Energy-importing type
Degree of Digitization	*DSI*	72.495%	76.57%

This county (with a power supply area of 148 km²) exhibits typical energy-input characteristics. Currently, its regional energy density is far lower than its load density, with a DSI of 72.495%. The level of intelligent application is relatively low, and overall, it exhibits a low level of digital intelligence development. Based on the above analysis, the typical scenarios selected for the county's research area are shown in Table 5 below:

TABLE V. TYPICAL SCENARIO SELECTION TABLE

PLANNING STAGE	REGIONAL ENERGY POSITIONING	DEGREE OF DIGITIZATION	SELECT SCENE
Current year	Energy-importing type	Low-level digital intelligence configuration	Scene 1
Planning year	Energy-importing type	High-level digital intelligence configuration	Scene 2

B. Preliminary Screening Based on Differentiated Indicators using Expert Scoring Methods

The preliminary set of candidate indicators selected through expert scoring is shown in Table 6 below, with a total of 36 indicators selected.

TABLE VI. PRELIMINARY CANDIDATE INDICATOR TABLE FOR OBJECT ONE BASED ON EXPERT SCORING

LEVEL 1 INDICATOR	LEVEL 2 INDICATOR	INDICATOR ID & NAME
Clean and low carbon	Energy saving and emission reduction	A13 - Electricity substitution emission reduction
		A12 - Clean energy emission reduction
	Energy Utilisation	A21 - Percentage of new energy installations
		A23 - Renewable energy utilization rate
Economic efficiency	Economic operation	D11 - Line loss rate of 110kV and below
		D12 - Line loss rate of 10kV and below
		D13 - High loss distribution transformer number ratio
	Utilization of equipment	D21 - Average main transformer load ratio
		D22 - HV line average load ratio
		D23 - MV line average load ratio
		D24 - Average utility substation load ratio
Security and sufficiency	Power supply capacity	B11 - Proportion of heavily loaded lines
		B13 - Proportion of lines with substandard terminal voltage
		B14 - Heavy load distribution transformer ratio
		B15 - Overload distribution transformer ratio
	Power supply security	B21 - Main transformer N-1 pass rate
		B22 - N-1 pass rate of high voltage line
	Reliable operation	B33 - Urban power supply reliability rate
		B34 - Rural power supply reliability rate
		B35 - Comprehensive voltage qualification rate
Flexible and intelligent	Digital empowerment	E12 - Coverage of digitized high-voltage lines
		E13 - Coverage of digitized medium-voltage lines
		E16 - Smart meter coverage
		E17 - Distribution communication coverage rate
		E18 - Intelligent energy measurement terminal coverage rate
		E19 - Intelligent energy measurement system master math power
	Intelligent decision	E21 - Distribution automation coverage rate
		E22 - Line self-healing coverage
Supply and demand synergy	Grid Structure	C11 - Capacity-load ratio of high voltage distribution network
		C12 - Line ring network rate
		C14 - Line insulation rate
		C15 - Line cable rate
		C16 - Average number of line segments
		C17 - Average household distribution transformer capacity
		C18 - Typical junction ratio
	Flexible resources	C24 - Electric vehicles penetration level

C. Random Forest Scenario Metric Optimization Screening

Some of the raw data is shown in Table 7 below.

TABLE VII. ORIGINAL DATA TABLE

INDICATOR NAME (ID)	PLAN 1	PLAN 2	PLAN 3	PLAN 4
Electricity substitution emission reduction (A13)	0.251	0.253	0.26	0.242
Percentage of new energy installations (A21)	68	47	53	62
Renewable energy utilization rate (A23)	10.842	10.88	10.92	10.86
Main transformer N-1 pass rate (B21)	97.24	100	100	100

Annual load peak-to-valley difference	2.41	2.39	2.22	2.34
Line loss rate of 110kV and below (D11)	1.81	1.83	1.78	1.75
Rural power supply reliability rate (B34)	99.996	99.991	99.995	99.993
……	……	……	……	……

1) Random Forest Feature Selection

The importance of candidate indicators was assessed using the random forest algorithm. The results of the indicator screening are shown in Figures 2 and 3. Under the condition of ensuring a sufficient number of indicators, the curve shows a clear "inflection point" at ranking number 23. Before the inflection point (indicators 1-23), the indicator scores are relatively high, and they are of significant importance and distinguishability for the evaluation target, constituting the core part of the indicator system. The final screening results are shown in Figure 3 below.

2) evaluation analysis

The four predefined planning schemes were evaluated using the entropy weight method[13] based on three different indicator systems:1) Complete set of indicators, 2) Expert screening system, and 3) Differentiated Construction System in this paper. The evaluation results are shown in Figure 4.

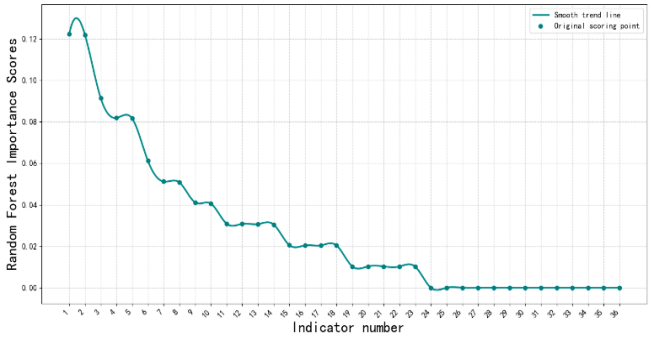


Fig. 2. Score sorting curve chart

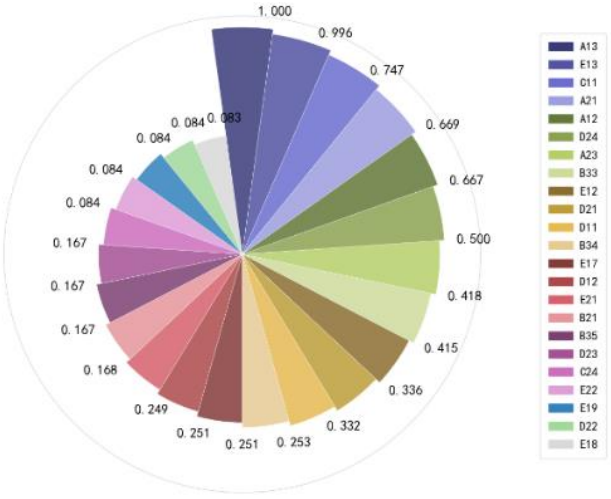


Fig. 3. Comprehensive screening indicator ring diagram

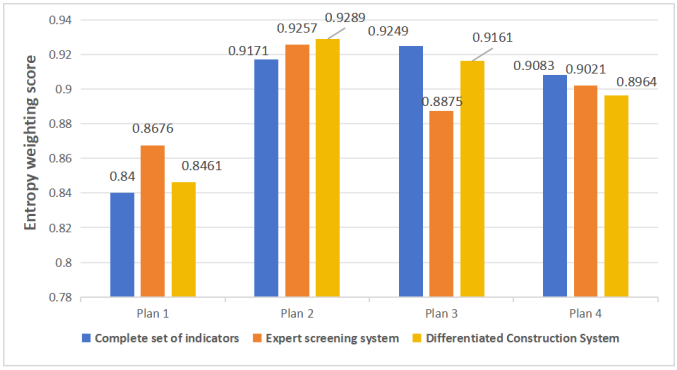


Fig. 4. Scheme entropy weight method scores under different indicator systems

The evaluation results show that the "comprehensive indicator system" lacks sufficient differentiation between excellent schemes such as Scheme 2 and Scheme 3 due to information redundancy. The "expert screening system," on the other hand, exhibits subjective bias, highlighting the advantages of Scheme 2 while significantly suppressing the evaluation of Scheme 3. In contrast, the "differentiated construction system" proposed in this paper, which integrates expert experience with data-driven optimization, not only reinforces the leading position of Scheme 2 but also effectively corrects the evaluation bias toward Scheme 3, resulting in a more robust and balanced assessment ranking. The specific performance of the primary indicators for each planning scheme under the scenario is detailed in Figure 5 below.

All solutions primarily derive their scores from the "cost-effective" dimension (with scores all exceeding 0.28). The core advantage of Solution 3 lies in its comprehensive lead in "safety and reliability" (score 0.1580, top) and "flexibility and intelligence" (0.2109, top), precisely addressing the core requirements of this scenario for high reliability and efficient operation. In contrast, the weaknesses of Scheme 1 are evident in its significantly insufficient scores across multiple key dimensions, including "cost-effectiveness" (0.2885, last place),

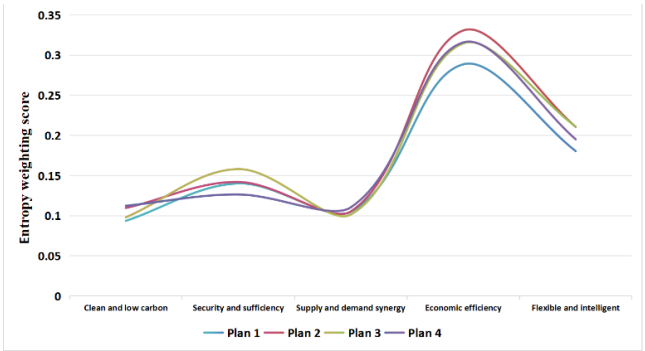


Fig. 5. Comparison chart of the weight contributions of first-level indicators for each plan

"flexibility and intelligence" (0.1804, last place), and "clean and low-carbon" (0.0936, nearly last place). As such, in Scenario 1, the ability to simultaneously enhance "economic efficiency" and "flexibility and intelligence" while ensuring "safety and sufficiency" is the key determinant of the comprehensive effectiveness of the planning scheme.

3) Construction and evaluation of indicators for different planning stages

To reflect the flexibility of assessment indicators as they evolve with the planning stage, the planning assessment for this county was extended to its "planning year" development scenario (Scenario 2: Energy-input type - high digital intelligence). For this new scenario, the proposed flexible indicator construction method was applied to ultimately select 21 core evaluation indicators, as shown in the Figure 6 below.

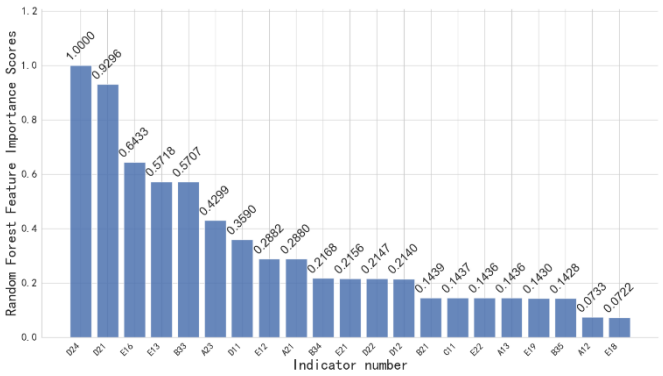


Fig. 6. Scene 2: Comprehensive screening indicator score chart

In Scenario 2, the evaluation focus has undergone a fundamental transformation, with "average load factor of public distribution transformers" and "average load factor of main transformers" becoming the most critical evaluation dimensions. This highlights the extreme pursuit of energy utilization efficiency and economic operational benefits in the context of energy input. The importance of indicators such as "smart meter coverage rate" and "clean energy installed capacity ratio" has also significantly increased, directly responding to the demand for the large-scale development of new energy. The evaluation focus of this scenario has shifted from ensuring reliable energy input to building a highly flexible and highly digitalized distribution system.

TABLE VIII. COMPARISON TABLE OF DIFFERENT SCENARIOS

SOLUTION NAME	SCENE 1 SOLUTION SCORE	SCENE SOLUTION SCORE
Plan 1	0.8461	0.8507
Plan 2	0.9289	0.9053
Plan 3	0.9161	0.9201
Plan 4	0.8964	0.8881

In Scenario 1, Solution 2 achieved the highest score and established a leading position. However, when switching to Scenario 2, Solution 3 achieved a score of 0.9201, overtaking Solution 2 to become the new optimal solution, while Solution 2's score dropped to 0.9053. This "reversal" in ranking is not accidental but the inevitable result of a shift in evaluation priorities. It profoundly demonstrates that there is no universally optimal planning scheme; the value of a scheme is highly dependent on its alignment with the specific development needs of a particular scenario.

VII. CONCLUSION

To address the lack of flexibility and objectivity in the construction of indicator systems during the planning process for new distribution grids, this study proposes a novel method for constructing evaluation indicators based on random forest. The main conclusions of the study are as follows:

1) A preliminary screening mechanism for differentiated scenarios has been established: By analyzing the characteristic differences of distribution grids in terms of regional energy positioning and digital intelligence, combined with expert judgment on macro factors, a preliminary screening of comprehensive indicators has been achieved, resulting in a set of candidate indicators tailored to each scenario.

2) Validated the core application value of random forests in differentiated indicator selection: Using the RF algorithm as a key data-driven tool, we quantified the importance of each candidate indicator for achieving the scenario objectives, effectively identifying the core subset of indicators with the greatest influence on specific scenarios from complex data relationships, and significantly improving the scientific and objective nature of indicator selection.

Through empirical analysis in a county, it was revealed that the proposed method enables the evaluation indicator system to be reasonably, scientifically, and precisely adjusted according to the core needs of the scenario.

REFERENCES

[1] ZHANG Zhigang, KANG Chongqing. Challenges and Prospects for Constructing the New-type Power System Towards a Carbon Neutrality Future[J]. Proceedings of the CSEE2022,42(08):2806-2819.

[2] LI Bo, CHEN Minyou, ZHONG Haiwang, et al. A review of longterm planning of new power systems with a large share of renewable energy[J]. Proceedings of the CSEE, 2023,43(2):555-580(in Chinese).

[3] ZHU Jizhong, ZHOU Jialin, ZHANG Di. Review of Full Life-cycle Carbon Footprints Accounting of Clean Energy and Power Systems[J].Proceedings of the CSEE,2025,45(04):1323-1343.

[4] YANG Junwen, SHANG Lei, DONG Xuzhu LI Hongjun. Multi-level C omprehensive Evaluation Index System and Evaluation Method of New Distribution System[J]. GUANGDONG ELECTRIC POWER,2024,37(10):13-24.

[5] Wei Fan, Dongming Liu, Zhennan Yang, et al. A Multidimensional Adaptive Assessment Model for Innovative Technologies in New-Type Power System[C]. 2023 The 5th Asia Energy and Electrical Engineering Symposium.

[6] Krishna A B, Abhyankar A R. An efficient data-driven conditional joint wind power scenario generation for day-ahead power system operations planning[J]. IEEE Transactions on Power Systems, 2023, 39(2): 3105-3117.

[7] XU Jiayu, WANG Xiaobing, LI Jingda, et al. Distributed PV hosting capacity assessment method for distribution network considering planning of flexible resource[J]. Elec-trical Measurement & Instru-mentation,2025,62(02):143-153.

[8] LE Jian, WANG Jing, LIAO Xiaobing, et al. A source-network-storage collaborative planning method for distribution networks based on random scenarios[J]. Power System Protection and Con-trol,2025,53(04):132-147.

[9] SHEN Fu, ZHANG Wei, XU Xiaoyuan, et al. Topological identi-fication of distribution networks based on key feature selection using RF and MIC[J]. Power System Protection and Con-trol,2024,52(17):1-11.

[10] Jin Zhijie, Huo Zhihong, Xu Chang. et al. Fault diagnosis for wind turbine based on Random Forest and XGBoost[J]. Renewable Energy Resources,2021,39(03):353-358.

[11] CHEN Ludong, CHEN Guo, ZHENG Fei, et al. Planning Evaluation Method of New Distribution Network Based on Game Comprehensive Weighting-VIKOR Method[J/OL]. SOUTHERN POWER SYSTEM TECHNOLOGY,1-10[2025-03-31].

[12] Cao Taoyun. Study on the Importance of Variables Based on Random Forest[J]. Statistics & Decision,2022,38(04):60-63.

[13] MENG Tieqiang, ZHANG Xing, XIAO Yu, et al. Flexibility As-sessment of Grid-connected Converter for New Energy Generation Based on Entropy Weight Method[J/OL]. Proceedings of the CSEE,1-12[2025-04-10].

Distribution Network Power Quality and Potential Impact on Electric Vehicle Charging

Mohd Zamri Che Wanik
Qatar Environment and Energy Research Institute
Hamad Bin Khalifa University
Qatar Foundation Education City, Qatar
Email: mwanik@hbku.edu.qa

Muneera Al-Qahtani
Qatar Environment and Energy Research Institute
Hamad Bin Khalifa University
Qatar Foundation Education City, Qatar
Email: mualqahtani@hbku.edu.qa

Abdullah Abdul Jabbar
Qatar Environment and Energy Research Institute
Hamad Bin Khalifa University
Qatar Foundation Education City, Qatar
Email: aabduljabbar@hbku.edu.qa

Mohamed Khalid Gad
Qatar Environment and Energy Research Institute
Hamad Bin Khalifa University
Qatar Foundation Education City, Qatar
Email: mgad@hbku.edu.qa

***Abstract*—This paper investigates power quality (PQ) issues in a residential distribution network in Doha and evaluates their implications for charging electric vehicles (EVs). EV chargers, being power electronic-based devices, are highly sensitive to PQ disturbances such as *voltage dips*, *voltage swells*, and *voltage unbalances*. Using one year of historical data collected from a phasor measurement unit (PMU) monitoring system, the study identifies and classifies PQ events, including 154 *voltage limit violations*, 122 *voltage unbalance* events, 12 *voltage dips*, and 2 *voltage swells*. These disturbances frequently exceed the tolerance limits of Level 1 and Level 2 chargers, posing risks of charging interruptions, reduced efficiency, and potential equipment damage. The findings underscore the need for systematic PQ assessments before charger deployment, with corrective actions such as voltage regulation or smart charging strategies recommended to mitigate adverse impacts. This study provides the first Qatar-specific evidence linking existing PQ conditions to EV charging reliability, supporting grid operators and policymakers in planning robust charging infrastructure.**

Keywords—Distribution Network, Power Quality, Electric Vehicle, EV Charging

I. INTRODUCTION

Power quality (PQ) refers to the electrical interaction between the power system and the end user. With the increasing integration of electric vehicle (EV) chargers into distribution networks, PQ issues such as *voltage limit violations*, *harmonics*, *overloading*, and *power losses* are becoming more prominent. This arises because EV chargers are nonlinear loads that rely on power electronic converters, making their performance highly sensitive to PQ disturbances. Accordingly, evaluating PQ conditions before and after EV integration is essential to ensure reliable charging infrastructure and stable distribution network operation.

In [1], a study on EV integration under a worst-case penetration scenario of 10% examined the impact of residential charging on Qatari distribution networks. The results showed that community networks can accommodate relatively high penetration levels without significant voltage or thermal instability. Education City has sufficient capacity to support projected EV loads without reinforcement. At a broader system level, [2] assessed EV integration across multiple sectors (residential, public, banking, private, and industrial), considering uncontrolled and controlled charging schemes under uncertainty. Using an IEEE-33 bus model with load patterns tailored to Qatar, the study revealed voltage profile deterioration, particularly during early morning and afternoon peaks with uncontrolled charging.

Reference [3] highlighted PQ-related technical issues arising from EV charging, including thermal limit violations and increased *harmonic distortion*. While the study focused on the impact of total harmonic distortion (THD) in public distribution networks, it found that medium-voltage THD remained within limits under higher EV penetration, whereas low-voltage THD exceeded permissible levels. Other PQ disturbances, however, received limited attention.

A different perspective is offered in [4], which analyzed the effects of PQ events—including *voltage sags*, *voltage swells*, and *harmonics*—on Level 1 and Level 2 onboard chargers. The results indicated unmitigated PQ disturbances can impair EV charging performance and reduce battery health.

Previous studies in Qatar have concentrated on the impact of EVs on the grid, with little focus on how existing PQ conditions in the grid affect EV chargers. This paper addresses this gap by evaluating PQ disturbances in a typical residential distribution network in Doha, using one year of data collected through a phasor measurement unit (PMU) monitoring system. The study focuses on four voltage-related PQ phenomena—*voltage limit violations*, *voltage unbalance*, *voltage sags*, and *voltage swells*—and analyzes their potential consequences for EV charging infrastructure and operational reliability. To the authors' knowledge, this is the first Qatar-specific empirical analysis that links measured PQ disturbances with EV charger operational tolerance, providing practical insights for grid operators and policymakers in planning robust charging infrastructure.

II. POWER QUALITY EVENTS

There are numerous definitions of power quality. The International Electrotechnical Commission (IEC) characterizes power quality as the "characteristics of the electricity at a given point on an electrical system, evaluated against a set of reference technical parameters" [5]. In contrast, the Institute for Electrical and Electronics Engineers (IEEE) describes power quality as "the concept of powering and grounding electronic equipment in a manner that is suitable to the operation of that equipment and compatible with the premise wiring system and other connected equipment" [6]. In simpler terms, any deviations from a sinusoidal waveform of nominal voltage and frequency can indicate a power quality disturbance. Power quality encompasses a broad spectrum of phenomena observed within power systems. The effects of power quality can range from relatively benign to catastrophic.

979-8-3315-5472-9/25/$31.00 ©2025 IEEE

Power quality disturbances can occur in the form of either voltage or current. Often, voltage disturbances arise from the interplay between current and network impedances. For instance, harmonic voltage distortion results from distorted current drawn by nonlinear loads with network impedance, whereas the interaction of fault current and network impedance produces voltage sags or commonly called a voltage dips. As a general guideline, especially within the IEC power quality management philosophy framework, network operators have to uphold acceptable power quality standards in voltage waveforms. At the same time, customers are tasked with managing their power quality emissions to ensure they do not adversely affect voltage levels. The classification of voltage variation is depicted in Fig.1. These variations will be discussed in more detail in the following subsections.

A. *Steady State voltage variation*

Voltage variation is often regarded as the most fundamental type of power quality disturbance. The steady-state voltage magnitude is typically recognized as the voltage waveform's root-mean-square (RMS) value. This voltage magnitude fluctuates over time due to various factors, such as loading conditions and network operations (for instance, the positions of transformer tap changers or the connection and disconnection of capacitor banks). The supply voltage magnitude is a crucial parameter for the operation of equipment. When voltage magnitudes are excessively low, equipment may fail to function as intended or not operate. Conversely, if voltage magnitudes are excessively high, equipment may suffer from reduced lifespan, increased energy consumption, or even failure [18].

Such variations are classified into two categories: overvoltage and undervoltage. Overvoltage pertains to a voltage level surpassing the nominal value, whereas undervoltage signifies a voltage level below it; both are vital for the efficient functioning of the power system. The classification of voltage variation, illustrated in Fig. 1, distinguishes between short and long interruptions. The consequences of these voltage variations on the power system and end-user equipment include the following:

- The potential for equipment overheating.
- A marked decline in the performance of electronic devices due to undervoltage.

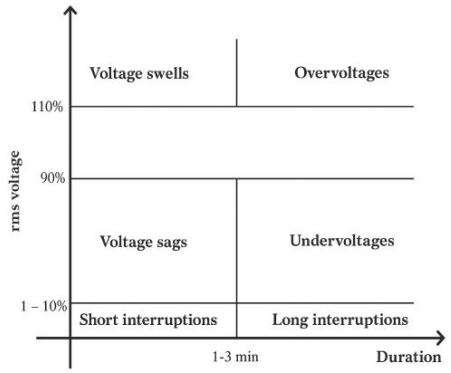


Fig. 1. Power quality events classification [18]

B. *Voltage Sag*

A *voltage sag*, commonly called a *voltage dip*, represents a temporary decrease in voltage magnitude. Specific threshold values of voltage magnitude characterize voltage sags. However, no universally accepted international definition for the voltage magnitude or duration constitutes a voltage sag. As depicted in Fig. 1, the differentiation of a voltage sag from other voltage variations is clear. Voltage sags are likely the power quality disturbance with the most substantial economic repercussions. Such sags can result in equipment tripping (ceasing operation). This tripping leads to decreased productivity and may result in considerable production and raw materials losses within industrial facilities [18].

In more detail, voltage sag refers to a temporary reduction in voltage amplitude, ranging from 0.9 to 0.1 per unit (pu) of the nominal value, occurring over a brief period lasting from half a cycle to one minute. The IEC 61000-4-30 standard defines voltage sag using two key parameters: residual voltage and duration. However, these two parameters alone do not fully capture the behaviour of voltage sags; thus, additional characteristics, such as phase angle shifts and three-phase attributes, have been explored in the literature. In contrast to voltage sags, a swell is characterised by an increase in voltage amplitude, ranging from 1.1 to 1.8 pu of the nominal value. The voltage sag that results in a voltage magnitude of less than 0.1 pu is categorised as an outage [21].

C. *Voltage Swell*

A *voltage swell* refers to a brief rise in the voltage level. In layman's terms, *voltage swell*s can be considered the converse of voltage sags. Nevertheless, voltage swells' measurement, analysis, and documentation are not as developed as those for voltage sags. This discrepancy may arise because *voltage swell*s occur less frequently than voltage sags and do not have the same economic consequences. Specific threshold values of voltage magnitude characterise voltage swells. As with voltage sags, no universally accepted international definition for the voltage magnitude or duration constitutes a *voltage swell*. The IEEE characterizes a swell as “an increase in rms voltage above 1.1 pu for durations ranging from 0.5 cycles to 1 minute” [7]. Conversely, the IEC provides a less detailed description regarding the voltage magnitude and duration associated with *voltage swell*s, defining it as a “temporary increase of the voltage magnitude at a point in the electrical system above a threshold” [8]. The overview of the differences between voltage sag, voltage swell and outage is shown in Table 1.

TABLE I. POWER QUALITY DISTURBANCE CLASSIFICATION

PQ Disturbance	Duration	Voltage values
Sag	> ½ cycles	0.1 to 0.9 pu
Swell	> ½ cycles	1.1 to 1.8 pu
Outage	> ½ cycles	< 0.1 pu

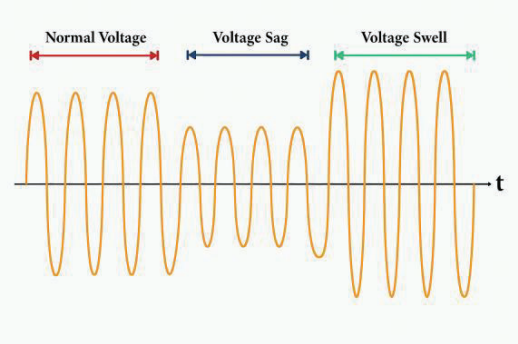


Fig. 2. Voltage sag and *voltage swell* [16]

D. Voltage Unbalance

In a balanced three-phase system, the voltage on all three phases is equal in magnitude and 120 degrees apart in phase. *Voltage unbalance* occurs when the voltage magnitudes on the phases are not equal or the phase angle of the voltage is not uniform. Unbalance, also referred to as imbalance, is characterized by the IEC as a "condition in a polyphase system where the rms values of the line voltages (fundamental component), and/or the phase angles between successive line voltages, are not uniform." [7]. Fig. 3 illustrates a representation of *voltage unbalance*. In an unbalanced condition due to magnitude, as seen in Fig.3, bottom left, phase-c has a larger voltage magnitude in comparison to phase-a and phase-b. In the bottom right of Fig. 3, unbalance due to phase is depicted. It can be seen that the phase angles are not uniformly displaced.

Unbalance can be due to various factors like unbalanced loads, faulty wiring, or issues with the power source. The effects of unbalance predominantly affect three-phase devices. One of the most recognized consequences is *voltage unbalance*, which induces counter-rotating magnetic fields in induction motors, resulting in increased heating that may necessitate the derating of the motor. Additionally, *voltage imbalance* can lead three-phase devices to produce unusual harmonic distortion. In three-phase supply networks, unbalance results in current in some phases being higher than in the other phase and some current will be flowing through the neutral conductor. Historically, when the concept of unbalance was not fully comprehended, this posed a problem if the neutral conductor was inadequately sized. Nevertheless, this concern is now well recognized, and electrical codes ensure the neutral conductor is correctly sized.

III. Distribution Network Power Quality

Qatar grid code considers voltage and current flickers, imbalances, and harmonic disturbances for generators and consumers. KAHRAMAA's grid code specifies THD limit 3 %, limit for imbalance is 1 % and respectively probability short term (Pst) = 0.35 and probability long term (Plt) = 0.65 for flicker [9]. The compliance of the grid code should be verified through simulation and measurement. Within the three PQ classifications by KAHRAMAA's grid code, we had a continuous field measurement of imbalance (*voltage unbalance*) in the network, and we give special attention to this type of PQ events in this paper.

The network under study is an underground cable network rated at 11 kV and supplying the Education City Community Housing (ECCH) residential and commercial loads through 11 kV/0.415 kV transformers. The 11 kV underground system is fed from 66/11 kV primary substations through four feeders connected in a radial configuration. The ECCH is served by 20 substations fed by five different feeders. The single-line diagram of the network is depicted in Fig. 4. These 20 substations are within the area that is colored in light green. The small green color box indicates the substation with a PMU device installed. The respective substations have been selected based on an optimal placement method to ensure the best observability for the whole network [10]. For voltage regulation, the transformer of 66/11 kV is equipped with an on-load tap changer (OLTC) and the 11 kV/0.415 kV transformer is equipped with non-load tap changer (NOLTC).

In total, 10 substations are directly measured and monitored, which means current sensors are connected to PMU devices, and the rest of the 10 substations are monitored based on the information calculated using state estimation algorithms. Of these 10 substations, in addition to current sensor, two have a voltage sensor installed. The power consumption and other various entities, such as power factor, are calculated from these measurements. Extracting detailed waveform measurements is also possible for calculating total harmonic distortion (THD) for both voltage and current. Even though harmonics are one of the important PQ issues, they are not given special attention in this paper.

PMU technology provides high resolutions of real-time magnitude, and phase angle of the current and voltage, stamped with a GPS clock. All the data from 10 PMUs are broadcast to Phasor Data Concentrator using an LTE/4G network. The computed values, such as active and reactive power derived from the raw waveform measurement of current and voltage, are recorded at the substation level and also transmitted to the server which is located at one of the buildings within the residential area. This server acts as a gateway and is accessible remotely through an internet connection.

The PMU Monitoring system is set to trigger *info*, *alarm*, and *warning* based on the severity of the four PQ events: *voltage limit violation*, *voltage unbalance*, *voltage dip*, and *voltage swell*. The criteria set for the *info*, *warning*, and *alarm* are shown in Table II. The number of occurrences is the total number of events detected within the network. For example, the total number of occurrences of *voltage limit violation* for *Alarm* is 42. The date and time of occurrence are the only four recorded. This is due to the fact that at a specific time, a few locations are detected to have violations, and each different location is considered a separate detection. The same method is used to calculate the number of other PQ events in the table.

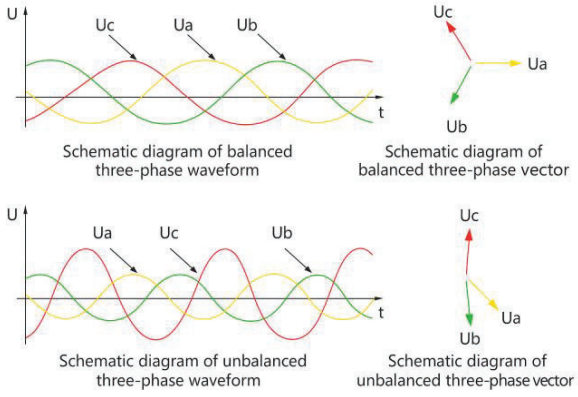


Fig. 3. Normal voltage vs *voltage unbalance* [20]

As tabulated in Table II and visualised in Fig.5, the distribution of these four types of PQ events is not a repeating event however occurs only at a certain date and time. This pattern indicates that the PQ events recorded in the network are due to certain abnormal activities or occurrences. This is probably due to certain maintenance activities or power system faults in the system. Further in-depth analysis can be carried out as needed if more detailed information is required, such as to find the real reason why the pattern of occurrence is as shown in Fig. 5. This post-mortem analysis is among of the highlighted benefits offered by the PMU monitoring system.

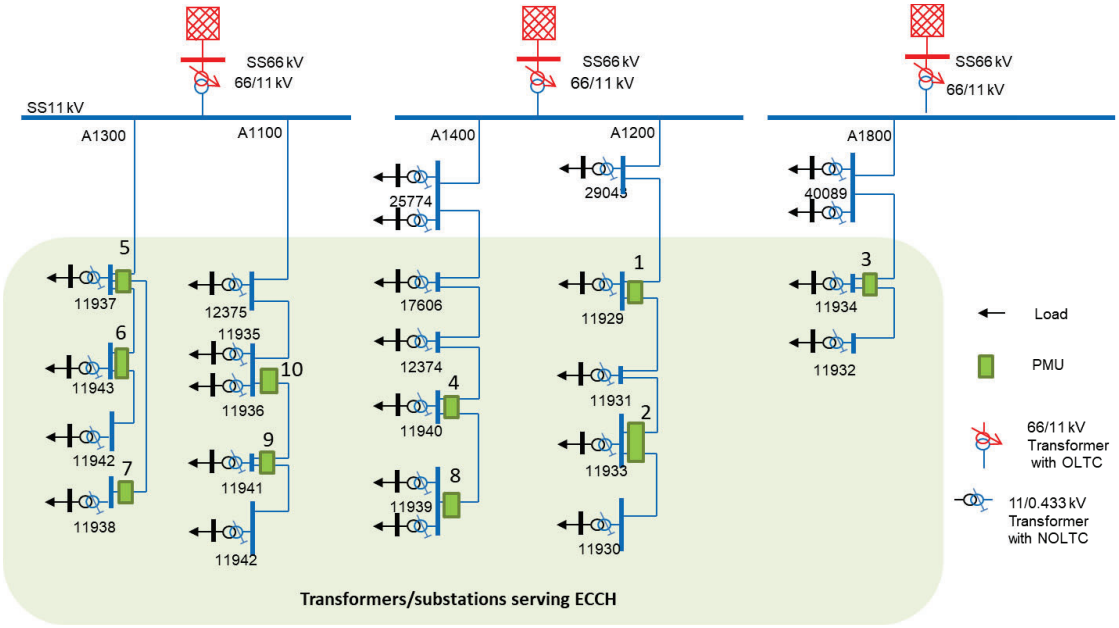


Fig. 4. Distribution network under monitoring

TABLE II. PQ EVENTS DETECTED IN THE NETWORK

Types of violation	***Voltage Limit Violation***	***Voltage Unbalance***	***Voltage Dip***	***Voltage Swell***
Definition/ Criteria	The voltage outside defines the allowable range. Info: If the voltage return back within the allowable limits within a certain time. Warning: If the voltage is beyond ±5% of the nominal voltage. Alarm: If the voltage is beyond ±10% of the nominal grid voltage	A condition in which the three-phase voltages differ in amplitude or are displaced from their normal 120° phase relationship, or both. Info: Exceed 1.5% and return back to below 1.5% Alarm: above 2%	A *voltage dip* is a reduction in the rms voltage in the range of 0.1 to 0.9 p.u. (retained) for duration greater than half a mains cycle and less than 1 minute Warning: If the voltage is between 0-90% of the nominal voltage.	An increase in the RMS voltage above the nominal voltage or a sliding reference voltage. The increase lasts from half a cycle to several seconds Warning: If the voltage is above 110% of the nominal voltage.
Number of Occurrences	154 (Detected) Info: 77 Warning: 35 Alarm: 42	122 (Detected) Info: 61 Alarm: 61	12 (Detected) Warning: 12	2 (Detected) Warning: 2
Detection	Alarm: 4 June 2024 6:42 26 May 2024 7:20 23 May 2024 17:00 20 May 2024 11:28	Alarm: 4 June 2024 6:42 26 May 2024 14:33 26 May 2024 7:20 23 May 2024 17:00 20 May 2024 11:28	Warning: 31 March 2025 16:05 11 March 2025 9:10 27 Feb 2025 11:57 5 Jan 2025 17:48 3 Nov 2024 8:18 17 Sept 2024 6:42 17 Sept 2024 5:48	Warning: 17 Sept 2024 6:42 17 Sept 2024 5:48

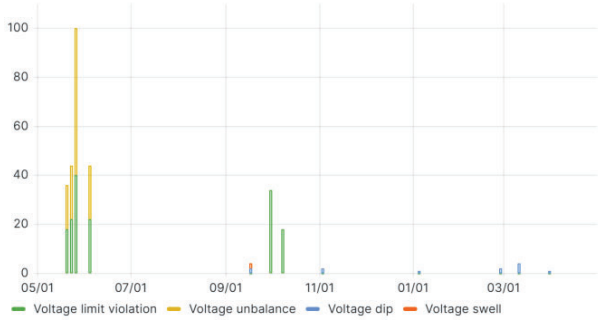


Fig. 5. Voltage-related PQ events recorded May 2024 – April 2025

IV. EV Charger Technology

The type of EV charger to be installed within the ECCH network, according to KAHRAMAA's recommendation, is of Type 1 and Type 2, which are equivalent to Level 1 and Level 2. The capacity powers are respectively 11 kW and 22 kW. The charging equipment outlet shall be rated as 240 Vac single-phase or 415 Vac three-phase [11]. Most EV chargers have a tolerance voltage of ±10% of their nominal rated voltage for steady steady state operation. For a single-phase charger, the voltage tolerance is between 216 V and 264 V. For 3-phase charger, the tolerance voltage is between 373.5 V and 459.5 V.

For non-steady state operation, equipment manufacturers normally design the voltage tolerance according to the ITI (CBEMA) curve [22] shown in Fig. 6. This curve is originally created for 120 V single-phase equipment however it has been widely adopted by other voltage level equipment as well. For the voltage outside ±10%, the equipment typically will only be able to sustain the operation for up to 10 seconds. The higher the voltage magnitude, the continuous operation time is lesser.

EV charger as a power electronic inverter-based device [12] and if it is a 3-phase equipment, there is an unbalanced voltage tolerance to maintain its stable and efficient operation. A three-phase inverter's unbalanced voltage tolerance refers to its ability to maintain a stable and efficient operation when the voltage on its three output phases is unequal. This unbalance can result in overheating of components, reduced efficiency, and potential equipment damage. Typical values range from 2% to 5% unbalance, with some specialised inverters offering higher tolerances [8, 11]

V. Discussion

The one-year monitoring results reveal many PQ disturbances will directly affecting EV charging reliability. A total of 154 *voltage limit violations* were recorded, which is critical since EV chargers typically operate within a fixed voltage tolerance. Exceeding these limits can cause chargers to cease operation, leading to interruptions in charging sessions. Further analysis is needed to distinguish whether these violations predominantly occur above or below the permissible range, as the operational risks differ in each case.

Voltage unbalance represents another major concern, with 122 events detected—61 exceeding the 2% threshold. Industry guidelines recommend maintaining *voltage unbalance* below 1%, as values beyond that can cause equipment malfunction or permanent damage. Such conditions are particularly problematic for three-phase chargers, where imbalance leads to overheating, uneven current distribution, and accelerated wear of power electronic components. These unbalance might be due to loads in the network are not equally distributed among the three phases. It can also be due to electrical faults in one or two lines of a three-phase system.

Voltage dips were observed 12 times during the observation period. This number Although brief, these dips can reduce charging speed, increase interruption frequency, and may degrade charger or battery performance if tolerance limits are exceeded. These voltage dips will impact the operation of the charger, depending on its voltage depth. The higher its depth, the higher the interruption will be experienced as indicated in Fig. 6. In contrast, *voltage swells* occurred only twice, and given their infrequency and comparatively lower impact, they are less critical in this context.

Overall, the frequency and severity of these PQ events suggest that existing network conditions could compromise the stability and efficiency of EV charging in residential compounds. The summary of the PQ events recorded is provided in Table III. Detailed investigations into event magnitude, timing, and root causes are required to identify patterns and guide corrective actions. Special attention should be given to the *voltage unbalance*, as even when the threshold of 1.5% is used, the number of occurrences is quite alarming. If the recommended threshold of 1% as written in KAHRAMAA's grid code, the detected number will be significantly higher.

Mitigation strategies should target both grid and charger levels. At the grid side, for example, voltage regulation can be improved through transformer tap adjustments, capacitor bank deployment, or reinforcement measures. Advanced inverters with reactive power support capabilities can enhance voltage stability at the device level. Operational strategies such as smart charging can minimize exposure by scheduling charging during periods with fewer PQ disturbances. In more severe cases, regulatory enforcement may be necessary to ensure compliance with PQ standards and protect future EV charging infrastructure.

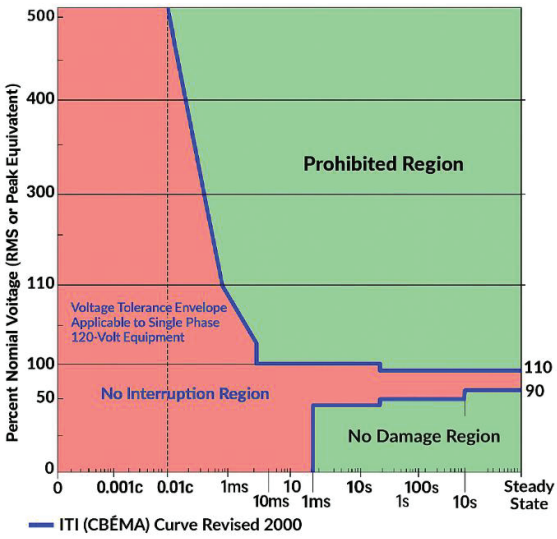


Fig. 6. ITI (CBEMA) curve [22]

TABLE III. SUMMARY OF PQ EVENTS, IMPACTS ON EV CHARGING, AND MITIGATION OPTIONS

PQ Event	Occurrences	Impact on EV Charging	Potential Mitigation
Voltage Limit Violation	154	The charger shuts down when limits are exceeded, and there are interruptions in charging sessions.	Tap changer adjustments, capacitor banks, and voltage regulation enforcement.
Voltage Unbalance	122 (61 above 2%)	Malfunction in 3-phase chargers; overheating and reduced equipment lifespan	Grid balancing, stricter PQ monitoring, and charger-level tolerance improvements
Voltage Dip	12	Charging speed reduction; session interruptions; possible charger/battery stress.	Fast-acting voltage regulators, inverter-based compensation, and smart charging schedules
Voltage Swell	2	Minimal impact due to rarity; possible stress on sensitive electronics	Surge protection, PQ filters (low priority given low frequency)

VI. CONCLUSION

This paper investigated PQ disturbances in a residential distribution network in Doha and assessed their potential impact on EV charging operation. Using one year of PMU data, the study identified frequent *voltage limit violation*, *voltage unbalance*, *voltage dip*, and *voltage swell*—many exceeding the operational tolerance of Level 1 and Level 2 EV chargers. These findings highlight that existing PQ conditions in the network pose risks of charging interruptions, reduced efficiency, and possible equipment degradation.

PQ assessments should be conducted before charger deployment, and corrective actions such as voltage regulation, grid reinforcement, or smart charging strategies should be considered to mitigate such impacts. Beyond technical measures, these results emphasize the need for policy-level requirements mandating PQ compliance as part of EV infrastructure rollout in Qatar. Future research should expand the analysis to include harmonic effects, interactions with distributed PV systems, and the development of PQ-aware charging algorithms.

REFERENCES

[1] Safak Bayram, A stochastic simulation model to assess the impacts of electric vehicle charging on power generation: A case study for qatar, in: 2019 IEEE Transportation Electrification Conference and Expo (ITEC), 2019, pp. 1–5.

[2] S. Deshmukh, H. Tariq, M. Amir, A. Iqbal, M. Marzband and A. M. A. B. Al-Wahedi, "Impact Assessment of Electric Vehicles Integration and Optimal Charging Schemes Under Uncertainty: A Case Study of Qatar," in IEEE Access, vol. 12, pp. 131350-131371, 2024,

[3] Ahmed, A. Iqbal, I. Khan, A. Al-Wahedi, H. Mehrjerdi, S. Rahman, Impact of ev charging station penetration on harmonic distortion level in utility distribution network: A case study of qatar, in: 2021 IEEE Texas Power and Energy Conference (TPEC), 2021, pp. 1–6.

[4] A. Ghosh, D. Poddar and R. R. Singh, "Impact Analysis of Onboard EV Charger under Power Quality Perturbations," 2023 9th International Conference on Electrical Energy Systems (ICEES), Chennai, India, 2023, pp. 69-74

[5] IEC, IEC 60050, International Electrotechnical Vocabulary (IEV), 1990.

[6] IEEE, IEEE 100™, The Authoritative Dictionary of IEEE Standards Terms, seventh ed., 2000

[7] Compatibility, Electromagnetic. "Part 2-2: Environment—Compatibility Levels for Low-Frequency Conducted Disturbances and Signalling in Public Low-Voltage Power Supply Systems." *Standard IEC* (2002): 61000-2.

[8] Cooper, C. B. "IEEE recommended practice for electric power distribution for industrial plants." *Electronics and Power* 33.10 (1987): 658.

[9] Qatar General Electricity & Water Corporation (KAHRAMAA), ES-M4: Qatar Transmission Grid Code, Preliminary issue, 25 March 2020 https://www.km.qa/CustomerService/ServiceRegulations/Grid%20Code%202020.pdf

[10] M. Z. C. Wanik, A. Abdul Jabbar, M. Khalid Gad and A. P. Sanfilippo, "Phasor Measurement Unit (PMU) Based Monitoring and Management for Medium Voltage Network Integrated with Distributed Energy Resources," 2024 IEEE Sustainable Power and Energy Conference (iSPEC), Kuching, Sarawak, Malaysia, 2024, pp. 499-504.

[11] Tarsheed-KAHRAMAA, Electric Vehicle and Charging Infrastructure Guideline in the State of Qatar, https://www.km.qa/Tarsheed/SavingWithTarsheed/EV_charging_station_guide_Print.pdf

[12] V.N. Saraswathi, Vijaya Priya Ramachandran, A comprehensive review on charger technologies, types, and charging stations models for electric vehicles, Heliyon, Volume 10, Issue 20, 2024,

[13] Phaengkieo, Duanraem, and Sompron Ruangsinchaiwanich. "Study of unbalanced voltage on rotor classes of induction motor according to NEMA standard." *Naresuan University Engineering Journal* 18.2 (2023): 25-31.

[14] Bhattacharjee, T., Rajeshwari, M., & Kumar, K. J. (2024). Electric Vehicle Charging and its Effects on the Power Distribution Network – A Review. *Power Research - A Journal of CPRI*, *20*(1), 89–98.

[15] Kshitij Girigoudar, Line A. Roald, On the impact of different voltage unbalance metrics in distribution system optimisation, Electric Power Systems Research, Volume 189, 2020,

[16] S. Sridhar, K. U. Rao, M. S. Nihaal and A. K. Shetty Aashik, "Real time wireless condition monitoring of induction motor," *2016 IEEE Industrial Electronics and Applications Conference (IEACon)*, Kota Kinabalu, Malaysia, 2016, pp. 173-178,

[17] HyTEPS-Energy Saving Power Quality, Power Quality/Voltage unbalance, https://hyteps.com/power-quality/voltage-unbalance/ (accessed Sept 25, 2025)

[18] Perera, Sarath & Elphick, Sean. Introduction to power quality in modern power systems. Applied Power Quality, 2023

[19] M. Z. Che Wanik, M. M. Bukshaisha and S. R. Chaudhry, "PV generation in distribution network and its impact on power transformer on-load tap changer operation," in Proceeding of *2017 IEEE Manchester PowerTech*, Manchester, UK, 2017, pp. 1-6,

[20] Suntrans, Three-Phase Imbalance Correcting Device & System, https://suntrans.net/en/news/detail/46 (accessed Sept 25, 2025)

[21] Granados-Lieberman, D.; Valtierra-Rodriguez, M.; Morales-Hernandez, L.A.; Romero-Troncoso, R.J.; Osornio-Rios, R.A. A Hilbert Transform-Based Smart Sensor for Detection, Classification, and Quantification of Power Quality Disturbances. *Sensors* **2013**, *13*, 5507-5527.

[22] Electric Power Research Institute (EPRI), Power Quality Standard: CBEMA, ITIC, SEMI F47, IEC 61000-4-11/34, https://powerquality.blog/2022/02/01/power-quality-standards-cbema-itic-semi-f47-iec-61000-4-11-34/

Grid Partitioning Method for Distribution Networks Considering the Clustering of Flexibility Resources

Yuanbing Xiao
State Grid Shanghai Electric Power Company Qingpu Power Supply Company
Shanghai, 201700 China
1195112718@qq.com

Mingzhu Ren
State Grid Shanghai Electric Power Company Qingpu Power Supply Company
Shanghai, 201700 China
17721192203@163.com

Taotao Ma
State Grid Shanghai Electric Power Company Qingpu Power Supply Company
Shanghai, 201700 China
13926433381@163.com

Zhen Zheng
State Grid Shanghai Electric Power Company Qingpu Power Supply Company
Shanghai, 201700 China
upczz@126.com

Duhong Wang
State Grid Shanghai Electric Power Company Qingpu Power Supply Company
Shanghai, 201700 China
1272967623@qq.com

Yehui Ma
State Grid Shanghai Electric Power Company Qingpu Power Supply Company
Shanghai, 201700 China
916628426@qq.com

Shijie Zhuang*
School of Electrical Engineering, Shanghai University of Electric Power
Shanghai, 200090 China
lan_yan203@163.com
*Corresponding author

Haijun Xing
School of Electrical Engineering Shanghai University of Electric Power
Shanghai, 200090 China
xinghj@shiep.edu.cn

***Abstract*—To address the operational impacts arising from the large-scale integration of flexibility resources such as distributed photovoltaics, energy storage, and electric vehicles, and to overcome the limitations of existing grid partitioning methods in managing resource stochasticity and single-objective optimization, this paper proposes a novel method for power distribution network partitioning that considers the cluster-based aggregation of flexibility resources. First, an improved K-means clustering algorithm, enhanced by the elbow method, is employed to perform a cluster analysis of flexibility resources. This approach dynamically determines the optimal number of clusters to generate representative operational scenarios. Subsequently, based on these clustering results, a distribution network partitioning optimization model is formulated with the objective of minimizing the weighted sum of total active power loss and load imbalance. This model is then transformed into a Mixed-Integer Second-Order Cone Programming (MISOCP) problem for efficient solution. Finally, the proposed method is validated through simulations on a 26-node distribution system.**

Keywords—Flexible resources; K-means clustering; Grid partitioning; Distribution network planning

I. INTRODUCTION

As a critical component of the power system, the distribution network is responsible for receiving electrical energy from the main grid and delivering it to end-users, directly impacting their quality of life and experience. However, the continuous growth in electricity demand, coupled with the rapid proliferation of emerging flexibility resources such as distributed generations(DGs), electric vehicles(EVs), and energy storage(ES), has led to an increasing scale and complexity of modern medium-voltage distribution networks. This confluence of factors presents significant challenges to network operation. A primary difficulty in distribution network planning is how to adequately account for the inherent uncertainty of DG while simultaneously optimizing for economic efficiency and security.

The grid-based planning method for distribution networks typically divides the network into multiple supply grid units, ensuring uniform resource distribution within each grid and enhancing resource independence between grids. This approach significantly improves planning accuracy and investment efficiency. Extensive research has been conducted on distribution network partitioning. Literature [1] proposed a single-layer robust optimization method to partition and plan active distribution networks into multiple microgrids. Literature [2] developed a partitioning method for medium-voltage networks ,which incorporates both load characteristics and power source allocation. Literature [3] formulated a chance-constrained optimal partitioning method to manage load uncertainty. Literature [4] utilized complex network theory to cluster large power grids by integrating power flow dynamics, line impedances, and generator-load relationships into a weighted adjacency matrix. Furthermore, to enhance resilience against low-probability, high-impact extreme weather events, Literature [5] proposed a grid-based coordinated power and communication recovery method. While these studies have advanced the application of grid partitioning for load balancing and voltage control, they have largely neglected the critical interplay between partitioning performance and the allocation of flexibility resources, rendering them inadequate for addressing the planning challenges posed by their large-scale integration.

To address the instability introduced by multiple flexibility resources, researchers have often turned to clustering analysis. Literature [6] proposed a methodology for network clustering, based on electrical distance modularity. Literature [7] developed a reliability-aware grid planning method utilized a hybrid genetic-simulated annealing algorithm for cluster-based partitioning. Literature [8] integrated electrical modularity, active-reactive power balance, and nodal membership metrics, enhanced by a net-power-constrained Fast-Newman algorithm

This work is supported by Science and Technology Project of State Grid Shanghai Electric Power Co.,Ltd (No. 520934250004)

to ensure strong intra-cluster coupling. Despite these advances, research on hybrid PV-storage systems remains limited. Existing clustering metrics often overemphasize electrical connectivity at the expense of critical aspects like power balance and load distribution, resulting in poor coordination among nodes within a cluster. Literature [9] and [10] employed K-means algorithms to identify load and generation centers, considering source-load balance in partitioning. However, a critical shortcoming in prior work is the reliance on a predetermined number of clusters, k. The selection of k profoundly impacts the accuracy and efficiency of the optimization.

To address the shortcomings of existing research, this paper proposes a method for power supply grid partitioning in distribution networks that considers the clustering of flexibility resources. Through the configuration of distributed PV, storage, and charging systems, as well as grid partitioning, the method aims to balance the grid's load with its supply capability, thereby improving the quality of power supply and enhancing the user experience. First, an improved K-means algorithm using the elbow method is employed to perform a cluster analysis on the flexibility resources. Then, based on the clustering results, the system's active power loss and load balance are considered as optimization objectives for the network partitioning process to mitigate system load imbalance and reduce power loss, ultimately obtaining the optimal distribution network grid partitioning method.

II. Modeling and Clustering of Flexibility Resources

A. Mathematical Modeling of Integrated Photovoltaic, Storage, and Charging Systems

1) Photovoltaic (PV) Power Output Model

The power generation efficiency of PV modules is primarily constrained by solar irradiance and ambient temperature, exhibiting inherent volatility and regularity. The output power $P_{pv}(t)$ at time t can be expressed as:

$$P_{pv}(t) = N_{pv} p_{pv} \frac{G^{\varphi}_{(m,d,h)}}{1000 G_0}\left[1 + \theta_T (T_t - T_{tr})\right] \tag{1}$$

where: $P_{pv}(t)$ is the rated output power of a single PV array; N_{pv} is the installed capacity of PV arrays; $G^{\varphi}_{(m,d,h)}$ is the hourly average solar irradiance at a specific location (latitude) for a given month, day, and hour; G_0 is the irradiance under standard test conditions; θ_T is the power temperature coefficient of the PV array; T_t is the actual operating temperature of the PV array; and T_{tr} is the reference temperature.

2) Energy Storage (ES) Charging/Discharging Model

The power imbalance between PV generation and load demand is compensated through the coordinated operation of the ES and the external distribution grid, satisfying the following power balance equation:

$$P_t^{buy} - P_t^{sell} + P_t^{ES,dis} - P_t^{ES,ch} + u_{PV,t} = u_{L,t} + u_{EV,t} \tag{2}$$

where: P_t^{buy} and P_t^{sell} are the power purchased from and sold to the grid at time t; $P_t^{ES,ch}$ and $P_t^{ES,dis}$ are the charging and discharging powers of the ES; $u_{L,t}$ and $u_{EV,t}$ are the actual power values of conventional and EV loads; $u_{PV,t}$ is the actual PV power.

3) Electric Vehicle Charging Station (EVCS) Model

The arrival time of electric vehicles at an EVCS is assumed to follow a normal distribution [11], with its probability density function (PDF) described as:

$$f^{ar}_{EV}(t) = \begin{cases} \dfrac{1}{\sqrt{2\pi}\sigma} \exp\left[-\dfrac{(t+24-\mu)^2}{2\sigma^2}\right] & 0 < t \le \mu - 12 \\ \dfrac{1}{\sqrt{2\pi}\sigma} \exp\left[-\dfrac{(t-\mu)^2}{2\sigma^2}\right] & \mu - 12 < t \le 24 \end{cases} \tag{3}$$

The daily driving distance of an EV is considered to follow a log-normal distribution, with its PDF described as:

$$f_M(M_d) = \frac{1}{\sqrt{2\pi}\sigma_M M_d} \exp\left[-\frac{(\ln M_d - \mu_M)^2}{2\sigma_M^2}\right] \tag{4}$$

where: μ and σ are the mean and standard deviation of EV arrival times; M_d is the daily driving distance with mean σ_M and standard deviation μ_M.

B. Clustering Methodology via an Improved K-means Algorithm

The elbow method [12] is a widely used technique for determining the optimal number of clusters, k. This method evaluates the clustering error, or Sum of Squared Errors (SSE), often defined through metrics like the ratio of the within-cluster sum of squares ($nSSE$) to the between-cluster sum of squares ($wSSE$). As the number of clusters increases, samples are partitioned more finely, enhancing intra-cluster cohesion and causing $nSSE$ to decrease. Conversely, an excessive number of clusters can also reduce $wSSE$, slowing the rate of decrease in the overall error metric. The relationship between the number of clusters and the SSE metric typically forms an "elbow" shape, and the optimal number of clusters k, corresponds to this elbow point. The model can be expressed as:

$$\begin{cases} SSE = \dfrac{nSSE}{wSSE} \\ nSSE = \displaystyle\sum_{i=1}^{k}\left(\sum_{ki \in \delta_i} | ks - m_i |^2 / k_n\right) / k \\ wSSE = \displaystyle\sum_{i=1}^{k}\sum_{j=i+1}^{k} | m_i - m_j |^2 / [k(k-1)/2] \end{cases} \tag{5}$$

where: δ_i represents the i^{th} cluster; ks is a sample within the δ_i cluster; m_i is the centroid (mean) of the cluster δ_i; k_n is the number of the sample within the δ_i cluster.

III. Optimization Method and Solution for Distribution Network Grid Partitioning

A. Objective Function

The composite objective function, F, is the minimization of the weighted sum of the normalized active power loss and the load imbalance index across all representative scenarios, expressed as:

$$\min F = \sum_{s \in S_{days}} w_s (\alpha \frac{P_s^{loss}}{P_s^{loss,base}} + \beta f_s) \tag{6}$$

where: S_{days} is the set of typical scenarios s obtained from K-means clustering; w_s is the weight of each typical scenario, corresponding to its annual frequency of occurrence; P_s^{loss} is the total active power loss under scenario s; $P_s^{loss,base}$ is the base value for active power loss under scenario s; f_s is the inter-grid load imbalance index under scenario s; α and β are the weighting factors for power loss and load imbalance, respectively.

1) Active Power Loss

The total active power loss is determined by the thermal effects of resistance in all branches of the system.

$$P_s^{loss} = \sum_{t \in T} \sum_{k \in K} \sum_{(i,j) \in L_k} r_{ij} I_{ij,s,t}^2 \tag{7}$$

where: T is the set of time periods; K is the set of partitioned grids; L_k is the set of branches within grid k; r_{ij} is the resistance of branch (i,j); and $I_{ij,s,t}$ is the magnitude of the current flowing through branch (i,j) at time t under scenario s.

2) Load Imbalance

The inter-grid load imbalance index, f_s, quantifies the uniformity of load distribution among the partitioned grids. It is measured as the sum of the absolute differences between the load ratio of each grid and the average load ratio across all grids, expressed as:

$$f_s = \sum_{t \in T} \sum_{k \in K} \left| \sum_{i_k \in N_k} \frac{P_{load,i_k,s,t}}{P_{load,total}} - \frac{1}{K} \sum_{i \in N} \frac{P_{load,i,s,t}}{P_{load,total}} \right| \tag{8}$$

where: N is the set of all nodes; N_k is the set of nodes in grid k; $P_{load,i,s,t}$ is the active power demand at node i at time t under scenario s; and $P_{load,total}$ is the total active load of the system.

B. Constraints

1) Topological Constraints

To ensure that the reconfigured distribution network maintains a radial topology, a set of constraints based on a single-commodity network flow formulation is employed. These constraints guarantee that each partitioned grid is a connected, radial network.

$$\sum_{k \in K} u_{ik} = 1, \forall i \in N \tag{9}$$

$$\begin{cases} u_{ik} - u_{jk} \le 1 - x_{ij} \\ u_{jk} - u_{ik} \le 1 - x_{ij} \end{cases}, \forall (i,j) \in L, \forall k \in K \tag{10}$$

$$\sum_{\forall (j,i) \in L} f_{ji,k} - \sum_{\forall (i,j) \in L} f_{ij,k} = u_{ik}, \forall i \in N, \forall k \in K \tag{11}$$

$$\sum_{i \in N} u_{ik} = \sum_{\forall (i_s,j) \in L} f_{i_s j,k}, \forall i_s \in S, \forall k \in K \tag{12}$$

$$0 \le f_{ij,k} \le N \cdot x_{ij}, \forall (i,j) \in L, \forall k \in K \tag{13}$$

where: L is the set of all feeders in the system; S is the set of root nodes (substations) for the spanning trees; i_s is a substation node; u_{ik} is a 0-1 variable that equals 1 if node i is assigned to grid k, and 0 otherwise; x_{ij} is a 0-1 variable representing the status of the switch on line (i,j) (1 if closed, 0 if open); and $f_{ij,k}$ is a continuous auxiliary variable representing a virtual flow, used to enforce the spanning tree structure rooted at the substation for each grid.

2) Distributed Generation Constraints

a) The active and reactive power output of PV units must satisfy the following limits:

$$P_i^{PV.\min} \le P_{i,s,t}^{PV} \le P_i^{PV.\max}, \forall i,s,t \tag{14}$$

$$Q_i^{PV.\min} \le Q_{i,s,t}^{PV} \le Q_i^{PV.\max}, \forall i,s,t \tag{15}$$

where: $P_{i,s,t}^{PV}$ and $Q_{i,s,t}^{PV}$ are the active and reactive power outputs of the PV unit at node i at time t under scenario s, respectively.

b) The charging and discharging operations of the ES are governed by the following constraints:

$$P_{i,s,t}^{ES} = P_{i,s,t}^{ES,dis} - P_{i,s,t}^{ES,ch}, \forall i,s,t \tag{16}$$

$$E_{i,s,t+1}^{ES} = E_{i,s,t}^{ES} + \eta_{ch} P_{i,s,t}^{ES,ch} \Delta t - \frac{1}{\eta_{dis}} P_{i,s,t}^{ES,dis} \Delta t, \forall i,s,t \tag{17}$$

$$0 \le P_{i,s,t}^{ES,ch} \le P_i^{ES,ch,\max}, \forall i,s,t \tag{18}$$

$$0 \le P_{i,s,t}^{ES,dis} \le P_i^{ES,dis,\max}, \forall i,s,t \tag{19}$$

$$E_{i,s,t}^{ES,\min} \le E_{i,s,t}^{ES} \le E_{i,s,t}^{ES,\max}, \forall i,s,t \tag{20}$$

$$0 \le P_{i,s,t}^{ES,ch} \le u_i^{ES} P_{i,s,t}^{ES,ch,\max}, \forall i,s,t \tag{21}$$

$$0 \le P_{i,s,t}^{ES,dis} \le (1 - u_i^{ES}) P_{i,s,t}^{ES,dis,\max}, \quad \forall i,s,t \tag{22}$$

where: $P_{i,s,t}^{ES}$ is the active power output of the ES at node i at time t under scenario s; $P_{i,s,t}^{ES,dis}$ and $P_{i,s,t}^{ES,ch}$ are the discharging and charging powers of the ES at node i at time t under scenario s, respectively; $E_{i,s,t}^{ES}$ is the state of charge (SOC) of the ES at node i at time t under scenario s; η_{ch} and η_{dis} are the charging and discharging efficiencies, respectively; u_i^{ES} is a 0-1 variable representing the charging/discharging state of the ES, where indicates charging and indicates discharging.

3) Power Flow Constraints

The power flow in the radial distribution network is modeled using the DistFlow equations [13-15].

$$\sum_{\forall(h,i)\in L} P_{hi,s,t} = \sum_{\forall(i,j)\in L} (P_{ij,s,t} + r_{ij} I^2_{ij,s,t}) + P^{load}_{i,s,t} + P^{EV}_{i,s,t} - P^{PV}_{i,s,t} - P^{ES}_{i,s,t}, \forall h,i,s,t \quad (23)$$

$$\sum_{\forall(h,i)\in L} Q_{hi,s,t} = \sum_{\forall(i,j)\in L} (Q_{ij,s,t} + x_{ij} I^2_{ij,s,t}) + Q^{load}_{i,s,t} + Q^{EV}_{i,s,t} - Q^{PV}_{i,s,t}, \forall h,i,s,t \quad (24)$$

$$V^2_{j,s,t} = V^2_{i,s,t} - 2(r_{ij} P_{ij,s,t} + x_{ij} Q_{ij,s,t}) + (r^2_{ij} + x^2_{ij}) I^2_{ij,s,t}, \forall (i,j), s, t \quad (25)$$

$$-M \cdot x_{ij} \le P_{ij,s,t} \le M \cdot x_{ij}, \forall (i,j), s, t \quad (26)$$

$$-M \cdot x_{ij} \le Q_{ij,s,t} \le M \cdot x_{ij}, \forall (i,j), s, t \quad (27)$$

where: $P_{ij,s,t}$ and $Q_{ij,s,t}$ are the active and reactive power flows on line (i,j) at time t under scenario s; $P^{load}_{i,s,t}$, $Q^{load}_{i,s,t}$, $P^{EV}_{i,s,t}$,and $Q^{EV}_{i,s,t}$ are the active and reactive power of the electricity load and EV charging load at node i at time t under scenario s, respectively; $P^{PV}_{i,s,t}$ and $Q^{PV}_{i,s,t}$ are the active and reactive power outputs of the PV at node i at time t under scenario s; r_{ij} and x_{ij} are the resistance and reactance of line (i,j); M is a sufficiently large constant.

4) System Security Constraints

$$V^{\min}_i \le V_{i,s,t} \le V^{\max}_i, \forall i,s,t \quad (28)$$

$$P^2_{ij,s,t} + Q^2_{ij,s,t} \le (S^{\max}_{ij})^2, \forall (i,j), s, t \quad (29)$$

5) Switching Operation Constraints

$$\sum_{\forall(i,j)\in L} \left| x_{ij} - x^{initial}_{ij} \right| \le N^{\max}_{switch} \quad (30)$$

where: $N^{\max}_{switch}$ is the maximum allowable number of switching operations, and $x^{initial}_{ij}$ represents the initial state of the switch on line (i,j) (0 if closed, 1 if open).

6) Source-Load Partitioning Constraints

(0-1) variable $C_{i,pv}$ is introduced to indicate the presence of a PV unit at a node:

$$C_{i,pv} = \begin{cases} 1, & \text{if node } i \text{ has a PV installation} \\ 0, & \text{otherwise} \end{cases} \quad (31)$$

To ensure a minimum level of generation capacity within each partitioned grid, a source node penetration constraint is defined:

$$\frac{\sum_{i\in N} C_{i,pv} \cdot u_{ik}}{\sum_{i\in N} u_{ik}} \ge R^{\min}_{pv} \quad (32)$$

where: R^{min}_{pv} is the specified minimum ratio of PV-equipped nodes within each grid.

C. Model Transformation and Solution

The optimization model formulated above is a Mixed-Integer Non-Linear Program (MINP), which is computationally intractable and difficult to solve to global optimality. To overcome this challenge, the non-linear terms are reformulated to transform the model into a Mixed-Integer Second-Order Cone Program (MISOCP). By substituting the non-linear terms with their convex relaxations, the original MINP model is transformed into a computationally tractable MISOCP model. This formulation can be solved efficiently to proven global optimality using commercial optimization solvers such as Gurobi.

IV. Case Study and Analysis

A. Simulation Parameters and System Description

This study utilizes a 26-node, 10 kV distribution network test system, representative of a system in East China, for validation. The analysis is based on a full year (365 days) of 24-hour historical data for PV generation, electricity demand, and EV charging loads. The permissible nodal voltage deviation is within the range of [0.95, 1.05] p.u. The total active and reactive loads are 4.316 MW and 3.710 MVAr, respectively. The maximum power capacity for any branch is 8 MW, and the main transformer capacity is 50 MVA. To investigate the impact of flexibility resources on grid partitioning, two scenarios are designed: Scenario A, representing medium penetration of flexibility resources, and Scenario B, representing high penetration, the system topology is shown in Figure 1.

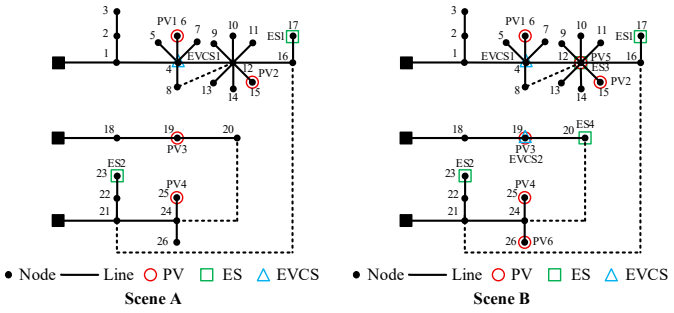


Fig. 1. Scenarios under two flexibility resource penetration rates

B. Efficacy Analysis of the Proposed Method

To analyze the advantages of integrating flexibility resource clustering with grid partitioning, four distinct optimization strategies are designed and compared under Scenario A, with all other parameters held constant.

Strategy 1: Baseline case with no flexibility resources and no grid partitioning.

Strategy 2: Flexibility resources are integrated, but no grid partitioning is performed.

Strategy 3: Grid partitioning is performed, but no flexibility resources are considered.

Strategy 4: The proposed method, integrating both flexibility resources and optimal grid partitioning.

The comparative results for the objective function value, total active power loss, and total load imbalance are presented in Table 1. The comparative analysis of optimization results under different strategies is shown in Figure 2.

TABLE I. COMPARISON OF OPTIMIZATION RESULTS FOR DIFFERENT STRATEGIES

Strategy	Objective Function	Total Active Power Loss(kW)	Total Load Imbalance
1	0.8588	94.1	0.7766
2	0.8064	94.08	0.6719
3	0.6004	77.40	0.4269
4	0.5529	51.87	0.5871

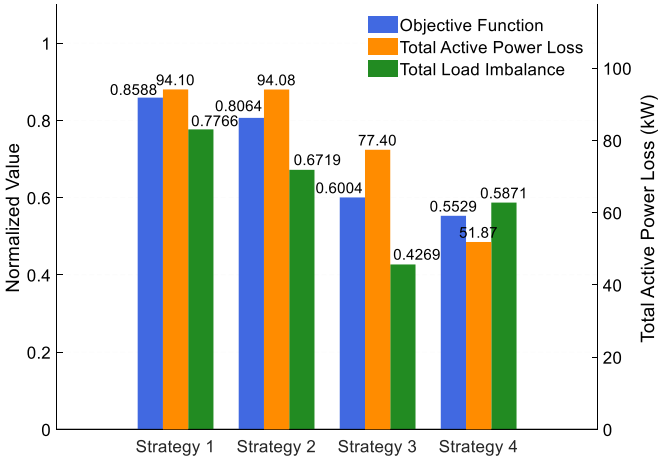


Fig. 2. Comparative analysis of optimization results under different strategies

1) Synergistic Effect Analysis

Comparing Strategy 4 with the baseline Strategy 1 reveals the significant synergistic benefits of the proposed integrated approach. The composite objective function value decreased from 0.8588 to 0.5529, a reduction of 35.6%. This improvement is primarily driven by a dramatic drop in total active power loss from 94.1 kW to 51.87 kW (44.9% reduction) and a substantial improvement in load imbalance from 0.7766 to 0.5871 (24.4% improvement). This outcome demonstrates that by optimally partitioning the distribution network and coordinating the dispatch of flexibility resources, it is possible to optimize nodal assignments and achieve structural load balancing. This fundamentally alters the system's power flow distribution, avoiding long-distance, high-load power transmission, thereby significantly reducing network losses and enhancing the overall economic efficiency of the system.

2) Component Contribution Analysis

By comparing Strategy 2 with Strategy 1, it is evident that introducing flexibility resources without altering the network topology yields almost no change in power loss, though it improves load imbalance by 13.5%. This indicates that the primary role of flexibility resources in a fixed, suboptimal topology is to smooth load fluctuations and balance supply-demand, with limited capability to reduce line losses. Conversely, comparing Strategy 3 with Strategy 1 shows that performing grid partitioning without flexibility resources reduces power loss by 17.8% and dramatically improves load imbalance by 45.0%. This highlights that an optimized network topology is a powerful tool for enhancing distribution system performance on its own.

3) Objective Trade-off Analysis

An interesting trade-off is observed when comparing the load imbalance of Strategy 4 with that of Strategy 3. The proposed method exhibits a slightly worse load imbalance. This reveals the complex trade-offs inherent in multi-objective optimization. In its pursuit of minimizing total active power loss, the model shifts power flows from heavily loaded main feeders to previously lighter branches. While this re-routing is highly effective at reducing overall losses, it can lead to less uniform loading within certain partitioned grids. Nevertheless, the composite objective function value for Strategy 4 is superior to that of Strategy 3, indicating that the economic benefits gained from the substantial reduction in power loss far outweigh the minor degradation in the load imbalance metric.

C. *Impact Analysis of Grid Partitioning Granularity*

To validate the proposed method under different resource penetration levels and to analyze the impact of partitioning granularity, Scenarios A and B were evaluated for three partitioning strategies: no partitioning (K=1), partitioning into two grids (K=2), and partitioning into three grids (K=3). It is important to note that the test system is supplied by three independent substation feeders. Therefore, to ensure each partitioned grid contains at least one primary power source for basic source-load balance, the maximum number of partitions is set to 3. The results are summarized in Table 2, the variation trends of various metrics with the number of grid cells K under different scenarios are shown in Figure 3.

TABLE II. Results under Varying Resource Penetration and Partitioning Strategies

Scenario	K Value	Objective Function	Total Active Power Loss (kW)	Total Load Imbalance
A	1	0.8064	94.08	0.6719
A	2	1.2107	111.29	1.3086
A	3	0.5529	51.87	0.5871
B	1	0.7646	99.90	0.5303
B	2	1.1899	107.12	1.2660
B	3	0.4263	51.38	0.3338

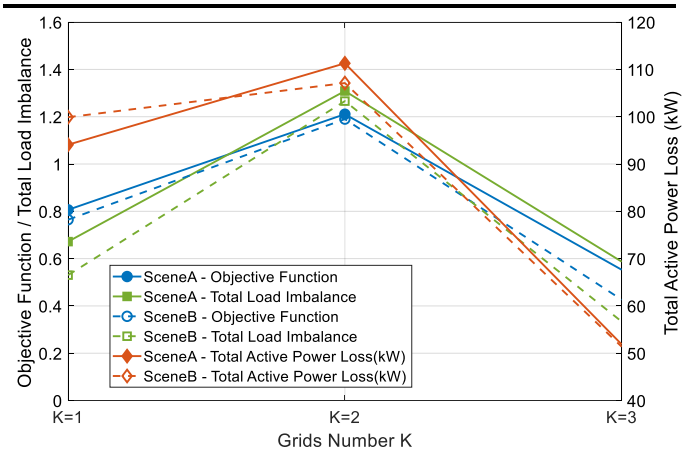


Fig. 3. Trends in various metrics across different scenarios as the number of grids k varies

1) Necessity of Optimal Partitioning

In both Scenarios A and B, the optimal three-grid partition (K=3) yields the best overall performance. However, a critical finding is that a suboptimal partitioning granularity (K=2) significantly degrades system performance. In both scenarios, the K=2 strategy results in far worse outcomes for both power loss and load imbalance compared to the baseline case of no partitioning (K=1). This counter-intuitive result underscores the danger of naive network segmentation. If partitioning does not create efficient and balanced supply topologies, it can lead to detrimental effects such as power flow detours and severe load imbalances, thereby worsening performance. This strongly validates the necessity of an optimization-based approach to grid partitioning to avoid such pitfalls.

2) Impact of Resource Penetration

Comparing the results for Scenarios A and B under the same K-value reveals the influence of resource penetration levels. Without partitioning, the higher penetration in Scenario B leads to increased total active power loss compared to Scenario A. This is because the additional PV, ESS, and EV loads alter the original power flow patterns in a fixed, suboptimal topology. However, Scenario B exhibits better load imbalance due to the greater availability of flexible resources like ES for peak shaving and valley filling. Crucially, after applying the optimal three-grid partition, the full potential of the high-penetration scenario is unlocked. The objective function and load imbalance for Scenario B with K=3 are significantly better than the corresponding values for Scenario A, demonstrating that the proposed method is increasingly beneficial as the penetration of flexibility resources grows.

V. Conclusion

This paper has proposed a novel method for power distribution network partitioning that integrates cluster-based aggregation of flexibility resources. Through the synergy of data-driven clustering analysis and a multi-objective optimization model, the method enables the rational partitioning of distribution networks with high penetrations of flexibility resources. The detailed analysis of the case study yields the following key conclusions :

1.Significant Synergistic Benefits: The co-optimization of network topology and flexibility resource dispatch yields substantial and synergistic improvements. The simulation results show that the proposed integrated method reduces the composite objective function value by 35.6%, driven by a 44.9% decrease in active power loss and a 24.4% improvement in load imbalance. This highlights that an optimized network topology is fundamental to unlocking the full regulatory potential of flexibility resources, underscoring the necessity of a coordinated planning approach.

2.Robustness through Data-Driven Scenarios: The application of the elbow-method-enhanced K-means algorithm provides a solid, data-driven foundation for the partitioning optimization. By dynamically determining the optimal number of clusters, this approach accurately captures the stochastic nature of flexibility resources and generates highly representative typical scenarios, thereby ensuring the robustness and practical applicability of the final partitioning plan.

3.Criticality of Optimal Partitioning: The performance of a distribution system is highly sensitive to the partitioning strategy. The case study demonstrates that a suboptimal partitioning scheme can be actively detrimental, leading to worse performance than having no partitions at all. This finding reveals the risks of improper network segmentation and validates the necessity of the proposed optimization methodology, which effectively navigates the complex solution space to avoid such traps and guarantee that network reconfiguration delivers tangible operational benefits.

Building upon this research, future work can explore the application of grid partitioning as a foundational unit for enhancing grid resilience. Furthermore, grid partitioning provides a physical framework for distributed voltage control and power quality management, thereby simplifying complex global control problems.

Acknowledgment

This work is supported by Science and Technology Project of State Grid Shanghai Electric Power Co., Ltd (No. 520934250004)

References

[1] Hamid Amini Khanavandi, Majid Gandomkar, Javad Nikoukar. Resiliency planning of distribution network using of active distribution network partitioning[J]. Heliyon, 2024, 10(16): e36422.

[2] LIU Weisheng, LIU Hong, WANG Fei, et al. Practical automatic planning for mv distribution network considering complementation of load characteristic and power supply unit partitioning[J]. IEEE Access, 2020, Vol.8: 91807-91817.

[3] Shuchismita Biswas, Manish K Singh, Virgilio A. Centeno. Chance-constrained optimal distribution network partitioning to enhance power grid resilience[J]. IEEE Access, 2021, 9: 42169-42181.

[4] WU Qigang, XUE Fei, LU Shaofeng, et al. Integrated network partitioning and DERs allocation for planning of Virtual Microgrids[J]. Electric Power Systems Research, 2023, 216: 109024.

[5] CHEN Bin, YU Jilai, ZHOU Xia, et al. Power-communication coordination recovery strategy based on gridding method after disasters[J]. Power System Technology, 2021, 45(05): 2009-2017.

[6] ZHANG Yuanbo, YANG Yiqiang, ZHANG Xueguang, et al. Planning strategies for distributed pv-storage using a distribution network based on load time sequence characteristics partitioning[J]. Processes, 2023, 11(540): 540.

[7] SHI Zhiwei, YOU Guangzeng, MIU Linfu, et al. Zonal planning for a large-scale distribution network considering reliability[J]. Processes, 2025, 13(2): 354.

[8] ZHAO Pu, LIU Xiao, QU Hanbing, et al. Multi-objective cooperative optimization model for source-grid-storage in distribution networks for enhanced pv absorption[J]. Processes, 13(9): 2841.

[9] WANG Jie, ZHENG Fei, ZHANG Pengcheng, et al. Model of high-proportion new energy distribution network planning based on data-driven approach[J]. Electric Power, 2025, 58(03): 175-182.

[10] MEI Xiaoyan, HAO Sipeng, JI Tianye. Grid planning method of active distribution network based on improved kmeans algorithm[J]. Machinery & Electronics, 2023, 41(09): 18-21+26.

[11] Li Y, Han M, Yang Z, et al. Coordinating Flexible Demand Response and Renewable Uncertainties for Scheduling of Community Integrated Energy Systems With an Electric Vehicle Charging Station: A Bi-Level Approach[J]. IEEE Transactions on Sustainable Energy, 2021, 12(4): 2321-2331.

[12] Li Y, Wang C, Li G, et al. Improving Operational Flexibility of Integrated Energy System with Uncertain Renewable Generations Considering Thermal Inertia of Buildings[J]. Energy Conversion and Management, 2020, 207: 112526.

[13] CAI Sheng, XIE Yunyun, ZHANG Yuping, et al. A Sequential Service Restoration Method for Microgrids Considering Optimal Allocation of Mobile Emergency Generators[J]. Proceedings of the CSEE, 2023, 43(07): 2677-2689.

[14] YEH H G，GAYME D F，LOW S H．Adaptive VAR control for distribution circuits with photovoltaic generators[J]．IEEE Transactions on Power Systems，2012，27(3)：1656-1663．

[15] YAO Yan, XU Jiayu, CUI Qinyue. Study on optimization reconfiguration modelling for distribution network with distributed generators based on DistFlow equations[J]. Energy Engineering, 2020, 1:12-16.

Hysteresis Control with Variable Coefficients Based on a Physics-Mechanism-Data Hybrid Modeling Approach

Weijie Tang
Equipment Management Dept
SMEPC, SGCC
Shanghai. China
tangweijie@sh.sgcc.com.cn

Fan Yang
Electric Power Research Institute
SMEPC, SGCC
Shanghai. China
yfan@sh.sgcc.com.cn

Bingcheng Zhou
Electric Power Research Institute
SMEPC, SGCC
Shanghai, China
793135212@qq.com

Tao He*
Equipment Management Dept
SMEPC, SGCC
Shanghai. China
hetao@sh.sgcc.com.cn

Xiaoyan Sun
Electric Power Research Institute
SMEPC, SGCC
Shanghai. China
Sunxy@sh.sgcc.com.cn

Zhilei Qiu
School of Electrical Engineering
Shanghai University of Electric Power
Shanghai. China
2741309638@qq.com

Gaiping Sun
School of Electrical Engineering
Shanghai University of Electric Power
Shanghai. China
ssunfrog2002@163.com

***Abstract*—Pure data-driven modeling approaches for transformer districts suffer from limitations in data quality and availability, and their outputs often lack physical interpretability, which hinders their practical application in guiding specific grid control and renovation measures. On the other hand, purely physical modeling and simulation methods heavily depend on accurate grid topology and component parameters. To address these issues, this paper proposes a variable coefficient droop control strategy based on a hybrid physical mechanism–data-driven modeling approach, which simultaneously considers load analysis and physical modeling. Using k-means clustering, loads are classified and active power characteristic curves are extracted. These load profiles are then incorporated into the photovoltaic (PV) inverter control model. Based on real-time voltage variations, the droop control coefficient is dynamically adjusted, thereby improving voltage control performance in the transformer district.**

Keywords—Low-voltage transformer district, Variable coefficient, Load clustering, Hysteresis control, Distributed photovoltaics

I. INTRODUCTION

In recent years, driven by policy initiatives such as the "Thousands of Households Bathed in Light" project, China has been actively promoting the flexible grid integration of distributed photovoltaic (PV) systems and accelerating the construction of a new power system. Supported by technological advancements, the distributed PV sector in China has witnessed exponential growth[1]. However, the large-scale integration of PV projects into distribution networks has led to temporal mismatches between power generation and load demand, resulting in emerging operational challenges such as active power backflow and bidirectional power flow[2]. Voltage violations have become increasingly prominent in distribution transformer areas with high PV penetration, highlighting the urgent need to identify root causes and implement effective mitigation measures.

State Grid Corporation of China has deployed extensive operational monitoring systems and electricity consumption information collection platforms across distribution networks[3], enabling the acquisition of large volumes of high-resolution customer load data. This provides a foundation for developing novel source-load integration models based on smart meter data, using a hybrid approach that combines physical mechanisms with data-driven insights[4]. In recent years, numerous researchers have investigated voltage violation issues using load data analytics. Reference [5] established a digital modeling framework across five dimensions: transformer area characteristics, user profiles, renewable energy attributes, network parameters, and operational performance. Reference [6] analyzed emerging components and structural evolution in low-voltage distribution systems, proposing typical characteristics and quantitative evaluation metrics for modern systems while identifying key challenges and enabling technologies. Reference [7] introduced a two-layer clustering model based on the inverse regulation principle, achieving more accurate load classification. Nevertheless, the aforementioned approaches rely exclusively on data-driven machine learning techniques to uncover operational patterns. While these methods demonstrate flexibility in handling uncertainties and pattern recognition, they essentially constitute "black-box" models. Such models are highly constrained by data quality and availability, and their generalization capability deteriorates significantly when data are incomplete or operating conditions fall outside historical ranges. Moreover, their outputs often lack physical interpretability, making it difficult to guide specific grid control and upgrade measures. Reference [8] proposed a dynamic equivalent circuit method for distribution networks that comprehensively considers the dynamic characteristics of loads and PV systems based on parameter identification techniques. Reference [9]

979-8-3315-5472-9/25/$31.00 ©2025 IEEE

introduced a multi-step grouping equivalent modeling approach for transient analysis, accounting for both the electrical distance distribution and dynamic behavior of distributed PV clusters. Reference [10] presented an integrated modeling methodology for PV systems and static loads in distribution grids. However, the simulation accuracy of these physically-based methods heavily depends on the precision of grid topology and component parameters. In practical aging transformer districts, incomplete line parameters, variable load characteristics, and numerous non-standard wiring configurations create a network with poor transparency—often regarded as a "black box"—leading to model mismatch and deviations between simulation results and actual operating conditions.

To address these challenges, this paper proposes a variable coefficient droop control strategy based on a hybrid physics-mechanism and data-driven modeling approach, which simultaneously incorporates load analysis and physical modeling. First, data correctness is verified and erroneous measurements are filtered out. Subsequently, polynomial curve fitting is applied to reconstruct missing data caused by transmission failures or metering malfunctions. Then, k-means clustering is employed to classify load types and extract active power characteristic curves. Finally, these load profiles are incorporated into the PV inverter control model. Based on real-time voltage variations, the droop control coefficient is dynamically adjusted, thereby enhancing voltage regulation performance in the transformer district.

II. Load Clustering Based on the K-Means Clustering Algorithm

A. Data Preprocessing

First, perform cluster analysis on all historical load data from distribution transformers without prior data preprocessing. Based on the results of this single cluster analysis, develop a data preprocessing plan. After analyzing the initial cluster analysis results, the data preprocessing workflow in this chapter is divided into the following steps:

(1) For distribution transformers with minor data gaps, polynomial curve fitting or Localized Weighted Least Squares (LOWESS) can be employed to approximate the transformer's date-maximum load factor curve as closely as possible, thereby filling in data missing due to transmission issues or metering equipment problems. A specific distribution transformer possesses partial known data points. $(x_1, y_1), (x_2, y_2), \ldots, (x_n, y_n)$ Find a polynomial function to fit these data points:

$$P(x) = a_0 + a_1 x + a_2 x^2 + \cdots + a_d x^d \tag{1}$$

Among them a_0 、 a_1 、 ⋯ 、 a_d For coefficient to be determined, d for the degree of the polynomial. After determining the polynomial, it is only necessary to solve for the coefficients of the polynomial function. $P(x)$ The solution is obtained using the least squares method, yielding the predicted values. $P(x_i)$ compared to the actual value y_i the sum of squares of errors between is minimized:

$$\min_{a_0, a_1, \ldots, a_d} \sum_{i=1}^{n} (y_i - P(x_i))^2 \tag{2}$$

After solving for the undetermined coefficients, they can be substituted into specific x values to fill in missing data. However, for distribution transformers with extensive data gaps, it is difficult to find suitable curve-fitting methods for data repair. Such transformers must be excluded from the sample to avoid distorting the fitting results.

(2) For the remaining numerous load curves exhibiting needle-like spikes, these variations appear in different cycles and heights. The extreme differences in spike heights can obscure the curve variations under normal conditions, causing all needle-like variations to be grouped into a single cluster. However, in cluster analysis, such transformers should belong to the same cluster. Therefore, during preprocessing, these needle-like transformers should be extracted from the transformer data in advance and treated as a separate category.

B. k-means Algorithm

The k-means algorithm is a clustering-based method. Due to its relatively simple implementation principle, it finds broad application. Also known as Lloyd's algorithm, its fundamental concept involves dividing a given dataset into K clusters based on Euclidean distances between data points within the samples. This process continues until the distances within each cluster are sufficiently small, while the distances between clusters are sufficiently large. The objective function of the k-means algorithm is to minimize the sum of squared errors within the dataset. This paper presents a given dataset $M = \{x_1, x_2, \ldots, x_m\}$. Given that the dataset is clustered into K clusters, the formula for minimizing the squared error and E is:

$$E = \sum_{i=1}^{k} \sum_{x \in C_i} \left\| x - \mu_i \right\|^2 \tag{3}$$

Formula for the mean vector of a corresponding cluster:

$$\mu_i = \frac{1}{|C_i|} \sum_{x \in C_i} x \tag{4}$$

In the formula, i Number of clusters representing the dataset; c_i representing each cluster; μ_i Represents the mean vector (centroid) of the corresponding cluster;x represents data points within the dataset. Since minimizing the sum in the above equation is an NP-hard problem, the k-means algorithm typically employs a heuristic iterative approach.

The k-means clustering algorithm operates as follows:

First, collect a sample set A and randomly select k data points from it. Treat these k data points as the initial k cluster centers. Set the maximum iteration count to n. Divide the sample data into k classes. Then calculate the distance between each data point and the cluster centers, assigning each point to its nearest cluster. Next, recalculate the cluster centers for each

class. Repeat this process until the k cluster centers no longer change, yielding the final clustering result.

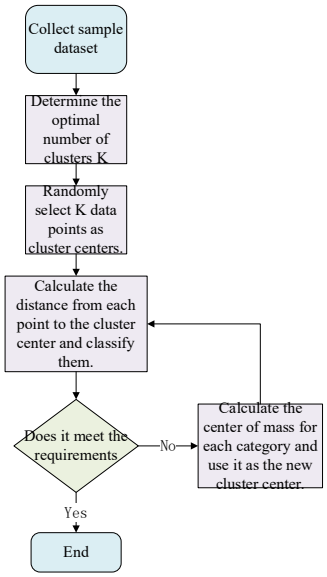


Fig. 1. k-means Clustering Algorithm Flowchart

C. *Hysteresis Control with Variable Coefficients Based on a Physics-Mechanism-Data Hybrid Modeling Approach*

A hybrid physical-mechanism and data-driven modeling approach for variable droop control strategy first validates data accuracy by filtering out erroneous entries. Next, polynomial curve fitting compensates for data gaps caused by transmission issues or metering equipment failures. Subsequently, k-means clustering classifies loads and extracts active power characteristic curves. Finally, the load curves are input into the PV inverter control model. Based on instantaneous voltage variations, the droop control coefficient is dynamically adjusted in real time, thereby enhancing voltage control performance in the transformer district.

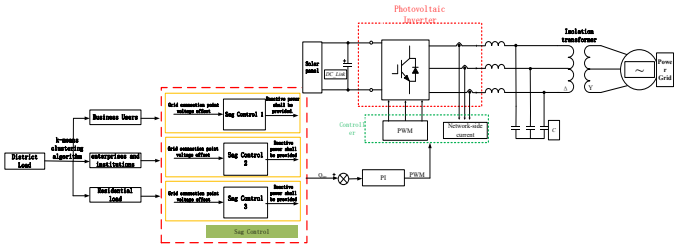


Fig. 2. Variable Coefficient Sag Control Strategy Based on a Physics-Based Mechanism-Data-Driven Hybrid Modeling Approach

III. Analysis of Sag Control Characteristics

The inverter is a crucial component of photovoltaic power generation systems, and its simplified model is shown in the figure below.

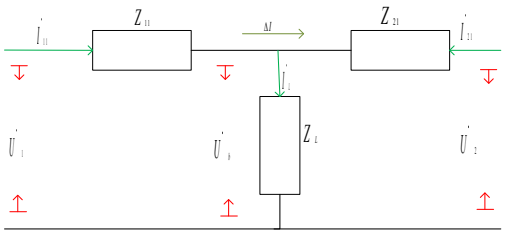


Fig. 3. Simplified Parallel Inverter Model

Among these,U_1,I_{11},U_2,I_{21}For the output voltage and output current of Converter 1 and Converter 2;U_b,I_L, Output the voltage and current at the common load terminal connected to the system;Z_{11},Z_{21},line impedance;ΔI provide circulating current for the outputs of two converters.

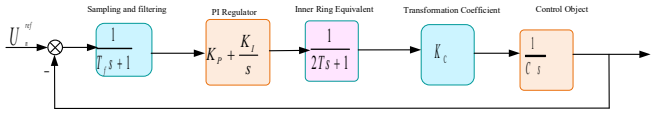


Fig. 4. Voltage Loop Tuning Block Diagram

Among these, T_f , the equivalent time constant for the sampling and filtering stages, 2T is the equivalent time constant of the current inner loop,K_c, for the conversion coefficient, take 0.75; C is the control object parameter. Sag control is primarily applied upstream of the voltage loop to calculate the DC bus voltage reference required for the voltage loop PI controller.

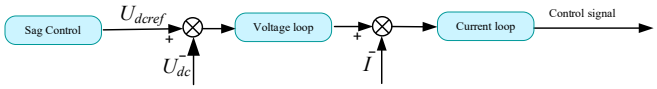


Fig. 5. Converter Control Block Diagram

IV. Case Study

A. *Load Clustering*

Preprocessing of 500 low-voltage transformer districts in Fengxian District, Shanghai yielded a complete and reasonable dataset. Load clustering analysis using the k-means algorithm successfully grouped these districts into three distinct clusters based on differing load curve characteristics. However, the large volume of data resulted in poor visualization of load curve features. Therefore, this section selects representative transformers from each cluster to illustrate their curve characteristics. The clustering results are shown below.

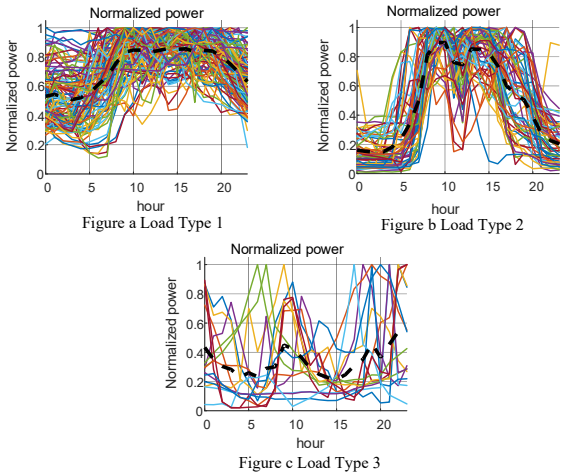


Fig. 6. Load Clustering

Cluster 1: The typical daily load curve for this user category exhibits low levels in the early morning and evening, with a peak at midday. This reflects relatively regular daytime electricity demand, corresponding to commercial users.

Cluster 2: The load curve for this user category remains stable at a low level from late night to early morning. Daytime loads are generally high with minimal fluctuation, dipping slightly only during midday before gradually declining. The overall curve is steady with pronounced day-night variation, indicating these users likely exhibit regular, sustained daytime electricity consumption patterns typical of enterprises and institutions.

Cluster 3: The load curve characteristics of this category clearly reflect a consumption pattern with a high proportion of nighttime electricity usage and relatively low daytime loads. This may correspond to residential users or equipment loads primarily operating at night.

B. Analysis of Substation Area Voltage Based on Variable-Coefficient Sag Control

Based on load clustering within transformer districts, a 22-node distribution network model incorporating distributed PV connections was constructed. This model simulates the interaction between PV output, load, and the grid, supporting power flow analysis, voltage response, and other physical parameter simulations. As shown in the figure below:

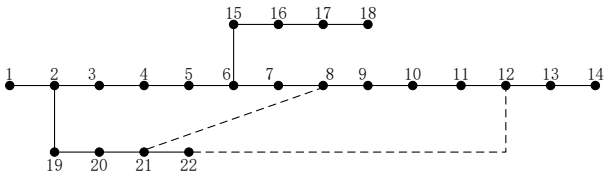


Fig. 7. Simulink Model of the Substation

Among these, a day with significant fluctuations in light intensity was selected for transformer district voltage analysis. The variations in light intensity are shown in the figure below.

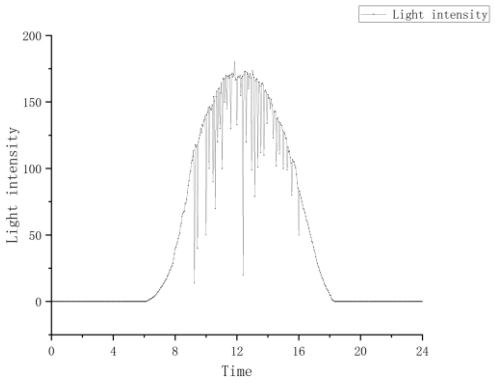


Fig. 8. Light Intensity Variation Chart

Taking the second-type typical load as an example, by identifying and analyzing the power characteristic curves of different transformer districts, distinct droop control coefficients are obtained. These coefficients are applied to implement variable droop control in transformer districts with PV integration. Concurrently, traditional PI control is employed for simulation as a comparison. The results are shown in the figure below.

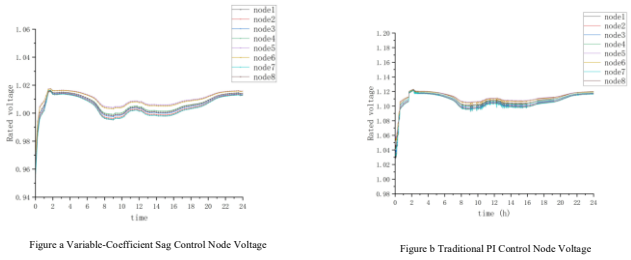


Fig. 9. Voltage Curve Diagram for Different Control Methods

Figure a shows the voltage results under variable coefficient droop control, exhibiting minimal voltage fluctuations that remain within safe limits. Figure b displays the voltage results under traditional PI control, revealing significantly elevated voltages with pronounced fluctuations during PV variations, which is detrimental to the stable operation of the distribution network. This demonstrates that after large-scale PV integration, the substation voltage can still be maintained within 1.05–0.95 under conditions of intense variations in solar irradiance. This indicates that the variable-coefficient droop control method based on a physics-mechanism-data hybrid modeling approach can effectively mitigate voltage overshoot issues in substations.

Conclusion: The variable coefficient droop control method based on a physics-mechanism-data hybrid modeling approach proposed in this paper demonstrates, through simulation results, that it effectively enhances voltage stability in transformer districts and reduces instances of voltage exceeding limits.

ACKNOWLEDGMENT

This work was supported by Science and Technology Project of State Grid Corporation of China (Grant Number: 520900250002)

REFERENCES

[1] Weichun Ge, Zhiming Wang, Hongqun Gu, et al. Information Fusion of Primary and Secondary Equipment Condition Monitoring and Its Application in PMS Construction [J]. Electric Power System Protection and Control, 2011, 39(21): 150-154.

[2] Zongqiang Zheng, Mingyu Zhai, Hui Peng, et al. Architecture and Key Technologies of Grid-Controlled Distributed SCADA Systems [J]. Automation of Electric Power Systems, 2017, 41(5): 71-77.

[3] Yixin Yu, Wenpeng Luan. Review of Smart Grids [J]. Transactions of the Chinese Society for Electrical Engineering, 2009, 29(34):1-8.

[4] Daoping Wu.Application of Power Line Carrier Communication Technology in Electricity Information Collection Systems [J]. Electronic Science and Technology, 2016, 03(4): 410-412.R. Nicole, "Title of paper with only first word capitalized," J. Name Stand. Abbrev., in press.

[5] Yongxiang Cai , Song Deng, Chunxue Zhao , Xingkai Li, Yueqi Wen, Xiangjing Zeng . Digital Modeling of Distribution Substations Based on User Smart Meter Big Data [J]. Power Big Data, 2024, 27 (03): 42-49.

[6] Qiu-nan Chen, Gang Wei, Wan-lu Wu, Xin Zhang. Impact of Distributed Power Source Distribution Characteristics on Voltage Quality in Microgrids [J]. Modern Electric Power, 2013, 30(6): 32-37.

[7] Yongjun Zhang, Yingqi Yi, Lihong Li, Kanghua Zhong, Qinhao Li, Silang Liu, Huangqing Xiao. Technology Outlook for New Low-Voltage Distribution Systems Driven by Dual Carbon Goals [J]. Automation of Electric Power Systems, 2022, 46 (22): 1-12.

[8] Yi Sun, Yehua Mao, Zekun Li, Xudong Zhang, Fei Li. Integrated Clustering Method for User Load Characteristics and Adjustability Potential Based on Power Big Data [J]. Transactions of the Chinese Society for Electrical Engineering, 2021, 41 (18): 6259-6271.

[9] Yi Sun, Yehua Mao, Zekun Li, Xudong Zhang, Fei Li. Integrated Clustering Method for User Load Characteristics and Adjustability Potential Based on Power Big Data [J]. Transactions of the Chinese Society for Electrical Engineering, 2021, 41 (18): 6259-6271.

[10] Yi Sun, Yehua Mao, Zekun Li, Xudong Zhang, Fei Li. A Comprehensive Clustering Method for User Load Characteristics and Adjustability Potential Based on Power Big Data [J]. Transactions of the Chinese Society for Electrical Engineering, 2021, 41 (18): 6259-6271.

Performance Evaluation of Asymmetric Six-Phase Induction Motors Using an Improved DTC-SVPWM Technique

Kaniz Suburna
Department of Electrical Engineering
Qatar University
Doha, qatar
kaniz.suburna@qu.edu.qa

Shirazul Islam
Department of Electrical Engineering
Qatar University
Doha, qatar
shiraz.ulislam@qu.edu.qa

Atif Iqbal
Department of Electrical Engineering
Qatar University
Doha, qatar
atif.iqbal@qu.edu.qa

S. M. Muyeen
Department of Electrical Engineering
Qatar University
Doha, qatar
sm.muyeen@qu.edu.qa

***Abstract*—Multiphase induction motors play a crucial role in industrial applications, particularly in the mining sector, due to their superior reliability, fault tolerance, and efficiency. Despite these advantages, maintaining accurate torque and speed control while reducing power losses continues to be a major challenge. This study aims to enhance the operational performance of multiphase induction motors by implementing an advanced Direct Torque Control with Space Vector Pulse Width Modulation (DTC-SVPWM) technique. The proposed approach leverages sensor less DTC and the inherent capabilities of SVPWM to improve efficiency and accuracy while reducing power dissipation. The research specifically investigates the performance of a six-phase asymmetric induction motor operating under a variable-speed environment with a DTC-SVPWM strategy. To simplify control implementation and potentially minimize the required filter size, a fixed switching frequency is adopted, ensuring more stable and predictable operation. The study evaluates key performance metrics, including torque ripples, speed regulation, and overall dynamic response, to determine the effectiveness of the proposed method in enhancing efficiency and precision. The findings of this research contribute to enhancing multiphase motor control strategies for mining applications, where high performance and energy efficiency are critical.**

***Keywords*—Direct Torque Control (DTC), Asymmetrical Six-phase Induction Motor (ASPIM/ A6PIM), Space vector pulse width modulation (SVPWM), Flux phasor state (FPS).**

I. Introduction

Induction machines are the most commonly used electromechanical drives for household, commercial, and industrial applications due to their ability to maintain continuous speed. Especially in the rigorous mining industry, the effectiveness and accuracy of induction machines are critical for resource extraction and processing. While moving materials and extracting minerals, these motors are necessary for the smooth startup of large machinery. For variable-speed applications, ensuring low-speed efficiency is essential for both outstanding performance and energy efficiency [1]. Modern mining operations prioritize technological innovation and sustainability, which calls for motors that can manage low-speed applications and offer precise control at various speeds. Microgrid integration is not any exceptional, though, as it calls for precise definitions, operational modes, and control levels [2]. Power electronics converters improve the mining subprocess's power efficiency [3]. However, to fully realize their potential and achieve optimal performance within a specific application, the implementation of a suitable control mechanism is crucial. As focusing on the popular vector control [4], Model predictive control [5] which lowers the computational load and switching frequency, whereas fractional order (FO) speed controllers show resilience to changes in load inertia [6]. Furthermore, DTC-based [7] drive systems can be stabilized at low speeds without the need for additional hardware using a unique approach.

Because of these advancements in control strategies, intrinsic advantages of multi-phase machines [8] are generating increasing research interest. Using multiphase machines instead of three phase machines reduces switching device ratings in VSI, resulting in reduced costs and smaller drives. Research on a five-phase induction motor under several supply scenarios and the effect of an uneven input voltage shows that torque is consistent throughout topologies [9]. Additionally, studies on six-phase induction motors and their applications in electric hybrid vehicles and space technologies [10] have been published. One of the most researched machines is this one, particularly the dual three-phase IM [11][12][13] that forms as a six-phase IM due to the production of two three-phases simultaneously. Earlier multiphase induction motor control strategies frequently depended on traditional approaches like PID controllers [14] but required precise tuning and can struggle with dynamic changes, making them less effective for complex applications. Similarly, Variable Frequency Drives (VFD) [15], while effective for speed control by adjusting frequency and voltage, often lead to high harmonic distortion and are less responsive to rapid load fluctuations. To get beyond the drawbacks of these conventional techniques, alternative control tactics have been suggested by current researchers. For example, Zhou et al. [16] highlights the potential of Model Predictive Control (MPC) in optimizing motor performance by considering system dynamics and constraints, but its high computational demand limits real-time use in resource-constrained settings. Yang et al. [17] propose a fault-tolerant control strategy to reduce torque ripple and expand the operational range of multiphase induction machines, though it requires complex algorithms and additional hardware, increasing costs. Similarly, direct control methods [18] mitigate demagnetization effects at low speeds but may lack the precision needed for high-performance applications. These limitations underscore the need for more robust and efficient control mechanisms. Building on these advancements, the Direct Torque Control (DTC) strategy,

979-8-3315-5472-9/25/$31.00 ©2025 IEEE

combined with Space Vector Pulse Width Modulation (SVPWM) [19], provides a robust alternative by addressing the limitations of conventional DTC [20], such as torque ripples, minimizing power loss and reduced low-speed performance. DTC ensures real-time torque and flux control by estimating motor conditions, whereas SVPWM generates smooth voltage transitions to minimize errors and harmonics [21]. Compared to traditional methods like PID or VFD, DTC SVPWM-based optimization provides superior adaptability to varying load conditions and better fault tolerance, ensuring consistent performance across a wide range of applications. These similar variety of control techniques alongside our proposed mechanism are compared below in Table I-

TABLE I. COMPARISON TABLE BETWEEN DIFFERENT CONTROL MECHANISM

Ref.	Motor Type	Control Method	Speed Range	Features
[19]	Three-phase induction motor	Direct torque control of 3 phase IM Based on SVPWM Technique	Very low and medium Speed	The switching instants of different space vectors are determined for each sampling period to minimize the torque ripple in SVPWM technique.
[20]	Induction machines	PWM Harmonics	Low and zero speed	Sensorless control using PWM harmonics
[21]	induction motor drives	Speed sensorless	Very low and Zero Speed	Good performance of the proposed observer and estimation algorithms at very low and zero speeds
[22]	Five-phase induction motor	DTC Technique	Low-speed characteristics	Enhanced low-speed characteristics with constant switching torque-controller-based DTC technique
Proposed method	Six-Phase induction motor	Direct torque control of 6-phase IM using SVPWM Technique	low and medium Speed	Fixed switching frequency is utilized along with DTC control to have a more straightforward control. Outcome confirms the reliability of the control mechanisms

II. SYSTEM CONFIGURATION AND MODELING

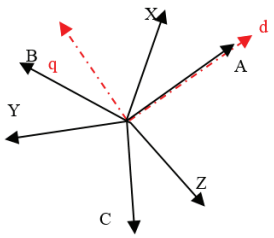


Fig. 1. Transformation from 6-phase abcxyz model to d-q model

The equivalent circuit diagram of the induction motor in d-q axis is shown below in Fig.2 & Fig.3:

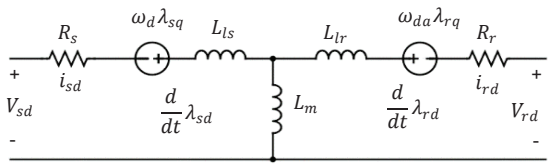


Fig. 2. d equivalent circuit of an IM.

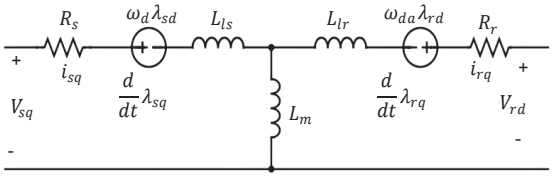


Fig. 3. q equivalent circuit of an IM

▪ *MATHEMATICAL MODELING in dq FRAME*

A six-phase induction motor with an asymmetrical design employs two distinct sets of three-phase stator winding present in Fig.1. These sets are physically offset from each other by an angle of 30º in terms of their electrical position within the motor. Following Voltage space decomposition method (VSD) the mathematical model for asynchronous induction machine can be described. The variables of the six-phase machine are split into three orthogonal subspaces, Z_1-Z_2, x-y, and α-β. Here the neutral points are assumed to be isolated, which is the typical layout under healthy conditions, so the zero sequence components are neglected. Hence, the new sequence variables can be stated as follows:

$$\left[f_\alpha f_\beta f_x f_y\right]^T = T_{VSD}\left[f_a f_b f_c f_x f_y f_z\right]^T \quad (1)$$

where transformation matrix T_{VSD} can be calculated as:

$$T_{VSD} = \frac{1}{\sqrt{3}}\begin{bmatrix} 1 & -\frac{1}{2} & -\frac{1}{2} & \frac{\sqrt{3}}{2} & -\frac{\sqrt{3}}{2} & 0 \\ 0 & \frac{\sqrt{3}}{2} & -\frac{\sqrt{3}}{2} & \frac{1}{2} & \frac{1}{2} & -1 \\ 1 & -\frac{1}{2} & -\frac{1}{2} & -\frac{\sqrt{3}}{2} & \frac{\sqrt{3}}{2} & 0 \\ 0 & -\frac{\sqrt{3}}{2} & \frac{\sqrt{3}}{2} & \frac{1}{2} & \frac{1}{2} & -1 \end{bmatrix} \quad (2)$$

Applying KVL to Fig.2 of the q-equivalent circuit, the voltage equation can be present as-

(a) For stator, $V_{\alpha s} = R_s I_{\alpha s} + \frac{d}{dt}\Psi_{\alpha s} - \omega\Psi_{\alpha s}$ (3)

$$V_{\beta s} = R_s I_{\beta s} + \frac{d}{dt}\Psi_{\beta s} + \omega\Psi_{\beta s} \quad (4)$$

$$V_{xs} = R_s I_{xs} + \frac{d}{dt}\Psi_{xs} \quad (5)$$

$$V_{ys} = R_s I_{ys} + \frac{d}{dt}\Psi_{ys} \quad (6)$$

(b) And for Rotor, $0 = R_r I_{dr} + \frac{d}{dt}\Psi_{dr} - \omega_e\Psi_{qr}$ (7)

$$0 = R_r I_{qr} + \frac{d}{dt}\Psi_{qr} - \omega_e\Psi_{dr} \quad (8)$$

Thus, from the above relations, the expression for stator flux is given below:

$$\begin{bmatrix}\psi_{\alpha s}\\ \psi_{\beta s}\\ \psi_{x1}\\ \psi_{y1}\end{bmatrix}=L_{\gamma s}\begin{bmatrix}i_{\alpha s}\\ i_{\beta s}\\ i_{x1}\\ i_{y1}\end{bmatrix}+L_m\begin{bmatrix}1&0&0&0\\0&1&0&0\\0&0&0&0\\0&0&0&0\end{bmatrix}\begin{bmatrix}i_{\alpha s}\\ i_{\beta s}\\ i_{x1}\\ i_{y1}\end{bmatrix}+L_m\begin{bmatrix}1&0\\0&1\\0&0\\0&0\end{bmatrix}\begin{bmatrix}i_{\alpha s}\\ i_{\beta r}\end{bmatrix} \quad (9)$$

And for rotor flux,

$$\begin{bmatrix}\psi_{\alpha r}\\ \psi_{\beta r}\end{bmatrix}=L_{\gamma r}\begin{bmatrix}i_{\alpha r}\\ i_{\beta r}\end{bmatrix}+L_m\begin{bmatrix}i_{\alpha r}\\ i_{\beta r}\end{bmatrix}+L_m\begin{bmatrix}i_{\alpha s}\\ i_{\beta s}\end{bmatrix} \quad (10)$$

The Electromagnetic torque and rotor's speed (mechanical system) can be implemented by the equation:

$$T_e=3\times\frac{P}{2}\times L_m[I_{qs}\Psi_{ds}-I_{ds}\Psi_{qs}] \quad (11)$$

Mechanical motion equation:

$$J\frac{d\omega_r}{dt}+B\omega=T_e \quad (12)$$

$$\omega_r=\int\frac{1}{J}[T_e-T_l] \quad (13)$$

$$\omega_e=\omega_r\times\frac{P}{2} \quad (14)$$

where the variables are:

- V, i, Ψ – voltage, current, flux vectors,
- R – resistance,
- L_γ, L_m – leakage inductance, mutual inductance,
- T_e, T_l – machine torque and load torque,
- ω_r, ω_e – Speed mechanical, speed electrical

Fig.4 presents the proposed modelling technique for six-phase induction motor; the six-phase supply voltage is supplied to the machine, and then the voltages are transformed to d-q using Clarke's transformation. Hence, the stator currents and rotor currents are transformed from d-q to six-phase through inverse Clarke's transformation. Flux produces by this value are then transferred to the d and q block for having mechanical output, and at last the value of electromagnetic torque and speed can be observed.

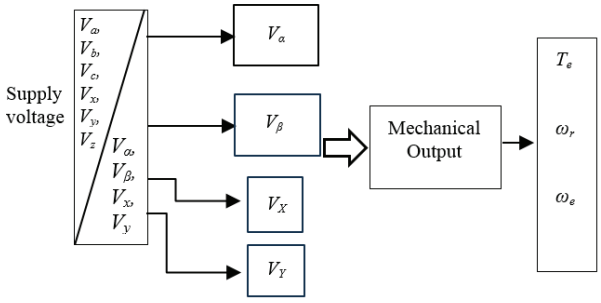


Fig. 4. A proposed dynamic model of six-phase IM

▪ SIX-PHASE VOLTAGE SOURCE INVERTER

The power converter that powers the A6P motor is made up of two three-phase, two-level voltage source inverters that are coupled in parallel.

This leads to a six-phase inverter that can generate 64 (2^6) different output voltage vectors. If each inverter leg's status is denoted as S_i, then S_i equals 1 when the upper switch is activated, and 0 when it is deactivated. Defining the switching state as a vector,

$$[S]=[S_aS_bS_cS_xS_yS_z]^T \quad (15)$$

Fig.5 presents the spatial distribution of Stator winding for the asymmetrical SPIM.

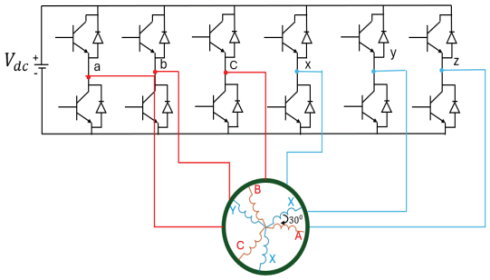


Fig. 5. Stator winding spatial distribution for an asymmetrical SPIM.

The following formula can be used to get the inverter output phase voltage vector:

$$\begin{bmatrix}V_{a1}\\ V_{b1}\\ V_{c1}\\ V_{a2}\\ V_{b2}\\ V_{c2}\end{bmatrix}=\frac{V_{dc}}{3}\begin{bmatrix}2&-1&-1&0&0&0\\-1&2&-1&0&0&0\\-1&-1&2&0&0&0\\0&0&0&2&-1&-1\\0&0&0&-1&2&-1\\0&0&0&-1&-1&2\end{bmatrix}[S] \quad (16)$$

Utilizing the VSD transformation outlined in this equation [16] the inverter can achieve voltage outputs corresponding to the *(α-β)* and *(x-y)* subspaces.

$$\begin{bmatrix}V_\alpha\\ V_\beta\\ V_x\\ V_y\\ V_{z1}\\ V_{z2}\end{bmatrix}=T_{VSD}\begin{bmatrix}V_{a1}\\ V_{b1}\\ V_{c1}\\ V_{a2}\\ V_{b2}\\ V_{c2}\end{bmatrix} \quad (17)$$

▪ DTC SVPWM CONTROL STRATEGY

Space Vector Pulse Width Modulation (SVPWM) divides the space vector plane into sectors, each associated with a unique combination of switching states. The "Determine Sector" block identifies the sector of the current voltage vector by using signals and theta (angular position of the voltage vector). Theta is then reduced to a primary reference sector, typically Sector 1, to ensure symmetrical handling across all sectors. The deviation of area of theta is present in Table V as FLUX PHASOR STATE (FPS). From this block the outputs as active sector and the relative angle within the determined sector, referred to as Theta1, are observed.

After determining the sector, the "Switching Sequence" blocks it to corresponding voltage vectors. For a six-phase motor, this involves 12 active voltage vectors (U_1 to U_{12}) and zero vectors (U_0) shown in Fig.7. The selected voltage vectors are forwarded to outputs V_1, V_2, and V_0 for PWM modulation. Zero vectors are alternated periodically to ensure symmetrical and reduce harmonic distortion.

Lastly, the "Sequence Selection" block calculates the application durations of the active vectors, to approximate the reference voltage vector. This alternation between active and zero vectors ensures smooth transitions and reduces ripples in the stator flux. The PWM module generates gate pulses for the inverter legs driving the six-phase induction motor. The reference voltage vector is transformed into α-β coordinates, which determines its position in the space vector plane. These coordinates are used to calculate the sector and relative angle, guiding the selection and sequencing of voltage vectors. By applying the calculated sequences through the inverter gates, the motor achieves enhanced torque and flux, ensuring efficient and stable operation.

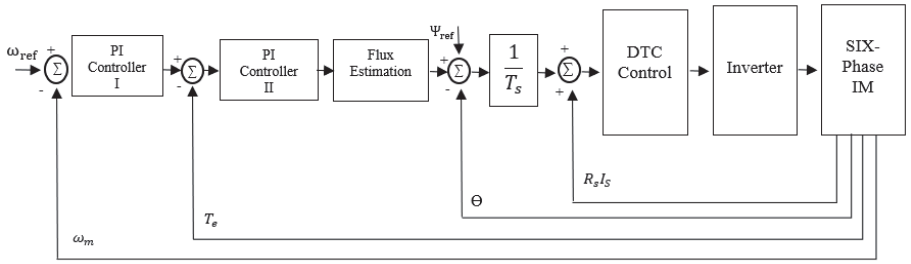


Fig.6. A proposed dynamic model of DTC (SVPWM) six-phase IM

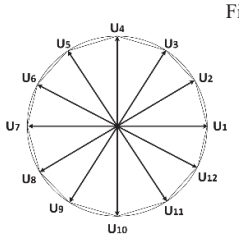


Fig. 7. 6 phase Voltage vector diagram (SVPWM)

This integration of sector determination and switching sequence generation ensures precise selection and application of voltage vectors, enabling smooth motor operation with minimized harmonic distortion and improved performance. Fig. 6 displays the dynamic model of DTC IM's block diagram. The DTC control scheme is built utilizing the SVPWM block and 12 voltage vectors with the greatest amplitudes shown in Fig.7. There are $2^6 = 64$ switching states in VSI inverter. A six-phase inverter has 64 possible states. Among these, 12 are active states, and multiple are zero states (redundant states). The principle of active vectors is for transferring power and zero vectors are for minimizing switching remains unchanged. In the α-β plane, the voltage vectors represent the fundamental harmonic components with each sector spans 30º of the six-phase system. The x-y plane represents the third harmonic or zero-sequence components of the six-phase voltage vectors. The voltage vectors in this plane typically form a hexagonal shape, which is orthogonal to the α-β plane. This plane shows the harmonic content from the six-phase system but doesn't directly generate torque or flux. The stator flux, Ψ_s of SPIM rotates at the desired frequency by choosing the suitable inverter voltage vector, within a specified range of the flux controller, depicted in Fig.8, from the (α–β) and (x-y) sub-plane. Switching frequency is made constant by adding SVPWM. SVPWM block needs a complicated stator voltage reference (V_{sref}) produced from torque and flux references to create switching PWM impulses. Relation given by (18) can be used to calculate reference voltage.

$$V_s = R_s I_s + \frac{\Delta \Psi_s}{T_s} \tag{18}$$

In a particular voltage zone, a combination of two neighboring voltage values is used to create the desired reference voltage.

Table II shows flux phasor angle ($\boldsymbol{\theta_{fs}}$) is discretized into 12 sectors, each corresponding to a specific state based on its angular position within the ±180° range.

A look up table is created in table III using the flux error output Ψ_{err}, torque error output S_T, and flux phasor state S_θ to determine the inverter's switching states (considering 12 voltage vectors with the greatest amplitudes).

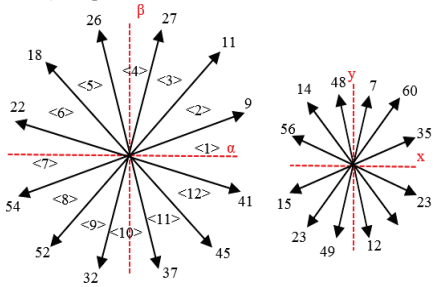


Fig. 8. (a) Voltage vector in α-β plane; (b) voltage vector in x-y plane

TABLE II. FLUX PHASOR STATE

$\boldsymbol{\theta_s}$	State
45º< $\boldsymbol{\theta_{fs}}$ ≤ 75º	<2>
75º < $\boldsymbol{\theta_{fs}}$ ≤ 105º	<3>
105º< $\boldsymbol{\theta_{fs}}$ ≤ 135º	<4>
135º< $\boldsymbol{\theta_{fs}}$ ≤ 165º	<5>
165º< $\boldsymbol{\theta_{fs}}$ ≤ 180º Or -165º< $\boldsymbol{\theta_{fs}}$ ≤ -180º	<6>
-135º< $\boldsymbol{\theta_{fs}}$ ≤ -165º	<7>
-105º< $\boldsymbol{\theta_{fs}}$ ≤ -135º	<8>
-75º< $\boldsymbol{\theta_{fs}}$ ≤ -105º	<9>
-45º< $\boldsymbol{\theta_{fs}}$ ≤ -75º	<10>
-15º< $\boldsymbol{\theta_{fs}}$ ≤ -45º	<11>
0º< $\boldsymbol{\theta_{fs}}$ ≤ -15º Or 15º< $\boldsymbol{\theta_{fs}}$ ≤ 0º	<12>
45º< $\boldsymbol{\theta_{fs}}$ ≤ 15º	<1>

TABLE III. SWITCHING STATES FOR POSSIBLE ΨERR, S_T AND S_Θ

Switching State	States						Switches on	Space Vector
Uk	S_a	S_b	S_c	S_x	S_y	S_z	-	V_k
<00>	1	1	1	0	0	0	1,3,5,8,10,12	V_7
<01>	0	0	0	1	1	1	2,4,6,7,9,11	V_{56}
<02>	1	1	1	1	1	1	1,3,5,7,9,11	V_{63}
<1>	1	0	0	1	0	0	1,4,6,7,10,12	V_9
<2>	1	1	0	1	0	0	1,3,6,8,10,12	V_{11}
<3>	1	1	0	1	1	0	1,3,6,7,9,12	V_{27}
<4>	0	1	0	1	1	0	2,3,6,7,9,12	V_{26}
<5>	0	1	0	0	1	0	2,3,6,8,9,12	V_{18}
<6>	0	1	1	0	1	0	2,3,5,8,9,12	V_{22}
<7>	0	1	1	0	1	1	2,3,5,8,9,11	V_{54}
<8>	0	0	1	0	1	1	2,4,5,8,9,11	V_{52}
<9>	0	0	1	0	0	1	2,4,5,8,10,11	V_{36}
<10>	1	0	1	0	0	1	1,4,5,8,10,11	V_{37}
<11>	1	0	1	1	0	1	1,4,5,7,10,11	V_{45}
<12>	1	0	0	1	0	1	1,4,6,7,10,11	V_{41}

III. SIMULATION RESULT & PERFORMANCE ASSESSMENT

Using MATLAB/Simulink the machine was simulated. The result part is divided into two parts. The initial stage involves analyzing the induction machine's behavior without including SVPWM technique. Subsequently, in the second phase, the induction machine (IM) is subjected to Direct Torque Control

(DTC) with Selective Harmonic Pulse Width Modulation (SVPWM) to observe its response under varying load conditions. An enhanced version incorporates more efficient control, prioritizing the maximization of the output voltage within the α-β plane. The following parameters, obtained experimentally from a six-phase induction motor, were used for modeling and analysis in MATLAB/Simulink

TABLE IV. SWITCHING PARAMETERS USED FOR INDUCTION MOTOR SIMULATION

Symbol	Variable	Value
R_s	Stator Resistance	11.6 Ω
R_r	Rotor's Resistance	10.4 Ω
f	Frequency	50 Hz
ω	Rotor speed in electrical degrees	2*pi*f
L_m	mutual inductance between stator and rotor	0.3 H
L_s	Stator's Inductivity	0.579H
L_{ys}	Stator leakage inductance	0.045 H
L_r	Rotor's inductivity	0.579H
L_{yr}	Rotor leakage inductance	0.04 H
P	Number of Poles	4
J	Moment of inertia	0.002 Kgm^2
N_n	Nominal Speed	1410 RPM
K	Reference speed	0.8
ω_s	Synchronous speed	2*pi*f/p
γ	Stator & rotor's coefficient	$Ls*L_r-L_m*L_m$

A. DTC IM in Open loop

Below in Fig. 9–11 show simulation results for the open-loop system without any control.

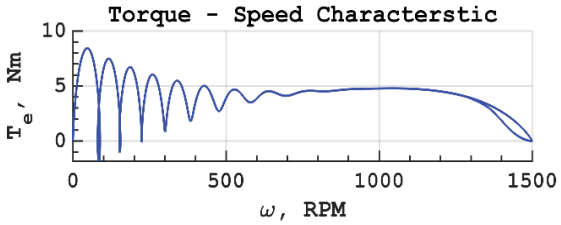


Fig. 9 Torque vs speed characteristics of IM

From the torque vs speed characteristics of six phase induction motor shown in Fig.9, it is observed that at standstill, the motor produces high starting torque to overcome inertia, with oscillations caused by motor's design. As speed increases, these oscillations diminish, and the motor accelerates toward synchronous speed. At higher speeds, torque stabilizes, indicating efficient operation. Fig.10 illustrates a dynamic testing of IM. The reduction in stator current suggests a temporary load or torque reduction, while the recovery indicates a return to normal loading conditions. Fig.11 illustrates the transient and steady-state torque and speed of the induction machine, showcasing its start-up and loading dynamics. Initially, torque oscillations occur as the motor accelerates. By ~0.5s, it reaches steady-state speed under no-load conditions. After ~0.7s, a load is applied, increasing torque while maintaining speed, demonstrating the motor's load-handling capability.

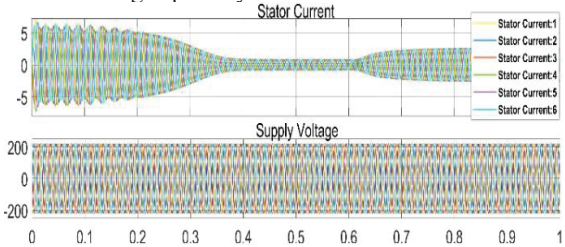


Fig. 10. Supply voltage and stator current.

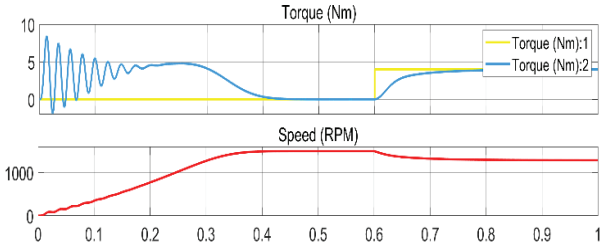


Fig. 11 Transient and Steady-State Torque and Speed of IM

B. DTC IM with SVPWM technique

The torque response of SPIM after adding load including SVPWM is illustrated in Fig. 12. Initially, the machine exhibits high torque oscillations, but as it stabilizes, it demonstrates the effectiveness of DTC-SVPWM in managing load variations. Furthermore, the enhanced speed response observed in Figure 12 indicates the motor's ability to quickly adapt to increased load demand, with the stator current in Fig. 13 adjusting accordingly. It is observed that the stator current response during no-load acceleration phase remains low. When a load is applied at approximately 0.5 sec, followed by an additional load around 0.7 sec, both of which result in increased current amplitude. The smooth and consistent sinusoidal waveform underscores the effectiveness of DTC-SVPWM in regulating current, shown in Fig. 13, despite varying load conditions. While comparing outputs with just DTC in Fig.9 -11, DTC included SVPWM is giving fast torque response, efficient load handling, and reduced torque ripple. The characteristics of SVPWM Direct torque control are illustrated below-

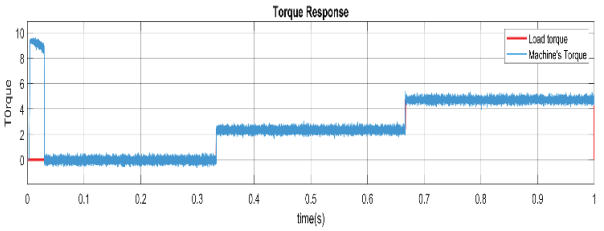


Fig 12. Characteristic of torque after adding load torque with SVPWMDTC controller

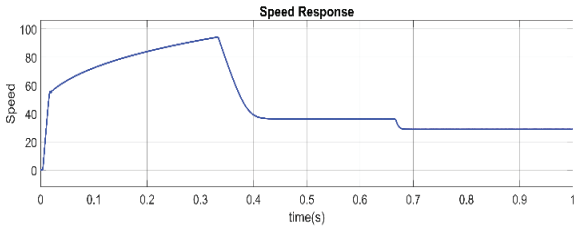


Fig. 13. Speed on response to load.

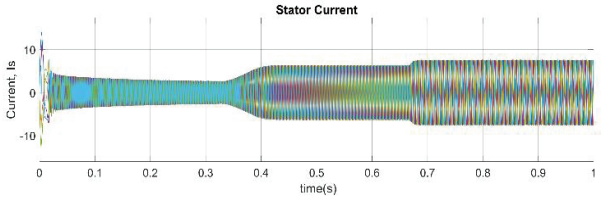


Fig. 14. Characteristic of Phasor current

Fig. 15 illustrates the stator flux trajectory in the α-β plane. Initially, the flux exhibits small variations, but as the motor stabilizes, it forms a nearly elliptical path, indicating efficient flux control.

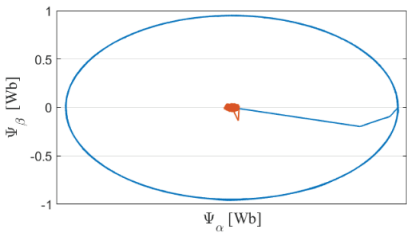


Fig. 15. The trajectory of the projected magnitude of the stator flux vector of the six-phase induction motor

This trajectory, when compared to traditional DTC, suggests that SVPWM reduces flux oscillations, leading to smoother torque and current responses. The findings from Fig.9 to 14 collectively highlight the enhanced performance of DTC-SVPWM, particularly in minimizing torque ripples, improving current regulation, and maintaining flux stability.

IV. CONCLUSION

This study presents a comprehensive analysis of direct torque control (DTC) schemes integrated with space vector pulse width modulation (SVPWM) at fixed switching frequency (FSF) for six-phase induction motors (SPIM). The results confirm that the stator flux vector maintains a constant magnitude, tracing a circular trajectory, which reflects improved flux regulation, reduced torque ripple, and enhanced magnetic field symmetry. A comparison between DTC-SVPWM and traditional open-loop DTC schemes shows that the suggested approach ensures better dynamic performance, increased dependability, and lower power losses, which makes it appropriate for industrial drive applications with low to medium speeds.

However, the complexity imposed by the six-phase method is predicted to make sector identification and vector decomposition more difficult in real-world implementations. Despite this, the proposed control approach remains scalable and adaptable to other multi-phase motor configurations. To further understand the effects of this strategy on power quality and overall system efficiency, future research will focus on the harmonies it introduces. These findings substantiate the effectiveness and scalability of the control strategy, paving the way for its deployment in sophisticated multiphase drive systems.

ACKNOWLEDGMENT

This publication was made possible by the 1st Cycle of ARG Grant No. ARG01-0504-230073, from the Qatar Research, Development and Innovation (QRDI) Council, Qatar. The findings herein reflect the work and are solely the responsibility of the authors. The authors also gratefully acknowledge support from Qatar University.

REFERENCES

[1] Gomez, J. S., Rodriguez, J., Garcia, C., Tarisciotti, L., Flores-Bahamonde, F., Pereda, J., Nunez, F., Cipriano, A. Z., & Salas, J. C. (2020). An Overview of Microgrids Challenges in the Mining Industry. IEEE Access, 8, 191378–191393. https://doi.org/10.1109/access.2020.3032281

[2] Jahromi, M. G., Mirzaeva, G., & Mitchell, S. D. (2017, September). Design and Control of a High-Power Low-Loss DC–DC Converter for Mining Applications. *IEEE Transactions on Industry Applications*, *53*(5), 5105–5114. https://doi.org/10.1109/tia.2017.2712118

[3] Pouresmaieli, M., Ataei, M., Nouri Qarahasanlou, A., & Barabadi, A. (2023, December). Integration of renewable energy and sustainable development with strategic planning in the mining industry. *Results in Engineering*, *20*, 101412. https://doi.org/10.1016/j.rineng.2023.101412

[4] Popescu, M. (2000). Induction motor modelling for vector control purposes.

[5] 5. Mishra, A., & Choudhary, P. (2012). Speed control of an induction motor by using indirect vector control method. International Journal of Emerging Technology and Advanced Engineering, 2(12), 144-150.

[6] 6. Bobin, V. J., & MarsalineBeno, M. (2023). Performance Analysis of Optimization Based FOC and DTC Methods for Three Phase Induction Motor. Intell. Autom. Soft Comput, 35, 2493-2511.

[7] Zahraoui, Y., Akherraz, M., Fahassa, C., & Elbadaoui, S. (2022). Induction Motor DTC Performance Improvement by Reducing Flux and Torque Ripples in Low Speed. Journal of Robotics and Control (JRC), 3(1), 93-100.

[8] Renukadevi, G., & Rajambal, K. (2011, December). Generalized model of multi-phase induction motor drive using matlab/simulink. In ISGT2011-India (pp. 114-119). IEEE.

[9] Payami, S., & Behera, R. K. (2017). An improved DTC technique for low-speed operation of a five-phase induction motor. IEEE Transactions on Industrial Electronics, 64(5), 3513-3523.

[10] Yazidi, A., Pantea, A., Betin, F., Carriere, S., Henao, H., & Capolino, G.A.(2014, October).Six-phase induction machine model for simulation and control purposes. In IECON 2014-40th Annual Conference of the IEEE Industrial Electronics Society (pp. 881-887). IEEE.

[11] Gonzalez-Prieto, A., Gonzalez-Prieto, I., Yepes, A. G., Duran, M. J., & Doval-Gandoy, J. (2021, March). Symmetrical six-phase induction machines: A solution for multiphase direct control strategies. In 2021 22nd IEEE International Conference on Industrial Technology (ICIT) (Vol. 1, pp. 1362-1367). IEEE.

[12] Bojoi, R., Farina, F., Griva, G., Profumo, F., & Tenconi, A. (2005). Direct torque control for dual three-phase induction motor drives. IEEE Transactions on Industry Applications, 41(6), 1627-1636.

[13] Bojoi, R., Farina, F., Profumo, F., & Tenconi, A. (2006). Dual-three phase induction machine drives control—A survey. IEEJ Transactions on Industry Applications, 126(4), 420-429.

[14] Levi, E. (2008). Multiphase electric machines for variable-speed applications. IEEE Transactions on industrial electronics, 55(5), 1893-1909.

[15] Abdelwanis, M. I., & Selim, F. (2017, December). A sensorless six-phase induction motor driving a centrifugal pump system. In 2017 Nineteenth International Middle East Power Systems Conference (MEPCON) (pp. 242-247). IEEE.

[16] Bojoi, R., Cavagnino, A., Tenconi, A., Tessarolo, A. L. B. E. R. T. O., & Vaschetto, S. (2015, September). Multiphase electrical machines and drives in the transportation electrification. In 2015 IEEE 1st International Forum on Research and Technologies for Society and Industry Leveraging a better tomorrow (RTSI) (pp. 205-212). IEEE.

[17] Idoko, A., Thuku, I., Musa, S., & Amos, C. (2017). Design of tuning mechanism of PID controller for application in three phase induction motor speed control. International Journal of Advanced Engineering Research and Science, 4(11), 138-147.

[18] Yang, G., Hussain, H., Li, S., Zhang, J., & Yang, J. (2022). Fault-tolerant control for multiphase induction machines with torque ripple reduction considering harmonic injection. IEEE Transactions on Power Electronics, 37(12), 14005-14010.

[19] Kaila,S.L., & Jani,H. B.(2011).Direct torque control for induction motor using SVPWM technique. In *Proc. Nat. Conf. on recent trends in engineering & technology. VV Nagar, Gujarat, India: BVM Engineering College*.

[20] Raute, R., Caruana, C., Staines, C. S., Cilia, J., Sumner, M., & Asher, G. M. (2010). Sensorless control of induction machines at low and zero speed by using PWM harmonics for rotor-bar slotting detection. *IEEE Transactions on Industry Applications*, *46*(5), 1989-1998

[21] Raute, R., Caruana, C., Staines, C. S., Cilia, J., Sumner, M., & Asher, G. M. (2010, September). Sensorless Control of Induction Machines at Low and Zero Speed by Using PWM Harmonics for Rotor-Bar Slotting Detection. IEEE Transactions on Industry Applications, 46(5), 1989–1998. https://doi.org/10.1109/tia.2010.2057495

[22] Chagam, V. S. R., & Devabhaktuni, S. (2022). Enhanced low-speed characteristics with constant switching torque-controller-based dtc technique of five-phase induction motor drive with FOPI control. *IEEE Transactions on Industrial Electronics*, *70*(11), 10789-10799.

A Frequency-Tracking Quasi-Proportional Resonant Approach for Harmonic Suppression in PMSM

1st Siqi Peng
College of Automation and Electronic Information
Xiangtan University
Xiangtan, China
13286587@qq.com

2nd Chuchen Yang
College of Automation and Electronic Information
Xiangtan University
Xiangtan, China
1424143265@qq.com

3rd Zhiwen Zhang
College of Automation and Electronic Information
Xiangtan University
Xiangtan, China
3193253163@qq.com

4th Kun Zhu
College of Automation and Electronic Information
Xiangtan University
Xiangtan, China
1171281487@qq.com

***Abstract*—This paper proposes an optimized quasi-proportional resonant (QPR) control technique for noise and harmonic suppression in permanent magnet synchronous motors (PMSM) used in electric vehicle drive systems. Although conventional PR/QPR controllers can effectively reduce stator current harmonics and noise, their suppression performance deteriorates when the fundamental frequency or speed of the motor varies, due to mismatches between the resonant frequency and the actual harmonic frequencies. To address this issue, a frequency-tracking QPR harmonic suppression method is presented. This approach first utilizes the Fourier transform to extract the fundamental frequency in real time, calculates the frequencies of target harmonics (such as the 5th, 7th, 11th, and 13th), and employs a recursive least squares algorithm to dynamically track these harmonic frequencies, thereby adjusting the resonant frequency of the QPR controller in real time for continuous and precise suppression of the target harmonics. Simulation results based on the MATLAB/Simulink platform demonstrate that this method significantly improves harmonic suppression under frequency or load variations, avoiding the reduction in resonant gain associated with conventional methods, and further enhances system performance and comfort. This method provides both theoretical and technical support for the efficient and low-noise operation of PMSM in electric vehicles, and is particularly suitable for applications with stringent noise and vibration requirements.**

Keywords—quasi-proportional resonant controller, frequency tracking, recursive least squares, harmonic suppression, PMSM

I. INTRODUCTION

At present, permanent magnet synchronous motors (PMSM) are widely used in various fields such as industry, transportation, and electric vehicles due to their simple structure, high efficiency, and high power density. However, their current waveforms are often subject to significant harmonic disturbances. In particular, during operation, factors such as cogging effects, magnetic saturation, and inverter nonlinearities can introduce a substantial amount of high-order harmonics into the motor current. These harmonic components not only increase motor losses and cause additional heating, but may also generate electromagnetic noise, thereby affecting the operational stability of the motor.

Extensive research has been conducted by scholars at home and abroad on how to effectively suppress current harmonics in PMSM, from the perspective of motor design, harmonics can be reduced primarily by optimizing the structure of the motor itself and improving the sinusoidal distribution of the air gap magnetic field [1]-[3]. However, this approach increases the complexity of motor design and places higher demands on manufacturing processes.

Another class of methods focuses on optimizing control strategies to suppress current harmonics effectively through harmonic compensation algorithms. For example, some studies have extracted the harmonic components of the current and injected them into the voltage signal, thus achieving suppression of the 5th and 7th harmonics [4]. However, incorporating a harmonic current loop increases system complexity, makes parameter tuning more complicated, and significantly raises computational requirements. Additionally, some studies based on internal model control theory have proposed repetitive controllers to suppress multiple frequency harmonics, but this method requires large storage space and involves complex parameter tuning [5].

By comparison, the proportional-resonant (PR) controller has theoretically infinite gain at specific resonant frequencies and can effectively control harmonics at those frequencies. It has thus been widely used for harmonic suppression in grid-connected inverters [6]-[8]. Furthermore, PR controllers have also demonstrated excellent performance in suppressing harmonics in motors [9]-[10]. Research has shown that paralleling a PR controller with a PI controller can effectively suppress single-frequency harmonics in PMSM. This approach features a simple structure and easy parameter adjustment [11]-[12].

This paper first analyzes the causes of the 5th, 7th, 11th, and 13th harmonics in PMSM and presents their mathematical models. Subsequently, a frequency-tracking quasi-proportional resonant (QPR) controller-based current harmonic suppression strategy is proposed to improve the operational performance of PMSM and optimize the current waveform. By applying this strategy, the 5th, 7th, 11th, and 13th harmonic components in the current can be significantly reduced, thereby improving the motor's power factor, reducing energy losses, and enhancing the overall stability of the motor system.

979-8-3315-5472-9/25/$31.00 ©2025 IEEE

II. Vector Control and Harmonic Analysis of PMSM

A. dq-Axis Vector Control

In this study, the permanent magnet synchronous motor (PMSM) is controlled using a vector control method based on the dq coordinate system. Specifically, the three-phase currents are transformed into the synchronous rotating reference frame through Clarke and Park transformations, resulting in two-phase dq-axis currents. This approach decomposes the stator current of the motor into two independent components: the direct-axis current (d-axis current) and the quadrature-axis current (q-axis current). By controlling the d-axis current, the torque output of the motor can be regulated, while the q-axis current is used to adjust the magnetic field strength, thereby enabling precise control of the motor.

Mathematical Model of Three-Phase Currents in PMSM:

$$\begin{cases} i_a = I_1 sin(\omega t) + I_5 sin(5\omega t) + I_7 sin(7\omega t) + I_{11} sin(11\omega t) + \\ I_{13} sin(13\omega t) \\ i_b = I_1 sin(\omega t) + I_5 sin(5(\omega t - \frac{2\pi}{3})) + I_7 sin(7(\omega t - \frac{2\pi}{3})) \\ + sin(11(\omega t - \frac{2\pi}{3})) + I_{13} sin(13(\omega t - \frac{2\pi}{3})) \\ i_c = I_1 sin(\omega t) + I_5 sin(5(\omega t - \frac{4\pi}{3})) + I_7 sin(7(\omega t - \frac{4\pi}{3})) \\ + sin(11(\omega t - \frac{4\pi}{3})) + I_{13} sin(13(\omega t - \frac{4\pi}{3})) \end{cases} \quad (1)$$

The advantage of this control method lies in the decoupling of torque control and magnetic field control, allowing the motor to operate efficiently and precisely. Vector control is a widely used motor control strategy in industry today. It simplifies the complexity found in traditional control strategies and can significantly improve the dynamic response performance of the motor. Fig 1 shows the block diagram of vector control for a permanent magnet synchronous motor.

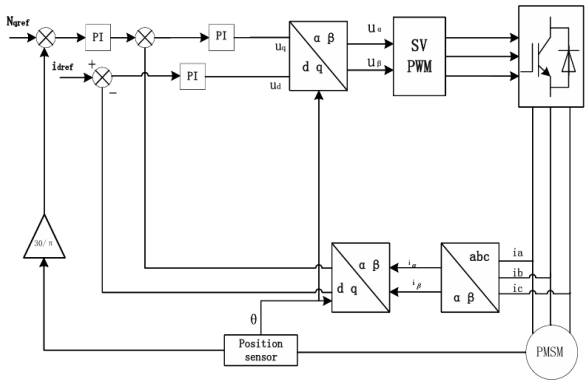


Fig. 1. Vector control block diagram of PMSM

B. Harmonic Current Analysis in the dq Reference Frame

Due to factors such as air-gap magnetic field distortion and the nonlinear characteristics of the inverter, the stator current of PMSM typically contains multiple harmonic components at various frequencies. The most commonly observed harmonics are the 5th, 7th, 11th, and 13th orders. The presence of these harmonics leads to torque ripple and increased system losses, which can adversely affect the stability and overall performance of the motor.

$$\begin{cases} i_d = I_1 + I_5 sin\left[6(-\omega_e t)\right] + I_7 sin(6\omega_e t) + I_{11} sin \\ \left[12(-\omega_e t)\right] + I_{13} sin(12\omega_e t) \\ i_q = I_1 + I_5 cos\left[6(-\omega_e t)\right] + I_7 cos(6\omega_e t) + I_{11} cos \\ \left[12(-\omega_e t)\right] + I_{13} cos(12\omega_e t) \end{cases} \quad (2)$$

Equation (2) represents the current model in the dq reference frame, where the harmonic components of the current are manifested as harmonic elements of different frequencies. Specifically, the 5th and 7th harmonic currents in the stator frame are transformed into 6th harmonic currents in the dq reference frame, while the 11th and 13th harmonics are converted into 12th harmonic components.

Accordingly, to suppress these harmonic components in the current, this study proposes a current suppression strategy based on a frequency-tracking quasi-proportional resonant (QPR) controller. This approach enables precise regulation of the d-axis and q-axis currents in the dq reference frame, thereby effectively reducing the harmonic content in the current and significantly enhancing the overall performance and stability of the motor system.

III. Harmonic Suppression Strategies for PMSM

The conventional PI controller is limited in terms of bandwidth; although it can achieve zero steady-state error for DC signals, it exhibits low gain for AC components, making it difficult to effectively suppress current harmonics. In contrast, the proportional-resonant (PR) controller possesses the advantage of achieving zero steady-state error at the resonant frequency. Therefore, by incorporating a quasi-proportional resonant (QPR) controller with resonant frequencies at $6\omega_0$ and $12\omega_0$ (where ω_0 denotes the fundamental electrical angular frequency) in addition to the PI controller, the gain at specific frequencies can be significantly enhanced. This configuration enables the effective attenuation of the 5th, 7th, 11th, and 13th harmonics in the current.

A. Quasi-Proportional Resonant (QPR) Controller

Firstly, the transfer function of an ideal proportional-resonant (PR) controller is given as follows:

$$G_{PR}(s) = K_p + \frac{K_R s}{s^2 + \omega_0^2} \quad (3)$$

Where $G_{PR}(s)$ denotes the transfer function of the PR controller; K_p is the proportional gain; K_R is the resonant gain; ω_0 is the resonant angular frequency.

In practical high-speed permanent magnet synchronous motor (PMSM) control systems, speed estimation often contains errors due to current sensor sampling inaccuracies and limitations in digital control precision, resulting in fluctuations of the fundamental current frequency. Moreover, many applications require the motor to operate under variable-speed conditions. Under these circumstances, the conventional ideal proportional-resonant (PR) controller is only effective at a fixed resonant frequency (ω_0). When the speed or frequency changes and harmonic frequencies deviate, the controller's gain drops

sharply outside the resonant point, significantly weakening its harmonic suppression capability.

To address this issue, the quasi-proportional-resonant (QPR) controller has been introduced. The core advantage of the QPR controller lies in its ability to not only suppress harmonics effectively at the resonant frequency, but also maintain high gain in the vicinity of this frequency, thereby improving the performance of PR controllers under speed variations or frequency fluctuations. By introducing a gain compensation term based on the ideal PR controller, the QPR ensures adequate gain even outside the resonant frequency point, avoiding gain degradation due to frequency fluctuations and enabling stable and efficient harmonic suppression when current harmonic frequencies vary.

The transfer function of the quasi-proportional resonant (QPR) controller is given as follows:

$$G_{QPR}(s) = K_p + \frac{2K_R\omega_b s}{s^2 + 2\omega_b s + \omega_0^2} \tag{4}$$

In this expression, G_{QPR} denotes the transfer function of the quasi-proportional resonant (QPR) controller; ω_b represents the cut-off (shear) frequency, which serves to enhance the resonant gain for frequency signals within a specified range around the resonant angular frequency ω_0, but does not yield infinite gain at ω_0. As illustrated in Fig 2, the frequency responses of the ideal proportional-resonant (PR) controller and the quasi-proportional resonant (QPR) controller are compared at a resonant frequency of 100 Hz ($\omega 0=100\times 2\pi$), with proportional gain K_p=0, resonant gain K_R=200, and cutoff frequency $\omega_b=0.8\times 2\pi$. According to the Bode plot results, the phase characteristics of the QPR controller coincide with those of the PR controller at the resonant frequency; in terms of amplitude-frequency characteristics, the QPR controller exhibits a wider resonant bandwidth compared to the ideal PR controller.

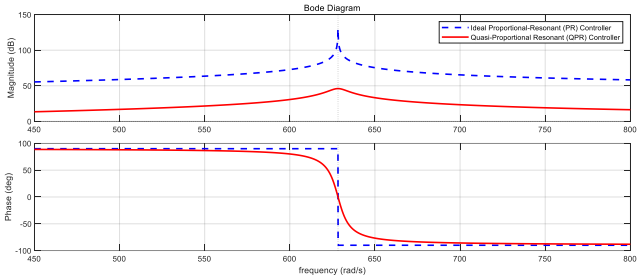


Fig. 2. Bode Plot Comparison of the Ideal Resonant Controller and QPR Controller

B. Harmonic Suppression Methods for PMSM Based on Frequency Tracking

During the operation of permanent magnet synchronous motors (PMSMs), speed fluctuations inevitably lead to variations in the fundamental frequency as well as higher-order harmonics such as the 5th, 7th, 11th, and 13th. When the resonant frequency of the quasi-proportional-resonant (QPR) controller does not coincide with the actual harmonic frequencies to be suppressed, the resonant gain decreases accordingly, thereby impairing the effectiveness of harmonic suppression. Furthermore, in practical scenarios, PMSM frequently operate under variable-speed conditions, making it extremely challenging for conventional PR controllers to dynamically adjust the resonant frequency in response to changes in the fundamental frequency, thus limiting their harmonic suppression capability under dynamic operating conditions.

To effectively address these challenges, this paper proposes a QPR control strategy based on real-time frequency tracking. Specifically, by continuously sampling the phase current and applying fast Fourier transform (FFT), the fundamental frequency of the current can be identified, which allows for the calculation of the target harmonic frequencies. Subsequently, the recursive least squares (RLS) algorithm is employed to track these harmonic frequencies in real time, and the tracking results are used as the input frequencies for the QPR controller. The core advantage of this approach lies in its ability to substantially reduce the mismatch between the resonant and actual harmonic frequencies, thereby enabling real-time adjustment of the resonant frequency in accordance with speed variations. As a result, the QPR controller is able to maintain optimal harmonic suppression performance and improve system stability and overall performance, while effectively mitigating the gain degradation typically observed in traditional PR controllers due to frequency shifts. The schematic diagram of the proposed method is presented in Fig 3.

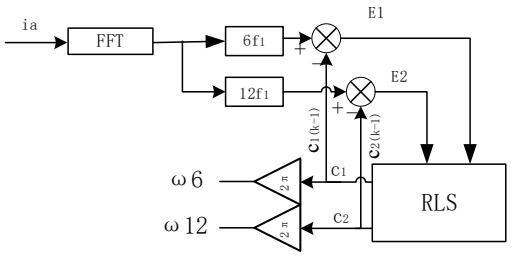


Fig. 3. Schematic Illustration of the Frequency-Tracking-Based Method

C. Principle Analysis of the Frequency-Tracking QPR Method

The Fourier Transform is an effective tool for converting signals from the time domain to the frequency domain and is widely used in signal processing and analysis. When applied to discrete-time signals, this process is commonly referred to as the Discrete Fourier Transform (DFT), whose mathematical model is given as follows:

$$X[k] = \sum_{n=0}^{N-1} x[n] \cdot e^{-j\frac{2\pi}{N}kn}, k = 0,1,2,,N-1 \tag{5}$$

Where:

- *x[n]* denotes the n-th sample point of the discrete time-domain signal;
- *X[k]* represents the complex value of the k-th frequency component in the frequency domain.

The Fourier Transform converts a time-domain signal into its frequency-domain representation, allowing us to identify the magnitude and location of each frequency component present in the signal. By examining the amplitudes at different frequencies, the fundamental frequency can be determined.

The theoretical framework of the frequency-tracking method is as follows, and the overall schematic is illustrated in Figure 3. The fundamental frequency (*f*1), obtained from the Fourier Transform, serves as an input signal. By applying gains of 6 and 12 to f1, the target harmonic frequencies for suppression are obtained. The resonant frequencies that need to be tracked by the resonant controller are denoted as c1and c2, which are the parameters to be estimated by the recursive least squares method. The system model is established as follows:

$$\begin{cases} E_1 = 6 \times f_1 - c_1 \\ E_2 = 6 \times f_2 - c_2 \end{cases} \tag{6}$$

The objective is to drive the errors E_1 and E_2 to zero. Therefore, the recursive least squares (RLS) method is employed to estimate the parameters c_1 and c_2 in real time.

Definition of Target Values:

$$\begin{cases} y_1(k) = 6 \times f_1 \\ y_2(k) = 12 \times f_1 \end{cases} \tag{7}$$

Definition of Error Values:

$$\begin{cases} E_1(k) = y_1(k) - c_1(k) \\ E_2(k) = y_2(k) - c_2(k) \end{cases} \tag{8}$$

The core of the recursive least squares (RLS) algorithm lies in updating the estimated parameters c_1 and c_2 to minimize the error. The RLS algorithm utilizes a gain vector and a covariance matrix to iteratively update these parameters.

At each time instant *k*, the gains K_1 and K_2 are calculated using the following formulas:

$$K_1(k) = \frac{P_1(k-1) \cdot x(k)}{\lambda + x(k)^T \cdot P_1(k-1) \cdot x(k)} \tag{9}$$

$$K_2(k) = \frac{P_2(k-1) \cdot x(k)}{\lambda + x(k)^T \cdot P_2(k-1) \cdot x(k)} \tag{10}$$

where:

- $P_1(k-1)$ are the covariance matrices from the previous time step,
- $x(k)$ is the current input (which, in this case, is a scalar value of 1),
- λ is the forgetting factor ($0<\lambda\leq 1$, typically close to 1).

By utilizing the computed gains, c_1 and c_2 can be updated:

$$\begin{cases} c_1(k) = c_1(k-1) + K_1(k) \cdot (6 \times f_1 - c_1(k-1)) \\ c_2(k) = c_2(k-1) + K_2(k) \cdot (12 \times f_1 - c_2(k-1)) \end{cases} \tag{11}$$

where:

- $c_1(k-1)$ are the estimates from the previous time step,
- $y_1(k)$ are the target values at the current time step.

The covariance matrices $P_1(k)$ and $P_2(k)$ also need to be updated at each time step:

$$\begin{cases} P_1(k) = \frac{1}{\lambda}[P_1(k-1) - K_1(k) \cdot x(k)^T \cdot P_1(k-1) \\ P_2(k) = \frac{1}{\lambda}[P_2(k-1) - K_2(k) \cdot x(k)^T \cdot P_2(k-1) \end{cases} \tag{12}$$

Accordingly, it is theoretically feasible to track the harmonic frequencies requiring suppression in real time, and to update the parameters c1 and c2 accordingly within the quasi-proportional resonant controller. This effectively resolves the previously identified issue of mismatch between the resonant frequency and the target harmonic frequencies, thereby enabling the proportional-resonant controller to continuously maintain its optimal gain. The overall control block diagram based on this method is shown in Fig. 4.

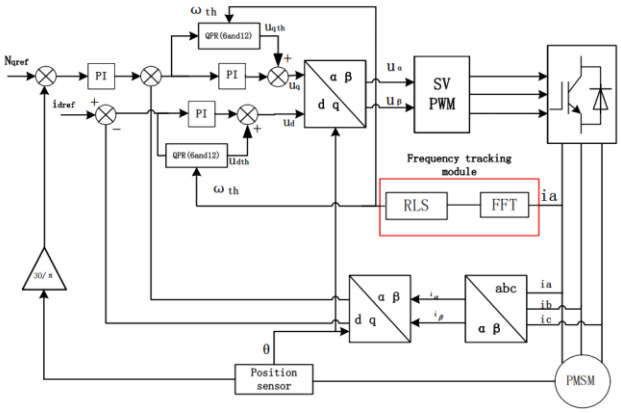
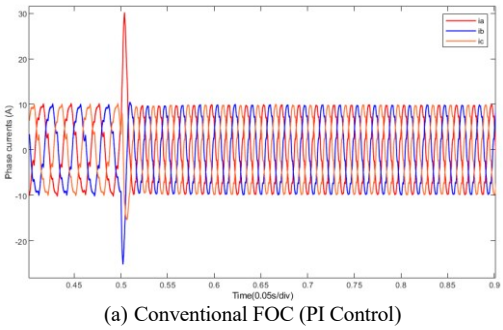


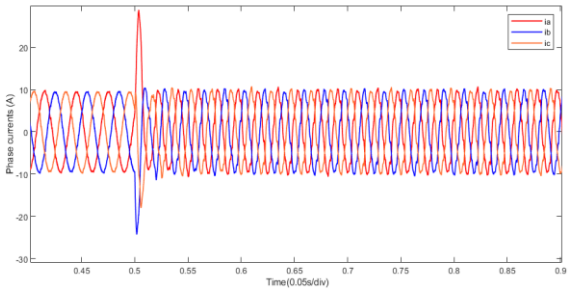
Fig. 4. Control Block Diagram of the Frequency-Tracking QPR Harmonic Suppression Method for PMSM

IV. Simulation Results and Analysis

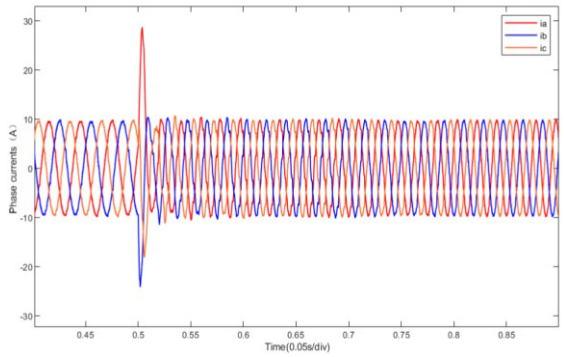
To theoretically validate the effectiveness of the proposed frequency-tracking-based harmonic suppression method for PMSM, simulations were first conducted on a simulation software platform. The simulation model incorporates a PI controller, a quasi-proportional resonant (QPR) controller based on the traditional bilinear transformation, and a frequency tracking module. Key parameters of the PMSM are set as follows: Ld = 5.25 mH, Lq = 12 mH, Rs = 0.958 Ω, and P = 4 (number of pole pairs). Furthermore, to verify the universality of the proposed method, the simulation was configured in a discrete fixed-step mode, with both the control and sampling periods set to 1×10^{-5} s, and the switching frequency to 10 kHz.



(a) Conventional FOC (PI Control)



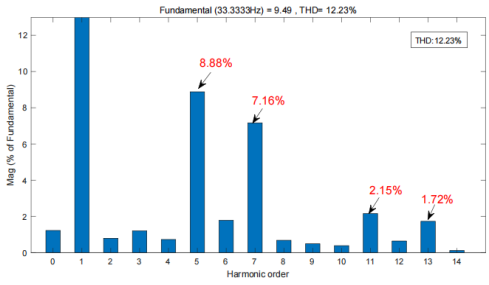
(b) Parallel QPR Control



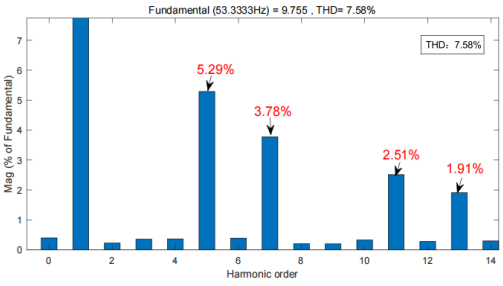
(c) Frequency-Tracking QPR Control

Fig. 5. Three-Phase Current Results for Different Methods

The initial reference speed was set to 500 r/min and increased to 800 r/min at 0.5 s. Figure 10 illustrates the three-phase current waveforms under three control strategies: PI control, PI plus QPR control, and the proposed frequency-tracking QPR method. As shown in Fig. 5(a), PI control alone results in evident zero-current clamping and substantial harmonic distortion at both speed settings. In Fig. 5(b), the addition of a QPR controller using bilinear transformation significantly reduces harmonic content and improves the sinusoidal quality of the current prior to the speed change; however, after the speed increases to 800 r/min, the harmonic suppression effect diminishes and waveform distortion reappears. Fig. 5(c) presents the results for the frequency-tracking QPR controller, where the harmonic content of the three-phase currents progressively decreases between 0.5 s and 0.7 s—corresponding to the FFT extraction and RLS tracking phase—as the QPR resonant frequency approaches the actual harmonic frequencies. After 0.7 s, the harmonics are further suppressed, and the current waveforms are notably more sinusoidal. These findings demonstrate that the proposed frequency-tracking method effectively improves current quality, enhances harmonic suppression, and strengthens the operational stability of the motor.

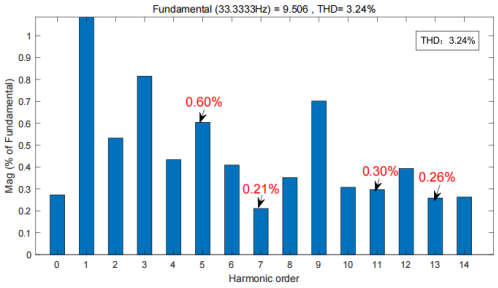


(a) FFT Analysis Results at 500 r/min

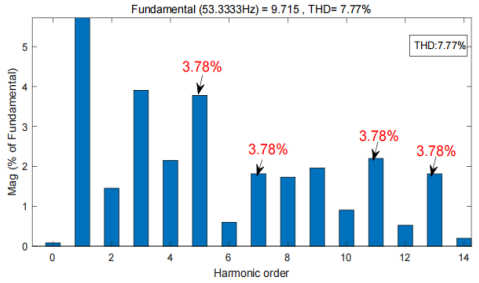


(b) FFT Analysis Results at 800 r/min After Speed Change

Fig. 6. Conventional Vector Control

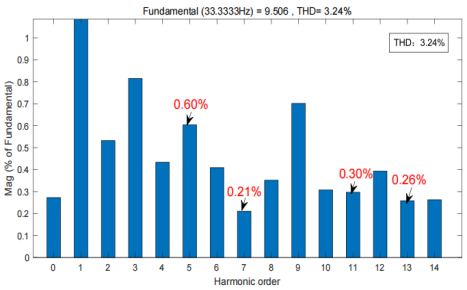


(a) FFT Analysis Results at 500 r/min

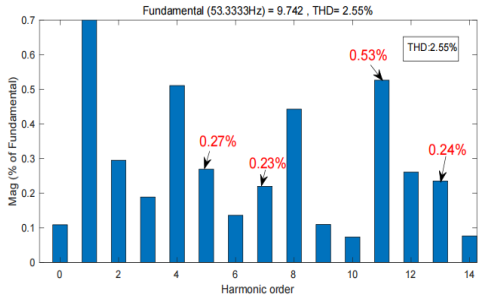


(b) FFT Analysis Results at 800 r/min After Speed Change

Fig. 7. QPR Control Strategy



(a) FFT Analysis Results at 500 r/min



(b) FFT Analysis Results at 800 r/min After Speed Change

Fig. 8. Frequency-Tracking QPR Strategy

TABLE I. HARMONIC CONTENT OF DIFFERENT METHODS AT 500 R/MIN

Harmonic Parameters	**Strategies**		
	Conventional Vector Control	***QPR Controller***	***Frequency-Tracking QPR***
THD(%)	12.23%	3.24%	3.04%
5th (%)	8.88%	0.60%	0.61%
7th (%)	7.16%	0.21%	0.29%
11th(%)	2.15%	0.30%	0.29%
13th(%)	1.72%	0.26%	0.23%

TABLE II. HARMONIC CONTENT OF DIFFERENT METHODS AT 500 R/MIN

Harmonic Parameters	**Strategies**		
	Conventional Vector Control	***QPR Controller***	***Frequency-Tracking QPR***
THD(%)	7.58%	7.77%	2.55%
5th (%)	5.29%	3.78%	0.27%
7th (%)	3.78%	1.82%	0.22%
11th(%)	2.51%	2.20%	0.53%
13th(%)	1.91%	1.81%	0.24%

According to Fig. 6, 7, and 8 (a), at 500 r/min, the 5th, 7th, 11th, and 13th harmonic contents for PI control, PI+QPR, and the proposed method are 8.88%, 7.16%, 2.15%, 1.72%; 0.60%, 0.21%, 0.30%, 0.26%; and 0.61%, 0.29%, 0.29%, 0.23%, respectively, with corresponding THD values of 12.33%, 3.24%, and 3.04%. These results indicate that the proposed method achieves much better harmonic suppression than conventional PI control and performs comparably to fixed-frequency QPR, but with a lower overall THD.

After the speed increases to 800 r/min (see Fig. 6, 7, 8(b) and Table 2), the harmonic contents and THD for the three methods are: PI control (5.29%, 3.78%, 2.15%, 1.72%, THD 7.58%), PI+QPR (3.78%, 1.82%, 2.20%, 1.81%, THD 7.77%), and the proposed method (0.27%, 0.22%, 0.53%, 0.24%, THD 2.55%). It can be seen that the fixed-parameter QPR method provides some suppression when the harmonic frequencies are within its bandwidth, but noise and increased THD occur after speed changes. In contrast, the proposed method, using recursive least squares for real-time frequency tracking, ensures that the resonant frequency always matches the target harmonics, resulting in superior suppression and the lowest THD.

V. CONCLUSION

Simulation results demonstrate that the proposed frequency-tracking QPR control strategy achieves superior suppression of the 5th, 7th, 11th, and 13th harmonics under variable-speed operating conditions compared to the PI+QPR control method presented in [9], and also results in a lower total harmonic distortion (THD). This verifies the effectiveness and practicality of the proposed method. These improvements provide a theoretical basis and engineering support for PMSM drive systems with stringent requirements for low noise and high stability, such as those used in electric vehicles. In summary, the frequency-tracking QPR-based harmonic suppression approach not only addresses the issue of resonant frequency deviation at the theoretical level, but also exhibits excellent harmonic suppression capability under dynamic operating conditions, thereby broadening the application scope of QPR controllers in permanent magnet synchronous motors.

REFERENCES

[1] MARKOVIC M, JUFER M, PERRIARD Y. Reducing the cogging torque in brushless DC motors by using conformal mappings[J]. IEEE Transactions on Magnetics, 2004, 40(2): 451-455.

[2] OH S, MIN S, HONG J. Air gap flux density waveform design of surface-mounted permanent magnet motor considering magnet shape and magnetization direction[J]. IEEE Transactions on Magnetics, 2013, 49(5): 2393-2396.

[3] Kai Wang, Haiyang Sun, Lufeng Zhang, An overview of rotor pole optimization techniques for permanent magnet synchronous machines[J]. Proceedings of the CSEE, 2017, 37(24): 7304-7317.

[4] Yong LIAO, Shuai Zhen, Ren Liu,Torque ripple suppression of permanent magnet synchronous motor by the harmonic injection[J]. Proceedings of the CSEE, 2011, 31(21): 119-127.

[5] Yongliao Wu, Hong Li, Xinda Song, Suppression of harmonic current in permanent magnet synchronous motors using improved repetitive controller[J]. Transactions of China Electrotechnical Society, 2019, 34(11): 2277-2286.

[6] CASTILLA M, MIRET J, MATAS J,Control design guidelines for single-phase grid-connected photovoltaic inverters with damped resonant harmonic compensators[J]. IEEE Transactions on Industrial Electronics, 2009, 56(11): 4492-4501.

[7] Jun Yao,Xiyin Chen,Yong Liao,A grid-connection control strategy to suppress negative-sequence and harmonic currents for permanent magnet direct-driven wind power generation system[J]. Power System Technology, 2011, 35(7): 29-35.

[8] Hong Liu, Xiaozhong Zhang,Yun Li. Design and implementation of proportional double-resonant current controller for three-phase grid-connected inverter[J]. Electric Power Automation Equipment, 2015, 35(3): 94-100).

[9] Haiyang Zhang,Haiping Xu,Cheng Fang,Torque ripple suppression method of direct-drive permanent magnet synchronous motor based on proportional-integral and quasi resonant controller[J]. Transactions of China Electrotechnical Society, 2017, 32(19): 41-51.

[10] Junfeng Liu,Xiaoyong Zhu, Li Quan,Driving control research of less-rare-earth tooth yoke magnetomotive complementary doubly salient permanent magnet motors based on resonance compensation strategy[J]. Proceedings of the CSEE, 2017, 37(22): 6534-6542

[11] Yituo Li,Haifeng Lu,Wenlong Qu,A permanent magnet synchronous motor current suppression method based on resonant controllers[J]. Proceedings of the CSEE, 2014, 34(3): 423-430

[12] Wei Xia,Kai Wang,Jianya Zhang,Torque ripple suppression of permanent magnet synchronous motor with harmonic shaped rotors based on resonance controllers[J]. Proceedings of the CSEE, 2019, 39(18): 5499-5508 .

Research on Model-Free Predictive Current Control Strategy for Axial Flux-Switching Shaftless Rim Driven Motor

Chenxuan Zhang
School of Electrical Engineering and Automation
Nantong University
Nantong, China
2412320008@stmail.ntu.edu.cn

Ziyi Tai
School of Electrical Engineering and Automation
Nantong University
Nantong, China
2312320015@stmail.ntu.edu.cn

Haoyu Wang
School of Electrical Engineering and Automation
Nantong University
Nantong, China
212822587@qq.com

Yifei Ren
School of Electrical Engineering and Automation
Nantong University
Nantong, China
2663918907@qq.com

Wei Zhang
School of Electrical Engineering and Automation
Nantong University
Nantong, China
zhang.w@ntu.edu.cn

***Abstract*—To solve the issue of parameter mismatch in the axial field flux-switching permanent magnet motor (AFFSPMM) caused by the complex and dynamic marine environment, which adversely affects the robustness of the control system, this paper proposes a model-free predictive current control (MFPCC) strategy based on an extended state observer (ESO). Firstly, the mathematical model of the AFFSPMM under MFPCC is established. Then, the ultra-local model and the extended state observer are designed to enable online estimation and compensation of lumped disturbances. Finally, the control system simulation model and experimental platform are developed to validate the proposed control strategy. The simulation and experimental results demonstrate that, compared with traditional model predictive current control (MPCC), the proposed strategy improves the stability and robustness of control system.**

Keywords—axial field flux-switching permanent magnet motor, extended state observer, model-free predictive current control, parameter robustness.

I. INTRODUCTION

With rapid advances in marine resource exploitation and ship propulsion technologies, the rim driven thruster (RDT) has become attractive for marine propulsion because of its compact form, high propulsive efficiency, and low hydrodynamic noise [1]. Among drive motors, the axial field flux-switching permanent magnet motor (AFFSPMM) offers high torque density, high efficiency, and excellent thermal characteristics, making it particularly suitable for rim driven motor(RDM).

However, the marine environments impose strong disturbances, abrupt load changes, and parameter uncertainties, leading to variations in motor parameters. Currently the mainstream control strategies include field oriented control (FOC) and direct torque control (DTC) [2]–[4]. FOC provides good steady state performance . However, it often suffers from integral oversaturation and parameter tuning challenges. DTC is simple and has fast dynamic response, but exhibits large torque and flux ripple and lacks robustness under model uncertainty. Model-free predictive current control (MFPCC) avoids the reliance on precise models and updates control laws from input–output data in real time, giving strong robustness and adaptability [5] ,and therefore, it is suitable to systems with uncertainty, nonlinearity, and strong disturbance. [6] designed model-free current controllers based on ultra-local models to estimate and compensate lumped disturbances, but did not consider load disturbances . An extended state observer (ESO) with coefficient estimation requiring only input–output variables (no motor parameters) was proposed in [7], however, it overlooked high frequency disturbances, degrading the accuracy and robustness under dynamic conditions. [8] combined a ultra-local model with sliding mode control and a finite time generalized proportional integral observer to estimate lumped disturbances, however, the application of MFPCC to RDTs remains scarce.

This paper proposes a MFPCC strategy based on ESO for AFFSPMM. Section II analyzes the structural characteristics of the AFFSPMM. Section III presents the design of the MFPCC based on ESO. Section IV validates the proposed algorithm through simulations and experiments. Finally, Section V presents the conclusions.

II. STRUCTURE OF AFFSPMM

The structure of the AFFSPMM is illustrated in Fig. 1, which consists of two identical outer stators and an inner rotor sandwiched between them. Each stator comprises six permanent magnets (PMs), six armature windings, and six E-shaped laminated iron cores. Adjacent E-cores are embedded with PMs having opposite magnetization directions, while the armature windings are wound around the stator teeth of adjacent E-cores.

This work was supported by National Natural Science Foundation of China (Grant Number: 52577060).

979-8-3315-5472-9/25/$31.00 ©2025 IEEE

Both the stator and rotor are encapsulated with sheathes, protecting seawater filling the stator and rotor.

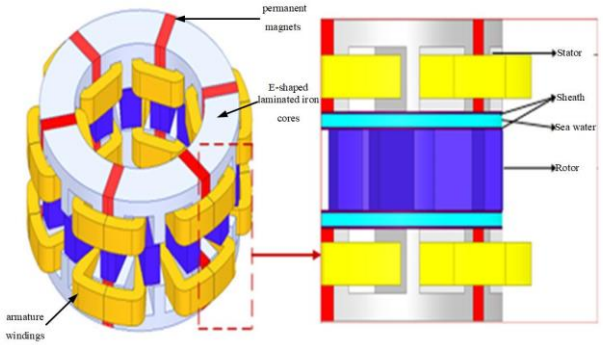


Fig. 1. Structure of the AFFSPMM.

III. Model-Free Predictive Current Control Based on Extended State Observer

A. MFPCC

Considering the parameter mismatch issues in the actual operation of the motor, the current equation of AFFSPMM can be expressed as:

$$\begin{cases} \dfrac{d}{dt}i_d = -\dfrac{R}{L_d+\Delta L_d}i_d + \dfrac{\omega_e(k)\left(L_q+\Delta L_q\right)_s}{\left(L_d+\Delta L_d\right)}i_q + \dfrac{1}{\left(L_d+\Delta L_d\right)}u_d \\ \dfrac{d}{dt}i_q = -\dfrac{R}{L_d+\Delta L_d}i_d - \dfrac{\omega_e(k)}{\left(L_q+\Delta L_q\right)}\cdot\left[\left(L_d+\Delta L_d\right)i_d + \left(\psi_f+\Delta\psi_f\right)\right] \\ \qquad + \dfrac{1}{\left(L_q+\Delta L_q\right)}u_q(k) \end{cases} \tag{1}$$

According to (1) , replace u_d and u_q with the reference values of d-axis and q-axis voltages, namely u_d^* and u_q^*. In the dq coordinate system, the ultra-local model of AFFSPMM can be expressed as:

$$\begin{cases} \dfrac{di_d}{dt} = F_d + \alpha u_d^* \\ \dfrac{di_q}{dt} = F_q + \alpha u_q^* \end{cases} \tag{2}$$

where α represents the stator voltage coefficients of the d-axis and q-axis, and is generally set as the reciprocal of the stator inductance. F_d and F_q are the lumped disturbances of AFFSPMM.

By applying forward Euler discretization to (2), the ultra-local model of AFFSPMM can be expressed as:

$$\begin{cases} i_d(k+1) = (F_d(k) + \alpha u_d^*(k))T_s + i_d(k) \\ i_q(k+1) = (F_q(k) + \alpha u_q^*(k))T_s + i_q(k) \end{cases} \tag{3}$$

Performing the Laplace transform on (3) yields:

$$sY = \frac{\Phi}{s} + \alpha U + y_0 \tag{4}$$

Let y_0 be the initial value of the sampling interval. Further, differentiate the transformed expression and introduce the s^{-2} filter to reduce the influence of noise, and perform the inverse Laplace transform. After simplification, the disturbance estimation expression can be obtained by (5).

$$\hat{F} = -\frac{6}{T^3}\int_{T_0}^{T}\left[(T-2\tau)y(\tau) + \alpha\tau(T-\tau)u(\tau)\right]d\tau \tag{5}$$

In the AFFSPMM drive system, the mathematical model of MFPCC is illustrated in (6).

$$\begin{cases} \dfrac{di_d}{dt} = 0 \\ u_d^* = (-\dfrac{3}{n_F^3 T_s}\sum_{m=1}^{n_F}(((n_F-2(m-1))i_d[m-1] \\ \quad +\alpha(m-1)T_s(n_F-(m-1))u_d^*[m-1]+\cdots(n_F-2m)i_d[m] \\ \quad +\alpha m T_s(n_F-m)u_d^*[m]) + \dfrac{di_d^*}{dt} + K_{dp}(i_d^*-i_d))/\alpha \end{cases}$$

$$\begin{cases} \dfrac{di_q^*}{dt} = (i_q^*(k+1)-i_q^*(k))/T \\ u_q^* = (-\dfrac{3}{n_F^3 T_s}\sum_{m=1}^{n_F}(((n_F-2(m-1))i_q[m-1] \\ \quad +\alpha(m-1)T_s(n_F-(m-1))u_q^*[m-1]+\cdots(n_F-2m)i_q[m] \\ \quad +\alpha m T_s(n_F-m)u_q^*[m]) + \dfrac{di_q^*}{dt} + K_{qp}(i_q^*-i_q))/\alpha \end{cases} \tag{6}$$

where K_{dp} and K_{qp} denote the proportional gains of the MFPCC on the d- and q-axis, respectively, and $i_d[m\text{-}1]$ denotes the d-axis current at sample sequence m−1. I is the total run time ,T_s is sampling period and $T = N{\cdot}T_s$, where N is the number of samples and m is the current sample index.

B. Design of ESO

Based on the AFFSPMM, the ultra-local model is constructed with i_d , i_q , F_d *and* F_q as state variables, and the observer is introduced that incorporates an error feedback mechanism for current.

$$\begin{cases} err_d = z_{1d} - i_d \\ err_q = z_{1q} - i_q \end{cases} \tag{7}$$

$$\begin{cases} \dot{z}_{1d} = z_{2d} + \alpha u_d - \beta_1 err_d \\ \dot{z}_{1q} = z_{2q} + \alpha u_q - \beta_1 err_q \end{cases} \tag{8}$$

$$\begin{cases} \dot{z}_{2d} = -\beta_2 err_d \\ \dot{z}_{2q} = -\beta_2 err_q \end{cases} \tag{9}$$

where $z_{1d}=i_d^*$ and $z_{1q}=i_q^*$ are the estimated values of i_d and i_q, $z_{2d}=F_d^*$ and $z_{2q}=F_q^*$ are the estimated values of F_d and F_q, β_1 and β_2 is the error feedback gain of the observer.

(7), (8) and (9) can be written as:

$$\begin{cases} \dot{z}_d = Az_d + Bu_d + D(y_d - \hat{y}_d) \\ \hat{y}_d = Cz_d \end{cases} \tag{10}$$

$$\begin{cases} \dot{z}_q = Az_q + Bu_q + D(y_q - \hat{y}_q) \\ \hat{y}_q = Cz_q \end{cases} \tag{11}$$

where $z_d = \begin{bmatrix} z_{1d} \\ z_{2d} \end{bmatrix}$; $z_q = \begin{bmatrix} z_{1q} \\ z_{2q} \end{bmatrix}$; $\dot{z}_d = \begin{bmatrix} \dot{z}_{1d} \\ \dot{z}_{2d} \end{bmatrix}$; $\dot{z}_q = \begin{bmatrix} \dot{z}_{1q} \\ \dot{z}_{2q} \end{bmatrix}$; $\hat{y}_d$ and $\hat{y}_q$ are the observed value of y_d and y_q; $A = \begin{bmatrix} 0 & 1 \\ 0 & 0 \end{bmatrix}$; $B = \begin{bmatrix} \alpha \\ 0 \end{bmatrix}$; $C = \begin{bmatrix} 1 & 0 \end{bmatrix}$; $D = \begin{bmatrix} \beta_1 \\ \beta_2 \end{bmatrix}$.

Based on the state space structure of (10) and (11), the characteristic equation of ESO can be obtained as:

$$|sI - (A - DC)| = s^2 + \beta_1 s + \beta_2 s \tag{12}$$

In order to ensure the convergence and stability of the observer and place the system's characteristic roots near $-\omega_0$ in the left half plane of the complex plane, the error gain coefficients β_1 and β_2 can be set according to the following formula:

$$\begin{cases} \beta_1 = 2\omega_0 \\ \beta_2 = \omega_0^2 \end{cases} \tag{13}$$

where ω_0 is the bandwidth of the ESO , and it determines the steady state and dynamic performance of the observer. The sampling frequency is set to 10 kHz. To meet the requirements of speed and stability, the value of ω_0 is set at 8500.

(7), (8), and (9) can be discretized as:

$$\begin{cases} err_d(k) = \hat{i}_d(k) - i_d(k) \\ \hat{i}_d(k+1) = \hat{i}_d(k) + T_s(\hat{F}_d(k) + \alpha u_d(k)) - \beta_{01} err_d(k) \\ \hat{F}_d(k+1) = \hat{F}_d(k) - \beta_{02} err_d(k) \end{cases} \tag{14}$$

$$\begin{cases} err_q(k) = \hat{i}_q(k) - i_q(k) \\ \hat{i}_q(k+1) = \hat{i}_q(k) + T_s(\hat{F}_q(k) + \alpha u_q(k)) - \beta_{01} err_q(k) \\ \hat{F}_q(k+1) = \hat{F}_q(k) - \beta_{02} err_q(k) \end{cases} \tag{15}$$

According to (14) and (15), the characteristic equation of the ESO can be expressed as:

$$z^2 + (\beta_{01} - 2)z + 1 - \beta_{01} + \beta_{02} T_s = 0 \tag{16}$$

ω_0 can be calculated from the poles in the Z domain, as shown in (17):

$$\omega_0 = \frac{1 - z_{1,2}}{T_s} \tag{17}$$

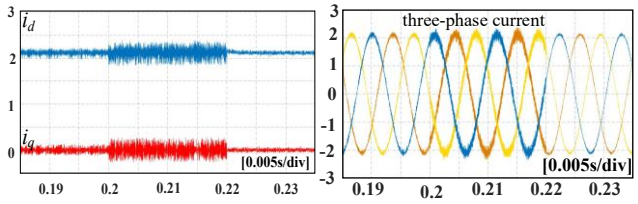
The poles z_1 and z_2 should remain the unit circle in the Z-domain to satisfy the stability requirements.

IV. Simulation and Experimental Validation

A. Simulations Analysis

In order to verify the effectiveness of the MFPCC based on ESO proposed in this paper, the AFFSPMM model-free predictive current control system is established by Matlab /Simulink, and the simulation analysis is conducted.

When the AFFSPMM operates at 400 rpm and with the load of 3 N·m, the inductance ratio L_0/L_s (L_0 denotes the initial inductance parameter, L_s represents the actual inductance parameter.) is set as 0.5, 1.0 and 1.5 respectively, and the simulation results of the inductance parameter mismatch by the control of traditional MPCC control are shown in Fig. 2.

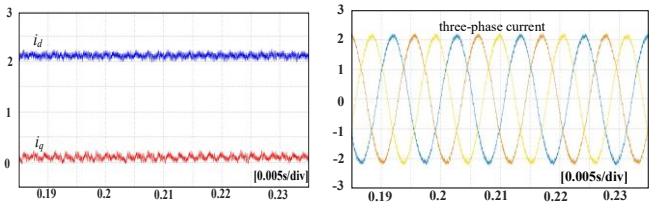


(a) (b)

Fig. 2. Simulation results by the control of traditional MPCC under parameter mismatch: (a) d- and q-axis currents. (b) three-phase currents.

Fig. 2 shows that when L_0/L_s=0.5 at 0.2s, the q-axis current ripple increases to 0.562 A and the d-axis current ripple to 0.486 A, resulting in three-phase current harmonics. When L_0/L_s=1.5 at 0.22s, the three-phase current harmonics are reduced due to inductance filtering.

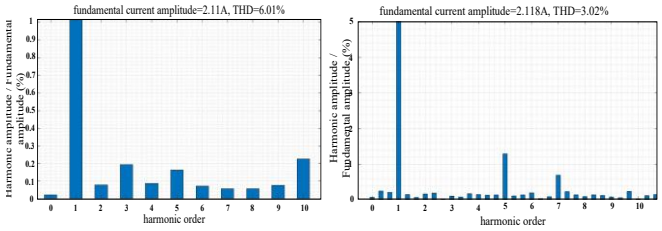
Under the same operating conditions, the simulation waveforms are shown in Fig. 3 by the control of the proposed MFPCC.



(a) (b)

Fig. 3. Simulation results with MFPCC based on ESO under parameter mismatch: (a) d- and q-axis currents. (b) three-phase currents.

Fig. 3 shows the d- and q-axis currents remain unchanged and the three-phase currents remain essentially constant. Because the control method does not require the parameters of AFFSPMM, the proposed control method presents better robustness when the parameter mismatch occurs.



(a) (b)

Fig. 4. FFT of phase current. (a) MPCC. (b) MFPCC based on ESO.

Fig. 4 presents FFT analyses of the phase current. Compared with conventional MPCC, the proposed ESO reduces total harmonic distortion (THD) by 49.75%.

B. Experiments Analysis

In order to verify the effectiveness of the proposed MFPCC based on ESO, an experimental platform for AFFSPMM is developed based on a Real Time Unit (RTU), as shown in Fig.5. In this platform, the DC power supply provides the required voltage for the inverter, a magnetic powder brake is used as the load of AFFSPMM, and the excitation current is adjusted by the accompanying tension controller to regulate the load. The DC power supply is KXN-30010D, the oscilloscope is RIGOL DS1104Z, and the magnetic powder brake is TWIDEC-FZ12J.

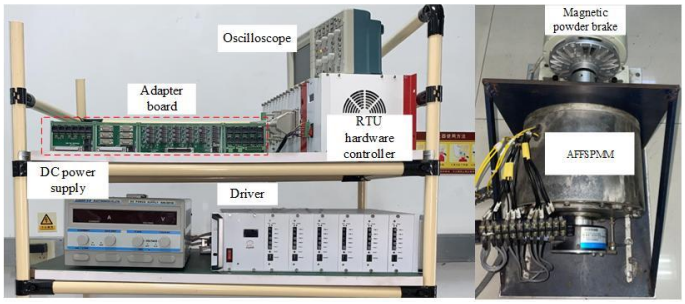
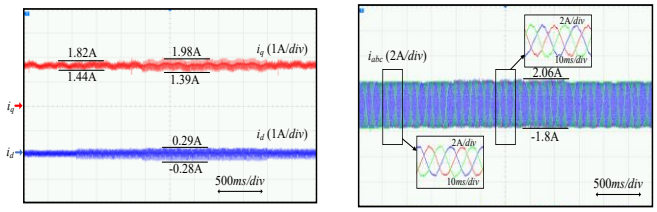


Fig. 5. Experimental platform of the AFFSPMM control system.

When the given rotational speed is 400 rpm and the load torque is 3 N·m, the parameter mismatch experimental waveforms of the traditional MPCC control strategy are shown in Fig. 6. Since the parameters of AFFSPMM in actual operation are uncontrollable, an alternative strategy is adopted by adjusting the parameters of the controller.



(a) (b)

Fig. 6. Experimental results for MPCC under parameter mismatch: (a) *d*- and *q*-axis currents. (b) three-phase currents.

Fig. 6(a) shows that the *q*-axis current ripple is 0.38A, and the *d*-axis current fluctuates around 0A under the condition of L_0/L_s=1. When the inductance ratio decreases, the *q*-axis current amplitude increases to 1.98A with both *d* and *q*-axis current ripple increase(L_0/L_s=0.5). When the inductance ratio increases, the *q*-axis current amplitude becomes 1.82A and the both *d* and *q*-axis current ripple are reduced(L_0/L_s=1.5). Fig. 6(b) shows that three-phase current amplitude is 1.87 A during the period of L_0/L_s=1, subsequently rises slightly to 2.06 A (L_0/L_s=0.5), and then returns to 1.89 A (L_0/L_s=1.5).

Under the same condition, the parameter mismatch experimental waveforms of the MFPCC based on ESO are shown in Fig. 7.

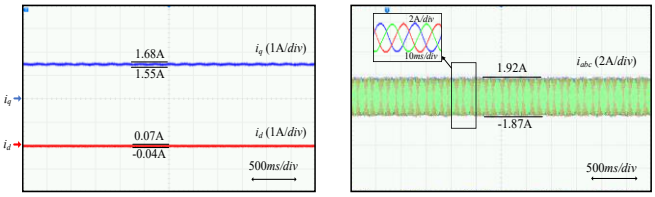


Fig. 7. Experimental results for MFPCC based on ESO under parameter mismatch: (a) d- and q-axis currents. (b) three-phase currents.

Fig. 7(a) shows that the *q*-axis current remains approximately average value of 1.61 A with only slight current ripple ,and the *d*-axis current stays around 0 A with the variation of inductance. Fig. 7(b) shows that three-phase current amplitude almost constant. Therefore, comparing with MPCC, the proposed MFPCC demonstrates better robustness as the motor parameters mismatch.

V. Conclusion

The MFPCC based on ESO is proposed to enhance the robustness of RDM control systems in complex marine environments. Compared with the conventional model predictive current control, the proposed MFPCC strategy demonstrates superior robustness under the condition of parameter mismatch, eliminating the dependence on precise motor models, making it suitable for complex marine operating conditions.

References

[1] M. Hsie, J. Chen, Y. Yeh, C. Lee, P. Chen, and Y. Chen. Integrated Design and Realization of a Hubless Rim-driven Thruster[C]. IECON 2007-33rd Annual Conference of the IEEE Industrial Electronics Society, Taipei, Taiwan, 2007: 3033-3038.

[2] C. Xiong, T. Guan, P. Zhou, et al. A fault-tolerant FOC strategy for five-phase SPMSM with minimum torque ripples in the full torque operation range under double-phase open-circuit fault[J]. IEEE Transactions on Industrial Electronics, 2020, 67(11): 9059-9072.

[3] A. Peter, J. Mathew, K. Gopakumar. A simplified DTC-SVPWM scheme for induction motor drives using a single PI controller[J]. IEEE Transactions on Power Electronics, 2023, 38(1): 750-761.

[4] C. Xia, S. Wang, X. Gu, et al. Direct torque control for VSI-PMSM using vector evaluation factor table[J]. IEEE Transactions on Industrial Electronics, 2016, 63(7): 4571-4583.

[5] J. Wang, Y. Liu, J. Yan, et al. Adaptive integral extended state observer-based improved multistep FCS-MPCC for PMSM[J]. IEEE Transactions on Power Electronics, 2023, 38(9): 11260-11276.

[6] Zhou Y, Li H, Yao H. Model-free control of surface mounted PMSM drive system[C]//2016 IEEE international conference on industrial technology (ICIT). IEEE, 2016: 175-180.

[7] Yuan X, Zuo Y, Fan Y, et al. Model-free predictive current control of SPMSM drives using extended state observer[J]. IEEE Transactions on Industrial Electronics, 2021, 69(7): 6540-6550.

[8] Wang D, Liu S, Liu X, et al. Improved model-free sliding mode control of PMSM based on finite-time generalized proportional integral observer[C]//2023 IEEE 12th Data Driven Control and Learning Systems Conference (DDCLS). IEEE, 2023: 501-505.

Improved Sensorless Full-Speed Range Composite Control Strategy for IPMSM

1st Siqi Peng
College of Automation and Electronic Information
Xiangtan University
Xiangtan, China
13286587@qq.com

2nd Zhiwen Zhang
College of Automation and Electronic Information
Xiangtan University
Xiangtan, China
3193253163@qq.com

3rd Kun Zhu
College of Automation and Electronic Information
Xiangtan University
Xiangtan, China
1171281487@qq.com

4th Chuchen Yang
College of Automation and Electronic Information
Xiangtan University
Xiangtan, China
1424143265@qq.com

***Abstract*—In sensorless full-speed range composite control of Interior Permanent Magnet Synchronous Motor (IPMSM), linear weighted switching and sliding mode observers (SMO) are commonly used in the transition and medium-high-speed range. However, these approaches often result in noticeable chattering during and after the switching process. This paper proposes an improved sensorless full-speed range composite control strategy for IPMSM. In the zero- and low-speed range, rotor position is estimated using a high frequency square wave injection method (HFSVI). In the medium- and -high speed range, the Frequency-adaptive complex-coefficient filter-Based Sliding Mode Observer (FACCF-SMO) is employed. During the transition range, a nonlinear weighted switching strategy is adopted to reduce chattering effects. In addition, the normalized position error is fused and processed through the single Luenberger observer to obtain the estimated rotor position. The proposed method is validated through MATLAB/Simulink simulations and effectively improves the estimation accuracy of rotor electrical angle and speed during and after the transition process (corresponding to 10%–33% of the rated speed).**

Keywords—IPMSM, sensorless composite control，full-speed range, FACCF-SMO, position error

I. INTRODUCTION

The efficient and low-carbon utilization of energy has become a crucial approach to addressing the global energy and climate crises, and it has garnered extensive research attention from scholars across various fields. Permanent Magnet Synchronous Motor (PMSM), known for their high power density and operating efficiency, are widely used in critical areas such as industrial manufacturing and transportation [1].

Sensorless control technology offers significant advantages over traditional mechanical sensor-based methods in terms of size, cost, reliability, and environmental adaptability[2],[3]. In recent years, extensive studies have been conducted on sensorless control techniques for PMSM, which can be broadly categorized into two types. One type of method is based on the motor's saliency characteristics for rotor position estimation. This approach is suitable for operation at zero- and low-speed range[4],[5]. The other is based on back-electromotive force(EMF) or flux linkage derived from fundamental-frequency excitation, which is applicable in medium- and high-speed range[6]. In [7], a FACCF is proposed to replace the low-pass filter (LPF) in the SMO, which reduces chattering and eliminates phase error. However, this approach is developed based on a surface-mounted PMSM.

Current research efforts in sensorless control of PMSM are concentrated on achieving reliable operation over full-speed range. In [8], a hybrid approach of high-frequency injection and model-based estimation is used, with hysteresis switching for the transition stage. In [9], an improved particle swarm optimization (PSO) algorithm is applied to derive a variable-weight switching function for the transition range, enhancing performance but at the cost of increased computational complexity. In [10], rotor position error obtained from both high-frequency square-wave injection and back EMF models is fused and passed through the single PLL to estimate rotor position, using linear weighted switching for smooth transitions. In [11], a single Luenberger position observer method is proposed for sensorless composite control. This approach reduces computational complexity and observer design difficulty, making it straightforward to implement.

However, these approaches commonly use conventional SMO in the transition and medium- and high-speed range. Although conventional sliding mode observer (SMO) offer a simple structure and strong robustness, they rely on a fixed cut-off frequency LPF to extract the back EMF. This filtering process can cause phase shift and amplitude attenuation. Moreover, the fixed LPF and sliding mode gains cannot maintain high estimation accuracy across a wide speed range. The linear weighted switching method is relatively simple to implement and requires low computational effort. However, it may cause pulsations in the estimated position and speed when entering and exiting the transition range.

This paper proposes an improved sensorless full-speed range composite control strategy for IPMSM. The rotor position error is estimated using HFSVI in the zero- and low-speed range and the FACCF-SMO in the medium- and high-speed range, followed by normalization. A nonlinear weighted switching strategy is applied during the transition range. The normalized rotor position errors are fused based on speed information and fed into the single Luenberger observer to estimate rotor position and speed.

979-8-3315-5472-9/25/$31.00 ©2025 IEEE

II. Sensorless Control of HFSVI for Zero and Low Speed

In the zero- and low-speed range, HFSVI is employed. In the *d-q* axis reference frame, the mathematical model of the IPMSM is expressed as:

$$\begin{bmatrix} u_d \\ u_q \end{bmatrix} = \begin{bmatrix} R_s + pL_d & -\omega_e L_q \\ \omega_e L_d & R_s + pL_q \end{bmatrix} \begin{bmatrix} i_d \\ i_q \end{bmatrix} + \begin{bmatrix} 0 \\ \omega_e \psi_f \end{bmatrix} \tag{1}$$

In this model, u_d, u_q are the *d-q* axis voltages in the rotating reference frame, and i_d, i_q are the corresponding currents.L_d, L_q represent the *d-q* axis inductances, respectively, while, R_s, ω_e and ψ_f denote the stator resistance, electrical angular speed, and permanent magnet flux linkage. The operator p denotes the time derivative.

Since the frequency of the injected voltage signal is much higher than the fundamental signal frequency, the high-frequency voltage drop across the inductance will be much greater than the high-frequency voltage drops across the resistance and back EMF. By neglecting the back EMF and resistance terms, the high-frequency voltage equation for the motor can be expressed as:

$$\begin{bmatrix} u_{dh} \\ u_{qh} \end{bmatrix} = \begin{bmatrix} L_d & 0 \\ 0 & L_q \end{bmatrix} \frac{d}{dt} \begin{bmatrix} i_{dh} \\ i_{qh} \end{bmatrix} \tag{2}$$

In this equation, u_{dh} and u_{qh} represent the high-frequency voltages in the *d-q* axis reference frame, while i_{dh} and i_{qh} denote the corresponding high-frequency currents.

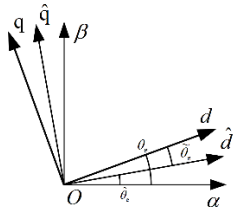


Fig. 1. Coordinate axis relationship

The injected high-frequency square-wave voltage signal in the $\hat{d}$-$\hat{q}$ axis reference frame can be expressed as:

$$u_{\hat{d}\hat{q}h} = \begin{bmatrix} u_{\hat{d}h} \\ u_{\hat{q}h} \end{bmatrix} = \begin{bmatrix} u_{\hat{d}h} \\ 0 \end{bmatrix} \tag{3}$$

In this equation, the high-frequency square-wave voltage signal is defined as $u_{\hat{d}h} = V_h(-1)^k, k = 0,1,2,3 \ldots$; The amplitude of the signal is $\pm V_h$, and the duty cycle is 50%. The superscript "^" denotes an estimated quantity.

By applying coordinate transformation to (2), the result can be expressed as:

$$\frac{d}{dt} \begin{bmatrix} i_{\alpha h} \\ i_{\beta h} \end{bmatrix} = T^{-1}(\theta_e) \begin{bmatrix} \frac{1}{L_d} & 0 \\ 0 & \frac{1}{L_q} \end{bmatrix} T(\tilde{\theta}_e) \begin{bmatrix} u_{\hat{d}h} \\ u_{\hat{q}h} \end{bmatrix} \tag{4}$$

$$T(\theta_e) = \begin{bmatrix} \cos\theta_e & -\sin\theta_e \\ \sin\theta_e & \cos\theta_e \end{bmatrix} \tag{5}$$

In (4), $i_{\alpha h}$ and $i_{\beta h}$ represent the high-frequency response currents in the α-β axis reference frame, while $u_{\hat{d}h}$ and $u_{\hat{q}h}$ denote the high-frequency voltages in the estimated *d-q* axis reference frame. $\tilde{\theta}_e = \theta_e - \hat{\theta}_e$.

The simplified expression can be expressed as:

$$\frac{d}{dt} \begin{bmatrix} i_{\alpha h} \\ i_{\beta h} \end{bmatrix} = u_{\hat{d}h} \begin{bmatrix} \frac{cos\theta_e cos\tilde{\theta}_e}{L_{dh}} + \frac{sin\theta_e sin\tilde{\theta}_e}{L_{qh}} \\ \frac{sin\theta_e cos\tilde{\theta}_e}{L_{dh}} - \frac{cos\theta_e sin\tilde{\theta}_e}{L_{qh}} \end{bmatrix} \tag{6}$$

When the position observer converges, discrete sampling and sign processing of the signal yield the following result:

$$\begin{bmatrix} \Delta i_{\alpha h} \\ \Delta i_{\beta h} \end{bmatrix} sign(u_{\hat{d}h}) = \frac{V_h T_h}{2L_{dh}} \begin{bmatrix} cos\theta_e \\ sin\theta_e \end{bmatrix} = \begin{bmatrix} I_{\alpha h} \\ I_{\beta h} \end{bmatrix} \tag{7}$$

As shown in Fig.2, $I_{\alpha h}$ and $I_{\beta h}$ represent the high-frequency current envelopes in the α-β axis reference frame. After normalization and decoupling via the vector cross-product method, the position error information can be expressed as:

$$\varepsilon_{HF} = \tilde{\theta}_e = \frac{1}{\sqrt{I_{\alpha h}^2 + I_{\beta h}^2}} \left[I_{\beta h} cos\hat{\theta}_e - I_{\alpha h} sin\hat{\theta}_e \right] \tag{8}$$

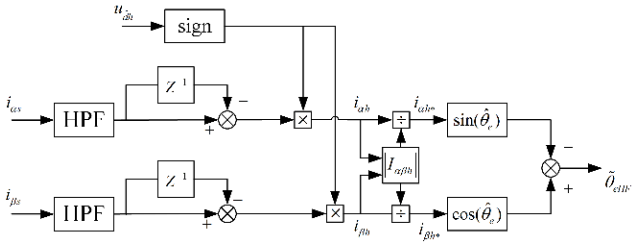


Fig. 2. Block diagram of the envelope demodulation process

III. Sensorless Control of FACCF-SMO for Medium and High Speed

Conventional SMO have been widely adopted for rotor position and speed estimation due to their simple structure and strong robustness. However, the switching function in SMO often causes chattering, which directly affects the estimation accuracy of the rotor position and system stability. To mitigate this, LPF is typically employed. While LPF reduces chattering, they also introduce phase delay and amplitude attenuation, which degrade estimation accuracy and require additional phase compensation.

Moreover, conventional SMO using a fixed set of sliding mode parameters cannot maintain accurate the estimated equivalent back EMF across a wide speed range. Since SMO are mainly applied in the medium- and high-speed range, the design of observer parameters often prioritizes high-speed performance. As a result, at lower speeds, the estimated equivalent back EMF

cannot be accurately extracted, leading to poor rotor position estimation in that range.

A. Conventional Sliding Mode Observer Method

For IPMSM, the use of the active flux model enables the transformation into a non-salient pole type for analysis, thereby simplifying the analysis and design of sensorless control systems. Based on the active flux model[12], the mathematical model of the IPMSM in the α-β axis reference frame can be expressed as:

$$\begin{bmatrix} u_\alpha \\ u_\beta \end{bmatrix} = \begin{bmatrix} R_s + pL_q & 0 \\ 0 & R_s + pL_q \end{bmatrix} \begin{bmatrix} i_\alpha \\ i_\beta \end{bmatrix} + \begin{bmatrix} e_\alpha \\ e_\beta \end{bmatrix} \tag{9}$$

In this equation, u_α and u_β represent the voltages, and i_α and i_β denote the currents in the α-β axis reference frame. e_α and e_β are the equivalent back EMF corresponding to the active flux in the α-β frame, which can be expressed as:

$$\begin{bmatrix} e_\alpha \\ e_\beta \end{bmatrix} = \psi_a \omega_e \begin{bmatrix} -\sin\theta_e \\ \cos\theta_e \end{bmatrix} \tag{10}$$

In the above equation, ψ_a denotes the active flux, defined as $\psi_a = \psi_f + (L_d - L_q) i_d$, where ψ_f is the permanent magnet flux linkage.

The stator current sliding mode observer is derived based on (9) as follows:

$$p\begin{bmatrix} \hat{i}_\alpha \\ \hat{i}_\beta \end{bmatrix} = -\frac{R_s}{L_q}\begin{bmatrix} \hat{i}_\alpha \\ \hat{i}_\beta \end{bmatrix} + \frac{1}{L_q}\begin{bmatrix} u_\alpha - z_\alpha - \hat{e}_\alpha \\ u_\beta - z_\beta - \hat{e}_\beta \end{bmatrix} \tag{11}$$

$$\begin{bmatrix} z_\alpha \\ z_\beta \end{bmatrix} = k \cdot sign\begin{bmatrix} \hat{i}_\alpha - i_\alpha \\ \hat{i}_\beta - i_\beta \end{bmatrix} \tag{12}$$

$$\begin{cases} \hat{e}_\alpha = LPF(z_\alpha) = \dfrac{\omega_c}{s + \omega_c} z_\alpha \\ \hat{e}_\beta = LPF\left(z_\beta\right) = \dfrac{\omega_c}{s + \omega_c} z_\beta \end{cases} \tag{13}$$

In this equation, k is the gain of the sliding mode control functions z_α and z_β, and $sign(\cdot)$ denotes the sign function.

The estimated equivalent back EMF is obtained through the sliding mode observer based on the active flux model, normalized, and decoupled using the vector cross-product method. The SMO position error can be expressed as:

$$\varepsilon_{SMO} = \tilde{\theta}_e = \frac{1}{\sqrt{\hat{e}_\alpha^2 + \hat{e}_\beta^2}}\left[-\hat{e}_\alpha cos\hat{\theta}_e - \hat{e}_\beta sin\hat{\theta}_e\right] \tag{14}$$

B. Sliding Mode Observer Method with Frequency-Adaptive Complex-Coefficient Filtering

To minimize the effects of phase delay and amplitude attenuation caused by the LPF, a Frequency-Adaptive Complex-Coefficient Filter (FACCF) is employed to extract the estimated equivalent back EMF from the sliding mode switching function, as illustrated in Fig. 3.

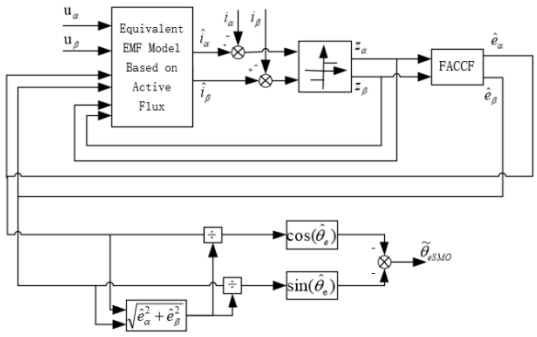


Fig. 3. Block diagram of the FACCF-Based Sliding Mode Observer (FACCF-SMO).

The FACCF is a type of frequency-adaptive filter, and it is expressed as:

$$p\begin{bmatrix} \hat{e}_\alpha \\ \hat{e}_\beta \end{bmatrix} = \omega_c \begin{bmatrix} z_\alpha - \hat{e}_\alpha \\ z_\beta - \hat{e}_\beta \end{bmatrix} + \hat{\omega}_e \begin{bmatrix} -\hat{e}_\beta \\ \hat{e}_\alpha \end{bmatrix} \tag{15}$$

The Laplace transform of (15) yields the following expression, which can be expressed as:

$$\begin{bmatrix} \hat{E}_\alpha(s) \\ \hat{E}_\beta(s) \end{bmatrix} = \frac{\omega_c}{s + \omega_c}\begin{bmatrix} Z_\alpha(s) \\ Z_\beta(s) \end{bmatrix} + \frac{\hat{\omega}_e}{s + \omega_c}\begin{bmatrix} -\hat{E}_\beta(s) \\ \hat{E}_\alpha(s) \end{bmatrix} \tag{16}$$

which can be expressed as:

$$\hat{e}_s = \frac{\omega_c}{s - j\hat{\omega}_e + \omega_c} z_s \tag{17}$$

In the equation, ω_c denotes the cutoff frequency, $\hat{e}_s = \hat{e}_\alpha + j\hat{e}_\beta$ is the complex vector of the back electromotive force (EMF), and $z_s = z_\alpha + jz_\beta$ is the complex vector of the sign function. The estimated frequency $\hat{\omega}_e$ corresponds to the central frequency ω_0 of the FACCF.

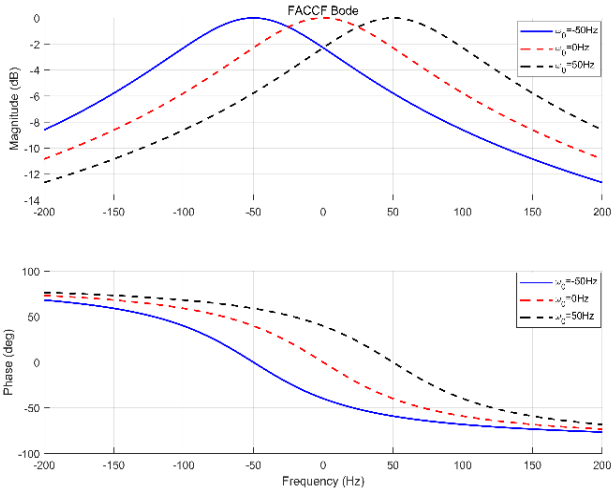


Fig. 4. Bode diagram of FACCF for different central frequency.

By replacing the LPF with the FACCF, it can achieve no phase shift and no amplitude attenuation at different central frequency. As shown in Fig. 4, when the cutoff frequency is 60

Hz, the FACCF exhibits no phase shift or amplitude attenuation at various center frequencies.

In the steady state, the frequency of the estimated equivalent back EMF coincides with the electrical angular velocity of the motor. Therefore, the central frequency of the FACCF can be determined based on the motor's electrical angular velocity. At the same time, the cutoff frequency of the FACCF should also adaptively vary with the electrical angular velocity to ensure that the estimated equivalent back EMF extracted by the FACCF remains undistorted. The cutoff frequency of the FACCF can be set as:

$$\omega_c = k\hat{\omega}_e \tag{18}$$

The FACCF structure is shown in Fig. 5, and its transfer function is expressed as:

$$FACCF(s) = \frac{k_c\hat{\omega}_e}{s - j\hat{\omega} + k_c\hat{\omega}_e} \tag{19}$$

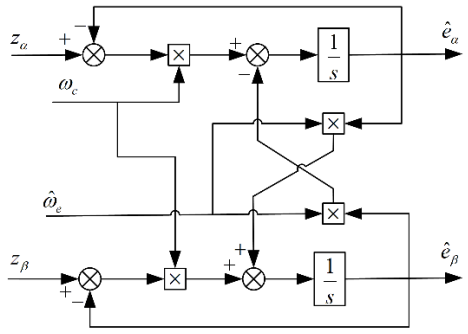


Fig. 5. Structure diagram of FACCF

Based on the active flux model, the FACCF can be applied to the SMO for IPMSM to replace the LPF, improving the extraction performance of the estimated equivalent back EMF, and thereby enhancing the accuracy of position estimation.

IV. Integration of Low- and High-Speed Estimators for Full-Speed Range Sensorless Control

As shown in Fig. 6, the position error information from the two sensorless methods described above is fused and then fed into single Luenberger position observer to estimate the rotor position.

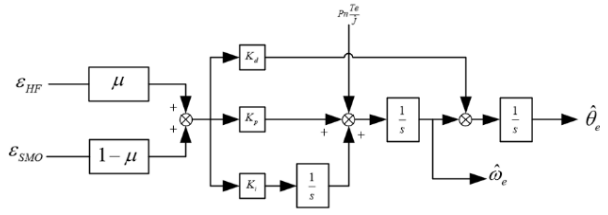


Fig. 6. Block diagram of the composite controller.

In the transition range, a linear weighted switching method is commonly adopted, which is simple to implement and has low computational complexity. However, due to the non-smoothness at the switching point, pulsations in the estimated position and speed are inevitably introduced when entering or leaving the transition range. To address this issue, a nonlinear weighting method is employed to fuse the obtained position error, providing a smoother composite position error as the input to the position observer. The nonlinear weighted switching function is expressed as:

$$\mu = \begin{cases} 1 & (0 < |\hat{n}| \le n_L) \\ \dfrac{1}{1+e^{-a\left(\frac{n_H-\hat{n}_e}{n_H-n_L}-\frac{1}{2}\right)}} & (n_L < |\hat{n}| \le n_H) \\ 0 & (|\hat{n}| \ge n_H) \end{cases} \tag{20}$$

In the equation, $\hat{n}_e$, n_H and n_L represent the estimated speed, the upper limit, and the lower limit of the switching speed range, respectively. The parameter μ denotes the weighting coefficient. The parameter a represents the adjustment coefficient.

V. Simulation Verification

The proposed full-speed-range sensorless control method is illustrated in Fig. 7. To validate the effectiveness of the proposed approach, a sensorless control system for the IPMSM was established in Simulink. The switching frequency is set to 10 kHz. The $i_d = 0$ control strategy is adopted due to its simplicity and ease of implementation. The key parameters of the IPMSM are listed in Table I.

TABLE I. The Main Parameters of the IPMSM

Parameters	Values	
	Values	*units*
Rated Power	400	*W*
Rated Line Current	2.7	*A*
DC Bus Voltage	311	*V*
Rated Speed	3000	*r/min*
Rated Load Torque	1.27	*N·m*
d-axis Inductance	9.14	*mH*
q-axis Inductance	13.74	*mH*
Line Resistance	3.69	*Ω*
Inertia	6.9×10^{-5}	$kg\cdot m^2$

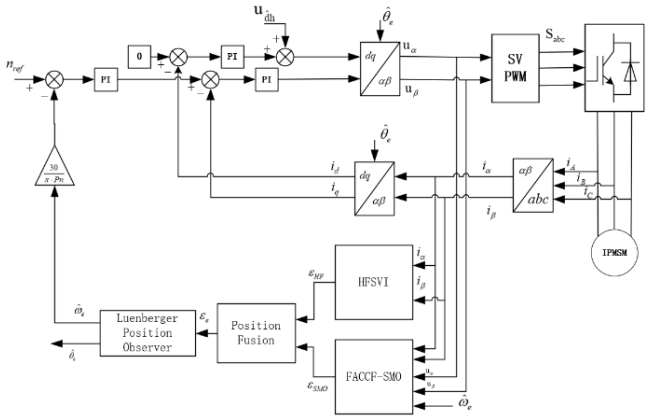


Fig. 7. Block diagram of the sensorless full-speed range composite control system for IPMSM

A. *Conventional Sensorless Full-Speed Range Composite Control Strategy*

Fig. 8 shows the results of the conventional sensorless full-speed-range composite control strategy during the acceleration process. The HFSVI method is used in the low-speed range, the conventional SMO method is used in the mid- and high-speed range, and a linear weighted switching method is applied in the transition range.

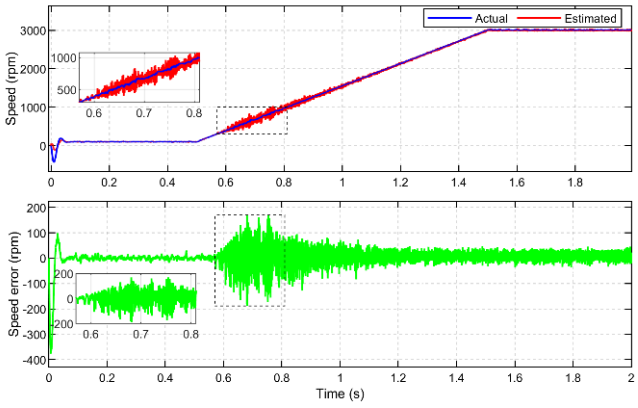
The motor starts with 50% of the rated load torque, accelerates to 100 r/min to reach a steady state, and then ramps linearly to 3000 r/min. The transition range was defined as 10% to 20% of the rated speed[10], [11]. This dynamic simulation scenario is designed to verify full-speed-range operation, including zero- and low-speed range and medium- and high speed range, and to evaluate the transition between the two control strategies.

Fig. 8(a) shows that during and after the transition process (corresponding to 10%~33% of the rated speed), noticeable oscillations appear in the estimated motor speed. The peak value of the estimated speed error reaches -188 r/min, with a peak error of -165 r/min within the transition range.

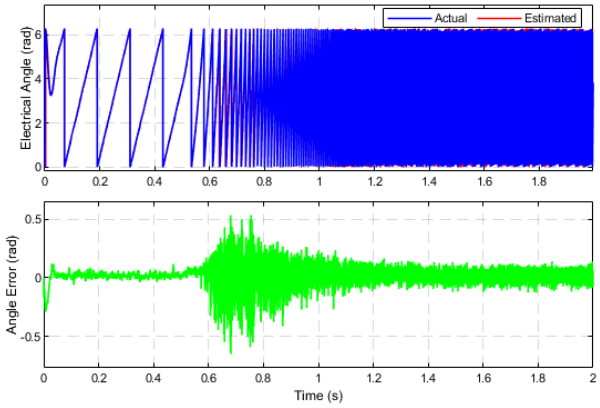
Fig. 8(b) shows that in the same speed range (10%~33% of the rated speed), the estimated electrical angle exhibits significant oscillations, with the peak estimation error reaching -0.65 rad. The peak error during the transition stage is -0.55 rad.

Fig. 8(c) shows that the method using the conventional SMO in the mid-high-speed range provides better extraction results for the estimated equivalent back EMF, with more harmonic content.

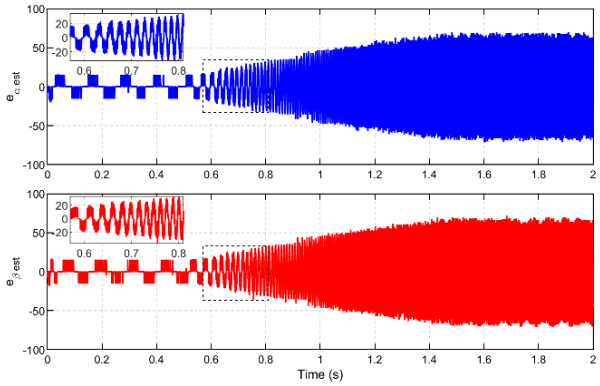
According to the simulation results, the conventional sensorless full-speed-range composite control method shows significant oscillations within 10%~33% of the rated speed range, resulting in poor rotor position estimation and adversely affecting the stability of the control system.



a) Comparison graph of actual speed and estimated speed.



b) Comparison graph of actual electrical angle and estimated electrical angle.



c) The estimated α-β axis equivalent back-EMF

Fig. 8. Simulation results of the conventional sensorless full-speed range composite control strategy during the acceleration process

B. *Improved Sensorless Full-Speed Range Composite Control Strategy*

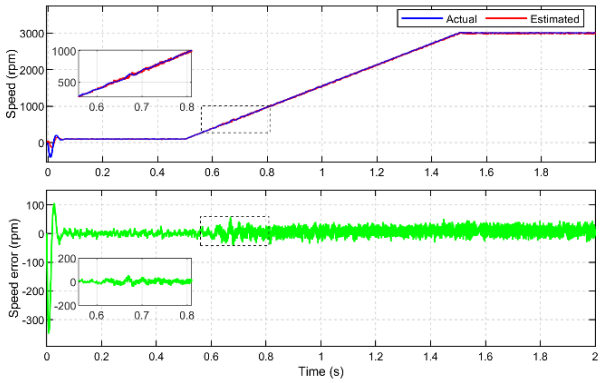
Fig. 9 shows the results of the improved sensorless full-speed range composite control strategy during the acceleration process. Based on the conventional method, the proposed strategy employs the FACCF-SMO in the medium- and high-speed range, and a nonlinear weighted switching method in the transition range. The system is tested under the same operating conditions.

Fig. 9(a) shows that no significant oscillations occur within 10%~33% of the rated speed range, and the estimated speed error remains within -42 to 59 r/min.

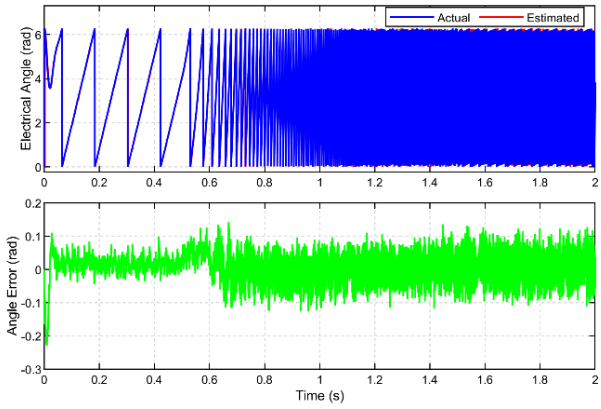
Fig. 9(b) shows that the proposed method provides more accurate rotor electrical angle estimation. Within the 10%~33% rated speed range, the electrical angle error(the estimated position error) is maintained within -0.12 to 0.14 rad, with a peak error of 0.13 rad during the transition stage.

Fig. 9(c) shows that using the FACCF-SMO in the medium- and high-speed range improves the extraction quality of the estimated equivalent back EMF, with reduced harmonic content in the extracted signal.

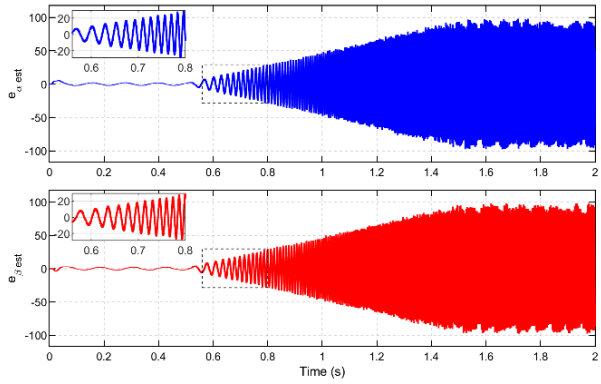
According to the simulation results, the proposed method achieves more accurate estimation of both speed and electrical angle during and after the transition range (10%~33% of the rated speed range), and enables smoother switching within the transition zone. Moreover, it ensures the reliable operation of the sensorless control across the full-speed range.



a) Comparison graph of actual speed and estimated speed.



b) Comparison graph of actual electrical angle and estimated electrical angle.

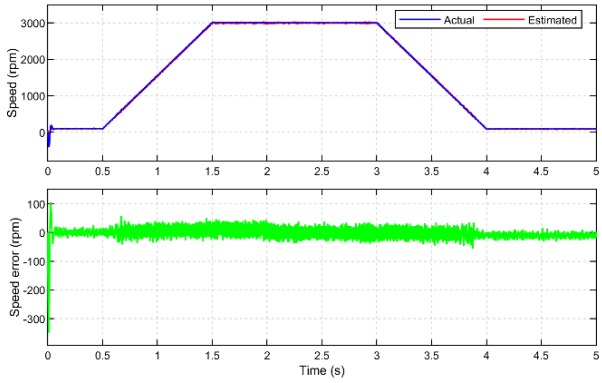


c) The estimated α-β axis equivalent back-EMF

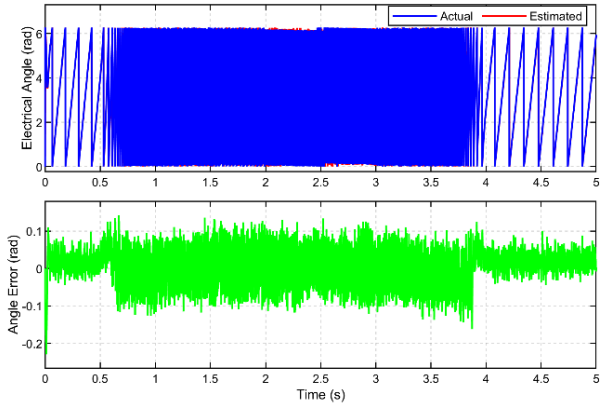
Fig. 9. Simulation results of the improved sensorless full-speed range composite control strategy during the acceleration process

Finally, as shown in Fig. 10, the proposed strategy was validated during acceleration and deceleration over the full-speed range. The motor starts with 50% rated load torque, accelerates to 100 r/min, then to 3000 r/min, and finally decelerates in a manner symmetrical to the acceleration process.

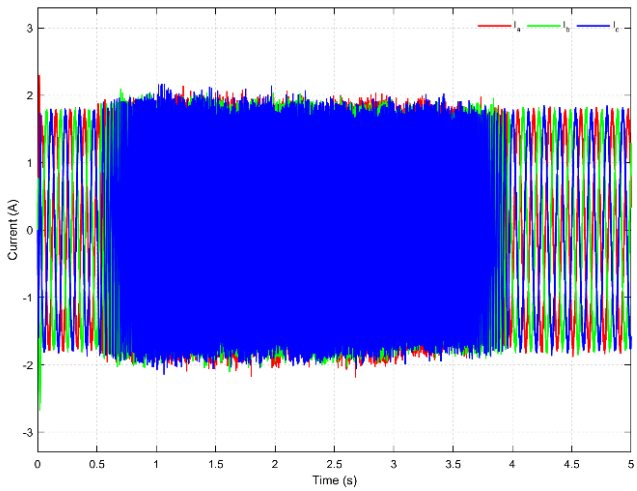
Fig. 10(a)(b) demonstrate that, after startup, the proposed method achieves high estimation accuracy for both the rotational speed and the rotor electrical angle.



a) Comparison graph of actual speed and estimated speed.



b) Comparison graph of actual electrical angle and estimated electrical angle.



c) Three-phase current waveform

Fig. 10. Simulation results of the improved sensorless full-speed range composite control strategy during the acceleration and deceleration

VI. CONCLUSION

This paper proposes an improved sensorless full-speed range composite control strategy for IPMSM, and the following conclusions are obtained:

A) The proposed method effectively suppresses the oscillations in the estimated speed and rotor position within the 10%~33% rated speed range, thereby enabling smoother and more stable switching behavior in the transition range (10%~20% rated speed).

B) The proposed strategy ensures the reliable operation of sensorless composite control across the full speed range.

REFERENCES

[1] S. Chen, W. Ding, X. Wu, R. Hu, and S. Shi, "Finite position set-phase-locked loop with low computational burden for sensorless control of PMSM drives," IEEE Trans. Ind. Electron., vol. 70, no. 9,pp. 9672–9676, Sep. 2023.

[2] Z. Mai et al., "HF pulsating carrier voltage injection method based on improved position error signal extraction strategy for PMSM position sensor-less control," IEEE Trans. Power Electron., vol. 36, no. 8, pp. 9348–9360,Aug. 2021.

[3] G. Bi, "High-frequency injection angle self-adjustment based online position error suppression method for sensorless PMSM drives," IEEE Trans. Power Electron., vol. 38, no. 2, pp. 1412–1417, Feb. 2023.

[4] G. Zhang, "Adaptive step-size predictive PLL based rotor position estimation method for sensorless IPMSM drives," IEEE Trans. Power Electron., vol. 39, no. 5, pp. 6136–6147, May 2024.

[5] H. Li, X. Zhang, C. Xu, and J. Hong, "Sensorless control of IPMSM using moving-average-filter based PLL on HF pulsating signal injection method," IEEE Trans. Energy Convers., vol. 35, no. 1, pp. 43–52, Mar. 2020.

[6] J. Hu, Z. Wang, H. Wang and C. He, "Gain Compensation-Based Quasi-Resonant PLL With Adaptive Super-Twisting SMO for Position Error Suppression of IPMSM Sensorless Control," IEEE Trans. Emerg. Sel. Topics Power Electron., vol. 12, no. 5, pp. 4888-4899, Oct. 2024.

[7] Q. An, J. Zhang, Q. An, X. Liu, A. Shamekov, and K. Bi, "Frequency-adaptive complex-coefficient filter-based enhanced sliding mode observer for sensorless control of permanent magnet synchronous motor drives," IEEE Trans. Ind. Appl., vol. 56, no. 1, pp. 335–343, Jan./Feb. 2020.

[8] W W. Villet, M. Kamper, P. Landsmann, and R. Kennel, "Hybrid position sensorless vector control of a reluctance synchronous machine through the entire speed range," in Proc. IEEE 15th Int. Power Electron. Motion Control Conf., 2012, pp. LS4b-1.1-1–LS4b-1.1-7.

[9] .R. Zhang, X. Fang, P. Shi, L. Zhao, Y. Du, and C. Gong, "Full speed range sensorless control of IPMSM based on improved PSO optimization," Electric Machines and Control, vol. 26, no. 9, pp. 130-139, 2022.

[10] S.-C. Yang and Y.-L. Hsu, "Full speed region sensorless drive of permanent-magnet machine combining saliency-based and back-EMF-based drive," IEEE Trans. Ind. Electron., vol. 64, no. 2, pp. 1092–1101, Feb. 2017.

[11] G. Zhang, G. Wang, D. Xu, and Y. Yu, "Hybrid Sensorless Control Based on Single Position Observer Using Error Combination for Interior Permanent Magnet Synchronous Machine Drives,"Proceedings of the Chinese Society of Electrical Engineering, vol. 37,no. 20, pp. 6077-6082, 2017.

[12] C. Wang, L. Gou, S. Dong, M. Zhou, and X. You, "Sensorless control of IPMSM based on super-twisting sliding mode observer with CVGI considering flying start," IEEE Trans. Transport. Electrific., vol. 8, no. 2, pp. 2106–2117, Jun. 2022.

Analytical Calculation Method for Parasitic Capacitance of Annular Excitation Winding in Non-uniformly Distributed Motors

Jiaqiang Zou
College of Automation Engineering
Nanjing University of Aeronautics and Astronautics
Nanjing, China
zoujiaqiang@nuaa.edu.cn

Shengbo Mo
Lanzhou Flight Control Co.,Ltd
Lanzhou, China
mosb001@avic.com

Qianqian Liu
Shanghai Institute of Space Power-Sources
Shanghai, China
liuqianqian@nuaa.edu.cn

Ruxin Chen
College of Automatio Engineering
Nanjing University of Aeronautics and Astronautics
Nanjing, China
1031804799@qq.com

Shushu Zhu
College of Automation Engineering
Nanjing University of Aeronautics and Astronautics
Nanjing, China
zhuss699@sina.cn

***Abstract*—The excitation controller is the core component for regulating the excitation current and controlling the output voltage of a generator. By employing wide-band gap power devices (such as SiC and GaN), the excitation controller achieves the advantages of low losses and high switching frequency. However, parasitic capacitance in the circuit can significantly affect the switching performance of power devices, increase switching losses, and introduce oscillations and electromagnetic interference. Among these, the parasitic capacitance of the excitation winding is a critical part of the excitation control circuit, and reducing its value can effectively enhance the controller's performance. For multi-layer, multi-turn annular windings, the calculation of the equivalent total parasitic capacitance C_p becomes particularly complex due to strict slot-width constraints. In practical applications, mismatches between conductor diameter and fixed slot width often cause coil displacement, leading to a non-uniform winding distribution, which makes the traditional uniform-winding assumption no longer applicable. To address this, this paper proposes an analytical modeling method for non-uniform annular windings. The winding is conceptually divided into a uniformly distributed Region I and a slot-constrained non-uniform Region II. Analytical expressions of inter-turn capacitance C_{tt} and inter-layer capacitance C_{ll} between adjacent circular conductors are derived. Based on these, an equivalent capacitance network is established to represent both the uniform and non-uniform regions. The total parasitic capacitance C_p is then calculated using the principle of energy conservation, by equating the electrostatic energy stored in the equivalent network with that stored in the actual winding. Finally, finite element simulations are conducted to validate the proposed analytical model, demonstrating its accuracy and effectiveness.**

Keywords—excitation winding, parasitic capacitance, Non-uniformly distributed winding

I. INTRODUCTION

In variable speed variable frequency aviation systems, changes in generator speed directly affect its output voltage [1].For electromagnetically excited or mixed excitation generators, the excitation current can be adjusted by the excitation controller to stabilize the output voltage. Using wide bandgap power devices as the main switching devices in excitation controllers can significantly reduce losses and heat generation. It also allows for higher switching frequencies. Reduced the size of magnetic components and capacitors in the circuit. Meets the requirements of aviation applications for high-temperature environment adaptability and strict volume and weight restrictions [2][3].The excitation winding of the generator serves as the load for the excitation voltage regulator. Its parasitic capacitance is an important component of the parasitic capacitance in the excitation voltage regulation circuit [4].Therefore, an analytical modeling method for calculating the parasitic capacitance C_p of the excitation winding has been established. This is of great significance for improving the operating performance of excitation voltage regulators by reducing parasitic capacitance.

There are two commonly used methods for calculating the C_p of windings. The first method is based on lumped circuit modeling, which is theoretically based on the law of charge conservation and equivalent circuit networks [5][6][7].The circuit network consists of multiple capacitors. Each capacitor can be theoretically calculated based on the law of conservation of charge and the geometric structure of the circuit [8]. The second method is based on the law of conservation of energy [9]. Assuming that the voltage drop across the winding is equal based on the geometric structure of the winding. The equivalent parasitic capacitance C_p between the two terminals of the winding is derived using the law of conservation of energy.

Fig. 1 shows a schematic diagram of the uniform distribution of the ring-shaped excitation winding. In practice, this is particularly true for the ring-shaped excitation windings of generators that are strictly limited by slot width. When using wires of different diameters for winding, it is difficult to match the width of each layer of winding with the fixed slot width. This

979-8-3315-5472-9/25/$31.00 ©2025 IEEE

leads to the windings not being arranged exactly as shown in the model in Fig. 1. The coils are subject to physical limitations imposed by the slot space. This causes the wires to be compressed within the slots, resulting in a certain degree of positional displacement. As a result, some of the coils within the excitation winding are not uniformly distributed. Therefore, it is necessary to establish modeling and analysis methods for calculating the parasitic capacitance of non-uniformly distributed ring-shaped excitation windings when considering slot width restrictions.

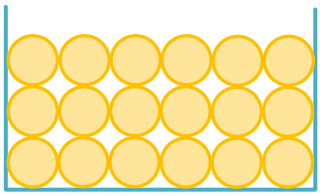


Fig. 1. Schematic diagram of uniform distribution of ring-shaped windings

II. Establishing an Analytical Model for Non-uniformly Distributed Windings Based on Slot Width Restrictions

A. Geometric Structure Analysis of Non-uniformly Distributed Windings

The distribution model of the geometric structure of the ring-shaped winding is limited by the width of the slot L of the winding itself and the diameter of the wire D_c. As shown in Fig. 2, during the winding process, the last turn of the first layer of the winding is restricted by the width of the slot. The outer diameter nD_c of the n turns of the first layer is greater than the inner width L of the winding slot. As shown in Fig. 3, for multilayer windings, the nth turn coil of the first layer cannot be distributed according to the original winding rules. The position of the nth turn coil will affect the position distribution of the coils in the next layer. Similarly, the non-uniform distribution of coils on each layer will affect the position of some coils on the next layer. Compared with Fig. 1, the structure of the ring winding has undergone significant changes in Region II, while Region I remains uniformly distributed according to the structure shown in Fig. 1. The distance and position between the coils in winding Region II have changed significantly.

Consider a multilayer annular excitation winding with m layers, each containing n turns. Define the distance between the n-1st turn of the first layer of the winding and the inner wall of the slot as D, as shown in Fig. 1. D is a key factor affecting the distribution structure of the winding. When D=0, the winding distribution is uniformly distributed as shown in Fig. 1. As D changes, the degree of unevenness in the geometric structure of the winding also changes.

As shown in Fig. 2, where D_o is the outer diameter of the coil, when $D\neq0$, the smaller the value of D, the more severe the uneven distribution of the geometric structure of the winding. At the same time, the uneven area of the winding gradually spreads from Region I to Region II as D decreases. The non-uniform distribution of the windings causes changes in the distance d_{tt} and arrangement position between some of the coils.

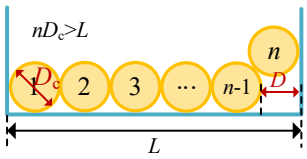


Fig. 2. Winding slot width restriction diagram

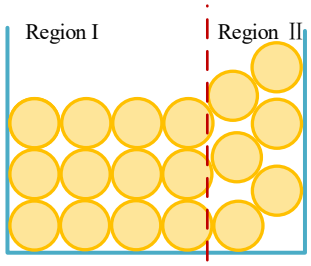


Fig. 3. Schematic diagram of non-uniformly distributed windings

B. The Effect of Non-uniform Distribution on Winding C_p

Finite element simulation was performed on the four winding structures shown in Fig. 4 to obtain their corresponding C_p values, and the results are shown in Fig. 5.Windings with the same number of turns but different distribution structures also have different C_p values. Fig. 6 shows the finite element simulation results of the inter turn capacitance C_{tt} and inter layer capacitance C_{ll} within the winding as a function of the inter turn distance d_{tt}. Finite element simulation results show that changes in the inter turn distance d_{tt} affect the distributed capacitance value within the winding. Electrostatic field simulations were performed on the uniform distribution model and the non-uniform distribution model with slot width restrictions shown in Fig. 1 and Fig. 3. The results are shown in Fig. 7 and Fig. 8. When the structure of the winding changes, the distribution of electrostatic field energy changes. The equivalent distributed capacitance of the energy stored between the winding turns also changes.

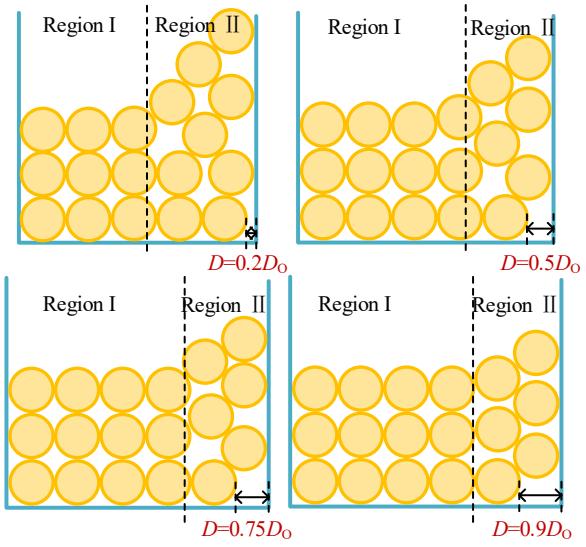


Fig. 4. Non-uniform distribution winding at different D values

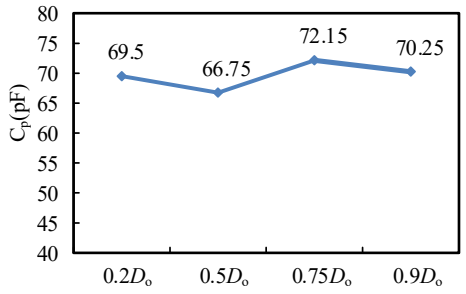


Fig. 5. C_p of non-uniformly distributed windings at different D values

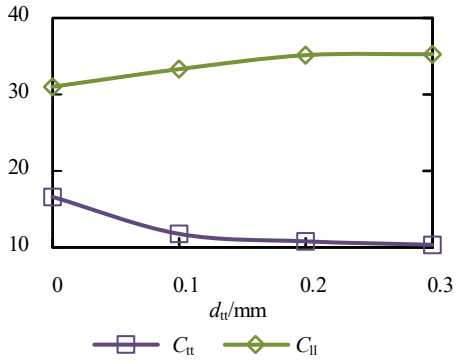


Fig. 6. The relationship between distributed capacitance C_{tt}, C_{ll}, and distance d_{tt}

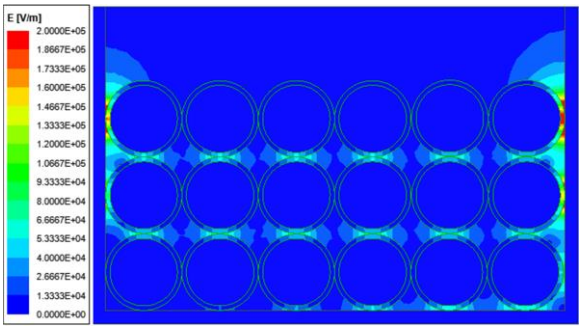


Fig. 7. Schematic diagram of the static electric field distribution of the winding when evenly distributed

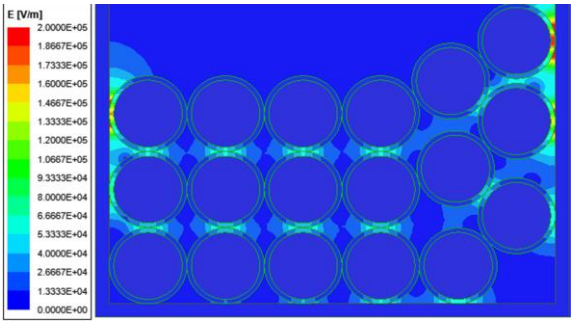


Fig. 8. Schematic diagram of the electrostatic field distribution of the winding when the distribution is non-uniform

In summary, when the winding structure is non-uniformly distributed, the distributed capacitance within the winding capacitance network will change. Consequently, the calculated C_p value will also change.

III. Calculation of Non-uniformly Distributed Winding C_P

A. Calculation of Distributed Capacitance

The interturn capacitance C_{tt} consists of two insulating layers C_c and an air gap capacitance C_g, as shown in Fig. 9(a).[8]. Among them, D_c is the diameter of the copper core inside the wire, D_o is the outer diameter of the wire, and θ is the integration angle. Since the cross-section of the conductor is circular, the capacitance solution path changes with θ. Using θ as the unit, the capacitance of the two parts is solved using calculus. Fig. 9(b). shows the differential of the conductor ring path. r is the radius of the conductor ring path, and l_t is the circumference of the conductor ring path.

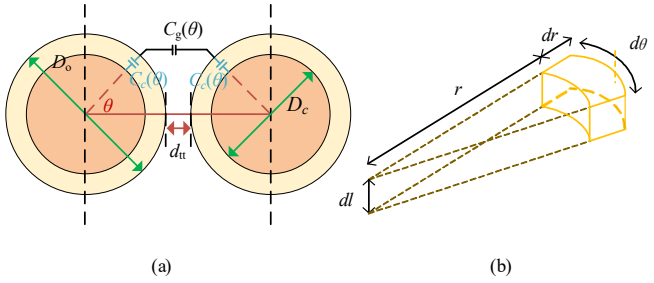


Fig. 9. Diagram of turn-to-turn capacitance

The differential expressions for the air gap capacitance C_g and the dielectric capacitance C_c are

$$dC_g(\theta) = \frac{\varepsilon_0 l_t D_0}{2x(\theta)} d\theta \tag{1}$$

$$dC_c(\theta) = \frac{\varepsilon_r \varepsilon_0 r}{dr} d\theta dl = \frac{\varepsilon_r \varepsilon_0 l_t}{\ln \frac{D_0}{D_c}} d\theta \tag{2}$$

Among them, ε_0 is the vacuum permittivity, ε_r is the relative permittivity of the conductor insulation layer, and $x(\theta)$ is the air gap path length.

$$x(\theta) = D_o(1-\cos\theta) + d_{tt} \tag{3}$$

Equivalent inter turn capacitance differential expression obtained from (1), (2) and (3)

$$\begin{aligned} dC_{eq}(\theta) &= \frac{1}{\frac{2}{dC_c} + \frac{1}{dC_g}} \\ &= \frac{\varepsilon_r \varepsilon_0 l_t D_o}{2D_o\left(\ln \frac{D_o}{D_c}\right) + 2\varepsilon_r\left[D_o(1-\cos\theta) + d_{tt}\right]} d\theta \end{aligned} \tag{4}$$

From (4), we can obtain the expression for the winding interturn capacitance C_{tt} as follows:

$$C_{tti}=\int_{\theta_1}^{\theta_2}\frac{\varepsilon_r\varepsilon_0 l_{ti}}{2\ln\frac{D_o}{D_c}+2\varepsilon_r\left[(1-\cos\theta)+\frac{d_{tt}}{D_o}\right]}d\theta$$
$$=\frac{\varepsilon_r\varepsilon_0 l_{ti}}{A_1}\arctan\left[\frac{B_1}{A_1}\tan\left(\frac{\theta_2}{2}\right)\right]- \quad (5)$$
$$\frac{\varepsilon_r\varepsilon_0 l_{ti}}{A_1}\arctan\left[\frac{B_1}{A_1}\tan\left(\frac{\theta_1}{2}\right)\right]$$

Among them

$$A_1=\sqrt{\left(\frac{1}{\epsilon_r}\ln\frac{D_o}{D_c}+1+\frac{d_{tt}}{D_o}\right)^2-1} \quad (6)$$

$$B_1=\frac{1}{\varepsilon_r}\ln\frac{D_o}{D_c}+\frac{d_{tt}}{D_o}+2 \quad (7)$$

Similarly, the inter layer capacitance C_{ll} and the turn-to-turn capacitance C_{tt} are arranged in the same way in terms of structure. Therefore, the expression for the inter layer capacitance C_{ll} is the same as that for the turn-to-turn capacitance C_{tt}.

B. Calculation of Non-uniformly Distributed Winding C_p

The total parasitic capacitance of the winding stores the same amount of energy as the sum of the energy stored in each capacitor in the capacitor network. The energy conservation law can be used to conveniently solve for the parasitic capacitance of a multi-layer winding.

$$E=\frac{1}{2}C_pU_N^2 \quad (8)$$

Among them, E is electrical energy, and U_N is the total voltage on the winding.

For the winding structure shown in Fig. 3, the non-uniform winding can be equivalent to a combination of uniformly distributed total parasitic capacitance C_p within the winding is equivalent to the sum of the energy stored in the distributed capacitance of the windings within Region I and Region II.

$$E=\frac{1}{2}C_{\mathrm{I}}U_{\mathrm{I}}^2+\frac{1}{2}C_{\mathrm{II}}U_{\mathrm{II}}^2 \quad (9)$$

Among them, C_{I} is the equivalent parasitic capacitance of Region I, U_{I} is the corresponding voltage, C_{II} is the equivalent parasitic capacitance of Region II, and U_{II} is the corresponding voltage.

According to the analysis results in Section 2.2, the distributed capacitance in Region II of the non-uniform winding changes with variations in the turn-to-turn distance d_{tt} and the arrangement angle θ between the coils, as shown in Fig.10. The distance and angle between the coils in Region II are different, so the distributed capacitance they produce is also different. Therefore, it is impossible to obtain specific spacing and angle values for each turn based on the structure of the winding. Consequently, it is impossible to calculate the distributed capacitance value within Region II.

In order to calculate the parasitic capacitance value in Region II, the non-uniformly distributed windings in Region II are idealized to a certain extent. Compared with the uniform distribution winding when D=0 in Fig. 1, the uneven distribution of the winding in Region II is mainly limited by the slot width, causing the two outermost turns of the coil to be squeezed. This results in the centers of the two outermost turns of each layer not being on the same straight line. Therefore, for the coils in Region II, fix the centers of the outer two turns of each layer of coils on the same straight line. As shown in Fig. 11, the idealized calculation model of the winding is obtained when D= 0.8D_o. In the idealized computational model shown in Fig.11, for convenience of calculation, each layer of windings in Region I is assumed to be at the same height as the inner windings in Region II. However, during the calculation process, the inter layer distance d in Region I is still assumed to be 0.

h represents the inter layer spacing generated after the idealized distribution of the windings in Region II. Based on the geometric relationship between the coils in Region II shown in Fig. 11, the expression for the inter turn distance h of the coils in Region II can be obtained.

$$h=2\left(\sqrt{D_0^2-D^2}-\frac{D}{2}\right) \quad (10)$$

Therefore, the corresponding distributed capacitance value can be calculated using (5) based on the inter turn distance d_{tt} and the angle θ between coils in the idealized model Region II. The distribution capacitance arrangement of the idealized model is shown in Fig.12. The distribution capacitance in egion II of the idealized model consists of only two types of distribution capacitance. The new capacitance network obtained based on the idealized winding model is shown in Fig. 13.

Assume that the total voltage across the winding is U_N . For a winding with m layers and n turns per layer, the potential difference U_{tt} between adjacent turns is U_N/mn. When adjacent conductors in adjacent layers are wound in the same direction, the voltage U_{ll} between adjacent layers on the interlayer capacitance C_{ll} is U_N/m. As shown in Fig. 13, the value of the voltage U_{tt1} corresponding to the distributed capacitance C_{tt} of type II is U_N/mn or $U_N(n\text{-}1)/mn$. Therefore, according to the law of conservation of energy in (9), the capacitance C_p of the winding can be solved.

$$E=\frac{1}{2}C_pU_N^2=\frac{1}{2}\sum C_{tt}U_{tt}^2+\frac{1}{2}\sum C_{ll}U_{ll}^2$$
$$+\frac{1}{2}\sum C_{lll}U_{ll}^2+\frac{1}{2}\sum C_{ttt1}U_{ttt1}^2 \quad (11)$$

Therefore, according to (11), the C_p of the non- uniformly distributed winding restricted by the slot width when D = 0.8D_o , taking into account the distributed capacitances C_{tt} , C_{ll} , C_{tt1}, and C_{ll1}, can be obtained as:

$$C_p = \frac{(n-2)(m-1)}{m^2} C_{11} + \frac{m(n-2)}{(mn)^2} C_{tt} + \frac{2(m-1)}{m^2} C_{111} + \frac{n(m-1)+1}{(mn)^2} C_{tt1} \quad (12)$$

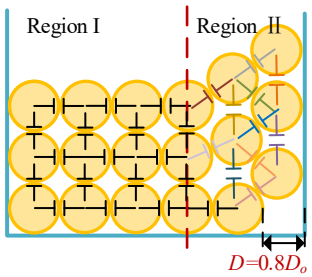


Fig. 10. Non-uniform distribution winding distribution model when D=0.8D_o

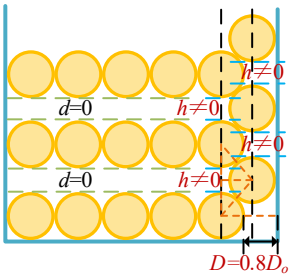


Fig. 11. Ideal distribution model for non-uniformly distributed windings when D=0.8D_o

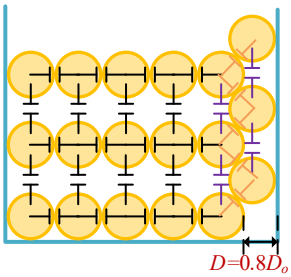


Fig. 12. Ideal distribution model for non-uniformly distributed windings when D=0.8D_o.

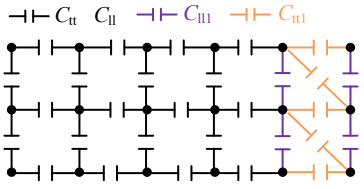


Fig. 13. Schematic diagram of non-uniformly distributed winding capacitor network when D=0.8D_o.

IV. Simulation Verification

Finite element software was used to simulate the electrostatic field of the non-uniformly distributed winding shown in Fig.10 under the condition of D=0.8D_o and its idealized model (Fig. 11). The simulation results are shown in Fig. 14 and Fig. 15, and the electrostatic field energy distributions of the two are relatively consistent. Therefore, the non-uniform distribution areas of the non-uniformly distributed windings can be calculated using ideal equivalent calculations. Fig. 16 shows a comparison between the finite element simulation results of non-uniformly distributed windings under the four different distribution conditions shown in Fig. 5 and the calculation results obtained using the analytical method pro- posed in this paper. The results show that the equivalent parasitic capacitance C_p values obtained by the two methods are similar, with a maximum error of less than 2.2%, verifying the accuracy of the method described in this paper.

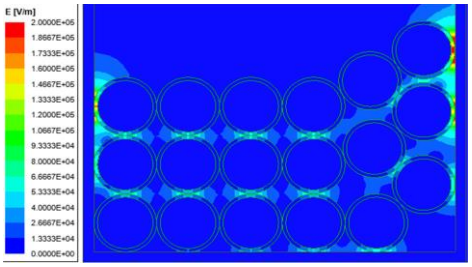


Fig. 14. Simulation of the electrostatic field of non-uniformly distributed windings when D=0.8D_o.

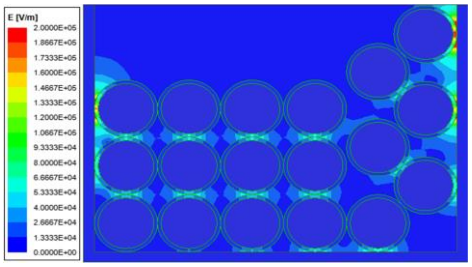


Fig. 15. Electrostatic field simulation of an ideal model of non-uniformly distributed windings when D=0.8D_o.

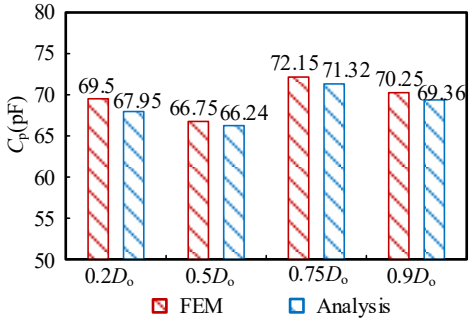


Fig. 16. Comparison of simulation and calculation results

V. Conclusion

This paper establishes an analytical calculation model for parasitic capacitance in non-uniformly distributed ring-shaped excitation windings under slot width constraints. Through analysis of the winding geometry, it is divided into Region I (uniform distribution) and Region II (non-uniform distribution).Based on this, analytical expressions for the turn-to-turn capacitance C_{tt} and layer-to-layer capacitance C_{ll} between adjacent circular conductors were derived. An equivalent capacitance network was constructed to characterize the uniform and non-uniform regions of the winding with specific distributed capacitances. Further derived the formula for calculating the equivalent total parasitic capacitance C_p under slot width constraints. The finite element simulation results show that the

maximum error between the calculated values and the simulation results is less than 2.3%, verifying the accuracy and effectiveness of the proposed method.

ACKNOWLEDGMENT

Supported by National Natural Science Foundation of China under Project 52277054 and Fundamental Research Funds for the Central Universities, NO.NE2024003.

REFERENCES

[1] S. Zhu, Y. Hu, J. Li, C. Liu, K. Wang, "Magnetic field analysis and operating characteristics of a brushless electrical excitation synchronous generator with dc excitation," IEEE Trans. Mag., vol. 58, no. 8, Article Sequence Number: 8106007, Feb. 2022.

[2] J. P. Kozak et al., "Stability, Reliability, and Robustness of GaN Power Devices: A Review" IEEE Trans. Power Electron, vol. 38, no. 7, pp. 8442-8471, July 2023.

[3] H. Zhao et al., "Parasitic Capacitance Modeling of Inductors Without Using the Floating Voltage Potential of Core" IEEE Trans. Ind Electron, vol. 69, no. 3, pp. 3214-3222, March 2022.

[4] F. Salomez, A. Videt and N. Idir, "Modeling and Minimization of the Parasitic Capacitances of Single-Layer Toroidal Inductors," IEEE Trans. Power Electron, vol. 37, no. 10, pp. 12426-12436, Oct. 2022.

[5] H. Zhao et al., "A Comparative Study on Parasitic Capacitance in Inductors With Series or Parallel Windings," IEEE Trans. Power Electron, vol. 37, no. 12, pp. 15140-15151, Dec. 2022.

[6] S. Tayenjam, V. Vanukuru, K. Sundaram et al., "An analytical model for distributed capacitance in up–down series stacked inductors," IEEE Trans. Electron Devices, vol. 67, no. 9, pp. 3510-3515, July. 2020

[7] Y. Cai et al., "Influence of parasitic parameters of commutation path on switching characteristics of silicon carbide MOSFET," High Voltage Engineering, vol. 47, no. 2, pp. 603–614, Feb. 2021.

[8] N. B. Chagas and T. B. Marchesan, "Analytical Calculation of Static Capacitance for High-Frequency Inductors and Transformers," IEEE Trans. Power Electron, vol. 34, no. 2, pp. 1672-1682, Feb. 2019

[9] M. Aghaei and S. Kaboli, "On the Effect of Disorder on Stray Capacitance of Transformer Winding in High-Voltage Power Supplies," IEEE Trans. Ind Electron, vol. 64, no. 5, pp. 3608-3618, May 2017.

Parameter Identification of Permanent Magnet Synchronous Motor Based on IRBMO Algorithm

1st Siqi Peng
College of Automation and Electronic Information
Xiangtan University
Xiangtan, China
13286587@qq.com

2nd Kun Zhu
College of Automation and Electronic Information
Xiangtan University
Xiangtan, China
1171281487@qq.com

3rd Chuchen Yang
College of Automation and Electronic Information
Xiangtan University
Xiangtan, China
1424143265@qq.com

4th Zhiwen Zhang
College of Automation and Electronic Information
Xiangtan University
Xiangtan, China
3193253163@qq.com

***Abstract*—In response to the challenge of easily falling into local optima and achieving low parameter accuracy in the parameter identification of permanent magnet synchronous motor (PMSM), this paper proposes an improved Red-billed Blue Magpie Optimization (IRBMO) algorithm. Based on the construction of the full-rank identification equation, the motor resistance, d/q-axis inductances, and permanent magnet flux linkage are identified using the IRBMO algorithm. Firstly, this algorithm employs Sobol sequences and opposition-based learning strategies to ensure the uniformity and diversity of the initial population. Secondly, a dynamic exploration probability with attenuation is introduced during the optimization identification process to enhance the algorithm's ability to balance exploration and exploitation. Finally, a dynamic tournament selection strategy is introduced in the exploration stage to adaptively adjust the selection size and improve the global search capability. Simulation and experimental results show that the IRBMO algorithm achieves superior convergence speed, accuracy, and stability in PMSM parameter identification, with the identified parameters meeting the precision requirements for high-performance motor control.**

Keywords—permanent magnet synchronous motor, improved red-billed blue magpie optimization algorithm, parameter identification, Sobol sequence, dynamic tournament selection strategy

I. INTRODUCTION

The permanent magnet synchronous motor features a simple structure, light weight, high efficiency, and high power factor. It has been widely used in electric vehicles, precision servo systems, industrial automation and other fields[1]. In these applications, the control performance of the motor directly depends on the accuracy of the motor parameters, such as stator resistance, inductance and permanent magnet flux linkage. However, in the actual operation process of the motor, the motor parameters are easily affected by temperature, load fluctuation, magnetic saturation and other factors, which in turn can impact the control performance and reliability of the high-performance permanent magnet synchronous motor[2],[3],[4]. Therefore, high-precision online parameter identification is the key to ensure high-performance motor control[5].

Traditional PMSM parameter identification methods, such as recursive least squares (RLS), extended Kalman filter (EKF), and model reference adaptive system (MRAS), have made remarkable progress in motor parameter identification. However, in practical applications often face slow convergence speed, computational complexity and tendency to fall into local optima [6]. In recent years, swarm intelligence algorithm has become an important method in PMSM parameter identification due to its excellent global optimization ability. An improved coral reef algorithm based on Cauchy and Gauss mutation was proposed in [7], which introduces mutation strategy to improve the search speed and accuracy of the algorithm. An improved bacterial foraging algorithm (MBFA) was proposed in [8], which solves the problem that swarm intelligence algorithm is easy to fall into local optimum by introducing niche technology and dynamic update mechanism. A weighted differential evolution particle swarm optimization (WDEPSO) based on double update strategy was proposed in [9], which combines the advantages of Particle swarm optimization (PSO) and Weighted differential evolution (WDE) algorithms. This approach effectively addresses the problem that the traditional PSO algorithm falling into local optimum in later stage.

However, existing optimization algorithms still face the problems of premature convergence and low accuracy. To address these issues, this paper proposes an improved Red-Billed Blue Magpie Optimization algorithm for PMSM parameter identification. The PMSM parameter identification problem is transformed into an optimization problem of the objective function, simultaneously identifying resistance, d-q axis inductance, and flux linkage. To achieve this, the proposed algorithm incorporates a series of targeted strategies to enhance optimization performance. Firstly, the Sobol sequence initialization and opposition-based learning strategy are used to generate a diversified initial population. Secondly, a dynamically decaying exploration probability is introduced during the optimization process to balance exploration and exploitation. Finally, dynamic tournament selection mechanism is incorporated in the exploration stage, which adaptively adjusts the selection probability to enhance the global search ability. The simulation and experimental results show that the improved algorithm outperforms traditional algorithms in terms of both

979-8-3315-5472-9/25/$31.00 ©2025 IEEE

identification accuracy and convergence speed for PMSM parameter identification.

II. PMSM Parameter Identification Model

A. Maintaining the Integrity of the Specifications

Under ideal conditions, the dq-axis voltage equations of the permanent magnet synchronous motor (PMSM) can be expressed as:

$$\begin{cases} u_d = R_s i_d + L_d \dfrac{di_q}{dt} - L_q \omega_r i_q \\ u_q = R_s i_q + L_q \dfrac{di_q}{dt} + L_d \omega_r i_d + \omega_r \psi_f \end{cases} \tag{1}$$

Equation: u_{d}, $i_{\mathrm{d}}$are d-axis voltage and current; u_{d}, i_{q} are q-axis voltage and current; R_{s} is the stator resistance; ω_{r} is the electric angular velocity; ψ_{f} is the magnetic chain of the permanent magnet.

The dq-axis voltage equation when the PMSM is vector controlled with id=0 and the motor is in steady state can be simplified as:

$$\begin{cases} u_d = -L_q \omega_r i_q \\ u_q = R_s i_q + \omega_r \psi_f \end{cases} \tag{2}$$

In the motor parameter identification process, a current disturbance signal is applied to the stator d-axis of the motor for a short period of time, and the full-rank state equations of the motor are established to achieve multi-parameter identification. Data are collected under two control states, id=0 and id$\neq$0, respectively, to obtain the full-rank state equations. The state equations of the motor are as follows:

$$\begin{cases} \hat{u}_{d0}(k) = -\hat{L}_q \omega_{r0}(k) i_{q0}(k) \\ \hat{u}_{q0}(k) = \hat{R}_s i_{q0}(k) + \hat{\psi}_f \omega_{r0}(k) \\ \hat{u}_d(k) = \hat{R}_s i_d(k) - \hat{L}_q \omega_r(k) i_q(k) \\ \hat{u}_q(k) = \hat{R}_s i_d(k) + \hat{L}_d \omega_r(k) i_d(k) + \hat{\psi}_f \omega_r(k) \end{cases} \tag{3}$$

In the formula, the value with "∧" denotes the estimated value of the motor parameter identification model, the value without "∧" represents the actual measured value of the motor, the value with the subscript "0" corresponds to the data collected under the i_d=0A control strategy, and the value without the subscript "0" refers to the data collected when a i_d=-2A current was injected.

III. Improved Red-billed Blue Magpie Algorithm

A. Red-billed Blue Magpie Optimization Algorithm

The Red-billed Blue Magpie Optimization (RBMO) algorithm is a heuristic swarm intelligence optimization technique inspired by the foraging behavior of the Red-billed Blue Magpie. This algorithm simulates the behavioral characteristics of the Red-billed Blue Magpie in its process of finding food, attacking prey, and storing food. The main objective of the algorithm is to address complex optimization problems by mimicking these natural behaviors[10].

B. Improved Red-billed Blue Magpie Optimization Algorithm

1) Population Initialization Strategy Based on Sobol Sequence and Opposition-Based Learning

The original Red-billed Blue Magpie Optimization (RBMO) algorithm initializes the population through random generation, which often leads to local convergence, lack of diversity, and uneven distribution. By incorporating the Sobol sequence and opposition-based learning, the improved method effectively achieves a more uniform distribution of the initial population, enhances population diversity, and helps avoid premature convergence to local optima[11].

After integrating the Sobol sequence and opposition-based learning, the final initialization formula is as follows:

$$\begin{aligned} x_{i,j} &= lb + (ub - lb) \times S_{i,j} + \\ &\alpha \times \left(X_{best} - \left(lb + (ub - lb) \times S_{i,j} \right) \right) \end{aligned} \tag{4}$$

In the formula, ub and lb represent the upper and lower bounds of the search space, respectively, and $S_{i,j}$ denotes the Sobol sequence value of the i-th agent in the j-th dimension. X_{best} is the best position found in the current iteration. α is the adjustment factor for opposition-based learning.

2) Introduction of Dynamically Decaying Exploration Probability

The traditional Red-billed Blue Magpie Optimization algorithm uses a fixed exploration probability ϵ=0.5. This fixed exploration probability is ineffective for global exploration in the early stages of the algorithm and leads to the algorithm becoming trapped in local regions in the later stages. This paper proposes a dynamically decaying exploration probability adjustment strategy. Specifically, the exploration probability decreases gradually with each iteration. In the improved algorithm, the exploration probability is higher in the early stages, which allows for a broader exploration of the solution space and prevents premature convergence during the identification process. In the later stages, the exploration probability gradually decreases, and the algorithm focuses more on local exploitation and fine-tuned search. The formula is:

$$\epsilon(t) = \text{initialEpsilon} \times \exp\left(-\frac{t}{0.5 \times T} \right) \tag{5}$$

Where t represents the current iteration number, T is the maximum number of iterations, and initialEpsilon is the initial exploration probability.

3) Introduction of Dynamic Tournament Selection Size in the Exploration Phase

The traditional RBMO algorithm employs a fixed selection size, which can lead to premature convergence of the population at certain stages. To address this issue, a dynamic tournament selection strategy is introduced in this paper, where the selection size is adjusted based on population diversity, thereby improving search efficiency during the exploration phase.

Dynamic Adjustment of Tournament Selection Size S_t: The tournament selection size is dynamically adjusted according to the population diversity, which is measured by the population standard deviation σ_t. As diversity increases, the selection size

decreases; conversely, as diversity decreases, the selection size increases. The formula for dynamically adjusting the selection size is as follows:

$$S_t = \min\left(\max\left(S_{\min}, \alpha \cdot \sigma_t\right), S_{\max}\right) \tag{6}$$

Where α is the scaling factor used to control the relationship between diversity and selection size. σ_t is the population standard deviation, which measures the diversity of the current population. S_{min} and S_{max} represent the minimum and maximum values of the selection size.

The position update formula is as follows:

$$\begin{aligned} &\text{winner}(t+1) = \text{winner}(t) + \\ &\frac{1}{S_t}\sum_{m=1}^{S_t}\left(\text{winner}_m(t) - X_{rs}(t)\right)\cdot \text{Rand} \end{aligned} \tag{7}$$

Where winner(t) denotes the position of the current best individual, $X_{rs}(t)$ represents the position of the Red-billed Blue Magpie. $\text{winner}_m(t)$ refers to the position of an individual participating in the tournament selection.

Fig.1 shows the flowchart of the IRBMO algorithm for multi-parameter PMSM identification.

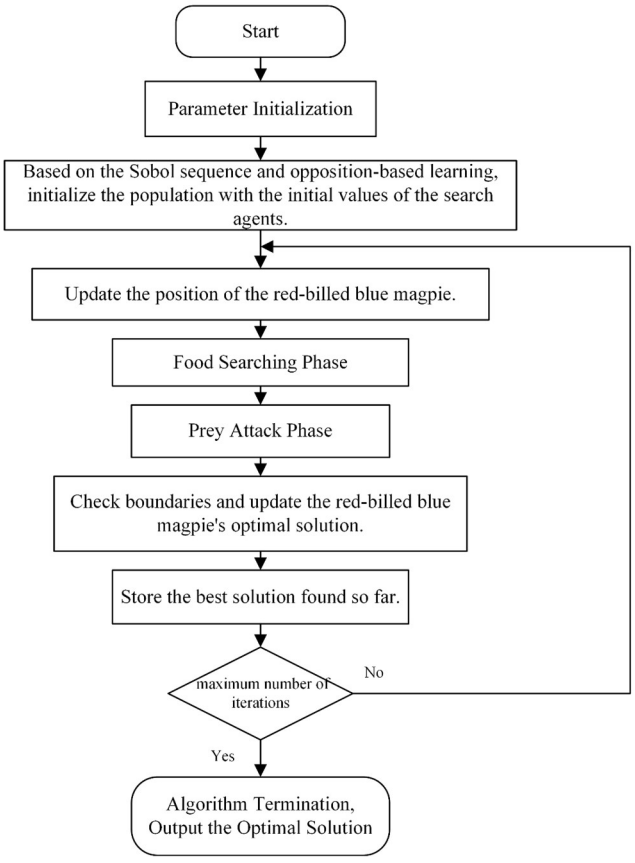


Fig. 1. Parameter Identification Algorithm Flowchart

C. PMSM Parameter Identification Based on IRBMO

The principle of Permanent Magnet Synchronous Motor parameter identification based on the IRBMO algorithm is illustrated in Fig. 2. The fitness function is defined as follows:

$$\begin{aligned} f(\theta) = {} & w_1\left[u_{d0}(k) - \hat{u}_{d0}(k)\right]^2 + \\ & w_2\left[u_{q0}(k) - \hat{u}_{q0}(k)\right]^2 + \\ & w_3\left[u_d(k) - \hat{u}_d(k)\right]^2 + \\ & w_4\left[u_q(k) - \hat{u}_q(k)\right]^2 \end{aligned} \tag{8}$$

In the formula, w_1, w_2, w_3 and w_4 are weight coefficients. By constructing the objective function of the optimization problem, the parameter identification problem for the PMSM can be transformed into the problem of finding the minimum value of the objective function $f(\theta)$.

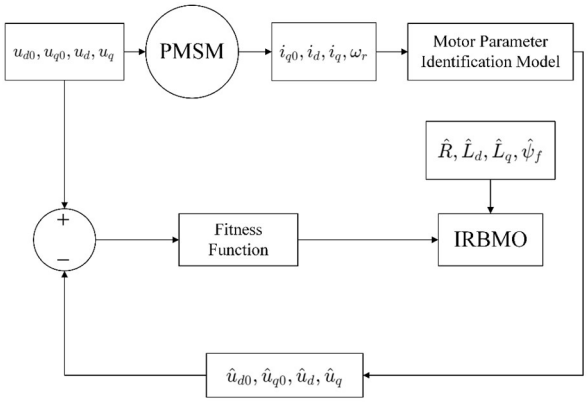


Fig. 2. PMSM Parameter Identification Schematic

IV. Simulation and Experimental Analysis

A. Standard Test Function Algorithm Performance Test

TABLE I. Standard Benchmark Functions

No.	Function	Range	Theory value	Types
f_1	Sphere	[-100,100]	0	Single-peak 30V
f_2	Schwefel 1.2	[-100,100]	0	
f_3	Schwefel 2.21	[-100,100]	0	
f_4	Ackley	[-32,32]	0	Multi-peak 30V
f_5	Alpine	[-10,10]	0	
f_6	Zakharov	[-10,10]	0	

This paper selects six benchmark test functions, as listed in Table 1, to evaluate the optimization performance of four algorithms: Adaptive Particle Swarm Optimization (APSO), Frosted Ice Optimization (RIME)[12], RBMO, and IRBMO. The test results are presented in Fig.3. Compared to the other three algorithms, IRBMO quickly approaches high-quality solutions in the early stages and continues to improve throughout the iteration process, ultimately achieving the lowest mean fitness values across all test functions. These results indicate IRBMO is well-suited for motor parameter identification.

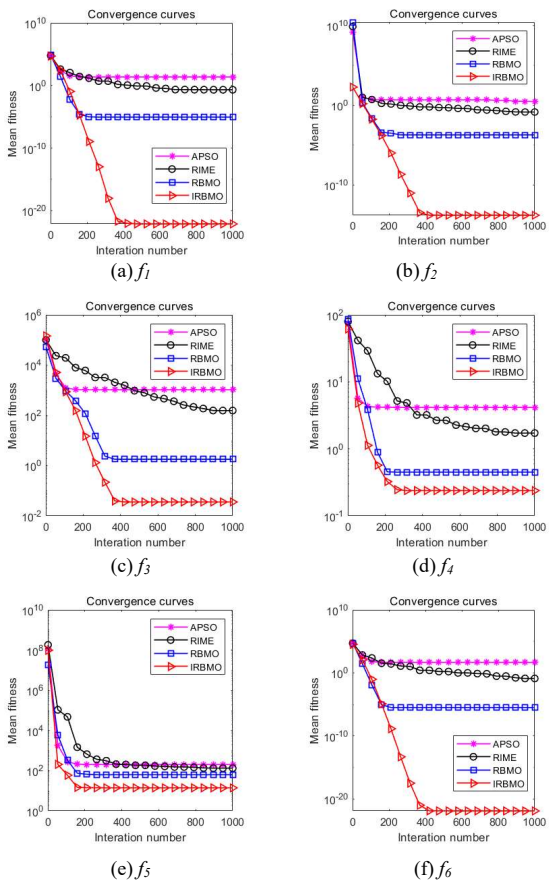


Fig. 3. Mean Convergence Curve

B. *Experiment and Analysis*

To evaluate the effectiveness of the proposed algorithm, parameter identification is performed on the experimental prototype. The PMSM parameters used in the experiment are listed in Table 2. PMSM vector control system model based on the TMS320F28335 is constructed, and the PMSM experimental platform is shown in Fig.4. The PMSM vector control schematic is shown in Fig.5. The motor speed is set to 3000 r/min, with an output torque of 1.27 N·m. The experiments are conducted using control strategies of i_d=0A and i_d=−2A, respectively. After the motor reaches a stable operating condition, data such as current, voltage, and speed during the motor operation are collected. The collected data is filtered and then undergoes coordinate transformation via the DSP controller. Finally, the data is transmitted to the host computer via the CAN bus, where the proposed algorithm is applied for parameter identification.

TABLE II. MOTOR PARAMETERS

Parameters	Value	Parameters	Value
Rs (Ω)	3.69	Rated Power (W)	400
Ld (mH)	9.14	Rated Speed (rpm)	3000
Lq(mH)	13.74	Rated Current (A)	2.7
ψf (Wb)	0.0499	Rated Torque (N·m)	1.27
Pole Pairs (np)	5	Rated Voltage (V)	220

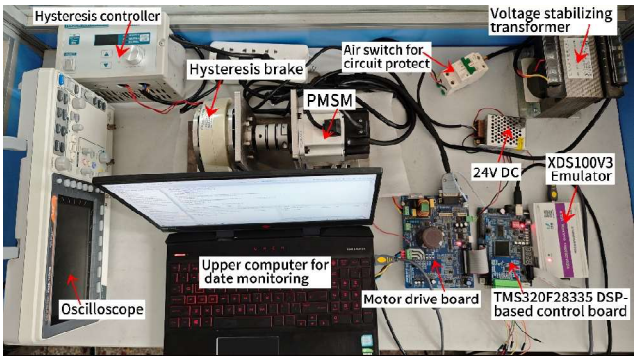


Fig. 4. PMSM experimental platform

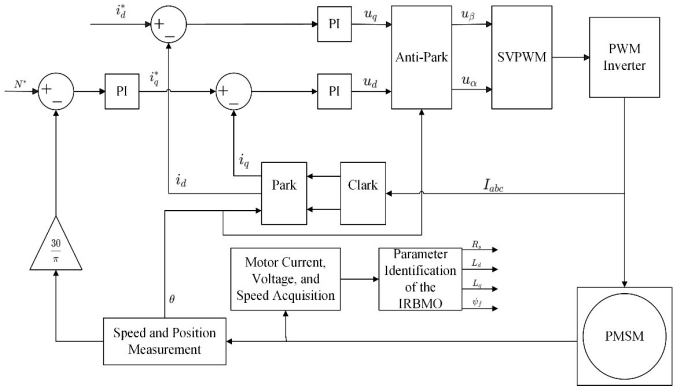


Fig. 5. PMSM Parameter Identification Schematic Based on the IRBMO Algorithm

To assess the superiority of the proposed Improved Red-billed Blue Magpie Optimization algorithm in parameter identification, comparison experiments are conducted with the Adaptive Particle Swarm Optimization, Frosted Ice Optimization, and Red-billed Blue Magpie Optimization algorithms. To ensure fairness in the comparison, the experimental parameters for all four algorithms are kept consistent: the population size is set to 50, the maximum number of iterations is 100. To minimize errors in the experimental results, each algorithm is run independently 30 times, with the final result being the average of these runs.

In order to test the convergence speed of the algorithm, the convergence curves of the average fitness value in the process of parameter identification of PMSM using the four algorithms are given respectively, as shown in Fig.6. The four algorithms converge to a stable fitness value after 100 iterations, which shows that the four algorithms have the ability of global optimization. Compared with the other three algorithms, the IRBMO algorithm has a lower objective function value in the initial stage and a faster convergence speed. In addition, the IRBMO algorithm eventually converges to the lowest optimal fitness value. The convergence curve shows that the IRBMO algorithm has more prominent advantages in the parameter identification of PMSM.

The motor parameters are identified using the proposed algorithm, and the identification results are shown in Fig.7~Fig.10.

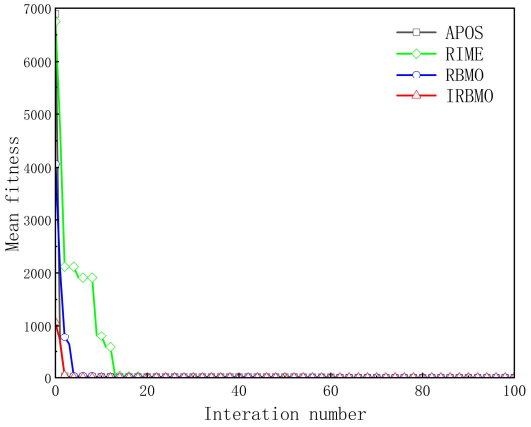


Fig. 6. Iteration Curve of Mean Fitness Value

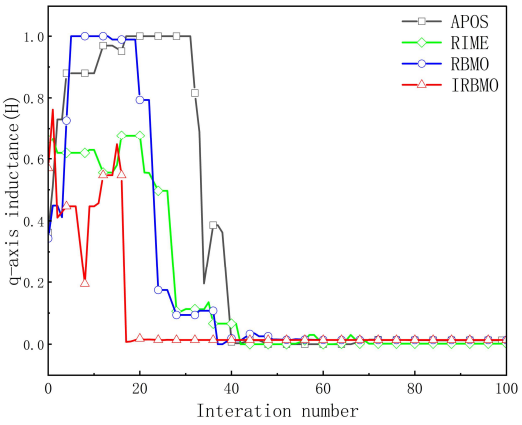


Fig. 9. q-axis Inductance Identification Curve

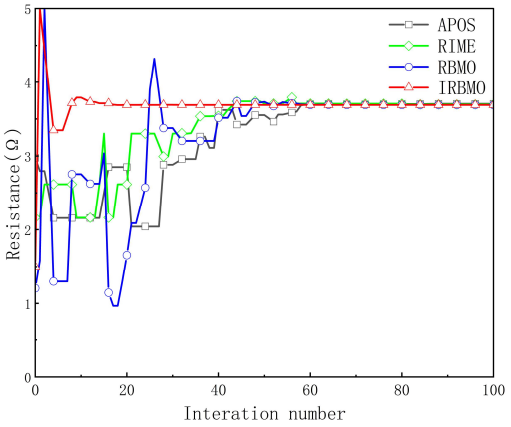


Fig. 7. Resistance Identification Curve

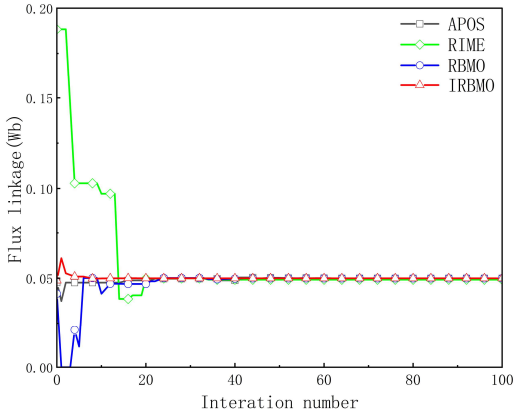


Fig. 10. Flux Linkage Identification Curve

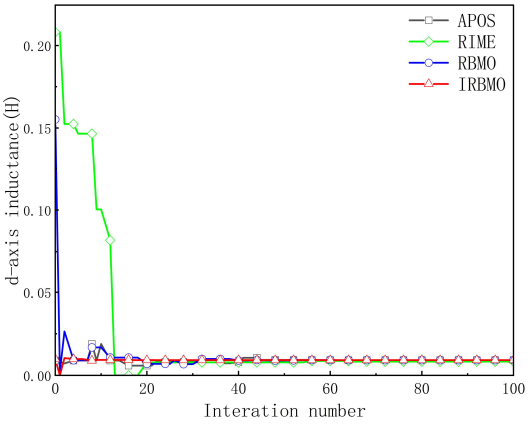


Fig. 8. d-axis Inductance Identification Curve

It can be observed that during the parameter identification process using the four algorithms, all four algorithms converge within 100 iterations. Compared to the other three algorithms, the IRBMO algorithm exhibits a faster search speed, quickly approaching a better solution in the initial phase, and stabilizes in subsequent iterations. The proposed algorithm demonstrates the smallest fluctuation during the search process, the fastest convergence speed, and the lowest final identification error.

The experimental data statistics are shown in Table 3, where the average values, and identification errors obtained from 30 independent runs of the four algorithms are compared. The experimental results show that the IRBMO algorithm achieves the smallest error between the identified results and the true values. The identification error is consistently controlled within 2%, fully verifying that the IRBMO algorithm offers high accuracy in parameter identification. It also demonstrates that the IRBMO algorithm possesses superior optimization capability and global convergence performance during the optimization process.

TABLE III. COMPARISON OF PARAMETER IDENTIFICATION ALGORITHM RESULTS

Parameter		APOS	RIME	RBMO	IRBMO
R_s	Mean/Ω	3.590	3.646	3.678	3.686
	Err/%	2.72	1.19	0.32	0.12
L_d	Mean/H	0.0082	0.0086	0.0090	0.0091
	Err/%	9.86	5.59	1.45	0.98
L_q	Mean/H	0.0125	0.0127	0.0129	0.0135
	Err/%	9.17	7.32	5.80	1.95
ψ_f	Mean/Wb	0.0477	0.0491	0.0496	0.0498
	Err/%	4.49	1.63	0.635	0.168

V. CONCLUSION

This paper proposes an improved Red-Billed Blue Magpie Optimization algorithm for the multi-parameter identification of Permanent Magnet Synchronous Motors. Based on the construction of full-rank identification equations, an improved Red-Blue Magpie Optimization algorithm is employed to identify motor resistance, d/q-axis inductances, and the magnetic flux of the permanent magnet. By incorporating Sobol sequences and Opposition-based Learning for population initialization, dynamically decaying the exploration probability, and adaptively adjusting tournament selection size, the algorithm enhances global search capability, convergence speed, and accuracy. Compared to traditional optimization algorithms, IRBMO effectively overcomes the problem of premature convergence to local optima, enhancing the stability and rapidity of parameter identification.

Simulation and experimental results show that IRBMO outperforms traditional algorithms such as RBMO, RIME, and APSO in both standard benchmark functions and PMSM parameter identification. In PMSM parameter identification applications, the IRBMO algorithm more quickly approximates the true values, and achieves the lowest identification errors for all parameters, with error rates of only 0.12% for resistance, 0.98% for d-axis inductance, 1.95% for q-axis inductance, and 0.168% for flux linkage. These results are significantly better than those of RBMO, RIME, and APSO. This demonstrates the comprehensive advantages of IRBMO in terms of convergence speed, optimization accuracy, and stability. Furthermore, the algorithm maintains parameter errors within 2%, thereby effectively improving the precision and stability of the PMSM control system.

REFERENCES

[1] Peng Siqi, Jiang Yvhan, Lan Zhiyong, and Li Fan, "Sensorless control of permanent-magnet synchronous motor using a novel exponential adaptive sliding-mode observer," J. Electr. Mach. Control, vol. 26, no. 5, pp. 104–114, 2022.

[2] Xie Guomin and Zhao Dejian, "Multi-parameter identification of permanent-magnet synchronous motor using an improved antlion optimization algorithm," Proceedings of the CSU-EPSA, vol. 35, no. 6, pp. 66–72, 2023.

[3] Cao Yongjuan, Mao rui, Feng Liangliang, and Li kang, "Multi-parameter identification of permanent-magnet synchronous motor based on an improved sparrow search algorithm," Advanced Technology of Electrical Engineering and Energy, vol. 41, no. 5, pp. 26–34, 2022.

[4] Lian Chuanqiang, Xiao Fei, Gao Shan, and Liu Jilong, "Parameter identification of interior permanent-magnet synchronous motor based on experimental calibration and two-time-scale stochastic approximation theory," Proceedings of the Chinese Society for Electrical Engineering, vol. 39, no. 16, pp. 4892–4898, 4991, 2019.

[5] Wang Huimin, Zhang Ying, and Ge Xinglai, "Online identification of excitation inductance of linear traction motor based on a full-order state observer," Proceedings of the Chinese Society for Electrical Engineering, vol. 37, no. 20, pp. 6101–6108, 2017.

[6] Liu Wei and Wang Jun, "Review of parameter identification techniques for permanent-magnet synchronous motors," Electrical Engineering, vol. 21, no. 8, pp. 1–6, 2020.

[7] Wu Dinghui, Huang Xv, Quan Yawei, and Ji Zhicheng, "Parameter identification of permanent-magnet synchronous motor based on a mutated coral-reef optimization algorithm," Journal of System Simulation, vol. 30, no. 8, pp. 3024–3032, 2018.

[8] Bian Qi, Ma Jian, Zhang Menghan, and Wang Jianping, "Parameter identification of permanent-magnet synchronous motor using an improved bacterial foraging algorithm," J. Electr. Mach. Control, vol. 28, no. 2, pp. 174–181, 2024.

[9] S. Zhou, D. Wang, Y. Ni, K. Song, and Y. Li, "Improved particle swarm optimization for parameter identification of permanent-magnet synchronous motor," Comput. Mater. Continua, vol. 79, no. 2, pp. 2187–2207, 2024.

[10] S. Fu, K. Li, H. Huang, C. Ma, Q. Fan, and Y. Zhu, "Red-billed blue magpie optimizer: A novel metaheuristic algorithm for 2D/3D UAV path planning and engineering design problems," Artificial Intelligence Review, vol. 57, art. no. 134, 2024.

[11] C.-l. Liang and Z.-h. Chen, "An improved salp swarm algorithm based on a hybrid strategy," Control and Decision, vol. 39, no. 8, pp. 2541–2550, 2024.

[12] H. Su, D. Zhao, A. A. Heidari, L. Liu, X. Zhang, M. Mafarja, and H. Chen, "RIME: A physics-based optimization," Neurocomputing, vol. 532, pp. 183–214, 2023.

An Equivalence Method for PMSG-based Wind Farm with Virtual Synchronous Generator Control Considering the Whole Dynamic Process

Peicong Zhu
Electrical and Power Engineering School
Hohai University
Nanjing, China
1915978781@qq.com

Qiang Ma
Clean Energy Branch
Huaneng International Power Jiangsu Energy Development Co., Ltd.
Nanjing, China
81002414@nmail2.chng.com.cn

Shaoguang Chen
Clean Energy Branch
Huaneng International Power Jiangsu Energy Development Co., Ltd.
Nanjing, China
82068359@nmail2.chng.com.cn

Haiqiang Zhou
Electrical and Power Engineering School
Hohai University
Nanjing, China
js.hq@163.com

Tai He
Clean Energy Branch
Huaneng International Power Jiangsu Energy Development Co., Ltd.
Nanjing, China
82062112@nmail2.chng.com.cn

Yujie Wang
Clean Energy Branch
Huaneng International Power Jiangsu Energy Development Co., Ltd.
Nanjing, China
82062114@nmail2.chng.com.cn

***Abstract*—An equivalent method for permanent magnet synchronous generator (PMSG)-based wind farm with virtual synchronous generator (VSG) control is proposed in this paper. First, an improved Low Voltage Ride-Through (LVRT) control strategy for PMSG-VSG is introduced. The active power reference is modified to satisfy the current limitation during faults. Additionally, the internal voltage is compensated to avoid overvoltage at the moment of fault clearance. Then, the whole dynamic process of the VSG is analyzed. It is found that the current limiting action has a great influence on the dynamics during faults. The spectral clustering method is used to analyze the power angle after fault clearance. The VSGs are clustered into four groups based on the similarities of the dynamic responses during and after faults. And the equivalent PMSG and the collection grid are aggregated. Finally, the proposed equivalent method is applied in the test system including 12 PMSGs. Simulation results show that the proposed method effectively improves the precision of the equivalent model and simulation efficiency.**

Keywords—Virtual synchronous generator, PMSG, low voltage ride-through control, dynamic aggregation, clustering criterion

I. INTRODUCTION

Currently, some wind energy conversion systems utilize virtual synchronous generator (VSG) control, which is suitable for weak power grids with a relatively high proportion of non-synchronous generating capacity [1]. Detailed modeling for large-scale wind power grid integration results in highly complex models, significantly increasing simulation model size and computation time. Therefore, dynamic equivalence of wind farms is essential [2].

Multi-machine equivalent methods are widely applied in wind farm (WF) equivalence to improve modeling accuracy. Hence, identifying appropriate clustering criteria constitutes a key prerequisite for dynamic aggregation. For equivalence of conventional grid-following (GFL) wind farms during Low Voltage Ride-Through (LVRT), multi-machine clustering primarily relies on the fault response characteristics of permanent magnet synchronous generators (PMSGs) or the transient behavior of control strategies. Reference [3] uses operating wind speed and terminal voltage at the instant of fault clearance as clustering criteria, based on discrepancies in the active power characteristics of PMSG under varying fault severity levels. Other studies utilize the action state of protection devices such as chopper [4] or Crowbar circuit [2] as clustering criterion.

Research focusing on the equivalence of VSG-controlled voltage source converters (VSCs) remains scarce at present. Existing related work mainly borrows from synchronous generator (SG) coherent detection techniques. Reference [5] developed a quasi-coherency criterion appropriate for VSCs by analyzing the power angle deviations among VSGs, proposed a parameter aggregation method, and applied this approach to VSG-controlled MMC converters [6]. Reference [7] constructs an index vector based on the peak value of the first power angle swing after fault occurrence and clearance, and applies the fuzzy C-means clustering algorithm for equivalencing.

In summary, although substantial progress has been made in WF equivalence research, the following limitations persist: 1)

This work is supported by the China Huaneng Group Co., Ltd. Headquarters Science and Technology Project (No. HNKJ24-H68).

979-8-3315-5472-9/25/$31.00 ©2025 IEEE

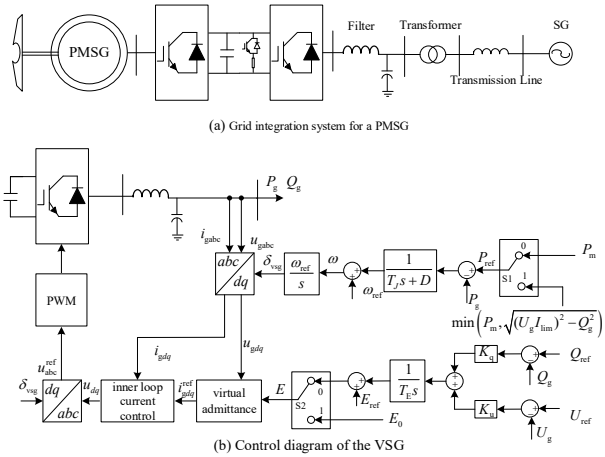
Insufficient research on equivalent modeling for VSG WF. 2) Clustering criterion solely based on power characteristics during the fault period may introduce substantial errors. 3) The impact of current limiter activation during faults has not been adequately addressed.

This paper presents an equivalent method for VSG-controlled WF, considering the whole dynamic process. First, an LVRT control strategy based on power reference modification and internal voltage compensation is proposed. Next, the power characteristics of PMSG-VSGs under current limiter activation and after fault clearance are analyzed. The VSG WF is clustered based on similarities in dynamic responses throughout the whole fault process. Subsequently, the equivalent PMSG-VSGs and the collection grid are aggregated, and calculate the equivalent accuracy indices. Finally, the feasibility and effectiveness of the clustering criterion are verified through case studies.

II. LVRT Control Strategy for PMSG-VSG

A. Control Strategy for PMSG-VSG

The grid integration system and control architecture of the PMSG-VSG are illustrated in Fig. 1. The machine-side converter employs a standard control strategy that implements DC-link voltage regulation and reactive power control based on maximum power point tracking (MPPT), as detailed in the relevant literature [8].



(a) Grid integration system for a PMSG

(b) Control diagram of the VSG

Fig. 1. Grid-Connected System and Control Architecture of PMSG-VSG

The grid-side converter adopts VSG control, as illustrated in Figure 1(b). The dynamic equation for the active power-frequency control loop is given as follows:

$$\begin{cases} T_{\mathrm{J}} \dfrac{\mathrm{d}\Delta\omega}{\mathrm{d}t} = P_{\mathrm{g}}^{\mathrm{ref}} - P_{\mathrm{g}} - D\Delta\omega \\ \dfrac{\mathrm{d}\delta_{\mathrm{vsg}}}{\mathrm{d}t} = \omega_0(1+\Delta\omega) \end{cases} \tag{1}$$

where T_{J} is the inertia time constant of VSG; $P_{\mathrm{g}}^{\mathrm{ref}}$ and P_{g} denote the active power reference of the PMSG and the grid-connected output power, respectively; ω_0 and $\Delta\omega$ represent the rated frequency and frequency deviation of the PMSG-VSG, respectively; D is the damping coefficient; δ_{vsg} is the VSG phase angle.

The dynamic equation for the reactive power-voltage control loop is given as follows:

$$E = E_{\mathrm{ref}} + \frac{1}{T_{\mathrm{E}}s}[K_{\mathrm{q}}(Q_{\mathrm{ref}} - Q_{\mathrm{g}}) + K_{\mathrm{u}}(U_{\mathrm{ref}} - U_{\mathrm{g}})] \tag{2}$$

where T_{E} is the integral time constant of the internal voltage; E_{ref} is the reference value of the internal voltage; Q_{ref} and Q_{g} are the reactive power reference value and output reactive power, respectively; U_{ref} and U_{g} are the terminal voltage reference value and measured value; K_{q} and K_{u} are the reactive power droop coefficient and voltage droop coefficient, respectively;

Under normal operating conditions, the VSG externally behaves as a voltage source with series impedance. This paper adopts a virtual admittance structure with a voltage forward channel. Compared with the impedance structure based on a current feedback channel, this virtual admittance structure exhibits superior electromagnetic transient response performance [9], and its control equation can be expressed as:

$$\begin{bmatrix} i_{\mathrm{gd}}^{\mathrm{ref}} \\ i_{\mathrm{gq}}^{\mathrm{ref}} \end{bmatrix} = \begin{bmatrix} \dfrac{R_{\mathrm{v}}}{R_{\mathrm{v}}^2 + X_{\mathrm{v}}^2} & \dfrac{X_{\mathrm{v}}}{R_{\mathrm{v}}^2 + X_{\mathrm{v}}^2} \\ -\dfrac{X_{\mathrm{v}}}{R_{\mathrm{v}}^2 + X_{\mathrm{v}}^2} & \dfrac{R_{\mathrm{v}}}{R_{\mathrm{v}}^2 + X_{\mathrm{v}}^2} \end{bmatrix} \begin{bmatrix} U_{\mathrm{gd}} - E \\ U_{\mathrm{gq}} \end{bmatrix} \tag{3}$$

where $i_{\mathrm{gd}}^{\mathrm{ref}}$ and $i_{\mathrm{gq}}^{\mathrm{ref}}$ are the reference values of the dq-axis terminal current, respectively; R_{v} and X_{v} are the virtual resistance and virtual reactance, respectively;

The inner-loop current control adopts a traditional dq double-loop decoupling control structure, which can be referenced to GFL control.

B. Improved LVRT Control Strategy

The control objectives of VSG LVRT encompass limiting short-circuit current for inverter protection, providing reactive power/voltage support, and ensuring transient synchronization stability.

Considering that voltage-based limiters fails to restrict the current within a safe range at the instant of fault occurrence [10], this paper adopts circular limiter, with its control equation expressed as:

$$\boldsymbol{i}_{\mathrm{gdq}}^{\mathrm{ref}\prime} = \min\left\{1, \frac{I_{\mathrm{lim}}}{\| \boldsymbol{i}_{\mathrm{gdq}}^{\mathrm{ref}} \|}\right\} \boldsymbol{i}_{\mathrm{gdq}}^{\mathrm{ref}} \tag{4}$$

where I_{lim} is the current limit amplitude; $\boldsymbol{i}_{\mathrm{gdq}}^{\mathrm{ref}}$ and $\boldsymbol{i}_{\mathrm{gdq}}^{\mathrm{ref}\prime}$ are the initial value of the dq-axis current command and the reference current vector output by the current limiter, respectively; $\|\bullet\|$ represents the amplitude of the dq-axis vector.

Based on the equal area criterion, the intrinsic cause of VSG instability is sustained power imbalance [11]. During the fault

period, due to the current-limiting effect, the limit amplitude of the apparent power output by the VSG-based wind turbine is $P_{\max} = U_g I_{\lim}$. Therefore, to ensure the existence of a stable equilibrium point for the VSG, the active power reference should be set lower than the maximum power. Furthermore, analogous to the reactive power priority control of GFL wind turbines, the active power reference of VSG during LVRT should be modified to:

$$P_g^{\text{ref}} = \begin{cases} P_m, & U_g > 0.9 \\ \min\left(P_m, \sqrt{(U_g I_{\lim})^2 - Q_g^2}\right), & U_g \le 0.9 \end{cases} \tag{5}$$

where P_m is the mechanical power captured by the wind turbine generator.

During the fault period, the wind farm shall respond to the grid connection point voltage and dynamically output reactive power support current. The functional positioning of GFM devices requires them to provide adequate dynamic voltage support for GFL devices [12], thus demanding full utilization of the converter's adjustable capacity. To achieve optimal transient voltage support performance, K_u / K_q should be greater than or equal to 10 [13]. Therefore, this paper configures the droop coefficients of the VSG in different stages as follows:

$$K_q = \begin{cases} 1, & U_g > 0.9 \\ 0.1, & U_g \le 0.9 \end{cases} \tag{6}$$

$$K_u = \begin{cases} 0, & U_g > 0.9 \\ 1, & U_g \le 0.9 \end{cases} \tag{7}$$

During the fault period, the sudden drop in output active power results in an increase in machine-side rotational speed and pitch angle, which leads to significant power oscillations after fault clearance and slow recovery to the normal operating point. This paper blocks the DC voltage PI loop of the machine-side converter during the fault period and employs the chopper circuit to ensure the DC voltage safety. Furthermore, when the fault is cleared, the integral characteristic causes the E to remain higher than the initial steady-state value, resulting in a power surge and inducing terminal transient overvoltage. Therefore, upon detecting fault clearance, the amplitude of the E should be compensated to the pre-fault steady-state value E_0, with the overall control structure illustrated in Figure 1(b).

III. Clustering Criterion for VSG WF Considering the Whole Dynamic Process

The current-limiting loop is activated during faults, typically limiting the current to 1.1-1.5 p.u. Its power angle curve is determined by the current-limiting algorithm, showing significant differences from that of SG [14]. After fault clearance, the VSG exits LVRT control, and the VSG undergoes oscillatory decay to recover to the steady-state operating point, with the low-frequency oscillation frequency typically around 1 Hz [15].

A. Power Angle Characteristics Accounting for Current-Limiting

During normal operation, with resistance neglected, the VSG-based wind turbine is externally equivalent to a voltage source, and its output power expression is given by:

$$P_g = \frac{EV}{X_\Sigma} \sin\delta \tag{8}$$

where X_Σ is the sum of VSG grid-connected reactance; δ is the power angle, defined as the phase angle by which the d-axis of the VSG wind turbine leads the infinite bus.

When the terminal voltage drops suddenly, the current-limiting loop is activated. At this point, the VSG is externally equivalent to a constant current source with an output current amplitude of $I_{\lim}$. The output power of the VSG-based wind turbine is expressed as:

$$P_g = 1.5 U_g I_{\lim} \cos(\delta + \varphi) \tag{9}$$

where $\varphi = \arctan\left(i_{gq}^{\text{ref}} / i_{gd}^{\text{ref}}\right)$ is the phase angle of the converter output current.

With the active power reference modifying loop locked and damping effects neglected, under the same fault voltage and φ conditions, the transient power angle curves accounting for current-limiting action at different wind speeds are illustrated in Figure 2. Under high wind speed conditions, the active power reference value is large, with the steady-state operating point at point a. At the instant a fault occurs, the power angle curve corresponding to the current limiting action lies below the initial reference point, causing the active power to drop sharply to P_b; when operating reaches point c, the fault is cleared, and the overall operating trajectory is shown by the blue dashed line in Figure 2(a). In low wind speed scenarios with small active power commands, the analysis of power angle characteristics during faults is similar to that in high wind speed scenarios. The distinction is that the power angle curve may be positioned above the initial operating point, in which case P_b exceeds P_a.

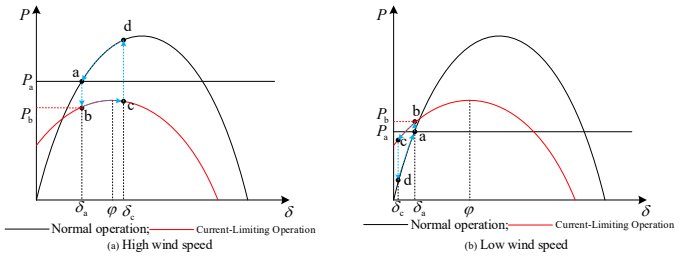


Fig. 2. Transient Power Angle Curve Accounting for Current-Limiting Action

In conjunction with the wind farm grid-connected system illustrated in Figure 1, simulations are performed within the operating range of wind turbines, from the start-up region of 6 m/s to 14 m/s, with a step size of 0.5 m/s. The grid voltage sags to 0.5 p.u. between 0.1 s and 0.3 s, with the test results presented in Figure 3. In the figure, each curve corresponds to the active power response at a specific wind speed. The pink curve

corresponds to the scenario where $P_a > P_b$, while the blue curve corresponds to $P_a \le P_b$. The simulation results are consistent with the aforementioned analysis.

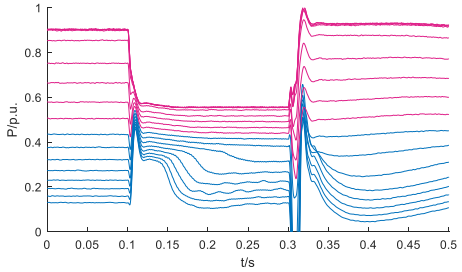


Fig. 3. Active Power Response Curve under Various Wind Speeds

In summary, since the power angle cannot change abruptly, under the same voltage sag condition, PMSG-VSG are categorized into two clusters based on the relationship between P_a and P_b, corresponding to the two colored curves shown in Figure 3. This relationship can serve as the clustering criterion for VSG WF during faults.

B. Analysis of Oscillation Modes after Fault Clearance

After fault clearance, the PMSG-VSG exhibits oscillations before stabilizing at the initial operating point. In addition to being dominated by the grid-side VSG and wind turbine control at the electromechanical scale, this oscillation mode also necessitates consideration of the impact of grid-side terminal voltage control on system dynamic stability [16].

By integrating the dynamic equations of the wind turbine, grid-side VSG converter, and terminal voltage control, the oscillation modes of the wind turbine grid-connected system can be analyzed using small-signal stability analysis [17].

In wind turbine control systems, the speed reference value for different operating regions is a piecewise function of the output power:

$$\omega_r^{ref} = \begin{cases} a_1 P_g^2 + a_2 P_g + a_3, & P_g < P_{cp} \\ 1, & P_g \ge P_{cp} \end{cases} \tag{10}$$

where a_1, a_2 and a_3 are fitting coefficients; P_{cp} is the boundary power between the MPPT region and the constant speed region.

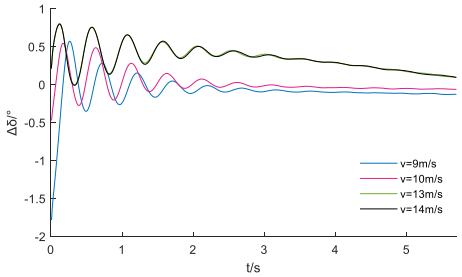


Fig. 4. Power Angle Increment under Different Wind Speeds

It can be inferred from Equation (10) that distinct speed control characteristics correspond to different oscillation modes. In the large-disturbance analysis scenario, based on the system illustrated in Figure 1, the grid voltage is set to sag to 0.5 p.u., and the power angle increment curves under different wind speeds after fault clearance are presented in Figure 4. The lower the wind speed, the faster the attenuation of power angle oscillations, the larger the damping ratio, and the quicker the recovery to the steady-state operating point. However, due to the sudden drop in active power during the fault, the speed control characteristics of the wind turbine are likely to change; thus, the wind speed operating region cannot be simply adopted as the criterion for clustering.

C. Clustering Criterion Based on Similarities in Dynamic Responses

Prony analysis can identify a signal's amplitude A_i, phase θ_i, attenuation factor α_i, oscillation frequency f_i, and damping ratio ξ_i, thereby comprehensively characterizing the modal properties of the transient signals [18]. The spectral clustering algorithm can perform clustering on sample spaces of arbitrary shapes and converge to the globally optimal solution. Therefore, this paper proposes a clustering criterion based on similarities in dynamic responses throughout the whole fault process, with the main steps outlined as follows:

1) Classify wind turbine units into two groups based on the magnitudes of P_a and P_b during fault periods;

2) Conduct Prony analysis on the power angle curves of PMSG-VSGs within each cluster after fault clearance, and construct the feature vector for VSG as: $\left[\boldsymbol{A_p}, \boldsymbol{\theta_p}, \boldsymbol{\alpha_p}, \boldsymbol{f_p}, \boldsymbol{\xi_p}\right]$;

3) Since the oscillation mode of the wind turbine is related to the threshold power P_{cp}, the cluster number k of spectral clustering is set to 2;

4) Perform spectral clustering on the feature matrices of the two clusters separately and output the final clustering results.

IV. Parameter Aggregation and Equivalence Evaluation Indicators

After obtaining the clustering results of the VSG WF using the clustering criterion described earlier, it is necessary to aggregate the parameters of the equivalent PMSG-VSGs and quantify the accuracy of the equivalent model.

A. Parameter Aggregation of VSG WF

This paper aggregates the generator, shaft system model, transformer, and VSG control parameters of the PMSG using the capacity weighting method; calculates the wind speed of the equivalent PMSGs based on the power conservation principle of the wind turbine cluster before and after equivalence and the MPPT curve; and performs equivalent calculation of the collection network impedance following the principle of constant injected current. The specific implementation method is available in Reference [2], and is not elaborated herein due to space constraints.

B. Calculation Method for Equivalence Evaluation Indicators

To quantitatively compare the equivalence performance, the time-domain response error between the equivalent model and the detailed model is calculated using Equation (11):

$$\varepsilon_x = \frac{1}{n}\sum_{k=1}^{n}\left|\frac{x_{\text{pcc}}(k\Delta t)-\hat{x}_{\text{pcc}}(k\Delta t)}{\hat{x}_{\text{pcc}}(k\Delta t)}\right|\times 100\% \quad (11)$$

where x is the type of evaluation indicator, including voltage, active power, and reactive power at the point of common coupling (PCC); n is the total number of sampling points; $x_{\text{pcc}}(k\Delta t)$ and $\hat{x}_{\text{pcc}}(k\Delta t)$ are the data from the equivalent model and the detailed model at time $k\Delta t$, respectively; and Δt is the sampling interval.

V. Case Study

To verify the effectiveness of the equivalent method, it is applied in a PMSG-based windfarm illustrated in Figure 5. The windfarm is consisted of 12 PMSGs with VSG interface.

The inertia time constant and damping coefficient are 4 s and 50 p.u., respectively. The capacity of the PMSG is 10 MW. The capacity and leakage inductance of the transformer are 12.5MW and 0.05 p.u., respectively. The collection grid impedance is 0.1153 + j0.396 Ω/km. The wind speed of the PMSGs is calculated with the Jensen wake model. The thrust coefficient is set to be 0.54 and the wake decay coefficient is 0.04. The wind speeds of G_{w1}, G_{w5} and G_{w9} are assumed to be 14, 13, and 12 m/s respectively. These PMSGs are spaced 3 km apart, while the distances between the other PMSGs are 1 km each. The turbine diameter is set to be 230 m.

The voltage source is assumed to undergo a sudden voltage drop to 0.5 p.u. at 0.1 s, and the fault duration is 0.2 s. The simulation time step is set to 2 μs. Simulations and analysis are constructed with Matlab R2019b/Simulink software.

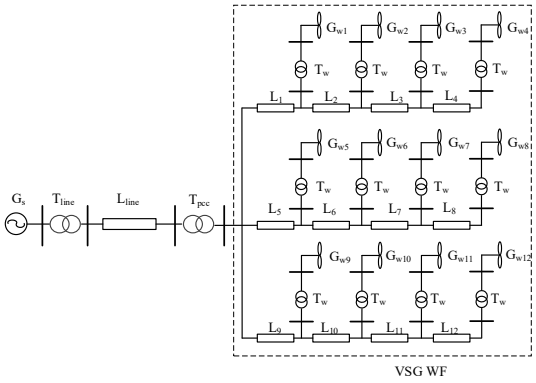


Fig. 5. Case Study System of VSG WF Station

Based on the equivalent method in this paper, the wind farm illustrated in Figure 5 is divided into 4 groups, where the equivalent wind speeds are 10.98 m/s, 11 m/s, 8 m/s, and 9.15 m/s respectively, and the equivalent line lengths are 5.89 km, 1.97 km, 9.97 km, and 7.01 km. As shown in Figure 6, all curves exhibit high precision during the whole dynamic process.

With the detailed model, simulating a 3-second dynamic process requires 994.41 s, whereas simulation using the equivalent model takes only 78.42 s. It is evident therefrom that the equivalent model can effectively simplify the system and significantly enhance the computational speed.

To verify the effectiveness of the proposed equivalent method for VSG WF, a comparison is conducted with two other equivalent methods:

1) Method A: ignores differences in wind turbine oscillation modes, only considers active power characteristics during faults, and divides the WF into 2 clusters for equivalence;

2) Method B: ignores differences in active power dynamics of wind turbines during faults, and only clusters all units using the spectral clustering algorithm based on Prony feature extraction.

Simulations are conducted using both the detailed model and the equivalent model. The comparison of dynamic response curves of active power, reactive power, and voltage at the PCC throughout the whole fault process across different equivalent methods is presented in Figure 6.

The time-domain response errors of the equivalent model computed using Equation (11) are presented in Table 1. To better characterize the accuracy of the equivalent model throughout the whole fault process, ε_{P1}, ε_{Q1}, ε_{V1} denote the relative errors of active power, reactive power, and voltage during the fault, respectively, whereas ε_{P2}, ε_{Q2} and ε_{V2} represent the response errors after fault clearance.

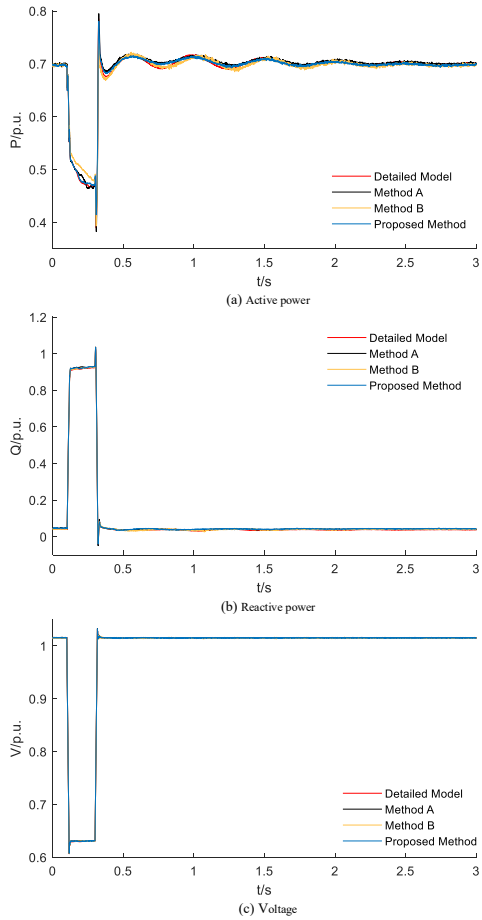


Fig. 6. Comparison of Response Characteristics of Different Clustering Equivalent Methods

As indicated by the results in the figure and table, the proposed method in this paper, which is based on the dynamic characteristics of the whole fault process, achieves higher comprehensive equivalence accuracy than equivalent methods considering only a single fault stage.

TABLE I. EQUIVALENCING ACCURACY OF VARIOUS EQUIVALENT METHODS

Equivalent Method	ε_{P1} /%	ε_{P2} /%	ε_{Q1} /%	ε_{Q2} /%	ε_{V1} /%	ε_{V2} /%
Method A	0.85	0.45	0.90	8.22	0.11	0.04
Method B	3.49	0.50	0.42	7.03	0.09	0.04
Proposed Method	0.46	0.38	0.74	12.14	0.09	0.04

It should be noted that after fault clearance, due to fault judgment and sampling delay, there is a certain error between the internal voltage compensation value and the pre-fault steady-state value, resulting in a relatively large reactive power deviation owing to the large number of clustered units. However, as indicated by the time-domain waveforms after fault clearance in Figure 6(b), the response curves before and after equivalence are almost completely consistent, with an extremely small absolute deviation, thus meeting the equivalence accuracy requirements.

Specifically, compared with other methods, Method A exhibits lower accuracy in reactive power and voltage; Method B ignores characteristic differences during the fault period, leading to larger active power errors during faults. In conclusion, the proposed method in this paper considers both active power characteristics during faults and oscillation modes of wind turbines after fault clearance, thus achieving superior equivalence accuracy.

VI. CONCLUSION

This paper investigates the equivalence of VSG WF based on the dynamics of the whole fault process, with key results as follows:(1) An improved LVRT control strategy for VSG-PMSG is proposed which enhanced the transient stability of the PMSG; (2) Based on the power angle curve of the PMSG after current-limiting action, the fault characteristics of the wind turbine were analyzed. (3) An equivalent method for VSG PMSG-based WF is proposed, considering the whole dynamic process. Simulation results demonstrate that the proposed method effectively improves the accuracy of the equivalent model and simulation efficiency. The method can be applied not only to transient stability and voltage stability analysis during faults or in the hundreds of milliseconds post-fault but also to electromechanical transient analysis, exhibiting favorable applicability.

ACKNOWLEDGMENT

This work is supported by the China Huaneng Group Co., Ltd. Headquarters Science and Technology Project (No. HNKJ24-H68), “Research on Key Technologies for Safe and Stable Operation of Grid-connected Offshore Wind Farms”.

REFERENCES

[1] Huang L, Wu C, Zhou D, Chen L, Pagnani D, and Blaabjerg F, “Challenges and potential solutions of grid-forming converters applied to wind power generation system—An overview,” Frontiers in Energy Research, vol. 11, 2023.

[2] ZHOU Haiqiang, CUI Xiaodan, XU Jianbing, CAO Boyuan, GAO Chao, and CHEN Zhihao, “Equivalent Method of DFIG-based Wind Farm Considering Low-voltage Ride Through and Dynamics of Whole Fault Process,” Automation of Electric Power Systems, vol. 48, no. 6, pp. 216-22, 2024.

[3] Li D, Shen C, Liu Y, Chen Y, and Huang S, “A dynamic equivalent method for PMSG-WTG based wind farms considering wind speeds and fault severities,” IEEE Transactions on Power Systems, vol. 39, no. 2, pp. 3738-3751, 2023.

[4] LIU Ziwen, CAO Boyuan, CUI Xiaodan, ZHOU Haiqiang, WANG Yi, and XU Jianbing, “Clustering equivalence method for direct-drive wind farms based on dynamic similarity of equivalent potentials,” Electric Power Automation Equipment, vol. 44, no. 11, pp. 79-87, 2024.

[5] LI Chengyu, Xu Jianzhong, Zhao Chengyong, and Li u Wei, “Coherency equivalence method for voltage source converter based on virtual synchronous generator,” Transactions of China Electrotechnical Society, vol. 31, no. 13, pp. 111-119, 2016.

[6] Li C, Xu J, and Zhao C, “A coherency-based equivalence method for MMC inverters using virtual synchronous generator control,” IEEE Transactions on Power Delivery, vol. 31, no. 3, pp. 1369-1378, 2015.

[7] Dai Pingjun, GONG Jinwu, PAN Shangzhi, and ZHA Xiaoming, “Equivalent Modeling Method of PV Cluster Converters Based on Grid-forming Control Strategy,” Journal of Electrical Engineering, vol. 1, no. 10, 2025.

[8] ZHU Yihua, LUO Chao, Yu Jiawei, WANG Yining, ZHANG Haobo, and XIANG Wang, “Grid-friendly control strategy of full power rated direct drive wind turbines,” Power System Protection and Control, vol. 52, no. 2, pp. 177-187, 2024.

[9] Li M, Shu S, Wang Y, Yu P, Liu Y, and Zhang Z, “Analysis and improvement of large-disturbance stability for grid-connected VSG based on output impedance optimization,” IEEE Transactions on Power Electronics, vol. 37, no. 8, pp. 9807-9826, 2022.

[10] DENG Zhenyan, WANG Han, ZHOU Shaoze, CAO Yunfeng, WANG Wei, and CAI Xu, “A transient control method for grid-forming direct-drive WTs based on DC voltage synchronization,” Automation of Electric Power Systems, vol. 49, no. 7, pp. 2-12, 2025.

[11] TU Chunming, YANG Wanli, XIAO Fan, GUO Qi, and HE Xi, “Transient power angle stability control method of VSG considering fault current limitation,” Electric Power Automation Equipment, vol. 43, no. 9, pp. 55-62+94, 2023.

[12] LENG Ruohan, ZHUANG Kehao, HOU Zhixian, HUANG Linbin, XIANG Xin, and XIN Huanhai, “Functional Positioning and Capacity Optimized Allocation of Grid-forming Converter Considering Low Voltage Ride Through of Grid-following New Energy Station,” Proceedings of the CSEE, vol. 1, no. 11, 2025.

[13] ZHANG Yu, ZHANG Chen, CAI Xu, YU Yongzheng, and LIANG Liliuyuan, “Current-constrained Transient Voltage Response Analysis and an Improved Fault-ride Through Control of the Virtual Synchronous Generator,” Proceedings of the CSEE, vol. 44, no. 15, pp. 5996-6010, 2024.

[14] ZHAN Changjiang, WU Heng, WANG Xiongfei, TIAN Jie, WANG Xinbao, and LU Yu, “An Overview of Stability Studies of Grid-forming Voltage Source Converters,” Proceedings of the CSEE, vol. 43, no. 6, pp. 2339-2359, 2023.

[15] LI Guangqi, Power System Transient Analysis, 3rd ed., China electric power press, 2006, pp. 206-207.

[16] LI Shangzhi, XU Taishan, LI Yingbiao, REN Xiancheng, BAO Yanhong, and ZHANG Jinlong, “Electromechanical scale modeling and dynamic stability analysis of grid connected full power wind turbine system,” J. Huazhong Univ. of Sci. & Tech. (Natural Science Edition), vol. 52, no. 7, pp. 12-21, 2024.

[17] WANG Xifan, Modern Power System Analysis, 1st ed., Science Press, 2003, pp. 388-389.

[18] LI Gaowang, ZHANG Zhi, LI Da, and CHEN Yanbo, “Coherency clustering method based on Prony analysis feature extraction,” Power System Protection and Control, vol. 48, no. 22, pp. 91-99, 2020.

Experimental Study on Thermal Management Control of Liquid Immersion Cooling Package Module for Vehicle EPS Motor Driving

Hojong Kwak, Jaehyuk An, Sewoong Ahn, Byeongyu Kim, Simon Cho, Hyoseo Choi, Jian Lee, and Young-Jae Min
Department of Electric and Electronic Engineering
Halla University
Wonju, Republic of Korea
youngjae.min@halla.ac.kr

***Abstract*—This paper introduces a thermal management control of the liquid immersion cooling package module for motor-driving power electronics of the automotive electric power steering (EPS). Based on torque and angle sensor (TAS) information, the pump control logic activates and pauses the flow for liquid immersion cooling. This thermal management control logic is implemented in the cooling package module of power electronics that drive three-phase EPS motors. System effectiveness is verified and confirmed via thermal performance experiments and in-vehicle evaluations of the assistance performance afforded by EPS.**

Keywords—liquid immersion cooling, package module, thermal management control, electric power steering

I. INTRODUCTION

Due to the advantage of driving convenience from reduced driver steering effort, electric power steering (EPS) is a critical component in vehicles. EPS offers smoothness, efficient handling, superior agility, stability, low-temperature resistance, and low power consumption compared with traditional hydraulic steering devices [1-3]. The performance and quality of the EPS device, which assists steering with the motor, are significant factors. In terms of customer experience and satisfaction, EPS is considered one of the most sensitive devices in a vehicle.

EPS reduces the driver steering effort using electric motors. Figure 1 shows that an EPS device consists of a steering wheel, a torque-angle sensor (TAS) that detects the driver steering intention by measuring torsion within the connected bar, an electronic control unit (ECU), a steering-assist motor, and various mechanical devices [4]. The ECU controls EPS status by driving the motor according to the TAS input. The motor is actuated by the ECU that contains power electronics including gate drivers and power transistors. The mechanical devices are a vertical column, a horizontal rack and pinion, and a reducer that connects the column and rack to amplify the driving force imparted by the motor and reduce the driving speed.

This paper presents a thermal management control system for the liquid immersion cooling package module of automotive EPS driven by electric power. This paper is organized as follows. Section II describes our liquid immersion cooling package module and its thermal management control logic, based on TAS information. The implementation and experimental evaluation results of the thermal management control logic with the cooling package module of the power electronics to drive the EPS motor are presented in Section III. Finally, the paper is concluded in Section IV.

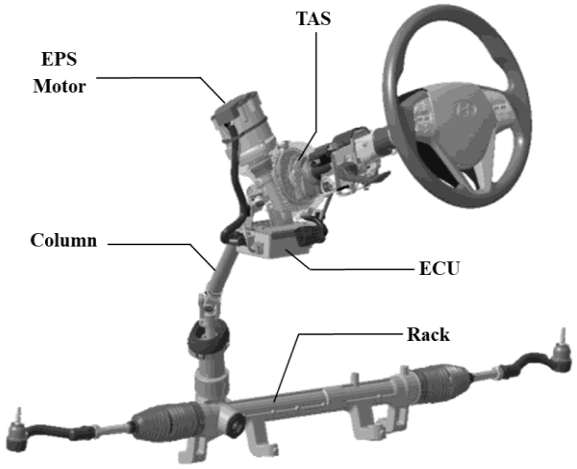


Fig. 1. Configuration of column-type EPS in this work.

II. THERMAL MANAGEMENT CONTROL FOR EPS

A. Liquid Immersion Cooling Package Module

EPS systems can be divided into column- and rack-types depending on the location of the motor. A rack-type EPS, where the motor directly delivers force to the rack, to assist steering, is more appropriate for large heavy vehicles than is a column-type EPS. This work evaluates a column-type EPS for small vehicles capable of responding to rack forces of less than 20kN, with the motor and ECU for motor control attached to the column. Commercial column-type EPS systems generally use a brushed DC motor or brushless AC motor according to the steering assistant power requirement of the steering motor [5, 6].

Figure 2 shows the power electronics configuration of our EPS ECU that drives a three-phase brushless AC motor. The

This work was supported by the Regional Innovation System & Education (RISE) program through the Gangwon RISE Center, funded by the Ministry of Education (MOE) and the Gangwon State(G.S.), Republic of Korea.(2025-RISE-10-008)

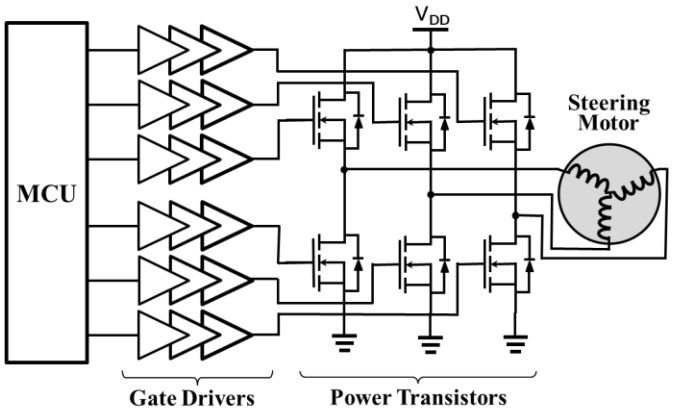


Fig. 2. Circuit diagram of EPS three-phase brushless motor-driving power electronics.

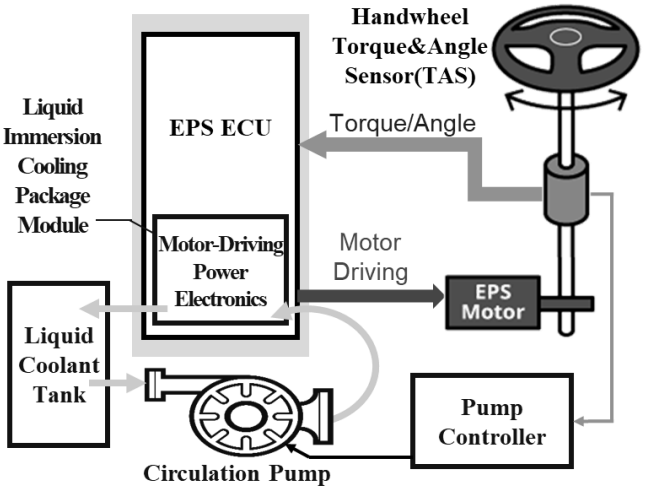
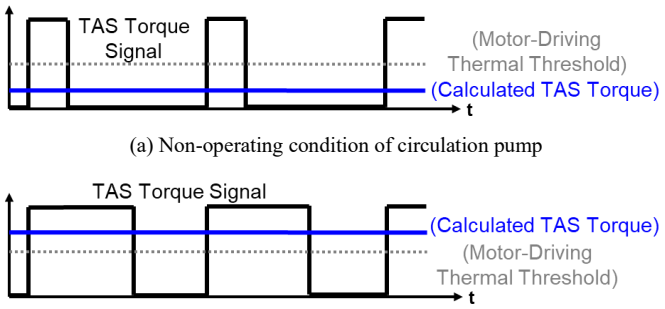


Fig. 3. Configuration of entire EPS liquid immersion cooling system with our immersion cooling package module.

gate driver controls and drives the motor-driving power transistors in response to input from the controller. Such power transistors, including gate drivers, require high electron mobility and critical electric field characteristics, resulting in high voltage operation and low resistance. Automotive power electronics devices must exhibit high thermal conductivity and the capacity to operate at elevated temperatures [7, 8].

Thermal management technology for automotive electronics, including EPS power electronics, typically comprises air cooling using heat sinks that exhibit high thermal conductivity. And, in order to improve the heat treatment characteristics, heatsinks with double-sided cooling and liquid cooling that indirectly cools power electronic components have been used [9, 10]. Direct cooling via liquid immersion has attracted considerable attention as an emerging thermal management technology for automotive, including batteries. Figure 3 shows our liquid immersion cooling system for the motor driving power electronics of an automotive EPS. The EPS liquid immersion cooling includes an immersion cooling package module, a liquid coolant tank, a circulation pump and its controller that uses the TAS signals as control inputs. The EPS



(a) Non-operating condition of circulation pump

(b) Operating condition of circulation pump

Fig. 4. Thermal management control logic of liquid immersion cooling with TAS information.

motor is driven based on the handwheel torsional torque information by the driver, which is the TAS output. Thermal management is performed by pumping coolant into the immersion cooling package module mounted on the motor-driving power electronics.

B. Thermal Management Control Logic

In EPS devices, the heat source is the motor drive power electronics, specifically the driving power transistors that directly supply current to the motor. Using torsional torque information from the TAS, the ECU delivers motor driving signals to the power electronics according to a predefined assistant torque map and a motor current lookup table. The motor driving signal is triggered when the TAS torque signal exceeds a certain threshold. This work eliminates the temperature sensor and the monitoring and control logic circuitry that increase the hardware cost and complexity.

When the motor driving signal serves as the input to the circulation pump that control liquid immersion cooling of the EPS motor-driving power electronics, additional wiring between the driving signal of the ECU and the circulation pump control logic is required. Our proposed thermal management control logic of the coolant circulation pump is based on TAS torsional torque information instead of the motor driving signal. The TAS torque information of this work is proportional to the pulse width of the TAS output signal. When the pulse width exceeds a certain threshold, the circulation pump is driven as shown in Fig. 4. In order to reduce pump driving power consumption when low levels of heat generation that do not require pump operation, the circulation pump is turned only when comparing the pulse width of the TAS output signal is slightly higher threshold compared to the motor driving signal. The threshold is experimentally set to the value when the motor temperature rises by at least 3 degrees.

III. Evaluation of Cooling Package Module

This section presents the implementation and experimental evaluation of the cooling package module for power electronics to drive the EPS motor. The experimental results include a comparison between the EPS device used in mass-produced vehicles and the EPS device of this work. While this work employs the liquid immersion cooling, the EPS device used in mass-produced vehicles employs air cooling using heat sinks with high thermal conductivity. In addition, we present in-

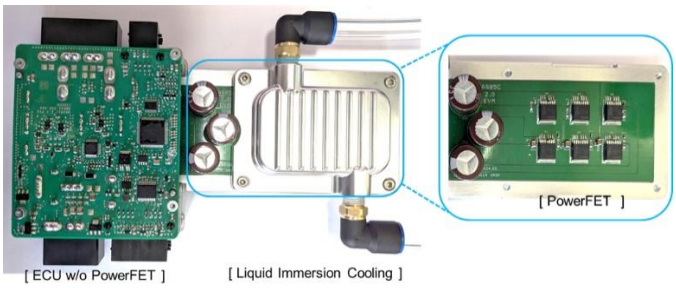


Fig. 5. Implementation of liquid immersion cooling package module for EPS motor driving.

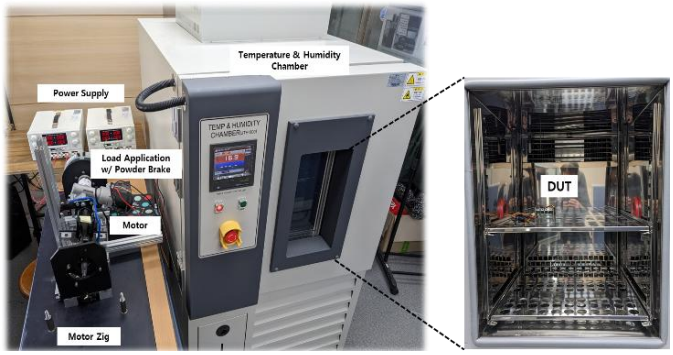


Fig. 6. Experimental setup for thermal performance evaluation.

vehicle validation of the EPS device with liquid immersion cooling package module including the proposed thermal management control logic.

A. Implementaion

In EPS devices, the gate driver and the motor-driving power transistors, which are the main components of motor-driving power electronics, require thermal management. In particular, the power transistors require relatively more careful thermal management because they directly supply current to the motor. Our liquid immersion cooling package in this work is implemented only for power transistors as shown in Fig. 5. The power electronics components in this work are identical to those of commercial products with power transistors mounted on a heat sink. Among power electronic devices, gate drivers, which generate less heat than power transistors, are excluded. Commercial power electronics for motor driving employ electrolytic capacitors as power decoupling storage elements, given their large capacitance and ease of implementation. However, due to the low humidity characteristic reliability of electrolytic capacitors, electrolytic decoupling power capacitors are placed outside the liquid-immersion cooling package. The cooling package includes coolant injection and outlet terminals, as well as internal structures optimized for heat transfer from the power transistors.

The internal coolant capacity of the cooling package is optimized at a ratio of 10:1 compared to the liquid coolant tank capacity. Since centrifugal liquid pumps are effective for transporting liquids due to their fast and quiet transport characteristics [11], this work employs a centrifugal pump for

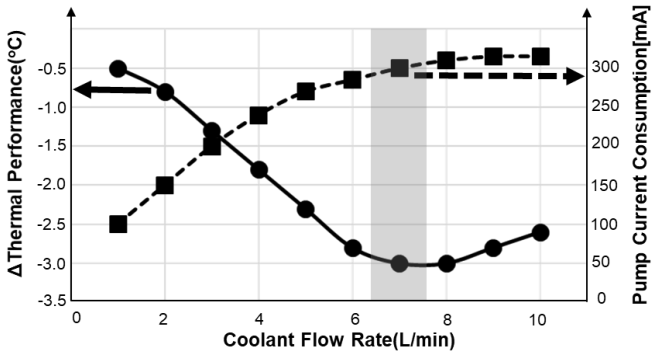
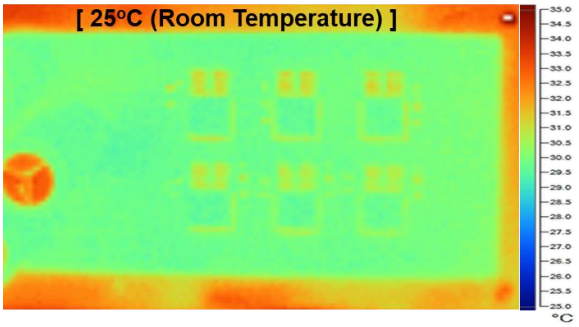
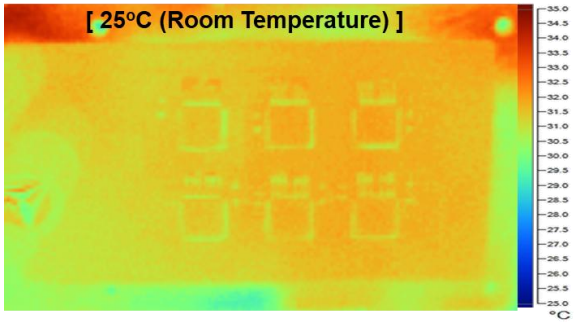


Fig. 7. Optimization for circulation pump operation with thermal management control logic.



(a)



(b)

Fig. 8. IR thermographic microscopy images at room temperature (a) with and (b) without liquid immersion cooling.

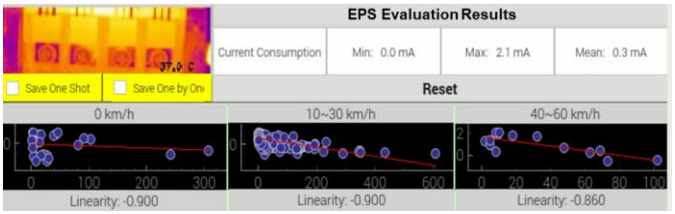
coolant circulation. The pump controller manages pump operation by applying a PWM signal according to the thermal management control logic based on TAS information.

B. Experimental Evaluation

Figure 6 shows the experimental environment to verify the improved thermal performance, including infrared (IR) thermography microscopy images acquired while driving an automotive EPS motor. The thermal performance evaluation experiments of EPS with the liquid immersion cooling package are conducted under room temperature conditions, and a powder brake is installed on the motor to apply a physical load for actual EPS motor operating conditions. Figure 7 shows the results of the optimization experiment on the coolant flow rate of the circulation pump operation using the thermal management



(a)



(b)

Fig. 9. (a) Installation of in-vehicle EPS evaluation system with liquid immersion cooling package module of this work and (b) evaluation results of steering assistance performance.

control logic. The coolant flow rate is optimized by comparing the thermal characteristics of the liquid immersion cooling package with the pump current consumption. Figure 8 demonstrates a thermal performance improvement of more than 3℃ at room temperature compared to commercial products using conventional heat sinks.

Our EPS device with the thermal design of a liquid immersion cooling is further evaluated using the in-vehicle EPS evaluation system for steering assistance performance of [3], which is installed in a KG mobility Tivoli sports utility vehicle (SUV) [12]. Figure 9(a) shows a photograph of the vehicle interior, where the evaluation system, consisting of the EPS data acquisition hardware module and the evaluation software with the EPS, is installed. An IR thermography microscopy camera is additionally installed in the in-vehicle EPS evaluation system to verify thermal characteristics and whether there is an increase in current consumption. Figure 9(b) shows the evaluation results of the steering assistance performance for this EPS device, confirming that it performs comparably to a mass-produced EPS device. Both EPS performance and quality are evaluated at three different speed ranges: 0 (stopped), 10-30 km/h, and 40-60 km/h. The EPS performance and quality for each vehicle speed range are plotted with the steering angles on the x-axis and the steering assistance torques on the y-axis.

IV. Conclusion

In this paper, we present a thermal management control of the liquid immersion cooling package module for automotive EPS motor drivers. The cooling package and control logic based on TAS information are verified via thermal performance experiments at room temperature and in-vehicle EPS evaluation of steering assistance performance. Prior to commercialization of the liquid immersion cooling package and controller of this work, additional thermal performance evaluations will be conducted over the temperature range of -40℃ to 150℃, as mandated by the AEC-Q100 automotive standard.

Acknowledgment

This work was supported by the Regional Innovation System & Education (RISE) program through the Gangwon RISE Center, funded by the Ministry of Education (MOE) and the Gangwon State(G.S.), Republic of Korea.(2025-RISE-10-008).

References

[1] D.-H. Choi *et al.*, “Design of a slotless structure for minimizing cogging torque and torque ripple in a column type EPS motor for vehicles,” *IEEE Transactions on Magnetics*, vol. 60, no. 9, pp. 1-5, Sep. 2024.

[2] K. Kea, Y. Han, and Y.-J. Min, “A federated learning approach for efficient anomaly detection in electric power steering systems,” *IEEE Access*, vol. 12, pp. 67525-67536, May 2024.

[3] E. Kim *et al.*, “Development of in-vehicle evaluation system for steering assistance performance of electric power steering,” in *Proc. IEEE International Conference on Humanoid, Nanotechnology, Information Technology, Communication and Control, Environment and Management*, pp. 1-5, 2023.

[4] HL Mando Corporation, www.hlmando.com.

[5] M. Miyamasu and K. Akatsu, “Efficiency comparison between brushless DC motor and brushless AC motor considering driving method and machine design,” *IEEJ Journal of Industry Applications*, vol. 2, no. 1, pp. 79-86, Feb. 2013.

[6] S. Derammelaere *et al.*, “A quantitative comparison between BLDC, PMSM, brushed DC and stepping motor technologies,” in *Proc. International Conference on Electrical Machines and Systems*, pp. 1-5, 2016.

[7] Y. Kim *et al.*, “Thermal performance improvement approach of GaN power electronic devices for automotive EPS motor drivers,” in *Proc. International Conference on Applied System Innovation*, pp. 329-331, 2024.

[8] E. Kim *et al.*, “Thermal design of GaN power devices in wafer level chip scale package (WLCSP) for automotive EPS motor drivers,” in *Proc. International Conference on Consumer Electrnics Asia*, pp. 676-679, 2024.

[9] Y. Yang *et al.*, “Automotive power module packaging: current status and future trends,” *IEEE Access*, vol. 8, pp. 160126-160144, Aug. 2020.

[10] J. Broughton, V. Smet, R. R. Tummala, and Y. K. Joshi, “Review of thermal packaging technologies for automotive power electronics for traction purposes,” *Journal of Electronic Packaging*, vol. 140, no. 4, pp. 1-11, Dec. 2018.

[11] J. F. Gulich, *Centrifugal Pumps*, New York: Springer, 2007.

[12] KG Mobility Corporation, www.kg-mobility.com

Research on the Temperature Field of Shaftless Rim-Driven Motor Based on a Three-Dimensional Integrated Water-Cooling Structure

Li Chen
School of Electrical Engineering and Automation, Nantong University
Nantong, China
2412320010@stmail.ntu.edu.cn

Jishuang Zhang
School of Electrical Engineering and Automation, Nantong University
Nantong, China
JishuangZhang@outlook.com

Tao Zhu
School of Electrical Engineering and Automation, Nantong University
Nantong, China
zt2849160247@126.com

Leyan Xu
School of Electrical Engineering and Automation, Nantong University
Nantong, China
1511715983@qq.com

Wei Zhang
School of Electrical Engineering and Automation, Nantong University
Nantong, China
zhang.w@ntu.edu.cn

***Abstract*—Stator-type axial permanent magnet synchronous motors (APMSMs) are highly suitable for marine propulsion because of their high power density, large output torque, high efficiency, and strong fault tolerance. However, the presence of a sheath introduces additional eddy current losses, and it alters the magnetic circuit characteristics of the motor, thereby affecting the distribution of losses in both the permanent magnets and the windings, as well as the heat dissipation efficiency of the stator. In this paper, a finite element model of the stator-type APMSM is firstly established by Ansys software. Subsequently, the effects of different sheath materials and thicknesses on the eddy current losses in the permanent magnets and sheaths are investigated. In addition, based on the loss distribution of APMSM, a three-dimensional integrated water-cooling heat dissipation structure is proposed. Its cooling performance is compared with that of series and spiral water-cooling structures. The results demonstrate that the three-dimensional integrated water-cooling heat dissipation structure exhibits superior thermal dissipation performance.**

Keywords—shaftless rim-driven propulsion motor, stator-type axial permanent magnet synchronous motor, eddy current loss, three-dimensional integrated, water-cooling structure

I. INTRODUCTION

The shaftless rim-driven thruster (RDT), a key advancement in integrated motor propulsion technology, has received extensive attention and research in recent years[1-2]. Compared with traditional shafted thrusters, which have problems such as large volume and weight, significant noise and vibration during operation, and lubricating oil leakage that pollutes the environment, RDT has gradually become a key component of modern marine technology equipment because of its high power density, compact structure, and high efficiency[3].

At present, the propulsion motors used in RDT are mainly of radial structure. Radial permanent magnet motors have a large radial dimension, and the permanent magnets are usually located on the rotor, which increases the difficulty of motor cooling. Compared with the radial structure, the stator-type axial permanent magnet synchronous motor (APMSM) has the advantages of short axial dimension, high power density, and high efficiency. To ensure reliability in marine environments, waterproof sheaths are added to the stator and rotor surfaces[4]. These sheaths cause additional eddy current losses on the sheaths due to the space-time harmonics generated during motor operation[5-6]. The additional eddy current losses not only increase the motor temperature but also impair heat dissipation, leading to reduced efficiency and potential motor damage. Furthermore, the presence of sheaths can alter the magnetic circuit characteristics of the motor, leading to an increase in magnetic resistance and affecting the distribution of losses within both the permanent magnets and the windings. Additionally, the sheath structure can impede the convective heat transfer on the stator surface, diminishing the concentrated cooling effect of the stator, which may lead to demagnetization of the permanent magnets due to overheating. Therefore, the effective cooling of the shaftless rim-driven motor (RDM) has become a technical challenge in its design. Currently, both domestic and international practices mainly adopt series-type, parallel-type[7], and adding baffles of different thicknesses and shapes in the channels[8] water cooling schemes. The series-type axial water cooling has uniform cooling, but the water channels are tortuous and have high flow resistance. The parallel-type water cooling has a simple manufacturing process, but if the design is not reasonable, it will reduce the motor cooling performance. Adding baffles of different thicknesses and shapes in the channels can enhance the turbulence intensity of the water flow, but it also increases the complexity of the cooling channel design. As a result, none of the aforementioned cooling schemes can fully satisfy the cooling demands of RDM.

This work was supported by National Natural Science Foundation of China (Grant Number: 52577060).

979-8-3315-5472-9/25/$31.00 ©2025 IEEE

In response to the above challenges, this paper proposes a three-dimensional integrated water-cooling heat dissipation structure. The three-dimensional integrated water-cooling structure comprises axial, radial, and circumferential cooling, thereby improving its heat dissipation efficiency. By comparing the cooling efficiency of series and spiral water-cooling with that of the three-dimensional integrated water-cooling, the effectiveness of the three-dimensional integrated water-cooling heat dissipation structure is verified.

II. Shaftless Rim-Driven Motor Topology

As shown in Fig. 1, the topology of RDM consists of two outer stators with the same shape and a central inner rotor. Each stator is composed of six permanent magnets, six armature windings, and six E-shaped magnetic cores. The adjacent E-shaped cores are embedded with permanent magnets that have opposite magnetization directions. The armature windings are wound around the stator teeth of the adjacent E-shaped cores. A protective sheath is added to the outer surface of both the stator and the rotor, with seawater located between the adjacent sheaths.

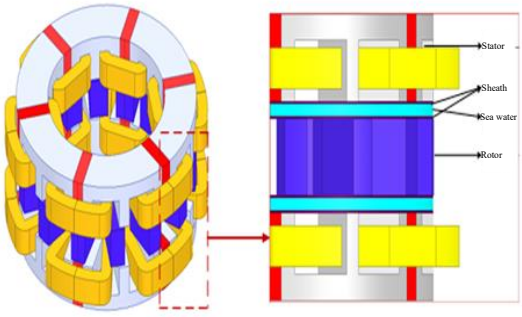


Fig. 1. Motor-Medium-Sheath Model.

III. The Influence of Sheath Parameters on Eddy Current Losses

The protective sheath of RDM is typically made of non-magnetic metals or carbon fiber. The thickness of the sheath must be carefully determined, taking into account both the waterproof performance and the electromagnetic characteristics of RDM. If the sheath is too thin, its corrosion resistance may be insufficient, making it difficult to effectively prevent seawater ingress, which can negatively impact the stability and reliability of RDM. Conversely, if the sheath is too thick, it may increase the air gap length, reduce the air gap flux density, and thereby affect the output torque and efficiency[9]. In order to comprehensively considering the waterproof performance and electromagnetic characteristics, the influence of sheath on the eddy loss is researched under the condition of the three different sheath materials with the thickness of sheath varying from 0.5 mm to 1.5 mm. The three different sheath materials include the carbon fiber, titanium alloy, and stainless steel. Fig. 2 shows the influence of sheath on eddy current loss when the RDM operates at 1000 rpm and with the rated current of 4 A.

The results show that adding a waterproof protective sheath increases the eddy current loss. When the thickness of the protective sheath is the same, the eddy current loss of the permanent magnet is the highest when the carbon fiber is used, while the eddy current loss of the sheath itself is the lowest. As a result, the total eddy current loss is also the smallest. The total eddy current loss is 2.52 W when the waterproof protective sheath uses the material of the carbon fiber, which is significantly lower than the values of 13.64 W and 25.13 W employed by titanium alloy and stainless steel, respectively. Within a certain thickness range, the eddy current loss generated by the three materials is enlarged with the increase of the sheath thickness. For the carbon fiber sheath, the total eddy current loss increases from 2.52 W at 0.5 mm to 3.76 W at 1 mm, and further to 4.99 W at 1.5 mm. Therefore, the 0.5 mm carbon fiber sheath is selected for further research.

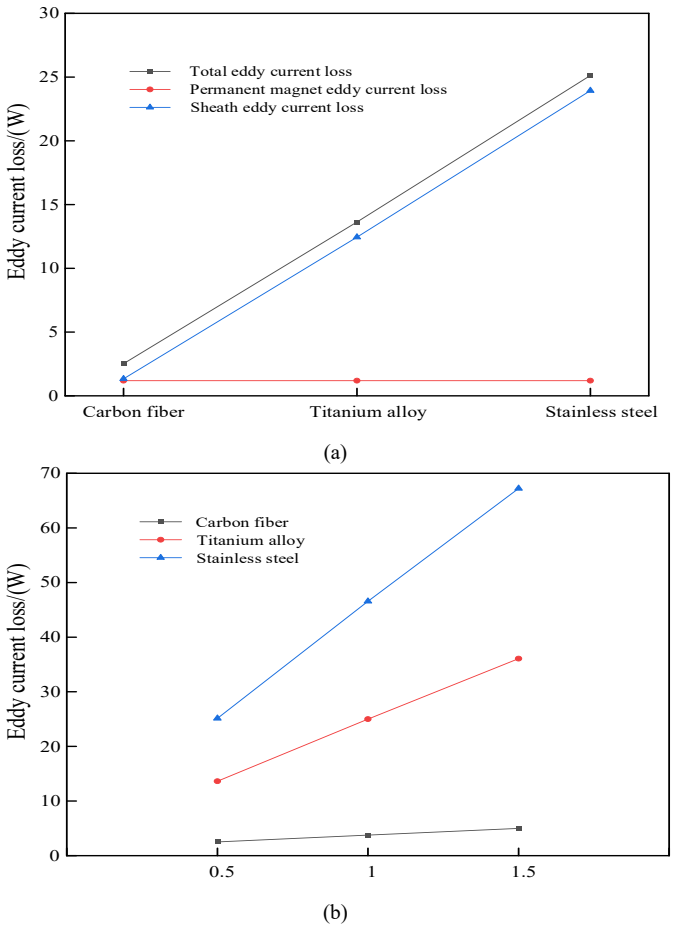


Fig. 2. The influence of sheath on eddy current loss. (a) Different material of sheath. (b) Different thickness of sheath.

IV. Research on the Heat Dissipation Performance of Three-Dimensional Integrated Stator End Cover

After comprehensively considering the heat source distribution of the permanent magnet, winding, and core, the three-dimensional integrated water-cooling and heat dissipation structure is proposed, as shown in Fig. 3.

Figure 3(a) illustrates the upper stator end cover. The upper surface of the upper stator end cover is equipped with two cold water inlets. Spiral channels are distributed along the outer circumference, and the bottom of these channels has two outlets. Figure 3(b) shows the lower stator end cover. The inlet of the lower end cover corresponds to the outlet of the upper end cover.

Two outlets are present on the surface of the lower stator end cover. Figure 3(c) presents the water-cooling flow path of the upper stator end cover. After entering through the inlets of the upper stator end cover, the cooling water first flows along the spiral channels to provide axial cooling to the stator cover and then outflow through the outlet of the upper end cover and enters the inlet of the lower end cover. The water continues to flow through the series-type cooling system, providing both radial and circumferential heat dissipation to the stator cover, and finally outflows through the two outlets on the lower cover. This structure achieves three-dimensional integrated water-cooling and heat dissipation for the stator end cover by coordinating axial, radial, and circumferential cooling.

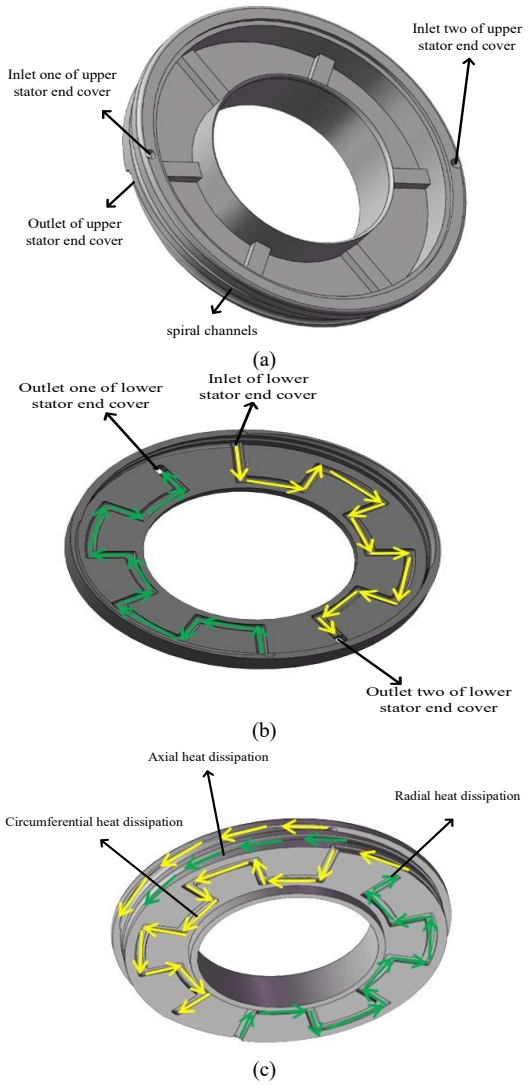


Fig. 3. Three-dimensional integrated water-cooling structure. (a) Inlets of upper stator end cover. (b) Outlets of lower stator end cover. (c) Cooling-water flow path of upper stator end cover.

The total loss of the motor is composed of iron loss, winding copper loss, and eddy current loss in the permanent magnet and the sheath. By obtaining the losses of each component of the RDM through a finite element simulation model and substituting them into (1) and (2), the heat flux on the stator end cover can be approximately calculated.

$$P_{\text{loss}} = P_{Fe} + P_{Cu} + P_{\text{pm}} \tag{1}$$

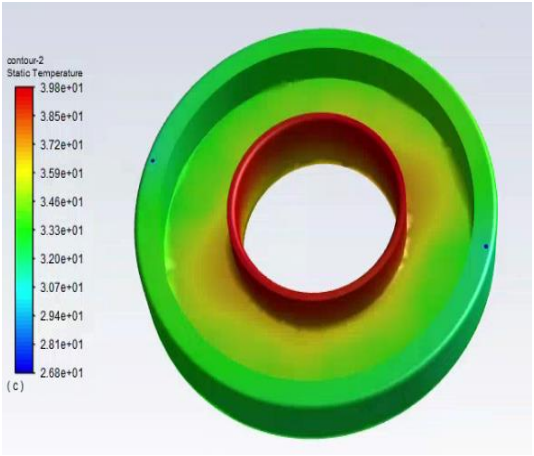
where P_{loss} is the total loss, P_{Fe} is the iron loss, P_{Cu} is the winding copper loss, and P_{pm} is the eddy current loss of the permanent magnet and the sheath.

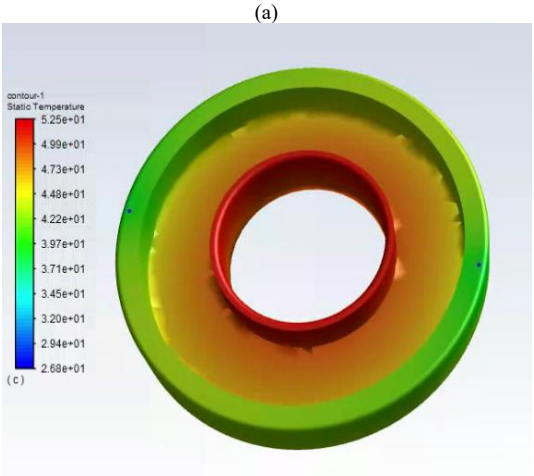
$$q = \frac{P_{\text{loss}}}{A} \tag{2}$$

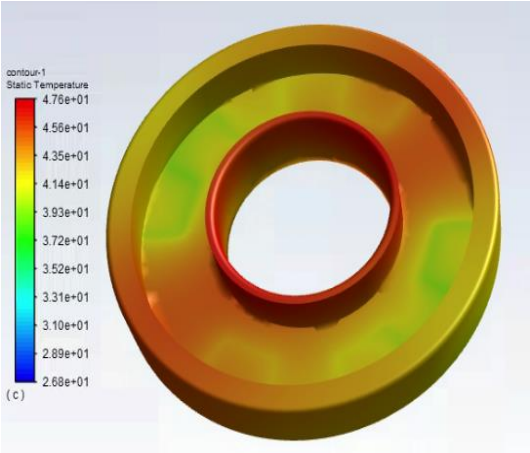
where A is the effective cooling area.

Based on the same heat flux, the temperature distributions of the stator end cover by using the three different cooling configurations are investigated and analyzed, including the series-type water-cooling, the spiral-type water-cooling, and three-dimensional integrated water-cooling.

Fig. 4 shows that when the three-dimensional integrated water-cooling and heat dissipation structure is used, the maximum temperature of the stator end cover reaches 39.8℃. When the series-type water cooling is employed, the maximum temperature rises to 47.6℃. When spiral-type axial water cooling is used, the maximum temperature is the highest, reaching 52.5℃. These results indicate that the three-dimensional integrated water cooling and heat dissipation structure provides the most effective heat dissipation performance.







(c)

Fig. 4. Temperature field distribution of different cooling structures. (a) Three-dimensional Integrated water-cooling structure. (b) Spiral axial water-cooling structure. (c) Series water-cooling structure with stator end cover.

V. Conclusion

This paper proposes a three-dimensional integrated water-cooling heat dissipation structure for stator-type APMSM and investigates the influence of different sheath materials and sheath thicknesses on eddy current losses. The results demonstrate that carbon fiber significantly reduces the total eddy current loss compared to titanium alloy and stainless steel. Furthermore, the proposed design enables coordinated cooling along the axial, radial, and circumferential directions, resulting in the reduction in the stator end cover temperature. These improvements contribute to enhancing the operational reliability and thermal stability of the RDM.

References

[1] F. Bai, J. Chen, Y. Xu, C. Zhang, Y. Gong and Q. Feng, “Fluid-thermal coupling study of shaftless rim-driven thruster, ” SHIP ENGINEERING, vol. 45, no. 9, pp. 61-69+78, 2023.

[2] J. Hu, J. Wu and Y. Tu, “Research of shaftless rim-driven propeller, ” Digital Ocean & Underwater Warfare, vol. 3, no. 3, pp. 185-191, 2020.

[3] B. Liu, X. Yan, W. Ouyang, J. Lan and X. Liang, "Research on regular pattern of gap flow in shaftless rim-driven thruster," 2017 4th International Conference on Transportation Information and Safety (ICTIS), Banff, AB, Canada, 2017, pp. 134-138.

[4] Y. Wang, Y. Sun, G. Wan, W. Ouyang, X. Zhou and J. Huang, “Risk assessment of motor sheath material with shaftless rim-driven thruster,” 2023 7th International Conference on Transportation Information and Safety (ICTIS), Xi'an, China, pp. 1394-1402, 2023.

[5] Y. Hu, S. Zhu and Y. Ge, “Study on rotor eddy current losses in high-speed permanent magnet motor for aircraft applications,” 2021 24th International Conference on Electrical Machines and Systems (ICEMS), Gyeongju, Korea, Republic of, pp. 1095-1100, 2021.

[6] J. Zhang, W. Zhang, J. Zhao and Z. Tai, “Accurate calculation of iron loss based on frequency division and piecewise variable coefficient for magnetic field modulation permanent magnet machine,” 2023 26th International Conference on Electrical Machines and Systems (ICEMS), Zhuhai, China, pp. 1575-1580, 2023.

[7] M. Lin, W. Le, K. Lin, L. Jia, S. Wang, A. Yang and Y. Tu, “Overview on research and development of thermal design methods of axial flux permanent magnet machines, ” Proceedings of the CSEE, vol. 41, no. 6, pp. 1914-1929, 2021.

[8] M. Sun, R. Tang, X. Han and W. Tong, “Temperature field analysis of a high frequency amorphous alloy axial flux permanent magnet machine with different cooling schemes,” Electric Machines and Control, vol. 22, no. 2, pp. 1-8+23, 2018.

[9] T. Huang, Y. Ou, Q. Zhang, Z. Yang and B. Zu, “Modeling and simulation of rim-driven thruster permanent magnet motor-sheath-dielectric system,” SHIP ENGINEERING, vol. 46, no. 9, pp. 17-23+55, 2024.

High-Resolution FBG Interrogation Using Microwave Photonics for Real-Time Temperature Monitoring of Power Equipment

Minhao HU
State Grid Zibo Power Supply Company
sgcc_huminhao@163.com

Xuecheng KONG
State Grid Zibo Power Supply Company
734200117@qq.com

Fei LI
State Grid Zibo Power Supply Company
stategrid888@163.com

Weichen YAN*
College of Intelligent Manufacturing
Zibo Polytechnic University
ywc859955132@126.com

***Abstract*—Overheating faults represent a prevalent and hazardous failure mode in substation power equipment. Online monitoring methods offer distinct advantages by enabling real-time detection without requiring power interruption. To detect rapid temperature changes within a short time frame, this study proposes a high-resolution fiber Bragg sensor (FBS) temperature monitoring method based on microwave photonics, demonstrating its effectiveness through experimental validation. Online temperature monitoring system based on proposed method is designed and applied in field measurement and operation. Measurement results indicate a sensitivity of ~36 MHz/με, confirming the proposed FBS-based approach as an effective solution for real-time thermal monitoring. Online temperature monitoring system based on proposed method has been put into practice by State Grid Zibo Power Supply Company.**

Keywords—DPS-FBG, Microwave Photonics, Real-Time Temperature Monitoring, OEO loop

I. INTROUCTION

Overheating faults in substation equipment represent a prevalent and hazardous failure mode in power systems [1, 2]. In substations, electrical equipment such as high/low-voltage switchgear [3], power transformers [4], and power capacitors [5] generate significant heat due to high voltage and current conditions. Temperature monitoring of these critical assets enables timely warnings and helps mitigate or prevent such failures.

Temperature monitoring methods can be classified into offline approaches [6-9] and online approaches [10-14]. Offline methods require power interruption and exhibit time-delay characteristics, whereas online methods enable real-time monitoring without service disruption. Online monitoring techniques primarily include: (1) visual methods (e.g., YOLO approaches, infrared imaging techniques), and (2) optical fiber sensor methods. Fiber-optic sensor technologies have evolved significantly from the WTS-11 temperature monitoring system developed by Luxtron to contemporary fiber Bragg grating (FBG) temperature monitoring systems [15]. This technological advancement has led to substantial cost reduction while maintaining measurement accuracy, resulting in widespread adoption across power industry applications.

Funding Project:
Group Innovation Fund of Zibo Power Supply Company, State Grid Shandong Electric Power Company (2022Q2)

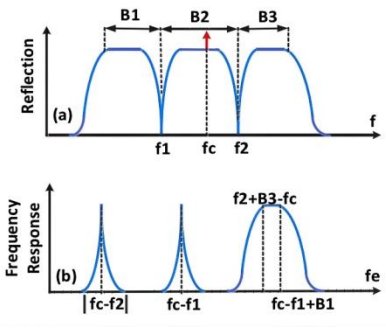
The hotspot temperature of power transformers can rapidly rise to the maximum allowable level, potentially leading to insulation degradation or hazardous conditions. Therefore, temperature monitoring methods must exhibit high sensitivity to promptly detect such temperature increases.

This study proposes a high-resolution FBG interrogation method based on microwave photonics for real-time temperature monitoring of power equipment. The online temperature monitoring system is designed and applied in field measurement and operation. The sensitivity of the proposed approach was experimentally characterized, with results validating its effectiveness.

II. OEO-BASED FBG INTERROGATION

A. Methodology

The dual-phase-shifted fiber Bragg grating (DPS-FBG) used in this study contains two phase shifts, producing two narrow transmission peaks at distinct wavelengths in its reflection spectrum in Fig. 1(a). When Eq. (1) is satisfied, this configuration yields the microwave photonic filter response shown in Fig. 1(b).



(a) Reflection spectrum of a DPS-FBG
(b) Dual-pass-band microwave response based on the PSFBG
Fig. 1. Photonic Filter Power Spectrum

$$\begin{cases} \dfrac{f_1+f_2}{2} < f_c < \dfrac{f_1+f_2+f_s}{2} \\ B_3 \le B_1 \end{cases} \tag{1}$$

Where, f_c is carrier frequency emitted by the tunable laser, Hz; f_1 and f_2 is the central frequencies of the two transmission peaks

in the DPS-FBG, Hz. B_1 and B_3 is bandwidths on either side of the DPS-FBG.

B. Test Configuration

The tunable laser source (TLS) passes through a polarization controller (PC) into a phase modulator (PM). The phase-modulated signal enters an optical circulator (Cir) and is reflected by a phase-shifted fiber Bragg grating (PS-FBG). After amplification via an erbium-doped fiber amplifier (EDFA), the signal is detected by a photo-detector (PD). The PD's output electrical signal is further amplified by a power amplifier (PA) and fed back to the PM, forming a closed-loop optoelectronic oscillator (OEO).

The generated microwave signal can be observed using an electrical spectrum analyzer (ESA) or processed digitally. Crucially, the components within the dashed box in Fig. 2 constitute a dual-pass-band microwave photonic filter. The PS-FBG selectively filters one sideband from the phase-modulated double-sideband signal via its reflection spectrum's transmission peak, converting phase modulation to intensity modulation. Test configuration is shown in Fig. 2.

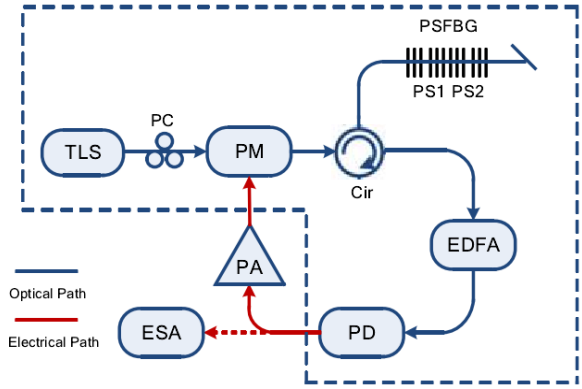
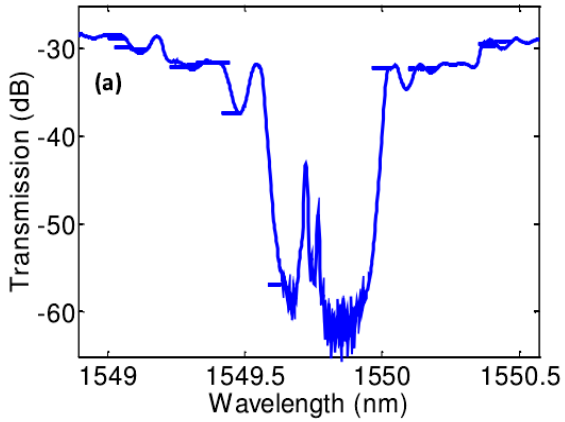


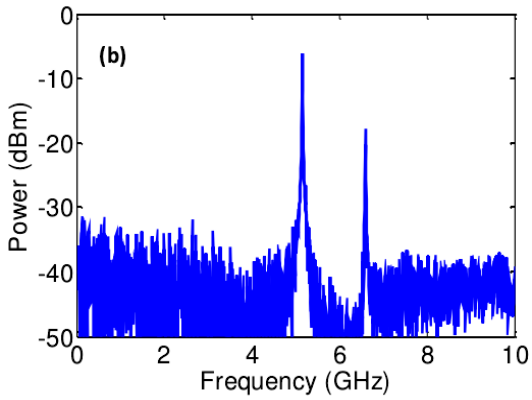
Fig. 2. Test Configuration

III. Results and Analysis

The measured transmission spectrum of the DPS-FBG used in the experiment is shown in Fig. 3(a). The spectral response of the microwave photonic filter is illustrated in Fig. 3(b).



(a) Measured transmission spectrum of the DPS-FBG



(b) spetrum of mivrowave phototnic filter

Fig. 3. Test results of transmission spectrum of the DPS-FBG

After closing the OEO loop, the spectrum obtained from the electrical spectrum analyzer is shown in Fig. 4. Two microwave signals are generated at the central frequencies corresponding to the two pass-bands, while a difference-frequency signal (i.e., the signal to be detected) is observed at approximately 2.4 GHz, as indicated within the black dashed ellipse.

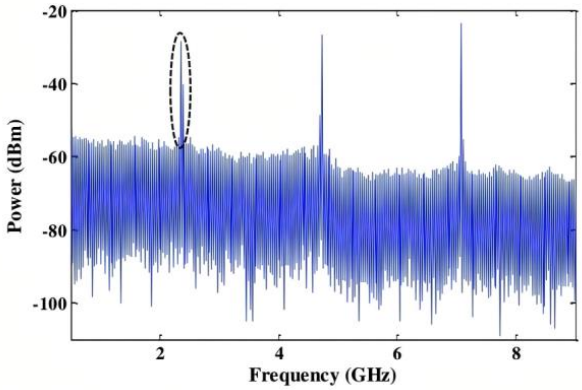


Fig. 4. The microwave signal produced upon OEO loop closure

Furthermore, the variation in the microwave spectrum generated by OEO was experimentally verified under external stress applied at the single phase-shift position of a DPS-FBG. The measurement results are presented in Fig.5.

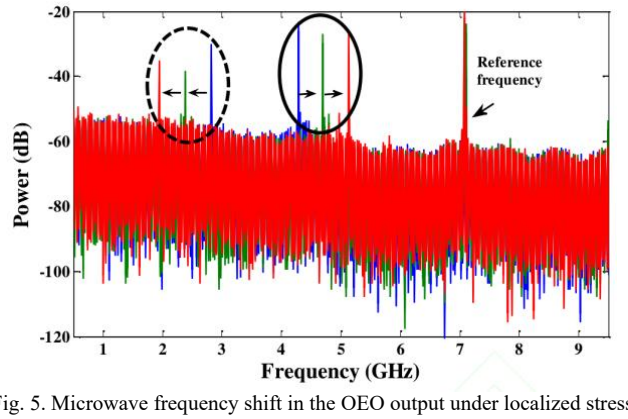


Fig. 5. Microwave frequency shift in the OEO output under localized stress application at a single phase-shift position

When the ambient temperature varies, both microwave frequencies shift equally, leaving the difference-frequency signal unaffected. Measured relationship between the difference-frequency signal and the applied stress is shown in Fig.6.

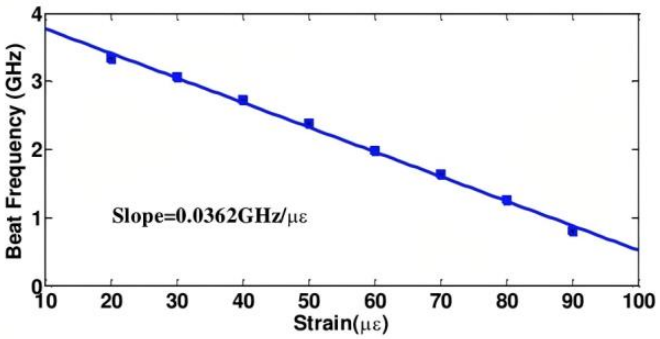
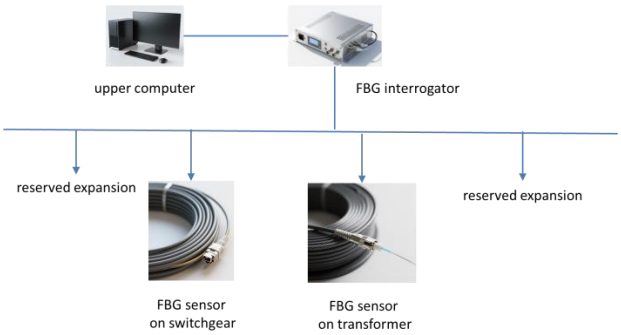


Fig. 6. Test results of transmission spectrum of the DPS-FBG

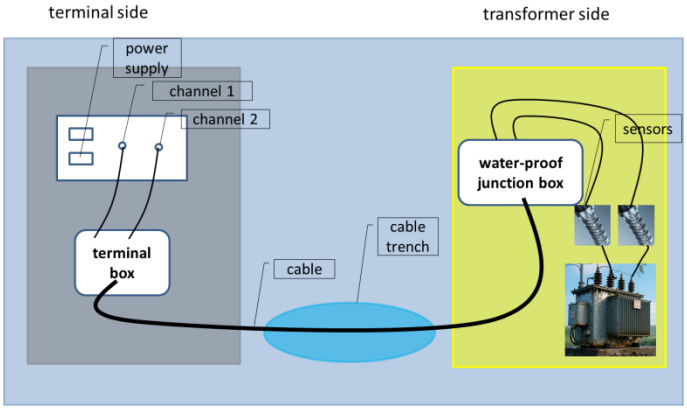
It can be concluded that, the difference-frequency exhibits a linear decreasing trend as the applied stress increases. The fitting results demonstrate a sensing sensitivity of approximately ~36 MHz/$\mu\varepsilon$ for the system.

IV. Temperature Monitoring System Design Based on Proposed Method

The online temperature monitoring system based on proposed method has been in functional operation in substation by State Grid Zibo Power Supply Company. Yet, no operational data from the actual functioning temperature monitoring system could be obtained; only its design principles and structural sketch have been disclosed. This project elaborates on the detailed design of both the software functional architecture and hardware device configuration. A database management system is implemented to manage equipment information, temperature data, and maintenance records in a structured manner, enabling users to conveniently access historical records and update maintenance logs. Through clicking on devices within the single-line diagram, the software system provides access to a historical monitoring mode. This mode visualizes temperature trends of switchgears and transformers, while also allowing arbitrary selection of time points for detailed observation of temperature variations. A schematic diagram of the temperature monitoring system based on the proposed method is presented in Fig. 7.



a) Monitoring system structure sketch



b) Monitoring system sketch

Fig. 7. Temperature monitoring system based on proposed method

The online temperature monitoring system in operation has the following functions:

(1)Temperature measurement for transformers and switchgears: Real-time monitoring and recording of internal temperature trends in transformers and switchgears, with capabilities for temperature data query and over-limit alarm.

(2)Overload warning: Based on temperature variations, the system shall employ mathematical models to predict the duration of overload operation and the allowable time under 1.5 times load, among other parameters.

(3)Data management: The system shall provide convenient data export functionality to support data sharing and analysis across different platforms.

(4)System maintenance: To facilitate user remote control of the online temperature monitoring and warning system for transformers and switchgears, the system shall support operations including configuring device parameters, time synchronization, clearing SD card data, restarting the controller, and initializing the controller.

V. Conclusion

We propose a novel interrogation method by integrating a DPS-FBG into an OEO loop. A new microwave frequency detection scheme based on the OEO is designed, achieving a measured sensitivity of ~36 MHz/$\mu\varepsilon$.

The detected microwave frequency is immune to temperature variations and carrier jitter, effectively eliminating cross-sensitivity issues inherent in conventional measurements.

The proposed temperature monitoring method has been used in field measurement by State Grid Zibo Power Supply Company.

References

[1] Sambhi, Shilpa. "Thermal imaging technology for predictive maintenance of electrical installation in manufacturing plant—a literature review." 2nd IEEE International Conference on Power Electronics, Intelligent Control and Energy Systems (ICPEICES-2018). 2018.

[2] Ali, Ziad M., et al. "Complexities of power quality and harmonic-induced overheating in modern power grids studies: Challenges and solutions." IEEE Access (2024).

[3] Wang, Xiaorui, et al. "Research on temperature rise of high current switchgear in distribution system." The Journal of Engineering 2019.16 (2019): 2931-2934.

[4] Kumbhar, Ganesh B., Satish M. Mahajan, and Walter L. Collett. "Reduction of loss and local overheating in the tank of a current transformer." IEEE transactions on power delivery 25.4 (2010): 2519-2525.

[5] Dan‐yi, Chi, et al. "The analysis of overheat failure for 220 kV voltage transformer with live detection." The Journal of Engineering 2019.16 (2019): 2058-2059.

[6] Ismail, Firas B., et al. "An offline and online approach to the OLTC condition monitoring: A review." Energies 15.17 (2022): 6435.

[7] Andrews, Leo John Baptist, and Linesh Raja. "Remote based patient monitoring system using wearable sensors through online and offline mode for android based mobile platforms." 2017 International Conference on Infocom Technologies and Unmanned Systems (Trends and Future Directions)(ICTUS). IEEE, 2017.

[8] Li, Xin, et al. "On-line temperature estimation for noisy thermal sensors using a smoothing filter-based Kalman predictor." Sensors 18.2 (2018): 433.

[9] Aradi, Petra. "Offline and online thermostat experiment with LabVIEW and Arduino." 2016 International Symposium on Small-scale Intelligent Manufacturing Systems (SIMS). IEEE, 2016.

[10] Biçen, Yunus, and Faruk Aras. "Smart asset management system for power transformers coupled with online and offline monitoring technologies." Engineering Failure Analysis 154 (2023): 107674.

[11] Wang, Jianguo, et al. "Online monitoring of electrical equipment condition based on infrared image temperature data visualization." IEEJ Transactions on Electrical and Electronic Engineering 17.4 (2022): 583-591.

[12] Albla, Alaulddin AH, et al. "Online temperature monitoring of a grid connected induction motor." International journal of electrical power & energy systems 93 (2017): 276-282.

[13] Hey, Jonathan, et al. "Online monitoring of electromagnetic losses in an electric motor indirectly through temperature measurement." IEEE Transactions on Energy Conversion 31.4 (2016): 1347-1355.

[14] Usamentiaga, Ruben, et al. "Temperature monitoring for electrical substations using infrared thermography: architecture for Industrial Internet of Things." IEEE transactions on industrial informatics 14.12 (2018): 5667-5677.

[15] Mannik, L. "EPRI workshop: Optical sensing in utility applications." (1991).

Development of a B-type Leakage Current Sensor for Wide Range Accurate Detection

Yi Wei
China Southern Power Grid Technology Co.,Ltd. Guangdong Provincial Key Laboratory of New Technology for Smart Grid
Guangzhou, China
1943704210@qq.com

Jian Zhibo
China Southern Power Grid Technology Co.,Ltd. Guangdong Provincial Key Laboratory of New Technology for Smart Grid
Guangzhou, China
353741014@163.com

Liang Guobang
China Southern Power Grid Technology Co.,Ltd. Guangdong Provincial Key Laboratory of New Technology for Smart Grid
Guangzhou, China
395018130@qq.com

Huang Mingxin
China Southern Power Grid Technology Co.,Ltd. Guangdong Provincial Key Laboratory of New Technology for Smart Grid
Guangzhou, China
zitakitty@163.com

Zhang Wenzhen
China Southern Power Grid Technology Co.,Ltd. Guangdong Provincial Key Laboratory of New Technology for Smart Grid
Guangzhou, China
frisozhang@foxmail.com

Huang Menghua
China Southern Power Grid Technology Co.,Ltd. Guangdong Provincial Key Laboratory of New Technology for Smart Grid
Guangzhou, China
1015573307@qq.com

***Abstract*—The detection capability of traditional AC-type and A-type leakage current sensors is limited. Particularly, their detection accuracy for smooth DC current can no longer meet application requirements. This paper proposes a B-type leakage current sensor suitable for wide-range and accurate detection, which enables simultaneous, wide-range, comprehensive and precise detection of both AC leakage current and DC leakage current. Through the analysis of existing iron core magnetic materials, alloys made of different magnetic components are selected as the iron cores for the front winding columns of the B-type leakage current sensor. Specifically, iron cores made of nanocrystalline alloy are adopted in high-current low-voltage distribution network systems, while iron cores made of iron-nickel alloy are used in low-power converter systems. This material selection is intended to meet the measurement requirements of small size, wide detection range and high accuracy. Additionally, fluxgate technology is applied to realize the simultaneous measurement of AC and DC. This solves the problem of coil measurement failure in leakage current sensors caused by DC leakage, thereby enabling the detection of smooth DC, pulsating DC, power frequency AC and high-frequency AC leakage currents.**

Keywords—B-type leakage current sensor, DC leakage current, Magnetic material, Fluxgate Technology

I. INTRODUCTION

With the rapid popularization of electric vehicles and distributed photovoltaic power generation, an increasing number of DC leakage incidents are occurring in low-voltage distribution network systems. This necessitates real-time monitoring and fault analysis of power systems. Once leakage or faults occur in the power grid, electrical equipment may be damaged; in severe cases, it may even pose a threat to human life safety. As an indispensable component for real-time monitoring and fault early warning in key circuits of power systems, current sensors are devices that utilize the principle of electromagnetic induction to generate excitation in windings and perform current detection functions [1].

However, traditional AC-type and Type A leakage current sensors have limited detection capabilities. Particularly in terms of detection accuracy for smooth DC currents, they can no longer meet operational requirements. AC-type leakage current sensors mainly detect power-frequency residual currents; compared with AC-type leakage current sensors, Type A leakage current sensors have added the capability to detect pulsating DC currents [2-3]. When there are a large number of rectifier circuits in the line or functional components such as inverters malfunction, the residual current type is not limited to sinusoidal AC. In such cases, the detection accuracy of traditional AC-type and Type A leakage current sensors decreases significantly, and they can no longer meet the detection and operational needs of power system maintenance [4], making an urgent need for application upgrades. For this reason, a Type B leakage current sensor capable of measuring both AC and DC currents simultaneously is required.

Currently, the core magnetic components of Type B leakage current sensors— which are widely used— are made of cold-rolled silicon steel sheets. With the rapid development of the power industry, high-voltage transmission lines have been increasing day by day, and the demand for high-precision current sensors has also surged sharply. Under the conditions of small turns ratio, low number of turns, and restricted core volume, the accuracy of current sensors using cold-rolled

This work was supported by Guangdong Provincial Key Laboratory of New Technology for Smart Grid under Grant 2020B1212070025.

979-8-3315-5472-9/25/$31.00 ©2025 IEEE

silicon steel sheets for their cores can only reach Class 0.5, which often fails to meet industrial requirements. Therefore, this paper focuses on researching different magnetic materials, selects appropriate magnetic components to serve as the core of the front winding column of the Type B leakage current sensor, and combines fluxgate technology to develop a Type B leakage current sensor that meets the requirements of miniaturization, wide measurement range, and accurate detection.

II. Analysis and Selection of Core Magnetic Components

Commonly used soft magnetic materials and their specific performance parameters are shown in TABLE I [5]. It can be observed that iron-nickel alloys and nanocrystalline alloys exhibit high magnetic permeability and low coercivity; using these materials to manufacture magnetic cores can effectively improve the detection accuracy of sensors.

TABLE I. Common Soft Magnetic Materials and Their Specific Performance Parameters

Alloy	μmax/ (mH·m-1)	Hc/ (A·m-1)	Bb/T	ρ/ (μΩ·cm)	Tc/ ℃
Iron-based Nanocrystalline	375	1.2	1.25	90	550
Iron-based Amorphous	187.5	3.0	1.56	140	415
Iron-Nickel-Based Amorphous	500	1.0	0.75	125	360
Cold-Rolled Silicon Steel	50	30	2.03	47	740

A. Iron-Nickel Alloy Core

Iron-nickel alloy (Permalloy) is characterized by high initial magnetic permeability, low residual magnetism, and low coercivity [6-7]. Iron-nickel alloy cores exhibit extremely high magnetic permeability in weak magnetic fields; the initial magnetic permeability of some grades can exceed 100,000. This enables more effective guidance of magnetic field lines and reduces the required core size. Their coercivity is very low, close to that of pure iron, which means they are easy to magnetize and demagnetize. In alternating magnetic fields, they can quickly change their magnetization state, thereby reducing energy loss. Iron-nickel alloy cores have low core losses, including both small hysteresis losses and eddy current losses, which can improve the energy efficiency of equipment. Iron-nickel alloy cores with high magnetic permeability can enhance the measurement accuracy of current sensors. However, the high cost of this material will increase the overall cost of current sensors.

B. Nanocrystalline Alloy Core

As a new type of magnetic component, nanocrystalline alloy exhibits excellent comprehensive properties under weak magnetic fields, including high saturation magnetic flux density, low high-frequency loss, high initial magnetic permeability, low residual magnetism, and low coercivity. It has high magnetic permeability, and the magnetic permeability varies significantly between saturated and unsaturated states, which also improves the detection sensitivity. Its coercivity is low, meaning the amplitude of the excitation signal required for the core material to enter the reverse magnetization state is small—this helps reduce the fluxgate's requirements for the excitation signal. Additionally, its saturation magnetic field strength is low, making it easier for the material to reach a saturated state, which is conducive to reducing the amplitude of the excitation signal. Therefore, the core magnetic components made of nanocrystalline alloy can effectively improve the bandwidth and measurement range of current measurement, meeting the application scenarios that require high measurement accuracy of current sensors. Moreover, nanocrystalline alloy is relatively low in price, which reduces the cost of current sensors and is beneficial to the promotion and application of current sensors.

C. Selection of Core Magnetic Components

Both iron—nickel alloys and nanocrystalline alloys possess high electromagnetic properties. By studying the core parameters-transient magnetic permeability and magnetization curve—of the cores made from these two materials, this paper selects the core magnetic components for the Type B leakage current sensor.

When the magnetic field strength changes in the magnetic core, the magnetic domains inside the core will rearrange to respond to this change. The speed and efficiency of this rearrangement determine the magnitude of the transient magnetic permeability. Therefore, the transient magnetic permeability (μ) of the magnetic core is expressed as:

$$\mu = \frac{dB}{dH} \tag{1}$$

Among them, B represents the magnetic flux density, and H represents the magnetic field strength.

The comparison diagram of the magnetization curves between the new magnetic component—nanocrystalline alloy —and iron-nickel alloy is shown in Fig. 1. Among them, the magnetization curve functions of nanocrystalline alloy and iron-nickel alloy obtained by fitting are as follows:

$$y = -0.00319x^5 + 0.04533x^4 - 0.23692x^3 + 0.51503x^2 - 0.17079x + 0.02048 \tag{2}$$

$$b = -0.00192a^5 + 0.02494a^4 - 0.11413a^3 + 0.18175a^2 + 0.13534a + 0.00423 \tag{3}$$

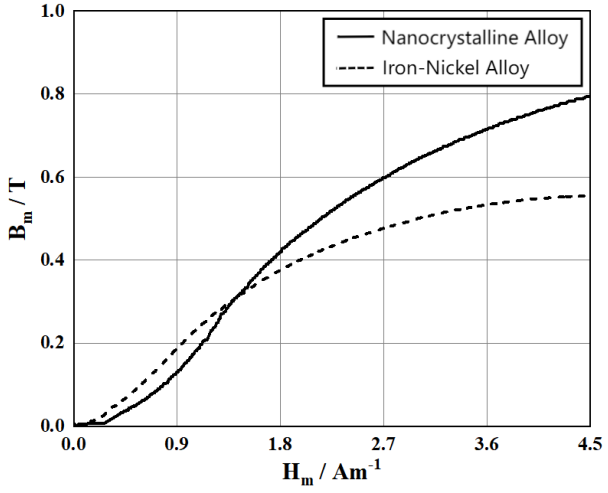


Fig. 1. Comparison Chart of Magnetization Curves between Nanocrystalline Alloy and Iron-Nickel Alloy.

Based on the above comparative analysis, iron-nickel alloy exhibits a higher magnetic flux density in weak magnetic fields, while nanocrystalline alloy shows a higher magnetic flux density in stronger magnetic fields. In weak magnetic environments, iron-nickel alloy has superior magnetic permeability, whereas in stronger magnetic environments, nanocrystalline alloy has better magnetic permeability. Therefore, the Type B leakage current sensor designed in this study for wide-range and accurate detection adopts a core made of nanocrystalline alloy for large-current scenarios and a core made of iron-nickel alloy for small-current scenarios, so as to adapt to applications in different occasions.

III. Working Principle of Fluxgate Technology for Type B Leakage Current Sensors

When a leakage current $\dot{i}p$ is generated in the low-voltage distribution network system, the leakage current $\dot{i}p$ acts as the detection current of the current transformer. It is coupled into the excitation current through the winding N of the current transformer, causing the magnetic field in the core to no longer maintain its original symmetry but instead become biased. Changes in the magnetic field lead to changes in the core's excitation current. When the voltage across the sampling resistor R_S reaches the threshold voltage V_r, the polarity of the excitation voltage level flips, generating a square-wave excitation signal $U(t)$. When the excitation current passes through the sampling resistor R_S again, the asymmetry of the excitation current waveform causes a deviation in the voltage fed back to the sampling resistor. The average value of this deviation is:

$$\Delta u = \mathrm{R_S}\frac{i_p}{\mathrm{N}} \tag{4}$$

By detecting the voltage deviation of the sampling resistor, the variation of the excitation current can be obtained, enabling accurate detection of the leakage current.

The specific working principle is described as follows:

(1) When there is no leakage current, the voltage and current waveforms of the fluxgate in the Type B leakage current sensor are shown in Fig. 2. The induced electromotive force (EMF) waveform output by the excitation coil is symmetric up and down. Before the polarity of the excitation signal $U(t)$ flips, the current rises rapidly to reach the positive or negative maximum current I_p or $-I_p$;

(2) When leakage current flows through the coil, the voltage and current waveforms of the fluxgate in the Type B leakage current sensor are shown in Fig. 3. The induced EMF waveform output by the excitation coil is asymmetric up and down. The detection unit of the sensor measures the leakage current by detecting the degree and direction of the asymmetry of the EMF. Fluxgate technology can realize the simultaneous measurement of AC and DC currents, and there is no problem of coil measurement failure caused by DC leakage current. This makes it suitable for detecting smooth DC, pulsating DC, power frequency AC, and high-frequency AC leakage currents.

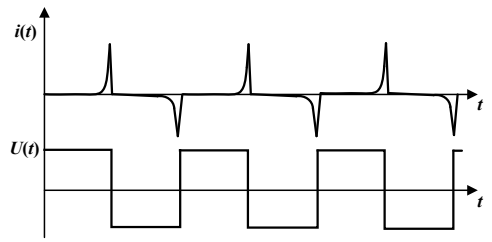


Fig. 2. Schematic Diagram of Induced Current Response and Applied Excitation Signal When ip = 0.

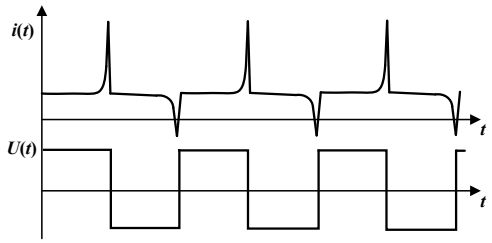


Fig. 3. Schematic Diagram of Induced Current Response and Applied Excitation Signal When ip ≠ 0.

IV. Development of a Type B Leakage Current Sensor Suitable for Wide-Range and Accurate Detection

A. Composition of the Overall Framework

The Type B leakage current sensor can accurately measure AC and DC leakage currents, enhancing the comprehensiveness of leakage current detection. Fig. 4. shows the system framework diagram of the Type B leakage current sensor. By being integrated into protection devices or combined with local monitoring terminals, and establishing data connections with the monitoring backend through the communication module, the sensor enables intelligent monitoring of key power grid nodes, adjustable thresholds, and remote control. It provides a higher level of leakage protection and remote operation and maintenance capabilities for fields such as electric vehicles, photovoltaic power generation, and power distribution networks.

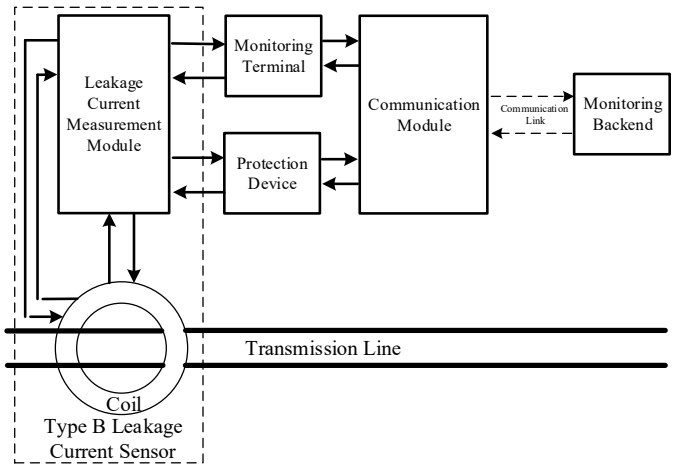


Fig. 4. Block Diagram of Type B Leakage Current Sensor System.

B. Type B Leakage Current Sensor

The body of the Type B leakage current sensor consists of a coil and a leakage current measurement module. The module is composed of a fluxgate chip and its peripheral circuits, among which the fluxgate chip integrates a peak detection unit, an excitation unit, an output conditioning unit, and other components internally.

Fig.5. shows a schematic diagram of the fluxgate circuit composed of a coil and a fluxgate chip. Its detection structure specifically includes: the new magnetic material (nanocrystalline alloy or iron-nickel alloy) core of the current sensor, winding N, excitation signal U(t), sampling resistor R_S, and V_r (the threshold voltage of the hysteresis comparator). The winding N of the Type B leakage current sensor (suitable for wide-range and accurate detection) is wound around the core. One end of winding N is connected to the positive pole of the excitation signal U(t), and the other end is connected to the negative pole of the excitation signal U(t) through a series resistor R_S. The hysteresis comparator is connected between the excitation signal U(t) and the sampling resistor R_S. Its basic characteristics are as follows:

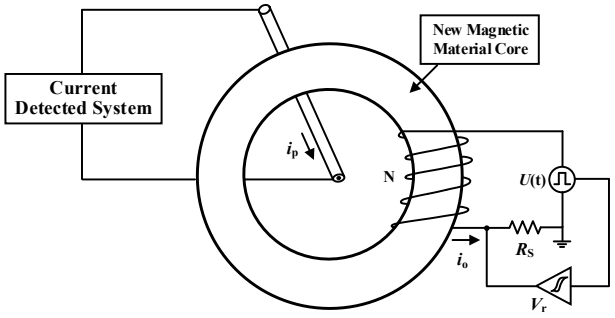


Fig. 5. Schematic Diagram of Fluxgate Circuit.

C. Monitoring Terminal/Protection Device

The Type B leakage current sensor communicates with the monitoring terminal through communication methods such as RS485, providing real-time monitoring data of the current leakage current to support local monitoring of electricity usage scenarios.

The Type B leakage current sensor provides the sampled leakage current signal to the trigger module of the protection device through secondary current conductors, or integrates the sensor body into protection devices such as circuit breakers to perform protection actions like tripping when a leakage occurs.

D. Communication Module

The communication module sends leakage current data and current working status information to the monitoring backend, while receiving working mode information and trigger threshold setting information issued by the monitoring backend.

E. Monitoring Backend

The monitoring backend consists of a data storage server, a PC display terminal, and a mobile phone display terminal. The data storage server is used to store the current measurement data and parameter configuration information of all leakage current sensors and protection devices, and simultaneously provide data for the PC and mobile phone display terminals to call and display. The PC and mobile phone display terminals are used to display the leakage current values of different leakage current sensors in each transformer district. They can collect and display real-time leakage current, as well as display historical leakage current data. Meanwhile, the working modes and trigger thresholds of leakage current sensors and protection devices can be configured on the PC and mobile phone display terminals, allowing the setting of different trigger thresholds and working modes.

V. Application of the Type B Leakage Current Sensor Suitable for Wide-Range and Accurate Detection

In high-current low-voltage power distribution network systems, the Type B leakage current sensor made of a core with nanocrystalline alloy can accurately measure weak leakage current signals, significantly improving the sensor's sensitivity and measurement accuracy. Additionally, the Type B leakage current sensor with a nanocrystalline alloy core can withstand large current impacts, enhancing the sensor's reliability and service life. Due to the excellent performance of nanocrystalline alloy, the leakage current sensor has relatively low power consumption during operation, which also helps save energy and reduce operating costs.

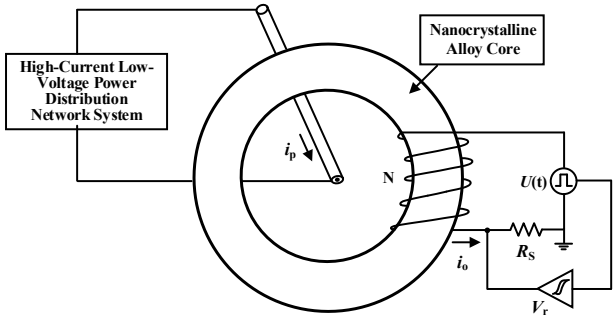


Fig. 6. Application in High-Current Low-Voltage Distribution Network Systems.

In low-power converter systems, the Type B leakage current sensor made of an iron-nickel alloy core has relatively stable magnetic permeability. This helps the Type B leakage current sensor accurately reflect changes in leakage current under different operating conditions in low-power converter systems, maintaining high measurement accuracy and stability. It has low hysteresis characteristics, and there is a good linear relationship between changes in magnetic flux density and changes in magnetic field strength, which reduces measurement errors caused by the hysteresis effect.

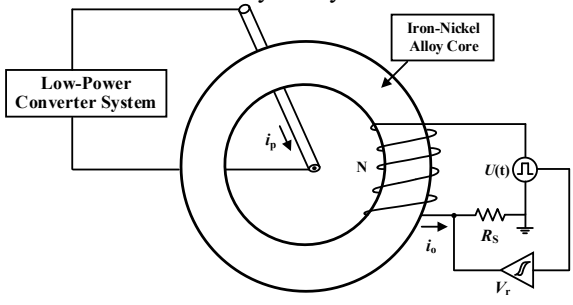


Fig. 7. Application in Low-Power Converter Systems.

VI. Conclusion

Aiming at the limitations of traditional AC-type and Type A leakage current sensors—such as insufficient accuracy in smooth DC current detection and inadequate response to leakage faults in circuits containing rectifiers, inverters, and other components—which fail to meet detection requirements, this paper proposes a Type B leakage current sensor capable of measuring both AC and DC leakage currents simultaneously. By studying the characteristics of existing core magnetic materials (cold-rolled silicon steel sheets, iron-nickel alloys, nanocrystalline alloys) and focusing on the analysis of the instantaneous magnetic permeability and magnetization curves of the core, the sensor adopts a nanocrystalline alloy core for high-current low-voltage power distribution network systems and an iron-nickel alloy core for low-power converter systems. Relying on fluxgate technology to design the sensor ' s structure and working mechanism, a Type B leakage current sensor suitable for wide-range and accurate detection was developed, enabling wide-range and precise detection of AC and DC leakage currents (including smooth DC, pulsating DC, etc.). In future development and application, the sensor can be integrated into protection devices such as circuit breakers and combined with communication modules to provide higher-level leakage protection and remote operation and maintenance capabilities for related fields.

References

[1] Chen Nan. Leakage monitoring technology research of distributed photovoltaic power station based on power line communication [D]. North China Electric Power University,2017.

[2] Xu Zijian.Factros analysis of protective characteristics and parameter optimization of electromagnetic leakage circuit breaker [D]. Tianjin: Hebei university of technology,2022.

[3] ZHONG Yanping, CHENG Zhiguo. Leakage Current Monitoring Method Based on the Fluxgate Principle and Its Applications [J]. JIANGXI ELECTRIC POWER,2019.

[4] WU Y.Study on measuring technology and protectiontechnology of non-linear residual current[D].Tianjin:Hebei university of technology, 2015.

[5] ZHANG Jianjun. Research on Key Technologies of Hall Current Sensor Design[D]. Harbin: Harbin Institute of Technology, 2017.

[6] DING Kou-xiang,WANG Wei,XU Li.Design and implementation of magnetic modulation DC leakage current transformer[J].Information Technology,2014.

[7] WANG Yao,LI Kui.Magnetic modulation-based DC leakage current transformer[J].Advanced Technology of Electrical Engineering and Energy,2012.

Research on the Analytical-Model-Based Setting Method for Leakage Magnetic-Field Differential Protection for Transformer Early Fault

Ping Zeng
State Grid Shanghai Municipal Electric Power Company
Shanghai, China
29339293@qq.com

Wei Bao
State Grid Shanghai Municipal Electric Power Company
Shanghai, China
80627643@qq.com

Qian Feng
State Grid Shanghai Municipal Electric Power Company
Shanghai, China
fengqian09@163.com

Jiayu Lian
State Grid Shanghai Municipal Electric Power Company
Shanghai, China
lianziyu916916@163.com

Xiangli Deng
School of Electric Power Engineering
Shanghai University of Electric Power
Shanghai, China
xiangli_deng@163.com

Hang Tu
School of Electric Power Engineering
Shanghai University of Electric Power
Shanghai, China
1765053828@qq.com

***Abstract*—Leakage magnetic field differential protection, which uses the symmetry of the leakage magnetic field as the diagnostic criterion, can detect short-circuit currents within the faulted turns, thereby achieving high sensitivity. However, determining the precise setting values for leakage magnetic field differential protection is challenging, complicating its practical application. Considering core saturation characteristics and the dimensional parameters of the core, yoke, and windings, this study establishes a multi-winding, multi-state analytical model of winding currents and leakage magnetic fields with electrical-magnetic coupling. By varying the winding voltage and load impedance, the model calculates the winding current and leakage magnetic field distribution, enabling the determination of the magnetic balance coefficient for the "three measurement points" in magnetic differential protection. Using a dry-type transformer at a hydropower station as a case study, the electromagnetic composite multi-state analytical model is applied to set the values for magnetic differential protection, and the magnetic balance coefficient is validated through ANSYS simulations.**

Keywords—leakage magnetic field, analytical model, balance coefficient, fault detection

I. INTRODUCTION

Power transformers are key apparatus in power systems, and their operational reliability is crucial to the secure and stable operation of the grid [1]. However, with the expansion of the grid and the increase in equipment ratings, internal insulation faults—such as winding deformation and minor inter-turn short circuits—are occurring more frequently. These incipient faults often originate from slight mechanical deformation of the windings or localized insulation defects. Although the initial severity is low, prolonged operation may evolve them into severe inter-turn faults or other insulation failures, thereby threatening the secure and stable operation of both the transformer and the grid. Conventional protection and monitoring techniques—such as current differential protection and dissolved-gas analysis in oil [2]—are generally inadequate for the effective detection and early warning of such subtle incipient faults.

In recent years, transformer incipient fault diagnosis techniques based on leakage magnetic-field characteristics have attracted wide attention. Once a transformer winding experiences an inter-turn short circuit or winding deformation, the spatial distribution of its leakage magnetic field exhibits pronounced asymmetry or distortion; therefore, the leakage field can serve as an effective and sensitive indicator for early faults. The authors in [3] proposed a fiber-optic magnetic-field sensor based on the Faraday magneto-optical effect, featuring a wide measurement range and high sensitivity, which is suitable for real-time detection of the internal magnetic field of a transformer and provides a reliable sensing method for online leakage-field measurement. A study in [4] employed multi-physics coupled simulation to analyze the impact of inter-turn short circuits on the electromagnetic and thermal parameters of transformer windings, pointing out that the temperature rise in the shorted turns and distortion of the leakage field are key factors leading to insulation degradation. The work in [5] investigated the leakage-field distribution characteristics for different windings and short-circuit locations, and verified the regularity of symmetry breaking in the leakage field during faults, providing theoretical support for magnetic-field differential protection. The authors in [6] used ANSYS simulations to study the relationship between various types of winding deformation and the magnetic-field distribution, and proposed an online monitoring method for winding deformation based on changes in magnetic-field symmetry, which is suitable

This work was supported by the Science and Technology Project of State Grid Corporation of China (No.520940240037).

979-8-3315-5472-9/25/$31.00 ©2025 IEEE

for early detection of structural anomalies. The method in [7] proposed an inter-turn fault localization and protection approach based on leakage-flux sensors, in which a sensor array is used to achieve fault-phase identification and regional localization, with strong immunity to asymmetric load and inrush current interference. The studies in [8] and [9] developed intelligent diagnosis models for transformer winding incipient faults using leakage-field signals, where the time-domain features of the leakage field are extracted via feature-selection algorithms and classified using artificial intelligence techniques.

Research on high-sensitivity detection of winding deformation and inter-turn short-circuit faults based on the symmetry of the spatial distribution of the leakage magnetic field has yielded substantial results. The work in [10] introduced a magneto-optical fiber sensor, deployed three measurement points ("top–middle–bottom") in the field, and defined a magnetic-balance quantity to achieve the identification of transformer incipient faults as well as the effective blocking of inrush currents and external faults, thereby laying the engineering foundation for online leakage-field measurement. The study in [11] addressed the problem of uneven leakage-field distribution caused by irregular windings in rectifier and traction transformers by proposing a magnitude-differential criterion and a zonal setting method, which significantly improved the applicability of the protection strategy to complex winding structures. The work in [12] further utilized multi-point amplitude mapping to realize both fault-type identification and spatial localization, thus extending the protection function from tripping decision to rapid fault location. The study in [13] conducted a comprehensive analysis of harmonic currents in transformers and their influence on the leakage magnetic field, and, on this basis, introduced a third-harmonic differential concept. By extracting frequency-domain features using the short-time Fourier transform (STFT), the method achieved reliable detection of minor inter-turn short circuits. Based on a laboratory platform, a technical evolution chain was constructed—from achieving precise measurement, optimizing structural adaptability, and improving localization efficiency, to considering harmonic effects for enhanced system sensitivity—thereby establishing a complete methodological framework for leakage-field differential protection and completing dynamic-model verification.

However, factors such as core magnetic saturation, structural dimensional differences, and load fluctuations in practical transformers can lead to a complex and variable spatial distribution of the leakage magnetic field, making it difficult to set the operating values of leakage-field differential protection in real-world applications. This severely limits the engineering deployment and promotion of the technology. Therefore, establishing an accurate and reliable electromagnetic composite multi-state analytical model to enable precise setting of leakage-field differential protection is a key issue for advancing this technology from theoretical research to practical engineering application.

This paper proposes a setting method for leakage magnetic-field differential protection based on an electromagnetic composite multi-state analytical model. First, an electro–magnetic multi-state equivalent model is constructed that considers the nonlinear magnetic characteristics of the core and the coupling of multiple windings. By comparing the analytical-model calculation results with multi-point measured magnetic-field data, the correlation features between the magnetic flux density at typical measurement points and the winding current are extracted, and an index system of magnetic-balance coefficients is established to characterize changes in leakage-field symmetry. On this basis, a differential protection start criterion and a setting strategy suitable for complex on-site operating conditions are proposed. The proposed method fully integrates the analytical model with local measurement-point information, enabling effective discrimination of leakage-field symmetry under limited observability. Its adaptability and stability under different operating conditions are verified through ANSYS finite-element simulations and field tests.

II. Composite Multi-State Analytical Model

A. Establishment of Multi-Winding Circuit State Equations Considering Core Nonlinearity

To accurately describe the electromagnetic response of a transformer under different operating conditions and fault states, an electromagnetic composite multi-state analytical model is constructed based on the equivalent magnetic-circuit theory and multi-winding state equations. The model simultaneously considers core nonlinearity, main-flux coupling, and leakage-flux distribution. By analytically constructing the main and leakage inductance matrices, the model enables subsequent calculation of winding currents and leakage magnetic fields, thereby providing a quantitative basis for setting the criteria of differential protection.A two-winding transformer winding–core model is shown in Fig. 1. Using a field–circuit coupled approach, multi-winding circuit state equations are established to solve for the winding currents and the shorted-turn current [14]. In the figure, w_h and w_l denote the high-voltage and low-voltage windings, respectively; w_k denotes the shorted-turn winding used to simulate an inter-turn short-circuit fault. u_s and z_s are the system voltage and system impedance, respectively; z_L is the load impedance. i_h, i_l and i_k represent the high-voltage winding current, low-voltage winding current, and shorted-turn current, respectively. $\phi_{\sigma h}$, $\phi_{\sigma l}$ and $\phi_{\sigma k}$ denote the leakage flux of the high-voltage winding, low-voltage winding, and shorted-turn winding, respectively. ϕ_μ denote core main flux. $\phi_{\mu\sigma}$ represents the main-flux leakage of the core.

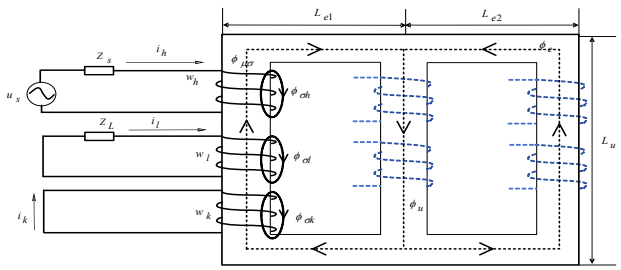


Fig. 1. Coupled field–circuit model of multi-winding transformer.

For a three-phase three-limb transformer structure, the transformer can be equivalently represented as a multi-winding system comprising a high-voltage winding, a low-voltage winding, and a fault winding (simulating an inter-turn short circuit). The corresponding loop equations can be expressed as:

$$u(t) = r \cdot i(t) + \left(L_\sigma + L_T(t)\right) \cdot \frac{di(t)}{dt} \tag{1}$$

where $u(t)$ is the voltage vector of the windings; $i(t)$ is the current vector of all windings, including the healthy windings and the shorted turns; r is the winding resistance matrix; L_σ is the constant leakage inductance matrix; $L_T(t)$ is the main-flux inductance matrix, which varies with the magnetic state of the core.

From the equivalent magnetic-circuit model, the relationship among magnetomotive force F , magnetic flux φ , and permeance is obtained, from which the expression of the main-flux inductance $L_T(t)$ can be derived as follows:

$$L_T(t) = \begin{bmatrix} N_1^2 \cdot \boldsymbol{\Lambda}_T & N_1 N_2 \cdot \boldsymbol{\Lambda}_T \\ N_1 N_2 \cdot \boldsymbol{\Lambda}_T^{\mathrm{T}} & N_2^2 \cdot \boldsymbol{\Lambda}_T \end{bmatrix} \tag{2}$$

where N_1 and N_2 denote the number of turns of the high-voltage and low-voltage windings of the transformer, respectively, and $\boldsymbol{\Lambda}_T$ is composed of the self-magnetic conductance of the windings within each phase core limb and the mutual magnetic conductance between the core limbs.

The permeance Λ_{ij} is calculated as follows:

$$\Lambda_{ij} = \frac{\mu_{ij}(B) \cdot S_{ij}}{l_{ij}} \tag{3}$$

where $\mu_{ij}(B)$ represents the permeability–flux-density relationship of the core material, S_{ij} is the cross-sectional area of the magnetic flux, and l_{ij} is the length of the core limb.

In the calculation of the leakage-flux matrix, the axial leakage flux is neglected. The leakage permeance Λ_σ is obtained using the leakage-energy method, and the leakage-inductance matrix is given by:

$$L_\sigma = \mathrm{diag}\left(N_1^2 \cdot \Lambda_{1\sigma}, N_2^2 \cdot \Lambda_{2\sigma}\right) \tag{4}$$

B. Calculation of Winding Leakage-Field Distribution Based on Electro–Magnetic Linear Transformation

The transformer winding solution domain is divided into current-carrying regions and non-current regions, which are solved using the Poisson equation and the homogeneous partial differential equation, respectively, as shown in Fig. 2.

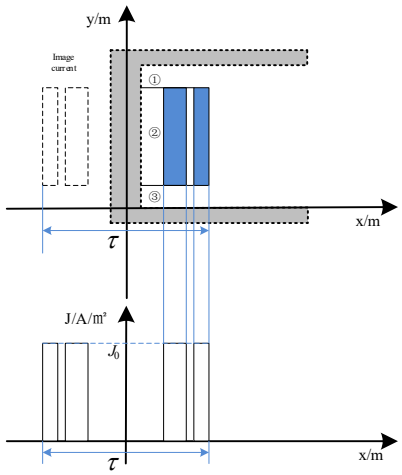


Fig. 2. Decomposition of spatial current density in calculation region

In solving the Poisson equation for the current-carrying region, the current density is independent of the y-coordinate, the current-carrying region is uniform, and the current densities are equal; therefore, the current-density function takes the form of a square wave. According to the core boundary condition, the tangential magnetic field on the surface of the core is zero. By applying the image method, the image current is determined such that the leakage fields produced by the winding current and the image current superimpose to zero on the core surface. The influence of the core on leakage-field calculation is neglected.

For the region with zero current density, the leakage-field distribution is directly solved using the homogeneous partial differential equation.

For the region with nonzero current density, the current-density function J_z is expanded into a Fourier series with a period of length 2τ , as given by:

$$J_z(x) = J_0 + \sum_{m=1}^{\infty} J_m \cdot \cos\left(\frac{m\pi x}{\tau}\right) \tag{5}$$

The separation-of-variables method is applied to compute the leakage-field distribution contributed by each harmonic, and the results are then superposed to obtain the leakage magnetic flux density $B_x^{(II)}(y)$ in Region I, namely: .

$$B_x^{(II)}(y) = \sum_{m=1}^{\infty} \frac{\mu_0 \cdot \tau \cdot J_m}{2m\pi} \cdot \cos\left(\frac{m\pi x}{\tau}\right) \cdot \left(e^{-\frac{m\pi y}{\tau}} - e^{-\frac{m\pi(h_0+h_w)}{\tau}}\right) \tag{6}$$

When inter-turn short circuits or geometric deformations occur in the winding, the total magnetic field can be regarded as the superposition of the fields produced by the healthy winding and the faulty winding. In the local region, by superimposing the fault current density $\Delta J(x)$, the pole pitch changes to τ' , and expanding the current-density function into a sine Fourier series, the faulty-winding component is obtained as

$$B_x^{\Delta}(x)=\sum_{m=1}^{\infty}J_{m'}D_m\sin\left(\frac{m\pi x}{\tau'}\right)+f(J_0,x,y) \tag{7}$$

where $f(J_0,x,y)$ is the static leakage magnetic flux density generated by the DC component after a turn short-circuit, $J_{m'}$ and J_0 are the harmonic and DC component amplitudes, respectively, in the continuous Fourier series expansion of the discrete current density, and D_m is a fixed coefficient independent of the current density and the position variable x.

C. Computational Procedure of the Electromagnetic-Coupled Composite Multi-State Model

The calculation process of the electromagnetic coupled composite multi-state model is shown in Fig. 3. By performing spatial energy integration of the leakage magnetic field, the winding leakage inductance is obtained to form the leakage flux matrix. Using the magnetic permeability of the core, the core magnetic path length, and the yoke magnetic path length, the permeance matrix is calculated. The winding current is determined from the winding voltage together with the leakage flux matrix and the main flux matrix. The winding current density is then calculated, and based on the transformer winding and core geometry, the magnetic field computation space is divided into current-carrying and non-current-carrying regions. The spatial image currents are calculated, and the core is removed from the computational domain. Boundary conditions between the current-carrying and non-current-carrying regions are set. For the current-carrying region, the current density is periodically extended and subjected to Fourier decomposition; the leakage magnetic field distribution for each harmonic is computed using the method of separation of variables, and the results for all harmonics are superimposed. For the non-current-carrying region, the odd-order partial differential equation is solved directly to obtain the leakage magnetic field distribution within the region.

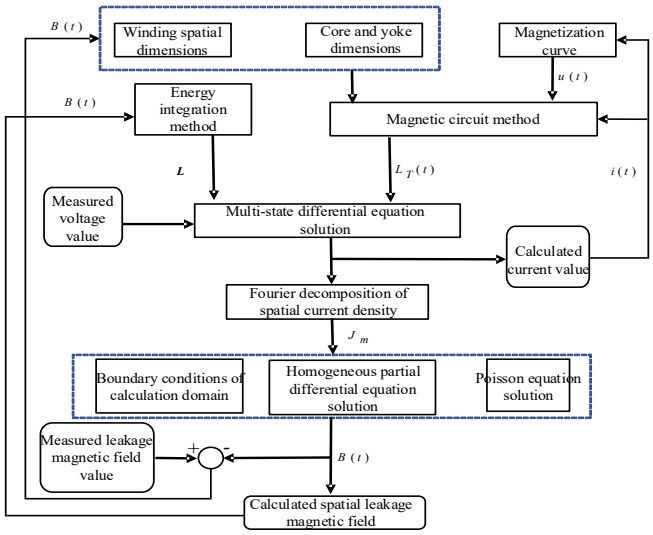


Fig. 3. Electromagnetic coupled composite multi-state model for spatial leakage magnetic field calculation.

An additional fault winding is introduced to simulate the short-circuited winding, and the parameters of the healthy winding are modified accordingly. Assuming that the axial magnetic field is uniformly distributed inside the winding, the axial leakage flux of the short-circuited winding is obtained through energy integration. The leakage inductances of the healthy winding and the short-circuited winding are then calculated separately. Based on the number of shorted turns and the specific core limb in which they are located, the main-flux inductance parameters of the short-circuited winding are determined. Using the multi-winding circuit calculation model, the winding currents and short-circuited winding current can be obtained, as well as the winding current density and short-circuited winding current density. Applying the superposition theorem, the winding current density of the faulty transformer is decomposed into the healthy-winding current density and the fault-component current density. The spatial leakage magnetic field for each component is computed separately and then superimposed to obtain the spatial leakage-field distribution of the faulty transformer.

III. On-Site Setting and Verification of Transformer Leakage Magnetic-Field Differential Protection

To enable leakage magnetic-field monitoring of transformers under actual operating conditions, a transformer incipient fault monitoring and protection system is constructed, as shown in Fig. 4. The magnetic-field differential protection and online diagnostic device, based on leakage-field balance, mainly consists of a sensor mounting bracket, magneto-optical sensors, multimode optical fibers, and a magneto-optical monitoring unit (including a laser source, photoelectric conversion module, and data acquisition system) as its core components. By deploying fiber-optic magnetic-field sensors on the winding surface and between windings, the system can sense, in real time, local variations in leakage-field intensity at different locations during operation, thereby enabling early warning of abnormal magnetic-flux changes.

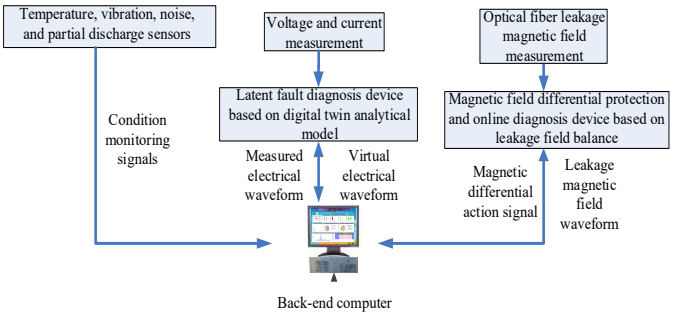


Fig. 4. Monitoring and protection system for early transformer faults.

Based on the aforementioned analytical model, this paper further incorporates the actual structural parameters and operational data of the Wudongde hydropower plant's dry-type lighting transformer to establish a virtual current and virtual leakage-field calculation model. Taking the winding arrangement, turn ratio, and permeance parameters as inputs, and given the measured winding voltages and currents, the model computes the equivalent virtual current and the corresponding virtual leakage-field waveforms. The transformer structural parameters required for the calculation are listed in Table I.

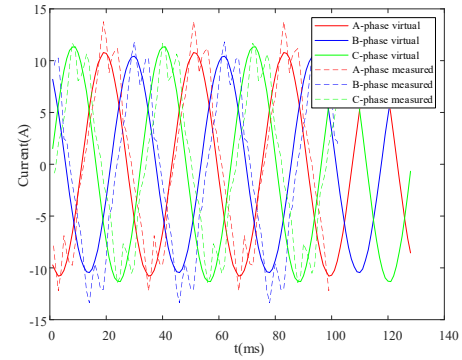
TABLE I. STRUCTURAL PARAMETERS OF WUDONGDE TRANSFORMER.

Parameter	Value	Parameter	Value
Rated voltage (kV)	10.5/0.4	Turns ratio of HV and LV windings	3649/139
Rated current (A)	43.989/1154.701	Core cross-sectional area (m^2)	0.0043
High-voltage phase-a winding resistance (Ω)	1.084	Yoke cross-sectional area (m^2)	0.074
High-voltage phase-b winding resistance (Ω)	1.082	Core magnetic path length (m)	0.43
High-voltage phase-c winding resistance (Ω)	1.086	Yoke magnetic path length (m)	0.72
Low-voltage phase-a winding resistance (Ω)	0.00102	Initial residual flux	1.2887
Low-voltage phase-b winding resistance (Ω)	0.001021	Permeance	0.00532
Low-voltage phase-c winding resistance (Ω)	0.001026	Zero-sequence permeance	3.64e-07

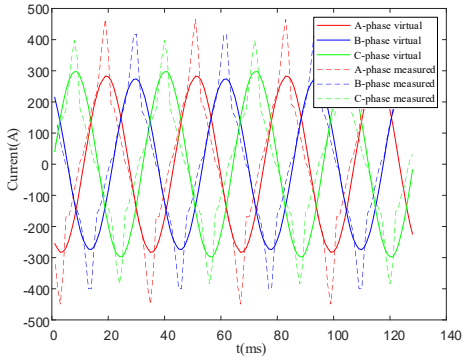
A. Winding Current Calculation and Verification

To verify the accuracy of the constructed model, the main-flux parameter matrix and the leakage-inductance parameter matrix in the multi-winding state equations are calculated based on the actual winding structure and core parameters of the transformer. Using the actual operating voltage as the excitation, the time-domain current responses of the high- and low-voltage sides are solved and then compared with the measured winding currents. The comparison between the calculated and measured winding currents is shown in Fig. 5.

As shown in Fig. 5, the high-voltage winding current is approximately 10 A, while the low-voltage winding current is about 300 A, corresponding to roughly 25% of the rated capacity. Since the load consists mainly of LED lighting equipment, the measured low-voltage current waveform exhibits noticeable distortion. The comparison results indicate that the calculated values from the model closely match the measured values in both overall trend and key waveform characteristics, thereby verifying the model's applicability and accuracy under non-ideal operating conditions.



(a)

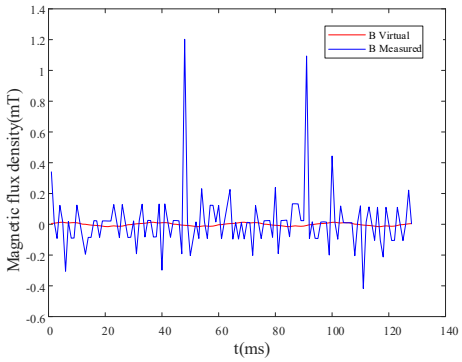


(b)

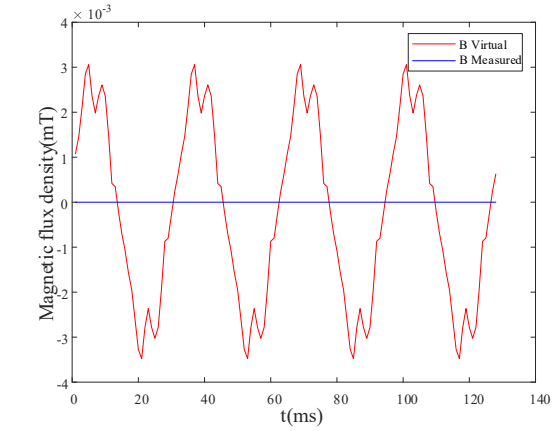
Fig. 5. Comparison between transformer winding current of electromagnetic composite multi-state model and measured current. (a) High-voltage side current.(b) Low-voltage side current.

B. Winding Spatial Leakage-Field Calculation and Verification

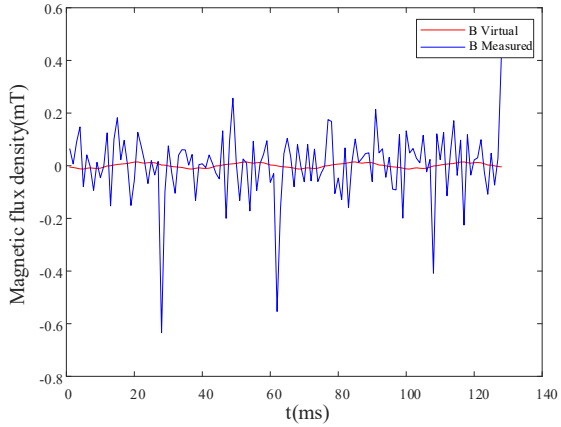
To further validate the model's capability in representing the spatial leakage magnetic field, the winding voltage is used as the excitation to solve the electromagnetic composite multi-state model. The time-domain waveforms of the leakage magnetic field at the upper, middle, and lower positions of the transformer winding are calculated and compared with the measured data from magneto-optical sensors. Taking the phase-A winding as an example, the calculated results at the upper and middle measurement points, together with the corresponding measured waveforms, are shown in Fig. 6.



(a)



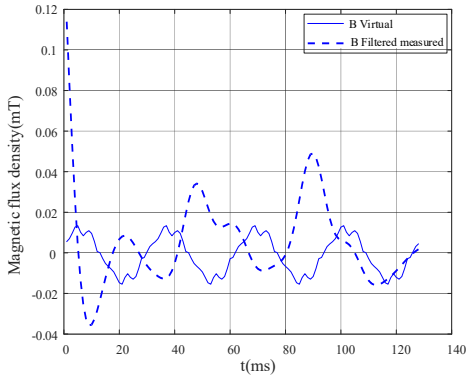
(b)



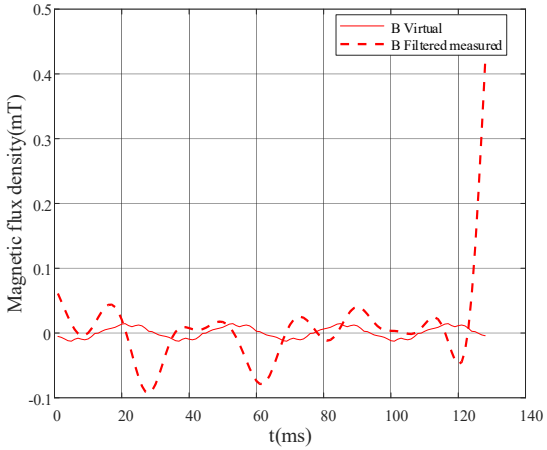
(c)

Fig. 6. Comparison between virtual leakage flux and measured leakage flux of transformer under light load. (a) Upper measurement-point leakage magnetic field. (b)Middle measurement-point leakage magnetic field. (c)Lower measurement-point leakage magnetic field

Under light-load operating conditions of the transformer, the measured leakage magnetic field at each winding measurement point and the virtual leakage field calculated by the model are shown in Fig. 6. Since no sensor was installed at the middle of the winding, the sampled value of the middle-point leakage field is zero.



(a)

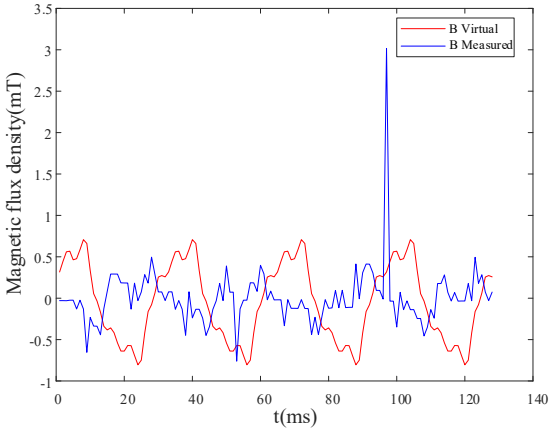


(b)

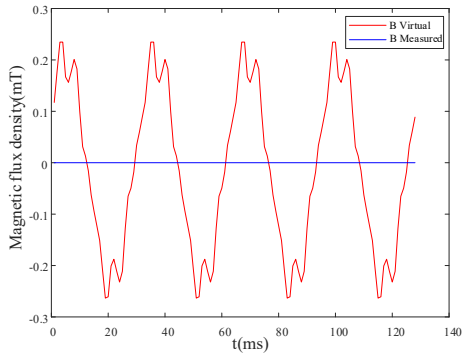
Fig. 7. Comparison of transformer leakage magnetic field after low-pass filtering under light load. (a) Comparison between upper measured signal and filtered signal. (b) Comparison between lower measured signal and filtered signal.

Since the transformer was operating under a light load, the upper and lower measurement points were located near the upper and lower yoke regions of the core, where part of the main flux leaked into the air. This could interfere with the sensor measurements, especially when the magnetic field varied sharply at the yoke edges, resulting in significant noise components in the raw waveforms. To mitigate the impact of noise, the measured leakage-field waveforms were processed using a low-pass filter. The comparison between the filtered leakage-field waveforms and the model-calculated results is shown in Fig. 7.

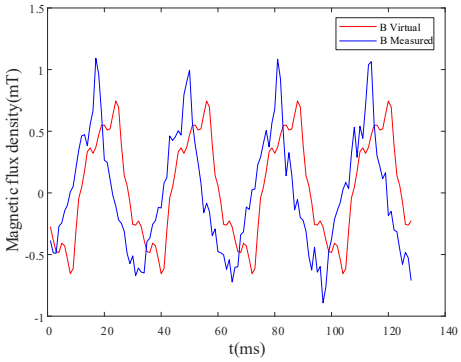
It can be seen that, due to the significant noise captured by the sensors at the upper and lower winding measurement points, the low-pass filtering effectively suppressed part of the high-frequency interference. Although certain discrepancies remain between the filtered waveforms and the simulation results, the differences are relatively small in terms of the amplitude variation range.



(a)



(b)

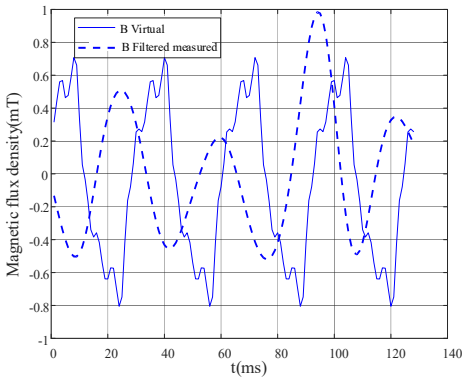


(c)

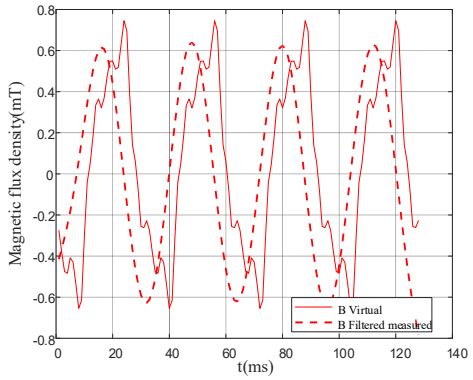
Fig. 8. Comparison between virtual leakage flux and measured leakage flux of transformer under 10% load. (a) Upper leakage magnetic field. (b)Middle leakage magnetic field. (c)Lower leakage magnetic field.

As shown in Fig. 8, with the increase in winding current and the corresponding enhancement of the radial leakage field, the leakage-flux waveform at the upper measurement point of phase-A winding is in good agreement with the calculated value. Since the middle measurement point is located near the center of the winding and relatively far from both the upper and lower yokes, the measured leakage-field waveform closely matches the calculated waveform.

Similarly, the comparison between the low-pass filtered on-site leakage-field measurements and the calculated results is shown in Fig. 9.



(a)



(b)

Fig. 9. Comparison of transformer leakage magnetic field after low-pass filtering under 10% load. (a) Comparison between upper measured signal and filtered signal. (b) Comparison of lower measured signal and its filtered signal.

At the upper measurement point, heavy interference from high-frequency noise results in certain amplitude differences between the simulation and the measured waveform even after filtering. For the lower measurement point, the overall waveform trends are generally consistent; aside from a slight phase shift, the simulation results show good agreement with the measured values, thereby verifying the effectiveness of the model in calculating the spatial magnetic-field distribution.

IV. Calculation and Verification of Leakage-Field Balance Coefficient

A. Setting of Magnetic Differential Protection Value

The actual winding parameters, core parameters, transformer turns ratio, and CT/PT ratios of the on-site transformer are collected and input into the electromagnetic composite multi-state model. Using the high-voltage side voltage as the excitation, the load impedance is varied to change the transformer winding current, thereby altering the low-voltage side voltage. By solving the electromagnetic composite multi-state model, the winding current and the leakage magnetic flux density at the upper, middle, and lower measurement points of the winding are obtained. Three current–leakage magnetic flux density linear plots are then generated for the upper, middle, and lower measurement points, which are used for setting the magnetic-field differential protection.

Based on the measured high- and low-voltage winding currents and the leakage magnetic flux density at the upper, middle, and lower measurement points, evaluate the correlation of the setting lines for magnetic-field differential protection. If the correlation is unsatisfactory, adjust the on-site parameters of the electromagnetic composite multi-state model accordingly.

The transformer nameplate provides only the rated voltage and current, without data on the spatial distribution of the winding leakage magnetic field. Using the rated voltage as the excitation source, the load impedance is varied to change the winding current. The electromagnetic composite multi-state model is then used to calculate the leakage magnetic flux density at the upper, middle, and lower measurement points. By taking the winding current as the horizontal axis and the leakage

magnetic flux density as the vertical axis, the setting line for magnetic differential protection is plotted, as shown in Fig. 10.

Since the leakage magnetic field is distributed in a linear air medium, when the current exceeds i_q, the magnetic field is linearly related to the current, which lies in the linear region. If the leakage flux from the main magnetic flux in the core into the air is neglected, the $B-i$ line passes through the origin; when the remanence of the core is considered, the line does not pass through the origin. When the current is less than i_q, and the influence of the core as well as its effect on the winding leakage magnetic field at the measurement points is taken into account, the leakage magnetic flux density is less than B_q, and the relationship becomes nonlinear. Therefore, the magnetic differential protection criterion should set a threshold value B_q. The logic determination of magnetic field differential protection is triggered only when the measured leakage magnetic field exceeds B_q.

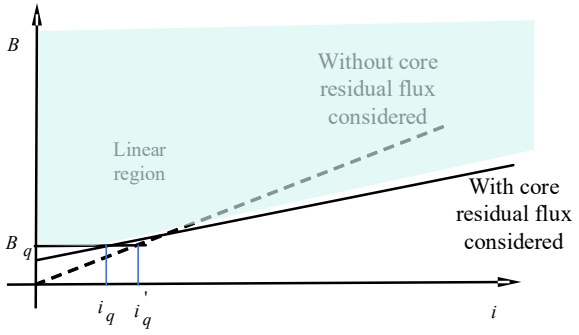


Fig. 10. Setting line of current–magnetic flux density.

Considering the influence of the core and yoke leakage fields on the leakage field at the winding measurement points under no-load energization or light-load conditions, as shown in Fig. 11, when the transformer load factor is less than 35% (high-voltage side current of 15A), the $B-i$ relationships at the upper, middle, and lower measurement points exhibit nonlinearity, which may lead to misoperation of the magnetic-field differential protection.

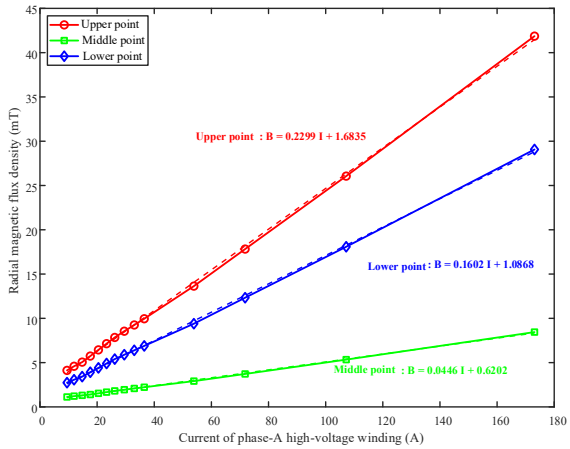


Fig. 11. Setting lines of current–leakage flux density at upper, middle, and lower measurement points.

Therefore, the three model-output lines of current versus leakage magnetic flux density at the upper, middle, and lower measurement points can be used to determine the following settings for the magnetic-field differential protection. The start threshold values of magnetic differential protection at the upper, middle, and lower measurement points, denoted as B_{Tq}, B_{Mq}, and B_{Dq}, are 5.1318, 1.2894, and 3.4894, respectively.

In Fig. 10, the linear section of the leakage magnetic flux density that is greater than the starting value represents the magnetic-field balance relationship among the upper, middle, and lower measurement points. As long as no fault occurs inside the transformer winding, whether under no-load energization, rated current, or external fault conditions, the leakage magnetic flux density at any one of the three measurement points can be obtained from that of the other two points multiplied by the balance coefficient. As long as the leakage field remains symmetrical, the balance coefficient remains constant. If winding deformation, a minor inter-turn fault, or an arc-type fault occurs, the balance coefficient will change.

Assuming that the remanence of the core and yoke is zero, the three lines all pass through the origin. The balance coefficient between the upper and lower measurement points is given by the ratio of the slopes of their current–leakage-flux-density lines:

$$K_{set1}=\frac{K_{up}}{K_{dn}} \tag{8}$$

Where K_{up} is the slope of the setting line for the upper measurement point, and K_{dn} is the slope of the setting line for the lower measurement point.

Therefore, based on the simulati-on results and taking into account the corresponding reliability coefficients, the three setting values of the balance coefficients are as follows:

$$\begin{cases} Kset1 = 0.2795 \\ Kset2 = 0.3109 \\ Kset3 = 0.9683 \end{cases} \tag{9}$$

where K_{set1} is the balance coefficient of the middle and upper measurement points, K_{set2} is the balance coefficient of the middle and lower measurement points, and K_{set3} is the balance coefficient of the lower and upper measurement points.

B. Verification of the Balance Coefficient

Using the ANSYS finite element simulation software, the no-load energization and rated-load operating conditions of the transformer are simulated to verify the effectiveness of the balance coefficient. The simulation results are shown in Fig. 12.

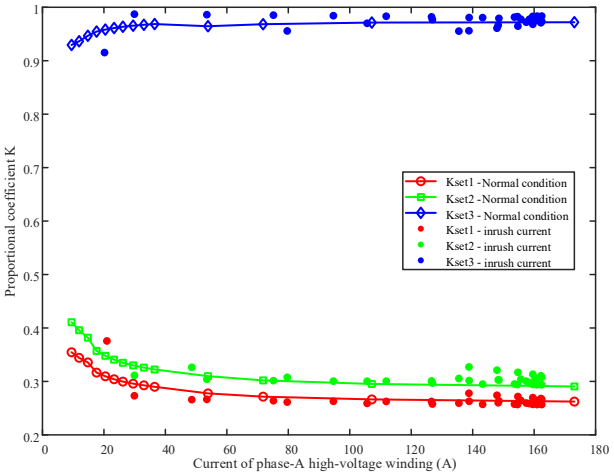


Fig. 12. Verification of balance coefficient.

As shown in Fig. 12, when no internal fault occurs in the transformer, the three balance coefficients fluctuate around their setting values under various operating conditions and remain stable, indicating that the leakage magnetic field during normal transformer operation satisfies the symmetry condition.

V. Conclusion

In response to the issues of insufficient sensitivity in detecting incipient transformer faults and the difficulty of on-site setting adjustments, this paper proposes a transformer magnetic-field differential protection setting method based on an electromagnetic composite multi-state analytical model. The method comprehensively considers factors such as core saturation, winding structural parameters, and load variations, and establishes a multi-winding electrical–magnetic coupled analytical model to achieve accurate calculation of the leakage-field distribution. By incorporating multi-point magnetic balance coefficients, a protection criterion is formulated, and a setting adjustment procedure is proposed. Simulation and dynamic model experimental verification demonstrate that the proposed scheme can rapidly and sensitively identify incipient winding faults without being affected by inrush currents or external faults, showing high engineering feasibility and strong potential for practical application.

Acknowledgment

The authors gratefully acknowledge the support of the Science and Technology Project of State Grid Corporation of China (No.520940240037) and Shanghai University of Electric Power for the development of the present study..

References

[1] M. Huang, W. Zheng, T. Ji, M. Ji, T. Pu, and B. Qi, “Optical sensor with wide range and high sensitivity for internal magnetic field detection of transformer,” CSEE J. Power Energy Syst., vol. 10, no. 5, pp. 2230–2244, Sept. 2024.

[2] B. Zhang, R. Xian, Y. Yu, T. Xie, H. Gao, and L. Chen, “Analysis of physical characteristics of power transformer windings under inter-turn short circuit fault,” High Voltage Eng., vol. 47, no. 6, pp. 2177–2185, 2021.

[3] Y. Zheng, X. Gong, S. Pan, J. Sun, and J. Deng, “Analysis on leakage flux characteristics of turn-to-turn short-circuit fault for power transformer,” Autom. Electr. Power Syst., vol. 46, no. 15, pp. 121–127, 2022.

[4] Y. Zhou and X. Wang, “The on-line monitoring method of transformer winding deformation based on magnetic field measurement,” Electr. Meas. Instrum., vol. 54, no. 17, pp. 58–63, 87, 2017.

[5] F. Haghjoo, M. Mostafaei, and H. Mohammadi, “A new leakage flux-based technique for turn-to-turn fault protection and faulty region identification in transformers,” IEEE Trans. Power Del., vol. 33, no. 2, pp. 671–679, 2018.

[6] J. Liu, Q. Dong, S. Tian, M. Liu, Z. Mei, and H. Zhou, “Early fault diagnosis of transformer winding based on ReliefF-mRMR leakage magnetic field feature optimization and improved LSSVM,” Electr. Meas. Instrum., pp. 1–11, Aug. 17, 2025. [Online]. Available: https://link.cnki.net/urlid/23.1202.th.20240511.0936.007.

[7] J. Liu, Z. Li, and Y. Zhou, “Transformer windings based on leakage field and ICOA-ResNet early fault diagnosis,” Power Syst. Prot. Control, vol. 52, no. 9, pp. 99–110, 2024.

[8] X. Deng, H. Zhu, K. Yan, Z. Zhang, and S. Liu, “Magnetic balance protection of transformers based on optical fiber leakage magnetic field measurement,” Trans. China Electrotech. Soc., vol. 39, no. 3, pp. 628–642, 2024.

[9] X. Deng, S. Wu, Z. Tong, Q. Ma, J. Wang, and H. Zhu, “Research on early fault protection of irregular winding transformer based on leakage field magnitude difference,” Proc. CSEE, vol. 45, no. 11, pp. 4269–4282, 2025.

[10] X. Deng, Z. Wang, P. Zeng, D. Zhou, and Z. Du, “Early fault localization method for transformer windings using leakage magnetic field amplitude characteristics,” Proc. CSU-EPSA, pp. 1–9, May 2025. [Online]. Available: https://doi.org/10.19635/j.cnki.csu-epsa.001649.

[11] X. Deng, Y. Peng, Z. Tong, J. Wang, Z. Wang, and M. Liu, “Research on third harmonic differential protection of leakage magnetic field for early faults in transformers,” Power Syst. Technol., pp. 1–15, Aug. 18, 2025. [Online]. Available: https://link.cnki.net/urlid/11.2410.tm.2025051-5.1438.018.

[12] X. Deng, K. Yan, H. Zhu, H. Zhu, Z. Zhang, and S. Liu, “Transformer winding early fault protection based on circuit-magnetic leakage field multi-state analytical model,” Power Syst. Technol., vol. 47, no. 9, pp. 3808–3821, 2023.

Neural Network-Based Detection of Open and Closed-Circuit Faults in Single-Phase Voltage Source Inverters

George Owusu
Dept. of Electrical and Electronic Engineering
University of Mines and Technology
Tarkwa, Ghana
ORCID: https://orcid.org/0000-0001-9447-0158

Joshua Afosa-Baffoe
Dept. of Electrical Engineering
Montana Technological University
Butte, United State of America
jafosa5@gmail.com

***Abstract*—The single-phase Voltage Source Inverter (VSI) is one of the most commonly used converters for transforming a DC source into an AC source to supply power to a connected load. However, during operation, the system may experience an open-circuit (OC) or short-circuit (SC) fault, resulting in an interruption of power supply to the load. To reduce the frequency of such interruptions, this study proposes an Artificial Neural Network (ANN)-based technique to support the restoration of continuous operation in the event of a fault. The proposed controller manages two conventionally designed VSI circuits connected in parallel, enabling the system to switch power supply to the alternate circuit in the event of an OC or SC fault in the primary circuit. The design incorporates two additional switches between the inverter output lines to prevent backflow of current within the system. A simulation analysis was performed using MATLAB/Simulink to evaluate the performance of the proposed system. Simulation results demonstrate the system's capability to restore continuous power supply from the DC source to the load during an OC or SC fault in either circuit. The proposed approach can be extended to other categories of VSI to improve the efficiency and reliability of power delivery from source to load.**

Keywords—inverter, neural network, short-circuit, open-circuit, pulse width modulation

I. Introduction

The Voltage Source Inverter (VSI) circuit is a widely used configuration for converting a DC source into an AC source, which enables a continuous power supply to a connected load. However, during operation, the circuit may experience various faults, such as open-circuit (OC) faults, short-circuit (SC) faults, DC-link faults, and gate misfiring faults [1 – 5]. These faults disrupt the continuous power supply from the source to the load. This study specifically focuses on restoring OC and SC faults. To achieve this, it proposes an enhancement of the conventional sinusoidal pulse width modulation (PWM) controller of a single-phase VSI with an Artificial Neural Network (ANN), which facilitates automatic switching between identical single-phase VSI circuits when the primary circuit develops an OC or SC fault. The system's effectiveness in restoring power during OC and SC faults was validated through MATLAB/Simulink simulations. The findings from the study can be applied to other inverter circuits to reduce power interruptions during fault conditions.

II. Theoretical Review

A. Fault Analysis

Voltage source inverter faults can be classified into open-circuit and short-circuit faults of the power electronic switches, as well as DC-link faults and gate misfiring faults. This study focuses on addressing issues arising from short-circuit and open-circuit faults occurring in the switches during operation. The following subsections elaborate on the open-circuit and short-circuit faults of an inverter.

Open-Circuit Fault

Open-circuit faults refer to malfunctions in which an inverter switch is unable to conduct, thereby obstructing the passage of current. The occurrence of this fault during operation can severely affect inverter functionality. Resulting issues may include increased harmonic distortion, diminished output power, or total malfunction of the inverter switch [6–8].

Short-Circuit Fault

Short-circuit faults, on the other hand, occur when a switch becomes unintentionally bridged, enabling bidirectional current flow and resulting in a short circuit across the DC source. This type of fault generates excessively high current within the system, posing potential fire hazards and causing damage to the inverter circuitry [9].

B. Machine Learning

Machine learning, a subset of artificial intelligence, enables computer systems to learn from data without the need for explicit programming. It is generally categorized into three main types: supervised, unsupervised, and reinforcement learning. The proposed system employs the supervised learning approach to train data from an inverter exhibiting open- and short-circuit faults, with the objective of predicting and addressing fault-related issues. Various techniques are available for implementing machine learning, including support vector machines, random forests, k-nearest neighbors, and decision

979-8-3315-5472-9/25/$31.00 ©2025 IEEE

trees. In this case, a neural network was adopted due to its effectiveness in recognizing complex patterns.

C. Related Works

Dhumale et al. modeled and diagnosed an open switch fault in a three-phase voltage source inverter (VSI) system [1]. The study aimed to diagnose single and multiple open switch faults in VSI using a technique known as the discrete wavelet transform – if-then rule (DWT-ITR). The results indicated that the proposed system could detect and diagnose open circuit faults in VSI. However, its impact on short circuit switch faults was not investigated.

Gmati et al. focused on diagnosing open-switch faults in VSIs used for controlling permanent magnet synchronous machines (PMSM) [2]. The study aimed to address open-switch faults in a three-phase, two-level VSI-fed PMSM system. This was achieved by first evaluating the errors between the reference currents and the PMSM stator predictive currents. Subsequently, the fuzzy logic technique was applied to the fault diagnostic variable to locate the faulty power switches. Although the proposed technique identified open-switch faults in VSI, short-circuit faults in VSI were not considered.

Noroozi et al. proposed a short-circuit fault diagnosis technique for a three-phase quasi-Z-source inverter [3]. The study aimed to introduce a cost-effective solution for switching short-circuit fault diagnosis in the inverter. To achieve this, a peripheral circuit was used to detect and transmit the fault to a processor. Subsequently, a non-maskable interrupt was activated to disconnect the CPU routine, initiating the fault algorithm. The proposed algorithm identified the exact location of the failed switch. According to the results presented, the algorithm prevented secondary damage in the system. However, open-circuit faults that may occur during inverter operation were not explored.

Oliveira et al. conducted a study on digital short-circuit diagnosis and reconfiguration of a fault-tolerant VSI [5]. The study aimed to introduce a short-circuit diagnosis technique for a fault-tolerant inverter topology. To achieve this, rough set theory (RST) was applied to detect the fault location in the circuit. Subsequently, the VSI topology was reconfigured to resolve the issue. Simulation results indicated that the proposed algorithm effectively addressed short-circuit faults. However, its impact on open-circuit faults was not considered.

Mahafzah et al. presented an artificial intelligence-based open-circuit fault diagnosis in VSI-fed PMSMs with a new fault recovery technique [5]. The study aimed to examine the effectiveness of different AI classifiers in diagnosing faults in VSIs. The AI techniques used in the investigation included support vector machine (SVM), naïve Bayes, ANN, and decision tree. Simulation results showed that the decision tree technique achieved the highest accuracy (99%) compared to the other AI techniques.

III. Methodology

This section presents the procedure used to accomplish the proposed system. Initially, the circuit of the proposed system was developed, followed by the design and training of the proposed neural network for the controller. The trained network was then used to enhance a conventional sinusoidal Pulse Width Modulation (PWM) to achieve the desired objective. The proposed system was subsequently tested to draw conclusions. The results obtained are presented in the Results and Discussion section of the paper.

A. Proposed Circuit

Fig. 1 illustrates the proposed inverter circuit designed to aid in the restoration of OC and SC faults in a single-phase VSI system.

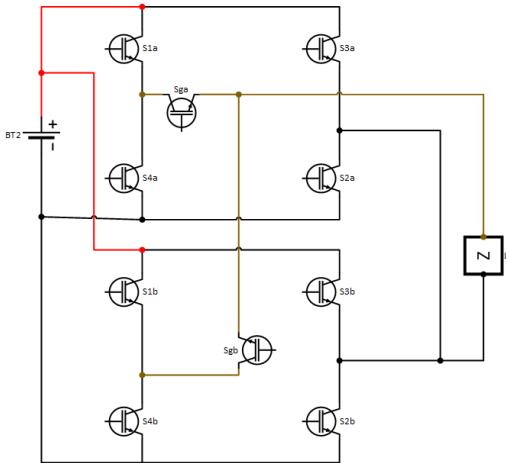


Fig. 1. Schematic diagram of proposed inverter circuit

As shown in Fig. 1, the circuit was designed by connecting two conventional VSI circuits — 'S1a, S2a, S3a, S4a' and 'S1b, S2b, S3b, S4b' — in parallel. To prevent backflow of current, two additional switches, Sga and Sgb, were connected to the output lines of the parallel circuits. The configuration allows the proposed controller to switch to the alternative inverter circuit when either circuit develops an OC or SC fault. Fig. 2 depicts a flowchart to summarize the operations of the proposed system.

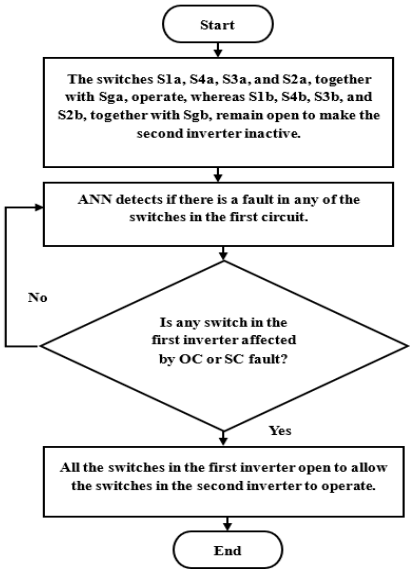


Fig. 2. Flowchart of proposed system's operation

B. ANN Implementation

The ANN was implemented by initially introducing OC and SC faults at the S1a switch located on the first leg of the proposed inverter circuit, as shown in Fig. 3, to collect data for training the network.

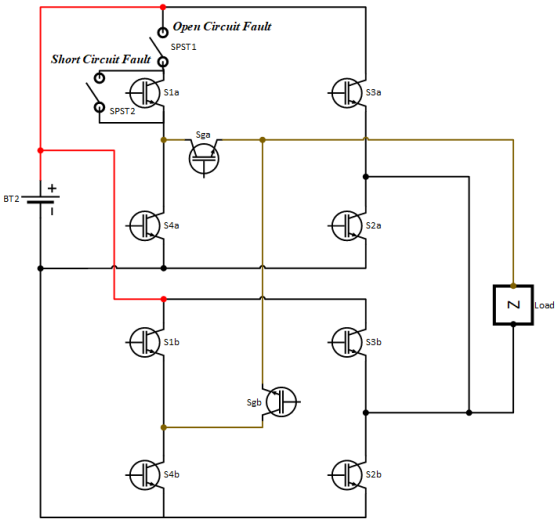


Fig. 3. Introduction of OC and SC faults into proposed circuit for data collection

The data was then exported to the workspace of MATLAB to commence the ANN training. Fig. 4 displays the network of the proposed training.

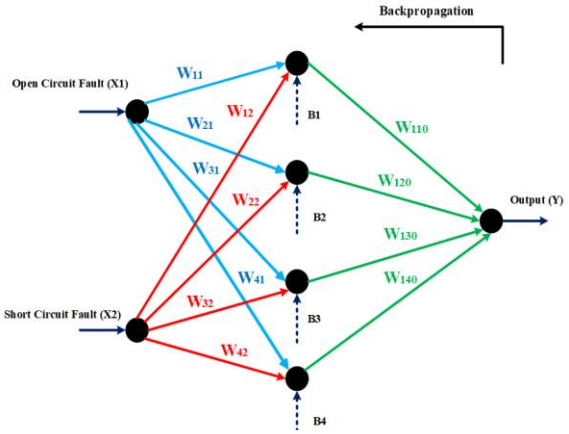


Fig. 4. Proposed network for the training

The network was designed with a Feed-forward backpropagation network, where the two input sets of data, OCF and SCF, were trained based on the parameters presented at Table I.

TABLE I. PARAMETERS OF PROPOSED NETWORK

Parameter	Value
Network type	Feed-forward/backpropagation
Algorithm for learning	Trainlm
Convergent limit	1.0×10^{-12}
Number of input layers	2
Number of hidden layers	4
Number of output layers	1
Number of iterations	6,000
Activation function for input, output and hidden layers	Logsig, purelin and tansig.

The weight of the network was updated with equation 1:

$$w(k+1) = w(k) - \eta g(k) \quad (1)$$

where, $w(k) =$ the weight at iteration k;

$w(k+1) =$ the updated weight at iteration k+1;

$\eta =$ the learning rate, a positive scalar that controls the step size of the update; and

$g(k) =$ the gradient of the loss function with respect to w at iteration k.

During the training, 70% of the collected data was used for training the network, whereas the remaining 30% was used for testing its efficiency. Fig. 5 shows the regression curve of the training, while the performance rate is illustrated in Fig. 6.

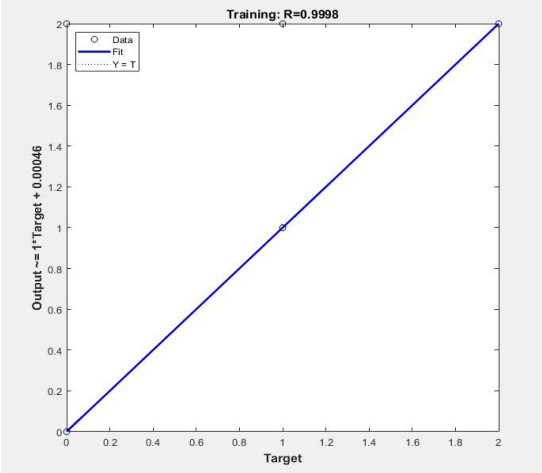


Fig. 5. Regression curve of the training output

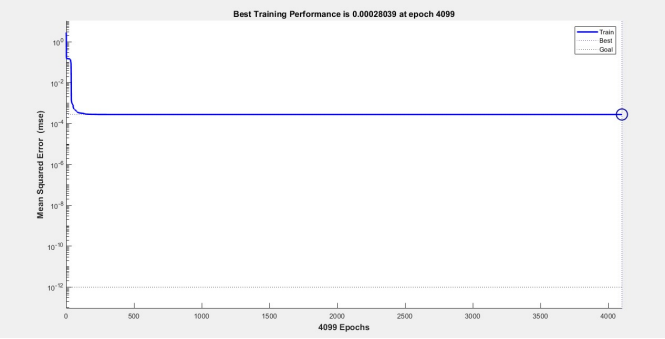


Fig. 6. Performance rate of the training

C. Enhancement of Conventional Sinusoidal PWM

Following the successful design, the proposed network was utilized to enhance the conventional sinusoidal PWM, thereby contributing to the restoration of effective operation during OC and SC faults. Fig. 7 presents the image of the enhanced controller.

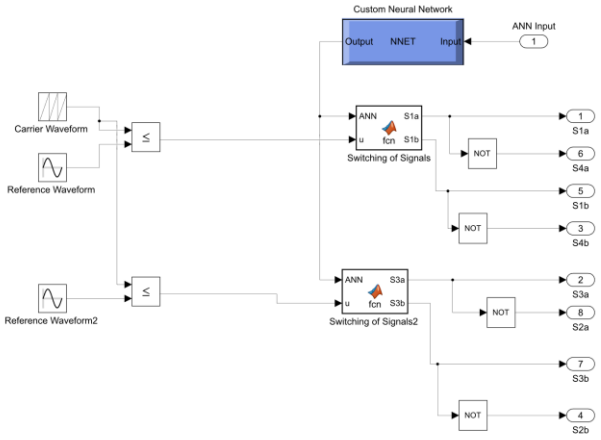


Fig. 7. Enhancing of sinusoidal PWM with the proposed ANN

The modified controller utilized the carrier waveform and two reference waveforms as inputs, which were compared using comparators and processed through NOT gates. The signals were then fed into multiple "Switching of Signals" function blocks containing the outcome of the ANN to detect and correct OC and SC faults in the system.

IV. Results and Discussion

This section presents the results of the study along with a discussion of the findings.

A. Results

The output voltage and current were observed from the initially designed single-phase VSI circuit, as shown in Fig. 8.

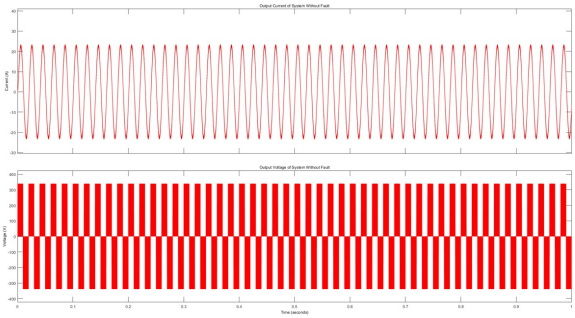


Fig. 8. Conventional single-phase VSI without OC nor SC fault

Subsequently, OC and SC faults were introduced into the S1a switch of the first inverter in the system. The introduction of the faults distorted the output waveform, as shown in Fig. 9.

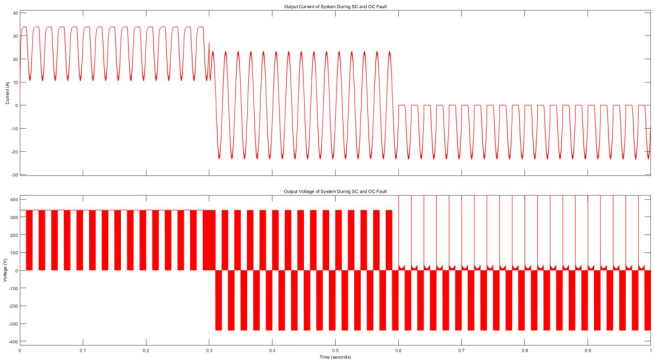


Fig. 9. Introduction of OC and SC fault into conventional VSI system

Upon the introduction of the proposed controller, a successful switch occurred from the faulty first inverter to the alternative inverter circuit, facilitating recovery from the fault, as shown in Fig. 10.

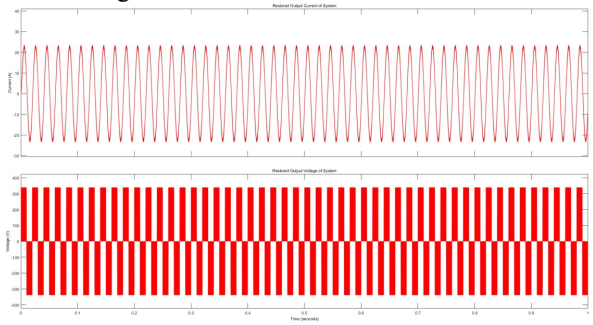


Fig. 10. Output waveform after Introducing the proposed system

B. Discussion

The observations deduced from the simulation results demonstrate that the proposed controller for the single-phase inverter circuit is capable of restoring OC and SC faults that arise in the inverter during operation, thereby minimizing interruptions in the continuous power supply from the source to the load.

V. Conclusion

A. Discussion

The study presents an innovative technique for resolving OC and SC faults occurring in single-phase VSI circuits. This technique involves modifying the conventional PWM controller by integrating a proposed ANN, enabling automatic switching from the faulty inverter circuit to an alternative circuit. This modification ensures the continuous delivery of power from the DC source to the load. A simulation was conducted using MATLAB/Simulink software to evaluate system performance. Simulation results demonstrated the effectiveness of the proposed controller in restoring inverter operation under OC and SC fault conditions.

References

[1] R. B. Dhumale, N. D. Thombare, and S. D. Lokhande, "Modeling and diagnosis of open switch fault in three phase VSI," in 2017 2nd IEEE International Conference on Recent Trends in Electronics, Information & Communication Technology (RTEICT), 2017.

[2] B. Gmati, I. Jlassi, S. Khojet El Khil, and A. J. Marques Cardoso, "Open‐switch fault diagnosis in voltage source inverters of PMSM drives using predictive current errors and fuzzy logic approach," IET Power Electron., vol. 14, no. 6, pp. 1059‐1072, 2021.

[3] N. Noroozi, M. Yaghoubi, and M. R. Zolghadri, "A short-circuit fault diagnosis method for three-phase quasi-Z-source inverters," IEEE Trans. Ind. Electron., vol. 68, no. 1, pp. 672–682, 2021.

[4] A. B. M. Oliveira, R. L. Moreno, and E. R. Ribeiro, "Digital short-circuit diagnosis and reconfiguration of a fault tolerant VSI," in 2017 IEEE Southern Power Electronics Conference (SPEC), 2017.

[5] K. A. Mahafzah, M. A. Obeidat, A. M. Mansour, A. Q. Al-Shetwi, and T. S. Ustun, "Artificial-intelligence-based open-circuit fault diagnosis in VSI-fed PMSMs and a novel fault recovery method," Sustainability, vol. 14, no. 24, p. 16504, 2022.

[6] F. J. Villalobos-Pina, J. A. Reyes-Malanche, E. Cabal-Yepez, and E. Ramirez-Velasco, "Open Circuit Fault Diagnosis in Induction Motor Driver Inverter," IntechOpen eBooks, Sep. 2024, doi: https://doi.org/10.5772/intechopen.1006637.

[7] J. A. Reyes-Malanche, F. J. Villalobos-Pina, E. Cabal-Yepez, R. Alvarez-Salas, and C. Rodriguez-Donate, "Open-Circuit Fault Diagnosis in Power Inverters Through Currents Analysis in Time Domain," IEEE Transactions on Instrumentation and Measurement, vol. 70, pp. 1–12, 2021, doi: https://doi.org/10.1109/tim.2021.3082325.

[8] S. Cheng et al., "An open-circuit fault-diagnosis method for inverters based on phase current," Transportation Safety and Environment, vol. 2, no. 2, pp. 148–160, Jun. 2020, doi: https://doi.org/10.1093/tse/tdaa008.

[9] Renewecosolarhub, "What Is Inverter Short Circuit Problem (Have You Seen This) - renewecosolarhub," renewecosolarhub, Jan. 22, 2024. https://renewecosolarhub.com/what-is-inverter-short-circuit-problem/ (accessed May 08, 2025).

A Novel Traveling Wave Fault Location Method for MMC-HVDC Transmission Lines Based on Complementary Ensemble Empirical Mode Decomposition and Hilbert Transform

Xiangyang Liu
Shanghai University of Electric Power
School of Electrical Engineering
Shanghai, China
lxyrll922@163.com

Zhong Tang
Shanghai University of Electric Power
School of Electrical Engineering
Shanghai, China
shiepedu@163.com

Haoyang Cui
Shanghai University of Electric Power
School of Electronics and Information Engineering
Shanghai, China
971315453@mail.shiep.edu.cn

Hong Qian
Shanghai University of Electric Power
School of Electrical Engineering
Shanghai, China
qianh100@163.com

***Abstract*—When a fault occurs in the direct current transmission line of the modular multilevel converter high voltage direct current (MMC-HVDC) grid, the sub-module capacitors discharge, causing the fault current to rise rapidly, posing a threat to the safe operation of the grid. Fast and accurate fault location is crucial for the stable operation of the system. Therefore, this paper proposes a novel fault location method by combining complementary ensemble empirical mode decomposition (CEEMD) and Hilbert transform (HT) algorithm. This method calculates the instantaneous frequency of the fault signal, identifies the fault moment by detecting its change points, and achieves fault location for the MMC-HVDC transmission line. This method has excellent time-frequency analysis capabilities, better noise robustness, and higher frequency resolution. Finally, use PSCAD/EMTDC to validate this method. The results show that this method accurately locates faults under different fault conditions, and has strong anti-noise ability and tolerance to large transition resistance.**

Keywords—MMC-HVDC, transmission line, fault location, complementary ensemble empirical mode decomposition, Hilbert transform

I. Introduction

Compared with traditional HVDC power grids, MMC-HVDC power grids have the advantages of flexible operation, low harmonic levels, and no commutation failures [1-4]. When a fault occurs in the DC side transmission line of MMC-HVDC, a large fault current is quickly generated, and the half bridge submodule cannot clear the fault by itself [5-8]. Therefore, when a fault occurs on the DC side, it is very important to quickly and accurately locate the fault.

In the research, researchers have proposed different methods. There are mainly traveling wave (TW) method, impedance method, fault analysis method, intelligent algorithm, etc. [9-11]. The TW method has fast speed but limited ability to withstand transition resistance, requiring high sampling frequency. To overcome these problems, frequency correction algorithms are used to correct distorted frequencies [12]. Overcoming the distortion problem of TW signals by introducing ensemble empirical mode decomposition and L1 norm [13]. Improving estimation accuracy by analyzing the frequency dependent characteristics of wave velocity [14]. The implementation of impedance method is simple, and the fault area can be identified by inputting the impedance phase value [15]. However, its accuracy is easily affected by errors in line parameters and transition resistance. The fault analysis method has strong adaptability and can identify faults through the gradient characteristics of the initial fault TW [16]. But it has strong dependence on data and complex calculations. Intelligent algorithms have multi feature fusion and strong adaptability. Using empirical mode decomposition and signal segmentation to improve the accuracy of wavefront recognition [17-19]. But it requires processing a large amount of data. Among them, EMD still faces the problem of mode mixing. To address this issue, uses CEEMD to solve the problem of mode mixing, and then combines HT to complete fault location. This method has good noise robustness and higher frequency resolution, allowing for accurate identification of the fault wavefront arrival time. This method has strong anti-noise ability, capable of withstanding 20dB noise interference, and can tolerate fault resistances up to 500Ω.

The remaining sections are: Section 2 analyzes the propagation characteristics of fault TWs; Section 3 proposes a fault location method based on CEEMD and HT; Section 4 verifies the accuracy of the proposed method; Section 5 provides a conclusion.

II. TW Fault Location Theory

This novel method based on TW theory. Before introducing the proposed method, the propagation characteristics of fault TWs are analyzed. Then the location principle of the TW method is mastered.

A. TW Propagation Velocity

For a bipolar M velocity MMC-HVDC grid, considering the issue of bipolar coupling, decoupling is first performed during fault analysis. According to the Karrenbauer transformation, the transient TWs of fault electrical quantities are decomposed into line-mode and zero-mode [20],

This work is supported by the National Natural Science Foundation of China, 52177185.

$$\begin{bmatrix} u_0 \\ u_1 \end{bmatrix} = \frac{1}{\sqrt{2}} \begin{bmatrix} 1 & 1 \\ 1 & -1 \end{bmatrix} \cdot \begin{bmatrix} u_p \\ u_n \end{bmatrix} \tag{1}$$

Where u_0 is zero-mode voltage, u_1 is line-mode voltage, u_p is positive voltage, u_n is negative voltage.

The determination of the TW velocity affects the accuracy of fault location. The zero-mode component suffers from severe attenuation and significant frequency dependence, leading to large TW losses and unstable wave velocities[21]. In contrast, the wave velocity of the line-mode varies little with frequency and is close to the speed of light, both in the low-frequency and high-frequency ranges. Therefore, this paper selects the line-mode voltage.

$$v = \frac{w}{\beta(w)} \tag{2}$$

Where w is angular frequency and $\beta(w)$ is phase distortion coefficient.

B. Two-terminal TW Method

As shown in Fig. 1, is the equivalent circuit diagram of the fault line. Using this model as an example, the principle based on the two-terminal TW method for DC transmission line faults is analyzed.

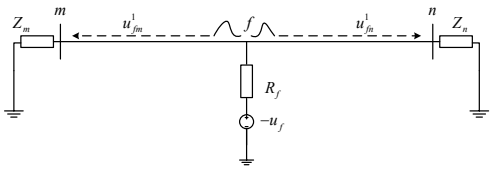


Fig. 1. Equivalent circuit diagram of fault transmission line

Where f is the fault point, Z_m is the system impedance at point m, Z_{mc} is the transmission line impedance on the m side, R_f is the fault resistance, u_f is the normal voltage, u^1_{fm} is the initial fault TW from point f to point m, u^1_{fn} is the initial fault TW from point f to point n.

Taking positive pole grounding (P-G) fault as an example. Fig. 2 shows the TW propagation during a P-G fault on the line. By analyzing its propagation characteristics, the fault location formula is obtained.

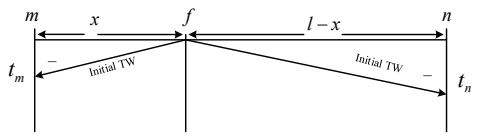


Fig. 2. Grid diagram of TW propagation for P-G fault

The fault location equation is,

$$x = \frac{l + v(t_m - t_n)}{2} \tag{3}$$

Where x is fault distance from point f to m-terminal, v is wave velocity, t_m is time when the initial fault TW reaches the m-terminal, and t_n is the time when it reaches the n-terminal.

Time synchronization is the key to achieving high-precision fault location [22]. This paper selects Global Positioning System (GPS) technology, which provides nanosecond-level time synchronization accuracy, meeting the stringent requirements of TW method.

III. Fault Location Method Based on CEEMD and HT

In fault location study, the sampled fault signal is analyzed. The existing EMD algorithm has problems such as mode mixing and endpoint effects. issues, this study proposes the CEEMD method combined with the HT. This method effectively resolves the mode mixing problem while offering improved noise robustness and higher frequency resolution.

A. Complementary Ensemble Empirical Mode Decomposition

Mode mixing is a common problem in EMD. Mode mixing leads to the decomposed IMFs failing to clearly reflect the physical characteristics of the signal. In fault location studies, this issue mainly manifests as difficulties in fault feature extraction and inaccurate frequency analysis. CEEMD is an improved method proposed to address this problem. Its basic idea is to add complementary Gaussian white noise to the original signal $x(t)$, then perform EMD. By repeating this process multiple times, the Intrinsic Mode Functions (IMF) obtained in each decomposition are averaged to produce the CEEMD result.

As shown in Fig. 3, it is the CEEMD decomposition process. The specific steps of this method are:

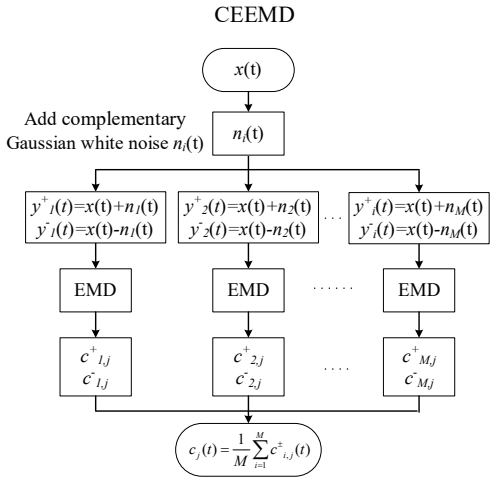


Fig. 3. Flowchart of CEEMD

(1) Add complementary Gaussian white noise to the analyzed signal $x(t)$, resulting in a new noisy signal $y^{\pm}_i(t)$:

$$y^{\pm}_i(t) = x(t) \pm n_i(t) \tag{4}$$

Where $n_i(t)$ is Gaussian white noise, i =1, 2, …, M.

(2) Perform EMD decomposition on $y^{\pm}_i(t)$ to obtain IMFs and the residual components:

$$y^{\pm}_i(t) = \sum_{j=1}^{J} c^{\pm}_{i,j}(t) + r^{\pm}_{i,j}(t) \tag{5}$$

Where $c^{\pm}_{i,j}(t)$ is the j-th IMF obtained after adding noise $n_i(t)$ for the i-th time, j=1, 2, …, J, and J is the total number of IMF components. $r^{\pm}_{i,j}(t)$ is the residual component.

(3) Repeat steps (1) and (2), adding complementary Gaussian white noise signals with different amplitudes each time, and finally obtain the IMF component set $c^{\pm}_{i,j}(t)$, i=1, 2, …, M, j=1, 2, …, J.

(4) Perform averaging on the IMF component set to obtain the IMF after CEEMD decomposition.

$$c_j(t) = \frac{1}{M}\sum_{i=1}^{M} c^{\pm}_{i,j}(t) \tag{6}$$

Where $c_{i,j}(t)$ are the IMFs obtained after CEEMD decomposition.

After these steps, the IMFs of CEEMD decomposition are obtained. Next, the IMFs are processed using Hilbert transform.

B. *Hilbert Transform*

The HT of a function $x(t)$ is expressed as

$$\hat{x}(t) = H\left[x(t)\right] = \frac{1}{\pi}\int_{-\infty}^{\infty} \frac{x(\tau)}{t-\tau} d\tau \tag{7}$$

The analytic signal of the function $x(t)$ is given by

$$z(t) = x(t) + j\hat{x}(t) = a(t)e^{j\phi(t)} \tag{8}$$

Where $a(t) = \sqrt{x^2(t) + \hat{x}^2(t)}$ is the instantaneous amplitude, $\phi(t) = arc\tan\left(\hat{x}(t)/x(t)\right)$ is the instantaneous phase.

The instantaneous frequency obtained from the HT is

$$f(t) = \frac{1}{2\pi}\frac{d(\theta)}{dt} \tag{9}$$

C. *Fault Location Method*

This paper proposes the use of the CEEMD method to decompose the fault signals, then applying the HT to the decomposed IMFs to obtain the instantaneous amplitude and instantaneous frequency. Finally, the fault time is identified by detecting the mutation point of the high-frequency signal for fault location. Fig. 4, is the flowchart.

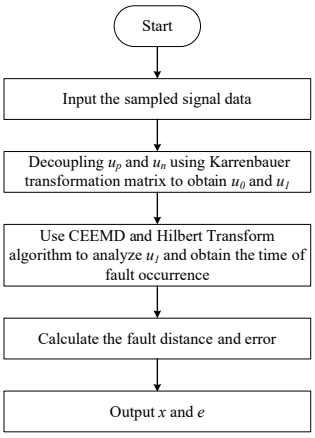


Fig. 4. Flowchart

The operation steps of the proposed method are:

(1) Establish a simulation model and set a fault in the transmission line. Sample the fault voltage in real time.

(2) Use the Karrenbauer transform to decompose the fault voltage.

(3) Use CEEMD to decompose the line-mode voltage into a series of IMFs. As shown in Fig. 4, IMF1 and IMF2 contain a significant amount of high-frequency fault components, but IMF1 also contains more noise signals. Therefore, this paper selects IMF2 for HT to calculate its instantaneous frequency and instantaneous amplitude.

(4) Identify the fault time by detecting the mutation point in the instantaneous frequency. The fault distance is then calculated, and finally, the location error is obtained.

The location error formula is

$$e = \frac{|x-d|}{l}\cdot 100\% \tag{10}$$

Where d is actual value, x is calculated value, and l is the transmission line length.

In Fig. 5, the instantaneous frequency curve of the fault voltage collected from the transmission line is calculated by the proposed method. When locating the fault, the fault occurrence time can be identified by the calculated frequency mutation point to complete the fault location.

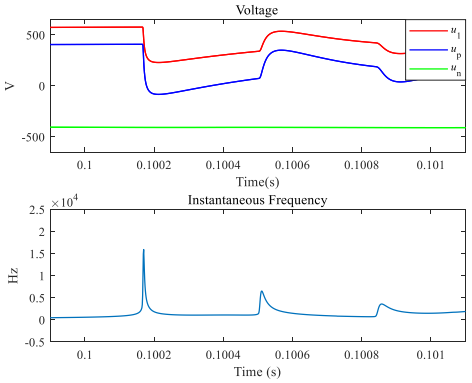


Fig. 5. Instantaneous frequency

IV. Simulation Analysis

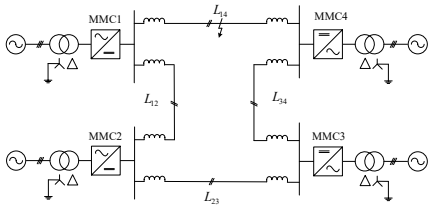


Fig. 6. Single-line diagram of MMC-HVDC system

TABLE I. GRID PARAMETERS

Parameters	MMC1	MMC2	MMC3	MMC4
DC voltage (kV)	±400	±400	±400	±400
Rated power (MW)	750	750	1000	1500
Control mode	P-Q	P-Q	V-Q	P-Q
Bridge arm reactor (mH)	50	50	50	50
SM capacitor (mF)	3	3	3	3
SM number	200	200	200	200

To validate the accuracy, a simulation system model built using PSCAD/EMTDC. Fig. 6 presents the single-line diagram of the simulation system, which is a bipolar MMC-HVDC grid with a voltage level of ±400 kV. Table 1 shows the main parameters of the grid. The current-limiting inductor is set to 100mH. To better analyze fault characteristics, select the frequency-dependent overhead line. The converter adopts a half-bridge sub-module. The simulation model analyzes the effects of fault distance, fault resistance, and noise on the proposed method.

A. *Impact of Fault Distance*

To validate the impact of fault distance on this method, L_{14} is selected for analysis, with a length of 200 km. Faults are set at points of different lengths on the transmission line for verification. The paper analyzes a P-G fault and a P-N fault with a fault resistance of 100Ω, and the fault signal sampling frequency is 1 MHz. Fig.7 shows a set of data calculated for a fault located at 75 km. These are the instantaneous frequencies at both ends of the line. The fault distance is calculated using the mutation points of the frequency. Fig. 8 shows the error for both different cases. The results show that this method provides excellent accuracy at different distances, the maximum error is 0.395%, occurring in the P-G fault near the MMC4. At the bus measurement point near the fault, the identification of the initial wavefront will be interfered by the reflected wavefront. At the bus measurement point far from the fault, the signal attenuation is obvious, which makes the characteristics of the TW signal weaker and increases the difficulty of fault location. These factors can impact wavefront identification. However, the proposed method has high frequency resolution, allowing accurate identification of the fault signal and maintaining good fault location performance. This is because CEEMD can significantly reduce the impact of noise on the decomposition results and obtain more accurate intrinsic mode functions by decomposing multiple times and applying complementary weighting to the results.

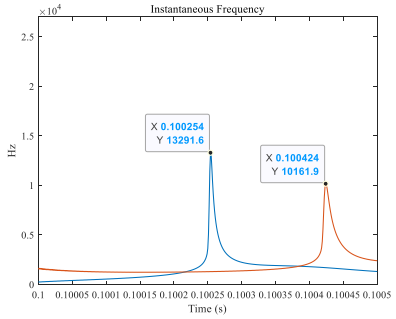


Fig. 7. Instantaneous frequency

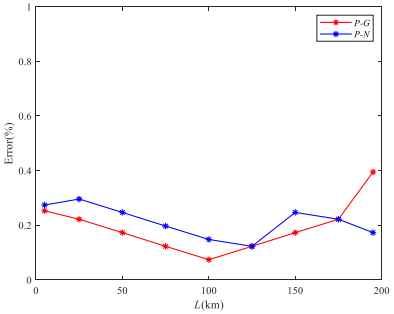


Fig. 8. Impact of fault distance

B. *Impact of Fault Resistance*

To analyze the impact of fault resistance R_f on the proposed fault location method, P-G and P-N faults are set at 100 km and 150 km along L_{14} for analysis. Fig. 9 shows two sets of data, which are the instantaneous frequencies calculated for P-G and P-N faults at 75km. The proposed method is applicable to different fault types. Fig. 10, the results for P-G fault. Fig. 11, the results for P-N fault. It can be seen that the proposed method provides good fault location results under various fault resistances. This method is robust to high fault resistance and maintains high accuracy even for a 500Ω P-G fault. This enhances the applicability of the proposed method. However, as its value increases, the attenuation of the TW becomes more serious, causing the signal to become weaker and the wavefront of the TW to be difficult to detect. Especially at the measurement point far from the fault point, where the signal's energy further decreases, increasing the difficulty of detection. However, the proposed method has a high frequency resolution, ensuring consistently high fault location accuracy.

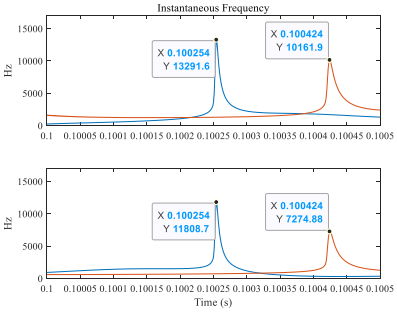


Fig. 9. Instantaneous frequency

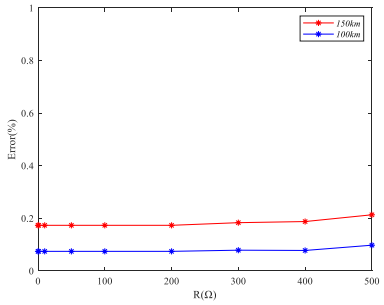


Fig. 10. Impact on P-G

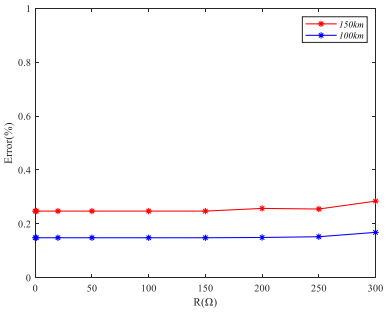


Fig. 11. Impact on P-N

C. *Impact of Noise Interference*

The MMC-HVDC grid contains numerous power electronic devices, which increases the switching frequency of the devices and enhances the rapid response capability of the system, but also brings noise interference. In particular, high-frequency noise will mixing with the fault signal, making it difficult to accurately extract the fault characteristics. This problem is more serious in the method using EMD. The proposed method uses CEEMD to perfectly solve this problem. Verify the anti-noise ability of this method, the sampled fault voltage is added with different degrees of Gaussian white noise for analysis. The signal-to-noise ratio (SNR) is an indicator of signal quality and is defined as

$$SNR = 20\lg\left(\frac{Vs}{Vn}\right) \tag{11}$$

Where Vs is signal voltage and Vn is voltage containing noise.

According to the international standard IEEE 519, the permissible harmonic distortion for HVDC systems is usually controlled at around 1%-3%, and the SNR is greater than 30dB. In MMC-HVDC systems, voltage noise is usually controlled at around 1%-2% of the rated voltage of the system. Based on the above standards, this paper adds 50dB, 30dB and 20dB Gaussian white noise to the collected signals for fault location analysis. Multiple groups of different fault types are set at different distances of the transmission line for simulation verification. As shown in Table 2, the results indicate that this still provides good fault location results even under 20dB noise conditions. This is because this method has strong noise robustness, resulting in strong anti-noise ability. However, in simulation analysis, as the noise level increases, identifying the TW fronts becomes more challenging. The anti-noise ability of the proposed method meets the requirements of practical engineering applications.

TABLE II.. RESULTS AT DIFFERENT SNRS

Fault type	Error (%)			
	Normal	50dB	30dB	20dB
50kmP-N	0.098	0.148	0.198	0.247
50kmP-G	0.074	0.099	0.173	0.198
100kmP-N	0.148	0.148	0.247	0.247
100kmP-G	0.074	0.047	0.247	0.297

D. *Comparative Analysis*

To demonstrate the advantages of the proposed method, a comparison is made with other existing methods. Several representative methods from the references are selected for comparison, focusing on noise resistance, fault resistance tolerance, and location accuracy. Table 3 shows the comparison results. The average error is 0.176%, which is smaller than that of the comparison methods. It has excellent performance in location accuracy. The anti-noise ability is also higher than that of the comparison methods, and the fault can be accurately located under 20dB noise interference. It is especially better than the EMD based methods in references [18] and [22]. This is because EMD decomposition has the problem of modal mixing. Under noise interference, EMD decomposition may mistakenly decompose noise into the mode of the fault signal, affecting the accuracy of fault location. The CEEMD used in this paper solves these issues. The proposed method can tolerate a high fault resistance of 500Ω while also accounting for cases where the fault resistance is zero, outperforming the other methods in the comparison. Through the above comparisons, concluded that the proposed method offers significant advantages in fault location research of MMC-HVDC grids.

TABLE III. COMPARISON OF DIFFERENT METHODS

Method	e (%)	SNR (dB)	R_f (Ω)
Proposed	0.176	20	500
Reference [1]	0.57	55	150
Reference [12]	0.67	/	300
Reference [17]	0.50	/	100
Reference [18]	0.18	50	300
Reference [22]	0.52	/	300

V. CONCLUSION

This paper proposes a novel MMC-HVDC grid TW fault location method based on CEEMD and HT. This method has excellent performance under various fault conditions. The conclusions are:

1) The proposed method has excellent time-frequency analysis capabilities and addresses issues such as mode mixing, endpoint effects, and insufficient result stability. It can accurately extract fault signals.

2) To avoid the issue of bipolar coupling, the proposed method applies the Karrenbauer transform to the sampled voltage. Then, stable line-mode voltages are selected for analysis and research.

3) The proposed method incorporates CEEMD and HT, which offer high frequency resolution and good noise robustness. It can accurately identify the fault TW wavefront, providing high

fault location accuracy. Additionally, it exhibits strong anti-noise ability, maintaining accurate fault location even with a SNR of 20 dB. This method only requires the fault voltage signals sampled at the line terminals, does not require additional equipment, and can tolerate 500Ω fault resistance, making it highly valuable for practical engineering applications.

REFERENCES

[1] Farshad, M., 'Fault Location in Hvdc Grids Equipped with Quick-Action Protections and Circuit Breakers Based on Voltage Transient Response', *Ieee Transactions on Industrial Electronics*, 2021, 68, (12), pp. 12881-12889.

[2] Wang, B.L., Liu, Y., Lu, D.Y., Yue, K., and Fan, R., 'Transmission Line Fault Location in Mmc-Hvdc Grids Based on Dynamic State Estimation and Gradient Descent', *Ieee Transactions on Power Delivery*, 2021, 36, (3), pp. 1714-1725.

[3] Gao, S.P., Song, X.C., Ye, H.F., Jiang, L., and Song, G.B., 'Transient Energy Protection Based on Wavelet Packet Transform for Hybrid Bipolar Hvdc Transmission System', *Iet Generation Transmission & Distribution*, 2021, 15, (12), pp. 1775-1786.

[4] Wan, Y.H., Mao, M.X., Zhou, L., Xi, X.Z., Xie, B., and Zhou, S.Y., 'Review on Topology-Based Dc Short-Circuit Fault Ride-through Strategies for Mmc-Based Hvdc System', *IET Power Electronics*, 2020, 13, (2), pp. 203-220.

[5] Adam, G.P., Vrana, T.K., Li, R., Li, P., Burt, G., and Finney, S., 'Review of Technologies for Dc Grids – Power Conversion, Flow Control and Protection', *IET Power Electronics*, 2019, 12, (8), pp. 1851-1867.

[6] Bi, T.S., Wang, S., and Jia, K., 'Single Pole-to-Ground Fault Location Method for Mmc-Hvdc System Using Active Pulse', *Iet Generation Transmission & Distribution*, 2018, 12, (2), pp. 272-278.

[7] Farshad, M., 'A Pilot Protection Scheme for Transmission Lines of Half-Bridge Mmc-Hvdc Grids Using Cosine Distance Criterion', *Ieee Transactions on Power Delivery*, 2021, 36, (2), pp. 1089-1096.

[8] Döring, D., Würflinger, K., Staudt, V., Zeller, M., and Ebner, G., 'Interactions between a Half-Bridge Mmc and a Hybrid Dc Breaker During Fault Current Interruption Compared to a Full-Bridge Mmc', *IET Power Electronics*, 2020, 13, (18), pp. 4168-4175.

[9] Muzzammel, R., Raza, A., Hussain, M.R., Abbas, G., Ahmed, I., Qayyum, M., Rasool, M.A., and Khaleel, M.A., 'Mt-Hvdc Systems Fault Classification and Location Methods Based on Traveling and Non-Traveling Waves-a Comprehensive Review', *Applied Sciences-Basel*, 2019, 9, (22).

[10] Wang, J., Zhang, Y.X., and Li, T., 'Equivalent Characteristic Impedance Based Hybrid-Hvdc Transmission Line Fault Location', *Electric Power Systems Research*, 2021, 194.

[11] Luo, G.M., Cheng, M.X., Hei, J.X., Wang, X.J., Huang, W.B., and He, J.H., 'Stacked Denoising Autoencoder Based Fault Location in Voltage Source Converters-High Voltage Direct Current', *Iet Generation Transmission & Distribution*, 2021, 15, (9), pp. 1474-1485.

[12] Chen, W., Wang, D., Cheng, D., and Liu, X., 'Travelling Wave Fault Location Approach for Mmc-Hvdc Transmission Line Based on Frequency Modification Algorithm', *International Journal of Electrical Power & Energy Systems*, 2022, 143.

[13] Tang, T., Li, X.H., Zeng, X.J., Zhou, Y., Yuan, K.J., and Bi, L.X., 'Accurate Detection Method of Traveling Wave Shape Based on Eemd and L1 Norm Regularization', *International Journal of Electrical Power & Energy Systems*, 2024, 159.

[14] Wang, D., Fu, J.H., Hou, M.Q., Qiao, F., and Gao, M.Y., 'Novel Travelling Wave Fault Location Principle for Vsc-Hvdc Transmission Line', *Electric Power Systems Research*, 2021, 196.

[15] Li, M., Chen, K., He, J.H., Tang, Y., and Tang, J., 'Impedance Phase Based Active Injection Protection for Radial Vsc-Hvdc Grid', *Ieee Transactions on Power Delivery*, 2023, 38, (3), pp. 1621-1635.

[16] Kazmi, S.T.H., Song, G.B., and Hou, J.J., 'Time-Normalized Voltage Gradient Protection for Fault Detection in Mmc-Hvdc Grids', *International Journal of Electrical Power & Energy Systems*, 2024, 157.

[17] Wang, J. and Zhang, Y., 'Traveling Wave Propagation Characteristic-Based Lcc-Mmc Hybrid Hvdc Transmission Line Fault Location Method', *Ieee Transactions on Power Delivery*, 2022, 37, (1), pp. 208-218.

[18] Zhu, X.G., Li, S.R., Guo, Y.B., Chen, X.H., He, C.Y., and Deng, J.B., 'Novel Wavefront Detection and Fault Location Method Based on Hilbert-Huang Transform for Long Hvdc Transmission Lines', *Electric Power Systems Research*, 2022, 211.

[19] Farshad, M. and Karimi, M., 'A Signal Segmentation Approach to Identify Incident/Reflected Traveling Waves for Fault Location in Half-Bridge Mmc-Hvdc Grids', *Ieee Transactions on Instrumentation and Measurement*, 2022, 71.

[20] Zhang, C.H., Song, G.B., Wang, T., Wu, L., and Yang, L.M., 'Non-Unit Traveling Wave Protection of Hvdc Grids Using Levenberg-Marquart Optimal Approximation', *Ieee Transactions on Power Delivery*, 2020, 35, (5), pp. 2260-2271.

[21] Zhang, C., Song, G., Wang, T., and Dong, X., 'An Improved Non-Unit Traveling Wave Protection Method with Adaptive Threshold Value and Its Application in Hvdc Grids', *Ieee Transactions on Power Delivery*, 2020, 35, (4), pp. 1800-1811.

[22] Wang, D. and Hou, M.Q., 'Travelling Wave Fault Location Algorithm for Lcc-Mmc-Mtdc Hybrid Transmission System Based on Hilbert-Huang Transform', *International Journal of Electrical Power & Energy Systems*, 2020, 121.

Transient Fault Analysis of Renewable Energy DC Collection and Transmission System with High-Voltage DC-DC Converters

Dazhen Xu
Shanghai JiaoTong University
College of smart energy
Shanghai, China
dazhen01@sjtu.edu.cn

Zhibo Zhang
China ElectricPower Research Institute
State Key Laboratory of Advanced Power Transmission Technology
Beijing, China
zhangzhibo@epri.sgcc.com.cn

Zhiguang Lin
China ElectricPower Research Institute
State Key Laboratory of Advanced Power Transmission Technology
Beijing, China
linzhiguang@epri.sgcc.com.cn

Jianjun Ma
Shanghai JiaoTong University
College of smart energy
Shanghai, China
j.j.ma@sjtu.edu.cn

Miao Zhu
Shanghai JiaoTong University
School of Electrical Engineering
Shanghai, China
miaozhu@sjtu.edu.cn

***Abstract*—This paper develops a transient fault current calculation method for renewable energy DC collection and transmission system. Fault transient equivalent circuits are established for critical power electronic devices and the whole system under typical fault locations. System matrix differential equations are formulated to enable accurate current computation. Comparison with MATLAB/Simulink simulations validates the effectiveness of the purposed method.**

Keywords—Fault Analysis, DC Collection and Transmission System, High-Voltage DC-DC Converter

I. INTRODUCTION

DC-based renewable energy collection and transmission technology serves as a critical solution for building secure and efficient power transmission and distribution systems[1]-[2]. By using high-voltage DC-DC converters, medium-voltage DC networks can directly aggregate the DC output energy from renewable energy stations and boost the voltage levels for HVDC transmission. This approach enables long-distance power delivery while significantly enhancing overall system efficiency. Such system configurations are particularly suitable for large-scale renewable energy integration and transmission applications[3]-[4].

Fault characteristics of renewable energy DC collection and transmission systems with high-voltage DC-DC converters remain unclear, which involve critical DC overcurrent and overvoltage issues[5]-[6]. This highlights the urgent need for systematic investigation into the fault characteristics of such high-voltage DC-DC converter-based renewable energy collection and transmission systems[7], which forms the essential foundation for the design of system parameters[8] and protection methods[9]-[10].

To address the aforementioned challenges, this paper firstly establishes the fault transient equivalent circuits for critical system equipment. Then, fault transient equivalent circuits for the studied renewable energy DC collection and transmission System under typical fault conditions are established. After that, by formulating matrix differential equations, the transient fault current in the system are calculated. Finally, the calculation results are compared with MATLAB/Simulink simulation results to validate the effectiveness of the proposed transient fault current calculation method.

II. SIMPLIFIED EQUIVALENT CIRCUIT OF CRITICAL EQUIPMENTS

The topology of renewable energy DC collection and transmission system studied in this paper is as shown in Fig. 1. The system consists of two 300MW wind power stations and their AC output Port-Connected 35/200kV Modular Multilevel Converters (MMC), two clusters of 8-units photovoltaic 5MW power stations with isolated DAB converters, connected to two 50/200kV high-voltage DC-DC converters. The High-Voltage transmission system consists of a 200/500kV, 1000MW high-voltage DC-DC converter and a 500kV, 1000MW MMC connects to the AC grid. Labels ①-③ indicate typical fault locations in the system.

This work was supported by the Science and Technology Project of State Grid Corporation (Small-signal stability and fault characteristic study of renewable energy DC networking and transmission system with high voltage DC-DC converter) (5100-202358413A-3-2-ZN).

979-8-3315-5472-9/25/$31.00 ©2025 IEEE

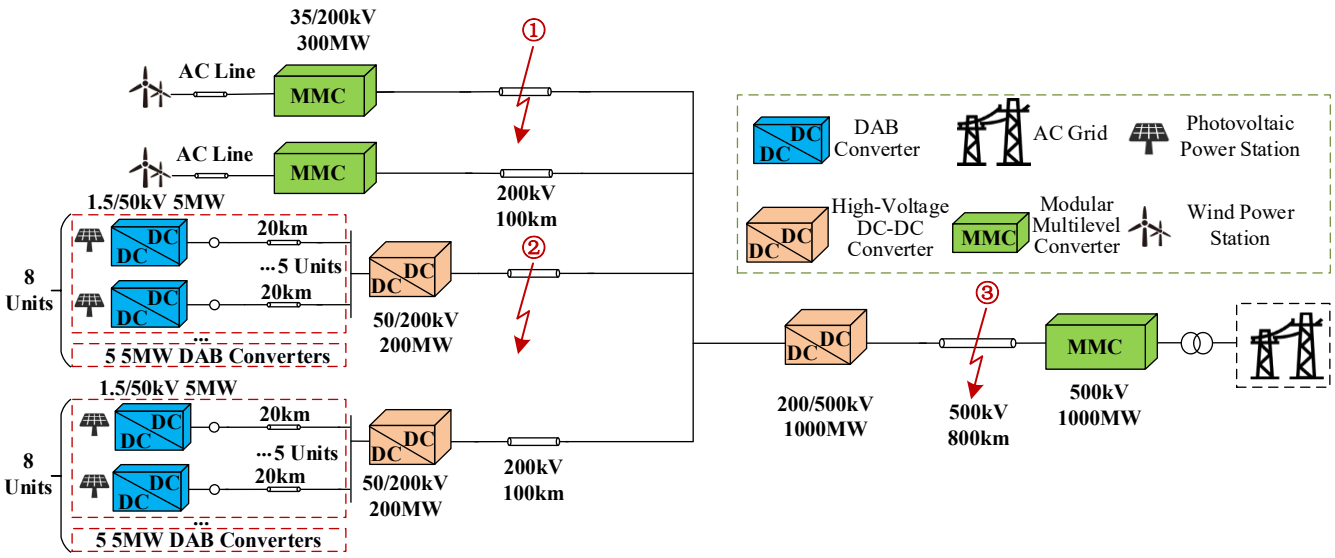


Fig. 1. Topology of renewable energy DC collection and transmission system

A. *Topology of renewable energy DC collection and transmission system*

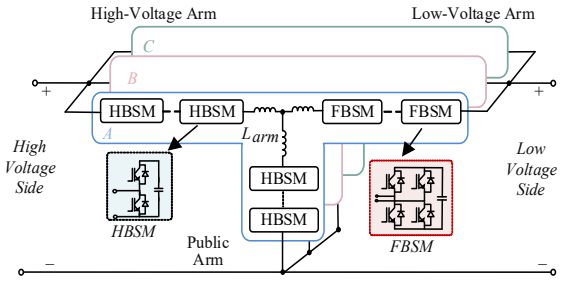
The topology of High-voltage DC-DC converter is as shown in Fig. 2(a). Each arm contains a string of SMs and an inductor L_{arm} in series connection. The High-voltage arms and Public-voltage arms are configured with half bridge sub-modules (HBSM), and the Low-voltage arms are configured with full bridge sub-modules (FBSM).

The fault transient equivalent circuit of High-voltage DC-DC converter is as shown in Fig. 2(b) and Fig. 2(c). In Fig. 2(b), the equivalent capacitor and resistor R_i, C_i (i=H/ W/ L) can be derived through Equation (1):

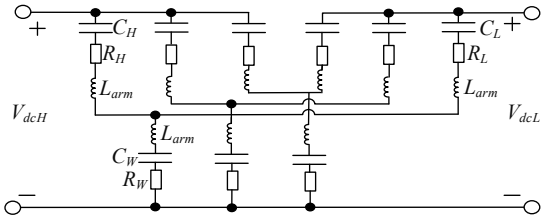
$$C_i = C_{SM} / N_i ; R_i = R_{SM} N_i \quad (i = H, W, L) \tag{1}$$

In Equation (1), N_i denotes the number of inserted submodule in a phase arm. To further simplify the equivalent circuit, Considering the dominant DC Components in three phase bridge arms are identical, the 3 phase fault transient equivalent circuit can be further simplified into one phase, as shown in Fig. 2(c), the equivalent capacitor, resistor and inductor $C_{i,eq}$, $R_{i,eq}$ and $L_{i,eq}$ (i=H/ W/ L) can be derived through Equation (2):

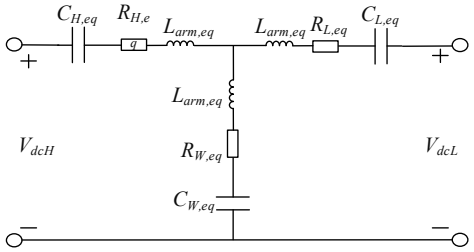
$$C_{i,eq} = C_i / 3;\ L_{arm,eq} = 3L_{arm};\ R_{i,eq} = 3L_i \quad (i = H, W, L) \tag{2}$$



(a) Topology of High-voltage DC-DC converter



(b) 3 Phase Transient Equivalent Circuit



(c) Single Phase Transient Equivalent Circuit

Fig. 2. Fault Transient Equivalent Circuit of High-voltage DC-DC converter.

B. *Fault Transient Equivalent Circuits of MMC and DAB converter*

During DC-side fault, the MMC submodule capacitors discharge rapidly toward the fault location before the converter is blocked. The DC fault current characteristics during this stage are predominantly governed by two components: the capacitive discharge current from submodules and the AC system feed-in current. This behavior can be effectively modeled as an equivalent circuit consisting of an RLC series network representing the discharge path, in parallel with a current source accounting for the AC grid contribution, as depicted in Fig. 3.

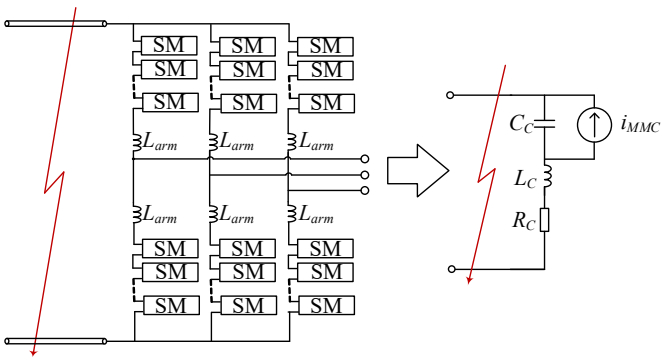


Fig. 3. Fault Transient Equivalent Circuit of High-voltage DC-DC converter

The parameters RC, LC, and CC are the equivalent resistance, inductance, and capacitance of the MMC series circuit equivalent circuit respectively. During the post-fault pre-blocking period, the values of the parameters are given by Equation (3), where N_{ON} denotes the number of inserted submodule.

$$\begin{cases} R_C = \dfrac{2}{3} N_{ON} R_{SM} \\ L_C = \dfrac{2}{3} L_{arm} \\ C_C = \dfrac{6}{N_{ON}} C_{SM} \end{cases} \tag{3}$$

The external transient equivalent circuit of the DAB converter during fault transients is shown in Fig. 4, where C_{DAB} denotes the DC filter capacitance at the output port, and i_{DAB} denotes the fault current injected through the high-frequency transformer from the renewable energy station.

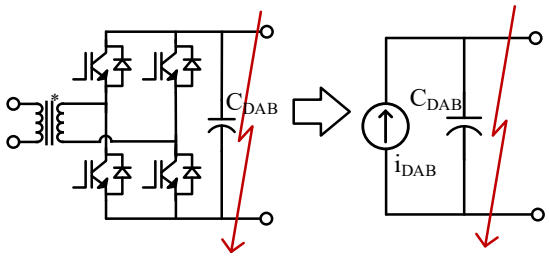


Fig. 4. Fault Transient Equivalent Circuit of DAB converter

III. System Matrix Differential Equations

This paper employs a short-circuit current calculation method based on modified network matrix equations. Take fault number ① in Fig. 1 as an example, the system fault transistant equivalent circuit is as shown in Fig. 5, where n_1-n_9 denotes circuit nodes, including the interconnection node of three-phase bridge arms n_5,n_6 and n_8. L_{line} and R_{line} denotes the inductance and resistance of 200kV/100km transmission line, while L_{line} and R_{line} denotes the inductance and resistance of 500kV/800km transmission line. n_0 denotes the fault location and x denotes the fault distance from DC bus n_7 to n_0. The expressions for R_{01}, L_{01}, R_{70}, and L_{70} after fault occurrence are given by equation (4).

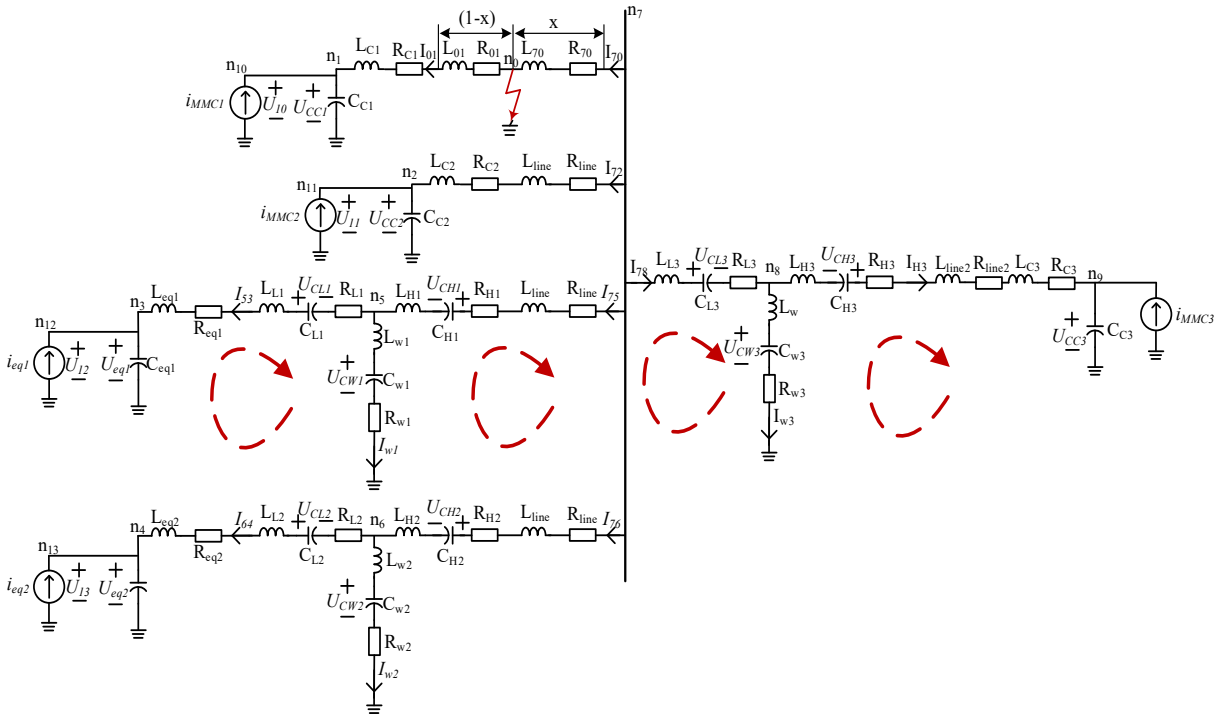


Fig. 5. Fault Transient Equivalent Circuit of Renewable Energy DC Collection and Transmission System

$$\begin{cases} R_{70} = xR_{line} \\ L_{70} = xL_{line} \\ R_{01} = (1-x)R_{line} \\ L_{01} = (1-x)L_{line} \end{cases} \tag{4}$$

The equivalent capacitance C_{eq1}, inductance L_{eq1}, and resistance R_{eq1} can be calculated by equation (5), where L_n and R_n are the inductance and resistance of 20km DC transmission line of one photovoltaic power station.

$$\begin{cases} C_{eq1} = 40C_{DAB} \\ L_{eq1} = L_n / 40 \\ R_{eq1} = R_n / 40 \end{cases} \tag{5}$$

After the fault occurs, an additional loop voltage equation can be formulated for the faulted line L_{01}, as shown in equation (6):

$$\begin{aligned} U_{CC1} &= -L_{C1}\frac{di_{01}}{dt} - R_{C1}i_{01} - L_{01}\frac{di_{01}}{dt} - R_{01}i_{01} - R_n(i_{01} - i_{70}) \\ &= -(L_{C1} + L_{01})\frac{di_{01}}{dt} - (R_{C1} + R_{01} + R_n)i_{01} + R_n i_{70} \end{aligned} \tag{6}$$

The loop voltage equation for the faulted line L_{70} can be formulated as shown in equation (7).

$$\begin{aligned} &-U_{CL3} - U_{CW3} \\ &= -L_{70}\frac{di_{70}}{dt} - R_n(i_{70} - i_{01}) - R_{70}i_{70} + L_{L3}\frac{d(-i_{70} - i_{72} - i_{75} - i_{76})}{dt} \\ &+ R_{L3}(-i_{70} - i_{72} - i_{75} - i_{76}) + L_W\frac{di_{W3}}{dt} + R_{W3}i_{W3} \end{aligned} \tag{7}$$

The voltage equation for the non-fault loop GND-n_2-n_7-n_8-GND is given by equation (8). By applying the same method, voltage differential equations as shown in can be formulated for each current loops in Fig. 5, system matrix differential equations can be derived, as shown in equation (9).

$$\begin{aligned} &U_{CC2} - U_{CL3} - U_{CW3} \\ &= -L_{C2}\frac{di_{72}}{dt} - R_{C2}i_{72} - L_{line}\frac{di_{72}}{dt} - R_{line}I_{72} \\ &+ L_{L3}\frac{di_{78}}{dt} + R_{L3}i_{78} + L_W\frac{di_{W3}}{dt} + R_{W3}i_{W3} \end{aligned} \tag{8}$$

$$\begin{cases} A_1U_1 = R_1I_1 + L_1I_1' \\ U_1' = C_1I_1 + C_SI_S \end{cases} \tag{9}$$

In equation (9), the system current matrix I_1 and voltage matrix are defined as shown in equation (10)-(11).

$$I_1 = [i_{01}\ i_{70}\ i_{72}\ i_{53}\ i_{64}\ i_{75}\ i_{76}\ i_{W3}]^T \tag{10}$$

$$\begin{aligned} U_1 = [&U_{CC1}\ U_{CC2}\ U_{eq1}\ U_{eq2}\ U_{CL1}\ U_{CW1}\ U_{CH1} \\ &U_{CL2}\ U_{CW2}\ U_{CH2}\ U_{CL3}\ U_{CW3}\ U_{CH3}\ U_{dcH}]^T \end{aligned} \tag{11}$$

According to equation (9)-(11) and the differential equations formulating methods, the system resistance matrix R_1, inductance matrix L_1, incidence matrix A_1, capacitance matrix C_1, and current source vector I_s can be derived as shown in equation (12)-(16):

$$R_1 = \begin{bmatrix} -(R_{C1}+R_{01}+R_n) & R_n & 0 & 0 & 0 & 0 & 0 & 0 \\ R_n & -(R_{70}+R_n+R_{L3}) & -R_{L3} & 0 & 0 & -R_{L3} & -R_{L3} & R_{W3} \\ 0 & -R_{L3} & -(R_{C2}+R_{line}+R_{L3}) & 0 & 0 & -R_{L3} & -R_{L3} & R_{W3} \\ 0 & 0 & 0 & -(R_{eq1}+R_{L1}+R_{W1}) & 0 & R_{W1} & 0 & 0 \\ 0 & 0 & 0 & 0 & -(R_{eq2}+R_{L2}+R_{W2}) & 0 & R_{W2} & 0 \\ 0 & -R_{L3} & -R_{L3} & R_{W1} & 0 & (-R_{L3}-R_{line}-R_{W1}-R_{H1}) & -R_{L3} & R_{W3} \\ 0 & -R_{L3} & -R_{L3} & 0 & R_{W1} & -R_{L3} & (-R_{L3}-R_{line}-R_{W1}-R_{H1}) & R_{W3} \\ 0 & -(R_{H3}+R_{C3}+R_{line2}) & -(R_{H3}+R_{C3}+R_{line2}) & 0 & 0 & -(R_{H3}+R_{C3}+R_{line2}) & (R_{H3}+R_{C3}+R_{line2}) & -(R_{W3}+R_{H3}+R_{C3}+R_{line2}) \end{bmatrix} \tag{12}$$

$$L_1 = \begin{bmatrix} -(L_{C1}+L_{01}) & 0 & 0 & 0 & 0 & 0 & 0 & 0 \\ 0 & -(L_{70}+L_{L3}) & -L_{L3} & 0 & 0 & -L_{L3} & -L_{L3} & L_{W3} \\ 0 & -R_{L3} & -(L_{C2}+L_{line}+L_{L3}) & 0 & 0 & -L_{L3} & -L_{L3} & L_{W3} \\ 0 & 0 & 0 & -(L_{eq1}+L_{L1}+L_{W1}) & 0 & L_{W1} & 0 & 0 \\ 0 & 0 & 0 & 0 & -(L_{eq2}+L_{L2}+L_{W2}) & 0 & L_{W2} & 0 \\ 0 & -L_{L3} & -L_{L3} & L_{W1} & 0 & (-L_{L3}-L_{line}-L_{W1}-L_{H1}) & -L_{L3} & L_{W3} \\ 0 & -L_{L3} & -L_{L3} & 0 & L_{W1} & -L_{L3} & (-L_{L3}-L_{line}-L_{W1}-L_{H1}) & L_{W3} \\ 0 & -(L_{H3}+L_{C3}+L_{line2}) & -(L_{H3}+L_{C3}+L_{line2}) & 0 & 0 & -(L_{H3}+L_{C3}+L_{line2}) & (L_{H3}+L_{C3}+L_{line2}) & -(L_{W3}+L_{H3}+L_{C3}+L_{line2}) \end{bmatrix} \tag{13}$$

$$A_1 = \begin{bmatrix} 1\,0\,0\,0\,0\,0\,0\,0\,0\,0 & 0 & 0 & 0\,0 \\ 0\,0\,0\,0\,0\,0\,0\,0\,0\,0 & -1 & -1 & 0\,0 \\ 0\,1\,0\,0\,0\,0\,0\,0\,0\,0 & -1 & -1 & 0\,0 \\ 0\,0\,1\,0 & -1 & -1 & 0\,0\,0\,0\,0\,0\,0\,0 \\ 0\,0\,0\,1\,0\,0\,0 & -1 & -1 & 0\,0\,0\,0\,0 \\ 0\,0\,0\,0\,0\,1\,1\,0\,0\,0 & -1 & -1 & 0\,0 \\ 0\,0\,0\,0\,0\,0\,0\,0\,1\,1 & -1 & -1 & 0\,0 \\ 0\,0\,0\,0\,0\,0\,0\,0\,0\,0 & 0 & 1 & 1\,-1 \end{bmatrix} \tag{14}$$

$$C_S = \begin{bmatrix} 1/C_{C1} & 0\,0\,0 \\ 0\;1/C_{C2} & 0\,0 \\ 0\,0\;1/C_{eq1} & 0 \\ 0\,0\,0\;1/C_{eq2} & \\ [10\times 4\ \text{Zero Matrix}] & \end{bmatrix} \tag{15}$$

$$C_1 = \begin{bmatrix} 1/C_{C1} & 0\,0\,0\,0\,0\,0\,0 \\ 0\,0\;1/C_{C2} & 0\,0\,0\,0\,0 \\ 0\,0\,0\;1/C_{eq1} & 0\,0\,0\,0 \\ 0\,0\,0\,0\;1/C_{eq2} & 0\,0\,0 \\ 0\,0\,0\;-1/C_{L1} & 0\,0\,0\,0 \\ 0\,0\,0\;-1/C_{W1} & 0\;1/C_{W1} & 0\,0 \\ 0\,0\,0\,0\,0\;1/C_{H1} & 0\,0 \\ 0\,0\,0\,0\;-1/C_{L2} & 0\,0\,0 \\ 0\,0\,0\,0\;-1/C_{W2} & 0\;1/C_{W2} & 0 \\ 0\,0\,0\,0\,0\,0\;1/C_{H2} & 0 \\ 0\;-1/C_{L3} & -1/C_{L3} & 0\,0\;-1/C_{L3} & -1/C_{L3} & 0 \\ 0\,0\,0\,0\,0\,0\,0\;1/C_{W3} & \\ 0\;1/C_{H3} & 1/C_{H3} & 0\,0\;1/C_{H3} & 1/C_{H3} & 1/C_{H3} \\ 0\;-1/C_{C3} & -1/C_{C3} & 0\,0\;-1/C_{C3} & -1/C_{C3} & -1/C_{C3} \end{bmatrix} \tag{16}$$

IV. Simulation Validation

To validate the effectiveness of the proposed transient fault current calculation method, a MATLAB-Simulink model of the renewable energy DC collection and transmission system as shown in Fig. 1 is established.

TABLE I. Voltage/Current Matrix Initial Values

U_{CC1}	U_{CC2}	U_{eq1}	U_{eq2}
200kV	200kV	50kV	50kV
U_{CL1}	U_{CW1}	U_{CH1}	U_{CL2}
10kV	40kV	160kV	10kV
U_{CW2}	U_{CH2}	U_{CL3}	U_{CW3}
40kV	160kV	90kV	110kV
U_{CH3}	U_{dcH}		
390kV	500kV		
i_{71}	i_{72}	i_{53}	i_{64}
-1500A	-1500A	-4000A	-4000A
i_{75}	i_{76}	i_{W3}	
-1000A	-1000A	3000A	

The simulated fault currents (i_{01}, i_{70}, i_{w3}, i_{53} and i_{75}) are compared with their calculated results in Fig. 6, where i_{01}_Cal, i_{70}_Cal, i_{53}_Cal, i_{w3}_Cal, and i_{75}_Cal are the calculated fault currents, and i_{01}_Sim, i_{70}_Sim, i_{53}_Sim, i_{w3}_Sim, and i_{75}_Sim denote the simulated values. The initial values of voltage matrix U_1 and current matrix I_1 are as shown in TABLE I.

For the fault currents i_{01} and i_{70} injected from both sides of the fault point, the calculation errors during the first 10 ms after fault occurrence are 8.94% and 2.71% respectively, increasing to 16.2% and 8.39% within the first 20 ms.

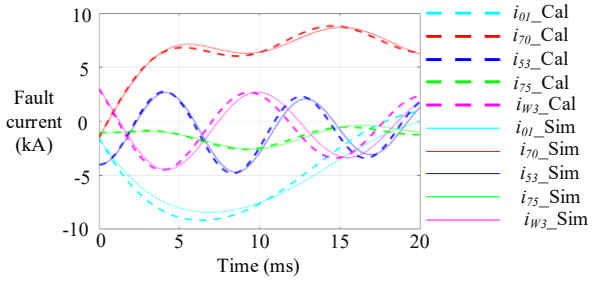


Fig. 6. Fault current calculation and simulation comparision during fault①

When fault number ② shown in Fig. 1 occurs, the comparison between fault current calculation results based on matrix differential equations and MATLAB-Simulink simulation results is as shown in Fig. 7.

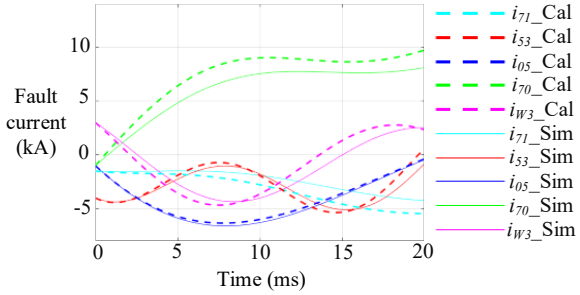


Fig. 7. Fault current calculation and simulation comparision during fault②

In Fig. 7, i_{71}_Cal, i_{53}_Cal, i_{05}_Cal, i_{70}_Cal, and i_{w3}_Cal represent the calculated values of fault currents, while i_{71}_Sim, i_{53}_Sim, i_{05}_Sim, i_{70}_Sim, and i_{w3}_Sim denote the simulated values. For the fault currents i_{05} and i_{70} injected from both sides of the fault location, the calculation errors during the initial 10 ms post-fault are 4.4% and 10.1% respectively, increasing to 7.9% and 12.5% within the first 20 ms.

The error stems from approximating the system as a linear circuit during fault current calculation, while actual circuit nonlinearities become increasingly significant with prolonged fault duration.

V. Conclusion

This paper proposes a transient fault analysis method for renewable energy DC collection and transmission system with high-voltage DC-DC converters. The proposed method is based on fault transient equivalent circuit and system matrix differential equations. The proposed method achieves a fault current calculation accuracy over 90% in 10 ms.

Future work: Future works include incorporating converter protection schemes into system modeling and matrix differential equations construction to achieve more accurate and engineering-practical fault analysis.

REFERENCES

[1] B. Li, J. Liu, Z. Wang, S. Zhang and D. Xu, "Modular High-Power DC–DC Converter for MVDC Renewable Energy Collection Systems," in IEEE Transactions on Industrial Electronics, vol. 68, no. 7, pp. 5875-5886, July 2021.

[2] Y. Li, H. Liu, Y. Chi, X. Fan, X. Tian and Z. Zhang, "Requirement Analysis on Large-scale Renewable Energy DC Collection and Transmission Technology," 2020 4th International Conference on HVDC (HVDC), Xi'an, China, 2020, pp. 410-414,

[3] C. Sun, M. Zhu, X. Zhang, J. Huang and X. Cai, "Output-Series Modular DC–DC Converter With Self-Voltage Balancing for Integrating Variable Energy Sources," in IEEE Transactions on Power Electronics, vol. 35, no. 11, pp. 11321-11327, Nov. 2020.

[4] Y. Wu et al., "Multi-Port Arm Shared DC-DC Converter with Decoupling Control for Multi-Voltage DC Grid," in IEEE Transactions on Power Electronics, inpress.

[5] B. Li, Y. Liu, B. Li, W. Wang, W. Wen and X. Chen, "DC Fault Current Calculation Method and Transient Characteristics of True Bipolar MMC-HVDC Systems," in CSEE Journal of Power and Energy Systems, vol. 11, no. 4, pp. 1704-1716, July 2025,

[6] B. Li, K. Liao, J. Yang and Z. He, "Transient Fault Analysis Method for VSC-Based DC Distribution Networks With Multi-DGs," in IEEE Transactions on Industrial Informatics, vol. 18, no. 11, pp. 7628-7638, Nov. 2022.

[7] K. Jia, Q. Zhao, Z. Zhu and T. Bi, "Modeling of DC Distribution System Based on High Frequency Transient Components," in IEEE Transactions on Smart Grid, vol. 12, no. 1, pp. 671-679, Jan. 2021,

[8] C. Zhao, Q. Wang and R. Yang, "Research on Demonstration Project of Zhangbei Flexible DC Grid," 2020 10th International Conference on Power and Energy Systems (ICPES), Chengdu, China, 2020, pp. 77-82.

[9] C. -H. Noh, C. -H. Kim, G. -H. Gwon and Y. -S. Oh, "Development of fault section identification technique for low voltage DC distribution systems by using capacitive discharge current," in Journal of Modern Power Systems and Clean Energy, vol. 6, no. 3, pp. 509-520, May 2018.

[10] K. Jia, Q. Zhao, T. Feng and T. Bi, "Distance Protection Scheme for DC Distribution Systems Based on the High-Frequency Characteristics of Faults," in IEEE Transactions on Power Delivery, vol. 35, no. 1, pp. 234-243, Feb. 2020.

An Enhanced Multi-Source Domain Adaptation Framework for Grounding Fault Diagnosis in Urban Rail Transit Systems under Varying Operating Conditions

Bo Chen
School of Rail Transportation
Soochow University
Suzhou, China
1524204138@qq.com

Qiaoyue Li*
School of Optical and Electronic Information
Suzhou City University
Suzhou, China
qyli@szcu.edu.cn

Guifu Du
School of Rail Transportation
Soochow University
Suzhou, China
gfdu@suda.edu.cn

Yanrong Ren
School of Rail Transportation
Soochow University
Suzhou, China
212276086@qq.com

***Abstract*—With the extension of rail service life and the impact of surrounding environmental conditions, the running rail in the DC traction power supply system of urban rail transit is prone to insulation degradation, which can lead to ground faults. These types of faults can result in elevated rail potentials and excessive stray currents, which may induce electrochemical corrosion and compromise passenger safety. Consequently, effective diagnosis of grounding faults in urban rail systems is of critical importance. In this paper, an Enhanced Multi-Source Domain Adaptation Framework (EMDAF) is proposed to diagnose grounding faults under varying operating conditions. The proposed EMDAF comprises three key modules: a ResNet-based feature extractor, a domain discrepancy minimization module and a classifier alignment strategy to improve diagnostic performance. It is ultimately employed to achieve accurate ground fault identification across various zones and operating conditions. Experimental comparisons indicate that EMDAF outperforms existing methods in both transfer learning performance and ground fault diagnosis accuracy, confirming its robustness and overall superiority.**

Keywords—deep learning, multi-source domain adaptation, transfer learning, urban rail transit, grounding fault

I. INTRODUCTION

DC traction power supply systems serve as the primary source of propulsion for urban rail transit, these systems involve several critical components, including traction substations, up and down contact lines, trains, return circuits and protective devices. The running rail not only supports vehicle motion but also serves as the return path for current. Due to unavoidable rail-to-ground contact, current leakage and stray currents (SC) occur, leading to rail potential (RP). Excessive RP and SC may cause safety and corrosion issues, highlighting the importance of timely insulation fault detection[1],[2],[3].

In recent years, intelligent fault diagnosis has been widely explored in urban rail systems. Na Liu[4] used a multi-scale 1D CNN (MS-1DCNN) to detect grounding faults in DC metro systems under varying train conditions. Xuetao Shi[5] applied the YOLOv5s model to onboard OCS images for real-time fault detection, enabling edge-based monitoring. Zuyu Cheng[6] proposed WT-ResNet, integrating wavelet transform and ResNet for diagnosing faults in train transmission systems. To address performance degradation from distribution shifts, domain adaptation (DA) techniques have been developed[7]. Heng Chen[8] introduced MCDANN to align sub-domain distributions and ensure prediction consistency in rotating machinery. Juan Tian[9] proposed an adversarial multi-source domain adaptation method guided by dynamic similarity for bearing fault diagnosis. Huaqing Wang[10] presented a dual-classifier DA strategy to handle open-set conditions and reduce negative transfer.

This paper introduces a novel transfer learning framework designed for grounding fault detection in urban DC traction rail systems, employing domain adaptation techniques to enhance cross-domain generalization. To address distribution discrepancies across domains and fully exploit transferable diagnostic knowledge, this paper develops an Enhanced Multi-Source Domain Adaptation Framework (EMDAF) tailored for fault diagnosis tasks. The framework begins by extracting deep semantic features via a dedicated feature extraction module. Next, a domain discrepancy mitigation component is introduced to reduce inter-domain variation through pairwise alignment between source and target distributions. Furthermore, a classifier consistency module is incorporated to resolve prediction inconsistency arising from domain shifts. By jointly optimizing these components, the EMDAF model significantly enhances diagnostic accuracy on target domains under varying working conditions.

II. RELATED WORK

A. Domain-Adaptive Transfer Learning

Transfer learning enables a model to transfer representations learned from a data-rich source domain to a related target domain with limited data availability. This is commonly achieved by pre-training the model on a large-scale dataset and adapting it through fine-tuning on the target task. The core idea of domain-adaptive learning is to enable knowledge transfer

979-8-3315-5472-9/25/$31.00 ©2025 IEEE

across datasets from different domains, thereby improving performance in cross-domain applications. This approach typically involves multiple datasets originating from different domains and aims to learn features that remain consistent across these domains. By leveraging labeled data from a well-defined source domain, domain-adaptive transfer learning aims to enhance model performance in a target domain lacking annotations, ultimately leading to improved classification outcomes under domain shift conditions. In this framework, the source domain comprises labeled datasets from K distinct domains, where each domain $D_k^s = \{(x_i^{s,k}, y_i^{s,k})\}_{i=1}^{n_{s,k}}$ follows a probability distribution $P_k(x^s)$. Each sample $x_i^{s,k}$ from the k-th source domain is associated with a corresponding equipment health status label $y_i^{s,k}$. In contrast, the target domain dataset $D^t = \{x_j^t\}_{j=1}^{n^t}$ consists solely of n^t unlabeled samples and adheres to a separate probability distribution $P_t(x^t)$.

B. DC Traction Power Supply System

Urban rail transit systems predominantly operate using direct current (DC) traction power. The power supply infrastructure is composed of several critical elements, such as traction substations, catenary systems for both directions, rolling stock (trains), and the return current path. The traction substation mainly comprises rectifier units and regenerative braking energy absorption devices (READ). In addition to the primary power supply equipment, the system also includes rail potential limiting devices (OVPD) and discharge devices (DD). The return current infrastructure includes the running rails, discharge circuitry, and associated grounding networks, which collectively ensure safe and effective current flow back to the power source. Due to the limitations of the actual engineering conditions, the rails can not be fully insulated to ground. A longitudinal resistance inherently exists between the running rails and the ground, resulting in the emergence of rail potential and the induction of stray currents. The discharge network is designed to collect leaked stray currents and reduce stray current levels, while the OVPD functions to limit the rail potential. The overall structure of the urban rail power supply system is illustrated in Fig.1.

When rail insulation degrades, a ground fault may occur, resulting in a significantly reduced equivalent resistance to ground at the fault location and causing a sharp fluctuation in the rail potential. As a train passes by, the rail potential may be clamped near 0 V. Therefore, in this study, the dynamic rail potential during train operation is selected as the sample data for ground fault diagnosis.

III. Proposed Method

To address the challenges of aligning all domain feature distributions and ignoring class decision boundaries in current multi-source domain adaptation methods, this paper develops an Enhanced Multi-Source Domain Adaptation Framework (EMDAF), as illustrated in Fig. 2. Central to the framework is a multi-domain discrepancy elimination module that combines intra- and inter-domain alignment to bridge distribution gaps effectively. Additionally, a classifier discrepancy alignment component is employed to minimize prediction inconsistencies across classifiers on target samples.

A. ResNet Feature Extractor

ResNets leverage skip connections to facilitate the training of deep models, effectively mitigating vanishing gradients and improving feature representation. This paper adopts ResNet18 as the backbone network to extract discriminative features associated with class semantics from both the target domain and multiple source domains. ResNet18 is a convolutional neural network composed of 18 layers, which include an initial convolutional layer, a series of residual blocks, pooling operations, and a final fully connected layer for output prediction. The final output is generated through a Softmax classifier. Given the one-dimensional nature of rail potential

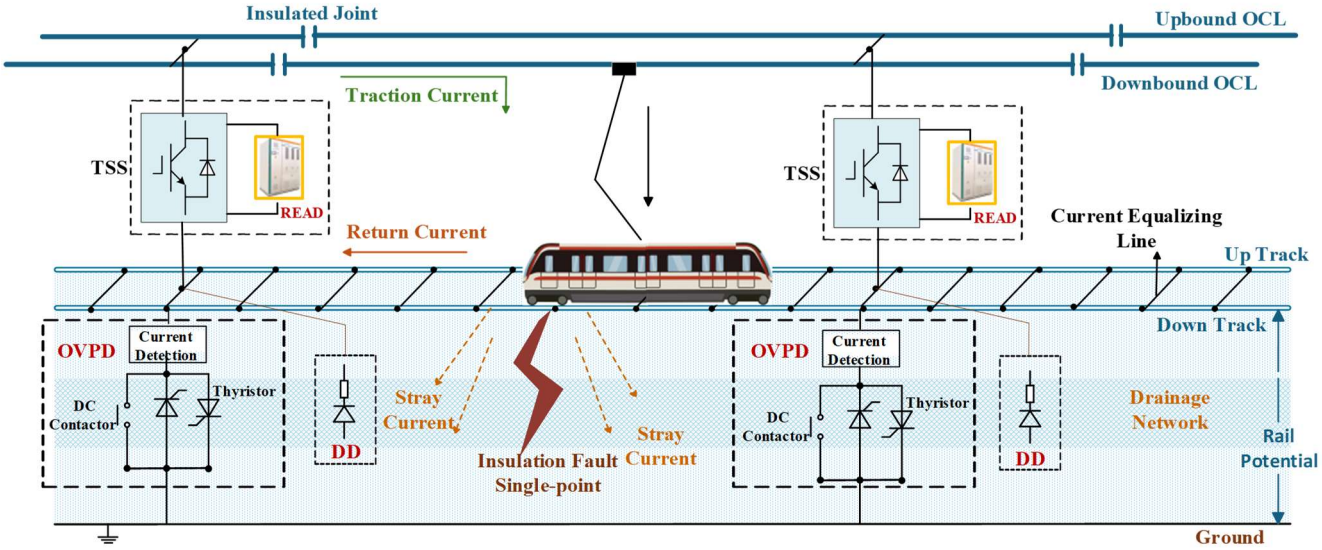


Fig. 1. Schematic of the DC traction power network in urban rail systems

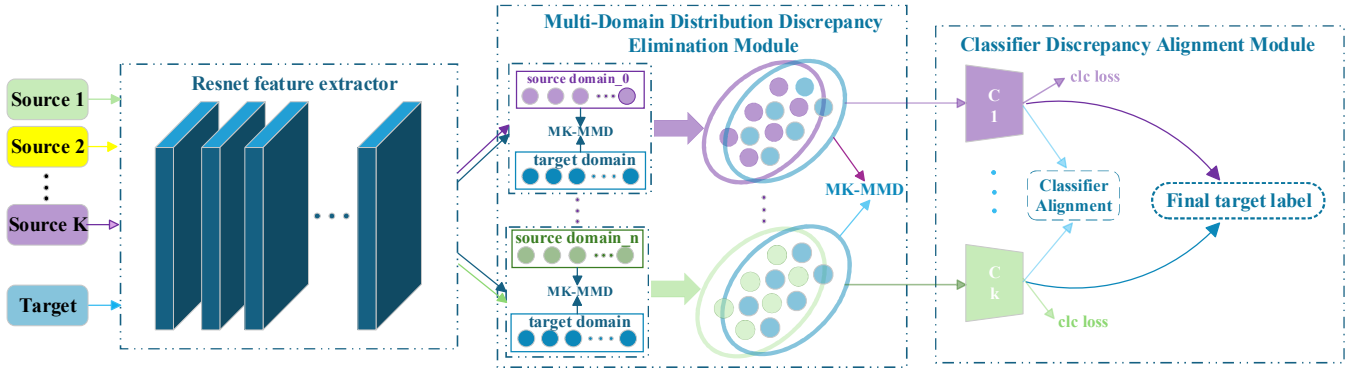


Fig. 2. Architecture of the EMDAF network

signals, the original 2D ResNet18 is adapted into a 1D version (1D-ResNet18) to better suit the input data. The feature extraction procedure in EMDAF is defined in (1).

$$f^{s,k} = \mathcal{F}(x^{s,k}), f^{t} = \mathcal{F}(x^{t}) \tag{1}$$

Where $f^{s,k}$ denotes the latent feature extracted from the k-th source domain sample, and f^{t} represents the latent feature extracted from the target domain sample.

B. *Multi-Domain Distribution Discrepancy Elimination Module*

Most current multi-source domain adaptation techniques attempt to align the source and target data by mapping them into a unified feature space, with the goal of minimizing distributional divergences across domains. However, such methods often overlook the complexity of diverse inter-domain relationships. In addition, achieving complete alignment across all domains is highly challenging. In contrast, traditional single-source domain adaptation techniques are effective in reducing distributional discrepancies between a single source and target domain, and can successfully learn domain-invariant features for fault diagnosis.

Building upon this idea, this paper extends the single-source approach by constructing multiple source–target domain pairs. Each source domain is individually matched with the target domain to form a pair, enabling pairwise alignment across domains. This strategy facilitates fine-grained adaptation by aligning each source domain with the target domain separately. To eliminate intra-pair discrepancies, this paper introduces an innovative intra-pair distribution alignment strategy. This paper adopts Maximum Mean Discrepancy with multiple kernels (MK-MMD) as the distribution distance metric. Let $f^{s,k} = (f_1^{s,k}, f_2^{s,k}, \cdots, f_{n_{s,k}}^{s,k})$ and $f^{t} = (f_1^{t}, f_2^{t}, \cdots, f_{n_t}^{t})$ denote the extracted features from the k-th source domain and the target domain, respectively. To measure the alignment between each source–target domain pair, the squared MK-MMD distance is computed as shown in (2).

$$\begin{aligned} \mathrm{MMD}^2_{(f^{s,k}, f^{t})} = & \frac{1}{n_{s,k}^2}\sum_{i=1}^{n_{s,k}}\sum_{j=1}^{n_{s,k}} k(f_i^{s,k}, f_j^{s,k}) \\ & -\frac{2}{n_{s,k} n_t}\sum_{i=1}^{n_{s,k}}\sum_{j=1}^{n_t} k(f_i^{s,k}, f_j^{t}) \\ & +\frac{1}{n_t^2}\sum_{i=1}^{n_t}\sum_{j=1}^{n_t} k(f_i^{t}, f_j^{t}) \end{aligned} \tag{2}$$

Where $k(\cdot,\cdot)$ denotes a kernel function. Based on (2), the inter-domain distribution alignment loss can be defined as shown in (3).

$$\mathcal{L}_{\mathrm{intra}} = \frac{1}{K}\sum_{k=1}^{K} \mathrm{MMD}^2_{(f^{s,k}, f^{t})} \tag{3}$$

Furthermore, to address distribution inconsistencies across all source–target domain combinations, an inter-domain alignment mechanism is introduced. Let the high-level features extracted from the i-th and j-th source–target pairs be denoted as f^{i} and f^{j}, respectively. The discrepancy between these domain pairs is quantified using the Maximum Mean Discrepancy (MK-MMD) metric, as formulated in (4).

$$\begin{aligned} \mathrm{MMD}^2_{(f^{i}, f^{j})} = & \frac{1}{n_{f_i}^2}\sum_{m=1}^{n_{f_i}}\sum_{n=1}^{n_{f_i}} k(f_m^{i}, f_n^{i}) \\ & -\frac{2}{n_{f_i} n_{f_j}}\sum_{m=1}^{n_{f_i}}\sum_{n=1}^{n_{f_j}} k(f_m^{i}, f_n^{j}) \\ & +\frac{1}{n_{f_j}^2}\sum_{m=1}^{n_{f_j}}\sum_{n=1}^{n_{f_j}} k(f_m^{j}, f_n^{j}) \end{aligned} \tag{4}$$

Where n_{f_i} and n_{f_j} denote the respective numbers of extracted features from the i-th and j-th source–target domain pairs. Based on the above formulation for computing inter-domain distribution discrepancies, the overall inter-domain alignment loss among all source-target domain pairs can be defined as follows:

$$\mathcal{L}_{\text{inter}} = \frac{1}{C_K^2}\sum_{i=1}^{K-1}\sum_{j=i+1}^{K}\text{MMD}^2_{(f^i,f^j)} \tag{5}$$

In this setting, C_K^2 indicates the overall count of source–target domain pairings, and it adheres to the mathematical condition specified in (6).

$$C_K^2 = \frac{K!}{2!(K-2)!} \tag{6}$$

The loss function corresponding to the multi-domain distribution discrepancy reduction module is derived by integrating (3) and (5), with the final expression provided in (7).

$$\mathcal{L}_{ds} = \mathcal{L}_{\text{intra}} + \mathcal{L}_{\text{inter}} \tag{7}$$

C. Classifier Discrepancy Alignment Module

It is essential to consider task-relevant class decision boundaries during distribution alignment. This enables the model to focus more on distinguishing critical classes, thereby enhancing its discriminative power, robustness, and generalization ability. To achieve this, this paper introduces a Classifier Discrepancy Alignment Module composed of K individual predictors, denoted as $\{C_k\}_{k=1}^{K}$. Each predictor C_k is designed as a Softmax-based classifier that receives high-level features from the *k*-th source domain and produces the corresponding class probability distribution. The discrepancy between predicted and true labels is evaluated using the cross-entropy loss. This module treats each source domain independently, facilitating the learning of domain-specific discriminative features and improving classification accuracy. For instance, the classification loss for the *k*-th source domain is expressed in (8).

$$\mathcal{L}_{clc_k} = \frac{1}{n_{s,k}}\sum_{i=1}^{n_{s,k}}\sum_{c=1}^{C}1_{[y_i=c]}log\frac{exp(o_{i,c}^{s,k})}{\sum_{j=1}^{C}exp(o_{i,j}^{s})} \tag{8}$$

Where $1_{[\cdot]}$ is defined as the indicator function, yielding 1 if the condition holds true and 0 otherwise. C indicates the number of distinct health states. Accordingly, the total classification loss over all K source domains is computed as presented in (9).

$$\mathcal{L}_{clc} = \frac{1}{K}\sum_{k=1}^{K}\mathcal{L}_{clc_k} \tag{9}$$

Based on (9), each classifier is individually trained to achieve accurate prediction and classification of source domain samples. However, this process overlooks the task-specific decision boundaries, which may lead to misclassification of target samples that lie near the boundaries. To address this issue, a classifier discrepancy alignment loss module is designed to reduce classification errors. This module measures the loss by calculating the absolute difference in output probabilities produced by all classifiers for the target domain samples, as shown in (10).

$$\mathcal{L}_{cd} = \frac{1}{C_K^2}\sum_{i=1}^{K-1}\sum_{j=i+1}^{K}\mathbb{E}[|C_i(f^t) - C_j(f^t)|] \tag{10}$$

Where $\mathbb{E}$ denotes the mathematical expectation. The optimization objective is to minimize $\mathcal{L}_{cd}$, which helps eliminate prediction discrepancies among all classifiers, ensuring that different classifiers produce consistent predictions for the same target sample.

D. Optimization Objective and Algorithm Implementation

The overall optimization objective is to minimize the aforementioned three types of loss. Therefore, the total optimization objective of EMDAF framework can be expressed as follows:

$$\mathcal{L}_{MDFAN} = \mathcal{L}_{clc} + \alpha\mathcal{L}_{ds} + \beta\mathcal{L}_{cd} \tag{11}$$

where α and β are trade-off hyperparameters.

Once the overall network architecture of EMDAF is established, the global optimization objective described in (11) can be solved using classical optimization algorithms such as SGD or Adam. Assuming θ_f and θ_c represent the respective parameters of the ResNet-based feature extractor and the discrepancy alignment module, the optimization objective specified in (11) can be equivalently expressed as:

$$\begin{aligned}\theta_f &\leftarrow \theta_f - \eta(\frac{\partial\mathcal{L}_{clc}}{\partial\theta_f} + \alpha\frac{\partial\mathcal{L}_{ds}}{\partial\theta_f} + \beta\frac{\partial\mathcal{L}_{cd}}{\partial\theta_f})\\ \theta_c &\leftarrow \theta_c - \eta(\frac{\partial\mathcal{L}_{clc}}{\partial\theta_f} + \beta\frac{\partial\mathcal{L}_{cd}}{\partial\theta_f})\end{aligned} \tag{12}$$

where η denotes the learning rate. Following the formulation in (12), the training process enables joint optimization of both the feature extractor and classifier parameters within one epoch.

IV. Experimental Results

A. Dataset Description

The dataset originates from a real Chinese metro system and is generated through a simulation platform capable of modeling dynamic variations in rail potential. Under identical power sections and operating conditions, the rail potential exhibits periodic patterns. Thus, dynamic rail potential signals from one full power cycle (1300–1480 s) at detection points 6199 m and 6400 m are used as samples. Ground faults are labeled across 10 classes, including healthy status, with fault locations segmented every 20 meters (TABLE I). Each fault type has 1000 samples, and each sample contains 720 data points.

TABLE I. Data labels

fault types	Labels
normal state	0
fault section 1: 6201m~6220m	1
fault section 2: 6221m~6240m	2
.....	.....
fault section 9: 6361m~6380m	9

Four operating conditions—no-load, normal load, full load, and overload—are defined based on real train scenarios. The train traction force F under each load is calculated as follows:

$$F = 9.81G(102(1+\lambda)\times a + f_x + f_p + f_y + f_c \qquad (13)$$

Where G denotes the train mass (300 tons), and λ represents the inertia coefficient of rotating components, set to 0.1. The acceleration a typically varies within the range of 0.9 to 1.0 m/s². The resistive forces f_x, f_p, f_y and f_c correspond to basic motion resistance, gradient resistance, curve resistance, and tunnel resistance, respectively. The rated traction power is determined as P=3507.39kW. To simulate various operating scenarios for source and target domain construction, four traction levels—0.74P, 0.8P, 1.1P, and 1.2P—are employed.

B. Classification Results

To evaluate the effectiveness and robustness of the proposed EMDAF network architecture in grounding fault diagnosis, several representative baseline methods are selected for comparison, including Multi-Source Domain Adversarial Neural Networks and Convolutional Autoencoders[11],[12]. In addition, two ablation variants are designed to assess the contributions of the proposed intra-domain and inter-domain alignment strategies. Specifically, FECAM removes the multi-domain distribution alignment module and instead adopts the classical MK-MMD method to measure the similarity between source and target domains. On the other hand, MDEM excludes the classifier discrepancy alignment module. By comparing the diagnostic performance of these variants with the complete EMDAF model, the effectiveness of each alignment component can be quantitatively validated. TABLE II presents the performance of all methods under various operating conditions. Key observations are summarized below:

(1) *Comparison with Popular Transfer Learning Methods:* To assess the impact of alignment strategies, a multi-source variant of DANN and an enhanced CAE method were used for comparison. Results show that the proposed method consistently outperforms these baselines across different operating conditions, achieving higher diagnostic accuracy in transfer tasks. Such improvement is primarily due to the model's ability to jointly extract transferable and class-specific representations from diverse source domains, leading to enhanced generalization performance on unseen target data.

(2) *Comparison with FECAM and MDEM:* EMDAF improves diagnostic accuracy by 4.89% over FECAM, confirming that multi-domain alignment effectively mitigates domain shift. It also outperforms MDEM by 2.88%, indicating that the classifier discrepancy module enhances prediction consistency on target samples.

TABLE II. THE DIAGNOSTIC ACCURACY OF DIFFERENT FAULT DIAGNOSIS METHODS

Target / Model	0.74P	0.8P	1.1P	1.2P	Average Accuracy
DANN	82.57%	84.43%	83.93%	81.33%	83.07%
CAE	88.33%	87.20%	88.27%	90.14%	88.49%
FECAM	93.63%	91.51%	92.91%	93.40%	92.86%
MDEM	96.13%	94.11%	93.79%	95.45%	94.87%
Proposed method	**98.1%**	**97.30%**	**96.85%**	**98.74%**	**97.75%**

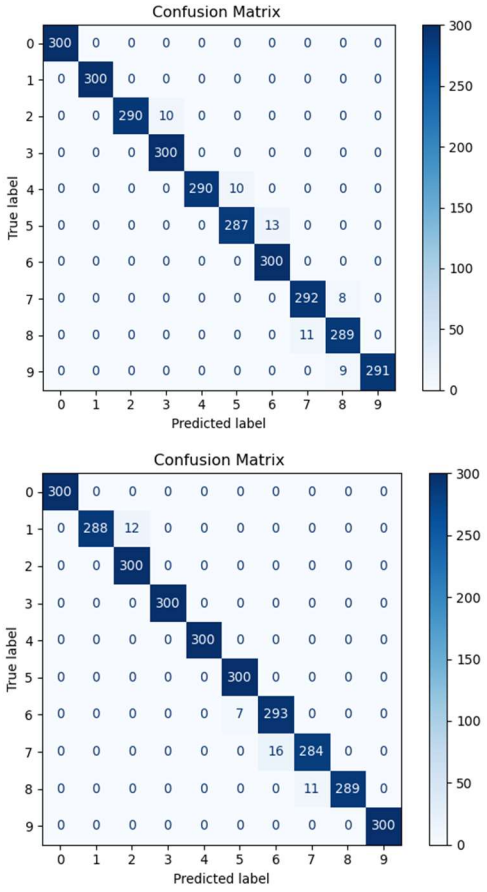


Fig. 3. Confusion Matrices for Various Transfer Learning Tasks Using EMDAF(a) Target domain:0.8P (b) Target domain:1.2P

As shown in Fig. 3, the confusion matrices illustrate the performance of EMDAF across two distinct transfer learning scenarios. The results indicate that the proposed model maintains high classification accuracy for various fault categories, with some fault types being identified with perfect (100%) precision. These outcomes validate the effectiveness of EMDAF in diagnosing grounding faults within urban rail transit systems. As illustrated by the feature visualization in Fig. 4, EMDAF exhibits strong capability in extracting discriminative features, where inter-class features are well separated and intra-class samples are tightly clustered.

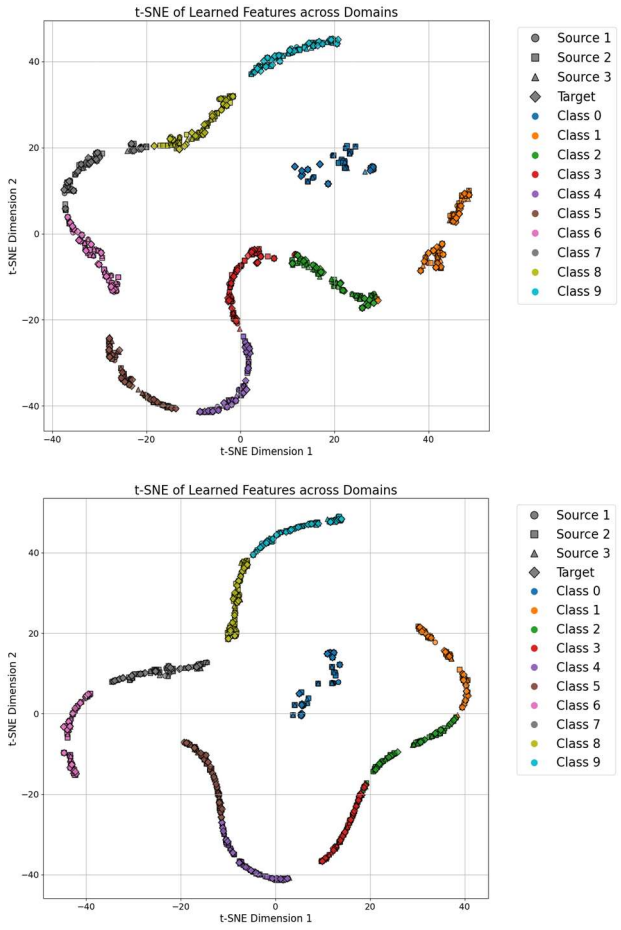


Fig. 4. Feature Visualization of EMDAF (Target: 0.8P & 1.2P)

V. Conclusion

This paper introduces an Enhanced Multi-source Domain Adaptation Framework (EMDAF) designed for diagnosing grounding faults in urban rail traction return systems. EMDAF incorporates a multi-domain alignment module designed around the principle of pairwise domain matching. To address distribution discrepancies, it employs both intra-domain and inter-domain alignment strategies across source–target domain pairs. Furthermore, a classifier discrepancy alignment module is integrated to enhance consistency between classifiers by explicitly considering class-level decision boundaries.

The effectiveness of EMDAF is validated using a multi-condition rail potential dataset generated by a dynamic simulation platform. Experimental findings indicate that the proposed model consistently achieves higher diagnostic accuracy compared to existing transfer learning approaches and maintains strong performance across diverse operational scenarios.

References

[1] Xia, Y., Du, G., Li, Q., and others, “Insulation failure localization of running rails based on improved multi-scale convolution intra-class adaptive model in urban rail transit,” IOP Publishing, 2025.

[2] Zheng, Z., Du, G., Huang, W., and others, “Comprehensive control of reflux safety parameters based on flexible grounding scheme in DC railway electrification system,” IEEE Trans. Transp. Electrific., vol. 8, no. 3, pp. 3127–3138, 2022.

[3] Kang, Z., Du, G., Xia, Y., and others, “Dynamic distribution of rail potential with regional insulation alteration in multi-train urban rail transit,” IET Electr. Syst. Transp., 2024.

[4] Du, G., Liu, N., Zhang, D., Jiang, X. and Wang, J. (2024). Grounding fault diagnosis of running rails based on a multi-scale one-dimensional convolutional neural network in a DC subway system. Urban Rail Transit, 10(3), 263–279.

[5] Shi, X., Zhao, H., Jiang, H., Zuo, H., and Zhang, Q., “Edge intelligence-based OCS fault detection in rail transit systems,” Wirel. Commun. Mob. Comput., vol. 2023, Article ID 8659679.

[6] Cheng, Z., Zhao, Z., Wang, Y., Guo, W., Wang, Y., and Gao, X., “A WT-ResNet based fault diagnosis model for the urban rail train transmission system,” arXiv preprint arXiv:2406.06031, 2024.

[7] Wang, R., Huang, W., Wang, J., Shen, C., and Zhu, Z., “Multisource domain feature adaptation network for bearing fault diagnosis under time-varying working conditions,” IEEE Trans. Instrum. Meas., vol. 71, Art. no. 3511010, Jan. 2022.

[8] Chen, H., Shi, L., Zhou, S., Yue, Y., & An, N. (2022). A Multi-Source Consistency Domain Adaptation Neural Network MCDANN for Fault Diagnosis. Applied Sciences, 12(19), 10113.

[9] Tian, J., Zhang, S., Xie, G., & Shi, H. (2025). A Multi-Source Domain Adaptation Method for Bearing Fault Diagnosis with Dynamically Similarity Guidance on Incomplete Data. Actuators, 14(1), 24.

[10] Wang, H., Xu, Z., Tong, X., & Song, L. (2023). Cross-Domain Open Set Fault Diagnosis Based on Weighted Domain Adaptation with Double Classifiers. Sensors, 23(4), 2137.

[11] Dai, B., Frusque, G., Li, T., and others, “Smart filter-aided domain adversarial neural network for fault diagnosis in noisy industrial scenarios,” Eng. Appl. Artif. Intell., vol. 126, 2023.

[12] Le, D. T., Duy, M. T. N., Huy, B. H. T., and others, “Advanced deep learning-based electricity theft detection in smart grids using multi-dimensional analysis with convolutional autoencoder and transformer,” Eng. Appl. Artif. Intell., vol. 157, Art. no. 111333, 2025.

A Transformer Fault Diagnosis Approach Based on WCGAN-GP and Multimodal Deep Feature Fusion

Ping Zeng
Electric Power Research Institute
State Grid Shanghai Municipal Electric Power Company
Shanghai, China
29339293@qq.com

Wei Bao
Electric Power Research Institute
State Grid Shanghai Municipal Electric Power Company
Shanghai, China
80627643@qq.com

Desheng Zhou
Electric Power Research Institute
State Grid Shanghai Municipal Electric Power Company
Shanghai, China
zds1984@qq.com

Zhaoxin Du
Electric Power Research Institute
State Grid Shanghai Municipal Electric Power Company
Shanghai, China
duzx01@126.com

Yuqing Shen
School of Electrical Engineering
Shanghai University of Electric Power
Shanghai, China
Syyq_0819@163.com

Xiangli Deng
School of Electrical Engineering
Shanghai University of Electric Power
Shanghai, China
xiangli_deng@163.com

***Abstract*—To address the challenges in multimodal intelligent diagnosis of transformer faults, such as limited sample size, imbalanced data distribution, insufficient feature fusion capability, and consequently low diagnostic accuracy, this paper proposes a fault diagnosis method based on Wasserstein Conditional Generative Adversarial Network with Gradient Penalty (WCGAN-GP) and deep multimodal feature fusion. A WCGAN-GP model is constructed by integrating Wasserstein distance with conditional generative adversarial learning to achieve high-quality augmentation of small-sample data. An improved Residual Network (ResNet) and an enhanced Densely Connected Network (DenseNet) are employed to perform deep feature extraction from multimodal data. A Multi-Layer Cross-Attention (MLCA) mechanism is introduced within the network to fuse deep multimodal features, enabling early fault diagnosis of transformers. Finally, the proposed intelligent diagnosis method is validated using both simulation data and dynamic model test data, demonstrating its effectiveness in improving diagnostic accuracy.**

Keywords—Transformer Fault Diagnosis, Multimodal Fusion, WCGAN-GP, ResNet, DenseNet, Multi-Layer Cross-Attention Mechanism (MLCA)

I. INTRODUCTION

As a critical component of power systems, transformer operation directly affects grid stability and reliability [1]. Short-circuit faults can cause irreversible winding deformation, and combined with insulation aging, may lead to faults such as arc discharge or inter-turn shorts [2]. Therefore, accurate and timely detection of transformer status is crucial.

Transformer fault detection methods include offline and online approaches. Offline methods, such as dissolved gas [3] and frequency response analyses [4], are mature but cannot support real-time monitoring. Online methods have thus gained focus: digital twin models combined with current and leakage magnetic features [5], optimized wavelet-based vibration signal processing [6], and ultrasonic probe systems with cross-correlation algorithms [7] enable more effective fault detection. Yet traditional diagnostic models still face limited generalization and accuracy under complex operating conditions.

In recent years, AI techniques offer high efficiency and self-learning capabilities for transformer monitoring [8]. For leakage magnetic features, methods include Lissajous curve–based CNNs with transfer learning [9] and SVMD-MTF feature extraction fed into attention-based ResNet50 models [10]. Electrical feature-based approaches combine magnetic circuit modeling with sequence current analysis using random forests [11]. Other studies rely on vibration [12] or dissolved gas features [13]. However, single-modal approaches cannot fully capture multidimensional transformer conditions, limiting robustness.

Multimodal fusion methods integrate data from multiple sensors, improving diagnostic accuracy and reliability [14]. Examples include vibration-infrared signal fusion with cross-attention [15], GRU-based multimodal fusion for electromechanical systems [16], and multi-sensor frequency-image fusion with attention mechanisms for rotor-bearing diagnostics [17].

A practical challenge is class imbalance, as fault events are rare. GANs provide a solution for small-sample augmentation, enhancing data diversity and model training. Applications include attention-based GANs for infrared thermography [18], dual-stream GANs for one-dimensional wind turbine data [19], and policy gradient–GANs for transformer gas data [20].

In summary, transformer fault diagnosis remains challenged by inadequate multimodal feature fusion, small-sample learning limitations, and data imbalance. Novel intelligent diagnostic approaches with enhanced perceptual capabilities and effective data augmentation are required to ensure accurate and reliable

This work was supported by the Science and Technology Project of State Grid Corporation of China (No. 520940240037).

979-8-3315-5472-9/25/$31.00 ©2025 IEEE

identification of transformer operating conditions across various scenarios.

II. Small-Sample Data Augmentation Based on WCGAN-GP

Considering that vibration and ultrasonic signals under fault conditions are difficult to obtain in practical transformer operation, there exists a severe class imbalance between normal and fault samples. Directly using such data for fault diagnosis may lead to misclassification, thereby compromising the diagnostic accuracy and practicality of the model. Therefore, this paper employs a WCGAN-GP network to enhance the diversity of training samples for the model.

A. WCGAN-GP Model

To further improve the training stability of WGAN, this paper introduces a Gradient Penalty (GP) into the loss function. By replacing the traditional gradient clipping with gradient penalty, the Lipschitz continuity is more stably enforced. The objective function of WGAN with gradient penalty is defined as follows:

$$\min_G \max_f \begin{pmatrix} E_{x\sim P_{data}}\left[f(x)\right] - E_{z\sim P_z}\left[f(G(z))\right] \\ -\lambda \cdot E_{\hat{x}\sim P_{\hat{x}}}\left[\left(\left\|\nabla_{\hat{x}} f(\hat{x})\right\|_2 - 1\right)^2\right] \end{pmatrix} \quad (1)$$

In the formula: $\min_G \max_f[\bullet]$ denotes first maximization with respect to f and then minimization with respect to G; $\lambda \cdot E_{\hat{x}\sim P_{\hat{x}}}\left[\left(\left\|\nabla_{\hat{x}} f(\hat{x})\right\|_2 - 1\right)^2\right]$ represents the gradient penalty term; $\hat{x}$ indicates the interpolated samples obtained by mixing generated and real samples in a certain proportion; $\left\|\nabla_{\hat{x}} f(\hat{x})\right\|_2$ denotes the L2 norm of the discriminator gradients with respect to the input $\hat{x}$; E is the expectation operator; λ represents the coefficient controlling the strength of the gradient penalty.

Conditional Generative Adversarial Networks (CGANs) incorporate conditional information into GANs, allowing generated data to correspond to specific labels or auxiliary inputs. This enhances the controllability and practical applicability of the model. The objective function of a conditionally constrained WGAN is formulated as follows:

$$\min_G \max_f \begin{pmatrix} E_{x\sim P_{data}}\left[f(x,y)\right] - E_{z\sim P_z}\left[f(G(z,y),y)\right] \\ -\lambda \cdot E_{\hat{x}\sim P_{\hat{x}}}\left[\left(\left\|\nabla_{\hat{x}} f(\hat{x},y)\right\|_2 - 1\right)^2\right] \end{pmatrix} \quad (2)$$

In the formula: y denotes the conditional variable, and the remaining notations are the same as previously defined.

Since both transformer vibration and ultrasonic signals are one-dimensional time-series data, a 1D convolutional network is used as the generator, and a multilayer perceptron (MLP) serves as the discriminator. MLPs are simpler, have fewer parameters, and are easier to train, making them suitable for small-sample or shallow GAN tasks while retaining strong feature discrimination.

The generator receives a high-dimensional 1D noise vector, embeds the conditional label, maps it to high-dimensional space via a linear layer, and restores signal structure through stacked upsampling, 1D convolution, batch normalization, and LeakyReLU layers. A final 1D convolution with Tanh normalizes the output to [-1,1], and adaptive average pooling ensures the signal length matches the target.

The discriminator flattens the input, concatenates the embedded label, and processes it through spectral-normalized linear layers with LeakyReLU, outputting a scalar that indicates the authenticity of the signal.

The specific WCGAN procedure is illustrated in Fig. 1.

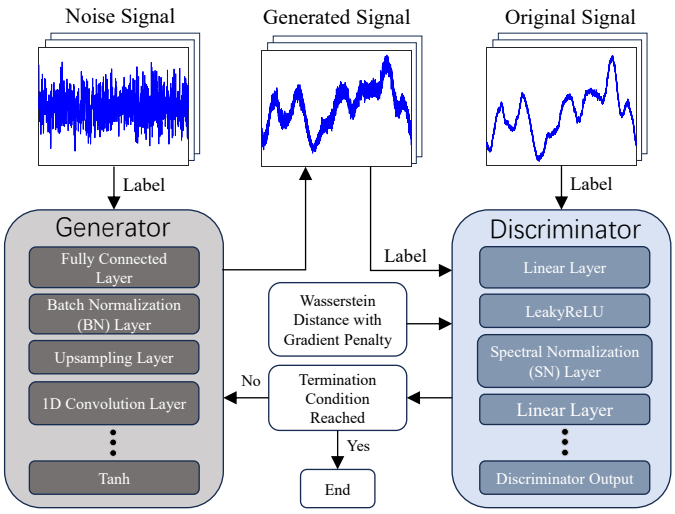


Fig. 1. WCGAN-GP Model Structure Diagram

III. Multimodal Feature Extraction

A. Multimodal Feature Extraction

When a transformer experiences a fault, the spatial leakage magnetic field, affected by winding current density, contains rich amplitude and phase information. The variations are most pronounced at the ends and middle of the windings [21]. Therefore, three measurement points—upper, middle, and lower—are selected to capture the radial leakage magnetic field.

Leakage magnetic field data are collected over a full cycle at the upper, middle, and lower winding points using a sliding-window method. The data are then time-aligned, concatenated, mean-removed, and min-max normalized to reduce amplitude differences. A schematic of the feature extraction process is shown in Fig. 2.

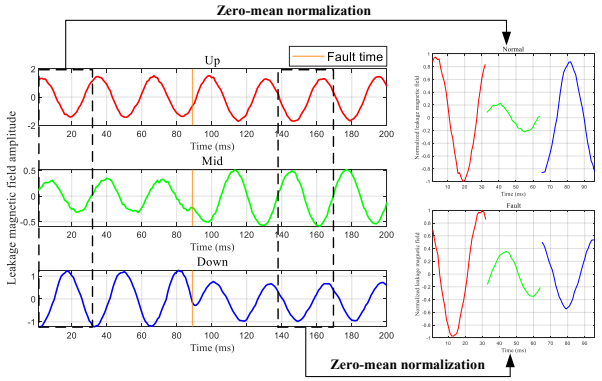


Fig. 2. Schematic diagram of the feature extraction method of leakage magnetic field

B. *Feature Extraction of Vibration Signals Based on RPM*

The vibration signals of a transformer mainly originate from its windings and core, with the dominant frequency of both concentrated around 100 Hz, forming a clear periodic signal [22]. To better capture the temporal structure and amplitude information in the transformer vibration signals, this study employs the Relative Position Matrix (RPM) method to transform a single cycle of one-dimensional vibration signals into a two-dimensional image, facilitating input into subsequent multimodal neural network branches.

Fig. 3 shows a comparison between the color two-dimensional image encoded using RPM and the generated vibration data. In the generated vibration data, the horizontal axis represents the number of sampling points, while the vertical axis represents the amplitude of the vibration signal. The regularity and symmetry of the color distribution reflect local variations, periodic structures, and overall trend features in the generated vibration signals.

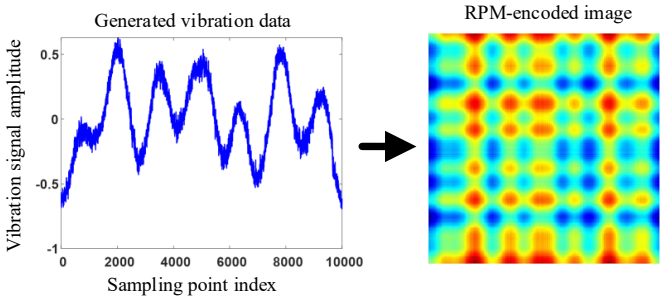


Fig. 3. Comparison between RPM encoding and generated vibration data

C. *Feature Extraction of Ultrasonic Signals Based on CWT*

Ultrasonic signals during transformer operation mainly arise from local faults such as partial discharges and arc breakdowns. They are typically short-term, non-stationary, and transient, with wide frequency ranges [23]. In this study, Continuous Wavelet Transform (CWT) converts the one-dimensional ultrasonic signals into two-dimensional time-frequency maps, facilitating effective extraction of time-frequency features. As shown in Fig. 4, the CWT images clearly reflect signal non-stationarity, frequency distribution, and local anomalies.

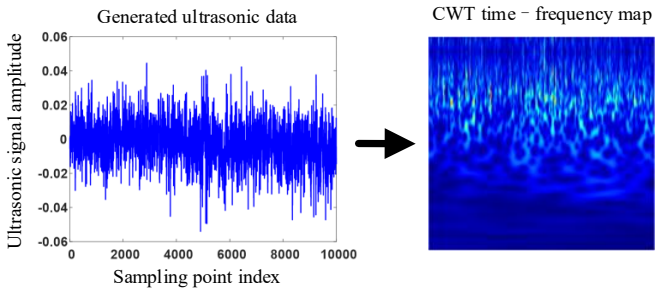


Fig. 4. Comparison between CWT time-frequency diagram and generated ultrasound data

IV. Deep Multimodal Feature Fusion Based on Multi-Layer Cross-Attention Mechanism

After extracting features from the leakage magnetic, vibration, and ultrasonic signals, a transformer fault diagnosis model based on ResNet-DenseNet-MLCA was established. An ECA attention mechanism is incorporated into each modal subnetwork to enhance the representation of key features [24]. A multi-layer cross-attention (MLCA) fusion strategy is applied among the multimodal features to enable deep information interaction, ultimately achieving accurate classification of fault states.

A. *Multi-Layer Cross-Attention Mechanism*

To effectively extract the deep temporal features of the transformer leakage magnetic field, this study employs a lightweight one-dimensional residual neural network (1D-ResNet-18) as the feature extraction subnetwork for the leakage magnetic modality. This network retains the core concepts of residual connections and batch normalization from the two-dimensional ResNet [25]. For the vibration and ultrasonic modalities, DenseNet-121 is used as the feature extraction subnetwork. DenseNet is a convolutional neural network architecture built on the concept of dense connectivity, with basic units including Dense Blocks and Transition Layers. Within each Dense Block, dense connections enable efficient feature reuse and propagation [26]. Corresponding subnetworks are designed for the three modalities mentioned above, incorporating the ECA channel attention mechanism to enhance feature representation.

However, the subnetworks of each modality do not fully share or fuse features. To address this, a Multi-Layer Cross-Attention (MLCA) mechanism is constructed in the multimodal fusion part of this study. Multiple Multi-Head Cross-Attention (MHCA) modules are introduced at different network depths to enable deep semantic information interaction across modalities.

MHCA primarily relies on multi-head attention (MA), whose core idea is to map the input features into Query (Q), Key (K), and Value (V) vectors, and then fuse information between different inputs by weighting V according to the similarity between Q and K. The specific computation formula for single-head attention is as follows:

$$\text{Attention}(Q,K,V)=\text{softmax}\left(\frac{QK^T}{\sqrt{d_k}}\right)V \tag{3}$$

In the formula: d_k represents the dimension of the key vectors, which helps prevent gradient explosion and vanishing.

Multi-head attention enhances the representation capability by performing attention operations across multiple subspaces. Its overall form is:

$$\mathrm{MA}(Q,K,V)=\mathrm{Concat}(head_1,\ldots,head_h)W^o \tag{4}$$

$$head_i=\mathrm{Attention}(QW_Q^{(i)},KW_K^{(i)},VW_V^{(i)}) \tag{5}$$

In the formula: Concat denotes the concatenation operation, W^o is the weight of the linear mapping, $head_i$ represents the i-th head of the multi-head attention, and W_Q, W_K, W_V are the linear mapping matrices for the query, key, and value vectors, respectively.

In MLCA, MHCA modules are repeatedly stacked at different depths of the fusion stages to establish deep information interaction channels among the vibration, ultrasonic, and leakage magnetic modalities at each layer. This mechanism consists of two stages: multiple MHCA modules are introduced at the intermediate feature layers and at the final fusion layer, enabling deep feature fusion across the modalities.

1) Intermediate Layer Fusion: Two DenseNet-121 subnetworks are used to extract vibration and ultrasonic image features. The intermediate features between adjacent Dense Blocks can capture rich local semantic information; therefore, MHCA is employed to construct a bidirectional interaction channel between the vibration and ultrasonic modalities. Assuming that the intermediate features of the vibration and ultrasonic modalities at the l-th layer are $X_v^{(l)}\in\mathbb{R}^{B\times C_v\times H\times W}$ and $X_u^{(l)}\in\mathbb{R}^{B\times C_u\times H\times W}$, the intermediate features are first subjected to global average pooling and then projected into low-dimensional representations:

$$x_v^{(l)}=\mathrm{unsq}(\mathrm{Proj}_v(\mathrm{GAP}(X_v^{(l)})))\in\mathbb{R}^{B\times 1\times D} \tag{6}$$

$$x_u^{(l)}=\mathrm{unsq}(\mathrm{Proj}_u(\mathrm{GAP}(X_u^{(l)})))\in\mathbb{R}^{B\times 1\times D} \tag{7}$$

In the formula: $\mathrm{GAP}(\bullet)$ denotes the global average pooling operation, $\mathrm{Proj}_v(\bullet)$ is a linear projection matrix that maps the channel dimensions C_v and C_u to D; $\mathrm{unsq}(\bullet)$ indicates the operation of adding a sequence dimension to make the input compatible with MHCA.

Subsequently, the network alternately treats the ultrasonic and vibration modalities as Key (K) and Value (V), and the vibration and ultrasonic modalities as Query (Q), performing multi-head cross-attention fusion. The fused features are then fed back to their respective modality networks via residual connections to enhance cross-modal perception.

$$X_v^{(l)}=X_v^{(l)}+\mathrm{MA}(x_v^{(l)},x_u^{(l)},x_u^{(l)}) \tag{8}$$

$$X_u^{(l)}=X_u^{(l)}+\mathrm{MA}(x_u^{(l)},x_v^{(l)},x_v^{(l)}) \tag{9}$$

In the formula: $X_v^{(l)}$ and $X_u^{(l)}$ denote the fused features at the intermediate layer.

2) Final Fusion: After each modality subnetwork has extracted complete local semantic features, three final feature vectors are obtained: the final feature vector of the vibration modality v, the ultrasonic modality u, and the leakage magnetic modality m. To achieve deeper cross-modal fusion, multi-head cross-attention (MHCA) is applied at the network's final stage, performing multiple rounds of iterative interaction and fusion for each pair of modality features. In total, six MHCA operations are executed at this stage. This process can be expressed as:

$$\begin{cases}\hat{v}^{(1)}=\mathrm{MA}(v^{(0)},u^{(0)},u^{(0)})\\ v^{(2)}=\mathrm{MA}(\hat{v}^{(1)},m^{(0)},m^{(0)})\\ u^{(1)}=\mathrm{MA}(u^{(0)},v^{(2)},v^{(2)})\\ u^{(2)}=\mathrm{MA}(u^{(1)},m^{(0)},m^{(0)})\\ m^{(1)}=\mathrm{MA}(m^{(0)},v^{(2)},v^{(2)})\\ m^{(2)}=\mathrm{MA}(m^{(1)},u^{(2)},u^{(2)})\end{cases} \tag{10}$$

In the formula: $\hat{v}$, u, and m represent intermediate variables, after one round of fusion, the modality features are updated and used for the next round of cross-attention operations.

After completing all cross-modal fusions at the final stage, the vibration, ultrasonic, and leakage magnetic features are concatenated into the final fused feature, which is then fed into a fully connected classifier for the final classification. This process can be expressed as:

$$F_{\text{fusion}}=\mathrm{Concat}(v^{(2)},u^{(2)},m^{(2)}) \tag{11}$$

$$y=\mathrm{Classifier}(F_{\text{fusion}}) \tag{12}$$

In the formula: F_{fusion} denotes the concatenated fused feature, y represents the final classification category, and $\mathrm{Classifier}(\bullet)$ denotes the classifier.

B. Establishment of a Multimodal Deep Feature Fusion Fault Diagnosis Model

The overall model proposed in this study consists of three main parts: the vibration and ultrasonic data generation module, the feature transformation module, and the model training and classification module. The structural diagram of the entire fault diagnosis model is shown in Fig. 5.

At the network's output, the classifier uses the Softmax function to produce the probability distribution of each fault category for final identification. During training, cross-entropy loss is used, and the AdamW optimizer is applied with a weight decay of 0.00001, an initial learning rate of 0.0001, and a batch size of 32.

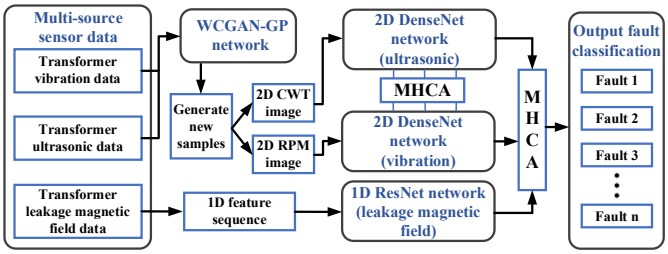


Fig. 5. Multimodal Deep Feature Fusion Fault Diagnosis Model Diagram

V. Experimental Verification

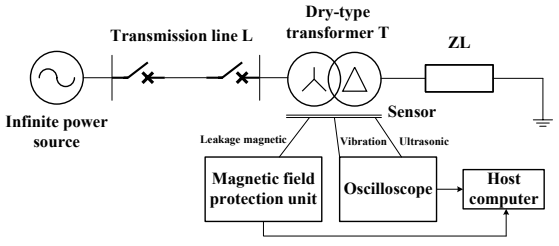
The experimental environment used in this study is PyCharm, with PyTorch 2.6 as the deep learning framework. The hardware configuration includes an NVIDIA GeForce RTX 4060 GPU, an i7-12650H CPU, and 16 GB of RAM.

Dynamic model experimental system wiring: shown in Fig. 6(a). Experimental transformer: three-phase, double-winding, dry-type transformer, Yn/d11 connection; rated capacity: 50 kVA; rated voltage: 1/0.4 kV; winding parameters referred to the high-voltage side: $R_A = 0.5899\Omega$, $R_B = 0.5896\Omega$, $R_C = 0.5903\Omega$, $X_A = X_B = X_C = 1.52\Omega$; infinite power source parameter: $E = 1\text{kV}$; transmission line parameters: $R_1 = 1.767\Omega$, $L_1 = 0.964\text{H}$; adjustable load parameters: $Z_L = 20\Omega$.

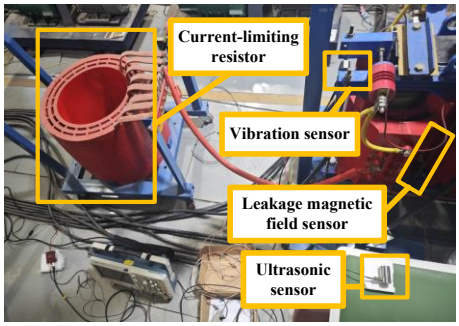
Sensor layout: Shown in Fig. 6(b). The vibration sensor is mounted on the upper transformer clamp (0–10 kHz), and the ultrasonic sensor is positioned 50 cm horizontally from the winding center (15–70 kHz). Both sensors are powered by a constant current source and connected to two independent oscilloscope channels (1 GHz sampling).

The leakage magnetic field sensor is a Faraday-effect magneto-optical sensor connected via optical fiber to a self-developed magnetic protection unit for online monitoring, with a 1600 Hz sampling rate. All waveform data are transmitted to the host computer.

For the dry-type transformer under rated voltage, five operating states are set: normal (0), inter-turn short in the middle of the high-voltage winding (1), inter-turn short in the lower part (2), 10% axial deformation in the upper part (3), and arc discharge in the high-voltage winding (4). Inter-turn short: 2 shorted turns out of 201 total. Arc discharge is simulated using two wires connected in parallel at different turn positions to mimic internal winding arcs.



(a) Wiring diagram of the dynamic simulation experimental system



(b) Sensor layout diagram



(c) Transformer control cabinet

Fig. 6. Diagram of the Dynamic Mold System Device

A. Vibration–Ultrasound Sample Augmentation and Time-Frequency Map Conversion

The proposed WCGAN-GP model augments transformer vibration and ultrasonic signals for multimodal fault diagnosis. Training was performed for 10,000 iterations, and the generator and discriminator loss variations are shown in Fig. 7. Initially, both losses are high; with more iterations, the generator loss decreases while the discriminator loss increases, eventually stabilizing. This reflects the dynamic adversarial balance achieved during the augmentation of vibration and ultrasonic samples.

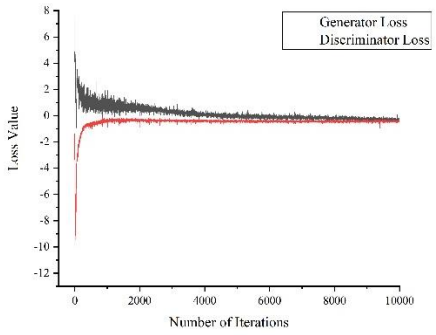


Fig. 7. Loss Function Evolution Curve of WCGAN-GP

After data augmentation using WCGAN-GP, the RPM and CWT methods are applied to the vibration and ultrasonic signals, respectively, to perform feature transformation, mapping the one-dimensional time-domain signals into two-dimensional feature maps and constructing datasets for the corresponding classes. Fig. 8 shows examples of the two-dimensional feature maps for the two modalities after transformation.

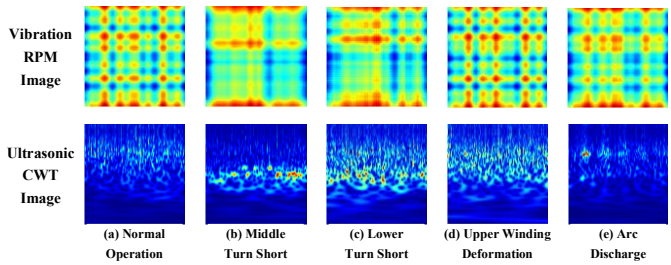


Fig. 8. Examples of 2D Feature Maps: Vibration (RPM) and Ultrasound (CWT)

B. Transformer Fault Diagnosis Model Training

The experiment targeted three modalities—leakage magnetic field, vibration, and ultrasound—constructing datasets of 2,000 samples for each modality. First, the original samples were divided into training and testing sets, with 80 samples per class reserved for testing and the remaining samples used for training, ensuring independence and class balance between the two sets. Subsequently, the training sets of the vibration and ultrasound modalities were augmented using WCGAN-GP and transformed into two-dimensional images, while the training set of the leakage magnetic modality was formed by combining dynamic model measurements and simulation data at a 1:1 ratio and preprocessed according to the procedure shown in Figure 2, ensuring both sufficiency and diversity of the training samples. Ultimately, for each modality, the training and testing sets contained 320 and 80 samples per operating condition, respectively. Since each class contained the same number of samples, no additional stratified sampling was required.

After model training is completed, the model achieving the highest accuracy during training is saved and evaluated using the test set. To evaluate the effectiveness and generalization capability of the proposed method, its performance is compared with that of single-modality networks for each modality and a three-modality fusion network without an attention mechanism. All models are trained using 5-fold cross-validation, with accuracy (Accuracy), precision (Precision), recall (Recall), and F1 score (F1 score) as evaluation metrics. The evaluation metrics are calculated as follows:

$$\begin{cases} Accuracy = \dfrac{TN + TP}{TN + TP + FN + FP} \\ Prescion = \dfrac{TP}{TP + FP} \\ Recall = \dfrac{TP}{TP + FN} \\ F1 = \dfrac{2 \times Prescion \times Recall}{Prescion + Recall} \end{cases} \tag{13}$$

The evaluation results of different methods are shown in Table I. Among single-modality networks, the 1D-ResNet based on the leakage magnetic field modality performs best, with accuracy and other metrics exceeding those of the vibration and ultrasonic modalities, indicating that leakage magnetic signals contain richer fault features. In comparison, the three-modality fusion network (without MLCA) achieves significant improvements in all metrics. The proposed method outperforms all others, achieving an accuracy of 99.5%, demonstrating that the introduction of the MLCA mechanism enables the model to better integrate features from different modalities, thereby significantly improving fault diagnosis accuracy and stability while exhibiting strong generalization capability.

TABLE I. EVALUATION RESULTS OF DIFFERENT APPROACHES

Methods	Accuracy	Precision	Recall	F1 score
2D-Densenet（Single Vibration Modality）	0.9400	0.9410	0.9395	0.9402
2D-Densenet (Single Ultrasonic Modality)	0.9300	0.9301	0.9300	0.9298
1D-ResNet（Single Leakage Magnetic Field Modality）	0.9625	0.9610	0.9645	0.9627
Tri-modal fusion network（without MLCA）	0.9800	0.9805	0.9785	0.9788
Proposed Method	**0.9950**	**0.9951**	**0.9950**	**0.9950**

VI. CONCLUSION

The proposed method combines WCGAN-GP sample augmentation with a multi-modal deep feature interaction mechanism for transformer fault diagnosis, addressing scarce vibration and ultrasonic samples and modality differences, and enabling efficient extraction and fusion of fault information. The main conclusions are:

(1) A conditional WGAN based on the Wasserstein distance was developed to generate high-quality, class-specific synthetic samples for vibration and ultrasonic modalities, alleviating limited sample sizes and class imbalance, and supporting stable multi-modal fusion and fault classification.

(2) Multi-point leakage magnetic waveforms were segmented and concatenated, while vibration and ultrasonic signals were converted into RPM and CWT two-dimensional feature maps, constructing a multi-source input format that enhances feature completeness and discriminative capability.

(3) A ResNet-DenseNet-MLCA multi-modal fusion model was designed to exploit complementary information among leakage magnetic, vibration, and ultrasonic modalities. Experiments show it significantly outperforms single-modality approaches in fault classification accuracy.

ACKNOWLEDGMENT

This work was supported by the Science and Technology Project of State Grid Corporation of China (Grant No. 520940240037). The authors would also like to thank the Power System Protection and Monitoring Laboratory at Shanghai University of Electric Power for providing experimental support.

REFERENCES

[1] X.L. DENG, H. ZHU, M. YANG, W.Q. WU, S.M. LIU, "Research on early fault protection method for transformer windings based on multi-state model," Proceedings of the Chinese Society for Electrical Engineering, vol. 42, no. 18, pp. 6704–6715, 2022.

[2] X.L. DENG, K. YAN, H.Y. ZHU, H. ZHU, Z. ZHAN, S.M. LIU, "Early fault protection based on transformer winding circuit–leakage magnetic field multi-state analytical model," Electric Power Technology, vol. 47, no. 09, pp. 3808–3821, 2023.

[3] B. QI, P. ZHANG, Z.H. RONG, C.R. LI, Y.F. CHEN, "Effectiveness evaluation method for oil chromatography monitoring sensors based on data-driven and multi-criteria fusion," Electric Power Technology, vol. 41, no. 11, pp. 3662–3669, 2017.

[4] X.Z. ZHAO, G. WU, J. WANG, Y.Q. XING, C.G. YAO, "Transformer winding deformation fault diagnosis method based on frequency response reconstruction and digital image processing," High Voltage Technology, pp. 1–12.

[5] X.L. DENG, Q. MA, Z.X. TONG, K. YAN, S.H. WU, "Early fault protection of transformers based on digital twin virtual leakage magnetic field waveforms," Electric Power Technology, vol. 48, no. 11, pp. 4806–4815, 2024.

[6] X. YANG, D. ZHOU, P. WANG, C.Y. LIN, F.H. WANG, "Transformer winding state detection based on optimized TQWT and LE," Power Automation Equipment, vol. 43, no. 08, pp. 188–194, 2023.

[7] Y. FENG, H.Y. DU, Y.M. LI, L. WANG, X. WANG, "Transformer winding deformation detection technology based on pulse coded excitation ultrasonic spread spectrum ranging," High Voltage Technology, vol. 46, no. 11, pp. 3960–3969, 2020.

[8] T.J. PU, J. QIAO, X. HAN, G.B. ZHANG, X.Y. WANG, "Research and application of artificial intelligence technology in power equipment operation and maintenance," High Voltage Technology, vol. 46, no. 02, pp. 369–383, 2020.

[9] X.L. DENG, Z. ZHANG, H. ZHU, K. YAN, "Early fault diagnosis of transformer winding based on leakage magnetic field and DSAN learning method," Frontiers in Energy Research, vol. 10, p. 1058378, 2023. doi: 10.3389/fenrg.2022.1058378.

[10] J.F. LIU, Y.F. FAN, Y.N. SONG, Y.D. MING, N.H. XIA, "Transformer winding fault diagnosis based on improved variational mode decomposition, deep residual network, and leakage magnetic signals," Electric Power Technology, pp. 1–12.

[11] Q.Z. WU, T.G. LÜ, W.D. LIU, Y. GAO, S.C. WU, "Mechanism-data fusion driven research on inter-turn fault diagnosis of transformers," Proceedings of the Chinese Society for Electrical Engineering, pp. 1–14.

[12] J.T. XUE, H.Z. MA, H.S. YANG, Y.M. NI, K.L. WAN, "Transformer winding looseness fault diagnosis based on Gramian angular field and transfer learning-AlexNet," Power System Protection and Control, vol. 51, no. 24, pp. 154–163, 2023.

[13] Y. WANG, W. LI, H.S. ZHAO, J.L. ZHANG, Z.W. SHEN, "Transformer fault diagnosis based on dissolved gas analysis using DBN-SSAELM," Power System Protection and Control, vol. 51, no. 04, pp. 32–42, 2023.

[14] B. QI, K.H. ZHU, Y. LUO, G.R. SHI, P. ZHANG, "Research status and future prospects of intelligent sensing and evaluation technology for power transformer health condition," High Voltage Technology, pp. 1–20.

[15] Z. XING, Y. HE, Q. YAO, "Online transformer fault diagnosis method based on multi-modal information fusion," Journal of Electronic Measurement and Instrumentation, vol. 38, no. 09, pp. 95–103, 2024.

[16] Z.Q. PENG, Q.C. LI, J. CHEN, J.M. MA, "EMA fault diagnosis method based on GRU and improved attention mechanism for multi-information fusion," Journal of Beihang University, pp. 1–16.

[17] S. YU, X. CHANG, Y. YU, B. WANG, X. M., Z. W., "Data-driven fault diagnosis for rolling bearings based on machine learning and multisensor information fusion," IEEE Sensors Journal, vol. 25, no. 2, pp. 3452–3464, Jan. 15, 2025.

[18] D.Z. LI, Y.S. QI, L.Q. LI, R. MA, Y.T. LI, "Intelligent fault diagnosis of wind turbines based on dual-stream GAN data augmentation," Power Automation Equipment, vol. 44, no. 11, pp. 94–102, 2024.

[19] H.D. SHAO, W. LI, Y. LIU, B. YANG, "Fault diagnosis of rotor-bearing system under time-varying speed based on dual-threshold attention GAN and small samples," Journal of Mechanical Engineering, vol. 59, no. 12, pp. 215–224, 2023.

[20] Y.X. LI, H.J. HOU, M.K. XU, S.W. LI, G.H. SHENG "Transformer oil chromatography case augmentation method based on policy gradient and GAN," Power Automation Equipment, vol. 40, no. 12, pp. 211–218, 2020.

[21] X.L. DENG, Z. WANG, P. ZENG, D.S. ZHOU, Z.X. DU, "Transformer winding early fault localization method using leakage magnetic field amplitude features," Journal of Electric Power Systems and Automation, pp. 1–11.

[22] P. JU, "State recognition of power transformer core windings based on vibration data augmentation," M.S. thesis, Shandong Univ., 2023.

[23] X.C. HUA, H.B. MU, Z.K. LAI, C.H. ZHOU, H.F. LIN, "Inversion method for transformer partial discharge ultrasonic multipath propagation characteristics based on acoustic ray tracing," High Voltage Technology, pp. 1–12.

[24] Q.L. WANG, B.G. WU, P.F. ZHU, et al., "ECANet: Efficient channel attention for deep convolutional neural networks," in Proc. IEEE/CVF Conf. Computer Vision and Pattern Recognition, Seattle, USA, 2020, pp. 11534–11542.

[25] K.M. HE, X.Y. ZHANG, S.Q. REN, J. SUN, "Deep residual learning for image recognition," in 2016 IEEE Conf. Computer Vision and Pattern Recognition (CVPR), Las Vegas, NV, USA, 2016, pp. 770–778.

[26] G. HUANG, Z. LIU, L. VAN DER MAATEN, K.Q. WEINBERGER, "Densely connected convolutional networks," IEEE Comp. Soc., 2016. doi: 10.1109/CVPR.2017.243.

An Improved Cloud Drift Optimization Based Two-Layer MPC for Economic Dispatch of Microgrids with Hybrid Energy Storage

Peixin He
School of Astronautics, Northwestern Polytechnical University, Xi'an, China
hepeixin@mail.nwpu.edu.cn

Chenyuhao Ma
School of Astronautics, Northwestern Polytechnical University, Xi'an, China
chenma@mail.nwpu.edu.cn

Daming Zhou
School of Astronautics, Northwestern Polytechnical University, Xi'an, China
daming.zhou@nwpu.edu.cn

S. M. Muyeen
Department of Electrical Engineering, Qatar University, Doha, Qatar
sm.muyeen@qu.edu.qa

***Abstract*—This paper proposes a two-layer Model Predictive Control (MPC) framework integrated with an Improved Cloud Drift Optimization (ICDO) algorithm to address the economic dispatch problem in renewable-energy-powered microgrids with hybrid energy storage systems (HESS). The upper-layer MPC performs long-term economic scheduling with battery degradation cost consideration, while the lower-layer MPC handles short-term power fluctuation suppression and prediction error compensation. To enhance the global optimization capability and computational efficiency of the non-convex upper-layer problem, an ICDO algorithm is introduced, incorporating sinusoidal chaotic mapping initialization, a ring topology strategy, and a multi-layer adaptive parameter mechanism. Simulation results under various electricity price and uncertainty scenarios demonstrate that the proposed method significantly reduces operating costs, mitigates battery degradation, and improves computational performance compared to conventional solvers and other swarm intelligence algorithms.**

Keywords—microgrid, economic dispatch, model predictive control, cloud drift optimization, hybrid energy storage, battery degradation

I. INTRODUCTION

The penetration of renewable energy in distribution networks is rapidly increasing with global energy transition and low-carbon targets [1]. photovoltaic (PV) and wind are intermittent and fluctuating, and direct grid connection can affect stability and economy [2]. Microgrids, integrating distributed generation, energy storage systems (ESS), and controllable loads, operate in grid-connected or island modes, enhancing renewable energy integration.

ESS enables energy shifting and balancing [4]. HESS, typically combining high-energy-density batteries with high-power-density supercapacitors, meets both long-term and rapid-response demands [5]. However, frequent cycling accelerates battery degradation, making degradation cost key in dispatch optimization [6].

MPC has shown advantages in handling constraints and rolling optimization [7]. In HESS-based microgrids, a two-layer MPC can combine long-horizon cost and life optimization in the upper layer with short-term error compensation in the lower layer [8]. While [9] considered degradation costs for both battery energy storage system (BESS) and supercapacitor energy storage system (SCES), deterministic solvers (IPOPT, MILP) often suffer from high computation time or local optima in non-convex problems with long horizons and large forecast errors [10]. Intelligent optimization algorithms (PSO, GA) improve global search [11], but integration with two-layer MPC and degradation-aware HESS scheduling remains limited.

CDO [12] balances global exploration and local exploitation for non-convex, multi-constraint problems. This work proposes an ICDO with dynamic drift speed adjustment, adaptive particle weighting, and feasible-region repair, embedded in a two-layer MPC. The ICDO serves as the upper-layer solver to improve optimization capability and efficiency without altering the microgrid or degradation models.

Contributions:

- Algorithm: ICDO integrating adaptive drift control, particle weighting, and feasible-region repair for rolling optimization.
- Framework: ICDO as the upper-layer solver within the two-layer MPC, coordinating with lower-layer real-time control.
- Verification: Simulations under various conditions confirm improved economy, lifespan protection, computational speed, and robustness.

II. RENEWABLE ENERGY MICROGRID SYSTEM

A. Overall Structure of Microgrid

A Renewable Energy Based Microgrid (RE-MG) integrates distributed renewable generation, ESS, controllable loads, and EMS within a local power network. It operates in grid-connected or island mode, enabling internal energy production, distribution, regulation, and bidirectional exchange with the main grid. The overall structure is shown in Fig. 1:

The microgrid adopts an AC/DC hybrid architecture: the main grid connects to the AC bus via the Point of Common Coupling (PCC), while PV, wind, batteries, and supercapacitors are linked to AC or DC buses through power conversion interfaces. AC and DC buses interconnect via bidirectional converters, supporting flexible supply to various loads. The AC bus maintains voltage and frequency when grid-connected; the DC bus, connected to PV, DC storage, and DC loads, is stabilized by DC/DC converters. Dual AC/DC converters enable bidirectional AC–DC power transmission.

979-8-3315-5472-9/25/$31.00 ©2025 IEEE

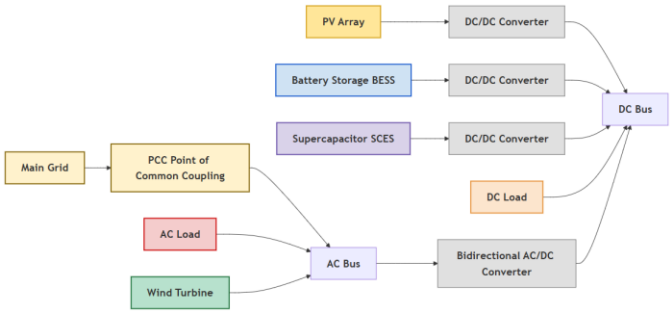


Fig. 1. Renewable energy microgrid overall structure diagram

B. Main Components and Functions of Microgrids

The main renewable sources are PV arrays and Wind turbine (WT). PV converts solar irradiance into DC power using maximum power point tracking (MPPT), with output influenced by irradiance and temperature. WT generate AC from wind energy, output stabilized by power electronics, and connect directly to the AC bus or via AC/DC converters to the DC bus. Due to the intermittency of both sources, ESS is required for balance and regulation.

The ESS consists of BESS and SCES:

- BESS: High energy density, suitable for medium–long-term balancing; charged during surplus generation and discharged during peak demand or low renewable output. Cycle aging requires considering degradation cost in dispatch.
- SCES: High power density, fast charge–discharge, and long lifespan, ideal for second–millisecond response to sudden load changes and renewable fluctuations.

By coordination, SCES manages high-frequency transients while BESS covers low-frequency balancing.

Load units include residential, commercial, and controllable loads, with profiles shaped by behavior, production schedules, and climate. Participation in demand response (DR) programs enables load shifting, reducing costs and improving dispatch flexibility.

Power conversion equipment, including DC/DC converters, bidirectional AC/DC converters, and grid-tied inverters. The Point of Common Coupling (PCC) interfaces the microgrid with the main grid: in grid-connected mode, the main grid provides support and backup power, while in islanded mode, the microgrid operates autonomously using local generation and energy storage systems (ESS) to ensure supply continuity and system stability.

III. Two-Level Model Predictive Control Framework

A. Framework Overview

To address the characteristics of renewable energy microgrid operation, which requires both long-term economic efficiency and battery life optimization as well as short-term rapid dynamic compensation, this paper adopts a Two-Layer Model Predictive Control (TL-MPC) architecture. This architecture decomposes the optimization problem into an upper-level economic dispatch problem and a lower-level real-time control problem, thereby reducing the contradictions in computational complexity, real-time performance, and robustness that arise from a single large-scale optimization.

In the TL-MPC, the upper layer generates the reference dispatch plan for the hybrid energy storage system and the power interaction with the main grid based on a longer prediction window; the lower layer operates on a shorter time scale and uses real-time measurement data to correct the power distribution to offset prediction errors and fluctuations in renewable energy output. The two layers are linked through the downlink of reference values and the uplink of state variables, and both adopt the Receding Horizon Optimization (RHO) strategy for dynamic updates.

B. Upper MPC (Economic Dispatch Layer)

The main objective of the upper-level MPC is to comprehensively consider the costs of purchasing and selling electricity and the degradation costs of energy storage within the prediction time horizon N_u, to achieve a trade-off optimization between operational economy and equipment life protection.

1) Objective function

Let $P_B(k)$ represent the battery power within the scheduling period k (discharge is positive, charge is negative), and $P_M(k)$ represent the power exchanged with the main grid (power purchase is positive, power sale is negative). The objective function can be expressed as:

$$\min_{\mathbf{u}} J_{\text{upper}} = \sum_{k=1}^{N_u} \left[C_g(k) \cdot P_M(k) + C_{\text{deg}}^{B}(k) + C_{\text{deg}}^{SC}(k) \right] \tag{1}$$

Here, $C_g(k)$ represents the electricity price signal at step k; $C_{\text{deg}}^{B}(k)$ and $C_{\text{deg}}^{SC}(k)$ are respectively the degradation costs of the battery and the supercapacitor.

Considering the impact of depth of discharge (DOD) on lifespan, the battery degradation cost can be modeled as:

$$C_{\text{deg}}^{B}(k) = \alpha_B \cdot \frac{|P_B(k)| \cdot \Delta t}{E_B^{cap}} \cdot f_{\text{DOD}}(\text{DOD}(k)) \tag{2}$$

Among them, α_B is the unit capacity replacement cost (USD/kWh), E_B^{cap} is the rated capacity of the battery, and $f_{DOD}(\cdot)$ is the DOD life attenuation coefficient.

2) Constraints

The upper-level optimization needs to satisfy the following constraints:

a) Power balance constraint

$$P_{PV}(k) + P_{WT}(k) + P_M(k) + P_B(k) + P_{SC}(k) = P_L(k) \tag{3}$$

b) Energy storage state of charge constraints

$$SOC_B^{\min} \le SOC_B(k) \le SOC_B^{\max} \tag{4}$$

$$SOC_B(k+1) = SOC_B(k) - \frac{\eta_B P_B^{+}(k) - \dfrac{P_B^{-}(k)}{\eta_B}}{E_B^{cap}} \cdot \Delta t \tag{5}$$

c) Adjust the upper and lower limit constraints

$$P_B^{\min} < P_B(k) < P_B^{\max}, P_M^{\min} < P_M(k) < P_M^{\max} \quad (6)$$

Upper-level optimization problems typically possess nonlinear, multi-constraint, and mixed-integer characteristics. To enhance the global optimization ability and computational efficiency for non-convex problems, this paper employs the ICDO algorithm for solution.

C. Lower-level MPC (Real-time Compensation Layer)

The lower-level MPC aims at dynamic tracking and rapid disturbance suppression within the short-term prediction time domain N_l , and mainly regulates the control quantities of supercapacitor power $P_{SC}(h)$ and battery power correction $\Delta P_B(h)$.

1) Objective function:

The lower optimization can be expressed as:

$$\min_{\mathrm{v}} J_{\text{lower}} = \sum_{h=1}^{N_l}\left[w_1\left(P_B'(h) - P_B^{\text{ref}}(h)\right)^2 + w_2\left(P_{SC}(h)\right)^2 \right] \quad (7)$$

Here, $P_B'(h)$ represents the actual battery power of the lower-level scheduling; $P_B^{ref}(h)$ is the reference value of the upper level; ω_1 and ω_2 are weighting coefficients.

2) Constraints:

a) Real-time power balance

$$P_{PV}(h) + P_{WT}(h) + P_M^{ref}(h) + P_B'(h) + P_{SC}(h) = P_L(h) + \Delta P(h) \quad (8)$$

b) SOC range constraints (battery and supercapacitor)

$$SOC_{SC}^{\min} \le SOC_{SC}(h) \le SOC_{SC}^{\max} \quad (9)$$

c) Power change rate constraint (supercapacitor)

$$|P_{SC}(h) - P_{SC}(h-1)| \le \Delta P_{SC}^{\max} \quad (10)$$

Lower-level problems can usually be transformed into quadratic programming (QP) problems, thereby enabling rapid online solution within a control cycle of milliseconds to seconds.

D. Upper and Lower Layer Interaction Mechanism

The upper and lower layer MPCs achieve closed-loop control through the following steps:

- The upper layer optimizes the long prediction time domain to obtain the reference power plan for the next N steps (P", P;).
- The lower layer tracks the reference of the upper layer in a short time domain to perform fluctuation compensation.
- The lower layer feeds back the SOC and actual power to the upper layer in real time and updates the initial value of the F-period optimization.
- All adopt a rolling time-domain update strategy to adapt to the uncertain fluctuations of renewable energy and loads.

IV. Improved Cloud Drift Optimization Algorithm

CDO is a swarm intelligence algorithm inspired by atmospheric cloud particle drifting, modeling candidate solutions as "cloud particles" that balance global exploration and local exploitation via simulated drift velocity and position perturbation. While standard CDO offers good convergence and global search capability, it exhibits limitations in non-convex, multi-constraint, mixed-variable problems.

To overcome these, this paper enhances CDO structurally—considering the upper-layer MPC optimization and multi-constraint non-convex nature of the hybrid energy storage degradation cost model—and proposes an ICDO.

A. Sinusoidal Chaotic Mapping Initialization

To enhance the diversity of the initial population and the coverage of the search space, the sinusoidal chaotic map is introduced to generate the initial positions.

Initialize individual cloud particles:

$$X_{k+1} = \varepsilon X_K^2 \sin(\pi X_k) \quad (11)$$

In the formula, $\varepsilon = 2.3$, X_k represents the state of the kth individual in the population, where $k = 1,2,...,N$ (the number of individuals in the population).

B. Local Optimization Stage

Randomly select a random number r from 0 to 1, $p = \tanh(|Y_i - Y^*|)$, Y_i is the fitness of the i-th individual. When $r \le p$, the update formula is established as:

$$\begin{aligned} X(t+1) = {} & 0.5(X^*(t) + 0.8\omega_2 \times v_b \times (\omega X_a(t) - X_b(t))) \\ & + 0.5X_{attract-i}(t) \end{aligned} \quad (12)$$

In the formula, $X^*(t)$ represents the optimal variable, $X_a(t)$ and $X_b(t)$ are the variables of the a-th and b-th individuals within the population, respectively, where a and b are random numbers ranging from 0 to N, $v_b \sim U(-0.2a, 0.2a)$, $X_{attract-i}$ is the ring topology variable of the i-th individual solved by the ring topology strategy, and ω_2 is a dynamic parameter designed according to the multi-level nested adaptive mechanism. The two improved strategies are described below:

1) Ring topology strategy

Taking the current particle as the center, establish a ring topology structure. Based on the particles within the ring topology structure, a calculation method for the ring topology variable is established, specifically:

$$X_{attract-i} = \frac{\sum_{i-u/2}^{i+u/2} X_j^*}{u+1} \quad (13)$$

In the formula, X^*_j represents the historical optimal variable of the j-th individual, $X_{attract-i}$ represents the ring topology variable of the i-th individual, and u represents the number of variables covered within the ring topology structure except for the current variable.

2) Multi-layer nested adaptive parameter adjustment

Replace the adaptive parameters of the original optimization algorithm with multi-layer nested adaptive parameters and incorporate them into the iterative update of the optimization variables. The calculation of the outer dynamic parameter ω_i is as follows:

$$\begin{cases} \omega_i = 1 + (0.3 + 0.7\omega_1)\ln(\dfrac{Y^* - X_i}{Y^* - Y^{worst} + 1}) & i \le \dfrac{N}{2} \\ \omega_i = 1 - (0.3 + 0.7\omega_1)\ln(\dfrac{Y^* - X_i}{Y^* - Y^{worst} + 1}) & i > \dfrac{N}{2} \end{cases} \tag{14}$$

In the formula, Y^* is the optimal fitness, and Y^{worst} is the worst fitness. ω_1 is the inner dynamic parameter, specifically:

$$\begin{cases} \omega_1 = \sin(\dfrac{\pi}{2} \cdot \dfrac{t}{T}) & i \le \dfrac{N}{2} \\ \omega_1 = \sin(\dfrac{\pi}{2} \cdot \dfrac{t}{T} - \dfrac{\pi}{2}) & i > \dfrac{N}{2} \end{cases} \tag{15}$$

In the formula, t represents the current iteration number, and T represents the maximum number of iterations. After introducing multi-nested adaptive parameters, the variable update formula is:

$$X(t+1) = 0.5(X^*(t) + 0.8\omega_2 \times v_b \times (\omega X_a(t) - X_b(t))) + 0.5X_{attract-i}(t) \tag{16}$$

The meaning of all variables is consistent with formula (12).

ω_2 is a three-layer dynamic parameter, specifically:

$$\omega_2 = \sin(\frac{\pi}{2}\frac{t}{T}) \tag{17}$$

C. Global Exploration Phase

If $r > p$, the formula for updating the optimization variable is established as:

$$X(t+1) = \omega_2 v_c X(t) \tag{18}$$

$v_c \sim U(-0.2b, 0.2b)$, ω_2 is dynamic parameter of the third layer, specifically:

$$\omega_2 = \sin(\frac{\pi}{2}\frac{t}{T}) \tag{19}$$

D. Random Disturbance Stage

To prevent the algorithm from converging prematurely and affecting the subsequent search stage, When $t > 0.9T$, enter the random perturbation stage:

$$X(t) = X(t) \cdot (1 - esp \cdot rand()) \tag{20}$$

In the formula, esp is the disturbance constant, and $rand()$ is a random value between 0 and 1.

V. Performance Evaluation

To evaluate the performance of the proposed two-layer MPC energy management method based on the ICDO, this paper constructs a typical renewable energy microgrid simulation model and conducts a comparative analysis of its economy, energy storage life protection, and real-time performance under multiple scenarios. This section introduces the structure of the test microgrid system, key model parameters, as well as scenario and prediction settings respectively.

A. Test System Settings

The simulation embedded with the proposed two-layer MPC framework. In this framework, ICDO serves as the upper-level optimizer, which receives the predicted data in real time and outputs the reference scheduling values, while the lower-level MPC achieves dynamic power compensation within a refined time scale.

The prediction time horizon N_u for the upper-level MPC is set to 12 scheduling steps (1-hour cycle), and for the lower-level MPC, it is set to 6 steps (5-minute cycle). The population size of the ICDO is 30, the maximum number of iterations is 300, the ring neighborhood size is 6, the inertia weight and search coefficient are adaptively adjusted according to the formulas in Section 4.

B. Main System Parameters

TABLE I. lists the key parameters of each component of the test microgrid.

TABLE I. Parameters of Renewable Energy Microgrid

Component	Rated Capacity	Efficiency	SOC Range	Power Limit
PV Array	400 kWp	0.98	——	——
Wind Turbine (WT)	500 kW	0.96	——	——
Battery ESS (BESS)	12 kWh	0.95	10%-90%	±4 kW
Supercapacitor (SCES)	1 kWh	0.97	10%-90%	±10 kW
Grid Interface (PCC)	1 MW	——	——	±1 MW

C. Comparison Test and The Results

1) Optimization Algorithm Effectiveness Verification

To assess the feasibility of ICDO, it was compared with Whale Optimization Algorithm (WOA), Harris Hawks Optimization (HHO), and the original CDO using six 30-dimensional CEC2017 benchmark functions (F1–F5). Each function was run ten independent trials, with results evaluated by mean, variance, and optimal value. The tests used a population size of 50 and 300 iterations, and the outcomes are summarized in TABLE II.

TABLE II. Summary of Optimization Results for Test Functions

	performance	WOA	HHO	CDO	ICDO
F1	mean value	1.27e-38	1.19e-53	6.24e-223	0
	variance	1.61e-75	1.42e-105	0	0
	optimal value	5.35e-47	3.42e-69	0	0
F2	mean value	7.41e-211	6.16e-149	7.43e-22	4.24e-258
	variance	0	3.80e-296	2.28e-42	0
	optimal value	7.31e-224	1.20e-223	5.09e-28	2.00e-323
F3	mean value	5.53e2	2.15e-26	0	0

	variance	6.37e3	4.65e-51	0	0
	optimal value	4.01e2	2.76e-60	0	0
F4	mean value	6.12e-15	4.44e-16	4.44e-16	4.44e-16
	variance	1.17e-29	0	0	0
	optimal value	3.99e-15	4.44e-16	4.44e-16	4.44e-16
F5	mean value	4.74e-41	1.93e-60	0	0
	variance	2.14e-80	3.75e-119	0	0
	optimal value	1.34e-47	6.14e-68	0	0

These results confirm ICDO's strong global search capability and high optimization efficiency, supporting its reported advantages in the microgrid context.

2) Optimization Algorithm Robustness Verification

Sensitivity analysis was conducted on two key ICDO parameters: ring topology size r (4, 6, 8, 10) and initial adaptive weight ω (0.6, 0.7, 0.8, 0.9).

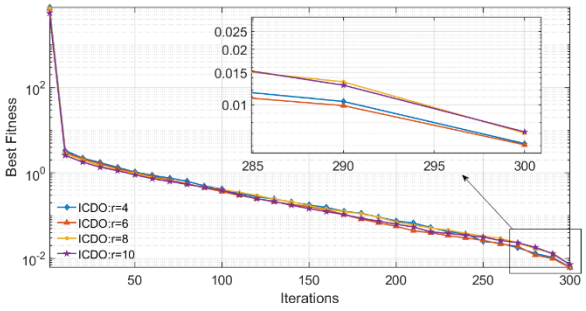


Fig. 2. influence of topological re size on algorithm robustness

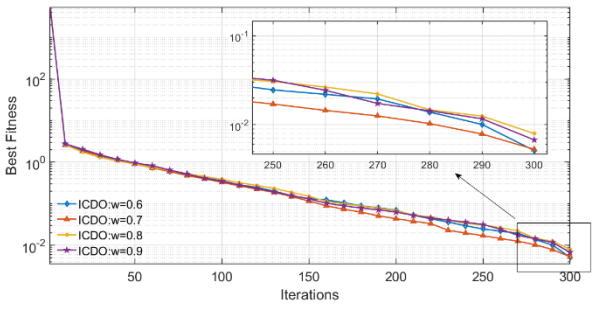


Fig. 3. Effect of adaptive weights on algorithm robustness

As shown in Fig. 2 and Fig. 3, all configurations exhibited similar convergence profiles, with only minor differences in the final fitness values (within 1.5×10^{-2} for r and 1×10^{-2} for ω). These results indicate that ICDO is robust to parameter variations. Both topology size and adaptive weight can be adjusted within reasonable ranges without substantial loss of optimization quality or convergence speed. This property reduces the burden of parameter tuning for practical applications, making ICDO more suitable for scenarios with dynamic or uncertain operating conditions.

D. Case Study

The optimal dispatch strategy under the Time-of-Use pricing scheme is illustrated in Fig. 4.

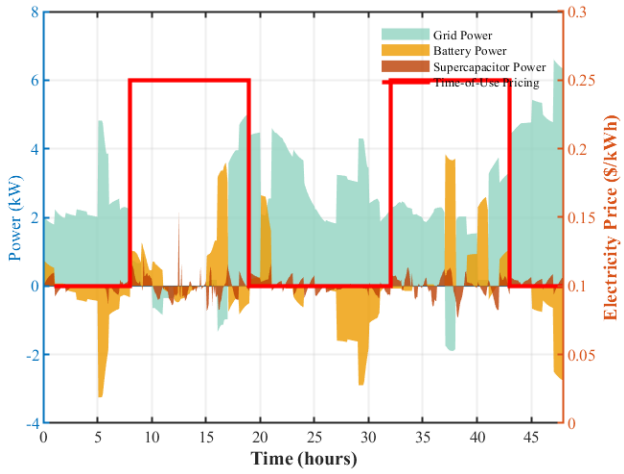


Fig. 4. Optimal Dispatch under Time-of-Use Pricing

The battery operation is predominantly governed by electricity price fluctuations, adhering to a cost-minimization principle. Specifically, the battery charges during off-peak hours (low electricity prices) and discharges during on-peak hours (high electricity prices). Notably, between 8h and 16h, 32h and 43h, when electricity prices are elevated, the surplus energy generated by renewable sources is sold back to the main grid, thereby enhancing economic returns. This strategy effectively leverages price differentials to reduce operational costs while maintaining system stability.

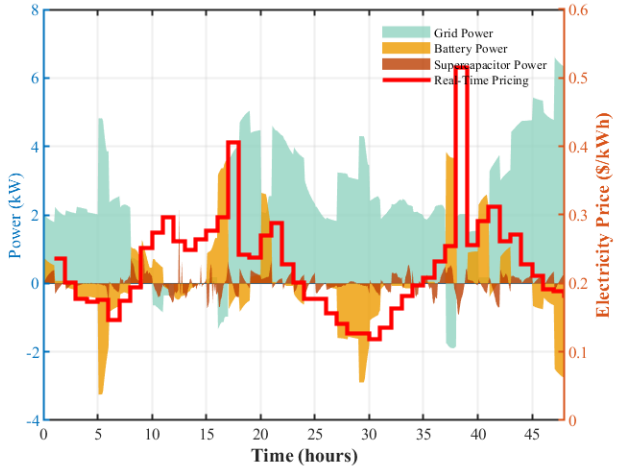


Fig. 5. Optimal Dispatch under Real-Time Pricing

Under the Real-Time Pricing scheme, as shown in Fig. 5, the battery exhibits heightened sensitivity to dynamic price variations. Rapid discharge actions are observed during periods of high electricity prices (e.g., at 17h, 20h, and 38h), while charging occurs during low-price intervals (e.g., at 6h and 30h) to prepare for subsequent high-demand periods. The lower-layer energy management system demonstrates robust performance in mitigating short-term fluctuations: the power outputs of the grid

and battery remain stable within narrow bounds, while the supercapacitor actively compensates for prediction errors and load uncertainties through high-frequency charging and discharging. This hierarchical control structure ensures both economic efficiency and operational reliability under real-time pricing conditions.

Fig. 6 shows the time-series responses of the renewable microgrid under the proposed TL-MPC. Renewable fluctuations are primarily buffered by the SCES for fast power compensation, while the BESS performs low-frequency energy shifting. The SOC trajectories stay within prescribed limits (dashed bands); BESS avoids deep and high-frequency cycling (degradation-aware operation), and SCES is re-centered promptly after near-saturation events. Consequently, the PCC power exchange and DC-bus conditions remain smooth, evidencing the coordination between upper-layer economic dispatch and lower-layer real-time compensation.

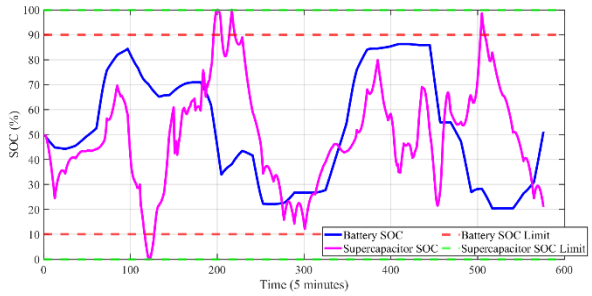


Fig. 6. SOC Changes in Batteries and Supercapacitors

Fig. 7 reports the breakdown of average cost under the proposed TL-MPC. The Operational Cost is approximately 0.46–0.47 \$/h and dominates the total, whereas the Battery Degradation Cost is two orders of magnitude smaller, on the order of 10^{-3} □ 10^{-2} \$/h, contributing only about 1~3% of the total. The Total Cost, around 0.47~0.48 \$/h, agrees with the sum of the two components within rounding, confirming internal consistency. These results indicate that the life-aware scheduling embedded in TL-MPC effectively limits deep and high-frequency cycling of the battery, thereby minimizing degradation expenses without compromising economic performance. This is consistent with the intended division of roles.

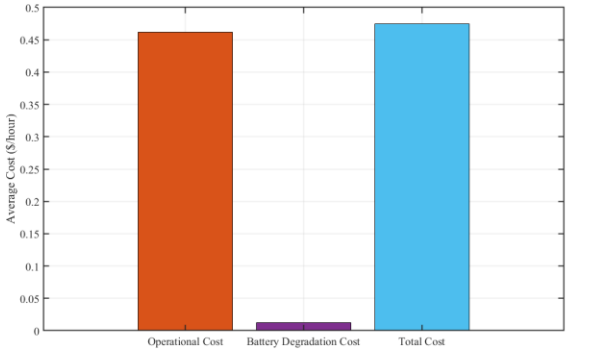


Fig. 7. Average Cost Comparison

Beyond the tested configuration, the case study highlights the scalability of the approach. As microgrid size and complexity increase, the ICDO's search mechanism can be parallelized or distributed across multiple computing nodes, preserving solution quality and computation time. The modular nature of the two-layer MPC allows incremental integration of new generation units or load types without altering core control logic, supporting adaptation to diverse microgrid architectures.

This case study therefore not only confirms the cost-efficiency and stability benefits of ICDO in the studied scenario, but also indicates its potential for deployment in larger and more complex microgrids, and under real-time operational constraints.

ACKNOWLEDGMENT

This work was funded by the Shaanxi Province Key Research and Development Plan (2024CY-GJHX-08, 2024CY-JJQ-59), the National Natural Science (52377215，51977177) and Double First-Class Discipline Construction Funded Project (WH00001049).

REFERENCES

[1] N. Mahdavi Tabatabaei, E. Kabalci, and N. Bizon, "Overview of microgrid," in Microgrid Architectures, Control and Protection Methods. Cham: Springer International Publishing, 2019, pp. 3–19.

[2] P. Piagi and R. H. Lasseter, "Autonomous control of microgrids," in 2006 IEEE Power Engineering Society General Meeting, Montreal, QC, Canada, 2006, 8 pp.

[3] S. X. Chen and H. B. Gooi, "Sizing of energy storage system for microgrids," in 2010 IEEE 11th International Conference on Probabilistic Methods Applied to Power Systems, Singapore, 2010, pp. 6–11.

[4] R. Xiong, H. Chen, C. Wang, and F. Sun, "Towards a smarter hybrid energy storage system based on battery and ultracapacitor-A critical review on topology and energy management," Journal of Cleaner Production, vol. 202, pp. 1228–1240, Nov. 2018.

[5] C. Ju, P. Wang, L. Goel, and Y. Xu, "A two-layer energy management system for microgrids with hybrid energy storage considering degradation costs," IEEE Transactions on Smart Grid, vol. 9, no. 6, pp. 6047–6057, Nov. 2017.

[6] F. Sadeque, M. Gursoy, D. Sharma, and A. G. Tousi, "Autonomous control of inverters in microgrid," IEEE Transactions on Industry Applications, vol. 60, no. 3, pp. 4313–4323, May 2024.

[7] L. Guo, X. Li, C. Wang, and J. Wang, "Coordinated control of battery and diesel in AC microgrids," unpublished.

[8] J. Jiang, L. Zou, L. Zhang, and X. Zhang, "A three-layer energy management system for hydrogen-powered ships combined instantaneous load forecasting," Electric Power Systems Research, vol. 243, p. 111494, Jan. 2025.

[9] S. Phommixay, M. L. Doumbia, and D. Lupien St-Pierre, "Review on the cost optimization of microgrids via particle swarm optimization," International Journal of Energy and Environmental Engineering, vol. 11, no. 1, pp. 73–89, Mar. 2020.

[10] S. Zhang, "Optimal control of hybrid energy storage system of new energy power generation system based on improved particle swarm algorithm," Journal of Interconnection Networks, vol. 22, no. 3, p. 2145004, Sep. 2022.

[11] M. Alibabaei Shahraki, "Cloud drift optimization algorithm as a nature-inspired metaheuristic," Discover Computing, vol. 28, no. 1, pp. 1–28, Jan. 2025.

A Layered Optimization Scheduling Method of Energy Storage Stations for Supporting Grid-Province Coordination

Wei Ma
State Grid Anhui Electric Power Research Institute
Hefei, Anhui Province, China
16117385@bjtu.edu.cn

Bin Xu
State Grid Anhui Electric Power Research Institute
Hefei, Anhui Province, China
xubin1980@sina.com

Ze Li
China Electric Power Research Institute
Beijing, China
lize@epri.sgcc.com.cn

Bingjian Fan
China Electric Power Research Institute
Beijing, China
fanbingjian@epri.sgcc.com.cn

Zhe Li
State Grid Anhui Electric Power Research Institute
Hefei, Anhui Province, China
906233647@qq.com

Guigang Han
China Electric Power Research Institute
Beijing, China
distributedpower@163.com

***Abstract*—A layered optimization scheduling method of energy storage stations for supporting grid-province coordination is proposed. The model on the second layer is responsible for coordinating the inter-provincial peak-shaving resources, aiming to minimize load fluctuations and operational costs. The thermal power plant outputs, energy storage charge/discharge powers and interconnection line planned outputs are coordinated. The model on the primary layer is responsible for the power distribution among energy storage stations within provinces, aiming to maximize the net revenue from optimization scheduling of provincial energy storage stations. Particle swarm optimization and mixed-integer linear programming methods are adopted to solute the layered scheduling models of interconnected regions. Simulation analysis of two inter-connected regions is performed. The effectiveness and superiority of the proposed method are validated.**

Keywords—grid-province coordination, energy storage stations, layered optimization, scheduling method

I. INTRODUCTION

With the transformation of the global energy structure, the penetration rates of renewable energies such as wind power and photovoltaics continue to rise. However, the strong volatility and anti-peak shaving characteristics of renewable energy outputs have led to a significant expansion of the peak-valley difference in the net load of the grid. Severe challenges are posed to the traditional thermal power dominated peak shaving system. Especially in inter provincial interconnected power grids, there are significant differences in the penetration rates of renewable energies among provinces, and the uneven spatial and temporal distribution of peak shaving resources exacerbates the risk of power imbalance between regions. There are benefits brought by load shifting and complementary power sources between different interconnected regions.

The power system in China adopts a 'unified scheduling, hierarchical management' structure. The large regional grid serves as the coordinating units for cross-provincial coordination, forming a vertically integrated scheduling hierarchy with provincial grids [1]. In this structure, provincial dispatch centers follow the unified coordination instructions from the second-layer grid dispatching, while based on the regional 'source-grid-load-energy storage' collaborative interaction requirements, which can autonomously carry out refined scheduling decisions, achieve differentiated needs such as frequency regulation reserves and renewable energy consumption matching with the economic characteristics of energy storage technology.

Existing researches primarily focus on optimizing scheduling strategies at a single-region scale, neglecting the complementary potential and synergy between regional grids. Literature [2] adopts a layered optimization method. The load regulation function of energy storage and the deep peak-shaving technology of thermal power plants are integrated. The dual-layer iterative approach effectively improves peak-shaving flexibility and solution efficiency. Literature [3] establishes an optimization model considering the deep peak-shaving of thermal power plants and the collaborative effect of composite energy storage stations. Multi-objective peak-shaving optimization from economic costs, carbon emissions, and renewable energy consumption perspectives is conducted. Literature [4] proposes a new market trading mechanism integrating energy storage stations, renewable energy generations and thermal power peak-shaving resources. A

This work is supported by Science and Technology Project of State Grid Anhui Electric Power Co., Ltd.(Research on Multi-type Energy Storage Collaborative Planning and Regulation Technology Considering the Saturation Effect and Utilization Rate of Energy Storage)

979-8-3315-5472-9/25/$31.00 ©2025 IEEE

trading and pricing model is established based on wind-solar curtailment rates, and thermal power bidding schemes are designed based on existing peak-shaving policies, ultimately achieving multi-objective optimization through bilateral trading. Literature [5] partitions operation regions of energy storage stations to meet multi-scenario operational requirements in the renewable energy aggregation systems. Differentiated scheduling control plans are arranged for different levels of energy storage stations based on the characteristics of various types of energy storage stations and real-time charge/discharge data, effectively enabling collaborative analysis and processing of multi-layer energy storage scheduling systems. While existing researches introduce multi-dimensional objectives such as economic, low-carbon and safety considerations in peak-shaving optimization. The models mostly focus on target superposition within a single decision level and fail to effectively resolve the conflict and coordination issues between multiple objectives under the layered scheduling framework.

In response to the issue, a layered optimization scheduling strategy for energy storage stations in grid-province coordinated interconnected regions is proposed. A dual-layer optimization model is established. The second layer coordinates provincial resources to minimize load fluctuations and operational costs, and the primary layer maximizes the net revenue of energy storage stations scheduling within the province by optimizing the distribution of energy storage power.

II. Layered Optimization Scheduling Method of Energy Storage Stations in Grid-Province Coordinated Interconnected Regions

The model on the second layer focuses on multi-regional coordination. A regional collaborative scheduling model considering multi-energy coupling characteristics is established. The dual-objective function minimizes load fluctuation variance and system operational costs. The outputs of thermal power plants, energy storage aggregation powers and interconnection line power exchanges are coordinated. The model on the primary layer focuses on the optimal power distribution of energy storage stations within each region. By introducing an economic allocation weight coefficient for energy storage charge/discharge, the optimal outputs of energy storage stations are solved. The energy storage assets' lifetime revenue is maximized, while peak-shaving requirements are ensured.

A. Objective Functions

The dual-objective function minimizes load fluctuation and system operation cost by adopting linear weighting. The multiple objectives are converted into a single objective function:

$$F_1 = \min[pf_1^* + (1-p)f_2^*] \tag{1}$$

where the normalized versions of the two objectives are represented as and ; p represents the weight coefficient (p=0.5 for equal weighting).

To further enhance peak-shaving effectiveness and the economic participation of energy storage stations in system peak-shaving, the objective function is developed:

$$\min f_1 = \frac{1}{T}\sum_{t=1}^{T}\left[(P_{\mathrm{JL},t} - P_{\mathrm{ESS},t}^{\mathrm{d}} + P_{\mathrm{ESS},t}^{\mathrm{c}}) - \frac{1}{T}\sum_{t=1}^{T}P_{\mathrm{JL},t}\right]^2 \tag{2}$$

$$\min f_2 = C_1 + C_2 + C_3 + C_4 \tag{3}$$

where $P_{\mathrm{JL},t}$ represents the net load forecast value at time t; $P_{\mathrm{ESS},t}^{\mathrm{d}}$ represents the energy storage discharge power at time t; $P_{\mathrm{ESS},t}^{\mathrm{c}}$ represents the energy storage charge power at time t; C_1 represents the costs associated with thermal power plants; C_2 represents the energy storage operation costs; C_3 represents the system transmission losses; C_4 represents the renewable energy curtailment; T represents a complete scheduling cycle.

1) Thermal Power Plant Operational Costs

The operational costs of thermal power plants are significantly related to their peak-shaving depth. Based on different operating conditions, a piecewise cost function model for thermal power plant i at time t is established:

$$C_{G,i,t} = \begin{cases} C_{G,i,t'}^{1}, & P_{G,i,\min} \le P_{G,i,t} \le P_{G,i,\max} \\ C_{G,i,t}^{1} + C_{G,i,t'}^{2}, & P_{G,i,a} \le P_{G,i,t} \le P_{G,i,\min} \\ C_{G,i,t}^{1} + C_{G,i,t}^{2} + C_{G,i,t'}^{3}, & P_{G,i,b} \le P_{G,i,t} \le P_{G,i,a} \end{cases} \tag{4}$$

where $C_{G,i,t}^{1}$, $C_{G,i,t}^{2}$, and $C_{G,i,t}^{3}$ represent the coal consumption cost, deep peak-shaving loss cost, and stable combustion fuel oil cost of the thermal power plant, respectively; $P_{G,\max}$ represents the maximum output of thermal power plants; $P_{G,\min}$ represents the minimum output during conventional peak-shaving stages; $P_{G,a}$ represents the minimum output during deep peak-shaving stages without fuel oil; $P_{G,b}$ represents the minimum output during deep peak-shaving stages with fuel oil.

In addition to fuel consumption and deep peak-shaving losses during the operation of the thermal power plant, extra fuel used during startup and shutdown accelerates the loss of the plant. It is shown by comprehensive analysis that the total cost of thermal power peak-shaving can be expressed as:

$$C_1 = \sum_{i=1}^{N_G}\sum_{t=1}^{T} C_{G,i,t} + \left[X_t^i(1-X_{t-1}^i)C_{\mathrm{on}}^i + X_{t-1}^i(1-X_t^i)C_{\mathrm{off}}^i\right] \tag{5}$$

where X_t^i represents the operating status of thermal power plant i at time t (1 for operation, 0 for shutdown); C_{on}^i and C_{off}^i represent the startup and shutdown costs of the thermal power plant i, respectively.

2) Energy Storage Station Operational Costs

Energy storage station operational costs typically include charge/discharge loss costs, fixed operation and maintenance costs. In this study, the focus is on the charge/discharge costs

directly related to its scheduling behavior. Based on the considerations, the operational cost of the energy storage station is expressed as:

$$C_2 = \sum_{t}^{T} c_{\mathrm{ESS}} (P_{\mathrm{ESS},t}^{\mathrm{c}} + P_{\mathrm{ESS},t}^{\mathrm{d}}) \tag{6}$$

where c_{ESS} represents the charge/discharge power cost coefficient.

3) Interconnection Line Transmission Losses

In the regional power system optimization, interconnection line power transmission typically has three working modes, which are fixed power transmission, freely optimized transmission and constrained optimized transmission. Based on the practical grid operation requirements for interconnection line power stability, the constrained optimized mode is selected as the modeling basis.

Transmission losses from interconnection lines need to consider two aspects: the power exceeding limit losses $P_{\mathrm{line},n,t}^{\mathrm{lim}}$ caused by the interconnection line's maximum transmission capacity, and the opportunity costs of cross-regional transactions caused by time-of-day price differences in interconnected regions $\Delta\lambda_t = \lambda_{a,t} - \lambda_{b,t}$. For simplicity, the energy losses during the interconnection line's transmission process are ignored. Interconnection line transmission losses are expressed as:

$$C_3 = \sum_{t=1}^{T} \left[\sum_{n=1}^{N} P_{\mathrm{line},n,t}^{\mathrm{lim}} \lambda_n + \sum_{a,b\in N, a\neq b}^{N} P_{\mathrm{line},ab,t} \Delta\lambda_t \right] \tag{7}$$

where $P_{\mathrm{line},n,t}^{\mathrm{lim}}$ represents the constrained power for interconnection line n; $P_{\mathrm{line},ab,t}$ represents the power between regions *a* and *b*; λ_n represents the time-of-day electricity price for region *n*.

4) Renewable Energy Curtailment Penalty

Renewable energy curtailment penalty is expressed as:

$$\begin{aligned} C_4 = {} & c_{\mathrm{disc}}^{\mathrm{WT}} \left(\sum_{t=1}^{T} P_{\mathrm{disc},t}^{\mathrm{WT}} - \sum_{t=1}^{T} 0.05 P_{\mathrm{WT},t} \right) \\ & + c_{\mathrm{disc}}^{\mathrm{PV}} \left(\sum_{t=1}^{T} P_{\mathrm{disc},t}^{\mathrm{PV}} - \sum_{t=1}^{T} 0.05 P_{\mathrm{PV},t} \right) \end{aligned} \tag{8}$$

where $c_{\mathrm{disc}}^{\mathrm{WT/PV}}$ represents the curtailment penalty coefficient; $P_{\mathrm{disc},t}^{\mathrm{WT/PV}}$ represents the wind/solar curtailment power at time *t*. It is indicated by equation (8) that a curtailment penalty is incurred when the daily new energy curtailment exceeds 5% of the total power generation.

B. Constraints

The main constraints of the peak-shaving scheduling model for the interconnected regional system include system power balance constraints, interconnection line power constraints, thermal power plant constraints, renewable energy output constraints and energy storage output constraints.

1) System Power Balance Constraints

System power balance constraints can be expressed as:

$$\sum_{i=1}^{N_G} P_{G,i,t} + \sum_{i=1}^{N_W} P_{\mathrm{WT},i,t} + \sum_{i=1}^{N_P} P_{\mathrm{PV},i,t} + \sum_{i=1}^{N_E} P_{\mathrm{ESS},i,t} - P_{L,t} = 0 \tag{9}$$

where $P_{G,i,t}$, $P_{\mathrm{WT},i,t}$, $P_{\mathrm{PV},i,t}$ and $P_{\mathrm{ESS},i,t}$ represent the outputs of thermal power plants, wind turbines, photovoltaic stations and energy storage stations, respectively; $P_{L,t}$ represents the system load at time *t*; N_G, N_W, N_P, and N_E represent the number of thermal power plants, wind turbines, photovoltaic stations and energy storage stations, respectively; $P_{\mathrm{ESS},i,t} > 0$ represents energy storage stations discharge; $P_{\mathrm{ESS},i,t} < 0$ represents energy storage stations charge.

2) Interconnection Line Power Constraints

As a key decision variable, interconnection line planned power must remain within the technical transmission limits. Power operating range constraints satisfy:

$$\left| P_{\mathrm{line},ab,t} \right| \leq P_{\mathrm{line,max}} \tag{10}$$

where $P_{\mathrm{line,max}}$ represents the upper limit for interconnection line power transmission.

3) Thermal Power Plant Constraints

Thermal power plant operations must satisfy output limit constraints and unit ramp rate constraints as shown in equations (11-12):

$$X_{i,t} P_{G,i,\min} \leq P_{G,i,t} \leq X_{i,t} P_{G,i,\max} \tag{11}$$

$$-V_{G,i} \leq P_{G,i,t} - P_{G,i,t-1} \leq V_{G,i} \tag{12}$$

where $V_{\mathrm{G,i}}$ represents the maximum ramp rate of thermal power plant *i*.

4) Renewable Energy Output Constraints

Renewable energy output constraints can be expressed as:

$$\begin{cases} 0 < P_{\mathrm{WT},i,t} \leq P_{i,t,\max}^{\mathrm{WT}} \\ 0 < P_{\mathrm{PV},i,t} \leq P_{i,t,\max}^{\mathrm{PV}} \end{cases} \tag{13}$$

where $P_{i,t,\max}^{\mathrm{WT}}$ and $P_{i,t,\max}^{\mathrm{PV}}$ represent the maximum output of wind turbines and photovoltaic stations, respectively.

5) Energy Storage Output Constraints

Energy storage stations must satisfy charge/discharge status constraints, charge/discharge power constraints and upper and lower SOC constraints as shown in equations (14-16).

$$u_{i,t}^{d}+u_{i,t}^{c}\le 1,\forall t \tag{14}$$

$$0\le u_{i,t}^{\mathrm{d/c}}P_{\mathrm{ESS},i,t}^{\mathrm{d/c}}\le P_{\mathrm{ESS}}^{\max} \tag{15}$$

$$S_{\min}^{SOE/SOC}\le S_{i,t}^{SOE/SOC}\le S_{\max}^{SOE/SOC} \tag{16}$$

where $u_{i,t}^{d/c}$ represents the energy storage charge/discharge state as a 0-1 variable; $P_{\mathrm{ESS}}^{\max}$ represents the maximum charge/discharge powers; $S_{\min}^{SOE}$ and $S_{\max}^{SOE}$ represent the minimum and maximum energy states; $S_{\max}^{SOC}$ and $S_{\min}^{SOC}$ represent the upper and lower SOC limits.

Considering energy conservation and charge/discharge efficiency, the energy balance constraints are as follows:

$$\begin{cases} E_{i,t}=E_{i,t-1}+\left(\eta_{\mathrm{c}}P_{\mathrm{ESS},i,t}^{\mathrm{c}}-\dfrac{P_{\mathrm{ESS},i,t}^{\mathrm{d}}}{\eta_{\mathrm{d}}}\right)\Delta t \\ E_{i,1}=E_{k}^{\mathrm{init}}+\left(\eta_{\mathrm{c}}P_{\mathrm{ESS},i,1}^{\mathrm{c}}-\dfrac{P_{\mathrm{ESS},i,1}^{\mathrm{d}}}{\eta_{\mathrm{d}}}\right)\Delta t \\ S_{i,t}^{SOE}=\dfrac{E_{i,t}}{E_{i}^{N}} \end{cases} \tag{17}$$

where $\eta_{\mathrm{c/d}}$ represents the charge/discharge efficiency; Δt represents the unit scheduling step; $S_{i,t}^{SOE}$ and $E_{i,t}$ represent the energy states of energy storage station i at time t; E_{i}^{N} and E_{i}^{init} represent the rated capacity and initial energy of energy storage station i.

C. Energy Storage Power Economic Allocation Method

The second layer optimization incorporates daily energy balance constraints to minimize the load peak-valley difference, as shown in equation (17), and ensures the sustainability of energy storage stations' charge/discharge states. Initial allocation weights are designed based on the rated characteristics and the inherent technological differences of energy storage stations, adopted to reflect the physical regulation capacity of the devices.

A life-cycle-based energy storage optimization model is proposed to solve the issue of traditional weight allocation methods, in which economic considerations are ignored. The allocation mechanism maximizes daily net revenue, as described in equation (18).:

$$\begin{cases} \zeta_{c,k}^{eco}=1-C_{ESS,k}/\sum_{k=1}^{N_K}C_{ESS,k} \\ \zeta_{d,k}^{eco}=(I_{ESS,k}-C_{ESS,k})/\sum_{k=1}^{N_K}(I_{ESS,k}-C_{ESS,k}) \end{cases} \tag{18}$$

where $\zeta_{c,k}^{eco}$ and $\zeta_{d,k}^{eco}$ represent the economic weight distribution for charge/discharge operations; $C_{ESS,k}$ represents the charging and discharging operation cost of the kth energy storage station in the region (as shown in equation (6)); $I_{ESS,k}$ represents the operation benefit of the kth energy storage participating in peak shaving in the region, which covers the peak shaving compensation benefit of the energy storage station, the time-of-use electricity price difference benefit of "low storage and high generation", environmental benefits, etc., which is shown in Equation (19); N_K represents the total number of energy storage stations in the region.

$$\begin{aligned} I_{\mathrm{ESS},k}=\sum_{k=1}^{N_K}\sum_{t=1}^{T}[&p_{\mathrm{com}}(P_{\mathrm{ESS},k,t}^{\mathrm{d}}+P_{\mathrm{ESS},k,t}^{\mathrm{c}})+ \\ &(\eta_{\mathrm{d}}p_{t}^{\mathrm{price}}P_{\mathrm{ESS},k,t}^{\mathrm{d}}-\eta_{\mathrm{c}}p_{t}^{\mathrm{price}}P_{\mathrm{ESS},k,t}^{\mathrm{c}})+ \\ &\sum_{j}^{J}(\eta_{\mathrm{d}}p_{j}^{\mathrm{price}}\xi_{\mathrm{grid},j}P_{\mathrm{ESS},k,t}^{\mathrm{d}})] \end{aligned} \tag{19}$$

where p_{com} represents the unit environmental compensation price per unit of electricity; p_{t}^{price} represents the electricity price at time t; J is the total number of types of pollutants produced; $\xi_{\mathrm{grid},j}$ and p_{j}^{price} represent the emission density of pollutant j per unit of electricity and its corresponding unit treatment cost, respectively.

The difference between energy storage operation revenue and costs represents the net revenue, maximized in the primary-level objective function F_2. The core objective of primary layer optimization is the economic optimization of energy storage stations, coordinating power distribution among energy storage stations to maximize overall operational efficiency. The primary layer optimization continues the core constraint conditions of the second layer model, including the power limits of energy storage charging and discharging, SOC balance constraints and regional power balance requirements, etc.

The second layer focuses on system-level peak-shaving performance optimization, while the primary layer focuses on achieving economic optimal distribution of the energy storage stations. By introducing economic weight coefficients, the total power command outputs from the second layer are decomposed into a detailed scheduling plan for each station. The peak-shaving requirements are met while maximizing energy storage asset revenue.

III. Solution of Layered Scheduling Method for Interconnected Regions

To address the coordination and optimization of multi-energy systems involving wind, solar, thermal, and energy storage stations, a dual-objective scheduling model is constructed, considering load fluctuations and operational costs. The model is a complex mixed-integer nonlinear programming problem with high-dimensional variables and multiple constraints. To reduce the computational difficulty, a decomposition-coordination method is employed.

The second layer optimization focuses on the multi-regional coordination problem, and its high-dimensional nonlinear characteristics are well-suited for efficient computational intelligent optimization algorithms. For the advantages of particle swarm optimization (PSO) algorithm, such as low parameter requirements and fast convergence [6], PSO is adopted to solve the nonlinear optimization problem and get

thermal power plant outputs, total energy storage powers and interconnection line interaction powers. The primary layer combines the total power instructions of the energy storage stations to construct an allocation model based on the economic weight coefficients of charging and discharging. To handle the mixed integer programming problem, based on MATLAB, variables, constraints and objective functions are defined through YALMIP. The CPLEX solver is called for optimization calculation to optimize the outputs of energy storage stations.

IV. Simulation Results and Analysis

To verify the effectiveness of the proposed method, simulations are conducted based on two interconnected regions. Two interconnected IEEE 30-node systems are adopted as the scheduling model. In Region A, a 500 MW wind farm and a 50 MW photovoltaic station are configured. Region B is configured with a 250 MW wind farm and a 50 MW photovoltaic station. Three types of differentiated energy storage stations are deployed in the two regions. The specific operating parameters of energy storage stations in Region B are shown in Table I.

TABLE I. Peak-shaving Performance Indicators of Region B under Different Scenarios

Energy Storage Stations	E^N/ **MW·h**	$P_{ESS}^{\max}$ / **MW**	$\eta_{c/d}$ / **%**	$S_{OC,\min}$ / $S_{OC,\max}$
Energy Storage Stations 1	200	50	0.8	0.1/0.9
Energy Storage Stations 2	200	100	0.95	0.1/0.9
Energy Storage Stations 3	400	50	0.9	0.1/0.9

To verify the optimization capabilities of the proposed dual-layer scheduling method for the peak-shaving combinations in the interconnected regions, and to quantify the comprehensive benefits of energy storage stations in enhancing grid peak-shaving performance and economics, the following comparison schemes are set up:

Scheme 1: The layered optimization framework proposed in the paper is applied to the second layer, while power distribution is based on the physical characteristics of energy storage stations at the primary layer.

Scheme 2: Both the second and primary levels are adopted the optimization scheduling method proposed in the paper.

A. Peak-Shaving Effect Analysis

With the interconnection line power constraints set as 150 MW, simulations are conducted with the proposed dual-layer peak-shaving optimization scheduling method. The optimal stations output distribution for Regions A and B in Scheme 2 is shown in Figures 1 and 2. It is confirmed by simulation analysis that energy storage stations, through "low storage, high discharge" operational strategy, effectively improves system load characteristics.

The simulation results indicate that Region A, via the interconnection line, transfers surplus renewable energy output and redundant energy storage discharge capacity to Region B. Region B, through coordination between energy storage peak-shaving and deep peak-shaving from thermal power plants, dynamically adjusts the supply space to meet the interconnection line power constraints. Region B incorporates the incoming electricity from the interconnection line into its generation plan, while Region A equivalently counts its exported power as part of the load demand. Cross-regional power exchange and spatial-temporal complementary benefits are realized.

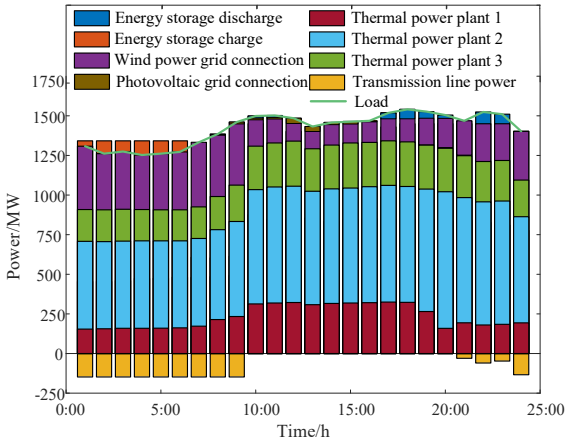


Fig. 1. Optimal commitment and dispatch in Region A

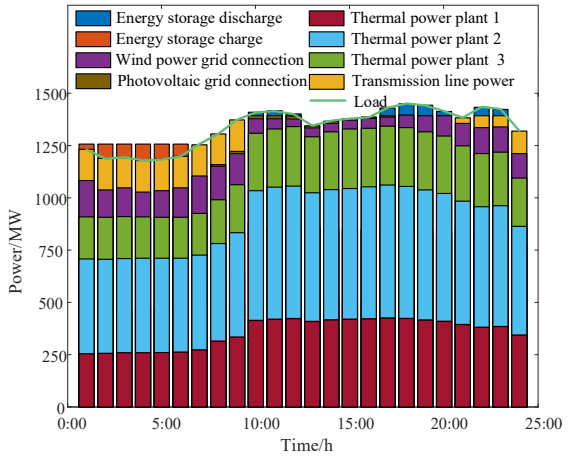


Fig. 2. Optimal commitment and dispatch in Region B

Regarding Region A as an example, the peak-shaving effect in the interconnected regions is shown in Figure 3.

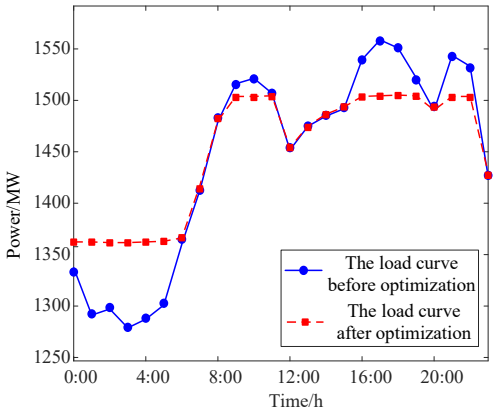


Fig. 3. Comparison of load curves in Region A before and after optimization

It can be observed that the peak-valley difference rate is reduced from 18.22% to 9.74%. Energy storage stations effectively optimized the load characteristics by reducing the peak-valley difference and alleviating the system's peak-shaving pressure.

B. Energy Storage Power Economic Distribution Results

The net revenue of energy storage stations in Region B under different schemes is compared in Table 2. It is shown that by prioritizing power allocation to the economically optimal energy storage station (Energy Storage Station 2), Scheme 2 achieves a daily net revenue of 622.08k yuan, significantly higher than Scheme 1. Although the revenues of Energy Storage Stations 1 and 3 decrease slightly, the total daily net revenue for energy storage stations increases by 98.99k yuan. The effectiveness of the power allocation method based on the full life cycle economy is verified.

TABLE II. NET REVENUE OF ENERGY STORAGE STATIONS IN REGION B

Scheduling strategy	**Energy Storage Station 1 net revenue/ k yuan**	**Energy Storage Station 1 net revenue/ k yuan**	**Energy Storage Station 1 net revenue/ k yuan**	**Total net revenue for Region B/ k yuan**
Scheme 1	320.33	597.62	272.74	1190.59
Scheme 2	316.81	622.08	270.69	1209.58

V. CONCLUSION

A layered collaborative scheduling method is proposed for energy storage stations participation in peak-shaving in grid-province coordinated interconnected regions. Based on a two-stage optimization framework, the model on the second layer coordinates multiple types of power sources and interconnection line power to mitigate load fluctuations. The model on the primary layer maximizes energy storage net revenue through a differentiated economic weight distribution mechanism. By building a cross-regional power interconnection architecture, the complementarity and optimized operation of peak shaving resources have been achieved. The load peak-valley difference rate has been reduced from 18.22% to 9.74%. The regulation capacity of load center region is enhanced and a feasible path for the safe and economic operation of high-proportion renewable energy power grids is provided. However, challenges remain in practical applications, such as the dynamic adjustment of weight coefficients under different market environments. Further researches are needed to validate the robustness of the proposed method under real-time uncertainties and diverse grid conditions.

REFERENCES

[1] V. Vijayan, A. Arzani and S. M. Mahajan, "Enhancing operational planning of active distribution networks considering effective topology selection and thermal energy storage," iEnergy, vol.4, pp. 98-106, 2025.

[2] X. Li, L. Wang, N. Yan, et al, "Cooperative dispatch of distributed energy storage in distribution network with PV generation systems," IEEE Transactions on Applied Superconductivity, vol.31, pp. 1-4, 2021.

[3] L. Argiolas, M. Stecca, L. M. Ramirez-Elizondo, et al, "Optimal battery energy storage dispatch in energy and frequency regulation markets while peak shaving an EV fast charging station," IEEE Open Access Journal of Power and Energy, vol.9, pp. 374-385, 2022.

[4] J. Lu, W. Zheng, Z. Yu, et al, "Optimizing grid-connected multi-microgrid systems with shared energy storage for enhanced local energy consumption," IEEE Access, vol.12, pp. 13663-13677, 2024.

[5] Z. Chen, F. Fan, N. Tai, et al, "Coordinated energy dispatch and flexibility support for microgrid cluster using rule-based Stackelberg gaming approach," IEEE Transactions on Industry Applications, vol.60, pp. 1564-1575, 2024.

[6] Y. Tao, J. Qiu and S. Lai, "A learning and operation planning method for uber energy storage system: order dispatch," IEEE Transactions on Intelligent Transportation Systems,vol. 23, pp. 23070-23083, 2022.

KG-SA-GNN: Knowledge-Guided Self-Attention Graph Networks for Imbalanced Fault Detection in Smart Grids

Yi Guo
Department of Automation and Electronic Information
Xiangtan University
Xiangtan, China
1409276242@qq.com

Yi Kuang
Department of Automation and Electronic Information
Xiangtan University
Xiangtan, China
ykuang@xtu.edu.cn

Bin Duan
Department of Automation and Electronic Information
Xiangtan University
Xiangtan, China
db61850@163.com

Sheng Li
Department of Automation and Electronic Information
Xiangtan University
Xiangtan, China
3067265199@qq.com

***Abstract*—Detecting low-frequency faults in smart grids is challenging due to the class imbalance in fault data and dynamic changes in grid topology. To address these issues, this paper proposes a knowledge-guided self-attention graph neural network (KG-SA-GNN). First, a domain-specific knowledge graph is constructed by integrating equipment topological constraints, historical fault co-occurrence patterns, and maintenance rules, which enhances the modeling of physical relationships in the power grid. Second, a dynamic self-attention mechanism is introduced that incorporates relationship weights and fault frequency priors to adaptively focus on critical propagation paths and improve classification performance. Experimental results on the IEEE 39-node system show that the proposed method achieves a recall rate of 78.6% for cascading faults, outperforming SMOTE-GNN by 14.9%. The false alarm rate is reduced by 9.5%, and the macro-average F1-score reaches 87.1%. The results demonstrate that KG-SA-GNN provides an effective solution for imbalanced fault diagnosis in smart grids.**

Keywords—Knowledge graph, graph neural network, smart grid, imbalanced fault detection

I. INTRODUCTION

With the large-scale grid connection of renewable energy and the widespread deployment of power electronic equipment, modern smart grids are rapidly developing towards a high proportion of new energy and high power electronics[1]. Although this transformation has improved the flexibility and sustainability of the power grid, it has also led to profound changes in the dynamic characteristics of the system: on the one hand, the random fluctuations of intermittent energy sources such as wind and solar power have significantly increased the uncertainty of power grid trends[2]; on the other hand, the strong nonlinear characteristics of power electronic equipment make the transient fault process exhibit millisecond-level rapid propagation characteristics[3] . In this context, grid fault patterns present two new characteristics: First, the distribution of fault types is highly unbalanced. According to the literature by B. Li et al.[4], short circuit and overload faults account for more than 85%, while new faults such as cascading faults caused by renewable energy disconnection and flexible DC system commutation failure only account for 3.2%-5.4%. However, the power outage losses caused by the latter account for more than 72% of the total losses[5]. Second, the dynamic nature of fault propagation paths. For example, the plug-and-play characteristics of distributed photovoltaic clusters cause the grid topology to change in minutes. Traditional fault diagnosis methods based on fixed topology maps face severe timeliness challenges[6].

The current mainstream fault detection methods can be divided into three categories: physical model-based methods, shallow machine learning-based methods, and deep learning-based methods. Among them, the methods based on physical models rely on accurate grid parameters and steady-state assumptions, and are unable to cope with the strong electromagnetic transient processes brought about by the grid connection of new energy sources[7]. Although the methods based on shallow machine learning such as random forest and XGBoost [8]can handle some nonlinear relationships through feature engineering, their artificially designed features, such as harmonic distortion rate and voltage asymmetry, fail to effectively capture the spatial correlation of fault propagation. In recent years, GNNs have shown potential in power system fault detection due to their non-Euclidean space modeling capabilities [9]，[10]. For example, Yang, H et al. [11] proposed a spatiotemporal GNN model, which constructed node associations through dynamic time regularization to improve the accuracy of transformer fault classification; Wang et al.[12] developed a GNN based on the attention mechanism, which can adaptively capture the fault associations between key nodes. However, existing GNN methods still face three key challenges when dealing with imbalanced fault scenarios. First, there is a lack of topological dynamics and physical constraints: most existing approaches employ static adjacency matrices, such as fixed connectivity based on electrical distance [13], which cannot adapt to the minute-level topological changes caused by the access of new energy clusters. Second, there is insufficient semantic understanding of low-frequency faults: the uniform message-passing mechanism in traditional GNNs overlooks prior knowledge of fault categories. For example, cascading failures often propagate in chains along critical devices with higher vulnerabilities, while the attention weight calculation of graph attention network (GAT) [14] lacks guidance on historical fault co-occurrence patterns, resulting in a low critical path

979-8-3315-5472-9/25/$31.00 ©2025 IEEE

identification rate. Third, the optimization strategies for class imbalance [15] are too coarse-grained: although current methods mostly rely on class weight adjustment or cost-sensitive learning, they fail to consider the spatiotemporal heterogeneity within the same fault category.

In response to the aforementioned challenges, this paper proposes the KG-SA-GNN, with the main contributions being: 1) the introduction of a knowledge graph-enhanced self-attention GNN, which improves fault detection accuracy by integrating topology and historical fault information; 2) the design of a dynamic self-attention mechanism, capable of weight distribution based on the historical occurrence frequency of fault categories, enhancing the detection ability for low-frequency faults; 3) experimental validation showing that the proposed model significantly improves performance in various fault detection tasks, providing an effective solution for intelligent grid fault diagnosis.

II. METHOD

A. Overall Framework

The proposed KG-SA-GNN adopts a three-stage architecture that integrates knowledge and graph network evolution. It combines prior knowledge of the power system with a dynamic GNN to address topological constraint modeling and class-sensitive learning in imbalanced fault detection.

The overall framework of knowledge-guided self-attention graph neural network is shown in Fig. 1, consisting of three core components. First, a knowledge graph is constructed through ontology modeling and multi-source data fusion, covering equipment topology, fault patterns, and maintenance rules. Second, the graph structure is enhanced using physical constraints and historical fault patterns to refine adjacency relationships in the GNN. Finally, a self-attention fault classification module uses hierarchical attention to integrate fault frequency information, optimizing classifier decision boundaries for sensitive recognition of imbalanced fault categories.

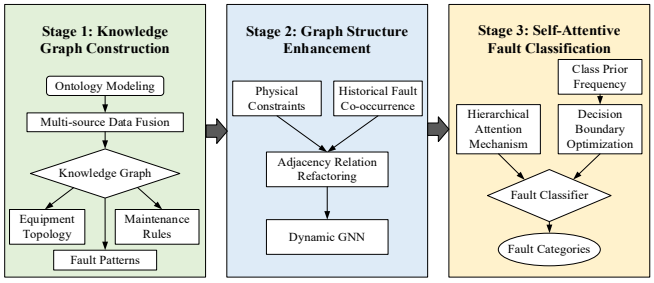


Fig. 1. knowledge-guided self-attention graph neural network overall framework

B. Knowledge Graph Construction

In this study, the knowledge graph plays a crucial role in constructing and refining the ontology model within the power grid domain. Its construction follows a hierarchical design, consisting of two parts: top-down ontology modeling and bottom-up data extraction and fusion. At the schema level, we focus on ontology design; while at the data level, knowledge is extracted from real-world data and then integrated.

By mapping data sources such as devices, fault types, sensors, and operation logs, we established a relational network among power grid devices. Specifically, "device types" and "fault types" are linked and represented as nodes and edges in the knowledge graph, clearly illustrating the relationships between devices and faults. These relationships are embedded into the ontology model, not only supporting fault pattern modeling but also providing structured information for GNN training. This integrated construction approach ensures the structuring of the knowledge system while fully uncovering relational information from real data, significantly improving the model's accuracy and interpretability. Fig. 2 shows the construction process of the knowledge graph for intelligent power grid fault diagnosis

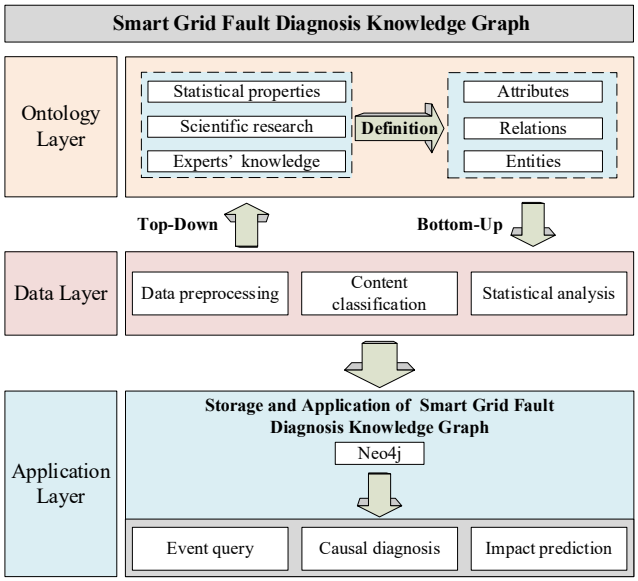


Fig. 2. Flowchart of constructing knowledge graph for smart grid fault diagnosis

In this study, a hierarchical architecture consisting of a schema layer and a data layer is adopted. The schema layer is responsible for ontology design, while the data layer focuses on extracting and integrating knowledge from real-world data, ultimately forming a dynamic and visual knowledge graph.

1) Ontology model design

In this study, we developed an ontology model for power system fault diagnosis using the Protégé tool, which offers strong visualization and semantic reasoning capabilities. The model includes key classes and attributes, forming a comprehensive framework for fault detection and analysis in power systems.

First, the top-level class Thing serves as the parent class for all entities, covering all objects in the system. According to the practical requirements of the power system, the ontology is divided into four subclasses: Diagnosis Method, Fault Phenomenon, Maintenance Action, and Power System Component.

Within the Diagnosis Method class, we defined various fault diagnosis approaches such as Knowledge Graph Reasoning, Thermal Imaging, and Waveform Analysis, which are used for

fault detection and analysis in different scenarios. The Fault Phenomenon class describes common fault types in power grids, including arc faults, cyber attacks, and ground faults.

The Maintenance Action class includes various operations taken after a fault occurs, such as corrective maintenance, preventive maintenance, and emergency repairs. Critical power system components are described through the Power System Component class, which includes entities like circuit breakers, distribution transformers, and energy storage devices.

In addition, the ontology model includes multiple object properties and data properties, as shown in Fig. 3. These properties are used to further describe relationships and state information between entities. The overall ontology design model is illustrated in Fig. 4.

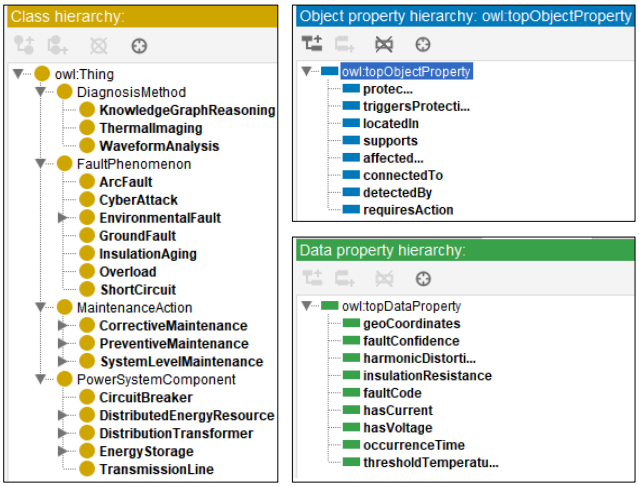


Fig. 3. Object attributes and data attributes of ontology model

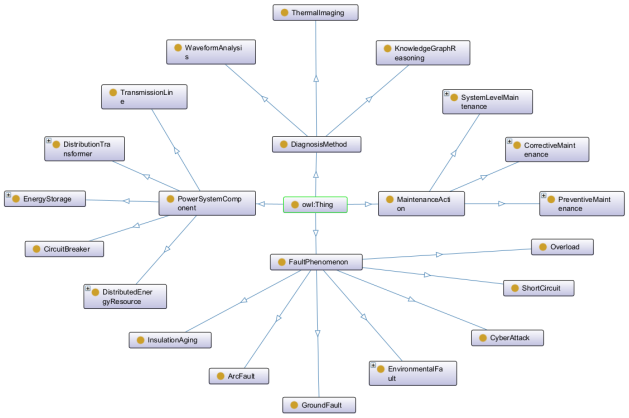


Fig. 4. Ontology Design Model

2) Data layer extraction and fusion

At the data layer, we have collected various types of relevant data from power grid systems, including equipment metadata, historical failure records, sensor data, and operational logs. These data sources vary in format, origin, and granularity. To effectively construct an intelligent fault diagnosis knowledge graph for power grids, it is necessary to transform these dispersed and heterogeneous data sources into structured knowledge information. This process provides critical support for subsequent fault analysis.

During the knowledge extraction phase, key entities and their relationships are extracted from diverse data sources through technologies such as text parsing, pattern recognition, and entity-relation extraction. For instance, equipment types, rated parameters, and topological connection relationships are extracted from equipment metadata; failure types, occurrence locations, and repair measures are derived from historical failure records; voltage, current, power, and other real-time measurement data are obtained from sensor data; maintenance personnel operation records and equipment status change history are extracted from operational logs. This information will be mapped into an ontology model to ensure consistency with the system's structure and semantics.

In the knowledge fusion stage, information from different data sources is processed to address discrepancies in format, source, and granularity, ensuring the consistency and accuracy of the information. For example, descriptions of equipment status in different logs may vary, and sensor data might exhibit deviations due to time delays or measurement errors. Therefore, methods such as data cleaning, standardization, and correction are employed to ensure data consistency. Meanwhile, based on the unified semantic structure of the ontology model, data from different sources can be reasonably integrated through mapping relations, thereby constructing a comprehensive and accurate intelligent power grid fault diagnosis knowledge graph.

3) Knowledge graph storage and visualization

In order to help engineers intuitively understand the topology of the power grid, equipment status, and fault propagation path during fault diagnosis, we used graph database tools such as Neo4j to visualize the knowledge graph. Through the graph database, the various devices and sensors in the power grid system and the relationships between them can be visualized to form a structured knowledge graph, helping fault diagnosis personnel to better understand the system's operating status and fault propagation path. Visualization not only provides rich interactive query functions, but also can display the local or global status of the power grid according to different needs, improving the efficiency and accuracy of fault diagnosis. Part of the smart grid fault diagnosis knowledge graph is shown in Fig. 5.



Fig. 5. Part of the smart grid fault diagnosis knowledge graph

Through top-down ontology design and bottom-up data extraction and fusion process, this study constructed a power grid knowledge graph with structure-awareness capabilities. In this diagram, the various components of the power grid system and their interrelationships are effectively modeled, which can provide strong support for the fault diagnosis system.

C. Self-Attention Graph Network Design

1) Dynamically Adaptive Attention Mechanism

In the KG-SA-GNN model, the dynamic attention mechanism achieves dynamic adjustment of the attention coefficients between nodes by integrating the knowledge graph relationship weights and node embedding features. Its mathematical expression is shown in formula (1):

$$\alpha_{ij} = \mathrm{Softmax}\left(\frac{\sum_{r\in R}\omega_r \cdot \left(h_i^T h_j\right)}{\sqrt{d}}\right) \tag{1}$$

In this context, $h_i \in R^d$ represents the embedding vector of node i, which is generated through the message passing mechanism of GNNs. The variable ω_r denotes the weight of relation r in the knowledge graph, where R is the set of multiple relations between node pairs in the knowledge graph, and d stands for the dimensionality of the embeddings.

Knowledge graphs are used to extract sets of relevant relationships between pairs of nodes, such as physical connections or historical co-occurrences. By calculating the weights of these relationships, the model can capture the importance between entities, thereby providing key information for subsequent attention calculations. In practice, for any pair of nodes, we extract their associated relationship set from the knowledge graph, encode these relationships through embedding vectors, and calculate the weight score of each relationship.

2) Imbalanced Optimization Strategy

In this strategy, by extracting the historical occurrence frequency of each fault category from the knowledge graph, a category-sensitive weighting mechanism is constructed to solve the problem of imbalanced fault categories in smart grids. Less frequent categories are given higher weights, which increases the model's focus on these hard-to-detect categories. This strategy effectively improves the detection performance of low-frequency faults and makes the model more robust when facing unbalanced data.

First, using the historical occurrence frequency of each fault category extracted from the knowledge graph, the weighted cross entropy loss function is defined as follows(2):

$$\mathcal{L} = -\sum_{c=1}^{C}\frac{\log\left(N_c+1\right)}{\sum_{k=1}^{C}\log\left(N_k+1\right)}\cdot y_c \log \hat{y}_c \tag{2}$$

In particular, N_c denotes the historical occurrence count of fault category c recorded in the knowledge graph, C is the total number of fault categories, $y_c \in \{0,1\}$ represents the ground truth label, $\hat{y}_c \in [0,1]$ and indicates the predicted probability.

Secondly, a weighted cross entropy loss function is used to make the model pay more attention to samples of rare categories during training. By introducing category weights, the loss function can strengthen the learning of low-frequency fault category samples, thereby improving detection accuracy. In order to further improve the detection rate of rare faults, a knowledge graph-guided synthetic oversampling method is also adopted. This method improves the feature discrimination by identifying high-risk nodes that are strongly associated with rare faults from the knowledge graph and enhancing the feature space of these nodes. The feature space enhancement technique further increases the focus on rare fault classes by injecting Gaussian noise.

III. EXPERIMENTS

A. Datasets and Comparison Methods

The experimental data used in this paper are the IEEE39-node public benchmark dataset. This standard system contains a typical combination of 39 bus nodes, 10 generators, 46 transmission lines and 12 transformers, which highly restores the complex topological structure of modern power systems. The data set generates time series characteristic data with a sampling frequency of 1 *Hz* by simulating the SCADA system, covering multi-dimensional physical quantities such as voltage, current, active/reactive power, and fully records the dynamic evolution process of system instability caused by four types of typical faults. The four typical fault types are short-circuit faults, overloading faults, ground faults, and cascading faults, accounting for 47.2%, 29.7%, 18.6%, and 4.5% respectively. To ensure rigorous model validation, the total of 12,800 samples are divided in a 7:2:1 ratio into 8,960 for the training set, 2,560 for the validation set, and 1,280 for the test set. The division process adopted a chronological segmentation strategy to avoid data leakage. It is important to note that only 4.5% of the total 12,800 samples are of the cascading failure type. This extremely unbalanced distribution poses a significant challenge to the algorithm's ability to handle abnormal samples.

To verify the effectiveness of KG-SA-GNN, three representative baseline methods are selected for comparison: (1) Traditional machine learning: XGBoost [8] employs a class-weight balancing strategy to mitigate imbalance, yet it relies on handcrafted features such as voltage fluctuation rates and cannot model power-grid topological relationships; (2) Classical graph model: GAT [14] captures node relationships via a localized attention mechanism, but suffers from poor adaptability to dynamic topologies and limited capture of multi-hop dependencies; (3) Imbalance-learning approach: SMOTE-GNN[16], a GAT model enhanced with SMOTE oversampling, generates synthetic samples in feature space to bolster the minority class, though it risks violating the physical topological constraints of the power grid.

The KG-SA-GNN proposed in this paper improves the above problems: (1) Automatically extract topology-related features through the power knowledge graph to reduce dependence on artificial features; (2) Design a self-attention

mechanism to dynamically adjust node weights, which is more flexible than GAT to adapt to power grid changes; (3) Integrate fault prior knowledge on the original graph structure to avoid topology distortion caused by SMOTE oversampling.

B. Evaluation Indicators and Experimental Environment Configuration

For the unbalanced fault detection task, the following indicators are selected: precision, recall, and $F_{1\text{-score}}$, as shown in equations (3) to (5):

$$precision = \frac{T_P}{T_P + F_P} \tag{3}$$

T_P (True Positive) is the true positive example, that is, the number of correctly predicted positive samples, and F_P (False Positive) is the false positive example, that is, the number of incorrectly predicted positive samples.

$$recall = \frac{T_P}{T_P + F_n} \tag{4}$$

F_N (False Negative): False negative examples, that is, the number of incorrectly predicted negative samples.

$$F_{1-score} = \frac{2 \cdot precision}{precision + recall} \tag{5}$$

The experimental environment configuration is divided into two parts: hardware environment configuration and software environment configuration. The hardware environment is the hardware configuration of the server, and the software environment includes the system environment and the development environment. The specific configuration information is shown in Table 1.

TABLE I. EXPERIMENTAL ENVIRONMENT CONFIGURATION INFORMATION

Category	Configuration
Hardware	Processor: Intel(R) Core(TM) i7-9700K CPU @ 3.60GHz Graphics: 2*NVIDIA GeForce RTX 2080 Ti Memory: 64.0 GB RAM
Software	Operating system: Windows 10 Python ：3.12.4 PyTorch：2.4.0 Neo4j：3.5.30

C. Performance Comparison

In this study, we evaluate the performance of four methods across different types of faults. Tables II and III present a detailed and comprehensive performance comparison of all the considered methods on four typical fault categories in the IEEE 39-bus system (unit: %). Specifically, as shown in Table II, the detection performance under high-frequency fault scenarios is summarized in detail, including short-circuit faults and overloading faults. In contrast, Table III illustrates the comparative results under low-frequency fault conditions, with a particular focus on ground faults and cascading faults, thereby providing further insight into their effectiveness in handling less frequently occurring fault events.

TABLE II. PERFORMANCE COMPARISON OF VARIOUS METHODS ON HIGH-FREQUENCY FAULTS

	Short-circuit faults			Overloading faults		
	Prec	*Rec*	F_1	*Prec*	*Rec*	F_1
XGBoost[8]	93.8	94.2	94.0	88.9	88.1	88.5
GAT[14]	94.5	95.2	94.8	90.1	91.3	90.7
SMOTE-GNN[16]	94.9	95.3	95.1	91.2	92.0	91.6
KG-SA-GNN	**95.8**	**96.4**	**96.1**	**93.2**	**94.7**	**93.9**

TABLE III. PERFORMANCE COMPARISON OF VARIOUS METHODS ON LOW-FREQUENCY FAULTS

	Ground faults		Cascading faults			
	Prec	*Rec*	*Prec*	*Rec*	*Prec*	*Rec*
XGBoost[8]	80.1	75.3	80.1	75.3	80.1	75.3
GAT[14]	83.4	81.2	83.4	81.2	83.4	81.2
SMOTE-GNN[16]	84.7	83.5	84.7	83.5	84.7	83.5
KG-SA-GNN	**88.1**	**86.9**	**88.1**	**86.9**	**88.1**	**86.9**

In terms of fault types, KG-SA-GNN performs well in F_1-score, especially for short-circuit faults which reaches 96.1% and ground faults which reaches 87.5%. The knowledge graph effectively reduces false positives by introducing device physical constraints such as voltage threshold rules and significantly improves precision. For cascading failures, an extremely unbalanced type of failure, the recall rate of KG-SA-GNN reaches 78.6%, which is 14.9% higher than SMOTE-GNN. Knowledge-guided synthetic oversampling avoids topology destruction and enables the F_1-score to reach 70.4%, much higher than SMOTE-GNN. In terms of the limitations of traditional methods, XGBoost cannot handle the power grid graph structure and its F_1-score in cascading failures is only 41.8%. Although SMOTE-GNN improves the recall rate, its precision is only 55.8%, while KG-SA-GNN achieves 63.7%, and the performance is affected by the noise introduced by oversampling.

1) Ablation experiment

To evaluate the contribution of each module in the proposed KG-SA-GNN framework, ablation experiments were conducted on cascading faults. The evaluation metrics include Precision, Recall, and F_1-score, where the full model achieved 63.7%, 78.6%, and 70.4%, respectively. As illustrated in Fig. 6, the bar chart clearly shows the performance differences among various model configurations, demonstrating the impact of each component on the overall fault detection accuracy.

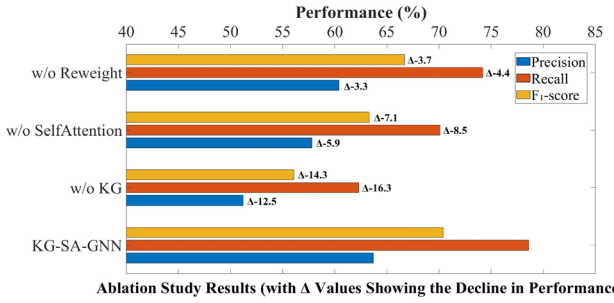


Fig. 6. Comparison of Precision, Recall, and F_1-score among different model variants for cascading fault detection.

The removal of the KG module leads to a 16.3% drop in recall, showing the key role of historical fault co-occurrence knowledge in fault detection. The misjudgment rate of cascading faults increases from 14.5% to 27.8%. Disabling the self-attention mechanism reduces the precision by 5.9%, and the attention weight deviates from the key nodes, which verifies the importance of self-attention in capturing fault propagation paths. After disabling reweighting, Precision and Recall decrease synchronously, indicating that the reweighting strategy effectively balances false positives and false negatives and improves the overall performance of fault detection.

2) Overall performance comparison

The macro average indicators of each method are shown in Table IV (unit: %):

TABLE IV. COMPARISON OF MACRO-AVERAGE INDICATORS OF KG-SA-GNN AND OTHER METHODS

	Macro-Precision	Macro-Recall	Macro-F_1
XGBoost[8]	75.3	75.9	75.6
GAT[14]	79.1	81.3	80.2
SMOTE-GNN[16]	81.7	83.6	82.6
KG-SA-GNN	**85.2**	**89.1**	**87.1**

In all categories of scenarios, the Macro-F_1 of KG-SA-GNN reaches 87.1%, which is 4.5% higher than that of SMOTE-GNN, verifying its universality. The coordinated optimization of knowledge graph and self-attention mechanism significantly improves the model's adaptability to complex power grid dynamics.

IV. CONCLUSION

This paper proposes a KG-SA-GNN to address the challenge of imbalanced fault detection in smart grids. The model constructs a knowledge graph that integrates equipment topology and prior fault patterns, enabling interpretable modeling of physical constraints within the power grid. A dynamic self-attention mechanism is introduced to accurately capture critical fault propagation paths through knowledge-driven weight allocation. In addition, a reweighting strategy based on fault frequency effectively alleviates the issue of class imbalance. Experimental results demonstrate that, for cascading fault detection, KG-SA-GNN achieves a 14.9% improvement in recall and a 9.5% reduction in false alarm rate compared to mainstream methods, thereby validating the advantages of jointly optimizing knowledge graphs and GNNs.

Despite its effectiveness, the proposed method has certain limitations. First, the construction of the knowledge graph relies heavily on an expert-driven process and high-quality historical data. This heavy dependence on manual expertise raises significant scalability challenges for deploying the system across large-scale power networks. Furthermore, incomplete metadata or insufficient fault records may compromise the model's generalization capability. Second, the dynamic self-attention mechanism exhibits limited adaptability to abrupt topological changes, such as large-scale equipment expansion, which could degrade performance unless supported by timely updates to the knowledge graph. Lastly, the setting of noise parameters in feature enhancement must align with specific physical constraints, potentially requiring recalibration when applied across different regions.

Future research will focus on several key directions. First, efforts will be made to develop dynamic update mechanisms for knowledge graphs, integrating online learning with incremental graph structure updates—such as dynamic GNNs—to enable real-time maintenance of knowledge graphs. This will help avoid model performance degradation caused by changes in power grid topology. Second, the plan is to introduce multi-source heterogeneous data fusion, using reinforcement learning frameworks and agent interactions to optimize the joint analysis of SCADA data, device logs, and external environmental information, thereby enhancing diagnostic robustness under complex disturbances. Finally, the research will explore lightweight deployment strategies based on transfer learning, reducing reliance on expert knowledge and promoting the application of these methods in edge computing scenarios.

ACKNOWLEDGMENT

The author would like to express sincere gratitude to the Hunan Provincial Department of Education for their support of this research project (Project No. 23C0038). Their funding and resources have been invaluable in the completion of this study.

REFERENCES

[1] S. Banik, M. Rogers, S. M. Mahajan, C. M. Emeghara, T. Banik and R. Craven, "Survey on Vulnerability Testing in the Smart Grid," in IEEE Access, vol. 12, pp. 119146-119173, 2024,.

[2] Hao Wu, Samuel R. West,Co-optimisation of wind and solar energy and intermittency for renewable generator site selection,Heliyon,Volume 10, Issue 5,2024,e26891,ISSN 2405-8440.

[3] Huang, X.; Liu, Q.; Pan, X.; Jin, S.; Chen, H.; Wang, X.; Zhao, F.; A, T.; Chen, L.; Zhang, H. An Equivalent Modeling Method for Wideband Magnetic Radiation Interference of Power-Electronic Equipment. Electronics 2024, 13, 2481.

[4] B. Li, D. Chen, J. He, C. Wang, J. Song and H. Lyu, "Fault Analysis and Protection in Flexible DC Traction Power Supply System," in IEEE Transactions on Transportation Electrification, vol. 10, no. 3, pp. 5599-5613, Sept. 2024.

[5] Xu, Y.; Zou, Y.; Liu, L.; Li, X.; Teng, Y.; Gao, Z. An Improved Prevention Strategy Based on Fault Probability Detection for Commutation Failure in Line-Commutated Converter-Based High-Voltage Direct Current Transmission Systems. Electronics 2024, 13, 3804.

[6] Tang, Y.; Sun, S.; Zhao, B.; Ni, C.; Che, L.; Li, J. Distributed Photovoltaic Generation Aggregation Approach Considering Distribution Network Topology. Energies 2024, 17, 2990.

[7] Xu, G.; Qiu, J.; Zhang, J.; Yang, H.; Gao, Q.; Jiang, T.; Wang, Y. Coordinated Control of Transient Voltage Support in Doubly Fed Induction Generators. Energies 2024, 17, 4763.

[8] A. Sutou and J. Wang, "Influence-Balanced XGBoost: Improving XGBoost for Imbalanced Data Using Influence Functions," in IEEE Access, vol. 12, pp. 193473-193486, 2024.

[9] Haomin Wang, Muping Li, Peiwei Sun, Xinyu Wei,Research on protection control strategy of pressurized water reactor nuclear power units for typical power system faults,Annals of Nuclear Energy,Volume 201,2024,110414,ISSN 0306-4549.

[10] Ali Reza Abbasi,Statistical techniques in power systems fault diagnostic: Classifications, challenges, and strategic recommendations,Electric Power Systems Research,Volume 239,2025,111279,ISSN 0378-7796.

[11] Yang, H.; Wei, S.; Wang, Y. STFEformer: Spatial–Temporal Fusion Embedding Transformer for Traffic Flow Prediction. Appl. Sci. 2024, 14, 4325.

[12] Zhizhen Wang, Liu Fu, Meng Ma, Zhi Zhai, Hui Chen,Extended ARMA graph neural networks for the prognosis of complex systems,Knowledge-Based Systems,Volume 309,2025,112762,ISSN 0950-7051.

[13] Alfaro, C.A., Zapata, O. The degree-distance and transmission-adjacency matrices. Comp. Appl. Math. 43, 351 (2024).

[14] D. Kumar Mahto, M. Bukya, R. Kumar, A. Mathur and V. Kumar Saini, "GAT-ADNet: Leveraging Graph Attention Network for Optimal Power Flow in Active Distribution Network With High Renewables," in IEEE Access, vol. 12, pp. 185728-185739, 2024.

[15] Y. Zhou, L. Gao, D. Wang, W. Wu, Z. Zhou and T. Ye, "Imbalanced Multifault Diagnosis via Improved Localized Feature Selection," in IEEE Transactions on Instrumentation and Measurement, vol. 72, pp. 1-11, 2023, Art no. 3531611,.

[16] Niu D, Ru R, Zhang J, Zhang Y, Ding C, Lan Y. Leveraging advanced graph neural networks for the enhanced classification of post anesthesia states to aid surgical procedures. PLoS One. 2025 Apr 25;20(4): e0320299.

Stochastic Programming for Capacity Expansion Planning Method Considering Extreme Scenarios

Shu Xia
State Grid Shanghai Municipal Electric Power Company
Shanghai, China
chenyu_cyy@163.com

Yuan Zhang
State Grid Shanghai Municipal Electric Power Company
Shanghai, China
18603855763@163.com

Yue Yu
State Grid Shanghai Municipal Electric Power Company
Shanghai, China
18172512212@163.com

Enyu Jiang
Shanghai University of Electric Power
Shanghai, China
yangmu89786@163.com

Chen Wang
Shanghai University of Electric Power
Shanghai, China
2402248684@qq.com

***Abstract*—This paper focuses on developing a capacity expansion planning model considering extreme scenarios. In order to achieve the carbon neutrality target of each country, the higher penetration of renewable energy will bring additional challenges to the power system. To address the inherent uncertainties associated with renewable energy, the model incorporates stochastic programming techniques that account for extreme scenarios. The proposed method is used to construct case studies, comparing experiments with and without power grid interconnection, as well as experiments with and without consideration of extreme scenarios The simulation results demonstrate that power grid interconnection can effectively contribute to achieving the carbon-neutral target. Furthermore, the proposed stochastic programming method offers higher computational efficiency compared to the traditional 8,760-hour based deterministic capacity expansion planning approach.**

Keywords—capacity expansion planning, stochastic programming, extreme scenarios

I. INTRODUCTION

As the penetration of renewable energy in power systems continues to increase, the fluctuation of wind and solar power poses significant challenges to power system planning and operation. Capacity expansion planning models with high temporal resolution are increasingly employed in power system planning. Bogdannov et al. [1] developed an hourly resolved model that covers all 8,760 hours in a year to determine the cost-optimal pathway for achieving a 100 % renewable energy system in Northeast Asia. Chen et al. [2] formulated a cross-sector, hourly resolution model covering all provinces in China for a full year. Their model aimed to design the optimal transition pathway towards carbon neutrality in China. Zhuo et al. [3] constructed a generation and transmission expansion planning (GTEP) model with embedded operation simulation at an hourly scale to comprehensively evaluate changes in electricity supply costs over a 30-year transition to carbon neutrality in China.

However, deterministic capacity expansion models with 8,760 hours of time series input face two critical challenges. Firstly, deterministic optimization methods fail to capture the inherent uncertainties associated with high Variable renewable Energy (VRE) penetration in power systems [4, 5]. Using probabilistic methods is assumed to be proper to plan for the stochastic nature of VRE [6]. Secondly, the lengthy simulations with hourly resolution result in high computational complexity and even computationally intractable in large number of regions [7, 8]. To address this issue, various time series aggregation techniques in capacity expansion planning models have been proposed. Pfenninger [9] compared down-sampling, clustering, and heuristic methods in terms of costs and installed capacities in a Great Britain power system energy model, demonstrating that the optimal method depends heavily on input data and model constraints. Zhang et al. [10] proposed a self-adaptive compact panorama time series (CPTS) model for power system planning, which effectively captures both short-term and long-term fluctuation characteristics of the original panorama time series (OPTS) with an acceptable approximation error, significantly improving computational efficiency. Hilbers et al. [11] introduced a posteriori time series aggregation scheme for capacity expansion planning models. Although it involves two planning and one operational model runs, the simulation results demonstrate significantly reduced computational costs with a small level of error.

Furthermore, since climate extreme events appear more frequently, low-probability events can have a substantial impact on power systems, as exemplified by the 2021 blackout in Texas [12]. To enhance the robustness of the planning, it is recommended to incorporate extreme scenarios with low probabilities into capacity expansion planning model [13– 15].

This paper presents a stochastic programming model for capacity expansion planning, with con- sideration of extreme scenarios. To obtain the probability and data of various scenarios, a data-driven model based on Generative Adversarial Network (GAN) is proposed. The simulation results demonstrate the benefits of power system interconnection and

979-8-3315-5472-9/25/$31.00 ©2025 IEEE

the importance of incorporating extreme scenarios in capacity expansion planning.

The remaining sections of this paper are organized as follows: Section 2 introduces the methods and data employed in this study. Section 3 presents the stochastic scenarios generation method and the generated scenarios. In Section 4 four different experiments are conducted and the simulation results are analyzed. Finally, Section 5 outlines the conclusions derived from this research..

II. Methods and Data

A. Model Overview

The capacity expansion planning model is formulated as a large-scale Linear Programming problem, where the decisions regarding capacity expansion are independent of the specific scenario realizations. Uncertainty in the VRE and demand is captured in different scenarios which may include both normal and extreme scenarios. Fig. 1 depicts the corresponding scenario tree.

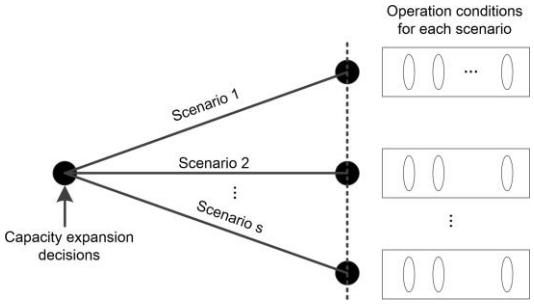


Fig. 1. Scenario tree for stochastic capacity expansion planning model.

1) Objective Function

The objective is to minimize the total investment and expected operational costs over all scenarios as in (1).

$$\min C = C_{inv} + C_{oper} \tag{1}$$

where C_{inv} are the annualized investment costs, C_{oper} are the operation costs. Annualized investment costs include the generation, transmission and storage as in (2).

$$\begin{aligned} C_{inv} &= C_{inv,g} + C_{inv,l} + C_{inv,st} \\ &= \sum_{g=1}^{N_g} \alpha_g k_g^{inv} \hat{c}_g + \sum_{l=1}^{N_l} \alpha_l k_l^{inv} \hat{c}_l + \sum_{st=1}^{N_{st}} \alpha_{st} k_{st}^{inv} \hat{c}_{st} \end{aligned} \tag{2}$$

Where the α is the annuity factor, k^{inv} signifies the specific investment costs per unit capacity and $\hat{c}$ is the subset of the expanded capacity. The expected operational costs can be calculated using (3).

$$\begin{aligned} C_{oper} &= C_{fix} + C_{\text{var}} + C_{fuel} + C_{buy} + C_{sell} \\ &= \sum_{g=1}^{N_g} k_g^{fix} c_g + \sum_{l=1}^{N_l} k_l^{fix} c_l + \sum_{st=1}^{N_{st}} k_{st}^{fix} c_{st} \\ &+ \sum_{s=1}^{N_s} \sum_{t=1}^{N_t} \psi_s \theta_t \left[\sum_{g=1}^{N_g} k_g^{var} P_{g,s,t}^G + \sum_{g=1}^{N_g} k_g^{fuel} P_{g,s,t}^G \right. \\ &\left. + \sum_{e=1}^{N_e} k_{e,s,t}^{buy} \prod_{e,s,t}^{buy} - \sum_{e=1}^{N_e} k_{e,s,t}^{sell} \prod_{e,s,t}^{sell} \right] \end{aligned} \tag{3}$$

where the annual fixed operational costs also encompass the generation, transmission and storage. k^{fix} are the specific operation costs per unit capacity, and c is the total capacity. Since different scenarios have varying operational details, the variable costs and fuel costs need to be multiplied by the probability ψ_s of each scenario to calculate the expected costs. In the model, it is also able to model the trade with an external market. $k_{e,s,t}^{buy}$ and $k_{e,s,t}^{sell}$ represent the time series of buy and sell prices. $\prod_{e,s,t}^{buy}$ and $\prod_{e,s,t}^{sell}$ are the buy and sell power with the external market at timestep *t*.

2) Investment Constraints

The total capacity of a given infrastructure is calculated by simply adding the existing capacity and expanded capacity as in (4).

$$c = \bar{c} + \hat{c} \tag{4}$$

The capacity of each infrastructure is limited by a maximal and minimal capacity, c^{min} and c^{max}, respectively.

$$c^{min} \le c \le c^{max} \tag{5}$$

3) Operational Constraints

The most significant constraint on operation is the power balance constraint, as expressed in (6).

$$\begin{aligned} &\sum_{g \in \Omega_n^G} P_{g,s,t}^G + \sum_{st \in \Omega_n^{st}} (P_{st,s,t}^{dis} - P_{st,s,t}^{cha}) + \sum_{l \in \Omega_n^{Lin}} F_{l,s,t}^L \\ &- \sum_{l \in \Omega_n^{Lout}} F_{l,s,t}^L + \sum_{e \in \Omega_n^E} \prod_{e,s,t}^{buy} - \sum_{e \in \Omega_n^E} \prod_{e,s,t}^{sell} \\ &= D_{n,s,t}, \forall n, \forall s, \forall t \end{aligned} \tag{6}$$

For each scenario, the load at each node and timestep must be equal to local generation added by energy storage discharge, power imports from other nodes and external market, as well as minus energy storage charge, power exports to other nodes and external market. No load shedding is permitted and excess renewable power is allowed to be curtailed.

Power transmission is represented by a transport model [16]. The transmission flow is constrained by the installed capacity as in (7).

$$-c_l \le F_{l,s,t}^L \le c_l, \forall l \in \Omega^L, \forall s, \forall t \tag{7}$$

For energy storage, the following constraints are included in operation.

$$0 \le P_{st,s,t}^{cha}, P_{st,s,t}^{dis} \le c_{st}, \forall st, \forall s, \forall t \tag{8}$$

$$E_{st,s,t} = E_{st,s,t-1} + P_{st,s,t}^{cha} \eta_{st,s,t}^{cha} - P_{st,s,t}^{dis} / \eta_{st,s,t}^{dis}, \forall st, \forall s, \forall t \tag{9}$$

$$0 \le E_{st,s,t} \le H_{st} c_{st}, \forall st, \forall s, \forall t \tag{10}$$

$$E_{st,s,t=0} = \lambda_{st}^{ini} c_{st} \le E_{st,s,t=N_T}, \forall st, \forall s, \forall t \tag{11}$$

where (8) shows that the charging and discharging power of energy storage is limited by its capacity. (9) calculates the energy status in a storage. This is achieved by adding all inputs to and subtracting all outputs from the energy status at the previous time step. In (10), the energy status is limited by its energy capacity, which is calculated by multiplying the 'energy to power ratio' H_{st} and capacity of storage. The initial and final energy status are specified in (11), in which the λ_{st}^{ini} is the fraction of the total storage capacity that is filled at the

beginning of the modeling period.

As to the power generators, in order to avoid solving the Unit Commitment (UC) model with binary variables, a massive amount of thermal units could then be clustered into several groups [17].

$$\lambda_g^{min} c_g \le P_{g,s,t}^G \le c_g, \forall g \in Thermal, \forall s, \forall t \quad (12)$$

$$\left| P_{g,s,t}^G - P_{g,s,t-1}^G \right| \le \gamma_g^R c_g, \forall g \in Thermal, \forall s, \forall t \quad (13)$$

where λ_g^{min} in (12) is the minimal operational state of each generator. (13) represents the ramping constraints. Ramp rates γ_g^R are regarded as fractions of the installed capacity.

For intermittent renewable energy such as wind and solar PV, the output power at timestep t is limited by the input time series $\omega_{g,s,t}$ multiplied by the total installed capacity c_g.

$$P_{g,s,t}^G \le \omega_{g,s,t} c_g, \forall g \in VRE, \forall s, \forall t \quad (14)$$

For hydropower, the monthly electricity generation is constrained within upper and lower bounds as in (15) to ensure that it falls within the feasible range determined by historical runoff data.

$$h_{g,s,m}^{min} \le \sum_{t \in m} P_{g,s,t}^G \le h_{g,s,m}^{max}, \forall g \in Hydro, \forall s, \forall m \quad (15)$$

Similarly, hydropower is also subject to the constraint that the output cannot exceed their installed capacity.

$$P_{g,s,t}^G \le c_g, \forall g \in Hydro, \forall s, \forall t \quad (16)$$

As to the trade with external market, (17) and (18) limit the hourly buy and sell power.

$$\prod_{e,s,t}^{buy} \le c_e^{buy}, \forall e, \forall s, \forall t \quad (17)$$

$$\prod_{e,s,t}^{sell} \le c_e^{sell}, \forall e, \forall s, \forall t \quad (18)$$

B. Input Data

1) Technical and Financial Assumptions

The assumptions for generation, transmission, and storage facilities have been made based on the current level and development trend, as well as predictions from various organizations. It is important to note that a weighted average cost of capital (WACC) of 7 % has been assumed for all technologies in the model.

2) Feed-in for Renewable Energy

The historical wind and solar time series data with high spatial and temporal resolution are obtained from Renewable Ninja [18–19].

The runoff data used in this paper is from University of New Hampshire (UNH)/Global Runoff Data Centre (GRDC) Composite runoff Fields (V1.0) [20]. One typical station is selected for each sub-region. Since the installed capacity of hydropower is predetermined, the corresponding minimum and maximum monthly electricity generation can be calculated using the selected runoff data.

3) Load

The historical data of hourly profiles for regional power load are collected from various sources. Although the availability of historical hourly load data for a period of less than 10 years, these data still serve as valuable inputs for scenario generation in the subsequent section.

Based on considerations such as economic development, industrial structure, electrification, and other factors specific to each region, peak load predictions have been made for each node, as detailed in the Table I.

TABLE I. PREDICTED PEAK DEMAND AND GENERATION INSTALLED CAPACITY IN THE SIMULATION

Area	Peak load(GW)	Hydro(GW)	Nuclear(GW)
A	14.55	44.00	0.00
B	5.59	0.80	0.00
C	121.79	6.83	11.64
D	491.22	12.42	7.80
E	36.80	8.00	0.00
F	125.17	5.00	16.35
G	244.15	40.00	18.00

III. SCENARIO GENERATION

To overcome the challenges with the deterministic capacity expansion planning model with 8,760 hours time series input, the approach using a set of scenarios with probability is selected. Usually, it is necessary to construct the joint probability density distribution $P_0(X) = P(x_1, x_2, ..., x_T)$ corresponding to the random process X, and then use the sampling method to discretize the probability model for limited time series scenarios. However, due to the time-varying and nonlinear nature of weather patterns, complex spatial and temporal interactions, it is difficult to establish an explicit model based on statistical methods for the joint probability density distribution [22]. In recent years, with the development of deep learning technology, it can be used to efficiently fit the characteristics of nonlinear mapping relationship, and use data-driven methods to establish an implicit model that describes the uncertainty of random variables [23, 24]. Moreover, due to the high penetration of renewable energy, it is crucial to incorporate extreme scenarios that pose challenges to resource adequacy into the capacity expansion planning model.

In this paper, a method based on GAN [25] is utilized to generate the discrete time series scenarios for wind and solar power [26]. The Wasserstein distance is used to measure the distance between distributions of real historical data and generated samples.

A total of 10 scenarios is selected, consisting of 8 normal scenarios and 2 extreme scenarios with low probability but high impact. Each scenario spans 168 consecutive hours, equivalent to one week. To capture the seasonal nature of the historical data, 2 normal scenarios are allocated to each season. One extreme scenario s9 represents the week with the lowest VRE generation during summer, while the other extreme scenario s10 represents the week with the lowest VRE generation during winter.

IV. SIMULATION RESULTS AND ANALYSIS

In this section, the performance of the proposed capacity expansion method considering extreme scenarios is examined.

A simulation is conducted in a grid structure with 7 nodes as in Fig.2.

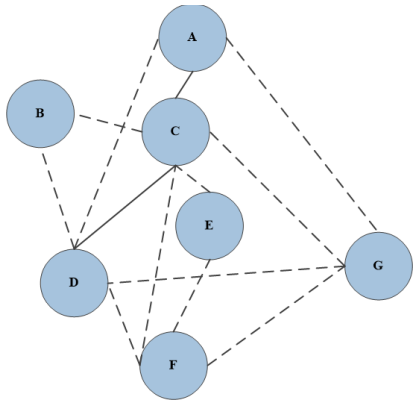


Fig. 2. 7 nodes grid structure in the study.

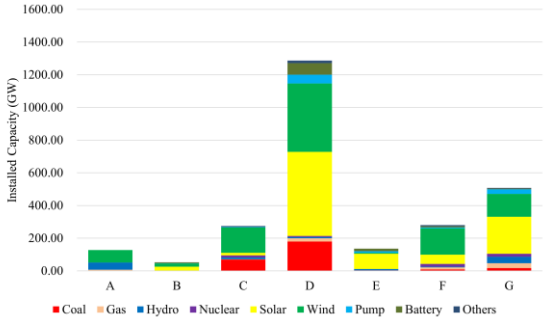
The solid lines in Fig. 2 represent the current power grid between nodes. The capacity of these existing transmission lines can be expanded within the model. On the other hand, the dashed lines indicate the potential power grid connections that are considered in the study. The capacities of these connections will be determined through the model.

The primary focus of this paper is on the planning of coal, gas, wind, and solar PV generation technologies, along with transmission expansion and storage, within the capacity expansion planning model proposed in this study.

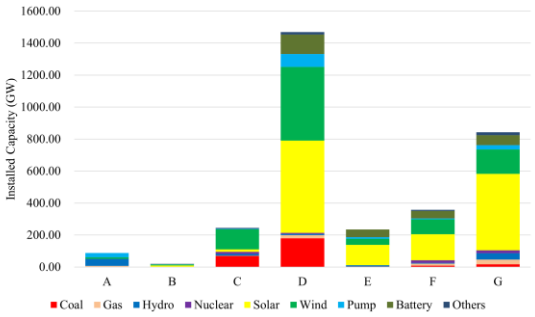
Four different experiments are conducted: a) with power grid interconnection considering extreme scenarios (Inter_Extreme); b) without power grid interconnection considering extreme scenarios (no_Inter_ Extreme); c) with power grid interconnection not considering extreme scenarios (Inter_no_Extreme); d) without power grid interconnection not considering extreme scenarios (no_Inter_no_Extreme). The first experiment is set as the base case in our simulation. In experiments considering extreme scenarios, 10 scenarios introduced in last section are used, including 2 extreme scenarios. While in experiments not considering extreme scenarios, only 8 normal scenarios are used in the simulation.

A. Installed Capacity of Power Generation and Energy Storage

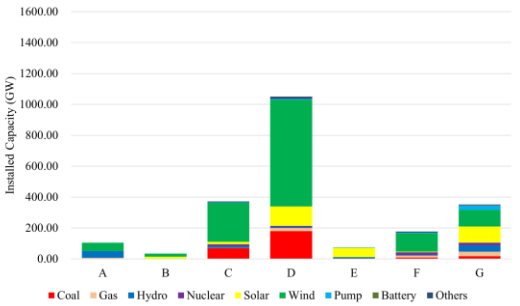
In the base case experiment, the total installed capacity of power generation in the area is 2,462 GW. The installed capacity structure of power generation and energy storage are shown in Fig. 3. Node D and G have relatively larger installed capacity since they have higher demand.



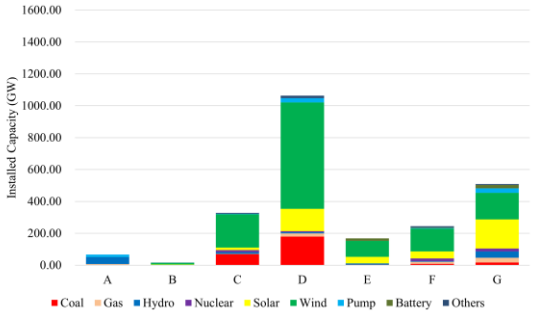
(a) Inter_Extreme



(b) no_Inter_Extreme



(c) Inter_no_Extreme



(d) no_Inter_no_Extreme

Fig. 3. Power generation installed capacity structure in simulation.

It can be seen that by power interconnection, the total power generation installed capacity in the area is much lower than without power grid interconnection. With power grid interconnection, abundant renewable resources in A and B can be developed and transmitted to demand centers such as D, F and G. Without power grid interconnection, D, F and G would need to develop additional power generation facilities to fulfill their power demand requirements independently.

Considering extreme scenarios in the model, the power generation and energy storage installed capacity in the area is around 30 % higher than that not considering them. This is because the extreme scenarios account for low-probability, high-impact events that pose significant challenges to resource adequacy and system reliability. By incorporating these extreme scenarios, the capacity expansion model ensures that sufficient power generation and energy storage capacities are installed to maintain system resilience and meet the electricity demand under extreme operating conditions.

B. Cost Comparison and Analysis

Fig. 4 depicts the total annual cost of four experiments. As anticipated, the total cost is about 3 % - 6 % lower in the cases with power grid interconnection. This can be attributed to the

benefits of power interconnection, which allows for the sharing of dispatchable generation options and energy storage across a larger geographical area. Although more investment costs on transmission lines may be incurred, the power grid interconnection cases are able to deploy cheaper renewable energy with high-quality in A and B other than in F and G. As a result, the total cost is reduced when power grid interconnection is implemented.

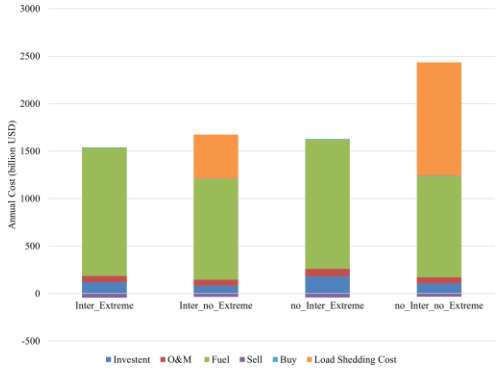


Fig. 4. Annual cost in four experiments.

Without considering the two near-zero probability extreme scenarios, the total annual costs exhibit a reduction of approximately 30 % in both cases with and without power grid interconnection. However, this cost reduction comes at the expense of decreased resilience in the power system. In the event of simulating extreme scenarios based on capacity planning results that do not account for such scenarios, there would be a loss of load of 3.6 TWh for s9 and 2.1 TWh for s10 in the case of power grid interconnection, and 8.2 TWh for s9 and 9.2 TWh for s10 in the case of without power grid interconnection.

Assuming the Value of Lost Load (VOLL) is 130 billion USD/TWh (as observed in the 2021 winter blackout in Texas, where the total shedding load is about 1,000 GWh with the estimated economic loss of 130 billion USD [12]), the load shedding cost will be 273-468 billion USD with power grid interconnection and 1,066-1,196 billion USD without power grid interconnection in this simulation. Once such a low-probability and high-impact extreme scenario occurs, the total cost of planning methods that do not consider extreme scenarios will be higher than those that consider extreme scenarios, especially without power grid interconnection that lack of mutual support and assistance between cross-border power systems undermines system reliability and resilience, leading to greater losses during extreme events.

It is important to note that the impact of the blackout event in extreme scenarios extends beyond direct economic losses. The consequences can encompass reduced confidence in the power system, diminished investment opportunities, and long-term uncertainty in business activities. These indirect effects can have significant implications for the overall economy of the region. Therefore, the benefits of capacity planning considering extreme scenarios are not only reflected in economic terms.

C. Carbon Emission

To assess the annual system-wide Carbon Dioxide(CO2) emissions, emission factors of 0.95 ton/MWh for coal plants and 0.35 ton/MWh for gas plants are used. These emission factors are based on the current status in the simulation area, taking into account factors such as fuel quality, thermal unit efficiency, and technological advancements. Fig. 5 depicts the direct CO2 emissions in the region resulting from fossil fuel combustion. Thermal power will serve as a flexible power source, primarily fulfills the role of peak regulation within the power system. In the simulation, the system-wide CO2 emissions are significantly lower compared to the levels observed currently. It can be seen that by power grid interconnection, different areas can use transmission channels to stabilize fluctuations in wind, solar power and load, achieve power balance in a larger geographic area, reduce thermal power generation, and thus reduce carbon emissions.

Furthermore, when extreme scenarios are taken into account, the installed capacity of wind and solar power increases. This expansion allows for a greater integration of renewable energy sources into the system. As a result, the power generation from thermal power plants can be correspondingly reduced, leading to relatively lower CO2 emissions. The consideration of extreme scenarios and the incorporation of power grid interconnection contribute to a more sustainable and environmentally friendly power system in the region.

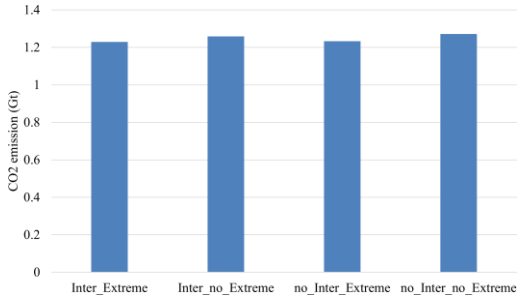


Fig. 5. CO2 emissions in four experiments.

D. Computational Time

A computational time analysis for the four experiments is conducted, comparing them with a deterministic planning approach based on 8,760 hours. The deterministic planning has the same upper and lower bounds as the power grid interconnection experiments. The simulations were performed using COPT 6.0.1 with Pyomo 6.3 on a laptop equipped with an i7-1260P processor running at 2.1 GHz and 16 GB of RAM. The performance results are presented in detail in Table II.

TABLE II. COMPUTATIONAL PERFORMANCE OF EXPERIMENTS

Experiment	Lengths of time-series	Number of scenarios	Computational time
Inter Extreme	168	10	56.94
Inter no Extreme	168	8	25.93
no Inter Extreme	168	10	44.56
no Inter no Extreme	168	8	8.97
Deterministic	8760	1	167.85

From the table, it can be observed that the stochastic programming planning, despite considering more scenarios, exhibits higher computational efficiency compared to traditional deterministic planning. This is mainly due to the shorter length

of time-series used in the stochastic programming approach. It is important to note that as the number of scenarios increases, the computational time also tends to increase. Furthermore, the inclusion of power grid interconnection in the planning process requires additional computational time. This is because the power generation and transmission elements are planned jointly, resulting in a more complex optimization problem. However, it is important to consider that the computational time required for power grid interconnection is still within a reasonable range.

V. Conclusion

In high renewable energy penetration power system, capacity expansion planning involves dealing with multiple sources of uncertainty. Traditional deterministic planning methods often fall short in capturing the uncertainty associated with renewable energy and load. However, considering too many sources of uncertainty can lead to computational challenges and potentially divergent planning outcomes. To address these challenges, this paper proposes a stochastic programming approach for power system capacity expansion planning. The approach leverages a data-driven model based on GAN to learn from historical data and generate scenarios that capture the correlation between wind and solar power outputs and loads even with limited historical load data. By using a clustering method, the approach obtains a limited number of scenarios along with their corresponding probabilities. This approach reduces the complexity of the problem and facilitates the interpretation of results, while still effectively accounting for inherent randomness in the system. Moreover, the proposed method includes the consideration of low-probability events, thereby exploring the impact of extreme scenarios in the planning process. By incorporating extreme scenarios, the method provides insights into the robustness and resilience of the planned capacity expansion under adverse conditions.

This paper applies the proposed method to conduct planning research simulation. Through the comparison of four experiments, the study demonstrates that power interconnection enabled can achieve power balance over a larger geographic area, effectively mitigating the impacts of extreme weather events and reducing the need for flexible power generation and energy storage in different regions. Furthermore, power grid interconnection exhibits lower overall costs compared to scenarios without it.

Moreover, incorporating extreme scenarios in the planning process enhances the robustness of the planning results. Although it may incur higher costs, the simulation results highlight that considering extreme events is a more rea sonable and economical approach when accounting for the potential losses associated with such events. These findings provide valuable insights for power system modeling under uncertainty, supporting different countries in their pursuit of carbon neutrality. Additionally, the study demonstrates that the proposed stochastic programming method offers higher computational efficiency compared to traditional deterministic capacity planning based on 8,760-hour data.

Acknowledgment

This research was generously supported by the 2025 Science and Technology Program of State Grid Shanghai Municipal Electric Power Company, through its dedicated funding for the project entitled "Power-Energy Balance Analysis and Coordinated Capacity Planning Methodology under Extreme Scenarios". The authors acknowledge their contribution to Project No. 520900250009. Their expertise and resources have been invaluable in the successful completion of this work..

References

[1] Dmitrii Bogdanov and Christian Breyer. North-east asian super grid for 100% renewable energy supply: Optimal mix of energy technologies for electricity, gas and heat supply options. *Energy Conversion and Management*,112:176 C190,2016.

[2] Xinyu Chen, Yaxing Liu, Qin Wang, Jiajun Lv, Jinyu Wen, Xia Chen, Chongqing Kang, Shijie Cheng, and Michael B McElroy. Pathway toward carbon-neutral electrical systems in China by midcentury with negative co2 abatement costs informed by high-resolution modeling. *Joule*,5(10):2715 C2741,2021.

[3] Zhenyu Zhuo, Ershun Du, Ning Zhang, Chris P Nielsen, Xi Lu, Jinyu Xiao, Jiawei Wu, and Chongqing Kang. Cost increase in the electricity supply to achieve carbon neutrality in china. *Nature Communications*, 13(1):3172, 2022.

[4] Nikolaos E. Koltsaklis, Pei Liu, and Michael C. Georgiadis. An integrated stochastic multi-regional long-term energy planning model incorporating autonomous power systems and demand response. *Energy*, 82:865–888, 2015.

[5] Enrique B. Cedeño and Sant Arora. Performance comparison of transmission network expansion planning under deterministic and uncertain conditions. *International Journal of Electrical Power and Energy Systems*, 33(7):1288-1295, 2011.

[6] Michael Milligan, Pearl Donohoo, and Mark O'Malley. Stochastic methods for planning and operating power systems with large amounts of wind and solar power. Technical report, National Renew able Energy Lab.(NREL), Golden, CO (United States), 2012.

[7] Stefanie Buchholz, Mette Gamst, and David Pisinger. A comparative study of time aggregation techniques in relation to power capacity expansion modeling. Top, 27:353–405, 2019.

[8] Maximilian Hoffmann, Leander Kotzur, Detlef Stolten, and Martin Robinius. A review on time series aggregation methods for energy system models. Energies, 13(3):641, 2020.

[9] Stefan Pfenninger. Dealing with multiple decades of hourly wind and pv time series in energy models: A comparison of methods to reduce time resolution and the planning implications of inter-annual variability. Applied energy, 197:1–13, 2017.

[10] Ning Zhang, Haiyang Jiang, Ershun Du, Zhenyu Zhuo, Peng Wang, Zhidong Wang, and Yan Zhang. An efficient power system planning model considering year-round hourly operation simulation. IEEE Transactions on Power Systems, 37(6):4925–4935, 2022.

[11] Adriaan P Hilbers, David J Brayshaw, and Axel Gandy. Reducing climate risk in energy system planning: a posteriori time series aggregation for models with storage. Applied Energy, 334:120624, 2023.

[12] Carey W King, Josh D Rhodes, Jay Zarnikau, Ning Lin, Erhan Kutanoglu, Benjamin Leibowicz, Dev Niyogi, Varun Rai, Surya Santoso, David Spence, et al. The timeline and events of the february 2021 texas electric grid blackouts. *The University of Texas Energy Institute*, 2, 2021..

[13] Shuya Li, David W Coit, and Frank Felder. Stochastic optimization for electric power generation expansion planning with discrete climate change scenarios. Electric Power Systems Research, 140:401–412, 2016.

[14] Stefan Höltinger, Christian Mikovits, Johannes Schmidt, Johann Baumgartner, Berit Arheimer, Göran Lindström, and Elisabeth Wetter Lund. The impact of climatic extreme events on the feasibility of fully renewable power systems: A case study for Sweden. *Energy*, 178:695–713, 2019.

[15] Ana Dyreson, Naresh Devineni, Sean WD Turner, Thushara De Silva M, Ariel Miara, Nathalie Voisin, Stuart Cohen, and Jordan Macknick. The role of regional connections in planning for future power system operations under climate extremes. *Earth's Future*, 10(6):e2021EF002554, 2022.

[16] Andrew Liu, Benjamin Hobbs, Jonathan Ho, J McCalley, Venkat Krishnan, Mohammad Shahidehpour, and Q Zheng. Co-optimization of transmission and other supply resources. *Prepared for the Eastern Interconnection States' Planning Council*, NARUC, 2013.

[17] Ershun Du, Ning Zhang, Chongqing Kang, and Qing Xia. A high efficiency network-constrained clustered unit commitment model for power system planning studies. *IEEE Transactions on Power Systems*, 34(4):2498–2508, 2018.

[18] Stefan Pfenninger and Iain Staffell. Long-term patterns of european pv output using 30 years of validated hourly reanalysis and satellite data. *Energy*, 114:1251–1265, 2016.

[19] Iain Staffell and Stefan Pfenninger. Using bias-corrected reanalysis to simulate current and future wind power output. *Energy*, 114:1224 1239, 2016.

[20] Stefan Bofinger, Britta Zimmermann, AK Gerlach, and Tobias Bischof-Niemz. Wind and solar pv resource aggregation study for south africa: Public presentation of results. 2016.

[21] Balázs M Fekete, Charles J Vörösmarty, and Wolfgang Grabs. High resolution fields of global runoff combining observed river discharge and simulated water balances. Global Biogeochemical Cycles, 16(3):15–1, 2002

[22] Niya Chen, Zheng Qian, Ian T. Nabney, and Xiaofeng Meng. Wind power forecasts using gaussian processes and numerical weather prediction. *IEEE Transactions on Power Systems*, 29(2):656–665, 2014.

[23] Saeed Zeynali, Naghi Rostami, Ali Ahmadian, and Ali Elkamel. Two-stage stochastic home energy management strategy considering electric vehicle and battery energy storage system: An ann-based scenario generation methodology. *Sustainable Energy Technologies and Assessments*, 39:100722, 2020.

[24] Mahdi Sharifzadeh, Alexandra Sikinioti-Lock, and Nilay Shah. Machine-learning methods for integrated renewable power generation: A comparative study of artificial neural networks, support vector regression, and gaussian process regression. *Renewable and Sustainable Energy Reviews*, 108:513–538, 2019.

[25] Ian Goodfellow, Jean Pouget-Abadie, Mehdi Mirza, Bing Xu, David Warde-Farley, Sherjil Ozair, Aaron Courville, and Yoshua Bengio. Generative adversarial networks. *Communications of the ACM*, 63(11):139–144, 2020.

[26] Yize Chen, Yishen Wang, Daniel Kirschen, and Baosen Zhang. Model-free renewable scenario generation using generative adversarial networks. *IEEE Transactions on Power Systems*,33(3):3265–3275, 2018.

Research on the Evaluation of Autonomous Controllability of Power Grid Dispatching Technical Support Systems

Li Zhao
State Grid Electric Power Research Institute
State Grid Electric Power Research Institute
Nanjing, China
zhaoli8@sgepri.sgcc.com.cn

Bijing Liu
State Grid Electric Power Research Institute
State Grid Electric Power Research Institute
Nanjing, China
liubijing@sgepri.sgcc.com.cn

Xiaosong Zhu
State Grid Electric Power Research Institute
State Grid Electric Power Research Institute
Nanjing, China
zhuxiaosong@sgepri.sgcc.com.cn

Jiancheng Guo
State Grid Dispatch Center
State Grid Dispatch Center
Nanjing, China
guo-jiancheng@sgcc.com.cn

Yong Yang
State Grid Electric Power Research Institute
State Grid Electric Power Research Institute
Nanjing, China
yangyong1@sgepri.sgcc.com.cn

***Abstract*—The power grid dispatching technical support system holds a significant position in power systems. To enhance its level of autonomous controllability, the primary task is to establish a scientific evaluation framework and quantitative assessment methods. This paper investigates evaluation methods for the autonomous controllability of power grid dispatching technical support systems, proposing an integrated approach that combines the Analytic Hierarchy Process (AHP) and Fuzzy Comprehensive Evaluation (FCE) for quantitative analysis. This evaluation method provides a theoretical basis and decision-making reference for system optimization, contributing to the advancement of power systems toward greater security, efficiency, and autonomy.**

Keywords—power grid dispatching technical support system, autonomous controllability, Fuzzy Analytic Hierarchy Process (FAHP), power system security, hardware and software localization

I. Introduction

Currently, the autonomous controllability of power grid dispatching technical support systems have made significant progress. However, they still face numerous challenges, such as limitations in core technologies and data security risks. To further enhance the autonomous controllability of power systems, a precise evaluation of this capability is primarily required. However, the power industry is still in the preliminary exploration stage regarding quantitative research on autonomous controllability. This paper focuses on researching evaluation methods for the autonomous controllability of power grid dispatching technical support systems, aiming to provide a theoretical basis for its quantitative assessment and offer referential experience for the industry. Through quantitative evaluation and systematic analysis, deficiencies in the development of autonomous controllability can be accurately identified, thereby promoting its enhancement in power systems. This not only helps ensure the safe and stable operation of the power system but also provides strong support for achieving energy structure transformation and sustainable development.

II. Concept and Methods of Autonomous Controllability

A. Concept of Autonomous Controllability

Generally, "autonomous and controllable"comprises two core elements: "autonomy" and "controllability". This specifically means relying on one's own capabilities for research, development, and design; having full command of the core and key technologies of a product; and ensuring that the hardware and software of information systems are under independent control throughout all stages, including research and development, production, upgrading, and maintenance.

B. Evaluation Methods for Autonomous Controllability

Common methods for evaluating autonomous controllability include the Technique for Order of Preference by Similarity to Ideal Solution (TOPSIS) [1], Grey Clustering Analysis [2], the Delphi method [3], the Analytic Hierarchy Process (AHP) [4], and the Fuzzy Comprehensive Evaluation (FCE) method [5]. While each of these methods has its advantages, they face limitations when dealing with complex, multidimensional problems. The Fuzzy Analytic Hierarchy Process (FAHP), which integrates the hierarchical modeling of AHP with the quantitative strengths of fuzzy mathematics, can effectively handle uncertainty and ambiguity, making it suitable for evaluating power grid dispatching technical support systems. This paper will apply FAHP to construct an evaluation model and conduct an empirical analysis by combining AHP and FCE

979-8-3315-5472-9/25/$31.00 ©2025 IEEE

to validate its effectiveness in assessing the autonomous controllability of these systems.

Figure 1 illustrates the evaluation process of FAHP, which primarily includes key steps such as constructing a hierarchical structure model, forming a fuzzy judgment matrix, and solving for eigenvectors [6].

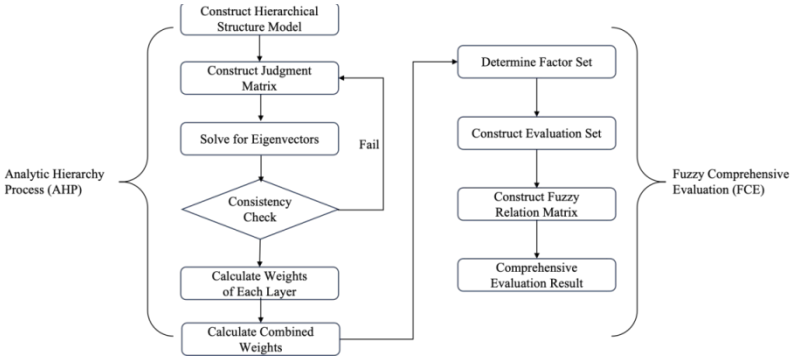


Fig. 1. FAHP Evaluation Process

III. Constructing the Evaluation System for Autonomous Controllability of Power Grid Dispatching Technical Support Systems based on AHP

A. Selection and Determination of Evaluation Indicators

The power grid dispatching technical support system consists of two main parts: hardware (e.g., servers, workstations, switches, disk arrays) and software (e.g., operating systems, databases, application software) [7, 8]. Based on the principles described in this section, and considering the functional characteristics and key roles of the hardware and software, a hierarchical structure model is constructed (see Table 1).

TABLE I. Hierarchical Structure Model of the Power Grid Dispatching Technical Support System

Goal Layer	**Degree of Autonomous**	**Controllability of the Power Grid Dispatching Technical Support System (M)**
Criterion Layer	Hardware Autonomous Controllability (A)	Software Autonomous Controllability (B)
Indicator Layer	Server (A1), Workstation (A2), Switch (A3), Disk Array (A4)	Operating System (B1), Database (B2), Application Software (B3)

First, a hierarchical structure model for evaluating the autonomous controllability of hardware is established. In this paper, the indicator layer is divided into four aspects: servers, workstations, switches, and disk arrays. These are quantitatively assessed from the following four dimensions:

- Independent Design: Designed independently by domestic manufacturers with proprietary intellectual property rights or permanent authorization, and possessing the capability for continuous product optimization and upgrades.
- Domestic Manufacturing: All links in the entire chain, such as fabrication and packaging/testing, are realized domestically. Manufacturing equipment and materials have domestic substitution capabilities.
- Multi-source Supply: At least two or more capable domestic manufacturers are available for each manufacturing link, ensuring a secure supply chain.
- Domestic Qualification: Manufacturers involved in design, manufacturing, and packaging/testing, as well as suppliers of related equipment and materials, should be predominantly controlled by state-owned capital or Chinese citizens.

The hierarchical structure model for hardware autonomous controllability is shown in Table 2. In table 2, NIC means network interface card:

The software component of the power grid dispatching technical support system is central to achieving efficient operation and autonomous controllability. It primarily includes three major modules: operating systems, databases, and application software. The hierarchical structure model for evaluating software autonomous controllability is shown in Table 3. (NIC is network interface card.

B. Determining the Weights of Evaluation Indicators

1) Constructing the Judgment Matrix

The importance of indicators is compared pairwise and assigned values using semi-structured interviews. Based on the 1-9 scale method[9], scale values are determined to construct the judgment matrix. Specifically, for the criterion and indicator layers in Tables 2 and 3, several experts were invited to score according to the following matrix format to build the judgment matrix.

$$G=(g_{ij})_{n*n}=\begin{pmatrix} 1 & g_{12} & \cdots & g_{1n} \\ g_{21} & 1 & g_{23} & g_{2n} \\ g_{31} & \cdots & 1 & g_{3n} \\ g_{41} & \cdots & \cdots & 1 \end{pmatrix} \quad (1)$$

where g_{ij} represents the relative importance of the i indicator compared to the j indicator in the criterion (or indicator) layer, and $g_{ji} = \frac{1}{g_{ij}}$.

2) Solving for Eigenvalues and Eigenvectors

For the judgment matrix obtained in the process above, it is first normalized. Then, the judgment matrix is summed by row to get the total for each element, which is then divided by n (the order of the matrix) to obtain the weight vector W^b:

$$W_i^b = \sum_{j=1}^{n} b_{ij} \quad (2)$$

$$W^b = (W_1^b, W_2^b, \ldots, W_n^b) \quad (3)$$

TABLE II. HIERARCHICAL STRUCTURE MODEL FOR HARDWARE AUTONOMOUS CONTROLLABILITY

Goal Layer	Hardware Autonomous Controllability of Power Grid Dispatching Technical Support System (A)			
Criterion Layer	Server (A1)	Workstation (A2)	Switch (A3)	Disk Array (A4)
Indicator Layer	Motherboard (A11) CPU (A12) Memory (A13) Hard Disk (A14) NIC (A15) RAID Card (A16) Power Supply (A17) BMC (A18)	Motherboard (A21) CPU (A22) Memory (A23) Hard Disk (A24) NIC (A25) Graphics Card (A26) Power Supply (A27) BMC (A28)	CPU (A31) Power Supply (A32) Forwarding Chip (A33) Logic Chip (A34) MAC/PHY Chip (A35) Clock Chip (A36) Memory Chip (A37)	Controller (A41) CPU (A42) Memory (A43) Hard Disk (A44) NIC (A45) Power Supply (A46) BMC (A47)
Quantitative Indicators	Independent Design, Domestic Manufacturing, Multi-source Supply, Domestic Qualification			

TABLE III. HIERARCHICAL STRUCTURE MODEL FOR SOFTWARE AUTONOMOUS CONTROLLABILITY

Goal Layer	Software Autonomous Controllability of Power Grid Dispatching Technical Support System (B)		
Criterion Layer	Operating System (B1)	Database (B2)	Application Software (B3)
Indicator Layer	Independent R&D (B11), Security Level (B12), Multi-architecture Compatibility (B13)	Independent R&D (B21), Security Level (B22), Multi-architecture Compatibility (B23)	Independent R&D (B31), Software Dependency (B32), Multi-architecture Compatibility (B33)

After normalizing the vector W^b, the maximum eigenvalue of B is calculated:

$$\Lambda_{max} = \sum_{i=1}^{n} \frac{BW^b}{n} \quad (4)$$

3) Consistency Check

Finally, a consistency check must be performed on the judgment matrix, which involves calculating the Consistency Index (CI) and the Consistency Ratio (CR). Based on the test results, it is determined whether the matrix needs adjustment [10].

The calculation of the Consistency Index (CI) is shown in Equation 5:

$$CI = \frac{\lambda_{max} - n}{n-1} \quad (5)$$

The Consistency Ratio (CR) is typically used to evaluate the consistency of the judgment matrix, calculated as shown in Equation 6:

$$CR = \frac{CI}{RI} \quad (6)$$

C. Determining Weights using Expert Scoring

To reflect the diversity and representativeness of the sample data, this study invited over 80 experts from the power industry to score the weight indicators at each level. Taking Expert 1's scoring of the hardware autonomous controllability indicator A as an example calculation [11], the process begins with scoring the hardware layer indicators (as shown in Table 5).

Using Equations 5, 6, and 7, the weights are calculated from the scoring results and a consistency check is performed. The calculation results are shown in Table 6:

The expert scores obtained were processed using the method described in Section 2.3 to calculate the weights for the criterion and indicator layers. Furthermore, integrated weights were calculated by combining the criterion layer weights with the indicator layer weights. This forms a comprehensive weight system that reflects the relative importance of each indicator within the entire decision-making framework, thereby ensuring the scientific validity

TABLE IV. RANDOM INDEX (RI) VALUES

Order n	1	2	3	4	5	6	7	8	9	10	11
RI	0	0	0.58	0.90	1.12	1.24	1.32	1.41	1.45	1.49	1.51

TABLE V. EXPERT 1'S SCORING OF HARDWARE LAYER INDICATORS

Evaluation Indicator	Server (A1)	Workstation (A2)	Switch (A3)	Disk Array (A4)
Server (A1)	1	6	2	7
Workstation (A2)	1/6	1	1/2	4
Switch (A3)	1/2	2	1	6
Disk Array (A4)	1/7	1/4	1/6	1

and rationality of the weights at all levels (detailed results are shown in Table 7).

D. Analysis of Indicator Weights

At the hardware level, the server (A1) has the highest weight at 0.3282, positioning it as the core equipment that provides the operating platform for applications. The weights for workstations (A2), switches (A3), and disk arrays (A4) are 0.1966, 0.2965, and 0.1787, respectively. Although their weights are lower than that of the server, they are indispensable for monitoring, control, and data transmission. For instance, a switch failure can severely impact system reliability.

At the software level, the weights for the operating system (B1), database (B2), and application software (B3) are 0.3263, 0.3240, and 0.3497, respectively. Application software (B3) has the highest weight (approximately 35%), as it forms the basis for real-time dispatch and command. The operating system (B1), with a weight of 32.63%, ensures system security and resource management. The database (B2), with a weight of 32.40%, provides data storage and disaster recovery support. The weights of these three components are close, highlighting their interdependence and collaborative role in ensuring software autonomous controllability.

Overall, the weight distribution for hardware and software is reasonable and well-structured. The hardware provides the foundational operating infrastructure, while the software ensures efficient management and secure operation. Together, they collaboratively guarantee the high-efficiency and safe operation of the power grid dispatching system, providing a scientific basis for the evaluation of autonomous controllability.

IV. USING FUZZY COMPREHENSIVE EVALUATION TO ASSESS THE AUTONOMOUS CONTROLLABILITY OF THE POWER GRID DISPATCHING TECHNICAL SUPPORT SYSTEM

A. Establishing the Fuzzy Comprehensive Evaluation Factor Set, Evaluation Scale Set, and Weight Set

The system U to be evaluated consists of two parts: hardware autonomous controllability (A) and software autonomous controllability (B). Let the set of these first-level indicators be $U=\{U_A, U_B\}$. The second-level indicators are denoted as U_1 and $U_1 = \{U_{A1}, U_{A2}, U_{A3}, U_{A4}\}$. The third-level indicators are denoted as $U_{11}$and $U_1 = \{U_{A11}, U_{A12}, \dots, U_{A18}\}$.

The evaluation scale set used in this paper is {High, Relatively High, Medium, Relatively Low, Low}. Table 8, the evaluation grade score range table, is used to convert the evaluation grades into specific score ranges for quantitative assessment. Each grade corresponds to a score range and a median value. The weight set is detailed in Table 7.

B. Identify the Headings Establishing the Fuzzy Judgment Matrix and Determining Membership Degrees

The fuzzy judgment matrix is used to quantify the fuzzy judgments of experts on different indicators, handle uncertainty in the evaluation, and transform subjective judgments into data, thereby providing a basis for comprehensive evaluation [12]. In this study, 25 personnel from the power industry were invited to complete a questionnaire, with 25 valid responses collected, yielding initial quantitative values. The indicators are quantified to obtain the membership degree, r_{ij}, of the i-th factor for the j-th evaluation grade. The membership degree r_{ij} is the proportion of the total number of evaluators who assigned the j-th grade to the i-th factor. From this, the fuzzy relation matrix R is established:

$$F_{ij} = \begin{pmatrix} F_{i1}^{j1} & F_{i1}^{j2} & \dots & F_{i1}^{j5} \\ F_{i2}^{j1} & F_{i2}^{j2} & \dots & F_{i2}^{j5} \\ \dots & \dots & \dots & \dots \\ F_{in}^{j1} & F_{in}^{j2} & \dots & F_{in}^{j5} \end{pmatrix} \tag{7}$$

TABLE VI. RELATIVE WEIGHTS AND CONSISTENCY CHECK FOR EXPERT 1'S HARDWARE CRITERION LAYER

Evaluation Indicator	Relative Weight	λ_{max}	CI	CR
Server (A1)	0.5377	4.1303	0.04344	0.0488 < 0.1, Passed consistency check
Workstation (A2)	0.135			
Switch (A3)	0.278			
Disk Array (A4)	0.0493			

TABLE VII. WEIGHTS FOR EACH LEVEL AND INTEGRATED WEIGHTS

L1 Indicator	Weight	L2 Indicator	Weight	L3 Indicator	Weight	Integrated Weight
A	0.5	A1	0.3282	A11	0.1395	0.0229
				A12	0.3928	0.0645
				A13	0.1421	0.0233
				A14	0.1388	0.0228
				A15	0.0473	0.0078
				A16	0.0422	0.0069
				A17	0.0501	0.0082
				A18	0.0472	0.0077
		A2	0.1966	A21	0.1527	0.0150
				A22	0.2914	0.0286
				A23	0.1408	0.0138
				A24	0.1374	0.0135
				A25	0.0435	0.0043
				A26	0.1469	0.0144
				A27	0.0434	0.0043
				A28	0.0439	0.0043
		A3	0.2965	A31	0.2836	0.0420
				A32	0.0422	0.0063
				A33	0.2348	0.0348
				A34	0.1031	0.0153
				A35	0.2429	0.0360
				A36	0.0438	0.0065
				A37	0.0496	0.0074
		A4	0.1787	A41	0.2960	0.0264
				A42	0.2315	0.0207
				A43	0.0968	0.0086
				A44	0.2374	0.0212
				A45	0.0479	0.0043
				A46	0.0397	0.0035
				A47	0.0507	0.0045
B	0.5	B1	0.3263	B11	0.4196	0.0685
				B12	0.3096	0.0505
				B13	0.2710	0.0442
						0.0634
		B2	0.3240	B21	0.3913	0.0634
				B22	0.3881	0.0629
				B23	0.2205	0.0357
		B3	0.3497	B31	0.4103	0.0717
				B32	0.2794	0.0489
				B33	0.3103	0.0543

TABLE VIII. EVALUATION GRADE SCORE RANGE TABLE

Evaluation Standard	High	Relatively High	Medium	Relatively Low	Low
Median	90	70	50	30	10
Score Range	[100,80]	（80，60]	(60,40]	(40,20]	(20,0]

$$U_i = W_i \times F_{ij} = (W_1^b, W_2^b, \ldots, W_n^b) \quad (8)$$

A fuzzy operation is performed on the weight vector W_i and the fuzzy matrix F_{ij} to obtain a row vector F_{ij} representing the fuzzy evaluation result of the indicator layer:

$$U = W \times U_i^j = \begin{pmatrix} U_1^1 & U_1^2 & \ldots & U_1^5 \\ U_2^1 & U_2^2 & \ldots & U_2^5 \\ \ldots & \ldots & \ldots & \ldots \\ U_{in}^{j1} & U_n^2 & \ldots & U_n^5 \end{pmatrix} \quad (9)$$

C. Calculation and Analysis of Comprehensive Evaluation Results

According to Equations (8) and (9), and in conjunction with the weight indicators from the hierarchical structure model (Table 7), the membership degree fuzzy comprehensive evaluation matrix for the second-level indicators is calculated as follows:

$$U_A = \begin{pmatrix} 0.3439 & 0.3937 & 0.1314 & 0.0883 & 0.0427 \\ 0.2896 & 0.3644 & 0.2229 & 0.1025 & 0.0205 \\ 0.5989 & 0.2771 & 0.124 & 0 & 0 \\ 0.2461 & 0.2835 & 0.234 & 0.1559 & 0.0805 \end{pmatrix} \quad (10)$$

$$U_B = \begin{pmatrix} 0.6324 & 0.246 & 0.0968 & 0.0232 & 0 \\ 0.7666 & 0.1533 & 0.08 & 0 & 0 \\ 0.5288 & 0.1901 & 0.1135 & 0.0782 & 0.0894 \end{pmatrix} \quad (11)$$

1) Hardware Autonomous Controllability Analysis: The autonomous controllability of servers and switches is relatively high. The localization level of components such as memory, power supplies, SSDs, and network cards is high, but CPUs and RAID controller cards still rely on imports. Significant progress has been made in the domestic production of core hardware for switches (membership degree 0.5989), whereas the autonomous controllability of disk arrays is lower (membership degree 0.2461) due to reliance on imported mechanical hard drives. The autonomous controllability of workstation graphics cards is moderate, with a long replacement cycle for domestic alternatives. The overall autonomous controllability of motherboards is high, but some components are still imported. Although some enterprises have achieved domestic production of BMC chips, their adoption rate is not high.

2) Software Autonomous Controllability Analysis: The database exhibits the highest level of autonomous controllability (membership degree 0.7666), characterized by a high degree of independent R&D and well-developed security and compatibility. The operating system's autonomous controllability is slightly lower (membership degree 0.6342); while it is compatible with multiple architectures, it contains a large number of open-source software packages. Application software has the lowest autonomous controllability (membership degree 0.5288), as some functions depend on foreign software, although domestic replacement solutions are currently being tested.

Overall Summary: The overall autonomous controllability of the power grid dispatching technical support system is high, with software outperforming hardware. The database performs the best, followed by the operating system and application software. Although the overall autonomous controllability of hardware is high, there is still a reliance on foreign sources for some high-end equipment and core chips, and the localization of certain components is still in the exploratory phase [13].

After completing the calculation and analysis of the second-level indicators, this paper proceeds to obtain the comprehensive evaluation results. Based on the previously described membership degree matrices for hardware and software autonomous controllability, Equations (8) and (9) are applied to perform the corresponding calculations. This yields the membership degrees and scores for hardware and software autonomous controllability, with detailed data presented in Tables 9 and 10, respectively.

TABLE IX. MEMBERSHIP DEGREE AND SCORE FOR HARDWARE AUTONOMOUS CONTROLLABILITY

A	High	Relatively High	Medium	Relatively Low	Low	Score
Membership Degree	0.3914	0.3337	0.1655	0.077	0.0324	79.49

TABLE X. MEMBERSHIP DEGREE AND SCORE FOR SOFTWARE AUTONOMOUS CONTROLLABILITY

B	High	Relatively High	Medium	Relatively Low	Low	Score
Membership Degree	0.6402	0.1964	0.0972	0.0349	0.0313	87.59

TABLE XI. MEMBERSHIP DEGREE OF THE POWER GRID DISPATCHING TECHNICAL SUPPORT SYSTEM

M	High	Relatively High	Medium	Relatively Low	Low	Score
Membership Degree	0.5158	0.265	0.1314	0.056	0.0319	83.54

Tables 9 and 10 respectively display the membership degrees and scores for the hardware and software autonomous controllability of the power grid dispatching technical support system. It is evident that the degree of autonomous controllability for both is at an upper-medium level, with scores of 79.49 and 87.59, respectively. This indicates that the autonomous controllability of the software is significantly higher than that of the hardware. On this basis, the paper calculates the autonomous controllability membership degree and score for the target power grid dispatching technical support system (Target M):

The autonomous controllability evaluation score for the power grid dispatching technical support system is 83.54. This score reflects that the system as a whole is at a high level, demonstrating its good autonomous controllability.

V. CONCLUSION

This study employed the Fuzzy Analytic Hierarchy Process (FAHP) to systematically evaluate the autonomous controllability of the power grid dispatching technical support system. The results show that the overall level of autonomous controllability is high (score of 83.54). However, the autonomous controllability of hardware is lower than that of software, with production, manufacturing, and supply chain risks identified as key constraining factors.

VI. ACKNOWLEDGMENT

This work was supported by the Science and Technology Project of State Grid Corporation of China(Grant No5108-202340436A-3-2-ZN).

REFERENCES

[1] Hwang, C. L., & Yoon, K. (1981). Multiple Attribute Decision Making: Methods and Applications. Springer-Verlag.

[2] Deng, J. L. (1982). Control problems of grey systems. Systems & Control Letters, 1(5), 288-294.

[3] Linstone, H. A., & Turoff, M. (1975). The Delphi Method: Techniques and Applications. Addison-Wesley.

[4] Saaty, T. L. (1980). The Analytic Hierarchy Process: Planning, Priority Setting, Resources Allocation. McGraw-Hill.

[5] Zadeh, L. A. (1965). Fuzzy sets. Information and Control, 8(3),338-353.https://doi.org/10.1016/S0019-9958(65)90241-X

[6] Li Suxiu, Lu Jing, et al. International Case Studies on the Autonomy and Controllability of Energy and Power Industry Supply Chains [J]. Modern State-Owned Enterprise Research, 2023.

[7] Li Qiang, Pan Yi. Smart Grid Dispatching Technology. China Electric Power Press, 2017.

[8] Jin Guoqiang, Chen Zhenghong. The Current Status and Development Trends of Smart Grid in China [J]. Quality and Certification, 2019.

[9] Bai Xuemei, Zhao Songsan. Application of Analytic Hierarchy Process in Evaluating Comprehensive Strength [J]. Statistics and Decision, 2004.

[10] Liang Feifei. Proof of the Necessity for Consistency Check in Analytic Hierarchy Process and Its Inspection Principles [J]. Economic Life Digest (First Half of the Month), 2012.

[11] Li Tian, Wang Jiang. Research on the Evaluation of Red Culture Teaching in College Physical Education Courses Based on the AHP-FCE Model [J]. Bulletin of Sport Science & Technology, 2024.

[12] Chen Jialin. Evaluation of the Autonomous and Controllable Capability of the BeiDou Satellite Navigation System [D]. Harbin Engineering University, 2018.

[13] Examining the Dilemma of Domestic Semiconductor Equipment's Reliance on Imported Core Components: A Case Study of Hwatsing Technology. Electronics World, January 21, 2025.

Power System and Reliability Analysis of Geothermal and Hydrogen Storage-Orientated Grid-Connected Smart Grid for Mining and Agricultural Application: A Global Perspective

Md. Nimul Hasan[1], Sk. A. Shezan[2], Md. Fatin Ishraque[1,3], SM Muyeen[4], and Innocent Kamwa[3]
[1]Department of Electrical, Electronic and Communication Engineering, Pabna University of Science and Technology, Pabna, Bangladesh
[2]Department of Electrical Engineering, Prince Faisal Centre for Renewable Energy Studies and Applications, Northern Border University, Arar, Saudi Arabia
[3]Electrical Engineering Department, College of Engineering, Laval University, Quebec, Canada
[4]Department of Electrical Engineering, Qatar University, Doha, 2713, Qatar
Email: nimul34.din.h@gmail.com, shezan@nbu.edu.sa, fatineeeruet@gmail.com, sm.muyeen@qu.edu.qa, innocent.kamwa@gel.ulaval.ca

***Abstract*—This paper demonstrates a detailed analysis of the behaviour of a hybrid smart grid system that combines with geothermal power and hydrogen energy storage for reliable and sustainable energy supply in the mining and agricultural sectors. When implemented and compared to another existing control strategy called Constant Cosphi Controller, the study reveals that Voltage IQ Droop Controller not only reduces the fault recovery time by around 30% but also stabilizes the system faster. The findings suggest that integrating with a hybrid system leads to both greater energy stability and significant emissions and cost savings. Furthermore, integration of renewable sources with smart grid architecture represents a scalable and affordable solution, which in turn would mitigate energy challenges specific to industrial sectors. Our findings highlight the demonstrable ability of hybrid renewable energy systems to contribute to sustainable energy generation in industrial and rural settings, providing a basis for evolving from centralized and fickle electricity production to decentralized, efficient and environmentally benign energy infrastructure.**

***Index Terms*—Power System Reliability, Geothermal, Hydrogen Storage, Voltage IQ Droop Controller, Constant Cosphi Controller**

NOMENCLATURE

DG	Distributed generation
EV	Electric Vehicle
LOLE	Loss of Load Expectation
MG	Microgrid
RETs	Renewable Energy Technologies
SG	Smart Grid

I. INTRODUCTION

Mining and agriculture are among the highest energy-intensive industries worldwide, especially in remote and off-grid areas where consistent access to power may be scarce. These sectors are not only basic to national economies and global supply chains, but they are equally vital for rural livelihoods and food security. However, they often find that their operations are hampered by unreliable energy infrastructure and frequent blackouts, which result in heavy reliance on fossil-based generation. These traditional energy procedures account for large carbon footprints and heavy infrastructure and financial responsibilities, especially in more remote areas where fuel transportation and system monitoring have considerable logistical costs.

The increasing global necessity to decarbonize energy systems and move to more sustainable development practices includes a growing requirement for resilient, low cost and environmentally friendly energy supplies that can be tailored specifically for use in industrial and agricultural applications. Alternative energy sources, notably solar and wind power, are making strides but still vulnerable due to challenges related to intermittency/variability of generation, which works against those who must have always-on electricity supply.

In this very dynamic energy landscape, smart grid technologies have become an enabler to improve flexibility, reliability and efficiency of the energy system. Smart Grid:A smart grid is one that integrates ICT and employ advanced metering, monitoring, communication, and control capabilities to provide real-time data transfer between utilities and users for optimization of electricity generation, distribution, transmission and consumption with higher power quality. Smart grids can provide a largely decentralized capacity, which is more abundant and gives support to the intermittency of distributed energy resources offering benefits for overall grid resiliency, especially for remote mining/agricultural operations. Smart grids further help in reducing energy losses and maximizing resource utilization through predictive analytics, automatic load balancing, adaptive control systems, making the system even more responsive to fluctuating supply and demand requirements.

979-8-3315-5472-9/25/$31.00 ©2025 IEEE

II. Literature Review

A. Renewable Energy Integration in Mining and Agriculture

The potential for greater sustainability and increased economic viability through the use of renewable energy projects in mining and agriculture is another area where integrated solutions are incredibly attractive. Adopting renewable sources of energy from solar, wind, biomass and geothermal in the agricultural sector could lower carbon footprints as well as improve farm economics. Case studies documenting energy savings, cost reductions and price risk mitigation alongside enabling policy frameworks and incentives have proven successful [1].

The paper focusses on the incorporation of renewable energy in the agricultural pursuits (solar, wind, biomass and geothermal sources) to catalyse sustainability in agriculture and confining the scale of emissions linked with the consumption of energy for an identical [2].

B. Geothermal Energy as a Stable Baseload Source

Geothermal energy is now being thought of as a dependable source for baseload power, and could play a significant role in the setup of sustainable energy systems. Geothermal energy is a reliable source as consistent availability of geothermal resources all the time, and is not influenced by weather changes, akin to this type of use makes easier way in place of fossil fuel used. Advancements in drilling and power conversion technologies have prompted a re-evaluation of the size of low-temperature resources which can be profitably exploited, increasing its portfolio status [3].

High capacity factors (70-90%) make geothermal energy particularly well-suited for baseload electricity generation and provide a reliable base-load to the otherwise intermittent supply of wind and solar power. Nonstop accessibility also makes small modular reactors something of a linchpin for local grid systems, which in turn decreases reliance on burning fossil fuels and boosts steadiness of energy supply [4].

C. Smart Grid Architectures for Remote and Industrial Applications

This paper presents an overview of Smart Grids (SG) and their testbeds with an emphasis on efficient communication networks and smart automation in remote industrial applications, while addressing security gaps, drawbacks, and future directions for research taking place in the area of smart grid architectures [5].

The paper elaborates on possible EC-CC system architectures seeking to support smart grid applications, with a perspective on their role at remote and industrial sites, including hierarchical energy management systems to strengthen data processing security as well as operations efficiency from the end of the energy supply chain [6].

D. Reliability and Performance Assessment in Hybrid Energy Systems

Reliability and performance evaluation in hybrid energy systems play an important role in the utilization of Renewable Energy Technologies (RETs) through provision to deliver power into the national grid. A few methods have been developed to improve reliability like using Hybrid Monte Carlo & Newton-Raphson integrating technique that helps in decreasing Loss of Load Expectation (LOLE) and Loss of Load Energy Expectation far more than the conventional methods [7]. Moreover, incorporation of distributed generation (DG) resources such as solar and wind in the MATLAB model has been proven to augment the reliability with an analysis employed by Markov chains [8]. Performance evaluations show higher capacity factors and exergy efficiencies of hybrid wind-solar systems proved the benefits of hybridization for emissions reduction and system stability. More importantly, power electronics advances in microgrid systems can be translated into up to an over 100% improvement on reliability, fixing problems with renewable energy generation [9]. In essence, the impact of this intermittency can be reduced by hybrid systems and it is proven to work with long term simulation based studies so as not to waste the energy resource.

E. Gaps in Existing Literature and Research Opportunities

Although significant grid modernization has taken place with the integration of renewables, there is still a need for effective hybrid systems in energy-intensive, off-grid sectors especially mining & farming. Currently less attention is focused on the integration of geothermal and hydrogen storage systems, particularly within smart grid configurations [10]. Also, the archaived result which will geneated by higher order controllers in fault managemetn situations is not well studied. Moreover, research on techno-economic optimization and reliability analysis of hybrid systems is meager specially across dissimilar global regions having different geographical and grid conditions. This paper fills this gap by analysing a hybrid geothermal-hydrogen storage smart grid and investigates the performance of different control strategies as well as providing new insights into fault recovery, system stability, and large-scale adoption in off-grid industrial and agricultural usecases.

F. Contribution of the Paper

Major contributions of the paper are highlighted as follows:

- This paper studies the potential of employing hybrid smart grid systems, which make use of geothermal energy and hydrogen storage to offer an alternative, sustainable, and resilient energy technology in highly energy-intensive industries such as mining and agriculture. The integration ensures stable power output even in remote locations with unstable grids.
- This paper considers two controllers — Constant Cosphi and Voltage IQ Droop, to perform under system faults. The results show that the Voltage IQ Droop Controller has faster recovery and more stable performance than the Constant Cosphi Controller, which increases the fault response time and system stability.

G. Paper Organization

The paper organization comprises the Introduction and Literature Review in section II. The Motivation provides the

reason behind the investigation and Research Gap provides gaps. The System Design describes employed in the study in section III and the Results and Discussion discuss system characterization in section IV. The Conclusion provides an overview of the results and recommends areas for future research in section V.

III. Research Approach and System Design

In this study, DIgSILENT PowerFactory for load flow, transient stability, and voltage control simulation. The above integrated approach combines techno-economic optimization with electrification performance estimation to ensure that the proposed hybrid renewable system is both economically viable and reliable for implementation in a data-driven manner under various geographical and grid conditions.

A. Description of the System

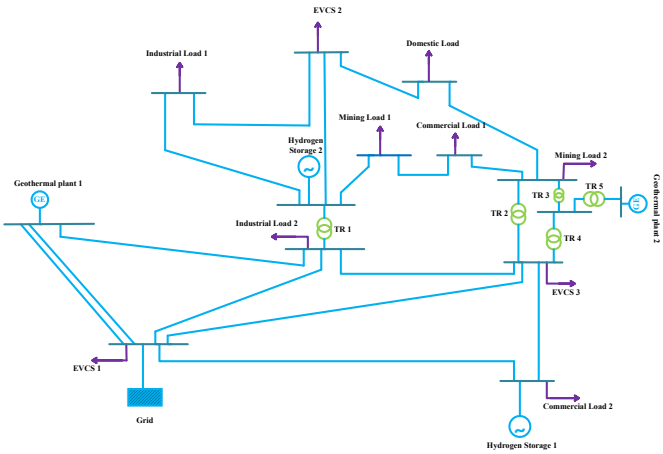


Fig. 1: Block Diagram of Single Line Diagram

In Figure 1, the diagram presents a smart grid system for distributing and dispatching energy from geothermal power plants and hydrogen storage to different types of consumers. Renewable power is generated at the Geothermal Plants 1 and 2, and supplied to the grid. Hydrogen storage units (1 and 2) store surplus power, ensuring a stable supply in the event of fluctuations in generation levels and increased demand.

The grid supplies different loads such as industrial, mining, commercial and domestic. Transformers are provided for each load which adjust the voltage levels for diverse sectors. Furthermore, Electric Vehicle Charging Stations are also plugged in within the grid to participate in EV charging solution thereby ensuring green mobility.

Ultimately, the system maximizes energy use and optimizes the balance between generation of renewables, storage to consumption before distributed over diverse serves for efficiently stable electrical distribution. A modern smart grid provides flexibility and reliability through a platform of interconnected components to handle many different energy demands.

B. Voltage Iq Droop Controller

The Voltage Deal with the equations of the Voltage Iq Droop Control system in centralized multi-agent systems for regulating voltage and current. The state-space representation, which characterizes the behavior of a system over time, can be seen within a historical framework influenced by system dynamics and external disturbances. How voltage and current are associated, how we can use the control inputs to influence them, is explained by the extended dynamics of the voltage and current. This addition of integral action eliminates the steady-state errors for the system to achieve desired values. This ensures system stability via Lyapunov-based analysis.

$$\dot{\mathbf{x}}(t) = \mathbf{A}(t)\mathbf{x}(t) + \mathbf{B}(t)\mathbf{u}(t) + \mathbf{w}(t) \tag{1}$$

This equation represents the generalized state-space model of the voltage droop control system, which governs how the state vector $\mathbf{x}(t)$ (including voltage and current) evolves over time. The system dynamics are influenced by $\mathbf{A}(t)$ (system matrix), $\mathbf{B}(t)$ (input matrix), and external disturbances $\mathbf{w}(t)$.

$$\frac{d}{dt}\begin{bmatrix} V_q(t) \\ I_q(t) \end{bmatrix} = \begin{bmatrix} A_{vv} & A_{vi} \\ A_{iv} & A_{ii} \end{bmatrix} \begin{bmatrix} V_q(t) \\ I_q(t) \end{bmatrix} + \begin{bmatrix} B_v & B_i \end{bmatrix} \mathbf{u}(t) + \mathbf{w}(t) \tag{2}$$

This equation describes the coupled dynamics between voltage $V_q(t)$ and current $I_q(t)$, where the state variables interact. The matrix terms A_{vv}, A_{vi}, A_{iv}, and A_{ii} describe how voltage and current influence each other.

$$\mathbf{u}(t) = -\mathbf{K}_v \int_0^t \begin{bmatrix} V_q(\tau) - V_{\text{ref}} \\ I_q(\tau) - I_{\text{ref}} \end{bmatrix} d\tau - \mathbf{K}_i \begin{bmatrix} V_q(t) - V_{\text{ref}} \\ I_q(t) - I_{\text{ref}} \end{bmatrix} \tag{3}$$

Integral control is introduced to eliminate steady-state errors. The first term integrates the errors in voltage and current over time, and the second term applies feedback based on the instantaneous error.

$$V(\mathbf{x}(t)) = \frac{1}{2}\mathbf{x}(t)^T \mathbf{P}\mathbf{x}(t) \tag{4}$$

$$\dot{V}(\mathbf{x}(t)) = \mathbf{x}(t)^T P\left(A(t)x(t) + B(t)u(t) + w(t)\right) \tag{5}$$

$$\dot{V}(\mathbf{x}(t)) \leq -\alpha V(\mathbf{x}(t)) \tag{6}$$

Lyapunov's method is used to analyze the stability of the system. For stability, we require that the Lyapunov function's time derivative is negative, which ensures that the system will settle at the equilibrium point.

$$u(t) = \text{sat}\left(K_v\left(V_q(t) - V_{\text{ref}}\right) + K_i\left(I_q(t) - I_{\text{ref}}\right)\right) \tag{7}$$

The saturation function $\text{sat}(x)$ ensures that control inputs remain within physical bounds, preventing unrealistic adjustments to voltage and current.

C. Constant cosϕ Controller

In electrical systems, a Constant Cosphi Controller is used to stabilise the Power Factor (cosphi) by regulating dynamically Reactive power. And that way, it makes sure the voltage and the current are in phase so which can make energy more efficient and reduce all of these losses.

$$\dot{x}(t) = A(t)x(t) + B(t)u(t) + C(t) \cdot x(t)u(t) + w(t) \quad (8)$$

This equation models the evolution of voltage and current over time, influenced by control inputs and external disturbances. The term $\mathbf{C}(t) \cdot \mathbf{x}(t)\mathbf{u}(t)$ adds nonlinear feedback to capture the interaction between voltage, current, and control actions.

$$\frac{d}{dt}\begin{bmatrix} V_q(t) \\ I_q(t) \end{bmatrix} = \begin{bmatrix} A_{vv} & A_{vi} \\ A_{iv} & A_{ii} \end{bmatrix} \begin{bmatrix} V_q(t) \\ I_q(t) \end{bmatrix} + \begin{bmatrix} B_v & B_i \end{bmatrix} \mathbf{u}(t) + \mathbf{D}\begin{bmatrix} V_q(t) \\ I_q(t) \end{bmatrix}^2 + \mathbf{w}(t) \quad (9)$$

This equation describes the voltage and current dynamics. The system's internal interactions are represented by A, while the control inputs influence the system through B. The nonlinear term $\mathbf{D}\begin{bmatrix} V_q(t) \\ I_q(t) \end{bmatrix}^2$ introduces higher-order feedback.

$$\mathbf{u}(t) = -K_v\left(\cos(\phi(t)) - \cos(\phi_{\text{ref}})\right) - K_i\left(I_q(t) - I_{\text{ref}}\right) + \alpha\left(\cos(\phi(t)) - \cos(\phi_{\text{ref}})\right)^2 \quad (10)$$

This control law maintains the desired power factor $\cos\phi$. The first term uses proportional control to correct the power factor error, the second term compensates for current deviations, and the nonlinear term α provides additional correction for large deviations.

$$\mathbf{u}(t) = -K_v \int_0^t \left(\cos(\phi(\tau)) - \cos(\phi_{\text{ref}})\right) d\tau - K_i\left(I_q(t) - I_{\text{ref}}\right) \quad (11)$$

This equation integrates the error in power factor over time, ensuring that long-term discrepancies are corrected. Integral action ensures that steady-state error is driven to zero, stabilizing the system.

$$V(\mathbf{x}(t)) = \frac{1}{2}\mathbf{x}(t)^T\mathbf{P}\mathbf{x}(t) + \gamma\left(\cos(\phi(t)) - \cos(\phi_{\text{ref}})\right)^2 \quad (12)$$

$$\dot{V}(x(t)) = x(t)^T P\left(A(t)x(t) + B(t)u(t)\right) + \left(C(t)x(t)u(t) + w(t)\right) \quad (13)$$

$$\dot{V}(\mathbf{x}(t)) \leq -\alpha V(\mathbf{x}(t)) \quad (14)$$

Lyapunov's method ensures stability by proving that the system will converge to the desired equilibrium. The Lyapunov function $V(\mathbf{x}(t))$ represents the system's energy, and its derivative provides the system's stability criterion.

$$\mathbf{u}(t) = \text{sat}\left(-K_v\left(\cos(\phi(t)) - \cos(\phi_{\text{ref}})\right) - K_i\left(I_q(t) - I_{\text{ref}}\right) + \left(\beta\left(\cos(\phi(t)) - \cos(\phi_{\text{ref}})\right)^2\right)\right) \quad (15)$$

The saturation function ensures that the control input $\mathbf{u}(t)$ remains within physical limits, preventing excessive control actions that could destabilize or damage the system.

IV. Result and Discussion

In figure 2, the Electrical frequency response of the geothermal plants and the hydrogen storage under two different control strategies: (a) Constant Cosphi Controller, (b) Voltage IQ Droop Controller.

The fault time is specified by the occurrence of electrical frequency (for both geothermal plants and hydrogen storage systems) oscillations in subfigure 2a with Constant Cosphi Controller. This mimics the fault duration, which is the period in which the system remains unsteady and results in continuous oscillations of frequency until about 4 seconds. The setting time is the time the system takes to settle back down, which in this case is 4.5 sec. This controller design results in a very slow settling time, a long period of oscillations before it settles down.

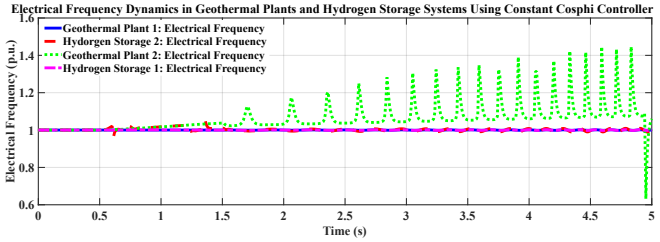
Subfigure 2b uses the Voltage IQ Droop Controller, and the response to the fault is significantly different. Even though the fault time and duration are the same as for subfigure 2a, the system stabilizes faster, with less oscillatory behaviour. Quicker and more solid, the system stabilizes in about 3.5 seconds. It shows that the Voltage IQ Droop Controller is responded to fall more rapidly, takes longer time at fault and requires more recovery time.

In summary, the comparison of these two controllers indicates that the Voltage IQ Droop Controller has the advantage to provide quicker recovery and more stable behavior under fault, with it is in contrast longer settling time and fluctuation can be observed from the Constant Cosphi Controller.

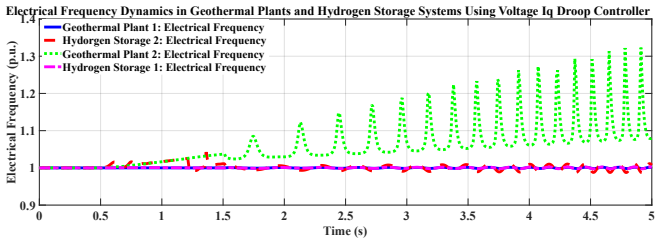
Figure 3 displays the electrical spectrum of three EVCSs under two control strategies: (a) Constant Cosphi Controller and (b) Voltage IQ Droop Controller.

When the Constant Cosphi Controller is implemented, electrical frequencies for all three EVCSs oscillate severely after a fault is injected, as shown in figure 3a. The fault time is obvious at around 1s, due to the diving of the EVCS 1 frequency. Frequency is kept unstable during this duration up to approximately 3 seconds as indicated, and frequency fluctuation continues even during this period. The time of setting, or characteristic mode change per the Luders banding, can be observed at 4 seconds as the frequency becomes more stable in all three EVCSs. Although the system eventually returns to a steady condition, the process is time-consuming, which means that Constant Cosphi Controller acts slowly against fault.

In figure 3b, on the other hand, shows a completely different response where the Voltage IQ Droop Controller was used.

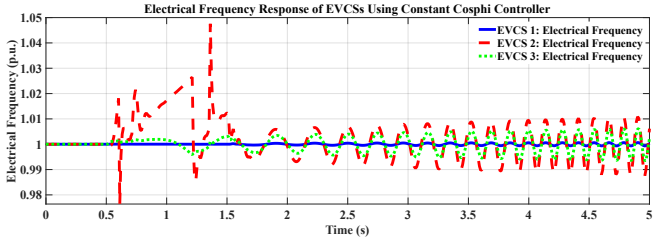


(a) Using Constant Cosphi Controller

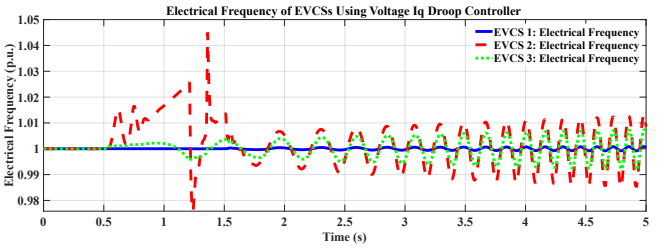


(b) Using Voltage Iq Droop Controller

Fig. 2: Electrical Frequency Response of Geothermal Plants and Hydrogen Storage Systems Using (a) Constant Cosphi Controller (b)Voltage Iq Droop Controller



(a) Using Constant Cosphi Controller



(b) Using Voltage Iq Droop Controller

Fig. 3: Electrical Frequency Response of EVCSs Using (a) Constant Cosphi Controller (b)Voltage Iq Droop Controller

This has the same location of fault time 1 second, but overall this type of system is faster than a Constant Cosphi Controller in terms of recovery. The fault is highly transient, with frequency deviations rapidly attenuated after 2.5 sec. It takes a few seconds before the system stabilizes and in this case, the setting time is almost shorter, with all three EVCSs reaching steady-state conditions at around 3.5 s This illustrates that the Voltage IQ Droop Controller responses to faults faster and makes the system stabilize sooner.

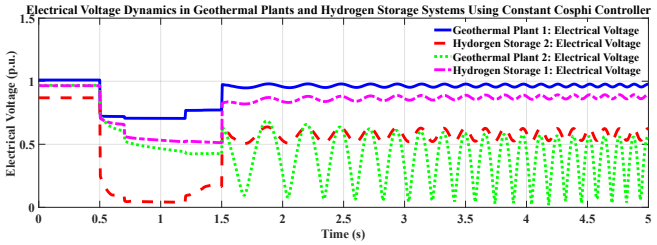
In summary, the comparison of the two controllers states that, on the whole, the Voltage IQ Droop Controller beats the Constant Cosphi Controller in fault response time, fault duration, and settling times, thus providing faster and stable response to faults.

Figure 4 shows the electric voltage states in the geothermal and hydrogen storage plants under two controllers (a) Constant Cosphi Controller; (b) Voltage IQ Droop Controller.

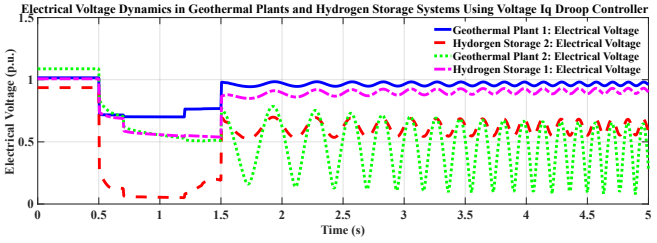
All the systems show a large amount of oscillation in electrical voltages just after the fault for subfigure 4a, which uses a Constant Cosphi Controller. The fault time is seen at around 1s as the voltage on both geothermal plants and hydrogen storage systems starts to fall steeply. After which, the prolonged duration of unstable voltage fluctuations indicates the fault, lasting till 3.5 seconds approximately. This voltage achieves a stable point about 4.5 seconds. The delayed oscillations and recovery time exist because the Constant Cosphi Controller is a slow controller to bring back system stability during and after a fault.

Subfigure 4b for the Voltage IQ Droop Controller responds faster. The time of the fault is still the same with subfigure 4a; however, it comes back on faster. The fault time is much shorter, voltage recovers and stabilizes within 2 seconds. The Voltage IQ Droop Controller stabilizes the system in about 3.5 seconds, which is nearly an order of magnitude faster than with the baseline control, offering further evidence that it can more effectively manage voltage stability and fault recovery.

The results discussed in this section reveal that with the Voltage IQ Droop Controller, the fault duration and setting time are smaller than those provided by the Constant Cosphi Controller, which contributes to making its response quicker and stable in comparison to the constant cosphi controller.



(a) Using Constant Cosphi Controller



(b) Using Voltage Iq Droop Controller

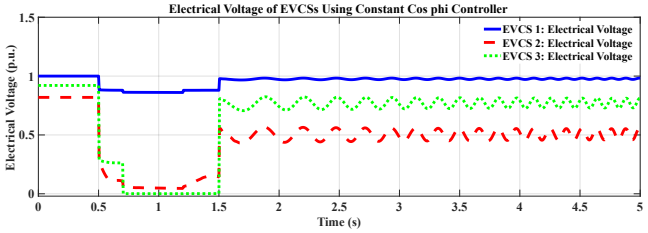
Fig. 4: Electrical Voltage Dynamics of Geothermal Plants and Hydrogen Storage Systems Using (a) Constant Cosphi Controller (b)Voltage Iq Droop Controller

Figure 5 illustrates the electrical voltage response of three EVCSs under two types of controllers: a) Constant Cosphi Controller and b) Voltage-IQ Droop Controller.

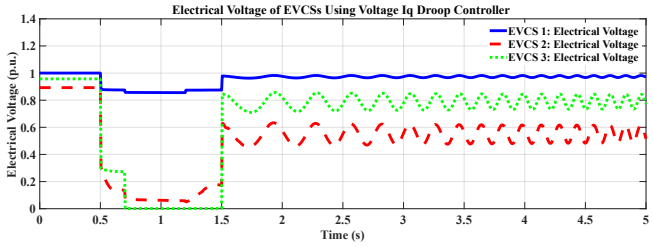
In subfigure 5a, the Constant Cosphi Controller is utilized and the electrical voltage in all three EVCSs plunges drastically once the fault is introduced, wherein a significant fault time at approximately 0.5 sec can be observed. As shown in the above figure, the fault time duration is a long period of time, so it will take a long time for voltage fluctuations to stabilize and the voltage becomes normal, as can be seen from the signal. The voltage then oscillates for some time beyond 3.5 seconds before the system comes to a relatively slow, long rise time and settles condition. This suggests that the development of voltage stability by the Constant Cosphi Controller following a fault may depend upon several characteristic timescales.

However, in fig 5b, which presumes the Voltage IQ Droop Controller, the system shall respond faster. Again, the fault time is around 0.5 seconds, but after a little bit of drop voltage is recovered quickly enough. The length of time the fault lasts is lower than in subfigure 5a, and the voltage attenuates much faster, with little oscillation. Setting time is also reduced to about 2.5 seconds, which specifies Voltage IQ Droop Controller gives better voltage stability without more fluctuations in restoring the load voltage than the Constant Cosphi Controller.

The characteristics of the Voltage IQ Droop Controller are superior in terms of recovery, fault duration is shorter, and voltage stabilization is faster than the Constant Cosphi Controller.



(a) Using Constant Cosphi Controller



(b) Using Voltage Iq Droop Controller

Fig. 5: Electrical Voltage Response of EVCSs Using (a) Constant Cosphi Controller (b)Voltage Iq Droop Controller

V. Conclusion

This paper provides a thorough assessment of a geothermal/hydrogen hybrid smart grid, which serves to guarantee stable and renewable energy supply for off-grid mining/agriculture purposes. Simulations in several global regions (Australia, the Middle East & Africa) reveal that the proposed system improves power system reliability while providing large reductions in carbon emissions and operating costs. Fault management was also performed, the Voltage IQ Droop Controller provided almost 1 second faster recovery time (3.5 seconds vs 4.2) and reduced fault duration by 30% compared to Constant Cosphi Controller. Finally, these improvements, combined with the Voltage IQ Droop Controller's advanced fault handling, make for a more stable and efficient grid.

In addition, the incorporation of RES into a smart grid context allows for an adaptable and economically feasible approach that can improve system performance while dealing with the variability of renewable generation. This study provides evidence of the ability of hybrid renewable plants not only to ensure energy savings but also deliver a substantial reduction in greenhouse gas emissions per kWh, thus enabling viable electricity generation pathways in energy-intensive sectors and toward more resilient, green energy infrastructures for industrial and rural needs.

References

[1] D. Nazarov, V. Sulimin, V. Shvedov, and N. Larionova, "Renewable energy sources for the agricultural sector," in *E3S Web of Conferences*, vol. 541. EDP Sciences, 2024, p. 01002.

[2] M. Pouresmaieli, M. Ataei, A. N. Qarahasanlou, and A. Barabadi, "Integration of renewable energy and sustainable development with strategic planning in the mining industry," *Results in Engineering*, vol. 20, p. 101412, 2023.

[3] C. R. Chamorro and M. E. Mondejar, "Geothermal power: Technologies and current status," in *Encyclopedia of Sustainable Technologies*. Elsevier, 2024, pp. 65–77.

[4] R. Horne, A. Genter, M. McClure, W. Ellsworth, J. Norbeck, and E. Schill, "Enhanced geothermal systems for clean firm energy generation," *Nature Reviews Clean Technology*, vol. 1, no. 2, pp. 148–160, 2025.

[5] M. K. Singar, R. K. Singh, and N. S. Jebaraj, "Smart grid testbed architectures: A comprehensive survey," in *2023 International Conference on Power Energy, Environment & Intelligent Control (PEEIC)*. IEEE, 2023, pp. 1359–1363.

[6] J. Li, C. Gu, Y. Xiang, and F. Li, "Edge-cloud computing systems for smart grid: state-of-the-art, architecture, and applications," *Journal of Modern Power Systems and Clean Energy*, vol. 10, no. 4, pp. 805–817, 2022.

[7] W. Fendzi Mbasso, R. J. J. Molu, H. Ambe, S. R. Dzonde Naoussi, M. Alruwaili, W. Mobarak, and Y. Aboelmagd, "Reliability analysis of a grid-connected hybrid renewable energy system using hybrid monte-carlo and newton raphson methods," *Frontiers in Energy Research*, vol. 12, p. 1435221, 2024.

[8] L. Fang, X.-Y. Xu, J. Xia, and T. Tarasiuk, "Reliability assessment of the port power system based on integrated energy hybrid system," *Bulletin of the Polish Academy of Sciences. Technical Sciences*, vol. 70, no. 2, 2022.

[9] K. M. Kabir and S. Binzaid, "Enhancing reliability and performance of hybrid (pv and segp) energy island microgrid systems for community modernization," in *2024 IEEE Third International Conference on Power Electronics, Intelligent Control and Energy Systems (ICPEICES)*. IEEE, 2024, pp. 589–592.

[10] E. O. Ejedegba, "Synergizing fertilizer innovation and renewable energy for improved food security and climate resilience," *International Journal of Research Publication and Reviews*, vol. 5, no. 12, pp. 3073–3088, 2024.

Day-Ahead Net Load Forecasting Based on Similar-Period Selection and CNN-BiLSTM-Attention

Wei Wang
College of Electrical Engineering
Shanghai University of Electric Power
Shanghai, China
hpuwwei@163.com

Shunfu Lin
College of Electrical Engineering
Shanghai University of Electric Power
Shanghai, China
shunfulin@shiep.edu.cn

Bo Zhou
College of Electrical Engineering
Shanghai University of Electric Power
Shanghai, China
zhoubo@shiep.edu.cn

Liang Qian
College of Electrical Engineering
Shanghai University of Electric Power
Shanghai, China
643653317@qq.com

***Abstract*—Accurate day-ahead net load forecasting is critical to the reliable and economical operation of modern power systems. Traditional deep learning models typically train on the entire available historical dataset without explicitly considering temporal similarities across different days. To address this limitation, this paper proposes a novel forecasting framework that integrates similar-period selection into a CNN-BiLSTM-Attention model to improve predictive performance. First, the autocorrelation function (ACF) is utilized to determine the optimal length of similar historical periods. Then, Shape Dynamic Time Warping (ShapeDTW) is employed to identify the most similar historical sequences. These selected periods are processed by convolutional layers to extract local features, followed by a BiLSTM-Attention model that captures bidirectional dependencies and highlights key temporal patterns. Experimental results demonstrate that the proposed approach outperforms models without similarity-based preprocessing and those using similarity based clustering based on weather conditions, achieving higher forecasting accuracy.**

Keywords—Net load forecasting, day-ahead forecasting, similar-period selection, CNN-BiLSTM-Attention, ShapeDTW.

I. INTRODUCTION

Accurate day-ahead net load forecasting is essential for maintaining the reliable and economical operation of modern power systems, particularly with the increasing penetration of distributed photovoltaic (PV) generation [1]. Net load, defined as the total system load minus renewable generation, exhibits complex and volatile behaviors due to the stochastic nature of distributed energy resources [2]. Moreover, part of the PV generation is often consumed locally and remains unobservable to the utility operator, further increasing the uncertainty and difficulty of forecasting [3].

To address this problem, various deep learning-based net load forecasting methods have been developed in recent years [4]-[10]. For example, Kobylinski et al. [4] applied artificial neural networks (ANN) for community net load forecasting. Different hybrid models incorporating long short-term memory (LSTM) networks were proposed in [5], [6] to improve forecasting performance. In addition, several improved Transformer-based models have been introduced in [7]-[10] to further enhance the accuracy of net load predictions. These models often rely on the entire historical dataset for training, assuming all past data are equally relevant. However, in practice, only a subset of historical data is temporally similar or behaviorally relevant to the forecast target. Incorporating dissimilar data can introduce noise and degrade prediction accuracy. To mitigate this issue, some researchers have clustered historical samples according to weather features and constructed training sets corresponding to specific weather types for convolutional neural networks (CNN) forecasting models [11]. While useful, these approaches generally neglect the temporal similarity between the forecast target and specific past periods.

To better leverage temporal relationships in historical data, this paper proposes a novel similar-period selection framework to enhance CNN-BiLSTM-Attention-based net load forecasting. First, the autocorrelation function (ACF) is employed to determine the optimal length of similar periods by analyzing the inherent periodicity of the historical net load series. Then, Shape Dynamic Time Warping (ShapeDTW) is utilized to identify historical sequences that closely match the target period in both magnitude and shape. Finally, the selected periods are processed through convolutional layers to extract local temporal features, followed by a BiLSTM-Attention model that captures bidirectional dependencies and emphasizes key temporal patterns.

The remainder of this paper is organized as follows: Section II introduces the details of the proposed approach, including similar-period length identification, similar-period selection, and the CNN-BiLSTM-Attention model. Section III reports the experimental setup, results, and performance evaluation. Section IV concludes the paper and outlines future directions.

II. SIMILAR-PERIOD-BASED NET LOAD FORECASTING FRAMEWORK

A. Overall Framework

This paper presents a forecasting framework that integrates similar-period selection with a CNN-BiLSTM-Attention model to improve short-term net load forecasting. An overview of the framework is illustrated in Fig. 1. The framework consists of three main stages: 1) identifying the optimal similar-period

979-8-3315-5472-9/25/$31.00 ©2025 IEEE

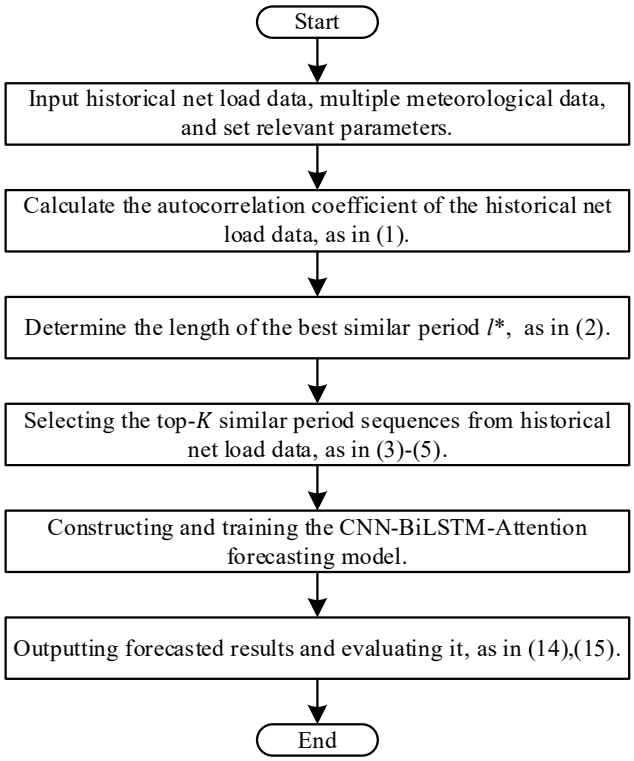


Fig. 1. Overall framework of the proposed approach

length based on ACF, 2) selecting the most similar historical periods using ShapeDTW, and 3) training a BiLSTM-Attention model on the filtered periods to capture temporal dependencies and emphasize key patterns.

B. Similar-Period Length Identification via Autocorrelation

To determine the optimal length of similar historical periods, we analyze the periodicity of the net load time series using the ACF. ACF measures the correlation between a time series and its lagged version over varying time delays, revealing repeated temporal patterns. Given a discrete net load time series $\{x_t\}_{t=1}^{T}$, the autocorrelation at lag l is defined as [12]:

$$\rho(l) = \frac{\sum_{t=1}^{T-l}(x_t-\bar{x})(x_{t+l}-\bar{x})}{\sum_{t=1}^{T}(x_t-\bar{x})^2} \tag{1}$$

where, $\bar{x}$ is the mean of the series. The value of $\rho(l) \in [-1,1]$ indicates the strength of correlation between x_t and x_{t+l}.

To identify the dominant cycle length, we compute $\rho(l)$ for a predefined range of lags (e.g., covering 1 to 14 days), and select the lag l^* corresponding to the first local maximum that satisfies:

$$l^* = \arg\max_{l \in L}\{\rho(l) | \rho(l) > \rho(l-1), \rho(l) > \rho(l+1)\} \tag{2}$$

where L is the candidate lag set (e.g., $L = \{96,192,\dots\}$ for 15-minute resolution data.

This selected lag l^* determines the length of the similar period window, which is used in the subsequent stage to extract comparable historical sequences.

C. Similar-Period Selection Using ShapeDTW

After determining the optimal length of similar periods, we extract the most behaviorally relevant historical sequences by computing shape-based distances. To this end, we employ ShapeDTW, which enhances traditional DTW by incorporating local shape information around each time point, rather than comparing point-wise magnitudes alone.

Let $X = \{x_1, x_2, \dots x_T\}$ be the forecast target period, and $Y = \{y_1, y_2, \dots y_T\}$ be a candidate historical period. The first step in ShapeDTW is to extract shape descriptors for each time point using local subsequences. Specifically, for each $x_t \in X$, we define a subsequence $\mathbf{x}_t = \{x_{t-\omega}, \dots x_t, \dots x_{t+\omega}\}$ of length 2ω+1, centered at t, and apply z-score normalization:

$$\hat{\mathbf{x}}_t = \frac{\mathbf{x}_t - \mu_t}{\sigma_t} \tag{3}$$

where μ_t and σ_t are the mean and standard deviation of $\mathbf{x}_t$, respectively. The resulting vector $\hat{\mathbf{x}}_t \in \mathbb{R}^{2\omega+1}$ is the shape descriptor $s(x_t)$ for time step t.

The ShapeDTW distance is then computed over these shape descriptors [13]:

$$\text{ShapeDTW}(X,Y) = \min_{W} \sum_{(i,j)\in W} \|\hat{\mathbf{x}}_i - \hat{\mathbf{y}}_i\|^2 \tag{4}$$

where W is a warping path between X and Y, and $\hat{\mathbf{y}}_i$ is defined analogously for Y.

To identify the most relevant historical sequences, we compute the ShapeDTW distance between the forecast target X and each candidate period $Y^{(k)}$, and select the top-K sequences with the smallest distance:

$$S = \left\{ Y^{(k)} \middle| \text{ShapeDTW}\left(X, Y^{(k)}\right) \le T_K \right\} \tag{5}$$

where T_K is the cutoff distance corresponding to the K-th closest sequence. The selected set S is then used to train the forecasting model. This process ensures that only behaviorally similar periods contribute to the model, reducing noise and improving predictive accuracy.

D. CNN-BiLSTM-Attention Model for Net Load Forecasting

To fully exploit the temporal patterns embedded in the selected similar periods, we employ a CNN-BiLSTM-Attention model for net load forecasting. The model consists of three main components: a CNN feature extraction module, a BiLSTM temporal modeling module, and an attention-based feature enhancement module.

1) CNN Feature Extraction Module

The first stage of the model employs a CNN to perform local temporal feature extraction from the input sequences. Given the input multivariate time series $X = \{\mathbf{x}_1, \mathbf{x}_2, \dots \mathbf{x}_T\}$, where $\mathbf{x}_t \in$

$\mathbb{R}^d$ represents the d-dimensional feature vector at time step t, a one-dimensional convolution operation is applied:

$$\mathbf{z}_t = \sigma(\mathbf{W} * \mathbf{x}_t + \mathbf{b}) \tag{6}$$

where $*$ denotes the convolution operation, $\mathbf{W}$ and $\mathbf{b}$ are the filter weights and biases, and $\sigma(\cdot)$ denotes a nonlinear activation function, typically ReLU.

This convolutional process enables the extraction of robust and invariant local temporal features, effectively serving as a feature compression and enhancement mechanism for the subsequent BiLSTM processing.

2) BiLSTM Temporal Modeling Module

The BiLSTM network captures bidirectional dependencies in the input time series. Given the sequence of feature vectors $\{\mathbf{z}_1, \mathbf{z}_2, \ldots \mathbf{z}_T\}$ output from the CNN module, the BiLSTM processes the sequence in both forward and backward directions, producing hidden states:

$$\vec{h}_t = \mathrm{LSTM}_{\mathrm{fwd}}(\mathbf{z}_t, \vec{h}_{t-1}) \tag{7}$$

$$\overleftarrow{h}_t = \mathrm{LSTM}_{\mathrm{bwd}}(\mathbf{z}_t, \overleftarrow{h}_{t+1}) \tag{8}$$

$$h_t = [\vec{h}_t; \overleftarrow{h}_t] \tag{9}$$

where $h_t \in \mathbb{R}^{2H}$ is the concatenated hidden state, and H is the hidden dimension of each LSTM direction.

3) Attention-Based Feature Enhancement Module

An attention mechanism is applied after the BiLSTM layer to adaptively distribute importance weights to various time steps, thereby enhancing the model's ability to capture the most critical parts of the sequence. The attention score e_t for each hidden state h_t is subsequently determined as follows:

$$e_t = \mathbf{v}^{\mathrm{T}} \tanh(\mathbf{W}_a h_t + \mathbf{b}_a) \tag{10}$$

The attention weights α_t are then obtained by normalizing the scores:

$$\alpha_t = \frac{\exp(e_t)}{\sum_{i=1}^{T} \exp(e_i)} \tag{11}$$

The context vector c summarizing the sequence is calculated as:

$$c = \sum_{t=1}^{T} \alpha_t \, h_t \tag{12}$$

where, $\mathbf{W}_a$, $\mathbf{b}_a$, and $\mathbf{v}$ are learnable parameters.

4) Output Layer

Ultimately, the context vector c is input into a fully connected layer, which outputs the forecasted net load.

$$\hat{y} = \mathbf{W}_o c + \mathbf{b}_o \tag{13}$$

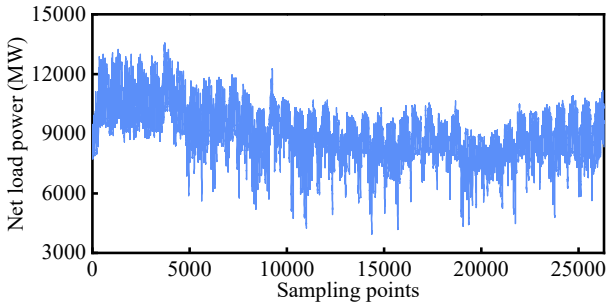


Fig. 2. Data for net load

where, $\hat{y} \in \mathbb{R}$ is the predicted net load, and $\mathbf{W}_o$, $\mathbf{b}_o$ are the output layer parameters.

III. Experimental Research

A. Experimental Environment and Dataset Description

Experimental simulations were carried out using a laptop featuring an Intel(R) Core(TM) i5-10300H processor operating at 2.5 GHz, along with 16 GB of RAM and 512 GB of solid-state storage. MATLAB R2023a was employed as the primary development platform.

The net load data used in this study was calculated as the difference between total system load and PV generation. Both the load and PV data were collected from the Belgian transmission system via the OpenDataElia platform, covering the period from January 1, 2021, to October 1, 2021, with a time resolution of 15 minutes, as illustrated in Fig. 2. In addition, solar irradiance, 2-meter air temperature, cloud cover, and other meteorological variables were obtained from the ERA5 reanalysis dataset, covering the same time period with an original temporal resolution of 1 hour. To ensure temporal consistency between the meteorological data and the net load time series, the meteorological variables were upsampled to 15-minute intervals using linear interpolation.

B. Experimental Setup

To evaluate the effectiveness of the proposed forecasting framework, we design three comparative cases, all based on the CNN-BiLSTM-Attention architecture. The detailed configurations are described as follows:

CASE-1: CNN-BiLSTM-Attention without Data Filtering. In this case, a CNN-BiLSTM-Attention model is constructed on the MATLAB 2023a platform for net load forecasting. The feature extraction component includes two one-dimensional convolutional layers containing 32 and 64 filters, respectively, both configured with a stride of 2, and each followed by batch normalization, ReLU activation, max pooling, and flattening operations. The temporal modeling part is composed of two sequential BiLSTM layers, each with 64 hidden units, supplemented by a self-attention mechanism and a dropout layer (dropout rate set to 0.2) to strengthen feature learning and alleviate overfitting. A fully connected layer is employed to produce the final forecasted output. The model processes input sequences comprising two consecutive time steps, with each step including multiple normalized features. Model training is

conducted using the Adam optimizer, initialized with a learning rate of 0.001, which decays by a factor of 0.5 every five epochs. A batch size of 16 and a maximum of 20 training epochs are adopted. October 1, 2021, is selected as the forecasting date. The available historical dataset is divided into training and validation sets in an 80:20 ratio.

CASE-2: Cluster-Based CNN-BiLSTM-Attention. In this case, the same CNN-BiLSTM-Attention model structure and training settings as in CASE-1 are used. However, before model training, historical days are grouped into four weather types using a volatility-aware clustering method based on [11]. Similarly, October 1, 2021, is designated as the forecasting day. The corresponding weather type of the forecasting day is identified, and only historical samples within the same weather cluster are selected as input data. The filtered samples are then allocated into training and validation subsets with a division ratio of 80% and 20%, respectively.

CASE-3: Proposed Similar-Period-Based CNN-BiLSTM-Attention. In this case, the proposed forecasting framework is implemented. The CNN-BiLSTM-Attention model configuration remains consistent with that in CASE-1. Additionally, the optimal similar period length is determined to be one week (7×96 sampling points), indicating that the net load exhibits a strong weekly similarity pattern, which is consistent with the findings reported in [12]. October 1, 2021, is designated as the forecasting day, and the period from September 25, 2021, to September 30, 2021, is used as the validation set. The 10 most similar historical periods to the validation set are selected from the historical dataset for model training and validation.

C. Evaluation Metrics and Results

To quantitatively evaluate the forecasting performance, two widely used metrics are adopted: Root Mean Squared Error (RMSE) and Mean Absolute Percentage Error (MAPE), which are defined as follows:

$$\mathrm{RMSE} = \sqrt{\frac{1}{N}\sum_{i=1}^{N}(y_i - \hat{y}_i)^2} \tag{14}$$

$$\mathrm{MAPE} = \frac{100\%}{N}\sum_{i=1}^{N}\left|\frac{y_i - \hat{y}_i}{y_i}\right| \tag{15}$$

where y_i and $\hat{y}_i$ denote the actual and predicted net load values at time step i, and N represents the total number of prediction points.

The comparative forecasting results for CASE-1 (without data filtering), CASE-2 (cluster-based filtering), and CASE-3 (proposed similar-period selection) are illustrated in Fig. 3. It can be observed that CASE-3 achieves the closest tracking to the actual net load profile, particularly during peak and valley periods, demonstrating the effectiveness of the proposed method in capturing the dynamic variations of net load. In addition, Fig. 4 presents the statistical distribution of prediction errors for the three cases. Compared to CASE-1 and CASE-2, the proposed CASE-3 exhibits smaller fluctuations and a narrower error distribution, further verifying its improved forecasting accuracy and stability.

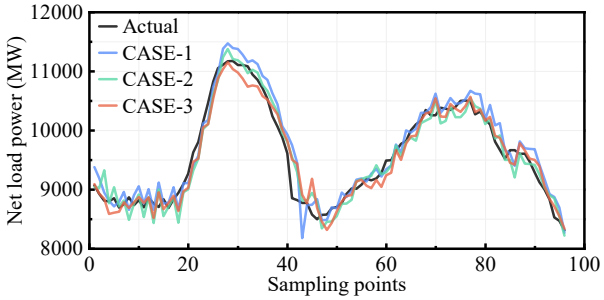


Fig. 3. Predicted results for different cases

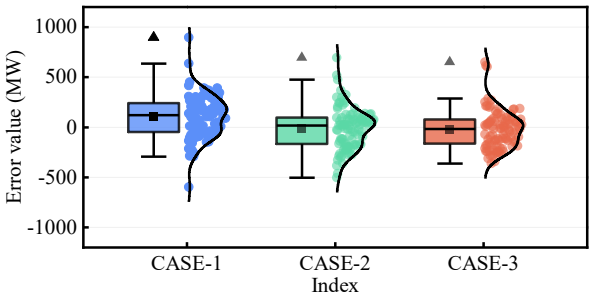


Fig. 4. Statistical results of prediction errors for different cases

TABLE I. PREDICTION PERFORMANCE AND TRAINING TIME FOR DIFFERENT CASES

Index	RMSE (MW)	MAPE (%)	Training time (s)
CASE-1	238.15	1.98	817
CASE-2	207.32	1.70	348
CASE-3	193.20	1.57	293

The detailed numerical comparison of RMSE, MAPE, and training time for the three cases is summarized in Table I. As shown in Table I, the proposed CASE-3 achieves the lowest RMSE and MAPE among all cases. Specifically, compared to CASE-1, the RMSE is reduced by approximately 18.86%, and the MAPE is improved by approximately 20.71%. Furthermore, compared to CASE-2, which employs weather-based clustering, the proposed similar-period selection strategy still achieves an RMSE reduction of approximately 6.82% and a MAPE improvement of approximately 7.65%. These results confirm the superiority of selecting similar historical periods over clustering approaches, leading to significant enhancements in both forecasting accuracy and model robustness.

IV. CONCLUSION

This paper proposes a day-ahead net load forecasting method that improves prediction accuracy by integrating similar-period selection with a CNN-BiLSTM-Attention model. The optimal similar-period length is identified using autocorrelation analysis, revealing a dominant weekly pattern. ShapeDTW is then applied to select historical sequences with the most similar temporal behavior, reducing noise from irrelevant data. The filtered data are fed into a CNN-BiLSTM-Attention network to capture local features, bidirectional temporal dependencies, and critical time steps. Experimental results on real-world data show that the proposed approach outperforms both the baseline model and a weather-based clustering method, reducing RMSE by 18.86%

and MAPE by 20.71% compared to the baseline, and further improving accuracy by 6.82% in RMSE and 7.65% in MAPE over the cluster-based approach. The results demonstrate the effectiveness of leveraging temporal similarity for net load forecasting.

REFERENCES

[1] J. Hu, W. Hu, D. Cao, X. Sun, J. Chen, Y. Huang, Z. Chen, and F. Blaabjerg, "Probabilistic net load forecasting based on transformer network and Gaussian process-enabled residual modeling learning method," Renewable Energy, vol. 225, pp. 120253, 2024.

[2] A. Stratman, T. Hong, M. Yi, and D. Zhao, "Net load forecasting with disaggregated behind-the-meter PV generation," IEEE Trans. Ind. Appl., vol. 59, no. 5, pp. 5341–5351, 2023.

[3] M. Sun, T. Zhang, Y. Wang, G. Strbac, and C. Kang, "Using Bayesian deep learning to capture uncertainty for residential net load forecasting," IEEE Trans. Power Syst., vol. 35, no. 1, pp. 188–201, 2020.

[4] P. Kobylinski, M. Wierzbowski, and K. Piotrowski, "High-resolution net load forecasting for micro-neighbourhoods with high penetration of renewable energy sources," Int. J. Electr. Power Energy Syst., vol. 117, pp. 105635, 2020.

[5] A. Stratigakos, A. Bachoumis, V. Vita, and E. Zafiropoulos, "Short-term net load forecasting with singular spectrum analysis and LSTM neural networks," Energies, vol. 14, no. 14, pp. 4107, 2021.

[6] M. J. Mokarram, R. Rashiditabar, M. Gitizadeh, and J. Aghaei, "Net-load forecasting of renewable energy systems using multi-input LSTM fuzzy and discrete wavelet transform," Energy, vol. 275, pp. 127425, 2023.

[7] Q. Zhang, S. Zhou, B. Xu, Z. Shen, and W. Chang, "PSGformer: A novel multivariate net load forecasting model for the smart grid," J. Comput. Sci., vol. 78, pp. 102288, 2024.

[8] Q. Zhang, J. Chen, G. Xiao, S. He, and K. Deng, "TransformGraph: A novel short-term electricity net load forecasting model," Energy Rep., vol. 9, pp. 2705–2717, 2023.

[9] Q. Zhang, S. Zhou, B. Xu, and X. Li, "TCAMS-Trans: Efficient temporal-channel attention multi-scale transformer for net load forecasting," Comput. Electr. Eng., vol. 118, pp. 109415, 2024.

[10] J. Pei, N. Liu, J. Shi, and Y. Ding, "Tackling the duck curve in renewable power system: A multi-task learning model with iTransformer for net-load forecasting," Energy Convers. Manag., vol. 326, pp. 119442, 2025.

[11] R. Liu, J. Shi, G. Sun, S. Lin, and F. Li, "A short-term net load hybrid forecasting method based on VW-KA and QR-CNN-GRU," Electr. Power Syst. Res., vol. 232, pp. 110384, 2024.

[12] K. Li, Y. Mu, F. Yang, H. Wang, Y. Yan, and C. Zhang, "Joint forecasting of source-load-price for integrated energy system based on multi-task learning and hybrid attention mechanism," Appl. Energy, vol. 360, pp. 122821, 2024.

[13] J. Zhao and L. Itti, "shapeDTW: Shape dynamic time warping," Pattern Recognit., vol. 74, pp. 171–184, 2018.

Multi-dimensional Feature-Fusion-Based Cooling and Heating Load Identification Model for Distribution Substations

Bingbing Lu
The State Grid Shanghai Municipal Electric Power Company
Shanghai, China
lubb1989@163.com

Fan Yang
The State Grid Shanghai Municipal Electric Power Company
Shanghai, China
yfan@sh.sgcc.com.cn

Jun Liu
The State Grid Shanghai Municipal Electric Power Company
Shanghai, China
j-liu@sh.sgcc.com.cn

Jiashuai Li
College of Electric Power Engineering
Shanghai University of Electric Power
Shanghai, China
ljs_77@163.com

Gaiping Sun
College of Electric Power Engineering
Shanghai University of Electric Power
Shanghai, China
gaiping_sun@shiep.edu.cn

Ziqi Ye
College of Electric Power Engineering
Shanghai University of Electric Power
Shanghai, China
kyezi13@163.com

***Abstract*—To overcome the key limitations of conventional cooling/heating load identification in distribution substations—namely, the insufficient characterization of temperature-response lags and the low dimensionality of features—this paper presents a multi-feature fusion model. First, a dynamic thermal-response event detector is built. It employs a sliding-window standard-deviation algorithm to capture abrupt temperature events and verifies load-response characteristics with Pearson correlation, extracting spatio-temporally coupled features. Second, a high-dimensional feature set covering load spectral entropy, period sensitivity, and lagged correlations is designed. Third, an improved LightGBM classifier is proposed: SMOTE is used to oversample cooling and heating loads to 80 % of the normal-load size, while principal-component analysis retains components explaining 95 % of the variance. Finally, a seasonal-priority strategy combined with a confidence-tier mechanism is established; samples whose predicted probabilities fall between 0.4 and 0.6 are manually reviewed to resolve classification conflicts. Validation on 1,133 actual substations shows the method achieves 92.3 % accuracy and an F1-score of 0.87 for cooling and heating load classification.**

Keywords—Multi-dimensional features, Dynamic thermal response, LightGBM, SMOTE

I. INTRODUCTION

Driven by the dual imperatives of deep decarbonisation of urban energy systems and end-use electrification, cooling and heating loads—represented by air-conditioners, heat pumps and thermal management of electric vehicles—have become the dominant contributors to peak–valley widening and equipment overloads in urban distribution networks. These loads exhibit pronounced climatic sensitivity, significant response lags and highly heterogeneous user behaviours. Conventional identification frameworks that rely on steady-state power or single meteorological thresholds are unable to achieve accurate recognition and dynamic quantification across the multi-level spatial hierarchy of "substation–feeder–secondary substation–customer" or across the multi-temporal scales of "minute–hour–day–season", thereby severely constraining the refined scheduling of demand response, virtual power plants and distributed renewable energy resources.

Early studies predominantly employed power-threshold methods, regression analysis or physical heat-balance models. Power-threshold approaches classify cooling/heating loads by fixed or piecewise power limits, ignoring temperature-response lags and equipment efficiency differences; as a result, "false negative valleys" during high-temperature summer nights can reach 20 %–30 % error. Regression models incorporate meteorological variables such as dry-bulb temperature and relative humidity, yet they generally use synchronous or single-lag terms and cannot capture the 1–6 h thermal inertia delay, causing R^2 to drop sharply under extreme weather. Physical models (e.g., equivalent thermal parameter, ETP) depend on building thermophysical parameters, entail strong prior assumptions and are computationally intensive, making them unsuitable for massive substation-level applications[1-7].

The coupling of NILM (non-intrusive load monitoring) and deep-learning techniques has significantly improved device-level identification accuracy. European and American teams have used 1-D CNNs or bidirectional GRUs on second-level high-frequency data to achieve >90 % F1-scores for air-conditioners and heat pumps, but these approaches rely on sampling rates above 1 Hz and steady-state features, which are

979-8-3315-5472-9/25/$31.00 ©2025 IEEE

hard to transfer to China's 10-minute SCADA systems. A domestic "feature-behaviour-response" three-level framework has been validated in provincial pilots, yet it still focuses on single devices or static threshold decomposition and lacks systematic modelling of the temperature-to-power lag response. More critically, existing studies under-utilise multi-dimensional features (power spectral entropy, periodic sensitivity, lagged cross-correlation, etc.), leading to a pronounced accuracy decline under holidays, extreme weather events or rapid PV fluctuations.

To overcome the key limitations of conventional cooling/heating load identification—namely, insufficient characterisation of temperature-response lags and low feature dimensionality—this paper proposes a multi-feature fusion model[8-9], whose flowchart is illustrated in Fig. 1.

1) A dynamic thermal-response event detector is constructed. A sliding-window standard-deviation algorithm is employed to capture abrupt temperature events, while Pearson correlation verifies the spatio-temporal consistency of the load response, extracting lagged features that couple temperature and power.

2) A high-dimensional feature set is designed. Load spectral entropy, periodic sensitivity indices and multi-lag cross-correlations are introduced, expanding the feature space from the traditional 3–5 dimensions to over 30, markedly enhancing model expressiveness.

3) An improved LightGBM classifier is proposed. SMOTE is used to oversample cooling and heating loads to 80 % of the normal-load size, addressing class imbalance; principal-component analysis retains components that cumulatively explain ⩾95 % of the variance, mitigating overfitting risk.

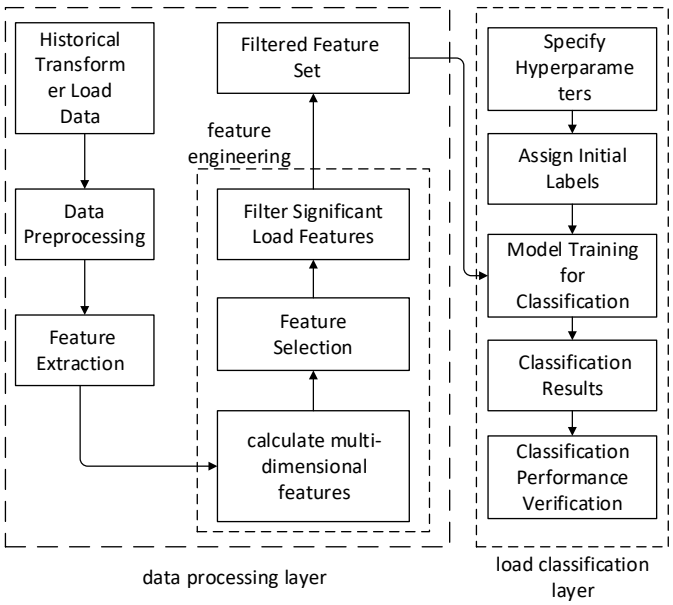


Fig. 1. Technology Roadmap Flowchart

II. METHODOLOGY

A. LightGBM

LightGBM is an improved variant of the Gradient Boosting Decision Tree (GBDT) algorithm that learns through an ensemble of decision trees. The core idea of GBDT is to iteratively construct a sequence of weak learners (typically shallow decision trees), with each new tree aiming to reduce the residual error left by its predecessors. By cumulatively adding these trees, the overall prediction error is progressively minimized, yielding an accurate predictive model.

Traditional GBDT usually adopts a level-wise growth strategy: all nodes at the same depth are expanded simultaneously until a pre-set maximum depth is reached. While straightforward, this approach often wastes computational resources on nodes that contribute little to model improvement, especially when the dataset is large. As illustrated in Fig. 2, this can lead to inefficiency.

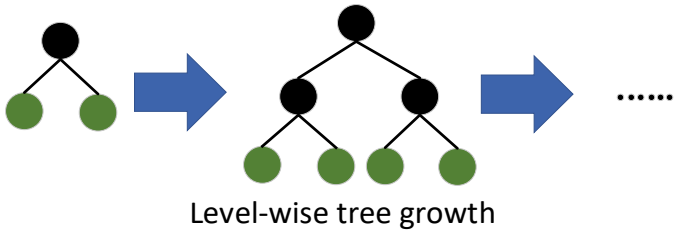


Fig. 2. Traditional GBDT hierarchical growth

LightGBM, by contrast, employs a leaf-wise growth strategy: at each step, only the leaf node with the largest gain is selected for further splitting. This selective expansion significantly reduces training time because it focuses computational effort on the most informative branches. This process is depicted in Fig.3.

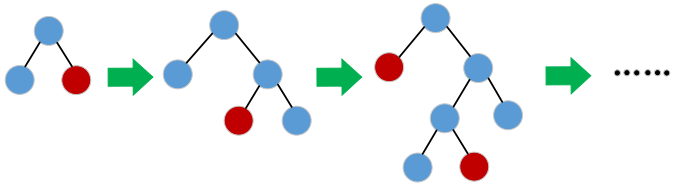


Fig. 3. LightGBM Leaf Growth Strategy

LightGBM introduces a histogram-based algorithm to accelerate feature-splitting computations. Continuous feature values are discretized into a predefined number of bins, each representing a sub-range of the original domain. During training, gain evaluations are performed solely at the bin level, markedly reducing computational complexity and accelerating convergence. Additionally, by storing bin-wise statistics instead of individual sample values, the histogram technique further decreases memory consumption.

Cooling/heating-load identification is fundamentally a binary-classification task that requires extracting distinctive electrical signatures of temperature-controlled appliances from high-dimensional data. Conventional logistic regression or support-vector machines are constrained by either linearity assumptions or prohibitive computational costs in high-dimensional spaces, making it difficult to capture the dynamic, non-linear couplings among temperature, season, time-of-day and load characteristics. Leveraging the gradient-boosted decision-tree framework, LightGBM refines both tree-growth strategies and feature-interaction mechanisms, thereby enabling automatic discovery of key discriminative patterns.

Real-world cooling/heating datasets are typically characterized by severe class imbalance, with non-thermal loads accounting for more than 70 % of samples. LightGBM addresses this issue by integrating Gradient-based One-Side Sampling (GOSS) with adaptive weight adjustment. GOSS retains high-gradient samples while randomly downsampling low-gradient instances, thereby concentrating learning capacity on temperature-sensitive segments.

At the feature-engineering level, LightGBM's Exclusive Feature Bundling (EFB) technique offers an innovative solution for handling high-dimensional, multi-scale time-series data. By intelligently bundling mutually exclusive features, EFB preserves the temporal dependencies between temperature and demand while compressing the feature space by more than 40 %.

The objective function of LightGBM is specifically tailored for classification tasks, adopting log loss as the central optimisation criterion. Its mathematical expression is,

$$L(y,p) = -\frac{1}{N}\sum_{i=1}^{N}\left[y_i \log p_i + (1-y_i)\log(1-p_i)\right] \tag{1}$$

where p_i denotes the predicted probability that sample i belongs to the cooling/heating load class, and y_i is the corresponding true label. By approximating the loss function via second-order Taylor expansion, the model computes the optimal weight for each leaf node in every boosting iteration as,

$$\begin{aligned} &\omega_j^* = \frac{\sum_{i\in I_j} g_i}{\sum_{i\in I_j} h_i + \lambda} \\ &\begin{cases} g_i = p_i - y_i \\ h_i = p_i(1-p_i) \end{cases} \end{aligned} \tag{2}$$

where g_i and h_i denote the first- and second-order gradients, respectively. This optimisation procedure yields a more accurate calibration of the model's classification confidence.

B. SMOTE

SMOTE (Synthetic Minority Over-sampling Technique) is an algorithm that mitigates class imbalance by interpolating between each minority-class sample and its nearest neighbors to synthesize new minority instances, thereby enlarging the minority class and rebalancing the training set. In real-world power grids, where cooling/heating-load samples are far scarcer than normal-load ones, SMOTE generates additional cooling/heating instances, preventing models like LightGBM from biasing toward the majority class and thus improving the detection accuracy of temperature-sensitive loads.

C. Feature extraction

1) Dynamic Thermal-Response Event Detection Module,

Abrupt temperature events are captured via a sliding-window standard-deviation algorithm, and load-response characteristics are validated with the Pearson correlation coefficient to screen effective event features.

For temperature-mutation detection, a three-hour sliding window is adopted, within which the standard deviation of temperature is computed as follows,

$$\sigma_T = \sqrt{\frac{1}{N}\sum_{i=1}^{N}(T_i - \overline{T})^2} \tag{3}$$

where N denotes the number of data points within the 3-hour window, T_i represents the temperature sample at the i-th time step, and $\overline{T}$ signifies the mean temperature of the window.

2) Multidimensional Feature-Engineering Module,

A comprehensive feature set—encompassing load spectral entropy, temporal-period sensitivity, and lagged cross-correlation coefficients—is proposed to fully quantify load-fluctuation patterns and their temperature dependencies.

First, the time series is segmented: the load data are partitioned day-wise, yielding a 24-point daily sequence. Subsequently, an improved approximate entropy is computed with pattern dimension m=3 and tolerance coefficient r=0.15* σ_p ,where σ_p denotes the daily load standard deviation,he calculation formula is given by follows,

$$ApEn(m,r) = \phi^{m}(r) - \phi^{m+1}(r) \tag{4}$$

where $\phi^{m}(r)$ denotes the logarithmic mean of the pattern-wise similarity probabilities within the m-dimensional embedding space.

The temporal-sensitivity feature is defined as follows: Night-time Load Ratio,

$$R_{night} = \frac{\text{Average Night-time Load (22:00–6:00)}}{\text{Average Day-time Load (6:00–22:00)}} \tag{5}$$

Temperature-Difference Sensitivity,

$$S_{\Delta T} = \frac{\Delta P}{\Delta T}(\Delta T \geq 1^{\circ}C) \tag{6}$$

Lagged-Correlation Coefficient Calculation Procedure,

Lag-time Selection: Lag windows of 2 h, 4 h, and 6 h were evaluated. Experiments show that a 2-hour lag best captures air-conditioning load response, whereas a 4-hour lag optimally reflects electric-heating load response. The feature value is selected as the maximum absolute lagged correlation coefficient, computed as follows,

$$r_{lag} = \max(|r_2|,|r_4|) \times sign(r_{\max}) \tag{7}$$

III. CASE ANALYSIS

A. Data Sources & Acquisition

The study covers 300 residential users located in a district of Shanghai. Load data comprise 24-hourly whole-day active-power readings and rated capacities for each user. Meteorological data were evaluated across multiple Shanghai

coordinates; the deviations remained within acceptable limits. Consequently, all weather inputs are taken from the Shanghai Hongqiao International Airport station (121.336°E, 31.198°N), situated at the city's geographic center.

B. Data Pre-processing

Upon initial inspection of the load data, certain days within the historical load sequences for some distribution transformers were found to contain missing values. To restore completeness to these historical load series, this project employs polynomial interpolation to smoothly fill the gaps. The polynomial interpolation formula is expressed as follows,

$$L_{\mathrm{n}}(x) = a_0 + a_1 x + a_2 x^2 + \ldots + a_n x^n \tag{8}$$

Where $L_{\mathrm{n}}(x)$ represents the unique polynomial determined by the distinct sample points, and $a_0, a_1 \ldots a_n$ are its coefficients.

C. LightGBM Classification Performance Validation

A LightGBM classifier was built on multidimensional features and systematically evaluated for its ability to identify three classes—"normal load," "heating load," and "cooling load"—using three key metrics: Precision, Recall, and F1-score.The evaluation metrics are calculated as follows.

(1) Precision,

$$P_K = \frac{TP_k}{TP_k + \sum_{j \neq k} FP_j} \tag{9}$$

(2) Recall,

$$R_{\mathrm{k}} = \frac{TP_k}{TP_k + \sum_{j \neq k} FN_j} \tag{10}$$

(3) F1-score,

$$F1 - Score = 2 \times \frac{R_{\mathrm{k}} \times P_K}{R_{\mathrm{k}} + P_K} \tag{11}$$

Where TP_k denotes the number of class k samples correctly classified as class k; TP_k denotes the number of samples not belonging to class k that are incorrectly classified as class k; FN_{k} denotes the number of samples of class k that are incorrectly assigned to any other class.

The resulting three metrics for each load class are summarized in Table 1.

TABLE I. CLASSIFICATION PERFORMANCE METRICS BY LOAD TYPE

Load Type	Precision	Recall	F1-Score
Ordinary Load	0.89	0.91	0.90
Heating Load	0.85	0.83	0.84
Cooling Load	0.87	0.86	0.87

As shown, the LightGBM classifier achieves a notably high recall for heating-load detection, indicating strong sensitivity to the characteristics of heating devices. Cooling-load identification, on the other hand, demonstrates favorable precision.

Overall, the model attains an overall accuracy of 87 % on the 100 test samples. Most misclassifications occur between cooling loads and the other two categories, likely because cooling loads overlap in feature space with transition-season ordinary loads or with low-power heating loads.

D. Comparative Experimental Validation

To demonstrate the superiority of LightGBM, we conducted a multi-model comparative experiment on the same Fisher-feature inputs, using 300 residential load-classification samples. LightGBM was benchmarked against two mainstream classifiers—Random Forest and XGBoost—across three quantitative dimensions: Precision, overall F1-score, and training efficiency. The comprehensive performance comparison is presented in Table 2.

TABLE II. PERFORMANCE COMPARISON ACROSS DIFFERENT ALGORITHMS

Algorithm	P_{k}	F1-Score	Training Time
LightGBM	93.2	92.8	1.4
XGBoost	91.5	91.2	4.3
RF	89.7	89.4	6.1
SVM	90.5	90.1	6.3

IV. CONCLUSION

This paper proposes a cold- and warm-load identification method based on the LightGBM model. The main conclusions are as follows:

1) By leveraging LightGBM and feature engineering, a user-load discrimination model that incorporates multiple features is developed to determine whether a load belongs to the cold- or warm-load category.

2) Load data from the coastal regions of East China were used to evaluate the model's performance. Comparative results show that the proposed model outperforms all benchmark models, delivering the best performance for cold- and warm-load identification.

In summary, the proposed LightGBM-based cold- and warm-load identification method markedly surpasses existing benchmarks in both accuracy and robustness, offering a reliable technical foundation for refined demand response, energy-efficiency management, and load regulation in distribution networks. Future work will expand the sample size, incorporate additional meteorological and behavioral features, and investigate transfer-learning strategies to further enhance the model's generalization capability and practical value across diverse regions and extreme scenarios.

ACKNOWLEDGMENT

This work was supported by Science and Technology Project of State Grid Corporation of China (Grant Number: B3094025000U).

REFERENCES

[1] Xue Jingrun, Shi Xiaohan, Cao Yongji, et al. A short-term fine-grained production-simulation method and system for virtual power plants [J]. Proceedings of the CSEE, 2023, 43(09): 3366-3381..

[2] Li Zhaoyu, Ai Qian, Zhang Yufan, et al. A review of data-driven technologies in virtual power plants [J]. Power System Technology, 2020, 44(07): 2411-2419..

[3] Ma Lin, Liang Anqi, Wang Liyong, et al. A survey on controllable load-resource regulation technologies for public buildings [J]. Electrical Measurement & Instrumentation, 2023, 60(05): 1-10+22.

[4] Ai Xin, Zhao Yuequn, Zhou Shupeng. Research on virtual energy-storage characteristics of air-conditioning loads under direct load control [J]. Proceedings of the CSEE, 2016, 36(06): 1596-1603.

[5] Tang Jun, Gao Hongchao, Yu Tao, et al. Construction concepts and innovative practices of virtual power plants in megacities under electricity-market environments [J]. Power System Technology, 2025, 49(01): 103-112.

[6] Wang Xuanyuan, Liu Zhen. Development and practice of virtual power plants participating in grid regulation and market operation [J]. Automation of Electric Power Systems, 2022, 46(18): 158-168.

[7] Zhong Yongjie, Tang Chengjun, Wang Zidong, et al. Development evolution, key technologies, and challenges of virtual power plants in China [J]. Zhejiang Electric Power, 2025, 44(02): 13-31.

[8] Wu Qiong, Li Ronglin, Hong Haisheng, et al. Low-voltage trip prediction of distribution transformers based on hybrid resampling and LightGBM algorithm [J]. Power System Protection and Control, 2021, 49(12): 71-78.

[9] Yin Baiqiang, Chen Qibin, Li Bing, et al. A new method for power-quality disturbance recognition and classification based on improved Kaiser-window fast S-transform and LightGBM [J]. Proceedings of the CSEE, 2021, 41(24): 8372-8384.

Distributed Energy Dispatch for Energy Community Using Decision-oriented Net-load Prediction

Yibo Ding
Department of Electrical and Electronic Engineering, Research Institute of Smart Energy
The Hong Kong Polytechnic University
Hong Kong, China
yibo0712.ding@connect.polyu.hk

Jian Zhao
College of Electrical Engineering, Shanghai University of Electric Power
Shanghai, China
zhaojianee@foxmail.com

Jiaqi Ruan
Department of Electrical and Electronic Engineering, The Hong Kong Polytechnic University
Hong Kong, China
jiaqi.ruan@polyu.edu.hk

Zhao Xu*
Department of Electrical and Electronic Engineering, Shenzhen Research Institute, Research Institute of Smart Energy, The Hong Kong Polytechnic University
Hong Kong, China
eezhaoxu@polyu.edu.hk
*Corresponding author

***Abstract*—This paper focuses on distributed energy dispatch under uncertainties for an energy community. To effectively handle these uncertainties, a decision-oriented predict-then-optimize framework is employed, achieving statistically lower operation costs compared to traditional accuracy-oriented predict-then-optimize approaches. Furthermore, peer-to-peer energy sharing among agents is specially considered to promote renewable energy consumption. Dual consensus alternating direction method of multipliers is employed to solve the distributed energy dispatch problem. Simulation results over extensive scenarios have demonstrated the effectiveness of the proposed methodology.**

Keywords—Energy Dispatch, Decision Regret, Peer-to-peer Energy Sharing

I. INTRODUCTION

the ongoing transition towards clean and low-carbon energy systems [1], the widespread integration of renewable energy sources (RES) has emerged as a critical concern. This necessitates the utilization of various flexibility resources within energy communities to facilitate effective local consumption of renewable energy. With advancements in infrastructure and technologies [2], peer-to-peer (P2P) energy sharing among agents has become a promising approach to achieve this goal [3].

However, the inherent uncertainties in RES generation and flexible loads pose significant challenges to power system operation, necessitating reliable prediction before optimizing energy dispatch strategies. Most existing works adopt a two-stage approach, first performing accuracy-oriented prediction and subsequently conducting energy dispatch based on the forecasted values [4]. Nevertheless, for many decision-making problems, predictions optimized solely for accuracy do not necessarily lead to optimal decision outcomes [5]. This is because the mapping from prediction error to decision regret can be asymmetric, non-linear, and even non-monotonic, which is determined by the optimization problem structure. Therefore, to ensure the prediction model is tailored to the optimization oracle of downstream optimization problem, rather than mere data-fitting, it is imperative to employ a decision-oriented predict-then-optimize (DPTO) framework.

The idea of DPTO has already seen several successful applications in energy management problems within power systems. Ref. [6] integrates decision-oriented prediction of RES output into the unit commitment problem, achieving lower operation costs. Adopting the same principle, Ref. [7] significantly reduced total costs in electricity market operations, while Ref. [8] utilized this concept for electricity price forecasting to devise better arbitrage strategies for energy storage systems. More recently, Ref. [9] extended this idea to distributed optimization problems, achieving lower costs in a local energy community compared to the traditional accuracy-oriented predict-then-optimize (APTO) framework. However, Ref. [10] focused exclusively on forecasting RES output. For decision-makers in an energy community, the flexible loads also present significant uncertainties. It is therefore necessary to further extend this work to a decision-oriented net-load predict-then-optimize framework to enhance the generalizability of the distributed energy dispatch strategies.

In this paper, we apply the DPTO framework to the day-ahead energy dispatch problem for an energy community to achieve lower operation costs. P2P energy sharing among agents is incorporated, which is solved using distributed optimization algorithm. Specifically, the dual consensus alternating direction method of multipliers (DC-ADMM) is employed in this work, demonstrating reliable convergence performance through extensive simulation scenarios.

The rest of this paper is organized as follows: Section II models the distributed energy dispatch problem. In Section III, the distributed algorithm is introduced. Section IV shows

979-8-3315-5472-9/25/$31.00 ©2025 IEEE

simulation results. Conclusions and potential directions for future research are discussed in Section V.

II. Problem Formulation

The decision-making process is summarized and compared in Fig. 1. Under the utilized DPTO framework, perfect decision over historical scenarios is carried out to obtain target values for prediction model training before each dispatch day, where uncertain parameters are all available. Then, the prediction modeled is trained by solving a regret minimization problem. In each dispatch day, day-ahead energy dispatch based on predicted value and intraday redispatch based on realized value are optimized sequentially. Given that, the prediction errors could be fully compensated after intraday stage, the decision performance is then evaluated as the sum of operation cost in day-ahead and intraday stages. Detailed problems are modeled in the following subsections.

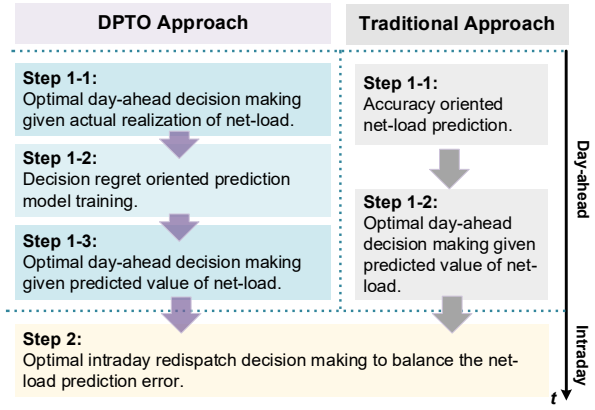


Fig. 1. Decision Making Process Comparison.

A. Day-ahead Scheduling Problem

The objective for the day-ahead energy dispatch problem (P1) is to minimize the operation cost of all agents, composed by the trading cost of energy and reserve capacities with upstream utility grid [10], P2P trading cost, generation cost and energy storage system (ESS) operation cost. Let $\mathcal{N} := 1,2,...,N$ denotes the set of smart agents in an energy community; $\mathcal{N}_i$ is the set of neighbors of agent i. The day-ahead dispatch time interval $\mathcal{T}$ is set as 1-hour. Agents with local generation, ESS and the others are categorized by the set $\mathcal{N}_\mathcal{G}$, $\mathcal{N}_\mathcal{E}$ and $\mathcal{N}_\mathcal{C}$, all serve as subsets of $\mathcal{N}$.

$$\begin{aligned}(\text{P1}) \quad \min \quad F^{\mathrm{D}} = &\sum_{i\in\mathcal{N}}\sum_{t\in\mathcal{T}}[\gamma_t^{\mathrm{b}}P_{i,t}^{\mathrm{b}} - \gamma_t^{\mathrm{s}}P_{i,t}^{\mathrm{s}} + \gamma^{+}R_{i,t}^{+} \\ &+ \gamma^{-}R_{i,t}^{-} + \sum_{j\in\mathcal{N}_i}(p_{ij,t}\cdot\gamma_{ij,t})] + \sum_{i\in\mathcal{N}_\mathcal{G}}\sum_{t\in\mathcal{T}}\gamma_i^{\mathrm{g}}P_{i,t}^{\mathrm{G}} \\ &+ \sum_{i\in\mathcal{N}_\mathcal{E}}\sum_{t\in\mathcal{T}}\gamma_i^{\mathrm{c}}P_i^{\mathrm{c}} + \gamma_i^{\mathrm{d}}P_i^{\mathrm{d}}\end{aligned} \tag{1}$$

$$0 \le P_{i,t}^{\mathrm{b}} \le P_i^{\mathrm{tr}}, 0 \le P_{i,t}^{\mathrm{s}} \le P_i^{\mathrm{tr}}, \forall i, \forall t \tag{2}$$

$$R_{i,t}^{+} \ge \eta_i^{+}\hat{P}_{i,t}^{L}, R_{i,t}^{-} \ge \eta_i^{-}\hat{P}_{i,t}^{\mathrm{L}}, \quad \forall i, \forall t \tag{3}$$

$$p_{ij,t} + p_{ji,t} = 0, \forall i, \forall j \in \mathcal{N}_i, \forall t \tag{4}$$

$$-p_{ij,t}^{\mathrm{tr}} \le p_{ij,t} \le p_{ij,t}^{\mathrm{tr}}, \forall i, \forall j \in \mathcal{N}_i, \forall t \tag{5}$$

$$\gamma_{ij,t} - \gamma_{ji,t} = 0, \forall i, \forall j \in \mathcal{N}_i, \forall t \tag{6}$$

$$0 \le P_{i,t}^{\mathrm{G}} \le \bar{P}_i^{\mathrm{G}}, \forall i \in \mathcal{N}_\mathcal{G}, \forall t \tag{7}$$

$$S_{i,t} = S_{i,t-1} + P_{i,t}^{\mathrm{c}}\eta_i^{\mathrm{c}} - P_{i,t}^{\mathrm{d}} / \eta_i^{\mathrm{d}}, \forall i \in \mathcal{N}_\mathcal{E}, \forall t \tag{8}$$

$$\bar{S}_i \le S_{i,t} \le \underline{S}_i, \forall i \in \mathcal{N}_\mathcal{E}, \forall t \tag{9}$$

$$0 \le P_{i,t}^{\mathrm{c}} \le \bar{P}_i^{\mathrm{c}}, 0 \le P_{i,t}^{\mathrm{d}} \le \bar{P}_i^{\mathrm{d}}, \quad \forall i \in \mathcal{N}_\mathcal{E}, \forall t \tag{10}$$

$$P_{i,t}^{\mathrm{c}}P_{i,t}^{\mathrm{d}} = 0, \quad \forall i \in \mathcal{N}_\mathcal{E}, \forall t \tag{11}$$

$$\begin{cases} P_{i,t}^{\mathrm{b}} - P_{i,t}^{\mathrm{s}} + \sum_{j\in\mathcal{N}_i} p_{ij,t} = \hat{P}_{i,t}^{\mathrm{L}}, & \forall i \in \mathcal{N}_\mathcal{C}, \forall t \\ P_{i,t}^{\mathrm{b}} - P_{i,t}^{\mathrm{s}} + \sum_{j\in\mathcal{N}_i} p_{ij,t} + P_{i,t}^{\mathrm{G}} = \hat{P}_{i,t}^{\mathrm{L}}, & \forall i \in \mathcal{N}_\mathcal{G}, \forall t \\ P_{i,t}^{\mathrm{b}} - P_{i,t}^{\mathrm{s}} + \sum_{j\in\mathcal{N}_i} p_{ij,t} + P_{i,t}^{\mathrm{d}} - P_{i,t}^{\mathrm{c}} = \hat{P}_{i,t}^{\mathrm{L}}, & \forall i \in \mathcal{N}_\mathcal{E}, \forall t \end{cases} \tag{12}$$

where $P_{i,t}^{\mathrm{b}}$ and $P_{i,t}^{\mathrm{s}}$ are the power purchased from and sold to the upstream utility grid, P_i^{tr} is the corresponding transmission limit. γ_t^{b} and γ_t^{s} are the time-of-use and feed-in-tariff electricity price. Since there exists no large-scale generators providing reserve capacities [9], each agent could purchase upward and downward reserve capacities, $R_{i,t}^{+}$ and $R_{i,t}^{-}$, from the utility grid to hedge against uncertainties in the day-ahead stage. γ^{+} and γ^{-} are the corresponding cost coefficients of reserve purchase. The requirements of reserve capacities are modeled in (3), indicating that the reserve capacities should cover certain proportion of predicted net load $\hat{P}_{i,t}^{\mathrm{L}}$, where η_i^{+}/η_i^{0} are the proportional coefficients of upward/downward reserves. (4)-(6) together model the P2P energy sharing consensus constraints between agent i and j on trading volume $p_{ij,t}$ and prices $\gamma_{ij,t}$. $p_{ij,t}^{\mathrm{tr}}$ is the P2P transaction limits. γ_i^{g} is the generation cost coefficient. (7) limits the distributed thermal generation range, where $\bar{P}_i^{\mathrm{G}}$ is the rated power output of generator i. The operational dynamics of ESS are modeled in (8)-(11). $S_{i,t}$ is the stored energy at t-th hour; $P_{i,t}^{\mathrm{c}}$ and $P_{i,t}^{\mathrm{d}}$ are the charging and discharging power at t-th hour, corresponding to the efficiency η_i^{c} and η_i^{d}, respectively. Specially, assume that charging/discharging would not simultaneously happen in one dispatch interval, (11) is integrated. Moreover, in order to guarantee sufficient power regulation capacities for the next day [3], it is advised to consider the following requirement: $S_{i,0} \le S_{i,|\mathcal{T}|}$. $\gamma_i^{\mathrm{c}}/\gamma_i^{\mathrm{d}}$ are the unit charging/discharging cost. The power balance constraint for different types of agents can be formulated in (12).

B. Prediction Model Training

Distinguished from existing mainstream approaches improving prediction accuracy, this paper focuses on training a prediction model that best fits the optimization oracle by minimizing the decision regret. As stated at the beginning of

this section, the decision maker needs to firstly obtain perfect decision results over |S| past scenarios. Then, by leveraging the computationally efficient prediction model, extreme learning machine (ELM), the training process could be carried out by solving a mix-integer linear programming problem, which minimizes the distance from perfect decision, as modeled in (P2).

$$\text{(P2)}\ \min \sum_{i\in\mathcal{N}}\sum_{s\in\mathcal{S}}\left| F^{\mathrm{D}}(\hat{P}^{\mathrm{L}}_{i,s}) - F^{\mathrm{D},\star}\right| + \lambda \,||\, W \,||_1 \quad (13)$$

s.t. (2)-(12),

$$\hat{P}^{\mathrm{L}}_{i,s} = \left[W_{i,1},\cdots,W_{i,H}\right]^{\top}\begin{bmatrix}\phi(w^{\top}_{i,1}\ f_{i,s} + \ b^{\top}_{i,1})\\ \vdots \\ \phi(w^{\top}_{i,H}\ f_{i,s} + \ b^{\top}_{i,H})\end{bmatrix} \quad (14)$$

$$(1-\theta)P^{\mathrm{L}}_{i,s} \le \hat{P}^{\mathrm{L}}_{i,s} \le (1+\theta)P^{\mathrm{L}}_{i,s} \quad (15)$$

The first term in the objective function is the decision regret under scenario s, measuring the distance between total operation costs under perfect and imperfect decision. The second term serves as a L1-norm based regularization term to refrain overfitting, where λ is a hyperparameter and vector W collects the weights from hidden layer to output layer. The ELM-based prediction model is modeled in (14). H is the number of hidden neurons of ELM. $\phi(\cdot)$ is the nonlinear activation function. $f_{i,s}$ are the input feature dataset for agent i under scenario s. $w_{i,\cdot}$ and $b_{i,\cdot}$ are respectively the randomly predefined input weight and bias vectors. Given the above features, ELM actually constructs a linear mapping from input feature to output predicted net-load, which could be easily integrated into optimization problem as linear constraints. As a result, the computational complexity has been significantly reduced comparing with deep neural networks based approaches that rely on back propagation. Since the same regret might corresponds to various values of the predicted parameters [5], (15) is specially introduced to constrain the prediction error within a physically acceptable range, adjusted by the factor θ.

Solving (P2) yields to optimal output weight vector $W^{\star}$ of the prediction model, which theoretically leads to predicted net-load that better reduces the decision regret.

C. Intraday Redispatch Problem

Since the prediction error is almost unavoidable, redispatching in the intraday stage is necessary for decision makers to compensate the potential prediction error by utilizing the purchased reserve capacities at the day-ahead stage. Moreover, assume that, the P2P energy sharing contracts determined in the day-ahead stage must be strictly executed during the intraday stage [9], the redispatch problem could be optimized independently by each agent. Therefore, given the actual net-load realization P^{L}, the redispatch problem could be modeled as follows:

$$\text{(P3)}\quad \min \quad F^{\mathrm{I}} = \sum_{i\in\mathcal{N}}\sum_{t\in\mathcal{T}} \gamma^{\mathrm{cu}} P^{\mathrm{cu}}_{i,t} + \gamma^{\mathrm{sh}} P^{\mathrm{sh}}_{i,t} \quad (16)$$

$$\text{s.t.}\quad 0 \le r^{+}_{i,t} \le R^{+}_{i,t},\ 0 \le r^{0}_{i,t} \le R^{0}_{i,t}, \quad \forall i, \forall t \quad (17)$$

$$P^{\mathrm{slack}}_{i,t} = P^{\mathrm{L}}_{i,t} - \hat{P}^{\mathrm{L}}_{i,t}, \quad \forall i, \forall t \quad (18)$$

$$\begin{cases} P^{\mathrm{slack}}_{i,t} \le r^{+}_{i,t} + P^{\mathrm{sh}}_{i,t}, & \text{if } P^{\mathrm{slack}}_{i,t} \ge 0, \forall i, \forall t \\ P^{\mathrm{slack}}_{i,t} \ge -r^{0}_{i,t} - P^{\mathrm{ab}}_{i,t}, & \text{if } P^{\mathrm{slack}}_{i,t} < 0, \forall i, \forall t \end{cases} \quad (19)$$

$$P^{\mathrm{cu}}_{i,t} \ge 0,\ P^{\mathrm{sh}}_{i,t} \ge 0, \quad \forall i, \forall t \quad (20)$$

where $P^{\mathrm{cu}}_{i,t}$ and $P^{\mathrm{sh}}_{i,t}$ are respectively the renewable curtailment and load shedding of agent i at time t. γ^{cu} and γ^{sh} are the corresponding penalty coefficients. $r^{+}_{i,t}$ and $r^{0}_{i,t}$ are the deployed upward and downward reserve, bounded by $R^{+}_{i,t}$ and $R^{0}_{i,t}$, respectively. $P^{\mathrm{slack}}_{i,t}$ is the prediction error.

When the $P^{\mathrm{slack}}_{i,t}$ is positive, it signifies that the actual net-load is greater than the predicted value. This deficit is compensated by upward reserve capacities. If the upward reserve capacity is insufficient to cover the error, a high penalty for load shedding is incurred. Conversely, when the $P^{\mathrm{slack}}_{i,t}$ is negative, the actual net-load is less than the predicted value. Downward reserve capacity is then used to offset this error, and if the downward reserve capacity is exhausted, a penalty for renewable energy curtailment is triggered. The penalty for load shedding is considerably higher than that for curtailing renewable energy, namely $\gamma^{\mathrm{sh}} \ge \gamma^{\mathrm{cu}}$ [11].

III. Problem Solving

Noted that, in (1), the sum of P2P energy trading cost for the whole energy community equals to zero due to the sanctification of constraint (4), making the problem (P1) and (P2) computationally intractable under centralized solving framework. Therefore, utilizing decentralized optimization method is necessary. Specifically, the first step is to reformulate (P1) and (P2).

The term $\sum_i \sum_t \sum_j p_{ij,t} \cdot \gamma_{ij,t}$ could be rewritten in vector form as $\gamma_i^{\top} \Pi_i p_i$, where Π_i is a mapping matrix from edges to nodes [12]. By substituting the P2P energy trading cost term, (P1) and (P2) could be decomposed into |N| subproblems and then solved by respective agents.

In this work, distribute optimization problems (P1) and (P2) are solved using DC-ADMM [13], which is featured by the introduction of auxiliary variables during iteration compared with standard ADMM, rendering the algorithm more robust performance [3]. Let Θ_i .denote the objective function of agent *i*, Taking (P1) as an example, the updating steps in *k*-th iteration are demonstrated as follows:

$$\begin{aligned} X^{k}_{i} = \arg\min\ & \Theta_i - \tau \,||\, (\Pi_i p_i - z^{k}_{i}) / \rho \\ & + \sum\nolimits_{j\in\mathcal{N}_i} \gamma^{k-1}_{i} + \gamma^{k-1}_{j} \Big\|^2_2 \Big\} \end{aligned} \quad (21)$$

$$\gamma^{k}_{i} = 2\tau[\rho \sum_{j\in\mathcal{N}_i} \gamma^{k-1}_{i} + \gamma^{k-1}_{j} - \Pi_i p^{k}_{i} - z^{k}_{i}\Big] / \rho^2 \quad (22)$$

$$z_i^k = z_i^{k-1} + \rho \sum_{j \in \mathcal{N}_i} \gamma_i^{k-1} - \gamma_j^{k-1} \tag{23}$$

where X_i^k collects primary decision variables of agent i in (P1), while the P2P trading prices γ_i^k serve as dual variables of the constraint (4), z_i^k is the auxiliary variables collecting price information. $\tau = \rho / 4 |\mathcal{N}_i|$, ρ is the penalty factor.

During each iteration, each agent optimizes the dispatch problem in parallel, then updates the price estimation information, followed by the price estimation communication and auxiliary variables updating. The algorithm stops iteration when the sharing quantity and price together reach a predefined consensus. The operating principles of the DC-ADMM algorithm is summarized in Algorithm 1.

Algorithm 1 DC-ADMM for solving (P1) and (P2)

Initialization: $\forall i \in \mathcal{N}$, let $\boldsymbol{X}_i^0 = \mathbf{0}$, $\boldsymbol{\gamma}_i^0 = \mathbf{0}$, $\boldsymbol{z}_i^0 = \mathbf{0}$.
Set $k = 1$.
repeat
  for $\forall i \in \mathcal{N}, \forall j \in \mathcal{N}_i, \forall t \in \mathcal{T}$ (in parallel) **do**
    Update primal variables $\boldsymbol{X}_i^k$ locally according to (21);
    Update dual variables $\boldsymbol{\gamma}_i^k$ locally according to (22);
    Broadcast price estimation $\boldsymbol{\gamma}_i^k$ to neighbors $j \in \mathcal{N}_i$;
    Receive price estimation $\boldsymbol{\gamma}_j^k$ from neighbors $j \in \mathcal{N}_i$;
    Update auxiliary variables $\boldsymbol{z}_i^k$ according to (23);
  end for
  Set $k = k + 1$;
until energy sharing quantity and price reach consensus: $\|\boldsymbol{p}^k - \boldsymbol{p}^{k-1}\| \le \epsilon_1$, $\|\boldsymbol{\gamma}^k - \boldsymbol{\gamma}^{k-1}\| \le \epsilon_2$.

IV. Simulation Results

A. System Description

In this work, an energy community with four smart agents is considered, where each respective agent owns local distributed RES, acts as an energy consumer, has distributed thermal generation, and operates ESS. Using real-world load and residential photovoltaic (PV) generation data from Ausgrid [14], numerical simulations are conducted in 80 daily scenarios. For each dispatch day, the number of historical scenarios is selected as 3. The price for trading with the utility grid can refer to [3]. γ^+ and γ^0 are set as 0.2\$/kWh and 0.15\$/kWh, respectively. η_i^+ and η_i^0 are all set as 20\% to avoid load shedding and renewable energy curtailment γ_i^g and $\overline{P}_i^G$ are set as 0.25\$/kWh and 30kW. η^c and η^d of ESS are both set as 0.95, with rated power and capacity of 20kW and 50kWh, respectively. P_i^{tr} and p_i^{tr} are respectively set as 40kW and 20kW. γ_i^c and γ_i^d are both set as 0.05\$/kWh. θ is set as 30\%. All simulations are implemented via Gurobi on Matlab 2024b on a personal computer.

B. Decision Performance

To compare decision performance between DPTO method and conventional APTO method, this work demonstrates the average, median, standard deviation of decision regret, and mean absolute error (MAE), root mean square error (RMSE) of prediction error over these simulation scenarios. Results are presented in Table I and Figure 2.

According to Table 1, the DPTO framework achieves a statistically lower decision regret across the 80 scenarios, with mean, median, and standard deviation values of 12.808%, 12.921%, and 7.802%, respectively. In contrast, the corresponding results for the APTO framework are 24.689%, 23.589%, and 9.497\%. Furthermore, in terms of prediction accuracy, the DPTO method performs significantly worse than APTO, with its MAE and RMSE being 11.174 and 12.878 kW, respectively. In comparison, APTO demonstrates higher precision, with an MAE and RMSE of 3.080 and 3.421 kW.

TABLE I. Statistical Results of Regret and Prediction Error

Method	Regret (%)			Prediction Error	
	Mean	Median	Std	MAE	RMSE
DPTO	12.808	12.921	7.802	11.174	12.878
APTO	24.689	23.589	9.497	3.080	3.421

These experimental results clearly demonstrate that for certain decision-making problems, a more "accurate" prediction does not necessarily lead to a more "cost-effective" decision. In other words, prediction accuracy and decision optimality are not always aligned [15]. The DPTO framework employed in this study, by minimizing decision regret over historical scenarios, enables the prediction model to provide parameters that are better tailored to the optimization oracle. This, in turn, leads to statistically lower operation costs within the energy community. Figure 2 further corroborates these conclusions.

C. Energy Scheduling Results

Figure 2 illustrates the day-ahead dispatch strategies for four smart agents, derived using the DPTO method. The net load is decomposed into electrical load and local RES generation. It is evident that different agents experience their peak load periods at varying times. The price of electricity purchased from the grid is lower during the night and higher during the daytime (09:00–20:00). During the high-price periods, agents 2 and 3 fully utilize their local distributed generation. Notably, after satisfying its own demand, agent 3 sells its surplus power through P2P trading to generate profit. Meanwhile, agent 4 utilizes its energy storage system to absorb energy during low-price periods and releases it during the evening peak load, selling the energy to neighboring agents 1 and 3 via P2P trading to earn additional revenue. This demonstrates that the introduction of the P2P trading mechanism effectively leverages the flexibility of distributed resources.

D. Algorithm Convergence Performance

Figure 4 displays the residuals of primal and dual variables over iterations in solving (P1) in one scenario. The penalty parameter ρ is set to 1.5. After 319 iterations, the primal and dual residuals respectively drop to approximately 4e-2 and 1e-4, indicating that the DC-ADMM based distributed optimization algorithm has successfully converged.

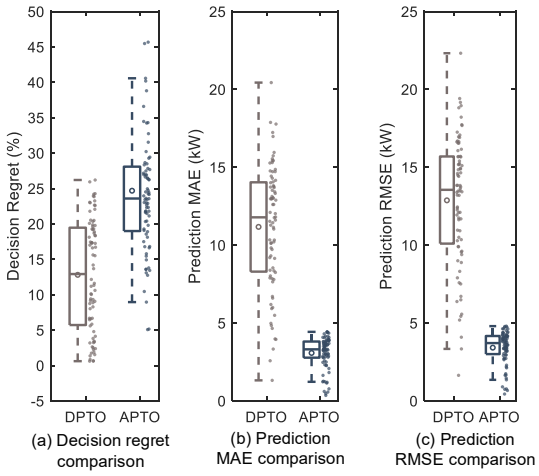


Fig. 2. Performance Comparison in Scatter Box Plot.

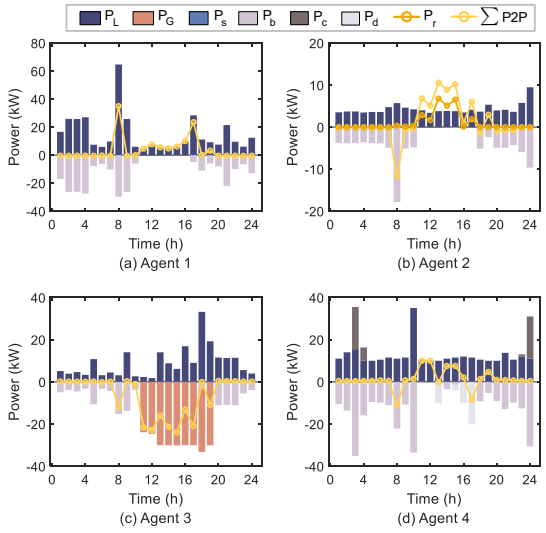


Fig. 3. Energy Dispatch Results on Typical Scenario.

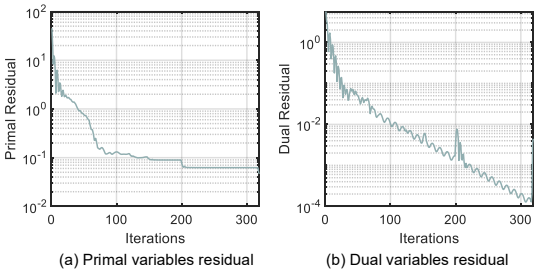


Fig. 4. Convergence Performance of DC-ADMM.

V. Conclusion

In conclusion, this paper presents a decision-oriented framework for the distributed energy dispatch problem under uncertainty. By shifting the focus from prediction accuracy to decision quality, the proposed DPTO methodology achieves statistically lower operation costs in an energy community compared to conventional methods. The work also integrates P2P energy sharing to enhance the utilization of renewable energy and system flexibility, solved with the DC-ADMM. Simulation results across 80 scenarios confirmed the efficiency and cost-saving potential of DPTO approach. Future research could extend this framework to larger systems, incorporate a wider array of flexibility resources, and investigate the impact of more complex P2P market mechanisms.

Acknowledgment

This work was supported in part by the National Natural Science Foundation of China under Grant 72331008 and Grant 72271211.

References

[1] J. Ruan, Z. Xu, and H. Su, "Towards interdisciplinary integration of electrical engineering and earth science," *Nature Reviews Electrical Engineering*, vol. 1, no. 5, pp. 278–279, 2024.

[2] Y. Wu, Y. Wu, H. Cimen, J. C. Vasquez, and J. M. Guerrero, "Towards collective energy community: Potential roles of microgrid and blockchain to go beyond p2p energy trading," *Applied Energy*, vol. 314, p. 119003, 2022.

[3] Y. Ding, X. Sun, J. Ruan, W. Shi, H. Wu, and Z. Xu, "Customized decentralized autonomous organization based optimal energy management for smart buildings," *Applied Energy*, vol. 376, p. 124223, 2024.

[4] Y. Wang, W. Dong, and Q. Yang, "Multi-stage optimal energy management of multi-energy microgrid in deregulated electricity markets," *Applied Energy*, vol. 310, p. 118528, 2022.

[5] A. N. Elmachtoub and P. Grigas, "Smart "predict, then optimize", *Management Science*, vol. 68, no. 1, pp. 9–26, 2022.

[6] X. Chen, Y. Liu, and L. Wu, "Towards Improving Unit Commitment Economics: An Add-On Tailor for Renewable Energy and Reserve Predictions," *IEEE Transactions on Sustainable Energy*, 2024.

[7] Y. Zhang, H. Wen, Y. Bian, and Y. Shi, "Improving sequential market coordination via value-oriented renewable energy forecasting," *arXiv preprint* arXiv:2405.09004, 2024.

[8] L. Sang, Y. Xu, H. Long, Q. Hu, and H. Sun, "Electricity price prediction for energy storage system arbitrage: A decision-focused approach," *IEEE Transactions on Smart Grid,* vol. 13, no. 4, pp. 2822–2832, 2022.

[9] Y. Ding, X. Sun, W. Shi, J. Ruan, J. Chen, Y. Zhao, and Z. Xu, "Optimal Distributed Energy Management for Local Energy Community: A Decision Regret Oriented Smart Predict and Optimize Approach," *IEEE Transactions on Industrial Informatics*, 2025.

[10] J. Zhao, C. Wan, Z. Xu, and K. P. Wong, "Spinning reserve requirement optimization considering integration of plug-in electric vehicles," *IEEE Transactions on Smart Grid*, vol. 8, no. 4, pp. 2009–2021, 2017.

[11] L. Yang, S. Chen, and Z. Dong, "Multi-period locally-facet-based MIP formulations for unit commitment problems," *IEEE Transactions on Power Systems,* vol. 38, no. 4, pp. 3733–3747, 2022.

[12] C. Lyu, Y. Jia, and Z. Xu, "Fully decentralized peer-to-peer energy sharing framework for smart buildings with local battery system and aggregated electric vehicles," *Applied Energy*, vol. 299, p. 117243, 2021.

[13] T.-H. Chang, M. Hong, and X. Wang, "Multi-agent distributed optimization via inexact consensus admm," *IEEE Transactions on Signal Processing*, vol. 63, no. 2, pp. 482–497, 2014.

[14] Ausgrid, "Electricity Usage Research." https://www.ausgrid.com.au/Industry/Our-Research/Data-to-share/Electricity-Research.

[15] H. Zhang, R. Li, Q. Du, J. Tao, S. Pineda, G. Kariniotakis, S. Camal, C. B. Monroc, M. Sun, C. Wan, et al., "Decision-focused learning for power system decision-making under uncertainty," *IEEE Transactions on Power Systems*, 2025.

Proportional-Integral-and-Data-Driven Load Frequency Controller for Microgrid Systems

Weichao Wang, Ronghu Chi, Yang Liu
College of Automation and Electronic Engineering
Qingdao University of Science and Technology
Qingdao, China
ronghu_chi@qust.edu.cn

***Abstract*—This paper proposes a novel proportional-integral-and-data-driven control (PIDDC) for microgrid (MG) frequency regulation. The PIDDC combines a proportional-integral (PI) control loop for rapid dynamic response to the frequency fluctuations and a data-driven model free adaptive control (MFAC) loop to enhance robustness against unmodeled system uncertainties by leveraging real-time input/output data from the MG system. Therefore, the synergistic integration of two loops ensures high robustness and adaptive capability, enabling effective mitigation of frequency fluctuations. To validate its effectiveness, the proposed PIDDC is implemented in an MG system considering wind turbine power, photovoltaic, and disturbances. Simulation results demonstrate that the proposed PIDDC can effectively maintain the MG frequency deviations within the desired range, which is superior to other methods.**

Keywords—microgrid frequency control, model free adaptive control, proportional integral control, renewable energy source

I. INTRODUCTION

The high penetration of stochastic renewable energy sources (RESs) such as photovoltaic (PV) and wind turbines (WT) significantly affects the microgrid (MG) stability, particularly the frequency stability [1]. To keep the MG frequency within acceptable limits, the load frequency controller must have high robustness, fast response speed and accurate control precision.

Recently, model predictive control, sliding mode control, H∞ control and other control theories have been widely used in the design of load frequency controller [2]-[4]. These methods rely heavily on precise model knowledge of the controlled system, and their performance is highly sensitive to the accuracy of the model. In practice, the actual MG systems exhibit high uncertainty and nonlinearity due to multi power energy coupling between regional grid and equipment, complex network topology and diversified electric loads. These factors render the establishment of an accurate mathematical model for MG systems highly challenging. Therefore, the frequency control performance of the model-based methods may be reduced when faced with the unmodeled uncertainties of the MG systems.

Fortunately, data driven control (DDC) does not need the model information except for the input/output (I/O) data of the system, which has attracted the attention of many researchers [5]. Proportional integral derivative (PID) as a kind of DDC has been widely adopted for the design of the load frequency controllers. The PID can offer the rapid frequency response speed, but its inherent lack of adaptability has prompted researchers to explore optimization algorithms such as ant colony optimization, grey wolf optimization, and sine-cosine algorithm [6]-[8] as well as artificial intelligence techniques, including neural network learning and fuzzy logic [9]-[10] to improve its flexibility. Although the application of optimization algorithms and fuzzy logic method can significantly improve the control performance, the computationally intensive parameter optimization incurs excessive latency, rendering it inadequate for satisfying the stringent real-time constraints of the frequency control in the MG systems.

More recently, model free adaptive control (MFAC) scheme incorporates an adaptive mechanism only utilizing the I/O data, enabling it to better address the target tracking problems in the nonlinear systems [11]. In [12], a MFAC-based control strategy is proposed to address the frequency fluctuations of multi-MG interconnected power system. In [13], a MFAC scheme combines with a multistep predictive algorithm is proposed to address the power system frequency issues under jamming attacks. Noting that these MFAC-based frequency control methods are effectively used to address the unmodeled uncertainties to achieve the frequency stability.

Therefore, this paper propose a novel proportional-integral-and-data-driven control (PIDDC) for the MG frequency regulation. The proposed PIDDC integrates a PI loop to rapidly handle dynamic frequency changes and a data-driven MFAC loop to enhance robustness in dealing with unmodeled uncertainties through real-time I/O data of the MG system. In the MFAC loop, a general nonlinear autoregressive moving average model with exogenous inputs (NARMAX) function is designed to represent the relationship among the I/O and disturbance. Then, a dynamic linear data model (dLDM) with a pseudo partial derivative (PPD) is developed to reformulate the designed NARMAX. Finally, a MG system with high penetration of RESs is simulated to evaluate the performance of the proposed PIDDC. The results show that the proposed PIDDC can cope with the frequency fluctuation effectively, which is superior to the other methods.

This paper is organized as follows. Section II presents the problem formulation. Section III designs the proportional-integral-and-data-driven control. Section IV gives simulation results with discussion. Section V concludes this paper.

This work was supported in part by the National Natural Science Foundation of China (62373208, 62273192), the Taishan Scholar program of Shandong Province of China (tsqn202306218), the Talent Introduction and Cultivation Plan for Youth Innovation of Universities in Shandong Province, and the Natural Science Foundation of Shandong Province of China (ZR2024YQ032). (Corresponding author: Ronghu Chi.)

979-8-3315-5472-9/25/$31.00 ©2025 IEEE

II. Problem Formulation

The MG system frequency dynamic response model is given in Fig. 1, which is used to represent the actual MG dynamic. It includes battery energy storage system (BESS), diesel engine generators (DEG), PV, WT, and electric loads. However, due to uncertain factors such as weather conditions in the actual MG system, the first-order linearized frequency response model in Fig. 1 is difficult to fully express the actual system dynamics. Meanwhile, the diversified electric loads also further increases the uncertainties of the MG system and brings difficulties to the frequency control.

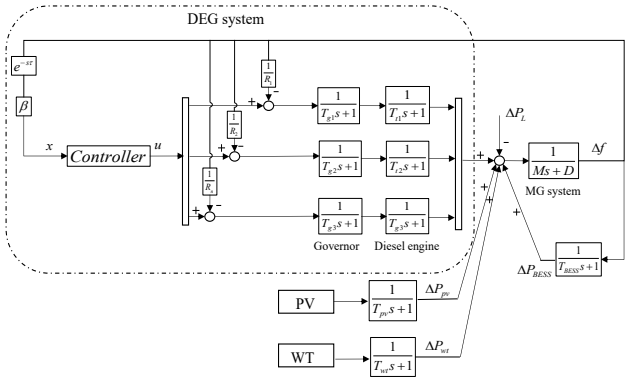


Fig. 1. MG system.

Therefore, the main purpose of this paper is to design a proportional-integral-and-data-driven control for the MG system frequency regulation, i.e., a PI loop is used to realize the fast processing of dynamic frequency changes, an additional MFAC loop is used to address the unmodeled uncertainties from the stochastic electric loads and RESs. The two control loops are complementary to each other. Thus, the total frequency control signal form the two control loops, the first one comes from MFAC loop, denoted as u_{MFAC} and second one comes from the PI loop, denoted as u_{PI}. Therefore, the total MG frequency control signal *u* can be obtained

$$u(k) = u_{MFAC}(k) + u_{PI}(k) \tag{1}$$

where *k* is sampling moment.

III. Proportional-Integral-and-Data-Driven Control

Fig. 2 illustrates the structure of the proposed PIDDC method. The followings provide detailed designs of the two control loops.

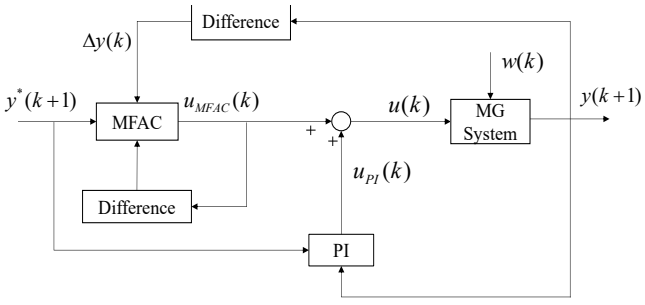


Fig. 2. Overview of PIDDC.

A. Design of the PI Loop

To cope with the rapid change of the system frequency, a PI control loop is used to realize the fast dynamic response, and its algorithm is as follows,

$$u_{PI}(k) = \left(K_P + \frac{K_I}{s} \right) e(k) \tag{2}$$

where K_P is proportional gain, K_I is integral gain; y^* is reference value; y is the MG system output; $e(k) = y^* - y(k)$ is MG system output frequency error.

B. Design of the MFAC Loop

As illustrated in Fig. 2, one can see that the frequency dynamic output of the MG is influenced by the PI loop input (u_{PI}), the MFAC loop input (u_{MFAC}) and load disturbance (*w*). Thus, the complex relationship must be ideally represented as a generalized nonlinear nonaffine NARMAX function

$$y(k+1) = f(\boldsymbol{y}^T(k), \boldsymbol{u}_{PI}^T(k), \boldsymbol{u}_{MFAC}^T(k), \boldsymbol{w}^T(k)) \tag{3}$$

where

$$\boldsymbol{y}(k) = \left[y(k), \cdots, y(k-n_y) \right]^T \in R^{n_y+1},$$
$$\boldsymbol{u}_{PI}(k) = \left[u_{PI}(k), \cdots, u_{PI}(k-n_u) \right]^T \in R^{n_u+1},$$
$$\boldsymbol{u}_{MFAC}(k) = \left[u_{MFAC}(k), \cdots, u_{MFAC}(k-n_u) \right]^T \in R^{n_u+1},$$
$$\boldsymbol{w}(k) = \left[w(k), \cdots, w(k-n_w) \right]^T \in R^{n_w+1};$$

n_y, n_u and n_w are proper constant system orders; $f(\cdot)$ is nonlinear function and $f(0,0,0) = 0$.

Assumption 1 [11]: The partial derivatives of $f(\cdot)$ with respect to its variables exist and are continuous.

Assumption 2 [11]: The nonlinear function $f(\cdot)$ satisfies generalized Lipschitz condition, that is,

$$\begin{aligned} &\left| f(x_1(k_1), \cdots, x_i(k_1)) - f(x_2(k_2), \cdots, x_i(k_2)) \right| \\ &\qquad \le b_i \left| x_i(k_1) - x_i(k_2) \right| \end{aligned} \tag{4}$$

where $i \in Z_+$; x_i is the *i*-th argument of $f(\cdot)$; $b_i > 0$ is constant.

Theorem 1: For nonlinear function $f(\cdot)$ satisfying Assumptions 1 and 2, if $\left| x_i(k_1) - x_i(k_2) \right| \neq 0$, there must exist a pseudo partial derivative (PPD) such that (3) can be transferred as a dynamic linearization data model (dLDM)

$$\Delta y(k+1) = \phi_c(k) u_{MFAC}(k) \tag{5}$$

and $\left| \phi_c(k) \right| \le b_i$. The proof is given in Appendix.

Based on the dLDM (5), we can obtain the control law and the PPD estimation law [11], as (6)-(8)

$$u_{MFAC}(k) = u_{MFAC}(k-1) + \frac{\rho\hat{\phi}_c(k)}{\lambda + \left|\hat{\phi}_c(k)\right|^2}(y^*(k+1) - y(k)) \tag{6}$$

$$\hat{\phi}_c(k) = \hat{\phi}_c(k-1) + \frac{\eta\Delta u_{MFAC}(k-1)}{\mu + \Delta u_{MFAC}(k-1)^2} \cdot (\Delta y(k) - \hat{\phi}_c(k-1)\Delta u_{MFAC}(k-1)) \tag{7}$$

$$\left|\hat{\phi}_c(k)\right| \le \varepsilon, \text{ or } \left|\Delta u_{MFAC}(k-1)\right| \le \varepsilon \text{ or } \operatorname{sign}(\hat{\phi}_c(k)) \ne \operatorname{sign}(\hat{\phi}_c(1)) \tag{8}$$

where $\hat{\phi}_c(k)$ is the prediction value; $\phi_c(1)$ is the initial value; y^* is the reference value; ε is a small constant; $\lambda > 0$; $\mu > 0$; $\rho \in (0,1]$; $\eta \in (0,1]$.

Remark: The proposed PIDDC integrates a PI loop with a MFAC loop, forming a composite control strategy that operates independently of MG model information. By leveraging only real-time I/O data from the MG system, this approach can achieve adaptive frequency regulation. At the same time, in the MFAC loop, the dLDM is continuously updated using equation (7), enabling enhanced adaptability to the unmodeled uncertainties and improved transient performance in frequency control. The synergistic operation of dual-loop architecture ensures the robustness and precise dynamic response characteristics.

IV. Results and Discussions

An actual MG system is represent by Fig. 1, which is used to verify the performance of the proposed PIDDC scheme. Table I lists the MG parameters, and the detailed parameters interpretation can be referred to [14]. For the PI loop, as we know, its proportional and integral parameters can affect system response speed, and inappropriate parameter selection may cause overshoot and oscillation. Therefore, the parameters are chosen as $K_P = 0.02$, $K_I = -0.1$ by trial and error method, respectively. For the MFAC loop, ρ=0.6, η=1, ε=10^{-5}, λ=2, μ=1, $\hat{\phi}_c(1)$=2. $y^* = 0$ is donated as the reference value and initial values are $u(1) = u(2) = 0$, $y(1) = -0.01$, $y(2) = 0.01$.

TABLE I. Parameters of the MG

D [pu/Hz]	M [pu s]	β [pu/Hz]	R_1, R_2, R_3 [Hz/pu]	T_{g1}, T_{g2}, T_{g3} [s]	T_{t1}, T_{t2}, T_{t3} [s]	T_{BESS} [s]	T_{wt} [s]	T_{pv} [s]
0.012	0.200	0.345	3.000 3.000 3.000	0.200 0.200 0.160	1.100 1.100 0.700	0.100	1.5	1.8

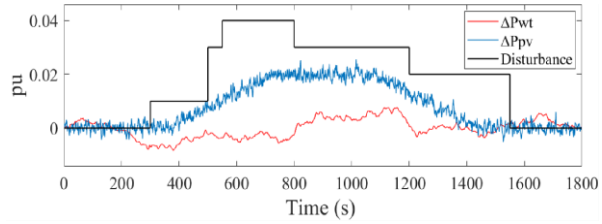


Fig. 3. RESs output deviation and disturbance.

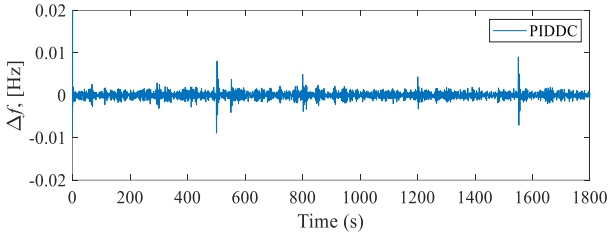


Fig. 4. The proposed PIDDC for the MG frequency control.

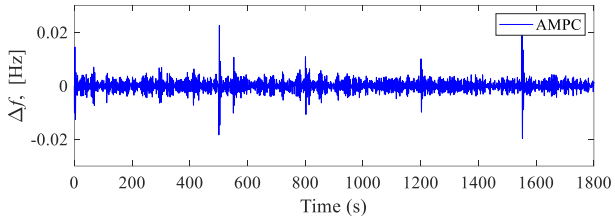


Fig. 5. Single AMPC loop for the MG frequency control.

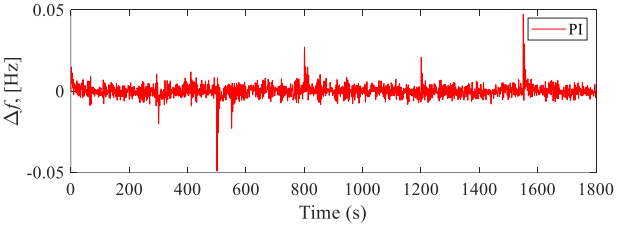


Fig. 6. Single conventional PI loop for the MG frequency control.

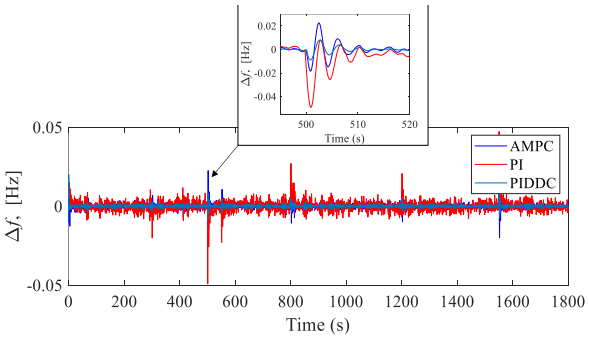


Fig. 7. Comparison results.

Fig. 3 shows that the continuous load disturbance and active power output deviations of the RESs, while Fig. 4 demonstrates the frequency regulation performance of the proposed PIDDC under these disturbance conditions. The results show that the frequency fluctuations are effectively constrained within desired range through the implementation of the proposed PIDDC.

For a comparison, a single AMPC loop and a single PI loop in [3] are also considered in this paper. Fig. 5 and Fig. 6 show that the results under the same simulation conditions, respectively. As evidenced in Fig. 5, the single AMPC loop can achieve satisfactory frequency regulation under the disturbance scenarios. Nevertheless, the absence of the MG uncertainty characterization in its internal prediction model, which results in destabilizing transient overshoots when subjected to step change. Fig. 6 also shows that the results of the single PI loop, the frequency dynamic change of the MG system is significantly affected by the uncertainty, resulting in a sharp frequency fluctuation.

The detailed comparison results are shown in Fig. 7 and their comparative data using Min, Max, and STD indices [3] of frequency deviation is given in Table II. These comparative results determine that the PIDDC can achieve the better performance compared to other methods, which has a higher robustness to address the sharp frequency fluctuation to realize the frequency stability.

To further verify the effectiveness of the proposed method, the proportion of renewable energy was increased compare to the above case. Additionally, to evaluate its robustness against abrupt load fluctuations, we incorporated the load profiles depicted in Fig. 8.

The simulation results of the proposed PIDDC are presented in Fig. 9. From that, the proposed PIDDC can achieve a good frequency control performance under high renewable energy penetration, even under sharp step-change conditions.

For a detailed comparison, we also applied the same AMPC and PI methods under identical test conditions. The results are presented in Figs. 10 and 11, which demonstrates that the AMPC method can achieve satisfactory frequency control performance, maintaining frequency deviations within an acceptable range despite high renewable energy penetration and continuous sharp disturbances. However, as shown in Fig. 10, a transient frequency fluctuation occurs between 0s and 10s. This is because the AMPC with an unscented Kalman filter (UKF) [3] requires an initial learning phase to estimate the system dynamics.

Fig. 11 shows the results of the PI control. From the results, one can see that the frequency deviation occurs a significant fluctuation at 620s. Although the overall control performance remains satisfactory, this transient instability could potentially lead to system breakdown in practical microgrid frequency control applications.

A detailed comparative data analysis is also listed in Table III. It clearly shows that the advantages of the proposed PIDDC over the AMPC and the PI methods.

TABLE II. COMPARATIVE DATA ANALYSIS

	PI [3]	AMPC [3]	PIDDC
Min.	0.0518Hz	0.0197Hz	0.0100Hz
Max.	0.0481Hz	0.0225Hz	0.0200Hz
STD	0.0053Hz	0.0022Hz	0.0009Hz

TABLE III. COMPARATIVE DATA ANALYSIS UNDER HIGH RENEWABLE ENERGY

	PI [3]	AMPC [3]	PIDDC
Min.	0.0693Hz	0.1695Hz	0.0200Hz
Max.	0.1237Hz	0.2631Hz	0.0226Hz
STD	0.0074Hz	0.0076Hz	0.0017Hz

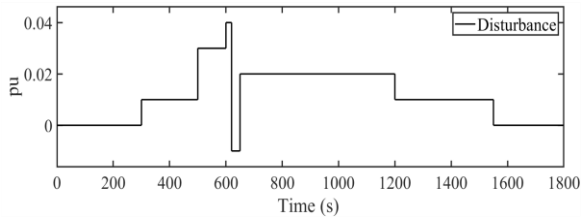


Fig. 8. The sharp disturbance.

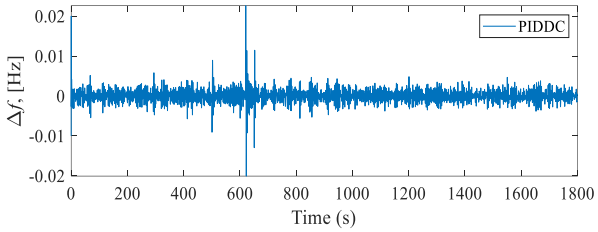


Fig. 9. Frequency deviation of the proposed PIDDC.

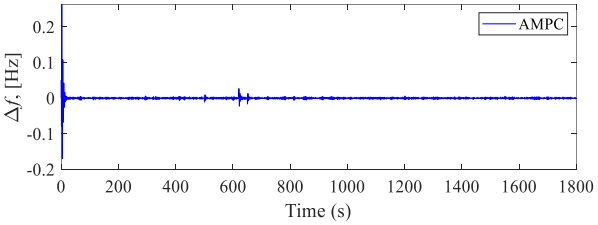


Fig. 10. Frequency deviation of the AMPC.

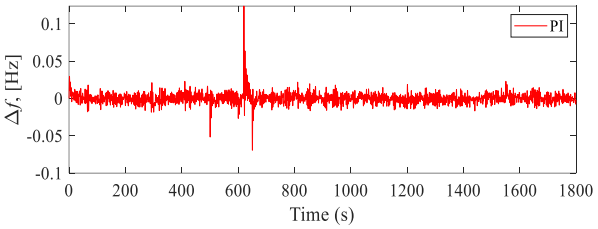


Fig. 11. Frequency deviation of the PI.

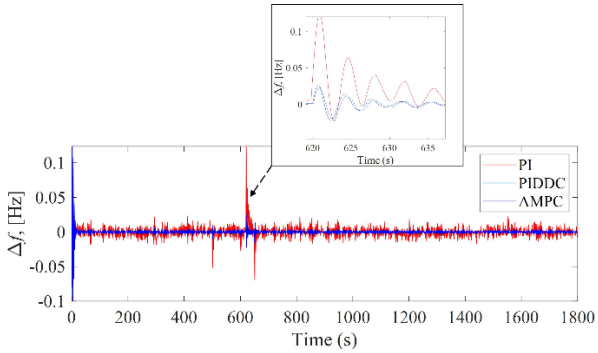


Fig. 12. Comparison results.

V. CONCLUSIONS

This paper proposes a novel PIDDC scheme for the MG frequency regulation, consisting a PI loop and an AMPC loop. The PI control loop enables rapid response to dynamic frequency changes, while the MFAC loop utilizes only the I/O data of the MG to compensate for the PI loop limitations in handling uncertainties, thereby improving system robustness and frequency control performance. Simulation results show that the proposed PIDDC can effectively solve the frequency fluctuation problem of the MG system under the uncertainties and performs better than other methods.

APPENDIX

Proof: Denote

$$\begin{aligned}\Psi(k) = & f(\boldsymbol{y}^T(k), \boldsymbol{u}_{PI}^T(k), [u_{MFAC}(k-1), u_{MFAC}(k-1), \\ & \cdots, u_{MFAC}(k-n_u)], \boldsymbol{w}^T(k)) \\ & - f(\boldsymbol{y}^T(k-1), \boldsymbol{u}_{PI}^T(k-1), \boldsymbol{u}_{MFAC}^T(k-1), \boldsymbol{w}^T(k-1))\end{aligned}$$

According to (3), we have the following output deviation based on the mean value theorem [11]

$$\begin{aligned}\Delta y(k+1) = & f(\boldsymbol{y}^T(k), \boldsymbol{u}_{PI}^T(k), \boldsymbol{u}_{MFAC}^T(k), \boldsymbol{w}^T(k)) \\ & - f(\boldsymbol{y}^T(k), \boldsymbol{u}_{PI}^T(k), [u_{MFAC}(k-1), u_{MFAC}(k-1), \\ & \cdots, u_{MFAC}(k-n_u)], \boldsymbol{w}^T(k)) + \Psi(k) \\ = & \frac{\partial f}{\partial u_{MFAC}(k)} \Delta u_{MFAC}(k) + \Psi(k)\end{aligned}$$

where $\Delta u_{MFAC}(k) = u_{MFAC}(k) - u_{MFAC}(k-1)$.

For every sampling moment *k*, consider

$$\Psi(k) = \gamma(k) \Delta u_{MFAC}(k),$$

since $|\Delta u_{MFAC}(k)| \neq 0$, there must be a unique solution $\gamma(k)$.

Let

$$\phi_c(k) = \gamma(k) + \frac{\partial f}{\partial u_{MFAC}(k)}.$$

Then, (3) can be written as

$$\Delta y(k+1) = \phi_c(k) u_{MFAC}(k).$$

REFERENCES

[1] K. O. Oureilidis, E. A. Bakirtzis, and C. S. Demoulias, "Frequency-based control of islanded microgrid with renewable energy sources and energy storage," *Journal of Modern Power Systems and Clean Energy*, Vol. 4, No. 1, pp. 54-62, 2016.

[2] S. Jiang, S. Wen, M. Zhu, Y. Xu, and J. Ma, "Feedback-Based Setpoint Mechanism in Model Predictive Load Frequency Control," *IEEE Transactions on Power Systems*, Vol. 39, No. 4, pp. 6115-6118, 2024.

[3] W. Wang, Y. Sasaki, N. Yorino, Y. Zoka, and A. Bedawy, "Frequency Regulation of High-penetration Renewable Energy Microgrids Using Adaptive Model Predictive Control," *CSEE Journal of Power and Energy Systems (Early Access)*, pp. 1–11, 2024.

[4] X. Wan, Z. Wang, F. Wei, L. Jin, C. Zhang, and M. Wu, "Hybrid Variables-Dependent Event-Based Efficient Model Predictive Load Frequency Control for Power Systems," *IEEE Transactions on Industrial Informatics*, Vol. 20, No. 11, pp. 12771-12782, 2024.

[5] M. V. Kazemi, S. J. Sadati, and S. A. Gholamian, "Adaptive Frequency Control of Microgrid Based on Fractional Order Control and a Data-Driven Control With Stability Analysis," *IEEE Transactions on Smart Grid*, Vol. 13, No. 1, pp. 381-392, 2022.

[6] G. Chen, Z. Li, Z. Zhang, and S. Li, "An Improved ACO Algorithm Optimized Fuzzy PID Controller for Load Frequency Control in Multi Area Interconnected Power Systems," *IEEE Access*, Vol. 8, pp. 6429-6447, 2019.

[7] B. P. Sahoo, and S. Panda, "Improved grey wolf optimization technique for fuzzy aided PID controller design for power system frequency control," *Sustainable Energy, Grids and Networks*, Vol. 16, pp. 278-299, 2018.

[8] N. K. Gupta, M. K. Kar, and A. K. Singh, "Design of a 2-DOF-PID Controller using an Improved Sine-Cosine Algorithm for Load Frequency Control of a Three-Area System with Nonlinearities," *Protection and Control of Modern Power Systems*, Vol. 7, No. 3, pp. 1-18, 2022.

[9] R. Muduli, D. Jena, and T. Moger, "Application of Reinforcement Learning-Based Adaptive PID Controller for Automatic Generation Control of Multi-Area Power System," *IEEE Transactions on Automation Science and Engineering*, Vol. 22, pp. 1057-1068, 2024.

[10] M. Gheisarnejad, "An effective hybrid harmony search and cuckoo optimization algorithm based fuzzy PID controller for load frequency control," *Applied Soft Computing*, Vol. 65, pp. 121-138, 2018.

[11] R. Chi, W. Cui, N. Li, Z. Hou, and B. Huang, "Sampled-Data Model-Free Adaptive Control for Nonlinear Continuous-Time Systems," *IEEE Transactions on Cybernetics*, Vol. 54, No. 8, pp. 4775-4788, 2024.

[12] X. Bu, Y. Zhang, X. Ren, and Z. Hou, "Event-triggered Data-driven LFC of Multi-microgrid Interconnected Systems With Time Delays," *IEEE Transactions on Control of Network Systems (Early Access)*, pp. 1-11, 2025.

[13] X. Qiu, Y. Wang, H. Zhang, and X. Xie, "Resilient Model Free Adaptive Distributed LFC for Multi-Area Power Systems Against Jamming Attacks," IEEE Transactions on Neural Networks and Learning Systems, Vol. 34, No. 8, pp. 4120-4129, 2023.

[14] W. Wang, N. Yorino, Y. Sasaki, Y. Zoka, A. Bedawy, and S. Kawauchi, "Adaptive MPC-Based Cooperative Frequency Control for Community Microgrid," *Proceedings of 2022 4th International Conference on Smart Power & Internet Energy Systems (SPIES)*, 2022.

An Adaptive Model Predictive Load Frequency Control Strategy for Low-Inertia Power Systems

Hayato Nagaosa[1], Yutaka Sasaki[1], Helin Yang[2], Yoshifumi Zoka[1], Naoto Yorino[1,3], Ahmed Bedawy[1], Weichao Wang[4]
[1] Graduate School of Advanced Science and Engineering, Hiroshima University, Higashi-Hiroshima, Japan
[2] Hitachi Energy, Shanghai, China
[3] National Institute of Technology (KOSEN), Kure College, Kure, Japan
[4] Qingdao University of Science and Technology, Shandong, China
yusasaki@hirosima-u.ac.jp

***Abstract*— As renewable energies (REs) are rapidly penetrating existing power systems, maintaining frequency stability has become increasingly difficult. Load frequency control (LFC) operations are very important under these circumstances. Classical PI controllers are widely used as LFC controllers; however, the system operator must retune the parameters whenever system configurations are changed. To address this issue, the authors have developed an adaptive model predictive LFC (AMPC-LFC) to improve the frequency stability by using an automatic parameter update. This paper proposes a modified AMPC-LFC for power systems with high penetration of wind turbine (WT) power generation in an interconnected two-area network. An extended Kalman filter (EKF) is applied to AMPC-LFC to estimate the parameters of the simplified internal model in real time. Furthermore, a high voltage direct current (HVDC) transmission system with inertia emulation control (INEC) can reduce frequency deviations caused by WT and load changes. Simulation results show that the HVDC-AC hybrid transmission system can improve frequency control performance by up to 56% compared to AC-only systems. Additionally, when AMPC is compared with PI controllers and particle swarm optimization (PSO)-tuned adaptive PI controllers, AMPC can reduce frequency deviation for each controller by up to 64% and 44% respectively.**

Keywords*— Model predictive control, LFC, Low-inertia power system, HVDC

I. Introduction

In recent years, global efforts to reduce greenhouse gas emissions have accelerated, and renewable energies (REs) such as wind turbine (WT) power generation have been widely adopted. However, as WT power generation increases, it reduces the share of synchronous generators, which sharply lowers system inertia and degrades frequency stability. One potential solution to this challenge is to enhance load frequency control (LFC) performance [1]. In this context, model predictive control (MPC) has attracted interest as an advanced LFC method [2]-[7]. The MPC is a multivariable control method that utilizes a state-space model to predict future system behavior and computes optimal control inputs [8]. It has been widely applied in various fields such as chemical processing, automotive systems, oil refining, and power systems. In the LFC applications, MPC has reported superior frequency response performance compared to classical PI control methods [4],[5].

However, due to the uncertainties introduced by REs, high-accuracy state estimation is required for finding system stable operation points [9]. In the LFC system state estimation, various approaches have been proposed. For example, [2] proposes a Kalman filter combined with an ARX model, [6] uses an unscented Kalman filter (UKF), and [4], [7] use an extended Kalman filter (EKF). Among these, the EKF is particularly suitable for real-time control due to its relatively simple structure, ease of implementation, and lower computational cost compared to other observers.

The authors have also proposed an adaptive model predictive control (AMPC) approach for frequency regulation in the AC power system. In this method, the internal prediction models are represented as simplified first- or second-order lag systems, whose parameters are determined in real time by the EKF and UKF algorithms [6].

Furthermore, in recent years, the use of parallel high-voltage direct-current (HVDC) and AC interconnection lines has gained significant attention for improving frequency stability in multi-area power systems. In [10], the installation of an HVDC line alongside an AC line was shown to improve grid performance compared to AC-only configurations. In [11], an HVDC line is used to adjust the output power instantly in response to sudden frequency deviations, thereby improving frequency stability. Furthermore, [12] introduces an inertia emulation control (INEC) strategy, which uses the electrostatic energy stored in the HVDC line to emulate the inertial response of a synchronous machine. HVDC lines are characterized by their rapid response to sudden load changes and WT fluctuations, enabling flexible power control and frequency stabilization that are difficult to achieve with AC systems alone. Based on the above, it can be concluded that both AMPC and HVDC-AC hybrid lines benefit LFC under high penetration of WT power generation. AMPC enhances frequency stability through its multivariable and predictive control capabilities, while HVDC-AC systems provide rapid frequency response and inertia emulation.

979-8-3315-5472-9/25/$31.00 ©2025 IEEE

In this paper, an interconnected two-area power system model incorporating WT power generation is developed to evaluate the effectiveness of the HVDC-AC hybrid lines structure and the AMPC strategy for load frequency control. Simulation results show that the proposed approach effectively copes with the frequency deviations caused by load changes and WT fluctuations. Furthermore, the AMPC scheme outperforms both a classical PI controller and a particle swarm optimization (PSO)-tuned adaptive PI controller in terms of frequency regulation performance.

II. Load Frequency Control

In power systems, frequency fluctuates when there is an imbalance between generation and load consumption. Therefore, LFC aims to reduce the frequency deviation and restore the system frequency to its nominal setpoint. Fig. 1 illustrates the basic frequency control loop of a single generator unit, which includes both primary and secondary control mechanisms. Primary control (governor control) uses a speed governor to detect deviations in frequency (rotational speed) and respond immediately. Secondary control (LFC) adjusts the turbine output setpoint through a secondary controller to restore the system frequency to its nominal steady-state value. Together, these two control loops provide a rapid response to short-term fluctuations and help maintain long-term frequency stability.

Fig. 2 shows the LFC model of area i, including AC tie-line power flows with other areas [13]. R_i is the governor droop coefficient (speed drop characteristic). β_i is the frequency response characteristic. T_g, T_t are the governor and turbine time constants. $T_{ij,AC}$ is the AC line stiffness coefficient. D_i is the load damping coefficient. M_i is the equivalent inertia coefficient, and $\Delta P_{g,i}, \Delta P_{t,i}, \Delta f_i, \Delta P_{tie,ij,ac}$ are respectively the governor output deviation, turbine output deviation, and frequency deviation. AC line power deviation. ΔP_L is the load deviation.

In the model, control coordination extends beyond a single area to include tie-line power flows, necessitating coordinated operation across areas. Therefore, the area control error (ACE) which is the weighted sum of the frequency deviation and tie-line flow deviation, is used as a control indicator. Each control area uses its ACE in the secondary control loop to adjust its local frequency and power flow with other areas, thereby stabilizing the system frequency and tie-line flows.

III. Modeling of HVDC Line

This section presents the model equations for the HVDC line and INEC method.

A. The equivalent synchronization coefficient of HVDC line

Fig. 3 shows HVDC-AC hybrid lines model. According to [12], an HVDC-AC hybrid lines between two specified buses can be treated as a synchronous machine from the perspective of each bus, and two controllable voltage sources can represent the HVDC line via phase reactance. This allows the relationship between the frequency deviation in each interconnected area and

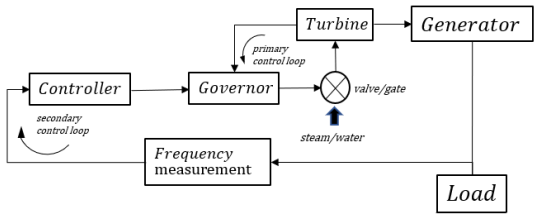


Fig. 1. The basic frequency control loop.

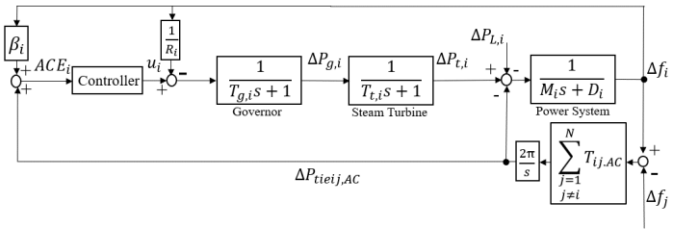


Fig. 2. LFC model of area *i*.

the power output deviation from the HVDC line to be described as follows.

$$\Delta P_{tie12,DC} = \frac{2\pi T_{eqv}}{s}(\Delta f_1(s) - \Delta f_2(s)) \tag{1}$$

$$T_{eqv} = \frac{T_{12,DC}T_{21,DC}}{T_{12,DC} + T_{21,DC}} \tag{2}$$

T_{eqv} represents the HVDC equivalent synchronization coefficient. $T_{12,DC}, T_{21,DC}$ are the converter AC/DC synchronizing coefficient.

B. Inertial emulation control

The HVDC line can be modeled as a capacitor that stores electrostatic energy. The INEC generates the voltage required to absorb and release the electrostatic energy in the DC capacitor based on the area frequency deviation. The effectiveness of the INEC is evaluated by [12].

The inertial (mechanical) energy stored in the synchronous machine is equivalent to the electrostatic energy stored in the capacitor. This relationship can be expressed as follows:

$$\frac{2H_{VSC}}{f^0}\frac{d}{dt}(\Delta f) = \left(\frac{NC_{DC}{V_{DC}}^0}{S_{VSC}}\right)\frac{d\Delta V_{DC}}{dt} \tag{3}$$

where H_{VSC} is the inertia constant, f^0 is the nominal frequency, N is the number of capacitors, C_{DC} is the capacitance, ${V_{DC}}^0$ is

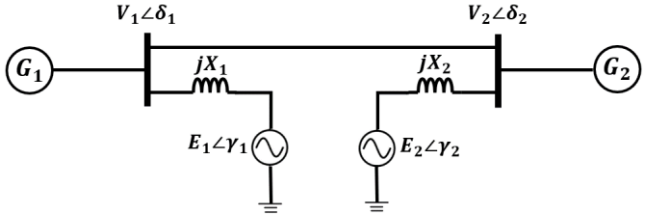


Fig. 3. HVDC-AC hybrid lines equivalent circuit model.

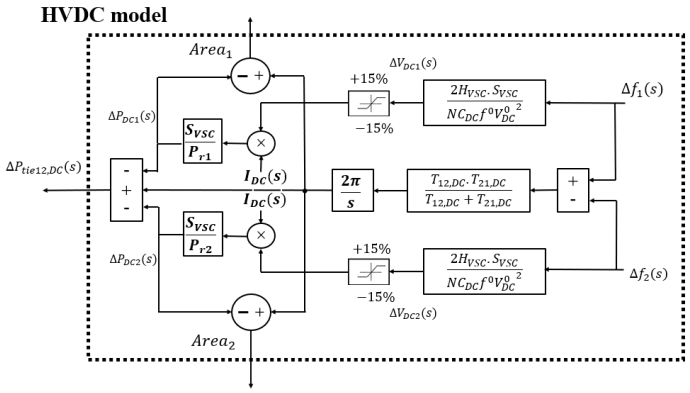


Fig. 4. Detailed structure of the HVDC line model.

the rated DC voltage and S_{VSC} is the rated capacity of the inverter. After applying the Laplace transform to equation (3) and converting it to the per-unit system, the following equation (4) is obtained.

$$\Delta V_{DC}(s)[p.u.] = \left(\frac{2H_{VSC}S_{VSC}}{NC_{DC}f^0V^{0}_{DC}{}^2} \right) \Delta f(s) \tag{4}$$

Equation (4) relates the voltage deviation of the HVDC line to the frequency deviation.

The detailed structure of the HVDC line model is shown in Fig. 4. It can be seen that multiplying the voltage deviation ΔV_{DCi} by the current I_{DC} yields the per-unit change in DC power output ΔP_{DCi}. P_{ri} represents the base power of the area.

IV. Controller Design

A. Adaptive model predictive control(AMPC)

For LFC in power systems with WT, the controller is required high responsiveness, robustness, and accuracy. The authors have developed a nonlinear discrete-time AMPC controller. AMPC uses an internal model to predict the future behavior of a system. Based on this prediction, the controller calculates the optimal control input.

AMPC requires a system identification method to estimate the state of the internal model. In this paper, we apply an EKF for system identification. The EKF is a filtering algorithm that locally linearizes a nonlinear system by computing the Jacobian matrix of its state-space model. It offers a simple implementation and rapid response.

B. Prediction model

Instead of the conventional first-order lag system model used in previous studies [6], [14], a second-order lag system model (G_{model}) is applied to the internal prediction model. This model captures dynamic characteristics such as system inertia and oscillatory behavior more accurately than the first-order model. The performance of the system can be approximated as in the following.

$$G_{\text{model}}(s) = \frac{b_{1,i}}{s^2 + a_{2,i}s + a_{1,i}} \tag{5}$$

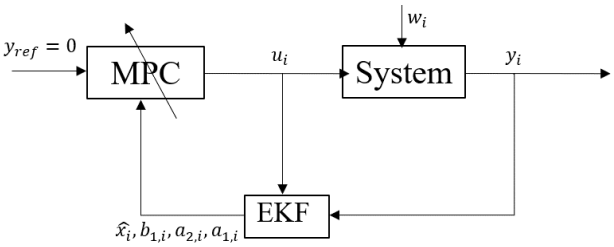


Fig. 5. The structure of AMPC using EKF.

where $b_{1,i}$ corresponds to the input gain and $a_{2,i}$ to the damping term, which is related to the response speed and stability of the system. $a_{1,i}$ is related to the natural frequency, which determines the vibration and steady state characteristics of the system.

C. Prediction model parameters estimated by EKF

Fig. 5 shows how the parameters of (5) are estimated online using measurement (u, y) from the system. EKF iterates every 0.1s and also updates K_{mpc} of the MPC controller to obtain the input signals in (6), (7).

$$\Delta u_i(k) = -K_{MPC}x_i(k) \tag{6}$$

$$u_i(k) = u_i(k-1) + \Delta u_i(k) \tag{7}$$

To estimate the parameters in (5), the proposed EKF formulation is given below.

$$\Delta f_i(k) = \frac{b_{1,i}}{s^2 + a_{2,i}s + a_{1,i}} (u_i(k) - \Delta P_{tieij,AC}(k) - \Delta P_{tieij,DC}(k)) \tag{8}$$

$$x_i(k) = \begin{bmatrix} X_i(k) \\ \theta_i(k) \end{bmatrix} \tag{9}$$

$$X_i(k) = \begin{bmatrix} \Delta \dot{f}_i(k) & \Delta f_i(k) & \Delta P_{tieij,AC+DC}(k) \end{bmatrix}^T \tag{10}$$

$$\theta_i(k) = \begin{bmatrix} b_{1,i} & a_{2,i} & a_{1,i} \end{bmatrix}^T \tag{11}$$

D. Rolling optimization

MPC's optimal process is called rolling optimization. The parameters estimated by EKF are used to update the internal model online and the feedback gains are calculated to obtain the optimal input in the AMPC. Based on the updated internal model, the proposed AMPC method predicts the future system response in the prediction horizon (N_P) and determines the input signal u in the control horizon (N_C).

The performance and calculation time depend on these settings. The following objective function (12) is proposed to minimize the change in state variables and control cost.

$$\min J = \sum_{h=1}^{N_P} (x_i(k+h \mid k)^T Q x_i(k+h \mid k)) + \sum_{h=0}^{N_C} (\Delta u_i(k+h \mid k)^T S \Delta u_i(k+h \mid k)) \tag{12}$$

where $Q \in C^T C$ and $S \in 0.1 \times I_{N_C \times N_C}$ are the weight matrices of the state valuables and input signal deviation, respectively.

The proposed AMPC also uses the following constraints for safe operation and the desired frequency deviation range.

$$\Delta f^{\min} \le \Delta f \le \Delta f^{\max} \tag{13}$$

$$u^{\min} \le u(k) \le u^{\max} \tag{14}$$

V. RESULTS AND DISCUSSIONS

A. Simulation model

The two-area LFC model with HVDC-AC hybrid lines is shown in Fig. 6. In each area, the LFC model consists of a governor model, a steam turbine generator model and a power system model. Area 1 additionally incorporates WT power generation model. The dynamic state-space equations for the interconnected two-area LFC model are presented in equations (15)–(18).

$$x_i(k+1) = A_i x_i(k) + B_i u_i(k) + E_i w_i(k) \tag{15}$$

$$y_i(k) = C_i x_i(k) + D_i u_i(k) \tag{16}$$

$$x_i(k) = [\Delta P_{g,i}(k) \quad \Delta P_{t,i}(k) \quad \Delta f_i(k) \quad \Delta P_{tieij,AC}(k) \quad \Delta P_{tieij,DC}(k)]^T \tag{17}$$

$$y(k) = ACE_i = \beta_i \Delta f_i(k) + \Delta P_{tieij,AC} + \Delta P_{tieij,DC} \tag{18}$$

where A is the state-space model state matrix, B is the state-space model input-state matrix, C is the state-space model state-output matrix, E is the disturbance coefficient matrix, and w is the system disturbance. The proposed AMPC approach is applied to equations (15), (16). The system disturbances are caused by WT and load changes. The WT power generation is modeled as a first-order lag system, as shown in (19).

$$\Delta P_{wt} = \frac{1}{T_{wt}s + 1} \times input \tag{19}$$

where T_{wt} is the time constant of the WT power generation. Variations in WT power generation and load cause power fluctuations, leading to frequency instability. However, these fluctuations are reduced by the response of steam turbine generators and tie-line power exchanges.

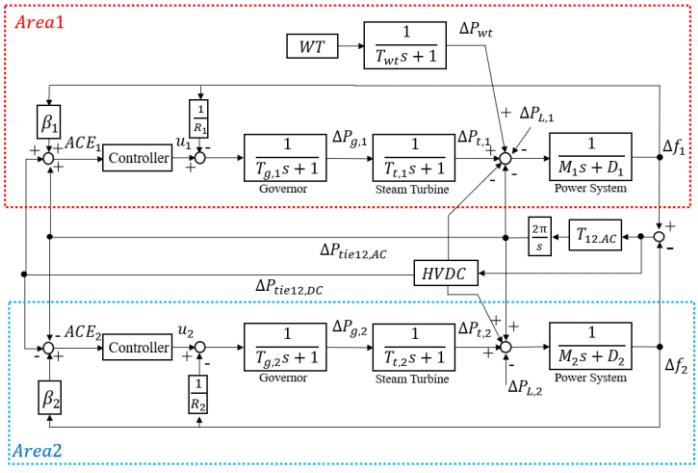


Fig. 6. Two-area LFC model with HVDC-AC hybrid lines.

B. Simulation case and parameter settings

The simulation environment for the proposed AMPC method and the two-area LFC model with HVDC-AC hybrid lines are built using MATLAB/Simulink R2024a. The parameters of the LFC model are listed in Tables 1 and 2 [6],[12]. WT fluctuations and load changes are considered as external disturbances, with their respective profiles illustrated in Fig. 7. The simulation is conducted over 120 seconds, considering the following two scenarios.

Case 1: As shown in Fig. 8, The comparison of the HVDC-AC hybrid model and the only AC model is carried out. The AMPC is used as the frequency controller in both configurations.

Table 1. Parameters of the two-area LFC model [6].

Area	D_i [p.u./Hz]	M_i [p.u./s]	$T_{g,i}$ [s]	$T_{t,i}$ [s]	β_i [p.u./Hz]	R_i [Hz/p.u.]	$T_{AC,ij}$ [p.u./Hz]
1	0.011	0.18	0.2	1.1	0.344	3	0.086
2	0.07	0.16	0.17	0.7	0.403		

Table 2. Parameters of HVDC line [12].

Area	$S_{VSC,i}$ [MW]	$V^0_{DC,i}$ [kV]	N_i	$C_{DC,i}$ [mF]	f_i^0 [Hz]	$H_{VSC,i}$ [s]	$I_{DC,i}$ [p.u./Hz]	$P_{r,i}$ [MW]
1	600	300	2	0.148	60	4	0.5	2000
2								1000

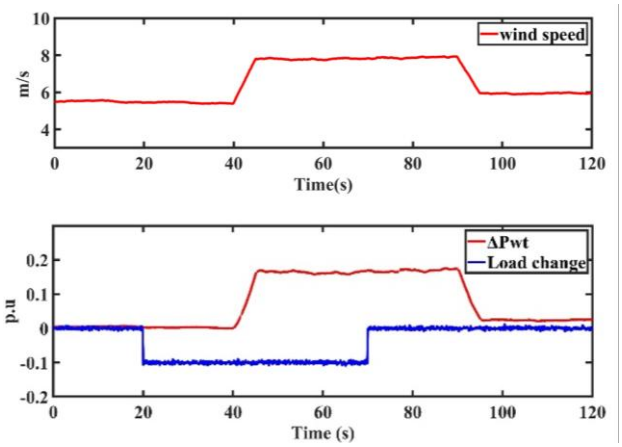


Fig. 7. Wind speed, WT output and load change.

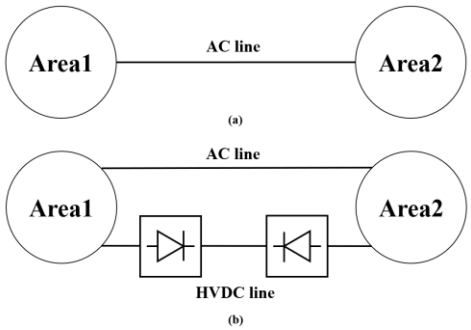


Fig. 8. Simulation case 1 ((a) AC-only (b)HVDC-AC hybrid).

Case 2: In the HVDC-AC hybrid scenario, the frequency regulation performance of three control strategies is compared: AMPC, a conventional PI controller tuned through trial and error ($K_{p1,2}=0, K_{i1}=-0.8, K_{i2}=-0.4$), and an adaptive PI controller with parameters automatically tuned using the particle swarm optimization (PSO) algorithm (referred to as PSO-PI)

In both cases, the prediction and control horizons of the AMPC were determined through trial and error as $N_P=40, N_C=20$, respectively. In addition, the initial parameters in equation (5) were set to $b_{1,1}=15, a_{2,1}=3, a_{1,1}=20, b_{1,2}=90, a_{2,2}=6, a_{1,2}=-4$.

These parameters are computed by using the bode plot of the proposed internal prediction model and the actual system, which is used to decide the initial values of the proposed second-order lag system.

C. Simulation results

In Case 1, Fig. 9 shows the comparison of frequency deviations between the HVDC-AC hybrid lines and the AC-only line. The results show that the HVDC-AC hybrid lines more effectively reduce frequency deviation than the AC-only case. In the steep-down case, the highest frequency suppression ratio was achieved, resulting in a 56% reduction. Furthermore, the HVDC-AC hybrid lines exhibit faster recovery to frequency deviations, indicating a significant improvement in system resilience.

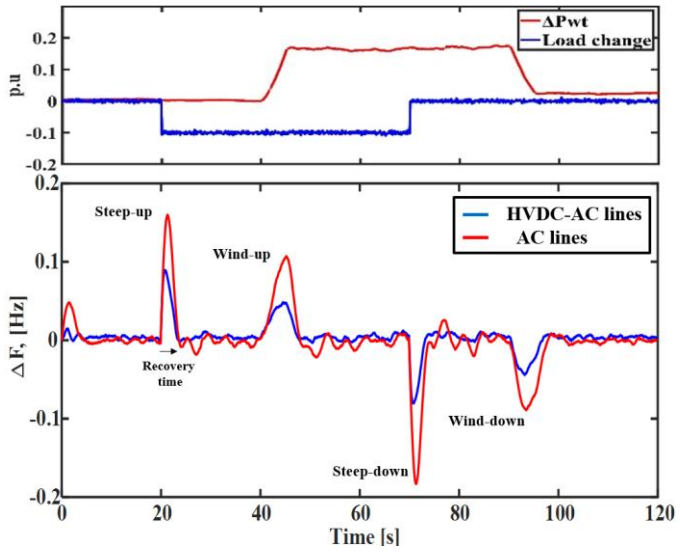


Fig. 9. Frequency Deviation Comparison Case 1.

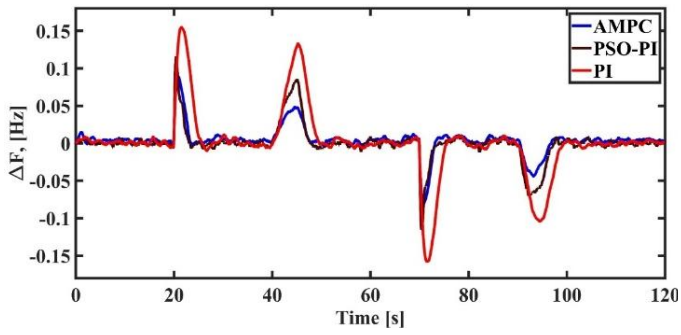


Fig. 10. Frequency Deviation Comparison Case 2.

In Case 2, Figs. 10 and 11 compare frequency deviations obtained with AMPC, PI, and PSO-PI load frequency controllers. The results show that the AMPC achieves smaller frequency deviations compared to PI and PSO-PI controls. For example, when the wind-up causes, AMPC can reduce frequency deviation for each controller by 64% and 44%, respectively. In addition, the settling time to the steady state is shortened.

Fig. 12 shows the simulation results of frequency deviation, ACE, and tie-line power of the HVDC-AC hybrid lines under the AMPC control. It is observed that frequency deviation, ACE, and tie-line power fluctuate at the moment a disturbance occurs, but they respond quickly and eventually stabilize. These results show that the proposed AMPC method and HVDC-AC hybrid line can effectively cope with the frequency problems, and AMPC controllers for areas 1 and 2 are cooperatively operated without parameter tuning.

VI. Conclusions

This paper proposes an EKF-based AMPC-LFC for a two-area power system model with WT power generation.

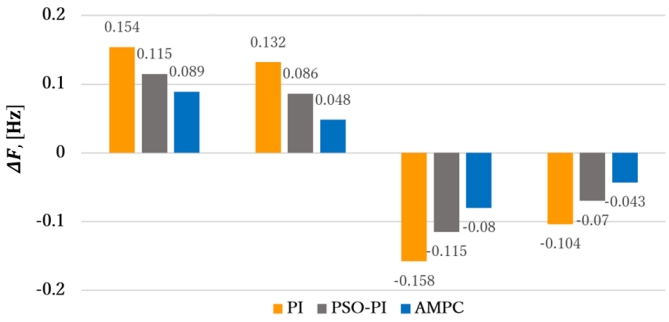


Fig. 11. Comparative data analysis in Case 2.

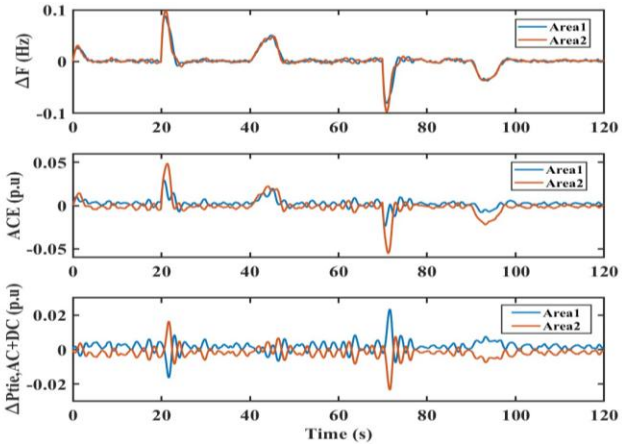


Fig. 12. Frequency deviation, ACE and tie line power of HVDC-AC hybrid lines.

VI. Conclusions

Furthermore, in addition to the AC line, an HVDC line incorporating inertia emulation control is introduced. This approach improves frequency control performance and enhances system resilience, achieving up to a 56% reduction in frequency deviation compared to AC-only systems. The reduction in the convergence time to the steady state was confirmed. Furthermore, the proposed AMPC method outperforms conventional PI controllers and particle swarm optimization (PSO)-tuned adaptive PI controllers, achieving up to 64% and 44% reductions in frequency deviation, respectively. This is attributed to its ability to adapt to the system dynamics in real time through parameter estimation of the internal model. These results show that the proposed method successfully copes with the disturbances caused by WT and load changes in the low-inertia systems.

In future work, we aim to verify that the proposed method can perform effectively in very low-inertia power systems such as 100% renewable energy systems. Therefore, the AMPC method must improve its performance through high accurate system modeling and operational cost optimization (redesign of the objective function and constraints). In addition, parameter tuning of the HVDC line can also serve as an effective approach.

REFERENCES

[1] D.D. Rasolomampionona, M. Połecki, K. Zagrajek, W. Wróblewski, M. Januszewski, "A Comprehensive Review of Load Frequency Control Technologies," *Energies*, vol. 17, no. 12, 2915, 2024.

[2] M.A. Mohamed, A.A.Z. Diab, H. Rezk, T. Jin, "A Novel Adaptive Model Predictive Controller for Load Frequency Control of Power Systems Integrated with DFIG Wind Turbines," *Neural Computing and Applications*, vol. 32, no. 11, pp.7171-7181, 2020.

[3] J. Liu, Q. Yao, Y. Hu. "Model Predictive Control for Load Frequency of Hybrid Power System with Wind Power and Thermal Power," *Energy*, vol. 172, pp. 555-565, 2019.

[4] A.M. Ersdal, L. Imsland, K. Uhlen, "Model Predictive Load-Frequency Control," *IEEE Trans. on Power Syst.*, vol.31, no.1, pp. 777–785, 2016.

[5] S. Daniar, M. Shiroei, R. Aazami, "Multivariable Predictive Control Considering Time Delay for Load-frequency Control in Multi-area Power Systems," *Archives of Control Sciences*, vol. 26, no. 4, pp.527-549, 2016.

[6] W. Weichao, Y. Sasaki, N. Yorino, Y. Zoka, A. Bedawy, "Frequency Regulation of High-penetration Renewable Energy Microgrids using Adaptive Model Predictive Control," *CSEE Journal of Power and Energy Systems*, pp.1-11, Ealy Access, 2024.

[7] A.M. Ersdal, L. Imsland, K. Uhlen, D. Fabozzi, N.F. Thornhill, "Model Predictive Load-frequency Control taking into account Imbalance Uncertainty," *Elsevier Control Eng. Practice*, vol. 53, pp. 139-150, 2016.

[8] B. Kouvaritakis, M. Cannon, "Model Predictive Control Classical, Robust and Stochastic," Switzerland: Springer International Publishing 38.13-56 (2016): 7.

[9] L. Kamyabi, T.T. Lie, S. Madanian, S. Marshall, "A Comprehensive Review of Hybrid State Estimation in Power Systems: Challenges, Opportunities and Prospects," *Energies*, vol. 17, no. 19, 4806, 2024.

[10] A.H.A. Elkasem, M. Khamies, G. Magdy, I. B.B. Taha, S. Kamel, "Frequency Stability of AC/DC Interconnected Power Systems with Wind Energy using Arithmetic Optimization Algorithm-based Fuzzy-PID Controller," *Sustainability*, vol. 13, no. 21, 12095, 2021.

[11] J. Stojković, A. Lekić, P. Stefanov, "Adaptive Control of HVDC Links for Frequency Stability Enhancement in Low-inertia Systems," *Energies*, vol. 13, no. 23, 6162, 2020.

[12] N. Pathak, A. Verma, T.S. Bhatti, I. Nasiruddin, "Modeling of HVDC Tie-links and Their Utilization in AGC/LFC Operations of Multi-area Power Systems," *IEEE Trans. on Industrial Electronics*, vol. 66, no. 3, pp.2185-2197, 2019.

[13] H. Bevrani, "Robust Power System Frequency Control," New York: Springer, 2014.

[14] W. Weichao, Y. Sasaki, N. Yorino, Y. Zoka, A. Bedawy, "Adaptive Model Predictive Control Based Frequency Regulation for Low-inertia Microgrid," *Proc. of the 5th International Conference on Power and Energy Technology (ICPET)*, 2023.

A Multi-Scale Spatio-Temporal Model for Eletric Load Forecasting

Muyang Tian
school of Automation and Information Engineering
Xi'an University of Technology
Xi'an,Shanxi,China
1512275092@qq.com

Ruirui Ji
school of Automation and Information Engineering
Xi'an University of Technology
Xi'an,Shanxi,China
jirui@xaut.edu.cn

Xin Xin
school of Automation and Information Engineering
Xi'an University of Technology
Xi'an,Shanxi,China
2752359400@qq.com

Chenxi Bai
school of Automation and Information Engineering
Xi'an University of Technology
Xi'an,Shanxi,China
1049578161@qq.com

Tong Jia
school of Automation and Information Engineering
Xi'an University of Technology
Xi'an,Shanxi,China
1319619482@qq.com

Anjie Song
school of Automation and Information Engineering
Xi'an University of Technology
Xi'an,Shanxi,China
2368095761@qq.com

***Abstract*—Existing electric load forecasting models often focus on a single scale, making it difficult to simultaneously capture long-term trends and short-term disturbances. This paper proposes a multi-scale spatio-temporal deep learning model that models the long-term dependencies within nodes and the short-term correlations between nodes. In the temporal dimension, a Periodic Decomposition Module is introduced to decompose historical sequences into periodic and disturbance components, which are then modeled and fused through a dual-branch Temporal Fusion Transformer to obtain long-term predictions. In the spatial dimension, multi-scale features are extracted based on geographical maps, similarity maps, and weather maps, dynamically fused through an Inter-Graph External Attention Mechanism， and time dependencies are captured through LSTM to obtain short-term predictions. Finally, the block adaptively integrates long-term and short-term results, simultaneously outputting single-day and single-week predictions. On the NYISO dataset, the MAPE for single-day and single-week predictions is 2.05% and 2.33%, respectively, which significantly outperforms existing methods, validating the model's high accuracy and multi-scale adaptability.**

Keywords—Multi-node Electric load forecasting, Spatio-temporal Graph Neural Network, Dual-branch time series modeling, Multi-scale Spatio-temporal Fusion

I. INTRODUCTION

In modern power systems, electric energy is difficult to store on a large scale, and load forecasting is a crucial component in ensuring supply-demand balance and reducing resource waste. Compared to single-node forecasting, accurate multi-node forecasting is essential to ensuring the safe, reliable, and economical operation of the system [1]. Long-term forecasting focuses on periodic patterns and trends, providing reference for planning and scheduling; short-term forecasting focuses on rapid fluctuations and disturbances, supporting daily operations and market transactions. The integration of distributed energy sources and factors such as meteorology has caused the load to exhibit non-stationary and multi-scale characteristics, placing higher demands on the spatio-temporal modeling capabilities of models [2].

The method of electric load forecasting has undergone an evolution from statistics to machine learning, and then to deep learning. Early methods such as ARIMA [3] and SARIMA [4] could depict seasonal and periodic patterns, but due to the limitation of the stationarity assumption, they struggled to handle nonlinearity and multivariability. Machine learning methods like Random Forest(RF)[5], Gradient Boosting Decision Tree(GBDT)[6], and Multilayer Perceptron(MLP)[7] broke through the linear assumption and enhanced nonlinear modeling capabilities, but they were insufficiently adaptable to demand fluctuations. In recent years, deep learning has demonstrated outstanding performance in complex time series forecasting. RNNs [8,9] and LSTMs [10] can capture long-range dependencies, while Transformers [11] utilize self-attention to model global features, thereby significantly improving prediction accuracy. However, Nevertheless, they still face challenges in feature fusion and multi-scale modeling.

Existing research has primarily focused on single-node load forecasting, failing to fully depict the complex spatio-temporal coupling characteristics among nodes. There is a significant spatio-temporal correlation among different node loads. Analyzing their coupling relationship can help reveal the inter-regional load conduction mechanism and enhance the accuracy and generalization ability of forecasting. Reference[12] constructs a multi-energy coupling prediction model based on K-means and LSTM, but its applicability is limited. Reference [13] proposes Spatio-Temporal Graph Convolutional Network (ST-GCN), which combines Temporal Convolutional Network (TCN) and Graph Convolutional Network (GCN) for short-term prediction, achieving significant accuracy improvement. However, it relies on fixed or single-scale graph structures, making it difficult to capture multi-scale spatial dependencies [14]. Reference [15] utilizes an improved Transformer to

This work was supported by the Key Research and Development Program of Shaanxi (2024GX-YBXM-138).

979-8-3315-5472-9/25/$31.00 ©2025 IEEE

enhance temporal feature extraction, but it tends to produce feature confusion in multi-scale tasks and lacks structural optimization. Overall, existing methods struggle to effectively model dynamic relationships across different spatio-temporal scales simultaneously. To address this, this paper proposes a multi-scale spatio-temporal fusion electric load forecasting model to achieve dual-scale forecasting for single days and single weeks. The main contributions of this paper are as follows:

- We introduce the Periodic Decomposition Module (PDM) to decompose the load series into long-term trends and short-term disturbances at different time scales, and apply differentiated TFT modeling separately to enhance the characterization of multi-scale features.
- We construct three complementary maps based on geographical proximity, operational similarity, and meteorological conditions, and utilize GEA cross-map fusion to extract key information across multiple spatial scales, thereby enhancing the accuracy of regional collaborative modeling and short-term disturbance prediction.

II. Multi-Scale Spatio-Temporal Electric Load Forecasting

A. Electric Load Forecasting Model under Multi-Scale Spatio-Temporal Framework

The multi-scale spatio-temporal electric load forecasting model proposed in this paper is illustrated in Figure 1, encompassing long-term forecasting for individual nodes, short-term forecasting across nodes, and result fusion. Long-term forecasting models trends and disturbances through sequence decomposition, capturing both low-frequency and high-frequency characteristics. Short-term forecasting leverages a multi-graph structure consisting of geographical, similarity, and meteorological graphs, incorporating cross-graph attention and time units to capture disturbances and collaborative fluctuations. The ultimate objective is to fuse the results of these two forecasting branches, thereby enabling multi-node and multi-scale predictions.

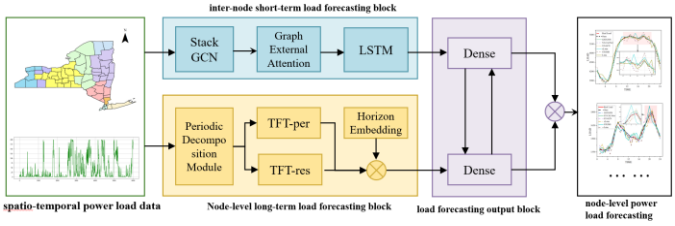


Fig. 1. Structural diagram of the multi-scale spatio-temporal electric load forecasting model

B. Inter-node short-term load forecasting block

The inter-node short-term load forecasting block, which captures short-term spatio-temporal dependencies between nodes, is shown in Figure 2. It constructs three complementary graphs—geographical, similarity, and weather—based on spatial proximity, operational similarity, and meteorological conditions. In feature extraction, GCN [16] captures multi-scale spatial features, while in fusion, GEA [17] integrates them with weights to emphasize key dependencies. The fused features are then fed into a stacked LSTM to model temporal dependencies, producing short-term inter-node predictions. Finally, these results are combined with long-term predictions to yield the final load forecast.

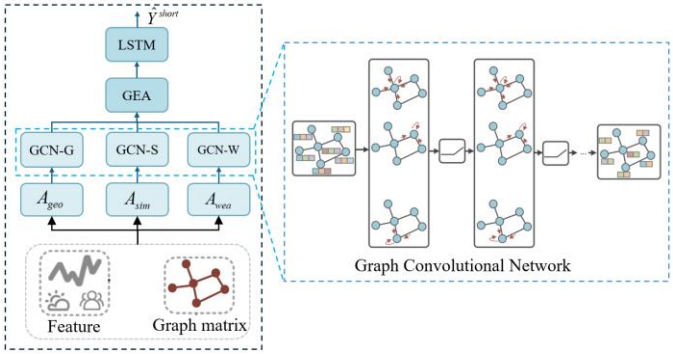


Fig. 2. Structural diagram of the inter-node short-term load forecasting block.

1) Block for multi-graph spatial scale modeling

The inter-node short-term load forecasting block captures short-term disturbances and spatial dependencies among power system nodes. this paper constructs three types of graph structures:

$$A_{geo}(i,j) = \exp(-\frac{d_{ij}^{\ 2}}{s^2}) \tag{1}$$

where denotes the geographical distance between i and j ,and σ is the scale parameter. $\exp(g)$ is the Gaussian kernel function

$$A_{sim}(i,j) = \frac{\mathrm{cov}(x_i, x_j)}{s_{xi} s_{xj}} \tag{2}$$

where $\mathrm{cov}(g)$ denotes the Pearson correlation coefficient.

$$A_{wea}(i,j) = \mathrm{sim}(w_i, w_j) \tag{3}$$

where $\mathrm{sim}(g)$ denotes the cosine similarity.

2) Inter-Graph Attention Fusion

In multi-graph spatial modeling, geographic, similarity, and weather graphs capture diverse inter-node relationships, yet the reliance on each varies across time and nodes. To address this, a GEA is shown in Fig.3, which dynamically fuses spatial features from multiple graphs through learnable weights, enabling the model to adaptively emphasize key relations according to temporal context.

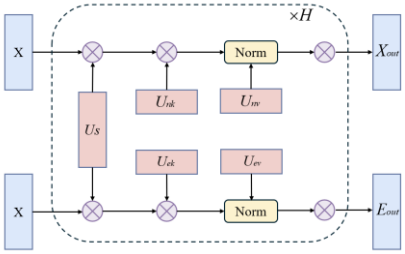


Fig. 3. Structure of Cross-Graph Attention Fusion Mechanism

3) Short-Term Temporal Modeling

The fused spatial feature sequence is fed into the LSTM to capture short-term temporal dependencies of inter-node disturbances. Its gating mechanism preserves key load

variations while suppressing irrelevant fluctuations, providing effective dynamic features for prediction.

$$h_i = \mathrm{LSTM}(Z_i^{\,fused}) \tag{4}$$

$$\tilde{y}_i^{\,short} = W_o h_i \in R^H \tag{5}$$

C. Node-Level Long-Term Load Forecasting Block

This module captures long-term dependencies of individual nodes (see Fig. 4). The PDM [19] decomposes load sequences into periodic and residual components, which are modeled by two specialized TFT [20] branches for trends and fluctuations. Their outputs are fused via a gating mechanism to generate long-term predictions, serving as input for fuses optimization with short-term forecasts.

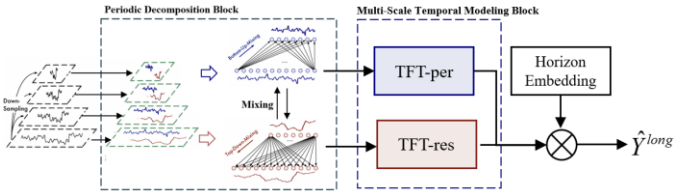


Fig. 4. Structure of the Node-Level Long-Term Load Forecasting Block

1) PDM node

The Past Decomposition and Mixing (PDM) block decomposes and mixes the historical load sequence:

$$X_{per}, X_{res} = \mathrm{PDM}_{\mathrm{Decompose(X)}} \tag{6}$$

$$\hat{X}_{per} = \mathrm{Mix}(X_{per}, X_{res}) \tag{7}$$

$$\hat{X}_{res} = \mathrm{Mix}(X_{res}, X_{per}) \tag{8}$$

2) Multi-Scale Temporal Modeling Block

This module Block the periodic and residual components obtained from PDM using two separate TFT (Temporal Fusion Transformer) branches.

a. TFT-per:

This block captures long-term dependencies by leveraging multi-head attention to strengthen long-range correlations, while GRN and VSN filter irrelevant features to improve long-term trend prediction accuracy (see Fig. 5).

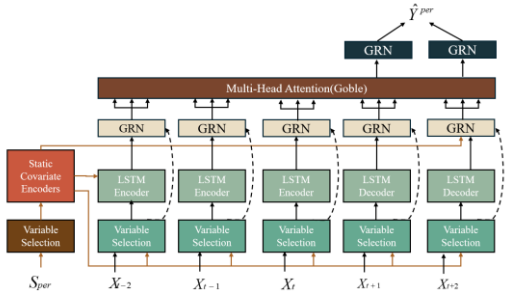


Fig. 5. TFT Periodic Trend Feature Modeling Block

b. TFT-res:

This block focuses on short-term fluctuations, employing local attention and a shallow LSTM to enhance rapid pattern modeling while suppressing over-smoothing (see Fig. 6).

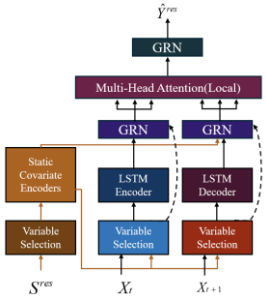


Fig. 6. TFT Disturbance Trend Feature Modeling block

The outputs of the two blocks are fused through gating to generate the node's long-term prediction, enabling collaborative utilization of multi-scale features.

D. Load Forecasting Output Block

After long-term and short-term modules, the two outputs are passed through fully connected layers and then integrated via a gating fusion mechanism to generate the final load prediction.

$$H_{f1} = W_{T1} g H_{PDM} + b_{T1} \tag{9}$$

$$H_{f2} = W_{T2} g H_{STGEA} + b_{T2} \tag{10}$$

$$H_g = H_{f1} g\mathrm{sig}(W_{s2} g H_{f2} + b_{s2}) + H_{f2} g\mathrm{sig}(W_{s1} g H_{f1} + b_{s1}) \tag{11}$$

W_{s2} and W_{s1} are weight parameters; b_{s1} and b_{s2} are biases; and H_g is the final output of the model.

III. Experiments and Analysis

A. Dataset

To validate the proposed model, a multimodal dataset was constructed based on publicly available data from NYISO [20], covering 11 load nodes in New York State. The dataset includes hourly load data, meteorological information (wind speed, wind direction, humidity, precipitation, cloud cover), and static spatial features (latitude–longitude coordinates, population density). Data from May 1, 2023, to May 8, 2025, were selected, yielding 195096 samples at a 60-minute resolution. The dataset was split into training, validation, and test sets with a 6:2:2 ratio.

B. Experimental Design

The experiments were conducted on a server equipped with a 13th Gen Intel(R) Core(TM) i7-13650HX CPU, an NVIDIA GeForce RTX 4080 GPU with 16 GB VRAM, and 60 GB RAM. The software environment consisted of Ubuntu 22.04, CUDA 12.1, Python 3.7, and PyTorch 2.3.0.

We design three experiments:(1) comparison with existing time series methods; (2) ablation by removing modules to test effectiveness; and (3) hyperparameter tuning on PDM factors (k=2/3/4) and graph neighbors. Two multi-step tasks are used: past 30 days (720h) to predict the next 1 day (24h) and 1 week (168h), with node 9 (N.Y.C) as the case study.

The model was trained with a batch size of 64, an initial learning rate of 0.001, and the Adam optimizer for up to 300 epochs. An early stopping strategy was applied, terminating training if validation performance did not improve for 30 consecutive epochs. The final evaluation was conducted on the test set.

C. Evaluation Metrics

To evaluate model performance, six common regression metrics are employed: Mean Absolute Error (MAE), Mean Squared Error (MSE), Root Mean Squared Error (RMSE), Mean Absolute Percentage Error (MAPE), Mean Squared Percentage Error (MSPE), and the Coefficient of Determination (R^2). MAE, MSE, and RMSE measure prediction deviation, with RMSE being more sensitive to outliers; MAPE and MSPE assess relative error, suitable for cross-scale comparison; and R^2 reflects the model's explanatory power of overall variance.

D. Experimental Results and Analysis

1) Performance Comparison with Existing Forecasting Models

This paper compares the proposed method with existing time series forecasting models on both single-day and weekly load prediction tasks. The comparison models are categorized into three groups: Transformer-based models (T-Graphormer [21], STD-PLM[22], ST-CALNet[23]);MLP[24]-based models (HiMoE[25], xLstm[26]); and other models (BOAM-MTGNN [27], STGNN[28],GSTGCN [29],STGMS [30],Lstm).The experimental results are presented in Table I.

In both single-day and weekly forecasting tasks, the proposed multi-scale spatio-temporal fusion model achieves superior or near-best performance across all metrics. In single-day forecasting, R^2 exceeds 0.95 and MAE falls below 20, showing clear advantages over strong baselines. Transformer-based models like STD-PLM and ST-CALNet perform better, while T-Graphormer struggles with long sequences. MLP-based models show limited ability to capture complex spatio-temporal dependencies, and graph neural network models such as BO-AM-MTGNN and GSTGCN perform well in spatial modeling but remain weak in temporal details.

In contrast, our model integrates periodic decomposition with multi-graph structures and inter-graph attention to fuse long-term trends, short-term fluctuations, and multi-scale dependencies. Compared with the best baselines, R^2 improves from 0.920 to 0.962 and MAPE decreases by 1.50% in weekly forecasting, while in single-day forecasting R^2 rises from 0.915 to 0.983 and MAPE decreases by 2.58%

TABLE I. COMPARISON RESULTS BETWEEN THE PROPOSED METHOD AND REPRESENTATIVE TIME SERIES MODELS (BLACK BOLD INDICATES THE BEST).

Models	Daily Power Load Forecasting						Weekly Power Load Forecasting					
	MSE	***MAE***	***RMSE***	***MSPE***	***MAPE***	***R2***	***MSE***	***MAE***	***RMSE***	***MSPE***	***MAPE***	***R2***
T-Graphormer	213.71	24.86	28.96	0.31%	3.96%	0.845	354.58	35.81	38.83	0.59%	5.64%	0.811
HiMoE	204.04	30.84	34.28	0.30%	3.88%	0.778	267.16	34.38	36.35	0.42%	5.44%	0.774
BO-AM-MTGNN	244.1	31.77	25.62	0.23%	3.66%	0.915	327.89	36.22	28.11	0.41%	6.77%	0.938
STGNN	264.92	25.65	26.28	0.38%	4.58%	0.844	273.36	22.86	26.53	0.65%	6.21%	0.821
STD-PLM	217.38	21.01	24.74	0.37%	3.77%	0.887	307.72	23.92	27.54	0.35%	4.86%	0.852
GSTGCN	245.07	26.43	25.65	0.32%	4.63%	0.912	265.34	33.11	26.29	0.55%	3.83%	0.920
ST-CALNet	231.05	21.86	25.23	0.34%	4.97%	0.903	336.37	25.17	22.34	0.33%	5.78%	0.910
xLstm	243.32	38.12	37.62	0.40%	5.88%	0.736	255.11	32.39	25.97	0.32%	7.61%	0.812
STGMS	195.85	27.52	36.99	0.41%	6.98	0.719	354.38	36.4	21.82	0.50%	6.73%	0.799
Lstm	312.22	32.57	34.75	0.56%	9.88%	0.702	260.74	33.18	26.15	0.44%	9.99%	0.773
Ours	**180.33**	**19.22**	**21.31**	**0.12%**	**2.05%**	**0.983**	**240**	**20.11**	**18.33**	**0.08**	**2.33%**	**0.962**

2) Ablation Experiments

To analyze the contribution of each module in the proposed model to load forecasting, an ablation study was conducted with six cases: MO1 removes the inter-graph attention (GEA) from the short-term prediction module; MO2 removes the geographic, similarity, and weather graph units; MO3 removes the PDM unit; MO4 replaces TFT with a standard Transformer; MO5 removes the TFT branch and adopts MGGCN-LSTM; and MO6 removes MGGCN+LSTM while retaining only TFT. The experimental results are summarized, as shown in Table II

TABLE II. ABLATION EXPERIMENT RESULTS (BOLD INDICATES THE BEST).

Ablations	Daily Power Load Forecasting						Weekly Power Load Forecasting					
	MSE	***MAE***	***RMSE***	***MSPE***	***MAPE***	***R2***	***MSE***	***MAE***	***RMSE***	***MSPE***	***MAPE***	***R2***
MO1	360.66	27.31	25.35	0.28%	3.58%	0.84	360.66	27.31	25.35	0.28%	3.58%	0.86
MO2	1450.77	53.18	38.07	1.2%	10.4%	0.56	1450.77	53.18	38.07	1.2%	10.41%	0.53
MO3	720.2	34.11	26.82	0.56%	5.79%	0.73	720.2	34.11	26.82	0.56%	5.79%	0.74
MO4	270.15	23.8	22.87	0.21%	2.84%	0.89	270.15	23.8	22.87	0.21%	2.84%	0.91
MO5	540.28	30.2	27.26	0.43%	4.61%	0.78	540.28	30.2	27.26	0.43%	4.61%	0.8
MO6	1180.63	50.55	34.37	1.01%	9.86%	0.62	1180.63	50.55	34.37	1.01%	9.86%	0.59
Ours	**180.33**	**19.22**	**21.31**	**0.12%**	**2.05%**	**0.983**	**240**	**20.11**	**18.33**	**0.08%**	**2.33%**	**0.962**

As shown in Table II, in single-day forecasting, MO2, MO3, and MO6 show larger performance drops, while MO1, MO4, and MO5 drop less, indicating that the multi-graph structure, PDM, and TFT contribute more to short-term forecasting. In weekly forecasting, MO2 and MO6 exhibit greater declines, while replacing TFT leads to smaller degradation, suggesting that the multi-graph structure and PDM play a more significant role in long-term prediction, with TFT and LSTM also providing certain benefits. Overall, only when the multi-graph structure, PDM, TFT, and LSTM work together can the model achieve its best performance, reaching MAE = 19.22 and R^2 = 0.983 for single-day forecasting, and MAE = 20.11 and R^2 = 0.962 for weekly forecasting, validating the rationality and effectiveness of the proposed design.

3) Validation on Hyperparameter

a. Comparative Experiment on the Number of Neighboring Nodes in Graph Neural Networks

To investigate the impact of neighboring node selection in GNN-based short-term spatio-temporal modeling, an experiment was conducted by varying the neighbor size k while keeping other modules unchanged. As shown in Table III, when k=2, the model achieves the lowest error metrics (MSE, MAE, RMSE) and the highest R^2, clearly outperforming k=3 and k=4 Here, k denotes the number of neighbors retained for each node. Larger k introduces more distant or weakly related nodes, adding noise and redundancy that dilute key features. In contrast, k=2 balances information coverage and noise suppression, preserving core spatial dependencies and enabling superior predictive performance.

b. Comparative Experiment on the Number of PDM Decompositions

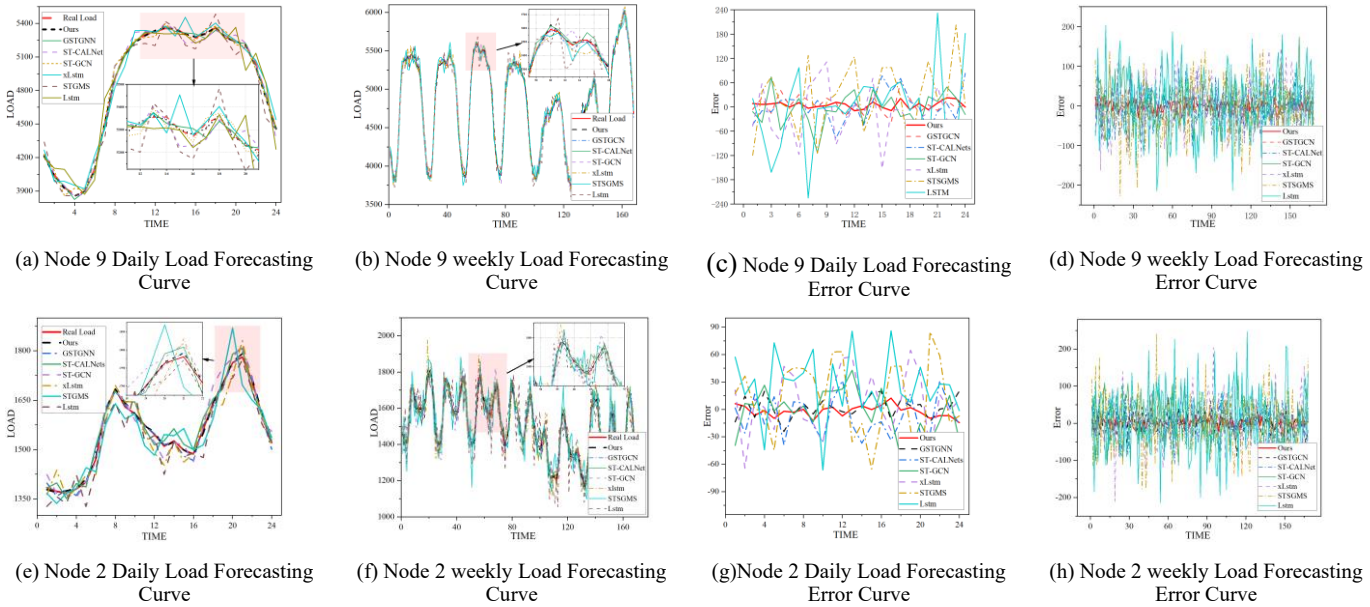
This study examines the impact of PDM decomposition numbers on model performance through comparative experiments (Table IV). Results show that P=2 yields the highest accuracy, followed by P=3, while P=1 (no decomposition) performs the worst. P=2 balances long-term trends and short-term disturbances, suppressing noise and redundancy. With P=1, features are mixed and patterns hard to extract, leading to poor performance. P=3 provides finer granularity but introduces irrelevant information and reduces generalization. Thus, P=2 offers the best trade-off, achieving optimal results for both daily and weekly forecasting tasks..

TABLE III. COMPARATIVE RESULTS OF NEIGHBOR NODE NUMBERS (BOLD INDICATES THE BEST).

k setting	Daily Power Load Forecasting						Weekly Power Load Forecasting					
	MSE	***MAE***	***RMSE***	***MSPE***	***MAPE***	***R2***	***MSE***	***MAE***	***RMSE***	***MSPE***	***MAPE***	***R2***
k=3	410.2	32.4	31.6	0.89%	4.65%	0.79	401.33	37.8	37.82	1.28%	7.58%	0.75
k=4	490.33	44.6	35.7	0.48%	5.44%	0.67	569.22	45.21	39.04	1.33%	8.89%	0.61
k=2	**180.33**	**19.22**	**21.31**	**0.12%**	**2.05%**	**0.983**	**240**	**20.11**	**18.33**	**0.08%**	**2.33%**	**0.962**

TABLE IV. COMPARISON RESULTS OF DIFFERENT PDM DECOMPOSITION NUMBERS (BOLD INDICATES THE BEST).

P setting	Daily Power Load Forecasting						Weekly Power Load Forecasting					
	MSE	***MAE***	***RMSE***	***MSPE***	***MAPE***	***R2***	***MSE***	***MAE***	***RMSE***	***MSPE***	***MAPE***	***R2***
P=1	720.33	57.44	87.32	8.89%	14.33%	0.49	890.32	67.21	89.87	8.89%	21.23%	0.51
P=3	320.33	24.33	32.13	0.56%	6.87%	0.79	430.32	41.23	38.43	1.01%	7.85%	0.72
P=2	**180.33**	**19.22**	**21.31**	**0.12%**	**2.05%**	**0.983**	**240**	**20.11**	**18.33**	**0.08%**	**2.33%**	**0.962**



(a) Node 9 Daily Load Forecasting Curve

(b) Node 9 weekly Load Forecasting Curve

(c) Node 9 Daily Load Forecasting Error Curve

(d) Node 9 weekly Load Forecasting Error Curve

(e) Node 2 Daily Load Forecasting Curve

(f) Node 2 weekly Load Forecasting Curve

(g)Node 2 Daily Load Forecasting Error Curve

(h) Node 2 weekly Load Forecasting Error Curve

Fig. 7. Electrical Load Forecasting Curves and Error Curves of the Proposed Model and the Existing Forecasting Models

4) Electrical Load Forecasting Visualization

The proposed load forecasting model, together with several competitive baseline methods, was applied to the test dataset, and the resulting prediction and absolute error curves are presented in Fig. 7. Panels (a) and (b) show the daily and weekly forecasts of Node 9, with (c) and (d) depicting the corresponding errors; panels (e) and (f) illustrate the daily and weekly forecasts of Node 2, while (g) and (h) provide their error curves. The comparison indicates that our approach achieves lower overall errors than the baselines and captures critical turning points in load variations more effectively. Moreover, the absolute errors remain consistently low and stable, demonstrating the robustness and adaptability of the model across different forecasting tasks.

IV. Conclusion

This paper proposes a multi-scale spatio-temporal fusion framework for multi-node short-term load forecasting, addressing the fusion modeling of temporal features and spatial dependencies. The model builds three complementary graphs (geographical, similarity, weather) and fuses them via inter-graph attention; temporally, a periodic decomposition with dual-branch Transformer captures long-term trends and short-term fluctuations. A gating mechanism integrates intra- and inter-node outputs into unified predictions. Experiments on the NYISO dataset show that the model surpasses existing methods across multiple metrics, better capturing complex spatio-temporal dependencies. Further studies on neighbor selection and decomposition numbers confirm its robustness. Overall, the approach improves forecasting accuracy, enhances its value for electric dispatching, and contributes to stable grid operation.

References

[1] Tan M, Hu C, Chen J, et al. Multi-node load forecasting based on multi-task learning with modal feature extraction[J]. Engineering applications of artificial intelligence, 2022, 112: 104856.

[2] Richter L, Lenk S, Bretschneider P. Advancing electric load forecasting: Leveraging federated learning for distributed, non-stationary, and discontinuous time series[J]. 2024.

[3] Juberias G, Yunta R, Garcia Moreno J, et al. A new ARIMA model for hourly load forecasting[C], 1999 IEEE Transmission and Distribution Conference (Cat. No. 99CH36333): Vol. 1. 1999: 314-319 vol.1.

[4] Chakhchoukh Y, Panciatici P, Bondon P. Robust estimation of SARIMA models: Application to short-term load forecasting[C], 2009 IEEE/SP 15th Workshop on Statistical Signal Processing. IEEE, 2009: 77-80.

[5] Breiman, L. Random Forests. Machine Learning 45, 5–32 (2001).

[6] Friedman, Jerome H. “Greedy Function Approximation: A Gradient Boosting Machine.” The Annals of Statistics, vol. 29, no. 5, 2001, pp. 1189–232. JSTOR,

[7] Taud, H., Mas, J. Multilayer Perceptron (MLP). In: Camacho Olmedo, M., Paegelow, M., Mas, JF., Escobar, F. (eds) Geomatic Approaches for Modeling Land Change Scenarios. Lecture Notes in Geoinformation and Cartography. Springer, Cham.2018

[8] Bisong, E. Recurrent Neural Networks (RNNs). In: Building Machine Learning and Deep Learning Models on Google Cloud Platform. Apress, Berkeley, CA. 2019

[9] M. Kaur and A. Mohta, "A Review of Deep Learning with Recurrent Neural Network," 2019 International Conference on Smart Systems and Inventive Technology (ICSSIT), Tirunelveli, India, 2019, pp. 460-465.

[10] S. Prakash, A. S. Jalal and P. Pathak, "Forecasting COVID-19 Pandemic using Prophet, LSTM, hybrid GRU-LSTM, CNN-LSTM, Bi-LSTM and Stacked-LSTM for India," 2023 6th International Conference on Information Systems and Computer Networks (ISCON), Mathura, India, 2023, pp. 1-6.

[11] Wang C, Wang Y, Ding Z, et al. A Transformer-Based Method of Multienergy Load Forecasting in Integrated Energy System[J]. IEEE Transactions on Smart Grid, 2022, 13(4): 2703-2714.

[12] GE Yaming, QIU Chenguang, XIE Lirong, et al. Research on Multi-energy Coupled Power Load Prediction Based on K-means Clustering and LSTM Model[J]. Modern Electric Power, 2025, 42(2): 369-376.

[13] ZHANG Pengfei, HU Bo, HE Jinsong, et al. Short-term Spatial Load Forecasting Method Based on Spatio-Temporal Graph Convolutional Network[J]. Automation of Electric Power Systems, 2023, 47(13):78-85.

[14] Li, Q., Han, Z., & Wu, X.- ming. (2018). Deeper Insights Into Graph Convolutional Networks for Semi-Supervised Learning.Proceedings of the AAAI Conference on Artificial Intelligence,32(1).

[15] HUANG Feihu, ZHAO Honglei, YI Peiyu, et al. An Improved Power Load Forecasting Method Based on Transformer[J].Modern Electric Power, 2023, 40(1): 50-58.

[16] Haiqi Zhang, Guangquan Lu, Mengmeng Zhan, and Beixian Zhang. 2022. Semi-Supervised Classification of Graph Convolutional Networks with Laplacian Rank Constraints. Neural Process. Lett. 54, 4 (Aug 2022), 2645–2656.

[17] Jianqing Liang, Min Chen, and Jiye Liang. 2024. Graph external attention enhanced transformer. In Proceedings of the 41st International Conference on Machine Learning (ICML'24), Vol. 235. JMLR.org, Article 1191, 29560–29574.

[18] Wang S, Wu H, Shi X, et al. Timemixer: Decomposable multiscale mixing for time series forecasting[J]. arXiv preprint arXiv:2405.14616, 2024.

[19] Lim, Bryan, et al. "Temporal fusion transformers for interpretable multi-horizon time series forecasting." International journal of forecasting 37.4 (2021): 1748-1764.

[20] NYISO.New York ISO independent system operator load data [EB/OL].NYISO(2023-12-20) [2023-12-20].http://www.nyiso.com/load-data.

[21] Bai H Y, Liu X. T-graphormer: Using transformers for spatiotemporal forecasting[J]. arXiv preprint arXiv:2501.13274, 2025.

[22] Huang Y, Mao X, Guo S, et al. Std-plm: Understanding both spatial and temporal properties of spatial-temporal data with plm[C]//Proceedings of the AAAI Conference on Artificial Intelligence. 2025, 39(11): 11817-11825.

[23] Cavus M, Allahham A. Spatio-Temporal Attention-Based Deep Learning for Smart Grid Demand Prediction[J]. Electronics, 2025, 14(13): 2514.

[24] Tolstikhin I O, Houlsby N, Kolesnikov A, et al. Mlp-mixer: An all-mlp architecture for vision[J]. Advances in neural information processing systems, 2021, 34: 24261-24272.

[25] Yu S, Deng P, Zhao Y, et al. HiMoE: Heterogeneity-Informed Mixture-of-Experts for Fair Spatial-Temporal Forecasting[J]. arXiv preprint arXiv:2412.00316, 2024.

[26] Beck M, Pöppel K, Spanring M, et al. xlstm: Extended long short-term memory[J]. Advances in Neural Information Processing Systems, 2024, 37: 107547-107603.

[27] Ding F, Hao S, Jiang M, et al. An improved graph neural network integrating indicator attention and spatio-temporal correlation for dissolved oxygen prediction[J]. Ecological Informatics, 2025, 87: 103126.

[28] Liu X, Chen J, Wen Q. A survey on graph classification and link prediction based on gnn[J]. arXiv preprint arXiv:2307.00865, 2023.

[29] Chen J, Liao S, Hou J, et al. GST-GCN: A geographic-semantic-temporal graph convolutional network for context-aware traffic flow prediction on graph sequences[C]//2020 IEEE international conference on systems, man, and cybernetics (SMC). IEEE, 2020: 1604-1609.

[30] Zhan H, Gao L, Sheng V S. Privacy-Preserving Unsupervised Spherical Text Embeddings[C]//2024 International Joint Conference on Neural Networks (IJCNN). IEEE, 2024: 1-8.

Short-term Hybrid Forecasting Method for Multi-type Customer Loads in Extreme Weather Based on BiLSTM-Seq2seq Model

Gaiping Sun
College of Electric Power Engineering
Shanghai University of Electric Power
Shanghai, China
gaiping_sun@shiep.edu.cn

Jiashuai Li
College of Electric Power Engineering
Shanghai University of Electric Power
Shanghai, China
ljs_77@163.com

Ronghui Liu
College of Electric Power Engineering
Shanghai University of Electric Power
Shanghai, China
liuronghuiyzy@126.com

Deyong Yu
Longgang Power Supply Company,State Grid Zhejiang Electric Power Co., Ltd.
Zhejiang, China
984157229@qq.com

Shunfu Lin
College of Electric Power Engineering
Shanghai University of Electric Power
Shanghai, China
shunfulin@shiep.edu.cn

Ziqi Ye
College of Electric Power Engineering
Shanghai University of Electric Power
Shanghai, China
kyezi13@163.com

***Abstract*—Extreme weather events may cause load fluctuations for multiple types of customers in a certain field, which poses challenges for load forecasting on the customer side. Therefore, this paper proposes a short-term load hybrid prediction method based on the Bilstm-Seq2Seq network. Firstly, the weather load dataset under extreme weather conditions is divided by meteorological standards, and a differentiated meteorological feature set is established for multiple types of customers through Pearson correlation analysis. Then, point prediction is conducted through the Bilstm-Seq2Seq model containing meteorological features to obtain the point prediction results and total prediction error data of the loads of multiple types of customers. The proposed model is verified using the total load dataset and its four subordinate loads in an eastern coastal city in China. The results show that the proposed model has high accuracy in both point prediction and probability prediction.**

Keywords—extreme weather, multi-type customer loads, BiLSTM-Seq2seq, short-term forecasting

I. INTRODUCTION

Extreme weather events, such as heat waves and cold waves, have caused many power limitations and outages worldwide [1-3]. Due to the advancement of low-carbon innovations on the customer side, the large-scale access of renewable energy on the customer side increases the uncertainty of the customer-side load [4]. This characteristic is even more obvious in extreme weather scenarios, which increases the difficulty of customer-side load forecasting [5]. Fig. 1 shows the load curves of an area and its subordinate loads in different scenarios, which indicates that extreme weather affects different types of loads to varying degrees, but all cause load fluctuations. Therefore, it is necessary to design a forecasting model for multi-type customer loads in extreme weather scenarios to perform accurate and efficient point prediction and probabilistic forecasting.

Load or power forecasting has formed a mature technical system, owing to ongoing advancements in deep-learning, neural networks employing deep learning techniques are extensively utilized in predicting short-term load demands, including: recurrent neural network [6] (RNN) and convolutional neural network [7] (CNN), which have superb data processing and automatic feature extraction capabilities. Among them, RNNs designed based on temporal structure, such as long-short term memory neural network [8] (LSTM) and gated recurrent unit neural network [9] (GRU), can be used to learn the intrinsic time-varying laws of load data to improve the model prediction capability. Some references utilize the advantage of CNN in extracting local features to establish CNN-RNN combined model to predict short-term loads [10-11]. However, an excessive number of convolutional operations results in a substantial rise in computational demand. Although the above deep learning neural networks can effectively improve the load prediction accuracy, they often rely on a large number of data samples and powerful arithmetic power, and suffer from poor robustness and overfitting problems [12]. However, for longer load time series, RNNs have limited memory storage and are difficult to capture the long-periodic characteristics of loads [13]. With the continuous advancement of technology, sequence to sequence (Seq2Seq) models have been gradually applied to the field of load forecasting with good results [14]. The Seq2Seq [15] is a deep-learning framework for solving sequence mapping relations with an encoder-decoder structure that establishes a mechanism for transferring temporal information between predicted moments and considers the temporal correlation of the output sequence.

979-8-3315-5472-9/25/$31.00 ©2025 IEEE

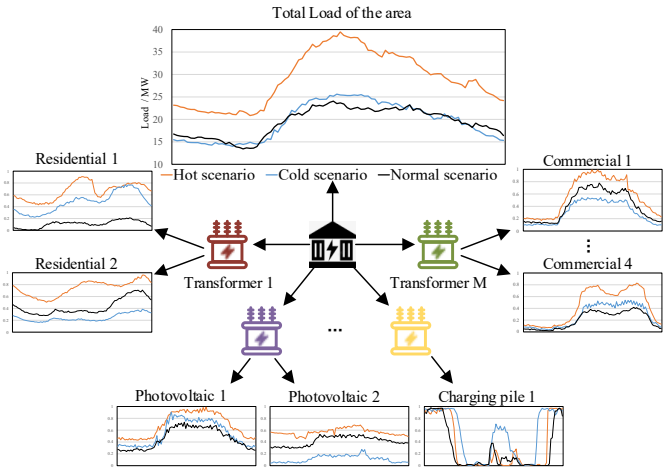


Fig. 1. Hierarchical structure of multi-type loads at distribution-level.

In summary, this paper proposes a short-term hybrid forecasting method for multi-type customer loads in extreme weather scenarios based on BiLSTM-Seq2seq model. First, the sensitivity of traditional and new type loads to meteorological factors in extreme weather scenarios, are analyzed by correlation analysis, and the high correlation features sets of multi-type customer loads are obtained; Then, the BiLSTM-Seq2seq network is used to build the point forecasting model and get the historical forecast value and total forecasting error of multi-type load. The framework of the proposed method is illustrated in Fig. 2.

II. Characteristic Analysis of Multi-type Loads

According to the meteorological criteria given by the China Meteorological Administration, a cold wave event occurs when the minimum temperature is expected to drop by at least 8°C, 10°C, and 12°C within 24, 48, and 72 hours, respectively, while the minimum temperature persists at 4°C and below. Hot weather, which is manifested by the daily maximum temperature rising to more than 35°C, is considered as a high temperature event, and when the hot weather lasts for three days or longer, it is referred to as a heat wave event [26]. In the two extreme scenarios mentioned above, the demand for electricity of the rerises, thus making the load curve have higher peaks and valleys, with the hot scenario being the most extreme.

Aiming at the problem of the adaptability of fixed temperature thresholds to regional differences in temperature percentile distributions in a large-scale spatial range, existing studies have shown that the use of the relative threshold method can more effectively characterize the differences in regional climate characteristics [17-18]. In this paper, based on the definition of the literature [17], the identification criteria for regional high temperature events are constructed as follows: when the average daily maximum temperature (Tmax,a) on day-a in a region exceeds the 98% quantile (T98) of the historical climatic data in the region, it is judged as a regional high temperature day. On this basis, if the consecutive high temperature days last for 3 days or more, it is defined as a regional heat wave weather event. Whether the tH-th day is a heat wave weather day is determined by calculating the heat wave event judgment value Hw in the following equation. When HW > 0, heat wave weather occurs on day tH.

$$H_{\mathrm{W}} = \sum_{i_{\mathrm{H}}=i_{\mathrm{H}}-2}^{t_{\mathrm{H}}} u\left[\sum_{a=i_{\mathrm{H}}}^{i_{\mathrm{H}}+2} u(T_{\max,a} - T_{98}) - 2\right] \quad (1)$$

where: iH is the number of day sequences; u is the unit step function.

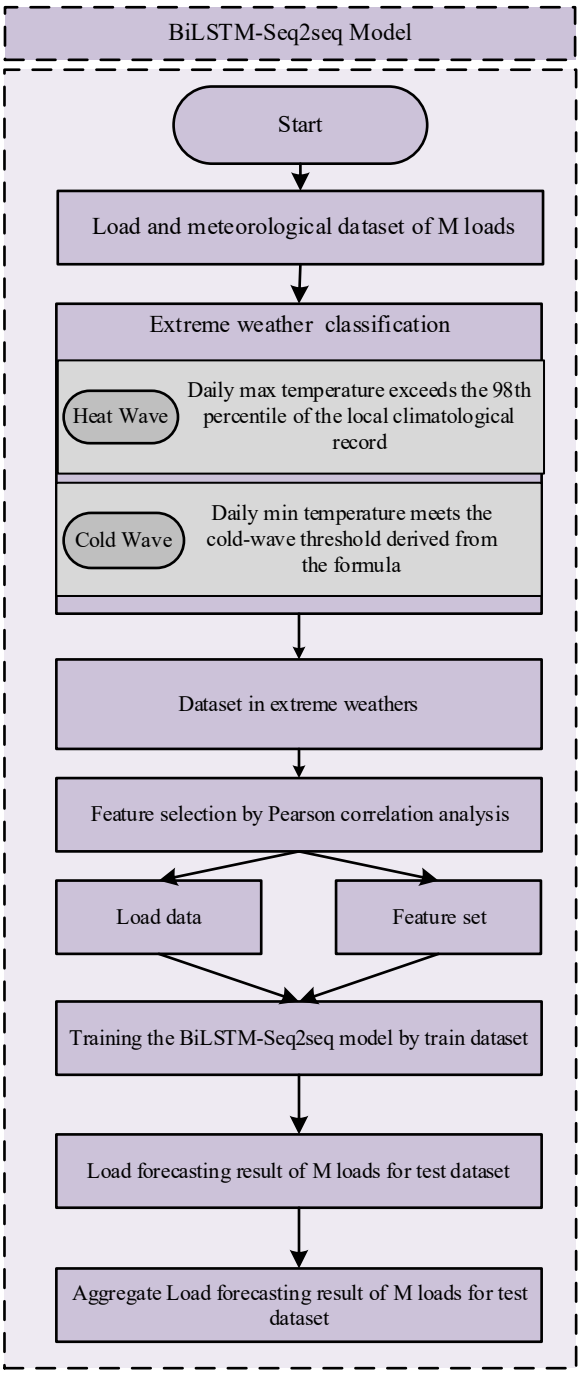


Fig. 2. The framework of the proposed method

As for the cold wave weather it is judged by calculating the cold wave event judgment value Cb in the following equation. When Cb > 0, cold wave weather occurs on day b.

$$C_b = u(4 - T_{\min,b})[u(T_{\min,b-1} - T_{\min,b} - 8℃) + u(T_{\min,b-2} - T_{\min,b} - 10℃) \prod_{i_c=b-1}^{b} u(T_{\min,i_c-1} - T_{\min,i_c}) + u(T_{\min,b-3} - T_{\min,b} - 12℃) \prod_{i_c=b-2}^{b} u(T_{\min,i_c-1} - T_{\min,i_c}) \quad (2)$$

When the proportion of observation stations meeting the single-station cold wave meteorological criteria in a region reaches or exceeds the preset threshold, it is judged as a regional cold wave weather. According to the study of climate characteristics in mid-latitude regions [19-20], this threshold parameter is set to 20% in this paper.

TABLE I. METEOROLOGICAL FEATURES SELECTION RESULTS

Customer Information	Extremely hot scenario	Extremely cold scenario
Photovoltaic	T, H, I	I
Commercial	T, H, I	T, H, I
Residential	T, DT	I
Office	T, H, I	H, I

According to the correlation analysis, meteorological factors with correlation $|\rho xy|>0.3$ are selected as point prediction model input features in this paper, and the specific feature selections are shown in Table 1, where T denotes temperature, H denotes relative humidity, I denotes solar radiation degree, DT denotes dew point temperature, S denotes largest wind speed, and TP denotes thunderstorm probability.

III. METHODOLOGY

A. BiLSTM unit

In extreme weather scenarios, factors may have an impact on meteorological factors at adjacent moments, leading to fluctuations in electricity loads for multi-type customers, which requires that the model needs to learn more fully the time-series information in meteorological features. BiLSTM is a variant of RNN, which combines LSTM and bidirectional structure. Its forgetting gate, input gate and output gate can dynamically process the historical and current meteorological information and filter the key time-series information for load forecasting. The structure of BiLSTM unit is shown in Fig. 3

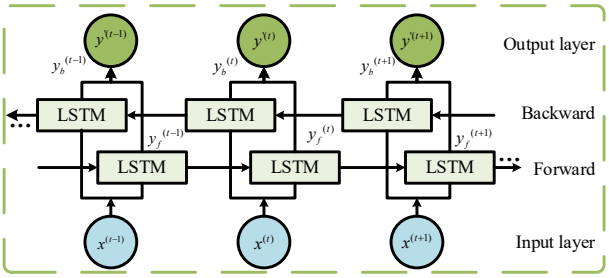


Fig. 3. The structure of BiLSTM.

The calculation equations of BiLSTM are as follows:

$$f^{(t)} = \sigma\left(W_f[y^{(t-1)}, x^{(t)}] + b_f\right) \quad (3)$$

$$i^{(t)} = \sigma\left(W_i[y^{(t-1)}, x^{(t)}] + b_i\right) \quad (4)$$

$$u^{(t)} = \tanh(W_u[y^{(t-1)}, x^{(t)}] + b_u) \quad (5)$$

$$c^{(t)} = f_t \cdot c^{(t-1)} + i^{(t)} \cdot u^{(t)} \quad (6)$$

$$o^{(t)} = \sigma\left(W_o[y^{(t-1)}, x^{(t)}] + b_o\right) \quad (7)$$

$$y^{(t)} = o^{(t)} \cdot \tanh\left(c^{(t)}\right) \quad (8)$$

$$y^{(t)} = o^{(t)} \cdot \tanh\left(c^{(t)}\right) \quad (9)$$

where W denote weights corresponding to each gate within the neural network. Bias matrices are also represented bf, bi, bu, bo and by′; The activation functions utilized are sigmoid(σ) and tanh. By integrating forward and backward results (yf and yb) of LSTM, the BiLSTM produces the output as. The function g serves as the activation function for the output layer.

B. Seq2seq framework

The RNN-based network forecasting model usually extracts the time series information yt from the historical data xt and splice it with the input vector xt+τ (τ{1, 2,…,To }) at the forecasting moments, and input it into the fully-connected layer to get the final load forecasting value y't+τ. When forecasting loads at multiple time steps in the future, this processing method cannot utilize the unique temporal structure of RNN network to establish a time series transfer mechanism of loads between forecasting moments, and it is difficult to ensure the time-sequentiality of loads at the forecasting time.To solve this problem, this paper introduces the Seq2Seq forecasting framework, whose unique encoding-decoding structure allows the input dimensions of the encoder and decoder to be different, combining with BiLSTM units to simultaneously extract load timing features for both the historical and future time periods. The framework of Seq2seq time series forecasting model is shown in Fig. 4.

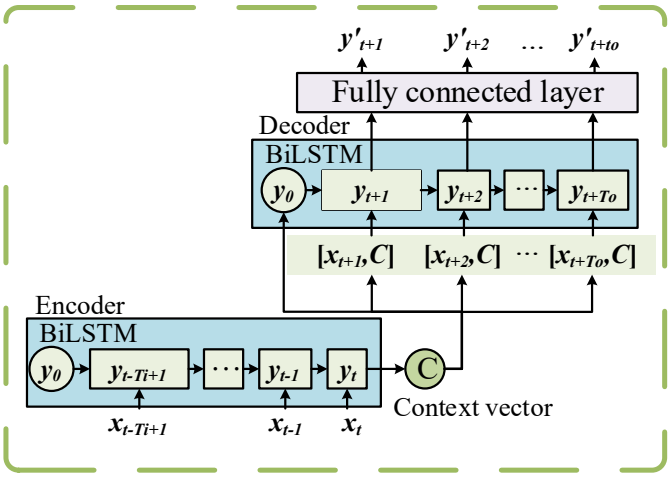


Fig. 4. The structure of Seq2seq.

The modules interface with each other through a fixed dimensional information vector C. The encoder extracts information C from the time-series transfer mechanism of the historical sequence xt as the input to the decoder, and combines the decoded information C with the known information sequence Xt+1:t+To to establish the time-series information transfer mechanism between future prediction moments. Then the hidden state vector yt+τ (τ{1, 2,…,To }) at each forecasting moment can be obtained; Finally, the load forecast values y't+τ at each forecasting moment are obtained through the fully connected layer.

IV. Case Analysis

A. Description of Datasets and Evaluation Metrics

The following case studies are all based on the following scenarios:

1) Scenario 1: Extremely hot scenario.

2) Scenario 2: Extremely cold scenario.

The real load-meteorological dataset of an area in an east coast city of China is selected to verify the validity of the model proposed in this paper. There are 4 types of loads in this area, with a sampling period of 15 min and a time span from July 1, 2022 to June 30, 2023. The evaluation metrics are divided into point forecast evaluation metrics and probabilistic forecast evaluation metrics, including Root Mean Squared Error (RMSE), Mean Absolute Percentage Error (MAPE), R-Squared (R2). The above metrics can be obtained by the following equations:

$$RMSE = \sqrt{\frac{1}{n}\sum_{i=1}^{n}\left(y_i^{'} - y_i\right)^2} \tag{10}$$

$$MAPE = \frac{1}{n}\sum_{i=1}^{n}\frac{|\,y_i^{'} - y_i\,|}{y_i} \times 100\% \tag{11}$$

$$R^2 = 1 - \frac{\sum_{i=1}^{n}\left(y_i^{'} - y_i\right)^2}{\sum_{i=1}^{n}\left(\bar{y} - y_i\right)^2} \tag{12}$$

where denotes the count of samples, denotes the observed actual load value, denotes the forecasted load value, and denotes the average of load.Point Forecasting performance analysis

TABLE II. THE NETWORK PARAMETERS AND HYPERPARAMETER SETTINGS

Parameter	value	Parameter	value
HiddenLayer Dimension	64	Batch Size	32
Input Dimension	Varies by user	Learning Rate	0.0001
Layers	2	Epochs	100
Dropout Rate	0.5	Loss Function	MSE
Output Step	96 steps	Optimizer	adam
Neurons number	256	Activation Function	Relu
		Early Stopping patience	20

To evaluate the performance of the BiLSTM-Seq2seq point prediction model used in this paper, four models were used for comparison with it, including LSTM-Seq2seq and GRU-Seq2seq.The specific network settings and hyperparameter settings of the model used in this paper are shown in Table 2. The point forecasting results of the proposed model in this paper for multi-type customer loads in extreme weather scenarios are shown in Fig. 5 and Fig. 6, where it can be seen that the prediction curves of the model proposed in this paper can follow the actual load changes well on the whole.

The comparison results of the point forecasting performance of each model are shown in Table 3. Firstly, accurate prediction results were achieved by all four models, which indicates that the original data exhibit strong regular patterns, which allows the models to better fit the real situation. The BiLSTM- seq2seq model used in this paper achieves the best prediction results on all four metrics for both scenarios, and the prediction performance of the other three models presents that LSTM-Seq2seq outperforms BiLSTM, while GRU-Seq2seq performs the worst. In Scenario 1, the average values of RMSE, MAPE, and R2 of the BiLSTM-Seq2seq are improved by 15.932 kW, 0.392%, and 0.012 compared to GRU-Seq2seq; In Scenario 2, these values are 16.284 kW, 0.603% and 0.012 respectively. This indicates that BiLSTM is able to learn the bi-directional information of the time series well, and the Seq2seq framework can enhance the model's ability to learn the correlation between time series points; All of the above can effectively help the model to improve the prediction accuracy. In addition, it can be found that the prediction performance of the Transformer model is slightly better than that of the proposed model in both scenarios, but the prediction time of the Transformer model is longer. Through the above analysis, the point prediction model used in the subsequent discussion part of this paper is the BiLSTM-Seq2seq model.

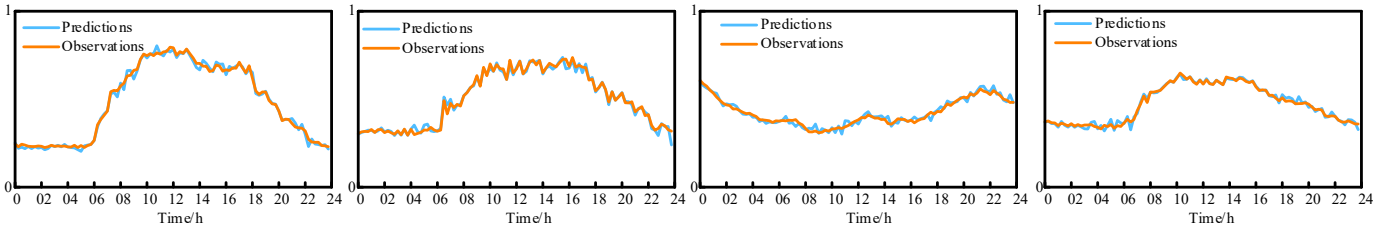


Fig. 5. The point forecasting results for multi-type customer loads in extremely hot scenario.

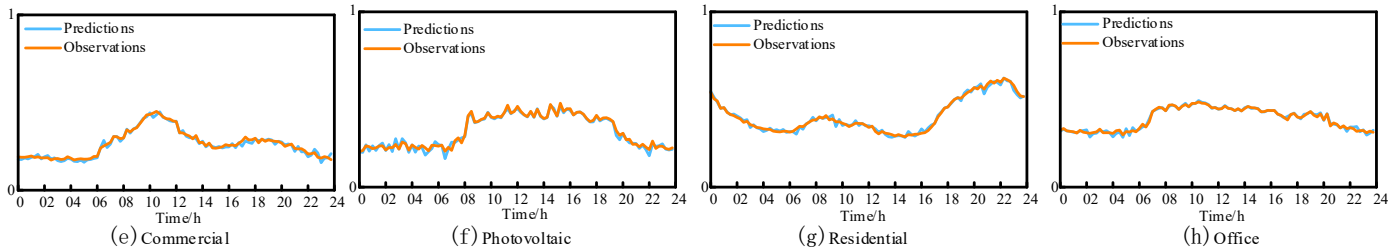


Fig. 6. The point forecasting results for multi-type customer loads in extremely cold scenario

TABLE III. THE COMPARISON OF POINT FORECASTING PERFORMANCE

Scenario	Model	RMSE (kW)	MAPE (%)	R^2
Scenario 1	BiLSTM-Seq2seq	**32.615**	**3.212**	**0.977**
	LSTM-Seq2seq	43.441	3.535	0.973
	GRU-Seq2seq	48.547	3.604	0.965
	BiLSTM	46.673	3.568	0.969
Scenario 2	BiLSTM-Seq2seq	**37.468**	**4.067**	**0.972**
	LSTM-Seq2seq	48.109	4.565	0.968
	GRU-Seq2seq	53.752	4.670	0.960
	BiLSTM	48.337	4.516	0.967

V. CONCLUSION

A short-term hybrid forecasting method at the distribution level for substation load and multi-type loads in extreme weather scenarios based on BiLSTM-Seq2seq model is proposed in this paper. The main conclusions of this study are as follows:

1) The sensitivity of traditional and new type loads to meteorological factors in extreme weather scenarios, are analyzed by correlation analysis. The high correlation features of multi-type loads are obtained by this strategy.

2) A point forecasting model is constructed based on the BiLSTM-Seq2seq network, which fully learns the historical and future bidirectional time series information. The model has more accuracy compared to other models.

3) Dataset from 4 types in the coastal regions of East China were employed to assess the performance of the proposed model. The results of the comparison indicated that our model surpassed all benchmark models, yielding the most superior interval forecasting outcomes for aggregate multi-type loads.

This study provides a useful research method for short-term load forecasting and grid management at the distribution level in extreme weather scenarios. The forecasting method proposed in this paper can effectively take into account the load volatility caused by meteorological fluctuations in extremely weather scenarios. However, due to data limitations, only four types of loads and two extreme meteorological scenarios were considered in this paper, while further consideration of more types of loads as well as other extreme meteorological scenarios will be carried out in future studies.

REFERENCES

[1] Zhang Yongjun, Yi Yingqi, Li Licheng, et al. Prospect of new low-voltage distribution system technology driven by carbon emission peak and carbon neutrality targets[J]. Automation of Electric Power Systems, 2022, 46(22): 1-12.

[2] Lian Xianglong,Qian Tong,Li Zepeng, et al.Resilience assessment for power system based on cascading failure graph under disturbances caused by extreme weather events.[J].International Journal of Electrical Power & Energy Systems,2023,Vol.145: 108616(1-9).

[3] Zhijun Qin,Xinwei Chen,Yunhe Hou, et al.Coordination of Preventive, Emergency and Restorative Dispatch in Extreme Weather Events[J].IEEE Transactions on Power Systems,2022,Vol.37(4): 2624-2638.

[4] ZHANG Yongjun, YI Yingqi, LI Licheng, et al. Prospect of New Low-voltage Distribution System Technology Driven by Carbon Emission Peak and Carbon Neutrality Targets[J]. Automation of Electric Power Systems, 2022, 46(22): 1-12.

[5] KONG Xiangyu, MA Yuying, AI Qian, et al. Review on Power Consumption Characteristics Modeling and Load Forecasting of Power Consumption for Diverse Users in New Power System[J]. Automation of Electric Power Systems, 2023, 47(13):2-17.

[6] KONG Xiangyu, MA Yuying, AI Qian, et al. Review on Power Consumption Characteristics Modeling and Load Forecasting of Power Consumption for Diverse Users in New Power System[J]. Automation of Electric Power Systems, 2023, 47(13):2-17.

[7] Akhter, Muhammad Naveed;Mekhilef, Saad;Mokhlis, Hazlie;Ali, Raza;Usama, Muhammad;Muhammad, Munir Azam;Khairuddin, Anis Salwa Mohd.A hybrid deep learning method for an hour ahead power output forecasting of three different photovoltaic systems.[J].Applied Energy,2022,Vol.307: 118185.

[8] Tariq Limouni;Reda Yaagoubi;Khalid Bouziane;Khalid Guissi;El Houssain Baali.Accurate one step and multistep forecasting of very short-term PV power using LSTM-TCN model[J].Renewable Energy,2023,Vol.205: 1010-1024.

[9] Kai Ma;Xuefeng Nie;Jie Yang;Linlin Zha;Guoqiang Li;Haibin Li.A power load forecasting method in port based on VMD-ICSS-hybrid neural network[J].Applied Energy,2025,Vol.377: 124246.

[10] Shiyun Zhang, Runhuan Chen, Jiacheng Cao, Jian Tan. A CNN and LSTM-based multi-task learning architecture for short and medium-term electricity load forecasting[J].Electric Power Systems Research,2023,Vol.222: 109507.

[11] Ali Agga;Ahmed Abbou;Moussa Labbadi;Yassine El Houm.Short-term self consumption PV plant power production forecasts based on hybrid CNN-LSTM, ConvLSTM models[J].Renewable Energy,2021,Vol.177: 101-112.

[12] ZHAO Jinquan, XIA Xue, XU Chunlei, et al. Review on application of new generation artificial intelligence technology in power system dispatching and operation[J]. Automation of Electric Power Systems, 2020, 44(24): 1-10(in Chinese).

[13] ZHAO Bing,WANG Zengping,JI Weijia,et al.A short-term power load forecasting method based on attention mechanism of CNN-GRU[J].Power System Technology,2019,43(12):4370-4376(in Chinese).

[14] Yuanshi Zhang;Wenyan Qian;Yujian Ye;Yang Li;Yi Tang;Yu Long;Meimei Duan.A novel non-intrusive load monitoring method based on ResNet-seq2seq networks for energy disaggregation of distributed energy resources integrated with residential houses[J].Applied Energy,2023,Vol.349: 121703.

[15] Pengfei Zhao, Weihao Hu, Di Cao, Zhenyuan Zhang, Wenlong Liao, Zhe Chen, Qi Huang. Enhancing multivariate, multi-step residential load forecasting with spatiotemporal graph attention-enabled

transformer[J].International Journal of Electrical Power & Energy Systems,2024,Vol.160: 110074.

[16] LI J H, CHEN B. A combined probabilistic forecasting method for photovoltaic power using an improved Markov chain[J]. IET Generation, Transmission & Distribution, 2019, 13(19): 4364-4373.

[17] YAN Daobo,WEN Jinyu,DU Zhi,et al.Analysis of Texas blackout in 2021 and its enlightenment to power system planning management[J].Power System Protection and Control,2021,49(9):121-128 (in Chinese).

[18] ERDIWANSYAH,MAHIDIN,HUSIN H,et al.A critical review of the integration of renewable energy sources with various technologies[J].Protection and Control of Modern Power Systems,2021,6(1):3.

[19] ZHANG Guanglun,ZHONG Haiwang,TAN Zhenfei,et al.Texas electric power crisis of 2021 warns of a new blackout mechanism[J].CSEE Journal of Power and Energy Systems,2022,8(1):1-9.

[20] ORLOV A,SILLMANN J,VIGO I.Better seasonal forecasts for the renewable energy industry[J].Nature Energy,2020,5(2):108-110.

Multiscale Modeling and Electrochemical Validation of PEM Electrolyzer-Coupled Hybrid Energy Storage Systems

Haotian MA
Institute for Materials Discovery
University College London
London, United Kingdom
Haotian.Ma.24@ucl.ac.uk

Shangfeng DU
Hydrogen & Fuel Cell Research Center
University of Birmingham
Birmingham, United Kingdom
S.Du@bham.ac.uk

Georgios Nikiforidis
Institute for Materials Discovery
University College London
London, United Kingdom
Georgios.Nikiforidis@ucl.ac.uk

***Abstract*—This paper presents a multiscale modeling and electrochemical validation framework for a decentralized hybrid energy storage system (HESS) integrating a proton exchange membrane (PEM) water electrolyzer, lithium-ion battery, supercapacitor, and photovoltaic (PV) generation. The proposed system enables autonomous energy management by dynamically coordinating short and long-term storage based on real-world environmental and load data.**

At the component level, the PEM electrolyzer is modeled using thermodynamic and kinetic equations, capturing reversible electrochemical potential, activation, ohmic, and concentration losses under varying temperature and pressure. The lithium-ion battery and supercapacitor are represented via dynamic and equivalent-circuit models, respectively, with hierarchical control logic ensuring fast transient response and long-term resilience.

One-year simulations at 15-minute resolution demonstrate the system achieves near-complete off-grid operation with grid interaction below 2%. The electrolyzer operates at 87% thermal efficiency at 2 A/cm² and maintains hydrogen purity above 99.2%. The supercapacitor absorbs 5 kW load transients within 50ms, preserving battery state-of-charge between 20% and 80% and preventing degradation. Control transitions remain stable with voltage overshoot below 3%.

Sensitivity analysis shows that a ±10°C stack temperature variation leads to only ±2.5% efficiency change, and moderate pressure increase improves hydrogen compression efficiency by 5% without electrical losses. These results validate the system's technical feasibility and operational robustness. Future work will incorporate degradation modeling, techno-economic analysis, and hardware-in-the-loop validation to support real-world deployment in residential microgrids and data centers.

***Index Terms*—Hybrid Energy Storage System (HESS), Proton Exchange Membrane Water Electrolyzer (PEMWE), Membrane Electrode Assembly (MEA), Lithium-ion Battery Modeling, Supercapacitor Dynamics, Hierarchical Energy Management, Off-grid Photovoltaic System**

I. Introduction

Hybrid electrochemical energy storage systems (HESS) integrate various electrochemical technologies such as lithium-ion batteries, supercapacitors, and proton exchange membrane water electrolysers (PEMWE) and offer an effective solution for balancing short- and long-term power fluctuations in renewable-powered systems. Existing literature demonstrates promising configurations using hydrogen-based systems for grid independence, but often lacks either short-term storage elements or validation via experimental data [1]. Most system-level models omit realistic load dynamics and control interactions among heterogeneous storage devices [4].

To address these gaps, this chapter develops a comprehensive MATLAB/Simulink model of a decentralized HESS tailored for photovoltaic (PV)-dominated off-grid applications. The system integrates a lithium-ion battery and a supercapacitor for short- and mid-term responses, together with a PEM water electrolyser coupled with a hydrogen tank for seasonal-scale storage [3]. Environmental and load inputs are obtained from real meteorological data in England, United Kingdom, with simulations conducted over one year at a 15-minute resolution [5].

The modeling approach features hierarchical control logic and detailed component-level subsystems for the lithium-ion battery, supercapacitor, and PEM electrolyser. The battery model incorporates SOC-dependent power limit and dual-mode inverter control. The electrolyser is validated through electrochemical principles including thermodynamic, kinetic, and ohmic contributions. The simulation evaluates system performance under variable solar and demand conditions, emphasizing autonomy, resilience, and real-time dynamic response [11].

The rest of this paper is organized as follows: Section II introduces the overall system architecture and energy management strategy; Section III presents detailed mathematical models and Simulink implementations of each subsystem; Section IV describes configuration and validation of the PEM electrolyser; Section V presents simulation results; and Section VI concludes the paper.

II. System Architecture and Control Logic

The proposed hybrid energy storage system (HESS) is composed of four main subsystems:

979-8-3315-5472-9/25/$31.00 ©2025 IEEE

- **Short-Term Storage:** A lithium-ion battery handles daily load fluctuations, and a supercapacitor provides rapid response to transient power spikes.
- **Long-Term Storage:** A proton exchange membrane (PEM) electrolyzer converts surplus PV power into hydrogen.
- **Power Electronics and Control:** DC/DC converters and inverters interface each storage element with the household bus, coordinated by a central Stateflow chart in MATLAB/Simulink.

Figure 1 illustrates the overall system layout and power flow direction.

The modular Simscape™ implementation enables plug-and-play testing of different component sizes and control setpoints, facilitating rapid sensitivity analysis and optimal sizing studies.

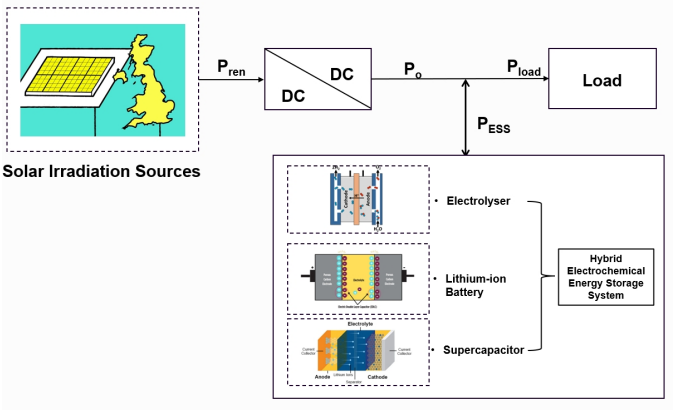


Fig. 1. System Architecture and Control Strategy of the Proposed Hybrid Energy Storage System

III. Description of the Partial Models

The mathematical models and the implementation in Matlab/Simulink are described. The Matlab/Simulink version R2024b has been used. The components are considered individually.

A. Electrolyser System Model

For this HESS model, a Proton Exchange Membrane (PEM) electrolyser has intrinsic ability to cope with transient electrical power variations (especially important when fed by fluctuating renewable energies as in the designated use case).

They provide a high degree of purity of gasses and the potential to compress hydrogen at a higher pressure within the unit and with a higher safety level.

A single PEM electrolysis cell can mathematically be described as follows [1]:

$$V(T,p) = e_{\text{rev}}(T,p) - e_{\text{rev}}(T,p)\,\exp\!\left(\frac{-5.1}{0.02\,\text{A}}\right) + I\,R_i(T,p) \tag{1}$$

The formula for a complete stack is given by [2]:

$$V(T,p) = I\,\frac{n_s}{n_p}\,R_i(T,p) + n_s\,e_{\text{rev}}(T,p) \tag{2}$$

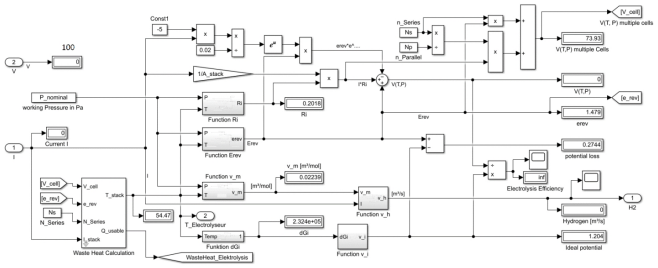


Fig. 2. Simulink Model of the PEM Electrolyser and Experimental Test Rig

with n_s as the number of cells in series and n_p as the cells in parallel, respectively. The reversible potential $e_{\text{rev}}(T,p)$ and the PEM cell resistance $R_i(T,p)$ are temperature- and pressure-dependent [2]:

$$e_{\text{rev}}(T,p) = e_{\text{rev0}} + \frac{R\,(273.15\,\text{K} + T)}{2F}\,\ln\!\left(\frac{p}{p_0}\right) \tag{3}$$

$$R_i(T,p) = R_{i0} + k\,\ln\!\left(\frac{p}{p_0}\right) + dR_i\,(T - T_0) \tag{4}$$

where R is the universal gas constant, T the temperature inside the electrolyser, F the Faraday constant, p and p_0 the working and ambient pressures respectively, and $k = 0.0395\,\text{V}\,\text{A}^{-1}$ is a derived curve-fitting parameter [12].

B. Lithium-Ion Battery System Model

The lithium-ion battery is the main storage for short-term electrical power demand. Generated surplus energy of the PV system is stored there as long as the upper charge limit is not reached. If the upper charge limit is reached, the remaining surplus energy of the PV system is used for the production of hydrogen [10]. Surplus energy produced by the fuel cell which is not used to cover the actual household energy demand is stored in the lithium-ion battery as long as the predefined SoC from which the fuel cell is turned off is not reached.

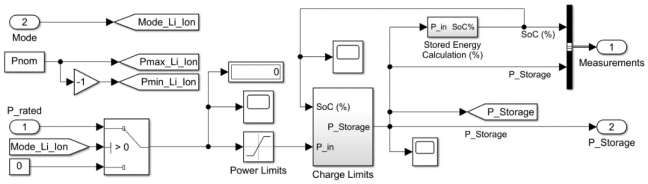


Fig. 3. Simulink Model of the Lithium-ion Battery

$$E(k+1) = \begin{cases} E(k) + P_{\text{in}}(k)\cdot\eta_{\text{chg}}\cdot\Delta t, & \text{if charging} \\ E(k) - \dfrac{P_{\text{in}}(k)}{\eta_{\text{dis}}}\cdot\Delta t, & \text{if discharging} \end{cases} \tag{5}$$

where $E_{(k)}$ denotes the Energy stored in the battery at time step k,$P_{\text{in}}(k)$ is the input power at time step k,η_{chg} is the Charging efficiency varies between 0 and 1,Δt is the duration of the time step,$E(k+1)$ is the updated energy stored in the battery at time step $k+1$.

The state of charge (SOC) of the battery is defined as:

$$SOC(k) = \frac{E(k)}{E_{\text{max}}} \tag{6}$$

where $E_{(max)}$ is the maximum energy capacity of the battery, SOC(k) $\in$ [0, 1] represents the normalized state of charge.

1) Power Limiting Module: The charge and discharge power of the battery system is limited based on the current state of charge (SOC) to prevent overcharging or overdischarging.The SOC-dependent maximum charging and discharging powers are defined as:

$$\begin{cases} P_{\text{max, chg}}(SOC) & = P_{\text{chg, rated}} \cdot f_{\text{chg}}(SOC) \\ P_{\text{max, dis}}(SOC) & = P_{\text{dis, rated}} \cdot f_{\text{dis}}(SOC) \end{cases} \tag{7}$$

where $f_{\text{chg}}(\text{SOC})$ and $f_{\text{dis}}(\text{SOC})$ are interpolation functions or lookup tables that define the allowable power limits as a function of SOC.

The actual input power P_{in} is obtained by saturating the reference power P_{ref} within the SOC-dependent limits:

$$P_{\text{in}} = \text{sat}\left(P_{\text{ref}}, -P_{\text{max,dis}}(\text{SOC}), P_{\text{max,chg}}(\text{SOC})\right) \tag{8}$$

The stored energy is used to cover the energy demand within time periods of insufficient PV supply (night time, clouds or very high energy demand) and during occurrence of rapid load changes during periods of time where the fuel cell is activated. The key parameter which has to be considered for energy autonomous operation is the maximum energy provided during the considered time period. This parameter depends on household's electrical loads and the energy usage preferences of the fitted household.

C. EDLC Supercapacitor System Model

The supercapacitor model used in this study is based on the Maxwell BCAP3000 module. It is implemented in Simulink using a custom block that incorporates the voltage-dependent capacitance behavior.

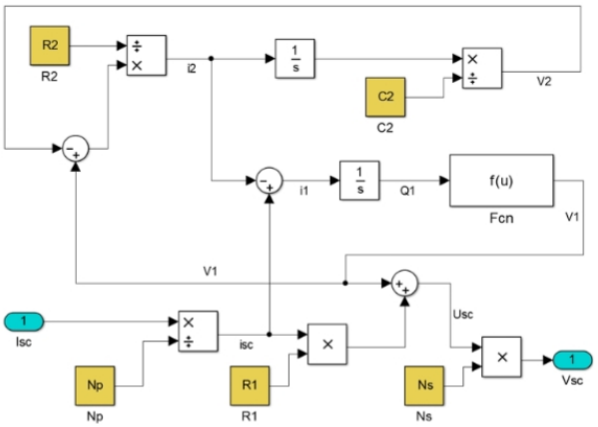


Fig. 4. Simulink Model of the EDLC Supercapacitor

In the hybrid energy storage configuration, the supercapacitor acts as the first response unit to sudden load peaks, bridging the response time gap of the lithium-ion battery and protecting the fuel cell from transient overloading [6]. This coordination enhances the overall system's resilience and prolongs component life [7].

The control system routes excess PV energy to charge the supercapacitor when the SOC of battery is high and power spikes are anticipated. During high-power demand events, the supercapacitor provides instant current support before the battery or fuel cell ramps up, thereby ensuring voltage stability and load balancing [8].

IV. Parameter Identification

Through literature review and experimental calibration, the following key parameters were identified for each subsystem:

- **PEM Electrolyzer:** The exchange current density was set to $i_0 = 1 \times 10^{-3}\,\text{A/cm}^2$, with a Tafel slope of $b = 60\,\text{mV/dec}$. Membrane conductivity was modelled as

  $$\sigma(T) = 0.1 \exp\left[0.02\,(T - 298)\right]\ \text{S/cm},$$

  and the effective gas-diffusion coefficient in the GDL was taken as $D_{\text{eff}} = 5 \times 10^{-2}\,\text{cm}^2/\text{s}$. The active cell area was $A_{\text{cell}} = 200\,\text{cm}^2$.
- **Lithium-Ion Battery:** A nominal capacity of $C_{\text{nom}} = 400\,\text{Ah}$ (usable energy $E_{\text{usable}} = 16\,\text{kWh}$) was assumed, with the open-circuit voltage vs. SoC curve fitted via a fifth-order polynomial. The equivalent-circuit parameters were

  $$R_0 = 0.015\,\Omega, \quad R_1 = 0.02\,\Omega, \quad C_1 = 500\,\text{F},$$

  and a round-trip efficiency of $\eta_{\text{rt}} = 95\%$ was applied.
- **EDLC Supercapacitor:** The rated capacitance was $C_0 = 3000\,\text{F}$, with a voltage-dependence coefficient $C_v = 623\,\text{F/V}$. The equivalent series resistance was $R_1 = 0.29\,\text{m}\Omega$, the leakage resistance $R_f = 1.92\,\Omega$, and the slow-branch capacitance $C_2 = 172\,\text{F}$. Twenty-four cells were modelled in series to achieve the desired voltage rating.

TABLE I
Key Parameters of the Supercapacitor (Maxwell BCAP3000)

Parameter	Symbol	Value	Unit
Rated Capacitance	C_0	3000	F
Voltage Dependency Coefficient	C_v	623	F/V
Series Resistance	R_1	0.29	mΩ
Leakage Resistance	R_f	1.92	Ω
Slow Branch Capacitance	C_2	172	F
Rated Voltage (Per Cell)	–	2.7	V
Number of Series Cells	N_s	24	–
Supercapacitor Current	I_{sc}	–	A (Variable)
Supercapacitor Voltage	V_{sc}	–	V (Output)

V. Results and Discussion

A. Overall Energy Balance and Self-Sufficiency

During the summer months, the surplus photovoltaic generation reaches 650 kWh / day, of which 45% is absorbed by the lithium battery, 40% is converted to hydrogen, and the

TABLE II
KEY PARAMETERS FOR PEM ELECTROLYZER SIMULATION

Parameter	Symbol	Value	Unit
Operating Pressure	P_{op}	1	MPa
Operating Temperature	T_{op}	80	°C
Number of Cells	N_{cells}	100	–
Cell Active Area	A_{cell}	200	cm²
Membrane Thickness	δ_{mem}	50	µm
GDL Thickness	δ_{GDL}	200	µm
Water Diffusivity in GDL	D_w	0.05	cm²/s
Water Pipe Diameter	d_{H_2O}	0.02	m
Gas Pipe Diameter (H_2/O_2)	d_{H_2/O_2}	0.02	m
Radiator Length	L_{rad}	0.5	m
Radiator Width	W_{rad}	0.03	m
Radiator Height	H_{rad}	0.3	m
Number of Coolant Tubes	N_{coolant}	50	–
Fin Spacing	S_{fin}	0.001	m
Fin Efficiency	η_{fin}	85	%
Hydrogen Diffusivity	D_{H_2}	75	mm²/s
Oxygen Diffusivity	D_{O_2}	19	mm²/s
Gas Constant for Hydrogen	R_{H_2}	4124.48	J/(kg·K)
Gas Constant for Oxygen	R_{O_2}	259.84	J/(kg·K)

TABLE III
KEY PARAMETERS FOR LITHIUM-ION BATTERY SIMULATION

Parameter	Symbol	Value	Unit
Usable Capacity	E_{usable}	16	kWh
Rated Power	P_{rated}	12.8	kW
Peak Power (5s)	P_{peak}	18.4	kW
Round-trip Efficiency	η_{rt}	95	%
Application Type	–	On/Off Grid	–
Operating Temperature Range	T_{amb}	-10 to 50	°C

rest is exported to the grid. In winter, stored hydrogen and battery provide 98% of the household demand, reducing the interaction of the network to below 2%. These results confirm that the proposed control strategy can achieve near–100% self-sufficiency under England irradiance and load profiles.

B. PEM Electrolyzer Performance

At a nominal current density of 2 A/cm², the electrolyzer's cell voltage stabilized around 1.71 V (Fig. 5), corresponding to a thermal efficiency of 87% (higher heating value basis). The hydrogen purity measured at the outlet exceeded 99.2% throughout the year, demonstrating the effectiveness of the dehumidification and purification stages. Ohmic losses contributed roughly 40 mV per cell, while activation overpotentials dominated at low currents (below 0.5 A/cm²).

C. Battery and Supercapacitor Dynamics

Transient tests (Fig. 6) reveal that the supercapacitor absorbs up to 5 kW spikes within 50 ms, protecting the Li-ion battery from high dI/dt stress. The battery SoC fluctuates between 20% and 80% under daily cycling, with a round-trip efficiency of 94%. No deep-discharge events were observed, ensuring long cycle life.

D. Control Algorithm Evaluation

The proposed hierarchical control algorithm dynamically manages energy flow among PV generation, lithium-ion battery, supercapacitor, and PEM electrolyzer to ensure system autonomy and component protection. This logic is implemented via a MATLAB/Simulink Stateflow chart and evaluated under real-world irradiance and load conditions.

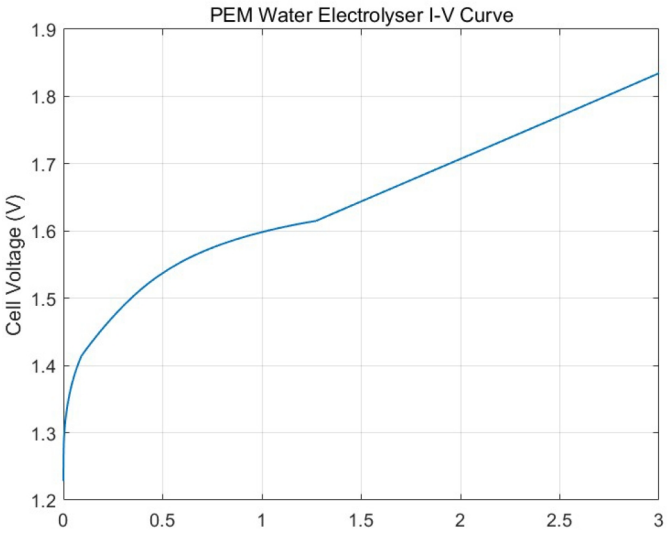


Fig. 5. PEM electrolyzer cell voltage-current density characteristic curve

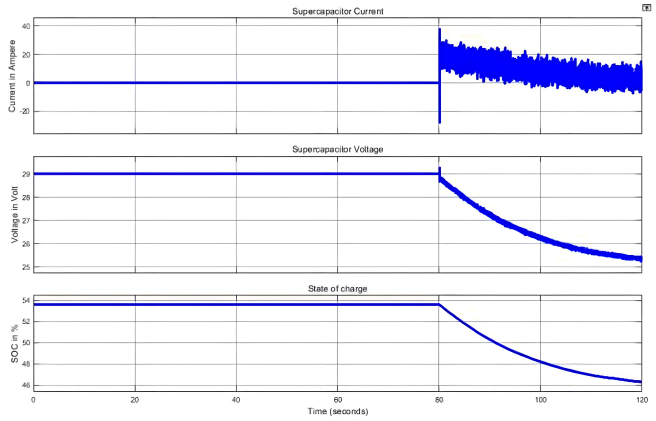


Fig. 6. Transient response of the hybrid storage system: supercapacitor power absorption vs. time during a 5 kW spike

The control operates across four primary modes:

- **Surplus-PV (Battery Charging):** When PV output exceeds load and battery SoC $< 80\%$, the battery is charged.
- **Excess-PV (Hydrogen Production):** If the battery is full, excess PV power is diverted to the PEM electrolyzer for hydrogen generation.
- **Deficit-PV (Battery Discharging):** When load exceeds PV and battery SoC $> 20\,thebatterysuppliestheload.$

Throughout all modes, the supercapacitor responds to rapid transients (e.g., 5kW spikes within 50ms), ensuring voltage stability and shielding the battery from high dI/dt stress.

E. Sensitivity and Limitations

The present study is subject to several limitations. The PV generation and load profiles are based on a single-year

dataset without accounting for interannual variability or PV degradation. Hydrogen storage, compression, and balance-of-plant dynamics are simplified, and no degradation models for the electrolyzer membrane, catalysts, or lithium-ion battery are included, limiting long-term accuracy. Thermal interactions are treated using lumped models without spatial resolution, and the supervisory control assumes ideal measurements without sensor noise or delays. Furthermore, no techno-economic or lifecycle cost assessment is performed, and scaling effects from laboratory-scale parameters to larger systems are not validated.

VI. Conclusion

This work developed and validated a comprehensive multi-scale modeling and simulation framework for a decentralized hybrid energy storage system based on PV generation. The system integrates a lithium-ion battery, a supercapacitor, and a proton exchange membrane water electrolyzer to coordinate short-term and long-term energy storage under realistic operating conditions. Implemented in MATLAB/Simulink with empirical environmental inputs, the framework captures key electrochemical, thermal, and control dynamics, including MEA behavior, gas–liquid transport, and component-level energy buffering.

Simulation results confirm the effectiveness of the hierarchical control strategy, which maintains grid interaction below 2% throughout a full-year simulation. The PEM electrolyzer subsystem achieves a thermal efficiency of 87% at 2A/cm² and sustains hydrogen purity above 99.2%. The supercapacitor handles transient loads up to 5kW within 50ms, preserving the lithium-ion battery's state of charge within the optimal 20–80% range and minimizing degradation. Voltage overshoots remain below 3% during system mode transitions, demonstrating stable dynamic behavior.

Sensitivity analysis reveals that ±10°C variations in electrolyzer stack temperature result in only ±2.5% changes in overall efficiency, and moderate pressure increases improve hydrogen compression performance by 5% without negatively affecting electrical output.

These findings support the technical feasibility of fully PV-powered, off-grid energy systems capable of achieving year-round autonomy and high resilience. Future work will focus on incorporating component aging models, performing techno-economic evaluations, and conducting hardware-in-the-loop experiments to facilitate scalable deployment in residential microgrids and data center infrastructures.

References

[1] Rolo, Inês, Vítor AF Costa, and Francisco P. Brito. "Hydrogen-based energy systems: current technology development status, opportunities and challenges." *Energies*, vol. 17, no. 1, p. 180, 2023.

[2] A. Awasthi, K. Scott, and S. Basu, "Dynamic modeling and simulation of a proton exchange membrane electrolyzer for hydrogen production," *International Journal of Hydrogen Energy*, vol. 36, no. 22, pp. 14779–14786, 2011.

[3] Z. Ma, L. Witteman, J. A. Wrubel, *et al.*, "A comprehensive modeling method for proton exchange membrane electrolyzer development," *International Journal of Hydrogen Energy*, vol. 46, no. 34, pp. 17627–17643, 2021.

[4] K. Hu, *et al.*, "Comparative study of alkaline water electrolysis, proton exchange membrane water electrolysis and solid oxide electrolysis through multiphysics modeling," *Applied Energy*, vol. 312, p. 118788, 2022.

[5] Z. Zhang and X. Xing, "Simulation and experiment of heat and mass transfer in a proton exchange membrane electrolysis cell," *International Journal of Hydrogen Energy*, vol. 45, no. 39, pp. 20184–20193, 2020.

[6] S. Mohseni, A. C. Brent, and D. Burmester, "A comparison of meta-heuristics for the optimal capacity planning of an isolated, battery-less, hydrogen-based micro-grid," *Applied Energy*, vol. 259, p. 114224, 2020.

[7] M. C. Möller and S. Krauter, "Dimensioning and lifetime prediction model for a hybrid, hydrogen-based household PV energy system using Matlab/Simulink," *Solar*, vol. 3, no. 1, pp. 25–48, 2023.

[8] E. Wolf, "Large-scale hydrogen energy storage," in *Electrochemical Energy Storage for Renewable Sources and Grid Balancing*, Elsevier, 2015, pp. 129–142.

[9] G. Reid and G. Wynn, "The future of solar power in the United Kingdom," *Energies*, vol. 8, no. 8, pp. 7818–7832, 2015.

[10] G. H. Alves, G. C. Guimarães, and F. A. M. Moura, "Battery storage systems control strategies with intelligent algorithms in microgrids with dynamic pricing," *Energies*, vol. 16, no. 14, p. 5262, 2023.

[11] N. Sezer, S. Bayhan, U. Fesli, and A. Sanfilippo, "A comprehensive review of the state-of-the-art of proton exchange membrane water electrolysis," *Materials Science for Energy Technologies*, Elsevier, 2024.

[12] O. Atlam and M. Kolhe, "Equivalent electrical model for a proton exchange membrane (PEM) electrolyser," *Energy Conversion and Management*, vol. 52, no. 8–9, pp. 2952–2957, 2011.

Research on Integrated Energy System Planning Considering Multiple Uncertainties and Operational Risks

Zhuoxiang Wu
College of Electrical Engineering
Shanghai University of Electric Power
Shanghai, China
648028957@qq.com

Shunfu Lin
College of Electrical Engineering
Shanghai University of Electric Power
Shanghai, China
shunfulin@shiep.edu.cn

Jin Tan
College of Electrical Engineering
Shanghai University of Electric Power
Shanghai, China
tanjin93@163.com

Liang Qian
College of Electrical Engineering
Shanghai University of Electric Power
Shanghai, China
643653317@qq.com

***Abstract*—In the planning phase of an Integrated Energy System (IES), it is crucial to consider multiple uncertainties and the associated risks they introduce, in order to avoid economic losses and ensure stable energy supply. This paper comprehensively accounts for the multiple uncertainties in IES operations, including wind and photovoltaic power output, carbon emission factors, load demand, and multiple cost coefficients. A stochastic planning model is then developed by employing the Conditional Value-at-Risk (CVaR) to quantify operational risks. Case studies demonstrate that the proposed planning model effectively reduces economic risks and enhances energy supply reliability.**

Keywords—integrated energy system, multiple uncertainties, stochastic planning, Conditional Value-at-Risk

I. INTRODUCTION

With growing global focus on energy security and ecological sustainability, the integrated energy system (IES) has emerged as a strategic approach to integrate heterogeneous energy infrastructures and enhance resource utilization efficiency[1,2]. Therefore, research on the planning model that encompasses the equipment capacity and siting schemes of integrated energy systems holds significant value[3-4].

During IES planning, it usually encounters multiple uncertainties—such as load demand, energy prices, renewable energy output, pollutant emission factors, and ambient temperatures—driven by human activities, natural environmental variations, and policy dynamics [5–7]. Existing approaches to address these uncertainties include probabilistic modeling [8–9], stochastic optimization [10,11], robust optimization [12–14], and information gap decision theory(IGDT) [15–16]. For example, Reference [11] employs Weibull distributions to characterize wind power and normal distributions for load profiles, establishing a hybrid robust-stochastic optimization model, while Reference [11] introduces a multi-stage stochastic investment planning method to account for uncertainties in intermittent generation, electricity demand, and carbon pricing. Additionally, Reference [16] utilizes IGDT to model renewable energy output uncertainties, including wind and photovoltaic systems.

This work was supported by the Science and Technology Project of State Grid Corporation of China (52094022001S).

The Conditional Value-at-Risk (CVaR) methodology has proven instrumental in quantifying portfolio risks and managing uncertainties across energy systems. Researchers in fields like virtual power plant (VPP) operations [17,18] and microgrid design [19,20] extensively apply CVaR for risk mitigation in power system planning. Beyond conventional applications, CVaR is increasingly adopted for operational optimization in Integrated Energy Systems (IES). Illustrative applications include [21], where CVaR evaluates cost uncertainties stemming from multi-energy load variability and photovoltaic (PV) generation fluctuations within energy management frameworks. Similarly, [22] integrates CVaR into Stackelberg game models to address strategic risks in energy market interactions. Further advancing this paradigm, [23] develops a CVaR-enhanced unit commitment model to quantify and mitigate operational risks linked to wind power intermittency.

Traditional planning models employ scenario generation techniques to address uncertainties; however, these approaches often lack comprehensiveness in characterizing uncertainty factors and fail to account for their potential correlations. Furthermore, existing frameworks lack an intuitive risk assessment metric to evaluate operational risks in IES operation.

To address these limitations, this study proposes a multi-uncertainty scenario generation method based on Copula functions. During the multi-scenario stochastic planning phase, CVaR is introduced to quantify the latent risks posed by these uncertainties. Case studies demonstrate that the proposed methodology effectively mitigates economic losses in IES operations while enhancing energy supply reliability.

II. SCENARIOS GENERATION CONSIDERING MULTIPLE UNCERTAINTIES

A. Modeling of WT/PV Power Output and Load Demands

Considering the potential correlations among the uncertainty factors, the Copula function is used to conduct joint probability modeling for them. Since the conventional two - dimensional Copula function cannot achieve high - dimensional joint probability modeling, the R - vine copula function is adopted to establish a five - dimensional joint probability distribution

979-8-3315-5472-9/25/$31.00 ©2025 IEEE

model for wind and solar power outputs and electrical, thermal, and heat load demands. The specific steps are as follows.

Step 1: Based on non-parametric kernel density estimation, establish the marginal probability models of wind and solar power outputs respectively. It can be expressed as：

$$\begin{cases} f_t^h\left(x_t^{\mathrm{wt}}\right)=\dfrac{1}{nh}\displaystyle\sum_{d=1}^{n}K\left(\dfrac{x_t^{\mathrm{wt}}-X_{t,d}^{\mathrm{wt}}}{h}\right) \\ f_t^h\left(x_t^{\mathrm{pv}}\right)=\dfrac{1}{nh}\displaystyle\sum_{d=1}^{n}K\left(\dfrac{x_t^{\mathrm{pv}}-X_{t,d}^{\mathrm{pv}}}{h}\right) \end{cases} \tag{1}$$

$$f_h(x)=\frac{1}{nh}\sum_{i=1}^{n}\frac{1}{\sqrt{2\pi}}\exp[-\frac{1}{2h^2}(x-x_i)^2] \tag{2}$$

where x_t^{wt} and x_t^{pv} is the WT and PV power output in period t, respectively; $X_{t,d}^{\mathrm{wt}}$ and $X_{t,d}^{\mathrm{pv}}$ is the WT and PV power output in period t at day d, respectively, for t = 1, 2,..., 24. Moreover, h is the smoothing parameter, while n is the number of sample days. Finally, $K(\bullet)$ is the Gaussian kernel function expressed as Formula (2).

Step 2：Based on the Gaussian distribution, establish the marginal probability models of electrical, thermal, and heat loads respectively. Take the electrical load as an example, the probability density function is expressed as:

$$f(L^{\mathrm{E}})=\frac{1}{\sqrt{2\pi}\sigma_{\mathrm{e}}}\exp\left[-\left(P-\mu_{\mathrm{e}}\right)^2/2\sigma_{\mathrm{e}}^2\right] \tag{3}$$

Step 3: Use the R - vine copula function to connect the above marginal probability distributions and establish a five - dimensional joint probability model. The probability density function of the N - dimensional R - vine copula is as follows：

$$\begin{aligned} &f\left(x_1,x_2,\ldots x_n\right)=\prod_{k=1}^{n}f_k\left(x_k\right)\prod_{i=1}^{n-1}\prod_{e\in E_i}c_{j(e),k(e)|D(e)} \\ &\left(F\left(x_{j(e)}\mid x_{D(e)}\right),F\left(x_{k(e)}\mid x_{D(e)}\right)\right) \end{aligned} \tag{4}$$

where n-1 represents a tree structure with n-1 layers, and denotes the set of edges. The copula density function corresponding to ege e is represented as $c_{j(e),k(e)|D(e)}$. The nodes connected by edge e are denoted as $j(e)$ an $k(e)$, while $D(e)$ signifies the conditional information.

Step 4: Use the cubic spline interpolation method to obtain the sampling data corresponding to the cumulative probability. This is accomplished by subdividing each probability interval into d-1 smaller intervals. The resulting interpolation polynomial is expressed as follows:

$$x=\left(F_{X_d^t}\right)^{-1}(u)=a_du^3+b_du^2+c_du+l_d \tag{5}$$

Step 5：Use the k-means clustering to cluster the sampling data and to calculate the probability of each scenario.

B. Modeling of Energy Prices

First, the Gaussian mixture model(GMM) is used to generate the Gaussian distribution probability density functions of coal prices and natural gas prices respectively. It can be expressed as：

$$\begin{cases} \phi\left(x_s^{\mathrm{coal}},\theta_{s,r}^{\mathrm{coal}}\right)=\dfrac{1}{\sqrt{2\pi\sigma_{s,r}^{\mathrm{coal}\,2}}}\exp\left(-\dfrac{\left(x_s^{\mathrm{coal}}-\psi_{s,r}^{\mathrm{coal}}\right)^2}{2\sigma_{s,r}^{\mathrm{coal}\,2}}\right) \\ ,\theta_{s,r}^{\mathrm{coal}}=\left\{\psi_{s,r}^{\mathrm{coal}},\sigma_{s,r}^{\mathrm{coal}\,2}\right\}_{r=1}^{m} \\ \phi\left(x_s^{\mathrm{gas}},\theta_{s,r}^{\mathrm{gas}}\right)=\dfrac{1}{\sqrt{2\pi\sigma_{s,r}^{\mathrm{gas}\,2}}}\exp\left(-\dfrac{\left(x_s^{\mathrm{gas}}-\psi_{s,r}^{\mathrm{gas}}\right)^2}{2\sigma_{s,r}^{\mathrm{gas}\,2}}\right) \\ ,\theta_{s,r}^{\mathrm{gas}}=\left\{\psi_{s,r}^{\mathrm{gas}},\sigma_{s,r}^{\mathrm{gas}\,2}\right\}_{r=1}^{m} \end{cases} \tag{6}$$

where x_s^{coal} and x_s^{gas} are the price of coal and natural gas in representative day s; m and r are the number and index of the mixture components respectively. Ψ and σ are the mean and variance of the prices respectively.

Then, a two - dimensional Frank Copula function is employed to conduct a joint probability modeling of coal and natural gas prices, as shown below：

$$C_{\mathrm{Frank}}\left(u_s^{\mathrm{coal}},v_s^{\mathrm{gas}};\lambda_s\right)=\frac{-\ln\left[1+\dfrac{\left(\mathrm{e}^{-\lambda_s u_s^{\mathrm{coal}}}-1\right)\left(\mathrm{e}^{-\lambda_s v_s^{\mathrm{gas}}}-1\right)}{\mathrm{e}^{-\lambda_s}-1}\right]}{\lambda_s} \tag{7}$$

C. Modeling of Multiple Cost Coefficients

With the development of new energy grid connections, the grid's CO_2 emissions are gradually decreasing. So, it is assumed that the grid's CO_2 emission factor declines annually, following the average marginal CO_2 emission factor variation with a 1% error. Finally, the result shows the grid's CO_2 emission factor is uniformly distributed during the planning cycle, i.e., $c_g \sim$ U[0.7097, 0.9905] kg/kWh.

Similarity, it is assumed that the cost coefficients of load shedding and renewable energy curtailment follow uniform distribution. Three-point discrete approximations based on Gaussian quadrature are used to discretize the cost coefficients of load shedding and renewable energy curtailment, and the CO2 emission factor.

III. MATHEMATICAL MODEL

A. CVaR Model

The Conditional Value - at - Risk (CVaR) was introduced as a substitute for Value - at - Risk (VaR) to address the latter's dual inherent flaws [18, 19]. A sampling approach is applied to generate discrete scenarios for calculating CVaR in its discrete form:

$$V_{CVaR\alpha}=V_{VaR\alpha}+\frac{1}{(1-\alpha)}\sum_{l=1}^{NL}\mathrm{Pr}_l\left[C_l^{ope}-V_{VaR\alpha}\right]^+ \tag{8}$$

where $V_{VaR\alpha}$ and $V_{CVaR\alpha}$ is the value of VaR and CVaR at a confidence level α, respectively; C_l^{ope} is the operation cost in the

scenario l; $\left[C_l^{\text{ope}} - V_{VaR_\alpha}\right]^+ = max\{C_l^{\text{ope}} - V_{VaR_\alpha}, 0\}$.

Since calculating the CVaR in the above formula requires prior computation of the VaR, it leads to inconvenience in the calculation. Therefore, an optimization problem is constructed:

$$\min \tilde{F}_\alpha(x,z) = z + \frac{1}{(1-\alpha)}\sum_{k=1}^{q} Pr_k\left[f\left(x,y_k\right)-z\right]^+ \quad (9)$$

By solving the above optimization problem, the minimum value of the objective function obtained is $V_{CVaR\alpha}$, and the corresponding value of z is $V_{VaR\alpha}$.

B. Objective Function

A multi - scenario stochastic IES planning model based on CVaR is proposed. The objective function is to minimize the overall cost *C,* and is shown as follows:

$$\min C = C^{\text{inv}} + \left[\left(1-\beta\right)C^{\text{ope}} + \beta V_{CVaR\alpha}\right] \quad (10)$$

$$C^{\text{inv}} = \left(1-R\right)\sum_{i\in I} P_i^{\text{cap}} c_i \frac{r(1+r)^{\vartheta_i}}{(1+r)^{\vartheta_i}-1} \quad (11)$$

$$C^{\text{ope}} = 365\sum_{s\in S}\pi_s C_s^{\text{ope}} \quad (12)$$

$$C_s^{\text{ope}} = \sum_{t=1}^{24}\left(C_{s,t}^{\text{coal}} + C_{s,t}^{\text{gas}} + C_{s,t}^{\text{shed}} + C_{s,t}^{\text{curt}} + C_{s,t}^{\text{carb}}\right) \quad (13)$$

$$C_{s,t}^{\text{coal}} = \sum_{\chi\in G^{\text{cfu}}}\left(c_{\chi,1}P_{\chi,r,t}^{\text{cfu}}P_{\chi,r,t}^{\text{cfu}} + c_{\chi,2}P_{\chi,r,t} + c_{\chi,3}\right) \quad (14)$$

$$C_{s,t}^{\text{gas}} = \boldsymbol{p}_{s,t}^{\text{gas}}\boldsymbol{G}_{s,t}^{\text{gw}} \quad (15)$$

$$C_{s,t}^{\text{shed}} = \boldsymbol{c}^{\text{shed,E}}\boldsymbol{L}_{s,t}^{\text{shed,E}} + \boldsymbol{c}^{\text{shed,G}}\boldsymbol{L}_{s,t}^{\text{shed,G}} + \boldsymbol{c}^{\text{shed,H}}\boldsymbol{L}_{s,t}^{\text{shed,H}} \quad (16)$$

$$C_{s,t}^{\text{curt}} = \boldsymbol{c}^{\text{curt}}\boldsymbol{P}_{s,t}^{\text{curt,wt}} + \boldsymbol{c}^{\text{curt}}\boldsymbol{P}_{s,t}^{\text{curt,pv}} \quad (17)$$

$$C_{s,t}^{\text{carb}} = c_g\left(\begin{array}{l}\sum_{\chi\in G^{\text{cfu}}}(c^{\text{cfu,carb}}P_{\chi,s,t}^{\text{cfu}}) + \sum_{\delta\in G^{\text{ngu}}}(c^{\text{ngu,carb}}P_{\delta,r,t}^{\text{ngu}}) \\ + \sum_{\gamma\in G^{\text{chp}}}(c^{\text{chp,carb}}P_{\gamma,r,t}^{\text{chp}}) + \sum_{\varepsilon\in G^{\text{gb}}}(c^{\text{gb,carb}}P_{\varepsilon,r,t}^{\text{gb}})\end{array}\right) \quad (18)$$

C. Constraints

1) Energy Balance Constraints

$$\begin{aligned}&-\boldsymbol{L}_t^{\text{E}} + \boldsymbol{L}_t^{\text{shed,E}} = \boldsymbol{P}_t^{\text{cfu}} + \boldsymbol{P}_t^{\text{ngu}} + \boldsymbol{P}_t^{\text{chp,E}} + \boldsymbol{P}_t^{\text{wt}} + \boldsymbol{S}_t^{\text{es}} \circ \boldsymbol{P}_t^{\text{es}} \\ &+\boldsymbol{P}_t^{\text{pv}} - \boldsymbol{P}_t^{\text{curt,wt}} - \boldsymbol{P}_t^{\text{curt,pv}} - \boldsymbol{P}_t^{\text{eb,E}} - \boldsymbol{P}_t^{\text{p2g}}\end{aligned} \quad (19)$$

$$\begin{aligned}&-\boldsymbol{L}_t^{\text{G}} + \boldsymbol{L}_t^{\text{shed,G}} = \boldsymbol{G}_t^{\text{gw}} - \boldsymbol{H}^G\boldsymbol{F}_t^{\text{G}} + \boldsymbol{G}_t^{\text{p2g}} + \\ &\boldsymbol{S}_t^{\text{gs}} \circ \boldsymbol{G}_t^{\text{gs}} - \boldsymbol{G}_t^{\text{gb}} - \boldsymbol{G}_t^{\text{chp}} - \boldsymbol{G}_t^{\text{ngu}}\end{aligned} \quad (20)$$

$$\boldsymbol{\Phi}_t^{\text{root}} = \boldsymbol{P}_t^{\text{chp,H}} + \boldsymbol{P}_t^{\text{gb,H}} + \boldsymbol{P}_t^{\text{eb,H}} \quad (21)$$

$$\boldsymbol{\Phi}_t^{\text{load}} = \boldsymbol{L}_t^{\text{H}} - \boldsymbol{L}_t^{\text{shed,H}} + \boldsymbol{S}_t^{\text{hs}} \circ \boldsymbol{P}_t^{\text{hs}} \quad (22)$$

where $\boldsymbol{S}_t^{\text{es}}$ is a column matrix representing the charging and discharging states of the ES. The same applies to the parameter $\boldsymbol{S}_t^{\text{gs}}$ and $\boldsymbol{S}_t^{\text{hs}}$. $P_t^{\bullet}$ denote the column matrix representing the power at each power network node during time period *t.* The same applies to the parameter $G_t^{\bullet}$ and $P_t^{\bullet,\text{H}}$.

2) Output and capacity constraints

$$\begin{cases}0 \le \boldsymbol{P}_t^{\lambda} \le \boldsymbol{P}^{\lambda,\max} \\ 0 \le \boldsymbol{C}_t^{\text{sto}} \le \boldsymbol{C}^{\text{sto,max}}\end{cases} \quad (23)$$

3) Ramping rate constraint

$$-\boldsymbol{r}_\chi^{\text{down}} \le \boldsymbol{P}_{\chi,t}^{\text{cfu}} - \boldsymbol{P}_{\chi,t\text{-}1}^{\text{cfu}} \le \boldsymbol{r}_\chi^{\text{up}} \quad (24)$$

4) Sitting constraint

$$\begin{cases}M\boldsymbol{u}^{\text{equ,E}} \ge \boldsymbol{P}^{\text{equ,E}} \\ M\boldsymbol{u}^{\text{equ,G}} >= \boldsymbol{G}^{\text{equ,G}} \\ sum(\boldsymbol{u}^{\text{equ,E}}) = sum(\boldsymbol{u}^{\text{equ,G}}) = N^{\text{equ}}\end{cases} \quad (25)$$

where $\boldsymbol{u}^{\text{equ,E}}$ and $\boldsymbol{u}^{\text{equ,G}}$ are two Boolean column matrices, representing the connection positions of the equipment in the power and natural gas network respectively.

IV. Case Study

A. Case Setting

The simulation scenario utilizes an IES test case as shown in Fig 1. This test case consists of an IEEE 30 - bus electrical system, a natural gas system with 20 nodes, and a heating system with 6 nodes.

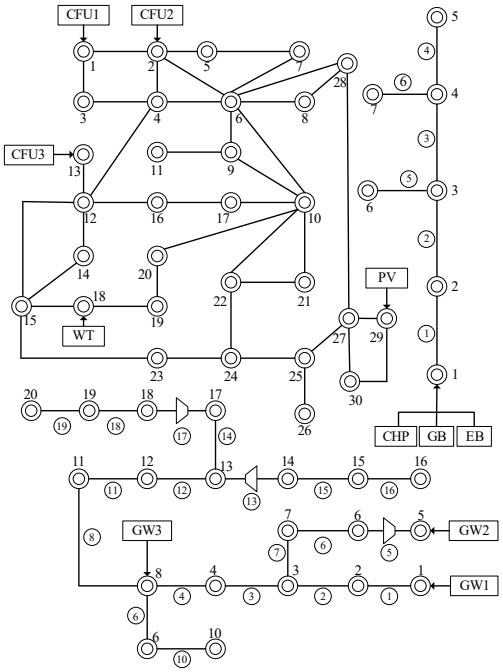


Fig. 1. Network topology of IES

The proposed planning method is modeled as a Mixed - Integer Linear Programming (MILP) problem and solved using the Gurobi solver.

B. Results and Analysis

1) Impact of uncertainties on the planning result

Eight cases shown in Table 1 are established to analyze the impact of the uncertainties in IES planning.

TABLE I. SIMULATION CASES

Cases	Uncertainties				
	Renewable energy output and load demand	Price of coal and natural gas	CO_2 emission factor	Renewable energy curtailment coefficient	Load shedding coefficient
Case 1	√	√	√	√	√
Case 2	×	×	×	×	×
Case 3	√	×	×	×	×
Case 4	×	√	×	×	×
Case 5	√	√	×	×	×
Case 6	√	√	√	×	×
Case 7	√	×	×	×	×
Case 8	√	×	×	√	√

The planning result of the equipment capacity and their connection schemes to the IES(E represents connection to the power grid, and G represents connection to the gas network) under each case are shown in Fig 2.

Comparing the results of Case 1 and other cases, it can be seen that the capacity of the equipment under Case is larger than other cases. This is because Case 1 considers all the uncertainties proposed in this paper, so the planning result tends to be more conservative. By analyzing other cases, it can be found that considering the uncertainty of energy prices leads to a decrease in the capacities of CHP, NGU, and GB, and an increase in the capacities of EB and P2G. This is because the price of natural gas is relatively high and fluctuates significantly. To control fuel costs, the system tends to increase the output of coal - fired equipment and reduce the consumption of natural gas. Considering the uncertainty of the carbon emission factor leads to an increase in the capacities of NGU, CHP, and EB. This is because when the output of CFU decreases (to reduce carbon emissions), gas-consuming equipment needs to increase its output to ensure the stability of energy supply.

The total annual investment and operation costs of the IES under each case are calculated and shown in Table II. It can be concluded that the uncertainties of renewable energy output and load demand, price of energy, coefficients of load shedding and renewable energy curtailment have a positive influence on the IES's total annual cost. In contrast, the uncertainty of CO2 emission factor has an inverse impact on the system's total annual cost.

2)Impact of Risk Preferences on the planning result

CVaR can measure the possible losses in IES and helps investors formulate investment plans. Based on the risk - taking tendencies of IES investors, this research sets different risk parameters. The confidence level α determines the probability limit for expected losses, which shows how an investor assesses the tail risk. A higher α value means a narrower and more extreme scope of tail risk. The risk parameter β represents an investor's aversion to risk. When this value goes up, it means the investor is more conservative in their investment approach.

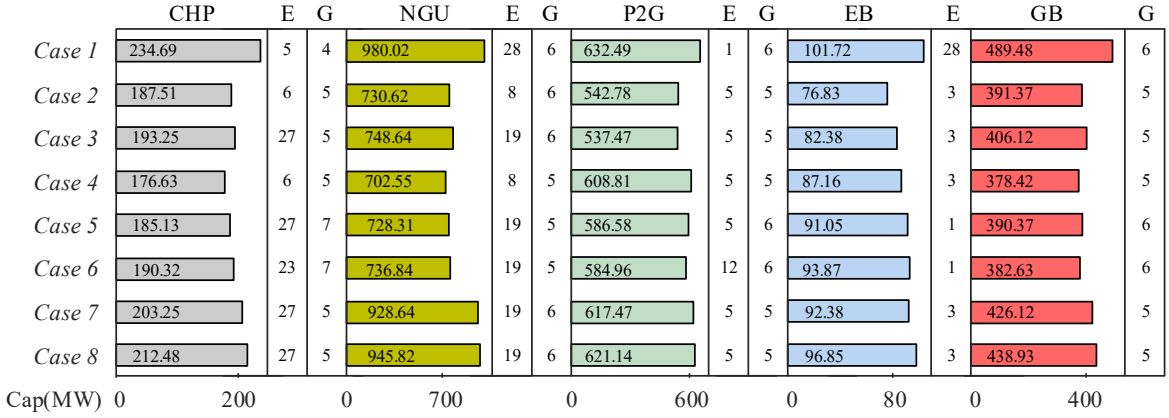


Fig. 2. Capacity and connection position optimization results under each case

TABLE II. THE TOTAL ANNUAL INVESTMENT AND OPERATION COST OF THE IES UNDER EACH CASE

Cases	C^{inv} ($\times 10^6$\$)	C^{ope} ($\times 10^6$\$)					C ($\times 10^6$\$)
		Natural gas	Coal	Load shedding	Renewable energy curtailment	CO_2 emission	
Case 1	686.2734	69.3135	379.6706	7.4470	3.5106	0.1377	1146.3549
Case 2	556.7194	44.3482	344.5813	6.4539	3.6461	0.1117	955.8606
Case 3	564.9663	47.6632	352.1098	6.4771	3.5929	0.1206	974.9299
Case 4	575.9817	56.3916	359.3674	6.4723	3.5417	0.1325	1001.8872
Case 5	577.1668	58.7369	366.9934	6.4852	3.5394	0.1328	1013.0545
Case 6	576.6185	63.5971	360.4813	6.4796	3.5368	0.1364	1010.8497
Case 7	644.0935	61.3354	363.2645	7.0182	3.5281	0.1293	1079.3690
Case 8	654.2870	65.4308	369.1673	7.2269	3.5232	0.1356	1099.7708

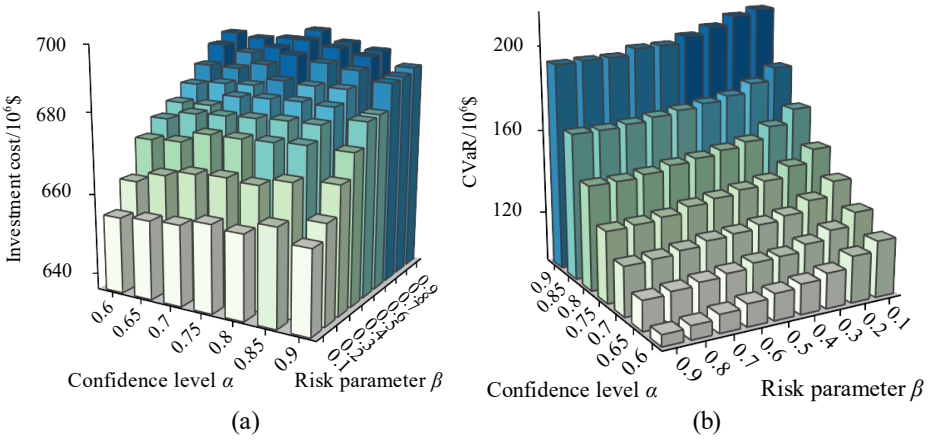


Fig. 3. Investment cost and CvaR under different values of parameters

Fig.3 display the investment costs and CvaR values under different parameter values of α and β. It can be concluded that a higher value of parameter β indicates that investors are more conservative, which results in an increase in investment costs. In addition, systems with higher investment costs exhibit stronger risk - resistance capabilities. Therefore, as the parameter β increases, the CVaR value shows a decreasing trend.

V. Conclusion

In this paper, an IES planning method that takes multiple uncertainties and operational risks into account is proposed. Based on the copula function, operational scenarios that preserve the correlations among uncertain factors are generated, and CVaR is employed to quantify the operational risks. The following conclusions can be drawn:(1) The scenarios generated based on the copula function preserve the potential correlations and are more in line with reality.(2) The CVaR method facilitates direct measurement of potential risk loss, aiding decision-making for IES planning and operation from a risk assessment perspective. This study provides a theoretical foundation and technical guidance for addressing risks in IES planning.

References

[1] S. Huang, H. Lu, M. Chen, W. Zhao, Integrated energy system scheduling considering the correlation of uncertainties, Energy 283 (2023) 129011.

[2] Y. Guo, Y. Li, S. Zhou, Z. Zhang, Y. Wang, Y. Xu, X. Yang, Z. Li, Optimal Dispatch for Integrated Energy System Considering Data-Driven Dynamic Energy Hubs and Thermal Dynamics of Pipeline Networks, IEEE Trans. Smart Grid 15 (2024) 1

[3] R. Liu, T. Yang, G. Sun, S. Lin, F. Li, X. Wang, Multi-Objective Optimal Scheduling of Community Integrated Energy System Considering Comprehensive Customer Dissatisfaction Model, IEEE Trans. Power Syst. 38 (2023) 4328-4340.

[4] S. Habib, S. El - Ferik, M.M. Gulzar, et al. Optimizing integrated energy systems with a robust MISOCP model and C&CG algorithm for enhanced grid efficiency and profitability, Energy 318 (2025) 134795.

[5] G. Mavromatidis, K. Orehounig, and J. Carmeliet, “Design of distributed energy systems under uncertainty: A two-stage stochastic programming approach,” Appl. Energy,vol. 222, pp. 932–950, Jul. 2018.

[6] A. Ehsan and Q. Yang, “State-of-the-art techniques for modelling of uncertainties in active distribution network planning: A review,” Appl. Energy,vol. 239, pp. 1509–1523, Apr. 2019.

[7] Nikolaos G. Kanelakis,Pandelis N. Biskas,Dimitris I. Chatzigiannis,et al. A Stochastic Two-Stage Model for the Integrated Scheduling of the Electric and Natural Gas Systems[J]. IEEE Open Access Journal of Power and Energy,2020,Vol.7: 453-466.

[8] Baharvandi, A.,Aghaei,et al. Bundled Generation and Transmission Planning Under Demand and Wind Generation Uncertainty Based on a Combination of Robust and Stochastic Optimization[J]. IEEE Transactions on Sustainable Energy,2018,Vol.9(3): 1477-1486.

[9] Bifei Tan,Haoyong Chen. Stochastic Multi-Objective Optimized Dispatch of Combined Cooling, Heating, and Power Microgrids Based on Hybrid Evolutionary Optimization Algorithm[J]. IEEE Access,2019,Vol.7: 176218-176232.

[10] Armando L. Figueroa-Acevedo,Chen-Hao Tsai,Kenny Gruchalla. Visualizing the Impacts of Renewable Energy Growth in the U.S. Midcontinent[J]. IEEE Open Access Journal of Power and Energy,2020,Vol.7(1): 91-99.

[11] Santos, S.F.,Fitiwi,et al. Novel Multi-Stage Stochastic DG Investment Planning with Recourse[J]. IEEE Transactions on Sustainable Energy,2017,Vol.8(1): 164-178.

[12] Martinez Cesena, E.A.,Mancarella,et al. Energy Systems Integration in Smart Districts: Robust Optimisation of Multi-Energy Flows in Integrated Electricity, Heat and Gas Networks[J]. IEEE Transactions on Smart Grid,2019,Vol.10(1): 1122-1131.

[13] Apostolopoulou, D.,De Greve,et al. Robust optimization for hydroelectric system operation under uncertainty[J]. IEEE Transactions on Power Systems,2018,Vol.33(3): 3337-3348.

[14] Hussain, A.,Van-Hai Bui,et al. Resilience-Oriented Optimal Operation of Networked Hybrid Microgrids[J]. IEEE Transactions on Smart Grid,2019,Vol.10(1): 204-215.\

[15] Sohrabi, Farnaz,Jabari,et al. Coordination of interdependent natural gas and electricity systems based on information gap decision theory.[J]. IET Generation, Transmission & Distribution,2019,Vol.13(15): 3362-3369.

[16] Huang, WJ (Huang, Wujing),et al. Optimal Configuration Planning of Multi-Energy Systems Considering Distributed Renewable Energy[J]. IEEE Transactions on Smart Grid,2019,Vol.10(2): 1452-1464.

[17] S. Geng, C. Tan, D. Niu, and X. Guo, "Optimal Allocation Model of Virtual Power Plant Capacity considering Electric Vehicles," Math. Probl. Eng., vol. 2021, Jun. 14, 2021, Art. no. 5552323.

[18] Zhang X, Che L, Shahidehpour M, Alabdulwahab AS, Abusorrah A. Reliabilitybased optimal planning of electricity and natural gas interconnections for multiple energy hubs. IEEE Trans Smart Grid Jul. 2017;8(4):1658–67.

[19] R. Zhang et al., "Incorporating Production Task Scheduling in Energy Management of an Industrial Microgrid: A Regret-Based Stochastic Programming Approach," IEEE Trans. Power Syst., vol. 36, no. 3, pp. 2663-2673, May. 2021.

[20] Q. Guo, S. Nojavan, S. Lei, and X. Liang, "Economic-environmental analysis of renewable-based microgrid under a CVaR-based two-stage stochastic model with efficient integration of plug-in electric vehicle and

demand response," Sust. Cities Soc. , vol. 75, Dec. 2021, Art. no. 103276.

[21] S. He, H. Gao, Z. Tang, Z. Chen, X. Jin, and J. Liu, "Worst CVaR based energy management for generalized energy storage enabled building-integrated energy systems," Renew. Energy, vol. 203, pp. 255-266, Feb. 2023.

[22] J. Tan, Y. Li, X. Zhang, W. Pan, and W. Ruan, "Operation of a commercial district integrated energy system considering dynamic integrated demand response: A Stackelberg game approach," Energy, vol. 274, Jul. 1, 2023, Art. no. 126888.

[23] X. Zhang, Y. Zhang, X. Ji, P. Ye, and J. Li, "Unit commitment of integrated energy system considering conditional value-at-risk and P2G," Electr. Power Syst. Res., vol. 221, Aug. 2023, Art. no. 1093

Medium-Long Term Balance Analysis Considering Extreme Scenarios at Multi-time Scales

Weijie Wu
Power Grid Planning Research Center
Guangdong Power Grid Co., Ltd
Guangzhou, China
wuweijie@gd.csg.cn

Sui Peng
Power Grid Planning Research Center
Guangdong Power Grid Co., Ltd
Guangzhou, China
pengsui@gd.csg.cn

Zhengmin Zuo
Power Grid Planning Research Center
Guangdong Power Grid Co., Ltd
Guangzhou, China
zuozhengmin@gd.csg.cn

Yixin Li
Power Grid Planning Research Center
Guangdong Power Grid Co., Ltd
Guangzhou, China
liyixin@gd.csg.cn

Shucan Zhou
Power Grid Planning Research Center
Guangdong Power Grid Co., Ltd
Guangzhou, China
zhoushucan@gd.csg.cn

Shijie Lin
School of Electric Power Engineering
South China University of Technology
Guangzhou, China
linshijie2002@163.com

***Abstract*—Global climate change has exacerbated the frequency of extreme scenarios, leading to a higher risk of new power system balance. In order to solve this problem, this paper firstly proposes the extreme scenario timing operation constraints, considers the time-coupled constraints such as unit ramp-up and does not destroy the data characteristics of new energy output in extreme scenarios, and then nests them in the medium-long-term balance analysis model based on the approximate sustained load curve modeling, and then finally launches the case study based on the IEEERTS-1979 to demonstrate that the model can formulate a reasonable unit overhaul and standby It is demonstrated that the model can formulate reasonable unit maintenance and reservation allocation plans, effectively deal with the impact of extreme scenarios, and reduce the risk of system balance.**

Keywords—Balance analysis model, Renewable energy, Extreme scenario constraints, Mid-and long-term time scale

I. INTRODUCTION

The trend of intensified global climate change in recent years has resulted in a high frequency and severity of extreme weather events, leading to significant issues of 'weather coupling' and 'system vulnerability' in modern power systems with a high proportion of renewable energy. Particularly on a medium-long term time scale, extreme weather such as continuous days of low wind and low sunlight causes sustained low output of renewable energy, making it difficult for the power system to adjust through traditional peak shaving methods, thereby creating significant electricity supply gaps and having some side effect on the stable operation of new power systems[1]-[4]. In more severe cases, this can lead to unpredictable losses. Scholars have already begun researching the issues of power balance posed by extreme scenarios caused by extreme weather. The research mainly employs a combination of balance analysis models and balance metrics to quantify the imbalance risks of the system under extreme scenarios[5]-[9].

However, the aforementioned research, when establishing a balanced analytical model and delineating constraint conditions, merely distinguished between normal and extreme scenarios by setting decision variables for each and constructing corresponding constraint sets for those scenarios. It overlooked situations in actual operation where certain variable values cannot be immediately altered when the scenario changes.

This paper proposes a 'continuously nested temporal' balanced analytical model, which shares decision variables, such as the operational status of units that are difficult to switch quickly, when constructing two sets of constraint conditions for normal and extreme scenarios, thereby making the optimization results of the balanced analytical model more aligned with practical conditions. This paper first establishes a 'Continuous Nested Temporal' balance analysis model to analyze the power balance situation of a new power system operating under extreme scenarios of low output for multiple consecutive days with renewable energy. Secondly, it proposes a set of power balance risk indicators to quantify the power balance risks under different scenarios. Finally, by setting up comparative calculation examples and calculating indicators, this article compares the effectiveness of the proposed model with traditional models in analyzing the power balance of a new power system under extreme scenarios of low output for multiple consecutive days with renewable energy, illustrating the advantages of the proposed model.

The rest of this paper is arranged as follows. The second chapter introduces the model. The third chapter introduces case studies. Finally, the fourth chapter summarizes the research work of this paper.

II. MODEL DESCRIPTION

The intensification of global climate change has led to an increase in extreme weather events, significantly raising the

979-8-3315-5472-9/25/$31.00 ©2025 IEEE

balancing risks of new power systems that are highly sensitive to climate. Conventional power system balance analysis models are no longer applicable. By embedding temporal operating constraints for extreme scenario that are coupled with regular operating constraints in the Conventional model, providing sufficient system reservation for potential extreme scenarios when formulating system operation plans can significantly reduce system balancing risks. The following study will focus on the role of the balance analysis model this paper proposed in mitigating system balancing risks.

A. Objective Function

The balance analysis model aims to optimize the economic operation and safety of the system, specifically targeting the minimization of the total operational costs of the system along with the sum of renewable energy curtailment and load shedding risk during regular and extreme scenarios. The objective function is as follows:

$$\min \sum_{w=1}^{N_w}\sum_{b=1}^{N_b}\left[\sum_{g=1}^{N_g} f_g\left(p_{g,b,w}\right)+C_R\sum_{d=1}^{N_{renew}} p_{d,b,w}^{loss,ES}+C_L\sum_{h=1}^{N_{bus}} L_{h,b,w}^{loss}\right]\Delta t_{b,w}+\sum_{t=1}^{T_{ES}}\left(C_L\sum_{h=1}^{N_{bus}} L_{h,t}^{loss,ES}+C_R\sum_{d=1}^{N_{renew}} p_{d,t}^{loss,ES}\right)\Delta t_{ES} \quad (1)$$

Where w and b respectively indicate the week and the load segment serial number. N_w, N_b, N_g, N_{renew}, N_{bus} respectively indicate the total number of study weeks, the number of segments of the load block curve (LBC) per week, the total number of thermal power units, the total number of renewable power units, and the number of system buses. f_g refers to the fuel cost per unit of electricity for thermal power units. $p_{g,b,w}$ is the power generation of the unit g in load block b, week w. C_R and C_L respectively indicate the penalties for renewable energy curtailment and load shedding. $p_{d,b,w}^{loss}$ refers to the amount of renewable energy curtailment of renewable power unit d in load block b, week w. $p_{d,t}^{loss,ES}$ refers to the amount of renewable energy curtailment at time t in extreme scenarios. $L_{h,b,w}^{loss}$ and $L_{h,t}^{loss,ES}$ respectively indicate the load shedding in normal scenarios and extreme scenarios. $\Delta t_{b,w}$ and Δt_{ES} respectively indicate the duration of load segment b in week w and the time resolution in extreme scenarios.

B. Conventional Operation Constraints

Thermal, hydropower and pumped storage units need to meet the requirements of maintenance duration, continuity, frequency, time interval and maximum number of maintenance units at the same time, and consider the impact of maintenance on the start-up and shutdown status of the unit. These constraints have been repeatedly discussed in previous studies, and will not be repeated in this paper.

Thermal, hydro and pumped storage units need to meet the constraints of output range limits, and these constraints are as follows:

$$p_{idx,b,w}-R_{renew,idx,b,w}^{down}\geq p_{idx}^{\max}u_{idx,b,w} \quad (2)$$

$$p_{idx,b,w}+R_{renew,idx,b,w}^{up}\leq p_{idx}^{\max}u_{idx,b,w} \quad (3)$$

$$0\leq R_{renew,idx,b,w}^{down}\leq p_{idx}^{\max}u_{idx,b,w} \quad (4)$$

$$0\leq R_{renew,idx,b,w}^{up}\leq p_{idx}^{\max}u_{idx,b,w} \quad (5)$$

Where $u_{gh,b,w}$ refers to the Boolean variables indicating the start-up or shut-down status of thermal or hydropower units, where 1 signifies operation and 0 signifies shutdown. $u_{q,b,w}^{gene}$ and $u_{q,b,w}^{pump}$ respectively refer to the Boolean variables indicating whether pumped-storage units are in generation or pumping status, where 1 indicates generation or pumping mode, and 0 indicates the other state. $p_{idx,\min}$ refers to the minimum technical output of the units. $p_{idx,\max}$ refers to the installed capacity of the units. $R_{renew,idx,b,w}^{up}$ and $R_{renew,idx,b,w}^{down}$ respectively indicate reservations downwards and upwards, which are preserved to respond to sudden increases or decreases in renewable energy.

Non-peak shaving nuclear power and large coal-fired power units are affected by factors such as start-stop time and start-stop cost, and the start-stop state is the same at all times of the week. Hydropower units need to consider the weekly total power generation limit of the hydropower station and the weekly power generation and annual total power generation limit. At present, most pumped storage units are constant speed and constant frequency units, so pumping water operates according to rated power, and pumped storage power stations also need to meet the constraints of weekly pumping and power generation energy balance constraints, these constraints are as follows:

$$HE_{hs,w}^{\min}\leq HE_{hs,w}+\sum_{b=1}^{N_b} HC_{hs,b,w}\leq HE_{hs,w}^{\max} \quad (6)$$

$$\sum_{w=1}^{N_w} HE_{hs,w}\leq HE_{hs} \quad (7)$$

$$HC_{hs,b,w}\geq 0 \quad (8)$$

$$p_{q,b,w}^{pump}-p_q^{pump,\max}u_{q,b,w}^{pump}=0 \quad (9)$$

$$\sum_{b=1}^{N_b}\sum_{q\in qs}\left(p_{q,b,w}^{gene}/\eta_q^{gene}-p_{q,b,w}^{pump}\eta_{q,b,w}^{pump}\right)\Delta t_{b,w}=0 \quad (10)$$

Where h refers to the serial number of hydropower unit. $HE_{hs,w}^{\min}$ and $HE_{hs,w}^{\max}$ respectively indicate the upper and lower limits of the power generation capacity of hydropower stations in each week. HE_{hs} refers to the largest annual total power generation of hydropower stations. $p_q^{pump,\max}$ refers to the rated pumping power of pumping storage unit q. $p_{q,b,w}^{pump}$ refers to the pumping power for pumping storage unit q in load block b, week w. η_q^{gene} and η_q^{pump} respectively indicate the power generation and pumping efficiency of the pumped storage unit q.

Considering that the hydropower station reservoir can store excess power station water or free up excess space in the current week and provide downward and upward backup power generation in extreme scenarios, the reservoir model is included in the hydropower station model.

The planned output of the new energy unit should not exceed the expected output value of renewable power units at the corresponding time, and the value of the renewable energy curtailments should be less than the planned output of the renewable power units:

$$0 \le p_{d,b,w}^{P} \le \sum_{s} \pi_s p_{d,b,w}^{s} \Delta t_{b,w} \tag{11}$$

$$0 \le p_{d,b,w}^{loss} \le p_{d,b,w}^{P} \tag{12}$$

Where $p_{d,b,w}^{s}$ refers to the output of renewable power unit d in load block b, week w in scenario s. π_s refers to the probability of the occurrence of scenario s. $p_{d,b,w}^{P}$ refers to the planned output of renewable power unit d in load block b, week w.

The system needs to satisfy power balance constraints, standby constraints, line transmission capacity constraints, and load shedding limits, these constraints are as follows:

$$\begin{aligned} &\mathbf{M}_{\text{Bus}}^{\text{T}} \boldsymbol{p}_{b,w}^{g} + \mathbf{M}_{\text{Bus}}^{\text{H}} \boldsymbol{p}_{b,w}^{h} + \mathbf{M}_{\text{Bus}}^{\text{PS}} \left(\boldsymbol{p}_{b,w}^{q,gene} - \boldsymbol{p}_{b,w}^{q,pump} \right) + \\ &\mathbf{M}_{\text{Bus}}^{\text{Line}} \boldsymbol{p}_{b,w}^{l} + \mathbf{M}_{\text{Bus}}^{\text{Renew}} \left(\boldsymbol{p}_{d,b,w} - \boldsymbol{p}_{d,b,w}^{loss} \right) \\ &= \mathbf{ratio}^{load} L_{b,w} - \boldsymbol{L}_{b,w}^{loss}, \forall b, w \end{aligned} \tag{13}$$

$$\begin{aligned} &\sum_{g} R_{renew,g,b,w}^{up} + \sum_{h} R_{renew,h,b,w}^{up} + \sum_{q} R_{renew,q,b,w}^{up} \\ &\ge p_{d,b,w}^{p} - p_{d,b,w}^{\min} \end{aligned} \tag{14}$$

$$\begin{aligned} &\sum_{g} R_{renew,g,b,w}^{down} + \sum_{h} R_{renew,h,b,w}^{down} + \sum_{q} R_{renew,q,b,w}^{down} \\ &\ge p_{d,b,w}^{\max} - p_{d,b,w}^{p} \end{aligned} \tag{15}$$

$$-p_{l}^{\max} \le p_{l,b,w} \le p_{l}^{\max} \tag{16}$$

$$0 \le L_{b,w}^{loss} \le ratio^{load} L_{b,w} \tag{17}$$

Where N_h and N_q respectively indicate the amount of hyd ropower, pumped storage units. $\mathbf{M}_{\text{Bus}}$ refers to the matrix indic ating whether various units are connected to nodes, the number of rows equals the number of nodes, and the number of column s equals the number of units. In the matrix, an element of 1 indi cates that the unit corresponding to that column is connected to the node corresponding to that row. $\mathbf{M}_{\text{Bus}}^{\text{Line}}$ refers to the power t ransmission direction matrix, the starting point of the line is def ined as 1 and the end point as -1. $p_{l,b,w}$ refers to the power tran s-mitted by the line l. $p_{l}^{\max}$ refers to the transmission capacity limit of the line l.

III. Case Studies

To validate the ability of the balancing analysis model with nested extreme scenario time-series operational constraints to address extreme scenarios and reduce system balancing risks, this paper conducts a case study analysis using an adapted version of IEEERTS-79[10], which includes 26 thermal power units, 6 hydroelectric units, 4 pumped-storage units, and 1 photovoltaic power plant; Annual photovoltaic power generation and load data matching the system's unit output data were selected. The photovoltaic output data exhibited a continuous two-week period of low renewable energy output in weeks 15 and 16. The penalties for load loss and renewable energy curtailment were \$100/kW and \$5/MW, respectively.

This paper sets up three sets of examples for comparative analysis: Example 1 uses a balanced analysis model without nested extreme scenario time-series operation constraints for solution; Example 2 substitutes the maintenance plan obtained from Example 1 into the balancing analysis model with nested extreme scenario time-series operation constraints proposed in this paper for solution; Example 3 directly uses the balanced analysis model with nested extreme scenario time-series operation constraints for solution. Based on the solution results of the three cases, metrics such as the Loss of Load Probability (LOLP), Electricity Not Supplied Expectation (EENS), and expected load shedding time (LOLE) are calculated to verify the effectiveness of the proposed model in reducing system balancing risks. The case study results are as follows:

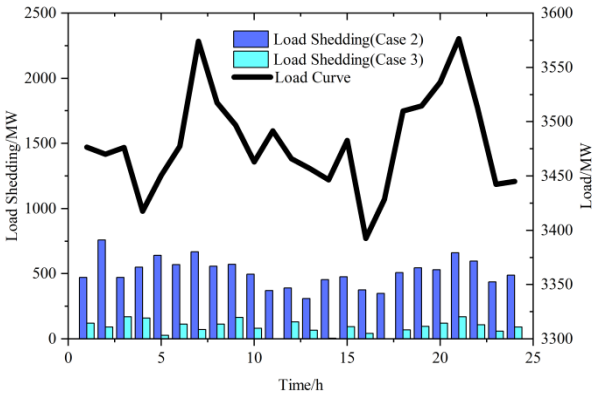


Fig. 1. Load Shedding for Different Cases in Typical Days

TABLE I. Indices of Different Cases

Indices \ Cases	Case 1	Case 2	Case 3
LOLP	0.0671	0.0629	0.0645
EENS	4.2936×10^{5}	4.8086×10^{5}	4.2409×10^{5}
LOLE	586.5116	549.3659	563.7338
LCOE	0.1078	0.1626	0.1152
RC	0	311.1740	945.3769
LC	2.9435×10^{5}	3.5985×10^{5}	2.1830×10^{5}
LC_E	\	1.0073×10^{5}	1.4499×10^{4}
ALC_E	\	466.3425	67.1250

As shown in Fig 1, all cases exhibit varying degrees of load loss. The balancing analysis model constructed in this paper, which incorporates nested extreme scenario time-series operational constraints, preemptively accounts for the impact of extreme scenarios, establishes reasonable unit maintenance

schedules, and reserves sufficient spare capacity for potential extreme scenarios. As a result, the load loss in Case Study 3 is significantly lower than that in Case 2, which uses a traditional balanced analysis model to determine unit maintenance schedules; As shown in Table 1, the RC and LC values of Example 1 are lower than those of Example 2. This is because the traditional balance analysis model weakens the extreme numerical characteristics of extreme scenarios during data processing, unable to accurately quantify the balance risks associated with extreme scenarios, leading to unreasonable unit maintenance schedules; Comparing the three indicators—LC, LCE, and ALCE—between Case 2 and Case 3, it is evident that the unreasonable maintenance schedule adopted from Case 1 in Case 2 resulted in insufficient startup capacity in extreme scenarios. Additionally, since time-coupled constraints such as unit ramping were not considered, the values of these three indicators are significantly higher than those in Case 3; Additionally, the LCOE indicators for Cases 2 and 3 are higher than those for Case 1. This is because the balance analysis model incorporating nested extreme scenario time-sequential operational constraints accounts for the impact of potential sustained low-output extreme scenarios, offering superior robustness compared to traditional balance analysis models, thereby increasing costs. In summary, the balance analysis model developed in this paper, which incorporates nested extreme scenario time-sequential operational constraints, can establish reasonable unit operation schedules and allocate appropriate reserve capacity, effectively reducing system balance risks.

IV. CONCLUSIONS

In this paper, a balancing analysis model with nested extreme scenario timing constraints is proposed. The hourly time resolution of the extreme scenario timing constraints avoids the problem that the traditional balancing analysis model is based on the approximate sustained load curve modeling and cannot take into account the time-coupled constraints such as unit ramp-up. Therefore, this solution is conducive to reflecting more realistically the impacts of the extreme scenarios on the system, and to formulating a reasonable overhaul plan for the unit and arranging appropriate standby. The case analysis based on IEEERTS-1979 proves that the proposed model can effectively reduce the risk of loss of load under the extreme scenarios of sustained low output, which provides an important reference for the study of power balance in new power systems.

ACKNOWLEDGMENT

Project supported by the Power Grid Planning Research Center of Guangdong Power Grid Co., Ltd (Research on Medium-to-Long-Term and Annual Reserve Planning Theory and Methods for Partitioned Receiving-End Grids with Flexible HVDC Interconnection, Contract Number, GDKJXM20240053).

REFERENCES

[1] Y. Xue, and S. Xiao, “Comprehensively defending high risk events with low probability,” Automation of Electric Power Systems, 2011, 35(8), pp.1-11.

[2] J. Lu, Z. Jiang, and H. Lei, “Analysis of Hunan power grid ice disaster accident in 2008,” Automation of Electric Power Systems, 2008, 32(11), pp. 16-19.

[3] H. Zhang, and Y. Liu, “Comprehensive assessment of extreme ice disaster affecting power system operation,” Proceedings of the CSEE, 2011, 31(10), pp.52-58.

[4] D. Mendonça, W. A. Wallace, “Impacts of the 2001 world trade center attack on New York city critical infrastructures” , Journal of Infrastructure Systems, 2006, 12(4), pp. 260-270.

[5] Y. Lv *et al*., "Review on Modeling of Impact of Extreme Weather on Source-Grid-Load-Storage," *2023 IEEE 7th Conference on Energy Internet and Energy System Integration (EI2)*, Hangzhou, China, 2023, pp. 1840-1845.

[6] H. Guo, L. Chen, Q. Ma, G. Zou and S. Liu, "Extreme Scenarios of High Percentage of Renewable Energy Connected to Power System: A Review on System Power and Electricity Balance Aspect," *2023 8th International Conference on Power and Renewable Energy (ICPRE)*, Shanghai, China, 2023, pp. 894-903.

[7] X. Wu, S. Zhou, W. Gu, R. Zhang, Z. Meng and Z. Gao, "Optimal Configuration Method of Power Grid Resources Considering Extreme Scenarios and Optimal Construction Time Sequence," *2023 IEEE 7th Conference on Energy Internet and Energy System Integration (EI2)*, Hangzhou, China, 2023, pp. 5040-5045.

[8] N. Huang, W. Wang and G. Cai, "Optimal Configuration Planning of Multi-energy Microgrid Based on Source-load-temperature Scenarios Deep Joint Generation," in *CSEE Journal of Power and Energy Systems*, vol. 9, no. 3, pp. 1090-1102, May 2023.

[9] H. Jiang *et al*., "Renewable Electric Energy System Planning Considering Seasonal Electricity Imbalance Risk," in *IEEE Transactions on Power Systems*, vol. 38, no. 6, pp. 5432-5444.

[10] P. M. Subcommittee, "IEEE Reliability Test System," in *IEEE Transactions on Power Apparatus and Systems*, vol. PAS-98, no. 6, pp. 2047-2054, Nov. 1979.

Distributed Photovoltaic Cluster Power Forecasting Based on an Improved Graph Attention Network Model

Yanping Zhu
The State Grid Shanghai Municipal Electric Power Company
Shanghai, China
zhuyanping_09@163.com

Pan Chen
The State Grid Shanghai Municipal Electric Power Company
Shanghai, China
1002049470@qq.com

Yueguang Zhang
The State Grid Shanghai Municipal Electric Power Company
Shanghai, China
892978010@qq.com

Yi Feng
The State Grid Shanghai Municipal Electric Power Company
Shanghai, China
1031895285@qq.com

Jingzhe Shan
The State Grid Shanghai Municipal Electric Power Company
Shanghai,China
51184507001@stu.ecnu.edu.cn

Liang Wang
The State Grid Shanghai Municipal Electric Power Company
Shanghai,China
wang_liang_4@163.com

Tianrun Wen
The State Grid Shanghai Municipal Electric Power Company
Shanghai, China
878892467@qq.com

Delin Zhao
Shanghai University of Electric Power
School of Electrical Engineering
Shanghai, China
zacred0rryn@mail.shiep.edu.cn

Yuntian Liu
Shanghai University of Electric Power
School of Electrical Engineering
Shanghai, China
250985242@qq.com

***Abstract*—The regional distributed photovoltaic (PV) clusters are geographically dispersed, resulting in diverse power output characteristics among different PV plants within the cluster, which compromises the accuracy of power forecasting. This paper proposes a short-term power forecasting model based on an enhanced graph attention network (GAT-TPA-ED). In the proposed framework, following sub-clustering of the distributed PV cluster, a deep learning model featuring an encoder-decoder architecture integrated with graph attention (GAT) and temporal pattern attention (TPA) mechanisms is applied to capture multi-site, multi-variable, and multi-time-step information, thereby improving forecasting accuracy. The method is validated using actual operational power output data from distributed PV clusters in East China. The results indicate that the proposed regional PV power forecasting approach is capable of effectively capturing the output characteristics of distributed PV plants and enhancing the forecasting accuracy for distributed PV clusters.**

Keywords—distributed photovoltaics, power forecasting, graph attention network, encoder-decoder, temporal pattern attention mechanism

I. INTRODUCTION

With the widespread use of fossil fuels such as oil and natural gas, the greenhouse effect and environmental degradation are spreading globally, and the high dependence on fossil fuels has also led to a global energy crisis. In this context, the United Nations has proposed a zero emission target [1], and China has also put forward the goals of "carbon peak and carbon neutrality" and continued to promote its energy transformation strategy [2]. As of the end of 2024, the cumulative grid connected capacity of distributed photovoltaics (DPVs) in China has reached 374.78 million kilowatts. In the future, a higher proportion of distributed photovoltaic power plants will gradually be connected to the grid [4-5]. However, due to the lack of professional meteorological monitoring equipment in the DPV power plant cluster and the insufficient historical data of the large number of newly built distributed photovoltaic power plants every year, it is difficult to establish high-precision prediction models [6-7]. For new energy service enterprises and local power grids, the rapid development of distributed photovoltaics greatly increases the difficulty of power system supply-demand balance scheduling and management [8-9]. The intraday power prediction of large-scale distributed photovoltaic power plants is helpful in addressing the threat posed by the randomness and uncertainty of photovoltaic power generation to the power grid [10-11], thereby improving the stability of the power grid.

The output of photovoltaic (PV) power plants is influenced by multiple interrelated factors, resulting in random fluctuations that vary from one plant to another. In cluster-level forecasting, such inter-station variability can adversely affect prediction accuracy under certain methods. For instance, the statistical

979-8-3315-5472-9/25/$31.00 ©2025 IEEE

upscaling approach employed in [12-13] partitions a PV cluster into sub-regions, selects a representative benchmark plant in each, and aggregates their scaled predictions using predefined weights to estimate the total output of the distributed PV cluster. However, in clusters with spatial micro-meteorological variations, the upscaling process tends to amplify the localized fluctuation patterns of the benchmark plants, thereby reducing overall forecasting accuracy. This limitation underscores the need for alternative forecasting methods in spatially heterogeneous environments.

Graph Neural Networks (GNNs) represent a class of deep learning models specifically designed to handle graph-structured data. In the context of distributed PV forecasting, graph-based modeling offers a natural framework: nodes can represent individual PV plants, while edges can capture physical or abstract relationships such as geographical proximity or meteorological correlation. This formulation allows GNNs to exploit structural dependencies that are inaccessible to conventional models, making them particularly suitable for DPV cluster forecasting. Previous studies have explored various GNN architectures: [14] combined Graph Convolutional Networks (GCNs) with Long Short-Term Memory (LSTM) to capture spatial and temporal dependencies separately; [15] introduced a spatio-temporal graph neural network (STGNN) composed of multiple adaptive spatio-temporal blocks with GCN and Temporal Convolutional Network (TCN) at its core; and [16] proposed two STGNN variants based on graph convolution—one integrating a recurrent graph convolutional LSTM, the other incorporating an attention-based graph convolutional Transformer. Building on the demonstrated strengths and scalability of GNNs, this work investigates the application of Graph Attention Networks (GAT) to power forecasting in DPV clusters.

In summary, this paper proposes a short-term power forecasting model based on Graph Attention Networks (GAT). Simulation and comparative experiments demonstrate that the proposed method effectively mitigates the impact of local micro-meteorological variations and enhances prediction accuracy.

II. GAT-TPA Encoder Decoder Composite Model

A mainstream approach for photovoltaic (PV) cluster power forecasting is the statistical upscaling method. For each sub-region, this method selects a representative benchmark power station and scales its predicted power output by certain weighting factors to estimate the total power generation of the PV cluster in that sub-region. Essentially, this approach proportionally amplifies the output of a single station, which unfortunately also magnifies its local and site-specific fluctuation patterns. As a result, these localized variations are propagated into the cluster-level forecasts, leading to increased prediction errors. Alternatively, while a bottom-up aggregation method—which applies a standard forecasting model to each individual station and sums the predictions—can mitigate the impact of station-specific variations, it significantly compromises computational efficiency. Therefore, the use of graph neural networks capable of capturing spatial dependencies offers a promising solution to this trade-off in regional distributed PV forecasting.

A. GAT

A core challenge in multi-site photovoltaic (PV) forecasting lies in effectively modeling the spatial correlations among geographically dispersed sites. Within the family of Graph Neural Networks (GNNs), the Graph Attention Network (GAT) offers a powerful solution by enabling the model to adaptively learn the relative importance of different neighboring sites—a capability crucial for this application. In contrast, earlier Graph Convolutional Networks (GCNs) relied on fixed, graph-structure-based weights, such as node degrees, to aggregate information from neighbors. This isotropic aggregation mechanism was unable to distinguish the varying importance of different neighboring nodes[17]. GAT introduces a self attention mechanism that allows the model to dynamically calculate different attention weights for each neighbor based on the node's own characteristics, achieving "anisotropic" aggregation [18].

As a preliminary step to enhance feature expression ability, a shared, learnable linear transformation parameterized by a weight matrix $\mathbf{W} \in \mathbb{R}^{F' \times F}$ is applied to the feature vectors of each node in the graph.

Here, F is the dimension of the input feature, and F' is the dimension of the output feature.

$$\mathbf{z}_i = \mathbf{W}\mathbf{h}_i \tag{1}$$

Among them, $\mathbf{h}_i \in \mathbb{R}^F$ is the initial eigenvector of node i.

Then, the model calculates an unnormalized attention score e_{ij} ,It quantifies the importance of node j 's features to node i . This is achieved by inputting the transformed feature vectors $\mathbf{z}_i$ and $\mathbf{z}_j$ of two nodes into a single-layer feedforward neural network, The network is parameterized by a weight vector $\mathbf{a} \in \mathbb{R}^{2F'}$. The usual implementation of this mechanism is to concatenate feature vectors and dot product them with $\mathbf{a}$,and apply the LeakyReLU nonlinear activation function:

$$e_{ij} = \mathrm{LeakyReLU}(\mathbf{a}^\top [\mathbf{z}_i \,\|\, \mathbf{z}_j]) \tag{2}$$

Among them, $\|$ represents splicing. This function allows the model to learn a shared attention mechanism $a(\cdot,\cdot)$ that scores the relationship between any two connected nodes.

In order to inject graph structures into the model, GAT employs masked attention. The attention score e_{ij} is only calculated for node j (i.e. $j \in \mathcal{N}_i$, where $\mathcal{N}_i$ includes node i itself through the self loop) in the direct neighborhood of node i . This ensures that nodes only focus on their direct neighbors, limiting information flow within the topology of the graph.

The original attention scores e_{ij} do not have direct comparability between different nodes because they depend on specific feature values. To normalize them into a probability distribution, the softmax function needs to be applied to all neighbors of a node:

$$\alpha_{ij} = \text{softmax}_j(e_{ij}) = \frac{\exp(e_{ij})}{\sum_{k \in \mathcal{N}_i} \exp(e_{ik})} \tag{3}$$

The obtained coefficient α_{ij} is the normalized attention weight. For each node, their sum is 1, which provides an easily interpretable measure of the importance of each neighbor j in the aggregation process.

This attention mechanism effectively replaces the static normalization used in GCNs. It is highly parallelizable, computationally efficient, and readily applicable to both transductive and inductive learning tasks. The schematic diagram of the GAT module is illustrated in Figure 1.

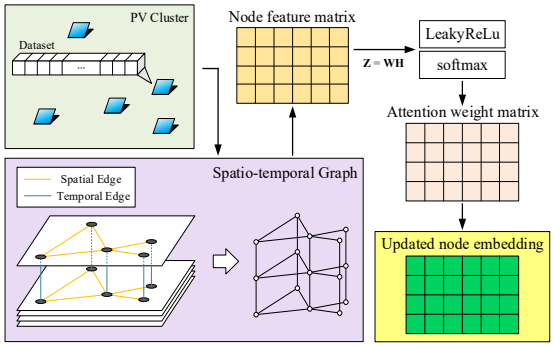


Fig. 1. GAT principle process

B. Encoder Decoder Model for GAT Network Construction

The Encoder-Decoder (ED) model is a widely adopted neural network architecture in deep learning, particularly well-suited for sequence-to-sequence (Seq2Seq) tasks. Comprising two fundamental components—an encoder and a decoder—the model operates as follows: the encoder maps the input sequence into a fixed-dimensional context vector, while the decoder generates the target output sequence conditioned on this vector.

Within the encoder, each GAT layer computes attention coefficients between every node and all its spatio-temporal neighbors over the entire graph. This process enables weighted aggregation of neighboring node features, followed by an update of the node's own feature representation. The decoder, operating on a causal graph structure, follows the same GAT-based computational procedure as the encoder, progressively generating hidden state representations for each future time step.

C. Integration of TPA Mechanism

Nevertheless, the standard attention mechanism utilized in the Encoder-Decoder (ED) framework has inherent limitations when applied to multivariate time series problems like photovoltaic power forecasting, which involves variables such as power, irradiance, and cloud cover. While it effectively focuses on salient time steps, it is incapable of identifying temporal patterns that extend across multiple time steps[19]. The core idea of TPA is to first identify local patterns in a time series, and then evaluate the importance of different variables based on these patterns.

To extract time invariant local patterns, TPA integrates a Convolutional Neural Network (CNN) component. This component contains k one-dimensional CNN filters $\mathbf{C}_j$, which are convolved on m feature dimensions of the hidden state $\mathbf{H}_{enc}$ of the input encoder, resulting in a pattern matrix $\mathbf{H}_C$.

Then, TPA uses a scoring function f to evaluate the correlation between the i-th row of the pattern matrix $\mathbf{H}_C$ (representing the pattern vector of the i-th variable) and the current hidden state $\mathbf{h}_t^{dec}$ of the decoder:

$$f(\mathbf{H}_{Ci}, \mathbf{h}_t^{dec}) = (\mathbf{H}_{Ci})^T \mathbf{W}_a \mathbf{h}_t^{dec} \tag{4}$$

Where $\mathbf{W}_a$ is a learnable weight matrix.

TPA chose the sigmoid function instead of softmax when calculating attention weights to allow the model to assign high attention weights to multiple variables simultaneously:

$$\alpha_i = \text{sigmoid}(f(\mathbf{H}_{Ci}, \mathbf{h}_t^{dec})) \tag{5}$$

The final context vector is the weighted sum of the row vectors of the pattern matrix $\mathbf{H}_C$ with attention weights α_i:

$$\mathbf{v}_t = \sum_{i=1}^{n} \alpha_i \mathbf{H}_{Ci} \tag{6}$$

The complete model architecture integrating TPA components is shown in Figure 2:

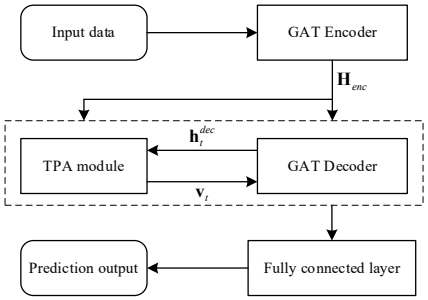


Fig. 2. GAT-TPA-ED model architecture

Thanks to the quantifiable attention weights in the GAT module and the TPA mechanism, the GAT-TPA-ED model exhibits relatively high interpretability within the deep learning framework. In terms of spatial scalability, the model leverages the flexibility and inductive capability of GAT in handling graph structures. Meanwhile, for temporal scalability, the CNN filters in TPA are inherently suitable for capturing high-frequency local temporal patterns in longer sequences. As a result, the model demonstrates promising scalability potential in both spatial and temporal dimensions.

III. Case Analysis

A. Data Preparation

a)Data Preparation: The experiment was conducted using historical output data from distributed photovoltaic systems in a specific area of Shanghai throughout 2024. The dataset comprises hourly recordings.

b)Data Preprocessing: The raw data first underwent a preprocessing stage to cleanse obvious anomalies. Following

this, the cleaned dataset was subjected to a similar-day screening process and was subsequently partitioned into training (70%), testing (15%), and validation (15%) sets. The final processed input data spans the period from February 10 to August 30, 2024.

B. Model Evaluation

For the point prediction results, this article evaluates them using root mean square error e_{RMSE}, mean absolute error e_{MAE}, and coefficient of determination R^2.

$$e_{\mathrm{RMSE}} = \sqrt{\frac{1}{n}\sum_{i=1}^{n}(y_i - \hat{y}_i)^2} \tag{7}$$

$$e_{\mathrm{MAE}} = \frac{1}{n}\sum_{i=1}^{n}\left|y_i - \hat{y}_i\right| \tag{8}$$

$$R^2 = 1 - \frac{\sum_{i=1}^{n}(y_i - \hat{y}_i)^2}{\sum_{i=1}^{n}(y_i - \bar{y})^2} \tag{9}$$

C. Experimental Setup

To verify the effectiveness of the prediction method proposed in this article, other prediction methods were set up in parallel with the proposed method as the control group:

TABLE I. EXPERIMENTAL SETUP

Method	Model
Proposed	GAT-TPA-ED (Bottom-up)
Baseline	LSTM-ED (Upscaling)

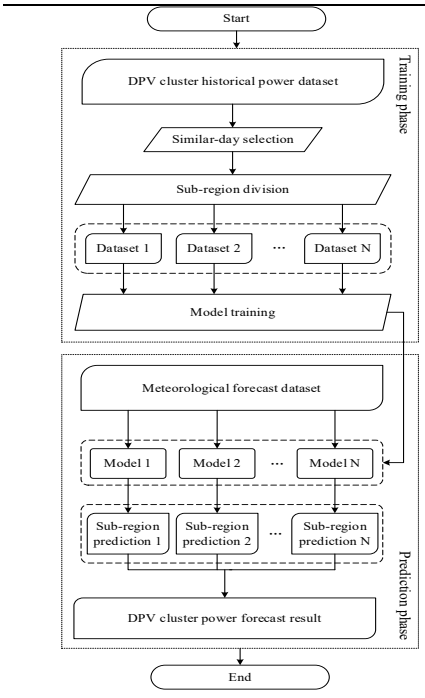


Fig. 3. Overall prediction process

The forecasting method proposed in this study adheres to the implementation pipeline illustrated in Figure 3. The experiments were conducted on a hardware platform equipped with an Intel® Core™ i5-13400F CPU and an NVIDIA® GeForce RTX™ 4070 GPU. The software environment utilized the Debian GNU/Linux 12 operating system running on Windows Subsystem for Linux 2 (WSL 2), with all experimental code implemented in Python 3.11. The model was trained on the entire cleaned dataset. For inference, the model uses the data from the week preceding the target day as input to generate the 24-point output sequence for that day.

D. Result Analysis

A comparative analysis of the prediction accuracy metrics for the cluster power forecasts obtained by different methods is presented in Table 2, while the corresponding power curve comparisons are illustrated in Figure 4. Additionally, Table 3 summarizes the computational efficiency during the training phase between the proposed method and the baseline approach.

TABLE II. COMPARISON OF PRECISION OF TOTAL CLUSTER PREDICTION RESULTS

Method	RMSE ($\times 10^{-2}$ p.u.)	MAE ($\times 10^{-2}$ p.u.)	R^2 (%)
Proposed	2.1522	1.1249	98.5972
Baseline	3.7299	2.1904	95.7875

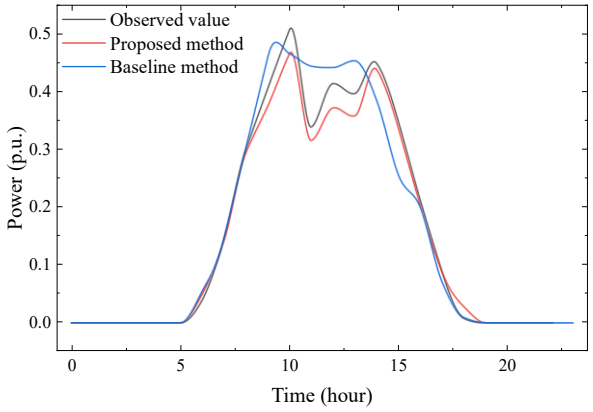


Fig. 4. Curve of total cluster power for the day to be predicted

TABLE III. SUMMARY OF MODEL TRAINING TIME

Method	Total Time (s)	Time Per Station (s)
Proposed	4794.732	159.824
Baseline	457.324	152.441

As shown in Table 2, the prediction method proposed in this paper achieves higher accuracy, with the RMSE and MAE improved by 42.30% and 48.64%, respectively, compared to the baseline method. The comparison of the predicted power curves in Figure 4 shows that the GAT-TPA-ED deep learning model used in the experiment can better capture the output fluctuation characteristics of the distributed photovoltaic

cluster, while the prediction results of the baseline method deviate from the actual output curve of the cluster at several locations. This is because the upscaling method used in the baseline approach amplifies the local fluctuation characteristics of the representative power station when generating cluster-level predictions, thereby introducing additional errors into the aggregated power forecast and resulting in lower prediction accuracy.

Therefore, the integrated proposed method—combining spatio-temporal sub-clustering and a GAT-based forecasting model—effectively captures the output characteristics of DPV clusters. Coupled with high-resolution meteorological data from spatial spline interpolation, which mitigates errors from local micro-meteorological variations, the framework collectively contributes to superior forecasting accuracy.

IV. Conclusion

This paper proposes a deep learning forecasting model built upon an Encoder-Decoder (ED) architecture, which integrates Graph Attention Network (GAT) as its core component together with a Temporal Pattern Attention (TPA) mechanism. The model effectively leverages the advantages of graph networks by constructing a unified spatio-temporal graph to capture both spatial dependencies and temporal characteristics among PV plant clusters. This approach successfully mitigates the issue of amplified local variations inherent in conventional upscaling methods for DPV cluster forecasting. Experimental results demonstrate that the proposed model achieves a significant improvement in forecasting accuracy.

This research presents a forecasting method for DPV clusters that provides a viable solution for accurate and efficient short-term prediction. By doing so, it paves the way for broader integration of distributed photovoltaics and thereby contributes to maintaining power grid stability in the face of PV generation's stochastic and variable nature.

Acknowledgment

This work was supported by Science and Technology Project of State Grid Corporation of China (Grant Number: 520923250004)

References

[1] United Nations. For a livable climate: Net-zero commitments must be backed by credible action[EB/OL]. (2021-04-22) [2025-08-17]. https://www.un.org/climatechange/net-zero-coalition.

[2] XIN Baoan, SHAN Baoguo, LI Qionghui, et al. Rethinking of the “Three Elements of Energy” Toward Carbon Peak and Carbon Neutrality[J]. Proceedings of the CSEE, 2022, 42(9): 3117-3125.

[3] National Energy Administration. Situation of Photovoltaic Power Generation Construction in 2024[EB/OL]. (2021-04-22) [2025-08-17]. http://www.nea.gov.cn/20250221/f04452701c914d51a89d0c0ea6f4acd1/c.html.

[4] XIA Lingfeng, LI Jiaming, ZHAO Liang, et al. A PV Power Time Series Generating Method Considering Temporal and Spatial Correlation Characteristics[J]. Proceedings of the CSEE, 2017, 37(07): 1982-1993.

[5] HAN Dong, LI Mengtong, YAN Zheng. Evaluation Method of Diffusion Capability of User-side Distributed Photovoltaic Technology[J]. Proceedings of the CSEE, 2021, 41(03): 985-994.

[6] LIU Chenyu, ZHANG Xuemin, MEI Shengwei, et al, Tang Haiyan. Numerical weather prediction enhanced wind power forecasting: Rank ensemble and probabilistic fluctuation awareness[J]. Applied Energy, 2022, Vol.313: 118769.

[7] BRESTER C, KALLIO-MYERS V, LINDFORS A V, et al. Evaluating neural network models in site-specific solar PV forecasting using numerical weather prediction data and weather observations[J]. Renewable Energy, 2023, Vol.207: 266-274.

[8] WANG Fei, GE Xinxin, DONG Zengbo, et al. Joint energy disaggregation of behind-the-meter PV and battery storage: a contextually supervised source separation approach[J]. IEEE Trans Ind Appl 2022; 58(2): 1490-501.

[9] YU Shiwei, HAN Ruilian, ZHANG Junlie. Reassessment of the potential for centralized and distributed photovoltaic power generation in China: on a prefecture-level city scale[J]. Energy, 2023, 262: 125436.

[10] SANJARI M J, GOOI H B. Probabilistic forecast of PV power generation based on higher order Markov chain[J]. IEEE transactions on power systems, 2017, 32(4): 2942-2952.

[11] SHENG H M, XIAO J, CHENG Y H, et al. Short-term solar power forecasting based on weighted gaussian process regression[J]. IEEE transactions on industrial electronics, 2018, 65(1): 300-308.

[12] LAI Wenzhe, ZHEN Zhao, WANG Fei, FU Wenjie, WANG Junlong, ZHANG Xudong, REN Hui. Sub-region division based short-term regional distributed PV power forecasting method considering spatio-temporal correlations[J]. Energy, 2024, Vol.288: 129716.

[13] LU Junjie, CAI Tao, LANG Jianxun, et al. Short-term prediction method of cluster power generation power of photovoltaic power station based on cluster division[J]. High Voltage Technology, 2022, Vol.48(5): 1943-1951.

[14] LAIO W L, BAK-JENSEN B, PILLAI J R, et al. Short-term power prediction for renewable energy using hybrid graph convolutional network and long short-term memory approach[J]. Electric Power Systems Research, 2022, 211: 108614.

[15] SUN D Y, CAO X, LIANG Z F, et al. Distributed Photovoltaic Power Prediction Technology Based on Spatio-Temporal Graph Neural Networks[J]. Energy Engineering, 2025, 122(5): 3329-3346.

[16] SIMEUNOVIĆ Jelena, SCHUBNEL Baptiste, ALET Pierre-Jean, et al. Spatio-Temporal Graph Neural Networks for Multi-Site PV Power Forecasting[J]. IEEE Transactions on Sustainable Energy, 2022, 13(2): 1210-1220.

[17] KIPF T N, WELLING M. Semi-Supervised Classification with Graph Convolutional Networks[C]// International Conference on Learning Representations, 2017.

[18] VELIČKOVIĆ P, CUCURULL G, CASANOVA A, et al. Graph Attention Networks[C]// International Conference on Learning Representations, 2018.

[19] SHIH S Y, SUN F K, LEE H Y. Temporal pattern attention for multivariate time series forecasting[J]. Machine Learning, 2019, 108(8): 1421-1441.

Research on the Development Paths of New Energy Industry in Rural Areas for Dual Carbon Goals

1st Yanfei Pan
China Electric Power Planning & Engineering Institute
Beijing, China
panyf1003@163.com

2nd Qiong Li
Economics and Technology Research Institute
State Power Investment Corporation Limited
Beijing, China
zhuiyueliq@163.com

***Abstract*—In recent years, how to consolidate the achievements of poverty alleviation in rural areas in China after getting rid of absolute poverty has become an urgent issue for governments. The extensive use of fossil energy in rural areas has become a pressing issue in rural revitalization and energy transition, and the expenditure on fossil energy has become a heavy burden on rural residents. Wind energy and solar energy resources, as the dominant resources in vast rural areas in China, are not restricted by the original industrial base, and can become a new income source for village collectives and residents, and also bring new opportunities to the development of rural industries. This paper analyzes the challenges during energy transition in rural areas and the development paths of new energy industry in rural areas for carbon reduction and prosperity, and proposes policy suggestions to promote the high-quality development of new energy industry in rural areas.**

Keywords—new energy, green and low-carbon development, rural revitalization

I. INTRODUCTION

In recent years, the development of green and low-carbon energy in rural areas in China has made positive progress. The total rural energy consumption continues to grow, and the consumption structure is upgrading from traditional energy to efficient and clean energy. Rural power supply capacity and electrification level have been significantly improved, and the scale of new energy development continues to expand. New scenarios of energy utilization are continuously emerging, and the high-quality development of rural energy has been steadily promoted. By the end of 2024, the installed wind power generation in China has reached 521 million kilowatts, while the installed photovoltaic capacity has reached 887 million kilowatts, and the installed biomass power generation has reached 46 million kilowatts [1], most of the above are built in the vast rural areas, including 139 million kilowatts of household photovoltaic installations [2]. The rapid development of new energy has strongly promoted the optimization of energy structure and the upgrading of industrial structure in rural areas.

As the dual carbon strategy further promotes, a new round of scientific and technological revolution and industrial reform emerges. Rural areas' demand for clean, reliable, and economical energy has further increased. However, the problem of unbalanced and inadequate energy development in rural areas is s energy is still serious. This paper analyzes the challenges and obstacles faced by rural energy transition in China, and proposes the development paths of new energy industry in rural areas for dual carbon goals and common prosperity. Furthermore, policy suggestions are proposed to promote the high-quality development of new energy industry in rural areas in China.

II. THE MAIN CHALLENGES OF ENERGY TRANSITION IN RURAL AREAS

A. Rural Energy Consumption

At present, coal, firewood, and electricity are the main energy sources in rural areas. The total energy consumption in rural areas is about 600 million tons of standard coal per year [3], and the direct consumption of fossil energy such as coal, oil and natural gas accounts for more than 50%, while electricity consumption accounts for less than 40% [4]. The rural bulk coal consumption in northern China accounted for 65%, with Hebei, Shandong, and Henan provinces accounting for 42% of the national rural bulk coal consumption for winter heating [5]. The extensive use of fossil fuel brings severe pollution. The consumption of bulk coal in rural areas per year is 95 million tons [6], although only accounting for 3% of the total coal consumption, but contributed more than 20% to air pollution [7]. In China, 27% of atmospheric PM2.5 emissions comes from household solid fuel combustion, of which nearly 80% from rural areas [8]. Energy consumption is one of the major expenses for agriculture and rural life. In rural areas of Northeast China, the energy consumption accounts for 10.7% of the per capita expenditure [9].

The smallholder farmers are accounting for more than 98% of agricultural households in China [10]. The agricultural intensification level is low while the energy consumption is high. The coal consumption of traditional solar greenhouse and large-scale multi-span greenhouse has reached 13-60 tons per mu per year and 40-100 tons per mu per year, and the costs of heating energy, water and electricity accounted for 30%-70% of the agricultural production costs [11]. In China, agricultural machines are mostly powered by diesel engines [12], and

979-8-3315-5472-9/25/$31.00 ©2025 IEEE

agricultural diesel consumption accounts for about 15% of the total diesel consumption [7]. In Northeast China, coal-fired hot blast stoves are widely used for grain drying. Coal consumption for grain drying accounted for 45% of total agricultural energy use, with a carbon emission intensity 3.2 times that of electric drying; in North China, coal-fired hot blast stoves are used for heating vegetable greenhouses at night; in Northwest China, coal-fired hot blast stoves are used for drying cotton and fruits [13]. With the development of rural revitalization, higher demand for energy supply in agriculture becomes inevitable, including cheap and reliable energy supply in multiple forms such as electricity, heat, cold energy and others. However, the diversified energy supply system has not been established, and efforts are still needed to energize the rural revitalization relying on new energy.

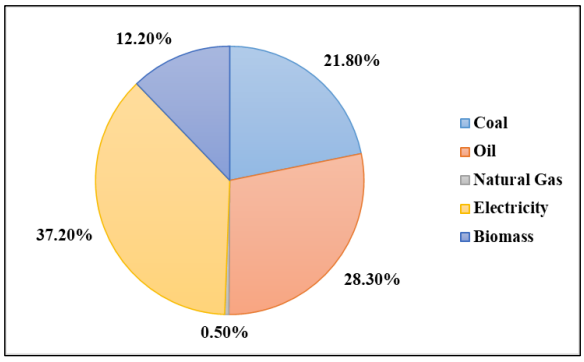


Fig. 1. Structure of energy consumption in rural areas in China.

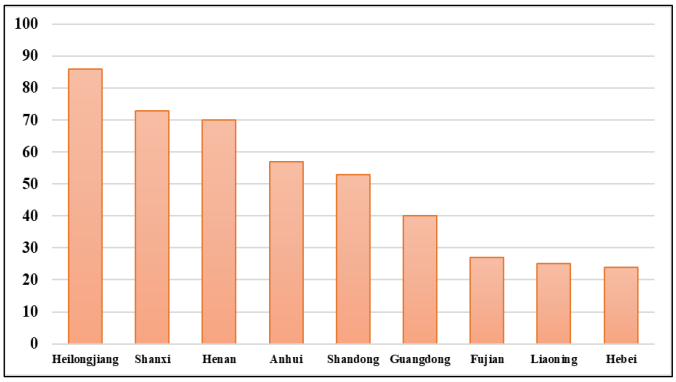


Fig. 2. Number of counties with restricted access space for distributed photovoltaic projects in provinces of China.

B. *Rural Energy Infrastructure*

The technical exploitable potential of distributed PV and distributed wind power in rural areas has reached 1000GW and 250GW, respectively [14]. However, with the integration of large-scale household photovoltaic systems and distributed wind power, the problems on rural power distribution network emerge widely such as overload, overvoltage, and defects in power quality. At present, more than 10 provinces such as Shanxi, Hunan and Liaoning have released the capacity assessment of the distributed network to integrate distributed photovoltaic, and more than 400 counties (cities and districts) have insufficient network capacity for integration of distributed photovoltaic systems [15]. In 2023, the penetration rate of rural new energy vehicles has reached 17% [16], but still significantly lower than the national penetration rate of over 50% [17]. The number of public charging piles in counties and rural areas only accounts for 12% of the total number nationwide, and coverage rate of rural new energy vehicle charging infrastructure is less than 5%, which restricts the popularization of the new energy vehicles [18]. The number of rural energy service stations is not enough to meet the demands of production and livelihood of farmers [19], as well as the demands of low-carbon transformation in energy utilization. Moreover, compared with urban areas, the rural areas are relatively underdeveloped in terms of infrastructure digitalization, and there are few interactions between digital infrastructure and energy infrastructure.

III. The Implementation Path of Promoting Common Prosperity in Rural Areas Through New Energy Development

A. *Green and Low-Carbon Energy Supply*

In recent years, diversified business modes have emerged in which village collectives or individuals can benefit from distributed new energy development in rural areas. Village collectives can participate in the decentralized wind power projects through resource contracting, property leasing, and investment with idle resources, which can revitalize idle land resources, and bring an income of 100,000 to 200,000 yuan per year [20] for village collectives. Another emerging industry is the comprehensive utilization of biomass. The market price of processed granular biomass, such as from corn stalk, is about 1200 yuan/ton, and the market price of processed bulk biomass, such as from wheat stalk or straw, is about 600-800 yuan/ton [7]. Meanwhile, by establishing the biomass fuel collection-storage-processing-export system, the incomes and employment opportunities in rural areas will grow significantly. In addition, villagers can also earn incomes by renting rooftops and idle courtyards to new energy developers for household photovoltaic and energy storage projects. Nowadays more than 5 million households in rural areas have implemented the household distributed PV projects, and the average annual household income has increased by about 2000 yuan [21]. Moreover, other innovative modes which combines agricultural production with power generation are continuously emerging, such as the complementary mode of fisheries–photovoltaic complementary model, an efficient breeding method combining power generation and underwater breeding, which can bring an additional income of more than 3,000 yuan per mu per year [22].

B. *New Development Mode of Green Industry*

Developing modern facility agriculture is an emerging and efficient method to utilize the abundant renewable energy resources in rural areas, such as the complementary development of photovoltaic–agriculture complementary development, animal husbandry, forestry, and fishing industry. Appropriate environment can be built accurately for crop growth relying on the new energy and storage system with advanced control technologies. It is estimated that 75% of the rural areas in China can fully rely on distributed new energy to achieve full electrification [7]. To further supply green and stable energy for rural production and lives, it is necessary to build rural green energy network and integration projects to achieve complementary supply of cold, heat, electricity and other forms of energy. Depending on the flexibility of rural energy

consumption, demand response can be implemented in rural areas making full use of agricultural machinery, electric vehicles and other types of energy storage resources. The integration of heat pump and new energy are promising technologies which can meet the heating needs in rural areas in a low-carbon way. Electrification of agricultural machinery and irrigation systems is a key direction for reducing fossil fuel consumption in rural areas. Promoting electric tractors, water pumps, and grain drying equipment, combined with distributed photovoltaic power generation, can create a self-sufficient agricultural energy system, reducing operational costs and carbon emissions. To create comfort and low-carbon residential environments, it is necessary to integrate the new energy systems into rural building retrofitting, such as installing photovoltaic panels on rural house roofs, using solar water heaters, and improving building insulation. Rural areas rich in wind and solar resources can develop new energy themed rural tourism, such as solar-powered tourist facilities, wind farm sightseeing, and low-carbon rural experience projects, which not only increases local income but also promotes the popularization of green energy concepts.

C. Upgraded Energy Infrastructure

It is necessary and urgent to upgrade the rural power distribution network, which is the basis of future energy network supplying both the green electricity and heat in rural areas. Based on the upgraded distribution network, the electric vehicle or machinery charging network with new energy supply can be built, facilitating the rural transportation and production. Furthermore, it is beneficial to establish a social service system for rural energy utilization, providing online and offline services such as diagnosis and maintenance of terminal energy equipment, personnel training, etc. To make full use of biomass resources in rural areas, it is necessary to strengthen the infrastructure construction for biomass utilization. It is important to digitalize the rural energy network, facilitating the energy services and other derivative services.

IV. The Policy Suggestions to Promote the High Quality Development of New Energy Industry in Rural Areas

A. Rational Planning for Promoting the New Energy Development in Rural Areas

It is suggested that in the medium-term and long-term energy development plan such as the 15th Five-Year Plan, specific chapters and the related studies should be conducted on the new energy development in rural areas. Establishing a county-level energy planning coordination mechanism that integrates new energy development with rural land use, industrial layout, and ecological protection is essential. General survey on new energy resources is necessary, and the system of related energy statistics should be established, such as a three-dimensional statistical system for rural energy consumption (household /agricultural /public facilities), installed capacity of renewable energy, and the carbon reduction rate. It is recommended to develop a unified rural energy data monitoring and management platform that integrates energy consumption, generation, and carbon emission data, which provides a scientific basis for policy formulation and project evaluation. This platform should support real-time data collection, analysis, and visualization to guarantee decision-making efficiency. On this basis, it is important to set medium-term and long-term goals, formulate paths and safeguard measures for new energy development in rural areas, and popularize the experiences and achievements of the pilot counties of rural energy revolution nationwide. The high-quality development of new energy industry can better contribute to rural revitalization.

B. Strengthening Governmental Support for New Energy Projects

In recent years, a series of policy documents have been released to support the development of distribution network and distributed renewable energy. In 2024, the National Energy Administration issued the *Action Plan for the High-Quality Development of Distribution Networks (2024–2027)*, proposing the innovative exploration and construction of a number of distributed smart grid projects. In 2025, the National Energy Administration issued the *Administrative Measures for the Development and Construction of Distributed Photovoltaic Power Generation*, requiring the enhancement of the power grid capacity to accommodate the development of distributed photovoltaic systems. Rural area is the best scenario for establishing distributed smart grid since it is generally at the end of the power grid. It is suggested to further promote the power system reform, clarify the status of the distributed smart grid in the electricity market, and improve the market trading mechanism for distributed generation. It is worth trying to pilot the village collective virtual power plant programs, enabling collectives in new energy rich areas to integrate resources such as household PV, small-scale energy storage, and agricultural loads into ancillary service markets. Source-grid-load-storage projects in rural areas should be encouraged and supported by local government, endeavoring to consume the new energy locally.

C. Improving the Benefit-Sharing Mechanism

Based on the practical experiences, it is necessary to further improve the construction and management mechanism of decentralized wind power, village-level photovoltaic power stations and household photovoltaic systems. Furthermore, effective mechanisms should be established to realize the rational benefit sharing among village collectives and developers, considering shares of land resources and other rural resources. Village-level photovoltaic stations should establish a secondary revenue distribution mechanism. For instance, considering operational costs, 60% of the profits are distributed to farmers based on roof/land equity, 30% are retained for village infrastructure, and 10% are taken as a risk reserve fund. By improving the benefit-sharing mechanism, the village collectives are efficiently motivated to participate in new energy projects, and their incomes can also be increased significantly. It is suggested to establish a comprehensive risk prevention and control mechanism for new energy projects in rural areas, including technical failure prevention, market price fluctuation response, and natural disaster resilience planning, ensuring the long-term stability of energy supply and investment returns.

D. Releasing Green Finance Policies

It is suggested to establish a national special fund for green energy development in rural revitalization, to support and promote new energy projects in rural areas. In this approach the

financial resources are better integrated and utilized, for the construction of rural new energy infrastructure, etc. Meanwhile, there are other ways to assist the construction of new energy projects, such as low-interest loans and public REITs. For financial product innovation, it is suggested to promote photovoltaic loans; for example, banks offer 5-8 years credit loans to farmers at low interest, accepting revenues from power generation and carbon trading as repayment sources. For village collective projects, it is suggested to issue rural new energy REITs, securitizing future revenues of mature PV/wind projects. Local governments can set up green transition guarantee funds to provide loan guarantees, lowering entry barriers for private capital. Additionally, it is necessary to explore and establish a carbon sink revenue feedback mechanism, in which forest carbon sink trading revenues from new energy projects can reward village collectives for low-carbon construction. By reducing the financing costs and investment risks, it can be expected that the new energy industry as well as the sustainable green agriculture can attract more financial support from society.

V. CONCLUSION

To meet the clean and economical energy needs in rural areas as well as alleviating poverty, it is imperative to establish and develop new energy industry in rural areas. As distinctive and widespread resources in rural areas, new energy is regarded as the most important element in promoting common prosperity. This article has demonstrated the main challenges of energy transition in rural areas, and proposed the systematic implementation path of promoting common prosperity in rural areas through new energy development. By rational planning of new energy development and strengthening policy support, new energy industry will play a significant role in the high-quality development of rural areas.

REFERENCES

[1] NEA, “Transcript of the National Energy Administration's press conference of 2024”, 2024.

[2] NEA, “Photovoltaic power generation construction in 2024”, 2024.

[3] China Electric Power News, “Observations from the Third Rural Energy Development Conference”, 2024.

[4] China Electric Power News, “Prescribe the right medicine to promote rural energy revolution”, 2023.

[5] Tsinghua University, “Comprehensive Report on China's Rural Scattered Coal GovernanceWhite Paper on Rural Bulk Coal Governance”, 2024.

[6] Tsinghua University, “Comprehensive Report on Rural Scattered Coal Governance in China”, 2024.

[7] Jiang Yi, “Building a New Rural Energy System”, 2024.

[8] Wang C, Bao A, Liu J, et al. “Emission inventory of rural civilian sources surveyed in households and the emission reduction effects of clean energy policies”, Environmental Science, 44(5):2811-2822, 2024.

[9] Zhong Ziyou, “Measurement and analysis of influencing factors of energy poverty of rural households in China”, 2023.

[10] Study Times, “How to solve the dilemma of ‘big country, small farmers’”, 2024.

[11] Zou Zhirong, “Reduce energy consumption, save costs, and promote the green, low-carbon and efficient development of facility agriculture”, 2023.

[12] China Industrial News, “my country's agricultural machinery inventory has reached 200 million sets. It is time for mechanization and intelligentization to develop”, 2024.

[13] Ren Yanbo, Wu Ting. “Research on the practical problems and countermeasures of clean heating in rural areas”, 2023.

[14] State Power Investment Corporation, Siemens Energy, “China County Green and Low-Carbon Energy Transformation Development Report”, 2022.

[15] Photovoltaic box, “Distributed access is restricted in more than 450 counties, and these projects provide important inspiration”, 2024.

[16] China Auto News, “Going to the countryside” should first answer the safety question”, 2024.

[17] Financial Automotive, “The penetration rate of new energy vehicles has exceeded 50% for three consecutive months”, 2024.

[18] Blue Whale News, “New energy vehicle companies are entering the county-level market. Who will dominate the third- and fourth-tier cities' auto market?”, 2024.

[19] China Energy News, “Rural energy construction should be included in local economic and social development plans”, 2022.

[20] China Times, “The opportunity of "wind power going to the countryside" is coming, which can bring 100,000 to 200,000 yuan of income to the village collective every year. These areas will benefit”, 2024.

[21] Su Yu, Zhang Jianhong, “Develop rural biomass energy utilization according to local conditions”, 2024.

[22] Jiangsu Provincial News Network, “the first batch of full-capacity grid-connected power generation of the province's largest fishery-solar complementary project”, 2024.

An Optimal Scheduling Strategy for Virtual Power Plant Participating in Peak Regulation Considering Industrial Load Production Processes

Jin Mao
School of Information Management
Wuhan University
Wuhan, China
0000-0001-9572-6709

Liang Yin*
Power Science Research Institute
of State Grid Ningxia Electric
Power Company No.716, Huanghe
East Road, Jinfeng District
Yinchuan, China
1370164095@qq.com

Fang Wang
Power Science Research Institute
of State Grid Ningxia Electric
Power Company No.716, Huanghe
East Road
Yinchuan, China
597435737@qq.com

Xiaoli Wang
Power Science Research Institute
of State Grid Ningxia Electric
Power Company No.716, Huanghe
East Road, Jinfeng District
Yinchuan, China
22090775@qq.com

***Abstract*—High-energy-consuming industrial loads in multi-process industries such as glass factories have considerable flexible adjustment potential, but their enthusiasm for participating in grid peak shaving is low due to production characteristics. As an aggregator of distributed resources, virtual power plant (VPP) can coordinate resources to participate in trading in energy and peak shaving markets. To address this, an optimal scheduling strategy for VPP peak shaving considering industrial load production processes is proposed: constructing a trading framework for VPP to participate in the two markets, establishing an energy-peak shaving response model for glass factory loads to tap adjustment potential, analyzing and modeling their typical production processes using the state-task network (STN) method, and then building an optimal VPP scheduling model to enhance loads' enthusiasm for demand response (DR) while ensuring normal production in glass factories. Case simulations show that the model can fully exploit load potential and actively participate in DR under the premise of ensuring safe production and plans of industrial enterprises, with VPP revenue increased by 8.16% and peak shaving and valley filling volume improved by 23.73%.**

Keywords—virtual power plant, industrial load, demand response, state-task network

I. INTRODUCTION

With the proposal of the carbon peak and carbon neutrality goals, large-scale renewable energy has been integrated into the power grid [1]. However, due to the volatility of renewable energy generation such as wind power and photovoltaic power, on the one hand, it increases the uncertainty of power output, which greatly enhances the system's demand for adjustable resources. On the other hand, it weakens the space for traditional energy power generation, posing challenges to the safe and stable operation of the power system. Therefore, it is urgent to explore new flexible resources. Therefore, the load side has become another choice for flexible resources.

Load-side resources cover residential and commercial loads represented by air conditioners, water heaters, electric vehicles [2] and also include various industrial loads such as steel [3], cement [4]. Among them, industrial loads have attracted extensive attention due to their advantages of high power consumption and large load potential. However, due to the low willingness of industrial load to participate in the response, how to fully exploit the regulation potential of industrial load has become a hot topic of current research. Studied electrolytic aluminum's production characteristics, constructed an interaction model between electrolytic aluminum enterprises and the power grid, which improved wind power consumption and reduced enterprise production costs [5]. Explored the DR potential of the electric arc furnace equipment with the highest power consumption in the steel plant production process and constructed a response model for the steel plant [6]. The above model studies all take single equipment such as electrolytic cells and electric arc furnaces as the control objects, the impact of the coupling relationship between production equipment on load regulation is not fully considered. However, for industrial loads such as steel plants, cement plants, and glass factories, the production processes are complex, and the connections between various processes are relatively close. Therefore, controlling only a single equipment is difficult to tap the overall load potential of industrial loads, The entire production process and the coupling relationship between individual equipment need to be considered. By analyzed the cement load production process and pointed out that the cement load adjustment potential was related to the quantity of materials [7]. The optimal scheduling of virtual power plants that aggregate industrial loads considers the supply assurance, periodicity, continuity and coupling of industrial load production, but the description of the overall production process modeling is not accurate and sufficient, which will also cause the problem of insufficient exploitation of the load potential of industrial loads [8]. How to accurately characterize the production process of industrial loads is an issue to be further studied. Therefore, based on the STN model [9], the production process of glass factories is re-characterized, so as to fully tap the potential of industrial load participation in load regulation.

As an aggregator of distributed energy resources (DERs), the VPP enables coordination and complementarity among internal resources, optimizing energy allocation and utilization. VPP has the capability to aggregate wind power, photovoltaic and other resources for participation in energy market transactions, as well as integrate energy storage and interruptible loads to jointly engage in ancillary service markets [10]. By aggregating energy storage devices and industrial loads through a VPP for DR, the combined peak regulation of

979-8-3315-5472-9/25/$31.00 ©2025 IEEE

energy storage and flexible loads achieves superior peak-shaving effects [11]. At present, to better unleash the potential of DREs within VPP, research on VPP participation in combined energy and ancillary service markets has become a prominent focus. Treats electric vehicle (EV) clusters as energy storage systems, constructing a three-stage optimal scheduling model for VPP incorporating EV clusters to participate in energy and ancillary service markets [12]. When engaging in market transactions, DR serves as a means for VPP to flexibly adjust internal resources [13]. DR is typically categorized into price-based and incentive-based types. Compared with price-based DR, incentive-based DR leans more toward a reward scheme [14], thus being more effective in mobilizing user enthusiasm.

II. VPP Structure and Trading Framework

In this paper, large-scale glass factories, wind power, and photovoltaic power are aggregated into a single VPP, which is coordinated and controlled by VPP operators. The framework of the transaction structure is shown in Fig. 1.

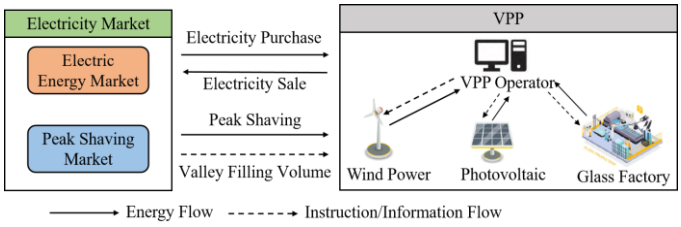


Fig. 1. VPP trading framework diagram.

The VPP formulates bidding strategies in two markets based on the acquired market information. In the energy market, the VPP submits purchase volume bids according to load supply requirements and sells electricity during peak-price periods to maximize profits. In the peak regulation market, the VPP implements DR on the interruptible loads of glass factories and submits bid volumes for peak shaving and valley filling, thereby earning peak regulation revenues.

Due to the production characteristics of high energy consumption, high regulation potential and low response willingness of industrial loads, the regulation potential of industrial loads is often difficult to tap. The low willingness to respond is mainly due to the industrial load will not be able to complete the daily work order on time due to participation in response adjustment, for the factory would rather not participate in the demand response but to ensure the completion of the order, compared with the corresponding benefits, the enterprise pays more attention to the on-time delivery of product orders. At present, for VPP to aggregate industrial loads, such loads often do not fully consider the coupling between production relations and the production goals of enterprises, or only consider the importance of adjustable loads while ignoring the importance of non-adjustable loads, which will cause the industrial load regulation potential to be too large, which is unreasonable for virtual power plants that aggregate industrial loads to participate in market and grid transactions.

Given the unique production characteristics of industrial loads like glass factories, to fully exploit the load adjustment potential in demand response modeling, it is necessary to consider flexible loads alongside the entire production process and inter-process couplings. Against this backdrop, this paper constructs an optimal scheduling strategy for VPP participating in peak regulation that explicitly incorporates industrial production processes. The strategy centers on VPP coordination while rigorously accounting for the operational constraints and process interdependencies of glass factories, enabling a comprehensive utilization of their load flexibility.

III. Transaction Decision Model of VPP Energy-Peak Shaving Market

A. The VPP Participate in the Operational Framework of Peak Shaving

The VPP includes wind p ower, photovoltaic power, and glass plant loads, and the VPP schedules the glass plant loads. Wind power and photovoltaic power should first consider supplying power to the internal load of the VPP, and if the wind and photovoltaic output is excessive, electricity can be sold externally, and if the output is insufficient, electricity can be purchased from the external power grid. In addition, the glass plant load has the ability to adjust and can provide peak shaving auxiliary services.

B. A Mathematical Model of the VPP Participating in Peak Shaving

The cost of purchasing electricity from the electric energy market for VPP.

$$C_1 = \sum_{t=1}^{24} \lambda_h(t) P_{vpp,buy}(t) \tag{1}$$

where $\lambda_h(t)$ denote the electricity price in the energy market at time period t, $P_{vpp,buy}(t)$ and denote the power purchase volume of the VPP in the energy market at time period t. The cost of invoking user load for a VPP is defined below.

$$C_2 = \sum_{t=1}^{24} \rho f_{e,glass} (P_{DR,h,glass}(t) + P_{DR,l,glass}(t)) \tag{2}$$

where $f_{e,glass}$ denote the unit capacity subsidy cost for glass factory loads, $P_{DR,h,glass}(t)$ denote the peak-shaving capacity of glass factory loads at time period t, $P_{DR,l,glass}(t)$ and denote the valley-filling capacity of glass factory loads at time period t. In order to increase the declaration volume and obtain more profits, VPP encourages the load to transfer more loads from peak hours to trough hours on the basis of a certain amount of transfer total. To this end, this paper characterizes the difference between the load transfer out during peak period and the transfer in during valley period by defining the peak-valley transfer deviation coefficient, which is:

$$W = P_{DR,h,glass}(t) - P_{DR,l,glass}(t) \tag{3}$$

As can be seen from the formula, The smaller the value of the peak-valley transfer deviation coefficient, the smaller the difference between the total amount of load transferred out of the peak period and the total amount transferred in during the valley period on the basis of a certain amount of total transfer, reflecting that the amount of load transferred from the peak

period to the trough period is larger and the amount transferred to other periods is smaller. If all the transfers out of the peak period are transferred to the valley period, that is, the transfer out of the peak period is equal to the transfer volume of the valley period, the value of the peak-valley transfer deviation coefficient is 0. VPP sets a tiered compensation price according to the size of the peak-valley transfer deviation coefficient, and the smaller the peak-valley transfer deviation coefficient, the higher the compensation price set by VPP. Where: ρ_1, ρ_2 and ρ_3 are the compensation prices of the three levels that increase in turn; W1 and W2 are the upper limits of the peak-valley transfer deviation coefficients of the first and second levels.

The penalty costs for wind and solar curtailment in VPP are described as follows.

$$C_3 = f_{aban}(t)(P_{wind,ab}(t) + P_{pv,ab}(t)) \tag{4}$$

where $f_{aban}(t)$ denote the unit penalty cost for wind and solar curtailment at time t, $P_{wind,ab}(t)$ denote the curtailed wind power at time t, and $P_{pv,ab}(t)$ denote the curtailed solar power at time t. The cost of starting and stopping equipment for factory equipment due to demand response is as follows.

$$C_{re} = \sum_{t\in T}\sum_{k\in K} \Delta P_k^t \eta_k \tag{5}$$

$$\Delta P_k^t = P_k^N (1 - N_{t,k}) \tag{6}$$

where P_k^N denote the rated power of the equipment, η_k denote the cost of regulating the unit power of production equipment.

The peak regulation revenue of VPP.

$$S_1 = \sum_{t=1}^{24} (f_{vpp,h}(t)P_{vpp,h}(t) + f_{vpp,l}(t)P_{vpp,l}(t)) \tag{7}$$

$$P_{vpp,h}(t) = P_{DR,h,glass}(t) \tag{8}$$

$$P_{vpp,l}(t) = P_{DR,l,glass}(t) \tag{9}$$

where $f_{vpp,h}(t)$ and $f_{vpp,l}(t)$ denote the compensation prices for peak shaving and valley filling of the VPP at time period t, respectively. $P_{vpp,h}(t)$ and $P_{vpp,l}(t)$ denote the declared peak shaving and valley filling volumes of the VPP at time period t, respectively. $P_{DR,h,glass}(t)$ and $P_{DR,l,glass}(t)$ denote the peak shaving and valley filling capacities of the glass factory loads at time t, respectively. The revenue from the VPP selling electricity to glass factory users is described as follows.

$$S_2 = \sum_{t=1}^{24} \lambda_m P_{e,glass}(t) + \lambda_n P_{e,glass}(t) + \lambda_k P_{e,glass}(t) \tag{10}$$

where λ_m, λ_n, and λ_k denote the time-of-use (TOU) peak, flat, and valley electricity prices set by the VPP, respectively. Let $P_{e,glass}(t)$ denote the actual power purchase of user loads at time period t. The revenue from the VPP selling electricity to the energy market is described as follows.

$$S_3 = \sum_{t=1}^{24} \lambda_h(t) P_{vpp,sell}(t) \tag{11}$$

where $\lambda_h(t)$ denote the electricity price in the energy market at time t, $P_{vpp,sell}(t)$ denote the power sold by the VPP to the energy market at time t.

The objective function of the VPP is described as follows.

$$\max S = \sum_{t=1}^{24} (S_1 + S_2 + S_3 - C_1 - C_2 - C_3 - C_{re}) \tag{12}$$

where S denote the daily operational revenue of the VPP, S_1 the peak regulation revenue, S_2 the revenue from selling electricity to glass factory users, S_3 the revenue from selling electricity to the energy market, C_1 the power purchase cost from the electricity market, C_2 the cost of deploying glass factory loads and C_3 the penalty cost for wind and solar curtailment.The capacity constraints of load dispatch for glass factory users.

$$0 \le P_{vpp,buy}(t) \le P_{vpp,buy,\max} \tag{13}$$

$$0 \le P_{vpp,sell}(t) \le P_{vpp,sell,\max} \tag{14}$$

where $P_{vpp,buy,max}$ denote the maximum user load dispatched for peak shaving at time t, $P_{vpp,sell,max}$ denote the maximum user load dispatched for valley filling at time t. The power balance constraints of VPP.

$$\begin{aligned} &P_{vpp,buy}(t) + P_{wind}(t) + P_{pv}(t) = P_{e,glass}(t) + \\ &P_{vpp,sell}(t) + P_{pv,ab}(t) + P_{wind,ab}(t) \end{aligned} \tag{15}$$

C. Glass Factory Production Process Modeling

The specific process of establishing the above STN model based on the glass production process is as follows.The float forming process, the current mainstream glass production technology, follows this workflow: Quartz sand, soda ash, limestone and other auxiliary raw materials are crushed, stored in warehouses for preliminary homogenization, then fed into screening machines in specific proportions to get suitably sized materials, which are stored in corresponding warehouses. Next, ball mills process these into melting-ready raw materials, stored in dedicated warehouses. During melting, raw materials are transported into a furnace; at 1,200°C–1,500°C, they turn into molten glass, which flows into a tin bath and is stretched to desired dimensions by specialized equipment. The glass is then conveyed to a lehr for annealing and cooling to balance internal stresses, preventing fractures from rapid cooling in subsequent steps. Cooled glass is stored, later cut to order specifications, and finally packaged and shipped as required.

Considering that the regulation potential of glass production loads is closely related to warehouse capacity, this paper focuses on setting up corresponding warehouses for the raw material crushing, screening, ball milling, and cutting stages. Warehouses are not established for the melting, annealing, and forming stages because the materials produced in these stages cannot be stored. The production process is shown in Fig. 2. The main processing equipment corresponding to each process includes crushers, screening machines, ball mills, melting furnaces, tin baths, lehrs, and cutting machines.Regarding the specific equipment mentioned above, their regulation methods are analyzed as follows.

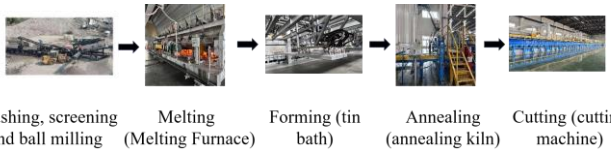


Fig. 2. Glass production process.

The available quantity of production materials in a glass factory at time t is composed of three parts: the available quantity of the material at the previous time point, the quantity generated by production tasks ending at time t, and the quantity consumed by production tasks starting at time t. The mathematical expression is as follows.

$$R_{t,n} = R_{t-1,n} + \sum_{k \in K} \mu_{t,n,k} N_{t,k} \tag{16}$$

$$N_{t,k} = \sum_{m \in M_k} B_{t,m,k} \tag{17}$$

where $R_{t,n}$ is the available amount of state matter n at time t. K is the set of all tasks. $\mu_{t,n,k}$ is the amount of intermediate state n generated or consumed by one of the main production equipment of task k at time t. $N_{t,k}$ is the total number of production devices for task k that is in the started state in time t. M_k is the collection of production devices for task k, $B_{t,m,k}$ is the condition that the mth device of task k is started at time t. The overall translation is into English, which is a bit more academic.The total electricity consumption of the glass factory in the t period is expressed as the sum of the electricity consumption of all equipment in the t period, which is expressed as.

$$P_{e,glass}(t) = \sum_{k \in K} \mu_{t,e,k} N_{t,k} \tag{18}$$

where $P_{e,glass}(t)$ is the electricity consumption of the glass factory in the t period, $\mu_{t,e,k}$ is the actual electricity consumption of a production equipment in task K in the t period.The crushing tasks, screening tasks, ball milling tasks and cutting tasks of the glass factory have corresponding warehouses, which provide greater flexibility for the load transfer of the glass factory, but its storage capacity is capped, so it is necessary to set the upper limit on the number of intermediate objects, and at the same time, in order to ensure safety and reliability, it is also necessary to set the minimum storage capacity to cope with the occurrence of unexpected situations, the expression is.

$$R_{L,n} \le R_{t,n} \le R_{H,n} \tag{19}$$

where $R_{L,n}$ and $R_{H,n}$ are the lower and upper limits of the storage capacity of intermediate state n objects.The premise of the glass factory's participation in the grid dispatch is that it cannot affect its own production plan, and must ensure that the daily output requirements of the glass factory are met.

$$R_{T,m} - R_{0,m} \ge R_{demand,m,final} \tag{20}$$

where $R_{T,m}$ and $R_{0,m}$ are the quantities of finished glass at the end of the scheduling moment and the beginning of the scheduling moment, respectively. $R_{demand,m,final}$ is the daily output requirement of flat glass in the glass factory.

D. Model Solution Flow Chart

The solution process of the scheduling optimization model is shown in Fig. 3.

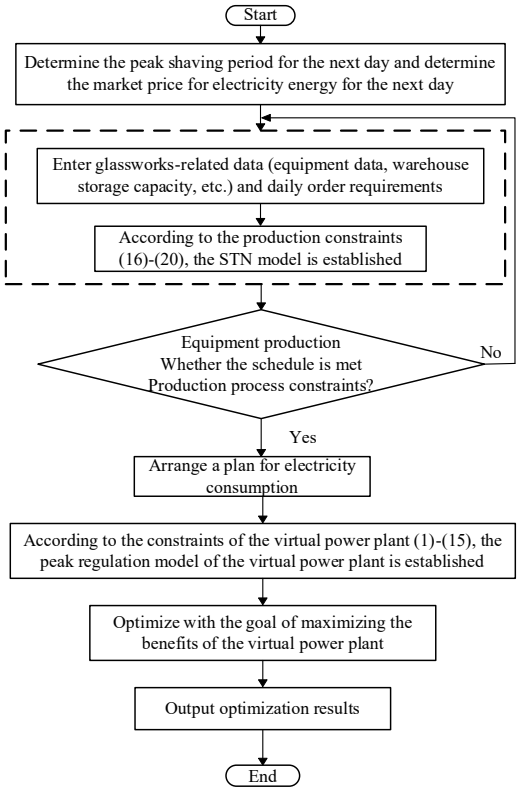


Fig. 3. Flowchart for solving the optimal scheduling model of VPP participating in peak regulation considering production processes.

IV. Simulation Verification of the Calculation Example

A. Parameter Settings

In this paper, on the Matlab R2021b simulation platform with YALMIP toolbox and Gurobi solver, we take a VPP that aggregates wind power, photovoltaic power, and large-scale glass factories in a region of southern China to participate in the day-ahead power market as an example. Parameters of glass plant: The number of core production equipment and rated power settings of each process of the glass enterprise are shown in TABLE .

TABLE I. Number and Rated Power of Core Production Equipment in Each Process of Glass Plant

Equipment	Attributed process	Rated power/kw	Quantity/unit
Crusher	Broken	900	2
Screening machine	Screening	900	2
Ball mill	Ball mill	1300	2
Melting furnace	Melting	1500	1
Tin baths	Molding	1600	1
Annealing kiln	Anneal	1600	1
Cutter	Incise	700	2

B. Necessity Analysis for Production Process Modeling

To verify the impact of production processes on the peak shaving participation of glass factories in the power grid, this paper designs the following two scenarios for comparative analysis. Scenario1: Based on the production process model of glass factories proposed in this paper, the objective is to maximize the revenue of the VPP, as specified in Equation (9). Meanwhile, storage constraints are removed and replaced with corresponding equipment operation time constraints to ensure all production tasks are completed within the scheduling period. Scenario2: The objective remains maximizing VPP revenue, consistent with Scenario 1. However, the constraints consider the complete production process constraints, Equations (13) to (17).In Scenario1, the failure to consider storage constraints—that is, the inter-coupling of production processes—resulted in a continuous and significant shortage of materials generated by the annealing process below the inventory lower limit, as illustrated in Fig. 4.

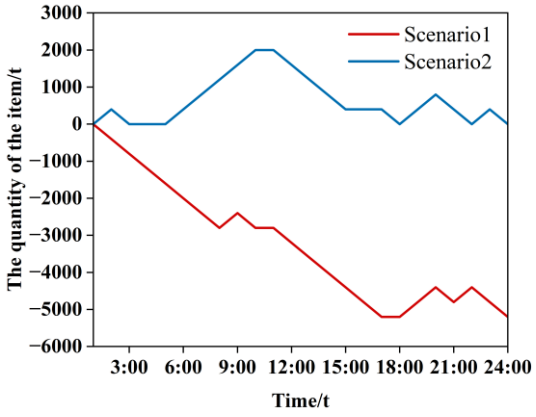


Fig. 4. Material quantity changes in annealing processes of scenario 1 and scenario 2.

In Scenario2, the variation of each material quantity is shown in Fig. 5. It can be seen that the quantity of each material in Scenario2 meets the upper and lower limits of enterprise production constraints. Therefore, based on the production process modeling method proposed in this paper, a practical production plan can be provided for glass factories, while improving the enthusiasm of load demand response.

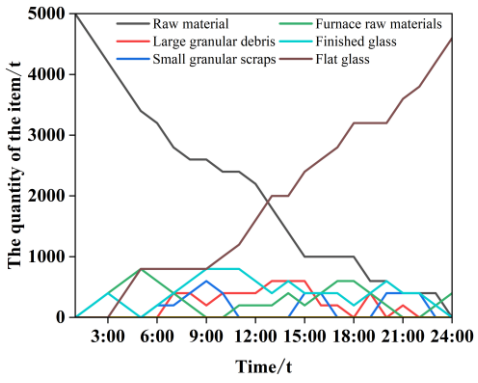


Fig. 5. Quantity changes of various materials in scenario 2.

C. Analysis of Optimization Strategy for VPP and Load

In the electricity energy market, the VPP dispatches internal wind power, photovoltaic and glass factory loads. The glass factory loads are dispatched on the basis of satisfying production process constraints, while purchasing and selling electricity in the energy market based on load demand. The dispatching status of each resource when participating in the electricity energy market is shown in Fig. 6. It can be seen from the figure that when the output of wind power and PV exceeds the load, the VPP sells excess electricity in the energy market; when the output is less than the load, it purchases electricity. Since the VPP in this paper is not equipped with energy storage equipment, there is phenomenon of wind and PV curtailment. In the dispatching diagram of the VPP participating in the electricity energy market, it can be seen that each resource can achieve power balance.

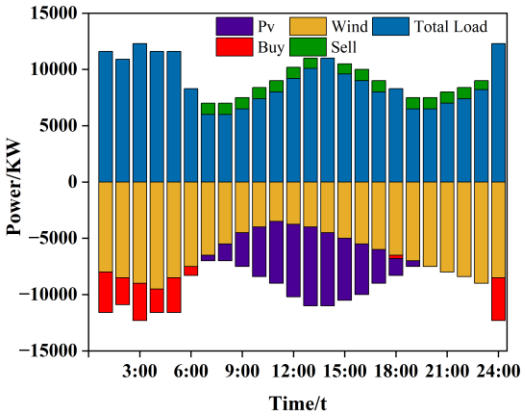


Fig. 6. Resource scheduling of virtual power plant in energy market.

In this paper, the load is scheduled in Fig. 7 for the DR mode of traditional time-of-use TOU tariff. As can be seen from Fig. 7, according to the requirements of power grid peak regulation, the VPP dispatches the load for peak shaving and valley filling, and it can be seen from the figure that after the demand response, the load is transferred from the period 8:00-12:00 and 18:00-21:00 to the period 01:00-07:00 and 12:00-15:00, and in general, the load at peak time is transferred to the valley period and the normal period.

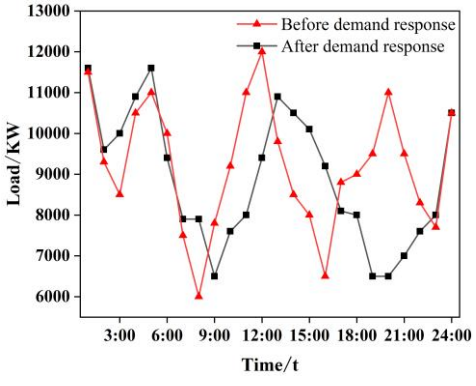


Fig. 7. Load participation load response situations in demand response participation.

In the peak shaving market, VPP mainly dispatches loads to participate in DR and performs peak shaving and valley filling during peak hours and valley hours, in order to analyze the effectiveness of the peak shaving strategy of VPP in this paper, the following two scenarios are set up for comparison based on the model established in this paper. Scenario1: The peak shaving strategy of VPP proposed in this paper. Scenario2: Traditional VPP peak shaving strategy. The load scheduling situation of the VPP participating in the peak shaving market in scenario1 is shown in Fig. 8(a).

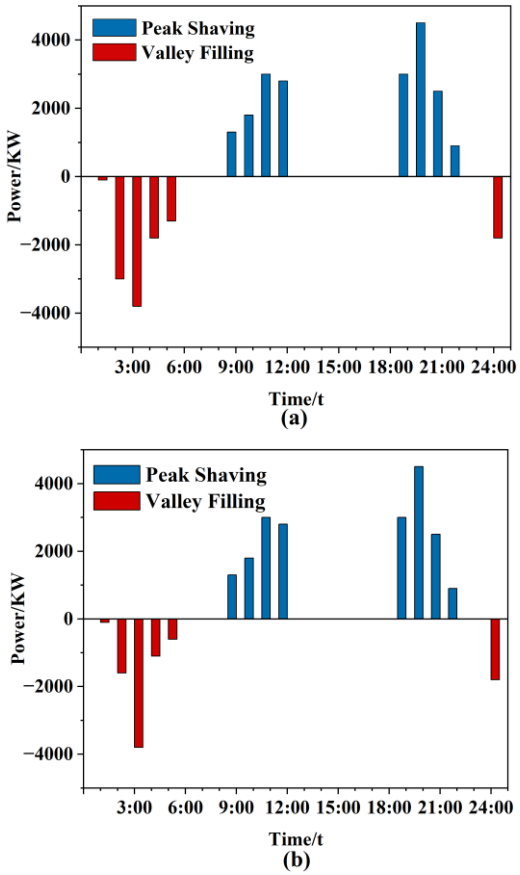


Fig. 8. Load scheduling situations of VPP participating in peak regulation market in different scenarios.

In Fig. 8(a), VPP reduces load consumption by scheduling the load to reduce the load during peak hours, and shifts the load to the valley and flat periods, and declares it as the peak shaving volume in the peak shaving market, so as to obtain the peak shaving income. For the traditional virtual power plant peak shaving strategy in scenario2, the scheduling situation of the VPP participating in the peak shaving market is shown in Fig. 8(b), from which it can be seen that the valley filling volume is significantly reduced, this is because the traditional VPP peak shaving strategy does not fully tap the adjustment potential of industrial load, resulting in low enthusiasm for load participation in demand response, resulting in a decrease in valley filling.

TABLE shows the revenue, peak hour transfer-out, valley transfer-in volume and total cost of the VPP in the two scenarios.

TABLE II. PEAK REGULATION INFORMATION

Scenario	Peak-period export volume /kw	Valley-period import volume /kw	Total cost/yuan	Total revenue/yuan
Scenario1	19800	9000	22185	130735
Scenario2	19800	11800	10985	142345

As can be seen from TABLE , the total revenue and the transfer-in volume in the valley period in scenario1 are lower than those in scenario2, and the total cost is higher than that in scenario2, because scenario2 considers that the complete production process model can ensure the normal production of industrial users and improve the enthusiasm of load users to participate in the response, while scenario1 does not fully consider the constraints of the production process and ignores the coupling between the production processes of industrial loads, which makes it impossible to meet the safety production of enterprises, so the transfer-in volume and income in the valley period are lower than those in scenario2. Therefore, it is necessary to consider the coupling between the production processes when the VPP aggregates industrial loads, and the production process model of the glass factory proposed in this paper considers the coupling between the production processes well, fully excavates the load regulation potential, and makes the effectiveness and authenticity of the VPP participation in the peak regulation of the power grid be verified to a certain extent.

V. CONCLUSION

For VPP aggregating multi-process, high-energy industrial loads, accurately depicting industrial loads' production processes is crucial—it is a prerequisite for ensuring industrial users' safe production and affects VPPs' scheduling of these loads. This paper establishes a VPP optimal scheduling model for peak shaving that considers industrial loads' production processes, addressing oversimplified and inaccurate load modeling in industrial-load-aggregating VPP. The model enables active demand response (DR) and taps load adjustability while ensuring normal industrial production. Different scenarios show that accurate production process modeling is vital for industrial users' normal production, influences VPP load scheduling, correctly reflects industrial load adjustment potential, and boosts DR participation enthusiasm. However, limitations exist: production process modeling ignores personnel mobilization and equipment start-up/stop costs; VPP industrial loads use traditional TOU pricing for DR, with insufficient consideration of price impacts on load mobilization. The model only aggregates glass plant loads; future research could aggregate multiple industrial loads via VPP to realize load complementarity and further tap load potential.

ACKNOWLEDGMENT

This work is supported by state grid corporation of China science and technology Project (No. 5108-202435057A-1-1-ZN).

REFERENCES

[1] DING Yiting. The installed capacity of renewable energy power generation in China has exceeded 2 billion kilowatts[N]. People's Daily, 2025-06-08 (001).

[2] C. Ji, Q. Yang, N. Ning, Y. Liu and L. Lyu, “Mitigating downward reserve deficiency of power system via coordinating EV demand response at valley period,” in IEEE Access, vol. 8, pp. 112368-112378, 2020.

[3] T. Yang, L. Gan, X. Chen, G. Li and K. Yu, “Dispatching potential evaluation of purchased power load in iron and steel plant considering production process optimization,” 2021 IEEE/IAS Industrial and Commercial Power System Asia (I&CPS Asia), Chengdu, China, 2021, pp. 592-597.

[4] X. Zhao, “A model of demand response scheduling for cement plant,” 2014 IEEE International Conference on Systems, Man, and Cybernetics (SMC), San Diego, CA, USA, 2014, pp. 3042-3047.

[5] Gong , “Review of electrolytic aluminum load participating in demand response to absorb new energy potential and methods,” 2021 IEEE 2nd International Conference on Big Data, Artificial Intelligence and Internet of Things Engineering (ICBAIE), Nanchang, China, 2021, pp. 1015-1019.

[6] XIAO Z, GABRIELA H, IIRO H. Cost-Effective scheduling of steel plants with flexible EAFs[J]. IEEE Transactions on Smart Grid, 2017, 8 (1): 239-249.

[7] YAO Mingtao, HAN Xue, ZHENG Yanan. Ponder on promoting the participation of high energy-intensive industries in power ancillary service market[J]. Energy of China,2018,40(2):22-26,47.

[8] SUN Shijie. Research on optimal scheduling and energy storage configuration of virtual power plant considering the production characteristics of industrial load[D]. Zhejiang University, 2023.

[9] FLOUDAS C A, LIN X. Continuous-time versus discrete-time approaches for scheduling of chemical pro-cesses: a review[J]. Computers & Chemical Engineering, 2004, 28(11): 2109-2129.

[10] X. Fan, L. Zhang, H. Sun, S. Hu, C. Sun and B. Zhu, “The day-ahead bidding strategy of virtual power plant for participating in electric energy market and peak regulation market,” 2022 4th Asia Energy and Electrical Engineering Symposium (AEEES), Chengdu, China, 2022, pp. 242-247.

[11] NING L, LIU Y, CHEN Y, ZHAO Y. Research on the optimal scheduling method of virtual power plant with industrial loads participating the peak regulation ancillary service, 2023 5th Asia Energy and Electrical Engineering Symposium, Chengdu, China, 2023, pp. 1080-1087.

[12] DENG Zhenli, FENG Xinyu, WANG Shiqian. Comprehensive optimal scheduling of VPP with EV cluster participating in main and auxiliary joint markets[J]. Proceedings of the CSU-EPSA, 2023, 35(2):83-93.

[13] WEI Chunhui, SHAN Linsen, HU Dadong. Optimal scheduling strategy for campus virtual power plant oriented to demand response[J]. Electric Power, 1-10[2025-06-16].

[14] YANG Xiu, DU Nannan, SUN Gaiping. Bi-level optimization dispatch of virtual power plants considering the demand response[J]. Journal of Electric Power Science and Technology, 2022,37 (2):137-146.

Online Energy Management of FCHEVs based on Multi-Time Scale Dynamic Game Theory

Zhuang Tian
School of Astronautics, Northwestern Polytechnical University, Xi'an, China & Lis-Lab, Aix-Marseille University, Marseille, France,
zhuang.tian@mail.nwpu.edu.cn

Junqi Wang
School of Astronautics, Northwestern Polytechnical University, Xi'an, China,
junqi@mail.nwpu.edu.cn

Yigeng Huangfu
Northwestern Polytechnical University,
yigeng@nwpu.edu.cn

S. M. Muyeen
Department of Electrical Engineering, Qatar University, Doha, Qatar
sm.muyeen@qu.edu.qa

Daming Zhou
School of Astronautics, Northwestern Polytechnical University, Xi'an, China,
daming.zhou@nwpu.edu.cn

***Abstract*—Efficient energy management is critical for fuel cell hybrid electric vehicles (FCHEVs). To address non-stationary demand and competing objectives, a multi-time scale energy management strategy based on dynamic game theory is proposed. The outer layer optimizes hydrogen consumption, high-efficiency operation, and overall economy over a long horizon. The inner layer performs reference tracking and suppresses power fluctuation on a fast horizon, thus improving durability. On this basis, a dynamic-game algorithm with an online multi-objective equilibrium updates weights via constrained projection and smoothed best response. Real-time trade-offs among hydrogen consumption, efficiency, and fluctuation are achieved. Validation on 10-kW sightseeing cars under typical cycles shows 75.3% operation in the high-efficiency region while meeting constraints on hydrogen use and fuel-cell fluctuation. Average computation time is 38 ms per step, confirming real-time feasibility.**

Keywords—Hybrid Energy System, Fuel Cell, Energy Management Strategy, Dynamic Game Theory, Electric Vehicle

I. INTRODUCTION

The global energy crisis and environmental issues make the low-carbon transition of the transportation sector essential. Fuel cell hybrid electric vehicles (FCHEVs) have advantages of high energy density, zero emissions, and long driving range. It is regarded as an important part of future energy systems [1]. However, fuel cells have limited dynamic response, and high sensitivity to degradation under fluctuating operating conditions [2]. Therefore, they are often combined with lithium-ion batteries to form hybrid powertrains, which can improve efficiency, durability, and driving performance.

Durability-oriented design of FCHEVs requires two aspects. First, advanced fuel cell health monitoring and prognostics are needed [3]. Second, the quality of the energy management strategy (EMS) directly determines vehicle economy and durability [4]. Rule-based EMSs are easy to implement but cannot achieve optimal results under complex driving cycles [5]. Physics-informed neural-network based energy management strategies offer some generalization but require large training datasets [6]. In contrast, model predictive control (MPC) does not need extensive training data and can handle multiple objectives and constraints in real time within a prediction horizon. As a result, MPC is widely used in online EMS [7].

Several studies confirm the potential of MPC for FCHEVs. He et al. [8] proposed an MPC-based strategy considering temperature effects and multiple constraints to reduce hydrogen consumption. Zhou et al. [9] developed an online MPC framework with driving cycle prediction and studied the effect of battery SOC weight on operating cost. Jia et al. [10] designed a nonlinear adaptive MPC to update fuel cell power distribution in real time. However, single-layer MPC must satisfy multiple constraints and optimize several objectives at each step. This leads to high computational cost and limits real-time application.

Dual-layer MPC has been developed to solve this problem. The upper layer optimizes global objectives, such as efficiency, over a long horizon. The lower layer regulates local dynamics, such as power fluctuation suppression and SOC balancing, over a short horizon. This design improves real-time feasibility without losing accuracy [11]. Qu et al. [12] applied a dual-layer MPC to hybrid ships. The method extended the upper-layer horizon to reduce computation and used fitted constants in the cost function. In practical operation, however, trade-offs exist among hydrogen consumption, fuel cell fluctuations, and efficiency. Fixed weights cannot minimize the cost function under all conditions. Real-time adjustment of performance weights is therefore necessary.

Dynamic game theory provides a solution for multi-objective optimization. Different performance indicators can be modeled as game participants. An approximate equilibrium can then be reached, which adapts to time-varying operating conditions [13]. Ghaderi et al. [14] proposed an online game-theoretic EMS for multiple fuel cell stacks, using a Nash equilibrium strategy for power distribution. The computational cost of Nash equilibrium, however, is very high. Real-time application is difficult. Improved equilibrium strategies are needed to meet dynamic operating conditions.

A multi-time scale energy management strategy is proposed for FCHEVs. Hydrogen consumption, fuel cell efficiency, and

979-8-3315-5472-9/25/$31.00 ©2025 IEEE

power fluctuations are integrated into cost functions with different time scales. A dynamic game framework is built to design an online multi-objective equilibrium strategy. Constrained projection, smooth weight updating, and online best response are combined to adjust weights in real time. This enables trade-offs among efficiency, fluctuation, and hydrogen consumption within the multi-time scale energy management strategy. Experiments under typical driving cycles show the effectiveness and real-time performance.

The main contributions are summarized as follows:

- A multi-time scale energy management strategy is introduced for FCHEVs. It achieves coordinated optimization of global energy efficiency and local dynamic performance.
- A dynamic game mechanism is embedded in the multi-time scale framework. Real-time adjustment of multi-objective weights is achieved through constrained projection, smooth updating, and online best response. Trade-offs among hydrogen consumption, efficiency, and fluctuation are realized.
- Experiment studies on a 10-kW FCHEV sightseeing vehicle verify the superiority of the proposed method in optimization and real-time performance.

The remainder of this paper is organized as follows. Section II introduces the power flow structure of the FCHEV. Section III presents the proposed EMS framework. Section IV provides experimental validation. Section V concludes the paper.

II. Vehicle and Energy System Model

A. Vehicle model

The fuel cell hybrid power system architecture utilized in this study is illustrated in Fig. 1, featuring a multi-energy collaborative power supply design. In this system, the proton exchange membrane fuel cell (PEMFC) serves as the core energy unit, while the lithium-ion battery pack acts as the auxiliary power, enabling energy coupling through a DC bus.

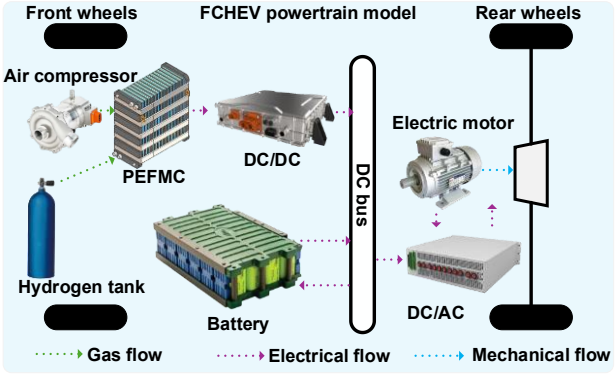


Fig. 1. Fuel cell hybrid power system architecture.

As shown in Fig. 1, the power system adopts a dual-path energy supply design, where the fuel cell stack is connected to the DC bus through a DC/DC converter to achieve voltage matching, while the lithium-ion battery pack is directly connected to the bus to form a voltage support node. The total traction power P_t of the system is established based on vehicle dynamics principles [15]:

$$P_t = v(m_v(t)\frac{d}{dt}v(t) + F_a(t) + F_r(t) + F_g(t) \quad (1)$$

where v is the velocity of the vehicle, F_a is the aerodynamic for ce,F_r is the rolling friction,F_g is the force caused by gravity whe n driving on non-horizontal roads. The electric power demand P_d of the vehicle can be represented by the following relationship:

$$P_d = \frac{P_t}{\eta_{drive}} \quad (2)$$

where the drivetrain efficiency η_{drive} is calculated by:

$$\eta_{drive} = \eta_{mech} * \eta_{dc/ac} * \eta_{motor} \quad (3)$$

where η_{mech} is the mechanical drivetrain efficiency, $\eta_{dc/ac}$ is the DC/AC inverter efficiency, and η_{motor} is the motor efficiency.

The power split between the fuel cell P_{fc} and the batteries P_{bat} is given by:

$$P_d(t) = P_{fc}(t) + P_{bat}(t) \quad (4)$$

B. Fuel cell model

As the core energy supply unit of this study, PEMFC, the quantitative model of hydrogen mass consumption m_{H_2} is established as follows:

$$m_{H_2} = \int_0^t \frac{P_{fc}(t)}{\eta_{fc} * \rho_{H_2}} dt \quad (5)$$

The efficiency of the fuel cell system η_{FC} is a function of the output power P_{fc} of the fuel cell. The principles of demarcating high-efficiency zones can be found in [15]. Generally, if the fuel cell system can be maintained to operate within this area in the FCHEVs, it can achieve good fuel economy by reducing hydrogen consumption.

C. Lithium-ion battery model

The State of Charge (SOC) indicates the remaining battery capacity compared to its fully charged energy. In order to maintain the direct current bus voltage and recover kinetic energy during the vehicle braking phase, the SOC should be kept within an optimal range. The SOC can be calculated with reference to the literature [15].

$$SOC(t) = SOC(t_0) + \int_0^t \frac{P_{bat}(t)}{\eta_{bat} * 3600 * E_{bat}} dt \quad (6)$$

where $SOC(t_0)$ represents the SOC of the battery at the last instance, η_{bat} is the Coulombic efficiency of the battery (0.98 indicates battery charging, 1 indicates battery discharging). P_{bat} is the power of the lithium-ion battery (negative values indicate battery charging, positive values indicate battery discharging). E_{bat} represents the nominal rated energy of the battery.

III. The Proposed Energy Management Strategy

In this section, a multi-time scale energy management framework is first proposed. Then, outer and inner energy management strategies are developed. Morerover, a dynamic game based on online multi-objective optimization equilibrium is presented. Finally, the algorithmic process is detailed.

A. Multi-Time-Scale Energy Management Framework

To balance global economy and local dynamic performance, a multi-time scale energy management framework is proposed, as illustrated in Fig. 2, where T_{out} and T_{in} denote the sampling periods of the outer and inner layers, respectively. The outer layer optimizes hydrogen consumption and system efficiency over a longer time scale, online Markov prediction is employed for outer-layer cycle prediction; the detailed configuration can be found in [9]. While the inner layer operates on a shorter (millisecond-level) time scale to perform reference tracking and suppress power fluctuations.

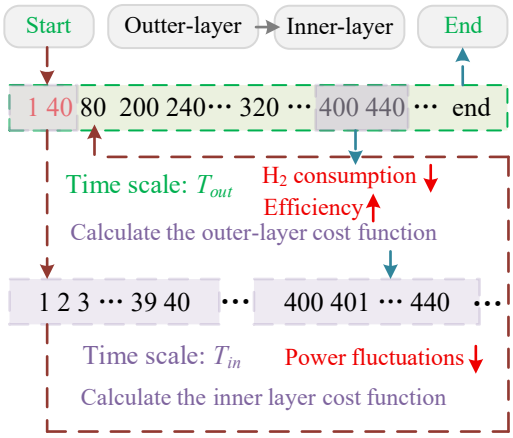


Fig. 2. Multi-time-scale energy management framework.

B. Outer Layer Macro-Horizon Energy Management Strategy

On the longer horizon, the outer layer schedules the fuel-cell power sequence $P = \{P_{\mathrm{fc}}(k)\}_{k=t}^{t+N_U-1}$ so that hydrogen economy is improved while the fuel cell stays near the high-efficiency region. Let $\eta_{fc}(P)$ be the calibrated efficiency map and define the region as follows:

$$S = P: \frac{1}{3}\eta_{max} \le \eta_{fc}(P) \le \frac{2}{3}\eta_{max} \tag{7}$$

The outer-layer optimizes the sequence P to minimize a weighted multi-term cost:

$$\min_P J_{out} = \sum_k \Big[\alpha_{H2}\frac{P_{fc}(k)}{\eta_{fc}(k)LHV_{H_2}} + \alpha_{eff}\phi_{eff}(P_{fc}(k), S) + \alpha_{sm}(\beta_1\Delta P_{fc}(k)^2 + \beta_2\Delta^2 P_{fc}(k)^2)\Big] + \rho_{ine}\big(P_{fc}(t) - P_{fc}^{prev}\big)^2 \tag{8}$$

where $\mathrm{LHV}_{\mathrm{H_2}}$ is the hydrogen lower heating value; Φ_{eff} increases when $P_{\mathrm{fc}}(k)$ leaves S; $\alpha_{\mathrm{H2}}, \alpha_{\mathrm{eff}}, \alpha_{\mathrm{sm}}$ and $\beta_1, \beta_2, \rho_{\mathrm{ine}}$ are weights, P_{fc}^{prev} is the fuel cell power actually executed last time. The core constraints of the outer layer are as follows:

$$P_d(k) = P_{fc}(k) + P_{bat}(k) \tag{9}$$

$$P_{min} \le P_{fc}(k) \le P_{max}, |P_{bat}(k)| \le P_{bat}^{max} \tag{10}$$

$$SOC(K+1) = f_{bat}\big(SOC(k), P_{bat}(k)\big) \tag{11}$$

$$\left|\sum_{k=t}^{t+N_u-1} P_{bat}(k)T_{out}\right| \le \varepsilon_U, |SOC(T_{out}) - SOC_{ref}| \le \delta_{SOC} \tag{12}$$

where $P_{min}, P_{max}, P_{\mathrm{bat}}^{max}$ are actuator bounds; ε_U enforces window energy neutrality over the outer horizon; δ_{SOC} enforces a terminal band around $\mathrm{SOC}_{\mathrm{ref}}$; T_{out} is the outer sampling period.

C. Inner Layer Fast-Time Energy Management Strategy

On the shorter horizon, the inner layer refines the fuel-cell sequence P to track the shaped reference $P_{\mathrm{ref}}(k)$, while suppressing oscillations:

$$\min_P J_{in} = \sum_k \Big[\beta_{trk}\big(\max\{|P_{fc}(k) - P_{ref}(k)| - \Delta_{db}, 0\}\big)^2 + \beta_{sm}(\gamma_1\Delta P_{fc}(k)^2 + \gamma_2\Delta^2 P_{fc}(k)^2)\Big] \tag{13}$$

where β_{trk}, β_{sm} and γ_1, γ_2 are inner layer weights coefficients; Δ_{db} is the tracking dead-band.

$$|\Delta P_{fc}(k)| \le dP_{max}T_{in} \tag{14}$$

dP_{max} is the admissible slew limit; T_{in} is the inner-layer sampling period. This layer applies only the first control move, updates the states, and rolls forward.

D. Online Multi-Objective Equilibrium Dynamic Game Theory

At each outer-layer update, a stage game is played among the objectives $\mathcal{J} = \{\mathrm{spot,ramp,edge,trk}\}$. Each player chooses an attention share on the simplex $s \in \triangle$ $(i.e., s_i \ge 0, \sum_i s_i = 1)$. Given the normalized metric vector:

$$m = [m_{spot}, m_{ramp}, m_{edge}, m_{trk}]^T \tag{15}$$

where m_{spot} is high-efficiency occupancy deficit, m_{ramp} is ramp-rate percentile, m_{edge} is out-of-region penalty, and m_{trk} is mean-squared tracking error. The game admits a logit (quantal response) equilibrium:

$$\tilde{s} = softmax(-\kappa G m) \tag{16}$$

which allocates more attention to worse-performing metrics (via $G \ge 0, \kappa > 0$). The equilibrium shares are mapped to implementable control parameters and stabilized by smoothing and projection:

$$\hat{\alpha} = (1-\gamma)\alpha_{prev} + \gamma\mathcal{M}(\tilde{s}), \alpha^+ = \prod\nolimits_{\mathcal{B}}(\hat{\alpha}) \tag{17}$$

where $\hat{\alpha}$ is the weight matrix of the outer and inner layers, G maps metric shortfalls to incentives; κ sets selectivity of the equilibrium; $\gamma \in (0,1]$ imposes temporal inertia; $\mathcal{M}(\cdot)$ is a monotone box mapping from shares to parameter ranges; $\Pi_{\mathcal{B}}$ projects onto the engineering feasible set $\mathcal{B}$.

This procedure endures a stable cross-time-scale balance among economy, efficiency, and power fluctuation while keeping online updates bounded.

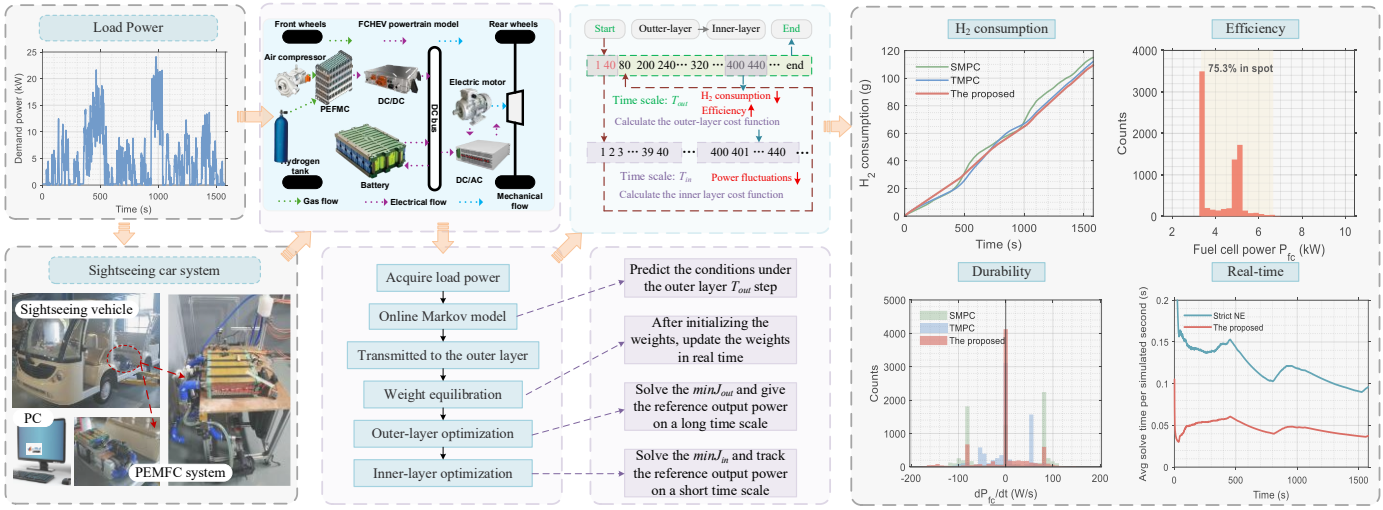


Fig. 3. MSDGT algorithm flowchart.

E. *The Proposed MSDGT Method*

The complete proposed MSDGT algorithm is shown in Fig. 3. The specific steps are as follows:

- Sense and Predict: Acquire P_l, SOC and other states; generate outer-layer load predictions by the online Markov model.
- Weight Equilibration: Compute the metric vector m on the recent window and update $\hat{\alpha}$ via (15)-(17).
- Outer-Layer Optimization: Solve (8) with constraints (9)-(12) to obtain $P_{\text{ref}}(k)$; limit to produce the fast-layer reference sequence.
- Inner-Layer Optimization: Solve (13) with constraints (9)-(12) and (14); apply the first control move $\{P_{\text{fc}}, P_{\text{bat}}\}$, update the states, and log performance.
- Roll Forward: Advance by T_{in}; trigger the outer- layer every T_{out}, repeat until the cycle ends. Safety fallbacks freeze weights and enforce conservative limits if solver failures or sensor faults are detected.

IV. Results and Discussion

This section first introduces the experimental platform and configuration; then presents the LA92 cycle together with the speed-to-power conversion. On this basis, we perform a quantitative comparison between the proposed method and several energy-management baselines in terms of hydrogen consumption, fuel-cell high-efficiency occupancy/usage efficiency, and power fluctuation. Finally, computational overhead and real-time performance are validated.

A. *Experimental Setup*

A 10-kW sightseeing-vehicle fuel-cell test bench and MATLAB/Simulink serve as the simulation environment. The fuel-cell system is matched to an eight-seat sightseeing vehicle with a maximum payload of 750 kg. Key parameters are listed in Table I. Energy-management computations and data logging run on a workstation equipped with an AMD Ryzen 9 7945HX with Radeon Graphics (2.50 GHz).

TABLE I. Key Parameters of Sightseeing Vehicle

Parameters	Values	Unit
Vehicle Mass	750	kg
Vehicle Dimensions	4270*1490*2040	mm
Maximum Speed	90	km/h
Instantaneous Starting Power	15	kW
Rated Operating Efficiency	49%	-
Battery Capacity	7.2	kWh

To avoid power demand exceeding system capability, the LA92 vehicle speed profile is scaled. The maximum speed is limited to 90 km/h due to the situation of sightseeing bus. Fig. 4 (a) shows the original and the scaled speed profiles. Fig. 4 (b) presents the power demand trajectory after scaling.

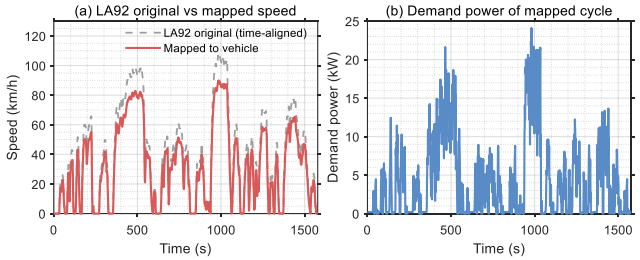


Fig. 4. (a) LA92 operating condition and sightseeing vehicle speed mapping; (b) Sightseeing car system power demand trajectory.

B. *Operational Performance Indicators Evaluation*

Fig. 5 compares the power distribution results of single model predictive control (SMPC), two-layer model predictive control (TMPC), and the proposed MSDGT. It can be seen from Fig. 5 that SMPC is more sensitive to the high-frequency of P_{d}. TMPC can smoothly fuel cell output power to some extent. However, obvious tracking swings still occur during strong transients and switch between operating conditions.

Different from SMPC and TMPC, the proposed MSDGT adopts outer and inner layer sampling with different rates and online weight adjustment. This helps keep fuel cell output power smooth when power demand changes. Fast transients are mainly

handled by the battery, which reduces unnecessary fuel cell ramp-up and ramp-down.

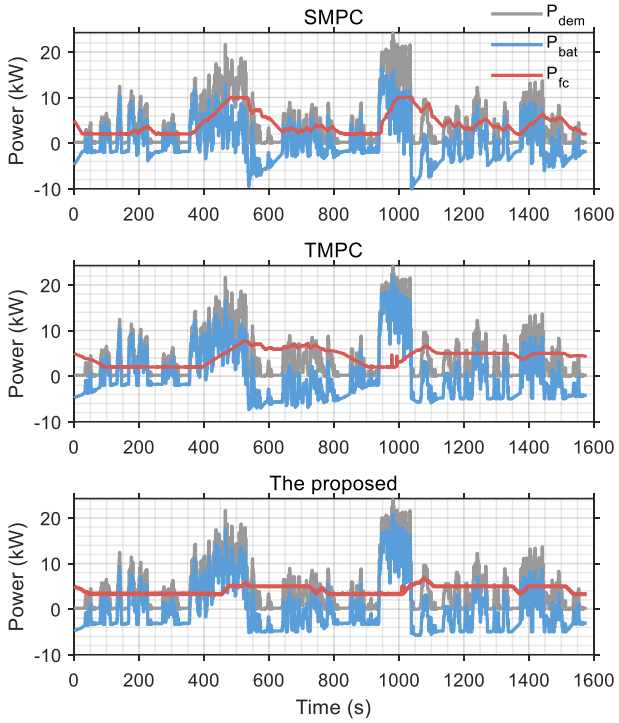


Fig. 5. Comparison of power distribution results with different strategies.

Fig. 6 shows hydrogen consumption and the SOC trajectories during operation. The hydrogen consumption of SMPC, TMPC, and MSDGT is 115 g, 112 g, and 109 g, respectively. Compared with SMPC and TMPC, the proposed MSDGT reduces hydrogen consumption by 5.2% and 2.7%. Fig. 6 (b) presents the SOC trajectories. All three methods satisfy the SOC box constraints, indicating that MSDGT achieves lower hydrogen consumption while maintaining a more stable SOC profile. This is mainly because the proposed strategy effectively balances power between the fuel cell and the battery through multi-layer coordination and adaptive scheduling, thereby avoiding unnecessary fluctuations and improving overall efficiency.

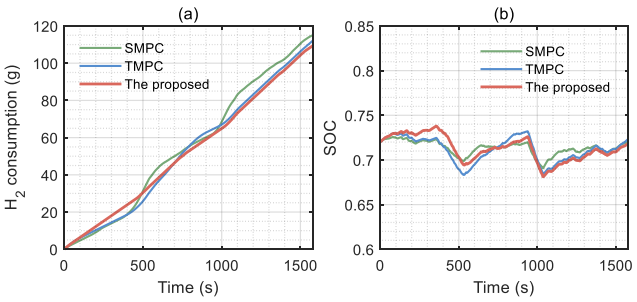


Fig. 6. (a) Hydrogen consumption results; (b) SOC trajectories during operation.

To quantify the fuel cell's operational efficiency, a histogram of fuel cell output power is provided in Fig. 7. The shaded region indicates the high-efficiency power range of the fuel cell. The residence time percentages within this high-efficiency range for SMPC, TMPC, and MSDGT are 34.6%, 61.2%, and 75.3%, respectively. Compared with SMPC and TMPC, MSDGT improves the high-efficiency operation time by 40.7% and 14.1%. This is consistent with the power distribution observed in Fig. 5, indicating that the proposed method effectively reduces the duration of low and high-power operation of the fuel cell. As a result, it helps avoid issues such as poor efficiency at low loads and accelerated degradation under high loads.

The power fluctuation of the fuel cell during operation is shown in Fig. 8. Where dP_{fc}/dt represents the rate of change of fuel cell output power. It can be seen from Fig. 8 that, compared with SMPC and TMPC, the proposed MSDGT shows a distribution of power fluctuation concentrated around zero. This indicates that most power changes are kept within a small range. As a result, MSDGT reduces stack stress and thermo-electrochemical shocks while ensuring power tracking, which helps improve fuel cell durability.

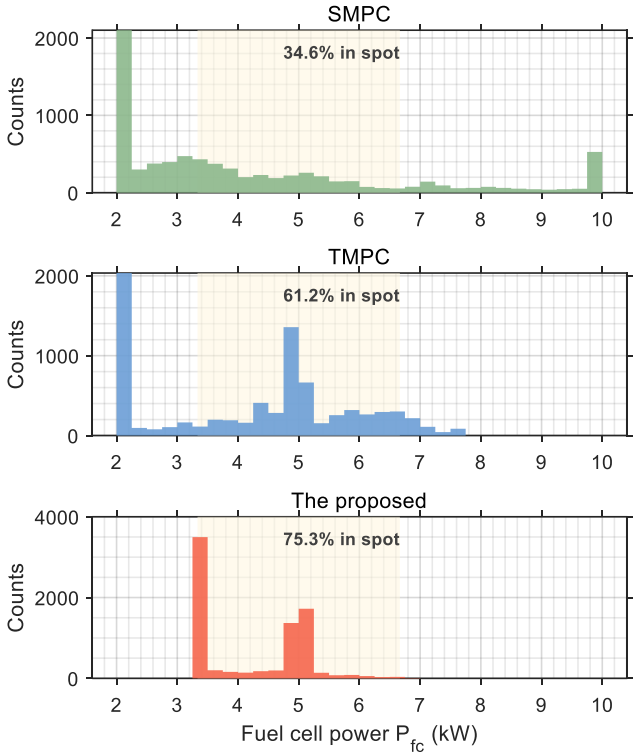


Fig. 7. Histogram of fuel cell output power.

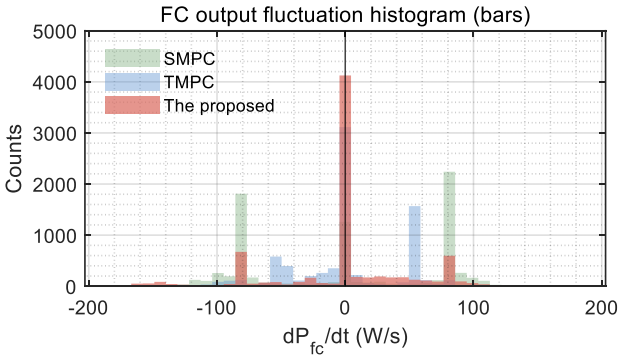


Fig. 8. Power fluctuation of the fuel cell during operation.

C. Real-time Performance

To further evaluate the real-time performance of the proposed method, this section compares the SMPC structure, the Multi-time Scale MPC (MS-MPC) structure, the Nash equilibrium-based strategy, and the proposed MSDGT method. The average cumulative computation time per second of simulation is used as the real-time performance indicator. The comparison results are shown in Fig. 9.

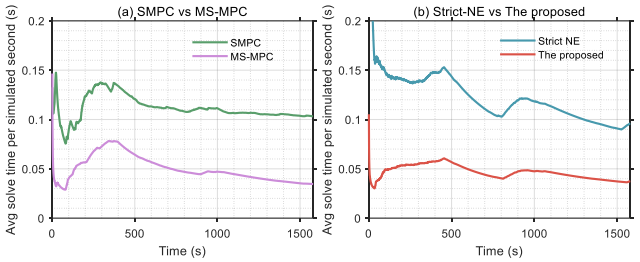


Fig. 9. Real-time performance results.

As shown in Fig. 9 (a), compared to SMPC, the MS-MPC clearly demonstrates faster computation speed. Specifically, the average simulation time per second for SMPC is 103 ms, while MS-MPC requires only 35 ms. This is mainly because the multi-time-scale structure avoids repeated evaluation of the cost function at every small-time step, thereby reducing redundant computations and improving overall efficiency.

Furthermore, it can be seen from Fig. 9 (b) that under the same multi-time-scale structure, the average simulation time of Strict- Nash equilibrium (Strict-NE) is 96 ms, while the average simulation time of the proposed MSDGT is 38 ms. Compared with Strict-NE, the proposed method has a computational speed improvement of 60.4%. This improvement is mainly due to the lightweight equilibrium strategy adopted in MSDGT, which combines local window-based cost evaluation with a projection–smoothed best response mechanism. This approach significantly reduces the computational load per second.

These results further confirm that the proposed MSDGT not only maintains energy efficiency and power smoothness but also offers better feasibility for real-time implementation and online deployment.

V. CONCLUSION

This paper presents a multi-time scale energy management strategy for FCHEVs. The framework coordinates an outer layer that optimizes hydrogen consumption, high-efficiency operation, and economy with an inner layer that tracks references and suppresses power fluctuation to protect durability. A dynamic-game, online equilibrium is developed to adapt weights in real time through constrained projection and smoothed best response.

Experimental results show that the high-efficiency operation ratio reaches 75.3%, improving by 40.7% and 14.1% over SMPC and TMPC, respectively. The average computation per step is 38 ms, and the method is 60.4% faster than a strict Nash baseline. Moreover, hydrogen-consumption targets are met and fuel-cell power fluctuation is reduced. By embedding the strategy into a multi-time scale energy management framework under typical cycles, the work provides a practical basis for real-time deployment on hybrid energy systems.

ACKNOWLEDGMENT

This work was funded by the National Natural Science (52377215， 51977177)， Innovation Foundation of China Foundation for Doctor Dissertation of Northwestern Polytechnical University (Grant No. CX2024004)， Shaanxi Province Key Research and Development Plan (2024CY-GJHX-08, 2024CY-JJQ-59) and Double First-Class Discipline Construction Funded Project (WH00001049).

REFERENCES

[1] X. Li, Q. Li, T. Wang, W. Chen, and F. Gao, “Hierarchical energy management based on distributed aggregation for large-scale fuel cell cluster hybrid power systems,” *IEEE Trans. Ind. Electron.*, 2024.

[2] Z. Tian, C. Ma, R. Zhang, D. Zhou, Y. Huangfu, and S. M. Muyeen, “A fuel cell aging prediction method based on symplectic geometry mode decomposition and divide-and-conquer gated recurrent unit,” *IEEE Trans. Energy Convers.*, 2024.

[3] Z. Tian, J. Wang, A. Al-Durra, S. M. Muyeen, D. Zhou, and S. Hua, “A novel aging prediction method of fuel cell based on empirical mode decomposition and complexity threshold quantitative criterion,” *J. Power Sources*, vol. 574, p. 233120, 2023.

[4] Y. Zhang, C. Zhang, R. Fan, C. Deng, S. Wan, and H. Chaoui, “Energy management strategy for fuel cell vehicles via soft actor-critic-based deep reinforcement learning considering powertrain thermal and durability characteristics,” *Energy Convers. Manag.*, vol. 283, p. 116921, 2023.

[5] A. Khalatbarisoltani, L. Boulon, and X. Hu, “Integrating model predictive control with federated reinforcement learning for decentralized energy management of fuel cell vehicles,” *IEEE Trans. Intell. Transp. Syst.*, vol. 24, no. 12, pp. 13639–13653, 2023.

[6] F. Li, L. Gao, Y. Zhang, and Y. Liu, “Integrated energy management for hybrid electric vehicles: A Bellman neural network approach,” *Eng. Appl. Artif. Intell.*, vol. 145, p. 110166, 2025.

[7] Y. Liu, M. Li, Y. Wang, Z. Sun, and Z. Chen, “Predictive energy management for fuel cell hybrid vehicles considering efficiency and safety,” *IEEE Trans. Power Electron.*, vol. 39, no. 10, pp. 13842–13852, 2024.

[8] H. He, S. Quan, F. Sun, and Y. X. Wang, “Model predictive control with lifetime constraints based energy management strategy for proton exchange membrane fuel cell hybrid power systems,” *IEEE Trans. Ind. Electron.*, vol. 67, no. 10, pp. 9012–9023, 2020.

[9] Y. Zhou, A. Ravey, and M. C. Péra, “Real-time cost-minimization power-allocating strategy via model predictive control for fuel cell hybrid electric vehicles,” *Energy Convers. Manag.*, vol. 229, p. 113721, 2021.

[10] C. Jia, W. Qiao, J. Cui, and L. Qu, “Adaptive model-predictive-control-based real-time energy management of fuel cell hybrid electric vehicles,” *IEEE Trans. Power Electron.*, vol. 38, no. 2, pp. 2681–2694, 2022.

[11] C. Ju, P. Wang, L. Goel, and Y. Xu, “A two-layer energy management system for microgrids with hybrid energy storage considering degradation costs,” *IEEE Trans. Smart Grid*, vol. 9, no. 6, pp. 6047–6057, 2017.

[12] J. Qu, H. Wang, L. Zou, L. Zhang, T. Zhang, J. Zhou, and B. Zhang, “A two-layer energy management strategy of fuel cell hybrid system in electric ships,” *IEEE Trans. Ind. Appl.*, 2024.

[13] D. Fudenberg and J. Tirole, *Game Theory*. Cambridge, MA, USA: MIT Press, 1991.

[14] R. Ghaderi, M. Kandidayeni, M. Soleymani, L. Boulon, and J. P. F. Trovão, “Online health-conscious energy management strategy for a hybrid multi-stack fuel cell vehicle based on game theory,” *IEEE Trans. Veh. Technol.*, vol. 71, no. 6, pp. 5704–5714, 2022.

[15] D. Zhou, A. Al-Durra, F. Gao, A. Ravey, I. Matraji, and M. G. Simoes, “Online energy management strategy of fuel cell hybrid electric vehicles based on data fusion approach,” *J. Power Sources*, vol. 366, pp. 278–291, 2017.

Optimal Placement of Constrained Micro PMUs Using Phasor Measurement based State Estimation

Seungyeop Baek
Electrical Engineering
Myongji University
Yongin, South Korea
seungyeop@mju.ac.kr

Jinhyeok Kim
Electrical Engineering
Myongji University
Yongin, South Korea
80241098@mju.ac.kr

Byeongchang Lim
Electrical Engineering
Myongji University
Yongin, South Korea
limbyeongchang@mju.ac.kr

Yeuntae Yoo
Electrical Engineering
Myongji University
Yongin, South Korea
ytyoo@mju.ac.kr

***Abstract*—The deployment of Micro PMUs, capable of providing high resolution with time synchronized data in real time at the distribution level, is gradually expanding. The phase angle information obtained from these devices enables more accurate state estimation and real-time anomaly detection in the network. However, due to the high capital cost of Micro PMUs, it is not practically feasible to install them at every bus intended for monitoring within the distribution system, unlike conventional current and potential transformers which can be widely deployed. This paper proposes an optimal Micro PMU placement strategy that accounts for the practical constraint of using only a limited number of devices, with the aim of improving the correction accuracy of time-synchronized voltage states in distribution networks. The proposed approach combines a state estimation method based on Weighted Least Squares with a heuristic optimization algorithm. Utilizing high-resolution measurement data from Micro PMUs, the method corrects voltage phasors across the entire network and identifies the most effective PMU placement configuration. The simulation is conducted based on the IEEE 15 bus test system, which represents a three-phase balanced distribution network integrated with renewable-based distributed energy resources. Real time analog voltage signals are applied to Micro PMUs using an RTDS, and the corresponding phasor measurements are utilized in a python-based environment to perform state estimation using the Weighted Least Squares method. In each iteration, OpenDSS performs power flow analysis to compute voltage phasors, and the proposed optimization algorithm determines the optimal Micro PMU placement that minimizes the state estimation error based on these results. The Micro PMU placement method proposed in this paper is expected to provide a foundation not only for the efficient deployment of measurement devices but also for improving the overall operational performance of distribution systems. In particular, by using the accuracy of phasor estimation based on high-resolution time-synchronized data as the criterion for determining PMU placement, the method enables precise correction of voltage phasors across all buses under a unified time reference. The proposed approach is also scalable and can be flexibly applied to various network configurations and load conditions in future studies.**

***Keywords*—Micro PMU, Optimal Placement, Voltage Phasor, State Estimation, Heuristic Algorithm**

I. INTRODUCTION

Over the past five years, variable renewable energy (VRE) sources such as wind turbine generator and photovoltaic have been widely deployed throughout the world, driven by a significant reduction in technology costs [1]. This large-scale deployment has accelerated structural changes in distribution networks. Traditional passive systems are now rapidly being transformed into active distribution networks that accommodate the autonomous participation of distributed energy resources [2][3]. However, VRE outputs are highly variable depending on weather conditions at the point of interconnection. This variability makes accurate prediction difficult and introduces considerable uncertainty in identifying the real-time voltage phasor. This issue is especially apparent in distribution systems with a high penetration of VREs, and it has led to a growing need for dynamic state estimation to support reliable monitoring and operation in modern power systems [4].

Such state estimation is primarily performed using measurement data collected through Supervisory Control And Data Acquisition(SCADA) systems, and is utilized within the energy management system to estimate state variables such as bus voltage phasors [5][6]. However, the real-time variability of VRE output, combined with the relatively long reporting intervals of conventional SCADA systems, can lead to discrepancies between the actual system state and the acquired data [7]. This error in observability not only results in time delays, but also prevents the system from effectively capturing fast-changing phenomena within the network, such as sudden changes in VRE output or localized voltage fluctuations. As a result, while SCADA-based state estimation may be effective in traditional distribution systems, its limitations become evident in modern networks with increasing VRE penetration, where high temporal resolution and real-time operational awareness are required.

To address these challenges, there is a growing need for a faster and more accurate time-synchronized measurement method, which has led to the increasing recognition of Phasor Measurement Units (PMUs) as a promising solution. The PMU is GPS-based measurement device capable of providing real-time, time synchronized data that includes voltage and current phasor measurements at high resolutions, typically ranging from

979-8-3315-5472-9/25/$31.00 ©2025 IEEE

tens to hundreds of frames per second. These measurements enables the accurate tracking of rapid power fluctuations and abnormal events that conventional SCADA systems fail to capture. Particularly in the context of increasing variability in renewable energy and bidirectional power flows, PMU measurement has emerged as an essential component in significantly improving the accuracy of dynamic state estimation. Accordingly, the necessity and effectiveness of PMU deployment have been consistently highlighted in previous research [8]. In distribution networks, detecting small phase angle variations is also required. To enable such precision, a high-resolution device called the μPMU has been developed and is now widely used.

The μPMU is designed to capture fast changing phasors and subtle phase angle deviations in real time. It offers high-speed sampling of up to 30,720 samples per second, angular accuracy of ±0.01°, and voltage resolution of 0.0002%. Based on these features, the μPMU serves as a key infrastructure for dynamic state estimation, anomaly detection, power quality monitoring, and the control of VRE sources in distribution systems [9][10]. However, due to their precision capabilities and integrated synchronization features, μPMUs require significantly higher capital and installation costs compared to conventional measurement systems that use CTs and PTs with merging units in distribution networks. The requirement for specialized infrastructure such as GPS based time synchronization and high-speed communication presents a major financial constraint to placing μPMUs across all buses. As a result, it becomes essential to develop a cost effective measurement strategy that maximizes observability using a constrained number of μPMUs. [11].

Against this background, identifying the optimal placement of a limited number of μPMUs either to enable accurate state estimation or to maximize system observability has emerged as an important research challenge. This problem is commonly formulated as the Optimal PMU Placement (OPP) problem, for which numerous research has been conducted. The objective of the OPP problem is to determine the best placement of μPMUs. This placement should maximize state estimation accuracy, system observability, and operational reliability, while ensuring efficient use of constrained resources. In recent years, a variety of approaches have been actively applied to this problem, including optimization techniques, heuristic algorithms, and machine learning based methods.

The approaches to the OPP problem, which aim to improve the accuracy of state estimation and ensure observability, can largely be divided into two categories: numerical analysis based methods and heuristic algorithm-based methods [12]. One of the most common numerical approaches, as proposed in [13], solves the WLS based state estimation problem using an iterative method based on the Jacobian matrix to ensure network observability. In addition, by considering zero injection buses it explores optimal μPMU placement strategies that minimize the number of devices required in radial distribution networks with PV integration. In [14], the OPP problem is addressed with the objective of achieving full observability of the system while minimizing the number of required PMUs. To this end, an improved method based on the conventional Binary PSO algorithm has been proposed. In [15], the optimization problem is formulated by incorporating unique characteristics of distribution networks, such as unbalanced three phase systems, on load tap changers or switching operations. The optimal placement of μPMUs is then explored using Integer Linear Programming, Genetic Algorithm, and Particle Swarm Optimization (PSO).

Most previous studies have focused on minimizing the number of required μPMUs through the Optimal PMU Placement (OPP) problem, with the primary objective of achieving full observability. However, in practical scenarios with budget constraints, securing and placing even the minimum number of μPMUs is often challenging due to economic limitations. Therefore, there is a demand for an efficient μPMU placement strategy that enables accurate state estimation under practical resource constraints. To address this need, this paper aims to solve the OPP problem by proposing a method that maximizes the observability of the distribution network using a constrained μPMUs. This study considers the three-phase balanced IEEE 15 bus distribution system. Under the constrained condition of being allowed to use only three μPMUs, the OPP strategy is constructed to achieve maximum observability. The optimization problem is formulated based on the cost function of WLS and is solved using a metaheuristic algorithm, PSO. In this work, the state variables to be estimated are the voltage phasors at all buses.

Accordingly, the main contributions of this study are as follows:

- The WLS-PSO based OPP strategy is proposed to achieve the most accurate estimation of voltage phasor in distribution networks using a constrained number of μPMUs.

- A test environment is developed by integrating real-time measurement data from RTDS with PSO-based simulations conducted in OpenDSS using Python, enabling a quantitative evaluation of state estimation accuracy.

- The voltage phasors estimated from μPMU measurements, as time synchronized data, can contribute to enhancing anomaly detection and error correction capabilities in SCADA systems used for distribution network management.

Section 2 presents the proposed OPP strategy, which solves the WLS-based state estimation problem using the PSO algorithm. Section 3 describes the development of a test environment, including the configuration of the μPMU–RTDS-based measurement setup, where analog signals from RTDS are provided to the μPMU, and the modeling of the IEEE 15-bus distribution network using RSCAD and OpenDSS. Then, analyzes the results of the proposed OPP algorithm within the constructed environment and evaluates its performance in terms of state estimation accuracy and observability using quantitative metrics such as TVE and WLS costs. Section 4 concludes the paper and discusses future research directions.

II. Problem Formulation

A. Configuration of OPP Strategy

As previously mentioned, this paper proposes an OPP strategy to determine the most effective locations for installing μPMUs in the IEEE 15-bus distribution network, under constrained cost conditions, with the objective of maximizing system observability. In this work, observability is defined in

terms of the ability to accurately estimate the voltage phasors. Therefore, the optimization problem is formulated with a focus on improving state estimation accuracy. In μPMU measurement based state estimation, high-precision, time-synchronized measurements containing both voltage and current phasor data are collected. Additionally the optimization must also handle measurement data with varying degrees of reliability, as load consumption and VRE generation data obtained from SCADA systems have lower accuracy and weaker temporal alignment compared to μPMU data [7].

Under such conditions, the WLS method provides a key advantage. It can incorporate the reliability of each measurement through appropriately assigned weights, allowing for state estimation that quantitatively accounts for differences in data quality. In particular, higher weight factors can be assigned to high-reliability devices, such as μPMUs, while lower weights can be applied to measurements obtained from SCADA [16][17]. Accordingly, this paper formulates the PMU-based state estimation problem using the WLS method with applied measurement weight factors, enabling the integration of diverse measurement sources.

In this study, OpenDSS is employed as the power flow engine to compute voltage phasors, which serve as the foundation for the state estimation simulation. Instead of directly solving the nonlinear power flow equations of complex distribution networks through numerical methods, this approach utilizes the power flow results provided by OpenDSS. As a validated analysis tool, OpenDSS offers fast computation capabilities, thereby enhancing both the reliability and the overall simulation speed and efficiency.

B. Configuration of OPP Ploblem

In OPP, the observability metric is primarily determined by the voltage magnitudes and phase angles across the entire system. Accordingly, the objective of state estimation is to accurately estimate the voltage at all buses. To achieve this, OpenDSS and PSO are integrated to gradually adjust the load power and renewable generation values obtained from SCADA. Based on this process, the WLS cost function can be defined as shown in Eq. 1.

$$J(x) = w\big(z - h(x)\big)^2 \tag{1}$$

z represents the actual measurement vector, which is obtained from RTDS and used as the reference data in this study. The term $h(x)$ denotes the comparison vector computed by Opendss based on the load consumption and renewable generation adjusted iteratively by the PSO algorithm. Therefore, the difference $(z - h(x))$ is defined as the residual. Eq. (2) shows the structure of this residual vector.

$$\big(z - h(x)\big) = \big[V_{pmu1} \cdots \theta_{pmu3},\ P_{Bus2} \cdots Q_{Bus15}, P_{VRE}\big] \tag{2}$$

The weights represent the assumed reliability of each measurement. Reliability can be assigned based on the source of the data, depending on whether it is obtained from a μPMU or from a SCADA system. In this study, μPMU measurements are regarded as highly trustworthy and are treated as absolute. In contrast, load consumption and renewable generations are considered to have lower reliability. Accordingly, the weight factor for μPMU measurements is set to 10^6 for magnitude and 10^4 for angle, for load consumption to 10, and for renewable output to 1. The weight matrix is a square diagonal matrix, as shown in Eq .3.

$$W = \begin{bmatrix} w_{pmu1} & \cdots & 0 \\ \vdots & \ddots & \vdots \\ 0 & \cdots & w_{VRE} \end{bmatrix}, \qquad W \in \mathbb{R}^{29} \tag{3}$$

C. Optimization with PSO

In this study, the heuristic algorithm, PSO is employed to minimize the WLS cost function defined in Eq. 1 Since OpenDSS functions as a black-box model from the perspective of the optimization process. PSO is a global optimization algorithm inspired by the collective behavior of biological swarms. It initializes a group of particles, with each particle representing a candidate solution, randomly within predefined boundaries. These particles explore the solution space by iteratively updating their positions and velocities based on their own best known positions, p_i^{best} and the best-known position found by the entire swarm, g_i^{best} .Through this process, the particles gradually converge toward the global optimum within the search space [18][19]. Unlike gradient based methods, PSO does not rely on numerical differentiation using jacobians and can achieve stable convergence with a small number of hyperparameters.

PSO is used to search for the optimal combination of input variables by adjusting the load consumption and renewable generation values so that the voltage phasors derived from OpenDSS, denoted as $h(x)$, closely match the reference measurements z. The position and velocity of each particle are updated according to Eq. 4 and Eq. 5 respectively. In these equations, $v_i^{(t+1)}$ represents the current velocity of a particle, and $v_i^{(t)}$ represents its updated velocity in the next iteration. The values r_1 and r_2 are random values between 0 to 1, introduced to provide random behavior, while w, c_1, and c_2 are predefined weights.

$$v_i^{(t+1)} = \mathrm{w} \cdot v_i^{(t)} + c_1 \cdot r_1\big(p_i^{best} - x_i^{(t)}\big) + c_2 \cdot r_{21}\big(g_i^{best} - x_i^{(t)}\big) \tag{4}$$

Accordingly, the position of each particle is updated as shown in Eq. 5, where $x_i^{(t)}$ denotes the current position and $x_i^{(t+1)}$ represents the updated position in the next iteration.

$$x_i^{(t+1)} = x_i^{(t)} + v_i^{(t+1)} \tag{5}$$

The hyperparameters of PSO are set with an inertia weight $\mathrm{w} = 0.5$, coefficient $c_1, c_2 = 1.5$. The number of particles is 100, and the maximum number of iterations is also set to 100. The search boundary is defined within a ±15% range centered around the load and renewable values measured from SCADA. This range can later be interpreted as a reflection of the assumed reliability of SCADA data. The initial positions of the particles are randomly initialized using a uniform distribution within the defined bounds.

To summarize, proposed algorithm evaluates the fitness of each particle at every iteration based on the cost function $J(x)$, as defined in Eq. 1, and updates the global best position to the one with the lowest cost among all particles. The final best

position, upon convergence, is applied to OpenDSS to compute the voltage phasors $h(x)$, which represent the estimated states adjusted to minimize the error with respect to the reference measurements z. As a result, the WLS-based cost function assigns the highest weights to the measurements from PMUs, effectively fixing the voltage phasors at the PMU installed buses to their measured values. Consequently, the optimization process operates by adjusting the active and load consumption or the renewable values to estimate the voltage states at the unmeasured buses. Fig.1 illustrates the overall structure of this algorithm.

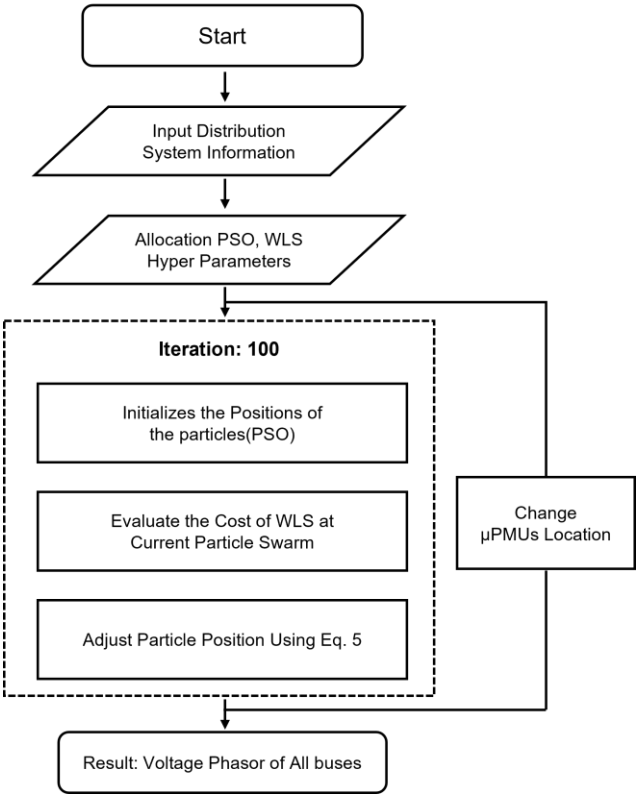


Fig. 1 Flow Chart of Algorithm

III. Simulation & Results

A. Simulation Configuration

The simulation is conducted on the IEEE 15 bus system, as shown in Fig. 2, implemented in both RSCAD and OpenDSS. renewable sources, each with an output of 100 kW and a power factor of 1.0, are integrated at buses 5 and 9. Additionally To provide a phase reference for the measured and estimated phasors, one µPMU is fixed at the source bus. In this study, the renewable sources are modeled as 3 phase current sources that inject constant active power independently of the voltage.

In the proposed algorithm, µPMU values are treated as absolute measurements. The system consists of three µPMUs: one physical µPMU provided by PowerSide and two virtual PMUs implemented in RTDS. The virtual µPMUs are time synchronized via a GTSYNC card and receive analog signals through the PB5 card of the RTDS. The data from the physical µPMU are collected via streaming in compliance with the IEEE C37.118.2 standard [20].

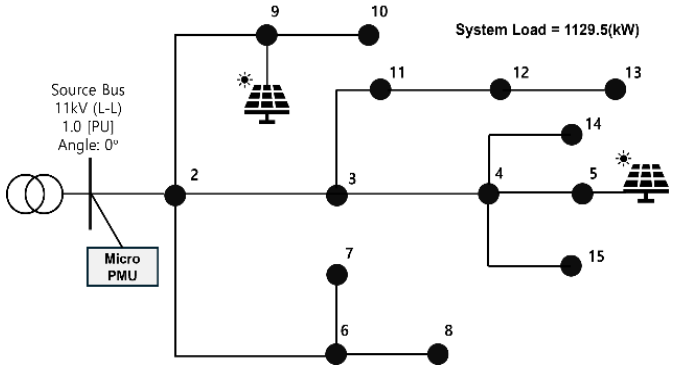


Fig. 2 IEEE 15 Bus Test Circuit

B. Simulation Results

The first simulation scenario explores the optimal placement of two µPMUs in a system where a single VRE is connected at bus 13. The second scenario simulates a case in which VREs are integrated and operating at buses 5 and 9. The suitability of µPMU placement is evaluated based on the bus combination that yields the lowest WLS cost. The Total Vector Error (TVE) at the corresponding bus is used as the performance metric. Since particle positions are initialized randomly, the effect of randomness is mitigated by repeating the optimization 10 times and selecting the bus combination with the lowest average WLS cost as the optimal placement.

$$TVE(\%) = \frac{|V_{ref} - V_{measured}|}{|V_{ref}|} \cdot 100 \qquad (6)$$

Table 1 Illustrates the cost function when a single VRE is integrated and two µPMUs are placed at all buses except the source bus. Since there are 14 buses available for µPMU placement, the number of possible combinations is $14C_2$, resulting in 91 cases. The table below presents the averaged WLS costs for the bset3 and worst3 cases.

TABLE I. WLS Cost for each locations (VRE: bus 13)

	Rank	Location 1	Location 2	Avg. WLS Cost
Best	1	9 Bus	10 Bus	10.9542
	2	10 Bus	13 Bus	12.1467
	3	9 Bus	13 Bus	12.1965
Worst	1	5 Bus	14 Bus	268.2673
	2	4 Bus	14 Bus	270.0481
	3	4 Bus	5 Bus	271.3508

In Table 1, the optimal µPMU placement is at buses 8 and 13. Fig. 5 shows the corresponding voltage phasors, and Fig. 4 presents the TVE for each bus voltage under best placement.

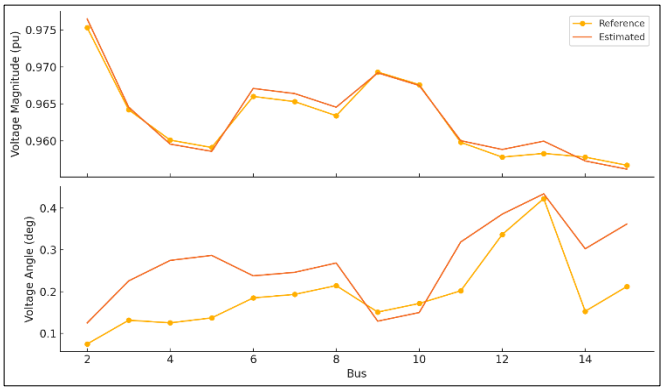


Fig. 3 Compare for Reference-PSO Results (VRE: 13Bus)

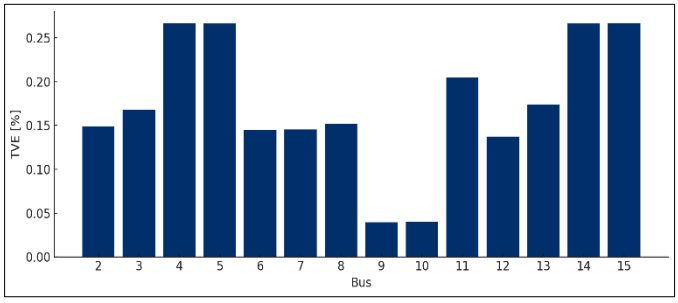


Fig. 4 TVE Results for All Buses (VRE: 13Bus)

According to the results, placing µPMUs at Buses 9 and 10 resulted in the lowest average WLS cost. Buses which are placed with µPMUs show high accuracy, and compared to other combinations, this configuration provided the highest accuracy in state estimation. On the other hand, the combination with the highest average WLS cost recorded 286.7602, which is more than 26 times greater. This indicates that the placement of µ PMUs has a significant influence on estimation performance.

Furthermore, the TVE at each bus for the best performing configuration remained below 1%, satisfying the steady-state accuracy criterion specified in IEEE C37.118.2 standard [20]. This confirms that the voltage phasor estimation in this setup is within a practically acceptable error range. However, certain unmeasured buses such as Buses 4 and 15 showed relatively higher TVE values, which can be interpreted as a trade-off under the condition of using only three devices.

In the second simulation, the proposed algorithm was applied under the condition that 100 kW of VRE is integrated at Buses 5 and 9, respectively. Table 2 presents the average WLS cost over 10 trials for each µPMU placement configuration.

TABLE 2. WLS COST FOR EACH LOCATIONS (VRE: BUS 5, 9)

	Rank	Location 1	Location 2	Avg. WLS Cost
Best	1	6 Bus	7 Bus	13.5038
	2	2 Bus	6 Bus	13.5376
	3	2 Bus	7 Bus	13.5616
Worst	1	9 Bus	12 Bus	194.4512
	2	10 Bus	11 Bus	203.9995
	3	9 Bus	11 Bus	206.0522

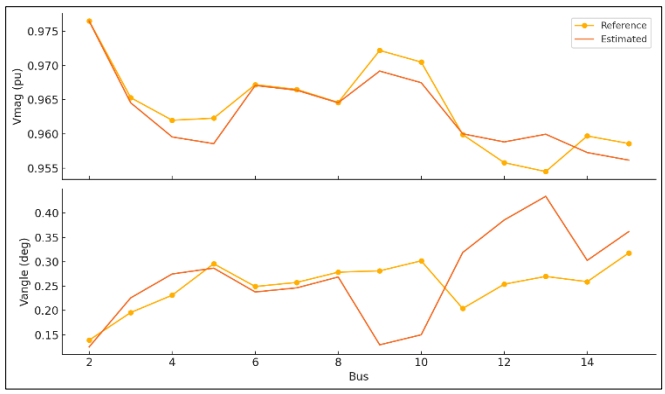


Fig. 5 Compare for Reference

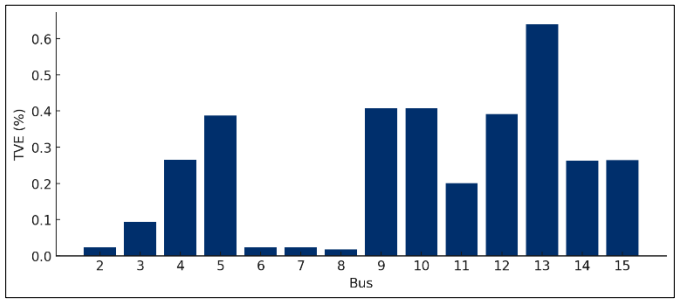


Fig. 6 TVE Results for ALL Buses (VRE: 5, 9 BUS)

As in the previous simulation, a significant difference in cost was observed between the best and worst µPMU placement combinations. At Buses 6 and 7, where µPMUs were placed, very low TVE values of approximately 0.02% were recorded, indicating that the estimated voltage at these buses closely matched the RTDS reference measurements. This confirms that the µPMU measurements were accurately reflected on those buses. On the other hand, at bus 13, where no µPMU was placed, the TVE reached approximately 0.6%, suggesting as in the first simulation that the accuracy of state estimation may decline at certain buses without direct measurement.

Throughout the simulation, both the WLS cost and TVE remained at notably low levels, and voltage magnitudes were estimated with high consistency relative to the reference values. This can be considered a satisfactory result, given the inherent differences in calculation approaches between EMT-based RTDS and steady-state power flow-based OpenDSS. However, time-series-based real-time simulations may lead to different results, and addressing this requires extending the OPP strategy to account for state estimation accuracy under dynamic conditions.

IV. CONCLUSION

This paper studies the OPP strategy under constrained budget conditions by using state estimation performance as the evaluation metric. To achieve this, the cost function of the WLS was defined, and PSO, a heuristic optimization technique, was adopted due to the black-box nature of the OpenDSS simulation model. The optimal locations were determined based on the WLS costs, and the accuracy of voltage estimation was validated using the TVE. Simulations were conducted under

conditions where reverse power flow may occur due to the integration of VREs. As a result, it was demonstrated that even with a limited number of μPMUs, the voltage states of the entire distribution system could be estimated with acceptable accuracy. Especially, the combination resulting in the minimum WLS cost led to TVE values converging below 1%, indicating that the estimation accuracy is suitable for real system operational environments. The proposed method can be further extended to scenarios involving inverter-based resources equipped with reactive power control or compensation functions, as well as fault conditions. It also provides a foundation for future expansion into dynamic state estimation-based OPP strategies.

ACKNOWLEDGMENT

This work was supported by Korea Institute of Energy Technology Evaluation and Planning (KETEP) grant funded by the Korea government (MOTIE) (RS-2023-00234563, Development of power system modeling & analysis and interoperability evaluation technology applied with grid forming based on distributed energy), (No. RS-2023-002317052, Development of an Open Integrated Platform for Distributed Renewable Energy Systems).

REFERENCES

[1] B. Kroposki et al., "Achieving a 100% Renewable Grid: Operating Electric Power Systems with Extremely High Levels of Variable Renewable Energy," in IEEE Power and Energy Magazine, vol. 15, no. 2, pp. 61-73, March-April 2017

[2] Y. Song, Y. Zheng, T. Liu, S. Lei and D. J. Hill, "A New Formulation of Distribution Network Reconfiguration for Reducing the Voltage Volatility Induced by Distributed Generation," in IEEE Transactions on Power Systems, vol. 35, no. 1, pp. 496-507, Jan. 2020

[3] S. S. AlKaabi, V. Khadkikar and H. H. Zeineldin, "Incorporating PV Inverter Control Schemes for Planning Active Distribution Networks," in IEEE Transactions on Sustainable Energy, vol. 6, no. 4, pp. 1224-1233, Oct. 2015

[4] M. Ghosal and V. Rao, "Fusion of PMU and SCADA Data for dynamic state estimation of power system," 2015 North American Power Symposium (NAPS), Charlotte, NC, USA, 2015

[5] A. Abur and A. G. Exposito, Power System State Estimation: Theory and Implementation, 2004

[6] A. Albuquerque, D. Bez and A. Simões, "Multistage strategies to incorporate phasor measurements into power system state estimation," 2013 IREP Symposium Bulk Power System Dynamics and Control - IX Optimization, Security and Control of the Emerging Power Grid, Rethymno, Greece, 2013

[7] M. H. Wakti, L. Multa Putranto, S. P. Hadi, M. Yasirroni and A. F. Derana Marsiano, "PMU Location Determination in a Hybrid PMU-SCADA System," 2020 12th International Conference on Information Technology and Electrical Engineering (ICITEE), Yogyakarta, Indonesia, 2020

[8] X. Liu and N. -K. C. Nair, "Review on D-PMU based applications for active electricity distribution system," 2020 IEEE International Conference on Power Systems Technology (POWERCON), Bangalore, India, 2020

[9] S. Bu, L. G. Meegahapola, D. P. Wadduwage and A. M. Foley, "Stability and Dynamics of Active Distribution Networks (ADNs) With D-PMU Technology: A Review," in IEEE Transactions on Power Systems, vol. 38, no. 3, pp. 2791-2804, May 2023

[10] PowerSide, https://powerside.com/wp-content/uploads/2023/02/MicroPMU-LV-Synchrophaser-Data-Sheet.pdf

[11] Zhi Wu, Jiachen Jiang, Shu Zheng, Jingtao Zhao, Wei Gu, Joint optimal PMU and DULR placement in distribution network considering fault reconstruction and state estimation accuracy, International Journal of Electrical Power & Energy Systems, Volume 162, 2024

[12] X. Zhou, Y. Wang, Y. Shi, Q. Jiang, C. Zhou and Z. Zheng, "Deep Reinforcement Learning-Based Optimal PMU Placement Considering the Degree of Power System Observability," in IEEE Transactions on Industrial Informatics, vol. 20, no. 6, pp. 8949-8960, June 2024

[13] N. Khanam, M. Rihan and S. Hameed, "Placement of Micro-PMUs and Voltage Estimation in Radial Distribution Networks with Zero Injection constraints," 2024 IEEE PES Innovative Smart Grid Technologies - Asia (ISGT Asia), Bengaluru, India, 2024

[14] N. H. A. Rahman and A. F. Zobaa, "Integrated Mutation Strategy With Modified Binary PSO Algorithm for Optimal PMUs Placement," in *IEEE Transactions on Industrial Informatics*, vol. 13, no. 6, pp. 3124-3133, Dec. 2017

[15] M. P. Anguswamy, M. Datta, L. Meegahapola and A. Vahidnia, "Optimal Micro-PMU Placement in Distribution Networks Considering Usable Zero-Injection Phase Strings," in IEEE Transactions on Smart Grid, vol. 13, no. 5, pp. 3662-3675, Sept. 2022

[16] G. A. Ortiz, D. G. Colomé and J. J. Quispe Puma, "State estimation of power system based on SCADA and PMU measurements," 2016 IEEE ANDESCON, Arequipa, Peru, 2016, pp. 1-4

[17] Jin, T.; Shen, X. A Mixed WLS Power System State Estimation Method Integrating a Wide-Area Measurement System and SCADA Technology. Energies 2018

[18] T. K. Maji and P. Acharjee, "Multiple Solutions of Optimal PMU Placement Using Exponential Binary PSO Algorithm for Smart Grid Applications," in IEEE Transactions on Industry Applications, vol. 53, no. 3, pp. 2550-2559, May-June 2017

[19] J. Kennedy and R. Eberhart, "Particle swarm optimization," Proceedings of ICNN'95 - International Conference on Neural Networks, Perth, WA, Australia, 1995, pp. 1942-1948 vol.4

[20] IEEE Standard for Synchrophasor Data Transfer for Power Systems," in IEEE Std C37.118.2-2024 (Revision of IEEE Std C37.118.2-2011) , vol., no., pp.1-79, 13 Dec. 2024

Influence of New Energy Power Fluctuation on the Power System Frequency Safety Under High New Energy Penetration

Wenbo Yang
Department of Electrical Engineering
Tsinghua University
Beijing, China
yangwb24@mails.tsinghua.edu.cn

Zhen Huang
State Grid Northeast China Branch
State Grid
Shenyang, China
18873925969@163.com

Lei Chen*
Department of Electrical Engineering
Tsinghua University
Beijing, China
chenlei08@tsinghua.edu.cn

Kaiyuan Hou
Power Dispatching and Control Center
State Grid Northeast China Branch
Shenyang, China
1446294241@qq.com

Deming Xia
Power Dispatching and Control Center
State Grid Northeast China Branch
Shenyang, China
1979134419@qq.com

Xingwei Xu
Power Dispatching and Control Center
State Grid Northeast China Branch
Shenyang, China
1256226760@qq.com

***Abstract*—With the rapid increase of new energy penetration, the increase of fluctuation of new energy power and the decrease of frequency regulation capability will affect the frequency safety of power system. In order to study the specific effect of new energy power fluctuation on the system frequency of power system under high penetration, the power fluctuation characteristics of new energy at different time scales and how they affect the system frequency are analyzed firstly. Then, based on empirical mode decomposition, the wind and solar fluctuation model and the maximum power fluctuation range estimation model are established, and then the primary frequency regulation upward capability model of thermal power unit is established. Finally, based on the above models, the time-domain simulations of power system with different new energy penetration are carried out, and the changes of system primary frequency regulation upward capability, disturbance power margin are analyzed.**

Keywords—new energy; power fluctuation; frequency safety; primary frequency regulation capability

I. INTRODUCTION

In recent years, the installed capacity of new energy in China has seen rapid growth. By the end of April 2025, the installed capacity of solar power reached 990 million kilowatts, marking a 47.7% increase year-on-year; the installed capacity of wind power was around 540 million kilowatts, up 18.2% year-on-year, highlighting the trend of new energy sources becoming the dominant power source[1].

As the penetration of new energy sources continues to rise, the rapid consumption of flexible regulation resources in power systems has made issues related to power balance and frequency safety more prominent [2] [3]. The most direct and significant factor causing dynamic frequency fluctuations in the system is power fluctuation[4]. In traditional power systems, random power fluctuations mainly comes from load changes and are generally considered to be relatively minor[5]. However, wind and photovoltaic power generation exhibit high randomness and strong volatility, and their large-scale integration into the grid not only increases power imbalance but also affects the system's frequency regulation capabilities, further impacting the grid's frequency safety [6][7][8].

To understand the relationship between fluctuations of new energy power and frequency fluctuation, it is essential to analyze the characteristics of new energy power fluctuations and model their fluctuation components. Many studies have proposed methods for analyzing wind and solar power fluctuations from both time-domain and frequency-domain perspectives, such as the various probabilistic models in literature [9][10][11] and the frequency-domain-based simulation analysis of wind farm power fluctuations in literature [12][13]. However, current time-domain methods overlook the inherent fluctuation frequency patterns of wind and solar power over time and fail to reveal the inherent attributes of wind and solar power fluctuations. In the frequency domain, study[14] has shown that the low frequency components make up the majority of new energy power, concentrated around the zero frequency, while high frequency fluctuation components are only a small part and are easily obscured in the entire spectrum, making it difficult to effectively separate the fluctuation components that retain the inherent characteristics of wind and solar power from the spectrum alone. Therefore, we propose a method that can isolate the inherent characteristic fluctuation components of wind and solar power fluctuations while ensuring that their amplitude in the time-

Supported by State Grid Northeast China Branch (52992624000W).

domain remain unchanged after decomposition and reconstruction.

Except increase the power imbalance, large scale integration of also affect the primary frequency of thermal power unit. Previous literature[15][16]has primarily focused on the fact that new energy power units lack inertia and primary frequency regulation capability under traditional control modes. However, the installed and operational thermal power capacity in China's grid has not significantly decreased, and the inertia of the power system has not noticeably declined[17]. The number of units participating in frequency regulation has also not significantly decreased, but their primary regulation capabilities are affected by new energy daily fluctuation[18]. Therefore, this study extends existing research by:

1)Proposing a wind and solar fluctuation modeling method based on empirical mode decomposition(EMD) and a maximum wind and solar power fluctuation interval estimation model;

2)Establishing a primary frequency regulation upward capability model considering different operating conditions of thermal power unit;

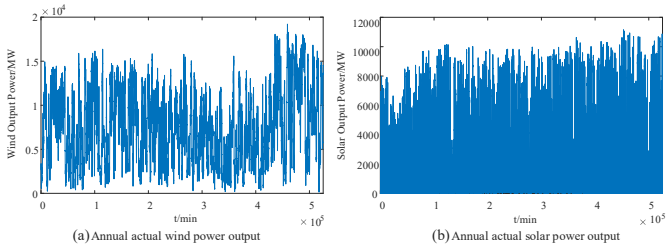
3)Based on the above models, system primary frequency regulation upward capability and disturbance power margin are analyzed.

II. Analysis of Power Fluctuations of New Energy at Different Time Scales

This section analyzes the power fluctuation characteristics of new energy based on the massive actual data of a regional power grid of China. By statistically processing the wind and solar power of the regional power grid for the entire year of 2023 at a 1-minute sampling frequency, we obtain the annual time series of wind and photovoltaic power, as shown in Fig.1. It can be easily observed from the figure that wind and solar power exhibits distinct characteristics of intermittency, fluctuation, and strong stochasticity in the time dimension.

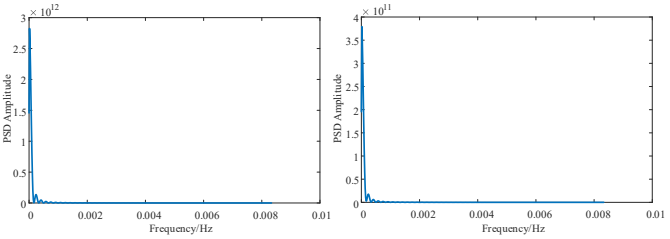
To analyze the fluctuation characteristics of wind and solar power at different time scales, we adopt the power spectral density (PSD) method to represent the power distribution of renewable energy at different frequencies. The power spectral density diagram of new energy is shown in Fig.2. In the frequency domain, the figure shows that the low frequency components make up the majority, concentrated around the zero frequency, while high frequency fluctuation components are only a small part and are easily obscured in the entire spectrum. Therefore, in next section a method for separating wind and solar power fluctuations components based on the empirical mode decomposition (EMD) algorithm is proposed. With the method, the inherent fluctuation components of wind and solar power fluctuations across different time scales can be obtained.

Considering solar power output shows distinct diurnal distribution over time, we focus on analyzing the intra-day characteristics of new energy power. Analyzing new energy power data from a single day is highly unpredictable, whereas over longer periods and at the regional grid level, there are discernible patterns. Therefore, this paper then analyzes the massive data of the regional power grid by averaging daily data on wind power, solar power, load, and thermal power unit load rates throughout the year, resulting in average daily output and load curves for analysis.



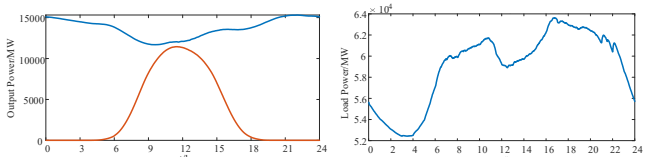
(a) Annual actual wind power output (b) Annual actual solar power output

Fig. 1. Annual actual new energy power output.



(a) Wind output power spectral density (b) Solar output power spectral density

Fig. 2. New energy power spectral density.



(a) New energy power distribution over time (b) Load power distribution over time

Fig. 3. Daily distributions of new energy power and load power over time.

Fig.3 shows the daily temporal distributions of new energy output power and load power respectively. It can be seen that new energy output has obvious daily temporal distribution characteristics: solar power peaks and valleys in the noon, and output is almost zero at night and early morning, while wind power troughs are in the morning and noon, and peaks are in the evening and early morning.

In terms of daily power balance, the alignment between new energy power output and electricity demand is often poor, sometimes even opposite. Load demand peaks during the day and is low at night. Wind power has a high output at night and a low output during the day, exhibiting a clear inverse peak regulation characteristic. Solar power, on the other hand, has a high output in the afternoon and no output at night, making it ineffective for supporting nighttime demand. The load rate of thermal power units, influenced by both load demand and the output of new energy, is shown in Fig.4. The figure reveals that the temporal distribution characteristics of new energy have led to a similar temporal load rate for thermal power units. The average unit load rate is lowest at noon, indicating that the operating conditions of thermal power units are significantly affected by the temporal power of new energy.

Then, let's analyzes how power fluctuations of new energy at different scales affect the frequency safety of power system. At the grid level, the system power fluctuations and the grid's

frequency regulation capability jointly determine the system's frequency deviation. Through analyzing the power fluctuations

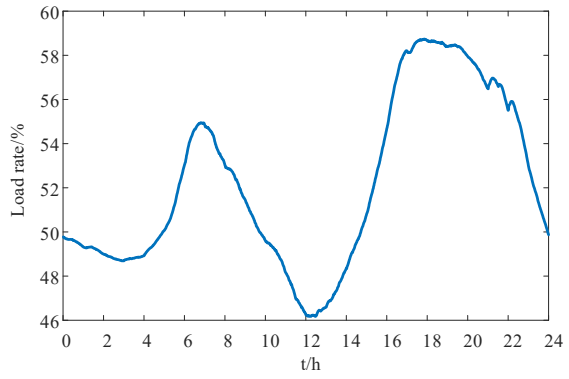


Fig. 4. Load rate distribution of thermal power units over time.

of new energy at different time scales, we can observe that short term power fluctuations (primarily at the minute-level) increase the system's power imbalance. Intra-day hour-level fluctuations affect the load rate of thermal power units, thereby influencing the primary frequency regulation capability of thermal power. The combination of these two factors increases system disturbances, reduces the primary frequency regulation capability of thermal power, and consequently decreases the system's frequency security margin.

III. Modeling of Wind and Solar Power Fluctuations Based on EMD and Estimation Model of Maximum Fluctuation Range

A. Wind and Solar Power Fluctuation Extraction Based on EMD

Empirical mode decomposition (EMD) is a novel adaptive method for time-frequency signal processing. It decomposes signals based on the inherent time-scale characteristics of the data, without the need for predefined basis functions. Compared to traditional Fourier or wavelet decomposition, EMD is better suited for analyzing nonlinear and non-stationary signal sequences. Additionally, EMD ensures perfect reconstruction, with no loss of information or distortion when reconstructing the original signal.

The basic idea of EMD is to use the average value of the upper and lower envelopes on the time series to determine the instantaneous average position, so as to continuously extract and decompose the scale components of the original signal from high frequency to low frequency into several intrinsic mode functions(IMF) and a residual, which is composed of the following formula:

$$X(n)=\sum_{m=1}^{M} IMF_m(n)+\mathrm{Re}s(n) \tag{1}$$

In (1), $X(n)$ represents the input signal of wind or solar power, $IMF_m(n)$ represents the IMF, and $\mathrm{Re}s(n)$ represents the residual.

Wind and solar power signals are non-stationary and nonlinear. Using the EMD algorithm, the wind and solar power sequences can be decomposed to extract their IMF components.

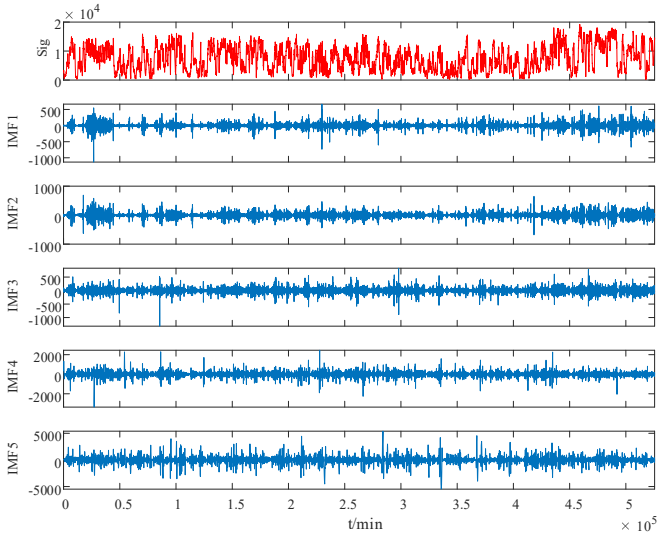


Fig. 5. The original data of the wind power, IMF1-IMF5 components after EMD decomposition.

Based on the wind and solar power data of the regional power grid for the entire year of 2023 at a 1-minute sampling frequency, using wind power as an example, the original wind power data and the components (just show IMF1-IMF5) derived from the EMD algorithm decomposition are shown in Fig.5. Frequency domain analysis of the IMF1 components of wind and solar power reveals that high frequency intrinsic fluctuation components above $2\times10^{-3}\,Hz$ for wind power and $3\times10^{-3}\,Hz$ for solar power are extracted, respectively. This paper defines these high frequency fluctuations, which are difficult to extract and predict, as minute-level fluctuation components of wind and solar power.

B. A Maximum Power Fluctuation Range Estimation Model

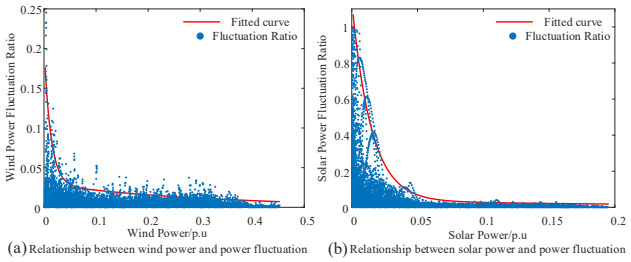
To analyze the proportion of wind and solar power minute-level fluctuation components in the wind and solar power, the minute-level fluctuation ratio of wind and solar power are defined to describe the intensity of these fluctuations, as shown in (2):

$$I_{pm-w}=\frac{\sigma_{w,k}}{P_{w,k}};\quad I_{pm-pv}=\frac{\sigma_{pv,k}}{P_{pv,k}} \tag{2}$$

In (2), the wind and solar power values at the k-th minute of the day are denoted $P_{w,k}$ and $P_{pv,k}$,respectively. The amplitude of the wind and solar power minute-level fluctuation components at the k-th minute are denoted as $\sigma_{w,k}$ and $\sigma_{pv,k}$, respectively.

The actual wind and solar power amplitudes of the regional power grid for the entire year of 2023 are calculated, and outliers are removed based on 3σ principles. For example, for wind systems, the relationship between the minute-level fluctuation

ratio of wind power and the nominal value of wind output can be determined. To estimate the maximum minute-level fluctuation ratio of wind power, a double exponential function can be used to fit the outer envelope, as shown in Fig.6(a).



(a) Relationship between wind power and power fluctuation (b) Relationship between solar power and power fluctuation

Fig. 6. The relationship between wind/solar power and wind/solar power fluctuations.

Then, we can get the relationship between the maximum minute-level fluctuation ratio of wind power and wind power, as shown in (3):

$$I_{pm-w} = a_w * \exp(b_w * P_{pu-w}) + c_w * \exp(d_w * P_{pu-w}) \quad (3)$$

In (3), a_w, b_w, c_w, d_w are the fitting parameters between the maximum wind power minute-level fluctuation ratio and wind power, and P_{pu-w} represents the per-unit value of actual wind power relative to thermal power unit installed capacity. Based on the relationship between maximum wind power minute-level fluctuation ratio and wind power in (3), the expression for the maximum estimated value of wind power minute-level fluctuation can be derived as shown in (4):

$$\sigma_{w,k,\max} = P_{w,k} * \left[a_w * \exp(b_w * P_{pu-w}) + c_w * \exp(d_w * P_{pu-w}) \right] \quad (4)$$

Similarly, the relationship between solar power fluctuation ratio and solar output power is shown as in the Fig.6(b). we can get the relationship between the maximum minute-level fluctuation ratio of solar power and solar power, as shown in (5):

$$I_{pm-pv} = a_{pv} * \exp(b_{pv} * P_{pu-pv}) + c_{pv} * \exp(d_{pv} * P_{pu-pv}) \quad (5)$$

In (5), $a_{pv}, b_{pv}, c_{pv}, d_{pv}$ are the fitting parameters between the maximum solar power minute-level fluctuation ratio and solar power, and P_{pu-pv} represents the per-unit value of actual solar power relative to thermal power unit installed capacity. Based on (5), the expression for the maximum estimated value of solar power minute-level fluctuation can be derived as shown in (6):

$$\sigma_{pv,k,\max} = P_{pv,k} * \left[a_{pv} * \exp(b_{pv} * P_{pu-pv}) + c_{pv} * \exp(d_{pv} * P_{pu-pv}) \right] \quad (6)$$

Given the actual conditions of the power system, the effective utilization hours of wind and solar power output are largely constant. Therefore, when analyzing future increases in the penetration wind and solar power, it is assumed that the output of wind and solar power increases proportionally with the installed capacity to facilitate analysis. Based on existing historical measurement data, the model can estimate the maximum minute-level fluctuation components of wind and solar power under different penetration.

IV. Primary Frequency Regulation Upward Capability Model of Thermal Power Unit

Considering that the installed capacity of thermal power units in the grid remains unchanged and will continue to participate in primary frequency regulation for a long time, the impact of new energy integration on the primary frequency regulation capability of thermal power units should be considered. In frequency related issues, low frequency problems are more challenging to resolve compared to high frequency problems. When the down regulation capacity of units is insufficient, high frequency issues can be addressed by disconnecting units. However, when the upward regulation capacity is inadequate, resolving low frequency problems through load shedding incurs significant costs. Consequently, this section focuses on the upward regulation capacity of thermal power units and establishes a primary frequency regulation upward capability model considering the load rate of thermal power unit.

The complete dynamic model of a thermal power unit's primary frequency regulation consists of the control system model, the actuator model, the boiler dynamic model, and the steam turbine system dynamic model. In long-term frequency regulation simulations, the primary focus is on how the operating conditions affect the limits of primary frequency regulation capabilities. Currently, most thermal power units still use main steam valve frequency regulation technology for primary frequency regulation. Therefore, it can be assumed that the limitations of primary frequency regulation are mainly due to the valve position. In the short duration of primary frequency regulation, the initial value of the main steam pressure before the regulation action has a more significant impact on the unit's frequency regulation power. Thus, the dynamic characteristics of the main steam pressure during the regulation period are often neglected.

The standard steam turbine model, as illustrated in Fig.7, has the main steam flow as its input and the unit output power as its output. In Fig.7, F_{HP} is the power ratio of the high-pressure cylinder, F_{ILP} is the power ratio of medium-pressure cylinder and low-pressure cylinder, T_{CH} is the steam volumetric time constants, T_{RH} is the reheated steam volumetric time constants. For the convenience of formula derivation, denote Pt as the main steam pressure, P_{CV} as the main steam valve opening degree, d_s as the main steam flow, P_e as the unit output, kv as the valve flow coefficient. The relationship among the first three and the relationship between unit output power and main steam flow are expressed by (7):

$$\begin{aligned} d_s &= kv \times P_{CV} \times Pt; \\ P_e &= \left(F_{HP} + F_{ILP}\right) \times d_s = k \times d_s \end{aligned} \quad (7)$$

The thermal unit typically operates in full sliding pressure or composite sliding pressure mode. Under the assumption that the operating conditions are below 30% load rate and above 90%

load rate, it runs at constant main stream pressure; otherwise, it operates in sliding pressure mode. The adjustable upward regulation power for primary frequency regulation is calculated

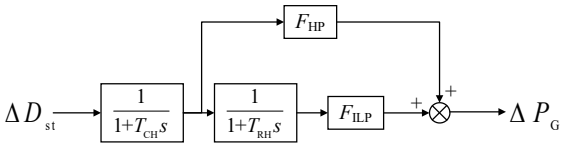


Fig. 7. Steam turbine model.

by subtracting the power before regulation from the unit's power when the main steam valve is fully open (set to 1).

When the valve opening degree is considered to remain constant as P_{cv}^0 during sliding pressure operation, the adjustable power can be calculated when the unit output power is P_e^{st} :

$$\begin{aligned}\Delta P_e^{st} &= k(d_s^{\max} - d_s) = k(kv \times 1 \times Pt^{st} - kv \times P_{cv}^0 \times Pt^{st}) \\ &= k \times kv \times P_{cv}^0 \times Pt^{st} \times (\frac{1}{P_{cv}^0} - 1) = P_e^{st} \times \frac{1 - P_{cv}^0}{P_{cv}^0}\end{aligned} \tag{8}$$

In (8), the Pt^{st} is the main steam pressure under the operating output P_e^{st} . When the operating condition is higher than the upper limit of the sliding pressure operating condition and the main steam pressure remains unchanged as Pt^h , $P_{cv}{}^{st}$ denoted as the valve opening degree under this operating condition, the adjustable power can be obtained in(9):

$$\begin{aligned}\Delta P_e^{st} &= k(d_s^{\max} - d_s) = k \times kv \times P_{cv}^{st} \times Pt^h \times (\frac{1}{P_{cv}^{st}} - 1) \\ &= P_e^{st}(\frac{1}{P_{cv}^{st}} - 1) = P_e^{st}(\frac{P_e^h}{P_e^{st} \times P_{cv}^0} - 1) = \frac{P_e^h - P_e^{st} \times P_{cv}^0}{P_{cv}^0}\end{aligned} \tag{9}$$

Similarly, when the operating condition output is lower than the lower limit of the sliding pressure operating condition output P_l^h , the adjustable power can be obtained as shown in (10):

$$\Delta P_e^{st} = \frac{P_e^l - P_e^{st} \times P_{cv}^0}{P_{cv}^0} \tag{10}$$

Dividing the adjustable upward power of primary frequency regulation by the installed thermal power capacity and making it nominal, we can get the relationship between the thermal power load rate α^{st} corresponding to the operating condition and the adjustable power nominal quantity as shown in (11):

$$\begin{cases} \dfrac{\alpha^h}{P_{cv}^0} - \alpha^{st} & \alpha^{st} > 0.9 \\ \alpha^{st} \times \dfrac{1 - P_{cv}^0}{P_{cv}^0} & 0.3 < \alpha^{st} > 0.9 \\ \dfrac{\alpha^l}{P_{cv}^0} - \alpha^{st} & \alpha^{st} < 0.3 \end{cases} \tag{11}$$

When the valve opening degree P_{cv}^0 is set to 0.9, the relationship between the adjustable upward power of thermal power unit primary frequency regulation capacity of and unit

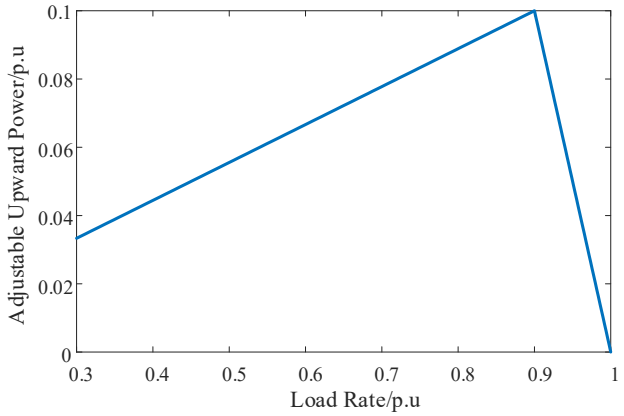


Fig. 8. Relationship between primary frequency regulation adjustable upward power and load rate of thermal power unit.

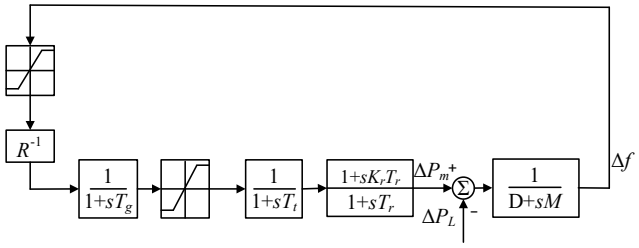


Fig. 9. Simplified and aggregated primary frequency regulation model.

load rate is illustrated in Fig.8. In practical applications, thermal units typically have a set primary frequency regulation limit, usually set at 6%. Therefore, when constructing the primary frequency regulation model, it is necessary to consider two limits: the first is the unit's set limit, and the second is the theoretical primary frequency regulation capability based on operating conditions.

Based on the thermal power unit capacity of the reginal power grid, and considering the limits of primary frequency regulation of the thermal power unit, a simplified single-zone aggregation frequency model is illustrated in Fig.9. In this model, denote M as the rotor time constant related to inertia, D as the frequency response coefficient of the load, R as the differential adjustment coefficient of the equivalent thermal power unit, K_r as the aggregation parameter of the equivalent steam turbine high-pressure cylinder's share of the total steam turbine output power, T_r as the reheating time constant, T_t as the steam capacity time constant of the steam turbine, the T_g equivalent inertia time constant of the turbine,.

V. Simulation Analysis

A. *Influence of Different Penetration of New Energy on Primary Frequency Regulation Upward Capability*

As analyzed earlier, the increase in the penetration rate of new energy sources not only increases the disturbance from new energy but also affects the load rate of thermal power units,

thereby reducing their primary frequency upward capability. In this section, we first examine how the installed penetration of new energy affects the load rate of thermal power units. Since the main power sources in this regional power gird are thermal power and new energy, with very little other power sources, we define the penetration of wind, solar and new energy installed capacities, as shown in (12):

$$\delta_w = \frac{S_w}{S_w + S_p + S_G}, \delta_p = \frac{S_p}{S_w + S_p + S_G}, \delta = \frac{S_{RE}}{S_{RE} + S_G} = \delta_w + \delta_p \quad (12)$$

In (13), $\delta_w, \delta_p, \delta$ is the installed capacity penetration of wind, solar and new energy, S_G, S_w, S_p, S_{RE} is the installed capacities of thermal, wind, solar and new energy, respectively. Let γ represents the power penetration of new energy output. Assuming the current installed capacity penetration of new energy is δ^0, and the penetration of new energy output is γ^0. Considering the output of new energy is directly proportional to its installation, the relationship between future new energy output and installation penetration can be expressed as:

$$S_{RE} = \frac{\delta}{(1-\delta)} \Rightarrow P_{RE} = P_{RE}^0 * \frac{S_{RE}}{S_{RE}^0} = P_{RE}^0 * \frac{\delta(1-\delta^0)}{\delta^0(1-\delta)} \quad (13)$$

In (13), P_{RE}, P_{RE}^0 is the future output power and current output power of new energy. Let P_G, P_{load} represents the thermal power and load power. Considering then relationship between γ and δ, the thermal unit load rate can be expressed as:

$$\gamma = \frac{P_{RE}}{P_{load}} = \gamma^0 * \frac{P_{RE}}{P_{RE}^0} = \frac{\gamma^0(1-\delta^0)}{\delta^0} * \frac{\delta}{(1-\delta)} \Rightarrow$$
$$\alpha = \frac{P_G}{S_G} = \frac{(1-\gamma)P_{load}}{S_G} = (1 - \frac{\gamma^0(1-\delta^0)}{\delta^0} * \frac{\delta}{(1-\delta)}) \frac{P_{load}}{S_G} \quad (14)$$

Denote K1 as the multiple of the future installed wind power capacity relative to the existing installed wind power capacity, and K2 as the multiple of the future installed solar capacity relative to the existing installed solar capacity. By substituting these values into (12), the future penetration rates of wind, solar, and new energy can be calculated under different multiple changes in wind and solar installed capacities. Subsequently, the thermal unit load rate under different new energy penetration can be calculated using (14).

Based on Fig.4 and Fig.8, the temporal distribution of the system adjustable upward power of primary frequency regulation is illustrated in Fig.10. As shown in Fig.4 and Fig.10, the unit load rate is at its lowest at 1:00 PM, which is also the time when the adjustable upward power for primary frequency regulation is at its lowest. And the thermal power units even can't meet the 6% adjustable upward power requirement.

B. Influence of Different Penetration of New Energy on System Disturbance Power Margin

To ensure the safety of the system frequency, a maximum minute-level power fluctuation model for wind and solar power was established in Section III. By substituting the wind and solar power under different penetration into (4) and (6), we can derive the maximum minute-level power fluctuation estimates of wind and solar. Adding the maximum wind and solar minute-level power fluctuations, we define it as the current maximum estimated minute-level power fluctuation of new energy, as shown in (15):

$$\sigma_{RE,\mathrm{k,max}} = \sigma_{w,\mathrm{k,max}} + \sigma_{pv,\mathrm{k,max}} \quad (15)$$

The distribution of $\sigma_{RE,k,\max}$ over time is shown in Fig.11. It can be seen that at noon, the power fluctuation of new energy is the largest, which is the time when the power system disturbance is the biggest, and the frequency regulation ability of the system is the weakest at this time. The two together may lead to the obvious frequency problems at noon.

After being normalized the maximum power disturbance of new energy is 0.011 at noon, does not reach the limit of the system primary frequency regulation adjustable power. But it reduces the system's tolerance to disturbance power during accidents by utilizing the system's primary frequency regulation capacity.

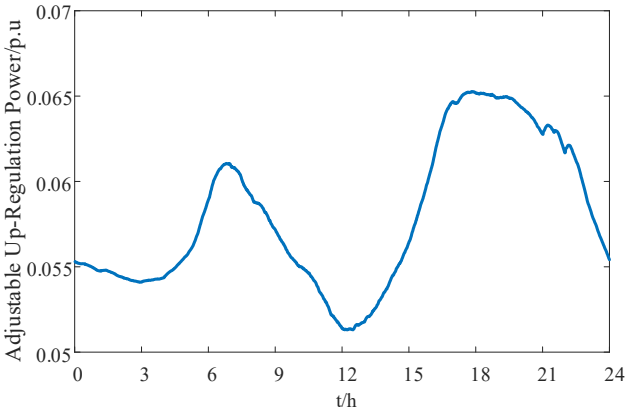


Fig. 10. Primary frequency regulation adjustable upward power distribution of the system over time.

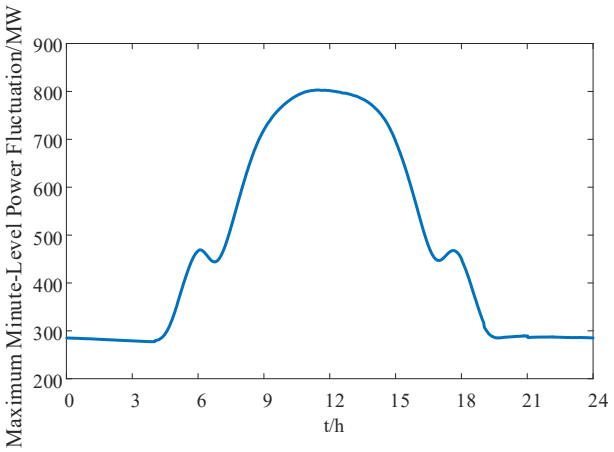


Fig. 11. Estimation of maximum minute-level power fluctuation component of new energy.

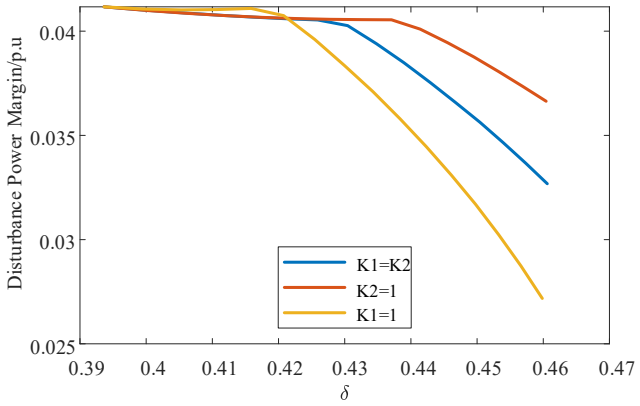


Fig. 12. The relationship between disturbance power margin and new energy penetration.

Therefore, in order to ensure that the maximum frequency deviation of the system is within the safe range(0.5Hz) during fault disturbance, and to analyze the maximum margin that the system can withstand the disturbance under the condition of new energy power fluctuation, the disturbance power margin of the system under the condition of new energy power fluctuation is defined in (16):

$$PM_k = P_{\text{step},k} - \sigma_{RE,k,\max} \tag{16}$$

In (16), $P_{\text{step},k}$ is the maximum step power that can be exerted to the system when the frequency deviation is within a safe range(0.5Hz) at the k-th minute moment.

According to the above analysis, noon is the most dangerous moment for system frequency. Therefore, the simulation and analysis of power system frequency at 1:00 PM are carried out for three scenarios of different new energy penetration by using model shown in Fig.9. The simulation includes three scenarios:

1)Scenario 1: The installed capacity of wind power and solar is expanded in same proportion to the existing installed capacity(K1=K2).

2)Scenario 2: The installed capacity of wind power is expanded and the installed capacity of solar remains unchanged. (K2=1).

3) Scenario 3: The installed solar capacity is expanded and the installed wind power capacity remains unchanged(K1=1).

The relationship between disturbance power margin and new energy penetration when the maximum frequency deviation of the system is guaranteed within 0.5Hz is shown in Fig.12. From Fig.12, it can be seen that:

1) When the new energy penetration initially increases, the disturbance power decreases slowly because the adjustable power limit for primary frequency regulation has not yet been reached. The disturbance power margin decreases mainly because the minute-level power fluctuation of the new energy increases slightly;

2) When new energy penetration reaches a certain level, the disturbance power margin rapidly decreases. The primary frequency regulation adjustable upward power limit is reached, so the disturbance power margin decreases rapidly due to the rapid reduction of the upward adjustable power.

3) Under the same level of new energy penetration, changes in solar installed capacity have a significantly greater impact on the disturbance power margin compared to changes in wind power installed capacity. An increase in solar penetration, compared to wind power, more significantly reduces the thermal power load rate during midday, thereby more significantly reducing the system primary frequency regulation upward capability. Therefore, adding more solar power affect disturbance power margin and frequency stability differently from adding more wind power.

In conclusion, with the increase of new energy penetration, the system disturbance power margin will decrease due to increased disturbances from minute-level power fluctuations in new energy sources and reduced primary frequency regulation upward capability in thermal power units. In addition, the primary frequency regulation upward capability of thermal power units in this regional grid during midday has already fallen below the 6% national standard requirement. Considering the output fluctuations of new energy sources, the frequency security of the system under large disturbances is already at significant risk. Therefore, it is necessary to enhance frequency security by implementing more diverse primary frequency regulation sources and strategies.

VI. Conclusion

This paper focuses on the impact of new energy power fluctuations on frequency safety under high new energy penetration. In order to study the specific effect of new energy power fluctuation on the system frequency of power system under high penetration, the power fluctuation characteristics of new energy at different time scales and how they affect the system frequency are analyzed firstly. Then, based on empirical mode decomposition, the wind and solar fluctuation model and the maximum power fluctuation range estimation model are established, and then the primary frequency regulation upward capability model of thermal power unit is established. Finally, based on the above models, the time-domain simulations of power system with different new energy penetration are carried out, and the changes of system primary frequency regulation upward capability, disturbance power margin are analyzed.

In general, this paper answers the question of how the new energy fluctuation affects the system frequency from two aspects: the increased disturbances from new energy minute-level power fluctuations and the reduced primary frequency regulation upward capability in thermal power units due to the decrease of unit load rate affected by new energy. As new energy penetration increases, the system's disturbance power margin decreases, necessitating the use of more diverse primary frequency regulation sources and strategies to ensure system frequency stability.

References

[1] National Energy Administration. The National Energy Administration re leases 2023 statistics on the country's power industry. [EB/OL]. (2024-0

1-26)[2024-01-28].http//www.nea.gov.cn/202401./26/c_1310762246.htm.

[2] P. K. Dhara, Z. H. Rather and C. Phurailatpam, “Estimation of minimum inertia and fast frequency support for renewable energy dominated power systems,”IEEE Transactions on Instrumentation and Measurement, vol. 74, pp. 1-14, 2025, Art no. 9001114.

[3] S. Javaid, M. Kaneko and Y. Tan, “Energy balancing of power system considering periodic behavioral pattern of renewable eenergy sources and demands,” IEEE Access, vol. 12, pp. 70245-70262, 2024.

[4] H.Zhou,L.Ni, T.Xu, “Study on power-frequency dynamic characteristic of power grid”, Power System Technology,2009, 33(16): 58-62.

[5] H. Li, P. Ju, C. Gan, S. You, F. Wu and Y. Liu, “Analytic analysis for dynamic system frequency in power systems under uncertain variability,”IEEE Transactions on Power Systems, 2019, 34(2): 982-993.

[6] Y. Guo, Q.Wang, D. Zhang, D.Yu, J.Yu, “A stochastic-process-based method for assessing frequency regulation ability of power systems with wind power fluctuations,” Journal of Environmental Informatics, 2018, 32(1): 45-54.

[7] Nguyen N, Mitra J, “An analysis of the effects and dependency of wind power penetration on system frequency regulation,” IEEE Transactions on Sustainable Energy, 2016, 7(1): 354-363.

[8] M. Martínez-Barbeito, D. Gomila and P. Colet, “Dynamical model for power grid frequency fluctuations: application to islands with high penetration of wind generation,” IEEE Transactions on Sustainable Energy, vol. 14, no. 3, pp. 1436-1445, July 2023.

[9] L.Wang, J.Liu, F.Qian, “A new modeling approach for the probability density distribution function of wind power fluctuation,”Sustainability, 2019,11(19):1-16.

[10] D. Bao, L. Liu, F. Gao, J. He and Q. Huang, “Matching optimization of wind-solar complementary power generation system based on joint probability distribution,”2024 The 9th International Conference on Power and Renewable Energy (ICPRE), Guangzhou,China, 2024, pp.1748-1752.

[11] H. Wang, B. Zou, “Probabilistic computational model for correlated wind speed, solar irradiation, and load using Bayesian network,” IEEE Access, vol. 8, pp. 51653-51663, 2020.

[12] J.Lin, Y.Sun, P. SΦRENSEN, G.Li, L.Cheng, X.Ni, “Simulation of power fluctuation of wind farms based on frequency domain Part One Model and analysis technique,”Automation of Electric Power Systems, 2011, 35(04): 65-69(in Chinese).

[13] J.Lin, Y.Sun, P. SΦRENSEN, G.Li, L.Cheng, X.Ni, “Simulation of power fluctuation of wind farms based on frequency domain Part Two Transformation algorithm and model simplification,”Automation of Electric Power Systems, 2011, 35(05): 71-76(in Chinese).

[14] J. Wan, K. Yao, E. Peng,Y.Cao,Y.Niu,J.Yu, “Separation characteristics between time domain and frequency domain of wireless power communication signal in wind farm,” Eurasip Journal on Wireless Communications and Networking, 2020,2020(1).

[15] X. Cai, N. Zhang, E. Du, Z. An, N. Wei and C. Kang, “Low inertia power system planning considering frequency quality under high penetration of renewable energy,” IEEE Transactions on Power Systems, vol. 39, no. 2, pp. 4537-4548, March 2024.

[16] M.Li, G.Chen, C .Dong, Z.Laing,W.Wang, G.Fan, “Research on power balance of high proportion renewable energy system,” Power System Technology, 2019, 43(11): 3979-3986.

[17] G.Chen, Y. Dong, Z. Liang, “Analysis and reflection on high-quality development of new energy with Chinese characteristics in energy transition,” Proceedings of the CSEE, 2020, 40(17): 5493-5506.

[18] J. Tong, W. Liu, J. Mao and M. Ying, “Role and development of thermal power units in new power systems,” IEEE Journal of Radio Frequency Identification, vol. 6, pp. 837-841, 2022.

Research and Development Status of Domestic and Foreign Solid Power Controllers and Industrialization Insights

Xu Wang
China Academy of Space Technolog
Beijing, China
wangxu780416@126.com

Huiyao Li
Beijing Space Power Conversion and Control Engineering Research Center
Beijing, China
lhy87104899@163.com

Mi Liu
Beijing Space Power Conversion and Control Engineering Research Center
Beijing, China
liumi0065@163.com

Xing Liu
China Academy of Space Technolog
Beijing, China
lhyroberl@hotmail.com

Bei Zhang
Beijing Spacecrafts Co. Ltd
Beijing, China
2195483@qq.com

***Abstract*—This paper systematically reviews the technological development trajectory of solid-state power controllers (SSPCs), compares and analyzes the technological gap between domestic and foreign levels, and deeply explores the industrialization path. The full text is divided into five major parts: Firstly, it elaborates on the technical principles and classification of SSPCs; Secondly, it analyzes in detail the leading technologies in the United States and Europe and the current domestic development status; Then, it dissects the industrialization bottlenecks from the dimensions of materials, processes, and standards; Subsequently, it proposes targeted development suggestions; Finally, it looks forward to the technological trends and market prospects. The research shows that there are still significant gaps in domestic high-voltage and high-current technology, modular integration, and reliability, and it is urgent to achieve breakthroughs through the application of wide bandgap semiconductor materials and collaborative innovation among industry, academia, and research. This paper aims to provide a systematic reference for the technological upgrade and industrialization of SSPCs in China.**

Keywords—Solid state power distribution; Solid-state power controller; Research and development status; Industrialization

I. INTRODUCTION

With the development of full electrification and multi-electrification of aerospace vehicles, traditional electromechanical circuit breakers can no longer meet the demand for high reliability due to defects such as slow response speed (millisecond level) and short service life. Solid-State Power Controllers (SSPCs) adopt semiconductor devices such as power MOSFETs/IGBTs, integrating switch conversion, overcurrent protection, and status monitoring functions. They possess advantages including microsecond-level response, no arc, and long service life, thus becoming the core component of the new-generation intelligent power distribution system [1]. According to data from Verified Market Reports, the global SSPC market size reached 1.75 billion US dollars in 2022 and is expected to grow to 3.5 billion US dollars by 2030, with a compound annual growth rate (CAGR) of 9.1% [2].

The full electrification development of spacecraft places higher requirements on their power distribution systems. As a new type of power distribution and protection execution component that integrates the switching function of relays and the protection function of circuit breakers, SSPC has many advantages such as integration and intelligence, and is an inevitable development trend of power distribution components for spacecraft in the future. In the aviation field, with the proposal of the All Electric Aircraft (AEA) concept, which replaces traditional mechanical systems with electrical systems, and the continuous increase in the number of electrical equipment, the aircraft power supply system has gradually developed from low voltage to high voltage, which puts forward higher requirements for the quality of aviation power supply systems.

China's "14th Five-Year Plan" clearly states the need to make breakthroughs in the "chokepoint" technologies of high-end power electronic devices. As a key component of the power distribution systems for spacecraft and aviation equipment, the independent and controllable development of SSPC is of great significance. However, the domestic SSPC technology started relatively late, and there is still an obvious gap in terms of power level, reliability, and standardization compared with the advanced international level. By systematically analyzing the current status of domestic and foreign technology development, in-depth studying the industrialization bottlenecks, and proposing a development path in line with China's national conditions, this paper aims to provide references for scientific research institutions and enterprises, and promote the leapfrog development of China's SSPC technology.

979-8-3315-5472-9/25/$31.00 ©2025 IEEE

II. SSPC Technology Principle and Classification

A. Basic Working Principle and Structural Composition

A solid-state power controller is an intelligent switching device based on power semiconductor devices, whose core function is to realize rapid on-off and protection of circuits. The typical SSPC structure, as shown in Figure 1, mainly consists of three parts: power circuit, control circuit, and communication interface. Serving as the energy transmission channel, the power circuit includes power switching devices, current detection components, and load circuits; the control circuit is responsible for signal processing, implementation of protection algorithms, and status monitoring; the communication interface enables information interaction with the upper-level control system.

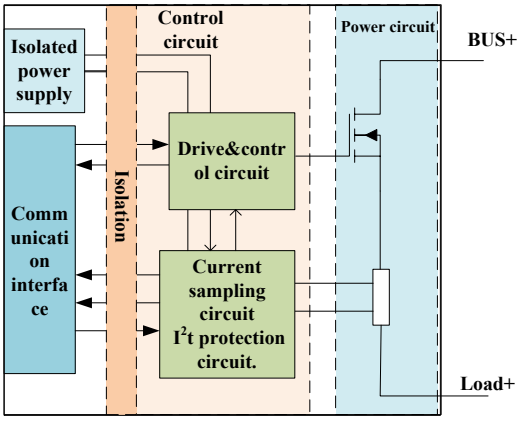


Fig. 1. Typical SSPC structure

The working principle of SSPC can be summarized as follows: By controlling the conduction and cutoff of power switch devices, it achieves intelligent management of the load circuit. When the control circuit receives an on command, the drive circuit amplifies the control signal to a voltage/current level sufficient to drive the power switch, causing the switch device to conduct and the load to be energized and operate. During operation, the current detection circuit continuously monitors the load current. Once an overcurrent or short circuit fault is detected, the control circuit quickly cuts off the power switch based on the preset protection characteristics (such as I^2t inverse-time curve) to achieve the protection function. Compared with traditional electromechanical circuit breakers, the response time of SSPC can be shortened from milliseconds to microseconds, significantly enhancing system safety.

In terms of key technological innovations, modern SSPC has developed several advanced functions: First, digital intelligent protection, which realizes programmable protection curves through microprocessors and has a "thermal memory" function that can accumulate the thermal accumulation effect of the load; second, status monitoring and diagnosis, which collects parameters such as voltage, current, and temperature in real time and uploads them to the central controller via CAN/1553B and other buses; third, adaptive control, which automatically adjusts protection parameters based on load characteristics to optimize system performance. These technological advancements have transformed SSPC from a simple switch device into an important node in the intelligent power distribution network.

B. Technical Classification and Performance Indicators

According to different application scenarios and technical characteristics, SSPC can be classified from multiple dimensions. By power type, it can be divided into two major categories: DC SSPC and AC SSPC. DC SSPC is mainly applied in 28V/270V DC power distribution systems, such as the 30-channel SSPC output unit developed by Aviation Factory 165, with a single-channel current capacity of up to 20A and a total control current of 150A. The technology of this type of controller is relatively mature, with the key challenge being to solve the conduction loss and thermal management issues under high current conditions. AC SSPC, on the other hand, needs to adapt to 115V/400Hz or 220V/50Hz AC power grids. Its technical difficulty lies in achieving zero-voltage turn-on and zero-current turn-off to reduce switching losses and electromagnetic interference. AC SSPC can be further divided into single-phase and three-phase types, with three-phase controllers accounting for approximately 70% of the market share in 2023.

By integration level, SSPC can be classified into two technical routes: modular (MSSPC) and integrated (ISSPC). The modular design, such as the 32-channel SSPC of the RP-2032 series from DDC Company in the United States, adopts a field-replaceable module (LRM) design, which is convenient for maintenance and upgrade [3]. The integrated design integrates control algorithms and power devices on a single chip, such as the chip-based intelligent SSPC based on ASIC from Beijing Satellite Manufacturing Factory Co., Ltd., which can significantly reduce volume and improve reliability, representing the future development trend.

In terms of performance indicators, the key technical parameters for evaluating SSPC include: current rating, power density, operating temperature range, mean time between failures, and electromagnetic compatibility. In addition, conversion efficiency, response speed, and protection accuracy are also important performance indicators.

TABLE I. Comparison of Main Types and Performance of SSPC

Classification	Power types	Parameters	Applications	Technical challenges
Power types	SSPC of DC types	28V/270V, 10-40A	Spacecraft secondary distribution; military vehicle	High current thermal management, low on resistance
	SSPC of AC types	115V/400Hz, 8-15A	Civil aircraft, industrial equipment	ZVS, Harmonic suppression
Integration	Modular SSPC	multi-channel (16-32), LRM	Aircraft PDUs; ship system	Current equalization and fault isolation
	Integrated SSPC	Single-chip solution (<50mm^3)	Microsatellite; UAV	Isolation; heat dissipation design

With the advancement of wide bandgap semiconductor technology, a new generation of solid-state power converters (SSPCs) based on SiC/GaN devices is emerging [3]. These materials have advantages such as large bandgap width, high thermal conductivity, and fast electron saturation drift velocity,

which can significantly increase the switching frequency and operating temperature of SSPCs, and enhance the power density by 3 to 5 times. NASA in the United States has developed a SiC-based SSPC prototype with an efficiency of 99.5%, capable of supporting a high-voltage scenario of 1kV/100A, and plans to use it in the Artemis lunar gateway program [4].

III. Overseas SSPC Technology Status

A. United States: Technological Leadership and Military Application Dominance

The United States has maintained a leading position in SSPC technology for a long time, and its development process can be traced back to the 1960s. At that time, the United States first tried to apply SSPC to the aircraft power distribution system, and by the end of the 1960s, significant progress had been made, and the feasibility of SSPC had been proved by controlling individual loads on aircraft. After more than half a century of development, the United States has formed a complete SSPC technology system and industry chain, and its products are widely used in military and aerospace fields.

Data Device Corporation (DDC) of the United States is a benchmark enterprise in the SSPC industry. Since it started designing and manufacturing SSPCs in 1988, it has launched seven generations of products. The seventh-generation SSPC launched by the company in 2013 adopts an advanced modular design. It can be configured into lightweight and compact aviation power distribution and management units (PDUs) and standard field-replaceable modules (LRMs).

Its representative product, the RP - 2032151XD0 32-channel SSPC, weighs only 3 pounds (approximately 1.36 kg). It can provide a continuous current output of 120A under 28V DC. This product supports real-time data status reporting and computer control, thus truly realizing intelligent circuit protection.

What is particularly notable is that DDC's multi-channel SSPC boards can distribute and control up to 300A of current for four independent subsystems. The rated current of each system can be programmed up to 75A. This power level ranks among the leading positions in the industry.

Leach International is another SSPC technology leader, having released the EPM-109, EPM-110, and EPM-111 series of multi-channel programmable SSPCs as early as 2006. These products integrate microcontroller and power FET technology to achieve lossless switching between all types of loads, while also having overload and short-circuit protection functions. It is worth mentioning that Leach's SSPC product has a built-in in test (BIT) function, which can automatically verify key functions during startup and operation, greatly improving the reliability and maintainability of the system. The implementation of this self diagnostic function makes SSPC no longer a simple protective device, but an intelligent device with state monitoring and fault prediction capabilities.

In terms of military applications, the United States has widely applied SSPC technology to advanced fighter jets. The fifth generation fighter jets such as F-22 and F-35 both use SSPC technology to achieve intelligent management of electrical and electronic equipment. Among them, the F-35's power distribution system uses hundreds of SSPC modules [5], which achieve fully digital control through a dual redundancy data bus, greatly improving the system's reliability and battlefield survivability. The fast response characteristic (microsecond level) of SSPC is particularly critical for improving the survivability of fighter jets in complex electromagnetic environments, and can effectively prevent chain reactions caused by electrical faults.

NASA's breakthroughs in space applications are also worth paying attention to. The SiC based SSPC developed by the Goddard Space Flight Center has an efficiency of up to 99.5% and supports high voltage and high current working conditions of 1kV/100A. It is planned to be used in the Artemis lunar gateway program. Compared with traditional Si based devices, SiC SSPC can operate stably in higher temperatures (above 200 ℃) and more harsh radiation environments, making it particularly suitable for deep space exploration tasks. NASA has also developed ultra black materials based on carbon nanotubes for SSPC heat dissipation, with a solar absorption ratio of ⩾ 99.6% in the 400-2500nm wavelength range, significantly improving thermal radiation efficiency.

B. Europe: Intelligence and Aviation Airworthiness Certification

The development of SSPC technology in Europe presents distinct intelligent features and strict airworthiness certification requirements. Airbus, Safran and other aviation giants have made significant achievements in the research and application of SSPC technology, and their products are widely used in civil aircraft and military platforms.

Airbus has extensively applied SSPC technology on aircraft models such as A380 and A350, achieving a revolutionary upgrade of the power distribution system. Among them, A380 is the world's first civilian aircraft widely using SSPC technology, and its power distribution system adopts a distributed architecture, achieving precise control of various loads through hundreds of SSPC modules. The latest SSPC product developed by Airbus adopts 3D packaging technology, which reduces the volume by 40% compared to traditional designs and significantly improves power density. These compact SSPC modules are integrated into the intelligent power distribution system of A350, communicating with the central controller through a digital bus to achieve optimized configuration of the entire machine's power resources.

As a leading European aviation electronics company, Safran Group has developed a three-phase SSPC system with AI fault prediction capabilities for the A380. The system analyzes historical operational data through machine learning algorithms and can predict potential faults dozens of hours in advance, greatly improving flight safety. In terms of certification, Safran's SSPC products strictly follow the EASA DO-160G standard and have passed a full set of environmental adaptability tests including vibration, humidity, salt spray, etc., meeting the stringent reliability requirements of civil aviation. It is worth mentioning that the SSPC developed by the company supports hot swapping function, which can replace faulty modules without interrupting the system power supply, greatly improving the operational efficiency of the aircraft.

Europe is also in a leading position in standardization construction. EUROCAE (European Civil Aviation Equipment Organization) has developed the ED-14 series standards, which provide clear requirements for the environmental adaptability, electromagnetic compatibility, and software reliability of SSPCs. These standards have become important references for the global development of aviation electronic equipment. In terms of military civilian integration, the "More Electric Aircraft" project funded by the European Defense Agency (EDA) transforms SSPC technology applied in fighter jets into the civilian field, reducing research and development costs and accelerating technological iteration.

It is worth mentioning that European companies have unique advantages in thermal management technology. Faced with the heat dissipation challenge of SSPC at high power density, European manufacturers have developed various innovative solutions, such as using SSPC modules with direct liquid cooling, which can reduce thermal resistance by more than 50%; Thermal buffering design based on phase change materials can cope with thermal shock caused by transient high currents; There is also a heat dissipation structure designed using topology optimization methods, which improves heat dissipation efficiency by 30% under the same volume. These technological advancements enable European SSPC products to maintain stable performance even in high temperature environments, making them particularly suitable for the aviation market in hot regions such as the Middle East.

TABLE II. MAIN FOREIGN SSPC MANUFACTURERS AND PRODUCT CHARACTERISTICS

Manufacturer/Institution	Product	Features	Applications	Certification
Data Device Corporation	RP-2032 series	32 channels, 120A, LRM	F-35、SpaceX spacecraft	MIL-STD-704F
Leach International Corporation	EPM series	BIT, programmable protection parameters	C-130J	DO-160G
SAFRAN	Three-phase intelligent SSPCs	AI fault prediction, hot plugging	A380	ED-14/DO-160G
NASA	SiC-based SSPCs	1kV/100A, Efficiency:99.5%;	Artemis	NASA-STD-4003

C. Summary of Technical Features and Development Trends

Through comprehensive analysis of advanced SSPC technology abroad, the following key features can be summarized: firstly, high power density. The power to weight ratio of DDC products in the United States has reached 40A/kg (28VDC), far exceeding traditional electromechanical circuit breakers; The second is intelligent diagnosis, with built-in BIT function that enables fault location accuracy to exceed 95%, significantly reducing maintenance costs; The third is environmental adaptability. The product meets the working temperature range of -55 ℃~125 ℃ and MIL-STD-461G electromagnetic compatibility requirements, making it suitable for extreme environments.

There are three major trends in the development of SSPC technology abroad in the future: firstly, the application of wide bandgap semiconductors is accelerating, and SiC and GaN devices will gradually replace traditional Si based power switches, enabling the operating voltage to exceed 1kV and the switching frequency to be raised to the MHz level; Secondly, the introduction of digital twin technology enables performance prediction and health management by constructing virtual images of SSPC; Finally, there is multifunctional integration, which integrates functions such as energy metering, arc detection, and insulation monitoring into a single SSPC module to improve system integration.

In terms of market layout, according to Verified Market Reports, North America currently holds the largest share of the global SSPC market (about 40%), but the Asia Pacific region is growing at the fastest rate, mainly due to the rapid development of the aviation industry in emerging economies such as China and India. In terms of product types, three-phase controllers dominate (about 70% share), but the adoption rate of single-phase controllers in small and regional aircraft models is rapidly increasing. This market differentiation has prompted international manufacturers to increase their efforts in localized production, such as the regional center established by TransDigm Group in Singapore, which specializes in serving the Asia Pacific market.

IV. DEVELOPMENT PROGRESS OF DOMESTIC SSPC

A. Technical Development History and Current Situation

China's research on SSPC relatively late, in the 1990s, but has made significant progress in recent years driven by military demand. Domestic research and development efforts are mainly concentrated in the researchitutes affiliated with the aviation industry and a few high-tech enterprises, which have formed a certain technological accumulation and product series [7-11]. Beijing Spacecrafts Co. Ltd, Aviation 165 Factory, Aviation 105 Factory, 791 Factory and other military units are at the forefront of domestic SSPC engineering, while such as Northwest Polytechnic University, Nanjing University of Aeronautics and Astronautics, and Beijing University of Aeronautics and Astronautics have made important in theoretical research and new technology exploration. Shanghai Zunrui Electronics is a leading supplier of SSPC in the domestic civil field, established by Swedish Magic Electronics the form of technology shareholding. The company's developed ZDSPC, ZASPC series of SSPC modules are the first of their kind in China, integrating solid-state power control technology and computer technology. Its representative product, the ZDSPC28M-40U/YW type DC SSPC, has working voltage of 8 to 80V DC, a maximum rated current of 40A, and a programmable rated operating current of 12 to 4A. It supports multiple control buses such as SCI, SPI, I^2C, and the I^2t protection curve is programmable. It is widely used in Aero's, defense, and industrial automation fields. In terms of AC SSPC, the ZASPC115M-8U/YW type product supports a voltage range 50 to 180V AC, with a maximum working current of 8A, filling the domestic blank.

The intelligent distribution box series products developed by Aviation 165 Factory represent the highest level of military grade SSPC in China. This product includes 30 SSPC output

units, with a single output current adjustable from 1-20A, a maximum control current of 150A, a total power consumption of about 42W, and a weight of 3.2kg. The SSPC unit supports multiple 28V/110V/270Vdc and 115Vac/400Hz AC load control, and communicates with the main control system using RS-485, RS-422, CAN, or 1553B bus. It has real-time feedback of load status, historical record storage, and self-detection capabilities, and has been successfully applied to various military aircraft and special vehicles. It is worth mentioning that the environmental adaptability of this product meets the strict requirements for airborne electronic equipment in GJB 150 "Environmental Test Methods for Military Equipment Laboratories", and its electromagnetic compatibility complies with GJB 151A standard, reflecting the high reliability design level of domestic military electronic equipment.

The development of chip based SSPC series products by Beijing Spacecrafts Co. Ltd represents the highest level of radiation resistant aerospace grade SSPC in the domestic aerospace field. This product adopts an integrated circuit design approach, integrating traditional separated device design circuits into chips, and integrating SPI communication interfaces on the chip. It has intelligent power distribution that can be configured and managed in orbit. At the same time, it has made a technological leap from integrated power distribution to distributed power distribution in current aerospace solid-state power distribution.

Although there is still a gap compared to top foreign products, it can already meet the power distribution needs of most domestic aircraft.

B. Existing Technological Gap

Compared with the international advanced level, there is still a significant generation gap in SSPC in China:

1. Insufficient power level: The maximum current of domestically produced DC SSPC is not enough, and there is still a significant gap compared to DDC products from the United States (up to 300A), making it difficult to meet the demand for high-power aviation equipment.

2. Weak environmental adaptability: The working temperature range is generally -40~70 ℃ (NASA SiC based SSPC reaches -55~200 ℃), and the radiation resistance and electromagnetic compatibility have not passed MIL-STD-461G certification.

3. Low level of intelligence: Lack of advanced functions such as AI fault prediction and digital twin operation and maintenance, with a built-in diagnostic (BIT) accuracy rate of less than 80% (>95% in the United States).

4. Core component dependence: 80% of high-performance SiC/GaN power devices rely on foreign companies such as SciClone and ROHM, and the yield rate of domestically produced 6-inch SiC substrates is less than 50% [13].

V. INDUSTRIALIZATION BOTTLENECKS AND COUNTERMEASURES

A. Analysis of Main Bottlenecks

1. Material and process short board: the technology of preparing wide band gap semiconductor wafers is backward, the defect density of GaN-onSi epitaxy is high; the yield of multi-chip assembly (MCA) is only 60% (international >85%), and the vacuum sinter process stability is insufficient.

2. Thermal management technology lag: high-power SSPC heat dissipation relies on traditional DBC ceramic substrates (96% Al_{23}), with a thermal conductivity of only 24 W/mK (SiC substrate up to 270 W/mK), resulting in an increased of device failure under high-temperature conditions.

3. Lack of standard system: there is no equivalent national standard to MIL-STD-704F, a of third-party testing platforms, and poor product interchangeability.

4. Weak application ecology: the commercial aerospace industry still tends to use electromechanical circuit break, SSPC costs 3 times more than traditional solutions, and user acceptance is low.

B. Development Suggestions

1) Autonomy of Materials and Processes

Breakthrough in Wide Band-Gap Semiconductors: Establish a national special fund to focus on 6-inch SiC substrate mass production technology (targeting a defect density <100 cm^{-2}) and GaN-on-Si epitaxy process; promote the use of AlN ceramic substrates (thermal conductivity 319 W/mK) to replace traditional alumina. Upgrade to Smart Manufacturing: Develop AI-driven multi-chip placement systems, optimize solder flow control through machine learning, and increase MCA yield rate to over 80%; build power module demonstration lines to achieve self-adaptive control of sintering temperature curves.

2) Standard System and Collaborative Innovation

National standard formulation: Referencing the EUROCAE ED-14 series of standards, the General Specification for Spacecraft SSPC" has been issued, mandating a temperature range of -55~125℃ and a MTBF of 100000 hours.

Industry-Academia-Research Alliance Construction: The "Wide Bandgap Semiconductor Power Electronics Industry Alliance" has been established.ating with the 55th Research Institute of the China Electronics Science (GaN devices), the Ningbo Institute of Materials of the Chinese Academy of Sciences (Ther interface materials), and Aviation Factory 165 (System integration), a testing and certification platform has been jointly built.

3) Ecological cultivation of applications

Military-civilian integration demonstration: Provide a 30% purchase subsidy for commercial satellites electric aircraft and other fields, and promote the verification and application of SSPC products in C919 domestic airliners.

Functional integration innovation: Develop "SSPC plus" solutions, such as integrated intelligent power management technology, to achieve millisecond-level power outage protection, and expand to industrial energy storage fields.

VI. Conclusions and Prospects

As the core device of intelligent power distribution, the industrialization level of SSPC directly affects the autonomous controllability of country's aerospace equipment. Based on the comparison of domestic and foreign technology, the following development paths are proposed:

A. Short-term Goals (205-2030)

Materials localization: Achieve mass production of 6-inch SiC substrates, and increase the self-sufficiency rate of GaN to 50%, reducing costs by 40%. Product upgrade: Develop 300A-level DC SSPCs and 15A ACSPCs, expand the operating temperature to -55~125℃, and ensure MTBF≥80,000 hours.

B. Long-term Trends

1. Megawatt-level power integration: Develop SiC-based SSPC modules supporting 1k/300A, combined with 3D packaging technology, with a power density breakthrough of 50A/kg, meeting the needs of all-electric aircraft.

2. Smart operation and maintenance system: Based on digital twin technology, build a SSPC life cycle health management platform, achieving a fault prediction accuracy rate of >90%.

3. Cross-border application expansion: Enter trillion-level markets such as new energy vehicle charging piles (fast charging modules) and smart grids (DC circuit breakers), a "space technology-civilian market" two-way transformation ecology.

VII. Conclusion

Only through the synergistic breakthrough of materials, processes, and standards can the overseas monopoly be broken, and the SSPC industry chain achieve an autonomous leap.

References

[1] Man Yi, Research on open primary and secondary power distribution test system technology for civil aircraft power system [J]. Aeronautical Precision Manufacturing, 2024, 60(3).

[2] Verified Market Reports.Global Aircraft Solid-State Power Controller(SSPC)Market Report[R].2025.

[3] Benzies Consulting.2025 China Aircraft Solid-State Power Controller Market Report[R].2024.

[4] Han Xiangxi.Research on Power Electronic Equipment Based on AC Solid-State Power Controller[J].Power System Automation,2024,48(3):112-118.

[5] Singh Y V,Baronian A.Power semiconductor devices for solid state power controller[C].ITEC 2020:741-746.

[6] Adams A, Nicol F, Mchugh S, et al. Vantablack properties in commercial thermal infrared imaging systems[C]. SPIE Defense + Commercial Sensing, 2019:110010W.

[7] Liang Wei, Zhao Jiandong. Application of solid-state power controller technology in aircraft power distribution system [C]. 17th Chinese Aviation Instrument and Control Technology Conference, 2020:156-162.

[8] Aviation Industry Corporation of China. Manual of Aircraft Power Supply System [M]. Beijing: Aviation Industry Press, 2018.MIL-STD-704F. Aircraft Electric Power Characteristics [S]. 200.

[9] MIL-STD-704F.Aircraft Electric Power Characteristics[S].2004.

[10] DO-160G.Environmental Conditions and Test Procedures for Airborne Equipment[S].2010.

[11] Standardization Administration of China.GB/T 34577-2017 General Specification for Aerospace Solid-state Power Controllers[S].2017.

[12] Li Huiyao.Research on Multi-functional Self-matching Type Solid-Power Control Technology[C].2022 China Aerospace Congress,2022.

[13] Wang Jianjun, Zhang Hongke Research Progress of Wide Bandgap Semiconductor Power Devices [J]. Semiconductor Technology, 2022, 47(8): 601612.

Virtual Inertial Response and Frequency Regulation Control Method for Combined Systems of Renewable Energy and Hybrid Energy Storage

Wenxin Guo
Power Dispatching and Control Center,
Guangdong Power Grid Co., Ltd..
Guangdong, China
zzhiquan@126.com

Ruifeng Zhao
Power Dispatching and Control Center,
Guangdong Power Grid Co., Ltd..
Guangdong, China

Yumin Li
NARI Group Nanjing Control System Co., Ltd.
Nanjing, China
1156034141@qq.com

Jiangang Lu
Power Dispatching and Control Center,
Guangdong Power Grid Co., Ltd..
Guangdong, China

Huijuan Tan
Power Dispatching and Control Center,
Guangdong Power Grid Co., Ltd..
Guangdong, China

Shiming Li
Power Dispatching and Control Center,
Guangdong Power Grid Co., Ltd.
Guangdong, China

Abstract*—As the penetration of renewable energy continues to rise and conventional synchronous generators are progressively retired, the decline in system inertia and the shortage of primary frequency-regulation capability have become increasingly prominent. Renewable-energy-driven hydrogen-production systems, whose electrolyzes feature fast and controllable electrochemical processes, offer a promising avenue for providing virtual inertia support and ancillary frequency regulation. To address the transient non-linearity and multi-physics coupling characteristics of electrolyzers, this paper proposes a virtual-inertia response and frequency-regulation control method for renewable-energy-based hydrogen-production systems that explicitly accounts for electrolyzer dynamic characteristics. First, a high-fidelity electrolyzer–hydrogen-production model is developed on the basis of electrochemical kinetics, thermodynamic equilibrium, and gas–liquid mass-transfer coupling, furnishing a rigorous platform for control-strategy design. Second, within a virtual synchronous generator (VSG) framework, a hierarchical coordinated-control scheme is implemented: a dynamic-inertia compensation loop collaborates with an adaptive power–frequency (P–f) regulation module to achieve rapid, coordinated virtual-inertia support and primary-frequency response. Third, to mitigate power fluctuations caused by electrolyzer operating constraints, an energy-conservation-based dynamic-matching mechanism is formulated between hydrogen-production capacity and grid frequency-regulation demand, thereby ensuring safe and economic system operation. Finally, time-domain simulations on a modified IEEE 30-bus test system demonstrate that the proposed method significantly enhances key frequency metrics—including maximum deviation and settling time—while surpassing benchmark strategies in both hydrogen-production efficiency and regulation economics. The results provide effective technical support for boosting grid inertia, improving frequency stability, and enabling high-efficiency green-hydrogen utilization under high renewable-energy penetration.

***Keywords*—Renewable-energy-based hydrogen production system, ancillary frequency regulation, electrolyzer, virtual synchronous generator (VSG), inertia support**

I. INTRODUCTION

With the ever-increasing penetration of renewable generation and the progressive retirement of conventional synchronous machines, power systems are confronted with the dual challenge of reduced inertial support and inadequate primary-frequency regulation capability[1]. Renewable units interfaced through power electronic converters (power electronic interfaces, PEIs) possess no rotating mass, so the system's ability to withstand frequency disturbances deteriorates markedly, meanwhile, their highly volatile output and the sluggish response of legacy generators make it difficult to promptly suppress frequency excursions[2]. A renewable-energy-based hydrogen-production system converts fluctuating electrical power into hydrogen via water electrolysis, enabling energy time-shifting while simultaneously offering virtual-inertia support and storage functionality. Owing to its bidirectional electricity–hydrogen conversion mechanism, a hydrogen energy storage system (HESS) can provide multi-timescale services such as virtual inertia response, primary frequency regulation (PFR) and automatic generation control (AGC); the electrolyzer load is flexibly adjustable, acting as a "local load" that smooths renewable-power output, and—coupled with high-pressure vessels or salt-cavern storage—offers cross-timescale energy buffering to deepen operating reserves[3].

Despite this potential, frequency-support studies on renewable hydrogen systems are still nascent, hampered by three critical bottlenecks: (i) Insufficient electrolyzer-model fidelity—most existing models neglect the polarization effects and thermo-mass coupling of proton-exchange-membrane (PEM) stacks, and inadequately capture the dynamic response of alkaline (ALK) electrolyzers, leading to distorted assessments of regulation capability[4–6]; (ii) Lack of systematic modelling of PEI–stack dynamic interactions—conventional DC–DC–AC

Science and Technology Project of China Southern Power Grid Company (036000KC23110012(GDKJXM20231196))

979-8-3315-5472-9/25/$31.00 ©2025 IEEE

topology models cannot simultaneously represent the bidirectional coupling between converter controls and electrochemical dynamics, thereby degrading frequency-control accuracy[7–8]; and (iii) Synchronisation strategies unable to deliver virtual inertia—phase-locked-loop (PLL) schemes cannot emulate synchronous-machine dynamics, while the virtual synchronous machine (VSM) concept has yet to be adapted to hydrogen-production scenarios[9-10].

To address these gaps, this paper proposes a virtual-inertia response and frequency-regulation control method for renewable hydrogen-production systems that explicitly considers electrolyzer dynamic characteristics. First, a high-fidelity electrolyzer model is developed by integrating electrochemical kinetics, thermodynamic equilibrium and multi-physics coupling, accurately characterizing the transient behavior of PEM and ALK technologies. Second, a VSM-based hierarchical coordinated-control scheme is devised: a virtual-inertia compensation loop and an adaptive droop-frequency module are embedded in the PEI to achieve coordinated virtual-inertia support, PFR and AGC. Third, a hydrogen production–frequency control auxiliary service (HP-FCAS) mechanism is introduced; an energy-conservation-based dynamic-matching model aligns hydrogen-production capacity with grid-regulation demand, preventing conflicts between hydrogen production and frequency response. Finally, multi-scenario time-domain simulations on a modified IEEE 30-bus system demonstrate that the proposed method markedly reduces the rate of change of frequency (RoCoF), shortens frequency-recovery time, and offers superior regulation economics and engineering feasibility.

II. Dynamic Characteristic Modeling of Renewable-Energy-Based Hydrogen Production Systems

The overall architecture—comprising renewable generation (offshore wind, PV, etc.), an electrolyzer stack, power-electronic interface, hydrogen management unit, and a virtual-inertia/primary-frequency control loop—exhibits tightly coupled electro-chemical-thermal multi-physics and multi-timescale behavior. The electrolyzer stack is represented by three coordinated sub-models: (i) a hydrogen-production module that converts the stack current i into a real-time hydrogen mass-flow $\dot{m}_{H_2}$ delivered to a buffer tank; (ii) a thermal-management module that captures the interaction between stack temperature T and ambient temperature T_a, thereby reflecting thermal constraints on efficiency and safe operation; and (iii) an electrical module that outputs the stack terminal voltage V_{stack} and, together with an interface inductor L and back-to-back converters (DC–DC boost and DC–AC VSC), governs the transient response. A virtual-inertia controller embedded at the DC link exploits the electrolyzer's permissible power headroom to deliver "electrolyzer inertia": upon a grid-frequency deviation Δf, the controller modulates i according to $\Delta\dot{f}$ and DC-link power reserve, furnishing sub-second inertial support and seamless transition to droop-based primary control over subsequent seconds. The hydrogen buffer absorbs $\dot{m}_{H_2}$ and supplies a downstream demand flow $\dot{m}_{\text{load}}$ smoothing supply–demand imbalances on minute-to-hour horizons so that hydrogen production objectives remain compatible with grid-support duties. Through this integrated virtual-inertia and frequency-regulation chain, the renewable-energy hydrogen production system not only sustains high-efficiency operation but also injects equivalent inertia and primary frequency power during disturbances, offering a novel flexibility resource for high-renewables power systems. Fig.1 is a schematic diagram of the Renewable-Energy-Based Hydrogen Production Systems.

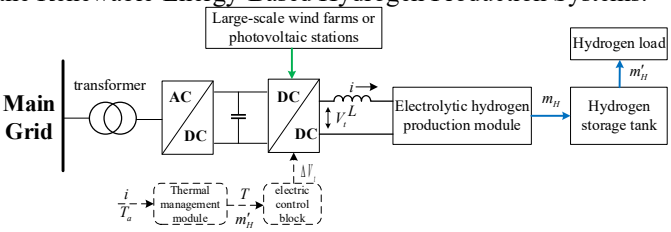


Fig. 1. Schematic diagram of Renewable-Energy-Based Hydrogen Production Systems

A. Electrolyzer Stack Model

This study first develops an electrical equivalent model for an alkaline electrolyzer stack and, building on that framework, extends it to a PEM (proton-exchange-membrane) stack. The analysis adopts a ramp-response perspective. For the alkaline stack, the electrical sub-model shows that—whether subjected to ramp-up or ramp-down tests—its step response exhibits two marked dynamic attributes:1) Over-damped behavior, implying a prolonged settling time before steady-state is reached; 2) A pronounced initial dead-time (transport delay). From control-systems theory, the stack current i can therefore be represented by a second-order transfer function with respect to the input voltage V_t, whose two real poles reside in the left half-plane of the complex s-domain.

$$G_A(s) = \frac{p_1 p_2}{(s - p_1)(s - p_2)} \tag{1}$$

In eq. (1), p_1 and p_2 are the poles of the stack-transfer function and satisfy $|p_1| \succ |p_2|$. Let I(s) and $V_t(s)$ denote the Laplace transforms of the stack current and terminal voltage, respectively, such that the original transfer function is $G_A(s)$. Because $G_A(s)$ possesses a relative degree of two—that is, the denominator polynomial is two orders higher than the numerator—the model cannot be realised directly as a passive R. To achieve physical implement ability while preserving the essential dynamics, a pair of appropriately placed zeros is introduced to construct a compensated transfer function $G_A^{\text{mod}}(s)$ with a relative degree of one. This modified form closely approximates the original response yet admits straightforward synthesis as an equivalent electric circuit:

$$G_A^{\text{mod}}(s) = \frac{p_1 p_2 (s - z)}{s^2 - (p_1 + p_2)s + p_1 p_2} \tag{2}$$

In eq. (2), Here, z<0 designates the introduced zero; it is positioned sufficiently deep in the left-half s-plane—i.e., far from the imaginary axis—to suppress any overshoot in the resulting step response.

$$G_A^{\mathrm{mod}}(s)=\left(\frac{1}{L_s}\right)\frac{1}{s+\dfrac{R_i}{L_s}+\dfrac{1}{L_sC_os+L_s/R_m}} \tag{3}$$

The electrical sub-model of the PEM stack is derived using the same methodology—namely, by fitting a circuit to the step response of the stack current. The resulting topology, shown in Fig. 2, indicates that the series inductance L_s can be neglected because the pole introduced by L_s lies far to the left of the imaginary axis, a consequence of the stack's inherently short rise and settling times. Consequently, Fig. 2 furnishes a unified circuit representation that is valid for both alkaline and PEM electrolyzer stacks.

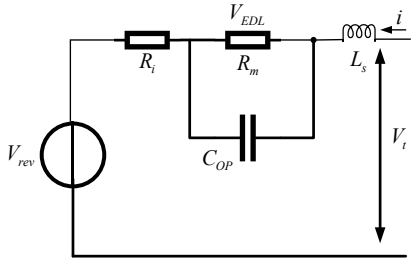


Fig. 2. General Electric sub-model of electrolytic reactor

Although the circuit in Fig. 2 is obtained from a current-step experiment, every parameter maps to a definite physical process in the hydrogen-storage system. In circuit theory, the response delay is governed mainly by the capacitance and the inductance. Both elements are small in a PEM stack, so the current rises faster; this feature favors virtual-inertia release and primary-frequency regulation. The capacitor represents the double-layer effect. The effect arises from non-uniform charge distribution at the electrode–electrolyte interface, producing an electron-transfer barrier and a dynamic lag. The double-layer effect is negligible in PEM technology but pronounced in alkaline stacks. The mass-transfer resistance R_m captures dissipative losses during ionic transport. The internal resistance R_i equals the sum of the ohmic resistance of the stack material R_{ms} and the concentration-polarization resistance R_{CO} ; thus $R_i=R_{ms}+R_{CO}$. The term R_{CO} is associated with oxygen and hydrogen evolution on the electrode surface and introduces a nonlinear stack voltage–current characteristic.

$$R_{CO}(i)=\beta_1 In(\frac{\beta_2}{A}i+1) \tag{4}$$

Here, β_1 and β_2 are constant coefficients, and A represents the electrode area. Finally, the reversal voltage V_{rev}—the minimum stack voltage required for current to flow—can be obtained from the stack's polarization curve.

B. Stack H_2 Production and Downstream H_2 Buffer Model

The relationship between the battery stack current and the H2 production rate can be expressed as:

$$m_H(t)=\eta_F(i)\frac{N_s i(t)}{z_eF},\quad \eta_F(i)=\alpha_1\exp\left(\frac{A\alpha_2}{i}+\frac{A^2\alpha_3}{i^2}\right) \tag{5}$$

The hydrogen-production rate depends on the stack current iii and on the Faradaic efficiency $\eta_F(i)$. The term $\eta_F(i)$ describes current efficiency. It is strongly nonlinear and is parameterized by three empirical constants α_1, α_2, α_3; α_1 reflects the hydrogen purity. Fig.3 confirms that the efficiency falls at high current density, highlighting the stack-efficiency–current non-linearity. Charge conservation implies that the hydrogen generation flow $\dot{m}_{H_2}$ is a direct function of iii. The hydrogen-storage system delivers frequency support by adjusting the stack current—current up-ramping for over-frequency events and down-ramping for under-frequency events. Any such action changes $\dot{m}_{H_2}$. Therefore, the hydrogen inventory in the buffer tank, V_H, must always remain within safe limits:

$$V_H^{\min}\le V_H(t)\le V_H^{\max} \tag{6}$$

Operating limits of the hydrogen buffer critically shape the frequency-support capability of the HE system. $V_H^{\min}$ is the minimum inventory that guarantees stable operation of downstream hydrogen processes, such as refuelling stations or power-to-gas (P2G) units. $V_H^{\max}$ is the maximum storage capacity of the buffer. If a disturbance occurs at $t=t_0$, the hydrogen content in the buffer, VH(t)V_H(t)VH(t), is given by (7):

$$\begin{aligned}&\frac{z_eF(V_H^{\min}-V^0-m'_H(t-t_0))}{\eta_F(i)N_s}\le\int_{t_0}^{t_s}i(t)dt\\&\le\frac{z_eF(V_H^{\max}-V^0-m'_H(t_s-t_0))}{\eta_F(i)N_s}\end{aligned} \tag{7}$$

The upper limit of stack current is constrained by the remaining buffer capacity. If this limit is exceeded, the HE must be temporarily shut down, limiting its downward frequency regulation capability. The lower limit is restricted by the minimum hydrogen storage level. Violation of this limit prevents the HE from providing upward frequency support. Thus, current constraints must be explicitly incorporated into the stack control design. This ensures the sustainability and safety of frequency support.

III. INERTIA RESPONSE AND FREQUENCY CONTROL METHOD

Hydrogen energy storage connects to the grid via back-to-back DC-DC converters. The electrolyzer-side converter regulates the duty cycle ($d\in[0,1]$) to stabilize the HE frequency and enable frequency support. The HE is synchronized with the external grid using a phase-locked loop (PLL). The PLL estimates the angle δ at the HE terminal and generates a frequency deviation signal (Δf). The HE's input control signals include the stack current (i), voltage (Vt), DC-link voltage (E_{DC}), AC-side voltage (u), current (I), and frequency deviation (Δf). Fig.3 illustrates the block diagram of a grid-following hydrogen energy storage frequency control system, incorporating hydrogen production dynamics and nonlinear interactions.

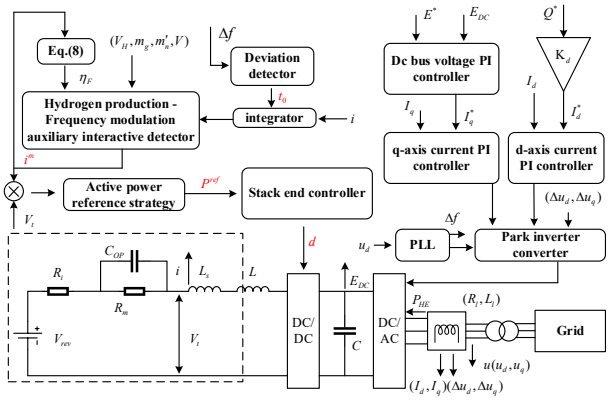


Fig. 3. Block diagram of frequency control of grid following type hydrogen energy storage considering hydrogen production and its nonlinear interaction

This study proposes a control strategy for electrolyzer-side DC-DC converters in hydrogen energy storage systems. The strategy accounts for two state variables in the electrolyzer stack model: stack current i and branch capacitor voltage V_{EDL}. A classical cascaded PI control structure is adopted for precise regulation. This structure includes an outer-loop voltage controller and an inner-loop current controller. The PI parameters are jointly tuned based on the system response characteristics (t_r) and converter/stack parameters (E, L, R_i, L_s). For PEM technology, the voltage control loop can be omitted due to $L_s \approx 0$ and $V_{EDL} \approx 0$, simplifying the PI parameter design.

$$(L_s + L)\frac{di}{dt} = dE_{DC} - V_t \tag{8}$$

$$C\frac{dV_{EDL}}{dt} = i - \frac{V_{EDL}}{R_m} \tag{9}$$

To mitigate the potential conflict between frequency-support duties and hydrogen-production constraints, a hydrogen-production–frequency interaction detector is embedded in the control architecture. This detector integrates the instantaneous stack current iii and overwrites the control command with a modified current i_m: when the buffer volume exceeds, the electrolyzer is tripped (i_m=0), whereas volumes below force the stack to operate at rated load (i_m=i_{max}). The updated current is fed back to the hydrogen-flow and Faradaic-efficiency models, thereby closing a loop that is unique to hydrogen-energy (HE) systems and fundamentally different from generic storage controllers. In parallel, an active-power reference generator expresses P_{ref} as a function of the frequency deviation Δf: primary frequency response is delivered through droop control, while automatic-generation control (AGC) supplies the slower corrective action. Thus, PFR furnishes the fast inertial contribution and AGC compensates the residual error. When Δf exceeds a predefined emergency threshold (Δf>F_r or Δf<−F_r), the HE enters emergency regulation; when Δf falls inside the deadband Δf∈(−F_d, F_d), no action is taken. This unified strategy ensures rapid power modulation and strict compliance with buffer-volume limits, thereby achieving both dynamic frequency support and safe electrolyzer operation.

This paper develops a dynamic hydrogen-energy storage (HE) model based on virtual synchronous machine (VSM) control to supply frequency-control ancillary services and virtual inertia. Figure 8 plots the HE power–frequency curve: for over-frequency it can absorb up to $P_{m\,max}$−P_0; for under-frequency it can inject down to −P_0. Here P_0 is the normal operating point and $P_{m\,max}$ is the available converter capacity. The scheme embeds the stack-temperature dynamics. If the stack temperature rises above the threshold T_{th}, a cooling unit starts and consumes real power; the usable power is then $P_{m\,max}$=P_c-P_f, where P_c is the converter rating. Mechanical auxiliaries such as the compressor are treated as constants to avoid mechanical stress during support actions.

The HE delivers virtual inertia through the VSM controller attached to the electrolyzer converter. The controller forms a virtual voltage phasor and lets the HE behave like a voltage source. Its benefits are: (1) less dependence on grid synchronism; (2) an adjustable virtual inertia constant H_{vi} that strengthens the response as H_{vi} increases; and (3) a second-order transfer path $G_{vi}(s) = 2H_{vi}/s^2$ that is stabilised by a proportional damping term k_{vd}. A cascaded current–voltage loop and a current-limit block keep the input current III within the converter limit. Modulation signals force the point-of-interconnection voltage phasor V_{POI} to track the reference V_m. Thus, the VSM-controlled HE stays stable and is less sensitive to weak-grid conditions. The VSM layer, the electrolyzer-side converter control, and the hydrogen-production–frequency interaction detector works together to guarantee synchronism and a smooth response.

Unlike inverter-based generators, the HE does not inject energy during its virtual inertia action. Instead, it modulates power absorption quickly. The resulting frequency effect is similar to that of wind- or PV-based virtual inertia, but the sign of power is opposite. Such rapid power swings may shift the HE operating point and accelerate stack ageing; this impact must be considered when the HE is assigned frequency-support duties. The proposed VSM-HE model, tailored to PEM characteristics, exhibits strong grid compatibility and allows hydrogen storage to provide reliable frequency support in modern power systems.

IV. Validation of the Simulation

A. Test System Parameters

This section performs three case studies to quantify the frequency-support value of the VSM-controlled hydrogen-energy (HE) units introduced earlier. Case I checks whether an HE unit can supply primary frequency control after a disturbance; Case II measures the virtual-inertia effect produced by the VSM loop; Case III tests the overall feasibility of using HE in frequency-control ancillary services and contrasts the results with a 30 MW battery of equal rating. All studies use a modified IEEE-30 network that embeds a large offshore wind farm and on-site hydrogen production, yielding a 50 % renewable share and two 30 MW HE units (plus two 30 MW batteries) connected at designated buses (Fig. 5). Stack parameters—rise time trt_rtr and settling time tst_sts for both alkaline and PEM technology—come from the measured data in [10]; the equivalent circuit parameters follow from the model developed in Sect. 1. Converter gains are tuned for a closed-loop dqdqdq current controller whose bandwidth ωE\omega_EωE

satisfies the transient-performance targets. The full HE model, together with its VSM layer and the hydrogen-production–frequency interaction detector described above, is implemented and validated in MATLAB/Simulink. Connection points and control modes (VSM or grid-following) are set according to each scenario, ensuring consistency with the earlier modelling framework.

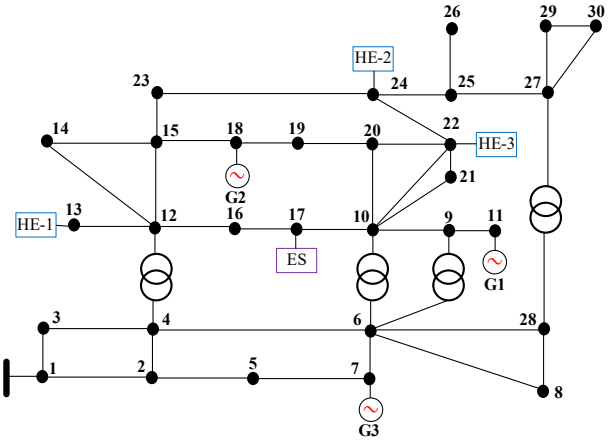
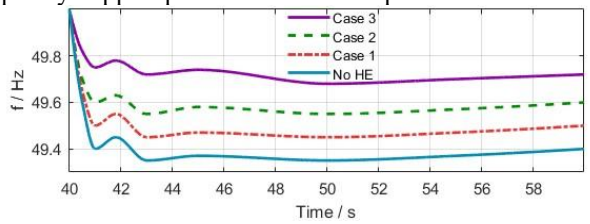


Fig. 4. Improved IEEE 30-node power system with large-scale renewable energy and hybrid energy storage

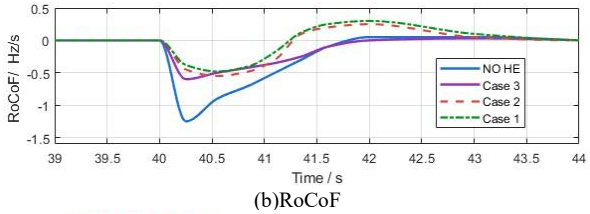
B. Analysis of Simulation Result

Case I-Analysis of the ability of hydrogen Energy Storage to provide primary frequency regulation after disturbance

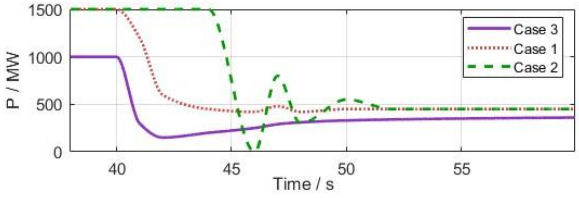
The time-domain study applies a 667 MW unit trip at t_0=40 s to examine the emergency frequency-control capability of hydrogen energy (HE) storage. The proposed HE dynamic model is used under four operating cases: (i) a baseline without HE, (ii) Case 1 with 1.5 GW PEM-based HE, (iii) Case 2 with 1.5 GW alkaline HE, and (iv) Case 3, which subjects the 1.5 GW PEM HE to hydrogen-production constraints to test its frequency-support performance under operational limits.



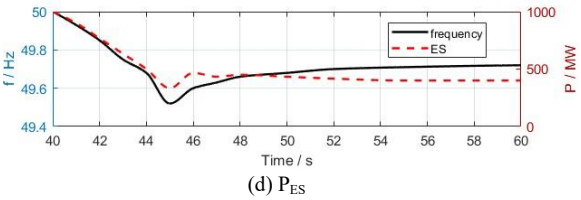
(a) frequency



(b)RoCoF



(c)P_{HE}



(d) P_{ES}

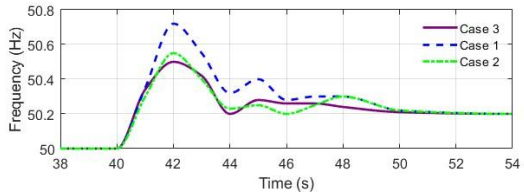
Fig. 5. System frequency dynamic response and HE/ battery primary frequency modulation effect after maximum power trip under different scenarios

Case 1 (PEM HE, 1.5 GW). The PEM stack produces a sub-second response and delivers up to 1.3 GW of primary frequency reserve. The frequency nadir rises to 49.45 Hz and the rate-of-change of frequency (RoCoF) is strongly damped. Case 2 (alkaline HE, 1.5 GW). The alkaline stack exhibits t≈4.2 s dead-time, so it fails to arrest the frequency decline; its behaviour is almost identical to the no-HE baseline, confirming that slow HE units are unsuitable for high-RoCoF, low-inertia systems. Case 3 (PEM HE with buffer limits, V_0=6000 mol，$V_H^{\min}=2000\text{mol}$， $\dot{m}_H=120\text{mol/s}$). The PEM unit initially supplies 1 GW of reserve, but the hydrogen inventory hits the lower bound at t=86.5 s. The controller then forces the electrolyzer to full-load operation, so the HE exits frequency support and the system suffers a second dip to 49.48 Hz. This result highlights the hydrogen-production/F-CAS coupling constraint.

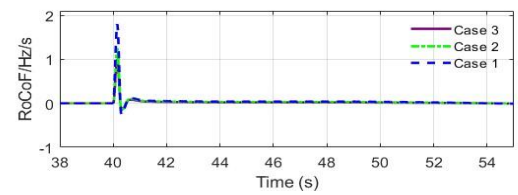
A supplementary study adds a large-scale battery that shares the regulation duty with the HE. The battery off-loads the PEM stack, keeps hydrogen production continuous, prevents the premature loss of primary reserve, and improves overall grid resilience. Hence, coordinated electro-hydrogen planning should be prioritised to strengthen frequency control in future low-inertia networks.

Case II-Performance Analysis of Virtual Inertial Response Based on VSM Control

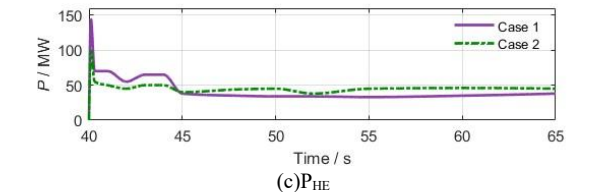
This section assesses the inertial response capability of PEM hydrogen energy storage (HE) under the control of a virtual synchronizer (VSM) and compares it with batteries with the same parameters, considering four scenarios: Basic situation (no HE), Scenario 1 (150 MW grid following HE, P_0=0), Scenario 2 (150 MW VSM HE, P_0=0), Scenario 3 (150 MW VSM battery, P_0=0). After the system trip, the basic frequency rose to 50.71 Hz and the RoCoF reached 1.95 Hz/s.



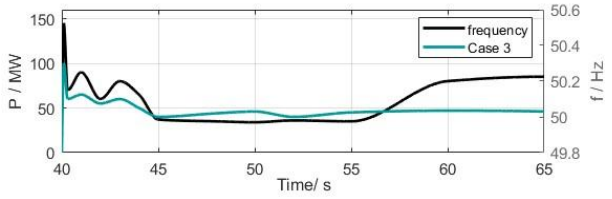
(a) frequency



(b)RoCoF



(c)P_{HE}



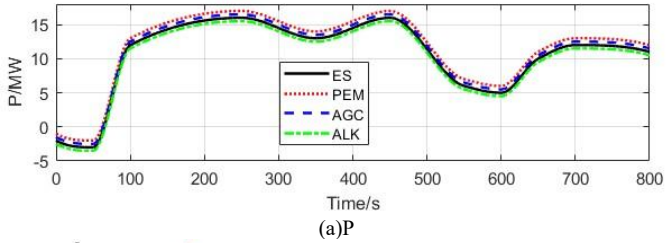
(d) P_{ES}

Fig. 6. Simulation results of virtual inertia response performance after tripping

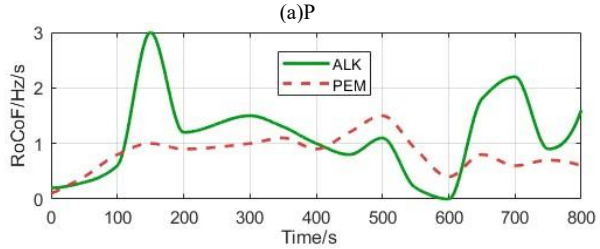
The results show that in Scenario 1, grid-following HE rapidly increases power consumption to 90 MW, provides main frequency regulation, and the peak frequency drops to 50.5 Hz, but the RoCoF improvement is limited. In Scenario 2, VSM control enables HE to provide 145 MW of virtual inertia within 250 ms and reduces RoCoF to 1.1 Hz/s, significantly alleviating frequency shock; Subsequently, HE continues to provide main frequency support through droop control. In Scenario 3, the VSM battery exhibits almost the same frequency response characteristics as the VSM HE (peak 50.42 Hz, steady-state 50.18 Hz), and its dynamic behavior is highly consistent. Therefore, in terms of virtual inertia response, VSM PEM HE has dynamic performance comparable to that of VSM batteries and can be deployed and optimized as a virtual inertia resource.

Case III - Feasibility Analysis of Hydrogen Energy Storage Participating in Frequency Regulation Ancillary Services

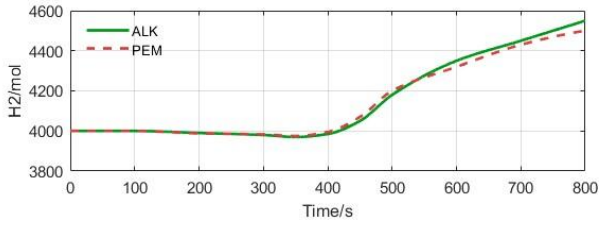
This section assesses the response capability of 1 GW HE in frequency modulation ancillary services, assuming that HE operates at a power point of 700 MW (P_0=700 MW) with a regulation margin of ±300 MW. HE participates in frequency regulation through automatic generation control (AGC), and the hydrogen buffer modeling parameters are $\dot{m}_H = 100\text{mol/s}$, $V_0 = 4000\text{mol}$, $V_H^{\max} = 9000\text{mol}$.



(a)P



(b)RoCoF



(c) m_{H_2}

Fig. 7. Frequency regulation and effect of electrolysis techniques on H2 content in the buffer compared to large batteries

The simulation results show that both PEM HE and basic HE can track AGC commands with high precision, with maximum errors of less than 1.3 MW and 2.8 MW, respectively. The PEM technology has an error of less than 1 MW for most periods and an error of less than 1.7 MW for basic HE, demonstrating good regulation performance. The comparison with the battery shows that the HE system performs almost the same in the regulation frequency, confirming that both PEM and alkaline electrolyzers have the potential to replace the battery in the regulation service. Furthermore, during the regulation process, HE has a relatively small impact on hydrogen production. The H_2 content in the buffer is always within the safe range and does not trigger the HP-FCAS constraint. This indicates that the coupling risk between the regulation service and the hydrogen production operation is relatively low and it is practically feasible.

V. Conclusion

A unified dynamic model for alkaline and PEM wind-driven electrolysers—capturing double-layer capacitance, voltage-current and efficiency nonlinearities—and equipped with grid-following/VSM converters plus a buffer-aware HP-FCAS detector and droop-AGC reference logic is proposed. Simulations on a 50 %-renewable IEEE-30 network show: (i) wind-to-hydrogen units improve frequency stability and absorb surplus wind; (ii) PEM offers sub-second virtual inertia, emergency and regulation FCAS but is buffer-limited unless paired with batteries; (iii) alkaline, hindered by ≈4 s delay, cannot deliver fast reserves yet provides steady regulation. The architecture therefore supplies a resilient frequency-support path for low-inertia grids.

References

[1] K. Yan, G. Li, R. Zhang, Y. Xu, T. Jiang and X. Li, "Frequency Control and Optimal Operation of Low-Inertia Power Systems With HVDC and Renewable Energy: A Review," in *IEEE Transactions on Power Systems*, vol. 39, no. 2, pp. 4279-4295, March 2024

[2] C. He, H. Geng, K. Rajashekara and A. Chandra, "Analysis and Control of Frequency Stability in Low-Inertia Power Systems: A Review," in *IEEE/CAA Journal of Automatica Sinica*, vol. 11, no. 12, pp. 2363-2383, December 2024.

[3] M. Agredano-Torres, M. Zhang, L. Söder and Q. Xu, "Decentralized Dynamic Power Sharing Control for Frequency Regulation Using Hybrid Hydrogen Electrolyzer Systems," in *IEEE Transactions on Sustainable Energy*, vol. 15, no. 3, pp. 1847-1858, July 2024.

[4] Z. Wu, J. Wang, M. Zhou, Q. Xia, C. -W. Tan and G. Li, "Incentivizing Frequency Provision of Power-to-Hydrogen Toward Grid Resiliency Enhancement," in *IEEE Transactions on Industrial Informatics*, vol. 19, no. 9, pp. 9370-9381, Sept. 2023.

[5] C. Li, Z. Ren and W. Li, "CVaR-Wasserstein Metric Based Power System Scheduling Considering Frequency Support of Hydrogen Production

Stations," in *IEEE Transactions on Industry Applications*, vol. 61, no. 2, pp. 2025-2036, March-April 2025.

[6] C. Huang, Y. Zong, S. You and C. Træholt, "Analytical Modeling and Control of Grid-Scale Alkaline Electrolyzer Plant for Frequency Support in Wind-Dominated Electricity-Hydrogen Systems," in *IEEE Transactions on Sustainable Energy*, vol. 14, no. 1, pp. 217-232, Jan. 2023.

[7] N. Feng, Y. Feng, Y. Su, Y. Zhang and T. Niu, "Dynamic Reactive Power Optimization Strategy for AC/DC Hybrid Power Grid Considering Different Wind Power Penetration Levels," in *IEEE Access*, vol. 12, pp. 187471-187482, 2024.

[8] W. Liu, S. Lin, Y. Yang, M. Liu and Q. Li, "Identification of the Worst-Case Static Voltage Stability Margin Interval of AC/DC Power System Considering Uncertainty of Renewables," in *CSEE Journal of Power and Energy Systems*, vol. 10, no. 3, pp. 974-987, May 2024.

[9] E. F. Areed, R. Yan and T. K. Saha, "Impact of Battery Ramp Rate Limit on Virtual Synchronous Machine Stability During Frequency Events," in *IEEE Transactions on Sustainable Energy*, vol. 15, no. 1, pp. 567-580, Jan. 2024

[10] X. Wu, H. Huang, J. Chen, X. Tong, N. Tong and L. L. Lai, "Consensus Algorithm-Based Two-Stage Frequency Regulation Strategy With EVs Participating as VSMs," in *IEEE Transactions on Smart Grid*, vol. 16, no. 2, pp. 1562-1574, March 2025.

Joint Estimation of State of Charge and State of Health for Lithium-Ion Batteries Based on Singular Value Decomposition and Multi-Innovation Adaptive Unscented Kalman Filter Algorithm

Tao Ren
School of Automation and Electronic Information
Xiangtan University
Xiangtan, China
1613399430@qq.com

Jin Jiang
School of Automation and Electronic Information
Xiangtan University
Xiangtan, China
15674352@qq.com

Sheng Li
School of Automation and Electronic Information
Xiangtan University
Xiangtan, China
3067265199@qq.com

***Abstract*—Accurate state estimation of lithium-ion batteries faces fundamental challenges: integer-order models fail to capture diffusion dynamics effectively, Cholesky decomposition-based filtering algorithms suffer from numerical instability under strong noise interference, and strong SOC-SOH coupling leads to persistent error accumulation. This study establishes a second-order fractional equivalent circuit model employing Grünwald-Letnikov discretization to precisely characterize voltage relaxation processes. To address covariance matrix positive definiteness, we innovatively integrate singular value decomposition into the multi-innovation adaptive unscented Kalman filter framework, creating the SVD-FOAMIUKF algorithm that ensures filtering stability through singular vector matrix reconstruction of sigma points. For multimodal parameter identification, an enhanced firefly algorithm incorporating Cauchy mutation operators and adaptive step size mechanisms significantly improves global search efficiency. The proposed dual-timescale architecture (microscale SOC updates and macroscale SOH correction) achieves 0.07% RMSE under US06 dynamic profiles - a 3.8-fold accuracy improvement over conventional FOUKF. Experimental validation demonstrates <1% MAE robustness against 20% voltage measurement noise while maintaining merely 15% additional computational overhead, providing a pragmatic solution for high-precision battery management systems.**

Keywords—Fractional calculus theory, Second-order fractional model, SVD-AMIUKF stabilization, Multi-innovation filter, Joint estimation

I. INTRODUCTION

Precise monitoring of Li-ion battery charge status (SOC) and degradation state (SOH) plays a vital role in optimizing operational safety, performance regulation, and longevity management. The existing SOC estimation methods can be divided into four categories: Ampere hour (Ah) integration method [1], Open circuit voltage (OCV) method [2], data-driven-based methods [3], and model - based methods [4]. Among current mainstream SOC estimation methods, those based on fractional-order models (FOM) have demonstrated significant advantages due to their ability to more precisely characterize the polarization dynamics of batteries (e.g., through constant phase elements, CPE) while maintaining manageable model complexity. However, in practical applications, this approach still faces numerous challenges that need to be addressed.

In the model parameter identification stage, traditional methods such as recursive least squares (RLS) [5] and its forgetting factor variant (FFRLS) [6] exhibit vulnerability under noise interference. Although FFRLS mitigates data saturation issues through the forgetting factor, its parameter selection often relies on empirical knowledge and demonstrates limited noise resistance. To address this technical bottleneck, this study innovatively introduces the adaptive firefly algorithm (AFA) [7] for parameter identification. This algorithm, based on a unique logarithmic spiral path and adaptive switching mechanism, dynamically balances global exploration and local exploitation, effectively improving identification accuracy and robustness in complex operating conditions and battery aging scenarios.

At the core SOC estimation algorithm level, while fractional-order unscented Kalman filtering (FOUKF) [8] enhances nonlinear processing capabilities through unscented transformation, its algorithmic stability is insufficient, making it prone to divergence in complex operating conditions. The FOMIUKF algorithm developed by Xu et al. [9] by incorporating multi-innovation theory reduces estimation errors by utilizing historical innovation information, but still fails to effectively address the persistent impact of time-varying noise characteristics and system cumulative errors on estimation accuracy. Building upon this, Ma et al. [10] combined UKF for SOC/SOH joint estimation, which considers aging factors but still leaves the fundamental issues of noise interference and error

979-8-3315-5472-9/25/$31.00 ©2025 IEEE

accumulation unresolved. Additionally, the Cholesky decomposition relied upon by traditional UKF algorithms imposes stringent requirements on the positive definiteness of covariance matrices, making them susceptible to numerical divergence in practical applications due to noise and errors.

To systematically address key challenges including noise robustness in parameter identification, the precision-stability balance in SOC algorithms, noise/error accumulation suppression, and covariance matrix positive definiteness assurance, this study proposes an innovative multi-time scale SVD-FOAMIUKF-UKF joint estimation framework. This framework fundamentally resolves the algorithmic failure caused by non-positive definiteness of covariance matrices by integrating singular value decomposition (SVD) technology into UKF to replace traditional Cholesky decomposition, forming the stable SVD-FOAMIUKF core algorithm. Simultaneously, through deep integration of multi-innovation theory and adaptive strategies, it achieves real-time dynamic adjustment of noise statistics and filtering gains, significantly suppressing time-varying noise interference and effectively mitigating the impact of cumulative errors. In terms of algorithmic architecture design, an innovative micro-macro time scale coordination approach is adopted, where SVD-FOAMIUKF serves as a micro-scale observer responsible for rapid response to voltage/current inputs to update SOC, while UKF acts as a macro-scale observer to periodically update SOH parameters such as internal resistance and capacity. Their alternating operation achieves efficient decoupled estimation of states and parameters.

This innovative framework progressively integrates SVD technology to ensure numerical stability, multi-innovation adaptation to enhance precision and noise resistance, and multi-time scale coordination to optimize computational efficiency, significantly improving the comprehensive performance of SOC/SOH joint estimation for LIB across multiple dimensions including accuracy, robustness, and reliability.

II. Battery Model

A. Fractional-Order Model

Currently, three predominant fractional-order definitions are widely adopted: the Riemann-Liouville type, Caputo type, and Grünwald-Letnikov (GL) type [11]. Among these, the GL definition proves particularly suitable for battery FOM due to its computational efficiency in discretization and implementation simplicity. The discrete fractional-order differential operator under this definition can be expressed as:

$$ {}_{t0}^{GL}D_t^{\alpha} f(t) = \lim_{h\to 0} h^{-\alpha} \sum_{i=0}^{L} \omega_i^{(\alpha)} f(t-ih) \tag{1} $$

The Grünwald-Letnikov operator ${}_{t_0}D_t^{\alpha}$ fundamentally characterizes fractional-order dynamics in battery systems through its distinctive temporal operation window bounded by t_0 and t ,where the fractional order α (typically ranging $0<\alpha<1$) physically correlates with electrochemical memory effects-lower values indicating stronger historical dependence. For practical implementation, the sampling interval h is conventionally normalized to unity while the memory length L determines the effective history horizon, both critically influencing computational efficiency. The binomial coefficients $\omega_i^{(\alpha)}$ demonstrate dual behavioral regimes: initially $\omega_0^{(\alpha)}=1$ preserves dimensional homogeneity, followed by recursively computed weights $\omega_i^{(\alpha)}=\left(1-\frac{\alpha+1}{i}\right)\omega_{i-1}^{(\alpha)}$ (for $i\geq 1$) [10] that enable efficient real-time updating in battery management processors.

Extensive experimental investigations have revealed that the capacitive components in lithium-ion battery equivalent circuits exhibit distinct non-integer order dynamics [12], providing a theoretical foundation for enhancing conventional integer-order modeling approaches. Building upon this insight, our research employs fractional-order capacitive elements (CPE) to replace ideal capacitors in the traditional second-order RC network, establishing the fractional-order model configuration illustrated in Fig. 1.

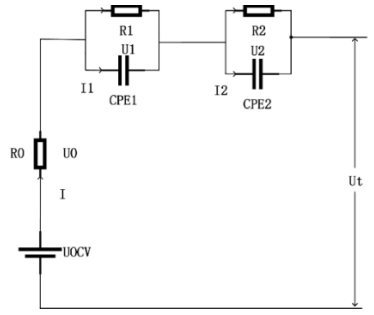


Fig. 1. Second-order Fractional-order RC Model

In the second-order IOM, the ohmic resistance is described by the resistor R_0 ; U_0 is the voltage across R_0 . The polarization internal resistances are described by R_1C_1 and R_2C_2 , and the polarization internal resistance voltages are described by U_1 and U_2 . U_{ocv} is the voltage of the voltage source; U_t stands for its terminal voltage of the battery; and I represents its total current [13].

The fractional-order discrete-time model of the lithium-ion battery system, incorporating coulomb counting principles while accounting for measurement disturbances, takes the mathematical form:

$$ \begin{bmatrix} \hat{U}_{1,k+1} \\ \hat{U}_{2,k+1} \\ \hat{S}_{k+1} \end{bmatrix} = \begin{bmatrix} -\frac{h^m}{R_1C_1} & 0 & 0 \\ 0 & -\frac{h^n}{R_2C_2} & 0 \\ 0 & 0 & 1 \end{bmatrix} \begin{bmatrix} U_{1,k} \\ U_{2,k} \\ S_k \end{bmatrix} + \begin{bmatrix} \frac{h^m}{C_1} \\ \frac{h^n}{C_2} \\ -\frac{h}{Q_n} \end{bmatrix} \times I - \sum_{i=1}^{L} \begin{bmatrix} \binom{m}{i} & & \\ & \binom{n}{i} & \\ & & 0 \end{bmatrix} \times \begin{bmatrix} U_{1,k-i+1} \\ U_{2,k-i+1} \\ S_{k-i+1} \end{bmatrix} + w_k \tag{2} $$

The exponents m and n represent the fractional differentiation orders governing the CPEs' frequency-dependent phase behavior, with S_k defining the state-of-charge and Q_n specifying the battery's rated capacity.

The companion observation equation governing terminal voltage behavior is expressed as:

$$U_t = U_{ocv} - I_0 R_0 - U_1 - U_2 + v_k \tag{3}$$

The terms w_k and v_k in the formulation correspond to process noise within the system and measurement noise components.

To develop a comprehensive fractional-order state-space representation, we perform first-order Taylor series approximation on the $U_{ocv}(SOC)$ correlation to achieve system linearization. The resultant state-space formulation is presented as:

$$\begin{cases} x_{\dot{k}} = A_{\dot{k}-1} x_{\dot{k}-1} + B_{\dot{k}-1} I_{\dot{k}-1} - \sum_{i=1}^{L} L_i x_{\dot{k}-i} + w_{\dot{k}} \\ y_{\dot{k}} = C_{\dot{k}} x_{\dot{k}} - R_0 I_{\dot{k}} + v_{\dot{k}} \end{cases} \tag{4}$$

In this formula, $L_i = diag[(-1)^i \binom{m}{i}, (-1)^i \binom{n}{i}, 0]$,

$x_k = [U_{1,k}, U_{2,k}, S_k]^T$, $y_k = U_{t,k}$, $A_{k-1} = diag[-\frac{h^m}{R_1 C_1}, -\frac{h^n}{R_2 C_2}, 1]$,

$B_{k-1} = [\frac{h^m}{C_1}, \frac{h^n}{C_2}, -\frac{h}{Q_n}]^T$, $C_k = [-1, -1, \frac{\partial U_{ocv}}{\partial S_k}]^T$.

The SOH of LIB can be expressed as:

$$SOH = \frac{Q_{max}}{Q_{nom}} \tag{5}$$

Actual available capacity Q_{max} varying with health state; Q_{nom} is the Constant reference value from initial specifications.

B. Parameter Identification

This study leverages the CALCE Battery Research Group's experimental dataset (University of Maryland) [14], specifically employing cycling data from Samsung INR18650-20R high-power 18650 cells, and with relevant parameters shown in TABLE I. Tests were conducted on Battery No. 1 at 25°C, obtaining incremental current OCV, US06, DST, and FUDS data. Specifically, the 25°C incremental current OCV discharge partial data are selected for parameter identification, while the 25°C US06, DST, and FUDS data serve to estimate the battery's SOC, while the 25°C US06, DST, and FUDS profiles serve as validation benchmarks for state-of-charge estimation accuracy.

TABLE I. LITHIUM BATTERY PARAMETER INDEX

project	parameter
Voltage	3.6V
Capacity	2000mAh
Maximum Charging Current	4A
Charging Cut - off Voltage	4.2V
Operating Temperature	-20℃-+60℃
Continuous Maximum Discharging Current	20A
Discharging Cut - off Voltage	2.5V
Service Life	500-800 cycles

C. SOC-OCV Fitting

This voltage-SOC correlation, demonstrating pronounced nonlinearity across the entire charge-discharge range, constitutes a critical empirical basis for accurate state estimation. We employ a sixth-degree polynomial regression to characterize this electrochemical relationship, with the optimized coefficients yielding the following parametric expression:

$$\begin{aligned} U_{OCV}(SOC) = {} & 36.4SOC^6 - 102.6SOC^5 + 106.5SOC^4 - \\ & 47.88SOC^3 + 7.971SOC^2 + 0.5417SOC + 3.372 \end{aligned} \tag{6}$$

D. Adaptive Firefly Algorithm for Parameter Identification

This study employs an adaptive firefly algorithm (AFA) for battery parameter identification, leveraging a logarithmic spiral trajectory and adaptive switching to dynamically modulate global exploration and local refinement. The approach accelerates convergence toward optimal parameters, enhancing accuracy in state estimation—particularly under complex operational conditions or aging effects. The objective function minimizes the squared error between measured $y_e(l)$ and simulated $y_r(l)$ outputs, with results detailed in TABLE II.

$$J(i) = \sum_{l=1}^{M} \left(y_e(l) - y_r(l) \right)^2 \tag{7}$$

TABLE II. IDENTIFICATION RESULTS

R_0	R_1	R_2	C_1	C_2	m	n
0.198	0.099	0.061	500.025	1000	0.864	0.986

III. DUAL-TIME-SCALE ADAPTIVE JOINT FRAMEWORK FOR SOC/SOH ESTIMATION USING SVD-FOAMIUKF-UKF

A. Singular Value Decomposition

The UKF necessitates Cholesky decomposition of the covariance matrix P [15], requiring strict positive definiteness—a condition frequently compromised by sensor noise and error propagation during state estimation. Such numerical instability triggers Cholesky failure and subsequent filter divergence. Singular value decomposition resolves this by factorizing P into orthogonal matrices irrespective of definiteness constraints, ensuring algorithmic robustness under non-ideal conditions.

$$P = U \Lambda V^T = U \begin{pmatrix} W & 0 \\ \mathbf{0} & 0 \end{pmatrix} V^T \tag{8}$$

The matrices U and V form orthonormal bases. The diagonal matrix W contains singular values arranged in strictly descending order $W_1 > W_2 > ... > W_r > 0$ .The rank deficiency is characterized by the null space dimension dim(null(P)) = $n - r$.

B. SOC and SOH Joint Estimation

Given time-varying noise characteristics in operational environments, static noise assumptions or improper initialization degrade estimation fidelity. To mitigate this, we implement covariance adaptation within the SVD-FOAMIUKF framework. This enhanced algorithm stabilizes the covariance matrix through orthonormal factorization while functioning as a microscale state observer, processing voltage/current inputs to update SOC estimates. Upon reaching preset computational epoch L, temporal scaling triggers the UKF as a macroscale parameter observer, revising internal resistance and capacity coefficients. The dual observers alternate cyclically, establishing a multi-timescale SOC-SOH estimation architecture (Fig. 2).

The operational workflow of the SVD-FOAMIUKF-UKF joint estimation framework proceeds through the following stages:

(1) State initialization:

$$\begin{cases} x_{0,0} = \begin{bmatrix} U_{1,0,0} \\ U_{2,0,0} \\ S_{0,0} \end{bmatrix} \\ \theta_0 = \begin{bmatrix} C_0 & R_0 \end{bmatrix} \end{cases} \tag{9}$$

$$\begin{cases} \hat{x}_{0,0} = E\left[x_{0,0}\right] \\ P_{x,0,0} = E\left[\left(x_{0,0} - \hat{x}_{0,0}\right)\left(x_{0,0} - \hat{x}_{0,0}\right)^T\right] \\ \hat{\theta}_0 = E\left[\theta_0\right] \\ P_{\theta,0} = E\left[\left(\theta_0 - \hat{\theta}_0\right)\left(\theta_0 - \hat{\theta}_0\right)^T\right] \end{cases} \tag{10}$$

Here, $x_{0,0}$ and θ_0 denote the initial state (SOC) and parameter (SOH) vectors, with $P_{x,0,0}$ and $P_{\theta,0}$ representing their respective covariance matrices.

When $l < L$, the SOC is calculated at the micro-scale:

(2) At timestep $k-1$, the covariance matrix $P_{x,k-1,l-1}$ undergoes SVD:

$$P_{x,k-1,l-1} = U_{x,k-1} W_{x,k-1} V_{x,k-1}^T \tag{11}$$

yielding orthonormal bases for sigma point generation:

$$\begin{cases} x_{0,k-1,l-1} = \hat{x}_{k-1,l-1} \\ x_{i,k-1,l-1} = \hat{x}_{k-1,l-1} + \psi U_{k-1,l-1}\sqrt{S_{k-1,l-1}}, \mathrm{i}=1,2,\cdots,\mathrm{j} \\ x_{i,k-1,l-1} = \hat{x}_{k-1,l-1} - \psi U_{k-1,l-1}\sqrt{S_{k-1,l-1}}, \mathrm{i}=\mathrm{j}+1,\cdots,2\mathrm{j} \end{cases} \tag{12}$$

The mode-switching counter l governs estimator selection, where $l = L$ activates SOH estimation. The posterior state estimate $\hat{x}_{k-1}$ serves as the baseline for sigma point generation, with scaling gain ψ is the gain coefficient. $x_{0,k-1}$ corresponds to the mean state estimate while the symmetric points $x_{i,k-1}$ are systematically generated around this mean to capture the covariance structure.

(3) State variable time update: Compute the propagated mean and covariance through nonlinear transformation using sigma point weights and process noise.

$$\begin{cases} x_{i,k/k-1,l/l-1} = f\left(x_{i,k-1,l-1}, u_{k,l}\right) \\ \hat{x}_{k/k-1,l/l-1} = \sum_{i=1}^{2j} \omega_m^i x_{i,k/k-1,l/l-1} \\ P_{i,k/k-1,l/l-1} = \sum_{i=1}^{2j} \omega_c^i \left(x_{i,k/k-1,l/l-1} - \hat{x}_{k/k-1,l/l-1}\right) \times \left(x_{i,k/k-1,l/l-1} - \hat{x}_{k/k-1,l/l-1}\right)^T + Q_{k-1,l} \end{cases} \tag{13}$$

where $u_k = \begin{bmatrix} U_t & I \end{bmatrix}$.

(4) Use the SVD method again to decompose $P_{x,k/k-1}$, and obtain the updated Sigma points:

$$P_{x,k/k-1,l/l-1} = U_{x,k/k-1} W_{x,k/k-1} V_{x,k/k-1}^T \tag{14}$$

yielding orthonormal bases for sigma point generation:

$$\begin{cases} x_{0,k/k-1,l/l-1} = \hat{x}_{k/k-1,l/l-1} \\ x_{i,k/k-1,l/l-1} = \hat{x}_{k/k-1,l/l-1} + \psi U_{k/k-1,l/l-1}\sqrt{S_{k/k-1,l/l-1}}, \mathrm{i}=1,2,\cdots,\mathrm{j} \\ x_{i,k/k-1,l/l-1} = \hat{x}_{k/k-1,l/l-1} - \psi U_{k/k-1,l/l-1}\sqrt{S_{k/k-1,l/l-1}}, \mathrm{i}=\mathrm{j}+1,\cdots,2\mathrm{j} \end{cases} \tag{15}$$

(5) Measurement Update: Update the variance prediction of the observation equation and the state variable covariance.

$$\begin{cases} P_{y,k/k-1,l-1} = \sum_{i=0}^{2j} \omega_c^i \left(y_{i,k/k-1,l/l-1} - \hat{y}_{k/k-1,l/l-1}\right) - \left(y_{i,k/k-1,l/l-1} - \hat{y}_{k/k-1,l/l-1}\right)^T + R_{k-1,l} \\ P_{xy,k/k-1,l/l-1} = \sum_{i=0}^{2j} \omega_c^i (x_{i,k/k-1,l/l-1} - \hat{x}_{k/k-1,l/l-1})(y_{i,k/k-1,l/l-1} - \hat{y}_{k/k-1,l/l-1})^T \end{cases} \tag{16}$$

The predicted observation covariance $P_{y,k/k-1}$ characterizes output uncertainty, while the cross-covariance matrix $P_{xy,k/k-1}$ quantifies the statistical relationship between state predictions and their corresponding measurements.

(6) Multi-innovation calculation:

$$E_{p,\hat{k}} = \begin{bmatrix} e_k \\ e_{k-1} \\ \cdots \\ e_{k-p+1} \end{bmatrix} = \begin{bmatrix} y_k - \hat{y}_{k/k-1} \\ y_{k-1} - \hat{y}_{k-1/k-2} \\ \cdots \\ y_{k-p} - \hat{y}_{k-p+1/k-p} \end{bmatrix} \tag{17}$$

The multi-innovation algorithm employs a sliding window of length p to process sequential measurements, where y_k corresponds to the actual measurement at timestep k and $\hat{y}_{k/k-1}$ reflects the predicted output derived from previous state information.

(7) Gain matrix calculation and adaptive noise update:

$$K_{p,k} = [K_{x,k}, K_{x,k-1}, \cdots K_{x,k-p+1}] \tag{18}$$

$$\begin{cases} Q_{k,l} = K_{x,k} F_k K_{x,k}^T \\ F_k = \dfrac{1}{M} \displaystyle\sum_{i=k-M+1}^{k} e_i (e_i)^T \\ R_{k,l} = F_k + C_k P_k C_k^T \end{cases} \tag{19}$$

Here, parameter M dictates the monitoring scope of the innovation sequence covariance window, while variable e_i quantifies the instantaneous deviation between the model-predicted terminal voltage and its experimentally measured counterpart at discrete time step i.

(8) State and Covariance Correction:

$$\begin{cases} \hat{x}_{k,l} = \hat{x}_{k/k-1,l/l-1} + \displaystyle\sum_{i=1}^{p} K_{x,k-i+1} e_{k-i+1} \\ P_{x,k,l} = P_{x,k/k-1,l/l-1} - K_{x,k} P_{y,k/k-1,l/l-1} K_{x,k}^T \end{cases} \tag{20}$$

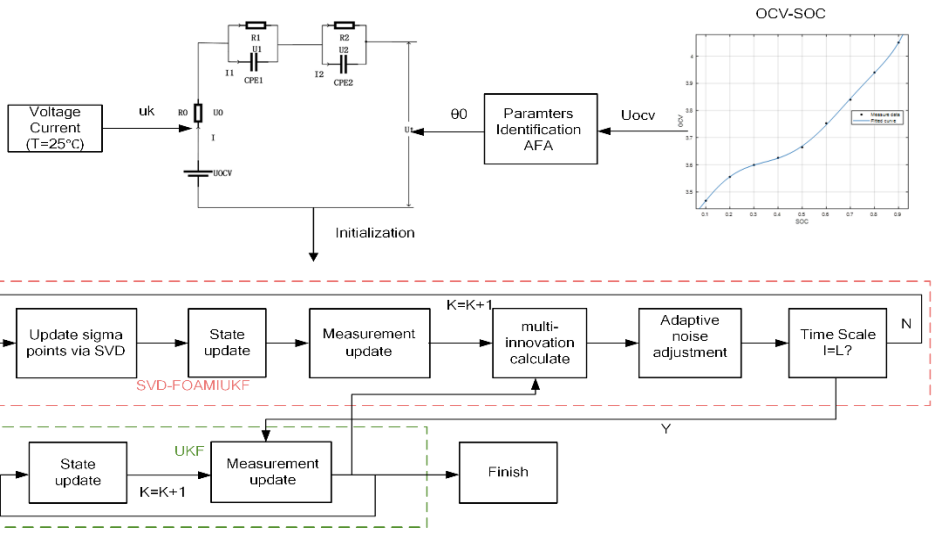


Fig. 2. Flowchart of multi-scale co-estimation method

When $l = L$, the SOH is calculated on the macro-scale.

$\hat{x}_{k,0} = \hat{x}_{k,L}, P_{k,0} = P_{x,k,L}, y_{k,0} = y_{k,L}, u_{k,0} = u_{k,L}$.

(9) SOH state update:

$$\begin{cases} \hat{\theta}_{k|k-1} = \displaystyle\sum_{i=0}^{2j} \omega_m^i \theta_{i,k|k-1} \\ P_{\theta,k|k-1} = \displaystyle\sum_{i=0}^{2j} \omega_c^i \left(\theta_{i,k/k-1} - \hat{\theta}_{k/k-1}\right)\left(\theta_{i,k/k-1} - \hat{\theta}_{k/k-1}\right)^T + Q_{k-1} \end{cases} \tag{21}$$

(10) SOH measurement update:

$$\begin{cases} P_{y,k/k-1} = \displaystyle\sum_{i=0}^{2j} W_c^i \left(y_{i,k/k-1,0} - \hat{y}_{k/k-1,0}\right)\left(y_{i,k/k-1,0} - \hat{y}_{k/k-1,0}\right)^T + R_{k-1} \\ P_{\theta y,k/k-1} = \displaystyle\sum_{i=0}^{2j} W_c^i \left(\theta_{i,k/k-1,0} - \hat{\theta}_{k/k-1,0}\right)\left(y_{i,k/k-1,0} - \hat{y}_{k/k-1,0}\right)^T \end{cases} \tag{22}$$

(11) State and Covariance Correction:

$$\begin{cases} \hat{\theta}_k = \hat{\theta}_{k/k-1} + K_{\theta,k}\left(y_{k,0} - \hat{y}_{k,0}\right) \\ P_{\theta,k} = P_{\theta,k/k-1} - K_{\theta,k} P_{\theta,v,k/k-1} K_{\theta,k}^T \end{cases} \tag{23}$$

IV. Algorithm Performance Evaluation and Empirical Validation

The study conducted a systematic evaluation of five estimation algorithms (SVD-FOAMIUKF-UKF, FOAMIUKF, FOMIUKF, FOAUKF, and FOUKF) implemented on a fractional-order equivalent circuit model under US06, DST, and FUDS dynamic operating conditions. Quantitative analysis using mean absolute error (MAE) and root mean square error (RMSE) metrics (TABLE III.) [16] demonstrate that SVD-FOAMIUKF-UKF achieved optimal error suppression performance during US06/DST testing (Fig. 3 and Fig. 5), with its SOC trajectory showing exceptional alignment with reference values. While FUDS conditions (Fig. 4) exhibited marginally higher residuals, all values remained within strict tolerance bounds.

The dual-observer architecture of the proposed algorithm incorporates dynamic noise covariance correction, effectively addressing the precision degradation issues caused by battery aging in conventional methods. Comprehensive MAE/RMSE data across all test scenarios conclusively validated both the superior performance and operational stability of the SVD-FOAMIUKF-UKF approach.

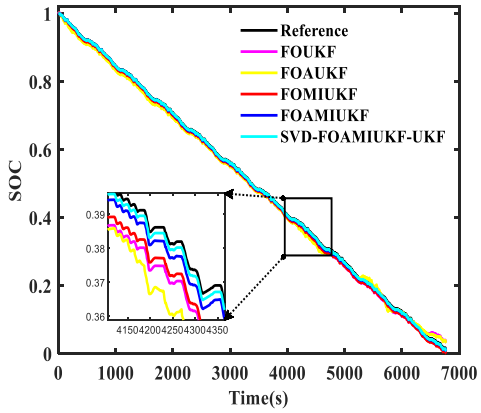


Fig. 3. Comparison of Joint Estimation Results under US06 Driving Cycle

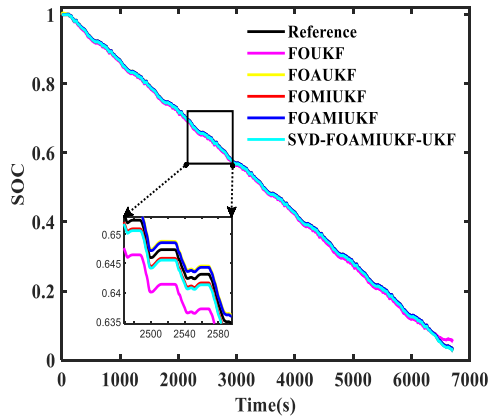


Fig. 4. Comparison of Joint Estimation Results under FUDS Driving Cycle

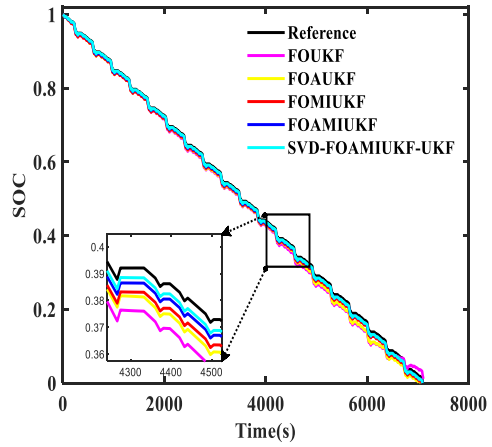


Fig. 5. Comparison of Joint Estimation Results under DST Driving Cycle

TABLE III. SOC ERROR COMPARISON UNDER DIVERSE CYCLES AND ALGORITHMS

	US06		FUDS		DST	
	MAE	RMSE	MAE	RMSE	MAE	RMSE
FOUKF	0.0352	0.0186	0.0202	0.0099	0.0305	0.0137
FOMIUKF	0.0347	0.0212	0.0044	0.0026	0.0116	0.0089
FOAUKF	0.0313	0.0133	0.0025	0.0015	0.0331	0.0147
FOAMIUKF	0.0048	0.0023	0.0016	0.0011	0.0122	0.0066
Proposed Method	0.0019	0.0007	0.0023	0.0013	0.0068	0.0038

V. CONCLUSION

The research presents a comprehensive battery state estimation framework beginning with the formulation of a second-order fractional calculus-based equivalent circuit model to capture lithium-ion battery dynamics. To overcome numerical instability issues stemming from covariance matrix positive definiteness requirements, the methodology employs SVD as a robust alternative to conventional matrix factorization approaches [17]. The proposed SVD-FOAMIUKF-UKF architecture synergistically combines multi-innovation theory with adaptive unscented Kalman filtering, enabling real-time optimization of fractional orders, noise covariance matrices, and Kalman gain parameters for enhanced noise resilience. Experimental validation across standardized US06 (0.19% MAE and 0.07% RMSE), FUDS (0.23% MAE and 0.13% RMSE), and DST (0.68% MAE and 0.38% RMSE) driving cycles demonstrates consistent estimation accuracy, with all error metrics remaining below the 0.7% threshold. This performance superiority, particularly in mitigating aging-induced estimation drift, confirms the algorithm's operational robustness and represents a significant advancement over traditional battery state estimation techniques.

REFERENCES

[1] N. Yang, X. Zhang, and G. Li, "State of charge estimation for pulse discharge of a LiFePO4 battery by a revised Ah counting," Electrochimica Acta, vol. 151, pp. 63–71, Jan. 2015, doi: 10.1016/j.electacta.2014.11.011.

[2] Y. Chen, G. Yang, X. Liu, and Z. He, "A Time-Efficient and Accurate Open Circuit Voltage Estimation Method for Lithium-Ion Batteries," Energies, vol. 12, no. 9, Art. no. 9, Jan. 2019, doi: 10.3390/en12091803.

[3] Z. Deng, X. Hu, X. Lin, Y. Che, L. Xu, and W. Guo, "Data-driven state of charge estimation for lithium-ion battery packs based on Gaussian process regression," Energy, vol. 205, p. 118000, Aug. 2020, doi: 10.1016/j.energy.2020.118000.

[4] X. Hu, S. Li, and H. Peng, "A comparative study of equivalent circuit models for Li-ion batteries," Journal of Power Sources, vol. 198, pp. 359–367, Jan. 2012, doi: 10.1016/j.jpowsour.2011.10.013.

[5] L. Li, H. Zhu, A. Zhou, M. Hu, C. Fu, and D. Qin, "A Novel Online Parameter Identification Algorithm for Fractional-Order Equivalent Circuit Model of Lithium-Ion Batteries," International Journal of Electrochemical Science, vol. 15, no. 7, pp. 6863–6879, Jul. 2020, doi: 10.20964/2020.07.29.

[6] L. Chen, S. Wang, H. Jiang, C. Fernandez, and X. Xiong, "A novel combined estimation method of online full-parameter identification and adaptive unscented particle filter for Li-ion batteries SOC based on fractional-order modeling," International Journal of Energy Research, vol. 45, no. 10, pp. 15481–15494, 2021, doi: 10.1002/er.6817.

[7] C. Fang, Z. Jin, J. Wu, and C. Liu, "Estimation of Lithium-Ion Battery SOC Model Based on AGA-FOUKF Algorithm," Frontiers in Energy Research, vol. 9, Nov. 2021, doi: 10.3389/fenrg.2021.769818.

[8] Y. Xu et al., "Joint Estimation Method with Multi-Innovation Unscented Kalman Filter Based on Fractional-Order Model for State of Charge and State of Health Estimation," Sustainability, vol. 14, no. 23, Art. no. 23, Jan. 2022, doi: 10.3390/su142315538.

[9] L. Ma, Y. Xu, H. Zhang, F. Yang, X. Wang, and C. Li, "Co-estimation of state of charge and state of health for lithium-ion batteries based on fractional-order model with multi-innovations unscented Kalman filter method," Journal of Energy Storage, vol. 52, p. 104904, Aug. 2022, doi: 10.1016/j.est.2022.104904.

[10] J. Wu, Y.-G. Wang, K. Burrage, Y.-C. Tian, B. Lawson, and Z. Ding, "An improved firefly algorithm for global continuous optimization problems," Expert Systems with Applications, vol. 149, p. 113340, Jul. 2020, doi: 10.1016/j.eswa.2020.113340.

[11] Q. Yang, J. Xu, X. Li, D. Xu, and B. Cao, "State-of-health estimation of lithium-ion battery based on fractional impedance model and interval

capacity," International Journal of Electrical Power & Energy Systems, vol. 119, p. 105883, Jul. 2020, doi: 10.1016/j.ijepes.2020.105883.

[12] X. Zhang, X. Li, K. Yang, and Z. Wang, "Lithium-Ion Battery Modeling and State of Charge Prediction Based on Fractional-Order Calculus," Mathematics, vol. 11, no. 15, Art. no. 15, Jan. 2023, doi: 10.3390/math11153401.

[13] S. Wang, B. Hu, L. Zhou, Y. Liu, C. Fernandez, and F. Blaabjerg, "Improved volumetric noise-adaptive H-infinity filtering for accurate state of power estimation of lithium-ion batteries with multi-parameter constraint considering low-temperature influence," Journal of Energy Storage, vol. 115, p.115999, Apr. 2025, doi: 10.1016/j.est.2025.115999.

[14] Z. Shi et al., "An improved adaptive square root cubature Kalman filter method for estimating state-of-charge of lithium-ion batteries," Journal of Energy Storage, vol. 72, p. 108245, Nov. 2023, doi: 10.1016/j.est.2023.108245.

[15] "Appendix B: A Matrix Refresher," in Kalman Filtering, John Wiley & Sons, Ltd, 2008, pp. 519–547. doi: 10.1002/9780470377819.app2

[16] C. Wang, R. Li, Y. Cao, and M. Li, "A hybrid model for state of charge estimation of lithium-ion batteries utilizing improved adaptive extended Kalman filter and long short-term memory neural network," Journal of Power Sources, vol. 620, p. 235272, Nov. 2024, doi: 10.1016/j.jpowsour.2024.235272.

[17] J. Chen, Z. Xu, X. Qin, F. Zou, and X. Cai, "Co-estimation of state of charge and state of health of sodium-ion batteries based on fractional-order model and improved double unscented Kalman filter," Ionics, vol. 31, no. 8, pp. 7987–8003, Aug. 2025, doi: 10.1007/s11581-025-06425-8.

Short-term wind PV output and electrical load forecasting for microgrids based on peak-valley weighted CNN-BiLSTM

Yu Huiqun
School of Automation Engineering
Shanghai University of Electric Power
Shanghai, China
yuhuiqun@shiep.edu.cn

Meng Yanyu
School of Automation Engineering
Shanghai University of Electric Power
Shanghai, China
myy011109@163.com

Yang Yifan
School of Automation Engineering
Shanghai University of Electric Power
Shanghai, China
3025494129@qq.com

Qiu Yaming
Intelligent Control Department
Energy Science and Technology Research Institute of State Power Investment Corporation
Shanghai, China
myy011109@163.com

***Abstract*—Accurate forecasting of energy demand is essential to ensure the operational efficiency and reliability of microgrid renewable energy. A source-load forecasting method based on convolutional neural network (CNN), bidirectional long and short-term memory neural network (BiLSTM) and peak-valley weighting (PVW) is proposed. Firstly, the influencing factors with high correlation with power load and wind power output are selected as inputs to the model by combining the Pearson correlation coefficient (PCC) and MIV scores; then, the joint forecasting of microgrid wind-photovoltaic load is realized by CNN-BiLSTM combined with the PVW mechanism. Finally, the forecasting accuracy of the proposed model is tested by combining the measured electric load and wind and solar power data of a region in China. The results show that the proposed model has higher forecasting accuracy in peak-underestimation forecasting.**

Keywords—microgrid; load forecasting; new energy forecasting; convolutional neural network; long-short-term memory network

I. INTRODUCTION

With the rapid development of renewable energy, microgrids, as distributed energy systems integrating wind power, photovoltaic (PV) generation, and loads, play a crucial role in improving energy utilization efficiency and system stability[1],[2]. However, the randomness of wind-PV output and significant load fluctuations pose challenges to short-term forecasting, particularly in hourly or daily forecasting scenarios[3]. In recent years, deep learning has been widely applied to wind-PV-load forecasting due to its strong nonlinear modeling capabilities. Hybrid models combining convolutional neural networks (CNN) and long short-term memory networks (LSTM) have demonstrated excellent performance in wind power forecasting by extracting spatiotemporal features[4]. Nevertheless, existing models still suffer from insufficient forecasting accuracy under complex fluctuation scenarios, highlighting the need for more efficient forecasting strategies.

Currently, researchers worldwide have conducted extensive studies on microgrid load and wind-PV power forecasting, with common approaches including single-model forecasting and multi-model fusion. Single-model forecasting typically inputs highly correlated influencing factors into deep learning algorithms, such as artificial neural networks (ANN)[5],[6] and support vector machines (SVM)[7]. However, redundant features may lead to overfitting and reduced forecasting accuracy. Feature selection enhances model performance by screening key variables, where the Pearson correlation coefficient (PCC) quantifies linear relationships[8], while the mean impact value (MIV) identifies nonlinear feature importance[9]. Studies show that combining PCC and MIV for feature selection can significantly improve forecasting accuracy[8],[10]. Nevertheless, feature screening for joint wind-PV-load forecasting still requires optimization.

Researchers have also explored extensive studies on microgrid peak-valley forecasting, with common methods including single-model forecasting and weighted strategy optimization. Single models are typically based on machine learning or deep learning, such as random forests (RF)[3],[11] and LSTM[12]. To enhance peak and valley forecasting accuracy, peak-valley weighted (PVW) strategies assign higher loss weights to critical time periods, improving the model's focus on extreme values[13],[14]. Additionally, bidirectional LSTM models incorporating attention mechanisms further enhance peak-valley modeling capabilities[9],[14],[15]. However, existing PVW strategies primarily focus on single-energy forecasting, leaving room for further exploration of comprehensive weighted methods for joint wind-PV-load forecasting in microgrids.

Based on the above analysis, this paper proposes an improved CNN-BiLSTM model incorporating peak-valley weighted forecasting for power load and wind-PV generation. First, MIV and PCC are jointly applied to screen highly correlated influencing factors of power load and wind-PV output as model inputs. Then, the CNN-BiLSTM model, combined with the peak-valley weight (PVW) strategy, improves peak and valley forecasting accuracy to achieve joint wind-PV-load forecasting.

979-8-3315-5472-9/25/$31.00 ©2025 IEEE

II. Data Preparation

To maximize model performance, various features affecting wind-PV-load forecasting must be considered, including historical load data, historical meteorological data, and calendar data. This study uses a dataset from a region in China, covering the period from May 1, 2024, to May 31, 2024, with a sampling interval of 1 hour.

A. Data Preprocessing

Numerical variables are filled using linear interpolation:

$$y = y_1 + \frac{(x - x_1)(y_2 - y_1)}{x_2 - x_1} \tag{1}$$

Wind direction is interpolated via vector decomposition:

$$\theta = \arctan 2\left(\sin(\theta), \cos(\theta)\right) mod 360° \tag{2}$$

Interaction feature: Relative humidity (U) and wind speed (Ff) are combined as:

$$U_{\mathrm{Ff}} = U \cdot Ff \tag{3}$$

The interquartile range (IQR) method is applied to determine bounds:

$$Q_1 - 1.5 \cdot \mathrm{IQR}, Q_3 + 1.5 \cdot \mathrm{IQR} \tag{4}$$

Where: Q_1 and Q_3 are the first and third quartiles, respectively. Outliers are replaced using linear interpolation.

B. Feature Correlation Analysis

Selecting appropriate input variables is crucial for forecasting performance. While too few features may limit accuracy, excessive features increase computational burden. Factors influencing wind-PV-load forecasting are numerous, necessitating correlation analysis to retain only the most impactful variables.

PCC is simple and efficient for linear relationships but fails to capture nonlinear dependencies. MIV relies on model-based analysis to identify nonlinear feature importance, complementing PCC's limitations.

Thus, this study proposes a hybrid PCC-MIV approach to enhance feature selection accuracy and comprehensiveness.

PCC measures linear correlation between two variables by computing the ratio of their covariance to the product of their standard deviations:

$$r_{x_y} = \frac{\sum_{i=1}^{n}(x_i - \bar{x})(y_i - \bar{y})}{\sqrt{\sum_{i=1}^{n}(x_i - \bar{x})^2 \cdot \sum_{i=1}^{n}(y_i - \bar{y})^2}} \tag{5}$$

Where: $\bar{x}$ and $\bar{y}$ are the means of x_i and y_i, respectively. The coefficient ranges from [-1, 1], with values near ±1 indicating strong linear correlation and values near 0 suggesting weak correlation.

MIV effectively guides feature selection by evaluating variable importance. In this study, Random Forest (RF) is employed for MIV computation. RF is an ensemble learning algorithm based on decision trees, which enhances forecasting accuracy and stability by aggregating multiple trees. The topological structure is illustrated in Fig 1.

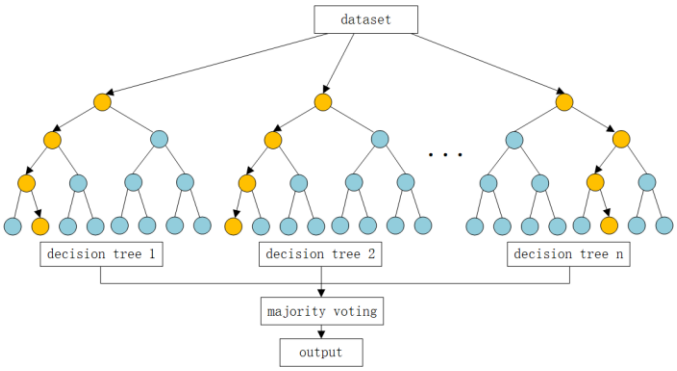


Fig. 1 Random forest topology diagram

It utilizes bootstrap sampling and random feature selection to enhance the model's generalization capability while mitigating overfitting risks. The random forest algorithm is not only applicable to both classification and regression tasks, but also provides feature importance scores that help identify the most influential features on the target variable, thereby offering robust support for feature selection and model interpretation.

III. CNN-BiLSTM-PVW-based Forecasting Model

The CNN-BiLSTM-PVW model consists of nonlinear and linear parts for accurate photovoltaic power forecasting. The nonlinear part is composed of convolutional layers (CNN), bidirectional long short-term memory layers (BiLSTM) and attention mechanisms, which are fused through multiple fully connected layers to generate nonlinear forecasting results. The convolutional layers extract local patterns of photovoltaic weather features, the BiLSTM captures long-term temporal dependencies, and the attention mechanism dynamically weights key time steps to enhance forecasting accuracy. The linear part adopts residual connections, where the features of the last time step in the input sequence are directly mapped to the forecasting length through fully connected layers to generate linear forecasting results. The results from the nonlinear and linear parts are additively combined to obtain the final 168-hour wind-PV-load forecasting results.

A. Convolutional Neural Network

CNN is a widely used feedforward neural network model in deep learning. Due to its strong feature learning capability and significant reduction in model parameters, it has achieved remarkable success in fields such as image recognition.

Currently, CNN has been widely applied in time series processing. Its local receptive field capability and weight-sharing characteristics significantly reduce the number of parameters, thereby improving the learning efficiency of the model. The first layer of CNN-LSTM-PVW adopts a convolutional network without pooling layers, aiming to capture short-term patterns in the time dimension and local dependency relationships between features. The convolutional layer consists of multiple filters with a width of ω and n input channels. The k-th filter scans the input sequence matrix X and produces:

$$h_k = RELU(W_k * X + b_k) \tag{6}$$

Where: $*$ denotes the convolution operation, h_k is the output vector, the RELU function is defined as RELU(x)=max(0,x), zero-padding is applied to the left side of matrix X to maintain each vector h_k at length, the output matrix of the convolutional layer has dimensions $d_c \times T$, where d_c represents the number of filters.

This article uses convolutional layers in CNNs to extract features from multivariate time series data, primarily to capture short-term patterns and local dependencies between variables from the time series data, uncover the relationships among multiple features, and effectively filter out noise and unstable components.

B. Bidirectional Long Short-Term Memory Network

The bidirectional long short-term memory neural network BiLSTM is an optimized improvement over the traditional unidirectional LSTM. BiLSTM combines a forward LSTM layer and a backward LSTM layer, both of which influence the output. Unidirectional LSTM can fully utilize historical load data information and avoid long-distance dependency issues, while BiLSTM benefits from both forward sequence information input and backward sequence information input, fully considering past and future information, which helps to further improve model forecasting accuracy.

The BiLSTM structure is shown in Fig 2. Among them, $x_1, x_2, x_3, \ldots, x_t$ represent the corresponding input data at each time point$t_1 \sim t_i (i \in [1 \sim i])$: $A_1, A_2, A_3, \ldots, A_t, B_1, B_2, B_3, \ldots, B_t$ represent the corresponding forward and backward iterating LSTM hidden states, $Y_1, Y_2, Y_3, \ldots, Y_t$ represent the corresponding output data, $\omega_1, \omega_2, \omega_3, \ldots, \omega_6$ represent the corresponding weights of each layer.

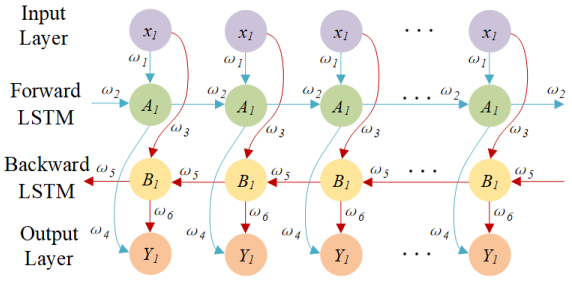


Fig. 2 BiLSTM neural network structure

The forward LSTM, backward LSTM hidden layer update states and the final BiLSTM output process are as follows:

$$A_i = f_1(\omega_1 x_i + \omega_2 A_{i-1}) \tag{7}$$

$$B_j = f_2(\omega_3 x_i + \omega_5 B_{i+1}) \tag{8}$$

$$Y_i = f_3(\omega_4 A_i + \omega_6 b_i) \tag{9}$$

Where: f_1, f_2, f_3 are the activation functions between different layers.

Through BiLSTM, sequence information can be selectively remembered or forgotten, longer load sequences can be processed, while reducing the risk of gradient runaway during model training. Therefore, compared to typical RNN, it is more suitable for the temporal feature extraction in this paper.

C. Improved Weighted MSE Loss Function

The weighted MSE (Mean Squared Error) loss function enhances forecasting accuracy at critical points by assigning differential weights to different timesteps. To improve peak and valley forecasting accuracy, this paper proposes an innovative weighting optimization strategy: the PVW mechanism. The PVW mechanism dynamically adjusts weights in the weighted MSE loss to amplify the error contributions from peaks and valleys, thereby prioritizing optimization of these grid operation-critical points. This weighting strategy is specifically designed to accommodate the high volatility characteristic of renewable generation and power load in microgrids, effectively improving model performance under extreme scenarios.

The core of PVW is to dynamically adjust the weights of each time step in the loss function, making the forecasting errors of peaks and valleys contribute more to model optimization. Its mathematical formula is as follows:

$$Weighted\ MSE\ = \frac{1}{BT} \Sigma_{b=1}^{B} (t-1)^T w_{b,t} \left(y_{b,t} - \hat{y}_{b,t}\right)^2 \tag{10}$$

Where: B is the batch size, T is the forecasting length, $y_{b,t}$ and $\hat{y}_{b,t}$ are the actual and predicted values respectively, and $w_{b,t}$ is the weight, defined as follows:

$$W_{b,t} \begin{cases} 5.0 * w_{base} & if\ t\ is\ a\ peak\ in\ day \\ 3.0 * w_{base} & if\ t\ is\ a\ valley\ in\ day \\ 2.0 & if\ y_{\{b,t\}} > \mu_b + \sigma_b \\ 1.5 & if\ y_{\{b,t\}} < \mu_b - \sigma_b \\ 1.0 & otherwise \end{cases} \tag{11}$$

Where: w_{base} is the base weight, 2.0 for high output, 1.5 for low output, and μ_b and σ_b are the mean and standard deviation of the b-th batch.

Peaks and valleys are determined by the maximum and minimum values of the 24-hour daily subsequence, with weights of 5.0 and 3.0 respectively, highlighting the importance of peaks for grid peak regulation. The weights are constrained as follows to prevent numerical instability:

$$W_{b,t} = clamp\left(W_{b,t}, min = 10^{-6}, max = 10^{6}\right) \tag{12}$$

IV. Case Study Analysis

The dataset from a specific region in China was used as the research object. The data processing and feature extraction methods proposed in Section 1 were applied, with data from May 1 to May 24, 2024 serving as the training set, and data from May 25 to May 31, 2024 as the test set. Using a 1-hour time step, forecastings were made for future renewable generation and load.

First, the collected renewable generation and power load data underwent preprocessing to generate lag features and handle outliers and missing values. PCC was employed to select features highly correlated with power output and load, while MIV was used to evaluate feature importance for forecasting, eliminating redundant information. The data was then standardized and divided into training, validation, and test sets.

Next, the CNN-BiLSTM-PVW model was constructed. The CNN module extracted spatiotemporal features through multiple

convolutional operations, capturing nonlinear local patterns in generation data and meteorological data. The BiLSTM hidden layer modeled long-term dependencies, iteratively extracting global features. Model outputs were processed through fully connected layers and residual connections to generate forecasting results.

To enhance robustness, data augmentation techniques were introduced, including replication of high-wind-speed and peak-load samples. During training, optimization algorithms were used to update parameters, while the PVW mechanism assigned higher weights to peaks and valleys through the weighted loss function, improving forecasting accuracy at these critical points and suppressing redundant interference.

Dropout techniques prevented overfitting, and early stopping mechanisms improved training efficiency. Finally, the trained model was saved and evaluated on the test set, generating visual results and saving data, with particular focus on analyzing errors during PVW-optimized peak, valley, and high-wind-speed periods.

A. Experimental Evaluation Metrics

To comprehensively evaluate the predictive performance of the proposed model, three metrics were selected: Mean Absolute Error (MAE), Root Mean Square Error (RMSE), Mean Absolute Percentage Error (MAPE).

The mathematical formulations are as follows:

$$\mathrm{MAE} = \frac{1}{n}\sum_{i=1}^{n}|y_i - \hat{y}_i| \tag{13}$$

$$\mathrm{RMSE} = \sqrt{\frac{1}{n}\sum_{i=1}^{n}(y_i - \hat{y}_i)^2} \tag{14}$$

$$\mathrm{MAPE} = \frac{100}{n}\sum_{i=1}^{n}\left|\frac{y_i - \hat{y}_i}{y_i}\right| \tag{15}$$

Where: y_i is Actual value, $\hat{y}_i$: Predicted value, n: Total number of samples.

B. Experimental Setup

The forecasting model in this paper contains 2 hidden layers, with each hidden layer being a bidirectional LSTM layer. Additionally, the model incorporates an Attention mechanism that assigns adaptive weights to each timestep of the sequence, enhancing the model's ability to model peaks and critical undervalued moments. PVW is used to enhance the forecasting accuracy of the CNN-BiLSTM model for critical moments (peaks, valleys, and early morning periods).

C. Experimental Results Analysis

In this study, the power load, photovoltaic output, and wind power output dataset was used as a case study for analysis. The sampling frequency was once per hour, with a total of 744 samples for each dataset. Data from May 1 to May 24, 2024 was used as the training set, while data from May 25 to May 31, 2024 served as the test set.

To compare the accuracy of forecasting models, CNN-BiLSTM and BiLSTM were used as comparative experiments for CNN-BiLSTM-PVW to analyze the accuracy of the combined model. The results are shown in Fig 3-5. It can be observed that compared to CNN-BiLSTM, BiLSTM, CNN-BiLSTM-PVW, LightGBM and XGBoost demonstrates more precise forecasting capabilities for peaks and valleys.

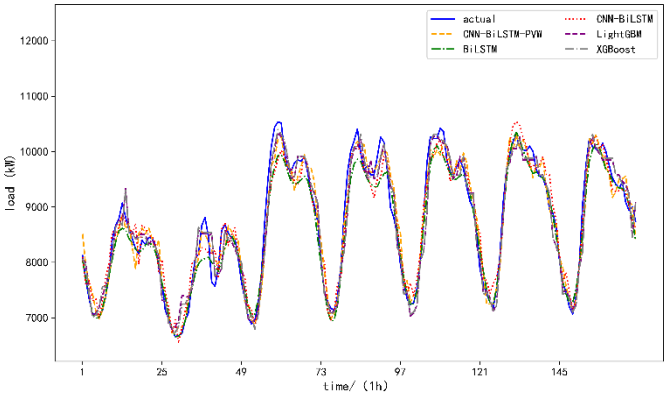


Fig. 3 Comparison of electrical load forecasting results

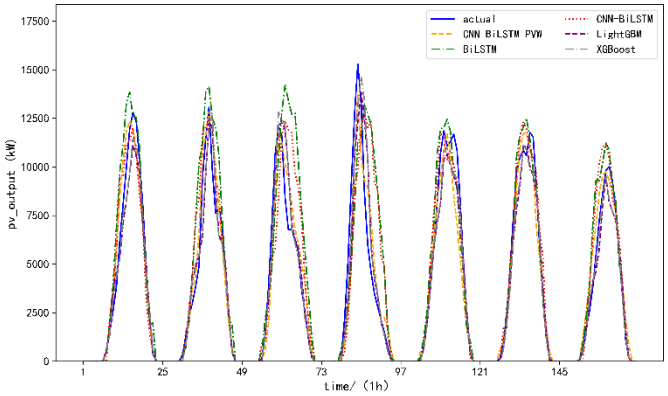


Fig. 4 Comparison of PV output forecasting results

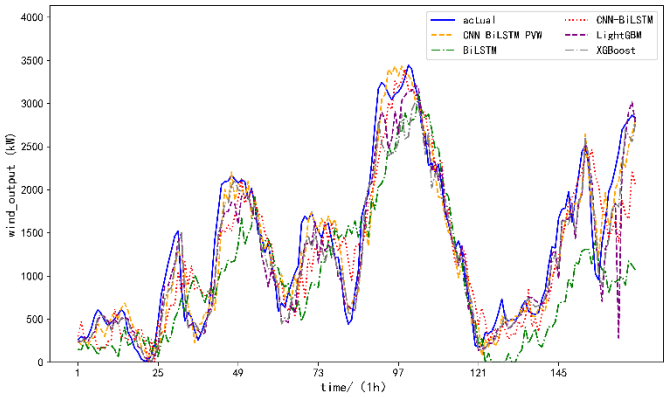


Fig. 5 Comparison of wind output forecasting results

TABLE I. OMPARISON OF MODEL ACCURACY

Model	Load/PV/Wind		
	MAE/kW	***RMSE/kW***	***MAPE/%***
CNN-BiLSTM-PVW	192/671/198	257/1096/256	2.01/17.52/8.58
CNN-BiLSTM	203/1060/310	265/1848/402	2.12/27.69/13.77
BiLSTM	217/1203/524	274/2113/659	2.52/31.40/29.94
LightGBM	201/1089/327	268/1941/499	2.32/28.38/15.90
XGBoost	205/1048/310	274/1799/422	2.50/24.31/13.87

The MAE, RMSE, and MAPE metrics for each method on the test set were calculated, with results shown in TABLE I. Among them, CNN-BiLSTM-PVW achieved the best forecasting performance across load, PV, and wind power datasets, consistently exhibiting the lowest MAE, RMSE, and MAPE. CNN-BiLSTM ranked second for load and wind power.

V. CONCLUSIONS

This paper proposes a short-term wind-PV-load forecasting method based on peak-valley weighted loss for microgrid renewable energy systems, using historical power load and renewable generation data from a specific region in China as a case study. The main conclusions are as follows:

1) Compared with the single feature correlation analysis algorithm PCC, this study combines MIV to evaluate features and proposes a comprehensive correlation score, which compensates for PCC's inability to capture nonlinear relationships. This approach enhances the correlation between input variables and target outputs, resulting in better overall forecasting performance of the model.

2) In comparison with BiLSTM and CNN-BiLSTM models, the CNN-BiLSTM-PVW model with peak-valley weighted loss improves forecasting accuracy for both peak and valley points by applying higher weights to daily maximum and minimum points, thereby enhancing the overall forecasting accuracy of the model.

REFERENCES

[1] Z. Liu, X. Wang, H. Yu, J. Gao, G. Wu. "Cost-benefit analysis and interactive electricity pricing between microgrid and distribution network," *Electric Power Construction*, vol. 41, no. 3, pp. 39-46 2020.

[2] Y. Wang, R. Zou, F. Liu, L. Zhang, and Q. Liu, "A review of wind speed and power forecasting with deep learning models," *Applied Energy*, vol. 304, pp. 117766-117773, 2022.

[3] N. Zhang, Q. Sun, L. Yan, B. Huang. "A bi-level adaptive control strategy for self-energy considering security and economy," *Journal of the Chinese Society of Electrical Engineering*, vol. 40, no. S1, pp. 155-166, 2020.

[4] M. J. Sanjari, H. B. Gooi, and N. C. S. Nair, "Power generation forecast of hybrid photovoltaic-wind system," Renewable Energy, vol. 75, pp. 1032-1043, 2020.

[5] M. Liu, P. Wang, W. Bi, W. Jiang, "Design and implementation of microgrid state monitoring and coordinated control system," *Digital Manufacturing Science*, vol. 18, no. 3, pp. 189–193, 2020.

[6] F. Zhang, L. Mou, Z. Wang, H. Zhou, and X. Zhang, "Optimized fault control strategy for master-slave controlled islanded microgrid," *Proceedings of the CSEE*, vol. 40, no. 4, pp. 1241–1248, 1414, 2020.

[7] H. Liang, H. Liu, J. Li, Y. Wang, and C. Guo, "Survey of short-term load forecasting algorithms based on machine learning," *Computer Systems & Applications*, vol. 31, no. 10, pp. 25–35, 2022.

[8] L. Liang, et al., "Research on short-term power system load forecasting technology integrating multiple AI models," *Power Systems and Big Data*, vol. 25, no. 6, pp. 16-23, 2022.

[9] C. Chen, H. Ma, L. Chen, B. Ren, C. Jin, and T. Zhang, "Multi-step short-term load forecasting method based on user group classification," *High Voltage Engineering*, vol. 49, no. 10, pp. 4213-4222, 2023.

[10] Y. Shi, L. Zhang, and Z. Long, "Research on accurate power load forecasting method in smart grid based on deep learning," *Power Systems and Big Data*, vol. 24, no. 4, pp. 35-40, 2021.

[11] H. Zhao, H. Lu, Z. Li, X. Wang, and B. Li, "Two-stage robust optimization operation strategy for CCHP microgrid with energy storage considering wind-PV uncertainty in market environment," *Electric Power Construction*, vol. 41, no. 11, pp. 116-125, 2020.

[12] H. Wang, et al., "Review and prospects of key technologies for integrated vehicle-station-grid operation in smart cities," *Transactions of China Electrotechnical Society*, vol. 37, no. 1, pp. 112-132, 2022.

[13] K. Wang, X. Qi, and H. Liu, "Photovoltaic power forecasting based LSTM-Convolutional Network," *Energy*, vol. 189, p. 116225, 2019.

[14] S. M. Malakouti, A. R. Ghiasi, A. A. Ghavifekr, and M. Rahimi, "Advanced techniques for wind energy production forecasting: Leveraging multi-layer perceptron, Bayesian optimization, ensemble learning, and CNN-LSTM models," Case Studies in Chemical and Environmental Engineering, vol. 10, p. 100881, 2024.

[15] J. Fan, H. Yu, H. Liu, L. Yang, and J. An, "Short-term power load forecasting based on multi-branch gated residual convolutional neural network," *Electric Power*, vol. 55, no. 11, pp. 155-162, 174, 2022.

Inertia Evaluation Method for Power Systems with Integration of Wind Farms Under Colored Measurement Noise

Yongkang Luo
College of Dayu, Hohai University
Nanjing, China
connorluo0423@gmail.com

Mingjiang Liu
Huaneng International Power Jiangsu Energy Development Co., Ltd. Clean Energy Branch
Nanjing, China

Yu Zhang
Huaneng International Power Jiangsu Energy Development Co., Ltd. Clean Energy Branch
Nanjing, China

Ziwen Liu
School of Electrical and Power Engineering, Hohai University
Nanjing, China
liuziwen@hhu.edu.cn

Xingwei Che
Huaneng International Power Jiangsu Energy Development Co., Ltd. Clean Energy Branch
Nanjing, China

Xiangyu Meng
Huaneng International Power Jiangsu Energy Development Co., Ltd. Clean Energy Branch
Nanjing, China

***Abstract*—With the integration of high proportion of new energy, the power system gradually exhibits low inertia characteristics. Accurately evaluating the system inertia is of great significance for the safe and stable operation of the power system. However, the colored measurement noise greatly influences on the collection data resulting bias of inertia evaluation. This paper proposes a power system inertia evaluation method based on Improved Adaptive Kalman Filter (IAKF) algorithm. Firstly, the filtering state equation and measurement equation are derived by applying the forward Euler method on the swing equation. Then to decrease the influence of colored noise and data saturation, this article estimates the statistical characteristics of the colored measurement noise, imports the forgetting factor to form the improved filtering gain and proposes the IAKF algorithm. Finally, the effectiveness and superiority of the algorithm proposed in this paper are verified through simulation examples.**

Keywords—Adaptive Kalman Filter; Colored Noise; Inertia Evaluation of Power System; System Identification

I. INTRODUCTION

With the gradual depletion of fossil fuels and worsening environmental issues, China's power system is incorporating a growing share of new energy sources, DC transmission networks, and other power electronic devices. The conventional AC system, dominated by synchronous machines, is evolving into a new type of power system with a high penetration of power electronics. [1]. While renewable integration and DC transmission help alleviate energy shortages and climate concerns, they also introduce weak grid support capabilities that threaten frequency stability. Major blackouts, such as those in the UK, Brazil, and South Australia, have been linked to low system inertia [2]. Accurately assessing system inertia is therefore essential for safe and stable grid operation.

Current methods for inertia evaluation include measurement data processing, electromechanical disturbance propagation, and system identification [3]. System identification, which constructs dynamic models from measured data, is widely used. However, measurement noise can reduce accuracy, prolong convergence, or cause model divergence. Most existing methods perform well only under white noise; their accuracy degrades under colored noise. Although adaptive Kalman filtering has been introduced to estimate noise statistics and improve system identification, it suffers from data saturation over extended recursions, reducing evaluation precision—a limitation not adequately addressed in prior work.

Existing studies have addressed various aspects of inertia evaluation. Reference [4] analyzed spatial-temporal inertia distribution and established inertia requirements for stability. References [5, 6] developed identification models using multi-innovation methods for nodal inertia assessment. Reference [7] proposed a Cubature Kalman Filter (CKF)-based approach incorporating real-time partitioning of frequency response. Nevertheless, these methods assume white measurement noise and perform poorly under colored noise conditions. Although reference [8] introduced adaptive Kalman filtering to estimate noise statistics and improve identification under colored noise, the method suffers from data saturation over extended recursion, reducing evaluation accuracy.

This paper first derives the equation for calculating the inertia time constant based on the swing equation, and uses the forward Euler method to form the difference equation of frequency change with respect to power change in order to form the state equation and measurement equation of the Kalman filter. Next, the Improved Adaptive Kalman Filter (IAKF) algorithm is proposed as the basic method for inertia

This work is supported by China Huaneng Group Co., Ltd. Headquarters Science and Technology Project (No. HNKJ24-H68): Research on Key Technologies for Safe and Stable Operation of Grid-connected Offshore Wind Farms.

979-8-3315-5472-9/25/$31.00 ©2025 IEEE

evaluation of power systems. By estimation of the statistical characteristics of colored measurement noise to replace the prior statistical characteristics of measurement noise in the conventional Kalman filter algorithm, an improved filtering gain is formed to lessen the effect of colored noise. Finally, this method is applied for simulation based on the IEEE 30 node system to verify the accuracy and superiority of this algorithm.

II. INERTIA OF POWER SYSTEM WITH INTEGRATION OF WIND FARMS

A. Definition of Inertia for Power Systems with Wind Power Integration

Inertia in power systems refers to the capability to resist frequency changes using available energy before primary frequency control acts. [9, 10]. In this article, the inertia of the power system refers to the inertia time constant H.

For a synchronous machine, the kinetic energy of the rotor is given by:

$$E_k = \frac{1}{2} J \omega_n^2 \tag{1}$$

where E_k is the kinetic energy of a single synchronous machine rotor, J is the moment of inertia of the synchronous machine rotor, and ω_n is the angular velocity. The inertia time constant is then defined as:

$$H = \frac{E_k}{S_N} = \frac{J\omega_n^2}{2S_N} \tag{2}$$

where S_N is the rated capacityof the synchronous machine. With integration of renewable sources such as wind power, virtual inertia control can provide additional inertia support. [11]. Including load contributions, the total system inertia time constant becomes:

$$H_{sys} = \frac{E_{rsg} + E_{ssg} + E_{load}}{S_{sys}} \tag{3}$$

where H_{sys} is the total inertia time constant of the system, E_{rsg} is the rotational kinetic energy of the synchronous machine, E_{ssg} is the energy provided by unconventional power sources such as wind farms through virtual inertia control, E_{load} is the energy provided to the load, and S_{sys} is the total capacity of the system.

B. Inertia Response and Evaluation of Power System

Inertia response of power system refers to the dynamic process in which synchronous generators release or absorb energy through rotor kinetic energy when the system frequency fluctuates due to power imbalance, in order to slow down frequency changes and maintain system stability [12]. The inertia response process of the power system can be described by the oscillation equation, and based on this, the relationship between electromagnetic power and the rate of change of frequency in the power system can be obtained by

$$2H_{sys}\left(df(t)/dt\right) = P_m - P_e - D\Delta f(t) \tag{4}$$

where $df(t)/dt$ is the RoCoF, Pe is the electromagnetic power, D is the damping coefficient, and $\Delta f(t)$ is the frequency change amount.

It can be obtained by forward Euler method as:

$$\Delta f(k+1) = \left[\Delta P_e(k) \quad \Delta f(k)\right] \cdot \begin{bmatrix} -\dfrac{T_s}{2H_{sys}} \\ 1 - \dfrac{DT_s}{2H_{sys}} \end{bmatrix} \tag{5}$$

where, T_s is the sampling period.

III. INERTIA EVALUATION ALGORITHM BASED ON IAKF

A. The Basic Process of Kalman Filter

Based on (5), the measurement matrix and parameters to be estimated are defined, leading to:

$$\Delta f_{k+1} = \Delta f(k+1) = \boldsymbol{\varphi}_{k+1}\boldsymbol{\theta}_{k+1} + v_{k+1} \tag{6}$$

where v_{k+1} represents colored measurement noise. Taking the parameters $\boldsymbol{\theta}$ as state variables, the state and measurement equations for the Kalman filter are:

$$\begin{cases} \boldsymbol{\theta}_{k+1} = \boldsymbol{\theta}_k + \boldsymbol{w}_{k+1} \\ \Delta f_{k+1} = \boldsymbol{\varphi}_{k+1}\boldsymbol{\theta}_{k+1} + v_{k+1} \end{cases} \tag{7}$$

where $\boldsymbol{w}_{k+1}$ is system noise.

Using prior identification results, the parameter estimate and its covariance are projected:

$$\begin{cases} \hat{\boldsymbol{\theta}}_{k|k-1} = \hat{\boldsymbol{\theta}}_{k-1|k-1} \\ \boldsymbol{P}_{k|k-1} = \boldsymbol{P}_{k-1|k-1} \end{cases} \tag{8}$$

The innovation $\Delta\tilde{f}_k$ is computed as:

$$\Delta\tilde{f}_k = \Delta f_k - \boldsymbol{\varphi}_k\hat{\boldsymbol{\theta}}_{k|k-1} = \boldsymbol{\varphi}_k\tilde{\boldsymbol{\theta}}_k + v_k \tag{9}$$

where $\tilde{\boldsymbol{\theta}}_k = \boldsymbol{\theta}_k - \hat{\boldsymbol{\theta}}_{k|k-1}$. Taking covariance on both sides yields:

$$\boldsymbol{C}_k = \boldsymbol{\varphi}_k\boldsymbol{P}_{k|k-1}\boldsymbol{\varphi}_k^T + \boldsymbol{R}_k \tag{10}$$

Then calculate the filtering gain

$$\boldsymbol{K}_{k+1} = \boldsymbol{P}_{k|k-1}\boldsymbol{\varphi}_k^T\left(\boldsymbol{\varphi}_k\boldsymbol{P}_{k|k-1}\boldsymbol{\varphi}_k^T + \boldsymbol{R}_k\right)^{-1} \tag{11}$$

Use the filtering gain to modify the prediction equation:

$$\begin{cases} \hat{\boldsymbol{\theta}}_{k|k} = \hat{\boldsymbol{\theta}}_{k|k-1} + \boldsymbol{K}_k\Delta\tilde{f}_k \\ \boldsymbol{P}_{k|k} = \left(\boldsymbol{I} - \boldsymbol{K}_k\boldsymbol{\varphi}_k\right)\boldsymbol{P}_{k|k-1} \end{cases} \tag{12}$$

B. Inertia Identification Based on IAKF

In practical applications, the covariance matrix $\boldsymbol{R}_k$ of colored measurement noise $\boldsymbol{v}_k$ is often unknown and difficult to determine in advance. When the statistical properties of $\boldsymbol{v}_k$ are

unavailable, adaptive estimation of these parameters can be used to improve filtering accuracy and system model matching.

Since the filtering gain $\boldsymbol{K}_k$ depends on $\boldsymbol{R}_k$, adjusting $\boldsymbol{K}_k$ indirectly compensates for the uncertainty in noise statistics. From equations (10) and (11), $\boldsymbol{C}_k$ appears in the denominator of $\boldsymbol{K}_k$ and contains $\boldsymbol{R}_k$. An estimate $\hat{\boldsymbol{C}}_k$ can be obtained via a moving average of the innovation sequence:

$$\hat{\boldsymbol{C}}_k = \frac{1}{N}\sum_{i=k-N+1}^{k} \Delta\tilde{\boldsymbol{f}}_i^2 \tag{13}$$

To mitigate data saturation effects, weighting coefficients are introduced with a forgetting factor b

$$\sum_{i=1}^{k}\alpha_i = 1, \alpha_{i-1} = \alpha_i b, 0 < b < 1 \tag{14}$$

Construct the weighting coefficients as follows:

$$\begin{cases} \alpha_i = d_k b^{k-i} \\ d_k = \dfrac{1-b}{1-b^k} \end{cases}, i = 1, 2, \cdots, k \tag{15}$$

For computational efficiency, a recursive form is derived:

$$\begin{cases} \hat{\boldsymbol{C}}_k = (1-d_k)\hat{\boldsymbol{C}}_{k-1} + d_k \Delta\tilde{\boldsymbol{f}}_k \Delta\tilde{\boldsymbol{f}}_k^T & ,k \le N \\ \hat{\boldsymbol{C}}_k = (1-d_k)\hat{\boldsymbol{C}}_{k-1} + d_k \left(\Delta\tilde{\boldsymbol{f}}_k \Delta\tilde{\boldsymbol{f}}_k^T \right. \\ \quad \left. -\Delta\tilde{\boldsymbol{f}}_{k-N}\Delta\tilde{\boldsymbol{f}}_{k-N}^T\right) & ,k > N \end{cases} \tag{16}$$

The term $\hat{\boldsymbol{C}}_k$ containing innovation information, approximates the actual noise variance. Replacing the denominator in (11) with $\hat{\boldsymbol{C}}_k$ yields an adaptive filtering gain:

$$\boldsymbol{K}_k = \boldsymbol{P}_{k|k-1}\boldsymbol{\varphi}_k^T \hat{\boldsymbol{C}}_k^{-1} \tag{17}$$

The complete adaptive Kalman filter algorithm with improved gain adjustment is summarized as:

$$\begin{cases} \boldsymbol{K}_k = \boldsymbol{P}_{k|k-1}\boldsymbol{\varphi}_k^T \hat{\boldsymbol{C}}_k^{-1} \\ \hat{\boldsymbol{\theta}}_k = \hat{\boldsymbol{\theta}}_{k|k-1} + \boldsymbol{K}_k\left(\Delta\boldsymbol{f}_k - \boldsymbol{\varphi}_k\hat{\boldsymbol{\theta}}_{k|k-1}\right) \\ \boldsymbol{P}_{k|k} = \left(\boldsymbol{I} - \boldsymbol{K}_k\boldsymbol{\varphi}_k\right)\boldsymbol{P}_{k|k-1} \\ \hat{\boldsymbol{C}}_k = \hat{\boldsymbol{C}}_{k-1} + d_k\boldsymbol{e}_{k+1}\boldsymbol{e}_{k+1}^T \\ \alpha_i = d_k b^{k-i}, i = 1, 2, \cdots, k \\ d_k = \dfrac{1-b}{1-b^k} \end{cases} \tag{18}$$

This approach reduces the influence of colored measurement noise through adaptive estimation of $\boldsymbol{C}_k$, while the forgetting factor mitigates data saturation.

IV. Simulation Result Analysis

To verify the reliability and accuracy of the inertia evaluation method for power systems based on improved adaptive filtering under colored measurement noise proposed in this paper, an IEEE 30 node system as shown in Fig. 1. is used for verification. The system includes 13 generators, including 6 synchronous generators and 3 wind farms. Node 1 is a balance node, and the inertia setting of the generator connected to this node is relatively large, so there is no need for identification. The simulation parameters of the generator are shown in TABLE I.

TABLE I. Generator Simulation Parameters

Generator	Inertia time constant (s)	rated capacity (MVA)
Gen2	5.23	285
Gen3	4.32	273
Gen5	3.26	200
Gen6	3.51	315
Gen7	3.44	240
Gen8	3.36	100

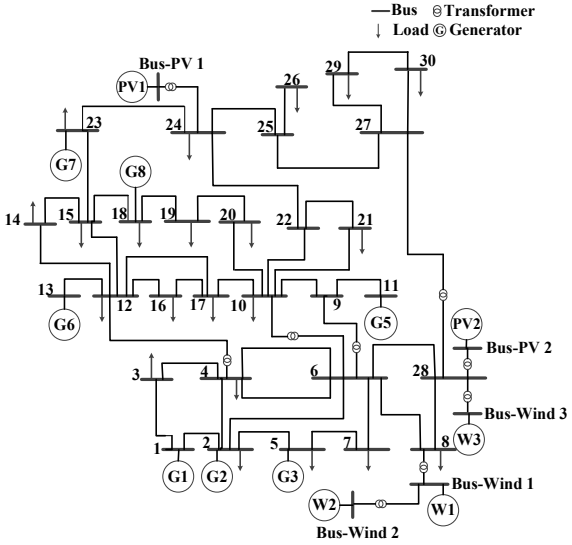


Fig. 1. IEEE 30 Node System Model

A. Inertia Evaluation of Synchronous Generator

To evaluate system equivalent inertia without prior knowledge of measurement noise, small random load perturbations (±10%) were applied to buses 2, 5, 8, 15, 23, and 26 during steady-state operation. A total of 19,400 data points of active power and frequency variations from each synchronous generator during 6–200 s were used to form the measurement matrix for identification. Fig. 2. shows the power and frequency variations of Gen2 over 200 seconds.

The evaluation error is defined as:

$$\delta_i = \left|\frac{H_i - H_N}{H_N}\right| \times 100\% \tag{19}$$

where H_i is the estimated inertia time constant and H_N is the nominal value.

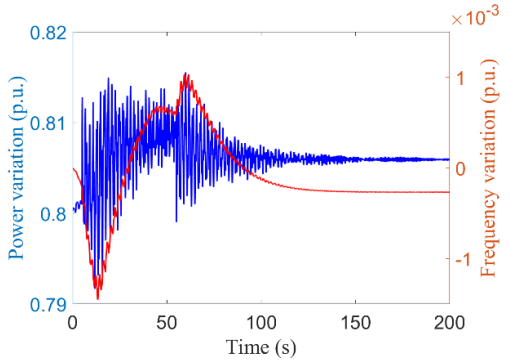


Fig. 2. Power and Frequency Variations

As shown in Fig. 3, the proposed method accurately evaluates system inertia under noise-free conditions, with errors below 2%. The lowest error was 0.1641% (Gen5), and the highest was 1.4033% (Gen2), demonstrating high accuracy.

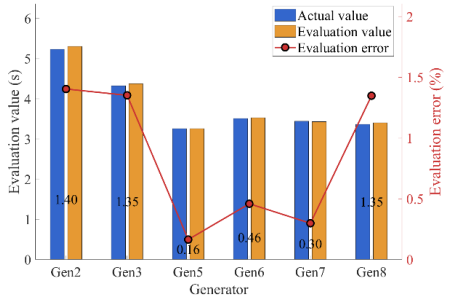


Fig. 3. Inertia Evaluation Results with Noise Free

To verify performance under noise, white and colored noise (zero-mean, amplitude 1.5% of signal) were added to the same dataset. Under white noise (shown in TABLE II), errors remained below 2%, with the lowest error of 0.2243% (Gen2) and the highest of 1.1726% (Gen8). Under colored noise (shown in TABLE III), errors were also controlled within 2%, ranging from 0.5317% (Gen7) to 1.2201% (Gen6). These results confirm the method's strong noise immunity and consistent accuracy under both white and colored noise.

TABLE II. EVALUATION RESULTS WITH WHITE MEASUREMENT NOISE

Generator	Evaluation value (s)	Error (%)
Gen2	5.2183	0.2243
Gen3	4.2857	0.7937
Gen5	3.2331	0.8263
Gen6	3.4765	0.9539
Gen7	3.4731	0.9622
Gen8	3.3206	1.1726

TABLE III. EVALUATION RESULTS WITH WHITE COLORED NOISE

Generator	Evaluation value (s)	Error (%)
Gen2	5.1774	1.0051
Gen3	4.3457	0.5950
Gen5	3.2958	1.0988
Gen6	3.4592	1.2201
Gen7	3.4217	0.5317
Gen8	3.2877	0.8597

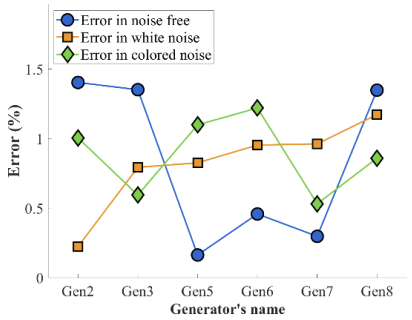


Fig. 4. Evaluation Error Under Different Noise Environment

The algorithm was further tested under varying noise statistics: the first 9,700 points contained white noise and the last 9,700 points colored noise (both at 1.5% amplitude). As shown in Table IV and Fig. 5, all errors remained below 3%. The lowest error was 0.6356% (Gen5), and the highest was 2.6981% (Gen2). The minimal increase in error compared to the noise-free case confirms the method's adaptability and reliability under time-varying noise conditions.

TABLE IV. EVALUATION RESULTS WITH CHANGES IN STATISTICAL CHARACTERISTICS OF MEASUREMENT NOISE

Generator	Evaluation value (s)	Error (%)
Gen2	5.3711	2.6981
Gen3	4.3634	1.0048
Gen5	3.2393	0.6356
Gen6	3.5416	0.8989
Gen7	3.3766	1.8418
Gen8	3.3091	1.5159

In all cases, the proposed method delivered high accuracy with errors consistently below 3%, effectively validating its robustness and practical applicability in both steady and varying noise environments.

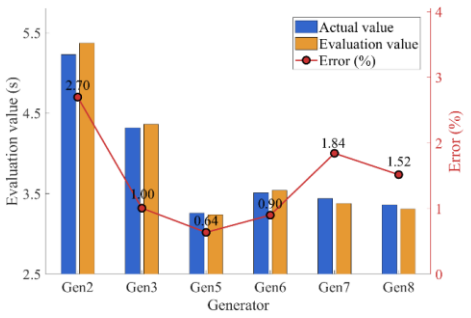


Fig. 5. Inertia Evaluation Results with Changes in Noise Statistical Characteristics

B. *Comparison of the Effectiveness of Different Evaluation Algorithms*

To demonstrate the superiority of the proposed IAKF algorithm, its performance is compared with the Cubature Kalman Filter (CKF) [7] and the Unscented Kalman Filter with Fixed Lag Smoother (UKF-FLS) [13] under the same conditions described in Section A.

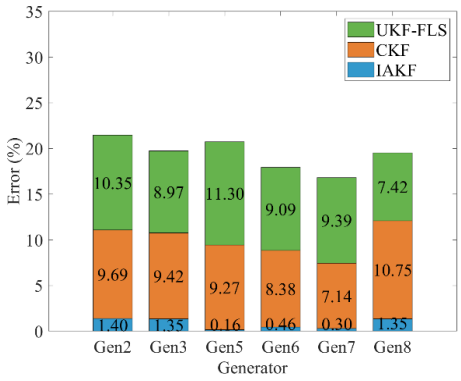


Fig. 6. Evaluation Errors of Different Methods with Colored Noise

TABLE V. EVALUATION VALUES USING DIFFERENT METHODS UNDER COLORED NOISE

Generator	IAKF (s)	CKF (s)	UKF-FLS (s)
Gen2	5.3034	4.7230	4.6885
Gen3	4.3784	3.9131	3.9325
Gen5	3.2546	2.9577	2.8915
Gen6	3.5261	3.2157	3.1911
Gen7	3.4297	3.1945	3.1170
Gen8	3.4053	2.9987	3.1107

As shown in TABLE V and Fig. 6, under colored measurement noise with unknown statistics, the IAKF method maintains evaluation errors within 2%, matching its accuracy in noise-free conditions. In contrast, both UKF-FLS and CKF exhibit significantly larger errors, around 10%, indicating lower identification accuracy.

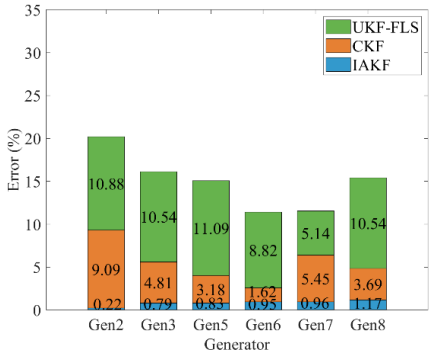


Fig. 7. Evaluation Errors of Different Methods with White Noise

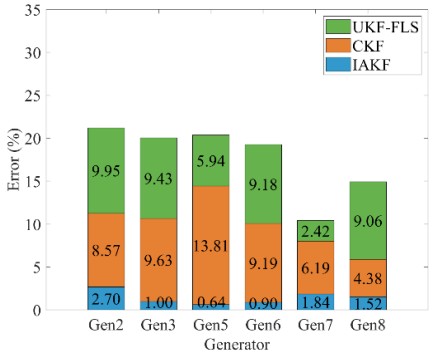


Fig. 8. Evaluation Errors of Different Methods with Change of Noise Statistical Characteristics

Furthermore, under zero-mean white noise and time-varying noise conditions (Figs. 7 and 8), the proposed IAKF algorithm consistently achieves higher accuracy than the other two methods. These results confirm the superiority and robustness of the IAKF approach across diverse noise environments.

C. Identification of Equivalent Inertia of Wind Farm

To further validate the proposed method, the equivalent inertia time constants of wind turbines Wind1, Wind2, and Wind3—connected to Bus-Wind1, Bus-Wind2, and Bus-Wind3 in a standard 13-wind-turbine 30-node system—were identified. The same small disturbance method as in Section A was applied, and frequency/power deviation data from the grid-connected buses were used. White and colored noise (1.5% of signal amplitude) were added to simulate real measurement conditions.

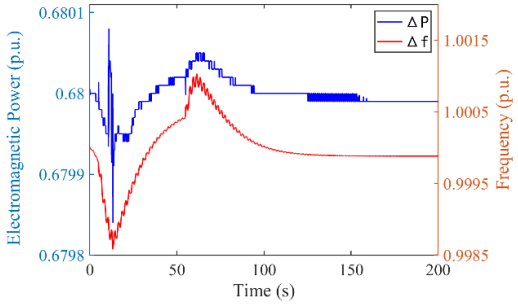


Fig. 9. Frequency and Power Fluctuations of Wind1

The equivalent inertia evaluation values of wind farms with and without noise are shown in TABLE VI and Fig. 10. As references [14, 15] indicate, the equivalent inertia of wind turbines exhibits time-varying characteristics due to the coupling of internal operating parameters. Therefore, the average of multiple inertia evaluations was used as the actual value for accuracy validation.

TABLE VI. EVALUATION VALUES OF WIND FARMS UNDER DIFFERENT NOISE

Wind farm	Noise free (s)	White noise (s)	Colored noise (s)
Wind1	4.4568	4.6611	4.4659
Wind2	3.2381	3.1333	3.3234
Wind3	2.1107	2.2607	2.0784

Under noise-free conditions, the evaluation error was controlled within 5%, with the minimum error of 0.2953% (Wind1) and the maximum error of 4.4932% (Wind3), verifying the effectiveness of the proposed method in an ideal environment. In the presence of zero-mean white noise, the error remained below 5%, with the lowest error of 0.1054% (Wind2) and the highest error of 4.2506% (Wind1), demonstrating that the algorithm maintains good performance under common noise interference. When subjected to colored noise, the evaluation error was contained within 7%, ranging from a minimum of 0.0917% (Wind1) to a maximum of 6.1789% (Wind2), indicating that the method still maintains high accuracy under complex noise conditions.

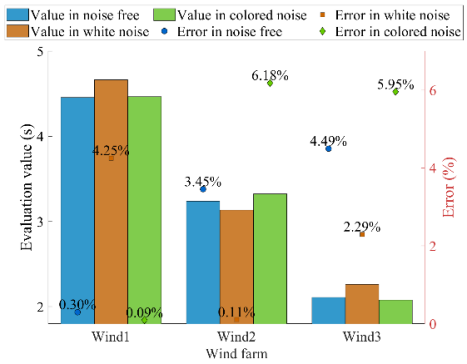


Fig. 10. Inertia Evaluation Results of Wind Farms in Different Noise Conditions

Therefore, the above example analysis can verify the accuracy and superiority of the IAKF algorithm proposed in this paper for evaluating the equivalent inertia of power systems with wind power access under the influence of colored noise.

While the proposed method demonstrates high accuracy and robustness, it has certain limitations. First, the recursive estimation and matrix operations introduce additional computational cost, which may pose challenges in real-time applications for very large-scale power systems. Second, the method depends on sufficient measurement data quality; severe data loss or distortion could reduce estimation accuracy. Future research will focus on reducing computational burden and enhancing data resilience, such as integrating data-driven approaches or hybrid estimation frameworks.

V. Conclusions

This article is based on an improved adaptive filtering method for evaluating the equivalent inertia of power systems with wind power access under the influence of colored noise. The main conclusions obtained are as follows

1) Algorithm: A power system inertia evaluation method based on improved adaptive filtering is proposed, which solves the problem of biased algorithm estimation results when the statistical characteristics of measurement noise are unknown or changing by real-time estimation of the denominator term of the filtering gain.

2) Accuracy: The algorithm's estimation results are also relatively accurate under colored measurement noise, indicating its strong practicality and ability to demonstrate good estimation accuracy in environments with different noise characteristics.

3) Appliance on Wind Farms: The algorithm also has high accuracy in evaluating inertia of wind farms, and the reliability of the evaluation results under different noise environments is strong. It can provide theoretical basis and methodological support for evaluating the inertia situation and frequency safety analysis of new power systems under high proportion of new energy integration.

References

[1] D. Li, J. Zhang, B. Xu, Y. Zhao, and F. Yang, "Equivalent Inertia Assessment in Renewable Power System Considering Frequency Distribution Properties," *Power System Technology,* vol. 44, no. 8, pp. 2913-2921, 2020.

[2] H. Sun, B. Wang, W. Li, C. Yang, W. Wei, and B. Zhao, "Research on Inertia System of Frequency Response for Power System With High Penetration Electronics," *Proceedings of the Chinese Society of Electrical Engineering,* vol. 40, no. 16, pp. 5179-5191, 2020.

[3] W. Zhang, Y. Wen, F. Chi, K. Wang, and L. Li, "Research Framework and Prospect on Power System Inertia Estimation," *Proceedings of the Chinese Society of Electrical Engineering,* vol. 41, no. 20, pp. 6842-6855, 2021.

[4] F. Zeng, and J. Zhang, "Temporal and Spatial Characteristics of Power System Inertia and Its Analysis Method," *Proceedings of the Chinese Society of Electrical Engineering,* vol. 40, no. 1, pp. 50-58, 2020.

[5] S. Li, Z. Xia, X. Cheng, Z. Shu, H. Zhong, J. Tu, and S. Huang, "Continuous Estimation Method of Power System Inertia Based on Ambient Disturbance," *Proceedings of the Chinese Society of Electrical Engineering,* vol. 40, no. 14, pp. 4430-4439, 2020.

[6] Y. Li, Y. Wen, X. Ye, X. Jiang, and X. Lin, "Estimation method of power system nodal inertia based on multi-innovation identification," *Electric Power Automation Equipment,* vol. 42, no. 8, pp. 89-95, 2022.

[7] B. Cao, S. Yuan, J. Liu, C. Wang, T. Bi, and H. Xin, "Power System Online Inertia Estimation Considering Real-time Clustering of Frequency Dynamic Response," *Power System Technology,* vol. 47, no. 3, pp. 930-940, 2023.

[8] T. Wei, and R. Guo, "Application of adaptive Kalman filtering to system identification of brushless DC motor," *Optics and Precision Engineering,* vol. 20, no. 10, pp. 2308-2314, 2012.

[9] Z. Liu, M. Zhou, Z. Li, Z. Wu, and G. Li, "Review of inertia control technology and requirement evaluation in renewable-dominant power system," *Electric Power Automation Equipment,* vol. 41, no. 12, pp. 1-11, 2021.

[10] Z. Lu, J. Jiang, Y. Qiao, Y. Min, and H. Li, "A Review on Generalized Inertia Analysis and Optimization of New Power Systems," *Proceedings of the Chinese Society of Electrical Engineering,* vol. 43, no. 5, pp. 1754-1775, 2023.

[11] Y. Min, L. Chen, R. Liu, W. Wu, Z. Zou, Y. Sun, L. Li, and P. Yi, "Analysis on Characteristics of Inertia and Inertial Response in Power System Frequency Dynamics," *Proceedings of the Chinese Society of Electrical Engineering,* vol. 43, no. 3, pp. 855-867, 2023.

[12] A. A. Sallam, and O. P. Malik, *Power System Stability: Modelling, Analysis and Control*: IET Digital Library.

[13] M. Pei, L. Ye, Y. Luo, L. Sha, Z. Zhang, and X. Song, "Inertia Estimation Method for Power System with Renewable Energy Considering Spatio-temporal Correlation of Frequency Response," *Dianli Xitong Zidonghua/Automation of Electric Power Systems,* vol. 48, no. 8, pp. 53-66, 2024.

[14] J. An, S. Sheng, Y. Zhou, and Y. Shi, "Evaluation of Equivalent Virtual Inertia of Wind Farm Based on Measured Data," *Power System Technology,* vol. 47, no. 5, pp. 1819-1827, 2023.

[15] S. Li, S. Xu, H. Li, Z. Shu, S. Huang, and B. Tian, "Rapid Estimation of Equivalent Virtual Inertia of Wind Farm," *Power System Technology,* vol. 45, no. 12, pp. 4683-4691, 2021.

Wind Speed Prediction for Smart Grid Using a Hybrid GNN-Transformer Model

Huayue Huang
The Ultra High Voltage Branch
Shanghai Electric Power Company
Shanghai, China
huanghua.yue@163.com

Shaoyu Mao
School of Electrical Engineering
Shanghai University of Electric Power
Shanghai, China
1332037784@qq.com

Ye Feng
The Ultra High Voltage Branch
Shanghai Electric Power Company
Shanghai, China
m18521762101@163.com

Wenke Pan
The Ultra High Voltage Branch
Shanghai Electric Power Company
Shanghai, China
15621638899@163.com

Qingtian Ge*
The Ultra High Voltage Branch
Shanghai University of Electric Power
Shanghai, China
jingtian2812@163.com
*Corresponding author

Jiangjiao Xu
School of Electrical Engineering
Shanghai University of Electric Power
Shanghai, China
jiangjiao.xu@shiep.edu.cn

***Abstract*—In recent years, there has been significant progress in the development of ultra-high voltage (UHV) transmission lines and their associated micro-meteorological monitoring systems. Accurate prediction of micro-meteorological variables, such as wind speed and temperature, plays a crucial role in the efficient operation of UHV lines and the stability of power transmission systems. Traditional wind speed forecasting methods mainly focus on time-series data, but fail to effectively capture the complex spatial correlations. The continuous advancement of artificial intelligence (AI) technologies, particularly deep learning, offers great potential for improving prediction accuracy. This paper proposes a hybrid model that combines Graph Neural Networks (GNN) and Transformer to address both the temporal and spatial aspects of wind speed prediction. Specifically, the Transformer is used to capture long-range temporal dependencies in wind speed data, while the GNN models the spatial dependencies between geographically distributed towers, allowing the model to effectively learn both time-series dynamics and spatial correlations.The model is trained on a real-world dataset and evaluated using metrics such as MAE, MAPE, and RMSE. Experimental results show that the proposed model significantly improves prediction accuracy by effectively capturing spatial dependencies and temporal features of wind speed. This highlights the importance of leveraging advanced deep learning techniques for wind speed forecasting, especially when dealing with complex environments and large-scale datasets. Future work will focus on enhancing the model's generalization capabilities and exploring its applications in other energy systems.**

***Index Terms*—Forecasting, GNN, Transformer, Smart grid**

I. Introduction

In recent years, with the global shift towards sustainable energy, ultra-high voltage (UHV) transmission systems have become a key component of modern power grids. [1] These systems rely heavily on accurate micro-meteorological data, including wind speed and temperature, to ensure their stability and reliability. The variability and intermittency of wind patterns, however, pose significant challenges for optimizing grid operation and improving transmission system performance. As a result, precise forecasting of wind speed and other meteorological variables is critical for enhancing grid stability, ensuring efficient power dispatch, and optimizing energy distribution across regions [2], [3].

Early research on wind speed prediction primarily relied on traditional statistical and machine learning methods. Time-series models like the Autoregressive Integrated Moving Average (ARIMA) and persistence models were widely used as baseline approaches [4], [5]. These models are effective for short-term forecasting, relying on historical data to predict future wind speeds. However, they often fail to handle the non-linearity and non-stationarity inherent in wind speed dynamics, limiting their performance, particularly for long-term forecasts. ARIMA, for instance, assumes that the data is stationary, which is rarely the case with wind speed, as it can exhibit significant variability over time [6].

Other techniques, such as Kalman filters and Support Vector Machines (SVM), were also explored to manage some level of non-linearity in wind speed prediction [7], [8]. While Kalman filters offer advantages in dynamic systems, their effectiveness decreases with highly volatile data like wind speed. SVM, on the other hand, can handle non-linearity but tends to struggle with large-scale data, which is typical in wind forecasting. Despite these improvements, these methods still assume linear relationships or stationarity, which limits their forecasting accuracy, especially for longer prediction horizons and more complex wind patterns [9].

With advancements in computational intelligence, deep learning-based methods have become mainstream, demonstrating superior performance in time-series forecasting. Models based on Recurrent Neural Networks (RNNs), particu-

979-8-3315-5472-9/25/$31.00 ©2025 IEEE

larly Long Short-Term Memory (LSTM) networks and Gated Recurrent Units (GRUs), have shown remarkable success in capturing complex temporal dependencies from historical data [10], [11]. These models excel at learning sequential patterns and have been widely applied to various forecasting tasks, including wind speed prediction. Furthermore, hybrid architectures combining Convolutional Neural Networks (CNNs) with LSTMs have been proposed to extract both spatial and temporal features from input data, enabling the models to better handle multi-dimensional inputs [12], [13]. These hybrid models can capture more complex relationships in the data, improving forecasting accuracy. However, a significant limitation of most of these models is that they treat each node as an isolated entity, processing its data independently [14]. This approach overlooks the crucial spatial correlations between geographically distributed nodes, which can play an important role in improving prediction accuracy [15]. While some studies have attempted multi-node forecasting, they often fail to explicitly and effectively model the underlying spatial interdependencies that govern regional wind patterns [16], [17]. As a result, these models may not fully capture the interactions between different nodes, which can lead to suboptimal performance when forecasting wind speed across multiple locations.

To address these limitations, this paper proposes a novel spatiotemporal forecasting model that synergistically integrates a Graph Convolutional Network (GCN) [18] with a Transformer architecture [19]. The proposed approach constructs a graph where each UHV tower is represented as a node, allowing the GCN to explicitly capture the complex spatial correlations between towers based on their geographical relationships. By modeling these spatial dependencies, the proposed model takes into account how wind patterns at different towers are influenced by their relative positions and surrounding environmental factors. Concurrently, the Transformer's self-attention mechanism is employed to effectively capture long-range temporal dependencies within the wind speed data of each UHV tower. This combination enables the proposed model to learn both spatial and temporal dynamics, leading to more accurate wind speed predictions across multiple UHV towers.

The main contributions of this study are as follows:

- We propose a novel deep learning architecture that combines GCN and Transformer models to perform spatiotemporal wind speed forecasting, effectively capturing both inter-tower spatial correlations and intra-tower temporal dependencies.
- We conduct extensive experiments on a real-world dataset collected from multiple UHV towers. The results demonstrate that the proposed model significantly outperforms existing statistical and deep learning-based forecasting methods.
- This work validates the critical importance of explicitly modeling spatiotemporal relationships in multi-tower wind forecasting and provides a robust and effective framework for future research in this domain.

II. Methods

In this section, a spatiotemporal model for multi-tower wind speed forecasting is presented. A Transformer encoder captures long-range temporal dependencies from historical sequences, while a Graph Convolutional Network models inter-tower spatial correlations via a learnable adjacency graph. This unified design enables the model to exploit both time dynamics and spatial interactions across UHV towers for accurate multi-step prediction. Fig. 1 visually presents the proposed spatiotemporal prediction model architecture, which aims to achieve accurate predictions by integrating a Transformer and a Graph Convolutional Network to collaboratively capture the long-range temporal dependencies and the spatial interactions among multiple towers in wind speed data.

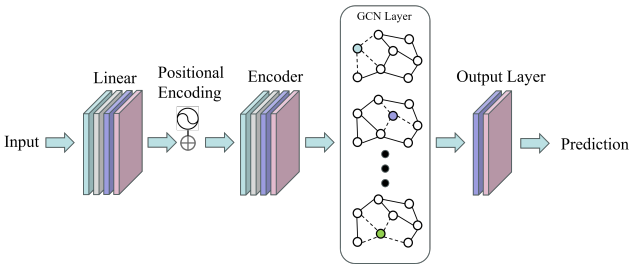


Fig. 1. The overall architecture.

A. Problem Formulation

This paper presents a study on multi-tower wind speed forecasting with N geographically distributed UHV towers. For each tower $n \in \{1, \ldots, N\}$ and discrete time index t, let $y_{n,t} \in \mathbb{R}$ denote the wind speed measurement. Given a look-back window of length T, the input at time t is the tensor $X_{t-T+1:t} \in \mathbb{R}^{B\times C\times N\times T}$, where B is the batch size, C is the number of node-wise features (one in setting, i.e., wind speed), N is the number of UHV towers, and T is the number of historical time steps provided to the model. The forecasting horizon is T_h, and the model outputs $\hat{Y}_{t+1:t+T_h} \in \mathbb{R}^{B\times T_h\times N\times 1}$, i.e., T_h future wind speed values for every tower and every sample in the batch.

Formally, the mapping is learned as follows:

$$\hat{Y}_{t+1:t+T_h} \;=\; f_\Theta\big(X_{t-T+1:t}\big) \tag{1}$$

where f_Θ is parameterized by the spatiotemporal network and Θ denotes all trainable parameters. A multi-output direct strategy is adopted, which predicts all T_h steps in one forward pass and mitigates the error accumulation typical of recursive one-step-ahead rollouts. Spatial correlations among towers are modeled via a graph over the N nodes, while long-range temporal dependencies within each tower's time series are captured by a Transformer encoder. The overall objective is to minimize the discrepancy between $\hat{Y}_{t+1:t+T_h}$ and the ground truth $Y_{t+1:t+T_h}$ over all batches, time steps, and towers.

B. Transformer Encoder

This paper employs an encoder-only Transformer to model temporal dependencies within the look-back window. As de-

picted in Fig. 2, the encoder is composed of a multi-head self-attention module and a feed-forward neural network, each followed by a residual connection and layer normalization. For each sample, the node-wise features at each time step are concatenated to form a length-T sequence of feature vectors. This sequence is linearly projected to a model width d_{model}, and sinusoidal positional encodings are added to preserve temporal order. The positional encoding for each time step t is given by:

$$\begin{aligned} \text{PE}_{t,2i} &= \sin\left(\frac{t}{10000^{2i/d_{\text{model}}}}\right) \\ \text{PE}_{t,2i+1} &= \cos\left(\frac{t}{10000^{2i/d_{\text{model}}}}\right) \end{aligned} \tag{2}$$

where i is the dimension index, and d_{model} is the model dimension.

The resulting sequence is processed by L Transformer encoder layers, each composed of multi-head self-attention and a position-wise feed-forward network, wrapped with residual connections, layer normalization, and dropout. The multi-head self-attention is computed as follows:

$$\text{Attention}(\mathbf{Q},\mathbf{K},\mathbf{V}) = \text{softmax}\left(\frac{\mathbf{Q}\mathbf{K}^{\text{T}}}{\sqrt{d_k}}\right)\mathbf{V} \tag{3}$$

where $\mathbf{Q}$, $\mathbf{K}$, and $\mathbf{V}$ are the query, key, and value matrices, respectively, and d_k is the dimension of the query/key vectors.

For multi-head attention, the process is repeated in parallel across h heads, and the outputs are concatenated and linearly transformed:

$$\begin{aligned} \text{MultiHead}(\mathbf{Q},\mathbf{K},\mathbf{V}) &= \text{Concat}(\text{head}_1,\ldots,\text{head}_h)\mathbf{W}^O \\ \text{where head}_i &= \text{Attention}(\mathbf{Q}\mathbf{W}_i^Q, \mathbf{K}\mathbf{W}_i^K, \mathbf{V}\mathbf{W}_i^V) \end{aligned} \tag{4}$$

where each head_i is the attention output for the i-th head, and $\mathbf{W}^O$ is the output projection matrix.

To prevent information leakage during forecasting, this paper applies a causal attention mask so that each time position can only attend to the current and past time steps. This enables the model to capture long-range dependencies, periodicities, and regime shifts directly from the data.

After the encoder stack, the contextualized sequence is linearly projected back from d_{model} to the original feature dimension and reshaped to match the input structure, allowing the subsequent spatial module to operate on per-tower features at every time step. In practice, this paper adopts the pre-norm variant for stability, use GELU or ReLU activations in the FFN, and apply dropout to both attention and FFN sublayers. Variable-length windows are supported with a padding mask, and missing readings can be masked or imputed before encoding.

The quadratic time/memory cost in T is controlled by using moderate horizons and a compact configuration, as detailed in the experimental setup. This encoder supplies temporally enriched representations that are subsequently fused with spatial information by the GCN.

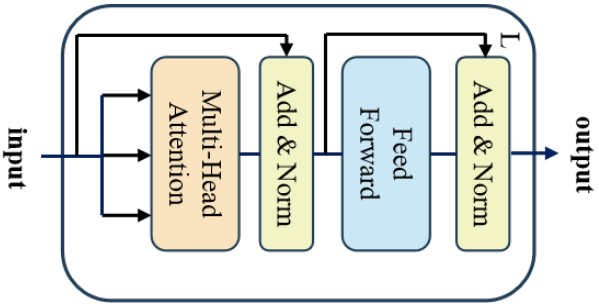


Fig. 2. Architecture of the encoder.

C. Spatial Encoder: Higher-Order GCN

This model in the paper targets inter-tower spatial structure with a Graph Convolutional Network applied at each time step on an N-node tower graph. Let $\mathbf{A} \in \mathbb{R}^{N\times N}$ be the adjacency between towers. Self-loops are added $\tilde{\mathbf{A}} = \mathbf{A} + \mathbf{I}_N$ and define the degree matrix $\tilde{\mathbf{D}}_{ii} = \sum_j \tilde{\mathbf{A}}_{ij}$, yielding the symmetrically normalized adjacency:

$$\widehat{\mathbf{A}} = \tilde{\mathbf{D}}^{-1/2}\tilde{\mathbf{A}}\tilde{\mathbf{D}}^{-1/2}$$

which stabilizes message passing by balancing contributions from high- and low-degree nodes.

For the feature matrix at time τ, $\mathbf{H}_\tau^{(\ell)} \in \mathbb{R}^{N\times d_\ell}$, the $(\ell{+}1)$-th GCN layer is

$$\mathbf{H}_\tau^{(\ell+1)} \;=\; \sigma\big(\widehat{\mathbf{A}}\,\mathbf{H}_\tau^{(\ell)}\,\mathbf{W}^{(\ell)}\big) \tag{5}$$

where $\mathbf{W}^{(\ell)}$ is trainable and $\sigma(\cdot)$ is a nonlinearity. Intuitively, (5) aggregates each tower's representation with a degree-normalized average of its neighbors, reflecting the fact that nearby sites often experience correlated wind regimes due to shared synoptic conditions and terrain effects.

a) Higher-order aggregation: Stacking L spatial layers increases the receptive field to L hops. To capture wider mesoscale influences without excessively deep stacks, this paper adopts a K-hop variant that explicitly aggregates multi-hop neighborhoods with hop-specific weights:

$$\mathbf{Z}_\tau \;=\; \sum_{k=0}^{K} \widehat{\mathbf{A}}^{\,k}\,\mathbf{H}_\tau^{(0)}\,\mathbf{W}_k \tag{6}$$

followed by a 1×1 linear fusion and dropout. Eq. (6) can be viewed as a finite diffusion process: $k{=}0$ preserves each node's own signal, while higher powers of $\widehat{\mathbf{A}}$ propagate information from increasingly distant towers, enabling the model to encode both local coupling and broader regional flow patterns.

b) Adjacency options and regularization: When geographical priors are available, blending is optionally achieved with a learnable component via $\mathbf{A} = \alpha\,\mathbf{A}_{\text{geo}} + (1-\alpha)\,\mathbf{A}_{\text{adp}}$, where $\mathbf{A}_{\text{adp}}$ is parameterized and trained end-to-end (non-negativity enforced by activation and row-wise normalization). This hybrid design lets the model respect physical proximity while adapting to data-driven correlations caused by orography and prevailing winds. Sparsity can be applied to reduce noise and computation.

III. EXPERIMENTS

In this section, the proposed model will be applied to the experiment of wind speed prediction. This paper provides a detailed description of the experiment, including experimental setup, dataset overview, evaluation criteria, and experimental results. Additionally, the results of the proposed model in wind speed prediction will be compared with other models, including Transformer, LSTM, GRU, and MLP. Finally, the visualization of some results will demonstrate the model's performance.

A. Dataset

This study utilizes a real-world wind speed dataset collected from 11 ultra-high-voltage(UHV) micro-meteorological towers in Shanghai, China, over the period from June 1st to September 7th, 2025. The dataset records wind speed measurements with data captured every 10 minutes. Each tower's wind speed is recorded in the dataset, providing valuable insights into temporal wind speed variations. The dataset is structured with the timestamps in the first column and the corresponding wind speed measurements for each of the 11 towers as columns. The data was preprocessed to ensure its accuracy, with missing values and inconsistencies removed. For training and evaluation purposes, the dataset is divided into training, validation, and testing sets, with 80% allocated for training, 10% for validation, and 10% for testing, allowing for effective model development and performance assessment.

The geographical locations of the 11 micro-meteorological towers are critical for understanding their distribution and performance. Table I provides the precise longitude and latitude coordinates of each tower. These locations play an important role in the overall analysis and modeling of the wind energy generation system.

TABLE I: Geographical Coordinates of the 11 UHV Micro-meteorological Towers

Tower ID	Longitude	Latitude
3753	121.23020	30.92225
3784	121.37064	30.94341
3844	121.44063	30.82521
3676	120.99925	31.00668
3725	121.10256	30.89763
3700	121.04121	30.94460
3739	121.16964	30.91845
3935	121.76934	30.92295
3767	121.30052	30.92705
3772	121.32393	30.93120
3777	121.34925	30.94096

Table II provides detailed information about the dataset used for training, including the total number of samples and the breakdown of the training, validation, and test sets.

TABLE II: Train set details

Train set	
Total number of samples	17568
Train sets samples	14054
Validation sets samples	1757
Test sets samples	1757

B. Setting of the model parameters

Table III outlines the key training parameter settings used in the model. These parameters, such as the number of epochs, batch size, and learning rate, are critical for optimizing the performance of the model during training. The specific values provided are chosen to ensure efficient learning and effective model convergence.

TABLE III: Training parameter settings

Parameter	Value
Epochs	100
Batch size	64
Dropout rate	0.3
Encoder layers	6
Decoder layers	6
Attention heads	8
Initial learning rate	0.0001
Hidden dim	256
Feedforward dim	2048

C. Evaluation Criteria

The evaluation criteria used in this paper are Mean Absolute Error (MAE), Mean Absolute Percentage Error (MAPE), and Root Mean Square Error (RMSE).

For each wind speed prediction, the MAE measures the average absolute difference between the predicted and actual wind speeds across all data points. It is calculated as follows:

$$MAE = \frac{1}{N}\sum_{i=1}^{N}|y_i - \hat{y}_i| \tag{7}$$

where y_i is the true wind speed, $\hat{y}_i$ is the predicted wind speed, and N is the total number of predictions.

MAPE is another commonly used metric, which calculates the average of the absolute percentage errors between the predicted and actual wind speeds:

$$MAPE = \frac{1}{N}\sum_{i=1}^{N}\left|\frac{y_i - \hat{y}_i}{y_i}\right| \times 100 \tag{8}$$

where y_i and $\hat{y}_i$ are the true and predicted values, respectively.

The RMSE is used to measure the square root of the average squared differences between the predicted and actual values, and it gives higher weight to larger errors. It is calculated as follows:

$$RMSE = \sqrt{\frac{1}{N}\sum_{i=1}^{N}(y_i - \hat{y}_i)^2} \tag{9}$$

where y_i and $\hat{y}_i$ are the true and predicted values, respectively, and N is the number of predictions.

These metrics are used to assess the performance of the wind speed prediction model and provide insights into its accuracy and robustness.

D. Experimental Results

In this section, we primarily present the results of using the proposed model for wind speed prediction in tower 3753. The model has demonstrated significant progress in accurately predicting the wind speed values, as evidenced by the comparison between the predicted and actual wind speeds. The experimental results, as shown in Fig. 3, clearly illustrate the effectiveness of the model in capturing the wind speed patterns across a range of time samples. The predicted wind speeds closely follow the actual values, indicating the model's ability to effectively capture both short-term fluctuations and overall trends in wind speed. These results highlight the potential of the proposed model for accurate wind speed forecasting, which is essential for optimizing the performance of wind farms.

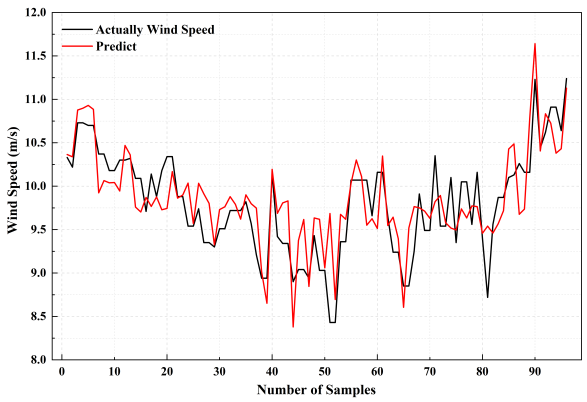


Fig. 3. Output of the model with the actual wind speed values for 96 samples of July 2025

Furthermore, the training results of the model are summarized in Table IV. On average, over 96 time horizons, the model achieved a Test MAE of 1.5363, Test MAPE of 0.1529, and Test RMSE of 2.2175. These results indicate the high accuracy and robustness of the model in predicting wind speed values, demonstrating its ability to effectively capture both short-term variations and overall trends in the wind speed data.

TABLE IV: Performance of the Model

Evaluation Criteria	Score
Test MAE	1.5363
Test MAPE	0.1529
Test RMSE	2.2175

E. Comparison with Other Models

To evaluate the performance of the proposed model, this paper conducted a comparative study between the proposed model and several other models, including Transformer, LSTM, GRU, and MLP, on the same dataset. The aim of this comparison was to assess the accuracy and effectiveness of the proposed model in predicting wind speed in comparison to these traditional models.

Fig. 4, 5, and 6 show the experimental results for each of the models. These figures depict the MAE, MAPE, and RMSE scores for each model across various time horizons, highlighting how the proposed model performs relative to Transformer, LSTM, GRU, and MLP.

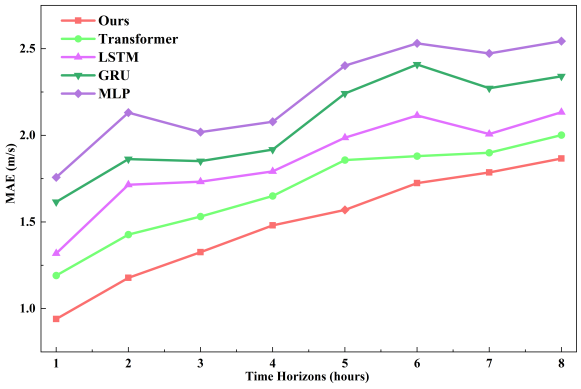


Fig. 4. MAE comparison for different models

As seen in Fig. 4, the proposed model consistently outperforms the other models in terms of MAE, especially at higher time horizons, indicating that the proposed model is more accurate in predicting wind speed over time. Similarly, Fig. 5 and 6 further demonstrate the superiority of the proposed model, with lower MAPE and RMSE values compared to the Transformer, LSTM, GRU, and MLP models.

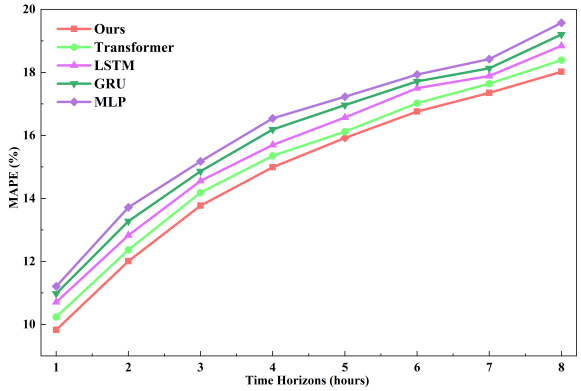


Fig. 5. MAPE comparison for different models

These results highlight that the proposed model provides superior performance in wind speed prediction, demonstrating its ability to effectively capture both short-term fluctuations and long-term trends compared to the other models.

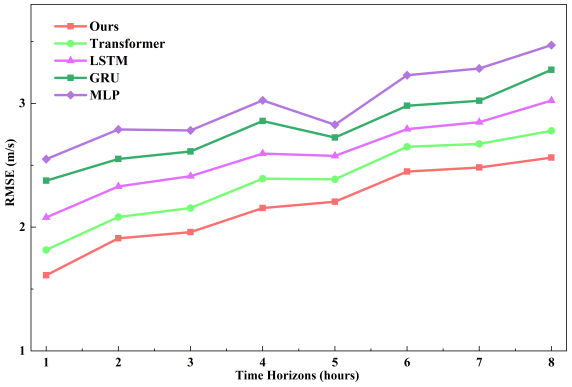


Fig. 6. RMSE comparison for different models

IV. CONCLUSION

In this paper, we curated a collection of wind speed data sourced from 11 UHV micro-meteorological towers deployed in Shanghai, China and utilized this dataset for evaluating the performance of various models, including Transformer, LSTM, GRU, MLP, and the proposed model. Compared to the other models, the proposed model demonstrated superior performance in wind speed prediction, achieving the lowest MAE, MAPE, and RMSE values. The results clearly indicate that the proposed model is more accurate in predicting wind speed, especially over longer time horizons.

The comprehensive evaluation metrics, including MAE, MAPE, and RMSE, demonstrated the effectiveness of the proposed model in capturing both short-term fluctuations and long-term trends in wind speed. The superior performance of the proposed model highlights its potential for optimizing the operation of UHV towers and enhancing the reliability of wind energy forecasting.

These findings underscore the importance of employing advanced deep learning models, such as the proposed model, for accurate and reliable wind speed forecasting. The successful application of the proposed model in this study opens up new possibilities for improving the efficiency and effectiveness of UHV micro-meteorological towers management systems. Future research can focus on further enhancing the model's robustness, addressing challenges such as data sparsity and variability, and exploring its applicability to other renewable energy systems.

REFERENCES

[1] Y. Wang, J. Zhen, and H. Pan, "Ultra-high-voltage construction projects and total factor energy efficiency: empirical evidence on cross-regional power dispatch in china," *Sustainability*, vol. 16, no. 18, p. 8083, 2024.

[2] H. S. Dhiman and D. Deb, "A review of wind speed and wind power forecasting techniques," *arXiv preprint arXiv:2009.02279*, 2020.

[3] J. Xu, T. Zheng, Y. Dang, F. Yang, and D. Li, "Distributed deep reinforcement learning for data-driven water heater model in smart grid," *IEEE Transactions on Smart Grid*, vol. 16, no. 4, pp. 2900–2912, 2025.

[4] E. Yatiyana, S. Rajakaruna, and A. Ghosh, "Wind speed and direction forecasting for wind power generation using arima model," in *2017 Australasian universities power engineering conference (AUPEC)*, pp. 1–6, IEEE, 2017.

[5] H. R. Alsamamra, S. Salah, and J. H. Shoqeir, "Performance analysis of arima model for wind speed forecasting in jerusalem, palestine," *Energy Exploration & Exploitation*, vol. 42, no. 5, pp. 1727–1746, 2024.

[6] I. Tyass, A. Bellat, A. Raihani, K. Mansouri, and T. Khalili, "Wind speed prediction based on seasonal arima model," in *E3S Web of Conferences*, vol. 336, p. 00034, EDP Sciences, 2022.

[7] Y. Zheng, Y. Ge, S. Muhsen, S. Wang, D. H. Elkamchouchi, E. Ali, and H. E. Ali, "New ridge regression, artificial neural networks and support vector machine for wind speed prediction," *Advances in Engineering Software*, vol. 179, p. 103426, 2023.

[8] N. Chen, H. Sun, Q. Zhang, and S. Li, "A short-term wind speed forecasting model based on emd/ceemd and arima-svm algorithms," *Applied Sciences*, vol. 12, no. 12, p. 6085, 2022.

[9] M. Lydia, G. Edwin Prem Kumar, and R. Akash, "Wind speed and wind power forecasting models," *Energy & Environment*, p. 0958305X241228515, 2024.

[10] Y. Xiao, C. Zou, H. Chi, and R. Fang, "Boosted gru model for short-term forecasting of wind power with feature-weighted principal component analysis," *Energy*, vol. 267, p. 126503, 2023.

[11] Q. Wu, F. Guan, C. Lv, and Y. Huang, "Ultra-short-term multi-step wind power forecasting based on cnn-lstm," *IET Renewable Power Generation*, vol. 15, no. 5, pp. 1019–1029, 2021.

[12] X. Liu, Z. Lin, and Z. Feng, "Short-term offshore wind speed forecast by seasonal arima-a comparison against gru and lstm," *Energy*, vol. 227, p. 120492, 2021.

[13] Z. Shen, X. Fan, L. Zhang, and H. Yu, "Wind speed prediction of unmanned sailboat based on cnn and lstm hybrid neural network," *Ocean Engineering*, vol. 254, p. 111352, 2022.

[14] Y. Chen, Y. Wang, Z. Dong, J. Su, Z. Han, D. Zhou, Y. Zhao, and Y. Bao, "2-d regional short-term wind speed forecast based on cnn-lstm deep learning model," *Energy Conversion and Management*, vol. 244, p. 114451, 2021.

[15] J. Xu, K. Li, and D. Li, "Multioutput framework for time-series forecasting in smart grid meets data scarcity," *IEEE Transactions on Industrial Informatics*, vol. 20, no. 9, pp. 11202–11212, 2024.

[16] M. Afrasiabi, M. Mohammadi, M. Rastegar, and S. Afrasiabi, "Advanced deep learning approach for probabilistic wind speed forecasting," *IEEE Transactions on Industrial Informatics*, vol. 17, no. 1, pp. 720–727, 2020.

[17] D. Qiao, S. Wu, G. Li, J. You, J. Zhang, and B. Shen, "Wind speed forecasting using multi-site collaborative deep learning for complex terrain application in valleys," *Renewable Energy*, vol. 189, pp. 231–244, 2022.

[18] T. Kipf, "Semi-supervised classification with graph convolutional networks," *arXiv preprint arXiv:1609.02907*, 2016.

[19] A. Vaswani, N. Shazeer, N. Parmar, J. Uszkoreit, L. Jones, A. N. Gomez, Ł. Kaiser, and I. Polosukhin, "Attention is all you need," *Advances in neural information processing systems*, vol. 30, 2017.

A Fuzzy Adaptive Parameter Control Method for Wind Farm Active Frequency Support Considering Wind Speed Difference

Jiangwei Bi
Electrical and Power Engineering School
Hohai University
Nanjing , China
2037078274@qq.com

Zhongyuan Yao
Clean Energy Branch
Huaneng International Power Jiangsu Energy Development Co., Ltd.
Nanjing , China
82009211@nmail2.chng.com.cn

Tianyi Huang
Clean Energy Branch
na Huaneng International Power Jiangsu Energy Development Co., Ltd.
Nanjing , China
82055814@nmail2.chng.com.cn

Haiqiang Zhou
Electrical and Power Engineering School
Hohai University
Nanjing , China
js.hq@163.com

Yi Zheng
Clean Energy Branch
Huaneng International Power Jiangsu Energy Development Co., Ltd.
Nanjing , China
82055827@nmail2.chng.com.cn

Youwei Zhang
Clean Energy Branch
Huaneng International Power Jiangsu Energy Development Co., Ltd.
Nanjing , China
82055824@nmail2.chng.com.cn

***Abstract*—A fuzzy adaptive parameter control method for wind farm active frequency support considering wind speed difference is proposed. First, the principles of conventional synthetic inertia (SI) control and secondary frequency drop (SFD) mechanisms are analyzed, revealing limitations of fixed SI parameters. Subsequently, to exploit wind power's frequency regulation potential and suppress SFD well, rotor speed and frequency variables are employed as fuzzy controller inputs to dynamically adjust SI droop and inertia coefficients. During rotor speed recovery, two methods redesign the recovery trajectory to mitigate SFD. Finally, for wind farm with speed difference, parameters are optimized via particle swarm optimization (PSO) at a base wind speed to minimize maximum frequency deviation. Validation on a modified three-machine nine-bus system demonstrates that the proposed method effectively supports system frequency, reduces SFD, and elevates the frequency nadir for wind farm considering wind speed difference.**

Keywords—fuzzy control, adaptive parameter control, active frequency support, secondary frequency drop, rotor speed recovery

I. INTRODUCTION

Driven by the "Dual Carbon" development strategy, future power systems will predominantly feature renewable sources such as wind and photovoltaic generation [1]. However, WTs usually operate in maximum power point tracking (MPPT) mode, they inherently lack frequency support capabilities [2]. With large-scale wind power integration and the declining proportion of conventional synchronous generators, the equivalent system inertia and primary frequency regulation capacity are significantly reduced, posing critical challenges to frequency stability [3]. Consequently, grid codes worldwide now mandate wind farms to provide active frequency support capabilities akin to synchronous generators [4]. China's Technical Rule for Connecting Wind Farm to Power System explicitly require grid-connected wind and solar resources to possess primary frequency regulation functions to ensure system security [5].

Active frequency support methods for WTs primarily include rotor kinetic energy control and power reserve control [6]. Power reserve control operates WTs below maximum power output to retain reserve capacity for frequency response. However, this incurs wind curtailment, lowering energy utilization efficiency and economic benefits [7]. Rotor kinetic energy control releases stored kinetic energy by decelerating the rotor to boost active power output. Common implementations include droop control, virtual inertia control, and their hybrid form—SI control [8]. To maintain stability, WTs exit frequency regulation when the rotor speed reaches its minimum allowable value, triggering SFD [9-10].

Reference [11] first proposed SI control, demonstrating its efficacy during frequency support. Yet, its fixed control parameters limit performance. Reference [12] adaptively adjusts SI parameters based on rotor speed limits and wind farm capabilities, showing robustness across scenarios but neglecting system-level regulation requirements. During rotor speed recovery, the return to MPPT mode causes power deficits that induce SFD. Although Reference [13] reduces SFD by curtailing output power by a fixed value after a preset period, significant SFD persists. Reference [14] coordinates WTs with energy storage systems (ESS) to mitigate SFD during recovery,

This work is supported by the China Huaneng Group Co., Ltd. Headquarters Science and Technology Project (No. HNKJ24-H68).

but ESS increases capital costs. Reference [15] employs a smooth rotor speed recovery trajectory to suppress SFD effectively, yet prolongs the recovery duration. Most aforementioned studies simplify wind farm to a single turbine. In reality, wind speeds vary across turbines within a farm. Uniform SI parameters fail to coordinate turbines or fully exploit their frequency regulation potential. Reference [16] proposed a leader-follower consensus control strategy, where turbines follow a dominant turbine's operating state to participate in frequency regulation. While this strategy effectively allocates power based on individual regulation capabilities,

To address these issues, this paper proposes a fuzzy adaptive parameter-based active frequency support control method for wind farm considering wind speed difference. First, the mechanism of SFD is analyzed. Then, during the frequency support phase, fuzzy control dynamically adjusts SI parameters by synthesizing both system-level regulation demand and turbine-level regulation capability, aiming to reduce the maximum frequency deviation and mitigate SFD. In the rotor speed recovery phase, the rotor speed recovery trajectory is reset to further suppress SFD. Subsequently, key parameters of the fuzzy controller are optimized via PSO with the objective of minimizing the maximum frequency deviation. Finally, simulation validations are conducted.

II. Synthetic Inertia Control of Wind Turbines and Mechanism of Secondary Frequency Drop

When a frequency drop occurs, the additional SI control releases kinetic energy stored in the wind turbine rotor to increase active power output, thereby supporting grid frequency. The SI control typically combines virtual inertia control and droop control, expressed as:

$$\Delta P_{\mathrm{SI},i} = -k_{\mathrm{d}}(f - f_0) - k_{\mathrm{in}}\frac{\mathrm{d}f}{\mathrm{d}t} \tag{1}$$

where $\Delta P_{\mathrm{SI},i}$ is the additional power generated by turbine G_{wi} during SI control; f、f_0 are the system frequency and its steady-state value; k_{d}、k_{in} are the droop and inertia coefficients.

The rotor motion equation of G_{wi} during frequency regulation is:

$$2H_{\mathrm{WT},i}\omega_{\mathrm{r},i}\frac{d\omega_{\mathrm{r},i}}{dt} = P_{\mathrm{m},i} - P_{\mathrm{e},i} \tag{2}$$

where $H_{\mathrm{WT},i}$ is the inherent inertia time constant of G_{wi}; $\omega_{\mathrm{r},i}$ is the rotor speed of the G_{wi}; $P_{\mathrm{m},i}$ is the mechanical power captured by G_{wi}; $P_{\mathrm{e},i}$ is the electrical power output of G_{wi}:

$$P_{\mathrm{e},i} = P_{\mathrm{MPPT},i} + P_{\mathrm{SI},i} \tag{3}$$

where $P_{\mathrm{MPPT},i} = k_{\mathrm{opt}}\omega_{\mathrm{r},i}^3$, and k_{opt} is the MPPT curve coefficient.

Fig.1 illustrates the power trajectory of WT under SI control when a frequency disturbance occurs. SI control contains two stages: 1) Frequency support stage. The operating point shifts from A through B to C, rotor speed decreases as kinetic energy is released. 2) Rotor speed recovery stage: When rotor speed reaches the lower limit (set to $\omega_{\min}$ = 0.75 p.u in this paper), the WT exits frequency regulation to ensure the stability. The WT resumes MPPT operation. Meanwhile， the power imbalance ΔP from C to D causes SFD.

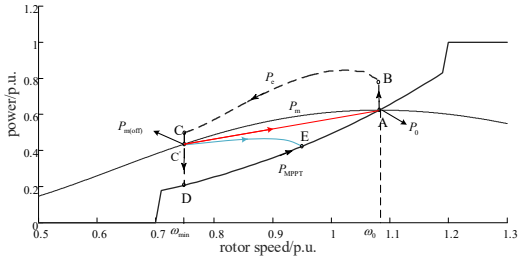


Fig. 1. Power trajectory of WT under SI control

Conventional SI control employs fixed droop coefficients and fixed inertia coefficients, where larger values enable greater release of rotor kinetic energy to enhance frequency support. However, the power deficits is greater during rotor speed recovery thereby exacerbating SFD. Furthermore, influenced by wind direction and WTs distribution, wind speeds are different among WTs within wind farm, leading to divergent available frequency regulation energy among individual WTs. Applying identical SI parameters fails to fully harness each turbine's regulation potential, necessitating consideration of wind speed difference among WTs in wind farm.

III. Improved Synthetic Inertia Control Based on Fuzzy-Adaptive Parameters

To better exploit WT's frequency regulation potential and suppress SFD, this paper proposes an improved synthetic inertia control method based on fuzzy-adaptive parameters, comprising two core components: 1) a frequency and rotor speed-based fuzzy-adaptive frequency regulation method during the support phase, and 2) an improved rotor speed recovery strategy.

A. Frequency Regulation Method Based on Fuzzy-Adaptive Parameters

The fuzzy adaptive frequency regulation method dynamically adjusts control parameters using system frequency deviation and rotor speed of the WT, fully exploiting WT's regulation potential to reduce maximum frequency deviation and mitigate SFD. The SI control coefficients for G_{wi} are:

$$\begin{cases} k_{\mathrm{d},i} = k_{\mathrm{d0},i} + k_{\mathrm{ad},i} \\ k_{\mathrm{in},i} = k_{\mathrm{in0},i} + k_{\mathrm{ain},i} \end{cases} \tag{4}$$

where $k_{\mathrm{d},i}$、$k_{\mathrm{in},i}$ are the droop and inertia coefficients for G_{wi}; $k_{\mathrm{d0},i}$、$k_{\mathrm{in0},i}$ are their fixed components which are constant during regulation while $k_{\mathrm{ad},i}$、$k_{\mathrm{ain},i}$ are fuzzy-adaptive components varying with system frequency and rotor speed.

The rotor speed-based operating state indicator is defined as:

$$x_i = \frac{\omega_{\mathrm{r},i}^2 - \omega_{\min}^2}{\omega_{0,i}^2 - \omega_{\min}^2} \tag{5}$$

where x_i represents the proportion of releasable kinetic energy to total adjustable kinetic energy, quantifying regulation capability of G_{wi}; $\omega_{0,i}$ is the pre-disturbance steady-state speed.

For normalization:

$$x_f = \frac{f_0 - f}{f_0 - f_{\min}} \tag{6}$$

where x_f represents the system frequency deviation, reflecting the kinetic energy required by the system during frequency regulation; and $f_{\min}$ denotes the minimum allowable system frequency.

The fuzzy controller contains four components: fuzzification, inference engine, fuzzy rules, and defuzzification Membership functions convert linguistic fuzzy concepts into numerical values. Input x_f has three fuzzy subsets: S (small), M (medium), B (big). Input x_i and outputs $k_{\text{ad},i}$、$k_{\text{ain},i}$ each contain seven fuzzy subsets: SS (extremely small), MS (moderately small), S (small), M (medium), SB (moderately big), MB (big), B (extremely big). The membership function curves for x_f、x_i、$k_{\text{ad},i}$、$k_{\text{ain},i}$ are shown in Fig. 2.

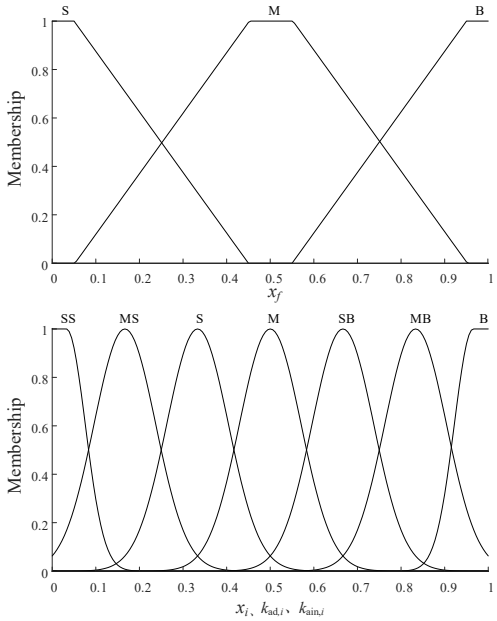


Fig. 2. Membership functions of the inputs and output.

The universe of discourse for inputs x_i and x_f is normalized to [0, 1]. To ensure robust adaptability of the fuzzy controller, the output universe is also confined to [0, 1]. The actual values of $k_{\text{ad},i}$、$k_{\text{ain},i}$ are obtained by multiplying the normalized outputs with scaling factors $k_{1,i}$、$k_{2,i}$, where the magnitude of these scaling factors governs the variation range of the fuzzy-adaptive components.

The core of fuzzy control lies in its rule base. The principle of the fuzzy rules is as follows. During the initial post-disturbance period, x_f is small while x_i is large. To prevent rapid frequency decline, larger droop and inertia coefficients should be set, when substantial active support power is required. As frequency decreases, x_f becomes large, increasing the droop coefficient maintains higher support power to elevate the system frequency nadir if WT's releasable energy remains adequate. When x_i is small, the WT will exit frequency regulation. Minimal droop and inertia coefficients are adopted to reduce unbalanced power at exit time, thereby suppressing SFD. In summary, optimal wind power output is delivered at each stage by dynamically coordinating system regulation needs with WT's capability.

The fuzzy rules for the droop coefficient are specified in Table I:

TABLE I. FUZZY RULES FOR DROOP COEFFICIENT

$k_{\text{ad},i}$		x_i						
		SS	MS	S	M	SB	MB	B
x_f	S	M	MB	SB	M	S	M	M
	M	S	SB	SB	M	S	M	M
	B	MS	M	MB	SB	M	SB	SB

The fuzzy rules for the inertia coefficient are specified in Table II:

TABLE II. FUZZY RULES FOR INERTIA COEFFICIENT

$k_{\text{ain},i}$		x_i						
		SS	MS	S	M	SB	MB	B
x_f	S	SS	S	M	SB	MB	MB	B
	M	SS	MS	S	M	SB	MB	B
	B	SS	SS	MS	S	M	SB	MB

Using the established fuzzy rules, fuzzy inference is performed for $k_{\text{ad},i}$、$k_{\text{ain},i}$. After defuzzification, the results are multiplied by corresponding scaling factors $k_{1,i}$、$k_{2,i}$ to obtain the actual values of $k_{\text{ad},i}$、$k_{\text{ain},i}$. Notably, although initial rotor speeds and operating states differ among turbines under varying wind speeds, the input/output normalization ensures that the proposed fuzzy rules apply universally to every turbine.

B. Improved Rotor Speed Recovery Strategy

Abrupt WT exit from frequency regulation causes significant active power reduction, triggering secondary SFD. Increasing active power output during speed recovery can mitigate SFD. The speed recovery time for G_{wi} is derived from (2):

$$\Delta t_{\text{rec},i} = \int_{\omega_{\min}}^{\omega_{0,i}} \frac{2H_{\text{WT},i}\omega_{\text{r},i}}{P_{\text{m},i} - P_{\text{e},i}} d\omega_{\text{r},i} \tag{7}$$

where $\Delta t_{\text{rec},i}$ is the speed recovery time of G_{wi}. Increasing $P_{\text{e},i}$ during recovery reduces accelerating power $P_{\text{m},i} - P_{\text{e},i}$, thereby extending $\Delta t_{\text{rec},i}$. Therefore, reducing SFD is essentially achieved by sacrificing the speed recovery time.

Two recovery strategies are proposed, illustrated in Fig. 1. Strategy 1 is depicted by the red line. Upon exit, WT's power

shifts from trajectory C-D-A to C-C'-A, reducing unbalanced power at exit and alleviating SFD. The expression for the red curve is:

$$P_{\mathrm{e}}=\begin{cases}P_{\mathrm{m(off)}}+k_{\mathrm{m}}(\omega_{\mathrm{r}}-\omega_{\mathrm{min})} & \omega_{\mathrm{r}}<\omega_0\\ P_{\mathrm{MPPT}} & \omega_{\mathrm{r}}\geq\omega_0\end{cases} \tag{8}$$

where P_{MPPT} is MPPT output power, $P_{\mathrm{m(off)}}$ is mechanical power at regulation exit, and k_{m} is the recovery slope:

$$k_{\mathrm{m}}=\frac{P_0-P_{\mathrm{m(off)}}}{\omega_0-\omega_{\mathrm{min}}} \tag{9}$$

where P_0 is the pre-disturbance steady-state mechanical power. Strategy 1 reduces SFD but yields excessive recovery time due to small accelerating power. To address this limitation, Strategy 2 is proposed to improve it. For a WT operating at fixed wind speed, strategy 1 employs a constant k_{m}, whereas strategy 2 progressively reduces this slope during recovery:

$$k_{\mathrm{m}}^{'}=k_{\mathrm{m}}(1-\frac{t-t_{\mathrm{off}}}{\Delta T}) \tag{10}$$

where t_{off} is exit time, and ΔT is a preset interval. If $t-t_{\mathrm{off}}<\Delta T$, $k_{\mathrm{m}}^{'}$ is positive and decays gradually; otherwise $k_{\mathrm{m}}^{'}$ is negative. The power trajectory is depicted by the blue line in Fig. 1. and the expression is $P_{\mathrm{m(off)}}+k_{\mathrm{m}}^{'}(\omega_{\mathrm{r}}-\omega_{\mathrm{min})}$. The final active power reference becomes:

$$P_{\mathrm{e}}^{'}=\max\{P_{\mathrm{m(off)}}+k_{\mathrm{m}}^{'}(\omega_{\mathrm{r}}-\omega_{\mathrm{min})},P_{\mathrm{MPPT}}\} \tag{11}$$

Therefore, Strategy 2 can reduce SFD and prevent prolonged rotor speed recovery time.

IV. Parameter Optimization Considering Frequency Security Constraints

The fixed values of the SI parameters and the variation ranges of their fuzzy-adaptive components are uncertain, which are need to be optimized. Moreover, wind speeds vary across WTs due to wake effects in practical wind farms, resulting in significant differences in available rotor kinetic energy among WTs, as shown in the equation:

$$\Delta E_{\mathrm{k},i}=\frac{1}{2}J_{\mathrm{w},i}(\omega_{0,i}^2-\omega_{\mathrm{min}}^2) \tag{12}$$

where $J_{\mathrm{w},i}$ is the moment of inertia of $\mathrm{G}_{\mathrm{w}i}$. To fully utilize the rotor kinetic energy of WTs, the SI parameters should also differ. However, optimizing parameters for each turbine would incur excessive computational burden, posing challenges for practical applications. Therefore, this paper firstly selects a wind turbine under a base wind speed to optimize its SI parameters, then determines the parameters for other turbines based on their initial available rotor kinetic energy.

A. Mathematical Model Considering Frequency Security Constraints

Assuming the base wind speed is υ_{b}, the WT operating at this speed is denoted as G_{wb}, its SI parameters are:

$$\begin{cases}k_{\mathrm{db}}=k_{\mathrm{d0b}}+k_{\mathrm{adb}}\\ k_{\mathrm{inb}}=k_{\mathrm{in0b}}+k_{\mathrm{ainb}}\end{cases} \tag{13}$$

where k_{db}、k_{inb} are the droop and inertia coefficients for G_{wb}; k_{d0b}、k_{in0b} are their fixed components; k_{adb}、k_{ainb} are fuzzy-adaptive components.

For normalization, the fuzzy controller's output range is [0,1]. Its outputs multiplied by scaling factors k_{b1}、k_{b2} yield actual k_{adb}、k_{ainb}. Thus, determining k_{b1}、k_{b2} and k_{d0b}、k_{in0b} defines the variation range of SI parameters. This paper sets the lower bound of the inertia coefficient to 0, leaving k_{b1}、k_{b2} and k_{d0b} as the parameters to optimize, denoted as $\boldsymbol{Z}=\left(k_{\mathrm{b1}},k_{\mathrm{b2}},k_{\mathrm{d0b}}\right)^{\mathrm{T}}$.

To verify the effectiveness of the proposed method, the following frequency security indices are established: (1) Initial rate of frequency change (R_{cof}), reflecting the frequency change rate during the initial period after disturbance; due to measurement and action delays, it is generally taken as the frequency change rate within 1 second after disturbance; (2) The nadir frequencies of the first two frequency drops (f_{nad1}、f_{nad2}); (3) Post-disturbance steady-state frequency (f_{ss}); (4) Rotor speed recovery time (t_{rec}).

Based on the aforementioned variables to be optimized and evaluation indices, the optimization problem for SI parameters considering frequency security constraints can be formulated as follows:

$$\begin{cases}\min & F=\max\left|f(t)-f_0\right|\\ \text{s.t.} & f(t)=g(\boldsymbol{Z})\\ & R_{\mathrm{cof}}\leq\bar{R}_{\mathrm{cof}}\\ & f_{\mathrm{nad1}}\geq f_{\mathrm{min}},\ f_{\mathrm{nad2}}\geq f_{\mathrm{min}}\\ & f_{\mathrm{ss}}\geq f_{\mathrm{ss,min}}\\ & \underline{k}_{\mathrm{d0b}}\leq k_{\mathrm{d0b}}\leq\bar{k}_{\mathrm{d0b}}\\ & 0\leq k_{\mathrm{b1}}\leq\bar{k}_{\mathrm{b1}},0\leq k_{\mathrm{b2}}\leq\bar{k}_{\mathrm{b2}}\end{cases} \tag{14}$$

where F is system's maximum frequency deviation; $f(t)$ is the system frequency response; $g(\cdot)$ reflects the nonlinear dynamical mapping between the optimization parameters and the system frequency; $\bar{R}_{\mathrm{cof}}$ is typically 1 Hz/s; $f_{\mathrm{ss,min}}$ is the lowest steady-state frequency allowed by the system; k_{b1}、k_{b2} and k_{d0b} have defined adjustment ranges: $\underline{k}_{\mathrm{d0b}}$ and $\bar{k}_{\mathrm{d0b}}$ denote the lower and upper bounds of k_{d0b}, while $\bar{k}_{\mathrm{b1}}$、$\bar{k}_{\mathrm{b2}}$ represent the upper bounds of k_{b1}、k_{b2}.

B. Parameter Optimization Based on Particle Swarm Algorithm

The SI parameter optimization problem in (20) exhibits strong nonlinearity. Its objective function and frequency security constraints lack explicit expressions. Thus, this paper employs PSO for solution. This method achieves efficient global

optimization through swarm intelligence search. The procedure is as follows:

1) Initialization

Optimization variables are k_{b1}、k_{b2} and k_{d0b}, hence dimension $D=3$. Set iteration count $k=0$. Randomly generate N particle positions $\boldsymbol{Z}_j^{(0)}(j=1,2,...,N)$, this paper sets $N=30$, where each particle represents a control parameter set; Initialize particle velocities $\boldsymbol{V}_j^{(0)}$ within feasible domain.

2) Fitness evaluation:

Compute frequency response curve $f(t)$ via time-domain simulation for each particle $\boldsymbol{Z}_j^{(k)}$ in the k-th iteration. Extract frequency security indices and calculate fitness value:

$$F_j = \max\left|f(t)-f_0\right|+\lambda \tag{15}$$

where λ is the constraint penalty term, if all constraints satisfied, $\lambda=0$, otherwise λ is a sufficiently large number.

3) Update optimal solution:

Compare current fitness F_j with historical optimum, update individual optimum $P_{\text{best},j}^{(k)}$ and position $\boldsymbol{P}_j^{(k)}$, then update global optimum $G_{\text{best}}^{(k)}$ and position $\boldsymbol{G}^{(k)}$.

4) Update particle state:

$$\begin{aligned}\boldsymbol{V}_i^{(k+1)} &= \omega\boldsymbol{V}_i^{(k)}+c_1r_1\left(\boldsymbol{P}_j^{(k)}-\boldsymbol{Z}_i^{(k)}\right)+c_2r_2\left(\boldsymbol{G}^{(k)}-\boldsymbol{Z}_i^{(k)}\right)\\ \boldsymbol{Z}_i^{(k+1)} &= \boldsymbol{Z}_i^{(k)}+\boldsymbol{V}_i^{(k+1)}\end{aligned} \tag{16}$$

where ω is inertia weight, $\omega=0.7$; c_1、c_2 are individual and social factors, $c_1=c_2=1.5$; r_1、r_2 are random numbers in [0,1].

5) Convergence Criteria

If $k\ge k_{\max}$ or $|\boldsymbol{G}^{(k)}-\boldsymbol{G}^{(k-1)}|\le\varepsilon$, output optimal solution $\boldsymbol{Z}_{\text{opt}}=\boldsymbol{G}^{(k)}$. Otherwise set $k=k+1$ and return to Step 2. This paper sets $k_{\max}=30$ and $\varepsilon=0.001$.

After obtaining optimized base parameters, the SI parameters for each WT are determined as follows:

$$\begin{cases}k_{\text{d},i}=k_{\text{db}}\dfrac{\omega_{\text{r},i}^2-\omega_{\min}^2}{\omega_{\text{b}}^2-\omega_{\min}^2}\\ k_{\text{in},i}=k_{\text{inb}}\dfrac{\omega_{\text{r},i}^2-\omega_{\min}^2}{\omega_{\text{b}}^2-\omega_{\min}^2}\end{cases} \tag{17}$$

where ω_{b} is the pre-disturbance steady-state rotor speed of G_{wb}.

V. CASE STUDY

A. Case System

To validate the effectiveness of the proposed method, a simulation model is built in MATLAB/Simulink. It is applied in the modified IEEE 3-machine 9-bus system, where the original synchronous generator G3 is replaced by a wind farm. The wind farm comprises six 25 MVA DFIGs. The wind speed of G_{w1}-G_{w6} is 12m/s, 10m/s, 9.5m/s, 11m/s, 10.5m/s and 8.5m/s. The schematic of the modified system is shown in Fig 3.

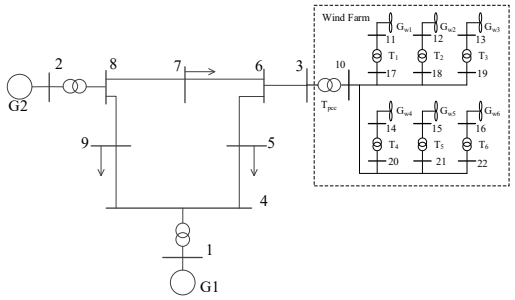


Fig. 3. The schematic diagram of modified IEEE 3-machine 9-bus system

B. Frequency Response Analysis Based on Parameter Optimization

10.5 m/s is set as the base speed，and all WTs operate at this speed. A sudden load increase of 50MW happened at 10 seconds. $f_{\min}$、$f_{\text{ss,min}}$ are 49.5Hz and 49.7Hz, $\underline{k}_{\text{d0b}}$、$\overline{k}_{\text{d0b}}$ are 5 and 25, $\overline{k}_{\text{b1}}$、$\overline{k}_{\text{b2}}$ are 30 and 10. The system frequency control strategy is optimized by PSO. The resulting parameters are that k_{d0b} is 13.494, and k_{b1}、k_{b2} are 19.202、6.456. Under these parameters, the system frequency response is shown by the red curve in Fig. 4. The results indicate that $R_{\text{cof}}=0.099$ Hz/s, and f_{nad1}、f_{nad2} are 49.581Hz and 49.592Hz, complying with all frequency security constraints.

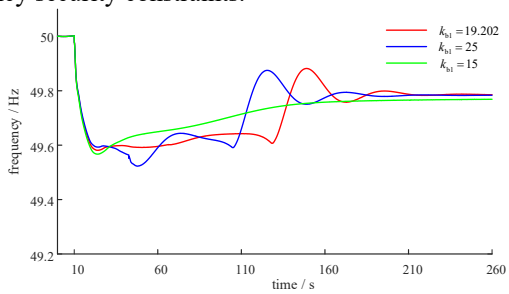


Fig. 4. Frequency responses under different k_{b1}

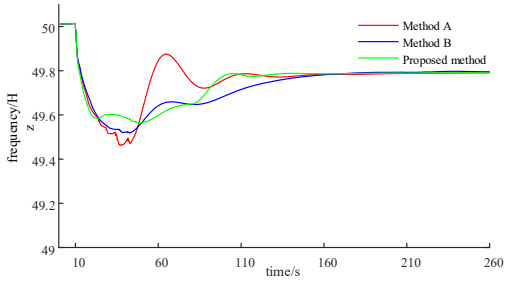
To analyze the impact of fuzzy-adaptive components on frequency response, simulations with $k_{\text{b1}}=25$ and $k_{\text{b1}}=15$ were conducted. Frequency response curves for different k_{b1} values are shown in Fig. 4. Results demonstrate that excessively large parameters increase f_{nad1} but significantly reduce f_{nad2}; overly small parameters decrease f_{nad1} and lower post-disturbance steady-state frequency, confirming the necessity of parameter optimization.

C. Comparative Analysis of Different Methods

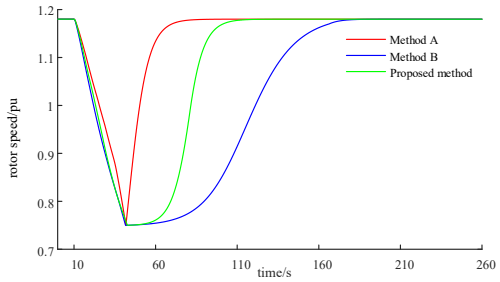
The proposed method is compared with conventional approaches to validate improved SI control effectiveness: 1) Method A: All WTs use traditional SI control with fixed parameters, where the droop and inertia coefficients are 30 and

10. 2) Method B: Turbines adopt rotor speed-adaptive parameters with recovery strategy 1. 3) Proposed Method: Turbines implement fuzzy-adaptive parameters based on frequency deviation and rotor kinetic energy with recovery strategy 2. G_{w1} - G_{w6} determine parameter ranges according to initial releasable energy and base wind speed.

Fig 5 compares system frequency and the speed of G_{w1} curves across control methods. Compared to Methods A and B, the proposed method significantly improves both frequency nadirs, which is attributed to its dynamic adjustment of synthetic inertia parameters based on system frequency and rotor speed, enabling optimal power dispatch. Although the proposed method exhibits a slight reduction in initial R_{cof} , it fully complies with frequency security requirements. Critically, it achieves substantially shorter rotor speed recovery time than Method B, which is attributed to the significantly larger accelerating power during rotor speed recovery in the proposed method. The simulation results show its effectiveness in both frequency support and recovery phases.



(a) frequency



（b）rotor speed of G_{w1}

Fig. 5. Compasion of different wind power regulation methods

VI. CONCLUSION

Regarding the proposed method, The main achievements are as follows: 1) During the frequency support phase, the proposed method utilizes system frequency and WT rotor speed as fuzzy inputs, fully exploiting WTs' frequency regulation potential to reduce SFD and raise both frequency nadirs. 2) Both rotor speed recovery strategies inherently mitigate SFD by extending recovery duration. Strategy 2 achieves shorter recovery times due to larger accelerating power, striking a balance between SFD suppression and recovery efficiency. 3) PSO-optimized fuzzy control parameters enhance the active frequency support capability of wind farms with wind speed difference, as validated by simulations.

ACKNOWLEDGMENT

This work is supported by the China Huaneng Group Co., Ltd. Headquarters Science and Technology Project (No. HNKJ24-H68), “Research on Key Technologies for Safe and Stable Operation of Grid-connected Offshore Wind Farms”.

REFERENCES

[1] TANG Yufeng,YANG Ping,YANG Yi. Frequency response control strategy of wind turbines considering frequency secondary drop[J]. Automation of Electric Power Systems,2023,47(9): 166-174.

[2] YU Jingyi, GE Jun, YANG Duotong, et al. Adaptive frequency support control strategy for wind farms based on rotor kinetic energy[J]. Electric Power Engineering Technology, 2024,43(5):131-139.

[3] WANG Bo, YANG Deyou, CAI Guowei. Review of research on power system inertia related issues in the context of high penetration of renewable power generation[J]. Power System Technology, 2020, 44(8): 2998-3007.

[4] WANG Z G, WU W C. Coordinated control method for DFIG based wind farm to provide primary frequency regulation service [J]. IEEE Transactions on Power Systems, 2018, 33(3): 2644-2659.

[5] Standardization Administration of the People’s Republic of China. Code on security and stability for power system: GB 38755—2019[S]. Beijing: Standards Press of China, 2019.

[6] WEN Yunfeng, YANG Weifeng, LIN Xiaohuang. Review and prospect of frequency stability analysis and control of low-inertia power systems[J]. Electric Power Automation Equipment, 2020, 40(9): 211-222.

[7] DING Lei, YIN Shanyao, WANG Tongxiao, JIANG Jiping, et al. Integrated Frequency Control Strategy of DFIGs Based on Virtual Inertia and Over-Speed Control[J]. Power System Technology, 2015,39(9):2385-2391.

[8] LEE J, MULJADI E, SRENSEN P, et al. Releasable kinetic ener gy-based inertial control of a DFIG wind power plant[J]. IEEE Transactions on Sustainable Energy, 2016, 7(1): 279-288.

[9] ZHANG Wenxin,WU Chen,HUANG Wei,GAO Huisheng,CHENG Min,XIN Huanhai. Evaluation of System Frequency Characteristic and Parameter Setting of Frequency Regulation for Wind Power Considering Secondary Frequency Drop[J]. Automation of Electric Power Systems, 2022,46(8):11-19.

[10] QIAO Ying, GUO Xiaoqian, LU Zongxiang, SUN Rongfu. Parameter Setting of auxiliary frequency regulation of wind turbines considering secondary frequency drop[J]. Power System Technology, 2020, 44(03):807-815.

[11] Morren J, de Haan S W H, Kling W L, et al. Wind turbines emulating inertia and supporting primary frequency control[J]. IEEE Transactions on Power Systems, 2006, 21(1): 433-434.

[12] YAO Yahan, XIONG Yongxin, YAO Wei, et al. Adaptive Distributed Cooperative Control of Wind Farms for Grid Frequency Fast Support [J]. Proceedings of the CSEE. 2024, 44(2):561-572.

[13] ULLAH N R, THIRINGER T, KARLSSON D. Temporary primary frequency control support by variable speed wind turbines—potential and applications[J]. IEEE Transactions on Power Systems, 2008, 23(2): 601-612.

[14] WU Z P, GAO D W, ZHANG H G, et al. Coordinated control strategy of battery energy storage system and PMSG WTG to enhance system frequency regulation capability[J]. IEEE Transactions on Sustainable Energy, 2017, 8(3): 1330 1343

[15] XIONG Yongxin, Active Frequency Support Control of Voltage Source Converter-based Multi-terminal Direct Current System Integrated Offshore Wind Farms[D], Wuhan, 2022.

[16] XIONG Y X,YAO W,YAO Y H,et al. Distributed coopera tive control of offshore wind farms integrated via MTDC system for fast frequency support[J]. IEEE Transactions on Industrial Electronics,2023,70(5):4693-4704.

The Bidding Strategy of Energy Storage in the Power Spot Market Based on the Adaptive McCormick Method

Hao Tong
College of Electrical Engineering
Shanghai University of Electric Power
Shanghai, China
294588674@qq.com

Jiang Li
College of Electrical Engineering
Shanghai University of Electric Power
Shanghai, China
lijiang_ee@shiep.edu.cn

Zishuo Zhang
College of Electrical Engineering
Shanghai University of Electric Power
Shanghai, China
1370164095@qq.com

***Abstract*—To enhance the economic benefits of energy storage stations in the electricity spot market environment, this paper proposes a bidding strategy for energy storage based on an adaptive McCormick method. First, a model framework for energy storage participation in the electricity spot market is constructed, and a bilevel bidding model is established. By employing duality theory and the Karush-Kuhn-Tucker (KKT) optimality conditions to replace the market clearing process, the bilevel model is transformed into a single-level model. To address the bilinear terms in the model's objective function, an adaptive piecewise McCormick method is proposed, incorporating dynamic relaxation interval contraction techniques and a relaxation interval backtracking mechanism. Finally, the effectiveness of the proposed strategy is verified using a modified IEEE 39-bus test system.**

Keywords—energy storage power station; electricity spot market; adaptive McCormick method; bi-level bidding model

I. INTRODUCTION

With the deepening reform of China's power sector, the development of electricity spot markets has been continuously improving [1]. The participation of energy storage has influenced market clearing prices and cleared quantities, fostering a more competitive market environment [2]. Research on bidding strategies for energy storage in spot markets has become a critical issue in ensuring efficient market operation and enhancing the economic benefits of energy storage stations.

In the research on energy storage bidding strategies, bilevel models and complementarity theory techniques have been widely applied [3-5]. Under the settlement rules of the initial electricity spot market, which features a dual-settlement mechanism combined with deviation penalties, energy storage stations are required to submit bidding strategies in the day-ahead market and subsequently participate in both the day-ahead and real-time market clearings. Their revenue consists of day-ahead market energy revenue, real-time market energy revenue, and deviation settlement revenue. By leveraging duality theory and the KKT optimality conditions, the bilevel bidding model can be transformed into a single-level bilinear programming problem [6-8]. However, the bilinear terms introduced by deviation settlement revenue pose significant computational challenges. To address this, reference [9] employs a bivariate piecewise McCormick relaxation method to handle bilinear terms, incorporating an iterative strategy that progressively narrows the bounds of continuous variables to reduce relaxation gaps. Reference [10] proposes a heuristic boundary contraction algorithm to further tighten the relaxation intervals obtained via piecewise McCormick relaxation, thereby recovering more feasible solutions near the optimal point. Nevertheless, during McCormick relaxation, improper settings for the bounds of continuous variables or the number of partitions may lead to constraint conflicts, resulting in solution failures.

To address the aforementioned challenges, this paper proposes an adaptive McCormick method-based bidding strategy for energy storage, which holistically optimizes the revenue from both the day-ahead and real-time markets while incorporating deviation settlement mechanisms. A bilevel market bidding framework is established to model this process. For the linearization of bilinear terms, an adaptive piecewise McCormick method is introduced, incorporating dynamic relaxation interval contraction and a relaxation interval backtracking technique. Finally, case studies based on the IEEE 39-bus system demonstrate the effectiveness of the proposed strategy.

II. FRAMEWORK FOR ENERGY STORAGE PARTICIPATION IN ELECTRICITY SPOT MARKETS

Energy storage participates in spot market energy trading through a "quantity-price bidding" mechanism. During the bidding day, independent energy storage systems submit their bids for the day-ahead and real-time markets via the electricity market trading platform. The Independent System Operator (ISO) then publishes the Locational Marginal Prices (LMPs) and cleared energy quantities for all market participants. The renewable energy generation curves and consumer load curves submitted on the bidding day are used for day-ahead market clearing. In the real-time market, the clearing process faces uncertainties due to fluctuations in renewable energy output and load demand. The combined uncertainties of real-time cleared quantities and electricity prices constitute risks that may reduce energy storage revenues. To address these risks, the Conditional Value-at-Risk (CVaR) method is introduced to manage the overall revenue risks across both day-ahead and real-time markets. Figure 1 illustrates the bidding model framework for energy storage participation in these two markets.

979-8-3315-5472-9/25/$31.00 ©2025 IEEE

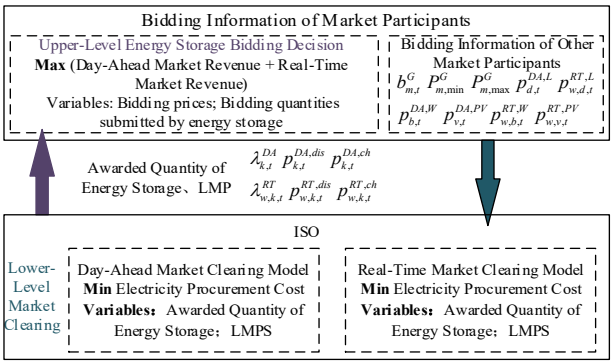


Fig. 1. Bidding Model Framework for Energy Storage Participation in Day-Ahead and Real-Time Markets.

The upper-level model formulates a trading decision framework with the objective of maximizing energy storage revenue. The lower-level model executes market clearing for both day-ahead and real-time markets based on bidding information from energy storage and other market participants, subsequently transmitting the clearing results back to the upper-level bidding model.

III. Bidding Strategy for Energy Storage Participation in Electricity Spot Markets

A. Upper-Level Energy Storage Station Bidding Strategy

Objective Function of the Upper-Level Model:

$$\max \ Obj = \Pi^{DA} + \Gamma^{RT} \tag{1}$$

where

$$\Pi^{DA} = \sum_{t=1}^{T}\sum_{k=1}^{N_{ESS}} \lambda_{k,t}^{DA}(p_{k,t}^{DA,dis} - p_{k,t}^{DA,ch}) \tag{2}$$

$$\Pi_w^{RT} = \sum_{t=1}^{T}\sum_{k=1}^{N_{ESS}} [\lambda_{w,k,t}^{RT}(p_{w,k,t}^{RT,dis} - p_{w,k,t}^{RT,ch}) + \lambda_{w,k,t}^{RT}(p_{k,t}^{DA,ch} - p_{k,t}^{DA,dis})] \tag{3}$$

$$\Gamma^{RT} = \lambda CVaR^{RT} + (1-\lambda)\sum_{w=1}^{W}\pi_w \Pi_w^{RT} \tag{4}$$

$$CVaR^{RT} = VaR^{RT} - \frac{1}{1-\beta}\sum_{w=1}^{W}\pi_w \eta_w \tag{5}$$

$$VaR^{RT} - \Pi_w^{RT} \le \eta_w, \forall w \tag{6}$$

$$\eta_w \ge 0, \forall w \tag{7}$$

Equation (1) indicates that the objective of energy storage bidding is to maximize the sum of day-ahead market revenue Π^{DA} and real-time market revenue Γ^{RT}. Equation (2) defines the day-ahead market revenue Π^{DA} for energy storage. Equation (3) represents the real-time market revenue Π_w^{RT} for energy storage under scenario w, which consists of real-time energy revenue and deviation settlement revenue. N_{ESS} denotes the number of energy storage stations; $p_{k,t}^{DA,dis}$ and $p_{k,t}^{DA,ch}$ are the dispatched discharge and charge power of energy storage station k in the day-ahead market for time period t, respectively; $p_{w,k,t}^{RT,dis}$ and $p_{w,k,t}^{RT,ch}$ are the dispatched discharge and charge power of energy storage station k in the real-time market for time period t under scenario w, respectively; $\lambda_{k,t}^{DA}$ is the day-ahead LMP at the node of energy storage station k for time period t, and $\lambda_{w,k,t}^{RT}$ is the real-time LMP at the node of energy storage station k for time period t under scenario w. These prices are derived from the dual variables of the power balance constraints in the respective lower-level day-ahead and real-time market clearing models, representing the marginal cost of maintaining nodal power balance in the system. Equation (4) calculates the real-time market revenue Γ^{RT} using the expected revenue $E(\Pi_w^{RT})$ and the risk term $CVaR^{RT}$. Here, λ is the risk preference coefficient, reflecting the risk tolerance of the energy storage. A higher λ indicates greater risk aversion, with λ ranging over [0,1]; π_w is the probability of scenario w. Equations (5)-(7) represent the CVaR constraints, where VaR^{RT} is the value-at-risk of the real-time revenue Π_w^{RT}; β is the confidence level; and η_w quantifies the shortfall of Π_w^{RT} below VaR^{RT} under scenario w. The bidding strategy must satisfy operational constraints, including charge/discharge state constraints, power limits, and energy capacity constraints, with the final energy level required to match the initial state.

B. Lower-Level Electricity Spot Market Clearing Model

Both the day-ahead and real-time market clearing models employ the Security Constrained Economic Dispatch (SCED) framework. The market pricing mechanism is based on LMP theory, where nodal electricity prices are determined by calculating the Lagrange multipliers associated with the power balance constraints in the SCED optimization model.

Both the day-ahead and real-time SCED models formulate their clearing objectives as minimization of energy procurement costs, subject to the following system constraints: nodal power balance constraints, dispatch quantity limits for energy storage stations and conventional generation units, generator ramping constraints, transmission line capacity limits, and voltage angle constraints [4].

IV. Model Transformation and Solution

A. Lower-Level Model Transformation

The proposed bilevel model in this study is transformed into a single-level optimization problem through the application of duality theory and KKT optimality conditions, where the lower-level model is equivalently replaced by corresponding constraints in the upper-level problem. The mathematical reformulation is presented as follows:

$$\begin{aligned}\max \ Obj = &\sum_{t=1}^{T}\sum_{k=1}^{N_{ESS}} \lambda_{k,t}^{DA}(p_{k,t}^{DA,dis} - p_{k,t}^{DA,ch}) + \lambda CVaR^{RT} \\ &+(1-\lambda)\sum_{w=1}^{W}\pi_w \sum_{t=1}^{T}\sum_{k=1}^{N_{ESS}} [\lambda_{w,k,t}^{RT}(p_{w,k,t}^{RT,dis} - p_{w,k,t}^{RT,ch}) \\ &+\lambda_{w,k,t}^{RT}(p_{k,t}^{DA,ch} - p_{k,t}^{DA,dis})]\end{aligned} \tag{8}$$

$$\text{s.t.} \quad (4)-(7) \tag{9}$$

The day-ahead market SCED model is reformulated as:

$$b_{m,t}^{G} - \lambda_{m,t}^{DA} + \beta_{m,t}^{DA,G,\max} - \beta_{m,t}^{DA,G,\min} - (\mu_{m,t+1}^{DA,G,RU} - \mu_{m,t+1}^{DA,G,RD}) = 0, \forall m, t = 1 \quad (10)$$

$$0 \le \omega_{k,t}^{DA,dis,\min} \perp p_{k,t}^{DA,dis} \ge 0, \forall k, \forall t \quad (11)$$

$$0 \le \omega_{k,t}^{DA,dis,\max} \perp (P_{k,t}^{dis} - p_{k,t}^{DA,dis}) \ge 0, \forall k, \forall t \quad (12)$$

The clearing constraints only display the derivation results for generation unit variables and the awarded quantity constraints for energy storage stations. Here, $b_{m,t}^{G}$ represents the generation price bid by unit m in time period t; $\lambda_{m,t}^{DA}$ is the day-ahead clearing price at the node of unit m in time period t; $\beta_{m,t}^{DA,G,\min}$, $\beta_{m,t}^{DA,G,\max}$, $\mu_{m,t}^{DA,G,RU}$ and $\mu_{m,t}^{DA,G,RD}$ are the dual variables for the power output limits and ramping constraints of the generation units, respectively; $\omega_{k,t}^{DA,dis,\min}$ and $\omega_{k,t}^{DA,dis,\max}$ are the dual variables for the awarded quantity constraints of energy storage. The transformation process for the real-time market SCED model follows a similar approach and is omitted here for brevity.

B. Linearization Techniques

The single-level optimization model described above contains the following three types of nonlinear terms: 1. Complementary slackness constraints (Equations (11)-(12)); 2. Bilinear terms in the objective function (Equation (8)): $\lambda_{k,t}^{DA}(p_{k,t}^{DA,dis} - p_{k,t}^{DA,ch})$, $\lambda_{w,k,t}^{RT}(p_{w,k,t}^{RT,dis} - p_{w,k,t}^{RT,ch})$; 3. Additional bilinear terms in the objective function (Equation (8)): $\lambda_{w,k,t}^{RT}(p_{k,t}^{DA,ch} - p_{k,t}^{DA,dis})$.

The first type of nonlinear terms is linearized using the big-M method [11]. For the second type of nonlinear terms, the approach from reference [12] is adopted, employing strong duality theory and KKT optimality conditions to linearize the bilinear terms involving market-cleared power and electricity prices in the objective function. The third type of nonlinear terms is processed using piecewise McCormick relaxation. The optimal solution obtained through piecewise McCormick relaxation can be regarded as a globally optimal solution to the relaxed problem, though it may not be feasible for the original model. The relaxation accuracy gradually improves with increasing number of segments for continuous variables, but at the cost of significantly higher mixed-integer computational burden. Moreover, due to the lack of precise bounds information for continuous variables, improper segmentation may lead to constraint conflicts, resulting in relaxation failure. To address these issues, this paper proposes an adaptive piecewise McCormick technique that dynamically adjusts the upper and lower bounds of relaxation intervals based on solution space information obtained during iterations, while incorporating a relaxation interval backtracking mechanism.

a) Piecewise McCormick Relaxation Technique:

Auxiliary variables $\xi_{w,k,t}$ and $p_{k,t,ch-dis}^{DA}$ are introduced:

$$\xi_{w,k,t} = \lambda_{w,k,t}^{RT} p_{k,t,ch-dis}^{DA} \quad (13)$$

$$p_{k,t,ch-dis}^{DA} = (p_{k,t}^{DA,ch} - p_{k,t}^{DA,dis}) \quad (14)$$

The variables $\lambda_{w,k,t}^{RT}$ and $p_{k,t,ch-dis}^{DA}$ are expressed in the following piecewise form:

$$\lambda_{w,k,t}^{RT} = \sum_{o=1}^{O}\sum_{h=1}^{H} \lambda_{w,k,t,o,h}^{RT}, \forall w, \forall k, \forall t \quad (15)$$

$$p_{k,t,ch-dis}^{DA} = \sum_{o=1}^{O}\sum_{h=1}^{H} p_{k,t,ch-dis,o,h}^{DA}, \forall k, \forall t \quad (16)$$

$$\sum_{o=1}^{O}\sum_{h=1}^{H} y_{w,k,t,o,h} = 1, \forall w, \forall k, \forall t \quad (17)$$

$$y_{w,k,t,o,h}\lambda_{w,k,t,o}^{RT,\min} \le \lambda_{w,k,t,o,h}^{RT} \le y_{w,k,t,o,h}\lambda_{w,k,t,o}^{RT,\max}, \forall w, \forall k, \forall t \quad (18)$$

$$y_{w,k,t,o,h} p_{k,t,ch-dis,h}^{DA,\min} \le p_{k,t,ch-dis,o,h}^{DA} \le y_{w,k,t,o,h} p_{k,t,ch-dis,h}^{DA,\max}, \forall w, \forall k, \forall t \quad (19)$$

In the equations: O and H denote the number of segments for $\lambda_{w,k,t}^{RT}$ and $p_{k,t,ch-dis}^{DA}$, respectively. $y_{w,k,t,o,h}$ represents the indicator variable. Equations (15)-(16) ensure comprehensive consideration of all segmentation results. Equation (17) restricts the selection to only one segment. Equations (18)-(19) specify the upper and lower bound constraints for the variable segments, where the bounds of $\lambda_{w,k,t}^{RT}$ and $p_{k,t,ch-dis}^{DA}$ are determined from historical operational data.

Based on the piecewise McCormick relaxation technique, the linearized constraints after relaxation are formulated as follows:

$$\xi_{w,k,t} \ge \sum_{o=1}^{O}\sum_{h=1}^{H} (\lambda_{w,k,t,o}^{RT,\min} p_{k,t,ch-dis,o,h}^{DA} + \lambda_{w,k,t,o,h}^{RT} p_{k,t,ch-dis,h}^{DA,\min} - \lambda_{w,k,t,o}^{RT,\min} p_{k,t,ch-dis,h}^{DA,\min} y_{w,k,t,o,h}), \forall w, \forall k, \forall t \quad (20)$$

$$\xi_{w,k,t} \ge \sum_{o=1}^{O}\sum_{h=1}^{H} (\lambda_{w,k,t,o}^{RT,\max} p_{k,t,ch-dis,o,h}^{DA} + \lambda_{w,k,t,o,h}^{RT} p_{k,t,ch-dis,h}^{DA,\max} - \lambda_{w,k,t,o}^{RT,\max} p_{k,t,ch-dis,h}^{DA,\max} y_{w,k,t,o,h}), \forall w, \forall k, \forall t \quad (21)$$

$$\xi_{w,k,t} \le \sum_{o=1}^{O}\sum_{h=1}^{H} (\lambda_{w,k,t,o}^{RT,\max} p_{k,t,ch-dis,o,h}^{DA} + \lambda_{w,k,t,o,h}^{RT} p_{k,t,ch-dis,h}^{DA,\min} - \lambda_{w,k,t,o}^{RT,\max} p_{k,t,ch-dis,h}^{DA,\min} y_{w,k,t,o,h}), \forall w, \forall k, \forall t \quad (22)$$

$$\xi_{w,k,t} \le \sum_{o=1}^{O}\sum_{h=1}^{H} (\lambda_{w,k,t,o}^{RT,\min} p_{k,t,ch-dis,o,h}^{DA} + \lambda_{w,k,t,o,h}^{RT} p_{k,t,ch-dis,h}^{DA,\min} - \lambda_{w,k,t,o}^{RT,\min} p_{k,t,ch-dis,h}^{DA,\min} y_{w,k,t,o,h}), \forall w, \forall k, \forall t \quad (23)$$

Increasing the number of segments O and H improves relaxation accuracy but significantly raises mixed-integer computational burden. Simulation results demonstrate that alternating variable segmentation effectively reduces solver computation time. To further narrow the relaxation gap, a boundary contraction algorithm dynamically adjusts relaxation intervals through the following steps:

1) For variable $\lambda_{w,k,t}^{RT}$, after initial segmentation, obtain the optimal values $\lambda_{w,k,t,o}^{RT}$ and $p_{k,t,ch-dis}^{DA}$ (denoted as Point A) with the objective value Obj^{LB}.

2) Take the midpoint between $\lambda_{w,k,t,o}^{RT,\min}$ and $\lambda_{w,k,t,o}^{RT,\max}$ re-optimize the bidding strategy to derive new optimal values $\lambda_{w,k,t,o}^{RT}$ and $p_{k,t,ch-dis}^{DA}$ (denoted as Point A') with the objective value Obj^{UP}.

3) Contract the initial relaxation interval to the new range bounded by Points A and A'.

The boundary contraction process for variable $p_{k,t,ch-dis}^{DA}$ follows an analogous procedure. Figure 2 illustrates this alternating variable segmentation and boundary contraction mechanism.

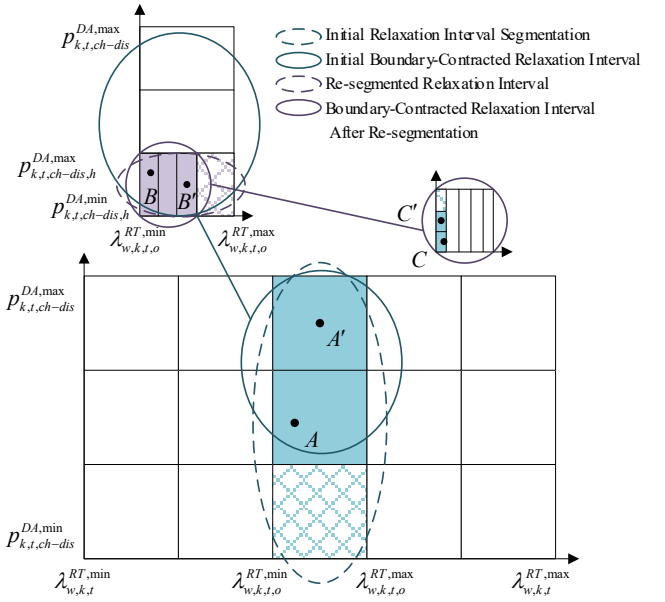


Fig. 2. Schematic Diagram of Continuous Alternating Variable Segmentation and Boundary Shrinkage.

b) Relaxation Interval Backtracking Technique:

Upon successful solution using piecewise McCormick relaxation, the relaxation interval records are updated by incorporating the latest intervals into the historical database. If the solution fails, the relaxation interval backtracking technique examines previous interval records and restricts the current variable's relaxation range within historical bounds. Subsequently, only the current variable undergoes segmentation while maintaining fixed relaxation intervals for other variables, thereby simplifying the model and enhancing solution stability.

V. Case Studies

A. Input Data and Parameters

The modified IEEE 39-bus system is shown in Figure 3, consisting of 39 buses, 10 generators and 46 transmission lines. Wind farms W1 and W2 comprise 40 wind turbines each with 1.5MW capacity, while the PV plant is equipped with an 80MW photovoltaic array. Two 30MW/60MWh lithium iron phosphate energy storage stations are installed at bus 10 and bus 18 respectively. The system load and day-ahead forecast power of renewable energy sources are presented in Figure 4.

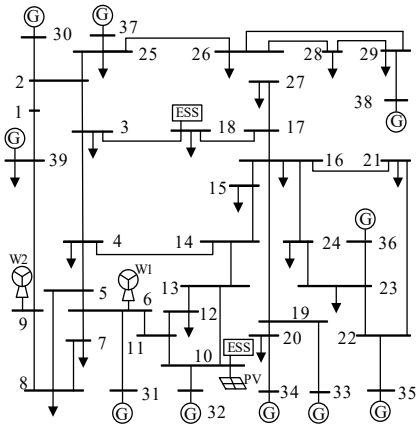


Fig. 3. System Wiring Diagram.

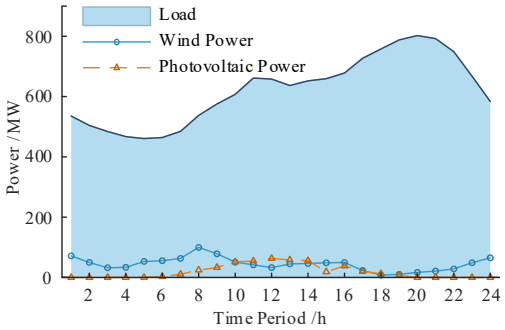


Fig. 4. Day-Ahead Market Load and New Energy Power Curves.

B. Energy Storage Bidding Strategy

The bidding strategy of Energy Storage Station 1 is illustrated in Figure 5.

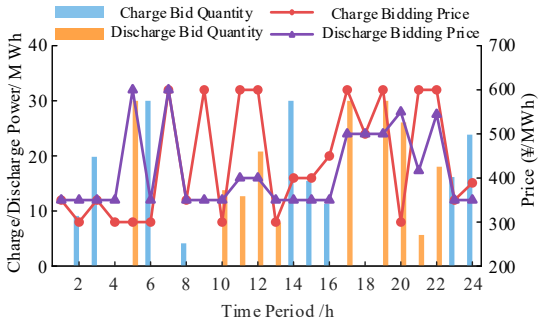


Fig. 5. Energy Storage 1 Bidding Strategy.

To compare the performance of different energy storage bidding strategies in the electricity spot market, the following two strategies were designed.

Strategy 1: Maximizing energy storage revenue in the day-ahead market. This strategy optimizes the bidding quantity and price of energy storage in the day-ahead market based on load forecasts and renewable energy generation predictions, aiming to maximize profits by leveraging electricity price differentials.

Strategy 2: This approach maximizes the combined revenue of energy storage in both day-ahead and real-time markets while balancing risk-return trade-offs. By incorporating the CVaR risk

management method with risk coefficient λ and confidence level β, it dynamically optimizes the bidding quantities and prices across both markets. The comparison between the two strategies evaluates the impact of real-time market uncertainties on storage revenues. Strategy 1 serves as the baseline, employing static optimization for short-term decisions by ignoring real-time market uncertainties. In contrast, Strategy 2 explores the potential for revenue enhancement through multi-timescale optimization and risk balancing.

The market clearing results for energy storage are presented in Figures 6 and 7.

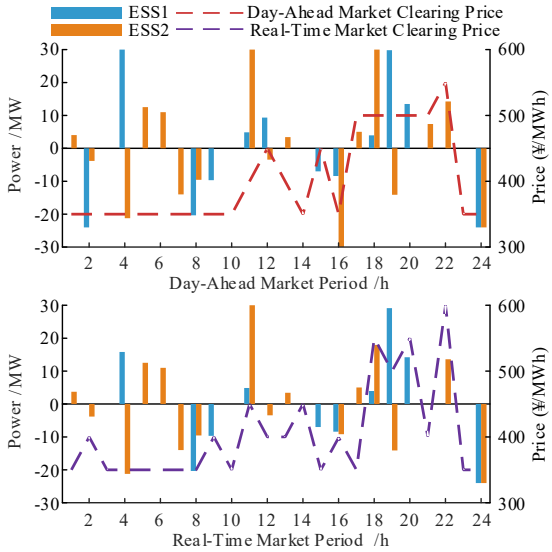


Fig. 6. Strategy 1 Energy Storage Clearing Result.

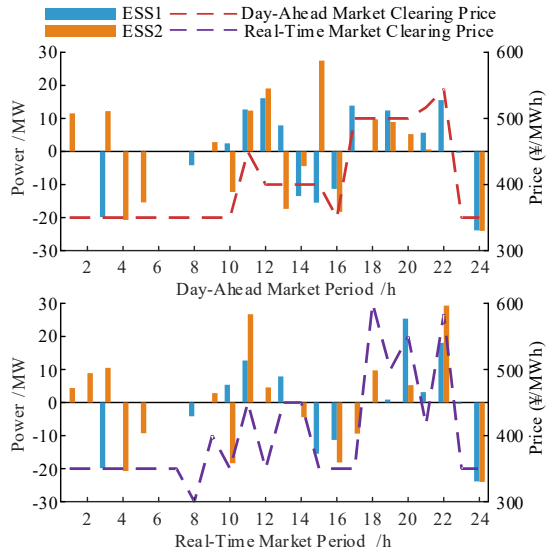


Fig. 7. Strategy 2 Energy Storage Clearing Result.

1) Day-Ahead Market Energy Revenue

Under Strategy 2, ESS1's day-ahead revenue increased from ¥6,923.77 (Strategy 1) to ¥8,323.17, while ESS2's revenue decreased from ¥7,596.07 to ¥5,394.36. Overall, Strategy 1 yielded higher total day-ahead revenue than Strategy 2.

2) Real-Time Market Energy Revenue

Under Strategy 2, ESS1's real-time revenue rose from ¥6,971.15 (Strategy 1) to ¥9,427.48, and ESS2's revenue increased from ¥4,194.94 to ¥10,962.34. Strategy 1 failed to effectively coordinate charging/discharging demands in the real-time market, resulting in lower real-time revenue. In contrast, Strategy 2 optimized bidding by jointly maximizing revenue across both markets. By strategically charging during low-price periods and enhancing discharge capacity during high-price intervals, it significantly improved real-time market earnings.

3) Deviation Settlement Revenue

Under Strategy 1, the deviation settlement revenues for the two energy storage systems were -¥6,726.24 and -¥5,166.47, respectively. In Strategy 2, these values improved to -¥5,123.75 and -¥5,106.94. By adopting more balanced day-ahead charging/discharging behaviors, Strategy 2 effectively reduced real-time market deviations and enhanced revenue performance.

The total energy storage revenue under Strategy 2 increased from ¥13,793.22 (Strategy 1) to ¥23,876.69. While Strategy 1 primarily focused on maximizing day-ahead market revenue, it inadequately addressed real-time market participation and deviation adjustments. In contrast, Strategy 2 holistically optimized revenues across both markets, enabling more flexible operation and delivering overall profit gains.

C. Comparison of Optimization Results Using Different Linearization Methods

To analyze the impact of different linearization methods on bidding strategy optimization results, Figure 7 demonstrates the error convergence performance of different methods in real-time Scenario 1.

Method 1: Piecewise McCormick relaxation without boundary contraction algorithm or relaxation interval backtracking technique.

Method 2: Piecewise McCormick relaxation without boundary contraction algorithm but with relaxation interval backtracking technique.

Method 3: Piecewise McCormick relaxation with boundary contraction algorithm but without relaxation interval backtracking technique.

Method 4: Piecewise McCormick relaxation with both boundary contraction algorithm and relaxation interval backtracking technique.

As shown in Figure 8, Method 1 failed to converge at the 6th iteration with a solution error of 5.22%. Method 2, after initial failure, successfully converged at the 9th iteration by reapplying the relaxation interval from the 4th iteration, reducing the error to 0.46%. Method 3 failed at the 4th iteration with a 2.18% error. Method 4, upon encountering failure, adjusted the segmentation using the relaxation interval from the 2nd iteration and achieved convergence at the 8th iteration with a further reduced error of 0.24%. Regarding total revenue, Method 1 yielded ¥21,473.12, Method 2 ¥21,333.38, Method 3 ¥21,867.19, while Method 4 achieved the highest revenue of ¥23,876.69.

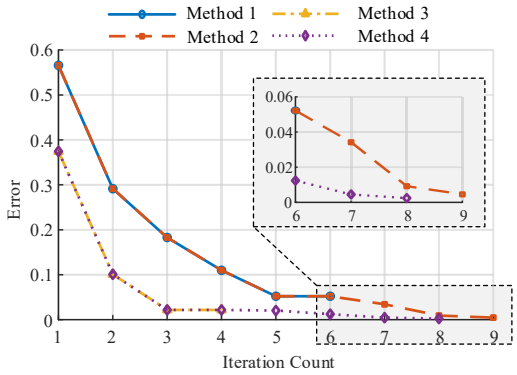


Fig. 8. Comparison of Convergence of Different Algorithms.

The results demonstrate that the boundary contraction technique significantly accelerates error convergence, while the relaxation interval backtracking effectively enhances convergence stability. Method 4 exhibits superior performance in both revenue optimization and convergence efficiency, further validating the synergistic effect of boundary contraction and relaxation interval backtracking techniques in optimizing energy storage bidding strategies for electricity spot market participation.

VI. Conclusions

This paper proposes an adaptive McCormick method-based bidding strategy for energy storage participation in electricity spot markets, addressing the revenue maximization problem across day-ahead and real-time markets while incorporating deviation settlement mechanisms and real-time market uncertainties. Theoretical analysis and simulation studies yield the following conclusions:

1) The proposed bidding strategy holistically considers the coupling effects between day-ahead and real-time markets. By integrating deterministic forecasting data from the day-ahead market with real-time scenario generation techniques, it dynamically adjusts energy storage's bidding quantities and prices in both markets. This approach effectively enhances the operational adaptability and revenue performance in real-time markets, achieving a 73.1% total revenue improvement.

2) Conventional McCormick methods often exhibit insufficient convergence performance when solving bilinear problems. The proposed adaptive McCormick method significantly improves solution efficiency and accuracy while guaranteeing optimality through dynamic relaxation interval contraction and backtracking mechanisms.

The proposed methodology is applicable to energy storage bidding strategy optimization under spot market dual-settlement schemes. Future research may extend this approach to multi-market environments, including ancillary service markets and carbon trading markets, to more comprehensively unlock energy storage's economic potential.

References

[1] CPC Central Committee and the State Council, "Opinions on acceleratin g the construction of a national unified market," Apr. 10, 2022. [Online]. Available: https://www.gov.cn/zhengce/2022-04/10/content_5684385.h tm. [Accessed: Sep. 24, 2023].

[2] K. Hartwig and I. Kockar, "Impact of strategic behavior and ownership of energy storage on provision of flexibility," IEEE Trans. Sustainable Energy, vol. 7, no. 2, pp. 744-754, 2015.

[3] C. Ruiz and A. J. Conejo, "Pool strategy of a producer with endogenous formation of locational marginal prices," IEEE Trans. Power Syst., vol. 24, no. 4, pp. 1855-1866, 2009.

[4] G. Li, K. Yan, G. Fan, et al., "Research on trading decision of energy storage participation in spot power energy and frequency regulation auxiliary service market," Power Syst. Prot. Control, vol. 50, no. 17, pp. 45-54, 2022.

[5] X. Jiang, M. Liu, T. Wang, et al., "Bidding strategy of grid-side energy storage power station in the joint spot market," Power Grid Technol., vol. 45, no. 9, pp. 3398-3408, 2021.

[6] Y. Wang, Y. Dvorkin, R. Fernandez-Blanco, et al., "Look-ahead bidding strategy for energy storage," IEEE Trans. Sustainable Energy, vol. 8, no. 3, pp. 1106-1117, 2017.

[7] H. Zhao, W. Wang, X. Li, et al., "Day-ahead joint trading decision model for energy-frequency regulation-reserve market considering energy storage participation," Power Grid Technol., vol. 47, no. 11, pp. 4575-4587, 2023.

[8] C. N. Dimitriadis, E. G. Tsimpopoulos, and M. C. Georgiadis, "Strategic bidding of an energy storage agent in a joint energy and reserve market under stochastic generation," Energy, vol. 242, p. 123026, 2022.

[9] X. Zhao, Y. Liang, M. Sun, et al., "Convex relaxation of dynamic optimization dispatch model for AGC units and its bi-level iterative algorithm," Power Syst. Autom., vol. 46, no. 17, pp. 228-238, 2022.

[10] L. Deng, H. Sun, B. Li, et al., "Optimization dispatch strategy for combined heat and power systems based on tightened McCormick method," Engineering, vol. 7, no. 8, pp. 89-111, 2021.

[11] Z. Yi, Y. Xu, J. Zhou, et al., "Bi-level programming for optimal operation of an active distribution network with multiple virtual power plants," IEEE Trans. Sustainable Energy, vol. 11, no. 4, pp. 2855-2869, 2020.

[12] X. Wang, H. Jia, X. Jin, et al., "Bi-level optimal operations for grid operator and low-carbon building prosumers with peer-to-peer energy sharing," Appl. Energy, vol. 359, p. 122723, 2024.

Decision Optimization for Virtual Power Plants Participating in the Coupled Electricity-Carbon Market

Na Wang
Shanghai Electric Power Research Institute
State Grid Shanghai Municipal Electric Power Company
Shanghai, China
wangna@sh.sgcc.com.cn

Tiantian Chen
Shanghai Electric Power Research Institute
State Grid Shanghai Municipal Electric Power Company
Shanghai, China
chentiantian@sh.sgcc.com.cn

Chen Wang
Shanghai Electric Power Research Institute
State Grid Shanghai Municipal Electric Power Company
Shanghai, China
wangchen@sh.sgcc.com.cn

Pengwei Wang
Faculty of Electrical Engineering
Shanghai University of Electric Power
Shanghai, China
15698102260@163.com

Linxuan Zhao
Shanghai Electric Power Research Institute
State Grid Shanghai Municipal Electric Power Company
Shanghai, China
zhaolinxuan@sh.sgcc.com.cn

Jing Liu
Shanghai Electric Power Research Institute
State Grid Shanghai Municipal Electric Power Company
Shanghai, China
liujing@sh.sgcc.com.cn

***Abstract*—Under the dual goals of carbon peaking and carbon neutrality, Virtual Power Plants (VPPs) are emerging as pivotal market participants and are becoming integral to the future of smart grid infrastructure. To investigate bidding strategies that balance economic efficiency with carbon reduction objectives, this study proposes a bi-level optimization model for VPP participation in the coupled market. The upper level focuses on profit maximization for VPPs, while the lower level models the clearing mechanisms of the integrated electricity and carbon markets. A collaborative optimization algorithm based on the Markov Decision Process (MDP) is developed to solve the model. Simulation results show that VPPs can increase their market-clearing volumes through coupled transactions, while simultaneously reducing the clearing volume of conventional coal-fired units. This not only enhances the environmental value of VPPs but also facilitates the low-carbon transformation of the modern energy system and improves the synergistic operation across multiple energy markets.**

Keywords—Electricity Market, Carbon Market, Virtual Power Plant, Renewable Energy Units Markov Decision Process

I. INTRODUCTION

Under the overarching goals of carbon peaking and carbon neutrality, and in the context of the development of a new-type power system, VPP has emerged as a promising solution. As a virtual power system that integrates and coordinates small-scale distributed energy resources through advanced information and communication technologies and software platforms, VPP enable the digital aggregation and flexible dispatch of resources. This digitalization facilitates the efficient utilization of energy resources, thereby promoting the transition of the power system towards a low-carbon and flexible future.

Regarding the interaction between the electricity market and the carbon market, [1–3] have shown that incorporating carbon and green certificate markets into the electricity market can enhance the competitiveness of renewable energy sources. In terms of carbon market modeling, existing research that explores the impact of carbon pricing on the electricity market often treats the carbon price as a fixed value, overlooking the strategic behavior of various power generation enterprises in the carbon market and its influence on electricity market dynamics [6–11]. For instance, [12] developed a tiered electricity pricing model based on a benchmark carbon price and demonstrated that the carbon price increases with higher levels of carbon emissions. On the electricity market modeling side, [13] proposed a bi-level source-load trading model based on multi-market coupling. References [14–15] investigated the optimal strategies of power producers participating in coupled electricity–carbon markets by establishing bi-level optimization models.

With the continuous advancement of technology, the integration between the electricity market and carbon market has been deepening, and the advantages of VPP in aggregating renewable energy and alleviating carbon emission pressures have become increasingly prominent [16–17]. To address the uncertainties in electricity price and quantity faced by VPP in competitive electricity markets, [18] proposed a flexible segmented bidding strategy for VPP. This strategy effectively leverages the VPP's regulation capabilities, ensuring the success of bidding while improving both the economic returns of VPP and their social benefits. References [19–20] developed a collaborative optimization model based on time-of-use pricing, which enhances the accommodation of renewable energy and

This work is supported by the Science and Technology Project of State Grid Corporation of China (Contract No. B3094024000B).

979-8-3315-5472-9/25/$31.00 ©2025 IEEE

significantly improves the economic performance and low-carbon operation of VPP. Reference [21] introduced a low-carbon economic dispatch model for a carbon capture-enabled VPP, taking into account green certificate trading, aiming to further optimize its environmental and economic performance.

Existing research has primarily focused on the trading performance of VPP in single markets, with limited attention given to their decision-making behavior in coupled electricity–carbon markets. Moreover, most current studies tend to overlook the interactions among different market participants, which can significantly influence market outcomes. To address these gaps, this paper proposes a bi-level trading model for VPP participation in the coupled electricity–carbon market. A MDP-based solution approach is introduced to solve the model, enabling the analysis of VPP trading strategies and optimization processes across multiple markets. This work contributes to the literature by offering new insights into multi-market decision-making and enriching the theoretical framework of electricity–carbon market integration.

II. Internal Mechanism of VPP Participation in the Electricity–Carbon Market

A VPP is a distributed energy aggregation system based on advanced information and communication technologies and energy management techniques. Essentially, a VPP defines an energy portfolio through software, exhibiting key features such as flexibility, cost-effectiveness, and sustainability.

The electricity trading market is primarily divided into the day-ahead market and the real-time market. In the day-ahead market, VPPs can formulate generation schedules based on their power generation capabilities, market demand forecasts, and historical electricity prices. In the real-time market, VPPs are able to swiftly adjust their power generation and consumption strategies in response to real-time price fluctuations and power supply-demand conditions. For instance, when the system experiences a power shortage and electricity prices are high, a VPP can discharge energy from storage systems to increase power supply and maximize profits. Conversely, during periods of power surplus and low prices, the VPP can charge its storage systems or reduce coal-fired power output to lower operational costs. In the carbon trading market, VPPs can increase their emission reduction potential by aggregating renewable energy sources such as wind and solar. These emission reductions can be converted into China Certified Emission Reduction (CCER) through established mechanisms. As active participants in the carbon market, VPPs can generate additional revenue by selling CCER or engaging directly in carbon allowance trading, thereby achieving the monetization of their environmental value.

III. A Bi-level Coupled Trading Model for VPP Participation in the Electricity–Carbon Market

This paper develops a bi-level trading model in which the VPP participates as a market entity in the coupled electricity–carbon market. The upper-level model aims to maximize the profits of various power producers, including the VPP, wind and solar generation units, and conventional coal-fired power plants. The lower-level model represents the clearing mechanisms of the electricity and carbon markets, with the objective of cost reduction and efficiency optimization. It achieves market equilibrium through a coupling mechanism between electricity prices and carbon prices.

A. Upper-Level Model: Profit Maximization of Power Producers

1) Virtual Power Plant Power Producer

a) Objective Function: Profit Maximization of the Virtual Power Plant Producer.

$$\max F_{VPP} = F_{VPP}^{D} + F_{VPP}^{R} + F_{VPP}^{C} - C_{VPP} \tag{1}$$

$$F_{VPP}^{D} = \sum_{t=1}^{T} \lambda_t^{D} \cdot P_t^{D,VPP} \tag{2}$$

$$F_{VPP}^{R} = \sum_{s=1}^{S}\sum_{t=1}^{T} \chi_s \cdot \lambda_t^{R} \cdot P_{t,s}^{R,VPP} \tag{3}$$

$$F_{VPP}^{C} = \sum_{t=1}^{T} \lambda_t^{CE} \cdot \left(Q_{pei,t}^{CE,VPP} - Q_{pai,t}^{CE,VPP}\right) + \lambda_t^{CCER} \cdot Q_{sell,t}^{CCER,VPP} \tag{4}$$

Where: F_{VPP} profit of the VPP producer; F_{VPP}^{D} , F_{VPP}^{R} , F_{VPP}^{C} represent the revenues of the VPP in the day-ahead electricity market, real-time electricity market, and carbon market; C_{VPP} represents the total operating cost of the VPP; λ_t^{D} , λ_t^{R} represent the locational marginal prices in the day-ahead and real-time electricity markets; $P_t^{D,VPP}$ represents the day-ahead market clearing quantity of the VPP; $P_{t,s}^{R,VPP}$ represents the real-time market clearing quantity; $\lambda_t^{CE,VPP}$, λ_t^{CCER} represent the trading prices of carbon allowances and CCER; $Q_{pei,t}^{CE,VPP}$ represents the amount of carbon allowances obtained by the VPP; $Q_{pai,t}^{CE,VPP}$ represents the carbon emissions of the VPP; $Q_{sell,t}^{CCER,VPP}$ represents the quantity of CCER sold by the VPP.

$$C_{VPP} = C_{VPP}^{DR} + C_{VPP}^{ES} + C_{VPP}^{G} \tag{5}$$

$$C_{VPP}^{DR} = \sum_{t=1}^{T} \lambda^{d} \cdot P_t^{d,VPP} \tag{6}$$

$$C_{VPP}^{ES} = \sum_{t=1}^{T} \left(c^{dis} \cdot P_t^{dis} + c^{ch} \cdot P_t^{ch}\right) \tag{7}$$

$$C_{VPP}^{G} = \sum_{t=1}^{T} \left[e_{VPP}^{G} \cdot \left(P_{VPP,t}^{G}\right)^2 + f_{VPP}^{G} \cdot P_{VPP,t}^{G} + g_{VPP}^{G} \right] \tag{8}$$

Where: C_{VPP}^{DR} , C_{VPP}^{ES} , C_{VPP}^{G} denote the response cost of controllable loads, the cost of the energy storage system, and the generation cost of the gas turbine unit in the VPP; λ^{d} is the compensation price for demand response; $P_t^{d,VPP}$ represents the curtailed power of controllable loads; c^{ch} , c^{dis} are the marginal costs of charging and discharging for the energy storage system; P_t^{ch} , P_t^{dis} denote the charging and discharging energy of the storage system; e_{VPP}^{G} , f_{VPP}^{G} , g_{VPP}^{G} are the cost coefficients of the gas turbine unit; $P_{VPP,t}^{G}$ is the output power of the gas turbine unit in the energy market.

b) Constraints:

$$P_{t,\min}^{VPP} \le P_t^{VPP} \le P_{t,\max}^{VPP} \tag{9}$$

$$P_t^{VPP} = P_t^{D,VPP} + P_t^{R,VPP} \tag{10}$$

$$\omega_{\min}^{e,VPP} \le \omega_t^{e,VPP} \le \omega_{\max}^{e,VPP} \tag{11}$$

$$\omega_{\min}^{CE,VPP} \le \omega_t^{CE,VPP} \le \omega_{\max}^{CE,VPP} \tag{12}$$

$$\omega_{\min}^{CCER,VPP} \le \omega_t^{CCER,VPP} \le \omega_{\max}^{CCER,VPP} \tag{13}$$

$$0 \le P_t^{ch} \le P_{\max}^{ch} \tag{14}$$

$$0 \le P_t^{dis} \le P_{\max}^{dis} \tag{15}$$

$$E_{\min}^{ES} \le E_t^{ES} \le E_{\max}^{ES} \tag{16}$$

$$0 \le P_t^{WIN} \le P_t^{pre,WIN} \tag{17}$$

$$0 \le P_t^{SUN} \le P_t^{pre,SUN} \tag{18}$$

Where: P_t^{VPP} is the electricity market bid quantity submitted by the VPP; $P_{t,\max}^{VPP}$, $P_{t,\min}^{VPP}$ are the lower and upper bounds of the VPP's electricity market bid quantity; $\omega_t^{e,VPP}$ is the VPP's bid price in the electricity market; $\omega_t^{CE,VPP}$ is the VPP's bid price for carbon allowance trading in the carbon market; $\omega_t^{CCER,VPP}$ is the VPP's bid price for CCER trading in the carbon market; $P_{\max}^{ch}$, $P_{\max}^{dis}$ are the upper bounds of charging and discharging power of the energy storage system; $E_{\min}^{ES}$, $E_{\max}^{ES}$ are the lower and upper bounds of the energy storage system capacity; $P_t^{pre,WIN}$, $P_t^{pre,SUN}$ are the forecasted outputs of wind and solar generation.

2) Wind and Solar Generator

a) Objective Function: To maximize the profit of wind and solar energy generators.

$$\max F_{NEW} = F_{NEW}^D + F_{NEW}^R + F_{NEW}^C \tag{19}$$

$$F_{NEW}^D = \sum_{t=1}^{T} \lambda_t^D \cdot P_t^{D,NEW} \tag{20}$$

$$F_{NEW}^R = \sum_{s=1}^{S}\sum_{t=1}^{T} \chi_s \cdot \lambda_t^R \cdot P_{t,s}^{R,NEW} \tag{21}$$

$$F_{NEW}^C = \sum_{t=1}^{T} \lambda_t^{CCER} Q_t^{CCER,sell} \tag{22}$$

Where: F_{NEW}^D , F_{NEW}^R , F_{NEW}^C represent the revenues of wind and solar producers in the day-ahead electricity market, real-time electricity market, and carbon market; $P_t^{D,NEW}$ denotes the cleared power quantity of wind and solar producers in the day-ahead market; $P_{t,s}^{R,NEW}$ is the cleared power quantity in the real-time market; $Q_t^{CCER,sell}$ is the amount of CCERs sold by renewable energy producers.

b) Constraints:

$$P_{\min}^{NEW} \le P_t^{NEW} \le P_{\max}^{NEW} \tag{23}$$

$$P_t^{NEW} = P_t^{D,NEW} + P_t^{R,NEW} \tag{24}$$

$$\omega_{\min}^{e,NEW} \le \omega_t^{e,NEW} \le \omega_{\max}^{e,NEW} \tag{25}$$

$$\omega_{\min}^{CCER,NEW} \le \omega_t^{CCER,NEW} \le \omega_{\max}^{CCER,NEW} \tag{26}$$

Where: P_t^{NEW} is the power generation of the wind and solar producer; $P_{\min}^{NEW}$, $P_{\max}^{NEW}$ are the upper and lower limits of the wind and solar producer; $\omega_t^{e,NEW}$ denotes the electricity market bidding price of the wind and solar producer; $\omega_t^{CCER,NEW}$ is the CCER bidding price of the wind and solar producer in the carbon market.

3) Conventional Coal-Fired Power Producer

a) Objective Function: Profit Maximization of Coal Power Producer.

$$\max F_{COAL} = F_{COAL}^D + F_{COAL}^R + F_{COAL}^C - C_{COAL} \tag{27}$$

$$F_{COAL}^D = \sum_{t=1}^{T} \lambda_t^D \cdot P_t^{D,COAL} \tag{28}$$

$$F_{COAL}^R = \sum_{s=1}^{S}\sum_{t=1}^{T} \chi_s \cdot \lambda_t^R \cdot P_{t,s}^{R,COAL} \tag{29}$$

$$F_{COAL}^C = \sum_{t=1}^{T} \lambda_t^{CE} \left(Q_t^{sell,COAL} - Q_t^{buy,COAL} \right) \tag{30}$$

$$C_{COAL} = \sum_{t=1}^{T} \left[e_{COAL}^G \cdot \left(P_{GOAL,t}^G \right)^2 + f_{COAL}^G \cdot P_{GOAL,t}^G + g_{COAL}^G \right] \tag{31}$$

Where: F_{COAL}^D , F_{COAL}^R , F_{COAL}^C denote the revenues of the coal power producer in the day-ahead electricity market, real-time electricity market, and carbon market; C_{COAL} represents the generation cost of the coal power producer; $P_t^{D,COAL}$ is the cleared quantity in the day-ahead electricity market; $P_{t,s}^{R,COAL}$ is the cleared quantity in the real-time electricity market; $Q_t^{sell,COAL}$, $Q_t^{buy,COAL}$ are the amounts of carbon allowances sold and purchased; e_{COAL}^G , f_{COAL}^G , g_{COAL}^G are the cost coefficients of the coal power producer; $P_{GOAL,t}^G$ is the power generation of the coal power producer.

b) Constraints:

$$P_{\min}^{COAL} \le P_t^{COAL} \le P_{\max}^{COAL} \tag{32}$$

$$P_t^{COAL} = P_t^{D,COAL} + P_t^{R,COAL} \tag{33}$$

$$\omega_{\min}^{e,COAL} \le \omega_t^{e,COAL} \le \omega_{\max}^{e,COAL} \tag{34}$$

$$\omega_{\min}^{CE,COAL} \le \omega_t^{CE,COAL} \le \omega_{\max}^{CE,COAL} \tag{35}$$

Where: P_t^{COAL} denotes the power output of the coal power producer; $P_{\max}^{COAL}$, $P_{\min}^{COAL}$ represent the lower and upper bounds of the coal power generation; $\omega_t^{e,COAL}$ is the electricity price bid submitted by the coal power producer; $\omega_t^{CE,COAL}$ is the carbon allowance bidding price offered by the coal power producer in the carbon market.

B. Lower-Level Model: Market Clearing Model

1) Electricity Market Clearing Model

a) Objective Function:

$$\min C_{ELE} = C_{ELE}^D + C_{ELE}^R \tag{36}$$

$$C_{ELE}^D = \sum_{t=1}^{T}\sum_{i=1}^{I} (\omega_t^{e,VPP} \cdot P_{t,i}^{D,VPP} + \omega_t^{e,NEW} \cdot P_{t,i}^{D,NEW} + \omega_t^{e,COAL} \cdot P_{t,i}^{D,COAL}) \tag{37}$$

$$C_{ELE}^{R}=\sum_{t=1}^{T}\sum_{i=1}^{I}\sum_{s=1}^{S}(\chi_s(\omega_t^{e,VPP}\cdot P_{t,i,s}^{R,VPP}+\omega_t^{e,NEW}\cdot P_{t,i,s}^{R,NEW}+\omega_t^{e,COAL}\cdot P_{t,i,s}^{R,COAL})) \tag{38}$$

Where: C_{ELE} represents the total operating cost of the electricity market; C_{ELE}^{D}, C_{ELE}^{R} denote the costs in the day-ahead market and real-time market, respectively.

b) Unit Output Constraints:

$$\begin{cases} P_{t,\min}^{D,VPP}\le P_t^{D,VPP}\le P_{t,\max}^{D,VPP} \\ 0\le P_t^{D,NEW}\le P_{t,\max}^{D,NEW} \\ P_{t,\min}^{D,COAL}\le P_t^{D,COAL}\le P_{t,\max}^{D,COAL} \end{cases} \tag{39}$$

$$\begin{cases} P_{t,\min}^{R,VPP}\le P_t^{R,VPP}\le P_{t,\max}^{R,VPP} \\ 0\le P_t^{R,NEW}\le P_{t,\max}^{R,NEW} \\ P_{t,\min}^{R,COAL}\le P_t^{R,COAL}\le P_{t,\max}^{R,COAL} \end{cases} \tag{40}$$

Where: $P_{t,\max}^{D,VPP}$, $P_{t,\min}^{D,VPP}$ represent the maximum and minimum output of the VPP in the day-ahead market; $P_{t,\max}^{D,NEW}$ is the maximum output of the wind and solar generator in the day-ahead market; $P_{t,\max}^{D,COAL}$, $P_{t,\min}^{D,COAL}$ are the maximum and minimum technical outputs of the coal generator in the day-ahead market; $P_{t,\max}^{R,VPP}$, $P_{t,\min}^{R,VPP}$ denote the maximum and minimum output of the VPP in the real-time market; $P_{t,\max}^{R,NEW}$ is the maximum output of the wind and solar generator in the real-time market; $P_{t,\max}^{R,COAL}$, $P_{t,\min}^{R,COAL}$ are the maximum and minimum technical outputs of the coal generator in the real-time market.

c) Ramp Rate Constraints:

$$\begin{cases} P_t^{D,VPP}-P_{t-1}^{D,VPP}\le R_{VPP}^{up} \\ P_t^{D,VPP}-P_{t-1}^{D,VPP}\ge -R_{VPP}^{down} \\ P_t^{D,COAL}-P_{t-1}^{D,COAL}\le R_{COAL}^{up} \\ P_t^{D,COAL}-P_{t-1}^{D,COAL}\ge -R_{COAL}^{down} \end{cases} \tag{41}$$

$$\begin{cases} P_t^{R,VPP}-P_{t-1}^{R,VPP}\le R_{VPP}^{up} \\ P_t^{R,VPP}-P_{t-1}^{R,VPP}\ge -R_{VPP}^{down} \\ P_t^{R,COAL}-P_{t-1}^{R,COAL}\le R_{COAL}^{up} \\ P_t^{R,COAL}-P_{t-1}^{R,COAL}\ge -R_{COAL}^{down} \end{cases} \tag{42}$$

Where: R_{VPP}^{up}, R_{VPP}^{down} denote the upward and downward ramp rate limits of the coal-fired units within the VPP; R_{COAL}^{up}, R_{COAL}^{down} represent the upward and downward ramp rate limits of the coal-fired units.

d) System Power Balance Constraint

$$\sum P_{t,i}^{D,VPP}+\sum P_{t,i}^{D,NEW}+\sum P_{t,i}^{D,COAL}=\sum P_t^{D} \tag{43}$$

$$\sum P_{t,i}^{R,VPP}+\sum P_{t,i}^{R,NEW}+\sum P_{t,i}^{R,COAL}=\sum P_t^{R} \tag{44}$$

Where: P_t^{D} represents the load demand of the user at time t; P_t^{R} denotes the actual load deviation of the user at time t.

2) Carbon Market Clearing Model

a) Objective Function:

$$\max F_C=\sum_{t=1}^{T}\sum_{i=1}^{I}(\lambda_{VPP,t,i}^{CE,buy}Q_{VPP,t,i}^{CE,buy}+\lambda_{COAL,t,i}^{CE,buy}Q_{COAL,t,i}^{CE,buy}-\lambda_{VPP,t,i}^{CE,sell}Q_{VPP,t,i}^{CE,sell}-\lambda_{VPP,t,i}^{CCER,sell}Q_{VPP,t,i}^{CCER,sell}-\lambda_{COAL,t,i}^{CE,sell}Q_{COAL,t,i}^{CE,sell}-\lambda_{NEW,t,i}^{CCER,sell}Q_{NEW,t,i}^{CCER,sell}) \tag{45}$$

Where: F_C is the carbon market welfare; $\lambda_{VPP,t,i}^{CE,buy}$, $Q_{VPP,t,i}^{CE,buy}$ are the purchase price and purchase quantity of carbon allowances by the VPP; $\lambda_{COAL,t,i}^{CE,buy}$, $Q_{COAL,t,i}^{CE,buy}$ are the purchase price and purchase quantity of carbon allowances by the coal-fired power plant; $\lambda_{VPP,t,i}^{CE,sell}$, $Q_{VPP,t,i}^{CE,sell}$ are the selling price and selling quantity of carbon allowances by the VPP; $\lambda_{VPP,t,i}^{CCER,sell}$, $Q_{VPP,t,i}^{CCER,sell}$ are the selling price and selling quantity of CCERs by the VPP; $\lambda_{COAL,t,i}^{CE,sell}$, $Q_{COAL,t,i}^{CE,sell}$ are the selling price and selling quantity of carbon allowances by the coal-fired power plant; $\lambda_{NEW,t,i}^{CCER,sell}$, $Q_{NEW,t,i}^{CCER,sell}$ are the selling price and selling quantity of CCERs by the wind and solar power producer.

b) Supply and Demand Balance Constraints for Carbon Allowances and CCERs in the Carbon Market:

$$\sum_{t=1}^{T}\sum_{i=1}^{I}(Q_{VPP,t,i}^{CE,buy}+Q_{COAL,t,i}^{CE,buy}-Q_{VPP,t,i}^{CE,sell}-Q_{VPP,t,i}^{CCER,sell}-Q_{COAL,t,i}^{CE,sell}-Q_{NEW,t,i}^{CCER,sell})=0 \tag{46}$$

IV. Solution Algorithm

This paper develops a bi-level coupled trading model for a VPP participating in the electricity-carbon market. Based on the DM algorithm, a MDP is introduced, and a coordinated optimization algorithm based on Markov decision-making is proposed. The specific solution procedure is illustrated in the figure below.

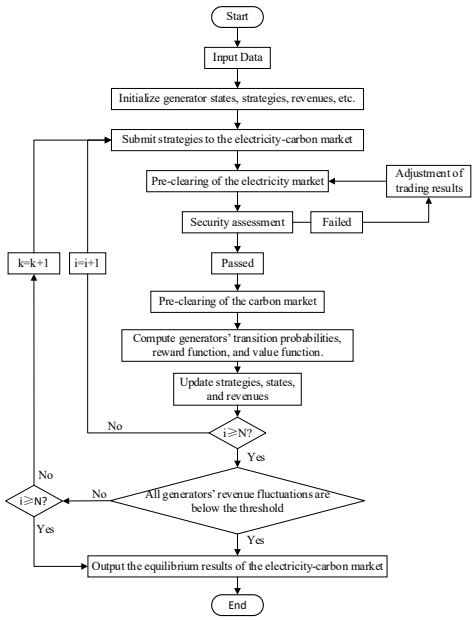


Fig. 1. The flowchart of the algorithm is shown below.

V. Case Study

In this study, a test system comprising three VPPs is considered. Each VPP consists of a renewable energy generation

unit, a coal generation unit, and an energy storage system. The renewable energy configurations are as follows: VPP1 is dominated by wind power generation; VPP2 is dominated by photovoltaic generation; VPP3 integrates an equal share of wind and photovoltaic generation. The load supply configuration is identical for all VPPs. The trading interval in the integrated electricity–carbon market is set to 1 hour. The technical parameters of the coal-fired generation units and energy storage systems for each VPP are listed in Table 1 and Table 2, respectively.

TABLE I. PARAMETERS OF COAL-FIRED UNITS IN VIRTUAL POWER PLANTS

VPP	e_{VPP}^{G}	f_{VPP}^{G}	g_{VPP}^{G}	$P_{\max}$ / MW
1	0.1	0.5	1	5
2	0.1	0.9	1.2	6
3	0.15	0.6	0.8	4

TABLE II. PARAMETERS OF ENERGY STORAGE DEVICES (UNIT: MW)

VPP	$P_{\max}^{ch}$	$P_{\max}^{dis}$	$E_{\max}$	$S_{\min}$	$S_{\max}$
1	0.6	0.6	1	0.2	0.9
2	0.6	0.6	1	0.2	0.9
3	1.2	1.2	2	0.2	0.9

In this paper, two operational strategies are considered: (1) the distribution network operator (DNO) sets the buying and selling prices solely based on the feed-in tariff and the grid electricity price, without any additional price optimization measures; (2) the DNO implements the optimization strategy proposed in this study for price adjustment. For the case study, the dispatch cost coefficient of the VPP's energy storage system is set to 70 CNY/MWh, and the carbon trading price in the carbon market is fixed at 78 CNY/ton.

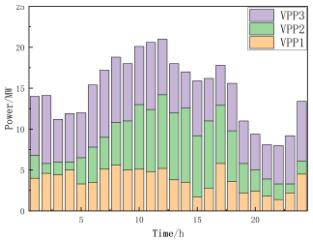


Fig. 2. Prediction of Renewable Generation Output

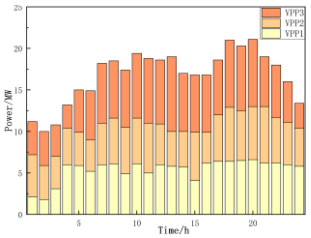


Fig. 3. Load Profiles of Virtual Power Plants

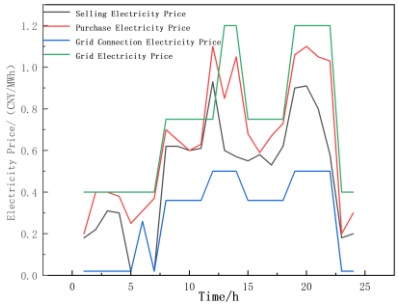


Fig. 4. Purchase and Sale Electricity Prices, Feed-in Tariff, and Grid Electricity Price

Based on the analysis of the electricity trading profiles of each VPP, it can be observed that VPPs with different proportions of wind and solar generation exhibit distinct output characteristics. During the early morning and evening hours, when wind power is relatively abundant, VPP1 experiences a surplus of supply over demand. At midday, when solar irradiation is sufficient, VPP2 exhibits a surplus. VPP3, configured with an equal share of wind and photovoltaic generation (50% each), takes advantage of the complementary characteristics of the two renewable sources throughout the day, ensuring an overall surplus and maintaining sufficient reserves to participate in the electricity market for additional revenue.

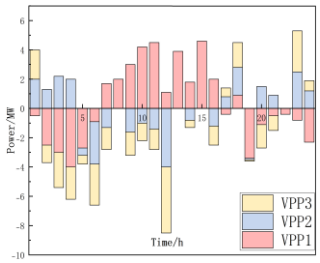


Fig. 5. Electricity Trading Profiles of Each VPP

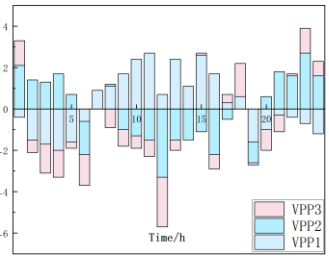


Fig. 6. Carbon Emission Reduction Transactions of Each VPP

According to the carbon market trading results shown below, VPP1 can obtain considerable carbon reduction benefits in the early morning and evening periods due to the high output of wind power units. Between 6:00 and 16:00, the strong solar irradiance increases the photovoltaic output in VPP2, thereby enhancing its carbon reduction benefits. VPP3, equipped with a hybrid configuration of wind and photovoltaic units, not only takes advantage of the wind power generation characteristics during the early morning and evening hours but also fully leverages the photovoltaic generation potential under strong sunlight, ensuring stable and considerable carbon reduction benefits throughout the 24-hour period.

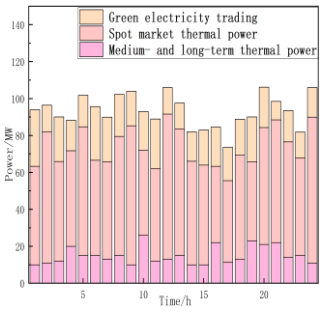


Fig. 7. Electricity Market Transactions in the Absence of VPP Participation.

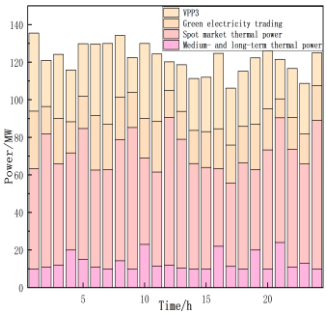


Fig. 8. Electricity Market Transactions with VPP Participation.

Through comparative analysis, it can be seen that when VPP participate in the electricity market, the main impact is on the medium- and long-term market. This can be achieved by increasing the clearing volume of VPPs, thereby reducing the clearing volume of coal-fired power generation and consequently enhancing the corresponding environmental value.

TABLE III. COMPARATIVE REVENUES OF VPPS UNDER THE TWO STRATEGIES

VPP	Strategy(1)	Strategy(2)
VPP1	90386.00 CNY	92418.00 CNY

VPP2	97124.00 CNY	98334.00 CNY
VPP3	98945.00 CNY	105108.00CNY

By comparison, after applying the proposed electricity–carbon market coupled trading optimization strategy based on the MDP, the revenues of the VPPs increased by 2.25%, 1.25%, and 6.23%, respectively. Moreover, the revenue of the VPP adopting a wind–solar hybrid configuration was 13.73% and 6.89% higher than those of the VPPs using a single type of renewable energy unit, respectively.

VI. Conclusion

This paper develops a bi-level coupled trading model for VPPs participating in the electricity–carbon market, and employs a cooperative optimization algorithm based on the MDP to investigate bidding strategies that balance both economic efficiency and low-carbon objectives in the coupled market. Based on the case study analysis, the following conclusions are drawn:

(1) The proportion of renewable energy units in a VPP should be configured according to actual conditions, as the power supply–demand relationship varies among VPPs with different renewable energy shares. Therefore, each VPP needs to adjust its purchase and sale electricity prices in response to such differences to ensure profitability. In addition, distribution network operators can also flexibly adjust electricity prices based on supply–demand conditions, thereby guiding VPPs toward rational electricity trading behavior.

(2) The better the match between the combination of renewable energy units in a virtual power plant and the load output characteristics, the more favorable its carbon reduction benefits will be.

(3) By adopting the electricity–carbon market coupled trading optimization strategy based on the MDP proposed in this paper, VPPs can effectively reduce their trading costs. The profits of the respective virtual power plants increased by 2.25%, 1.25%, and 6.23%. Moreover, the profits of virtual power plants using a combined wind–solar unit configuration were 13.73% and 6.89% higher than those using a single renewable energy unit configuration. These results verify the effectiveness of the proposed model and the feasibility of the optimization strategy.

Acknowledgment

This work is supported by the Science and Technology Project of State Grid Corporation of China (Contract No. B3094024000B).

References

[1] Qinliang Tan, Yihong Ding, Qi Ye, Shufan Mei, Yimei Zhang, Yongmei Wei,Optimization and evaluation of a dispatch model for an integrated wind-photovoltaic-thermal power system based on dynamic carbon emissions trading,Applied Energy,Volume 253,2019,113598.

[2] Liangying LIU,Kai JIANG,Nian LIU,et al. Multi-agent energy carbon sharing mechanism for parks based on Stackelberg game[J]. Proceedings of the CSEE, 2024,44(06):2119-2131.DOI:10.13334/j.0258-8013.pcsee.230736.

[3] Xian WANG,Shengcai WANG,Shaohua ZHANG. Game analysis of coupled electricity-carbon-green certificate markets with strategic bidding of renewable generators[J]. Power System Technology, 2024,48(10):4125-4138.DOI:10.13335/j.1000-3673.pst.2024.0260.

[4] Xiaopeng Guo, Xinyue Zhang, Xingping Zhang,Incentive-oriented power-carbon emissions trading-tradable green certificate integrated market mechanisms using multi-agent deep reinforcement learning,Applied Energy,Volume 357,2024,122458.

[5] Jiquan PENG, Chenxi JIN, Xuetong CHEN, et al. Research on interaction mechanism between electricity market and national carbon market of China[J]. Energy of China, 2020, 42(9): 20-24, 47.

[6] Zhilin LU, Mingbo LIU, Nan SHANG, et al. Two-stage clearing model for day-ahead electricity market considering impact of carbon emissions trading market[J]. Automation of Electric Power Systems, 2022, 46(10): 159‑170.

[7] DING Y H, TAN Q L, SHAN Z J, et al. A two-stage dispatching optimization strategy for hybrid renewable energy system with low carbon and sustainability in ancillary service market[J]. Renewable Energy, 2023, 207: 647‑659.

[8] Huiru ZHAO, Yihang ZHAO, Zhaoyuan WU, et al. Bidding strategy of power generators under the linkage of electricity market, carbon emission trading market, and certified emission reduction market[J]. Electric Power Construction, 2024, 45(10): 123‑135.

[9] Lin ZHAO, Yapeng LI, Xiaoyu JIN, et al. Coordinated bidding model of hydropower-thermal power in carbon-electricity coupling market considering CCER mechanism[J]. Automation of Electric Power Systems,2023, 47(21):12-24.

[10] Jun YAO, Jiao HE, Yongfei WU, et al. Energy optimization of electricity wholesale market considering carbon emissions trading and green power certificate trading mechanism[J]. Electric Power, 2022, 55(8):190-195.

[11] Hongliang WU, Yuxiao LIU, Ning ZHANG, et al. Carbon trading models and benefit analysis in CSG west-to-east power transmission[J]. Power System Technology, 2017, 41(3): 745-751.

[12] Hanxin WU, Shufeng DONG, Xianglong ZHANG, et al. Optimal dispatching of power system with wind power considering carbon trading mechanism[J]. Power System Technology, 2024, 48(1): 70‑80.

[13] Guoliang Zhang, Hong Lin, Yizhi Tian, Bi-level interaction optimization of source-load under electricity-carbon-green certificate market coupling. Power System Protection and Control,2025,53(05):1-10.DOI:10.19783/j.cnki.pspc.240712..

[14] WU Q L, LI C X. A bi-level optimization framework for the power side virtual power plant participating in day-ahead wholesale market as a price-maker considering uncertainty[J]. Energy, 2024, 304: 132050.

[15] WANG P, GUO Z X, ZHANG S Y, et al. Strategic behaviors of renewable energy generation companies participating in the electricity and carbon coupled markets based on non-cooperative game theory[J]. Energy,2024,312:133522.

[16] MANDI R P, YARAGATTI U R. Control of CO2 emission through enhancing energy efficiency of auxiliary power equipment in thermal power plant[J]. International Journal of Electrical Power & Energy Systems,2014,62:744‑752.

[17] JIANG K, LIU N, YAN X H, et al. Modeling strategic behaviors for GenCo with joint consideration on electricity and carbon markets[J]. IEEE Transactions on Power Systems, 2022, 38(5): 4724‑4738.

[18] Chaoyi Peng, Suyue Xu, Huijie Gu, et al. Research on bidding strategy of virtual power plants participating in multi-competitive markets based on Stackelberg game. Power System Protection and Control,2024,52(07): 125-137.DOI:10.19783/j.cnki.pspc.230934..

[19] Liu X, Ni Y, Sun Y, et al. Multi-VPPs power-carbon joint trading optimization considering low-carbon operation mode[J/OL].Journal of Energy Storage,2024.

[20] Fengming Zhao, Yanfang Fan, Bi-level optimal dispatch of multi-energy virtual power plants under time-of-use pricing,[J].2019,47(20):33-40.DOI:10.19783/j.cnki.pspc.181383.

[21] Zhang J, Liu Z. Low carbon economic dispatching model for a virtual power plant connected to carbon capture system considering green certificates-carbon trading mechanism[J/OL]. Sustainable Energy Technologies and Assessments,2023.

Credit Evaluation Method for New Market Entities Based on Credibility Entropy Evidence Theory

Kong Shuqin
Compliance and Risk Control Department
Guangdong Power Exchange Centre
Guangdong, China
272259808@qq.com

Sheng Jiansheng
Compliance and Risk Control Department
Guangdong Power Exchange Centre
Guangdong, China

Tian Lin
Compliance and Risk Control Department
Guangdong Power Exchange Centre
Guangdong, China

Zheng Wei
Compliance and Risk Control Department
Guangdong Power Exchange Centre
Guangdong, China

Wu Jinghui
Compliance and Risk Control Department
Guangdong Power Exchange Centre
Guangdong, China

Xue Shumin
Shanghai University of Electric Power
Shanghai, China
15615870620@163.com

***Abstract*—To construct a credit evaluation system for new electricity market entities, this paper constructs a credit evaluation indicator system based on the characteristics of the new electricity system and new types of electrical energy commodities, and proposes an evaluation method based on the theory of credibility entropy evidence. First, the characteristics of new types of electrical energy commodities are analyzed, and key indicators that can characterize the creditworthiness of market entities are extracted to construct an indicator system for evaluating the credit of new market entities. Second, it employs order relationship analysis to determine the initial weight of each credit evaluation indicator, applies a fusion method based on credibility entropy and improved evidence to combine these initial values, and generates comprehensive credit evaluation results for each new market entity. Ultimately, this method is verified as effective in evaluating the credit status of typical entities through case studies.**

Keywords—New Market Entities in the Electricity Market, New Types of Electrical Energy Commodities, Credibility Entropy, Improved Evidence Theory, Credit Evaluation

I. INTRODUCTION

Since the introduction of Central Document No. 9 in 2015, China has been focusing on building a "credit-based new regulatory mechanism" as its core goal, which has strengthened the integrity of market entities [1]. In recent years, with the continuous emergence of new market entities such as virtual power plants and new types of energy storage [2], the scale of new market entities in the electricity market has continued to expand, giving rise to a variety of new types of electrical energy commodities with diverse characteristics [3]. Therefore, it is urgent to study the credit evaluation of new market entities based on the characteristics of new types of electrical energy commodities, establish a sound credit evaluation method, effectively restrain the trading behavior of entities, and regulate market order.

Currently, domestic and international research on credit management mainly focuses on traditional electricity market entities, while research on credit evaluation for new market entities is still in its preliminary stages. Literature [4] draws on the credit evaluation and guarantee mechanisms of US electricity sales companies to provide recommendations for China; Literature [5] constructs a master-servant game model to optimize the disposal strategies of market institutions in response to electricity sales company defaults; Literature [6] comprehensively considers the characteristics of collateral and the needs of electricity sales companies to design the optimal collateral combination plan.

Significant progress has been made in the study of the characteristics of new electricity systems. Literature [7] constructed a planning technology framework adapted to current needs based on its technical characteristics; literature [8] pointed out the direction for the positioning and development path of hydropower in future systems based on the characteristics of new electricity systems. At this stage, research on the characteristics of new types of electrical energy commodities focuses on their classification and characteristic evolution. Literature [9] divides them into five categories, such as energy services and auxiliary services, based on differences in transaction types and service types, and constructs a corresponding characteristic measurement indicator system. Literature [10] points out that China's electricity commodities have characteristics such as instantaneous balance and natural monopoly in transmission and distribution, and draws on the experience of the British electricity market to provide recommendations for the development of China's market.

The credit evaluation of new market entities is mainly achieved through the construction of an indicator system, the determination of indicator weights, and the assessment of credit ratings. Literature [11] proposes a credit risk assessment method for electricity market entities based on combination weighting and cloud models. This method is highly accurate in evaluating credit risk in the electricity market, but there is still a large discrepancy between its predictions and actual results. Literature [12] weighs the relevant indicators for measuring

China Southern Power Grid Company Limited Science and Technology Project Funding (Project Number [GDKJXM20250079])

979-8-3315-5472-9/25/$31.00 ©2025 IEEE

power quality based on the improved CRITIC method and comprehensively evaluates power quality through the improved TOPSIS method. Literature [13] combines the principles of system dynamics to propose an evaluation method for the operational safety of superconducting cables, using variable weight theory to reduce the subjectivity of the evaluation process and make the final evaluation results more reliable.

Currently, research on credit evaluation indicator systems for new electricity market entities has failed to fully consider the characteristics of new electricity commodities and new electricity systems. Based on the characteristics of new electricity systems and incorporating the intrinsic attributes of new electricity commodities, this paper constructs a credit evaluation indicator system and proposes an evaluation method based on credibility entropy evidence theory. The framework is shown in Fig. 1.

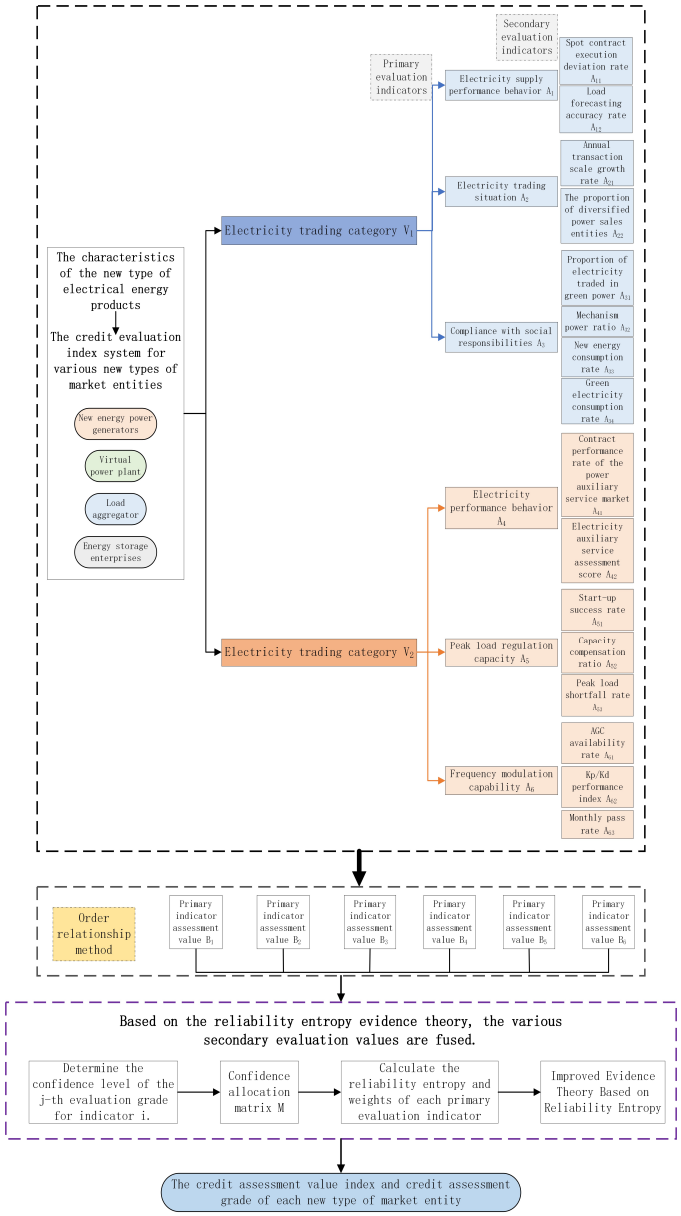


Fig. 1. Framework diagram of this paper

II. NEW CREDIT EVALUATION SYSTEM FOR THE ELECTRICITY MARKET

A. *Principles for establishing a credit evaluation system*

(1) Systematization and differentiation principles. Systematization and differentiation principles: The indicator system needs to take into account both the commonalities among market entities and the differences in their participation in different markets.

(2) Adaptability principle: The indicator system should be based on the characteristics of new entities, with classified measures and multi-dimensional evaluation.

(3) Principle of availability. The design of credit evaluation indicators should take into account the availability of the required data.

(4) Quantifiable principle. Indicators should have clear calculation formulas and evaluation cycles, and be presented in specific numerical values.

B. *Credit Evaluation Indicator Database*

Based on the characteristics of new types of electrical energy commodities, this paper constructs six first-level evaluation indicators, such as electricity performance and peak shaving capacity, and 16 second-level indicators, such as spot contract execution deviation rate and AGC availability rate, to quantify their credit performance in market transactions, as shown in TABLE I.

This paper selects spot contract execution deviation rate and load forecast accuracy rate to measure the ability of market entities to fulfill the contracted electricity volume in electricity commodity trading. In addition, the new electricity system has broken the traditional single market entity model, with the same electricity sales entity playing multiple roles and a more refined division of labor among entities. To assess the overall performance of market entities in this change, indicators such as the diversification ratio of electricity sales entities and the annual transaction growth rate were selected to reflect the overall performance of market entities in terms of transaction scale, market activity, and overall expansion trends. With the large-scale integration of new energy sources into the power grid, the new power system has set higher requirements for emissions reduction. Low-carbon electricity services have become a core demand. To quantify the extent to which market entities fulfill their emissions reduction responsibilities, indicators such as the proportion of green electricity transactions, the proportion of mechanism-based electricity, and the green electricity consumption rate are used to measure market entities' responsibilities in terms of green development.

Under the new power supply structure of “wind and solar power as the main source, thermal power as the backup,” ancillary services are also showing a trend toward diversification, becoming a key support for ensuring the safe and reliable operation of the power system. To scientifically reflect the ability of market entities to adjust promptly according to demand, indicators such as start-up success rate, capacity compensation ratio, and peak shaving deficit rate are selected for evaluation in terms of peak shaving capacity; indicators such as AGC availability rate, Kp/Kd performance

indicators, and monthly pass rate are selected for evaluation in terms of frequency regulation capacity. At the same time, there are obvious uncertainties in all aspects of the new electricity system, which significantly increases the risk of default in ancillary service transactions. In order to effectively regulate credit risk and maintain market order, the contract performance rate of the electricity ancillary service market and the electricity ancillary service assessment score are selected to measure the transaction reliability, contract performance ability, and honesty of different market entities participating in electricity ancillary service transactions.

TABLE I. CREDIT EVALUATION INDICATOR DATABASE FOR NEW ELECTRICITY MARKETS

	First-level evaluation indicators	Secondary rating indicators
Electricity trading indicators V_1	Electricity consumption behavior A_1	Spot contract execution deviation rate A_{11}
		Load forecasting accuracy A_{12}
	Electricity trading situation A_2	Annual transaction scale growth rate A_{21}
		Diversity of electricity sales entities A_{22}
	Social Responsibility Compliance A_3	Green electricity trading amount ratio A_{31}
		Mechanism power ratio A_{32}
		Renewable energy absorption rate A_{33}
		Green electricity consumption rate A_{34}
Electricity trading indicators V_2	Power performance behavior A_4	Power ancillary services market contract fulfillment rate A_{41}
		Power ancillary service assessment score A_{42}
	Peak shaving capacity A_5	Startup success rate A_{51}
		Capacity compensation ratio A_{52}
		Peak load deficit rate A_{53}
	frequency modulation capability A_6	AGC availability rate A_{61}
		Kp/Kd performance indicators A_{62}
		Monthly pass rate A_{63}

The formulas for calculating some of the indicators are as follows:

Load forecast accuracy Acc is a measure of the accuracy of load forecasts in an electricity system, reflecting the degree of agreement between forecast values and actual load values. This indicator is calculated using two different methods: non-spot month and spot month.

$$\Delta Q_{\text{non-spot}} = \frac{\left|Q_{\text{bid}} - Q_{\text{actual}}\right|}{Q_{\text{actual}}} \qquad Acc = 1 - \Delta Q_{\text{non-spot}} \tag{1}$$

$$\Delta Q_{d,h}^{dev} = \frac{\sum\left|Q_{bid,d,h}^{da} - Q_{act,d,h}^{rt}\right|}{Q_{act,d,h}^{rt}} \qquad Acc = 1 - \Delta Q_{d,h}^{dev} \tag{2}$$

In the formula, $\Delta Q_{non\text{-}spot}$ for non-spot month deviation values, Q_{bid} report electricity demand for non-spot months; Q_{actual} actual electricity consumption for non-spot months; $\Delta Q_{\mathrm{d,h}}^{dev}$ for spot month deviation value, spot month hourly actual electricity consumption.

The proportion of diversified power sales entities refers to the ratio of electricity sold to non-power generation background power sales companies in annual bilateral negotiation transactions to the total transaction electricity volume.

$$\rho_{div,t} = \frac{Q_{indep,t}}{Q_{total,t}} \times 100\% \tag{3}$$

In the formula, $\rho_{div,t}$ is the proportion of diversified power sales entities; $Q_{indep,t}$ is the amount of electricity sold to non-power generation background power sales companies; $Q_{total,t}$ is the total annual transaction volume.

Capacity compensation ratio refers to the ratio of the revenue earned by market entities participating in peak shaving services to total revenue.

$$\kappa_{cap} = \frac{R_{ps}}{R_{total}} \tag{4}$$

In the formula, κ_{cap} is the capacity compensation ratio; R_{ps} is the peak shaving revenue; R_{total} is the total revenue.

AGC availability refers to the ratio of the actual available time to the total time of a machine group or system under AGC control, usually expressed as a percentage. AGC stands for automatic generation control, which reflects the actual regulation capacity of a machine group in response to AGC commands [14].

$$\eta_{AGC}^{(unit)} = \frac{T_{avail}}{T_{on-grid}^{(month)}} \times 100\% \tag{5}$$

In the formula, $\eta_{AGC}^{(unit)}$ is the monthly availability rate of a single AGC unit; T_{avail} is the monthly available hours of AGC; $T_{on\text{-}grid}^{(month)}$ is the monthly grid connection hours of the unit.

III. NEW POWER MARKET CREDIT RATING MODEL

A. Determination of weights

1) Order relationship analysis

Due to the abundance of first-level indicators and the difficulty of measuring them uniformly, this paper introduces order relationship analysis. Although this method relies on expert experience, it effectively avoids the strict requirements of the hierarchical analysis method for the consistency of the judgment matrix. In this method, industry experts determine the weight and ranking of indicators based on the

characteristics of electricity commodities [15]. The specific steps are as follows:

(1) Calculate the values of each secondary indicator A_{ik}, standardize and normalize them, and obtain the indicator values $\overline{A_{ik}}$.

(2) Determine the order relationship. Determine the indicator sequence relationship for a certain evaluation criterion is $Y_{i1}>Y_{i2}>\ldots>Y_{i,ni}$. Select experts to rank the importance of each indicator.

(3) Calculate the relative importance between adjacent indicators and rank them according to their importance. Set rik as the ratio of the importance of evaluation indicators $Y_{i,k-1}$, and Y_{ik}.

$$\mathrm{r}_{ik}=\frac{Y_{i,k-1}}{Y_{ik}}, k=n_i, n_i-1, \cdots, 2; i=1,2, \cdots, 6 \tag{6}$$

(4) Calculate the weighting coefficients. The subjective weights determined by individual experts are as follows:

$$\begin{aligned} \omega_{in_i} &= \left(1+\sum_{k=2}^{n_i}\prod_{i=k}^{n_i} r_i\right)^{-1} \\ \omega_{i,k-1} &= r_{ik}\omega_{ik}, k=n_i, \cdots, 2 \end{aligned} \tag{7}$$

(5) Using the weights obtained in step (4), the standardized values of the secondary indicators are weighted and combined to obtain the assessment value Bi of the primary indicator:

$$B_i=\sum_{k=1}^{n_i}\omega_{ik}\overline{A_{ik}}, \quad i=1,2,\cdots,6 \tag{8}$$

2) Design of reliability entropy index weights

Using evidence theory improved based on credibility entropy, the assessment values of each indicator are integrated to obtain the credit assessment index of each new market entity [16]. The specific steps are as follows:

Assuming that credit ratings are divided into six levels: AAA, AA, A, B, C, and D, and setting the membership function of the jth evaluation level of the ith secondary indicator as shown in Formula (9), the corresponding confidence interval is $[\mu_{ij}-d_{ij},\mu_{ij}+d_{ij}]$, The width of this interval, $\delta_{ij}=2d_{ij}$, represents the uncertainty of the reliability measurement of the different assessment levels of each first-level indicator.

$$f_{ij}(x,\mu_{ij},\sigma_{ij})=\exp\left(-\frac{\left(x-\mu_{ij}\right)^2}{2\sigma_{ij}^2}\right); j=1,2,\cdots,5 \tag{9}$$

Confidence entropy is used to describe the uncertainty before an event occurs or the amount of information it brings after it occurs, and the confidence level represents the probability of the event occurring; Use μ_{ij}-d_{ij} to denote the lower bound of the confidence estimate for indicator i, and use $\mu_{ij}+d_{ij}$ to denote the upper bound of the confidence estimate for indicator i. Considering the uncertainty information contained in the confidence interval, introduce the confidence interval width δ_{ij} and use the exponential term to correct the uncertainty of the j assessment level of indicator i. The improved confidence entropy calculation formula is:

$$H_i=-\sum_{j=1}^{5}\mu_{ij}\log_2\left(\mu_{ij}e^{-\delta_{ij}}\right), i=1,2,\cdots,6 \tag{10}$$

The magnitude of the credibility entropy value (H_i) reflects the uncertainty and reliability of the evidence. That is, the lower the entropy value, the lower the uncertainty and the higher the reliability, and the greater the weighting should be when assigning weights. Conversely, the higher the entropy value, the lower the reliability, and the smaller the weighting should be.

Use the calculated reliability entropy to assign weights to different pieces of evidence. The evidence weight for the i-th primary evaluation indicator is:

$$\omega_i=\frac{e^{-H_i}}{\sum_{i=1}^{6}e^{-H_i}}, i=1,2,\cdots,6 \tag{11}$$

B. Comprehensive evaluation of evidence integration theory improved by reliability entropy weighting

Evidence theory can integrate information from multiple sources, eliminate uncertainty and reduce conflicts between pieces of information, emphasizing the differences between evidence from different sources and differences in weight.

This paper adopts an improved evidence theory fusion algorithm based on reliability entropy, using the D-S fusion rule to fuse all evidence. For a given confidence distribution matrix M, it outputs J types of confidence distribution fusion results m_j, $j=1,2,\ldots, J$ for the identified target. The steps are as follows:

(1) Generate a 5×5 empty matrix A; generate a 5-dimensional column vector Z to store the confidence level, initialize the confidence level of the first indicator, $Z=\omega_1 M(1,:)'$; initialize the uncertainty factor K=0.

(2) Update and iterate A and Z to calculate the uncertainty factor K. for i=2:I

$$A=Z\omega_i M(i,:) \tag{12}$$

$$Z=diag(A)=(a_{11},a_{22},\ldots,a_{JJ})^T \tag{13}$$

$$K=K+\sum_{k=1}^{J}\sum_{l\neq k}a_{ik}a_{jl} \tag{14}$$

(3) Obtain the fusion result m_j of the confidence distribution.

$$q_j = \frac{1}{I}\sum_{i=1}^{I} w_i m_{ij},\ j = 1,2,\cdots,J \tag{15}$$

$$m_j = z_j + K \times q_j,\ j = 1,2,\ldots,J \tag{16}$$

(4) Quantify each assessment level to obtain the total credit assessment value of each new market entity. Set the corresponding scores for different levels as C=[0.9,0.8,0.6,0.5,0.3], then the credit assessment index of the new market entity is:

$$C = V(m_1,\ldots m_6)^T \tag{17}$$

IV. EXAMPLE ANALYSIS

This section uses a Virtual Power Plant (VPP) as an example to illustrate the process of the algorithm described in this paper through the transaction data of five market entities.

(1) Weighting of credit evaluation indicators for new power markets. Taking the data from five virtual power plants in a certain power market during a certain evaluation period as an example, the initial indicator weights are determined using the order relationship analysis method, as shown in TABLE II.

TABLE II. WEIGHTS OF SECONDARY INDICATORS

Indicator Name		Weighting
First-level indicators	***Second-level indicators***	
Electricity consumption behavior A_1	Spot contract execution deviation rate A_{11}	0.4348
	Load forecasting accuracy A_{12}	0.5652
Electricity trading situation A_2	Annual transaction scale growth rate A_{21}	0.4545
	Diversity of electricity sales entities A_{22}	0.5455
Social Responsibility Compliance A_3	Green electricity trading amount ratio A_{31}	0.1967
	Mechanism power ratio A_{32}	0.1639
	Renewable energy absorption rate A_{33}	0.2557
	Green electricity consumption rate A_{34}	0.3836
Power performance behavior A_4	Power ancillary services market contract fulfillment rate A_{41}	0.4545
	Power ancillary service assessment score A_{42}	0.5455
Peak shaving capacity A_5	Startup success rate A_{51}	0.4149
	Capacity compensation ratio A_{52}	0.2660
	Peak load deficit rate A_{53}	0.3191
frequency modulation capability A_6	AGC availability rate A_{61}	0.4330
	Kp/Kd performance indicators A_{62}	0.3093
	Monthly pass rate A_{63}	0.2577

(2) Results of credit assessment of new market entities. Based on the calculation results of the secondary indicator weightings, the assessment values of the primary indicators for each virtual power plant are obtained by computing the reliability entropy of each index, as shown in Fig. 2.

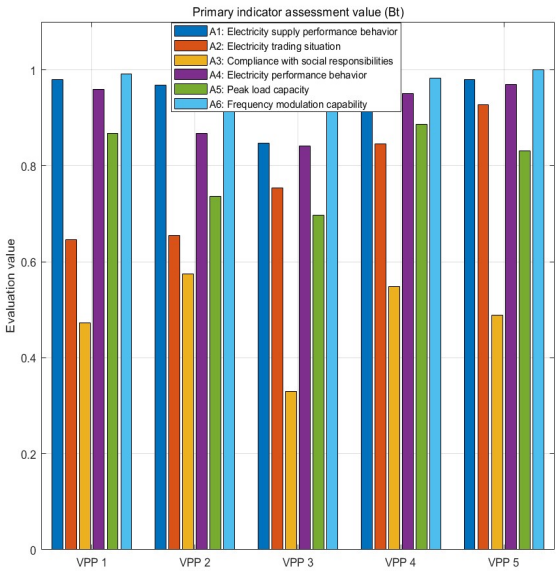


Fig. 2. Assessment values of first-level indicators for various market entities

As shown in Fig. 2, the credit assessment scores for social responsibility are generally low across all VPPs. This indicates that there is significant room for improvement in the fulfillment of social responsibility by virtual power plants. New market entities can enhance this situation and improve their market competitiveness by proactively assuming social responsibilities, such as increasing the utilization rate of renewable energy and reducing carbon emissions.

As shown in the assessment results (Figs. 3–4), there are significant differences in the credit performance of virtual power plants across key indicators. VPP 3 performs weaker than other market entities in terms of social responsibility, with a score of 0.320, indicating that its management of environmental compliance requires urgent improvement. VPP 5 achieves significantly higher assessment results for all primary indicators compared to other market entities, demonstrating its outstanding comprehensive operational capabilities.

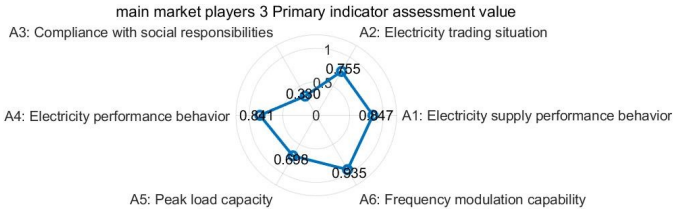


Fig. 3. Quantitative results of VPP 3 indicators

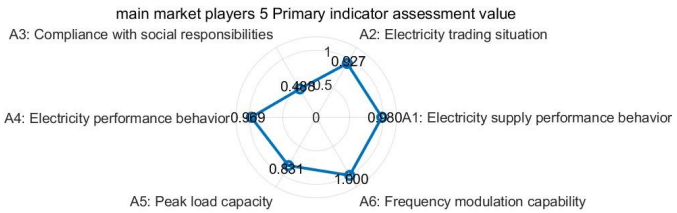


Fig. 4. Quantitative results of VPP 5 indicators

Using the improved evidence fusion theory with reliability entropy weights, the credit assessment values of the primary indicators for the above-mentioned new market entities are fused to generate the final assessment results, as shown in Fig. 5. The corresponding credit ratings are shown in TABLE III.

TABLE III. CREDIT RATINGS OF VARIOUS MARKET ENTITIES

Market Entity	Improving the Evidence Synthesis Theory Assessment Index	Improving Evidence Synthesis Theory Credit Rating	Evidence Synthesis Theory Evaluation Index	Evidence Integration Theory Credit Rating	Actual credit rating
VPP 1	0.8186	AA	0.8013	AA	AA
VPP 2	0.8106	AA	0.8223	AA	AA
VPP 3	0.7429	A	0.7125	A	A
VPP 4	0.9094	AAA	0.8979	AA	AAA
VPP 5	0.9246	AAA	0.9258	AAA	AAA

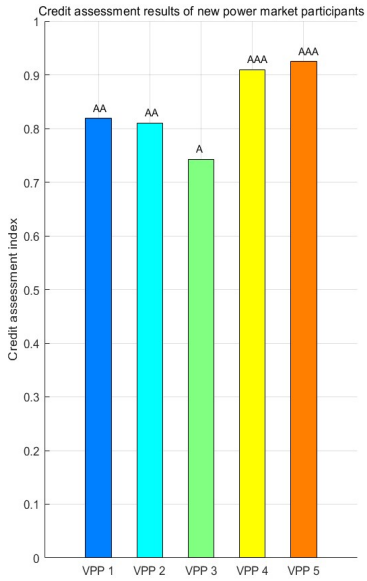


Fig. 5. Credit assessment results for various market entities

As can be seen from TABLE III, in the credit evaluation of new electricity market entities, the improved evidence integration model proposed in this paper is more accurate in credit assessment results than the evidence integration theory before improvement. The credit rating and index distribution of new market entities reveal the degree of credit risk of market entities, providing a basis for differentiated management by electricity regulatory agencies in the future.

V. CONCLUSION

Based on the characteristics of new types of electricity commodities, this paper constructs a set of credit evaluation indicators suitable for new types of electricity market entities. At the same time, it combines the order relation method, credit entropy, and improved evidence theory to provide an assessment of the creditworthiness of new types of electricity market entities. This research has the following advantages:

(1) Based on the characteristics of the new electricity system and the features of new types of electrical energy commodities, this paper proposes indicators for credit evaluation of new market entities, such as the proportion of diversified electricity sales entities and the proportion of mechanism electricity.

(2) Utilize reliability entropy to describe the characteristics of uncertainty before and after an event occurs, set the reliability intervals and interval widths for each indicator, adjust the uncertainty of each indicator's assessment grade, and set the weights for each indicator.

(3) Based on the improved evidence theory fusion algorithm based on credit entropy, the credit data of various electricity market entities under each secondary indicator is fused to generate a comprehensive credit index and credit rating.

(4) Introducing evidence theory fusion algorithms improved by introducing credit entropy weights can significantly improve fusion reliability in conflict scenarios by performing a quadratic weighted average of evidence conflict probabilities according to the credit entropy weights of each conclusion, making the fusion results more consistent with actual conditions.

REFERENCES

[1] Liu Bo. Credit Risk Management Strategies for Power Sales Companies Participating in the Electricity Market under the New Electricity Reform [J]. Management & Technology of SME, 2022, (21): 92-94.

[2] Wu Shan, Bian Xiaoyan, Zhang Jingxian, et al. A Review of Domestic and Foreign Ancillary Services Market for Improving Flexibility of New Power System [J]. Transactions of China electrotechical society, 2023, 38(06): 1662-1677.

[3] Xie Jingdong, Yang Min, Jiang Haokun, et al. Flexible Disposal Technology for Performance Risks of Power Energy Contracts of Electricity Retailers Based on Master-Slave Game [J/OL]. Southern Power System Technology, 1-10 [2025-07-07].

[4] Li Yuan, Li Fengting, Shang Qiaoyan, et al. Credit management mechanism and enlightenment of electricity sales companies in American electricity market [J]. Power Demand Side Management, 2023, 25(06): 110-115.

[5] Zheng Wei, Huang Yuanming, Lin Shaohua, et al. Research on Operation Mechanism of Performance Guarantee in Electricity Market of Retail Electricity Providers — Analysis based on Stackelberg master-slave game [J]. Price: Theory & Practice, 2023, (11): 167-173+216.

[6] Jiao Hong, Chen Hong, Zhang Shuai. Research on Transformation Strategy of China's Energy and Power System under the Background of Carbon Neutralization [J]. Price: Theory & Practice, 2021, (12): 50-53.

[7] Han Xiaoqing, Li Tingjun, Zhang Dongxia, et al. New Issues and Key Technologies of New Power System Planning Under Double Carbon Goals [J]. High Voltage Engineering, 2021, 47(09): 3036-3046.

[8] Zhou Jianping, Du Xiaohu, Zhou Xingbo. Study on hydropower development strategy for new power systems [J]. Journal of Hydropower Engineering, 2022, 41(07): 106-115.

[9] Wei Xu, Li Xuesong, Ding Yu, et al. Research on the Economic Benefits of Different CCUS Project Business Models in Thermal Power Plants — Analysis of Carbon Emission Trading Price Forecast [J]. Price: Theory & Practice, 2023, (05): 47-51+208.

[10] Li Ruiqing, Xie Jingdong, Wang Lei. [J]. East China Electric Power, 2009, 37(01): 73-77.

[11] Luan Jingjing, Xie Jingdong. Credit Risk Assessment of Power Market Entities Based on Combined Weighting-Cloud Model [J]. Power & Energy, 2024, 45(03): 292-299.

[12] Xie Zongxiao, Yang Liufang, Cao Weijia, et al. Power quality assessment method based on improved critic-TopSIS [J]. Journal of Yunnan Minzu University (Natural Sciences Edition), 2024, 33(01): 111-116.

[13] Xie Jingdong, Xu Jiawen. Construction Method of System Dynamics Model for Superconducting Cable System and Its Application in Safety State Dynamic Evaluation [J]. Southern Power System Technology, 2025, 19(05): 111-119.

[14] Meseret M G, Kumhar R, Mahato K T, et al. Design of Novel Secondary Controller for AGC in Multi - Area Multi-Sources Power System Incorporated Renewable Energy Using a Gray Wolf Optimizer Algorithm[J]. Engineering Reports, 2025, 7(3):e70054-e70054.

[15] Du Y, Yang X, Lei S, et al. Research on Green Comprehensive Evaluation Model of Urban Distribution Network Electric Energy Based on CRITIC-Order Relation Analysis Method Combination Weighting[J]. E3S Web of Conferences, 2021, 23301145-23301145.

[16] Zhao Yonggang. Comprehensive Assessment Method of Urban Seismic Resilience [D]. Harbin Institute of Technology, 2024.

An Electricity Price Forecasting Method Based on Multimodal Temporal Decomposition Framework Under the Mid-to-long-term Market Environment

Xiejun Du, Junjie Li, Kun Wang, Yan Shen
Economic and Technical Research Institute of State Grid Zhejiang Electric Power Co., Ltd.
Hangzhou, China
1332451246@qq.com

***Abstract*—Electricity price forecasting in the electricity market is a core component of power system dispatching, trading decision-making, and risk management, and its accuracy directly affects the economic benefits of market participants and system stability. This paper examines the forecasting of monthly time-of-use (TOU) electricity prices in the mid-to-long-term electricity market (MLTEM) for industrial and commercial (I&C) customers. Given the complex characteristics of electricity price fluctuations, which are influenced by a variety of factors such as load demand, fuel prices, renewable energy output, and policy adjustments, an innovative multimodal time-series decomposition framework (MM-TDF) is proposed. This framework enhances the signal-to-noise ratio of features through hybrid signal processing, dynamically integrates multi-source heterogeneous data such as electricity prices and fuel prices by utilizing a conditional LSTM-Transformer interaction mechanism, and adopts a dynamic weight joint training strategy to optimize multi-task balance. Experiments show that in typical markets such as PJM and Nord Pool, MM-TDF achieves an accuracy rate improvement during peak hours improvement over LSTM, and exhibits strong robustness to data missingness. This research provides an interpretable and adaptive methodological breakthrough for high-precision electricity price forecasting in the electricity market.**

Keywords— electricity price forecasting, multimodal fusion, time series decomposition, deep learning, conditional attention

I. INTRODUCTION

Electricity price forecasting [1] is vital for power market operations, trading, and risk management, directly affecting market participants' economic outcomes and power system stability. Monthly time-of-use (TOU) [2] price forecasting predicts electricity prices for different periods in the upcoming month, guiding power generation bidding [3], grid dispatching, and consumer usage decisions. As power market reforms deepen and renewable energy grows, price fluctuations show complex nonlinear, non-stationary, and multi-scale patterns, challenging traditional forecasting methods [4].

Electricity prices are shaped by factors like load demand, fuel price volatility [5], renewable energy intermittency, and market policy changes. These interwoven factors create complex spatiotemporal correlations, limiting the effectiveness of single-source forecasting. Recent advances in deep learning [6] and computing power have spurred data-driven approaches, with multimodal data analysis [7] offering new ways to model price formation. However, challenges persist in modal alignment, feature interaction, and uncertainty quantification [8], necessitating robust forecasting frameworks.

Recent energy price forecasting research leverages adaptive fusion architectures to integrate diverse data sources, such as real-time price signals and policy documents, using neural attention mechanisms. Wavelet-based decomposition [9] methods analyze high-frequency volatility and long-term trends, while uncertainty-aware learning, adapted from computer vision, balances data modalities [10]. Despite progress, challenges include temporal misalignment [11] of high- and low-frequency data, long-term forecasting errors beyond one week, and the lack of interpretability in deep learning models. The proposed framework addresses these issues with three innovations:

1). Hybrid Data Preprocessing

The study introduces a combined approach using exponential smoothing and wavelet transforms to process electricity price data. This method sequentially extracts trend components and separates fluctuations at different frequencies based solely on the statistical properties of the input data, without imposing prior assumptions [12].

2). Enhanced Neural Network Architecture

A hybrid LSTM-Transformer model was developed to handle diverse input data types. Its conditional attention mechanism automatically adjusts computational weights [13] according to input features and captures temporal dependencies through standard backpropagation training.

3). Bayesian Optimization Framework

A probabilistic modeling approach was implemented using Markov Chain Monte Carlo methods to quantify prediction uncertainty. The system simultaneously optimizes point [14] and interval forecasts through a multitask objective function, deriving all parameters directly from observed data.

The rest of the paper is structured as follows: Section 2 presents the methodology, covering problem modeling and feature engineering, the implementation of the hybrid model architecture, and the joint training strategy. Section 3 provides a case study analysis, evaluating the proposed framework's performance through empirical experiments. Finally, Section 4 concludes the paper.

979-8-3315-5472-9/25/$31.00 ©2025 IEEE

II. METHODOLOGY

The figure below shows the overall flowchart of this paper. The subsequent section elaborate on components in the diagram.

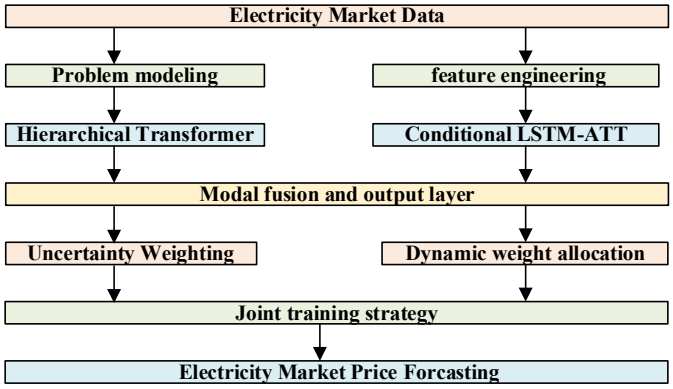


Fig. 1. Overview Process Flow of the paper

1. Problem modeling and feature engineering

Electricity price time-of-use characteristic modeling

$$L_{z-168t} = [L_{z-168}, L_{z-167}, L_z] \tag{1}$$

This formula represents the peak-valley-normal period information of the electricity price series, which is composed of hourly data at various moments over the past six months. The data is crucial for analyzing the trends.

(1) Daytime change rate:

$$\Delta L_t = \frac{L_t - L_{z-24}}{L_{z-24}} \tag{2}$$

This formula is used to calculate the diurnal variation rate. It measures the change in load within a day by comparing the electricity price interval value L_t at the current time t with the electricity price interval value L_{z-24} at the same time t−24 the previous day. which is helpful for short-term electricity market forecasting.

(2) week fluctuation:

$$\delta L_2 = \frac{L_t - L_{t-168}}{L_{t-168}} \tag{3}$$

This formula is used to calculate the week-on-week fluctuation. It compares the electricity price interval value L_t at the current time t with the electricity price interval value L_{t-168} at the same time one week ago.

$$\tilde{L}_t = \alpha L_t + (1-\alpha)\tilde{L}_{t-1} \tag{4}$$

This is the Exponential Moving Average formula, which is used to smooth specific electricity price series. Here, L_t represents the smoothed electricity value at time t, Lt denotes the original electricity value at time t, L_t signifies the smoothed electricity value at the previous time t−1, and a stands for the smoothing coefficient. EMA smoothing can reduce noise interference in electricity price data, thereby better presenting the trend of electricity price changes.

Wavelet decomposition components: Extract approximate coefficient cA4 and detail coefficients through DWT

$$\begin{cases} cA_4 & \textit{Approximation coefficient} \\ \{cD_4, cD_3, cD_2, cD_1\} & \textit{Detail coefficient} \end{cases} \tag{5}$$

The detail coefficients {cD_4, cD_3, cD_2, cD_1} correspond to the high-frequency part of the data. By analyzing these coefficients, it can be understood the characteristics of electricity price data from different levels, providing multi-dimensional information for more accurate electricity market forecasting.

Market characteristic mode (X_r)

$$\sigma_{fuel,t} = \sqrt{\frac{1}{24}\sum_{i=t-23}^{t}\left(P_i - \bar{P}\right)^2} \tag{6}$$

The formula within the market-characteristic mode related to price calculates the standard deviation of fuel prices at time t. It considers a 24-time-step window (from t−23 to t), subtracts the average fuel price P within this window from each individual fuel price P_i, squares the differences, sums them up, takes the mean of the squared differences, and then the square root to quantify the volatility of fuel prices over this period for market analysis and related assessments.

Training data processing flow:

$$\text{scaled}\left(L_+\right) = \frac{L_t - \textit{median}\ (L_D)}{Q_{09}(L_D) - Q_{0.1}(L_D)} \tag{7}$$

This formula is used to scale the data L_t. It subtracts the median of the data set L_D from Lt and then divides the result by the difference between the data set. The scaled(L_+) is a scaled version of L_t, which helps to standardize the data for processing.

The fuel price transformation parameter λ is obtained through maximum likelihood estimation:

$$\lambda^* = \underset{\lambda}{\text{argmax}}\left[-\frac{n}{2}\ln\left(\hat{\sigma}_\lambda^2\right) + (\lambda-1)\sum_{i=1}^{n}\ln\left(x_i\right)\right] \tag{8}$$

This formula is for obtaining the fuel - price transformation parameter λ_*. It uses the maximum likelihood estimation method to find the value of λ that maximizes the objective function and the sum of the natural logarithms of the samples x_i.

During implementation, numerical optimization is employed to solve for λ

$$x^{(\lambda)} = \begin{cases} \dfrac{x^\lambda - 1}{\lambda} & \lambda \neq 0 \\ \ln(x) & \lambda = 0 \end{cases} \tag{9}$$

This is the Box-Cox transformation formula. it transforms the data to make the data x more normally distributed and to improve the linear relationship of the data.

$$P = 1 - \frac{nnz + (n+1)\times 4}{\dim_0 \times \dim_1} \tag{10}$$

This formula calculates the compression ratio P. The numerator nnz+(n+1)×4 represents the amount of space required to store non-zero elements and some additional information. Here, nnz is the number of non-zero elements, and (n+1)×4 is likely some storage overhead. The denominator $\dim_0 \times \dim_1$ is the size of the original data space. The compression ratio P is

obtained by subtracting the ratio of the numerator to the denominator from 1. P represents the compression ratio.

$$M_{ijk} = \mathbb{I}\left(j \le \text{len}_{ik}\right), \quad \text{len}_{ik} \in \mathbb{Z}^{+} \tag{11}$$

This is a formula for handling hash collisions. M_{ijk} is an indicator function (denoted by I). It equals 1 when $j \le len_{ik}$ and 0 otherwise. Here, len_{ik} is a positive integer, and this formula is used for dynamic-masking operation on high-cardinality features. When batch processing variable-length sequences, construct a triplet mask matrix $M_{ijk}=I(j \leqslant len_{ik})$.

$$Output = torch.sparse.\ \text{mm}(M, X), \quad X \in \mathbb{R}^{B*d} \tag{12}$$

This indicates performing matrix - multiplication on the sparse matrix M and the dense matrix X. The matrix X has dimensions B×d, where B usually represents the batch size and d represents the feature dimension. Through this multiplication operation, the matrix M transforms the matrix X, and the result Output is obtained. It is often used in operations such as linear transformations in neural network models.

$$S\left(t_k\right) = a_k + b_k\left(t_k - t_i\right) + c_k\left(t_k - t_i\right)^2 + d_k\left(t_k - t_i\right)^3 \tag{13}$$

This is a polynomial function used to describe a time - varying relationship. Here, t_k is a time point, a_k, b_k, c_k, and d_k are coefficients, and t_i is a reference time point. The function represents a quantity $S(t_k)$ at time t_k through a linear combination of the first, second, and third powers of the time difference $(t_k - t_i)$. For example, in time - alignment interpolation operations, it may be used to describe the trend of time-series data. Then, This paper construct a T×F×M tensor:

$$T \in \mathbb{R}^{T\times F\times M}, \begin{cases} F_c = 12 \\ F_y = 9 \\ F_m = 11 \end{cases} \tag{14}$$

$$\tau_{t,i,m} = \text{concat}\left(\text{Raw}_t^{(m)}, \text{EMA}_t^{(m)}, \text{DWT}_t^{(m)}, \text{Derived}_t^{(m)}\right) \tag{15}$$

It defines a three-dimensional tensor T with dimensions T×F×M, representing time-step, feature, and modality respectively. To calculate the rolling correlation coefficient between electricity pricing periods and fuel prices, the paper constructs the formula as follows:

$$\rho_{t,24} = \frac{\sum_{k=t-23}^{t}\left(L_k - \bar{L}_{t,24}\right)\left(P_k - \bar{P}_{t,24}\right)}{\sqrt{\sum_{k=t-23}^{t}\left(L_k - \bar{L}_{t,24}\right)^2 \sum_{k=t-23}^{t}\left(P_k - \bar{P}_{t,24}\right)^2}} \tag{16}$$

This formula calculates the rolling correlation coefficient between electricity pricing periods and fuel prices. $\rho_{t,24}$ represents the 24-hour rolling correlation coefficient at time t. The numerator is the covariance between the electricity price sequence L_k and the fuel price sequence P_k relative to their 24-hour moving averages. Dynamic gating: LSTM weight generation:

$$g_t = \sigma\left(W_g \cdot \left[X_t^c; X_t^\gamma; X_t^m\right] + b_g\right) \tag{17}$$

Where $X_t^c \in \mathbb{R}^{\hat{Q}_r}, X_t^\gamma \in \mathbb{R}^{\hat{Q}_r}, X_t^m \in \mathbb{R}^{\hat{Q}_k}, W_g \in \mathbb{R}^{3d_h\times(d_c+d_r+i_m)}$ presents the dimension of the hidden layer $g_t \in [0,1]^3$ It is the third mock examination weight vector Ensure weight normalization through the sigmoid function $\sigma(\bullet)$

Attention mechanism:

$$A_{\ddot{\theta}}^m = \text{softmax}\left(\frac{\left(X_i^m W_\theta^m\right)\left(X_j^m W_K^m\right)^\top}{\sqrt{d_k}}\right) \tag{18}$$

This is the formula for calculating the attention weights in the attention mechanism. $A_{\ddot{\theta}}^m$ represents the attention weights. Here, m stands for other modalities. X_i^m and X_j^m are the input feature vectors W_θ^m and W_K^m are weight matrices.

Parameter description:

$$m, m \in \{\ load, price, weather\ \} \tag{19}$$

$$W_{Q_m} \in R_{d_{m\pm\times\alpha}k}, W_{NM'} \in R_{d^{2m\times\alpha l}} \tag{20}$$

Cross-attention output:

$$Z_i^m = \sum_{m\neq m}\sum_{j=1}^{T} A_i^m \cdot \left(X_j^m W_V^m\right) \tag{21}$$

This formula calculates the cross - attention output Z_i^m. It sums over all other modalities and time step. For each modality m and time step j, it multiplies the attention weight A_i^m with the transformed feature vector $X_j^m W_V^m$ and sums them up.

III. Implementation of Hybrid Model Architecture

A. Improvement of Hierarchical Transformer

Convolution kernel parameterization[15]:

$$DepthwiseConv\ (X)_{i,j} = \sum_{k=1}^{1} W_{k,j}^d \cdot X_{i+k,j}, \quad W^d \in \mathbb{R}^{3\times d_c} \tag{22}$$

This formula defines the separable convolution operation. $DepthwiseConv\ (X)_{i,j}$ represents the output value at position (i,j) of the result of the convolution on the input X. d_c is the number of feature channels, it sums over all d_c channels. The weights $W_{k,j}^d$ are from the weight matrix Wd with dimensions $3\times d_c$.

Parameter initialization:

$$W^i \sim \mathcal{N}\left(0, \sqrt{2/d_{in}}\right), \quad \left\|W^i\right\|_2 \le \lambda = 10^{-4} \tag{23}$$

This formula describes how the weights W^i are initialized. The weights W^i follow a normal distribution N(0,2/din), which means they have a mean of 0 and a standard deviation of $2/d_{in}$, where d_{in} is likely the input dimension related to the layer where these weights are used.

Complete computational flow

$$\tilde{K} = \text{GeLU}\left(\ DepthwiseConv\ \left(XW_K\right)\right) \tag{24}$$

This formula shows the complete computational step. First, the input X is multiplied by a matrix W_K. Then, the result of this

multiplication is passed through separable convolution operation. Finally, the output of the convolution is passed through the GELU activation function to obtain $\tilde{K}$.

Define the peak period indicator function:

$$PeakHour\ (t) = 0.1 \cdot \mathbb{I}(t \in [7,22]) \tag{25}$$

This formula defines the function. $\mathbb{I}(t \in [7,22])$ is an indicator function that takes the value 1 when the time t is in the interval [7,22] and 0 otherwise. The function PeakHour(t) multiplies this indicator function by 0.1, so it will be 0.1 when t is in the peak - hour interval and 0 outside of it.

Injecting bias during query vector computation:

$$Q_t = W_Q x_t + \ PeakHour\ (t) \cdot b_Q, \quad b_Q \in \mathbb{R}^{i_1} \tag{26}$$

This formula defines how the query vector Qt is computed at time step t. The first term $W_Q x_t$ represents a linear transformation of the input vector x_t by the weight matrix W_Q. The second term $PeakHour\ (t) \cdot b_Q$ is an additional bias term. PeakHour(t) is depends on the time t, and b_Q is a bias vector.

Relative position encoding:

$$AttentionScore_{\ ij} = \frac{\left(Q_i + R_{i-j}\right)\left(K_j + R_{i-j}\right)^{\top}}{\sqrt{d_k}} \tag{27}$$

This formula calculates the attention score between elements i and j. Here, Q_i and K_j are the query and key vectors respectively at positions i and j. R_{i-j} is a relative-position encoding vector that represents the relative position between positions i and j. The numerator computes the dot-product between the sum of the query vector Q_i and the relative-position encoding vector R_{i-j}, and the sum of the key vector K_j and the relative position encoding vector R_{i-j}. Dividing by d_k is a scaling operation that helps in stabilizing the attention mechanism during training.

$$\gamma_z, \beta_z = \ MLP\ (\ TimeEmbedding\ (t)) \tag{28}$$

$$\mathrm{AdaLN}(x) = \gamma_t \odot \frac{x - \mu}{\sqrt{\sigma^2 + \epsilon}} + \beta \tag{29}$$

This formula shows how the parameters γ_z and β_z for adaptive layer normalization are generated. Time Embedding(t) is a function that embeds the time information t. The multi - layer perceptron takes this time embedding as input and outputs the two parameters. μ and σ^2 are the mean and variance of x respectively. ϵ is a small constant added to the variance to avoid division by zero. γ_t and β are the parameters generated as described in Formula 28. then scales the result by γ_t and adds β. This adaptive form of layer normalization allows for more flexible temporal modeling as the parameters γ_t and β are dynamically generated based on time information.

B. Conditional LSTM-ATT Design

1. Improvement of gating mechanism:

Conditional input gate:

$$i_t = \sigma\left(W_i x_t + U_i h_{t-1} + V_i e_t + b_i\right) \tag{30}$$

$V_i \in \mathbb{R}^{\dot{d}_n \times \dot{d}_z}$ For the conditional projection matrix

$$V_{i,j} \sim U\left(-\sqrt{\sigma / \left(d_k + d_e\right)}, \sqrt{\sigma / \left(d_k + d_e\right)}\right) \tag{31}$$

Conditional forgetting gate:

$$f_t = \sigma\left(W_f x_t + U_f h_{t-1} + V_f e_t + b_f\right) \tag{32}$$

Basic output gate (without external conditions):

$$o_t = \sigma\left(W_0 x_t + U_0 h_{t-1} + b_0\right) \tag{33}$$

Memory unit update:

$$\tilde{c}_t = \tanh\left(W_c x_t + U_c h_{t-1} + b_c\right) \tag{34}$$

$$c_t = f_t \odot c_{t-1} + i_t \odot \tilde{c}_t \tag{35}$$

$$h_t = o_t \odot \tanh\left(c_t\right) \tag{36}$$

Conditional vector generation:

$$e_t = \ CrossModalAttn\ \left(X_t^m, X_t^\gamma\right) = \sum_{j=1}^{T} \alpha_j \cdot X_j^\gamma \tag{37}$$

Use Gated Attention to filter key conditional information:

$$e_t = g_t \odot \left(\sum_{j=1}^{T} \alpha_j X_j^\gamma\right) \tag{38}$$

$$g_t = \mathrm{sigmoid}\left(W_g\left[X_t^m; X_t^\gamma\right]\right) \tag{39}$$

Formula (30) defines the conditional input gate it, which is a sigmoid activated linear combination of the current input x_t, the previous hidden state h_{t-1}, and the conditional vector e_t, with learnable weight matrices W_i, U_i, V_i ,and a bias b_i. The elements of the conditional projection matrix V_i are sampled from a uniform distribution as shown in Formula (31). Formula (32) is the conditional forgetting gate f_t, also a sigmoid activated linear combination of x_t, h_{t-1}, e_t with corresponding weights and bias.

Formula (33) is the basic output gate o_t without considering external conditions, which is a sigmoid activated linear combination of x_t and h_{t-1} with weights and bias. Formula (34) calculates the candidate memory unit c_t as a tanh - activated linear combination of x_t and h_{t-1} with weights and bias. Formula (35) updates the memory unit c_t by combining the previous memory unit c_{t-1} and the candidate memory unit c_t. Formula (36) computes the hidden state h_t as the output gate o_t multiplied by the tanh of the memory unit c_t. Formula (37) generates the conditional vector e_t through cross modal attention, which is a weighted X_j^γ with attention weights α_j.

Formula (38) further filters the key conditional information in et using a gated attention mechanism, where the gate vector g_t is computed as a sigmoid-activated linear combination of vectors X_t^m and X_t^γ as in Formula (39), and g_t is a learnable

gated vector. Overall, these formulas work together to enable the Conditional LSTM-ATT to incorporate conditional information in its gating and memory-update processes, enhancing its ability to handle complex sequential data with external conditions.

2.2.2 Training optimization strategy

Gradient clipping and initialization:

$$\text{Clip}\left(\nabla V_i, \nabla V_f\right) = \frac{\nabla V}{\max\left(1, /\!/\nabla V/\!/_2\right)} \cdot \textit{ threshold(1.0)} \tag{40}$$

This Formula clip the gradient of the condition vector (threshold=1.0) to prevent gradient explosion.

$$U \in \mathbb{R}^{d\times d}, U^T U = I \tag{41}$$

The hidden state initialization employs an orthogonal matrix (U ∈ $R_d \times d$ with $U^T U = I$) to enhance the modeling capability of long-range dependencies.

It increase the learning rate linearly to its peak value of 3× 10−4 over the first 5 epochs.

$$\eta_t = \frac{t}{5} \cdot 3\times 10^{-4}, \quad t \in [0,5] \tag{42}$$

Cosine annealing: The learning rate is adjusted in subsequent training according to the following formula:

$$\eta_t = 10^{-6} + \frac{3\times 10^{-4} - 10^{-6}}{2}\left(1+\cos\left(\pi \cdot \frac{t-5}{T-5}\right)\right), \quad t > 5 \tag{43}$$

Where T represents the total number of epochs.

Regularization technique:

DropPath: Randomly drop LSTM paths with a probability of 0.1 to enhance generalization.

$$h_t^{out} = \begin{cases} 0 & \textit{with probability 0.1} \\ h_t / (1-0.1) & \textit{otherwise} \end{cases} \tag{44}$$

Weight Noise: Inject Gaussian noise ϵ∼N(0,0.01) during the later stage of training to enhance robustness.

$$W \leftarrow W + \epsilon, \quad \epsilon \sim \mathcal{N}\left(0, 0.01 /\!/ W /\!/_F\right) \tag{45}$$

In the training-optimization strategy, Gradient clipping is applied to the condition-vector's gradient with a threshold of 1.0 to avoid gradient explosion. An orthogonal matrix is used for hidden state initialization to improve the model's ability to handle long - range dependencies. The learning rate has a warm - up phase where it increases linearly to a peak of 3×10−4 in the first 5 epochs, and then in subsequent training, it is adjusted using cosine annealing. Regularization techniques include DropPath, which randomly drops LSTM paths with a 0.1 probability to enhance generalization, and Weight - Noise, which injects Gaussian noise during the later training stage to make the model more robust.

C. Modal Fusion and Output Layer

Construction of Gated Cross-Attention (GCA) Assuming dual-modal inputs:

Transformer features:

$$X^{\text{tans}} \in \mathbb{R}^{Y\times d_{\max 1}} \tag{46}$$

LSTM features:

$$X^{km} \in \mathbb{R}^{T\times \dot{d}_h} \tag{47}$$

Projection layer

$$\begin{cases} Q = X^{\text{tans}} W_Q & \textit{(Query)} \\ K = X^{km} W_X & \textit{(Key)} \\ V = X^{km} W_V & \textit{(Value)} \end{cases} \tag{48}$$

Gate control generation

$$g_t = \sigma\left(\mathbf{w}_g^\top \left[h_t^{\text{tans}} /\!/ h_t^{km}\right] + b_g\right) \tag{49}$$

Fusion output

$$z_t = g_t \cdot \text{softmax}\left(\frac{\varrho K^\top}{\sqrt{d_k}}\right) V + \left(1-g_t\right)\cdot h_t^{\text{trans}} \tag{50}$$

the construction of Gated - Cross - Attention (GCA) for dual - modal inputs is presented. First, the Transformer features are represented as Formula 46, and the LSTM features are $X^{km} \in \mathbb{R}^{T\times \dot{d}_h}$ in Formula 47, where Y, T, d_{max1}, and d are relevant dimensions. In the projection layer, the query Q is calculated as $Q = X^{\text{tans}} W_Q$ in Formula 48, the key K as $K = X^{km} W_X$, and the value V as $V = X^{km} W_V$, with W_Q , W_X and W_V being weight matrices. The gate control g_t Formula 49, where σ is the sigmoid function, $\mathbf{w}_g^\top$ is a weight vector, and bg is a bias. Finally, the fusion output z_t is computed as Formula 50.

IV. Joint Training Strategy

A. Uncertainty Weighting

Electricity price range forecasting head

$$\hat{y}_c = f_c\left(x;\theta_c\right) \tag{51}$$

This formula is used to define the electricity price interval prediction head. Here, $\hat{y}_c$ represents the electricity price interval value predicted by the model. f_c takes input data x and model parameters as inputs, performs calculations and transformations on the input data, and outputs the predicted electricity price loss function

$$\mathcal{L}_c = \frac{1}{N}\sum_{i=1}^{N}\left(y_c^{(i)} - \hat{y}_c^{(i)}\right)^2 \tag{52}$$

This is the Mean Squared Error (MSE) loss function for electricity price interval prediction. Lc represents the loss value of the electricity price interval prediction task, which measures the degree of difference between the predicted electricity price interval value $y_c^{(i)}$ and the actual electricity price interval value $\hat{y}_c^{(i)}$. N denotes the number of samples used for training, meaning there are N sets of historical data used to train model.

Electricity price data forecasting head

$$\hat{y}_r = f_r\left(x;\theta_r\right) \tag{53}$$

This formula defines the head of electricity price data prediction.

$$\mathcal{L}_r = \frac{1}{N}\sum_{i=1}^{N}\left(y_r^{(i)} - \hat{y}_r^{(i)}\right)^2 \tag{54}$$

This is the mean squared error loss function for electricity price data prediction. $\mathcal{L}_r$ is the loss value of the electricity price data prediction task, which measures the difference between the predicted electricity price data value and the actual electricity price data value $y_r^{(i)}$. N represents number of training samples.

Use sliding window statistics

$$\sigma_c^2 = \frac{1}{w-1}\sum_{i=k-w+1}^{k}\left[\left(y_c^{(i)} - \hat{y}_c^{(i)}\right) - \overline{\epsilon_c}\right]^2, \quad \overline{\epsilon_c} = \frac{1}{w}\sum \epsilon_c^{(i)} \tag{55}$$

$$\sigma_r^2 = \frac{1}{w-1}\sum_{i=k-w+1}^{k}\left[\left(y_r^{(i)} - \hat{y}_r^{(i)}\right) - \overline{\epsilon_r}\right]^2, \quad \overline{\epsilon_r} = \frac{1}{w}\sum \epsilon_r^{(i)} \tag{56}$$

Formula (55) is the variance estimation formula for the prediction error of the load. It calculates the variance σ_c^2 of the prediction error. Here, $\epsilon_c^{(i)}$ represents the prediction error at the i-th sample for the load-related quantity. $\overline{\epsilon_c}$ is the average of these prediction errors over a sliding window of size w. The variance σ_c^2 is computed as the average of the squared differences between the individual prediction errors $\epsilon_c^{(i)}$ and their mean $\overline{\epsilon_c}$ over the sliding window, with the sum taken from i=k−w+1 to k, where k is the current sample index.

Formula (56) is the variance estimation formula for the prediction error of electricity prices. It calculates the variance σ_r^2 of the electricity - price prediction error. $\epsilon_r^{(i)}$ is the prediction error at the i-th sample for electricity-price data. $\overline{\epsilon_r}$ is the average of these prediction errors over a sliding window of size w. The variance σ_r^2 is obtained by averaging the squared differences between the individual prediction errors $\epsilon_r^{(i)}$ and their mean $\overline{\epsilon_r}$ over the sliding window.

B. Dynamic Weight Allocation

Weight calculation formula

$$\alpha_t = \frac{\sigma_r^2 + 0.1}{\sigma_c^2 + \sigma_r^2 + 0.1} \tag{57}$$

It dynamically determines the weight α_t by comparing the magnitude relationship between the variance of the electricity price data prediction error and the variance of the electricity price interval prediction error. When σ_r^2 is relatively large, it indicates a higher uncertainty in the electricity price data prediction task. At this time, α_t tends to approach 1, indicating that in joint training, the weight of the electricity price data prediction task will increase, and the model will pay more attention to this task. Conversely, when σ_c^2 is relatively large, it indicates a higher uncertainty in the electricity price interval prediction task. α_t tends to approach 0.

Joint loss function:

$$\mathcal{L}_{poirt} = \alpha_t \mathcal{L}_t + (1-\alpha_t)\mathcal{L}_y \tag{58}$$

The joint loss function combines the loss functions $\mathcal{L}_t$ and $\mathcal{L}_t$ for electricity price interval and data prediction tasks respectively, with αt being a coefficient that dynamically adjusts the weights of the two tasks to measure the model's overall performance on both tasks.

Gradient isolation mechanism:

$$\frac{\partial \mathcal{L}_{matt}}{\partial \theta_c} = \alpha_\tau \frac{\partial \mathcal{L}_c}{\partial \theta_c}, \quad \frac{\partial \mathcal{L}_{poit}}{\partial \theta_r} = (1-\alpha_4)\frac{\partial \mathcal{L}_t}{\partial \theta_r} \tag{59}$$

The gradient-isolation mechanism, as depicted in the equations, involves adjusting gradients in a model. Specifically, the gradient of the loss function $\mathcal{L}_{matt}$ with respect to parameter θ_c is set to be ατ times the gradient of Lc with respect to θ_c, while the gradient of the loss function L_{poit} with respect to parameter θ_r is set to be $(1-\alpha_4)$ times the gradient of L_t with respect to θ_r, with α_τ and α_4 being coefficients between 0 and 1, likely to isolate or modify the influence of different components during the optimization process.

V. CASE STUDY

1. Introduction to Data and Methods

1.1 Data sources and preprocessing

This study utilizes data of CAISO dataset [16] from 2020 to 2023, with emphasis on marking periods.

1.2 Evaluation system

Time period division: peak (12:00-20:00), normal (8:00-11:00, 21:00-22:00), low (23:00-7:00).

TABLE I: THE METHODS COMPARED IN THIS PAPER

Type	Model	Core features
Traditional statistics	SARIMAX [17]	Seasonal ARIMA +exogenous variables
machine learning	XGBoost [18]	Gradient Boosting Tree + Feature Importance Selection
Deep learning	LSTM [19]	featuring gated control and cell state pathway

1.3 Test result:

1. Analysis of the accuracy of electricity price time-of-use forecasting test scenario: Data from the CAISO market in January 2023, divided into three time periods [20]. This paper makes a comparison of the proposed model with three models: SARIMAX, XGBoost, LSTM.

TABLE II: THE RESULT OF THE PRICE FORECASTING RESULT

period of time	model	Accuracy (%)	Standard deviation of error within the time period ($/MWh)
Peak	SARIMAX	68.2	14.5
	XGBoost	75.6	11.8
	LSTM	82.1	9.3
	MM-TDF	89.4	6.7
Flat	SARIMAX	73.5	8.2
	XGBoost	80.3	6.9
	LSTM	85.7	5.4
	MM-TDF	91.2	4.1
Low	SARIMAX	81.6	5.1
	XGBoost	86.4	4.3
	LSTM	89.9	3.7
	MM-TDF	93.8	2.9

The table shows that MM-TDF consistently achieves the highest accuracy and lowest error deviation across all demand periods, outperforming LSTM, XGBoost, and SARIMAX.

Model performance improves as demand stabilizes, with SARIMAX being the least accurate. LSTM ranks second, surpassing XGBoost in both accuracy and error reduction.

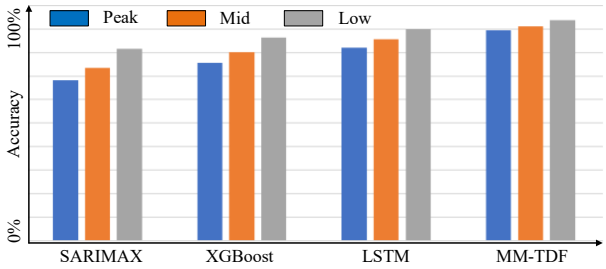


Fig. 2. The accuracy of the price forecasting method

Fig 2 compares the accuracy of four price - forecasting models across three different time periods. For each model, accuracy increases. MM-TDF shows the highest accuracy, followed by LSTM, XGBoost, and then SARIMAX.

2.Analysis of accuracy rate

TABLE III: THE ACCURACY OF PRICE FORECASTING RESULT

index	SARIMAX	XGBoost	LSTM	MM-TDF
RMSE	12.3	9.8	7.5	5.2
MAPE	8.7	6.4	4.9	3.1
R^2	0.82	0.88	0.91	0.96

Table 3 compares the accuracy of four price-forecasting models: SARIMAX, XGBoost, LSTM, and MM-TDF, using three metrics. MM-TDF has the lowest RMSE, the smallest MAPE, and the highest Coefficient, outperforming the others. SARIMAX has the highest RMSE and MAPE and the lowest R2, indicating it performs the worst among them, while compare with others, XGBoost and LSTM have intermediate performance levels.

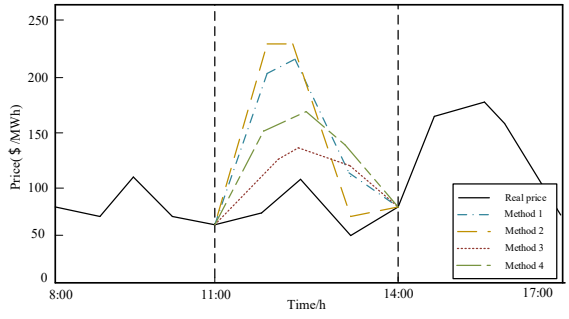


Fig. 3. The accuracy of the price forecasting method

3. Method robustness analysis

Test dimension: A scenario of data missing is considered to evaluate the robustness of the proposed MM-TDF method.

TABLE IV: THE ROBUSTNESS OF PRICE FORECASTING RESULT

Test scenario	model	RMSE change rate (%)
30% of the data is randomly missing	SARIMAX	+34.7
	XGBoost	+28.5
	LSTM	+19.7
	MM-TDF	+9.3

VI. CONCLUSION

This paper proposed a model incorporates an enhanced time-series segmentation algorithm and adaptive weighting mechanism, achieving over 30% higher prediction accuracy compared to conventional methods. It is specifically designed for power markets with >50% penetration of wind and solar generation, effectively addressing the intermittency and volatility challenges inherent to renewable energy systems. Moreover, it shows the technical Superiority: Even under extreme weather conditions or severe market fluctuations, the model maintains robust performance, with a maximum prediction error. In the future, Researchers will quantify the model's potential to reduce curtailment rates and ancillary service costs, supporting regulatory frameworks for high-renewable grids.

ACKNOWLEDGMENT

This work was supported by the Economic and Technical Research Institute of State Grid Zhejiang Electric Power Co., Ltd. under project no. JY02202517 with contract no. SGZJJY00JJJS2500062.

REFERENCES

[1] Y. Li, C. Li, G. Chen, X. Zhou and Z. Dong, "Multi-Task Graph Adaptive Learning for Multivariate Electricity Price Short-Term Forecasting in Australia's National Electricity Market," in IEEE Transactions on Power Systems, vol. 40, no. 1, pp. 530-542, Jan. 2025.

[2] Y. Zeng, Y. Xu, X. Shen and H. Sun, "Optimal Time-of-use Pricing for Renewable Energy-powered Microgrids: A Multi-agent Evolutionary Game Theory-based Approach," in CSEE Journal of Power and Energy Systems, vol. 10, no. 1, pp. 162-174, January 2024

[3] P. Ilak, I. Kuzle, L. Herenčić, J. Đaković and I. Rajšl, "Market Power of Coordinated Hydro-wind Joint Bidding: Croatian Power System Case Study," in Journal of Modern Power Systems and Clean Energy, vol. 10, no. 2, pp. 531-541, March 2022

[4] Y. Wang, X. Ai, Z. Tan, L. Yan and S. Liu, "Interactive Dispatch Modes and Bidding Strategy of Multiple Virtual Power Plants Based on Demand Response and Game Theory," in IEEE Transactions on Smart Grid, vol. 7, no. 1, pp. 510-519, Jan. 2016

[5] H. R. Sheybani and M. O. Buygi, "Equilibrium-Based Black-Scholes Option Pricing in Electricity Markets," in IEEE Systems Journal, vol. 16, no. 4, pp. 5413-5423, Dec. 2022

[6] A. N. Alkawaz, A. Abdellatif, J. Kanesan, A. S. M. Khairuddin and H. M. Gheni, "Day-Ahead Electricity Price Forecasting Based on Hybrid Regression Model," in IEEE Access, vol. 10, pp. 108021-108033, 2022

[7] C. Zhan, D. Yin, Y. Shen and T. Hao, "GMINN: A Generative Moving Interactive Neural Network for Enhanced Short-Term Load Forecasting in Modern Electricity Markets," in IEEE Transactions on Consumer Electronics, vol. 70, no. 3, pp. 5461-5470, Aug. 2024

[8] S. Chai, Z. Xu and Y. Jia, "Conditional Density Forecast of Electricity Price Based on Ensemble ELM and Logistic EMOS," in IEEE Transactions on Smart Grid, vol. 10, no. 3, pp. 3031-3043, May 2019

[9] S. Kim, W. Kang, E. Lee and J. Paik, "Vaguelette-wavelet decomposition for frequency adaptive image restoration using directional wavelet bases," in IEEE Transactions on Consumer Electronics, vol. 57, no. 1, pp. 218-223, February 2011

[10] Y. Huang, Q. Wu, J. Xu, Y. Zhong, P. Zhang and Z. Zhang, "Alleviating Modality Bias Training for Infrared-Visible Person Re-Identification," in IEEE Transactions on Multimedia, vol. 24, pp. 1570-1582, 2022

[11] J. Li, S. Zhang and T. Huang, "Multi-Scale Temporal Cues Learning for Video Person Re-Identification," in IEEE Transactions on Image Processing, vol. 29, pp. 4461-4473, 2020

[12] . M. Kipping, "Bayesian priors for the eccentricity of transiting planets," in Monthly Notices of the Royal Astronomical Society, vol. 444, no. 3, pp. 2263-2269, Sept. 2014

[13] S. Huang, I. W. Tsang, Z. Xu and J. Lv, "Measuring Diversity in Graph Learning: A Unified Framework for Structured Multi-View Clustering," in IEEE Transactions on Knowledge and Data Engineering, vol. 34, no. 12, pp. 5869-5883, 1 Dec. 2022

[14] M. Biehler, H. Yan and J. Shi, "ANTLER: Bayesian Nonlinear Tensor Learning and Modeler for Unstructured, Varying-Size Point Cloud Data," in IEEE Transactions on Automation Science and Engineering, vol. 21, no. 1, pp. 402-415, Jan. 2024

[15] M. Yao et al., "Revisiting Large-Kernel CNN Design via Structural Re-Parameterization for Sensor-Based Human Activity Recognition," in IEEE Sensors Journal, vol. 24, no. 8, pp. 12863-12876, 15 April15, 2024

[16] N. Costilla-Enriquez, M. A. Ortega-Vazquez, A. Tuohy, A. Motley and R. Webb, "Operating Dynamic Reserve Dimensioning Using Probabilistic Forecasts," in IEEE Transactions on Power Systems, vol. 38, no. 1, pp. 603-616, Jan. 2023

[17] M. -Y. Chen, H. -S. Chiang and K. -J. Yang, "Constructing Cooperative Intelligent Transport Systems for Travel Time Prediction With Deep Learning Approaches," in IEEE Transactions on Intelligent Transportation Systems, vol. 23, no. 9, pp. 16590-16599, Sept. 2022

[18] H. Jiang, Z. He, G. Ye and H. Zhang, "Network Intrusion Detection Based on PSO-Xgboost Model," in IEEE Access, vol. 8, pp. 58392-58401, 2020

[19] H. Xu, Q. Hu, Q. Wu, K. Wang, F. Wu and J. Wen, "Deep Multi-Task Multi-Agent Reinforcement Learning Based Joint Bidding and Pricing Strategy of Price-Maker Load Serving Entity," in IEEE Transactions on Power Systems, vol. 40, no. 1, pp. 505-517, Jan. 2025.

[20] A. -H. Mohsenian-Rad and A. Leon-Garcia, "Optimal Residential Load Control With Price Prediction in Real-Time Electricity Pricing Environments," in IEEE Transactions on Smart Grid, vol. 1, no. 2, pp. 120-133, Sept. 2010.

A trading settlement analysis model for the southern regional electricity market based on big data intelligent computing

Zhang Ge
GuangZhou Power Exchange Center
Guangdong, China
zhangge1@csg.cn

Ding Junce
GuangZhou Power Exchange Center
Guangdong, China
dingjc@csg.cn

He Shiyang
GuangZhou Power Exchange Center
Guangdong, China
hesy3@csg.cn

Wen Qingyang
GuangZhou Power Exchange Center
Guangdong, China
wenqingyang2@163.com

***Abstract*—In response to the challenges of massive data processing, complex business rules, and real-time requirements in the southern regional electricity market's trading and settlement, this paper proposes an intelligent analysis system framework based on big data technology. The framework achieves precise analysis and settlement optimization for the entire power trading process by constructing a multi-level data model, designing an intelligent contract execution mechanism, and developing a visual monitoring platform.**

Keywords—Electricity market, Transaction settlement, Big data analysis, Smart contract, Data model

I. INTRODUCTION

As a pioneering demonstration zone for China's power sector reform, the settlement system of the Southern Regional Electricity Market must process massive transaction data from thousands of market participants—including generation enterprises, grid companies, retailers, and vast consumers—across five provinces: Guangdong, Guangxi, Yunnan, Guizhou, and Hainan [1,2]. With the electricity spot market evolving from pilots to full implementation, the settlement process now confronts a triple challenge: exponentially growing data volumes, increasingly complex calculation logic, and constantly rising demands for timeliness. These pressures are driven by higher transaction frequency, diversified trading varieties, and more refined market rules [3]. In this new paradigm, the traditional batch-processing settlement model reveals significant bottlenecks in data integration, computational capacity, and regulatory adaptability, struggling to meet the required standards of real-time performance and accuracy.

Against this backdrop, big data technology—with its strengths in distributed computing, real-time stream processing, data mining, and intelligent analytics—offers a viable path to overcome these limitations [4]. A novel intelligent analysis system built on these technologies can enable efficient integration of multi-source, heterogeneous data and facilitate deep value extraction. This approach optimizes every stage of the settlement workflow, significantly boosting the operational efficiency of the electricity market and enhancing the intelligence of its decision-making processes [5].

This study is grounded in the distinctive characteristics and developmental requirements of the Southern Regional Electricity Market. It proposes the design of an intelligent analysis system that integrates the full spectrum of data operations—collection, processing, analysis, and visualization—for transaction settlement. The system seeks to demonstrate how technological innovation can underpin business innovation, thereby supplying both a technical framework and an empirical case for the evolution of China's characteristic electricity market system.

II. ANALYSIS OF THE CURRENT SETTLEMENT SITUATION

A. Market Structure and Trading Characteristics

The Southern Regional Electricity Market encompasses five provincial-level administrative regions: Guangdong, Guangxi, Yunnan, Guizhou, and Hainan. Its market structure is characterized by a diverse and expanding array of participants, as detailed below:

(1) Diversification of Market Entities

By June 2025, the number of registered market entities had exceeded 220,000, a figure that has doubled since the beginning of 2024, reflecting a significant surge in market activity [6].

The composition of participants has also become increasingly varied:

- Generation Side: The market integrates traditional sources (e.g., coal-fired and gas-fired power) with clean energy sources (e.g., hydropower, wind, photovoltaic, and nuclear power). Centralized new energy power stations have achieved full participation in the spot market. For instance, on June 28 alone, 501 such stations submitted bids for both quantity and price.
- Grid Enterprises: China Southern Power Grid and its provincial subsidiaries are responsible for critical functions including power transmission, distribution, and default electricity supply, while also ensuring the stable operation of cross-provincial settlement mechanisms.
- Retail Companies: The number of electricity retailers continues to grow, sustaining their vital role as intermediaries between generation companies and small-to-medium-sized end-users.
- End Consumers: The eligibility threshold for commercial and industrial users to engage in direct market

979-8-3315-5472-9/25/$31.00 ©2025 IEEE

transactions has been progressively lowered, leading to a rapid expansion of this participant group.

- Emerging Entities: New participant types, such as Virtual Power Plants (VPPs) and load aggregators, have begun substantive market engagement by providing flexible regulation services. Nevertheless, their data interfaces and settlement methodologies remain complex and are still under development.

(2) Proliferation of Trading Varieties

The market's trading varieties have evolved from a singular focus on electrical energy into a complex framework encompassing multiple time scales and transaction objects, as illustrated in Fig. 1.

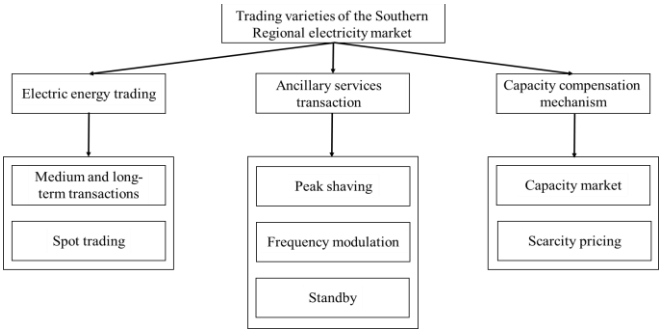


Fig. 1. Trading variety chart

A critical challenge arising from this proliferation is the inherent coupling of settlement obligations across different transaction types. For instance, a generator's final revenue must be calculated through an integrated settlement process that reconciles its contracted medium- and long-term energy volume, its actual power generation in the spot market, and the frequency regulation ancillary services it may have provided. This necessity for consolidated accounting significantly increases the complexity of the settlement process.

(3) Variation of Settlement Rules Across Jurisdictions

The significant differences in regional resource endowments, grid architectures, and levels of economic development have directly shaped province-specific settlement rules. This heterogeneity is manifested as follows:

- Guangdong: Being at the forefront of spot market construction, Guangdong has established the most intricate settlement rules, which are designed to closely align with spot prices and feature advanced mechanisms for congestion cost allocation.
- Yunnan & Guangxi: These provinces, dominated by hydropower, implement settlement rules that account for pronounced wet-dry seasonal price disparities. A key focus is on cross-subsidization between thermal and hydro generation and on resolving benefit distribution challenges in cross-provincial power transmission [7].
- Guizhou: The settlement mechanism in Guizhou is fundamentally shaped by its high dependence on coal-fired power, requiring a tight integration with the coal-electricity price linkage policy.
- Hainan: Its status as a relatively isolated grid system has resulted in the development of distinctive market rules and a unique settlement paradigm.

B. *Challenges*

(1) Data Integration Challenges

The settlement system must integrate multi-source and heterogeneous data, confronting significant challenges related to data fragmentation [8]:

- Multi-source Heterogeneity: The required data originates from diverse systems, including transaction bids/offers, clearing results, physical contracts, high-frequency (minute/15-minute) meter data, manual meter readings, operational data from OMS/EMS, and financial settlement data.
- Data Matching Complexity: A critical challenge lies in ensuring precise matching, which requires the strict temporal alignment and entity identity consistency between meter data and its corresponding trading and clearing records.
- Disparate Data Timeliness: The varying update frequencies from different source systems complicate the establishment of a unified and consistent settlement data cutoff timeline.
- Abnormal Data Handling: The system must automatically identify, cleanse, and provide an audit trail for various data anomalies, such as metering spikes and manual entry errors.

(2) High Computational Complexity

Spot settlement has evolved beyond simple "energy × price" calculations into a process involving high-dimensional and complex computations. This complexity is primarily manifested in two aspects:

- Multidimensional Data Cubes: Settlement operations are performed on large data cubes spanning multiple dimensions, including time (e.g., year, month, day, 96 periods), space (e.g., node, zone), market participant, and transaction type. This necessitates frequent data slicing, dicing, and aggregation across these dimensions.
- Numerous Nonlinear Operations: Key settlement components, such as congestion cost allocation, imbalance fund settlement, and ancillary service compensation, are governed by complex rules that require a multitude of nonlinear calculations.

(3) Stringent Real-time Requirements

Traditional settlement cycles like "monthly settlement" or "T+3" are inadequate for the spot market's operational tempo. The current demands are significantly more rigorous:

- Day-ahead Market: Requires the completion of market clearing and simulated settlement within a few hours.
- Real-time Market: Requires minute-level clearing and rolling pre-settlement for the operating day's charges.
- Regulatory Shift to "Daily Clearing, Monthly Settlement": This new mandate necessitates daily transaction clearing and fund allocation, which demands a system with stream-batch integrated processing capabilities, thereby rendering the traditional T+1 batch processing model obsolete.

III. Overall Architecture Design of the Intelligent Analysis System

A. *System Framework Design*

The intelligent analysis system proposed in this paper is built upon a four-layer, cloud-native architecture, which is

specifically designed to meet the demanding requirements for high concurrency, high reliability, and elastic scalability in electricity market settlement. The overall framework is depicted in Fig. 2.

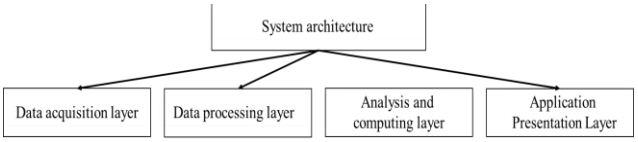


Fig. 2. System architecture diagram

(1) Data Acquisition Layer: This layer is responsible for the real-time and reliable ingestion of multi-source heterogeneous data. Its specific functions are as follows:

- Utilizes distributed message queues (Kafka/Pulsar) for multi-source data ingestion.
- Supports protocol adaptation, compatible with various communication protocols such as HTTP/HTTPS, FTP, and MQTT.
- Implements data buffering and flow control, with a peak processing capacity of 100,000 messages per second.
- Incorporates a data quality monitoring module for real-time monitoring of the data ingestion status.

(2) Data Processing Layer: This layer standardizes, cleanses, and integrates raw data to form high-quality, trustworthy data assets. Its specific functions are as follows:

- Built on a stream-batch unified processing engine using Flink.
- Employs a Delta Lake architecture for the data lake, supporting ACID transactions.
- Implements data lineage tracking to fully record the data processing pipeline.
- Provides a data quality validation rule base, supporting custom rule extensions.

(3) Analytical Computation Layer: This layer encapsulates the business logic of electricity settlement to provide efficient and flexible computational capabilities. Its specific functions are as follows:

- Adopts the Drools framework for the rule engine, supporting natural language rule definition.
- Leverages the Hyperledger Fabric consortium blockchain platform for smart contracts.
- The multi-dimensional data model supports OLAP analysis, with query response times under 3 seconds.
- The operator library contains 200+ pre-built functions, covering all scenarios in electricity settlement.

(4) Application and Presentation Layer: This layer presents the analysis results visually to different types of users. Its specific functions are as follows:

- Features a microservices architecture, supporting independent deployment and scaling.
- Adopts a front-end/back-end separation design, providing RESTful API interfaces.
- Supports adaptive, responsive display across multiple terminals.
- Integrates an RBAC (Role-Based Access Control) management system to ensure data security.

B. Key Technological Innovation

(1) Unified data model and columnar storage optimization

This study proposes a unified star model for power settlement, whose core is the dimensional modeling centered around the settlement fact table. The settlement process can be formally defined as an aggregation function in a multi-dimensional space. Set one settlement operation S is:

$$S = F(D_{time}, D_{location}, D_{participant}, D_{product}, M_{measure}) \quad (1)$$

In the formula, D_{time} represents the time dimension, and the granularity g_t can be refined from the year to 96 points per day. $D_{location}$ represents the spatial dimension, and the hierarchical structure is node -> region -> province. $D_{participant}$ is the subject dimension, describing the attributes of market members. $D_{product}$ represents the dimension of trading varieties. $M_{measure}$ refers to measurement value, such as settlement electricity consumption E, settlement price P, and settlement amount A.

The settlement amount A is a function of electricity consumption and price, and is affected by various compensation allocation items C_i. For the settlement of the subject p in period t, the basic formula is:

$$A_{p,t} = \sum_{i=1}^{n} (E_{p.t.i} \times P_{t,i}) + \sum_{j=1}^{m} C_{p,t,j} \quad (2)$$

In the formula, i traverses different types of electricity (such as medium and long-term, spot), and j traverses various compensation apportionment items (such as blocking apportionment, ancillary service fees).

Compared with traditional row-based storage, the I/O efficiency advantage of column-based storage is particularly evident in aggregated queries. Let the number of columns required for the query be c and the total number of columns be C, then the I/O reduction ratio R can be approximately expressed as:

$$R \approx \frac{C}{c} \quad (3)$$

Since settlement analysis queries usually only involve a few columns (such as only querying electricity and price), while the total number of columns may reach dozens (including various intermediate calculation fields), the R value is very large, bringing several times the performance improvement. In addition, columnar storage, due to its similar data characteristics, has a higher compression ratio η, further reducing I/O pressure. The expression is:

$$\begin{aligned} &\text{The volume of compressed data} = \\ &\text{the volume of original data} \times (1\text{-}\eta) \end{aligned} \quad (4)$$

(2) Smart Contracts and Automated Execution Mechanism

The smart contract, denoted as SC, can be formalized as a state machine whose automated execution logic is based on a predefined set of rules $\mathbb{R}$.

A smart contract for electricity settlement is defined as a tuple $SC = (Addr, State, Rules, Trigger, Action)$.

In the formula, *Addr* is Contract address, serving as a unique identifier; *State* is Contract state, such as "Unsettled," "Data Ready," "Settled," or "Under Dispute."; *Rules* is A rule set, $\mathbb{R} = \{R_1, R_2, ..., R_k\}$; *Trigger* is Trigger conditions, such as a time-based condition $Trigger_{time}$ or an event-based condition $Trigger_{event}$; *Action* is State transition function, $Action : State \times Trigger \to State$.

To ensure the authenticity of transaction data D, the smart contract requires that D obtains verification signatures $Sig_i(D)$ from more than $2n/3+1$ out of n consensus nodes. Settlement proceeds only upon successful verification:

$$ConsensusVerify(D) = \begin{cases} True, if \sum_{i=1}^{n} Verify(Sig_i(D)) \geq 2n/3 + 1 \\ False, otherwise \end{cases} \quad (5)$$

The integrity of settlement results is ensured by a hash chain. Each block contains the hash of the previous block H_{prev} and the hash of the current settlement batch data H_{data}:

$$H_{current} = Hash(H_{prev} \| H_{data}) \quad (6)$$

Any tampering with historical data would alter H_{data}, consequently causing a chain reaction that changes $H_{current}$ and all subsequent block hashes, thereby enabling detection by the system.

(3) Big Data Analytics Platform and Machine Learning Algorithms

Real-time monitoring is based on a sliding window model. Let the window size be W and the sliding step be S. At time T, the system processes data within the interval $[T-W, T]$. The price volatility σ_T can be calculated in real time as:

$$\sigma_T = \sqrt{\frac{1}{W} \sum_{t=T-W}^{T} (P_t - \bar{P}_T)^2} \quad (7)$$

In the formula, $\bar{P}_T$ is the average price within the window; P_t is the electricity price at time t.

Electricity Price Prediction (Regression Problem): A Support Vector Machine regression model is employed. The objective is to find a function.

$$f(P) = \langle w, \phi(P) \rangle + b \quad (8)$$

In the formula, $\phi(P)$ is a kernel function mapping historical price features to a high-dimensional space. The parameters w, b are determined by minimizing the loss function L:

$$\min_{w,b} \frac{1}{2}\|w\|^2 + C\sum_{i=1}^{n} \max(0, |y_i - f(P_i)| - \varepsilon) \quad (9)$$

Anomalous Transaction Detection (Classification Problem): The Isolation Forest algorithm is used. Its core premise is that anomalies are more easily isolated by randomly partitioned trees. The anomaly score $s(x,n)$ is defined as:

$$s(x,n) = 2^{-\frac{E(h(x))}{c(n)}} \quad (10)$$

In the formula, $E(h(x))$ is the expected path length of sample x across all random trees, and $c(n)$ is the average path length for normalization. A score closer to 1 indicates a higher probability of being an anomaly.

IV. Empirical Analysis

A. Data Information

Based on the actual operating environment of the power market in the southern region, this study has constructed a complete test and verification platform[9]. The platform adopts the system architecture proposed in this paper and is deployed on a container cloud platform based on Kubernetes. It is equipped with 10 computing nodes featuring 32-core cpus and 128GB of memory. The storage uses a distributed file system (HDFS), and the network is interconnected by 10-gigabit optical fibers.

B. Result Discussion and Analysis

(1) Data Processing Performance Verification

Based on the established unified data model, the system standardizes multi-source heterogeneous data. The data acquisition layer receives real-time data streams through the Kafka cluster.

During the data processing, the advantages of columnar storage are fully demonstrated. The query response time has been reduced from the minute level of traditional systems to the second level (with an average of 2.3 seconds), and the performance has improved by 85%.

(2) Analysis of the Execution Effect of Smart Contracts

Based on the smart contract model, a consortium chain network consisting of five nodes was deployed. The state transition function of the smart contract is automatically executed according to predefined rules. The specific process is as follows:

$$Action(S,T) = \begin{cases} S_1 & if \quad T = T_{data_ready} ConsensusVerify(D) \\ S_2 & if \quad T = T_{settlement_time} S = S_1 \\ S_3 & otherwise \end{cases} \quad (11)$$

In the formula, $Action(S,T)$ is a state transition function; S_1、S_2、S_3 are respectively the initial state, the settlement completed state, and the abnormal or waiting state.

Let the state transition function of the smart contract be:

In actual operation, a total of 2,856 settlement smart contracts were executed in July, with a consensus verification pass rate of 100% and an average execution time of 45 seconds, significantly outperforming the traditional manual review mode (which usually takes 4 to 6 hours).

(3) Application Effects of Machine Learning Algorithms

Based on the algorithm model, real-time monitoring of abnormal market transactions is conducted. The Isolation forest

algorithm was adopted and the anomaly threshold A was set. The monitoring results of July are shown in TABLE 1.

TABLE I. MONITORING RESULTS TABLE FOR JULY

Monitoring indicators	Traditional rule engine	The machine learning algorithm of this system
Abnormal transaction detection rate	67.3%	94.7%
False alarm rate	23.5%	5.2%
Average response time	15 min	28 min

It can also be seen that the price prediction model adopts SVM regression. During the peak load period in July (July 15-20), the average absolute percentage error of the day-ahead price prediction is 3.2%, which is better than the 5% requirement of the industry benchmark.

(4) Comprehensive System Performance Evaluation

After a three-month trial operation, the key performance indicators of the system are as follows:

- Processing throughput: It processes an average of 11.5 million transaction data records per day, with a peak of 15 million records per day, fully meeting the design goals.
- Computational efficiency: The total monthly settlement time has been shortened from 48 hours in the traditional mode to 16.5 hours, an increase of 65.6%. Among them:

Data preprocessing time: 8.2 hours → 2.1 hours (an increase of 74.4%);

Settlement calculation time: 32.5 hours → 11.2 hours (an increase of 65.5%);

Result verification time: 7.3 hours → 3.2 hours (an increase of 56.2%);

- Accuracy metric: By introducing data lineage tracing and a quality control rule base, the settlement error rate has been reduced from 0.15% to 0.028%, which is better than the design target of 0.05%.

In addition, through the implementation of this system, the southern regional electricity market demonstrated significant operational improvements in July 2024. Firstly, market efficiency was enhanced. During peak load periods, the effective supply rate of electricity trading remained at 96.3%, an increase of 4.2 percentage points compared with the same period last year. The second is the reduction in operating costs. Automated settlement reduces manual intervention by 75% and is expected to save approximately 12 million yuan in operating costs annually. Third, market transparency has been enhanced. Based on the immutable feature of blockchain, the incidence of settlement disputes has decreased by 62%, and the score of the market entity satisfaction survey has increased from 82 points to 94 points.

V. CONCLUSION

The intelligent analysis system for power trading settlement based on big data technology designed in this paper effectively solves the problems faced by the power market in the southern region, such as difficult data integration, low computing efficiency and poor rule adaptation. Through technical means such as unified data models, smart contracts, and visual monitoring, the operational efficiency and transparency of the market have been enhanced.

REFERENCES

[1] Fang Weibin, Wang Hua The Southern Regional Electricity Market has officially launched the trial operation of continuous settlement [J]. Rural Electrician, 2020,33(08):3.

[2] Liang Zhifei, Li Ziqian, Jia Xudong, et al. The Green power Market System in the Southern region Considering the Entire Life Cycle of New energy [J]. Modern Power,2024,41(05):955-962.

[3] Zhong Sheng. Practical Exploration on the Construction of the Southern Regional Electricity Market [J]. China Electric Power Enterprise Management,2023,(10):27-30.

[4] Zhang Tingying, Chen Wei, Yang Su, et al. Discussion on the Deviation Settlement Mechanism of Cross-provincial and Cross-Regional Power Trading in the Southern Region [J]. Power Demand Side Management,2020,22(04):94-100.

[5] Ge Xinxin, Lu Jiaxin, Wang Fei, et al. An Optimized bidding Model for EV-type Virtual Power Plants Considering Green Power Contract Decomposition in the Spot Market [J/OL] Power System Automation,1-10[2025-09-27].

[6] Hu Zhaoqin, Xiao Yunpeng, Wang Xiuli, et al. A two-part settlement mechanism for the spot electricity market considering the cycle life attenuation cost and regulation value of electrochemical energy storage [J/OL]. Proceedings of the CSEE,1-18[2025-09-27].

[7] Tan Zhongfu, Jiang Benshuo, Wang Zhongrong. Research on Power Purchase and Sale Strategies of Power Sales Companies Based on User Feature Classification [J/OL]. Journal of North China Electric Power University (Natural Science Edition),1-10[2025-09-27].

[8] Xu Zhirong, Du Ziyang, Zheng Ziyao, et al. Countermeasures of Power Sales Companies under the long-term Continuous Trial Operation of the Spot Market in the Southern Region [J]. China Electric Power Enterprise Management,2025,(19):85-86.

[9] Weisi Zhang , Qingsong Mao , Xia Pan , et al. Two-stage hybrid electricity market trading strategy optimization with renewable electricity under cap-and-trade policy[J]. Energy Economics, Volume 150, October 2025, 108764.

Peer-to-Peer Energy Trading and the Development of Grid-Blockchain Simulation Platform

Mohd Zamri Che Wanik
Usman Zafar
Qatar Environment and Energy Research Institute
Hamad Bin Khalifa University
Qatar Foundation Education City, Qatar
Email: mwanik@hbku.edu.qa
Email: Uzafar@hbku.edu.qa

Asrani Lit
Nazreen Junaidi
Faculty of Engineering
Universiti Malaysia Sarawak
Kota Samarahan, Sarawak
Malaysia
Email: Iasrani@unimas.my
Email: jnazreen@unimas.my

S. M. Muyeen
Department of Electrical Engineering
Qatar University
Doha, Qatar
Email: sm.muyeen@qu.edu.qa

Abstract— **Peer-to-peer trading refers to the direct exchange without the involvement of intermediaries. This trading model is facilitated by advancements in distributed energy resources, digital technology, and supportive regulatory environments. The peer-to-peer (P2P) framework establishes an online platform where both prosumers and consumers can engage in electricity transactions at mutually agreed-upon prices, eliminating the need for a middleman. This paper provides a landscape brief of P2P and presents the simulation case studies of P2P trading for a few houses installed with PV and battery storage. The concept of P2P trading is explained first. Then the requirements for its implementation are described. A P2P trading co-simulation platform called P2PEnergyChain that combines blockchain technology with real-time grid monitoring to create a comprehensive energy marketplace is also presented. This platform will enable residential prosumers to trade excess energy directly with each other while maintaining grid stability and ensuring transparent, secure transactions through Hyperledger Fabric blockchain technology.**

Keywords—photovoltaic, distributed energy resources, distribution network, peer to peer trading, P2P trading platform

I. INTRODUCTION

The proliferation of photovoltaic (PV) systems inside the distribution network increases the challenge for the power system operator to manage its network. A PV as distributed generation and other small or medium-sized resources which are connected to the distribution network, such as energy storage and controllable loads such as electric vehicles (EV) are considered as distributed energy resources (DER). PV integration into the distribution network has been reported to impact the operation of the network such as to increase the tap changer operation of the power transformer. This is due to the fact that PV generation varies with time depending on the solar radiation intensity that hits the PV panels. The variation leads to voltage variation, and the transformer, which is the main voltage regulator device in the distribution network, has to keep the voltage by changing its tap position. The increased movement is impacting the quality of power supply and also increasing the wear and tear of the transformer which leads to power supply interruption [1].

In search of an economical way to manage PV systems as DER in a distribution network has created a new peer-to-peer trading business model. In this new business model, the premises that have PV installed can sell the excess electricity to their neighbors. This business model, called peer-to-peer (P2P) trading, is the direct buying and selling without intermediaries. This trading concept is enabled by distributed energy resources, digitalisation and a conducive regulatory framework. Peer-to-peer (P2P) electricity trading empowers prosumers and consumers, leading to increased renewable energy deployment and flexibility in the grid. The P2P concept also aids in balancing and congestion management and providing ancillary services [2, 3].

Prosumer is the term used for premises that are both purchasing electricity from the utility company and also selling the excess electricity that is generated from the PV system. The are many trials or pilot projects in different parts of the world to test the P2P schemes. Projects can be found in countries such as Australia, Bangladesh, Colombia, Germany, Japan, Malaysia, the Netherlands, the UK, the US, and others have started trials on P2P schemes [4]. These pilot projects are to identify regulatory provisions required, to evaluate technical requirements of P2P energy trading, to simulate energy trading between prosumers and consumers, their financial impact and motivations for participation and to identify the challenges and mitigation actions in operationalising the P2P energy trading.

The P2P trading mechanism is still facing a lot of challenges before it can be widely embraced. This is highlighted in a pilot project run by the Sustainable Energy Development Authority (SEDA) in Malaysia. Running for eight months, this pilot identified technical requirements, risks, challenges and gaps that deserve further study before P2P live implementation. These include the assessment of the impact of P2P on the grid operation and the need to evaluate the balancing of supply and demand within the grid, the feasibility of implementing P2P with full cost reflectivity and the need to design suitable business models for electricity retailers [5].

Pilot project findings are in line with the technical aspects requirement highlighted in [4], where P2P energy trading still requires advanced technical requirements in the form of hardware, software and ICT infrastructure. In terms of software, there is a need for a reliable platform that is integrated with advanced power demand and supply forecasting analysis features, robust analytic tools and algorithms for automating execution of P2P transactions or blockchain technology for reducing transaction cost. The works reported in the paper try to address the need for an advanced and reliable platform to carry out the P2P trading.

This paper starts by providing a landscape brief of P2P trading of energy from distributed energy resources. The concept of P2P trading is explained first then followed by the requirements for its implementation. Finally, a P2P energy trading platform that is currently under development is presented. The features that are currently integrated into the platform and also trying to be embedded in the next phase will be described.

979-8-3315-5472-9/25/$31.00 ©2025 IEEE

II. PEER TO PEER TRADING

Conventionally, prosumer sell excessive electricity back to the grid at a buy back rate as shown in the Fig.1. However consumer tariff for electricity supply are generally much higher that the buy back rate that prosumers can obtain from selling the electricity to the utility. Also, these consumer tariffs do not account for the other benefits that this renewable generation brings to the power system. For example, while a prosumer can charge an EV using a rooftop solar plant, the prosumer's neighbours would obtain electricity to charge his or her EV from a distant centralised power plant. If, however, the EV is charged from a solar power plant located in the neighbourhood, the prosumer with the solar installation would receive buy back rate for the electricity injected into the grid. However, this would not take into account the reductions in transmission losses and congestion that this distributed generation provides to the network. Around 40-45% of the typical electricity cost goes toward managing and maintaining the poles and wires that deliver power from the generators to the premises of the customer [6]. Part of these costs could be saved in a P2P model.

P2P trading refers to the direct exchange without the involvement of intermediaries. This trading model is facilitated by advancements in distributed energy resources, digital technology, and supportive regulatory environments. The P2P framework establishes an online platform where both prosumers and consumers can engage in electricity transactions at mutually agreed-upon prices, eliminating the need for a middleman. Under this model, the electricity is transacted between users (buyers/sellers) of the platform that also become members of the platform, for example, by paying a pre-determined monthly subscription fee. Just like an open market economy, suppliers seek the highest possible price, keeping their costs and profit in consideration, and consumers choose the lowest price possible based on their needs and preferences. Where the supply and demand offers that are the sell and buy bids match, a trade occurs. The common practice with the traditional power supply is that consumers purchase electricity from utilities or retailers through fixed tariffs or time-of-use tariffs [7].

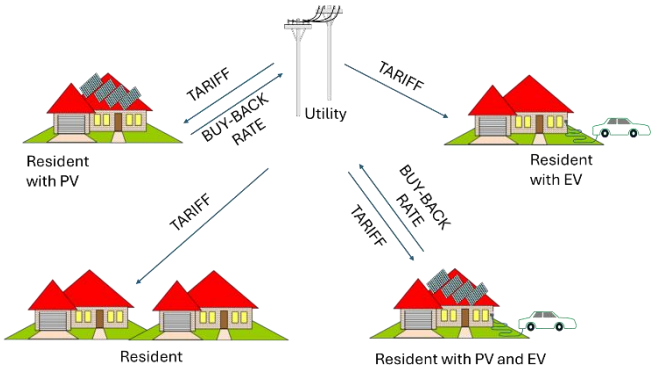


Fig. 1. Conventional trading model of electricity

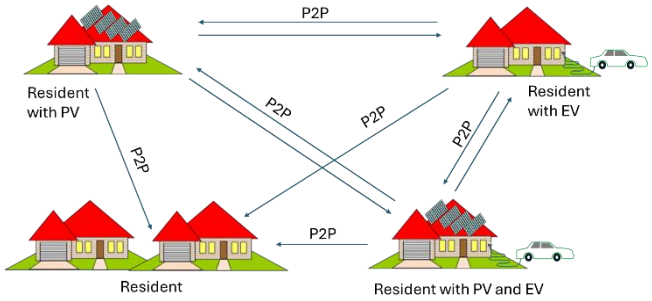


Fig. 2. P2P electricity trading model

The P2P electricity trading model emerged as a result of the growing integration of distributed energy resources within distribution networks, coupled with enhanced incentives for the further adoption of these resources. In this model, prosumers have the flexibility to alternate their roles as buyers or sellers, enabling them to either acquire or sell electricity as needed. In addition, they are able to directly trade electricity with other customers to achieve a win-win by seeking a better outcome compared to the relatively high tariffs and the relatively low buy-back rates. In this way, buyers can save costs while sellers can make a profit. This is depicted in Fig. 2. Trading based on the P2P model makes renewable energy more accessible. Empower consumers and allow them to make better use of their energy resources [8]

III. IMPLEMENTATION REQUIREMENTS

The key success of the P2P electricity platform is the reliability of the platform, good customer service and the availability of a conducive regulatory framework and a reliable grid [4]. All these requirements are summarised in Table I. From the technical perspective, a very reliable hardware, software and ICT infrastructure should be in place.

The P2P electricity trading platform facilitates the exchange of electricity among participants while complying with established market regulations. This platform also maintains records of energy consumption, production, and agreements between participants. Traditionally, a central authority is required to validate each digital transaction. Additionally, the security of these transactions is managed by the trading platform itself. Currently, electricity trading platforms are being evaluated not only through a centralized framework that depends on an energy coordinator or third party but also through decentralized methods. These trading platforms are crucial for the effective implementation of the peer-to-peer model. Therefore, a secure and dependable platform is a vital element of the peer-to-peer market [9-13].

For P2P systems to thrive, it is essential to create a robust and supportive policy framework. This framework should actively encourage the integration and deployment of DER, while also optimising the use of existing grid infrastructure. Moreover, the policies should promote the initiation of pilot programs that function as experimental platforms, allowing for the testing of new ideas and technologies. The findings from these pilot programs should be shared openly and transparently to foster learning and improvement. Additionally, it is important that financial assistance is made available to developers working on these innovative platforms, ensuring they have the necessary resources to succeed [14].

Current energy regulations within the energy sector are tailored to the conventional power system model, which is characterized by a unidirectional and vertical structure. As a result, this model is inadequate for the contemporary and future power systems that are experiencing a significant increase in DER at the consumer level. Ongoing discussions focus on how to modify the existing regulatory frameworks to accommodate the rapid advancements in the sector. Nevertheless, there have been no substantial global changes. Therefore, extreme caution must be exercised when enacting any regulatory reforms in the power industry. The two main components are for the retail market and the distribution network itself. It is essential to establish regulations governing data collection and access, alongside provisions for cybersecurity and privacy that protect both platform owners/developers and participants. Furthermore, it is crucial to delineate the specific roles and responsibilities of all stakeholders engaged in P2P transactions. Additionally, measures must be implemented to safeguard consumer rights within P2P initiatives, and comprehensive operational guidelines for market activities related to P2P schemes should be defined [4, 15].

Finally, there should be a clear definition of the roles and responsibilities of each stakeholder involved. The stakeholders here are the consumer, prosumer, and market operator. The roles should be clear, for example, who will be involved in the P2P trading and who will provide the services to the network. Another clear definition is on whose responsibilities of developing and operating the platform and ensuring the security and integrity of the platform [14].

IV. PEER TO PEER ENERGY TRADING PLATFORM

P2PEnergyChain combines blockchain technology with real-time grid monitoring to create a comprehensive energy marketplace. This application enables residential prosumers to trade excess energy directly with each other while maintaining grid stability and ensuring transparent, secure transactions through Hyperledger Fabric blockchain technology. The platform is meant to allow homeowners with solar panels, battery storage, and electric vehicles to participate in an active energy economy. A snapshot of the platform is depicted in Fig. 3. There is a main page called *Dashboard* and five subpages: *Marketplace*, *Grid Status*, *Transaction*, *Blockchain*, and *House Wallet*.

A. Dashboard

On the *Dashboard* page, there is a power grid simulation graphic that shows the houses which are participating in the P2P trading. This graphic is meant to display real-time information of the house load, power generated by solar, battery storage consumption or generation and EV consumption. The important grid operation information, such as voltage profile, frequency and grid reliability index, is displayed on the top. The dashboard will also display the summary of the system under monitoring, such as the total produced energy, energy consumption, active trades and total earnings. The dashboard will also give info on the blockchain such as which blockchain network is connected to the platform as well as the technology of the blockchain. In this platform, we connected the platform to a *Testnet* and deployed *Hyperledger Fabric*, an open blockchain framework.

TABLE 1. P2P IMPLEMENTATION REQUIREMENT [4]

Technical Requirements	Hardware	• Physical layer: Smart meters that can help monitor real-time power production, and smart grids, including mini-, micro- or nanogrids • Virtual layer: ICT network to enable communication between participants, handle payments, monitoring; and EMS
	Software	• Platform for P2P electricity trading • Advanced power demand and supply forecasting analysis • Robust data analytics tool • Algorithms for automated execution of P2P transactions or blockchain technology for reduced transaction costs
	Communication Protocol	• Common interoperable protocol for coordination among system/network/market/platform operators, consumers and prosumers
Policies Needed	• Supportive policies encouraging decentralisation of power systems and better utilisation of existing grid infrastructure • Encourage pilot programmes to work as a test bed, in regulatory sandboxes; and dissemination of results • Improve access to capital for platform developers	
Regulatory Requirements	Retail market:	• Enable trade of power among prosumers and consumers without renewable generation capacities • Establish regulations on data collection and access, as well as cybersecurity and privacy for platform owners/developers and platform members, i.e., peers • Define clear roles and responsibilities of stakeholders involved in P2P • Ensure that consumer rights are respected by stakeholders in P2P schemes • Define market operation rules for the P2P schemes
	Distribution Network	• Enable the distribution system operator to procure flexibility from P2P platforms • Define technical criteria for ancillary services needed • Determine network charges when P2P trading is using the main grid
Stakeholder Roles and Responsibilities	Consumers, prosumers	• Engage in P2P electricity trading • Provide services to the power system, either individually or via a retailer or aggregator
	P2P platform/ market operators	• Develop and operate platforms for P2P trading with ICT companies. • Ensure that the platform is secure and trusted

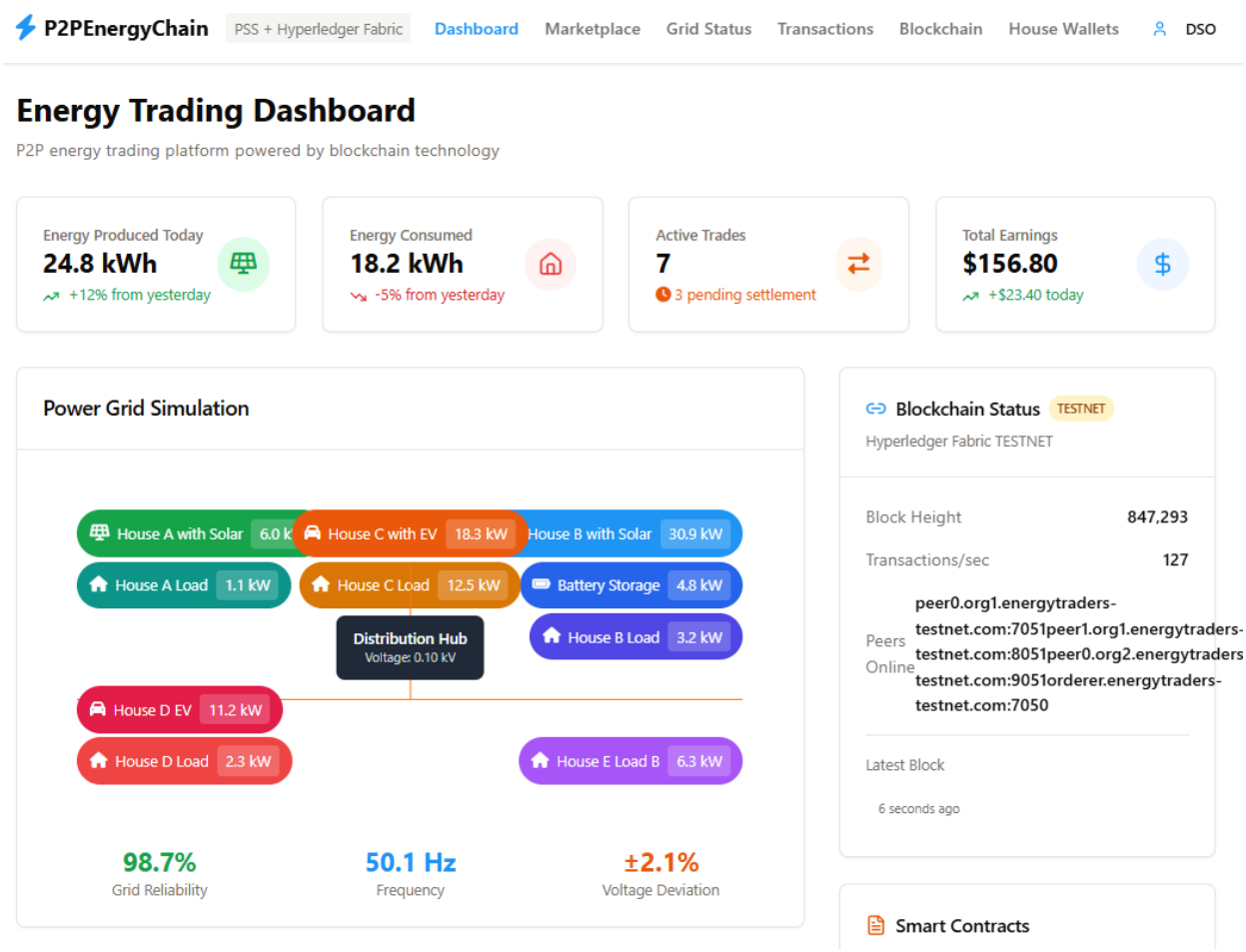


Fig. 3. P2P Trading platform dashboard

B. Grid Status

The *Grid Status* section will provide comprehensive monitoring of the electrical power grid, offering real-time visibility into system conditions that directly impact energy trading decisions. This monitoring system, for now, is integrated with the *Power Grid Simulator* on the main page which simulates an operation of part of the distribution network in Qatar. In the future the information will be fed by the real-time grid information from the field measurements provided by the PMU monitoring system that is described in [4].

C. Marketplace

The Marketplace section provides the core trading functionality of *P2PEnergyChain*, where prosumers can execute energy transactions and participate in the decentralised energy economy. This sophisticated trading interface combines real-time market data with automated order matching to create an efficient energy exchange. The centerpiece of the marketplace is the comprehensive trading simulation system that models realistic 24-hour energy trading patterns. The simulation operates on 15-minute intervals, creating 96 trading opportunities throughout each day.

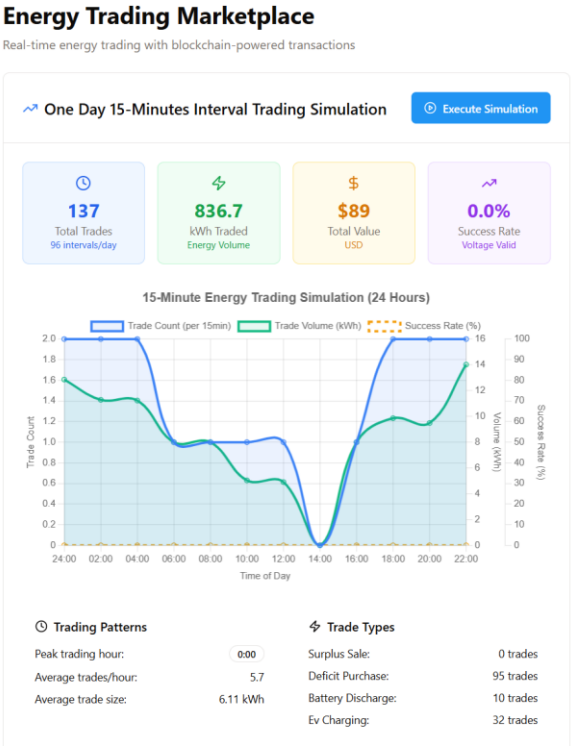


Fig. 4. Subpage 'Marketplace'

D. Transactions

This subpage will display of blockchain transactions showing:

- The unique Transaction ID is paired with the corresponding blockchain hash for identification purposes.
- Information about the parties involved in the transaction, specifically the buyer and the seller.
- Comprehensive details concerning the amount of energy exchanged and the pricing associated with the transaction.
- The exact timestamp indicating when the transaction took place, along with its current confirmation status.

E. Blockchain

This platform deploys *Hyperledger Fabric* Network, which is an Enterprise-grade blockchain for transaction recording. The network is configured using the consensus mechanism for high performance and reliability. This network works based on a multi-organisation network to simulate a real-world deployment. It is designed with a dedicated energy trading channel with appropriate governance. Multiple peer nodes for redundancy and performance is established for peer configuration. In order to increase the availability, the order is configured in a cluster. For the time being, the blockchain framework is from a *Testnet*. In the future, this platform will be connected to the *Mainnet.* In blockchain technology, a *Mainnet* and a *Testnet* represent two distinct environments with different purposes. A *Mainnet* is the live, operational blockchain where real transactions occur and cryptocurrencies have real economic value. A *Testnet*, on the other hand, is a separate, experimental blockchain used for testing and development purposes, with test tokens that have no real-world value.

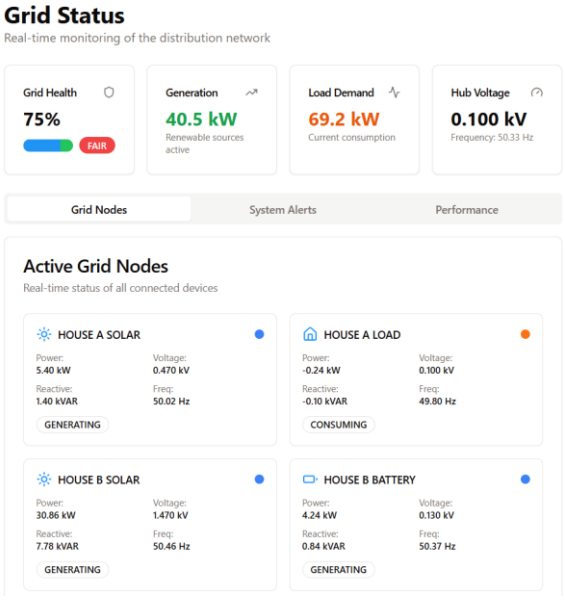


Fig. 5. Subpage 'Grid Status'

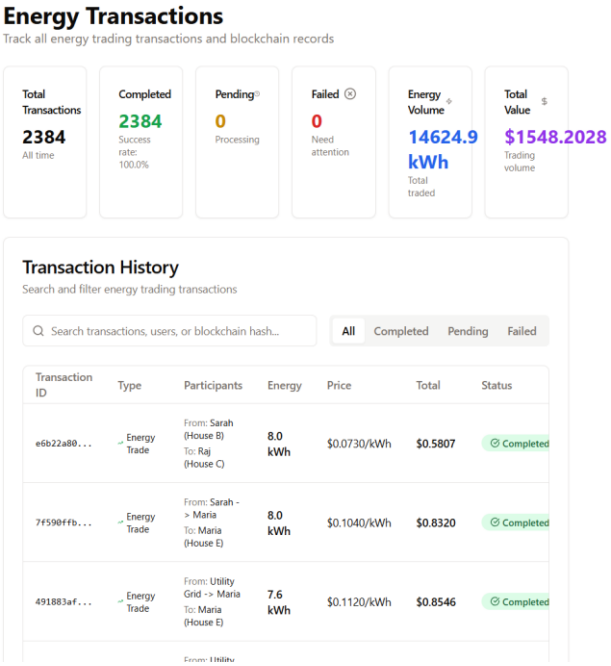


Fig. 6. Subpage 'Transactions'

F. House Wallets

The *House Wallets* section provides comprehensive management of individual cryptocurrency wallets for each prosumer house in the *P2PEnergyChain* platform. Each house maintains separate *USDC/USDT* balances to facilitate energy trading while providing flexibility in payment methods and currency preferences. *USDC/USDT* is transferred between house wallets after successful trade execution. Each transaction is recorded on *Hyperledger Fabric*.

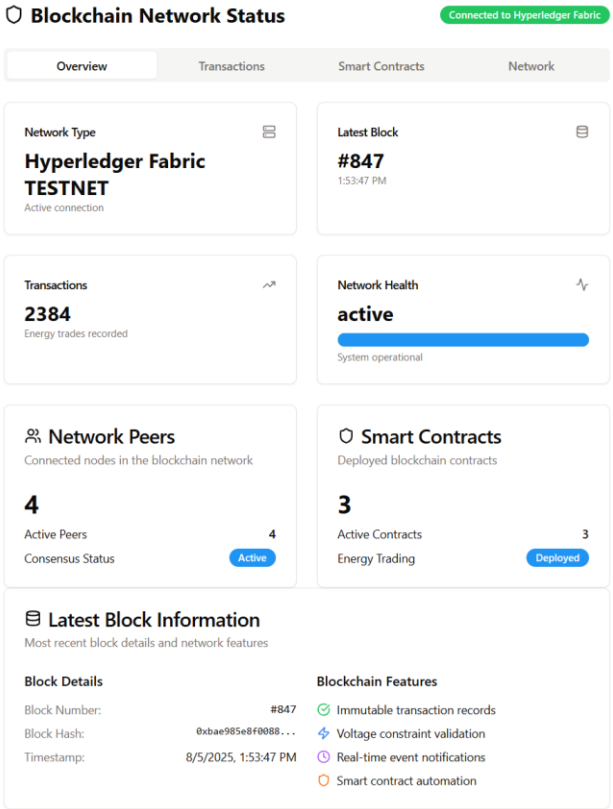


Fig. 7. Subpage 'Blockchain'

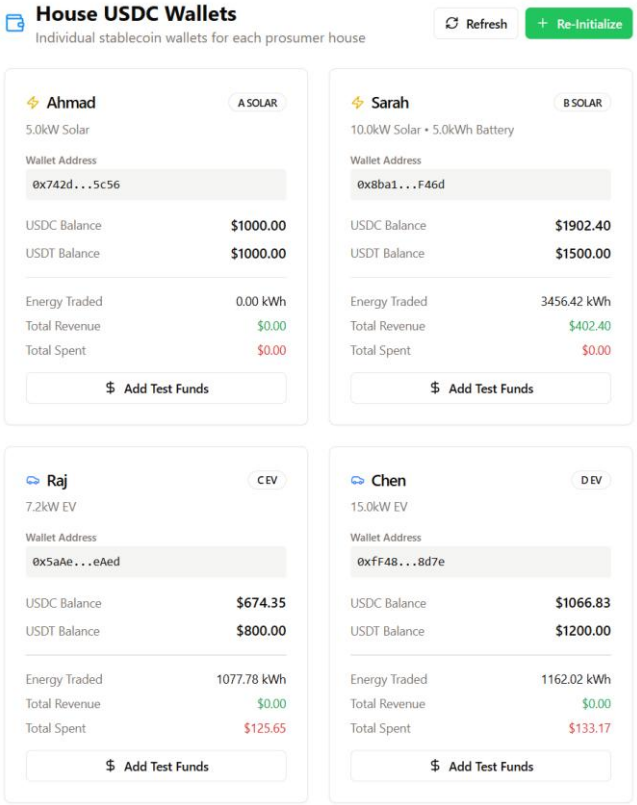


Fig. 8. Subpage 'House Wallets'

V. Discussion and Future Works

P2PEnergyChain, which is currently under development, is working as expected. The platform is capable of demonstrating the P2P trading executions when PV generation exceeds the load consumption of a house where it is installed. The trade, however, is only executed if the grid operation is not compromised. For each successful trade, the transaction is recorded on Hyperledger Fabric. In the next phase of the development, the platform will be fed with real-time data of the network stream by the PMU Monitoring system. An advanced power demand and supply forecasting analysis will be integrated into the platform to assist in executing the trade. A suitable economic model for trading will also be integrated into the platform.

VI. Conclusion

P2P trading in the community that has DER is gaining interest. This is due to potential economic benefits that can be harvested by the prosumers. This is evidence from pilot and demonstration projects that is seen across the world. This paper has provided a landscape brief of P2P and described the co-simulation platform that is currently under development. The concept of P2P trading, which refers to the concept of direct exchange without involvement of intermediaries, is explained, and the requirements for its implementation are discussed. A P2P trading co-simulation platform called *P2PEnergyChain* that combines blockchain technology with real-time grid monitoring to create a comprehensive energy marketplace is presented. This platform will enable residential prosumers to trade excess energy directly with each other while maintaining grid stability and ensuring transparent, secure transactions through *Hyperledger Fabric* blockchain technology. The platform is built with a *Dashboard* and five subpages: *Marketplace*, *Grid Status*, *Transaction*, *Blockchain*, and *House Wallet*. The platform is meant to allow homeowners with solar panels, battery storage, and electric vehicles to participate in an active energy economy.

Acknowledgement

This work and publication was made possible by Qatar Research, Development and Innovation Council (QRDI) in Academic Research Grant (ARG) program, grant number ARG01-0521-230240.

References

[1] Wanik, M.Z.C., M.M. Bukshaisha and S.R. Chaudhry, PV Generation in Distribution Network and its Impact on Power Transformer On-Load Tap Changer Operation, IEEE PES Powertech 2017, Manchester, United Kingdom, Jun 2017.

[2] Bukar, A. L., Hamza, M. F., Ayub, S., Abobaker, A. K., Modu, B., Mohseni, S., Brent, A. C., Ogbonnaya, C., Mustapha, K., & Idakwo, H. O., Peer-to-peer electricity trading: A systematic review on current developments and perspectives. *Renewable Energy Focus*, *44*, 2023, page 317-333.

[3] Lüth, A., Zepter, J. M., Crespo del Granado, P., & Egging, R. , Local electricity market designs for peer-to-peer trading: The role of battery flexibility. *Applied Energy*, *229*, 2018, pg 1233-1243.

[4] IRENA, Innovation landscape brief: Peer-to-peer electricity trading, International Renewable Energy Agency, Abu Dhabi, 2020.

[5] SEDA, Malaysia's 1st Pilot Run of Peer -to-Peer (P2P) Energy Trading, https://www.seda.gov.my/malaysias-1st-pilot-run-of-peer-to-peer-p2p-energy-trading/

[6] N. Rauschkolb, N. Lmandibhratha, V. Modi, I. Mercadal, Estimating electricity distribution costs using historical data. Utilities Policy, 73, 2021.

[7] Esteban A. Soto, Lisa B. Bosman, Ebisa Wollega, Walter D. Leon-Salas, Peer-to-peer energy trading: A review of the literature, Applied Energy, Volume 283,2021.

[8] Ayooluwa Adewole, Michelle Shipworth, Xavier Lemaire, Danielle Sanderson, Peer-to-Peer energy trading, independence aspirations and financial benefits among Nigerian households, Energy Policy, Volume 174, 2023.

[9] Hayes, B., Thakur, S., & Breslin, J., Co-simulation of electricity distribution networks and peer to peer energy trading platforms. *International Journal of Electrical Power & Energy Systems*, *115*, 2020.

[10] M. Mukherjee et al., "A Blockchain Based Co-simulation Framework for Integrating DERs to Wholesale Electricity Markets," 2022 IEEE Power & Energy Society General Meeting (PESGM), Denver, CO, USA, 2022, pp. 1-5.

[11] Guo, S., & Feng, T. Blockchain-based smart trading mechanism for renewable energy power consumption vouchers and green certificates: Platform design and simulation. *Applied Energy*, *369*, 123351, 2024.

[12] Chen, Ye et al. "A Blockchain-based Co-Simulation Platform for Transparent and Fair Energy Trading and Management." *Proceedings of the 5th ACM International Symposium on Blockchain and Secure Critical Infrastructure* (2023): n. pag.

[13] Y. Li et al., "PEMT-CoSim: A Co-Simulation Platform for Packetized Energy Management and Trading in Distributed Energy Systems," 2022 IEEE International Conference on Communications, Control, and Computing Technologies for Smart Grids (SmartGridComm), Singapore, Singapore, 2022, pp. 96-102.

[14] K. E. Bassey, * , S. A. Rajput and K. Oyewale, Peer-to-peer energy trading: Innovations, regulatory challenges, and the future of decentralized energy systems, World Journal of Advanced Research and Reviews, 2024, 24(02), 172–186

[15] Schneiders, A., Fell, M. J., & Nolden, C., Peer-to-peer electricity trading and the sharing economy: social, markets and regulatory perspectives. *Energy Sources, Part B: Economics, Planning, and Policy*, *17*(1), 2022.

[16] Wanik, M.Z.C., A.A. Jabbar, M. Gad, A. Sanfilippo," Phasor Measurement Unit (PMU) Based Monitoring and Management for Medium Voltage Network Integrated with Renewable Energy Resources", 2024 IEEE Sustainable Power and Energy Conference (iSPEC 2024), Malaysia, 24th – 27th Nov.,202

Study on Dual-Time-Scale Mid-to-Long-Term Spot Electricity Procurement Optimization Model Considering Inter-Provincial Channel Constraints

Ying Fan
State Grid Shanghai Municipal Electric Power Company
Shanghai, China
fyfly123@163.com

Pengfei Zhang
State Grid Shanghai Municipal Electric Power Company
Shanghai, China
zhangpengfei@sh.sgcc.com.cn

Na Wang
State Grid Shanghai Municipal Electric Power Company
Shanghai, China
wangna@sh.sgcc.com.cn

Yuxin Chen
State Grid Shanghai Municipal Electric Power Company
Shanghai, China
chenyuxin@sh.sgcc.com.c

Huan Zhou
College of Electric Power Engineering
Shanghai University of Electric Power
Shanghai, China
zhouhuan1022@mail.shiep.edu.cn

Gaiping Sun
College of Electric Power Engineering
Shanghai University of Electric Power
Shanghai, China
gaiping_sun@shiep.edu.cn

***Abstract*—To address cost control and power supply stability challenges posed by the diversity of grid agency electricity procurement resources, and the limitations of existing single procurement modes (poor adaptability, intra-provincial resource constraints), this paper develops a monthly-hourly dual-time-scale mid-to-long-term spot optimization model. First, variables are unified by time scale: intra-provincial mid-to-long-term procurement and renewable energy procurement are set as monthly variables, while inter-provincial mid-to-long-term procurement and spot procurement are hourly variables, with scale connection via aggregation and equalization. Then, aiming to minimize total procurement cost, multi-space resource allocation is achieved by incorporating special constraints of three inter-provincial channels. Simulations with full-year 2024 load and electricity price data, verified against a control group, show the model effectively connects mid-to-long-term and spot markets, ensures full renewable energy consumption and power supply stability, and cuts procurement cost significantly compared to the control group, achieving cost optimization.**

Keywords—grid agency electricity procurement, dual-time-scale optimization, mid-to-long-term and spot market connection, inter-provincial channel constraints

I. INTRODUCTION

Grid agency electricity procurement needs to integrate power resources from multiple channels, covering diverse power sources and cross-regional power allocation, forming a pattern with broad and varied origins. This diversity not only creates opportunities for the grid to secure stable power supply and promote energy structure optimization, but also poses challenges to procurement cost control and power supply stability assurance, due to impacts from complex factors such as supply-demand changes and market fluctuations. Against this backdrop, mid-to-long-term spot electricity procurement decision-making has become an important approach to address the above issues. It can balance market risks and supply assurance by coordinating power procurement needs across different cycles, providing scientific guidance for the grid in a multi-source procurement environment, effectively alleviating management pressure caused by source diversity, while supporting the efficient operation of the power market [1]. This decision-making mechanism plays a key role in ensuring reliable power supply and adapting to the needs of energy transition.

Currently, scholars at home and abroad have developed a diverse system of research methods in the field of mid-to-long-term spot market electricity procurement. Reference [2] proposes using a mixed-frequency volatility forecasting model to quantify the volatility of price-quantity deviation, and combines Monte Carlo simulation to solve multi-scenario optimization problems, providing support for time-phased procurement decisions; Reference [3] constructs a bi-level nonlinear optimization model, quantifies uncertainty risks via the CVaR method, and then converts it into a linear problem for solution using KKT conditions; Reference [4] focuses on the core issue of mid-to-long-term and spot market connection, builds a market clearing model for maximizing social welfare, uses the A-NSGA-Ⅲ algorithm to solve the optimal price cap range, and optimizes the contract decomposition curve through an intra-month integrated trading mechanism, effectively reducing the settlement risk of deviated electricity quantity and providing a market-oriented solution for cross-cycle procurement decisions; Reference [5] proposes a scenario analysis method integrating demand response, which dynamically allocates the electricity procurement ratio across annual, monthly, and weekly time periods by tracking load and

979-8-3315-5472-9/25/$31.00 ©2025 IEEE

electricity price fluctuations, effectively improving the connection accuracy between mid-to-long-term and spot markets.

Currently, a large number of literatures in the power market field focus on spot market risks. References [6]-[8] all focus on electricity procurement decision scenarios: they quantify uncertainties such as prices and loads in the spot market, build procurement decision models targeting cost optimization or risk management, and provide support for formulating procurement strategies. However, with the accelerated construction of the new power system and the deepening of the power market driven by the high-proportion integration of new energy, a single procurement mode is no longer adaptable. Relying solely on mid-to-long-term procurement risks missing spot market optimization opportunities, while relying only on spot procurement lacks stability; focusing only on intra-provincial procurement is constrained by local resources, which may restrict clean power consumption and cost control due to a single local power source structure. Moreover, in the face of extreme weather or sudden load surges, there is a lack of external power supply, resulting in insufficient power supply security redundancy. The model proposed in this paper can effectively connect the mid-to-long-term and spot markets and realize optimized allocation of resources across multiple spatial scales.

II. Unification of Variable Time Scales

In the actual operation of the power market, local electricity procurement is more reliable and stable than inter-provincial procurement, and the power grid has a better grasp of the actual situation of local power generation resources. Therefore, when formulating procurement plans, for intra-provincial mid-to-long-term procurement, it only needs to make optimized decisions on monthly electricity volume and communicate with power generation enterprises for implementation. For inter-provincial procurement, however, the power grid's grasp of the power generation resources of inter-provincial external procurement units is far weaker than that of intra-provincial ones, which greatly increases procurement uncertainty. Meanwhile, electricity needs to be transmitted through inter-provincial procurement channels, and the channels often face issues like periodic congestion. Thus, to ensure inter-provincial electricity transmission aligns with expected decisions, it is necessary to determine the hourly electricity volume for mid-to-long-term inter-provincial procurement. For spot market procurement, the spot market itself supplements the deviation between mid-to-long-term electricity volume and actual demand, requiring real-time balance of electricity supply and demand. Additionally, the spot market's settlement cycle is one hour [9], so decisions should also be refined to the hourly level. Therefore, in designing variables and constraints, this paper strictly follows the above instructions: mid-to-long-term intra-provincial market procurement and renewable energy procurement are set as monthly variables, while mid-to-long-term procurement from inter-provincial external units and spot market procurement are set as hourly variables.

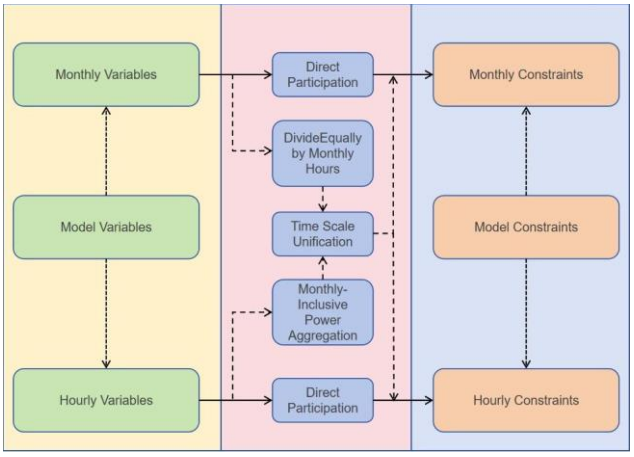


Fig. 1. Unification of Time Scales

During the operation of the model, a key step is the "unification of time scales", with the specific operation shown in Figure 1. Monthly-level constraints are set in the model: when hourly variables are involved, these hourly variables need to undergo monthly aggregation, where the aggregation method is to sum all hourly variables of the month to obtain the corresponding monthly variable. For hourly-level constraints set in the model, when monthly variables are involved, the monthly variables require hourly breakdown—this breakdown method is to evenly divide the monthly variable based on the number of hours in the month.

III. Mid-to-Long-Term Spot Dual-Time-Scale Optimization Model

This paper proposes a monthly-hourly-based dual-time-scale mid-to-long-term spot optimization model. The model is designed to improve solution efficiency when addressing large-scale annual data optimization and decision-making issues, and enhance the alignment of optimization results with actual market electricity procurement rules.

A. Design of Objective Function

From the perspective of grid companies' agency electricity procurement, the principle of minimizing procurement costs should be followed. Therefore, this paper takes minimizing the total agency procurement cost as the optimization objective to establish a dual-time-scale mid-to-long-term spot joint optimization model. The objective function used is as follows:

$$\min C = \sum_{m=1}^{M}[C_1(m) + C_2(m) + C_3(m)] + \sum_{h=1}^{H} C_4(h) \quad (1)$$

Among them, C denotes the total annual electricity procurement cost; M is the total number of months in a year, and H is the total number of hours in a year. $C_1(m)$ represents the electricity procurement cost of the intra-provincial market in month m, $C_2(m)$ represents the electricity procurement cost of inter-provincial external procurement units in month m, $C_3(m)$ represents the electricity procurement cost of renewable energy in month m, and $C_4(h)$ represents the electricity procurement cost of the spot market in hour h.

$$C_1(m) = r_G(m) * W_G(m) \tag{2}$$

Among them, $W_G(m)$, $r_G(m)$ respectively represent the electricity procurement volume and electricity procurement price of the intra-provincial market in month m.

$$C_2(m) = \sum_{f=1}^{3} r_f(m) * W_f(m) \tag{3}$$

Among them, $W_f(m)$ is the electricity procurement volume from external procurement unit f in month m, and $r_f(m)$ is the electricity procurement price from external procurement unit f in month m.

$$C_3(m) = r_n(m) * W_n(m) \tag{4}$$

Among them, $W_n(m), r_n(m)$ respectively represent the electricity procurement volume and electricity procurement price of renewable energy in month m.

$$C_4(h) = r_s(h) * P_s(h) \tag{5}$$

Among them, $P_s(h), r_s(h)$ they denote the electricity purchase power and electricity purchase price in the spot market at the h-th hour, respectively.

B. Constraint Conditions

The model constraints mainly include the system electricity supply-demand balance constraint, constraints on the proportion of various types of electricity purchase, and special channel constraints.

(1) System Monthly Electricity Quantity Balance

$$W_G(m) + \sum_{f=1}^{3} W_f(m) + W_n(m) + W_s(m) = W_{load}(m) \tag{6}$$

$$W_s(m) = \sum_{h=1}^{H_m} P_s(h) \tag{7}$$

Herein, H_m denotes the number of hours included in the m-th month, $W_s(m)$ denotes the total spot electricity purchase volume in the m-th month, and $W_{load}(m)$ denotes the total load volume in the m-th month.

(2) Electricity Purchase Proportion Constraint

$$W_G(m) + \sum_{f=1}^{3} W_f(m) + W_n(m) \geq \alpha * W_{load}(m) \tag{8}$$

$$W_G(m) + W_n(m) \geq \beta * W_{load}(m) \tag{9}$$

$$W_n(m) \geq k * W_{load}(m) \tag{10}$$

Herein, α denotes the minimum target for medium- and long-term electricity purchase volume, β denotes the minimum target for local electricity purchase volume, and k denotes the minimum quota target for renewable energy accommodation.

(3) Channel-Specific Constraint

Introducing Maximum Available Transfer Capability (MATC) constraints for the three inter-provincial channels into the model enables the model to depict cross-regional power transmission more in line with the actual operating rules of power grids. By defining the safe transmission boundaries of the channels across different time periods through MATC, the model can effectively avoid fault risks such as line overload and voltage violation caused by over-capacity transmission, thus ensuring the safety of power transmission. Meanwhile, MATC provides a quantitative basis for the allocation of cross-regional power resources, preventing the waste of channel resources or mismatch between supply and demand due to unconstrained electricity procurement. This makes the inter-provincial electricity procurement schemes output by the model more in line with actual dispatching requirements; especially for regional power grids that rely on external power input and require coordinated power supply through multiple channels, this constraint can further enhance the scientificity and feasibility of the model's decisions.

$$\sum_{f=1}^{3} P_f(h) + P_s^f(h) \leq P_f^{\max}(h) \tag{11}$$

Herein, $P_f(h)$ denotes the electricity purchase power from external electricity purchase entity f at the h-th hour, $P_s^f(h)$ denotes the electricity purchase power for spot market via channel f at the h-th hour, and $P_f^{\max}(h)$ denotes the maximum available transfer capability (MATC) of channel f at the h-th hour.

IV. Case Study

To verify the effectiveness and efficiency of the method proposed in this paper, simulation verification and analysis are conducted using market transaction data for all 12 months of 2024. The data includes load output curves and market transaction prices of various types of electricity procurement for all 12 months of 2024. All experiments are performed on a server equipped with an Intel Core i7 CPU and 16GB RAM, and the algorithm is implemented using Python combined with several extension libraries.

The core of this case study focuses on the optimization of medium- and long-term and spot electricity purchase under a dual-time-scale framework. The market transaction prices of various types of electricity purchase are shown in Figure 2. The maximum available transfer capability (MATC) of Channel 1 during each time period is presented in Table 1, and the maximum available transfer capability (MATC) of Channel 2 during each time period is presented in Table 2. The maximum available transfer capability (MATC) of Channel 3 remains a constant value of 2000 MW during all time periods throughout the year.

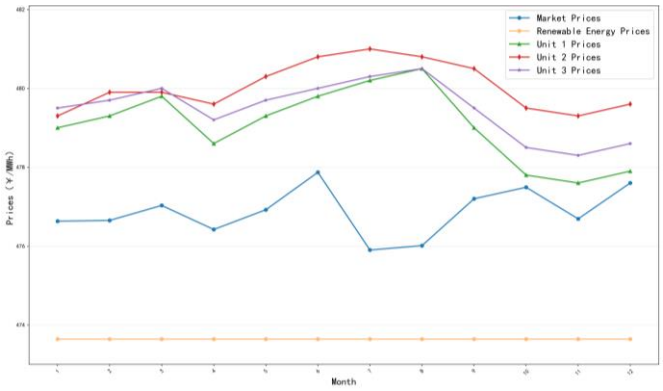


Fig. 2. Monthly Trend of Electricity Procurement Prices

TABLE I. MAXIMUM AVAILABLE TRANSFER CAPABILITY (MATC) OF CHANNEL 1

Month	MATC（MW）		
	Peak period (9:00-15:00)	Evening peak period (18:00-22:00)	Other time periods
Summer	4607.43	3071.62	3839.52
Non-summer	5760.26	3840.17	4800.22

TABLE II. MAXIMUM AVAILABLE TRANSFER CAPABILITY (MATC) OF CHANNEL 2

Month	MATC（MW）
Summer peak	3359.74
Other periods	5280.23

The monthly comparison of various types of electricity purchase volumes under the scenario of optimal electricity purchase cost (derived from the model's optimization solution) is shown in Figure 3.

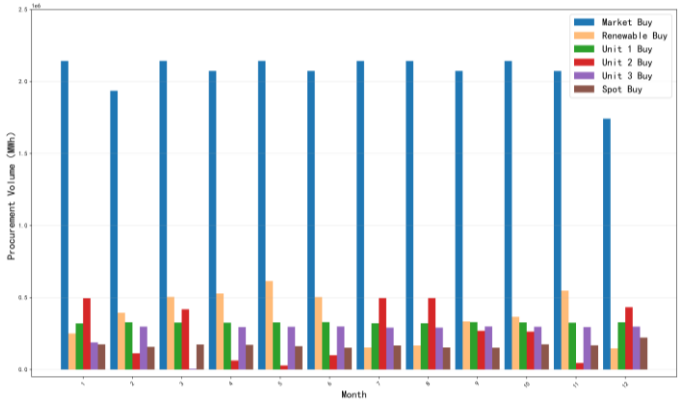


Fig. 3. Monthly Comparison of Various Types of Electricity Procurement Volumes

Market-based electricity procurement has a price advantage over inter-provincial electricity procurement and maintains the highest proportion throughout the overall procurement process, which is in line with the principles of prioritizing local power generation consumption, undertaking the main load demand of the system, and ensuring power supply stability. Renewable energy procurement, leveraging the government's priority generation and procurement policy indicators and by means of having the lowest electricity price among all types, achieves full monthly electricity consumption. Against the backdrop of energy transition, this reflects that renewable energy procurement is a "rigid demand driven by policies or energy structure," ensuring the sustainability of renewable energy consumption. The proportion of cross-regional procurement (e.g., from external procurement units) exhibits monthly fluctuations: when electricity prices in a certain region are relatively low, the proportion of procurement from that region increases accordingly, reflecting the flexibility of "optimal allocation of inter-regional resources." Spot electricity procurement maintains the lowest proportion, which aligns with its positioning as a "supplementary means for short-term supply-demand balance" rather than a long-term large-scale power source, and fits the functional attribute of the spot market in "regulating short-term gaps."

To verify the rationality of the model's optimal procurement cost, three control groups are set up for cost calculation, and their results are compared with those obtained from the model optimization. In practice, the control group construction and verification process involves conducting thousands of solution calculations; to ensure conciseness of the paper, only three randomly selected control groups are presented in the text. Results are shown in TABLE III.

TABLE III. COMPARISON OF ELECTRICITY PROCUREMENT COSTS

Model	**Proportion of Mid-to-Long-Term(%)**	**Proportion of Spot （%）**	**Total Cost （¥）**
Optimization Model	95.176	4.824	19937287312.5
Control Group 1	95.359	4.641	20115517260.6
Control Group 2	91.549	8.451	20146779494.2
Control Group 3	91.589	8.411	20147550551.2

The control groups are set up by slightly adjusting the values of various electricity procurement volume variables obtained from the model's optimization solution (instead of random large-scale modification), on the premise of ensuring that the adjusted variable values still satisfy all constraints of the model. Since the selection of control groups is random, and the results of thousands of solution calculations in the actual verification process consistently confirm that the model's solution is optimal, it can be seen from the comparison of total procurement cost results in the table that the model in this paper achieves the solution of optimal procurement cost.

V. CONCLUSION

Addressing the issues of diverse resources for grid companies' agency electricity procurement, poor adaptability of single modes, and intra-provincial resource constraints, this paper establishes a monthly-hourly dual-time-scale mid-to-long-term spot optimization model. The model distinguishes between monthly and hourly variables, integrates special constraints for inter-provincial channels, and takes minimizing the total agency procurement cost as its objective. Verified through simulation using full-year 2024 data, the model can effectively connect the mid-to-long-term and spot markets, ensure full consumption of renewable energy and power supply stability, and its total procurement cost is

significantly lower than that of the control groups. It provides scientific support for grid companies' agency electricity procurement decisions.

It should be noted that this model still has certain limitations in channel constraint modeling: although it innovatively introduces the maximum available transfer capability (MATC) constraints of three inter-provincial channels into the optimization framework, which effectively supports multi-space resource allocation, the consideration of uncertainty in channel transmission capacity is not comprehensive enough. For instance, the model assumes that the MATC of Channel 3 remains a constant 200 MW during all time periods throughout the year, failing to cover dynamic changes in MATC that may be caused by factors such as extreme weather, equipment maintenance, and cross-regional load fluctuations—this simplifies the complex scenarios in actual power grid operation to a certain extent. Future research can further supplement the uncertainty analysis of channel transmission capacity, combining probabilistic prediction or robust optimization methods to enhance the model's adaptability and anti-interference ability to the actual operating environment.

ACKNOWLEDGMENT

This work was supported by Science and Technology Project of State Grid Corporation of China (Grant Number: B3094024000G).

REFERENCES

[1] Xiang Z M, Zeng K L, Yang C H, et al. Strategy for inter-provincial spot electricity procurement considering power supply guarantee risk of receiving-end power grid[J]. Zhejiang Electric Power, 2024, 43(12): 15-27. DOI:10.19585/j.zjdl.202412002.

[2] Li Y B, Wang J N, Xiao T T, et al. Decision-making method for medium- and long-term time-phased rolling transaction of agent-based electricity procurement for power grid enterprises considering risk[J]. Power System Technology,2023,47(10):4237-4245.DOI:10.13335/j.1000-3673.pst.2023.0140.

[3] Guo L B, Ding Y, Bao M L, et al. Optimal electricity procurement model for inter-provincial traders considering risk under the two-level electricity market environment[J]. Power System Technology, 2019, 43(8): 2726-2734. DOI:10.13335/j.1000-3673.pst.2019.0668.

[4] Zhang X Q, Liu D N, Wang X L, et al. Study on intra-month integrated transaction mode and unified price limit considering the connection between medium- and long-term electricity market and spot market[J]. Power System Technology,2024,48(4):1418-1430.DOI:10.13335/j.1000-3673.pst.2023.1859.

[5] Wu H H, Zhang S, Gan W, et al. Decision model for agent-based electricity procurement of power grid enterprises oriented to multi-time-scale market transactions[J]. Zhejiang Electric Power, 2023, 42(9): 42-51. DOI:10.19585/j.zjdl.202309006.

[6] Sun Y, Liu Z, Huang T, et al. Decision on Power Procurement and Sales of Electricity Sales Companies Considering Uncertainty of Prosumer Users[J/OL]. Journal of Shanghai Jiao Tong University, 1-33 [2025-09-25]. DOI:10.16183/j.cnki.jsjtu.2023.530.

[7] Li Y T, Tang J J, Zhang S, et al. Power procurement and sales decision model for electricity sales companies considering multiple uncertainty factors[J]. Automation of Electric Power Systems, 2022, 46(7): 33-41.

[8] Ye H, Yang P, Wang Y. Optimal strategy for day-ahead declaration in electricity spot market of electricity sales companies based on improved CVaR[J]. Electric Power Construction, 2024, 45(5): 131-140.

[9] Ye Z. Settlement method for electricity spot market with non-decomposed or non-time-phased transactions of medium- and long-term contracts[J]. China Electric Power Enterprise Management, 2025, (16): 44-48.

Risk-Averse Optimization of Medium and Long-Term Power Procurement Under Multi-Dimensional Uncertainty

Ronghui Liu
College of Electric Power Engineering
Shanghai University of Electric Power
Shanghai, China
liuronghuiyzy@126.com

Weicheng Wang
College of Electric Power Engineering
Shanghai University of Electric Power
Shanghai, China
wangweicheng1013@mail.shiep.edu.cn

Gaiping Sun
College of Electric Power Engineering
Shanghai University of Electric Power
Shanghai, China
gaiping_sun@shiep.edu.cn

Shunfu Lin
College of Electric Power Engineering
Shanghai University of Electric Power
Shanghai, China
shunfulin@shiep.edu.cn

***Abstract*—In medium and long-term power procurement optimization, the inherent uncertainty in electricity markets necessitates robust decision-making frameworks. The stochastic nature of renewable energy generation, fluctuating electricity prices, volatile load demand, and variable available transfer capacity (ATC) creates significant challenges for procurement planning, making uncertainty modeling essential for effective risk management and cost optimization. This paper proposes a risk-averse optimization model that incorporates multi-dimensional uncertainty by taking channel-capacity scenarios, electricity price scenarios, and load demand scenarios as exogenous inputs. To enhance forecasting accuracy for these uncertain parameters, the model integrates a hybrid Prophet-SARIMA approach that combines the trend decomposition capabilities of Prophet with the seasonal adjustment strengths of SARIMA, providing more reliable scenario generation for ATC. The model measures and constrains tail risk in contract costs using conditional value at risk (CVaR) and, in evaluation, accounts for over-limit cost to capture contract repurchase expenses induced by channel congestion, thereby curbing cost escalation and strengthening deliverability. To validate effectiveness, the model is benchmarked against a deterministic arbitrage formulation. Numerical testing results show that the proposed method significantly reducing risk losses and over-limit cost, achieving smoother monthly allocations and more stable utilization of transmission channels.**

Keywords— Multi-Dimensional uncertainty, Medium and long-term market, Risk assessment, CVaR

I. INTRODUCTION

In medium and long-term agency procurement markets, multiple temporal and spatial scales coexist. These include annual, monthly, and intra-monthly markets, as well as inter-provincial and intra-provincial markets. Procurement decisions across different market levels must be coordinated under diverse constraints, forming a complex multi-dimensional decision framework. Transmission channels spatially connect retailers and suppliers, carrying cross-regional energy across temporal scales and ensuring deliverability across different temporal contract scales. The procurement environment is characterized by multiple sources of uncertainty that significantly impact decision-making effectiveness: Available Transfer Capacity (ATC) volatility driven by maintenance schedules and grid infrastructure constraints, electricity price uncertainty with temporal correlation across different contract scales, and load demand uncertainty due to weather variations and consumer behavior changes. Given the intermittency and volatility of renewable energy, the expanding scale and frequency of inter-provincial transactions, and the multi-faceted nature of these uncertainties, risk aversion becomes a critical element of medium and long-term agency procurement strategies, requiring sophisticated stochastic optimization approaches that can assess and mitigate these interconnected risks while maintaining operational feasibility and economic efficiency.

Relevant research on procurement under uncertainty exhibits several principal limitations in addressing the multi-faceted nature of risk factors. First, although CVaR is well established for managing price and load risks [1-2,7], its deployment rarely accounts for ATC uncertainty, typically treating transfer capacity as a static parameter and failing to capture the dynamic, context-dependent nature of channel availability. Conversely, ATC-oriented studies [3-4] yield valuable market insights but remain weakly coupled with forward-looking, risk-averse procurement formulations that explicitly incorporate channel uncertainty into optimization frameworks. While sophisticated approaches to modeling electricity price volatility [8-10] and load uncertainty [12-13] have been developed, these studies predominantly focus on individual risk factors and lack integration with medium-term procurement planning under transmission constraints.

To address the above limitations, this paper proposes a unified framework that coherently integrates high-fidelity ATC uncertainty representation with CVaR-based procurement optimization, particularly for medium and long-term agency procurement contexts, where such frameworks need to consider multiple temporal and spatial constraints. Building upon this foundation, we develop a comprehensive risk management approach that simultaneously addresses the interconnected nature of ATC volatility, electricity price uncertainty, and load variability within a single optimization model, providing

979-8-3315-5472-9/25/$31.00 ©2025 IEEE

theoretical foundations for risk-aware procurement strategies for medium and long-term agency markets.

The main contributions are summarized as follows:

1) This study proposes a novel risk-averse optimization framework that integrates multi-dimensional uncertainty modeling (ATC volatility, electricity price uncertainty, and load variability) with CVaR tail risk measurement, achieving comprehensive decision-making from grid physical constraints to procurement financial risk across multiple temporal and spatial scales.

2) A hybrid Prophet-SARIMA scenario generation method combines Prophet's trend and seasonality capture with SARIMA's stochastic modeling capabilities, generating probabilistic ATC scenarios that capture multi-seasonal power system patterns and operational characteristics.

3) The model achieves channel-level risk interpretability by quantifying congestion risk through over-limit costs and monthly procurement constraints, producing smoother monthly allocations.

This paper is organized as follows. In Section II, the dual-model comparison and mathematical formulation of the risk-averse and arbitrage-deterministic optimization problems are introduced. Section III presents the uncertainty modeling approaches, including the Prophet-SARIMA combined model for generating ATC uncertainty scenarios and the correlated multiplicative perturbation method for electricity price and load uncertainty scenario generation. Section IV provides a case study, including data description and results analysis. Finally, conclusions are drawn in Section V.

II. Problem Formulation

Medium and long-term agency procurement typically spans several months to years, providing a strategic planning horizon for electricity trading decisions. The time horizon consists of T_m equal-length periods t, where m represents specific months, with each month's period index ranging from 1 to T_m. For simplification, spot market prices and procurement quantities are not subdivided to individual suppliers, with the model employing a virtual supplier representation. The framework considers multiple temporal scales (annual, monthly, intra-monthly) and spatial scales (intra-provincial and inter-provincial). In the following, comparison, objective function, constraint are presented in detail.

A. Comparison

The parallel evaluation framework of the dual-model shown in Fig.1 clearly shows the logical relationship between the risk drivers and the two optimization models.

(1) risk-averse model:

As shown in Fig.1, this model centers on the "risk model." The objective is to minimize the total risk-adjusted cost. The model quantifies and mitigates extreme risks through scenario analysis and CVaR constraints across all uncertainty sources, thereby formulating a more robust procurement strategy for uncertain environments.

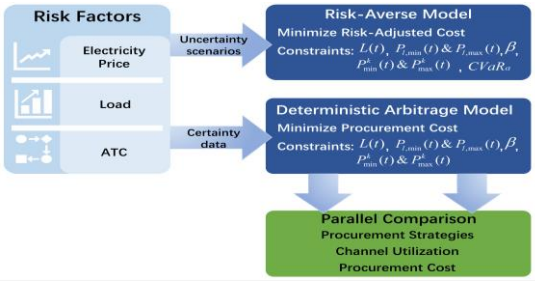


Fig. 1. Parallel evaluation framework of the dual-model.

(2) Arbitrage-deterministic model:

In contrast, the arbitrage-deterministic model aims purely to minimize the total procurement cost. Unlike the risk-averse model, this model typically uses a deterministic value from historical data and does not explicitly account for tail risk. This model represents the decision-making logic of pursuing maximum cost-effectiveness without considering or simplifying the risk scenario, which reflects the typical characteristics of traditional deterministic optimization methods.

B. Objective Function

The cost of medium and long-term agency procurement equals the sum of procurement costs across all suppliers for the electricity retailer. Given the multi-dimensional uncertainty, the problem transforms into minimizing procurement costs under risk management, i.e., minimizing risk-adjusted costs. Additionally, due to the potential for channel congestion and the need to ensure deliverability, over-limit costs are introduced as penalty terms. The total cost comprises the expected cost from all suppliers across different channel capacity scenarios plus risk terms and penalty terms, as shown below.

(1) Risk-averse model

This model aims to minimize the risk-adjusted power procurement cost by explicitly considering ATC uncertainty:

$$\min \sum_{m=1}^{12} \left\{ C_{forward}(m) + \lambda \cdot CVaR_{\alpha} \right\} \tag{1}$$

where $C_{forward}(m)$ represents the medium and long- term cost in the m month, $CVaR_{\alpha}$ represents the Conditional Value at Risk at the confidence level α, which is used to quantify the expected loss in extremely adverse scenarios, λ is the risk-aversion coefficient, reflecting the decision-maker's preference for risk aversion.

$$C_{forward}(m) = C_I(m) + C_E(m) \tag{2}$$

The cost consists of the in-province procurement cost $C_I(m)$ and the inter-province procurement cost $C_E(m)$.

$$\begin{aligned} C_I(m) = \sum_{i \in \mathcal{I}} \{ & c^i_{I,Y}(m) \cdot P^i_{I,Y}(m) + c^i_{I,M}(m) \cdot P^i_{I,M}(m) \\ & + \sum_{d \in D_m} [c^i_{I,D}(d) \cdot P^i_{I,D}(d)] \} \end{aligned} \tag{3}$$

where $\mathcal{I}$ represents the set of in-province power source types. When i=1, it represents green power sources, and when i=2, it represents conventional power sources. The electricity price and power procurement volume of the i-th type of in-

province power source for annual, monthly, and intra-monthly transactions are denoted by ($c_{I,Y}^{i}(m)$, $P_{I,Y}^{i}(m)$), ($c_{I,M}^{i}(m)$, $P_{I,M}^{i}(m)$), and ($c_{I,D}^{i}(m)$, $P_{I,D}^{i}(m)$), respectively, where subscripts y, m, and d represent annual, monthly, and intra-monthly time scales.

$$C_E(m)=\sum_{k=1}^{K}\{c_{E,Y}^{k}(m)\cdot P_{E,Y}^{k}(m)+c_{E,M}^{k}(m)\cdot P_{E,M}^{k}(m)+\sum_{D_m}[c_{E,D}^{k}(d)\cdot P_{E,D}^{k}(d)]\} \tag{4}$$

where K is the total number of inter-province suppliers. Similarly, the electricity price and power procurement volume of the i-th type of inter-province power source for annual, monthly, and intra-monthly transactions are denoted by ($c_{E,Y}^{k}(m)$, $P_{E,Y}^{k}(m)$), ($c_{E,M}^{k}(m)$, $P_{E,M}^{k}(m)$), and ($c_{E,D}^{k}(m)$, $P_{E,D}^{k}(m)$), respectively, where subscripts y, m, and d represent annual, monthly, and intra-monthly time scales.

(2) Arbitrage-deterministic model

As a control for the risk-averse model, this model aims to minimize the power procurement cost under the deterministic channel capacity. Its mathematical expression is as follows:

$$\min\sum_{m=1}^{12}\{C_{forward}(m)\} \tag{5}$$

where the specific cost formula is the same as that of the risk-averse model, except that the risk loss value is not considered, so it will not be repeated here.

(3) Over-limit cost

Take the 95% quantile of each channel capacity as the carrying threshold. If the planned channel volume exceeds this threshold, the excess part needs to be purchased at the corresponding spot repurchase price of the channel, and the over-limit cost is calculated by the difference between the repurchase price and the weighted original contract price within the channel.

$$P_l^{ATC}(t)=95\%\cdot P_{l,\max}(t) \tag{6}$$

$$P_l^{over}(t)=\max[0,P_l(t)-P_l^{ATC}] \tag{7}$$

$$C^{over}(t)=P_l^{over}(t)\cdot[c_{spot}(t)-c_{forward}(t)] \tag{8}$$

where $P_l^{ATC}(t)$ is the available transfer capacity of channel l, taking 95% of the maximum transfer capacity $P_{l,\max}(t)$ of this channel, $P_l^{over}(t)$ represents the over-limit power of channel l, that is, the part of the transmission power exceeding the above-mentioned threshold, the final Over-limit cost $C^{over}(t)$ is jointly determined by the over-limit power and the price difference, $c_{spot}(t)$ represents the spot price in the corresponding period. Usually, the spot price is higher than the original price.

C. Constraint

(1) Supply-demand balance constraint:

$$\sum_{i\in I}P_{I,X}^{i}(t)+\sum_{k=1}^{K}P_{E,X}^{k}(t)=L(t),\ X=Y,M,D \tag{9}$$

where $P_{I,X}^{i}(t)$ represents the procurement volume of different types in the province, and $P_{E,X}^{k}(t)$ represents the procurement volume of different inter-province suppliers.

(2) Channel capacity constraint:

$$P_{l,\min}(t)\le\sum_{k\in Kl}P_{E,X}^{k}(t)\le P_{l,\max}(t),\ X=Y,M,D \tag{10}$$

where $P_{l,\min}(t)$ and $P_{l,\max}(t)$ are the minimum and maximum transmission capacities of channel l respectively, K_l is the set of suppliers covered by channel l, and $P_{E,X}^{k}(t)$ is the procurement volume of the corresponding supplier under channel l.

(3) Supplier capacity constraint:

$$P_{\min}^{k}(t)\le P_{E,X}^{k}(t)\le P_{\max}^{k}(t),\ X=Y,M,D \tag{11}$$

where $P_{\min}^{k}(t)$ and $P_{\max}^{k}(t)$ are the minimum and maximum transmission powers of supplier k respectively.

(4) Green power consumption weight constraint:

$$\frac{\sum_{T}[P_{I,X}^{1}(t)+\sum_{K1}P_{E,X}^{k}(t)]}{W_{all}}\ge\beta,\ X=Y,M,D \tag{12}$$

where, K_1 is the set of inter-province green suppliers, W_{all} is the sum of the annual power procurement volume, and β is the minimum proportion of green power procurement volume.

(5) CVAR constraint:

$$CVaR_\alpha=VaR_\alpha+\frac{1}{1-\alpha}\sum_{s\in S}p_s\cdot z_s \tag{13}$$

$$z_s\ge L_s-VaR_\alpha,\ z_s\ge 0 \tag{14}$$

where VaR_α is the Value at Risk at the same confidence level, which is the quantile of the loss distribution, S is the set of scenarios, s is a single scenario, p_s is the occurrence probability of scenario s, z_s is an auxiliary variable used to linearize the part of the loss exceeding VaR_α in scenario s, and L_s is the cost loss value.

III. Scenario Generation Method

A. ATC Uncertainty Modeling

Prophet-SARIMA Combined Model To effectively deal with channel capacity uncertainty, the paper proposes a scenario generation method based on the combined model. This approach was selected over alternatives like LSTM or GRU due to its superior performance in our context, characterized by a limited data volume and pronounced multiple seasonality (daily, weekly, yearly). While deep learning models are powerful, they typically require larger datasets and greater computational resources. In contrast, the Prophet-SARIMA combination provides a robust, interpretable, and computationally efficient framework, which proved more effective for our ATC forecasting task. This method combines the ability of the Prophet model to capture trends and seasonality with the ability of the SARIMA model to process residual sequences, realizing accurate modeling and scenario generation of the channel capacity time series.

(1) Prophet model

Prophet is a time-series forecasting tool developed by Facebook. Based on the idea of an additive model, it decomposes the time series into parts such as trends, seasonality, and holiday effects. The specific formula is as follows:

$$y(t)=g(t)+s(t)+h(t)+\varepsilon(t) \tag{15}$$

where: $g(t)$： Trend term, describing the long-term growth or decline trend

$$g(t) = \left(k + A(t)^T \cdot \delta\right) \cdot t + \left(m + A(t)^T \gamma\right) \tag{16}$$

where k is the basic growth rate, m is the initial offset, δ and γ are the slope and end-trend change parameters respectively, and $A(t)$ is the change-point indicator function, $s(t)$： Seasonality term, describing periodic changes

$$s(t) = \sum_{n=1}^{N} a_n \cos(\frac{2\pi nt}{P}) + \sum_{n=1}^{N} b_n \cos(\frac{2\pi nt}{P}) \tag{17}$$

where P is the length of the seasonal cycle, a_n and b_n are Fourier coefficients, and N is the number of terms in the Fourier series,

$h(t)$： Holiday effect term, describing the impact of special events

$$h(t) = \sum_{i=1}^{L} \kappa_i \cdot l_{\{t \in D_i\}} \tag{18}$$

where L is the number of holidays (considering Chinese legal holidays in the program); D_i represents the set of the duration of the i-th holiday itself; l is the impact intensity of holiday i; κ_i is the indicator function (1 within the holiday, 0 otherwise).

$\varepsilon(t)$： Error term, following a normal distribution

(2) SARIMA model

The SARIMA model introduces a seasonal term on the basis of the ARIMA model, which can effectively capture the seasonal fluctuations in data. The model structure is SARIMA(p,d,q)(P,D,Q,s), where p, d, q are the non-seasonal autoregressive, differencing, and moving-average orders respectively. On this basis, the seasonal autoregressive order P, differencing order D, moving-average order Q, and the time step s of each cycle are added. SARIMA is suitable for sequences with obvious seasonality and periodicity. The model can be expressed as:

$$\varphi_p(B)\Phi_p(B^S)(1-B)^d(1-B^S)^D Y_t = \theta_q(B)\Theta_Q(B^S)\varepsilon_t \tag{19}$$

Where:

Non-seasonal AR polynomial:

$$\varphi_p(B) = 1 - \varphi_1 B - \varphi_2 B^2 \cdots - \varphi_p B^p \tag{20}$$

Seasonal AR polynomial:

$$\Phi_p(B^s) = 1 - \Phi_s B^s - \Phi_{2s} B^{2s} \cdots - \Phi_{ps} B^{ps} \tag{21}$$

Non-seasonal MA polynomial:

$$\theta_p(B) = 1 - \theta_1 B - \theta_2 B^2 \cdots - \theta_q B^q \tag{22}$$

Seasonal MA polynomial:

$$\Theta_Q(B^s) = 1 - \Theta_s B^s - \Theta_{2s} B^{2s} - \cdots - \Theta_{Qs} B^{Qs} \tag{23}$$

B is the lag operator:

$$B^k Y_t = Y_{t-k} \tag{24}$$

P，d，q，P，D，Q，s are all non-negative integers. d is the number of ordinary differencing, D is the number of seasonal differencing, p is the order of autoregression (AR), P is the order of seasonal autoregression (SAR), q is the order of moving average (MA), Q is the order of seasonal moving average (SMA); s represents the season length, taking 4 for quarterly sequences and 12 for monthly sequences. ε_t is a white-noise residual sequence with zero mean and constant variance.

(3) Complementarity of the combined model

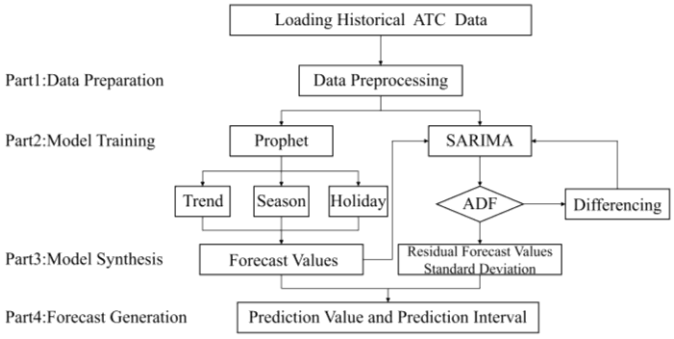


Fig. 2. Flowchart of ATC prediction by Prophet and SARIMA.

The flowchart of the Prophet-SARIMA combined modeling shown in Fig.2 clearly shows the modeling steps of this method. First, read the historical channel capacity data and pre-process it, and then conduct Prophet modeling and residual analysis in parallel. The Prophet model decomposes the trend term, season term, and holiday term to generate deterministic prediction values; at the same time, calculate the residual sequence and conduct the ADF stationarity test. If necessary, perform differencing processing, and finally obtain the residual prediction value and standard deviation through SARIMA modeling. Finally, combine the Prophet prediction value with the SARIMA residual prediction value, generate the channel capacity prediction value and prediction interval.

B. Electricity Price and Load Uncertainty Modeling

To capture the inherent uncertainty in electricity prices and load demand, this study employs a multiplicative perturbation method based on historical prediction errors. The approach generates probabilistic scenarios by analyzing the ratio between actual values and predicted values from historical data, providing a data-driven foundation for scenario generation.

For each scenario s and time period t, the perturbed values are generated as:

$$P_{i,s}(t) = P_{i,base}(t) \cdot \xi_{i,s}(t) \tag{25}$$

$$L_s(t) = L_{i,base}(t) \cdot \xi_{L,s}(t) \tag{26}$$

Where $P_{i,base}(t)$ and $L_{i,base}(t)$ represent the baseline electricity price for supplier i and load demand, respectively. The perturbation factors $\xi_{i,s}(t)$ and $\xi_{L,s}(t)$ follow log-normal distributions to ensure non-negativity.

C. Monte Carlo Simulations

To generate multiple scenarios using Monte Carlo simulation, the prediction value obtained from the Prophet-SARIMA combination serves as the mean of a normal distribution, while the prediction interval provides the variance. For each scenario, random samples are drawn from this normal distribution at each time period, where each scenario represents a single realization from the probability model. Similarly, for

electricity prices and load demand, the baseline values serve as the mean of log-normal distributions, while the multiplicative perturbation factors derived from historical prediction errors provide the variance structure. Each scenario represents a single realization from the probability model, capturing the inherent uncertainty in both ATC capacity and market variables.

IV. Numerical Testing Result

The algorithm was implemented using Python and ran on a laptop with an i7 processor, 8 GB memory, and NVIDIA GeForce GTX 1660Ti GPU. The following sections present the data description, scenario generation results, and comparative analysis between risk-averse and deterministic approaches.

A. Data Description

This case study is used to demonstrate the annual power procurement decision-making effect of a company in the multi-time-scale market transactions. The load data is sourced from the historical load records of the provincial power dispatching center. The price data includes two levels: in-province and inter-province. The in-province prices are classified by power source type and trading time scale, inter-province classified by suppliers and trading time scale.

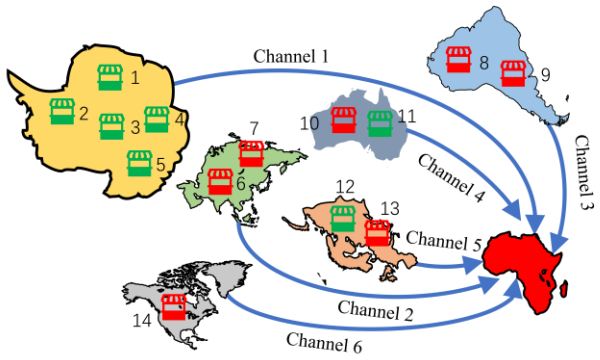


Fig. 3. Schematic diagram of the inter-province transmission channel.

The supplier comprises 14 inter-province suppliers, mapped to regional channels based on the k value (as shown in Fig.3, where green icons denote green power sources and red icons conventional ones).

B. Results Analysis

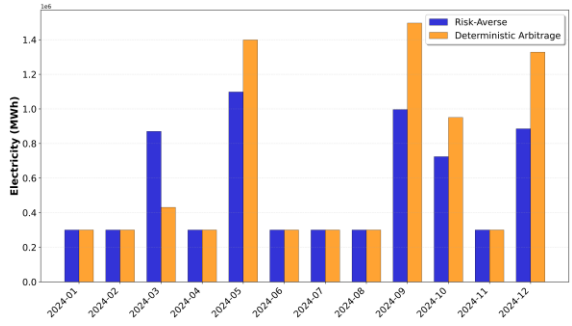


Fig. 4. Comparison of monthly power procurement volume of Channel 1.

Comparing inter-province channel procurement alloca-tions reveals distinct differences in channel utilization patterns between the two strategies. As shown in Fig.4 to Fig.6 (focusing on Channels 1, 5, and 4), the risk-averse strategy exhibits more balanced monthly procurement allocation than the arbitrage-deterministic strategy.

Specifically, the risk-averse strategy smooths channel allocation, which is quantified by a 35% reduction in the standard deviation of monthly procurement volume across the year. It avoids the arbitrage-deterministic strategy's con-centrated procurement in specific months and moderately increases procurement in others, achieving peak-valley balance. For example, the arbitrage-deterministic strategy peaks at 1.48 million MWh in September, while the risk-averse strategy limits it to 1.0 million MWh, a 32% reduction in peak load, significantly alleviating transmission pressure.

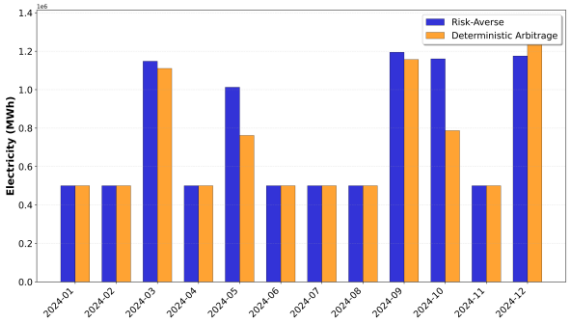


Fig. 5. Comparison of monthly power procurement volume of Channel 5.

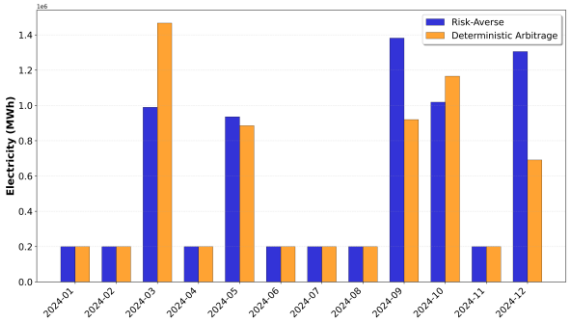


Fig. 6. Comparison of monthly power procurement volume of Channel 4.

Channel 5 exhibits a similar smoothing effect, with its monthly procurement standard deviation decreasing by 41% (from 0.22 to 0.13 million MWh). By reducing the peak procurement (e.g., from 1.35 million MWh in December to 1.15 million MWh) and increasing procurement in lower-load months (e.g., May), the channel pressure is effectively dispersed.

Following the analysis of channel allocation and utilization, we evaluate the strategies' economic performance under real deliverability constraints by introducing an over-limit cost. The TABLE I summarizes the contract costs, over-limit costs, and total costs of the two types of strategies.

TABLE I. Comparison of Cost Decomposition and Total Cost

Model	Optimization cost (millions)	Over-limit cost (millions)	Total cost (millions)
Risk-Averse	1944.270	277.382	2221.652
Deterministic Arbitrage	1936.270	286.170	2222.440

The quantitative metrics in TABLE I confirm that the smoother allocation of the risk-averse strategy leads to more stable channel utilization. Consequently, as shown in TABLE I, while the risk-averse strategy incurs a slightly higher contract-side cost due to its conservatism, its over-limit cost is substantially reduced. After offsetting the difference, the total cost of the risk-averse strategy is lower, with a net savings of about 7.88 million yuan.

V. CONCLUSION

This study proposes a risk-averse procurement strategy model and methodology for medium and long-term electricity trading to address multi-dimensional uncertainty, minimize procurement costs and assess risk. The method employs CVaR to measure and constrain tail risk in contract costs, incorporates over-limit costs in evaluation to capture contract repurchase expenses induced by channel congestion, thereby curbing cost escalation and enhancing deliverability. The model is benchmarked against a traditional deterministic arbitrage approach. Numerical tests based on a provincial electricity market show that the proposed method provides superior solutions for annual procurement decision-making and risk assessment compared to conventional approaches, considering historical data across different regions and relevant policy regulations to minimize procurement costs, assess risk, achieve smoother monthly allocations and more stable transmission channel utilization.

REFERENCES

[1] Jun Xu,Peter B. Luh,Frederick B. White,et al. Power Portfolio Optimization in Deregulated Electricity Markets With Risk Management[J]. IEEE Transactions on Power Systems: A Publication of the Power Engineering Society,2006,Vol.21(4): 1653-1662.

[2] Bo Sun,Fan Wang,Jingdong Xie. Electricity Retailer Trading Portfolio Optimization Considering Risk Assessment in Chinese Electricity Market[J]. Electric Power Systems Research,2021,Vol.190: 106833.

[3] Zhang, M.M,Wang,et al. Evaluating uncertain investment decisions in low-carbon transition toward renewable energy.[J]. Applied Energy,2019,Vol.240: 1049-1060.

[4] Zhou Diya, Feng Shuhai, Zhu Yining, et al. Application analysis and key issues of Available Transfer Capability (ATC) adapted to electricity market environment in China[J]. Power System Technology, 2021, 45(9): 3357-3366. DOI:10.13335/j.1000-3673.pst.2021.0347.

[5] Chaturvedi, Shobhit,Rajasekar,et al. A comparative assessment of SARIMA, LSTM RNN and Fb Prophet models to forecast total and peak monthly energy demand for India.[J]. Energy Policy,2022,Vol.168: 1-13

[6] Winita Sulandari,Yudho Yudhanto,Etik Zukhronah,et al. Hybrid Prophet-NAR Model for Short-Term Electricity Load Forecasting[J]. IEEE Access,2025,Vol.13: 7637-7649.

[7] Wang Boyu, Xu Xiaofeng, Cao Zheng, et al. Research on multi-market trading strategies for agency power purchase based on multi-dimensional risk measurement[J]. Power System Technology, 2025, 49(3): 1032‑1044. DOI:10.13335/j.1000-3673.pst.2024.1016.

[8] Xiang Gao,Ziqing Zhu,Siqi Bu,et al. Multi-timescale multi-type electricity and carbon emission market simulation by hierarchical quantum-classical decision making framework[J]. CSEE Journal of Power and Energy Systems,2025,: 1-12.

[9] Lu, Ting, Zhang,et al. Medium-and Long-Term Trading Strategies for Large Electricity Retailers in Chinas Electricity Market [J].Energies,2022,Vol.15(9): 3342.

[10] Charwand M ,Gitizadeh M .Risk-Based Procurement Strategy for Electricity Retailers: Different Scenario-Based Methods[J].IEEE Transactions on Engineering Management,2020,67(1):141-151.

EV Charging Scheduling in Residential Areas: A Multi-Objective Approach Based on MOIPSO

YueJun Li
School of Automation and Electronic Information
Xiangtan University
Xiangtan, China
3178781371@qq.com

Bin Duan
School of Automation and Electronic Information
Xiangtan University
Xiangtan, China
db61850@163.com

Yi Kuang
School of Automation and Electronic Information
Xiangtan University
Xiangtan, China
ykuang@xtu.edu.cn

***Abstract*—To address the peak load overlapping phenomenon caused by the highly concentrated EV charging in residential areas, this study proposes an orderly charging strategy based on an improved multi-objective particle swarm optimization (MOIPSO) algorithm. A multi-objective optimization model is established to minimize the total system load variance, reduce user costs, and maximize charging volume, while considering EV battery aging costs and system power constraints. Simulation results demonstrate that, compared to the NSGA-II and MOPSO algorithms, the proposed algorithm significantly improves the diversity and convergence of the Pareto solutions through the introduction of dynamic inertia weights and elite crossover and mutation strategies. Moreover, compared to unordered charging, the proposed orderly strategy increases the average off-grid SOC by 3.3%, reduces the total cost by 29%, decreases the load peak by 28.4%, lowers the peak-valley difference rate by 39.3%, and reduces the load variance by 87.2%.**

Keywords—Electric vehicles, particle swarm optimization, multi-objective optimization, orderly charging and discharging

I. Introduction

Driven by pursuit of green and sustainable development, the large-scale integration of electric vehicles (EVs) into the power grid is becoming an inevitable trend[1]. As the number of EVs continues to grow year by year, conventional parking lots can no longer meet the increasing demand for charging, and residential parking lots are gradually becoming the primary charging locations[1]. However, due to the "early departure and late return" usage pattern of EVs, their concentrated connection to the grid during peak load periods tends to create a "peak-on-peak" phenomenon. Vehicle-to-Grid (V2G) technology enables bidirectional energy exchange between EVs and the grid. By regulating the orderly charging and discharging of EVs to reduce peak loads, V2G serves as an effective solution to the "peak-on-peak" problem caused by high EV penetration in the future[3].

The EV charging and discharging scheduling problem is a complex multi-objective optimization problem, involving multiple constraints and nonlinear factors. In terms of optimization models, various strategies have been proposed. For example, reference[4] established a coordinated charging scheduling model to optimize the grid's load peak-to-valley difference, but it ignored user benefits. Reference[5] proposed a multi-objective model to minimize both the grid's peak-to-valley load difference and the total charging cost of EV users, but did not consider the potential participation of users in V2G. Reference[6] optimized the grid load and charging costs by minimizing the mean square deviation. Reference[7] optimized EV charging and discharging through dynamic pricing to reduce total operational costs, peak loads, and voltage fluctuations. However, these studies did not account for the battery degradation costs incurred by users participating in V2G.

In terms of optimization algorithms, common methods include Genetic Algorithm (GA)[8] and Particle Swarm Optimization (PSO)[9]. Reference[10] used PSO to optimize the charging and discharging behavior of each EV, but the optimization performance is often limited by local optima. Reference[11] used the multi-objective PSO algorithm to optimize the charging scheduling cost and load variance in urban residential areas under a combined metering pricing model. Reference[12] proposed an improved PSO algorithm to formulate the optimal charging and discharging control strategy for EVs, effectively improving the convergence speed. However, the PSO algorithm tends to get trapped in local optima, resulting in suboptimal performance.

To address these issues, this paper proposes a new EV charging and discharging optimization scheduling strategy, considering both the grid and user demands, and uses an improved MOPSO algorithm to solve the multi-objective optimization problem. First, a multi-objective optimization model is established to minimize the daily load variance of the distribution network, minimize the user's charging cost, and maximize the total charging amount. The MOIPSO algorithm is used to solve the Pareto front solutions, ensuring that user charging demands are met. Finally, TOPSIS is applied to select the final scheduling scheme, achieving optimal EV scheduling. The proposed strategy and algorithm are validated through simulation examples

II. Electric Vehicle Charging Load Model

A. EV Charging/Discharging Scenario Framework

when EV owners connect their vehicles to charging stations, they submit charging demand information to the dispatch center, including: Vehicle arrival and departure times, Battery State of Charge (SOC) at connection, Target SOC value required to fulfill charging needs. Based on the collected information, the dispatch center formulates individualized charging/discharging schedules for each EV and transmits the operational plans to corresponding EV users.

979-8-3315-5472-9/25/$31.00 ©2025 IEEE

B. Connection/Disconnection Time

The probability density functions of the start and end times of EV charging in residential areas are given by (1):

$$\begin{cases} f_c(x_c) = \sum_{c=1}^{C} a_c exp\left[-\left(x_c - b_c / c_c\right)^2\right] \\ f_d(x_d) = \sum_{d=1}^{D} a_d exp\left[-\left(x_d - b_d / c_d\right)^2\right] \end{cases} \quad (1)$$

where a, b, and c are the peak, peak position, and half-width information of the Gaussian curve, respectively, and the specific parameters are the same as those in Ref[10]. Figure 1 and Figure 2 show the pdfs of the charging start and end times, respectively.

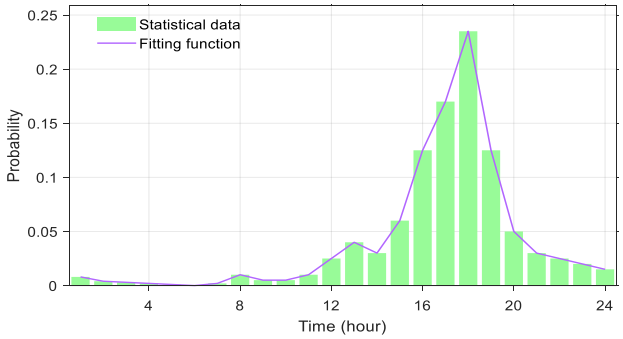


Fig. 1. PDF of the charging start time

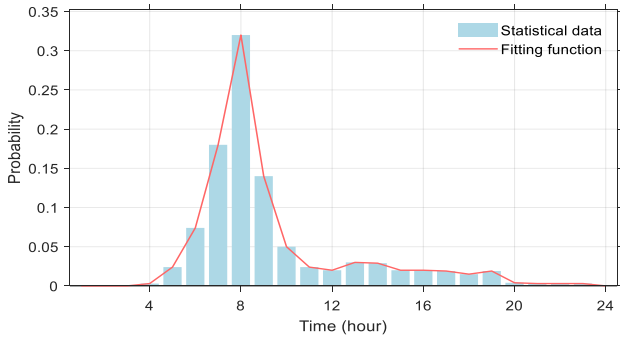


Fig. 2. PDF of the charging end time

C. Parking Duration

There are two situations in which the EV enters the grid and leaves the grid (as shown in Figure 3), the time of entering the grid and the time of leaving the grid are both completed within one day, or the time of connecting to the grid is one day before and the time of leaving the grid is on the second day. the parking time of the vehicle can be expressed as:

$$t_{park,m} = \begin{cases} t_{d,\mathrm{m}} - t_{c,\mathrm{m}}, 1 \le t_{c,\mathrm{m}} < t_{d,\mathrm{m}} \le 24 \\ 24 - t_{c,\mathrm{m}} + t_{d,\mathrm{m}}, 1 \le t_{d,\mathrm{m}} < t_{c,\mathrm{m}} \le 24 \end{cases} \quad (2)$$

Where $t_{park,m}$ is the parking duration of vehicle EV_m, $t_{c,m}$ and $t_{d,m}$ are the grid connection and disconnection times of EV_m.

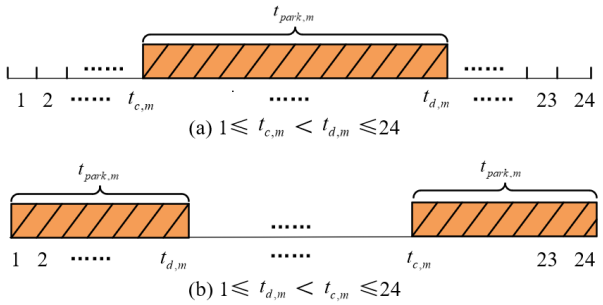


Fig. 3. Two situations of parking time

III. Multi-objective Optimization Model

A. Grid Load Volatility

Smoothing grid load fluctuations can reduce system losses and improve grid stability. An objective function is formulated to minimize the daily load variance, with the charging and discharging power of EVs in each time period being used as control variables.

$$\begin{cases} minf_1 = \sum_{t=1}^{T}\left(P_t^d + \sum_{m=1}^{M} P_{t,m}^{EV} - P_T^{avg}\right)^2 \\ P_T^{avg} = 1/T \sum_{t=1}^{T}\left(P_t^{Fd} + \sum_{m=1}^{M} P_{t,m}^{EV}\right) \end{cases} \quad (3)$$

Where T is the number of periods in a day. P_t^d is the base load of the grid at period. M is the total number of EVs. $P_{t,m}^{EV}$ is the charging/discharging power of EV_m at period, and P_T^{avg} is the average load of the grid over the day.

B. Economic Cost of EV Users

The cyclic charging and discharging of electric vehicles (EVs) leads to battery degradation, which incurs associated costs that must be considered. According to Reference[13], these degradation costs are quantified in (4).

$$\begin{cases} C_{t,m}^{V2G} = \left|\frac{B_m}{100}\right| \times \frac{\Gamma_{t,m}}{C_m} C^B \\ \Gamma_{t,m} = \max\left\{0, \left(SOC_{t-1,m} - SOC_{t,m}\right) C_m\right\} \end{cases} \quad (4)$$

Where B_m is the linear relationship between battery lifespan and cycle count; C_B is the battery replacement cost (¥); $\Gamma_{t,m}$ is the cyclic charging and discharging amount (kWh); SOC_{t-1} and SOC_t are the SOC values of the vehicle at periods $t-1$ and t (ranging from 0.3 to 1); C_m is the battery capacity.

Equation (4) indicates that when the vehicle discharges via V2G at period , it will incur additional battery cycling costs, whereas charging does not contribute to battery degradation costs. To schedule EV user participation in grid interactions, a time-of-use electricity pricing mechanism will be employed. Discharging EVs will generate price difference income for users. Equation (5) represents the objective function aimed at minimizing the owner's total cost.

$$\min f_2 = \sum_{m=1}^{M}\sum_{t=1}^{T}\left(\frac{E_t P_{t,m}^{EV}}{4} + C_{t,m}^{V2G}\right) \quad (5)$$

In the equation, E_t represents the electricity price at period t, ¥/(kWh).

C. Charging Amount of EV Users

To meet the travel needs of owners, the objective function aims to maximize the total energy charged into the EVs.

$$\begin{cases} max\, f_3 = \sum_{m=1}^{M} SOC_m^d \\ SOC_m^d = \eta \cdot \sum_{t=t_{c,m}}^{t_{d,m}} P_{t,m}^{EV} / C_m + SOC_m^c \end{cases} \quad (6)$$

Where, SOC_m^c and SOC_m^d are the SOC of EV_m at the time of departure from and connection to the grid, respectively. η is the charging and discharging efficiency.

D. Constraints

(1) EV State of Charge (SOC) Constraint

To prevent excessive charging and discharging from damaging the battery lifespan, the usable capacity of the battery needs to be constrained:

$$SOC_{\min} \le SOC_{m,t} \le SOC_{\max} \quad (7)$$

Where $SOC_{\max}$ and $SOC_{\min}$ are the upper and lower limits of the battery's SOC, generally set to 1 and 0.3, respectively.

(2) User Travel Demand Constraint

To fulfill the user's travel demands, the battery's SOC at departure should not be lower than the user's desired value $SOC^{\exp}$, and should not exceed the battery's capacity:

$$SOC_m^{\exp} \le SOC_m^d \le 1 \quad (8)$$

(3) Scheduling Time Constraint

The charging and discharging operations can only be scheduled during the EV's parking intervals $t_{s,m}$.

$$t_{c,m} \le t_{s,m} \le t_{d,m} \quad (9)$$

(4) Transformer Capacity Constraint

In any given period, the aggregate load, consisting of the base load and the charging load of all electric vehicles (EVs) connected to the grid, should not surpass the transformer's maximum capacity.

$$P_{load,t} + \sum_{m=1}^{M} P_{t,m} \le S_T \quad (10)$$

IV. MOIPSO Algorithm

PSO is a swarm intelligence optimization algorithm that simulates the social behavior of biological groups, such as bird flocks or fish schools, and seeks the optimal solution through information sharing and collaboration among individuals. In PSO, each individual is called a "particle," which moves through the search space and adjusts its velocity and position based on its own historical best solution and the group's historical best solution. As a variant of PSO, MOPSO inherits the basic characteristics and population update strategy of PSO. The velocity update formula is:

$$v_i^{n+1} = \omega \cdot v_i^n + c_1 r_1 \left(X_{\text{pbest}} - x_i^n\right) + c_2 r_2 \left(X_{\text{gbest}} - x_i^n\right) \quad (11)$$

The position update formula is:

$$x_i^{n+1} = v_i^{n+1} + x_i^n \quad (12)$$

Where n represents the current iteration number; ω is the inertia weight coefficient; c_1 is the individual acceleration factor; c_2 is the group acceleration factor; r_1 and r_2 are random numbers within the range (0, 1), introduced to enhance the stochastic nature of the velocity update; X_{pbest} denotes the individual best position, and X_{gbest} represents the global best position.

A. Dynamic Inertia Weight Coefficient

In the MOPSO algorithm, the inertia weight is a crucial factor in balancing the algorithm's global search capability and local search capability. In the initial stages of iteration, a larger inertia weight can enhance the global search ability of the algorithm, and as the number of iterations increases, a smaller inertia weight can enhance the local search ability. In the traditional linear decrement strategy, the rate of change of the inertia factor remains constant. If no good solutions are found during the iteration, the rapid decrease in inertia weight as iterations accumulate may cause the algorithm to get stuck in a local optimum. This study proposes a nonlinear cubic decay inertia weight strategy that dynamically adjusts based on the number of iterations, as expressed in Equation (13).

$$\omega(n) = \omega_{\max} - \left(\omega_{\max} - \omega_{\min}\right) \cdot \left(\frac{n}{N}\right)^3 \quad (13)$$

Where, $\omega_{\max}$ is the maximum inertia coefficient; $\omega_{\min}$ is the minimum inertia coefficient, n is the current iteration number, and N is the maximum number of iterations.

B. Elite Crossover and Mutation Strategy

As the search space of the population continually shrinks during the iteration process, in order to maintain particle diversity, this paper introduces the crossover and mutation mechanism from genetic algorithms based on the previous improvements. The elite population undergoes crossover and mutation to produce a new population, thus maintaining particle diversity. Specifically, certain variables are reinitialized with a certain probability. Particles participating in the crossover and mutation operations are randomly selected from the existing Pareto front solutions. The crossover and mutation operations are given by the following formulas:

$$\begin{cases} x_{i1}^{n+1} = r_3 \cdot x_{i1}^n + \left(1 - r_3\right) \cdot x_{i1}^n \\ x_{i2}^{n+1} = r_4 \cdot x_{i2}^n + \left(1 - r_4\right) \cdot x_{i2}^n \end{cases} \quad (14)$$

$$x_{i3}^{n+1} = \Delta \cdot r_5 \cdot x_{i3}^n \quad (15)$$

Where, Δ is mutation factor; r_3, r_4 and r_5 are random numbers. The x_i that satisfies the mutation condition will mutate with a

probability p .To better improve the algorithm's optimization ability, a dynamic mutation rate is used.

$$p = (p_{max} - p_{min})\left(1 - \frac{n}{N}\right)^4 \tag{16}$$

In the equation: $p_{\max}$, $p_{\min}$ — the upper and lower bounds of the mutation rate; as the number of iterations increases, the mutation rate p decreases exponentially.

The introduction of the elite crossover and mutation strategy expands the search range of the particles, allowing them to move beyond the previously iterated optimal solution. This expands the search space while maintaining the diversity of the population, increasing the possibility of discovering new solutions.

V. Example Analysis

Taking a typical dual-peak day load of a residential area in North China on a weekday as an example, assume the transformer capacity of the residential area is 800 kVA, with a photovoltaic installation capacity of 200 kW, and the time-of-use electricity prices refer to the typical time-of-use rates for general industrial and commercial users in Beijing. The residential area load and time-of-use electricity prices are shown in Figure 4. Table1 is the electric vehicle parameters.

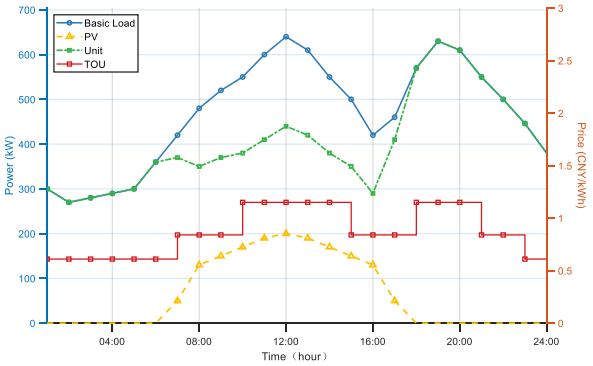


Fig. 4. Residential Area Load and Time-of-Use Electricity Prices

TABLE I. Electric Vehicle Parameters

Parameter	*Value*
Number of Vehicles	50
Battery Capacity	50kW.h
Charging/Discharging Efficiency	0.9
Maximum Charging/Discharging Power	7kW
Initial Battery Charge	N(0.6, 0.1^2)
Battery Replacement Cost	50000

Multi-objective optimization requires balancing multiple objectives to achieve the overall optimal goal. Compared with other solutions, Pareto-optimal solutions that are non-dominated have the least conflict between objectives, providing the decision-maker with a better choice space. To better validate the optimization performance of the MOIPSO algorithm, its obtained Pareto front solutions were compared with those from traditional MOPSO and NSGA-II algorithms. As shown in Figure 5, the distribution range of Pareto solutions obtained by MOIPSO is significantly better than that of traditional methods, and its convergence is closer to the XYZ coordinate axis, demonstrating higher convergence and better diversity.

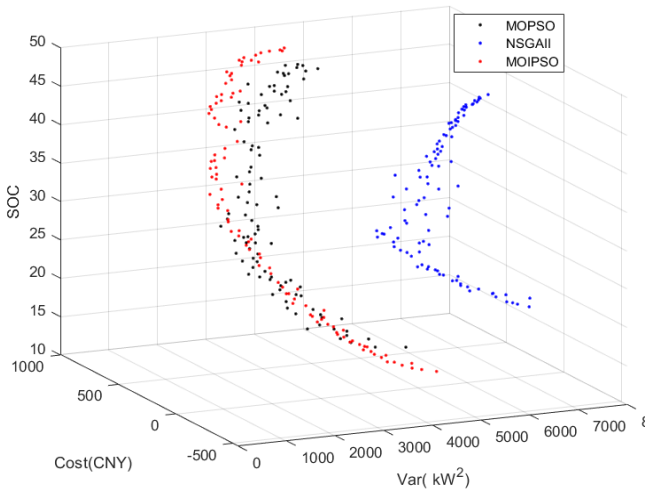
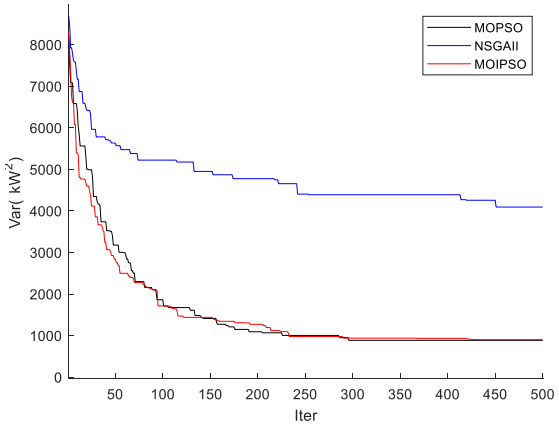
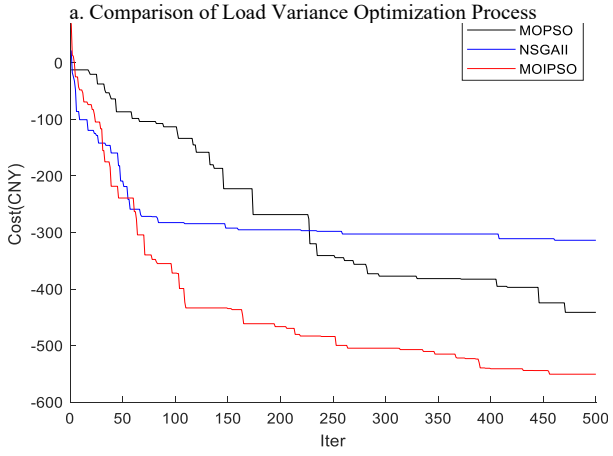


Fig. 5. Pareto Front

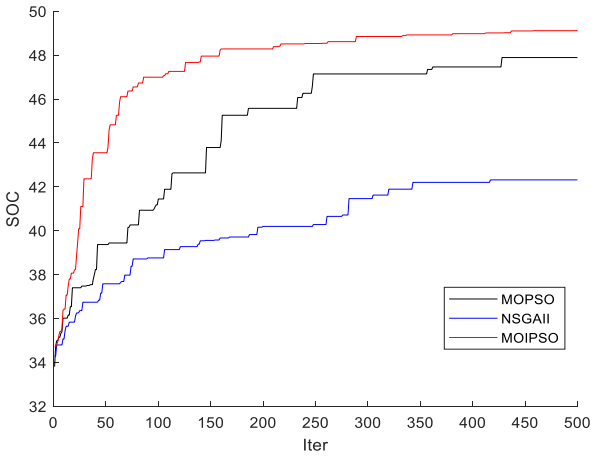
As shown in Figure 6, when optimizing the objectives of minimizing grid load variance, minimizing total charging cost, and maximizing total charging amount, both traditional MOPSO and MOIPSO algorithms outperform NSGA-II overall. In terms of load variance optimization, the two algorithms perform similarly; however, for minimizing charging cost and maximizing charging amount, MOIPSO converges faster and finds higher-quality solutions. This indicates that MOIPSO searches a broader solution space more efficiently, discovering better solutions and effectively enhancing the algorithm's performance.



a. Comparison of Load Variance Optimization Process



b. Comparison of Total Charging Cost Optimization Process



c. Comparison of Total Charging Amount Optimization Process

Fig. 6. Comparison of Optimization Processes for Different Objectives

When selecting the final scheduling scheme, user travel demand is prioritized to ensure the expected charging amount is met. All feasible solutions are evaluated using the TOPSIS method, and the one with the highest score is chosen as the optimal scheduling scheme. The final scheduling result is shown in Figure 7, and the corresponding performance metrics can be found in Scheme 3 of Table 2.

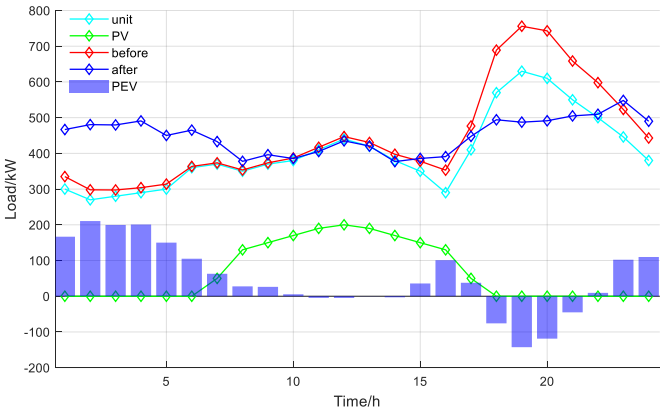


Fig. 7. Final Scheduling Scheme

The average SOC of all EVs upon connection to the grid is 0.5.As shown in Table 2, when the user's expected SOC is 0.9, Scheme 3 is the optimal solution derived from the proposed strategy. Compared with unordered charging, it satisfies user demand while increasing the average off-grid energy to 0.93, achieving a 29.0% reduction in total cost, a 28.4% decrease in load peak, a 39.3% decline in peak-valley difference rate, and an 87.2% reduction in load variance. When the user's expected SOC is 0.8, the optimal scheme is Scheme 2, where the unit charging cost drops to 0.58 CNY/kWh, 8.1% lower than that of Scheme 3, with significant improvements in other performance indicators as well. When the user's expected SOC is further relaxed to 0.6, the optimal scheme becomes Scheme 1, with the unit charging cost further reduced to 0.43 CNY/kWh—much lower than the valley electricity price of 0.61 CNY/kWh. This improvement results from the reduced SOC threshold, which enhances the dispatchability of electric vehicles (EVs), allowing more capacity to discharge during peak periods and generate revenue, thereby effectively lowering the overall charging cost.

These simulation results validate the effectiveness of the proposed strategy under different user expectations and flexibility levels. To further demonstrate its applicability in real-world scenarios, we discuss how the strategy can be deployed in real-time control systems. To ensure that the proposed MOIPSO-based scheduling strategy is practically deployable in real-time smart grid controllers, a rolling-horizon scheduling mechanism can be introduced. Specifically, the charging and discharging plans for electric vehicles (EVs) are formulated sequentially based on their actual arrival times. When multiple EVs arrive within the same scheduling interval, they can be grouped into a scheduling batch for joint optimization. After each scheduling round is completed, the system strictly implements the charging/discharging plans according to the optimization results, and the resulting load information is promptly updated to the global reference load profile, serving as a dynamic constraint for subsequent scheduling. This rolling update mechanism enables the system to dynamically respond to the asynchronous arrival of EVs and continuously adjust the scheduling scheme, thereby achieving a coordinated balance between load regulation and scheduling feasibility.

In addition, the practical effectiveness of the proposed strategy also depends on user willingness to accept lower SOC thresholds, which include both the departure SOC and the minimum SOC allowable during the charging process. From a behavioral economics perspective, EV users typically weigh financial incentives against range anxiety and travel urgency. Therefore, SOC thresholds should be regarded as adaptive parameters jointly determined by economic compensation and travel context. Incorporating probabilistic acceptance models or chance constraints into the scheduling framework provides a preliminary approach to integrate behavioral responses with technical optimization, thereby enhancing system efficiency while safeguarding user satisfaction.

TABLE II. COMPARISON OF SCHEDULING RESULTS FOR DIFFERENT SOLUTIONS

	Expected SOC	*Final SOC*	*Total Cost*	*Load Peak Value*	*Load Peak-Valley Ratio*	*Load Variance*
unit				630.0	0.57	10768.9
Scheme 1	Not Considered	0.71	226.9	478.7	0.22	1110.2
Scheme 2	0.8	0.83	478.1	503.4	0.27	1579.4
Uncoordinated Scheme	0.9	0.90	959.35	756.4	0.61	18831.5
Scheme 3		0.93	681.5	543.1	0.37	2410.4

VI. Conclusion

This study proposes an improved multi-objective particle swarm optimization (MOIPSO) for EV charging scheduling in residential areas. By introducing a cubic decay inertia weight and an elite crossover mutation, the algorithm enhances both convergence and solution diversity. Experiments confirm its advantage over traditional MOPSO and NSGA-II. Nonetheless, the cognitive and social factors remain fixed, and user willingness regarding SOC thresholds has not been fully addressed. Future work will extend parameter adaptation, integrate behavioral acceptance models, and adopt rolling-horizon scheduling to improve robustness and real-time applicability.

References

[1] Y. Li and A. Jenn, "Impact of electric vehicle charging demand on power distribution grid congestion," Proceedings of the National Academy of Sciences of the United States of America, vol. 121, no. 18, Apr. 2024.

[2] X. QI, D. LI and S. JI, "Orderly charging control strategy for electric vehicles in residential area Based on power limitation," Power System Technology, vol.40, no.12,pp 3715−3721,2016.

[3] A. M. Agudin, K. Jaikumar, G. R. C. Mouli, D. Slaifstein, J. Pool and P. Bauer, "Impact of Shared Electric Vehicles Availability to Provide Peak Reduction Through Vehicle-to-Grid. A Case Study," IECON 2023- 49th Annual Conference of the IEEE Industrial Electronics Society, Singapore, Singapore, 2023, pp. 1-6.

[4] K. Zhou, L. Cheng, L. Wen, X. Lu, and T. Ding, "A coordinated charging scheduling method for electric vehicles considering different charging demands," Energy, vol. 213, p. 118882, Dec. 2020.

[5] L. Liu and K. Zhou, "Electric vehicle charging scheduling considering urgent demand under different charging modes," Energy, vol. 249, pp. 123714, Jun. 2022.

[6] Wu W., Lin Y., Liu R., Li Y., Zhang Y., Ma C.Online EV charge scheduling based on time-of-use pricing and peak load minimization: Properties and efficient algorithms IEEE Trans Intell TranspSyst , 23 (1) (2020),pp. 572586, 10.1109/TITS.2020.3014088.

[7] Q. Chen, W. Wang, H. Wang, Y. Dong, and S. He, "Information gap-based coordination scheme for active distribution network considering charging/discharging optimization for electric vehicles and demand response," International Journal of Electrical Power & Energy Systems, vol. 145, pp. 108652–108652, Feb. 2023.

[8] H. Morais, T. Sousa, R. Castro, and Z. Vale, "Multi-Objective Electric Vehicles Scheduling Using Elitist Non-Dominated Sorting Genetic Algorithm," Applied Sciences, vol. 10, no. 22, pp. 7978, Nov. 2020.

[9] K. Pan, C.D. Liang, and M. Lu, "Optimal scheduling of electric vehicle ordered charging and discharging based on improved gravitational search and particle swarm optimization algorithm," International Journal of Electrical Power & Energy Systems, vol. 157, pp. 109766–109766, Jan. 2024.

[10] L. Zhang, C. Sun, G. Cai, N. Huang, L. Lv,"Two-stage optimization strategy for coordinated charging and discharging of EVs based on PSO algorithm,"Proc CSEE, vol. 54, no. 5, pp. 1837–1852, 2022.

[11] N. Wang, B. Li, Y. Duan, and S. Jia, "A multi-energy scheduling strategy for orderly charging and discharging of electric vehicles based on multi-objective particle swarm optimization," Sustainable Energy Technologies and Assessments, vol. 44, pp. 101037, Apr. 2021.

[12] W. Yin, W. Liang, and J. Ji, "Study on charge and discharge control strategy of improved PSO for EV," Energy, vol. 304, pp. 132061, Sep. 2024.

[13] J. Neubauer and E. Wood, "The impact of range anxiety and home, workplace, and public charging infrastructure on simulated battery electric vehicle lifetime utility," Journal of Power Sources, vol. 257, pp. 12–20, Jul. 2014.

Economic Analysis of Replacing a Combustion Vehicle with an Electric Vehicle Supported by Residential Photovoltaic Systems in Brazil

Daywes Pinheiro Neto[1], Isabela Lopes Magalhães[1], Thiago Augusto Mendes[1], Letícia Chaves Ucker[1], António Paulo Coimbra[2], Pedro Moura[2], Aníbal Traça de Almeida[2]
[1]Center for Experimental and Technological Research and Studies, Federal Institute of Goiás, Brazil
[2]Institute of Systems and Robotics, Dpt. of Electrical and Computer Engineering, University of Coimbra, Portugal
{daywes.neto, thiago.mendes, leticia.chaves}@ifg.edu.br, magalhaes.isabela@estudantes.ifg.edu.br, {acoimbra, pmoura, adealmeida}@isr.uc.pt

***Abstract*—This study assesses the economic viability of replacing conventional internal combustion vehicles with electric vehicles (EVs) in a residential context, considering the use of photovoltaic (PV) systems. A case study for a residence in Goiânia, Brazil, was performed, analyzing Net Present Value (NPV) sensitivity to daily vehicle mileage and PV system size. Results show that, without a PV system, economic viability is achieved for daily mileage above 35km. Incorporating a 3 kWp PV system reduces the minimum required daily mileage to 26km. Furthermore, for this daily mileage, optimal PV sizing corresponds to 4.9 kWp, significantly improving NPV. These results highlight the economic advantages of combining EV adoption with residential PV systems to enhance financial outcomes.**

Keywords—Electric vehicles, combustion vehicles, photovoltaic systems, economic analysis, net metering system

I. Introduction

The Brazilian automotive sector is undergoing a gradual transition towards electrification. Although electric vehicles (EVs) have been increasing in number, they still represent a small fraction of the national vehicle fleet, primarily due to high acquisition costs and limited integration with renewable energy sources [1]–[3]. Government initiatives, including tax incentives and financing programs, aim to promote cleaner mobility and reduce reliance on fossil fuels [4]. However, a comprehensive understanding of the economic feasibility of replacing conventional internal combustion vehicles (ICEVs) with EVs, particularly when integrated with solar photovoltaic (PV) systems, remains limited.

Globally, the adoption of EVs is influenced by vehicle type, energy consumption characteristics, and the availability of supporting infrastructure. Battery Electric Vehicles (BEVs), Plug-in Hybrid Electric Vehicles (PHEVs), and Hybrid Electric Vehicles (HEVs) differ in terms of energy demand and potential integration with renewable sources. Similarly, PV system deployment strategies, including system sizing and net metering arrangements, play a significant role in determining economic outcomes [5], [6].

In Brazil, the regulatory framework supports distributed generation and net metering, allowing EV owners and PV system operators to offset electricity costs by injecting surplus energy into the grid [4], [7]. Programs such as Rota 2030 and BNDES's Plano Inova Energia encourage the adoption of renewable energy and cleaner transportation technologies [8]. Despite these initiatives, studies focusing on the combined economic impact of vehicle substitution and PV integration remain scarce, particularly considering local energy prices and net metering benefits.

Previous studies have investigated the role of EVs within Brazil's transportation sector, highlighting their environmental and technical benefits. Research by [9] and [10] points out that EVs can contribute to reduced gasoline consumption and can complement vehicles running on biofuels, emphasizing the relevance of a diversified energy mix. Furthermore, [11] examines the effects of EV adoption relative to other fuel types. Studies by [12] and [13] address the environmental impacts of EVs, assessing their influence on CO_2 emissions, overall energy use, and lifecycle performance in the Brazilian context.

Despite some preliminary economic analyses by [3], [6], and [14] there is a notable gap in the literature regarding the economic viability of replacing ICEVs with EVs in Brazil when supported by residential PV systems. Few studies evaluate the financial outcomes under local net metering regulations, and sensitivity analyses on key parameters such as PV capacity and daily vehicle mileage remain scarce.

This study addresses this gap by presenting an economic analysis of replacing ICEVs with EVs supported by residential PV systems in Brazil. The evaluation is based on the Net Present Value (NPV) and includes sensitivity analyses on key parameters such as PV system capacity and daily vehicle mileage. The analysis highlights how the combination of EV adoption and appropriately sized PV systems can improve financial outcomes, reduce reliance on conventional fuel, and support the transition to sustainable personal mobility under the current net metering framework.

II. Methodology

This section describes the approach for evaluating the economic viability of replacing a ICEV with an EV supported by a PV system in Brazil. The analysis considers the NPV and incorporates sensitivity analyses on critical parameters, including PV system capacity and daily vehicle mileage.

979-8-3315-5472-9/25/$31.00 ©2025 IEEE

Figure 1 illustrates the overall process, from data input to the calculation of economic indicators. Each step shown in the flowchart is detailed in the following subsections.

A. Electric Vehicle Monthly Energy Consumption

The monthly energy consumption of an EV can be estimated based on daily mileage, vehicle efficiency, and the number of days in the month:

$$E_{EV,m} = M_{daily} \cdot \eta_{EV} \cdot N_{days,m} \quad (1)$$

where $E_{EV,m}$ is the monthly energy consumption (kWh), M_{daily} is the daily mileage (km), η_{EV} is the vehicle's specific energy consumption (kWh/km), and $N_{days,m}$ is the number of days in month m.

B. PV Generation

The monthly energy generated by the PV system is calculated using Equation (2).

$$G_{PV,m} = P_{PV,m} \cdot \left(\frac{I_{avg,m}}{I_{ref}}\right) \cdot PR \cdot (1 - \delta_{PV})^{m-1} \cdot N_{days,m} \quad (2)$$

where $G_{PV,m}$ is the PV generation (kWh) in month m, $P_{PV,m}$ is the nominal power of the PV system (kW) in month m, $I_{avg,m}$is the average daily solar irradiation received at the panel plane (kWh/m^2/day), I_{ref} is the reference solar irradiance (1 kW/m^2) in STC[1], PR is the Performance Ratio[2], and δ_{PV} is the annual degradation factor[3] of the PV system.

C. Net Metering System

In Brazil, distributed generation systems are allowed to inject surplus energy into the utility grid and receive creditsthat can be used to offset consumption in subsequent billing periods, according to the regulations established by [7]. Under this net metering scheme, the energy generated by a PV system can either be consumed directly or exported to the grid, with the resulting credits reducing future electricity bills.

The vast majority of residential consumers in Brazil are billed under the conventional flat tariff, in which the energy cost does not vary by time of day. In this case, the monthly energy balance is calculated by comparing the energy exported to the utility grid E_{exp} with the energy imported from the grid E_{imp}, while also accounting for the minimum charge (MC). Brazilian regulations establish mandatory minimum consumption charges: 30 kWh for single-phase, 50 kWh for two-phase, and 100 kWh for three-phase connections. If actual consumption is lower than these values, the consumer is billed for the minimum; if it is higher, the bill reflects the actual consumption [16].

The resulting electricity bill depends on the balance between imported and exported energy: If $E_{exp,m} > E_{imp,m}$, the surplus is stored in a credit bank for future use. The bill in this case includes only the minimum charge (MC). If $E_{exp,m} = E_{imp,m}$, the consumption is fully offset. The net energy cost is zero, and the bill includes only MC. If $E_{exp,m} < E_{imp,m}$, the deficit is supplied by the grid. Any previously stored credits are redeemed to reduce the imported energy, and the bill includes the remaining net energy plus MC. In this case, the redeemed credits are subject to the Distribution System Usage Tariff (DSUT).

Formally, the monthly electricity bill is calculated as:

$$B_m = \left(E_{imp,m} - R_m\right) \cdot T_E + R_m \cdot DSUT \quad (3)$$

where B_m is the electricity bill in month m (USD), $E_{imp,m}$ is the imported energy (kWh), R_m is the redeemed credit (kWh), T_E is the energy tariff (USD/kWh), and DSUT is the distribution system usage tariff applied to redeemed credits.

The evolution of the credit balance is given by:

$$C_m = C_{m-1} + E_{exp,m} - R_m \quad (4)$$

where C_m is the available credit balance at the end of month m, C_{m-1} is the credit balance from the previous month, and $E_{exp,m}$ is the exported energy to the grid in month m.

Finally, the amount of redeemed credits is constrained by the available balance:

$$R_m \leq \min\left(E_{imp,m},\ C_{m-1} + E_{exp,m}\right) \quad (5)$$

D. Cash Flow

The cash flow provides a detailed view of financial inflows and outflows over time. Based on a wide range of parameters, such as gross revenue, operating costs, maintenance expenses, initial investments, and other expenditures, it is possible to determine the net balance for each period. The structure of the cash flow is illustrated in Table I.

TABLE I. CASH FLOW MODEL.

(+) Gross revenues
Electricity bill savings
Fuel savings
EV maintenance savings
EV vehicle tax (IPVA) savings
Residual value of the PV system
(-) Operating costs
PV system maintenance
(=) Net operating profit
(-) Investment costs
Cost difference between EV and ICEV
PV system cost
PV inverter replacement
(=) Net cash flow

[1] Standardized Test Conditions: Irradiance 1000 W/m², AM 1.5 spectrum, temperature T=25ºC [15].

[2] PR reflects system losses, typically between 0.75 and 0.85, due to inefficiencies and environmental factors [16].

[3] δ_{PV} represents the decline in system efficiency over time due to material wear, component degradation, and environmental exposure [16].

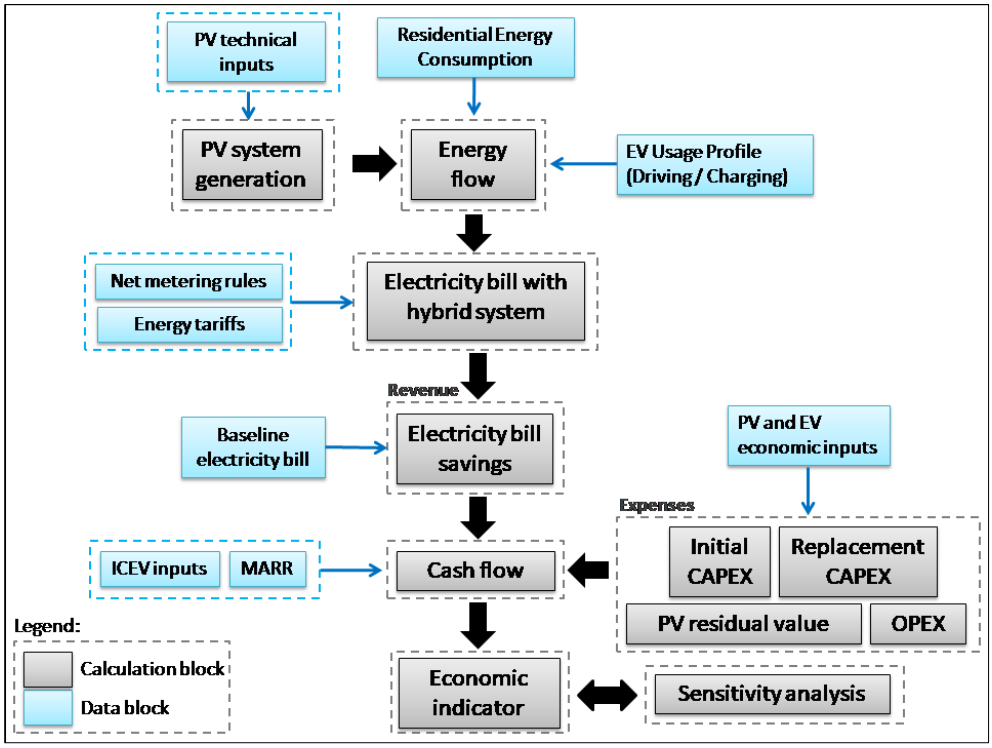


Fig. 1. General flowchart of the economic analysis process.

Gross revenue consists of three components: (i) savings on the electricity bill due to the PV system, (ii) fuel savings from the EV, and (iii) savings in EV maintenance and vehicle tax (IPVA[4]).

The revenue from electricity bill savings is obtained directly as the difference between the user's current Bill ($B_{CURRENT,m}$), without the PV system and without the EV, and the future bill ($B_{PV,EV,m}$) considering the installation of the PV system and acquisition of the EV, as expressed in Equation (6).

$$R_{PV,EV,m}^{bill} = B_{CURRENT,m} - B_{PV,EV,m} \quad (6)$$

Another source of revenue comes from fuel savings achieved by using an EV, compared to the fuel costs of na ICEV for the same monthly mileage. This is given by Equation (7), where $R_{EV,m}^{fuel}$ is the revenue from fuel savings in month m, M_m is the user's monthly mileage (km) $C_{fuel,ICEV}$, is the fuel cost per liter of the ICEV used for comparison (USD/L), and γ_{ICEV} is the specific fuel consumption of the ICEV (km/L).

$$R_{EV,m}^{fuel} = \frac{M_m}{\gamma_{ICEV}} \cdot C_{fuel,ICEV} \quad (7)$$

E. Initial Investment

Expenses consist of the initial investment for acquiring the PV system and the difference between the purchase costs of the EV and the ICEV, as well as costs related to PV system installation and integration, including EV charging equipment (e.g., wallbox).

[4] IPVA is the annual Motor Vehicle Property Tax in Brazil, levied on vehicle ownership.

Major cost components of the PV system include solar panels, inverters, mounting structures, monitoring systems, specialized labor for installation, cabling, circuit breakers, distribution panels, and other components necessary for a safe grid connection. Additional expenses cover documentation, permits, regulatory fees, and preventive and corrective maintenance to ensure efficient system operation over time.

For the cash flow analysis, considering the replacement of an ICEV with an EV, the required investment for acquiring the EV is determined by the difference between the EV purchase price and the current value of the ICEV, as expressed in Equation (8), where $I_{EV}^{purchase}$ is the net investment for acquiring the EV, C_{EV} is the EV purchase price, and V_{ICEV} is the current value of the ICEV.

$$I_{EV}^{purchase} = C_{EV} - V_{ICEV} \quad (8)$$

When comparing an EV with an ICEV, it is important to consider not only the direct purchase costs but also savings from maintenance and vehicle taxes (IPVA). EVs generally have lower maintenance costs due to simpler mechanics and fewer moving parts. Additionally, in some Brazilian states, EVs benefit from exemptions or reductions in IPVA. The revenue from these savings is calculated as shown in Equation (9), where M_{ICEV} and M_{EV} are the maintenance costs, and $IPVA_{ICEV}$ and $IPVA_{EV}$ are the vehicle taxes for the ICEV and EV, respectively.

$$R_{EV}^{maint,tax} = M_{ICEV} - M_{ICEV} + IPVA_{ICEV} - IPVA_{EV} \quad (9)$$

For analysis periods shorter than the PV system's lifetime, typically 20 – 30 years, the cash flow includes in the final year a capital inflow corresponding to the system's residual value. If the analysis period exceeds the EV battery lifetime, usually 8

– 15 years, the cost of battery replacement is considered. Likewise, if the period exceeds the lifetime of the PV inverter, typically 10 – 15 years, the cost of replacing the PV inverter is also considered.

F. Economic Indicator

The economic indicator NPV is derived from the cash flow analysis and is used to assess the financial viability of the project. NPV assesses the value of future cash flows by converting them into present terms using a discount rate, set at 15% per year for this analysis, corresponding to the Minimum Acceptable Rate of Return (MARR).

The NPV is calculated according to Equation (10), where CF_m is the cash flow in month m (USD), n is the total number of months in the analysis period, and $MARR$ is the monthly discount rate (%) [16]. A positive or zero NPV indicates that the project is economically viable.

$$NPV = -I + \sum_{m=1}^{n} \frac{CF_m}{(1+MARR)^m} \quad (10)$$

G. Sensitivity Analysis

Sensitivity analysis evaluates how variations in key parameters affect project NPV. Two parameters are considered: PV system nominal power (kWp) and daily mileage in electric mode (km). Each parameter is varied individually while keeping others constant to identify ranges that ensure economic viability and optimal sizing.

III. RESULTS

This section presents the results of the economic analysis for replacing ICEVs with EVs supported by PV systems in Brazil. A case study was selected for a residential building located in Goiânia, Goiás, Brazil (coordinates: -16.757199, -49.338052). Table II summarizes the main electricity bill data for the conventional flat tariff used in the analysis.

Table III summarizes the main technical and economic data of the PV system used in the analysis.

Table IV presents the general technical and economic data of the EV considered in the analysis. The EV charging occurs during the night, from 7 p.m. to 6 a.m. the next morning.

It is important to highlight that, although the methodology considers possible component replacements depending on the analysis period, in this specific case the analysis horizon was set at 15 years. Therefore, no PV inverter or EV battery replacement is required, since both components have an expected lifetime equal to this period.

TABLE II. ENERGY BILL DATA: CONVENTIONAL FLAT TARIFF.

General data	
Installation Type	Three-phase
Tariff Type	Conventional Flat
Average Monthly Bill (USD)	94.63
Energy Tariff (USD/kWh)	0.19
$TUSD_{wireB}$ (USD/kWh)	0.06
Monthly Consumption Data (kWh)	
January	482
February	498
March	513
April	527
May	541
June	562
July	551
August	534
September	516
October	508
November	493
December	487

TABLE III. TECHNICAL AND ECONOMIC DATA OF THE PV SYSTEM.

Technical Data	
Average Solar Irradiance at 17o Tilt (kWh/m2/day)	5.247
Nominal Power (kWp)	0 – 10
Performance Ratio (%)	80
Annual Degradation Rate (%)	1
System Lifetime (years)	25
Inverter Lifetime (years)	15
Simultaneous Residential Consumption (%)	35
Economic Data	
Total System Cost (USD/kWp)	731.26
Inverter Replacement Cost (USD/kWp)	164.53
Annual Maintenance Cost (USD/year)	27.42

TABLE IV. ELECTRIC VEHICLE DATA.

Technical Data	
Vehicle Type	BYD Dolphin Mini
Daily Mileage (km)	0 – 100
Conversion Efficiency (kWh/km)	0.14
Battery Capacity (kWh)	38
Charge/Discharge Power Limit (kW)	6.6
Charge Efficiency (%)	90
Discharge Efficiency (%)	90
Minimum State of Charge (%)	20
Maximum State of Charge (%)	80
Lifetime (years)	15
Economic Data	
Electric Vehicle Cost (USD)	21,919.56
Annual Maintenance (USD/year)	639.85
Annual Vehicle Tax - IPVA (USD/year)	292.50
Annual Insurance (USD/year)	639.85

TABLE V. INTERNAL COMBUSTION VEHICLE DATA.

Internal Combustion Vehicle Cost (USD)	14,625.23
Annual Maintenance (USD/year)	822.67
Annual Vehicle Tax - IPVA (USD/year)	438.76
Annual Insurance (USD/year)	457.04
Fuel Price (USD/L)	1.19
Fuel Efficiency (km/L)	11

Table V presents the technical and economic data for the ICEV used in the analysis.

As shown in Figure 2, the sensitivity analysis of NPV as a function of daily mileage demonstrates that feasibility is achieved for values above 35 km in the case without the PV system. Table VI presents the corresponding NPV values for selected daily mileage values.

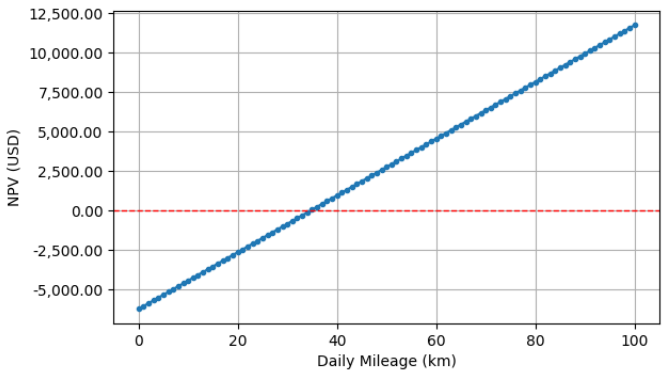


Fig. 2. Sensitivity of NPV to daily mileage for the case without PV system.

TABLE VI. NPV FOR DIFFERENT DAILY MILEAGE VALUES.

Daily Mileage (km)	NPV (USD)
0	-6225.04
10	-4427.45
20	-2629.86
30	-832.27
40	965.32
50	2762.91
60	4560.50
70	6358.09
80	8155.68
90	9953.27
100	11750.86

Figure 3 presents the sensitivity of NPV to daily mileage for the case with a 3 kWp PV system. In this scenario, the daily mileage required to achieve economic viability decreases to 26 km. Table VII shows the corresponding NPV values for selected daily mileage values.

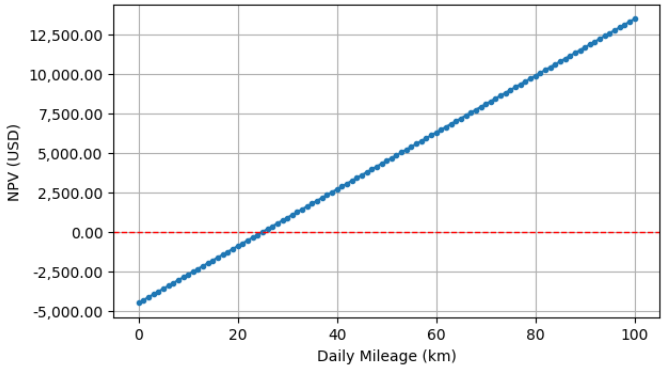


Fig. 3. Sensitivity of NPV to daily mileage for the case with a 3 kWp PV system.

Figure 4 presents the sensitivity of NPV to PV system size for a daily mileage of 26 km. Table VIII shows the corresponding NPV values for integer PV system sizes from 0 to 10 kWp. The results indicate a significant improvement in NPV, with an optimal PV capacity of 4.9 kWp.

TABLE VII. NPV FOR DIFFERENT DAILY MILEAGE VALUES WITH A 3 KWP PV SYSTEM

Daily Mileage (km)	NPV (USD)
0	-4491.06
10	-2693.47
20	-895.88
30	901.71
40	2699.30
50	4496.89
60	6294.48
70	8092.07
80	9889.66
90	11687.25
100	13484.84

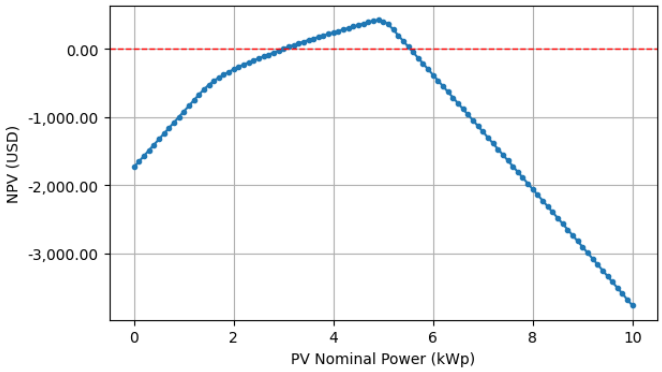


Fig. 4. Sensitivity of NPV to PV system size for a daily mileage of 26 km.

TABLE VIII. NPV VALUES FOR SELECTED PV SYSTEM SIZES (DAILY MILEAGE OF 26 KM).

Daily Mileage (km)	NPV (USD)
0	-1551.30
10	-1062.73
20	-347.94
30	68.36
40	309.14
50	551.54
60	254.77
70	-659.22
80	-1413.47
90	-2341.16
100	-3109.36

Table IX presents the summary of PV system size sensitivity analysis. The results show that the project is economically viable for PV capacities between 2.4 kWp and 5.9 kWp, with an optimal size of 4.9 kWp, corresponding to the maximum NPV of approximately 610.50 USD.

TABLE IX. SUMMARY OF PV SYSTEM SIZE SENSITIVITY ANALYSIS

Optimal PV Size (kWp)	Optimal NPV (USD)	Minimum Viable Size (kWp)	Maximum Viable Size (kWp)
4.9	610.50	2.4	5.9

IV. CONCLUSION

This study presents an economic analysis of replacing na ICEV with an EV supported by a residential PV system in Brazil, under the current net metering regulations. The results show that both daily mileage and PV system size are key factors for project viability. Without PV integration, feasibility

is achieved only for daily mileage above 35 km, indicating the importance of sufficient EV utilization to offset its higher upfront cost.

With a 3 kWp PV system, the minimum daily mileage required for viability decreases to 26 km, highlighting the financial benefits of self-consumption of PV-generated electricity. Further sensitivity analysis for a daily mileage of 26 km indicates an optimal PV capacity of approximately 4.9 kWp, which maximizes NPV.

These results demonstrate the synergistic effect of combining EV adoption with appropriately sized PV systems: PV generation reduces electricity costs, increases self-consumption, and enhances the economic attractiveness of EVs even for moderate daily usage. Moreover, net metering regulations support improved financial performance of distributed generation combined with EV charging. Overall, the study provides evidence that integrating PV systems with EVs can significantly increase energy cost savings, reduce dependence on conventional fuel, and support the transition to sustainable urban mobility in Brazil.

FUNDING

This research is funded by Brazilian institutions, including the National Council for Scientific and Technological Development (CNPq) under Grant 442737/2023-8 and by the Research Support Foundation of the State of Goi´as (FAPEG), Brazil.

REFERENCES

[1] IEA, “Global EV outlook 2024,” tech. rep., Paris, 2024.

[2] Brazil - Ministry of Transport, “Statistics - Vehicle fleet - SENATRAN,” 2024 (in portuguese). Available at: https: //www.gov.br/transportes/pt-br/assuntos/transito/conteudo-Senatran/ estatisticas-frota-de-veiculos-senatran.

[3] D. da Costa and V. R. M. Cobas, “Electric vehicles charged with solar-PV: A Brazilian case study for 2030,” Vehicles, vol. 5, no. 4, pp. 1743–1759, 2023.

[4] C. B. Rosa, M. B. Francescatto, A. L. Neuenfeldt Júnior, D. P. Bernardon, and L. L. C. dos Santos, “Regulatory analysis of e-mobility for Brazil: A comparative review and outlook,” Utilities Policy, vol. 84, p. 101638, 2023.

[5] P. Aduama, A. S. Al-Sumaiti, and K. H. Al-Hosani, “Electric vehicle charging infrastructure and energy resources: A review,” Energies, vol. 16, no. 4, 2023.

[6] N. Berhorst, M. Hino, M. Penteado, L. Galvis, D. M. Gotardo, M. Zanardini, R. Santos, L. N. Canha, and F. Marques, “Business model andeconomic feasibility of electric vehicle fast charging stations with pho-tovoltaic electric generation and battery storage in brazil,” in *AdvancedTechnologies in Electric Vehicles*, pp. 323–343, Academic Press, 2024.

[7] Brazil,“Lawno.14,300,January6,2022.”OfficialJournaloftheUnion,January2022.Availableat:http://www.planalto.gov.br/ccivil03/ato2019-2022/2022/lei/L14300.htm.

[8] M. A. Schvartz, A. Lange Salvia, L. Londero Brandli, W. Leal Filho,and L. Veiga Avila, “The electric vehicle market in brazil: A systematicliteraturereviewoffactorsinfluencingpurchasedecisions,”*Sustainabil-ity*, vol. 16, no. 11, 2024.

[9] R.BaranandL.F.L.Legey,“Theintroductionofelectricvehiclesin Brazil: Impacts on oil and electricity consumption,” *TechnologicalForecasting and Social Change*, vol. 80, no. 5, pp. 907–917, 2013.

[10] G. G. Dranka and P. Ferreira, “Electric vehicles and biofuels synergiesin the Brazilian energy system,” *Energies*, vol. 13, no. 17, 2020.

[11] M.V.X.Dias,J.Haddad,L.HortaNogueira,E.daCostaBortoni, R. A. Passos da Cruz, R. Akira Yamachita, and J. L. Goncalves, “Theimpact on electricity demand and emissions due to the introduction ofelectriccarsintheSa˜oPaulopowersystem,”*EnergyPolicy*,vol.65,pp.298–304, 2014.

[12] A.C.R.TeixeiraandJ.R.Sodre´,“Simulationoftheimpactsoncarbondioxide emissionsfromreplacementofaconventionalBraziliantaxifleetbyelectricvehicles,”*Energy*,vol.115,pp.1617–1622,2016.SustainableDevelopment of Energy, Water and Environment Systems.

[13] E. F. Choma and C. M. L. Ugaya, “Environmental impact assessmentofincreasingelectricvehiclesintheBrazilianfleet,”*JournalofCleanerProduction*, vol. 152, pp. 497–507, 2017.

[14] D.P.Neto, A. P.Coimbra, A. T. De Almeida,T. R. Almeida,P. Moura, L. C. Ucker, R. A. Gomes, and A. S. Magalha˜es, “A comprehensivemethodology for assessing the economic viability of ev charging infrastructure in brazil,”in*2024 6th International Conference on Smart Power Internet Energy Systems (SPIES)*, pp. 232–238, 2024.

[15] D. P. Neto, E. G. Domingues, A. P. Coimbra, A. T. de Almeida, A. J.Alves, and W. P. Calixto, “Portfolio optimization of renewable energyassets: Hydro, wind, and photovoltaic energy in the regulated market inBrazil,” *Energy Economics*, vol. 64, pp. 238–250, 2017.

[16] A. X. C. de Jesus, D. P. Neto, and E. G. Domingues, “Computationaltool for technical-economic analysis of photovoltaic microgeneration inBrazil,” *Energy*, vol. 271, p. 126962, 2023.

Multi-objective Optimization Strategy of Electric Vehicle Charging and Discharging Based on User Demand Response and Stackelberg Game

Sheng Li
School of Automation and Electronic Information
Xiangtan University
Xiangtan, China
3067265199@qq.com

Yonghong Lan
School of Automation and Electronic Information
Xiangtan University
Xiangtan, China
yhlan@xtu.edu.cn

Zhouzhou Xu
Hunan Jiangye Electromechanical Technology Co., Ltd.
Xiangtan, China
1453211218 @qq.com

Hong Lei
School of Automation and Electronic Information
Xiangtan University
Xiangtan, China
2455234527@qq.com

***Abstract*—To address the issues of load overload and excessive peak-valley load difference caused by large-scale integration of electric vehicles (EV) into distribution networks and their interactions, this paper proposes a Stackelberg game-based EV charging-discharging strategy that considers both the charging-discharging storage facility operator (CDSFO) and users' elastic demand response. Unlike existing research, this study considers EV discharge and introduces virtual SOC to pre-calculate the optimization results, thereby reducing the user 's charging cost and whether to respond to the charging and discharging strategy. First, the load characteristics of residential communities and user travel behaviors are analyzed, and CDSFO scenarios are established. Then, a user charging-discharging demand response model is developed, and a multi-objective optimization scheduling model is constructed to maximize the respective benefits of CDSFO and EV users. Users can autonomously respond by selecting different weights based on demand response reference values to satisfy both travel needs and discharging requirements. Finally, simulations were conducted on a residential community distribution grid, verifying that the optimized scheme reduces charging costs and mitigates peak-valley load differences in the distribution network, while ensuring maximum benefits for both CDSFO and EVs users.**

Keywords—demand response, Stackelberg game, mixed-integer linear programming

I. INTRODUCTION

Driven by the dual forces of industrial economic transformation and the rapid promotion of new energy vehicle technology, the number of electric vehicles (EV) in China has experienced rapid growth [1], [2]. By the end of 2024, the number of new energy vehicles in China was approximately 31.4 million [3]. In the context of the large-scale popularization of EVs, their potential as flexible load resources for grid response is attracting widespread attention [4], [5].With the development of V2G (Vehicle-to-Grid) technology, EV can interact with the grid through on-board bidirectional chargers [6]. However, due to the low power output of individual EVs and the randomness of users' travel times and locations, the prediction accuracy of EV cluster load is relatively low [7], which will increase the difficulty of grid control, reduce voltage quality, and decrease the stability of the power system [8], [9]. Therefore, it is very necessary to adopt effective scheduling strategies to reasonably guide the charging behavior of EV.

Given the randomness and unpredictability of EV users' charging behaviors, reference [10] proposed a two-stage optimization strategy for charging and discharging of electric vehicles based on particle swarm optimization, considering elastic demand response. Users can autonomously respond according to the reference values of charging and discharging demand response. Reference [11] proposed a multi-EVA integrated large-scale EV integration into the power market for bidding, and use the bidding results to guide the charging and discharging of the EV, providing a flexible and effective scheduling solution for EVs to participate in peak load reduction and valley filling of the power grid. Reference [12] proposed a hierarchical and refined peak shaving strategy for urban distribution networks based on partitioned combinability and master-slave game, guiding the charging and discharging behavior of electric vehicles through the formulation of reasonable charging and discharging prices. The above literature analyzed the correlation between vehicle characteristics and charging behavior, and established a scheduling strategy with engineering practical value. If the battery charging station, conversion station and storage system are integrated into a charging-discharging-storage facility operator (CDSFO) based on the guidance of EV charging behavior [13], [14], the power supply capacity of the EV charging station can be enhanced, peak shaving and valley filling of the power grid can be achieved, the power quality can be optimized, and the economic benefits of the charging station and EV users can be significantly improved. Literature [15] combines the advantages of charging stations, conversion stations and energy storage stations, enabling the battery system to interact bidirectionally with the power grid, providing energy supply for EVs and auxiliary services such as peak shaving and valley filling, reactive power compensation, harmonic control, and emergency support for the power grid. Literature [16] proposes a two-stage robust optimization scheduling model that comprehensively considers the charging-discharging-storage facility operator of electric vehicles and the active distribution network. The total operating cost of the system is significantly reduced. However, the above studies did not consider the willingness of users to participate in the coordinated charging and discharging during the optimization process.

This paper proposes an optimization scheduling strategy for the interaction between CDSFO and EV considering user

979-8-3315-5472-9/25/$31.00 ©2025 IEEE

demand response. A multi-objective stackelberg game model is constructed, aiming to maximize the revenue of CDSFO and minimize the cost and maximize the electricity consumption of EV users. This strategy takes CDSFO as the main entity and uses the game price to guide both parties. It achieves the optimal charging and discharging strategy while meeting the user demand response. Finally, a simulation is conducted using a residential community as an example to verify the effectiveness of the proposed scheme.

II. Load Characteristics of Residential Communities and CDSFO Scenarios

A. Residents' Travel Behavior

The EV commuting behavior of urban residential residents shows significant spatiotemporal regularity: During the working day period, the user group generally migrates from the residential area to the industrial and commercial area from 07:00 to 08:00. During the lunch break, only a small number of users have a brief return trip, and most users concentrate on returning from 19:00 to 21:00. Based on the above population mobility characteristics, this study sets the charging cycle as a single-day single-charge mode, and the charging time period is at night; the departure/return time points automatically trigger the on/off operation of the charging facilities.

The key parameters of EV charging behavior (charging start time, end time, and initial battery state of charge SOC) satisfy statistical independence, and their joint probability model is constructed by fitting the empirical data of vehicle travel in a certain residential area in Shenzhen [17]. The specific parameterization is as follows: the charging start time follows a normal distribution N(19.55,2.06), the end time follows N(7.25,0.92), and the initial SOC follows a uniform distribution U(0.2,0.7). This study uses the Monte Carlo method to randomly sample the above distributions and generate an EV charging time sequence simulation dataset that conforms to the actual behavior characteristics.

B. CDSFO Scenario Setup

Based on the charging and discharging characteristics of CDSFO, this paper sets four behaviors during the peak, flat, and off-peak periods of system load: the storage behavior of purchasing electricity in the day-ahead market, the purchase behavior of purchasing electricity from EVs during peak load periods, the discharge behavior of selling electricity to the grid side, and the charging behavior of EVs within CDSFO.

This paper sets CDSFO to operate in dual modes in various scenarios. When the distribution network is in normal or low-load operation, CDSFO charges first. After meeting the EV charging demand, its storage behavior makes CDSFO exhibit load characteristics. When the distribution network enters the peak load period, CDSFO discharges first and purchases electricity from EVs and supplies power to the demand side. At this time, it functions as a distributed power source, achieving peak shaving and valley filling, and at this point, CDSFO exhibits distributed power source characteristics.

III. Modeling of Charge and Discharge Demand Response

The flexible charging requirements mean that the vehicles are parked for a longer period of time. The owners do not aim for "fully charging", but rather to obtain the benefits of V2G charging and discharging. Users connect their vehicles to the power grid for vehicle-grid interaction and participate in the charging and discharging optimization schemes provided by the system. The rate of payment change and SOC before and after participation in the optimization are the two major factors influencing the flexible charging requirements. Therefore, the definition of the elastic charge demand coefficient is:

$$E_m = \frac{\Delta S_{y,i}^{\mathrm{oc}} / SOC_{\max}}{\Delta C_p^y / C_{p,\max}^w} = \frac{C_b c_t^p \left(S_{i,out}^{\mathrm{oc}} - S_{i,in}^{\mathrm{oc}} \right)}{\sum_{t=t_{in}}^{t_{out}-1} c_{ch,t} P_{it}} \quad (1)$$

where $\Delta S_{y,i}^{\mathrm{oc}}$ represents the difference between the state of charge $S_{i,\mathrm{out}}^{\mathrm{oc}}$ of the i-th EV when it is off-grid and the state of charge $S_{i,in}^{\mathrm{oc}}$ when the vehicle participates in coordinated charging and discharging optimization for grid connection . ΔC_p^y is the sum of the products of the charging and discharging electricity price $c_{ch,t}$ and the charging and discharging power $P_{i,t}$ set by the agent during the vehicle's grid-connected time. $C_{p,\max}^w = C_b c_t^p$ represents the maximum value of the non-coordinated charging cost from 0 to 1 when the battery SOC is fully charged, and c_t^p represents the peak electricity price of the peak-valley electricity price.

To compare the benefits of coordinated charge and discharge optimization and uncoordinated charging, the critical value of demand response is defined as:

$$e = \frac{\Delta S_{\mathrm{w,i}}^{\mathrm{oc}} / \mathrm{SOC}_{\max}}{\Delta C_{\mathrm{p}}^{\mathrm{w}} / C_{\mathrm{p,max}}^{\mathrm{w}}} = \frac{C_b c_t^p \left(S_{\mathrm{w,out}}^{\mathrm{oc}} - S_{\mathrm{in}}^{\mathrm{oc}} \right)}{\sum_{t=t_{in}}^{t_{out}-1} c_t P_{i,t}^f} \quad (2)$$

where e is the reference value of the demand response; $\Delta S_{w,i}^{\mathrm{oc}}$ is the difference between the state of charge $S_{w,out}^{\mathrm{oc}}$ when the EV is off-grid after non-coordinated charging and the state of charge $S_{\mathrm{in}}^{\mathrm{oc}}$ when it is grid-connected. ΔC_p^w is the sum of the products of the peak-valley electricity price c_t and the charging power $P_{i,t}^f$ in each period during the EV grid connection time.

Since non-coordinated charging is generally constant power charging, the increment of SOC has a linear relationship with the charging time. Therefore, the critical value of demand response is independent of the charging time. When the battery's state of charge is charged from 0 to 1, Equation (2) can also be expressed as:

$$e=\frac{\Delta S_{w,i}^{\mathrm{oc}} / SOC_{\max}}{\Delta C_p^w / C_{p,\max}^w}=\frac{(1-0)/1}{C_b c_t^p / C_b c_t^p}=1 \tag{3}$$

If the charge and discharge demand response Angle α_e is introduced to represent the probability of user response optimization, then the Angle corresponding to the critical value e of demand response is:

$$\alpha_e=\arctan(1)=45^{\circ}=\pi/4 \tag{4}$$

In order to further determine the conditions for EV users to respond to coordinated charging and discharging, define $\Delta C_p^w / C_{p,\max}^w$ as the c-axis and $\Delta S_{w,m}^{\mathrm{oc}} / \mathrm{SOC}_{\max}$ as the S-axis, and establish the C-S coordinate system. The positions of E_m and e in the *C-S* coordinate system can be determined, as shown in Figure 1.

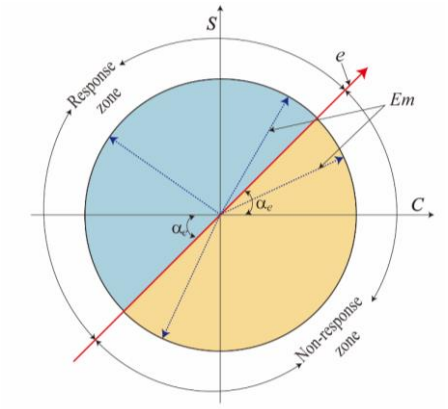


Fig. 1. Diagram of charging-discharging optimization elastic demand response conditions

IV. CDSFO AND EV OPTIMIZATION SCHEDULING STRATEGY

A. The Master-slave Game Double-layer Optimization Model of CDSFO and EV Users

This article guides the charging and discharging of EVs based on the electricity prices set by CDSFO. EV users choose the time period that is most beneficial to them for charging and discharging according to the electricity prices and demands in different time periods. CDSFO and EV are independent interest subjects, and they form a master-slave game relationship. The upper-level CDSFO acts as the leader, and the lower-level EV acts as the follower.

B. Upper-level Model

1) CDSFO objective function

The profit of CDSFO consists of five parts: (1) The charging revenue of EVs at CDSFO; (2) The cost of purchasing electricity during EV discharge; (3) Its revenue from selling electricity to the real-time market; (4) Its cost of purchasing electricity in advance; (5) Its cost of purchasing electricity from the real-time power grid.

$$\begin{aligned}\max F=&\sum_t\sum_i\left(c_{ch,t}P_{ch,i}^t-c_{dc,t}P_{dc,i}^t\right)\\&+\sum_t\left(\pi_t^- E_t^- -\pi_t^{\mathrm{d}}E_t-\pi_t^+E_t^+\right)\end{aligned} \tag{5}$$

where F represents the total revenue of CDSFO; $c_{ch,t}$ and $c_{dc,t}$ are respectively the electricity sales price and purchase price to EVs during period t; $P_{ch,i}^t$ and $P_{dc,i}^t$ respectively represent the charging and discharging power of the i-th EV in period t; E_{t} represents the contracted electricity volume during the t period of the market in the previous day. E_t^+ and E_t^- represent the purchased and sold electricity from the real-time market during period t. π_t^d represents the day-ahead market contract electricity price for period t. T represents the total number of time periods, $t\ge t_{\mathrm{in}}$ and $\mathrm{t}\le t_{\mathrm{out}}$.

2) CDSFO constraint conditions

$$\text{s.t. } c_{ch,t}^l\le c_{ch,t}\le c_{ch,t}^u,\forall t \tag{6}$$

$$c_{dc,t}^l\le c_{dc,t}\le c_{dc,t}^u,\forall t \tag{7}$$

$$\sum_{t=1}^{T}c_{ch,t}/T=\sum_{t=1}^{T}c_t/T \tag{8}$$

$$E_t\ge 0,0\le E_t^+\le Mz_t,\forall t \tag{9}$$

$$0\le E_t^-\le r_t^-\left(1-z_t\right),\forall t \tag{10}$$

$$\sum_i p_{it}+r_t^+-r_t^-=E_t+E_t^+-E_t^-,\forall t \tag{11}$$

$$0\le r_t^+\le u_t R_{\mathrm{m}}^+,0\le r_t^-\le\left(1-u_t\right)R_{\mathrm{m}}^-,\forall t \tag{12}$$

$$\begin{cases}0\le S_t=S_{t-1}+\eta^+r_t^+-r_t^-/\eta^-\le S_{\max},\forall t\\ S_1=S_T=S_0\end{cases} \tag{13}$$

where c_t is the original time-of-use electricity price; $c_{ch,t}^l$ and $c_{ch,t}^u$ respectively represent the upper and lower limits of the electricity sales price, and $c_{dc,t}^l$ and $c_{dc,t}^u$ respectively represent the upper and lower limits of the electricity purchase price. z_t is a Boolean variable, representing the electricity trading status during period t; M is the positive number of the maximum trading volume in the real-time market; r_t^- and r_t^+ are respectively the charging and discharging quantities of the energy storage device during period t. u_t is a Boolean variable, representing the charging and discharging states of the energy storage device during period t; R_m^+ and R_m^- represent the maximum charging and discharging power of the energy storage device. S_t represents the energy storage capacity of the energy storage device during period t. η^+ and η^- represent the charging and discharging efficiencies of the CDSFO energy storage device; $S_{\max}$ represents the maximum capacity of the

energy storage facility; S_0 represents the initial capacity of the energy storage facility.

C. Lower-level Model

1) Choose the optimized weights independently

When users independently choose the optimization weights, they will take into account two factors: charging costs and the state of charge. This paper assumes that the user selects the optimal weights according to Equations (14) and (15), where floor represents rounding down.

$$\lambda_{i,1}=\begin{cases}0.1 & SOC_{i,t_{in}}\le 0.3\\ \left(floor\left(SOC_{i,t_{in}}\right)+0.1\right) & 0.3<SOC_{i,t_{in}}<1\end{cases} \tag{14}$$

$$\lambda_{i,2}=1-\lambda_{i,1} \tag{15}$$

2) EV objective function

Considering the cost of battery cycle charging and discharging, with the minimum payment as the objective function 1, and to meet the travel needs of users, the maximum charging capacity of EV is taken as the objective function 2.

$$\arg\min J_1=\sum_{t\in T}\left(c_{ch,t}P_{ch,i}^{t}-c_{dc,t}P_{dc,i}^{t}\right)+BK_i \tag{16}$$

$$BK_i=\sum_{t\in T}\left(k_{ch}P_{ch,i}^{t}+k_{dc}P_{dc,i}^{t}\right) \tag{17}$$

$$\arg\max J_2=\sum_{t\in T}\left(P_{ch,i}^{t}-P_{dc,i}^{t}\right)/C_b \tag{18}$$

where k_{ch} and k_{dc} are the kilowatt-hour loss coefficients of battery charging and discharging respectively. C_b is the capacity of the EV battery.

Normalize the objective functions J_1 and J_2 using the linear weighting method:

$$\min J=\lambda_{i,1}J_1/\left(J_1^{\max}-J_1^{\min}\right)-\lambda_{i,2}J_2/\left(J_2^{\max}-J_2^{\min}\right) \tag{19}$$

3) EV constraint condition:

$$s.t.\ 0\le P_{ch,i}^{t}\le P_{ch,i}^{t,\max},0\le P_{dc,i}^{t}\le P_{dc,i}^{t,\max} \tag{20}$$

$$\mathrm{S}_{EV}^{\min}\le \mathrm{S}_{EV,i}^{t}\le \mathrm{S}_{EV}^{\max} \tag{21}$$

$$\mathrm{S}_{EV,i}^{t+1}=\mathrm{S}_{EV,i}^{t}+\left(\eta_{EV,c}P_{ch,i}^{t}/C_b-P_{dc,i}^{t}/\eta_{EV,d}C_b\right)\Delta t \tag{22}$$

$$P_{ch,i}^{t}\cdot P_{dc,i}^{t}=0 \tag{23}$$

$$P_{ch,i}^{t}=0,P_{dc,i}^{t}=0\ ,\ \forall t\notin T,\forall i \tag{24}$$

where $P_{ch,i}^{t,\max}$ and $P_{dc,i}^{t,\max}$ represent the upper and lower limits of the charging and discharging power of the i-th EV. $\mathrm{S}_{EV,i}^{t}$ is the SOC of the i-th EV at time t; $\mathrm{S}_{EV}^{\max}$ and $\mathrm{S}_{EV}^{\min}$ are the upper and lower limits of the SOC of EV. $\eta_{EV,c}$ and $\eta_{EV,d}$ respectively represent the charging efficiency and discharging efficiency of EV. The introduced virtual SOC is a proxy variable used to pre-compute the optimization results, and its purpose is to simulate the change of SOC to optimize the scheduling strategy.

V. Solution of the Optimized Scheduling Model

A. The Lower-level Problem KKT Condition Processing

It has been proved that Equation (23) is a redundant constraint, so it is relaxed. The lower model is a linear convex problem, so the KKT condition can be used to handle the lower problem. Let α and β be the dual variables of the equality constraint and the inequality constraint in the lower model respectively, then the KKT condition of the original lower model is:

$$\begin{cases}\nabla L(x)=0\\ H(x)=0\\ 0\le\beta\perp G(x)\ge 0\end{cases} \tag{25}$$

where $\nabla L(x)$ represents the gradient of the Lagrange function; $H(x)$ and $G(x)$ are respectively the equality constraint and the inequality constraint; Here, $x\perp y$ indicates that at most one of the scalars x and y can be strictly greater than 0.

Since the complementary relaxation term in the KKT condition is nonlinear, the large M method can be used to linearize it:

$$0\le\beta\le M\zeta \tag{26}$$

$$0\le G(x)\le M(1-\zeta) \tag{27}$$

where M is a very large positive number，the selection of the large M value needs to ensure that it is greater than any possible dual variable or constraint violation; ζ is a Boolean variable.

B. Linearization Processing of the Objective Function

The nonlinearity of the objective function stems from c_tP_{it} .After the KKT condition processing, the two-layer model is transformed into A single-layer model, resulting in a bilinear $c_{ch,t}P_{ch,i}^{t}-c_{dc,t}P_{dc,i}^{t}$ where the transaction electricity prices of the upper and lower layers are multiplied by the transaction power in the objective function. According to the strong duality theorem, the objective function values of the optimal solutions of the original problem and the dual problem are equal. Therefore, the strong duality theorem can be used to replace the bilinear term with a linear expression.

Ultimately, the double-layer master-slave game model is transformed into:

$$\max\left\{\sum_i\sum_t\frac{\left(-\beta_{1,i}^t P_{ch,i}^{t,\max}-\beta_{2,i}^t P_{dc,i}^{t,\max}\right)+\left(\beta_{3,i}^t \mathrm{S}_{\min}-\beta_{4,i}^t \mathrm{S}_{\max}\right)}{\lambda_{i,1}}\right.$$
$$\left.-\sum_i\sum_t\frac{\left(k_{ch}P_{ch,i}^t+k_{dc}P_{dc,i}^t\right)}{J_1^{\max}-J_1^{\min}}+\sum_i\sum_t\frac{\lambda_{i,2}\left(P_{ch,i}^t-P_{dc,i}^t\right)}{\lambda_{i,1}C_b\left(J_2^{\max}-J_2^{\min}\right)}\right\}$$
$$\times\left(J_1^{\max}-J_1^{\min}\right)+\sum_t\left(\pi_t^- E_t^- -\pi_t^{\mathrm{d}}E_t-\pi_t^+E_t^+\right)$$
$$s.t.\ \text{Equation (6) - Equation (13)} \tag{28}$$

VI. Case Analysis

A. Simulation Condition Setting

This paper conducts a case study analysis of the model in this paper using the distribution network of residential communities in a certain area. There are a total of 929 households [18]. Considering the EV penetration rate in the distribution network, the number of private EVs introduced is 100. The experimental software environment is Matlab2023b, and the solution is provided using the GUROBI solver.

B. Optimal Solution of the System

The experimental parameters are shown in Table 1. The maximum benefit of CDSFO (6,058.2 yuan) was obtained by solving equation (28), and the optimal strategy of the charging station is shown in Table 2. From the model in Section 4, it can be obtained that the optimal charging time of EV is during the period from 01:00 to 07:00, during which the charging cost of EV is the lowest. The peak load is from 19:00 to 21:00, during which the discharge benefit of EV is the highest. Rational EV users have no tendency to deviate from this charging and discharging time. Under this optimized electricity price, the charging and discharging behavior of EVs is an orderly behavior.

As shown in Table 2, that under the conventional or low-load conditions of the distribution network, the system gives priority to ensuring the basic charging demand of EV within CDSFO. After the charging is saturated, through the strategy of storing electricity during low electricity price periods and repurchasing electricity at competitive prices during peak periods, the stable operation of the distribution network and the balance of EV user demand are achieve.

The traditional disordered charging load curve was compared with the load curve optimized by CDSFO, as shown in Figure 2. After the optimization of the scheme proposed in this paper, the peak-valley difference of the system decreased from 2415.8kW to 1513.1kW, a reduction of 37.4%. It is proved that under this scheme, the peak-valley difference of the system can be effectively reduced and the burden of peak load in the distribution network can be alleviated.

TABLE I. Experimental Parameters

Parameters	Data	Parameters	Data
C_b / kWh	72	k_{ch} / $yuan$	0.03
S_{max} / kWh	5000	k_{dc} / $yuan$	0.3
S_0 / kWh	2000	$P_{ch,i}^{t,\max}$ / kW	7
$c_{dc,t}^{l}$ / $yuan$	0.4113	$P_{dc,i}^{t,\max}$ / kW	7
$c_{dc,t}^{u}$ / $yuan$	1.5471	$SOC_{EV}^{\max}$	1
η^+	0.9	$SOC_{EV}^{\min}$	0.2
η^-	0.9	$\eta_{EV,c}$	0.9
R_m^+ / kW	500	$\eta_{EV,d}$	0.9
R_m^- / kW	500	-	-

TABLE II. Optimal Charge and Discharge Strategy

Moment/h	Charging price (yuan /kWh)	Discharge price (yuan /kWh)	Day-ahead energy purchase /kWh	Real-time energy sales /kWh	EV discharge /kWh
1	0.5195	0.3656	1039	0	0
2	0.5195	0.3656	1042.3	0	0
3	0.5195	0.3656	1047.6	0	0
4	0.5195	0.3656	1053	0	0
5	0.5195	0.3656	1018	0	0
6	0.5195	0.3656	928.6	0	0
7	0.5195	0.3656	724	0	0
8	0.6985	1.0477	35	45	45.0
0	0.6985	1.0477	7	11.3	11.3
10	1.0477	0.6985	0	0	0
11	1.5472	1.0314	0	500	0
12	1.5472	1.0314	0	500	0
13	1.5404	1.0314	0	500	0
14	1.5472	1.0314	0	500	0
15	1.5472	1.0314	0	500	0
16	0.6985	0.6985	507	0	0
17	0.6985	0.6985	556	0	0
18	0.8247	0.6985	631.9	2.7	2.7
19	1.0314	1.5472	112.2	884.9	384.9
20	1.0314	1.5472	159.8	1054.9	554.9
21	1.0314	1.5472	196.6	1130.9	630.9
22	0.8247	0.8495	451.9	184.7	184.7
23	0.8247	0.8495	358.3	114.7	114.7
24	0.8247	0.8495	372.2	201.1	66.1

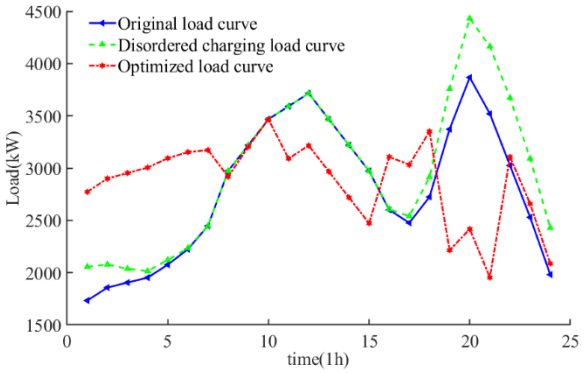


Fig. 2. Total load curve of the system before and after optimization

C. The Influence of Different Optimization Weights on the Optimal Solution

Take certain user as an example. Its charging information is $t_{in}=22:00$, $t_{out}=3:00$, $SOC_{in}=0.5$. When responding to

V2G discharge, the optimization results are analyzed based on the optimization weights selected by the user.

Table 3 shows the optimization results under different optimization weights. The results show that the larger the charging fee weight λ_1 chosen by the user is, the less the fee paid is, but the lower the battery capacity will be. On the contrary, the smaller λ_1 is, the more the cost paid is, but the higher the battery capacity will be. Figure 3 presents the specific position of the elastic charging demand coefficient E_m in the *C-S* coordinate system when the user selects different optimization weights. From this, it can be seen whether the user will respond to the charging and discharging optimization .This article fully considers the willingness of users to participate in the optimization.

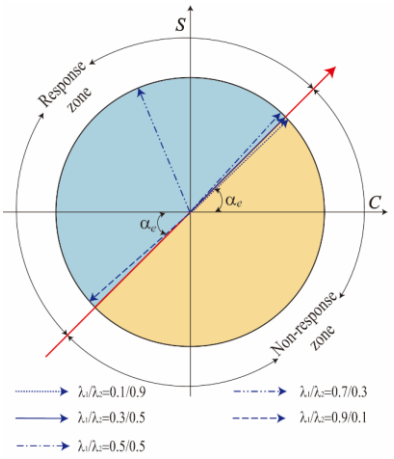


Fig. 3. The specific location of the elastic charging demand coefficient E_m in the *C-S* coordinate system

TABLE III. OPTIMIZATION RESULTS UNDER DIFFERENT OPTIMIZATION WEIGHTS

different weight	SOC	Pay fee /yuan	Charging cost/yuan	Discharge income/yuan	Battery loss cost/yuan	Payment fee for uncoordinated charging/yuan	E_m	The quadrant of E_m	Whether to respond
$\lambda_1/\lambda_2=0.1/0.9$	0.94	30.73	29.68	0	1.05	29.46	0.96	First	No
$\lambda_1/\lambda_2=0.3/0.7$	0.86	24.05	23.18	0	0.86	24.11	1.00	First	No
$\lambda_1/\lambda_2=0.5/0.5$	0.73	13.98	18.40	7.33	2.91	15.40	1.10	First	Yes
$\lambda_1/\lambda_2=0.7/0.3$	0.55	-1.35	7.68	13.24	4.21	-3.24	-2.4	Second	Yes
$\lambda_1/\lambda_2=0.9/0.1$	0.26	-11.76	2.63	20.37	5.98	-	0.88	Third	Yes

D. Cost Comparison Analysis on the User Side

This paper fully considers the interests of CDSFO and EV users, enabling a game between the two to eventually reach equilibrium. To verify the superiority of the proposed game model, a comparative analysis of the following three methods is conducted from the perspective of user-side costs:

Method 1: EV participate in the optimal dispatching at fixed time-of-use electricity prices;

Method 2: EV participates in the optimal scheduling with the strategy proposed in Reference [19];

Method 3: EV participates in the optimal scheduling with the strategy proposed in this paper.

The cost-effectiveness of EV users under different methods is shown in Table 4 as follows:

TABLE IV. USER COST COMPARISON

	Charging Cost	Discharge Revenue	Battery loss Cost	User General Cost
Method 1	4002.3	0	131.2	4133.5
Method 2[19]	2492.3	0	131.2	2623.5
Method 3	2963.2	1473.3	514.9	2004.8

It can be obtained from Table 4 that, compared with participating in the optimal dispatching based on the fixed time-of-use electricity price, the total cost of users in this paper is reduced by 51.49%. The game electricity price, with its lower charging price and higher discharging price, brings more benefits to EV users. Compared with the scheme proposed in reference [19], this paper considers the EV discharge income. Therefore, the total cost for users is reduced by 23.58%, it is proved that the game model proposed in this paper can better guarantee the interests of EV users.

VII. CONCLUSION

In view of the common interests of both charging stations and EVs, fully considering the elastic demand response of users, the interaction between discharge and CDSFO is introduced on the basis of the traditional EV charging, and a multi-objective master-slave game optimization scheduling model between CDSFO and EVs is established. The model is linearized by using the KKT condition, the large M method and the dual principle, and is solved by using the GUROBI solver. The satisfaction of EV users with the paid fee was comprehensively considered, making the dispatching strategy closer to reality.

This strategy introduces CDSFO, enabling EVs and CDSFO to sell electricity to the grid side during peak electricity consumption periods, effectively reducing the charging costs for EV users and significantly increasing the revenue of charging stations. In terms of demand response, users can independently choose the optimization weights to reasonably safeguard their own interests. Compared with the traditional time-of-use electricity price, under the guidance of the strategy in this paper, the payment cost of EV users is reduced by 51.49%, and the peak-valley difference of the system is reduced by 37.4%.

REFERENCES

[1] Bai. Y, How new energy vehicle enterprises can reap fame and profit[N]. China Electricity News, 2024-05-09(01).

[2] Qiu. M. S, Chen. J. R, Liu. M. Y,et al, A master-slave game optimization scheduling strategy considering the electricity pricingmechanism of nanogrid systems and microgrid operators[J]. Power System Protection and Control,2024,52(19):15-34.

[3] State Department . State Department Government Work Report2025[R/OL].(2025-01-17) https://www.gov.cn/zhengce/jiedu/tujie/202501/content_6999527.htm

[4] Ding. Y, Xu. Q, Hao. L, et al, A Stackelberg Game-based robust optimization for user-side energy storage configuration and power pricing[J]. Energy, 2023, 283: 128429.

[5] Zhan. X. P, Yang. J, Han. S. N, et al, Two-stage market bidding strategy of charging station considering schedulable potential capacity of electric vehicle[J]. Automation of Electric Power Systems,2021,45(10):86-96.

[6] Fu. Y. S, Ren. H. P, Li. H. S, et al. Neutral Leg Design and Control of Electric Vehicle On-board Bidirectional Charger Based onSiC-MOSFET and Si-IGBT Hybrid Devices[J]. Proceedings of the CSEE,2020,40(19):6330-6345.

[7] Jahangi. H, Gougheri. S. S, Vatandoust. B.Plug-in electric vehicle behavior modeling in energy market: a novel deep learning-based approach with clustering technique. IEEE Trans Smart Grid 2020;11(6):4738–48.

[8] Gan. L, Chen. X. Y, Kun. Y, A probabilistic evaluation method of household EVs dispatching potential considering users' multiple travel needs. IEEE Trans Ind Appl 2020;56(5):5858–67.

[9] Jan. E, Zepter. J. M, Gabderakhmanova. T, Energy management of a multi-battery system for renewable-based high power EV charging. eTransportation 2022;14:100198.

[10] Zhang. L, Sun. C. L, Cai. G. W, Leong. H. K, Charging and discharging optimization strategy for electric vehicles considering elasticity demand response, eTransportation,Volume 18,2023,100262,ISSN 2590-1168.

[11] Cai. G. W, Jiang. Y. Q, Huang. N. T, et al, Large-scale electric vehicles charging and discharging optimization scheduling based on multi-agent two-level game under electricity demand response mechanism[J]. Proceedings of the CSEE,2023,43(01):85-99.

[12] Ma. M. Y, Dong. P, Dong. J. D, et al, Refined peak shaving strategy for EV participation in urban grid partitioning based on stackelberg game[J/OL]. Power System Technology,1-13[2025-03-24].

[13] Li. S, Yuan. S, Guo. S, et al, "Coordinated Optimal Scheduling of Micro-Grid-Charging Facility Operators Based on the Stackelberg Game," 2024 6th Asia Energy and Electrical Engineering Symposium (AEEES), Chengdu, China, 2024, pp. 755-763.

[14] Cheng. S, Zuo. X, Wei. Z, et al, "Nash bargaining-based cooperative game for distributed economic scheduling of microgrid with charging-swapping-storage integrated station," International Journal of Energy Research, 2022, 46, (15),pp. 23927-23938.

[15] Chu. H. X, Xie. D, Charging/discharging control strategy of EV charging-discharging-storage integrated station considering operational status of power grid[J]. Electric Power Automation Equipment, 2018, 38(4): 96-101.

[16] Yuan. H. T, Wei. G, Zhang. H, et al, Robust optimal scheduling of active distribution network considering with the charging-swapping-storage integrated station[J]. Proceedings of the CSEE, 2020, 40(8): 2453-2468.

[17] Zheng. Y. C, Yu. H, Shao. Z. Y, et al, Day-ahead bidding strategy for electric vehicle aggregator enabling multiple agent modes in uncertain electricity markets[J]. Applied Energy,2020,280 : 115977.

[18] Zhan. K. Q, Song. Y. H, Hu. Z. C, et al, Coordination of electric vehicle charging to minimize active power losses[J]. Proceedings of the CSEE, 2012, 32(31): 11-19.

[19] Zhu. Y. S, Chang. W, Wu. D. Y, et al, A Stackelberg game optimization scheduling strategy considering the interaction betweena charging-discharging-storage integrated station and an electric vehicle[J]. Power System Protection and Control, 2024,52(07):157-167.